5th INTERNATIONAL SYMPOSIUM on DAM SAFETY

27 October - 01 November 2018
DSI-Orhantepe Convention Center
Cevahir Asia Hotel - ISTANBUL / TURKEY

5 UBGS 2018 Istanbul Turkey

www.damsafety2018.com

PROCEEDINGS: VOLUME I

General Directorate of State Hydraulic Works
was established
for use of earth and water resources in Turkey
by Law No. 6200.
We think that
all intellectuals throughout the country
have to support its institutional studies.

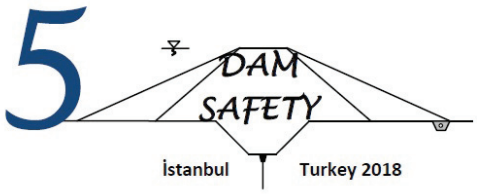

5th INTERNATIONAL SYMPOSIUM
on
DAM SAFETY

27 October – 1 November 2018

İstanbul / TURKEY

VOLUME I

Edited by:

Prof. Dr. Hasan TOSUN

Prof. Dr. M. Emin EMİROĞLU

Assoc. Dr. Şerife Yurdagül KUMCU

C. Eng. Turgut Vatan TOSUN

Proceedings for dam safety 2018

ISBN: 978-9444-0782-7-6

BASKI: Uzman Matbaacılık Kağıt Yayın Ticaret Ltd. Şti
İvedik Org. San. Bölgesi Matbaacılar Sitesi 1514 Sk.
No:44 İvedik /Ankara

Organizing Committee

Chairman
Hasan TOSUN
Co-Chairman
Murat DAĞDEVİREN
Co-Chairman
Feyza ÇİNİCİOĞLU
Co-Chairman
Sedat ÖZPINAR
Secretary
Kasım YENİGÜN
Co-Secretary
Şerife Yurdagül KUMCU, NEÜ
Members
Mustafa Hakkı AYDOĞU, HÜ
Tevfik Baran ÖNDER, BGD
Mehmer BERİLGEN, YTÜ
Veysel GÜMÜŞ, HÜ
Murat HATİPOĞLU, DSİ
Müge İNANIR, ZMGM
İlker PEKER, DSİ
Saim ŞEN, BGD
Turgut Vatan TOSUN, BGD
Mustafa TUNÇ, FÜ
Hasan USUL, BGD
Kemal YÜKSEL, DSİ

Members of The Honor Board

Binali YILDIRIM, Chairman of the Grand National Assembly of Turkey
Bekir PAKDEMİRLİ, Minister of the Agriculture and Forestry
Fatih DÖNMEZ, Minister of Energy and Natural Resources
Akif ÖZKALDI, Deputy Minister of the Agriculture and Forestry
Mücahit DEMİRTAŞ, Deputy Minister of Environment and Urban Planning
Mevlüt UYSAL, Mayor of İstanbul Metropolitan Municipality
Prof. Dr. Erhan GÜZEL, Rector of Kultur University
Prof.Dr. Kemal ŞENOCAK, Eskişehir Osmnagazi University
Hasan MANDAL, President of Scientific and Technological Research Council
Mehmet GÜLLÜOĞLU, Head of Disaster and Emergency Management
Presidency Mevlüt AYDIN, General Director of State Hydraulic Works
Fatih TURAN, General Director of Istanbul Water and Sewerage Administration.
Zekai ŞEN, Director of Water Foundation
Hasan TOSUN, President of National Dam Safety Association
İlyas DEMİRCİ, General Secretary of TDMMB

Local Advisory Committee

Dincer AYDOĞAN, DSİ
M.Emin EMİROĞLU, FÜ
Kamil EREN, İKÜ
Nazmi KAĞNICIOĞLU, DSI
Zafer KARAYILANLIOĞLU, YEGM
Celal KOLOĞLU, İNTES
Selami OĞUZ, BGD
Mehmet Uğur YILDIRIM, DSİ
Turgut UZEL İKÜ
Kasım YENİGÜN HÜ
Kemal KARAKUŞ, DSİ
Seyfullah YILMAZ, Eti Maden
Mithat YÜKSEL, EUAŞ
Munis ÖZER, TMMMB
Cemal GÖKÇE, İMO

International Advisory Committee

Altan Abdulamit, Romania
Mevlüt Aydın, Turkey
Marla Barnes, USA
Erich Bauer, Austria
Tony Bennett, Canada
George Dounias, Greece
Tuncer Edil, USA
Jean Jacques Fry, France
Mazza Guido, Italy
Michel Lino, France
Dimitur Kisliakov, Bulgaria
E. Miljkovic, Bosnia Herz.
Laurent Mouvet, Switzerland
Rakesh Nath, India
Ali Noorzad, İran
Vladimir Pelehtin, Russia
Ljupcho Petkovski, Macedonia
Mahdi Rashid Mahdi, Iraq
Illahi B. Shaikh, Pakistan
Anton J.Scheiss, Switzerland
Vache Tokmajyan, Armenia
G.Vashetti, Italy
Martin Wieland, Switzerland
Tracey Williamson, UK
Gerald Zenz, Austria
P. Zielinski, Canada

International Scientific Committee

Mohammad Alembagheri, Iran
M. Amin Hariri-Ardebili, USA
Eduardo E. Alonso, Spain
Arash Barjasteh, Iran
Erich Bauer, Austria
David S.Bowles, USA
Laura Calderia, Portugal
Georges R. Darbre, Switzerland
Behrouz Gordan, Iran
Dean B. Durkee, USA
Babak Ebrahiman, Iran
Tuncer Edil, USA
Mohsen Ghaemian, Iran
Yusof Gnaaat, USA
Feng Jin, China
Seyedmehdi Mohammadizadeh, Iran
Laurent Mouvet, Switzerland
Ljupcho Petkovski, Macedonia
Adrian Popovic, Romania
Anton J.Scheiss, Switzerland
Carlos Ventura, Canada
Jin-Ting Wang, China
Martin Wieland, Switzerland
Gerald Zenz, Austria
Andy P. Zielinski, Canada
Fu Zhongzhi, China

Local Scientific Comittee

Süleyman Adanur, Karadeniz Technical University
Necati Ağıralioğlu, Antalya Bilim University
Ahmet Can Altınışık, Karadeniz Technical University
S.Oğuzhan Akbaş, Gazi University
Mustafa Tamer Ayvaz, Pamukkale University
Mehmet Berilgen, Yıldız Technical University
Ayla Bilgin, Çoruh University
Barış Binici, Middle East Technical University
Zekai Celep, İstanbul Teknik Üniversitesi
Barış Sevim, Yıldız Technical University
Zafer Bozkuş, Middle East Technical University
U.Şafak Çavuş, Süleyman Demirel University
Yusuf Calayır, Fırat University
S.Feyza Çinicioğlu, Özyeğin University
Ayşe Edinçliler, Boğaziçi University
Kemal Önder Çetin, Middle East Technical University
Erdal Çokça, Middle East Technical University
Ender Demirel, Eskişehir Osmangazi University

Ahmet Doğan, Yıldız Technical University Şebnem
Şeker Elçi, İzmir İnstitute of Technology M.Emin
Emiroğlu, Fırat University
Mustafa Erdik, Boğaziçi University
Kamil Eren, İstanbul Kültür University
Erol Güler, Boğaziçi University
Necati Gülbahar, İstanbul Gelişim University Murat
Günaydın, Gümüşhane University
Ayhan Gürbüz, Gazi University
Tefaruk Haktanır, Erciyes University
Yılmaz İçağa, Afyon Kocatepe University
Mete İncecik, İstabul Teknik University
Yunus Kalkan, İstanbul Technical University
Halil Karadeniz, İstanbul University
Muhammet Karaton, Fırat University
Murat Emre Kartal, İzmir Demokrasi University
C. Melek Kazezyılmaz ALHAN, Istanbul University
Ayhan Koçbay, DSİ
Selami Oğuz, Dam Safety Association
Ali Rıza Öç, Temelsu Int.
Kutay Özaydın, Yıldız Technical University
A.Tolga Özer, Okan University
Evren Seyrek, Dumlıpınar University
Zekai Şen, Water Foundation
Gökmen Tayfur, İzmir İnstitute of Technology
Kasım Yenigün, Harran University
Yalçın Yüksel, Yıldız Technical University
Turgut Uzel, İstanbul Kültür University

Study Groups

Technical Committee on Dictionary for Dams and Auxiliary Structures
Technical Committee on Design of Tailing Dams
Technical Committee on Upstream Flood Control for Reservoir and Siltation
Technical Committee on Slope Stability in Reservoir

Awards

Competition on M.S Thesis
Competition on Ph.D Thesis

Dear Ladies and Gentlemen,

Working under the Ministry of the Agriculture and Forestry, there are main governmental agencies responsible for development of water resources all over Turkey. In terms of water resources, we consider two main problems in Turkey: Flood and Drought. These natural disasters can result in social and economic damages. Scientific studies point out that as a result of the global warming and climate change, water related natural disasters experienced in many countries have been occurring more destructive with larger scales than those happened in the past. Impacts of global warming and climate change have been intensified with each passing day in the world and in our region. These conditions add to the weight of water administration in the semiarid zones in which Turkey is located as well.

Our Ministry and other related organizations have accomplished a great deal towards completing facilities mitigating the adverse effects of flood and drought disasters. I would like our national organizations to continue on achievements and efforts for this challenge. We also try to discuss water resources problems in conferences, congresses and symposiums. This international symposium and exhibition is one of the important events to discuss our water problems with neighboring countries. We think that special technical sessions will be presented on large dam projects, which have been completed or under construction now in Turkey and other countries.

The purpose of this symposium is to provide opportunity for the dam safety community to share important information, lessons learned and new technology.

We are very glad to see you and your family members in Istanbul and wish you many stimulating professional and personal experiences.

Have a great symposium!

Dr. Bekir PAKDEMİRLİ
Minister of the Agriculture and Forestry

Dear Participants,

Turkey is in the semi-arid zone and so the precipitation shows differences according to regions and seasons. In recent years, upwards trends in temperature and changing precipitation patterns have been recorded all around the world due to the climate change impacts. Moreover, climate change in most regions will likely increase the probability and severity of floods. Although a large amount of rain falls down usually during the winter season however the water consumption increases a large amount in the summer times. Parallel to the population growth, there is a large increase in water demand in drinking, use and industry sectors, especially in agriculture in our country as well as in the world. As a consequence of climate change, receding in the amount of water brings need for effective and sustainable water resources utilization and enforces the countries to implement water saving technologies in all water sectors, particularly in irrigation.

Water demand of the future generation should be guaranteed without compromising the ability of them to meet their own needs by water storage structures for achieving water sustainability. Water resources should also be increased in order to avoid water scarcity problems, in particular, in arid periods. Preservation and extension of life-time of storage facilities has vital importance in Turkey. On the other hand, as Turkey is one of the most quake-prone countries in the world, the safety of the water storage facilities in all stages like from planning and design to construction and operation must also be planned by taking into account of the deformation risk of the construction materials. For this purpose, technical and academic studies are extensively carried out in Turkey. The fifth International Symposium on Dam Safety and Exhibition activity is a part of the our studies. We will be very pleased to see you among us at this symposium.

I would like to say “welcome” for all guests and participants in order to have enjoyable time and see the beauties of Istanbul and also Turkey and I wish the event has a great success.

Akif ÖZKALDI
Deputy Minister of the Agriculture and Forestry

Ladies and Gentlemen,

Turkey is rich by means of land resources and sufficient in terms of water resources. Almost one third of Turkey's total area (78 million ha) is arable land (28 million ha). Comprehensive studies pointed indicate that 8,5 million ha of the arable land is economically irrigable in Turkey. 5,9 million ha of this irrigable area have been equipped with irrigation facilities being 3,61 million ha developed by DSİ with modern irrigation network systems.

The average annual precipitation of Turkey is 501 cubic km (501 billion cubic m) per year. 274 billion cubic m of this amount is assumed to evaporate from surface and transpire through plants. 69 billion cubic m of precipitation directly recharges the aquifers, whereas 158 billion cubic m forms the precipitation runoff. There is a continuous interaction between surface runoff and groundwater, but it is estimated that a net 28 billion cubic m of groundwater feeds the rivers.

In summary, surface water and ground water potential has an average of 112 billion cubic m per year and of which 44 billion cubic m is consumed.

The General Directorate of State Hydraulic Works (DSI) is the primary executive state agency of Turkey and the main objective of DSI is to develop planning and designing projects for efficiently use of all water and land resources in Turkey. Additionally, it follows closely the improvements related with its subject and efforts for cooperating with organizations such as ICOLD in order to find out technical solutions rationally. 5th International Symposium on Dam Safety and Exhibition is one of these collaborations. Many scientists, researchers and field engineers of various countries are expected to participate this symposium and many presentation will be held on by invited speakers who are professional in their area.

Turkey has an important amount of knowhow about the assessment of water and land resources. I wish this conference will give an opportunity to share these knowledges and to exchange informations between the participants. I hope that this conference in which many issues discussed will be very useful for all of you and I as the President of TRCOLD would like to invite all of you to Istanbul.

Mevlüt AYDIN
General Director of State Hydraulic Works

Dear Colleagues, Ladies and Gentlemen,

Fifth International Symposium on Dam Safety was organized by National Association on Dam Safety, TRCOLD, Water Foundation, National Association on Soil Mechanics and Geotechnical Engineering and Eskisehir Osmangazi University between October 27 and November 1, 2018 in Istanbul, Turkey. On behalf of the Organizing Committee, I am very glad to join with you in the 5th International Symposium on the Safety of Dams. The Conference Center is located in a pleasant, calm and intimate atmosphere of the historic city of Istanbul, which lies on and around the Bosphorus between Asia and Europe.

The aim of the symposium is to provide participants with a forum to exchange experiences and information about new technologies. The Organizing Committee works extremely hard to present an interesting and innovative program that will also include excursions to dams in Istanbul. In addition to workshops and lectures, there are also be a special technical meeting on the major dam projects already completed or under construction in Turkey and neighboring countries. In the symposium, we organized information days for some countries with presentations on local water resources and hydraulic structures and panel discussions on safety of dams and other related structures.

The organizing committee is proud to offer the opportunity to the delegate taking part a high technical program including 240 abstracts and 132 full papers with different subject. The papers focused on the topics such as geotechnical problems of foundation and embankments, innovative technology on hydrology, use of geographical information system for dam issues, static and dynamic stability analyses, dam surveillance, maintenance, instrumentation and monitoring, foundation treatments and cut-off structures, environmental issues and also hydro politics.

I hope that the symposium has been an opportunity for engineers, consultants and scientists working in the field of dam safety and other dam issues to meet and to present new ideas, achievements and experiences and to incorporate of the latest knowledge into practice. Also it has provided an enjoyable experience for cultural and social activities with the background of ancient city of the World for the delegates and accompanying people.

Discover the historical, cultural and culinary side of Turkey.

We look forward to welcoming you to Istanbul.

Have a great symposium.

Prof. Dr. Hasan TOSUN, Chairman
Organizing Committee

CONTENTS

INVITED SPEAKERS

5th International Symposium on Dam Safety

October 27-31, 2018

THE SAFETY CHALLENGE OF RIVER DIVERSION DURING CONSTRUCTION OF DAMS

Anton J. SCHLEISS [1]

ABSTRACT

The appropriate design of a river diversion system during construction of dam is an essential task since dramatic consequences in view of cost and time overrun may be involved. After a short outline of the different methods of river diversion and its main structural elements, the paper focuses on critical issues in relation with the design of diversion tunnels. For a proper hydraulic functioning of a diversion tunnel a flow acceleration stretch at the entrance is essential, to avoid a too early pressurized flow with rapid increase of the water level upstream of the cofferdam which may lead to overtopping and failure of the latter. The technical challenges of river closure are addressed, which is often a critical phase during construction of a dam. The choice of an economical optimal design discharge of tunnel diversion system is outlined taking into account the risk of flooding of the ongoing construction works. In order to reduce the risk of failure of the cofferdams and the diversion tunnel in the case the design flood is exceeded, the design of novel protection methods against erosion of the cofferdam after overtopping as well as against scouring at the outlet of diversion tunnels are presented.

Keywords: Cofferdam, design, diversion tunnel, risk assessment, river closure, surface protection.

INTRODUCTION

The construction of a dam across closing a valley with its river by the help of river diversion is a major engineering challenge involving considerable risk. The purpose of the river diversion is to put the foundation site of the future dam with his appurtenant structures into dry conditions before starting construction. A dry construction pit is required to perform the following works:

- final geological and geotechnical investigations
- excavation of the foundation
- improvement of the underground by injections
- realization of the dam with his appurtenant structures

The notion “river diversion” comprises all structural measures for governing the river during construction. The task of an appropriate river diversion is to divert probable floods during the execution works of the dam in order to protect the construction site against any damages. The river diversion has also to ensure that the presence of the construction site doesn’t increase the risk of flooding upstream as well as downstream. Floods arriving during construction are particularly dangerous because since the dam with its appurtenant structures as powerhouse is not yet finalized and thus very vulnerable. The appropriate selection of design discharge for a river diversion is crucial in order to limit the risk of catastrophic cofferdam failure. Although the river diversion is often

[1] Professor and Honorary President ICOLD, ENAC – PL-LCH, Ecole polytechnique fédérale de Lausanne (EPFL), Switzerland
e-mail: anton.schleiss@epfl.ch

composed of temporary structures, they have to be designed correctly to ensure proper functioning during any flood event considering costs and risks involved.

METHODS OF RIVER DIVERSION AND MAIN STRUCTURAL ELEMENTS

In principal, a river diversion can be achieved by three different methods:

- Integral river diversion (Figure 1)
- Diversion of river through construction site (Figure 2)
- Balancing of river and its constriction during construction (Figure 3)

The first method consists of diverting fully or integrally the river by the help of a diversion tunnel or channel around the construction site, which allows to fully drying the river at the future dam site. The diversion structures as tunnels or channel can be built independent from the river and its discharge. Nevertheless, important construction works have to be realized for the integral river diversions with the following sequences:

a) Construction of small cofferdams at the entrance and outlet of the diversion tunnel in order to protect its construction. In the case of a favorable topography the natural terrain can replace the cofferdams, which will be excavated before putting into operation of the diversion tunnel.
b) Realization of the diversion structure as tunnel or channel (② on Figure 1) and preparation of the closure device (normally concrete stop logs)
c) River closure by advancing the lower part of the cofferdams ③ and ④ across the river (cf. Figure 1) in order to force the river to enter into the diversion structure. The river closure has normally to be done during dry season with low discharges.
d) Dewatering the construction pit between the cofferdams ③ and ④ (see Figure 1) by pumps with lowering groundwater table and finalizing the construction of the cofferdams
e) Execution of the final hydraulic structure (dam, intake, weir, powerhouse, a.s.o.)
f) Destruction of cofferdam (upstream normally completely, downstream partially)
g) Closure of derivation with stop logs

The closure of the river and of the temporary diversion is often a critical operation, which can strongly influence the planning and duration of the works.

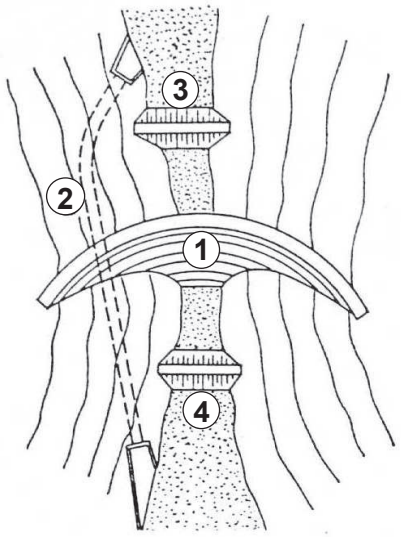

Figure 1: Integral river diversion: ① dam under construction, ② diversion tunnel, ③ upstream cofferdam, ④ downstream cofferdam (Schleiss 2015)

The diversion of river directly through construction site may be feasible in wide valleys by the help of a diversion through concrete culvert or tunnel excavated in the rock, which is situated below the foundation of the future dam (Figure 2). The diversion structure has to be built during the dry season with low discharge under protection of a temporary upstream and downstream cofferdam.

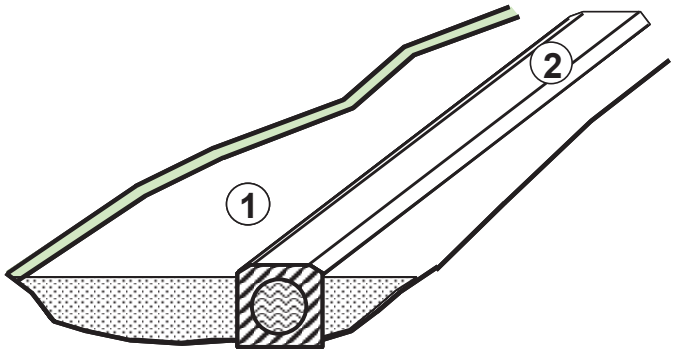

Figure 2: Diversion of river directly through construction site: ① dam foundation,② concrete culvert or tunnel (Schleiss 2015)

In the case of river balancing the latter remains in the valley but is constricted locally by a cofferdam, which protects a certain phase of the construction works (Figure 3). This method feasible in enough wide valleys allows minimizing the works related to the river diversion. Furthermore, the perturbation of the river flow regime is limited, which is a must in cases where the ship navigation has to be maintained during construction.

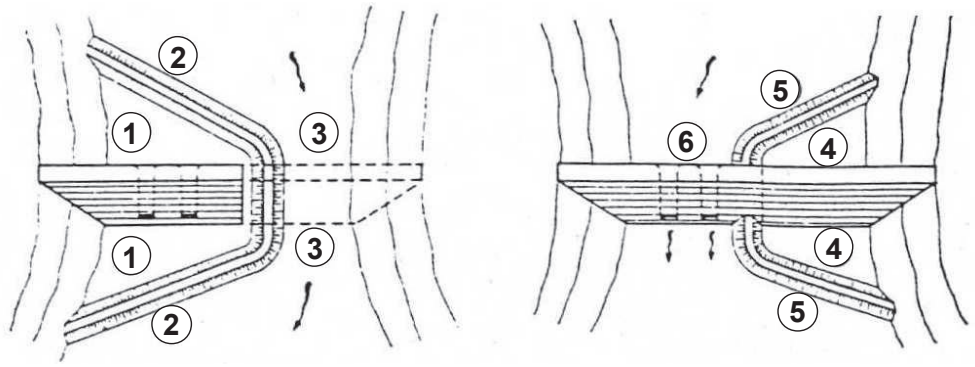

Figure 3: Balancing of river and its constriction during construction: ① zone of construction phase 1, ② cofferdam phase 1, ③ constricted river,④ zone of construction phase 2, ⑤ cofferdam phase 2, ⑥ openings in the final dam (for example low level flushing outlets) (Schleiss 2015)

In general, a river diversion is composed of the following structural elements:

- Cofferdams
- Diversion structures as tunnels, culverts, openings or orifices in the dam
- Closure structure as stop logs at the upstream portal of diversion tunnels

All these structural elements can be temporary or permanent structures. From economical point of view there is an interest to use the structural elements of river diversion as part of a final structure like bottom outlets or spillways. In the case of embankment dams, the cofferdams can be integrated in the final dam section.

In the following some important aspects in combination with diversion tunnels, mostly used in relatively narrow valleys, are discussed and highlighted.

Figure 4 shows the arrangement of the river diversion used at Karakaya Dam in Turkey consisting of two diversion tunnels. The tunnel portal is combined with a closure structure. Two cofferdams protect the construction site of the gravity-arch dam.

Figure 4: Intake portals of diversion tunnels of Karakaya Dam (Turkey) during construction (*Hydraulic Engineering Works* Italstrade: Milan 1990)

ARRANGEMENT OF DIVERSION TUNNELS

In narrow valleys, the integral diversion of the river during construction has to be done by the help of diversion tunnel (Figure 5).

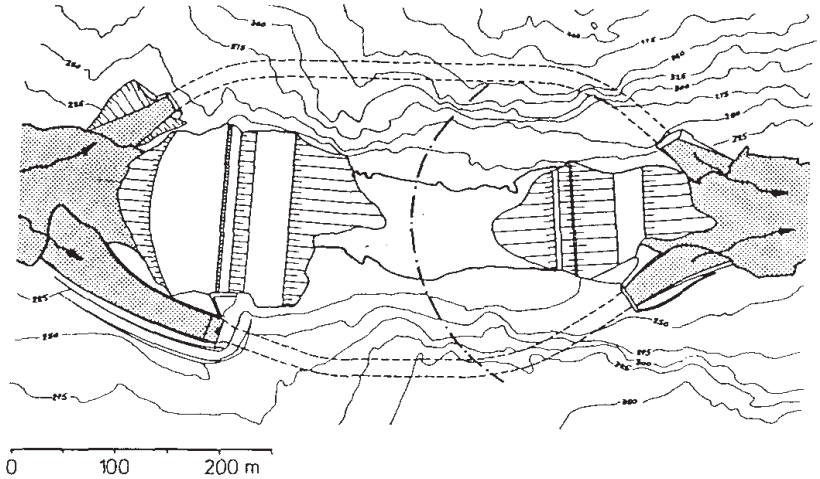

Figure 5: Example of a system of diversion tunnels (Cabora-Bassa in Mozambique)

Often several diversion tunnels on the same or on both sides of the valley are required in order to release the design flood. Until today the largest realized diversion tunnels reach a capacity of about 2500 m^3/s having diameter up to 16 m. The maximum feasible tunnel diameter depends on the rock quality:

- Excellent rock quality: $D_{max} \approx$ 16 m
- Good rock quality: D_{max} = 8 to 11 m

- Mean rock quality: $D_{max} < 8$ m

In general, the diversion tunnels have to be lined by concrete in order to limit friction losses and abrasion in the case of bed load transport. Nevertheless, abrasion can be managed only reasonably if the flow velocity remains below 10 m/s together with bed load transport. Up to the design discharge the diversion tunnels should operate under free surface flow conditions.

The layout of the diversion tunnel depends, besides the footprint of the dam foundation, on the available bottom slope depending on topography of the river stretch in question. The available riverbed slope in narrow valleys normally also results in diversion tunnel slopes generating supercritical uniform flow. Thus, an acceleration reach is mandatory at the tunnel entrance in order that the uniform, equilibrium flow velocity is reached at the beginning of diversion tunnel with constant slope (Fig. 6). This acceleration reach reduces the available slope for the diversion tunnel. In the case of several diversion tunnels, one of them may be built with a higher entrance invert and used during dry season as access tunnel between downstream and upstream. Then the slope of the diversion tunnel respectively its acceleration stretch is limited to 15% in maximum.

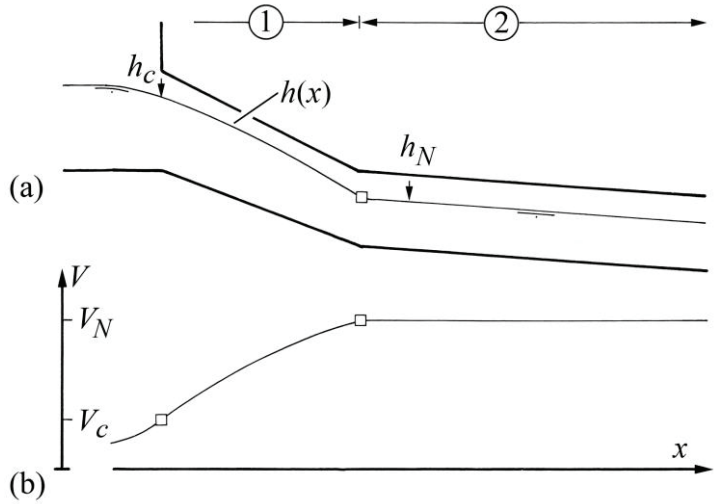

Figure 6: Intake of diversion tunnel (a) section, (b) stream wise increase of average velocity with ① Acceleration reach with *h(x)*, ② Equilibrium reach with uniform flow conditions with flow depth h_N *and flow velocity* V_N (critical flow with h_c and V_c) (Hager et al. 2018)

HYDRAULIC DESIGN OF DIVERSION TUNNEL

For a given design discharge the required flow area of the diversion tunnel i.e. its diameter has to be designed for uniform free surface flow conditions ensuring sufficient aeration by limiting the filling degree of the tunnel to 80% in maximum.

For uniform flow conditions the can be obtained from Manning-Strickler equation as follows:

$$V_N = K \times J^{1/2} \times R^{2/3} \tag{1}$$

Where V_N is the uniform flow velocity, K the Strickler friction coefficient, J the slope of the diversion tunnel and R the hydraulic radius of the tunnel flow section.

The approach flow velocity in the river upstream of the entrance to the diversion tunnel is normally well below the uniform flow velocity in the diversion tunnel. As a consequence, and as already

mentioned, an acceleration stretch is required. The latter is often built as a funnel shape steep transition (Figure 7). The required length and slope of this acceleration stretch has to be designed such that flow is accelerated to the uniform flow velocity at the beginning of the diversion tunnel.

In the acceleration stretch the flow passes trough the critical flow depth h_{cr}. In the case of a funnel shape transition this section corresponds to section along this transition stretch with the highest critical head H_{cr} (see Figure 7).

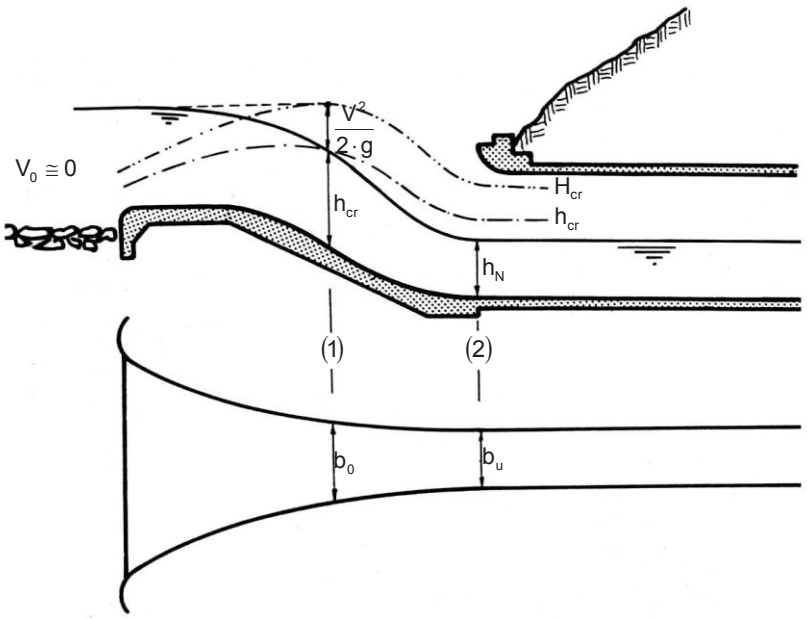

Figure 7: Acceleration stretch at the beginning of a diversion tunnel

For a rectangular cross section in the acceleration stretch the critical flow depth h_{cr} is obtained by:

$$h_{cr} = \sqrt[3]{\frac{Q^2}{g \cdot b_o^2}} \tag{2}$$

With the critical head

$$H_{cr} = \frac{3}{2} \cdot h_{cr} \tag{3}$$

Assuming that the acceleration stretch has a constant slope α, which should be below 15% if the diversion tunnel is used as an access tunnel during dry period, the required length L_{req} of the acceleration stretch can be obtained by applying Bernoulli equation between section (1) and (2) shown in Figure 7:

Section (1)
$$H_1 = \frac{3}{2} \cdot h_{cr} + \underbrace{L_{req} \cdot \sin\alpha}_{\Delta z} \tag{4}$$

Section (2)
$$H_2 = h_N + \frac{V_N^2}{2 \cdot g} + \Delta H_f \tag{5}$$

According Bernoulli $H_1 = H_2$, which results in:

$$L_{req} = \frac{h_N - \frac{3}{2} \cdot h_{cr} + \frac{V_N^2}{2 \cdot g} + \Delta H_f}{\sin\Delta} \tag{6}$$

The friction loss ΔH_f may be neglected in rather short and steep acceleration stretches. For other cases ΔH_f can be calculated approximately by the Manning-Strickler formula:

$$\Delta H_f = \frac{V_m^2 \cdot L_{req}}{K^2 \cdot R_m^{4/3}} \tag{7}$$

With $V_m = (V_N + V_o)/2$ and $R_m = (R_N + R_o)/2$ for a almost linear converging acceleration stretch.

This leads finally to:

$$L_{req} = \frac{h_N - \frac{3}{2} \times h_{cr} + \frac{V_N^2}{2 \times g}}{\sin\alpha - \frac{V_m^2}{K^2 \times R_m^{4/3}}} \tag{8}$$

It has to be mentioned that the slope α of the acceleration stretch and the slope J of the diversion tunnel are directly related by the available level difference between the tunnel entrance and outlet. Furthermore, it has to be ensured that the entrance sill of the acceleration stretch, characterized by L_{req} and α, is long enough to allow river closure. The formation of the critical flow section entrance of the acceleration stretch needs a water level upstream in the river during closure which corresponds to the critical head H_{cr} according Figure 8, since the flow velocity in the river, not perpendicular to the tunnel entrance, has to be neglected.
As will be explained in the next chapter, river closure by advancing the cofferdams across the river is only possible if the water level increase upstream

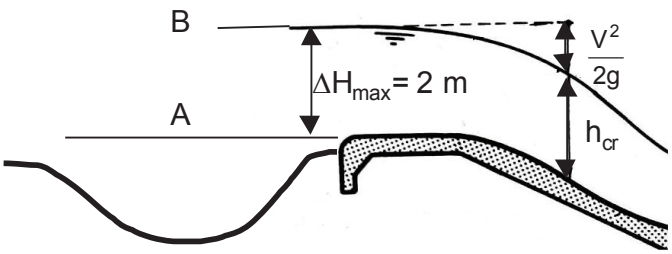

Figure 8: Increase of water level in the river at the entrance of the diversion tunnel. A) Water level before river closure (low level during dry period), B) Water level after river closure with operation of diversion tunnel.

THE CHALLENGE OF RIVER CLOSURE

The derivation of a river into a diversion channel or tunnel requires the closure of the river by the help of cofferdams. Generally, the river is forced to enter into the diversion tunnel by an increase of the water level, which results from the closure of the upstream cofferdam by advancing its construction across the river (Figure 9).

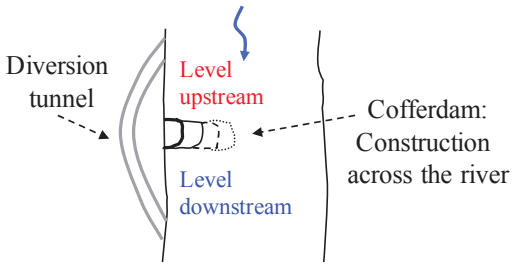

Figure 9: Put into operation of diversion tunnel by closure of cofferdam

According the length of the diversion tunnel, the water levels upstream and downstream of the cofferdam are influenced by its closure operation.

Short diversion

In the case of a short diversion, the water level downstream of the cofferdam is not influenced by its closure. The resulting head difference between upstream and downstream of the cofferdam depends only on the water level increase in the river during closure of the cofferdam (Figure 10). The capacity of the river diversion depends directly upon this level difference.

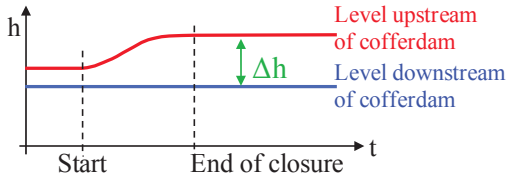

Figure 10: Water level upstream and downstream of a diversion tunnel in the case of a short diversion

Long diversion

In the case of a long diversion, that means a long diversion tunnel, both the upstream and downstream water levels are influenced by the river closure. The water level downstream of the cofferdam decreases since the river can even dry out (Figure 11). The level difference due to river closure becomes more important which makes the closure of the cofferdam more difficult.

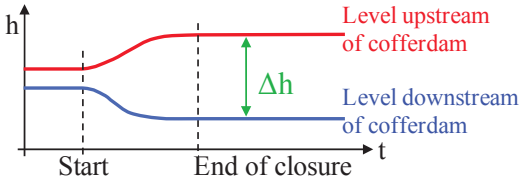

Figure 11: Water level upstream and downstream of a diversion tunnel in the case of a long diversion

Experience shows that with a single cofferdam built across the river, only a head difference of some 2m is feasible when using rock blocks or concrete elements of about 2 to 5 tons for the closure of the final breach. If the head difference becomes higher these blocks are washed away by the constricted river when trying to close the breach (Figure 9). If a higher head difference is required in order to force the river into the entrance of the diversion tunnels, several cofferdams have to be built simultaneously across the river. Each of these cofferdams can create a head difference of some 2m.

In general, river closure is a delicate and costly operation, which can be often successful only during the dry season with low discharge in the river. A careful logistic planning of the closure operation is required with a large enough stock of rock blocks or concrete elements for the final breach closure as

well as the required transportation equipment for fast construction of the cofferdams across the river. In the case of failure of the completion of the cofferdam, i.e. river closure operation, the risk is that the next feasible conditions are present only at the next dry season, which may delay the construction planning by one year.

SELECTION OF DESIGN FLOOD AND RISK ASSESSMENT

The design flood of a river diversion is chosen in order to minimize the risk of the inundation of the construction site during the ongoing work and by taking into account the expected consequences i.e. damages. Nevertheless, as already mentioned, the presence of the construction site and the ongoing works should not increase the risk of flooding upstream as well as downstream. The selection of the design flood of the river diversion depends on the vulnerability of the works under construction in the case of flooding. Consequently, the damage potential influences the choice of the design flood for the river diversion for a certain construction site. If the damage potential is small, for example in the case of concrete dams under construction with cofferdams, which can be overtopped without failure, a design flood between 5-years and 20-years flood may be adequate. In the case of embankment dams under construction, obviously, the damage potential is much higher even if the cofferdams can be overtopped without failure in the case of resistant surface protection. Then a design flood of the river diversion between a 20-years and 50-years flood may be required.

Nevertheless, in the case that only economical risks are involved, the design flood can be chosen by an optimization between the cost of the diversion system and the expected cost of damages when the system fails.

The inundation or flooding risk r of the construction site can be calculated as follows:

$$r = 1 - \left(1 - \frac{1}{n}\right)^{m} \tag{9}$$

Where n is the return period of the design flood of the diversion system and m is the duration of the construction works.

The economical capacity of the river diversion system can be determined by the optimization mentioned above. As long as the flood doesn't exceed the design flood of the diversion system, no damages will occur. Knowing the financial consequences C_d in case of a higher flood than the design flood, the probable value of the damages V_d is obtained by:

$$V_d = r \times C_d \tag{10}$$

Where r is the flooding risk as defined by Equation (9).

The probable value of the damages V_d diminishes when the return period of the design flood is increased. On the other hand, the required investments C_c for construction of the diversion system is higher for an increasing design flood of the latter. Thus, it exists an economical capacity Q_{opt} of the diversion for a certain system chosen as illustrated in Figure 11.

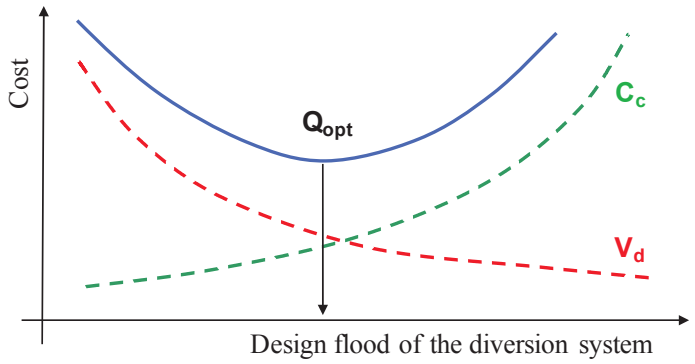

Figure 12: Economical capacity of a river diversion system

Since the hydrology at the dam site, especially the expected yearly return period of floods may have a certain uncertainty, a more detailed reliability analysis of the diversion system is recommended following the approach of Sinniger et al. (1988).

EROSION PROTECTION AT DIVERSION TUNNEL OUTLETS

Overview of protection measures

Water released from diversion tunnels into rivers should not result in riverbed scour, endangering the stability of the tunnel outlet itself or cause failure of any hydraulic structures near the scour zone such as cofferdams. Outlet structures are therefore required to reduce flow velocity and to ensure energy dissipation without dangerous scour (Emami et al. 2006a, b).

Knowing the expected scour depth and extension, the stability of the outlet structure (or tunnel portal) may be guaranteed by cut-off walls. These reinforced concrete walls have to be designed deep enough and founded on sound rock. Another possibility is to protect the mobile riverbed by a concrete slab or even a stilling basin. As non-permanent structures, these solutions are expensive and difficult to build in the presence of water, however.

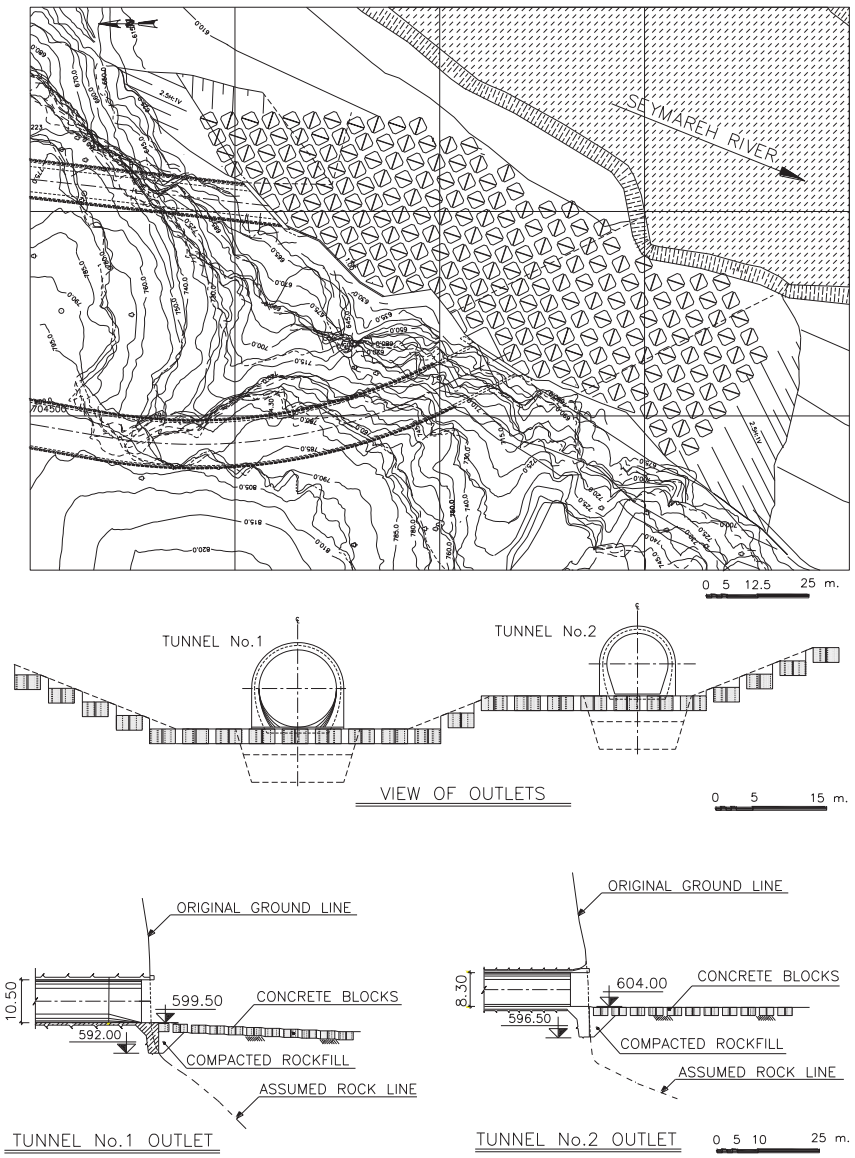

Figure 13. Seymareh Dam in Iran (a) plan, (b) cross-section of concrete prisms placed as erosion protection at diversion tunnel outlets with ① Tunnel 1, ② Tunnel 2, ③ outlet of Tunnel 1, ④ outlet of Tunnel 2, ⑤ original ground line, ⑥ concrete blocks, ⑦ compacted rockfill, ⑧ assumed rock line (Emami *et al.* 2006a)

The existence of deep alluvium at the diversion tunnel outlets of the Seymareh and Karun IV Dams in Iran revealed execution problems for these traditional erosion protection structures at the tunnel outlet resulting in high construction cost. Thus, as an innovative protection measure against scour, large unreinforced concrete prisms were placed in the riverbed close to the outlet of the diversion tunnels (Figures 13). These prisms result from dividing concrete cubes diagonally. This method was used successfully as bank and bed erosion protection measures in steep mountain rivers in Switzerland (Schleiss et al. 1998, Meile et al. 2004).

The applications at Karun IV and Seymareh Dams have demonstrated that the protection of the alluvial riverbed with concrete prisms is a promising solution for limiting scour from the points of view safety and economy (Emami et al. 2006b). Figure 14 illustrates the use of concrete prisms as an

erosion protection at the outlets. To proof the innovative concept and to establish general design criteria, systematic physical model tests have been performed (Emami 2004).

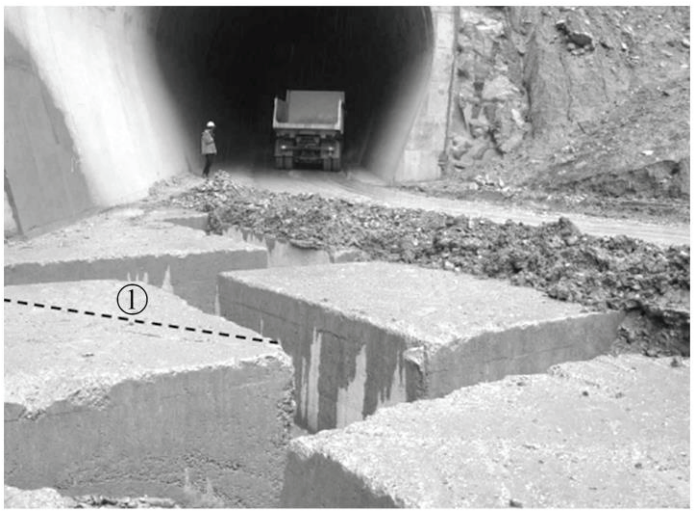

Figure 14: Diagonally divided concrete cubes placed as erosion protection at Diversion Tunnel 1 of Seymareh Dam in Iran with ① lost formwork (Emami et al. 2006a) (Courtesy: S. Emami)

For the cases with and without protection, a total of 24 tests were performed in the wide parameter range varying tailwater level, prism size, discharge intensity, length of protected area and densimetic Froude number involving the river bed material (Emami 2004). The test set-up is shown in Figure 15 with the scour geometry at the end of two tests.

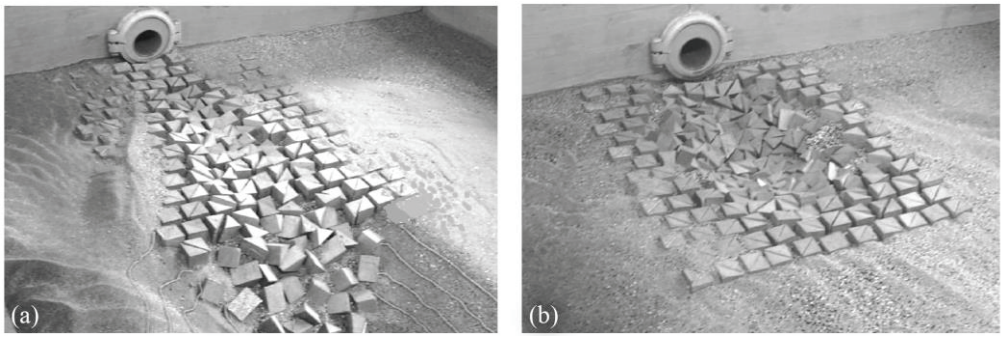

Fig. 15: Experimental set-up showing scour hole versus tailwater level h_{TW} relative to tunnel diameter D for Q=12.5 l/s and tailwater ratio h_{TW}/D = (a) 1.1 (high), (b) 0.2 (low) (Emami et al. 2006a)

In a first step, the variation of the maximum scour depth $y_{TW}=h_{TW}/D$ downstream of diversion tunnels without any protection was analyzed versus the densimetric Froude number $F_o = V_o/[(\rho_s/\rho-1)gd_{50}]^{1/2}$ and the tailwater depth h_{TW}. Here, V_o is the velocity at the tunnel outlet of diameter D, ρ_s is sediment density with grain size d_{50} and ρ is fluid density. The ratio h_{TW}/D ranged from 0.1 to 1.1 as is typical at diversion tunnels of dams. The test results were fitted semi-logarithmically as

$$y_{TW} = a_{TW} \cdot \ln F_o + b_{TW} \tag{11}$$

According to the tests, the tailwater level significantly influences the scour hole geometry. The scour hole is moved downstream from the outlet with increasing tailwater level. Consequently the coefficients a_{TW} and b_{TW} in Equation (11) are affected by h_{TW}. Within the tested parameter ranges, coefficients a_{TW} and b_{TW} depend linearly on h_{TW}/D, as stated in Table 1 for the various scour

characteristics including the maximum scour depth d_{sc}/D, maximum scour length L_{TW}/D, the distance of maximum scour depth from the outlet x_{TW}/D, and the maximum scour hole width w_{TW}/D.

Table 1: Coefficients a_{TW} and b_{TW} of Eq. (11) versus relative tailwater depth for $8.5<F_o<14.5$ and $0.10<h_{TW}/D<1.10$ (Emami et al. 2006a)

Scour hole characteristics	y_{TW}	a_{TW}	b_{TW}
Maximum scour depth	d_{sc}/D	$-0.60\cdot(h_{TW}/D)+1.80$	$1.23(h_{TW}/D)-2.25$
Maximum scour length	L_{TW}/D	$-0.38(h_{TW}/D)+13.20$	$6.08(h_{TW}/D)-21.95$
Distance of d_{sc} from pipe outlet	x_{TW}/D	$0.86(h_{TW}/D)+4.49$	$1.00(h_{TW}/D)-7.97$
Maximum scour width	w_{TW}/D	$-0.42(h_{TW}/D)+3.53$	$-3.33(h_{TW}/D)+0.78$

Empirical scour relations

To develop dimensionless relations for the protection of scour holes by *concrete prisms*, the so-called prism or block Froude number F_b was introduced based on the concept of the densimetric Froude number as

$$F_b = V_o \Big/ \sqrt{(\rho_b/\rho - 1) g V_{\text{cube}}^{1/3}} \tag{12}$$

Here ρ_b the block density whereas the equivalent cube size is $V_{\text{cube}}^{1/3} = (a_b^3/2)^{1/3}$, with a_b as the side length of a diagonally sliced cube.

The scour data in terms of F_b follow again a linear fit of the form $y_b = a_b \cdot F_b + b_b$. The coefficients a_b and b_b depend almost linearly on the tailwater depth divided by the equivalent cube dimension $h_{TW}/V_{\text{cube}}^{1/3}$ (Emami 2004). Based on the test data, the coefficients of the following scour characteristics are specified (Figure 16, Table 2):

- Maximum scour depth d_{sc}/D
- Scour depth at pipe or tunnel outlet d_{toe}/D
- Maximum scour width w_{sc}/D
- Up- and downstream limits of scour hole x_1/L_P, x_3/L_P
- Distance of deepest scour point from pipe or tunnel outlet x_2/L_P
- Required length of protected area L_{Req}/D

Note from Table 1 that only the maximum scour width is independent of h_{TW}.

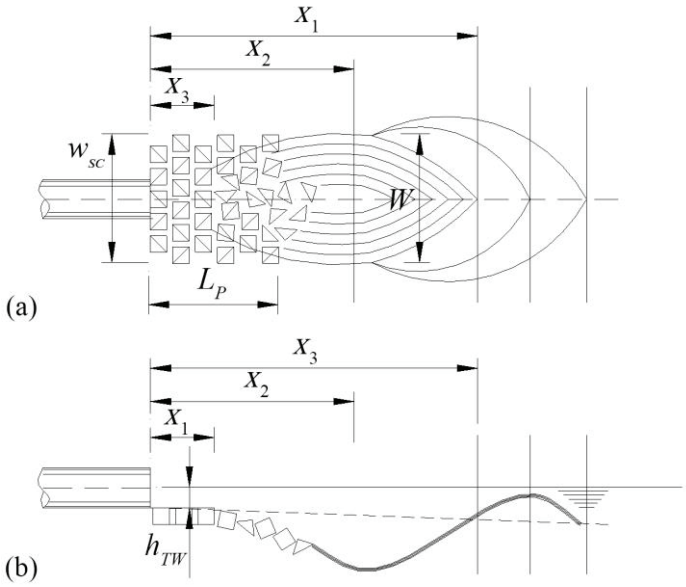

Figure 16: Definition of scour hole characteristics downstream of diversion tunnel outlet (a) plan, (b) streamwise section

Table 2: Coefficients a_b and b_b of equation $y_b = a_b \cdot \mathsf{F}_b + b_b$ for scour hole characteristics with protection by concrete prisms (Fig. 16)

Scour hole characteristics	y_b	a_b	b_b
Maximum scour depth	d_{sc}/D	$-0.01(h_{TW}/V_{\text{cube}}^{1/3}) + 0.87$	$0.38(h_{TW}/V_{\text{cube}}^{1/3}) - 1.00$
Scour depth at pipe outlet	d_{toe}/D	$-0.11(h_{TW}/V_{\text{cube}}^{1/3}) + 0.38$	$0.09(h_{TW}/V_{\text{cube}}^{1/3}) - 0.37$
Maximum scour width	w_{sc}/D	2.00	1.50
Upstream boundary of scour	x_1/L_P	$-0.27(h_{TW}/V_{\text{cube}}^{1/3}) + 0.09$	$0.88(h_{TW}/V_{\text{cube}}^{1/3}) - 0.29$
Distance of d_{sc} from pipe outlet	x_2/L_P	$-0.07(h_{TW}/V_{\text{cube}}^{1/3}) + 0.36$	$0.62(h_{TW}/V_{\text{cube}}^{1/3}) - 0.50$
Downstream boundary of scour	x_3/L_P	$-0.25(h_{TW}/V_{\text{cube}}^{1/3}) + 1.13$	$1.00(h_{TW}/V_{\text{cube}}^{1/3}) - 1.45$
Required length of protected area	L_{Req}/D	$-0.37(h_{TW}/V_{\text{cube}}^{1/3}) + 3.63$	$0.39(h_{TW}/V_{\text{cube}}^{1/3}) + 0.38$

Failure criteria

Any failure of the area protected by concrete prisms occurs in principle if either the scour extends over the protected area and/or if the concrete prisms are swept away by the flow (Emami 2004, Emami *et al*. 2016a). The experimental study revealed that the failure of prisms is affected by the velocity at the pipe outlet V_o, the mass densities of the prisms and water, the prism size $V_{\text{cube}}^{1/3}$, the tailwater depth h_{TW} and the length of the protected area L_P. Based on observations, the failure of the protected area occurred if one or more of the following conditions were met (Figure 15):

- Scour depth at tunnel outlet higher than 50% of tunnel diameter
- Maximum scour depth higher than 2 times tunnel diameter
- Maximum scour width higher than width of protected area

It was noted from the tests that the failure of the protected area strongly depends on the protection length L_P and the tailwater level h_{TW} for a given prism size expressed by the prism Froude number F_b. To define a dimensionless failure diagram to protect prisms, the relation between the prisms Froude

number F_b and parameter h_{TW}/L_P was plotted (Figure 17). Based on the above criteria, the failure diagram was divided into the three regions "No movement", "Acceptable movement" and "Failure".

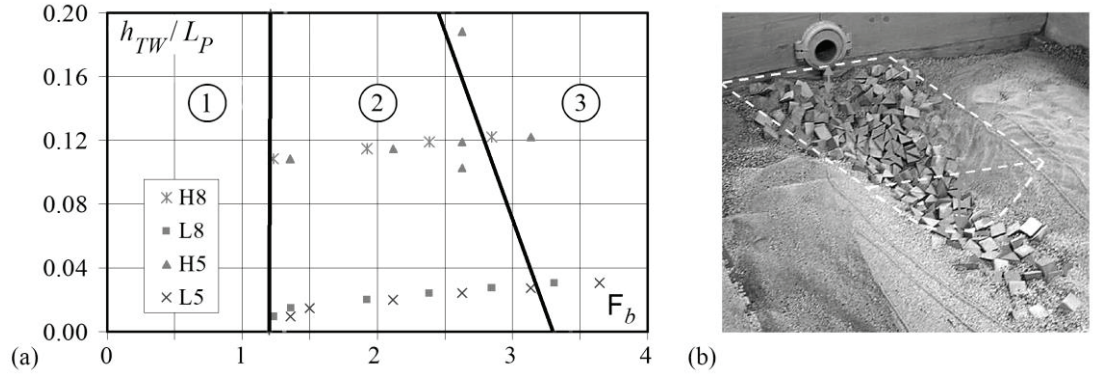

Figure 17: (a) Failure diagram for prism protection h_{TW}/L_P versus prism Froude number F_b, (–) Eq. (13) with ① No movement, ② Acceptable prism movement, ③ Prism failure, (b) example of failure of protected area (Emami et al. 2006a)

Figure 17b shows the successive failures of the area protected by concrete prisms with increasing discharge. The minimum required protection length L_{Req} downstream of the outlet to avoid any failure in the protected area is

$$F_b = 3.32–4.26(h_{TW}/L_{P,\text{Req}}) \tag{13}$$

The location of the scour hole was analyzed for protection lengths $6<L_p/D<11$. The required protection length was then defined if the following conditions were satisfied:

- Prisms are not eroded from downstream due to high tailwater
- Maximum scour is pushed by (1 to 2)D downstream of outlet (low tailwater)

The latter ensures the stability of the tunnel outlet. The minimum required protection length L_{Req} follows the empirical formula given in Table 2 resulting from the tests. If a protection length $L_P>L_{\text{Req}}$ is selected, the prism size can be reduced according to the failure diagram (Figure 17). The width of the protection area was always $w_P/D=7.5$, selected according to the flow diffusion angle for maximum discharges released from the tunnel. It can be considered as design value.

Design recommendations

The design discharge for checking the prism stability results from an analysis of the diversion system in view of construction cost and damages during floods at the construction site. The required prism size should then be determined by considering a safety factor. For the design discharge, a safety factor of $\beta_s=1.3$ is recommended for prisms obtained by dividing cubes diagonally. The safety factor is applied on the prism number when using the failure diagram ($\beta_s \cdot F_b$). The prism stability should be checked for the safety discharge ($\beta_s \geq 1$) corresponding to the maximum capacity of the diversion system under extreme conditions.

Within the application range of the developed scour formulas ($0.10<h_{TW}/V_{\text{cube}}^{1/3}<2.90$ and $8.5<F_o<14.5$), the minimum required prism size $a_{b,\min}$ should be close to 45% of the tailwater depth ($a_{b,\min} \geq 0.45 h_{TW}$) for the design discharge. The required prism dimension is then checked by using the failure diagram (Figure 17). According to the tests, the maximum acceptable prism spacing should not exceed 40% of the prism size ($s_b \leq 0.40 a_b$). A minimum prism spacing of 0.50 m is recommended for construction reasons (excavation and formwork). The length of the protected area should correspond at least to the required length as defined in Table 2. The width of the protected area should be at least 7.5D.

Concrete prisms should be used by dividing cubes diagonally, as they are the most resistant, and the design criteria have been developed for them. As long as they are not too flat, prisms obtained from square blocks are also acceptable. Since the prism Froude number is based on the equivalent cube size, the design criteria and design formulae still apply. If rather flat prisms are used (prism height 60 to 80% of its side length), the safety factor should be increased to $\beta_s = 1.5$.

The concrete prisms can be cast in place after excavation of the cube using a diagonal lost formwork to create them. The alternate solution is to precast a reinforced concrete formwork and fill it on site with mass concrete. A cement content of 250 kg/m^3 should be used for the concrete to ensure a sufficient shear and tensile strength of the prisms. Since erosion of material between the prisms can be accepted, no filter is required. Furthermore, in prototype applications, such a filter is practically not feasible. Once the material between the prisms is eroded, the latter tilts and forms a structure which protects against further erosion.

SURFACE PROTECTION OF COFFERDAMS

Since there is a practical limit of the discharge capacity of diversion tunnels regarding their maximum feasible excavation diameter (currently up to 16 m in excellent rock), the cofferdams may be overtopped during critical construction phases. To avoid the complete failure of cofferdams with catastrophic concerns in view of construction cost and time, their surface can be reinforced by adequate overlays to resist controlled overtopping. Widely used surface protection measures are:

- Riprap
- Reinforced slopes by anchored wire mesh
- Gabions
- Pre-casted concrete slabs and blocks

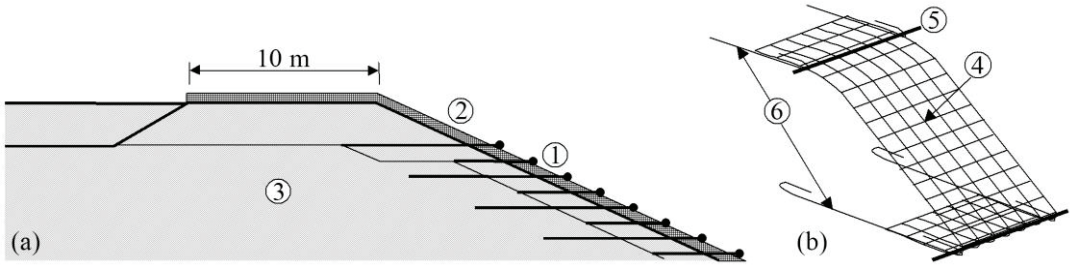

Figure 18: Protection by reinforcing slopes with anchored wire mesh including (a) ① steel bars 4 m and 10 m long, ② wire mesh, ③ riprap, (b) details of ④ wire mesh ⑤ thick steel bar ⑥ anchor bars (Schleiss, 2015)

A *riprap protection* is based on the critical surface velocity V_{cr} (Isbash 1945)

$$V_{cr} = 1.2\left[\frac{\rho_b - \rho}{\rho} 2gd_b \cos\phi_d\right]^{1/2} \tag{14}$$

Here, d_b is the equivalent block diameter, ρ_b block density (typically 2,650 kg/m^3), ρ water density and ϕ_d the downstream angle of the cofferdam. Schematic examples of reinforced slopes by anchored wire mesh and gabions are shown in Figs. 18 and 19. The surface protection of the upstream cofferdam of Cabora Bassa Dam is seen in Figure 20.

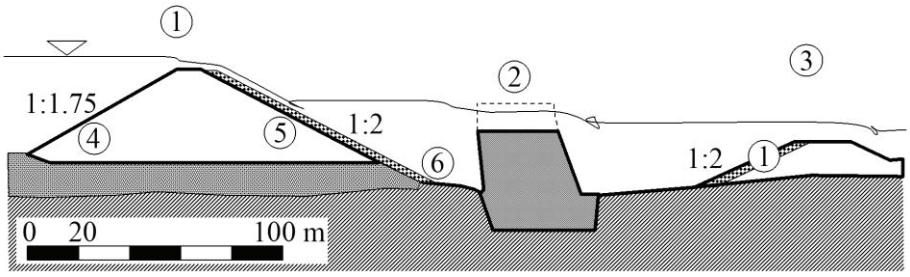

Figure 19: Surface protection using gabions with ① upstream cofferdam, ② dam under construction, ③ downstream cofferdam, ④ riprap, ⑤ surface protection, ⑥ toe of cofferdam (Schleiss 2015)

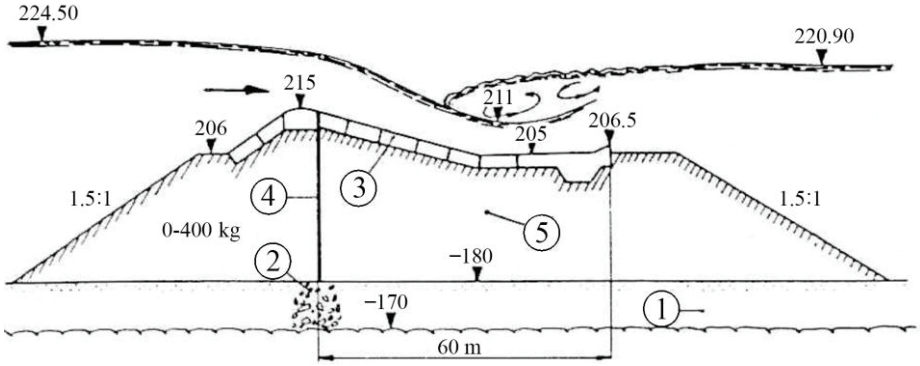

Figure 20: Protection of Cabora Bassa cofferdam with concrete slabs 3 m thick and size of 7×7 m^2 with ① alluvial river bed, ② grouting ③ concrete slabs, ④ sheet pile ⑤ riprap (GT-CFGB 1973).

Concrete slabs have the disadvantage to accelerate the flow along the downstream cofferdam side and thus enhance the risk of toe erosion. This risk can be mitigated by using a macro-roughness lining system as protection consisting of precast concrete elements (Manso *et al*. 2002). The main difference between this system and other existing concrete element systems is the stability concept, based on the self-weight of the blocks. Several types of elements were developed and tested in a physical model for a typical dam slope of 1V:3H (Figure 21) (Manso 2002). Failure conditions were identified after submitting the elements to increasing discharges.

The largest element, the 44° negative sloped step (Type 1), does not present any advantage in terms of stability compared with other stepped-like elements, or at least not within the range of discharges tested. The 30° negative step element (Type 2) is clearly the solution withstanding highest discharges. By addition of an end sill (Type 2+ES), higher energy-dissipation efficiency seems likely to occur by increasing the momentum exchanges at the pseudo-bottom interface. The pyramid element (Type 3) is a good alternative for moderate discharges, creating a highly complex flow pattern and presenting the lowest velocities for the observed range of discharges.

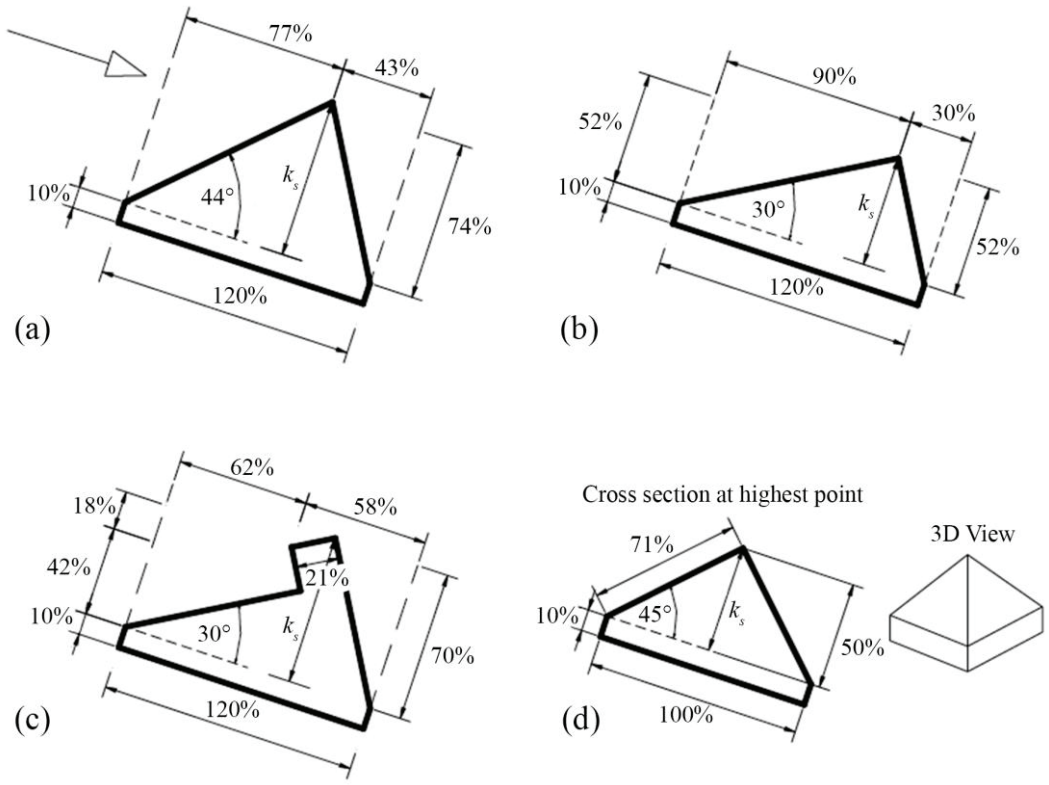

Figure 21: Dimensionless geometry of tested types of concrete lining blocks on a 1V:3H slope (Manso *et al*. 2002) (a) Type 1, (b) Type 2, (c) Type 2+ES, (d) Type 3. Roughness height k_s and block geometry are defined as multiple of element width b_E=100% (Manso *et al*. 2002).

For the preliminary design of the concrete elements, the design charts of Figs. 22 to 25 apply. These exclude any drainage layer below the concrete elements, the recommended conservative design assumption. For a detailed stability analysis, the procedure of Manso *et al*. (2002) should be considered.

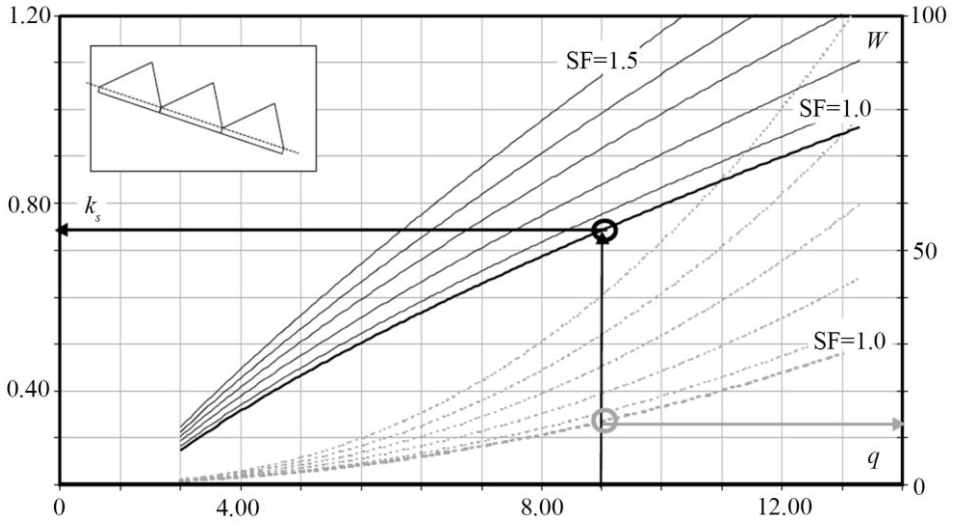

Figure 22: Design chart for 44° negative slope step (Type 1). Safety Factor values SF between 1 and 1.5, without drainage, versus roughness height k_s [m], unit discharge q [m^2/s], and weight W [kN] for concrete density of 2,400 kg/m^3; dam slope 1V:3H. (○) Experimental observation (Manso *et al*. 2002). Roughness height k_s of elements according to Fig. 21

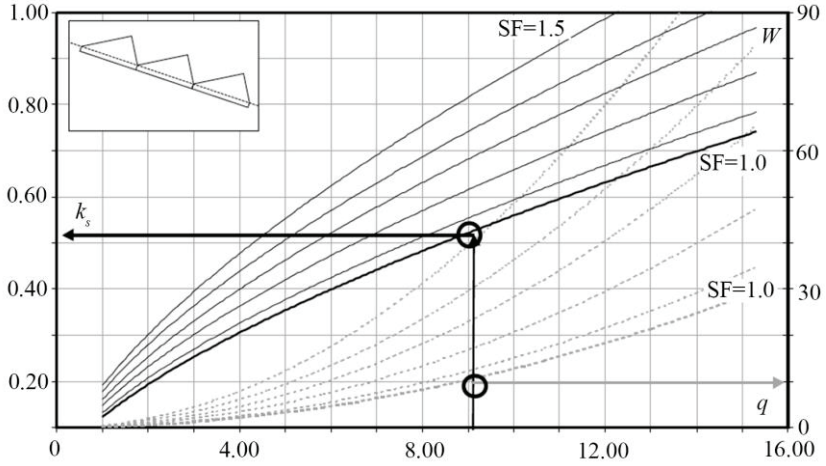

Figure 23: Design chart for 30° negative slope step (Type 2). Safety Factor values SF between 1 and 1.5, without drainage, versus roughness height k_s [m], unit discharge q [m^2/s], and weight W [kN] for concrete density of 2,400 kg/m^3; dam slope 1V:3H. (○) Experimental observation (Manso *et al*. 2002). Roughness height k_s of elements according to Fig. 21.

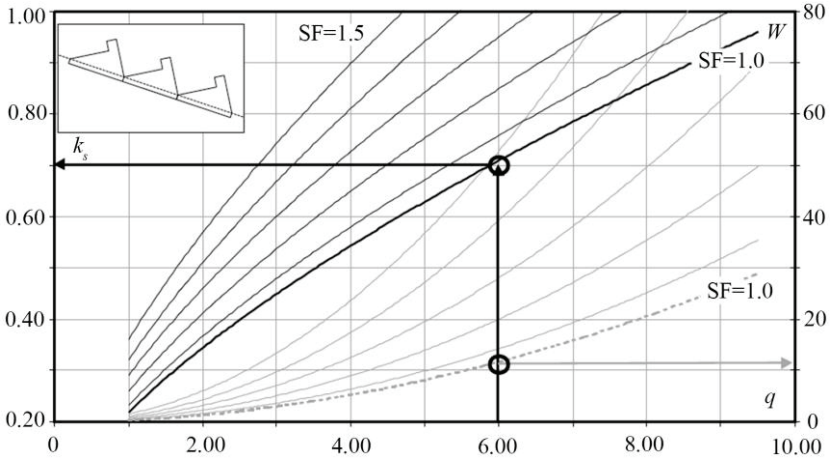

Figure 24: Design chart for 30° negative slope step (Type 2+ES). Safety Factor values SF between 1 and 1.5, without drainage, versus roughness height k_s [m], unit discharge q [m^2/s], and weight W [kN] for concrete density of 2,400 kg/m^3; dam slope 1V:3H. (○) Experimental observation (Manso *et al*. 2002). Roughness height k_s of elements according to Fig. 21.

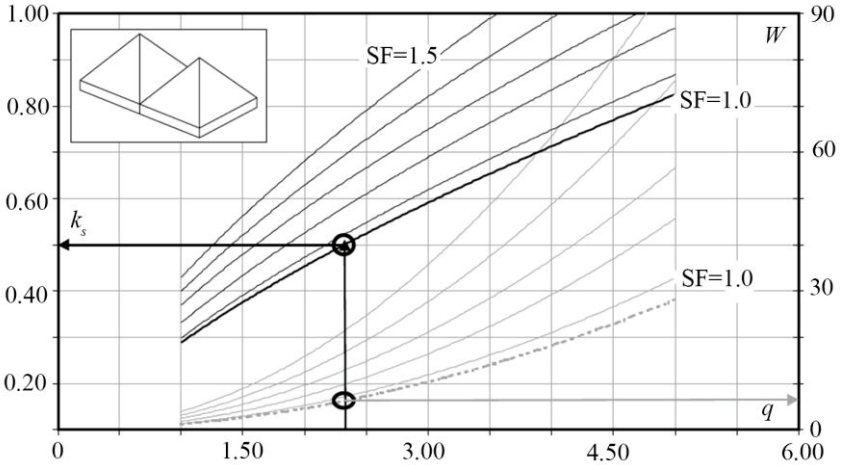

Figure 25: Design chart for 30° negative slope step (Type 3). Explanations as in Figure 24.

CONCLUSIONS

The river diversion during the construction of a dam is often an engineering and execution challenge, which not correctly designed and planned can have dramatic consequences on construction cost and time. When using diversion tunnels, which allow an integral diversion of the rivers around the construction site, some basic requirements for the safe hydraulic functioning of the system have to be respected. Above all it is important to foresee an acceleration stretch at the portal of the diversion tunnel which puts the flow into a velocity corresponding to the prevailing flow velocity in the diversion tunnel due to normal flow free surface conditions. Without such an acceleration stretch the tunnel may be pressurized before the design discharge is reached resulting in a fast increase of the water level upstream of the tunnel entrance and consequently a high risk of overtopping of the cofferdam as experienced in many cases. Furthermore, the entrance sill of the acceleration stretch has to be long enough in order to allow river closure by dumping and constructing the cofferdams across the river. River closure has to be carefully planned with appropriate hydraulic of the diversion entrance to the acceleration stretch. An issue is also the energy dissipation at the outlet of diversion tunnels, which should avoid any stability problem of the outlet portal without any risk of stability and consequently failure of the diversion system. Finally, the remaining risk may be also handled by reinforcing the surface of the cofferdams with an overlay of concrete elements which allow overtopping without failure up to a certain discharge.

REFERENCES

GT-CFGB (1973). Groupe de travail du Comité Français des Grands Barrages: Méthodes de dérivation pendant la construction. Proc. 11th ICOLD Congress Madrid, Q36(R16): 565-590 (in French).

Hager W., Schleiss A.J., Boes R., Pfister M. (2018). *Hydraulics of Dams.* Balkema: Rotterdam (under preparation)

Emami, S. (2004). Erosion protection downstream of diversion tunnels using concrete prisms: Design criteria based on a systematic physical model study. Communication 18. Laboratory of Hydraulic Constructions (LCH), A. Schleiss, ed. LCH-EPFL: Lausanne.

Emami, S., Schleiss, A.J. (2006a). Design of erosion protection at diversion tunnel outlets with concrete prisms. Canadian J. Civil Engineering 33(1): 81-92.

Emami, S., Schleiss, A.J. (2006b). Performance of large concrete prisms as erosion protection at Seymareh diversion tunnel outlets during a large flood. Proc. 21th Congress of the Intl. Commission of Large Dams - CIGB-ICOLD, Barcelona, Vol. V, Communication C12: 99-813.

Izbash, S.V. (1935). Construction of dams and other structures by dumping stones into flowing water. Izvestiya VNIIG 17: 12-66 (in Russian, with English summary).

Meile, T., Bodenmann, M., Schleiss, A., Boillat, J.-L. (2004). Flood protection concept for the river Gamsa in Canton Wallis. Intl. Symp. Interpraevent, Riva/Trient, Italy, Theme VII: 219-230 (in German).

Manso, P.A. (2002). Stability of linings by concrete elements for surface protection of overflow earthfill dams. Communication 12, A. Schleiss, ed. Laboratory of Hydraulic Constructions, LCH-EPFL, Lausanne, Switzerland.

Manso, P.A., Schleiss A.J. (2002). Stability of concrete macro-roughness linings for overflow protection of earth embankment dams. Canadian J. Civil Engineering 29(5): 762-776.

Schleiss, A., Aemmer, M., Philipp, E., Weber, H. (1998). Erosion protection at mountain rivers with buried concrete blocks. Wasser Energie Luft 90(3/4): 45-52 (in German).

Schleiss A. (2015). Aménagements hydrauliques. Polycopié EPFL, Section de Génie Civil (484 p.). EPFL: Lausanne (in French).

Sinniger R., Bourdeau P.L. (1988). Probability-based design of temporary diversions. Proc. 16th *ICOLD Congress* San Francisco, Q63(R21): 319-344

5 DAM SAFETY
İstanbul Turkey 2018

5th International Symposium on Dam Safety

October 27-31, 2018

MODELLING OF COLLAPSE SETTLEMENTS AND LONG-TERM DEFORMATIONS OF ROCKFILL DAMS

Erich BAUER [1]

ABSTRACT

In the present paper three deformation mechanisms of rockfill materials are distinguished: instantaneous deformations, collapse settlements and long-term deformations. The main factors of influence are the type of rockfill material, the pre-compaction, the state of weathering, the loading history, and the time dependent process of degradation of the solid hardness. The latter is related to progressive mechanical and chemical weathering of the solid material caused by repeated changes of the temperature and moisture. A change of moisture can take place due to leakage through the foundation, defects in the upstream sealing of the dam and repeated rainwater infiltration. For the constitutive modelling of these effects the solid hardness and the pressure dependent relative density are the main key parameters in the model proposed. The evolution equation for the degradation of the solid hardness is decomposed into a part related to long-term creep deformations and a part related to collapse deformations. The degradation of the solid hardness is coupled with a reduction of the pressure dependent limit void ratios and the critical void ratio, which are embedded in an extended hypoplastic constitutive model. Thus the model proposed allows a unified description of the interaction between the current density, the stress, the rate of deformation, the state of weathering of the solid hardness and its rate. The performance of the model proposed is shown by comparing the results of numerical simulations with experimental data. The concept for simulation of post-construction deformations is discussed for an artificial concrete face rockfill dam.

Keywords: Rockfill Dams; Solid Hardness, Collapse Settlements; Creep, Hypoplasticity

INTRODUCTION

The accurate prediction of post-construction deformations of rockfill dams is still a challenging task. Long-term deformations can be an accumulation of deformations related to various events and the interpretation of the relevant physical and thermo-chemical mechanisms is important both for the evaluation of the data obtained from monitoring and for numerical modelling. A general distinction can be made between time independent deformations, which are the instantaneous part of the deformation due to load changes, and time dependent deformations, which can also take place under constant load. The former, for instance, can be initiated by rapid changes of the water level in the reservoir, the change of effective stresses caused by a change of suction of fine grained materials, hydraulic fracturing and piping as a result of the seepage-driven internal erosion of solid particles. Time dependent deformations are usually related to the rheological properties of the rockfill material and influenced by the mineralogical composition of the solid material, the grain size distribution, the pre-compaction, the moisture content, the stress state, and the evolution of weathering. Progressive weathering caused by chemical weathering or by the frequency and the orientation of micro-cracks

[1] Professor, Institute of Applied Mechanics, Graz University of Technology, Graz, Austria
e-posta: erich.bauer@tugraz.at

has a significant influence on the time dependent process of the degradation of the solid hardness and as a consequence on the deformation behaviour of the rockfill material. In dam engineering it is common to differentiate between long-term creep deformations and so-called collapse settlements. While the former is related to the rheological properties of the rockfill material and controlled by gravity load and the effect of water impounding, the latter can be observed immediately after a change of the moisture content of the stressed rockfill material. Depending on the state of weathering of the rockfill material a change of the moisture content can initiate an acceleration of the crack propagation of stressed rockfill particles, which leads to a reduction of the solid hardness. Collapse settlements, also called wetting deformations are characterized by pronounced plastifications of grain contacts and grain crushing, which brings about local instabilities in the grain skeleton (Terzaghi, 1936). Changes of the moisture content can be caused by different events like climate changes, leakage related to defects of the dam sealing and the dam foundation, as well as by rainwater infiltration into the dam body.

(Figure 1a) shows the time dependent deformation of two different rockfill materials under a constant vertical stress of 0.8 MPa in an oedometer device (Sowers et al., 1965). The course of the deformations is qualitatively similar for greywacke and sandstone and can be divided into three parts. After applying the vertical stress on the initially dry material, an instantaneous settlement can be detected, which is larger for sandstone. Under constant stress creep can be observed in the dry state as well after a sudden flooding of the specimen. Flooding leads to a jump of the settlement rate but there is no jump in the settlement. It is therefore obvious that so-called collapse settlements are also time dependent. While for the dry material the creep velocity decreases slowly, the high settlement rate immediately after flooding fades out very fast. The amount of wetting deformations strongly dependents on the pre-compaction of the material, which is also clearly visible in (Figure 1b). The experimental results by (Kast, 1992) also show that the compressibility is generally higher for the wet material than for the dry material.

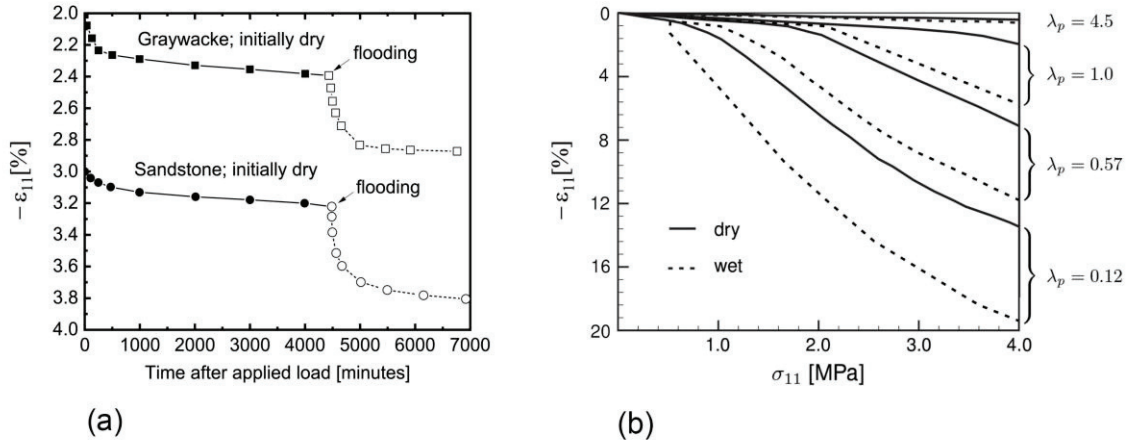

Figure 1. (a) Time dependent behaviour of two different rockfill materials under a constant vertical stress of 0.8 MPa in an oedometer device (Sowers et al., 1965); (b) oedometric compression behaviour of broken granite under dry and water saturated conditions and for different pre-compactions, i.e. λ_p denotes the relative pre-compaction energy (Kast, 1992)

Great efforts were made to explain the complex mechanisms of wetting deformations at the micro- and macro-level, e.g. (Sowers et al., 1965; Nobari and Duncan, 1972; Marsal, 1973; Brauns et al., 1980; Kast, 1992; McDowell and Bolton, 1998; Alonso and Oldecop, 2000; Oldecop and Alonso, 2001, 2007; Oldecop and Agreda, 2004; Hu et al., 2009; Alonso and Cardoso, 2009; Ham et al., 2010; Klammer and Dietzel, 2011; Alonso, 2014; Ovalle et al., 2014, 2015). For numerical simulations of the behaviour of rockfill dams, however, a material model on the macro-level is needed to capture the essential properties of weathered and moisture sensitive rockfill materials. For practical applications the material parameters involved should be easy to calibrate based on data from standard laboratory experiments or field tests.

For modelling time dependent deformations, the solid hardness and the pressure dependent relative density are the two key parameters considered in the present paper. To reflect the state of weathering on the compression behaviour of rockfill materials the concept of solid hardness was introduced by (Bauer, 2009) for modelling time dependent deformations. The solid hardness for the weathered material is lower and the degradation of the solid hardness caused by progressive weathering is described using an evolution equation (Bauer, 2009; Bauer et al., 2010; Bauer and Fu, 2011; Bauer et al., 2012; Li et al., 2016; Bauer et al., 2017; Bauer, 2018).
In the present paper a brief overview of how to calibrate the solid hardness and the creep parameter is given. It is shown that it is sufficient to consider the compression curves and creep curves obtained under isotropic or oedometric loading. To simulate time dependent deformations under general 3-D conditions the concept of the solid hardness is embedded as a state parameter into an extended hypoplastic material model. The capability of the constitutive model proposed is demonstrated by comparing the results of numerical simulations with laboratory experiments carried out by (Li, 1988) with a rockfill material used in the Xiaolangdi dam in China. Finally, an approach to simulating post-construction deformations is discussed for an artificial concrete face rockfill dam.
Throughout the paper the sign convention of rational solid mechanics is adopted, i.e. compressive stress and strain are negative. All stresses are effective stresses. Other effects of partly saturated materials like inter-particle capillary forces are negligible for coarse grained rockfill materials.

CONSTITUTIVE MODELLING OF THE LONG-TERM BEHAVIOUR OF ROCKFILLS

Definition of the solid hardness in the sense of a continuum description

For the constitutive modelling of the mechanical behaviour of rockfills it is convenient to define the solid hardness for the grain assembly rather than a single particle. To this end the compressibility of the rockfill material is described by the following relationship between the maximum void ratio e_i and the mean effective pressure $p = -(\sigma_{11} + \sigma_{22} + \sigma_{33})/3$ (Bauer, 1995, 1996):

$$e_i = e_{i0} \exp\left\{-\left(\frac{3p}{h_s}\right)^n\right\}. \tag{1}$$

Herein the constant e_{i0} denotes the void ratio for $p \approx 0$, and n is a dimensionless constant. The quantity of h_s is called solid hardness and defined for the pressure $3p$, at which the compression curve in a semi-logarithmic representation shows the point of inflection as illustrated in (Figure 2a). (Equation 1) is consistent within the whole pressure range and thus it also takes into account the influence of grain crushing depending on the mean pressure (Bauer et al., 2017).

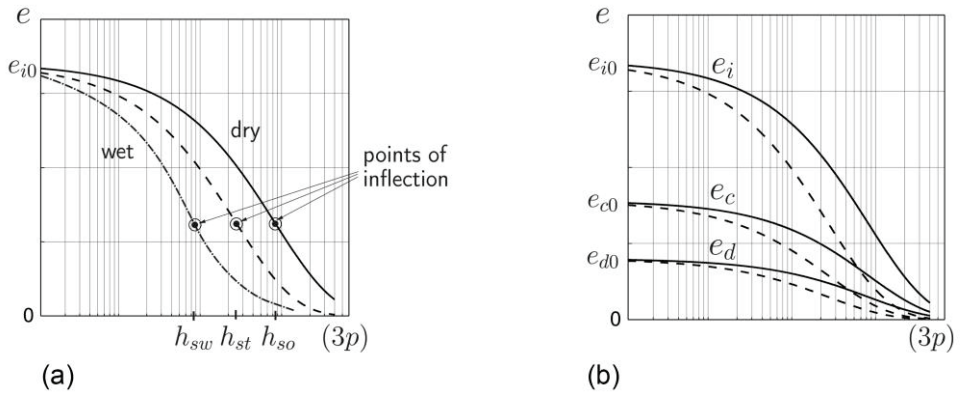

Figure 2. (a) Illustration of the compression curve for the dry state and the wet state of the material; (b) limit void ratios related to the initial solid hardness h_{so} (solid curves) and for the degraded solid hardness h_{sw} (dashed curves)

The time dependent process of degradation of the solid hardness

Weathered and moisture sensitive rockfill materials show a higher compressibility under wet states than under dry one (Figure 1b). In order to model the degradation of the solid hardness the constant solid hardness in (Equation 1) is replaced by a state variable, h_{st}, which depends on the history of mechanical and thermo-chemical weathering. A degradation of h_{st} is also related to a change of the compression curve as shown in (Figure 2a). To model the time dependent process of degradation of h_{st} the following evolution is considered (Bauer, 2009):

$$\dot{h}_{st} = -\frac{1}{c}(h_{st} - h_{sw}) \,. \tag{2}$$

Herein $\dot{h}_{st}$ denotes the rate of the current state of the solid hardness h_{st}, which ranges within the upper limit h_{so} and the lower limit h_{sw}. The quantity h_{so} denotes the initial value of the solid hardness, and h_{sw} is the final degraded state of the solid hardness. The integration of (Equation 2) yields for the solid hardness depending on the time *t*:

$$h_{st(t)} = h_{sw} + \left(h_{so} - h_{sw}\right)\exp\left\{-\frac{t}{c}\right\}. \tag{3}$$

Parameter c in (Equation 2) scales the velocity of degradation and can be calibrated from a creep test as outlined in the following. To this end a creep test in an oedometer device is considered. For a constant vertical stress σ_{11} the lateral stress can be approximated using the formula by (Jaky, 1948), i.e. with the friction angle φ_c the lateral stress is $\sigma_{22} = (1-\sin\varphi_c)\sigma_{11}$, so that the mean pressure can be computed as $p = -\left(1-(2/3)sin\,\varphi_c\right)\sigma_{11}$. For a constant mean pressure, the time derivative of (Equation 1) yields the following creep law (Bauer, 2009):

$$\dot{e} = ne\left(\frac{3p}{h_{st}}\right)^n \frac{\dot{h}_{st}}{h_{st}} \,. \tag{4}$$

With respect to $\dot{e} = \left(1+e\right)\dot{\varepsilon}_v = \left(1+e\right)\dot{\varepsilon}_{11}$ for oedoemetric compression condition, the integration of (Equation 4) yields for the axial strain ε_{11} as a function of $h_{st(t)}$:

$$\varepsilon_{11(t)} = \ln\left[\frac{e_o \exp\left\{\left(3p/h_{so}\right)^n - \left(3p/h_{st(t)}\right)^n\right\}+1}{\left(1+e_o\right)}\right], \tag{5}$$

Where e_o denotes the initial void ratio and $h_{st}(t)$ is taken from (Equation 3). For $t \to \infty$ the corresponding creep strain is:

$$\varepsilon_{11\infty} = \ln\left[\frac{e_o \exp\left\{\left(3p/h_{so}\right)^n - \left(3p/h_{sw}\right)^n\right\}+1}{\left(1+e_o\right)}\right]. \tag{6}$$

For a known value of $\varepsilon_{11\infty}$ the final degraded value of the solid hardness, h_{sw}, can be calculated from (Equation 6). With the initial inclination γ of the creep curve (Figure 3a) the value of parameter *c* can be computed:

$$c = \frac{n}{\tan\gamma}\frac{e_o}{\left(1+e_o\right)}\left(\frac{3p}{h_{so}}\right)^n\left(1-\frac{h_{sw}}{h_{so}}\right) \tag{7}$$

Based on (Equations 3, 5, 6, 7) and an assumption of the initial void ratio e_0 the experimental result by (Sowers, 1965) can be simulated as shown in (Figure 3b). In particular, the initially constant solid hardness h_{so} can be computed from the instantaneous settlement in part I, and the degradation of the solid hardness in part II, i.e. h_{sw}^{II}, can be obtained with an estimated value for the long-term creep strain $\varepsilon_{11\infty}^{\mathrm{II}}$. The degraded solid hardness h_{sw}^{III} in part 3 is a combination of the influence of long-term creep and the effect of collapse deformation caused by flooding at time $t = 4500$ minutes, i.e. h_{sw}^{III} can

be calculated from an estimated value for $\varepsilon_{11\infty}^{\mathrm{III}}$ and the condition $\dot{h}_{st}^{\mathrm{III}} = \dot{h}_{st}^{\mathrm{II}} + \dot{h}_{st}^{\mathrm{III}*}$, where $\dot{h}_{st}^{\mathrm{III}*}$ is the part of the degradation related to the collapse deformation. The creep velocities in part II and part III are different and the corresponding parameters c^{II} and c^{III} can be obtained using the relationship in (Equation 7). The comparison of the numerical result with the experiment in (Figure 3b) shows that the proposed model can simulate instantaneous settlements as well as long-term creep and collapse settlements in a unified manner.

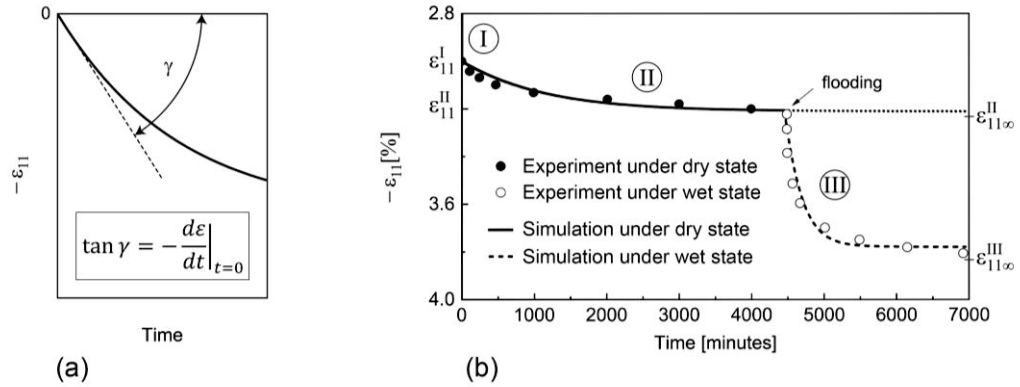

Figure 3. (a) Illustration of the initial inclination of the creep curve; (b) creep test under dry and wet conditions and a constant vertical stress of 0.8 MPa (experiments by Sowers et al., 1965)

Influence of the degradation of the solid hardness on the limit void ratios and critical void ratio
The range of possible void ratios is bounded by the maximum void ratio e_i and the minimum void ratio e_d. These limit void ratios as well as the critical void ratio e_c decrease with increasing pressure according to the postulate by (Gudehus, 1996), i.e.

$$\frac{e_i}{e_{io}} = \frac{e_c}{e_{co}} = \frac{e_d}{e_{do}} = \exp\left\{-\left(\frac{3p}{h_{st}}\right)^n\right\} . \tag{8}$$

It follows from (Equation 8) that a degradation of the solid hardness is connected with a decrease of the limit void ratios and the critical void ratio as illustrated by the dashed curves in (Figure 2b). This means that a degradation of the solid hardness leads to reduction of the pressure dependent stiffness and that the range of possible void ratios becomes smaller.

Embedding the concept of the solid hardness into hypoplasticity
In order to simulate the influence of degradation of the solid hardness for general loading paths, the hypoplastic constitutive model by (Bauer, 1996) and (Gudehus, 1996) was extended with an additional term to describe creep and stress relaxation in a unified manner. To take into account a degradation of h_{st} according to (Equation 2) the extended hypoplastic constitutive equation for the stress rate reads (Bauer, 2009):

$$\sigma_{ij}^{\triangledown} = f_s\,[\hat{a}^2\dot{\varepsilon}_{ij} + (\hat{\sigma}_{kl}\,\dot{\varepsilon}_{kl})\hat{\sigma}_{ij} + f_d\,\hat{a}(\hat{\sigma}_{ij} + \hat{\sigma}_{ij}^{*})\sqrt{\dot{\varepsilon}_{kl}\,\dot{\varepsilon}_{kl}}\,] + \frac{\dot{h}_{st}}{h_{st}}\left[\frac{1}{3}\sigma_{kk}\,\delta_{ij} + \kappa\sigma_{ij}^{*}\right]. \tag{9}$$

Herein the objective stress rate, $\sigma_{ij}^{\triangledown}$, is a non-linear function of the rate of deformation, $\dot{\varepsilon}_{ij}$, the effective Cauchy stress, σ_{ij}, its normalized quantity, $\hat{\sigma}_{ij} = \sigma_{ij}/\sigma_{kk}$, the deviatoric part $\sigma_{ij}^{*} = \sigma_{ij} - \sigma_{kk}\,\delta_{ij}/3$, its normalized quantity, $\hat{\sigma}_{ij}^{*} = \hat{\sigma}_{ij} - \delta_{ij}/3$, and factors f_s, f_d and $\hat{a}$. Factor $\hat{a}$ is a function of the friction angle, φ_c, and the invariants of the stress deviator according to the stress limit condition by (Matsuoka and Nakai, 1977) as shown in detail by (Bauer, 2000). The effect of pressure level and current void ratio on the incremental stiffness is taken into account with factors f_s

and f_d. In particular, the pressure dependent relative density factor f_d represents a relation between the current void ratio e, the critical void ratio, e_c and the minimum one e_d, i.e.

$$f_d = \left(\frac{e - e_d}{e_c - e_d} \right)^{\alpha} , \tag{10}$$

and the stiffness factor f_s reads:

$$f_s = \left(\frac{e_i}{e} \right)^{\beta} \frac{h_{st}}{\hat{\sigma}_{kl}\,\hat{\sigma}_{kl}} \frac{(1+e_i)}{n\,k_i\,e_i} \left(\frac{h_{st}}{3p} \right)^{n-1} \quad \text{with:} \quad k_i = 3\hat{a}_o^2 + 1 - \sqrt{3}\,\hat{a}_o \left(\frac{e_{io} - e_{do}}{e_{co} - e_{do}} \right)^{\alpha} . \tag{11}$$

Herein , α and β are constitutive constants (Bauer, 1996).

NUMERICAL SIMULATIONS

Comparison of the performance of the hypoplastic model with laboratory experiments

The 11 parameters involved in the hypoplastic constitutive model proposed were calibrated by (Bauer et al., 2012) to experimental data obtained by (Li, 1988) for a broken sandstone used in the Xiaolangdi dam in China. For the initially dry material the values of the parameters are: $\varphi_c = 40°$, $h_{so} = 47$ MPa, $n = 0.3$, $e_{io} = 0.59$, $e_{co} = 0.48$, $e_{do} = 0.20$, $\alpha = 0.18$ and $\beta = 2.50$. The additional constitutive constants for modelling the degradation of the solid hardness caused by wetting are: $h_{sw} = 11.5$ MPa, $\kappa = 0.7$ and $c = 3$ days.

The comparison of the results of the numerical simulations of triaxial compression tests with experiments is shown in (Figures 4a,b) for a lateral stress of -100 kPa and in (Figures 4c,d) for a lateral stress of -1000 kPa. As can be seen in (Figures 4a,c), the course of the deviatoric stress ($\sigma_{11} - \sigma_{33}$) and the volumetric strain ε_v against the axial strain ε_{11} is strongly influenced by the confining pressure and it is different for the dry and the water saturated materials. In (Figures 4b,d) the behaviour after water saturation at different deviatoric stresses is considered. As can be seen, the axial creep is more pronounced for a higher deviatoric stress while the inclination of volume strain curve is larger under a lower deviatoric stress. The volumetric creep paths are almost linear and also in good agreement with the experimental data for both lower and higher confining pressures.

Simulation of the long-term deformation of rockfill dams

The accumulated degradation rate, $\dot{h}_{st}$, of the solid hardness related to long-term creep, i.e. $\dot{h}_{st}^{\mathrm{II}}$, and to collapse settlements, i.e. $\dot{h}_{st}^{\mathrm{III}*}$, can be expressed by the following sum:

$$\dot{h}_{st} = \dot{h}_{st}^{\mathrm{II}} + \sum \dot{h}_{st}^{\mathrm{III}*} . \tag{12}$$

The evaluation of monitoring data of rockfill dams indicates that in contrast to long-term creep the effect of rain water infiltration on collapse settlements fades out with the number of rainfall events (Justo and Durand, 2000). This means that the number of wetting induced contributions of the second term in (Equation 12) are usually limited.

For the numerical simulation of the post-construction deformation an artificial concrete face rockfill dam is considered, with a height of 160 m and a slope ratio of 1:1.5 on both the upstream and downstream sides (Figure 5). The numerical simulation is carried out with the finite element program ABAQUS. The constitutive parameters are calibrated based on the experimental data obtained for a weathered broken granite. The large scale experiments were carried out by (Kast, 1992) and the calibration is described by (Bauer, 2009). For the dry material the values of the parameters are: $\varphi_c = 42°$, $h_{so} = 75$ MPa, $n = 0.6$, $e_{io} = 0.85$, $e_{co} = 0.39$, $e_{do} = 0.2$, $\alpha = 0.125$ and $\beta = 1.05$. With respect to a higher pre-compaction of the rockfill material the values for the wetted state of the material are assumed to be higher than in the experiments, i.e. $h_{sw} = 68.8$ MPa, $\kappa = 1.0$ and $c = 2$ years (Khosravi et al, 2017, 2018). For the compacted state of the rockfill material after construction a void ratio of 0.33 and a density of 2200 kg/m^3 is considered.

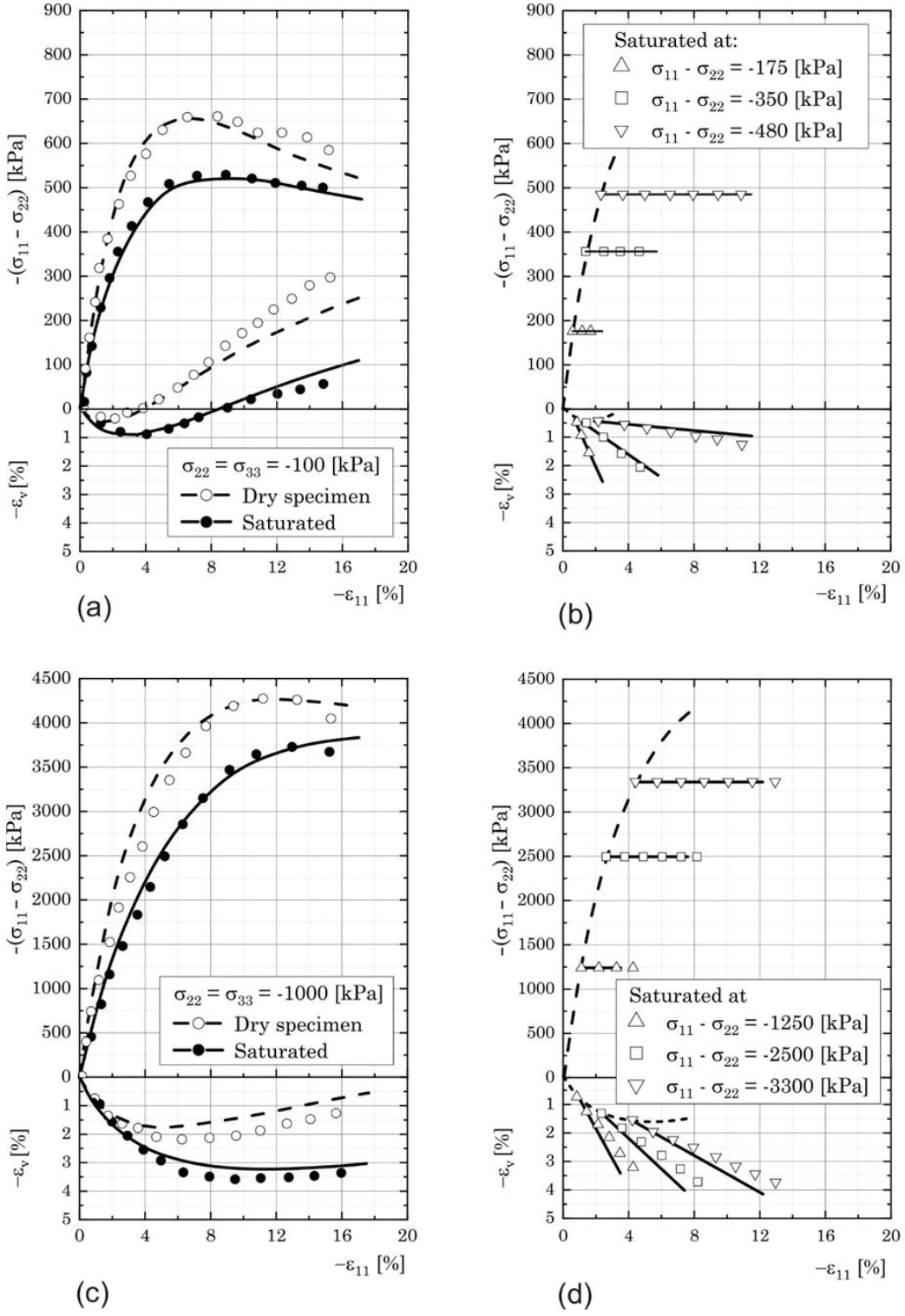

Figure 4. Response of broken sandstone under triaxial compression: dashed curves and solid curves are numerical responses for the dry and the water saturated specimens of broken sandstone, respectively (Bauer et al., 2012), shapes denote the experimental data by (Li, 1988)

(Figure 5a) shows the contours of the void ratio after water impounding, i.e. for the instantaneous deformation with $h_{so} = \text{constant}$. It is clearly visible that the reduction of the void ratio is pronounced in the upstream part of the dam body and concentrated close to the concrete slab. The change of the void ratio caused by water impounding and the degradation of the solid hardness over a period of 14 years is shown in (Figure 5b). The time dependent process of the degradation of the solid hardness

leads to an additional reduction of the void ratio, which is much higher compared to the instantaneous compaction and affects the whole dam body. In this context it is worth noting that for high rockfill dams the effect of rainwater infiltration on the rockfill material can be restricted to a certain area of the dam body (Khosravi et al., 2018) and that the prediction of post-construction deformation is usually a challenging task.

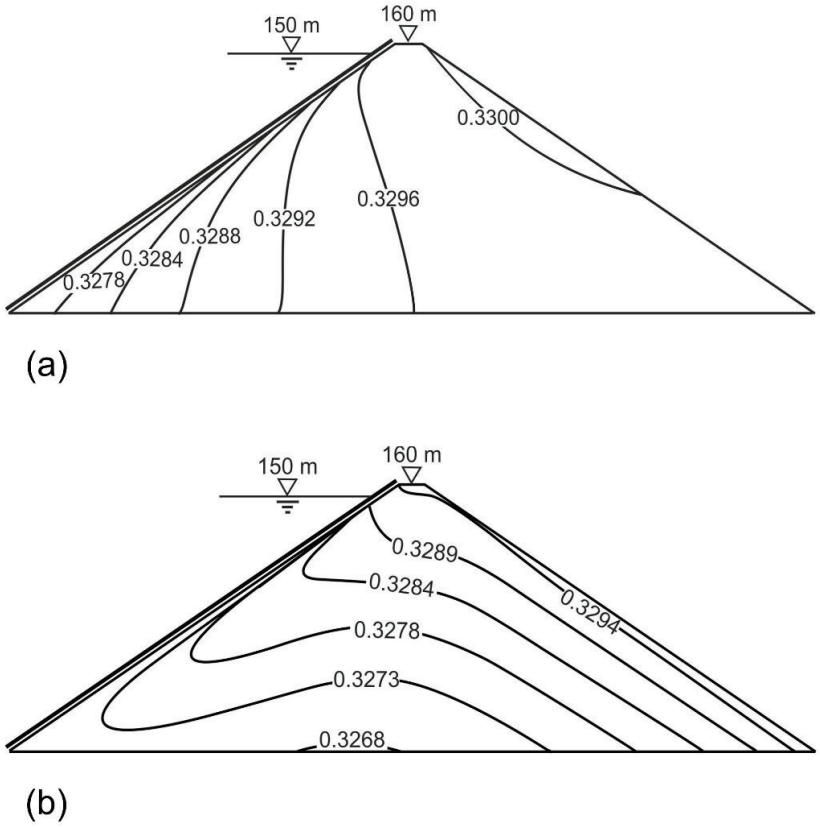

Figure 5. Contour of the void ratio of the rockfill material: (a) after water impounding; (b) with respect to water impounding and degradation of the solid hardness over a period of 14 years

CONCLUSION

In the present paper the mechanical behaviour of rockfill materials is modelled using an extended hypoplastic approach. Three different deformation mechanisms are distinguished: instantaneous deformations, collapse settlements and long-term deformations. The key parameters in the model are the solid hardness, which depends on the state of weathering, and the pressure dependent relative density. It is shown that for the calibration it is sufficient to consider the compression curves and creep curves obtained under isotropic or oedometric loading. The capability of the constitutive model proposed is demonstrated by comparing the results of numerical simulations with laboratory experiments. It is shown that the proposed model can simulate instantaneous settlements as well as long-term creep and collapse settlements in a unified manner.

AKNOWLEDGEMENTS

The author wishes to thank Dr. Z. Fu for the fruitful discussions and for providing extended numerical tools for some simulations. The assistance of Mr. S. Safikhani, Mr. L. Li and Mr. M. Khosravi in preparing the drawings presented in the paper is gratefully acknowledged.

REFERENCES

Abaqus 6.13, Dassault Systèmes Simulia Corp, Johnston, Rhode Island, United States.

Alonso, E. E., Oldecop, L. A., 2000. "Fundamentals of rockfill collapse". Proceediengs of the 1st Asian Conf. on Unsaturated Soils, (eds.) Rahardjo H., Toll DG., Leong EC., Balkema Press, Rotterdam, pp. 3-13.

Alonso, E. E., Cardoso, R., 2009. "Behaviour of Materials for Earth and Rockfill Dams: Perspective from Unsaturated Soil Mechanics". Proceedings of the 2nd Int. Conf. on Long Term Behaviour of Dams, (eds.) Bauer, Semprich and Zenz, Publisher by Verlag der Technischen Universität Graz, ISBN 978-3-85125-070-1, pp. 1-38.

Alonso, E. E., 2014. "Fracture mechanics and rockfill dams". Soils and Rocks, An International Journal of Geotechnical and Geoenvironmental Engineering, São Paulo, 37(1), pp. 3-35.

Bauer, E., 1995. "Constitutive modelling of critical states in hypoplasticity". Proc. of the 5th International Symposium on Numerical Models in Geomechanics, (eds.) Pande and Pietruszczak, Balkema press, pp. 15-20.

Bauer, E., 1996. "Calibration of a Comprehensive Hypoplastic Model for Granular Materials". Soils and Foundations, Vol. 36, N.1, pp. 13-26.

Bauer, E., 2000. "Conditions for embedding Casagrande's critical states into hypoplasticity". Mechanics of Cohesive-Frictional Materials, Vol. 5, pp. 125-148.

Bauer, E., 2009. "Hypoplastic Modelling of Moisture-Sensitive Weathered Rockfill Materials". Acta Geotechnica, Vol. 4, N.4, pp. 261-272.

Bauer, E., Fu, Z., Liu, S., 2010. "Hypoplastic Constitutive Modeling of Wetting Deformation of Weathered Rockfill Materials". Frontiers of Architecture and Civil Engineering in China, Vol. 4, N.1, pp. 78-91.

Bauer. E., Fu, Z., 2011. "Modeling of weathered and moisture sensitive granular materials". Proc. of the 9th International Workshop on Bifurcation and Degradation in Geomaterials. Eds: S. Bonelli, C. Dascalu, F. Nicot, Springer Series in Geomechanics and Geoengineering, pp. 333-338.

Bauer, E., Fu, Z., Liu, S. 2012. "Influence of pressure and density on the rheological properties of rockfills". Frontiers of Structural and Civil Engineering, 6, DOI 10.1007/s11709-012-0143-0, 25-34.

Bauer, E., Li, L., Khosravi, M., 2017. "Modelling grain damage under plane strain compression using a micro-polar continuum". In Proceedings of the 11th International Workshop on Bifurcation and Degradation in Geomaterials Dedicated to Hans Muhlhaus, Limassol, Cyprus, 21-25 May 2017, Papamichos, E., Papanastasiou, P., Pasternak, E., Dyskin, A. (eds.), Springer Series in Geomechanics and Geoengineering, DOI 10.1007/978-3-319-56397- 8, pp. 539-546.

Bauer, E., 2018. "Constitutive Modelling of Wetting Deformation of Rockfill Materials". International Journal of Civil Engineering, pp. 1-6, doi: 10.1007/s40999-018-0327-7.

Brauns, J., Kast, K., Blinde, A., 1980. "Compaction Effects on the Mechanical and Saturation Behaviour of Disintegrated Rockfill". Proceedings of International Conference on Compaction, Paris, Vol. 1, pp. 107-112.

Gudehus, G., 1996. "A Comprehensive Constitutive Equation for Granular Materials". Soils and Foundations, vol. 36, N.1, pp. 1-12.

Ham, T. G., Nakata, Y., Orense, R., ASCE, M., Hyodo, M., 2010. "Influence of Water on the Compressive Behavior of Decomposed Granite Soil". Journal of Geotechnical and Geoenvironmental Engineering, Vol. 136, N.5, pp. 697-705.

Hu, W., Frossart, E., Hicher, P. Y., Dano, C., 2009. "A new method to evaluate the mechanical behavior of granular material with large particles". Theory and validation. Proceedings of the 2nd Int. Conf. on Long Term Behaviour of Dams, (eds.) Bauer, Semprich and Zenz, Publisher by Verlag der Technischen Universität Graz, ISBN 978-3-85125-070-1, pp. 437-478.

Jaky, J., 1948, "Pressure in soils". Proc. 2nd ICSMFE, Rotterdam, Vol. 1, pp. 103-107.

Justo, J.L., and Durand, P., 2000. "Settlement-time behaviour of granular embankments". International Journal for Numerical and Analytical Methods in Geomechanics, 24(3), pp. 281–303.

Khosravi, M., Li, L., Bauer, E., 2017. "Numerical simulation of post-construction deformation of a concrete face rockfill dam". Proceedings of the 4th International Conference on Long-Term

Behaviour and Environmentally Friendly Rehabilitation Technologies of Dams, LTBD 2017, (eds.) Noorzad, A., Bauer, E., Ghaemian, M., Ebrahimian, B., Published by Verlag der Technischen Universität Graz, ISBN 978-3-85125- 564-5, pp. 307-314.

Khosravi, M., Li, L., Safikhani, S., Bauer, E., 2018. "Numerical simulations of the wetting effect on the long-term behavior of concrete face rockfill dams". Proceedings of the 5th International Symposium on Dam Safety, Istanbul, Turkey.

Kast, K., 1992. "Mechanisches Verhalten von Granitschuettungen". Veröffentlichungen des Institutes fuer Bodenmechanik und Felsmechanik der Universität Fridericiana in Karlsruhe, Heft 125.

Klammer, D., Dietzel, M., 2011. "Weathering of Natural Minerals and Rocks – Effect of Composition and Structure of Solids and Solution Chemistry". Proceedings of the 6th Int. Conf. on Dam Engineering, (eds) Pina, Portela and Gomes, Lisbon, Portugal.

Li, G. X., 1988. "Triaxial wetting experiments on rockfill materials used in Xiaolangdi earth dam". Research report from Tsinghua University.

Li, L., Wang, Z., Liu, S., Erich Bauer, E., 2016. "Calibration and performance of two different constitutive models for rockfill materials". Water Science and Engineering, 2016, Vol. 9, N.3, pp. 227-239.

Marsal, R.J., 1973. "Mechanical properties of rockfill". In: Embankment Dam Engineering. (eds.) Casagrande. R.C. Hirschfeld and S.J. Poulos, John Wiley & Sons, New York, pp. 109-200.

McDowell, G.R. and Bolton, M.D., 1998. "On the micromechanics of crushable aggregates". Géotechnique, 48:5, p. 667-679.

Matsuoka, H., Nakai, T., 1977. "Stress-Strain Relationship of Soil Based on the SMP". Proceedings of 9th ICSMFE, Constitutive Equations of Soils, pp. 153-162.

Nobari, E. S., Duncan, J. M., 1972. "Effect of reservoir filling on stresses and movements in earth and rockfill dams". Department of Civil Engineering, Report No. TE-72-1. University of California.

Oldecop, L. A., Alonso, E.E., 2001. "A model for rockfill compressibility". Géotechnique, Vol. 51, N.2, pp. 127-139.

Oldecop, L. A., de Agreda, E., 2004. "Testing Rockfill under Relative Humidity Control". Geotechnical Testing Journal, vol. 27, N.3, pp. 269-278.

Oldecop, L. A., Alonso, E.E., 2007. "Theoretical Investigation of the Time-Dependent Behaviour of Rockfill". Géotechnique, vol. 57, N.3, pp. 289-301.

Ovalle, C., Frossard, E., Dano, C., Hu, W., Maiolino, S., Hicher, P.Y., 2014. "The effect of size on the strength of coarse rock aggregates and large rockfill samples through experimental data". Acta Mechanica, Vol. 225(8), pp. 2199–2216, https://doi.org/10.1007/s00707-014-1127-z.

Ovalle, C., Dano, C., Hicher, P.Y., Cisternas, M., 2015. "Experimental framework for evaluating the mechanical behavior of dry and wet crushable granular materials based on the particle breakage ratio". Canadian Geotechnical Journal, vol. 52, pp. 587-598, https://doi.org/10.1139/cgj-2014-0079.

Sowers, G. F., Williams, R. C. and Wallace, T. S., 1965. "Compressibility of broken rock and settlement of rockfills". Proc. 6th ICSMFE, Montreal, Vol. 2, pp. 561-565.

5th International Symposium on Dam Safety

October 27-31, 2018

TWO-DIMENSIONAL DAM-BREAK FLOOD MODELING AND MAPPING FOR THE USA

Mustafa ALTINAKAR[1], Marcus MCGRATH[2], Vijay RAMALINGAM[3], James DEMBY[4], Gokhan INCI[5]

ABSTRACT

Developed by the National Center for Computational Hydroscience and Engineering, the University of Mississippi, DSS-WISE™ Lite is a web-based platform that provides web-based, automated dam-break flood modeling and mapping capability to the stakeholders of Dams Sector. DSS-WISE™ Lite system is accessed through the secure web portal DSS-WISE™ Web, which combines a map server with a graphical users interface for quickly setting up and lunching simulations, viewing the results of the simulations, and managing user groups. The numerical engine solves conservative form of full dynamic shallow water equations over complex topography using a state-of-the-art two dimensional finite volume model employing a shock-capturing upwind scheme. The funding for the development, and operation and maintenance of the capability and the web platform was provided by the U.S. Federal Emergency Management Agency (FEMA). The DSS-WISE™ Lite system has currently more than 600 accredited users from FEMA, other stakeholder federal agencies, ten FEMA regional offices, and the individual states. DSS-WISE™ Lite system is being used to track the hazard classification of dams, screening and prioritizing of dams, emergency action planning, and real-time operational modeling.

Keywords: Dam break flood, automated two-dimensional modeling, flood mapping, emergency.

INTRODUCTION

The label “Critical Infrastructure and Key Resources” (CIKR) refer to the assets of the United States essential to the nation's security, public health and safety, economic vitality, and way of life. U.S. Department of Homeland Security (DHS) defines (HSDP-7 2007 and PPD-21 2013) CIKR’s as “assets, systems, and networks, whether physical or virtual, so vital to the United States that their incapacitation or destruction would have a debilitating effect on security, national economic security, public health or safety, or any combination thereof.” The National Infrastructure Protection Plan (NIPP) integrates the wide range of efforts for the protection and resiliency of the eighteen CIKR’s identified by the DHS into a single national program. These eighteen CIKR form a highly interconnected and interdependent network. Failure in one of the CIKR may lead to cascading failures

[1] Research Professor, National Center for Computational Hydroscience and Engineering, University of Mississippi, University, MS, US, e-mail: altinakar@ncche.olemiss.edu
[2] Research & Development Engineer, National Center for Computational Hydroscience and Engineering, University of Mississippi, University, MS, US, e-mail: mzmcgrat@ncche.olemiss.edu
[3] Research Scientist, National Center for Computational Hydroscience and Engineering, University of Mississippi, University, MS, US, e-mail: virjay@ncche.olemiss.edu
[4] Senior Technical and Policy Advisor, National Dam Safety Program (NDSP), U.S. Federal Emergency Management Agency (FEMA), e-mail: james.demby@fema.dhs.gov
[5] Civil Engineer and Research Lead, National Dam Safety Program (NDSP), U.S. Federal Emergency Management Agency (FEMA), e-mail: gokhan.inci@fema.dhs.gov

in others. A large number of assets are owned by public and private entities. Thus, the management of risk and resiliency of CIKR requires a strong collaboration between federal, state, local, tribal, and territorial entities, and public and private owners and operators of critical infrastructure.

Dams are identified as one of the eighteen CIKR. They provide vital services such as flood protection, recreation, drinking water supply, water supply for industry and agriculture, hydroelectric power, waste management, river navigation, and wildlife habitat,. The failure of a dam, however, may lead to catastrophic floods with loss of life and property, disrupt the vital services it is providing, and cause cascading failures in other CIKR.

The need for a web-based automated, two-dimensional dam-break flood modeling and mapping capability, such as DSS-WISE™ Lite system presented in this paper, stems from the unique characteristics dam sector in the United States and the its specific challenges it is facing. There are currently 90,580 dams registered in the National Inventory of Dams (NID), which contain the records of all dams meeting at least one of the two criteria: 1) The dam has a height equal to or greater than 7.62 m (25 ft.) and the storage volume exceeds 18,502 m^3 (15 acre ft.); or 2) The storage volume exceeds 61,674 m^3 (50 acre ft.) and the dam height exceeds1.83 m (6 ft.). Embankment dams account for 86.4% of the dams. In the U.S., federal guidelines for dam safety (FEMA, 2004) adopt a hazard potential classification system with three categories based on the downstream consequences in case of failure or faulty operation. "Low hazard" dams are not expected to cause loss of life, and the economic and environmental losses are expected to be low and largely limited to owner. "Significant hazard" dams are not expected to cause loss of life either but they have the potential to cause substantial economic, environmental, and lifeline losses. "High hazard" classification is reserved for dams whose failure can potentially cause loss of life. These dams are expected to cause also considerable economic, environmental, and lifeline losses, but loss of life alone is sufficient for classifying a dam as high hazard. NID records show 15,5498 (17%) high hazard dams and 11,882 (13%) significant hazard dams. According to the law, an Emergency Action Plan (EAP) must be prepared for for high-hazard and significant-hazard dams. Despite significant efforts, about 19% of high hazard dams and 33% of significant hazard dams do not yet have an EAP. Considering the fact that many existing EAP's are either outdated or not prepared according to standards, it can be argued that the percentages of high-hazard and significant-hazard dams that do not have an EAP are probably higher.

One of the primary challenges is that 64% of the dams listed in the NID are privately owned. Often, the private owners do not fully understand their responsibility to ensure the safety of their dam or their liability in case of a failure. Moreover, many private owners do not have the financial resources to hire an engineering company to prepare an EAP. The situation is exacerbated by the fact that the hazard classification of dams may evolve in time based on new downstream development and other factors. Dam safety, however, is under the responsibility of the states. The state dam safety offices needed a robust and easy to use tool that can help them track the hazard classification of thousands of dams under their jurisdiction quickly, efficiently and economically. It was in response to this need that DSS-WISE Lite system was originally developed. Later, the exceptional computational performance of DSS-WISE Lite led federal agencies and state dam safety offices to adopt DSS-WISE Lite as a real-time emergency simulation tool for emergency response planning.

DESCRIPTION OF DSS-WISE WEB

DSS-WISE Lite capability is accessed via DSS-WISE Web portal hosted on a cluster at NCCHE[6]. The organizational chart of the portal is shown in Figure 1. Using an internet browser, the user connects to the secure portal by providing valid login credentials. Referring to Figure 1, the landing page provides access to three modules and the documentation page:

- "DSS-WISE Web Viewer" module is a map server with a graphical user interface. The viewer provides access to two different tools. "Terrain Profile Tool" allows the user to explore the based layer digital elevation model (DEM) by creating elevation profiles along the cross

[6] https://dsswiseweb.ncche.olemiss.edu/index.php

section lines that are drawn on the map by clicking the vertices of a polyline. The user can export the profile to a third party program such as a spreadsheet program, for further analysis. "DSS-WISE Lite Prep Tool" is a user interface to set up and submit user-defined dam break simulations quickly and efficiently by responding to a minimum set of questions.

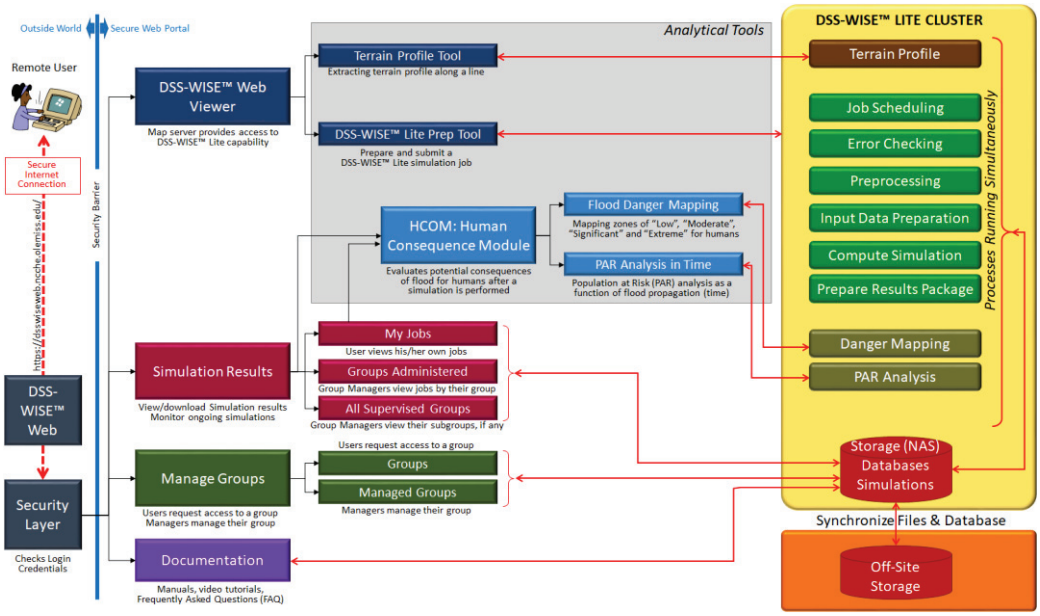

Figure 1 Organizational chart of DSS-WISE Web portal.

- "Simulation Results" module offers three options. "My Jobs" option provides access to the list of all simulations launched by the user. The user can click on a simulation to activate the "Status and Results" page which displays the flood extent on a map for viewing and allows user to download the results produced by DSS-WISE Lite. While the simulation is running, the flood extent is refreshed every 5 minutes to allow the user to monitor results. After the simulation is completed, the maximum flood extent is displayed. The options "Groups Administered" and "All Supervised Groups" are only available to group managers. The first allows a group manager to see the list of all simulations performed by the members of the group, and download the results. The latter allows the group manager to see the list of the subgroups of the group he/she is managing. The group manager, however, cannot view or download the results of the subgroups. The concept of group and group manager will be explained in the next subsection.
- "Manage Groups" offers two options. "Groups" option is available to all users and allows them to request membership to a group. "Managed Groups" option is only available to group managers and it allows them to manage the group (accepting or rejecting membership requests, removing users from membership, etc.)

A number of processes running simultaneously under the "DSS-WISE Lite Cluster" handle all simulations submitted by users. "Job Scheduling" handles the flow of submitted jobs. "Error Checking" verifies the data provided by the user to make sure that there are no errors. "Preprocessing" parses the input data, populates the appropriate fields in the databases, and places the simulation job in the input-data preparation queue. "Input Data Preparation" processes the jobs waiting in this queue sequentially. It automatically prepares all the input data files required by the DSS-WISE Lite computational engine. When the input files are successfully completed, the job is placed in the simulation queue. "Compute Simulation" processes the simulations waiting in the queue sequentially. Once the simulation is completed, "Prepare Results Package" analyzes the final results files to prepare the final report in PDF format, loads results files on the network attached storage (NAS) and makes them available for download on the "Status and Results" page.

Self-Managing User Groups

In order to run simulations on the DSS-WISE Lite system, the user has to be the member of at least one user group. The hierarchical structure of the groups is shown in Figure 2. NCCHE is the system administrator at "LEVEL 0". "FEMA HQ" group is at the root ("LEVEL 1") of the tree structure and has an oversight on the entire system. The "LEVEL 2" contains the groups for nine federal agencies and ten FEMA regional offices. The states under the jurisdiction of each FEMA regional office are "LEVEL 3" of the tree structure. FEMA Region 9 has also a technical assistance group for two counties in California, which are located at "LEVEL 4". In addition, the group "CALIFORNIA" has a special subgroup called "CA-NODES", which allows running simulations using their private compute-servers that are located at NCCHE. Each group is assigned a specific geographic area. The federal agencies are assigned the entire USA. The groups of FEMA regional offices are assigned the entire area of the states under their jurisdiction. The groups for the states are assigned the entire territory of the state and the counties the entire area of the county.

Each group is managed by a group manager approved by FEMA HQ. The group manager decides to approve or reject membership requests submitted to the group. The simulation is launched under a specific group and the simulation belongs to the group. The user who launched the simulation has access to the results of the simulation as long as he/she remains a member of the group. The group manager can access the results of all the simulations performed by the group members. The manager of a group can see the list of all the simulations launched by its subgroups, but cannot access the results.

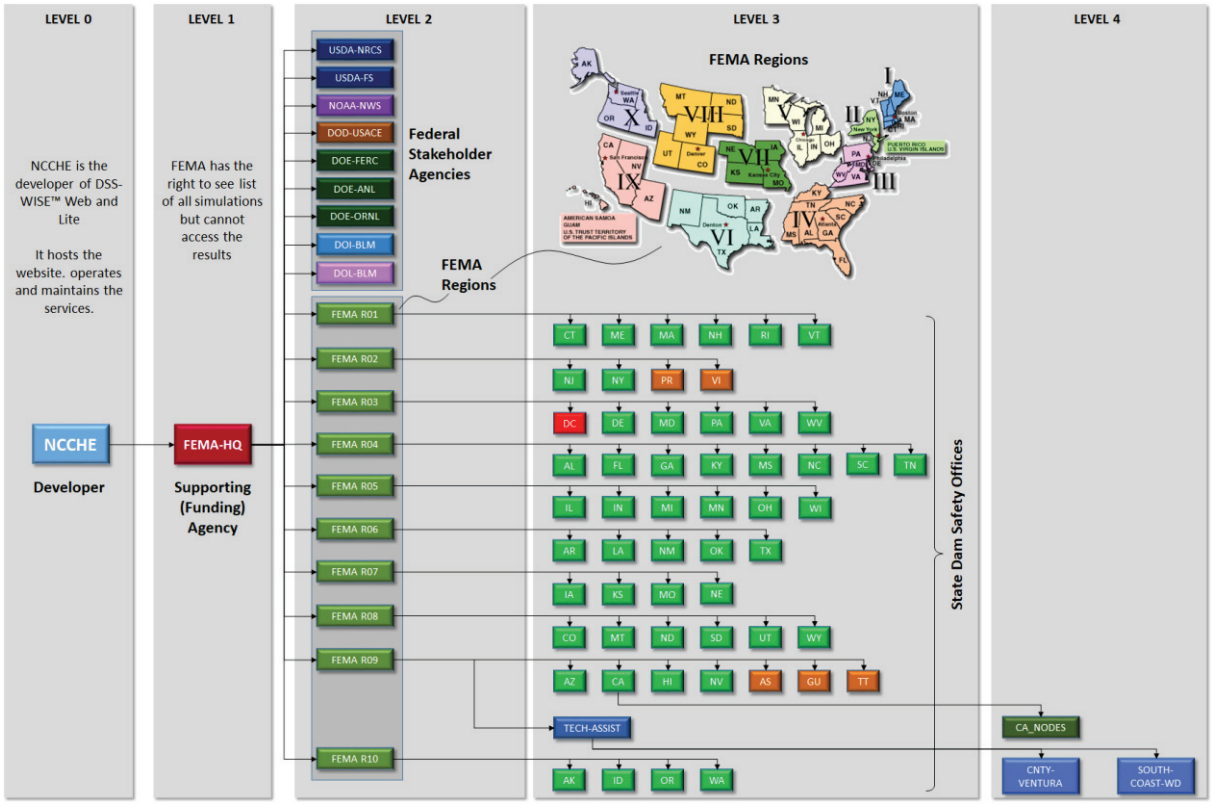

Figure 2. Hierarchical structure of self-managed user groups.

PREPARING AND LAUNCHING A DAM-BREAK SIMULATION USING DSS-WISE LITE

DSS-WISE Web Viewer

"DSS-WISE Web Viewer" shown in Figure 3 has two panels. The right panel is the map panel and initially displays a background layer provided by OpenStreetMap. The left panel displays two tabs. The "Modules" tab provides access to "DSS-WISE Lite Prep Tool" and the "Elevation Profile Tool". The "Layers" tab allows user to control the "Base Layers" and the "Overlay Layers" that are displayed

in the map panel. Base layers are mutually exclusive and only one of them can be displayed at a given time. The user can display any number of overlay layers simultaneously and modify their stacking order any time. The floating window in the foreground is the DSS-WISE Lite Prep tool window, which allows the user to set up and submit a dam break simulation. It has been activated by clicking on the "DSS-WISE Lite Prep Tool" button.

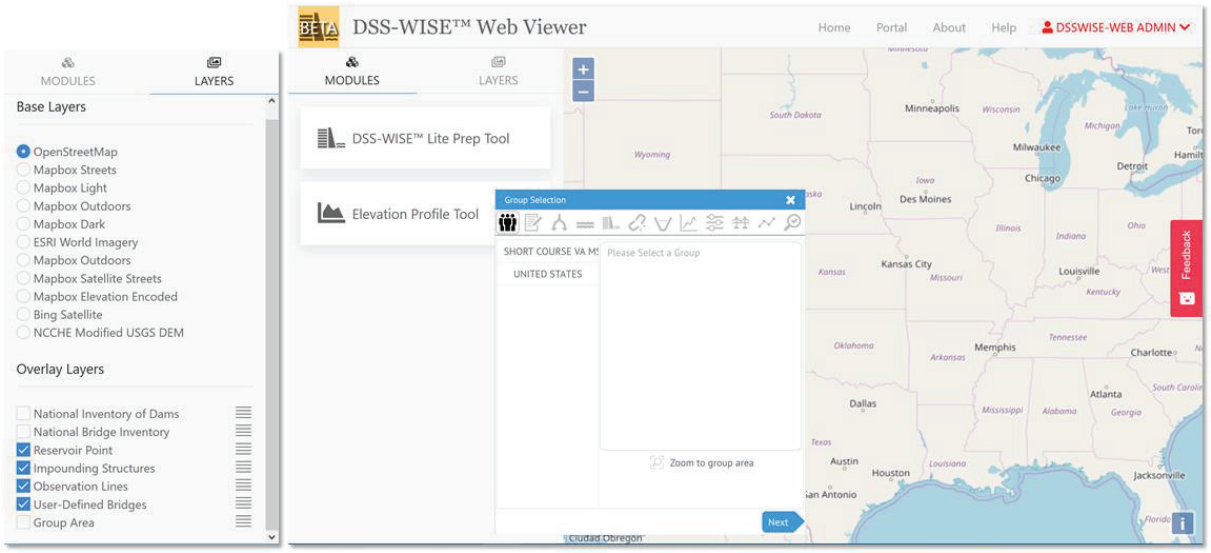

Figure 3 DSS-WISE Web Viewer with DSS-WISE Lite Prep Tool activated. The contents of Layers tab is shown on the left.

DSS-WISE Lite Prep Tool

DSS-WISE Lite Prep Tool (Figure 3) is a graphical user interface (GUI) for setting up and submitting two-dimensional (2D) dam break flood simulations by answering a minimal set of questions grouped under 12 data entry tabs, which are displayed side by side under the blue ribbon. The GUI is designed to provide an intuitive environment with real-time error checking to guide the user during the simulation setup process. The user advances from one tab to the next in a sequential order from left to right. However, it is possible to return to any previous tab any time to modify the data fields. Table 1 lists the input data the user is expected to enter under each tab:

1. Tab No 1 allows the user to select the group under which the simulation will be submitted.
2. Tab No 2 gathers the metadata that will help identify the simulation later. Optionally, if the simulated dam is registered in the NID, the simulation can be linked to its NID ID number.
3. Tab No 3 asks the user to choose the type of simulation. In "Reservoir-Type" simulation, the reservoir is represented as a water body with a user-defined water surface elevation. When the dam is breached the impounded water flows downstream. The breach discharge passing over the dam crest line is recorded as computed breach hydrograph. In "Hydrograph-Type" simulation, however, the reservoir is not modeled. The user provides a breach hydrograph (time vs. discharge pairs), which is imposed at the toe of the dam and propagated downstream.
4. Under Tab No 4, the user identifies the location of the reservoir by clicking a point in the reservoir on the map. Storage volume and elevation pairs for maximum and normal pool levels are entered only in case of reservoir-type simulations.
5. The impounding structures are defined under Tab No 5. All structures impounding a reservoir must be defined by providing its type, hydraulic height, and crest elevation. Each impounding structure is also located geospatially by drawing a polyline following its crestline on the map.
6. Tab No 6 defines the conditions at failure. For reservoir-type simulations, pool elevation and storage volume at the time of failure are entered. These are then used to fill the reservoir up to the specified volume. The breach center is defined for both reservoir-type and hydrograph-type simulations because it identifies the structure to be breached. In this tab, the user is asked to choose one of the two breach types. "Total Breach" option assumes that the entire dam disappears suddenly and completely and the original estimated valley profile is recovered.

"Partial Breach" option assumes that the dam breaches over a specified width and the failure occurs during a specified formation time. The latter requires additional information, which are provided by the user in the following tab.

Table 1 List of input data to be entered under different tabs.

Tab #	Tab Name	Data Field	R = Required; O = Optional			
1	Group Selection	Choose "Group"	R		R	
2	Scenario Description	Project Name	R		R	
		Scenario Name	R		R	
		Scenario Description	R		R	
		NID ID	O		O	
3	Simulation Type	Select "Simulation Type"	Reservoir-Type		Hydrograph-Type	
4	Reservoir Information	Click "Upstream Point"	R		R	
		Max. Storage Elevation	R			
		Max. Storage Volume	R			
		Normal Storage Elevation	R			
		Normal Storage Volume	R			
5	Impounding Structures (as many as necessary)	Name	R		R	
		Type (Emb., Gravity, Arch)	R		R	
		Hydraulic Height	R			
		Crest Elevation	R		R	
		Draw "Dam Crest Line"	R		R	
6	Conditions at Failure	Reservoir Storage Elevation	R			
		Reservoir Storage Volume	R			
		Click "Breach Center"	R		R	
		Choose "Breach Type"	Total Breach	Partial Breach	Total Breach	Partial Breach
7	Partial Breach Information	Breach Bottom Elevation		R		
		Breach Width		R		R
		Formation Time		R		
8	Breach Hydrograph	Breach Hydrograph			R	R
9	Simulation Parameters	Cell Size	R	R	R	R
		Downstream Distance	R	R	R	R
		Simulation Duration	R	R	R	R
10	Bridges (as many as necessary)	Click "Bridge Center"	O	O	O	O
		Name	O	O	O	O
		Span Length	O	O	O	O
11	Observation Lines (up to 10)	Name	O	O	O	O
		Draw "Observation Line"	O	O	O	O
12	Review and Submit	Verify Input Data and Submit	R	R	R	R

7. Under Tab No 7, breach bottom elevation, breach width and breach formation time are specified if the user has chosen a reservoir-type simulation with partial failure. If the user has chosen hydrograph type simulation with partial failure, only the breach width is specified.
8. The Tab No 8 is activated only if the user has chosen a hydrograph-type simulation. The user enters the time discharge pairs in a tabular form.
9. The Tab No 9 allows the user to set the simulation parameters, which are Cell Size, Downstream Distance, and the Simulation Duration. Cell Size can range from 6.1 to 61 m (20 to 200 ft.). Downstream Distance can range from 8 to 627 km (5 to 390 miles). The Simulation Duration can be varied from 1 day to 60 days. The selected combination of these parameters define the computational effort and duration. In general, the smaller cell size, the longer the downstream distance and the simulation duration, the greater is the computational effort and longer the duration of computations. The total allowed wall-time for a simulation is 24 hours due to limited computational resources. This limits is imposed to prevent long

waiting times. If the simulation is not completed within 24 hours, and if there are other jobs waiting in the queue, the simulation is terminated earlier than the scheduled end time, and the final-results files are written. Therefore, the user must choose a reasonable combination of the simulation parameters.

10. DSS-WISE Lite system uses 1/3 arc-second digital elevation model tiles prepared by U.S. Geological survey as the base map layer. In these tiles, normally the bridge decks have been removed to create a passage for the flow of water. Any bridges that may have remained can be removed using Tab No 10. The user identifies the bridge by clicking its center on the map and provides the span width that must be cleared. As many bridges as necessary can be defined.
11. Observation lines are polylines defined by the user by drawing them on the map using Tab No 11. They represent cross sections of interest. DSS-WISE Lite extracts discharge and cumulative volume passing over each cross section as a function of time and writes into a separate comma separated value (csv) file. The user can define up to 10 observation lines. In reservoir-type simulations, the polyline representing the crest line of the breached structure is automatically treated as an additional observation line that provides the breach hydrograph.
12. Tab No 12, allows the user to review and correct, if necessary, the input data entered under different tabs before the simulation is submitted to the system. The user can display and verify the storage volume curve generated by the system by fitting a cubic spline to the entered volume elevation pairs (normal pool, maximum pool and failure pool), and the zero volume elevation computed by subtracting hydraulic height from maximum pool elevation. The simulation is submitted to the DSS-WISE Lite Cluster by clicking on the submit button.

Automated Input Data Preparation

All input files needed by the DSS-WISE Lite computational engine are generated automatically by a process running on DSS-WISE Cluster.

1. Using the USGS 1/3 arc-second USGS DEM tiles, the computational grid is prepared as a virtual raster covering a square area with the dam at its center. The edge length of the square domain is twice the downstream distance specified by the user. The virtual raster allows the program to reference the large source tiles at the specified cell size without the need to mosaic them beforehand. During the simulation, as the flood propagates, the individual portions of the DEM are loaded into the memory when they are needed. The operations of mosaicking, warping, and resampling at the user specified cell size are performed on the fly.
2. The National Levee Database contains the data roughly for 29,000 km (18,000 miles) of levees. If there are any levees in the computational domain, these are burned into the topography at the specified cell size with the appropriate levee crest elevations.
3. In reservoir-type simulation, the water surface that is usually represented in the DEM tiles as a quasi-flat topography is removed. The unknown reservoir bed topography hidden by the water surface is estimated using specially developed skeletonization optimization with the constraint that at the failure elevation, the volume of the estimated topography will be the same as the failure volume specified by the user.
4. The cells are assigned Manning's roughness coefficients based on the classified land use/cover data from the National Land Cover Database 2011 (NLCD 2011)[7]. The seamless classified land use/cover map the default Manning's roughness values for the 21 land use/cover classes are listed in Figure 4. These default values are assigned to the computational cells.
5. For reservoir-type simulations the reservoir is initialized by filling it up to the specified failure elevation. The downstream is considered dry by assuming a sunny day simulation.
6. Outflow boundary conditions is defined at the edges of the computational domain.

Status and Results Page

The Status and Results page lists all the simulations performed by the user. The status of each simulation is indicated (input data preparation queue, simulation queue, simulation running, simulation completed). The user can click on any simulation to display the corresponding Simulation Status and Results page, as shown in Figure 5. The viewer panel on the upper left displays the computed flood

[7] http://www.mrlc.gov/nlcd2011.php

extent. During the simulation, the flood extent polygon shows the current extent, which is updated every five minutes. After the completion of the simulation, only the maximum flood extent polygon is displayed. The right panel provides information on the simulation. The files available for download are listed below the map viewer panel. The results package include the following files: 1) Final report in PDF format; 2) shape file of the inundation extent polygon; 3) Google Earth KMZ file of the final inundation extent; 4) combined polygon shapefile of arrival time; 5) combined polygon shapefile of maximum flood depth; 6) collection of point and polyline shapefiles of input data and extended structure lines; 7) collection of comma separated value (csv) files of hydrographs at observation lines; 8) DEM of the inundated area; 10) Raster files of arrival time, maximum flood depth, final flood depths at the end of the simulation maximum specific discharge, arrival time of maximum specific discharge, maximum velocity. Raster files and shapefiles can be opened using any GIS[8] software.

Color Code	Class Code	n ($m^{-1/3}s$)	Short Description
	0	0.0350	Unclassified
	11	0.0330	Open Water
	12	0.0100	Perrenial Snow / Ice
	21	0.0404	Developed, Open Space
	22	0.0678	Developed, Low Intensity
	23	0.0678	Developed, Medium Intensity
	24	0.0404	Developed, High Intensity
	31	0.0113	Barren Land
	41	0.1000	Deciduous Forest
	42	0.1000	Evergreen Forest
	43	0.1200	Mixed Forest
	51	0.0350	Dwarf Scrub*
	52	0.0400	Shrub/Scrub
	71	0.0400	Grassland/Herbaceous
	72	0.0350	Sedge/Herbaceous*
	73	0.0350	Lichens*
	74	0.0350	Moss*
	81	0.0350	Hay/Pasture
	82	0.0700	Cultivated Crops
	90	0.1500	Woody Wetlands
	95	0.1825	Emergent Herbaceous Wetlands

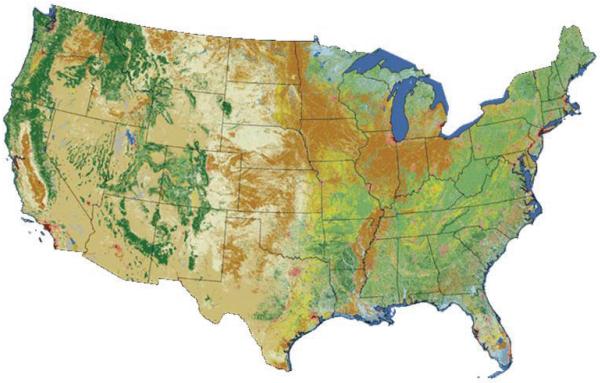

Figure 4 NLCD 2011 land use classification and the default Manning's coefficients assigned to each land use/cover class.

[8] Geographic Information System

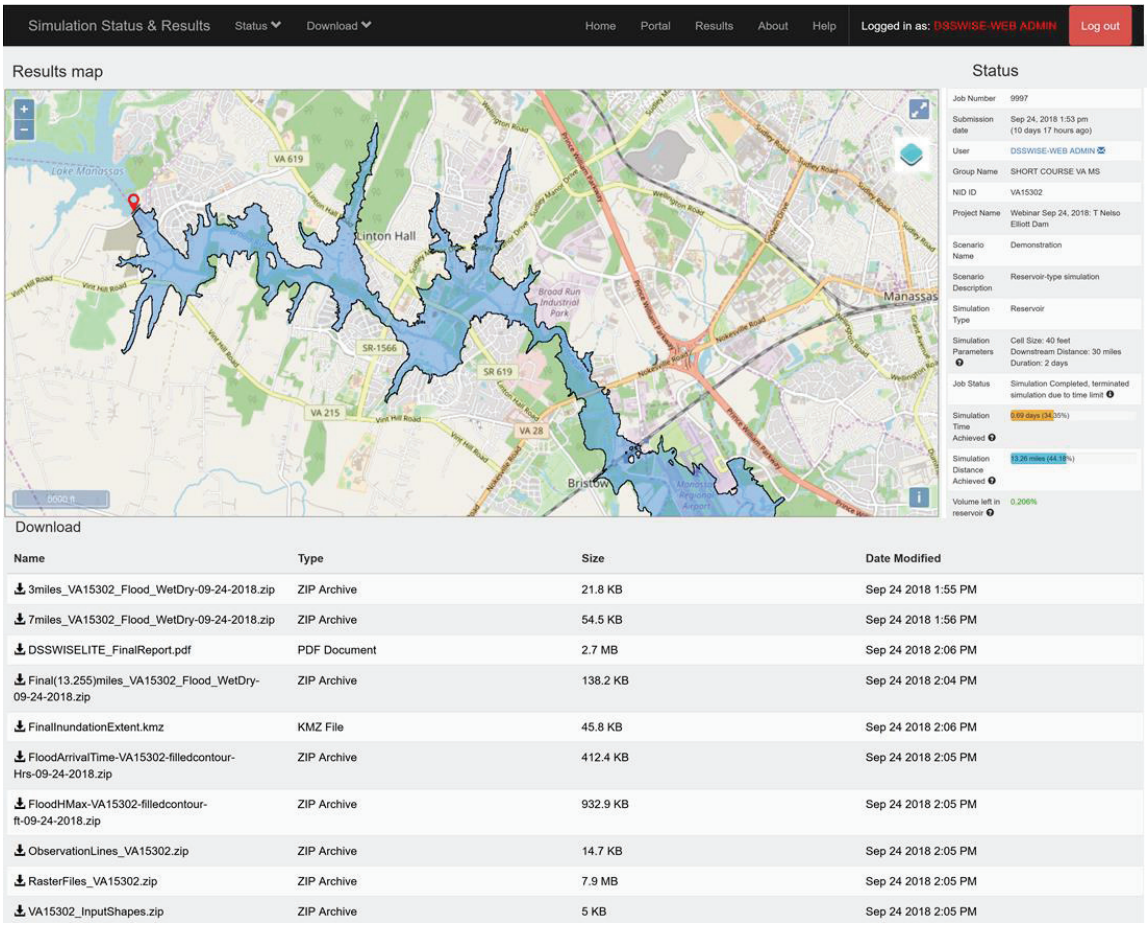

Figure 5 Simulation Status and Results page.

COMPUTATIONAL ENGINE OF DSS-WISE LITE

Governing Equations of Free-Surface Flows

The two-dimensional full dynamic shallow water equations (2D-SWE) that govern the propagation of flood over complex natural topography form a system of three nonlinear partial differential equations

$$\begin{aligned} \frac{\partial h}{\partial t} + \frac{\partial hu}{\partial x} + \frac{\partial hv}{\partial y} &= q_v \\ \frac{\partial hu}{\partial t} + \frac{\partial (huu + gh^2/2)}{\partial x} + \frac{\partial huv}{\partial y} &= -ghS_{fx} - gh\,\frac{\partial z_b}{\partial x} \\ \frac{\partial hv}{\partial t} + \frac{\partial huv}{\partial x} + \frac{\partial (hvv + gh^2/2)}{\partial y} &= -ghS_{fy} - gh\,\frac{\partial z_b}{\partial y} \end{aligned} \tag{1}$$

The first equation is the conservation of mass. The second and third equations are the equations of conservation of linear momentum in in x- and y-directions, which define the horizontal plane. The direction z is perpendicular to the horizontal plane. Referring to the definition sketch in to Figure 6a, t represents time, z_b the bed elevation with respect to a datum, h the flow depth, and g the gravitational acceleration. The friction slopes in x- and y-directions, S_{fx} and S_{fy}, respectively, are expressed using the Manning's roughness coefficient, n, as follows:

$$S_{fx} = \frac{un^2\sqrt{u^2+v^2}}{h^{4/3}} \quad \text{and} \quad S_{fy} = \frac{vn^2\sqrt{u^2+v^2}}{h^{4/3}} \tag{2}$$

The system of three nonlinear partial differential equations can be written in vector form as follows

$$\frac{\partial \tilde{U}}{\partial t} + \frac{\partial \tilde{F}(\tilde{U})}{\partial x} + \frac{\partial \tilde{G}(\tilde{U})}{\partial y} = \tilde{S}(\tilde{U}) \tag{3}$$

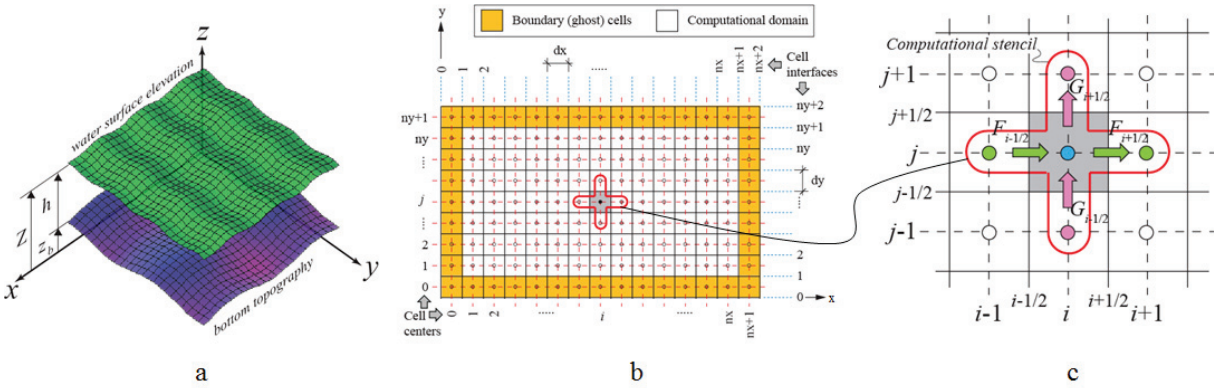

a b c

Figure 6. (a) Definition sketch; (b) regular Cartesian mesh used as computational grid; and (c) enlarged view of the computational stencil.

The vector of conserved variables, $\tilde{U}$, the vectors of the fluxes in x- and y-directions, $\tilde{F}(\tilde{U})$ and $\tilde{G}(\tilde{U})$, respectively, and the vector of source terms due to friction and topography are given as:

$$\tilde{U} = \begin{bmatrix} h \\ hu \\ hv \end{bmatrix} \quad \tilde{F}(\tilde{U}) = \begin{bmatrix} hu \\ huu + gh^2/2 \\ huv \end{bmatrix} \quad \tilde{G}(\tilde{U}) = \begin{bmatrix} hv \\ hvu \\ hvv + gh^2/2 \end{bmatrix} \quad \tilde{S}(\tilde{U}) = \begin{bmatrix} q_v \\ -ghS_{fx} - gh\dfrac{\partial z_b}{\partial x} \\ -ghS_{fy} - gh\dfrac{\partial z_b}{\partial y} \end{bmatrix} \tag{4}$$

Discretization of Governing Equations

Finite-volume discretization of Equation (3) over the regular Cartesian mesh shown in Figure 6b, leads to the following explicit algebraic expression

$$\tilde{U}_{i,j}^{m+1} = \tilde{U}_{i,j}^{m} - \left(\frac{\Delta t}{\Delta x}\right)\left(\tilde{F}_{i+\frac{1}{2},j}^{m} - \tilde{F}_{i-\frac{1}{2},j}^{m}\right) - \left(\frac{\Delta t}{\Delta y}\right)\left(\tilde{G}_{i,j+\frac{1}{2}}^{m} - \tilde{G}_{i,j-\frac{1}{2}}^{m}\right) + \Delta t \tilde{S}_{i,j}^{m} \tag{5}$$

The bed elevation, z_b, the flow depth h, and the specific discharges hu and hv are defined at the center of square cells of size $dx = dy$. Equation (5) is a vector equation that expresses three equations, one for each of the three conserved variables, h, hu and hv. Thus the system is closed and Equation (5) can be used to solve for the new values of the conserved variables $\tilde{U}_{i,j}^{m+1}$ at time step $m+1$ based on their known values $\tilde{U}_{i,j}^{m}$ at the current time step m. Referring to Figure 6b and c, the discretized fluxes in x-direction, $\tilde{F}_{i+\frac{1}{2},j}^{m}$ and $\tilde{F}_{i-\frac{1}{2},j}^{m}$, are defined at the east and west intercell boundaries whereas the discretized fluxes in x-direction, $\tilde{G}_{i,j+\frac{1}{2}}^{m}$ and $\tilde{G}_{i,j-\frac{1}{2}}^{m}$, are defined at the north and south intercell boundaries. The method used to calculate these intercell fluxes based on the values of conserved variables at the center of the cells forming the computational stencil (Figure 6c) is extremely important and defines the properties of the numerical scheme.

Numerical Scheme Used in DSS-WISE Lite

DSS-WISE Lite uses a first-order Godunov-type (Godunov, 1959, and Godunov et al., 1976) upwind scheme. Piecewise constant representation of the conserved variables in each cell leads to a Generalized Riemann Problem (GRP) (Toro, 1999 and 2001) across each intercell boundary. In the present context, the GRP corresponds to a generalized dam-break problem across the edge separating two neighboring cells. The classical dam-break problem constrains the water at the upstream and downstream of the dam to be stagnant. In the generalized dam-break problem, this constrained is

relaxed. The dam-break problem transforms into a discontinuity in flow depth and/or specific discharge perpendicular to the edge. The solution of the GRP problem provides the discretized intercell flux during the time step Δt.

Various methods are available to solve the GRP. DSS-WISE Lite uses the approximate HLLC Riemann solver (Toro et al., 1992, and Toro et al., 1994), which is a modified version of the HLL (Harten, Lax and van Leer) approximate Riemann solver originally proposed by Harten et al., 1983. The letter "C" stands for the "*contact wave*", such as a scalar quantity across the discontinuity. The version of HLLC implemented in DSS-WISE Lite implicitly handles wetting and drying interfaces. A linearization technique is used to handle large topographic source terms that may arise due to complex natural topography. More detailed information can be found in Altinakar et al., 2012.

Characteristics of the Numerical Code and its Validation

The numerical code developed using the techniques described in the previous paragraphs of this section is robust and reliable, which is extremely important when developing a web-based automated system. The implemented upwind scheme handles wetting and drying fronts and simultaneous presence of mixed flow regimes (subcritical, transcritical, and supercritical) in the computational domain, and captures shocks (i.e. discontinuities), such as standing or traveling hydraulic jumps. The implemented HLLC scheme does not require any entropy fixes to avoid convergence to non-physical solutions. The computational engine is parallelized to achieve high computational performance on commodity compute servers with multi-core architecture. To further increase the computational speed, the computational domain is partitioned into regions that are loaded into memory only when needed, and special data structures are implemented to track and calculate only wet cells and their neighbors.

The computational engine of DSS-WISE Lite has been verified using analytical solutions and validated based on laboratory experiments and field data from past experiments (Altinakar et al., 2010). In a blind study undertaken in collaboration with U.S. Army Corps of Engineers, sunny day failure of five selected dams using DSS-WISE Lite were compared with simulations using 1D HEC-RAS and FLO-2D (Altinakar et al., 2012).

PERFORMANCE STATISTICS OF DSS-WISE LITE

The cumulative number of DSS-WISE Lite simulations submitted to the system are plotted in Figure 7. The insert shows a map of the locations of the simulations. DSS-WISE Lite was released for general use on Nov 8, 2016. Since then, the number of simulations has been increasing steadily. At the time of writing this article (Sep 22, 2018), the total number of simulations handled was 9633. The system handles about 25 simulations per day.

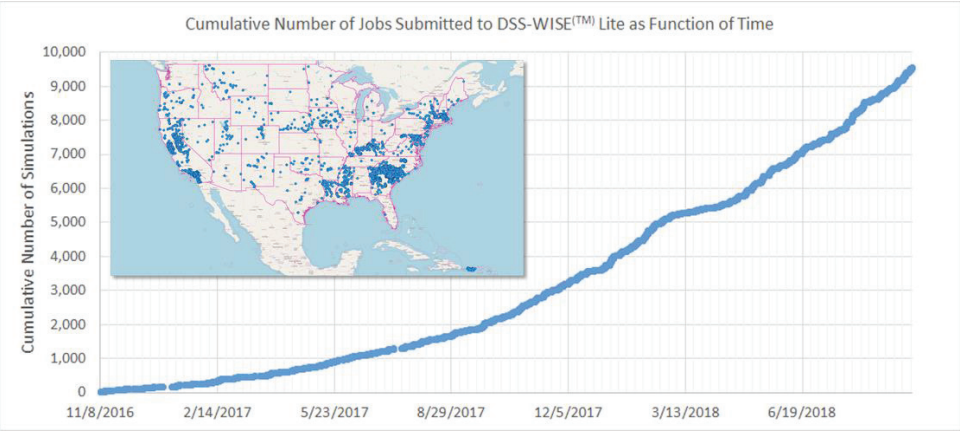

Figure 7 Evolution of the number of simulations submitted and their location on the map.

The statistical analysis provides the following information:

1. 97% of the simulations are specified with a downstream distance of 75 miles or shorter,

2. 49.2% of the simulations cover an inundation area less than 100,000 cells whereas 99.6% of the simulations have an inundation area less than 5,000,000 cells. The largest simulation had an inundation area of 19,000,000 cells.
3. 74.6% of the simulations have a specified cell size less than or equal to 9.15 m (30 ft.).
4. For 79% of the simulations, the automated input data preparation took less than 1 minute.
5. For 85.1% of the simulations, the final results were made available within ½ hour after the user clicked the submit button.
6. 75.1% of the simulations are being carried out with computational speeds 100 to 1,000 times faster than reality.

CONCLUSIONS

In less than two years, DSS-WISE Lite has quickly become an invaluable computational tool at the service of dam safety engineers and emergency managers in FEMA and its regional offices, stakeholder federal agencies, and state dam safety offices. Several states have adopted DSS-WISE Lite as the principal tool for their dam safety program. The large number of simulations successfully performed by the DSS-WISE Lite system shows that it is robust and can handle even complex simulation setups. Automated input data preparation tools have been continuously refined over time to handle various types of special situations encountered. The success rate for the simulations that are accepted into the simulation queue is almost 100%. Some simulations are rejected during input data verification. The rejections are mostly due to erroneous elevation data entered by the user, or the problems with the accuracy of the 1/3 arc-second USGS DEM tiles. New development work is now being undertaken to make use of higher resolution DEM products developed by the USGS, and the LIDAR based DEM products that can be provided by the individual states. Ability to set up simulations quickly using DSS-WISE Lite Prep Tool and the exceptional computational speed has led the users to adopt DSS-WISE Lite as a real-time operational model that can be used during emergencies. DSS-WISE Lite was used extensively to run real-time emergency simulations during various incidents. Some of the examples are 1) Oroville Dam spillway incident in California, in February 2017; 2) inundations in Texas due to Hurricane Harvey in August 20017; 3) emergency simulations of 37 dams in Puerto Rico due to Hurricane Maria (September 2017); and 4) inundations and dam failures in South Carolina and North Carolina due to Hurricane Florence (September 2018), etc.

ACKNOWLEDGEMENTS

It is gratefully acknowledged that the funding for the development of the DSS-WISE™ Lite and DSS-WISE™ Web and its operation and maintenance was provided by the U.S. Department of Homeland Safety (DHS), Federal Emergency Management Agency (FEMA) through a 5-year sole-source contract. DHS-FEMA also provided additional funding for the development of the Elevation Profile Tool module and for organizing short courses and webinars. We also gratefully acknowledge two additional funding sources: 1) the Division of Safety of Dams (DSOD) of the California Department of Water Resources has provided additional funding for the development of a new version with numerous additional capabilities to be released in 2019; and 2) U.S. Department of Energy, Argonne National Laboratory (ANL) provided funding for the development of a new module for the assessment of human consequences of dam-break floods and the preparation of flood hazard maps.

REFERENCES

Altinakar, M.S., McGrath, M.Z., Matheu, E.E., Ramalingam, V.P., Seda-Sanabria, Y. Breitkreutz, W., Oktay, S., Zou, J.Z., Yezierski, M. (2012). Validation of Automated Dam-Break Flood Simulation and Assessment of Computational Performance. Proceedings of the Dam Safety 2012, ASDSO Annual Conference, September 16-20, Colorado Convention Center, Denver, CO.

Altinakar, M.S., McGrath, M.Z., Ramalingam, V.P. and Omari, H. (2010). 2D Modeling of Big Bay Dam Failure in Mississippi: Comparison with Field Data and 1D Model Results. Proc. of the Int. Conference on Fluvial Hydraulics (River Flow 2010), September 8-10, Braunschweig, Germany.

Altinakar, M.S. and McGrath, M.Z., 2012. Parallelized Two-Dimensional Dam-Break Flood Analysis with Dynamic Data Structures. ASCE-EWRI, 2012 World Environmental & Water Resources Congress, Albuquerque, New Mexico, May 20-24, 2012.

FEMA, 2004. Federal Guidelines for Dam Safety: Hazard Potential Classification System for Dams. Prepared by the Interagency Committee on Dam Safety. U.S. Federal Emergency Management Agency, Report No: FEMA 333, April, 2004.

Godunov, S.K., 1959. A Difference Scheme for Numerical Solution of Discontinuous Solution of Hydrodynamic Equations. Math. Sbornik, 47, 271–306, transl. US Joint Publ. Res. Service, JPRS 7226, 1969.

Godunov, S.K., Zabrodine, A., Ivanov, A., 1976. Résolution numérique des problèmes multidimensionnels de la dynamique des gaz. Editions MIR de Moscou, 1976.

Harten, A., Lax, P., van Leer, D., 1983. On Upstream Differencing and Godunov-type Methods for Hyperbolic Conservation Laws. SIAM Review 25, pp. 35–61.

Homer, C.G., Dewitz, J.A., Yang, L., Jin, S., Danielson, P., Xian, G., Coulston, J., Herold, N.D., Wickham, J.D., and Megown, K. (2015). Completion of the 2011 National Land Cover Database for the conterminous United States-Representing a decade of land cover change information. Photogrammetric Engineering and Remote Sensing, v. 81, no. 5, p. 345-354.

HSPD-7 (2007). Homeland Security Presidential Directive 7 on “Critical Infrastructure Identification, Prioritization, and Protection”. December 17, 2003. https://www.energy.gov/sites/prod/files/HSPD-7.pdf

PPD-21 (2013). Presidential Policy Directive 21 on Critical Infrastructure Security and Resilience. February 12, 2013. https://www.dhs.gov/sites/default/files/publications/PPD-21-Critical-Infrastructure-and-Resilience-508.pdf.

Toro, Eleuterio F., 1999. Riemann Solvers and Numerical Methods for Fluid Dynamics. Berlin: Springer Verlag.

Toro, E.F., 2001. Shock-Capturing Methods for Free-Surface Shallow Flows. Wiley and Sons Ltd., Chichester, U.K.

Toro, E.F., Spruce, M., Speares, W., 1992. Restoration of the Contact Surface in the HLL–Riemann Solver, Technical Report CoA–9204, Department of Aerospace Science, College of Aeronautics, Cranfield Institute of Technology, UK.

Toro, E.F., Spruce, M., Speares, W., 1994. Restoration of the contact surface in the HLL-Riemann Solver. Shock Waves, Volume 4, No 1, pp. 25-34.

5th International Symposium on Dam Safety

October 27-31, 2018

Probabilistic Cracking, Ageing and Shaking of Concrete Dams

V.E. Saouma[1]
M.A. Hariri-Ardebili[2]

Abstract

Through various illustrations, this two-parts paper will highlight methodology to perform risk based safety assessment of concrete dams. In the first part State-of-the-Art deterministic analysis procedure to address dam cracking, aging (through alkali-aggregate reaction), or seismic excitation is presented. In the second part, a paradigm to perform probabilistic investigation of the above is presented through sensitivity and uncertainty quantification of existing aleatoric and epistemic uncertainties. End result will be a fragility curve that assess damage/failure probability in terms of a selected ground motion intensity measure.

keywords: Seismic analysis; nonlinear analysis; Fragility Curve; Concrete Dam, Earthquake. Uncertainty, Damage

Introduction

With increased understanding of local seismicity, and resulting new regulations there is a concern that many dams previously deemed to be safe under extreme cases may no longer be. Furthermore, many dams built in the ∼50's are aging and show sign of alkali aggregate reaction (AAR). Both conditions could result in structural cracking. Finally, given the various uncertainties assoiated with both capacity and demands, it is becoming imperative to assess dam safety through a probabilistic prism.

This paper, will report the experience of the authors in the development, implementation and usage of modern computational techniques to perform nonlinear safety assessment of dams based on the State of the Art and not necessarily conform with "established" methods.

First modeling techniques for a deterministic analysis will be addressed for cracking, aging and shaking of dams. Then related probabilistic methods will be presented. Equations will be avoided to the extent possible, and emphasis will be placed on qualitative explanations.

Nonlinear Deterministic Analyses

The limitations of a linear elastic analysis are highlighted in Figure 1(a) where the adoption of a linear analysis may result in a very expensive proposition if the ultimate response is to be captured, or (more importantly) it is dangerous in capturing the full nonlinear response where displacements/strains are invariably much higher than those predicted by a linear one. Furthermore, one should be attentive to the holistic nature of a nonlinear analysis, as ultimately it would be just as good as the weakest consideration, Figure 1(b).

Hence, following is a brief description of the model deemed to be appropriate by the authors for a "modern" nonlinear analysis of concrete dams.

[1]Professor, Dept. of Civil Engineering, University of Colorado, Boulder CO USA; Partner X-Elastica.com
e-posta: saouma@colorado.edu
[2]Post-Doctoral Research Associate, Dept. of Civil Engineering, University of Colorado, Boulder CO USA; Partner X-Elastica.com
e-posta: mohammad.haririardebili@colorado.edu

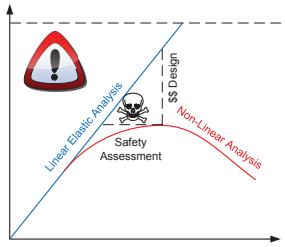

(a) Dangers of linear elastic analysis of a structure with a nonlinear response

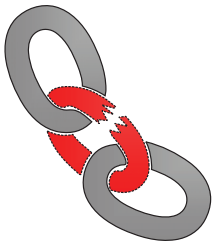

(b) Analysis is as accurate as its weakest link

Figure 1: Concerns with nonlinear analysis

Cracking

Cracking are unavoidable consequences of strong demand on dams once elastic limits have been reached. Crack models in concrete fall into two categories: smeared and discrete. The former has been extensively used in dams, though it is best when multiple cracks are present (as in reinforced concrete structures). in particular through the model of . However, it is well known that this model has been unable to localize a crack, and as a result one ends u with a "cloud" of cracked elements. Typically those models are based on the theory of plasticity or damage mechanics, and have to be "tweaked" to somehow localize. Many authors have used the model of Lee and Fenves (1998), which has exhibited convergence problems in implicit analyses. As such, this model is often used in explicit codes resulting in very fine mesh, and a lack of insurance that indeed convergence has been reached (explicit codes are much more forgiving than the implicit ones).

The other crack model (preferred by the authors) is the so-called discrete crack where a discontinuity in the mesh is introduced. This model is rooted in nonlinear fracture mechanics Hillerborg, Modéer, and Petersson (1976), and is most appropriate when few cracks are present such as along the base or at lines of discontinuity in a dam. Furthermore, uplift pressure can readily be accounted for and can be automatically adjusted with the progression of the crack.

In the following analysis, Figure 2(a) there is an extensive use of fracture mechanics based interface elements to model vertical joints, and the rock-concrete interface, Figure 2(b). At first those joints are "zipped" together, and they open or slide when a hyperbolic failure criteria (accounting for combined tensile and shear failures) is met. It should be noted that there is no need for adaptive remeshing in these analysis as (most often) it is unlikely that new cracks will develop in the concrete, since the joints constitute "fuses" which would open first and redistribute the stresses.

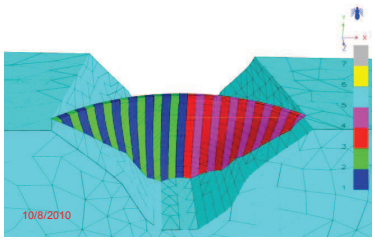

(a) Dam

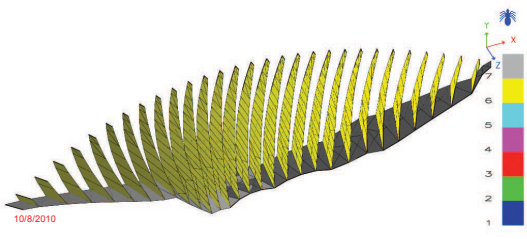

(b) Explicitly defined interface elements modeling all the joints

Figure 2: Nagawado Dam

In another case study, an old gravity dam, Figure 3(a), raised much concern to the surrounding

population in light of its apparent deterioration. Much silt had accumulated, it was overtopped numerous times, and simple 2D rigid body analysis failed to yield a sufficiently high factor of safety against sliding.

(a) Old gravity dam

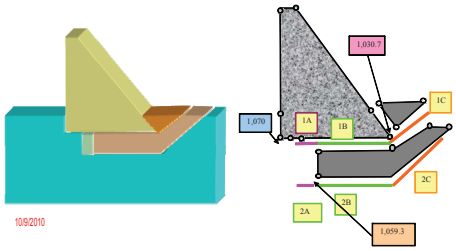

(b) Potential failure modes

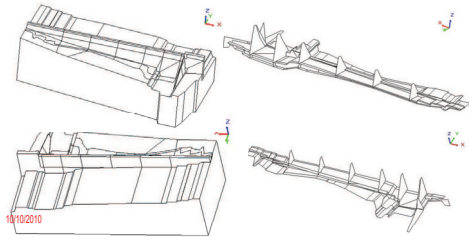

(c) Idealization

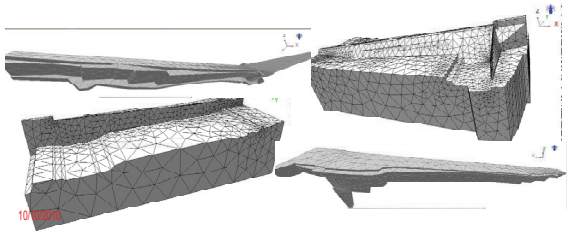

(d) FE mesh

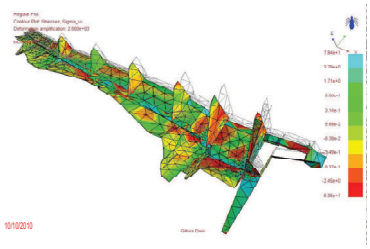

(e) Vertical joints and potential failure joints

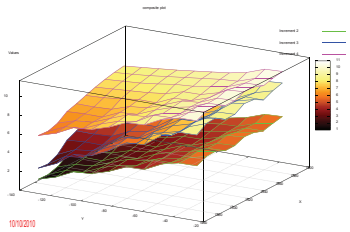

(f) Uplift pressures

Figure 3: Old gravity dam

A particularly challenging aspect was the complex geometry: the dam had a shear key, is partially built under existing rock, and has complex geometry which includes a stiff wall at one end.

Hence, the first task was to identify potential failure modes. Fig. 3(b) is an idealization of the two most likely one. The first cuts across the shear key, goes along the rock/concrete interface and then daylights at approximately 45 degrees. The second assumes a strong shear key, and failure initiates below it, propagates horizontally, and then again daylights at about 45 degrees. To further complicate matters, this was a 3D analysis with not only varying longitudinal geometry , but also spatially varying rock properties (cohesion, angle of friction). Idealization is shown in Figure 3(c), while the actual mesh is shown in Figure 3(d), and the joints (deformed shapes) are in Fig. 3(e).

Given the complex geometry, it was critical to ensure that the mesh was indeed well put together. This was critical as if two nodes across a potential failure modes are not connected by an interface element (i.e. tightly coupled), then no failure would occur (albeit close examination of the deformed shape and stress contour would reveal an irregularity). This was ensured by applying a sufficiently high hydrostatic load upstream to trigger "failure", and thus ascertain that the potential failure modes can be captured.

Another complexity is the ability to adjust uplift pressures automatically as the crack develop, and most importantly translate the results of a finite element analysis into a safety factor

against sliding. The first was addressed by the computer program, and Fig. 3(f) is a graphical representation of the 3D uplift distribution between two parallel vertical joints in terms of the hydrostatic pressure. The second resulted in a slight modification of our computer program to compute the safety factor. In 2D hand calculations, the safety factor can be easily determined from SF=$cL_{uncr}+\Sigma F_v \tan\phi/\Sigma F_h$. In the 3D analysis, this was far more complex to determine, as cohesion, angle of frictions, total horizontal and vertical forces all varied spatially and the vertical had to also include the effects of the uplift pressures. However the inclusion of the interface elements along the failure path greatly facilitated this task as all the required quantities were state variables of the code. Nevertheless, another question was to differentiate between localize (single Gauss point) safety factor *versus* the average one based on the integration over a certain area (such as in between two adjacent vertical joints).

Seismic Modeling

Modern nonlinear seismic modeling is best illustrated through a a few figures.

Given that modeling the dam foundation with its mass, the seismic excitation (applied at the base of the foundation must be determined from recorded surface ones. This identification requires a deconvolution process illustrated by Fig. 4(a) where a sequence of pre-analyses are needed and fast fourrier transforms (FFT) are involved.

Once the base excitation is identified, modeling requires two other important features: radiation damping and accountability of the excitation of the so-called free-field (the infinite part of the foundation outside the one explictly modeled by the finite element mesh). Whereas the first has often been (quite successfully and easily) modeled by dash-pots dampers (Lysmer and Kuhlemeyer, 1969), the second is more problematic. In this context, the first author has proposed a simple model that proved very successful Saouma et al. (2011) and is schematically illustrated by Fig, 4(c). Essentially, this requires a series of separate analyses of the external free field with either only horizontal or vertical excitation. Displacements and velocities are then transferred to dash-pots and springs that in turn apply them to the foundation.

Another important consideration in the seismic analysis the separation of static from dynamic analysis. Whereas associated with each one of them are separate sets of elastic properties, the dynamic analysis must be performed as a restart from the static one to account for the built-in state of stress before the earthquake occurs (particularly important in a non-linear analysis where the principle of superposition can not be applied).

In this context one must consider the impact of rocking. The dam's center of gravity being offset from the base, the numerical model must accommodate for it through: a) zero thickness interface elements along the dam-foundation interface; and b) a change in the boundary conditions associated with the base. This last step entails the provision of base support during the static analysis phase as they are needed to provide stability through reactions. In the subsequent dynamic phase, those supports are removed, and the reactions are in turn applied as nodal forces at the base of the foundation.

Finally, uplift merits also special consideration. Too often, and erroneously, models adopt an uplift distribution that accounts only for the presence of a drain, but not for the crack propagation. Indeed, the location of the crack front will substantially alter the uplift pressure distribution (Dewey, Reich, and Saouma, 1994; Slowik and Saouma, 2000), and this may affect results locally (which is the most fragile part of the dam: rock/concrete interface). Hence uplift pressure should be updates within each increment of a nonlinear analysis as shown in Fig. 5(a).

As to dynmaic uplift, the problem has been recognized for many years but experimental data are very scarce. During a seismic excitation, the crack is subjected to opening and closure. During ipening, there is a negative pressure that will "suck" the water out, while during closure the fluid inside the crack will act as a wedge resulting in a substantially increased uplift, Fig. 5(b).

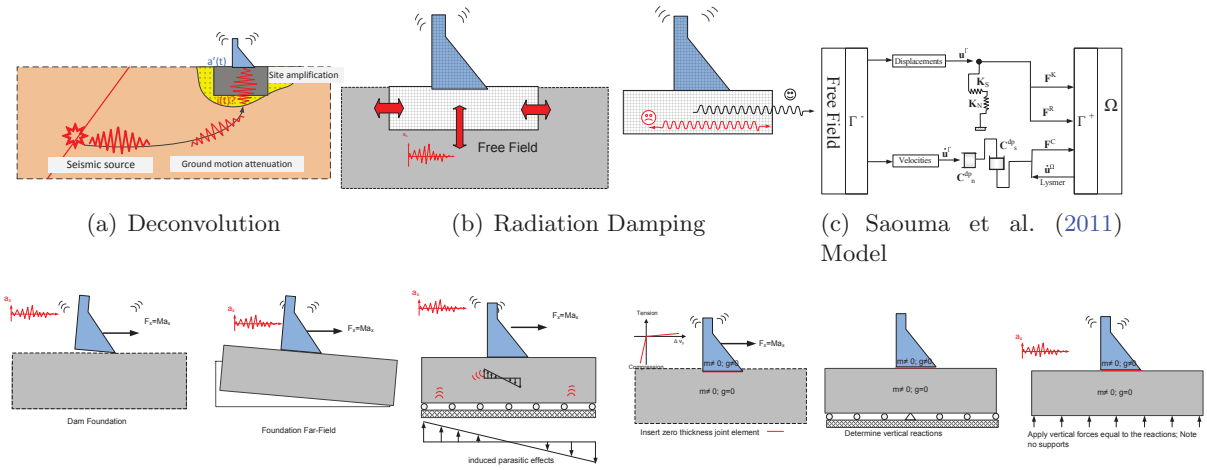

(a) Deconvolution (b) Radiation Damping (c) Saouma et al. (2011) Model

(d) Rocking; Problem (e) Rocking; Solution

Figure 4: Nonlinear analysis methodology

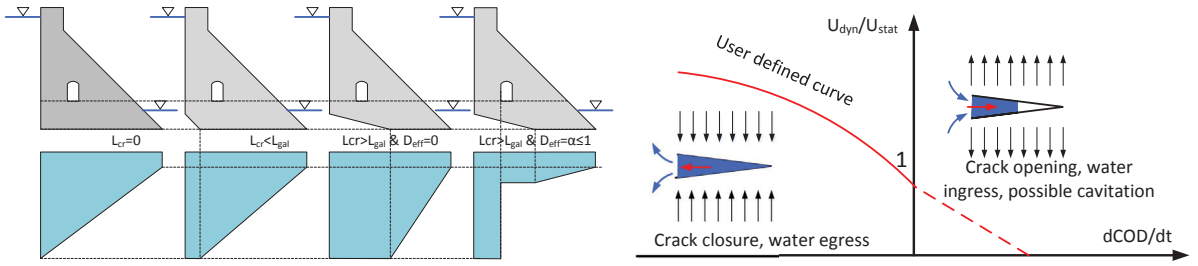

(a) Static (b) Dynamic

Figure 5: Uplift models

Modeling AAR

Many old concrete structures suffer from alkali aggregate reactions (AAR) which result in volumetric expansion. Whereas this may be merely a nuisance for small structures, it is of major concern in massive concrete ones as the constrained expansion is likely to result in structural cracking, inability to operate spillway gates, or worst yet misalignment of the turbines.

		January		February		March		April		May		June	
Incr.		**6.00**	**7.00**	**7.00**	**8.00**	**9.00**	**10.00**	**11.00**	**12.00**	**13.00**	**14.00**	**15.00**	**16.00**
Body force		dam											
Hydrostatic	**Pool Elevation**	1596.47	1593.53	1593.53	1592.94	1590.59	1589.71	1588.24	1586.76	1591.47	1598.24	1602.65	1604.00
	Incremental Elevation	-5.03	-2.94	0.00	-0.59	-2.35	-0.88	-1.47	-1.47	4.71	6.76	4.41	1.35
Uplift	**Pool Elevation**	1596.47	1593.53	1593.53	1592.94	1590.59	1589.71	1588.24	1586.76	1591.47	1598.24	1602.65	1604.00
	Incremental Elevation	-5.03	-2.94	0.00	-0.59	-2.35	-0.88	-1.47	-1.47	4.71	6.76	4.41	1.35
Temperature [°C]	**Air**	-3.10	-2.14	-1.67	-1.43	0.24	1.90	2.14	2.38	4.76	6.90	8.10	8.81
	Water	1.00	1.00	1.00	1.00	1.00	1.50	3.00	3.00	5.00	6.00	8.00	8.00

		July		August		September		October		November		December	
Incr.		**17.00**	**18.00**	**19.00**	**20.00**	**21.00**	**22.00**	**23.00**	**24.00**	**25.00**	**26.00**	**27.00**	**28.00**
Body force		dam											
Hydrostatic	**Pool Elevation**	1602.35	1602.65	1602.65	1602.65	1600.59	1595.29	1595.88	1593.24	1596.76	1598.53	1598.24	1601.50
	Incremental Elevation	-1.65	0.29	0.00	0.00	-2.06	-5.29	0.59	-2.65	3.53	1.76	-0.29	3.26
Uplift	**Pool Elevation**	1602.35	1602.65	1602.65	1602.65	1600.59	1595.29	1595.88	1593.24	1596.76	1598.53	1598.24	1601.50
	Incremental Elevation	-1.65	0.29	0.00	0.00	-2.06	-5.29	0.59	-2.65	3.53	1.76	-0.29	3.26
Temperature [oC]	**Air**	9.76	10.24	11.43	12.38	11.43	10.24	6.67	3.57	0.95	-1.19	-2.62	-4.05
	Water	9.00	10.00	11.00	11.00	11.00	8.50	6.00	4.00	3.00	3.00	2.00	1.00
AAR	**AAR**	**Activated**											

Figure 6: Data preparation, cyclic load

AAR is a very slow thermodynamically driven reaction, and many years (over 20) may pass before the dam instrumentation can with certainty indicate that we are in presence of an irreversible deformation (typically upstream, and a crest elevation).Though nothing can stop this reaction, it is of paramount importance for dam owner to assess the evolution (kinetics) of

the swelling with appropriate models, (Saouma and Perotti, 2006). Of critical importance is the right and timely application of the various incremental loads in an AAR analysis. This is illustrated by Figure 6 where the sequence of loads is looped for many years.

(a) Arch dam suffering from AAR

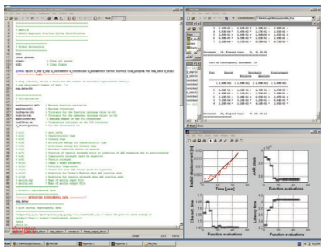

(b) GUI of system identification process

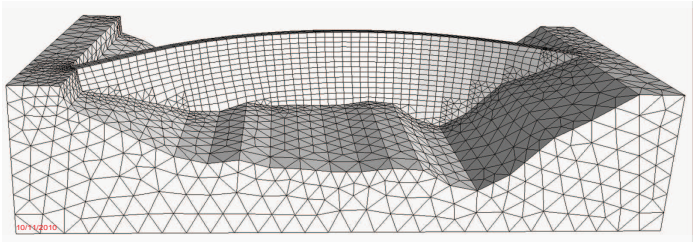

(c) Finite element mesh

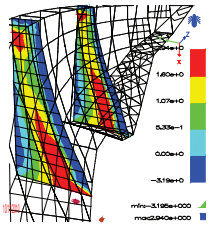

(d) Internal Stress contour plots

(e) Observed cracks along internal the gallery and inside a borehole

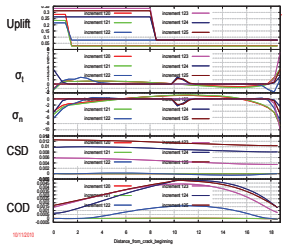

(f) COD, CSD, uplift, σ_n and σ_t

Figure 7: Arch gravity dam suffering from AAR

Figure 7(a) is an arch dam suspected of suffering from AAR (it turned out not to be AAR but another chemically induced reaction in the concrete which results in a volumetric expansion too). The AAR model (Saouma, 2013)is in terms of three critical material properties, maximum AAR induced volumetric strain, latency and characteristic times. However whereas those parameters can not be determined from laboratory testing for an existing structure, and since all we have is the historical record of the crest displacement, a system identification procedure must be used. Fig. 7(b) is the graphical user interface of a Matlab based program which automatically seeks to determine the three material properties by minimizing the square of the error between computed and recorded displacements. It should be noted that each analysis entails a full 3D, 20 years simulations of the dam with 3 months time increments. Fig. 7(c) is the finite element mesh used. It should be noted that vertical joints were not modeled, however it was deemed indispensable to model the rock concrete interfaces with interface elements. Fig. 7(d) shows the internal stresses, and we note the zone of high tensile stresses in the center which may result in some hidden cracks. Indeed a crack was observed along the gallery, and a borehole drilled to determine its extent, Fig. 7(e), as it had not "daylighted" on the downstream face (yet). More details can be found in (Saouma, Perotti, and Shimpo, 2007).

It should be noted that this analysis was preceded by a transient thermal analysis to determine

internal temperatures at three months interval. Subsequently, input data entailed a 20 years simulation in which temporal variation of thermal load, pool elevation, and uplift pressures had to be accounted for.

Finally, it has always been a matter of concern that concrete properties are extracted from few concrete cylinders, and then applied to an entire dam. Hence, the impact of heterogeneity of concrete properties, hereby referred to QoI for quantity of interest (which can be any user defined value) can be analyzed by first identifying a mean value and its coefficient of variation. Then the properties will be randomly assigned to elements while retaining quantum values acceptable.

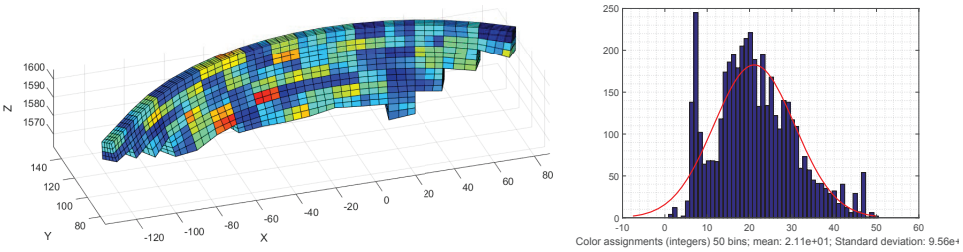

(a) Final QoI assignment

(b) Actual QoI distribution in generated mesh

Figure 8: HMG

Probabilistic Considerations

Next-Generation of PBEE

In 1997 the Pacific Earthquake Engineering Research Center (PEER) decided to develop a more robust methodology for performance-based earthquake engineering, called as next generation PBEE (also called as PBEE-2 or PEER PBEE). The PEER PBEE framework developed by PEER facilitates direct calculation of the effects of uncertainty and randomness on each step in the performance based procedure (Porter, 2003).

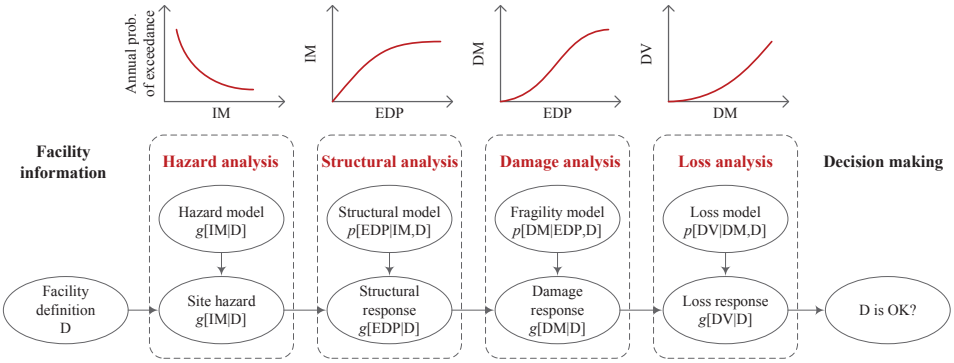

Figure 9: General framework of PEER PBEE methodology (Porter, 2003)

The general framework for PEER PBEE is shown in Figure 9. It breaks the seismic performance assessment into four primary steps: 1) ground motion hazard characterization, 2) structural response analysis, 3) damage analysis, and 4) loss assessment (Haselton et al., 2008). The results of each of these steps are represented as generalized variables, Intensity Measure (IM), Engineering Demand Parameter (EDP), Damage Measure (DM), and Decision Variable (DV).

Seismic Hazard Analysis

Seismic design of many structures, especially critical infrastructures such as dams needs to a clear vision on seismic potential of the region that the structure is going to be constructed. Parameters such as importance of the structure, risk of the failure, financial concerns, and even the technological problems may affects the method of the seismic hazard analysis. Figure 10(a) shows the different steps that are required for seismic hazard analysis of a concrete dam in context of the PBEE.

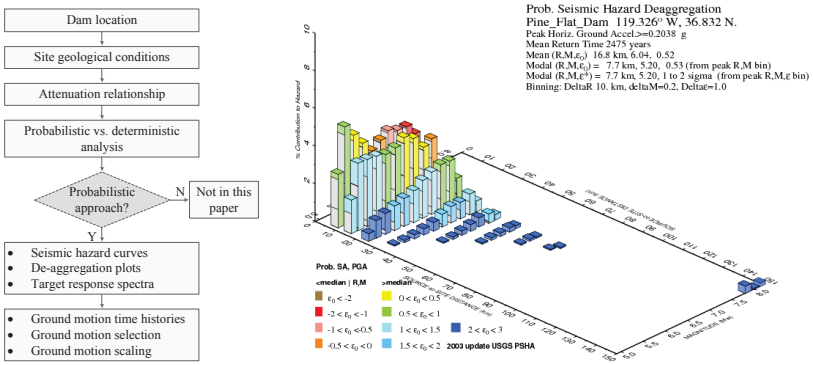

(a) Seismic hazard analysis

(b) Seismic de-aggregation

Figure 10: Seismic hazard assessment of the dams and identification of dominant scenario

In general, there are two approaches for obtaining site-specific ground motions, i.e. probabilistic seismic hazard analysis (PSHA) and deterministic seismic hazard analysis (DSHA). Within the PBEE concept, PSHA is used to obtain the appropriate suit of ground motions.

Probabilistic Seismic Hazard Analysis: PSHA approach uses the elements of the DSHA and adds an assessment of the likelihood that ground motions of a given magnitude would occur. The probability or frequency of occurrence of different magnitude earthquakes on each significant seismic source and inherent uncertainties are directly accounted for in the analysis. The possible occurrence of each magnitude earthquake at any part of a source is directly incorporated in a PSHA. The results of a PSHA are used to select the design earthquake ground motion parameters based on the probability of exceeding a given parameter level during the service life of the structure or for a given return period. Results from the PSHA approach can also be used to identify which combinations of magnitudes and distance is the largest contributor to hazard. Identification of these controlling earthquakes can then be used in scenario or DSHA analyses (FEMA, 2005).

Seismic Hazard De-aggregation: are useful since they can provide a clear vision on contribution of the different parameters in record selection process. Also they can be used for the source identification controlling the hazard at the dam site. Figure 10(b) shows the seismic hazard de-aggregation plots for Pine Flat dam with 2475 years of return periods (USGS 2003, 2003). The modal distance, magnitude, and inter-event term can be found in each case.

Ground Motion Selection and Scaling for Dams: It is recommended to amplitude scaling of the ground motions in a way that provide acceptable consistency, both individually and in a mean sense, to the target spectrum over a desired period range, T_{min} to T_{max}. The dam's small-amplitude fundamental period of vibration is denoted here by T_1. Motions are scaled at this period. After a target spectrum has been defined ground motions are selected and scaled to be consistent with the target spectrum over a period range $[T_{min}, T_{max}]$. T_{max} is taken as $2T_1$ and period T_{min} should typically be taken as $0.2T_1$ (Applied Technology Council, 2012). If substantial response and damage can occur due to response in modes having periods smaller than T_{min}, T_{min} should be selected to be sufficiently small to capture these important behaviors.

Potential Intensity measure Parameter: As mentioned in the previous sections, the first step in the PBEE-2 framework is to determine the ground motion intensity measure (IM) parameter. Hariri-Ardebili and Saouma (2016) provided a comprehensive list of possible IM parameters for concrete dams. They are reviewed here and the "optimal" one will be selected in the next sections. Those seven distinct categories are: a) Category I: Unscalable IMs, b) Category II: Ground Motion Dependent Scalar IMs, c) Category III: Ground Motion Dependent Compound IMs, d) Category VI: Structure-Independent Spectral IMs, e) Category V: Structure-Dependent Spectral IMs, f) Category VI: Vector-Based IMs, g) Category VII: IM for Multiple-Component Ground Motions.

Probabilistic Methods

Sensitivity Analysis: determines the impact of a variation in an input parameter on output results. Mathematically, this corresponds to the partial derivative of the output function with respect to an input parameter at a given design point.

The procedure starts with the identification of the basic RVs, $\mathbf{X} = (X_1, \cdots, X_n)$, and their corresponding distributional model (e.g. normal, log-normal). Then, $2n + 1$ analyses are performed Army Corps of Engineers (1992) using mean (X_i^{mean}), minimum (X_i^{min}) and maximum (X_i^{max}) values of the RVs. A reference response Θ^{Ref} is first computed in terms of the n RVs in $S = \{1, 2, ..., n\}$ equal to their mean values. Then $2n$ analyses are performed, each corresponding to a given maximum or minimum of a RV, while all others are set to their mean value. The swing for each of the n RVs is computed next and are sorted in descending order. Finally, the Tornado diagram is plotted and one has to arbitrarily decide what are the most sensitive RVs, figure 11(a).

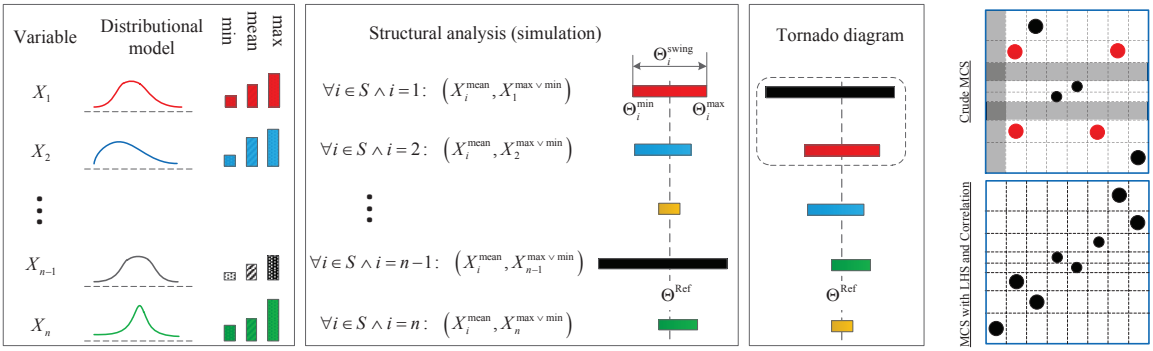

(a) Tornado diagram (b) Sampling

Figure 11: Sensitivity analysis and uncertainty quantification

Uncertainty Analysis: The uncertainty of input parameters is often expressed in terms of probability distributions; it can also be specified by samples of measured values, i.e. empirical probability distributions. The uncertainties of the different input parameters may have dependencies on each other, i.e. they may be correlated. Generally, the main reason of performing an uncertainty analysis is to assess the uncertainty in the model output that arises from uncertainty in the input RVs.

It is possible to account for the correlation among the RVs. The correlation coefficient is bounded by $[-1, +1]$. It will have value of zero when the covariance (among the RVs) is zero and value of ± 1 when the RVs are perfectly correlated or anti-correlated. Figure 11(b) illustrated two case with crude MCS, and correlated LHS where only two RVs are assumed to exists.

Probabilistic Structural Analyses

Having a detailed finite element model, with the capability of accounting for the material and modeling uncertainties, one of the following advanced structural analysis techniques can be

adapted to apply the ground motion record-to-record variability as well:

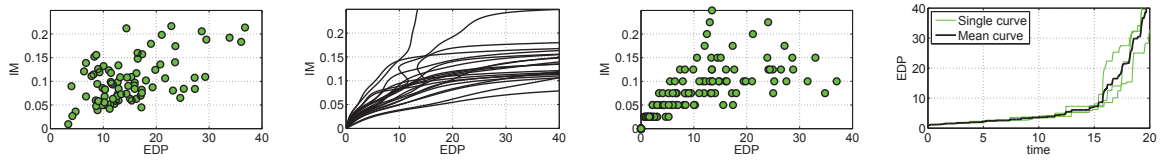

(a) CLA (b) IDA (c) MSA (d) ETA

Figure 12: Application of advanced nonlinear analysis techniques on concrete dams

Cloud Analysis (CLA) is a procedure in which first a dam is subjected to a (relatively large) set of (un-scaled or as-recorded) ground motions and is analyzed numerically. If the ground motion records are taken from a bin, they can represent an earthquake scenario defined by (M_{bin}, R_{bin}), the magnitude and distance representative of the bin (Jalayer, 2003). Then, from the results, EDP *vs.* IM are determined and form the so-called cloud response, figure 12(a).

Incremental Dynamic Analysis (IDA) is a dynamic procedure in which first a set of N (usually $\sim$30) ground motions are selected. Each ground motion is scaled successively to multiple IM levels (Vamvatsikos and Cornell, 2002). Each of the scaled ground motions, are then applied to the dam separately and the maximum EDP is computed. A single-record IDA curve connects the resulting EDPs corresponding to each ground motion. Finally, a multiple-record IDA curve is developed, which is a group of N single-record IDA curves, figure 12(b). A full IDA procedure for each ground motion results dam failure under high scale factors. It corresponds to a flat-line in IDA curve.

Multiple Stripe Analysis (MSA) is a procedure in which a set of m seismic intensity levels (SIL) or stripes are selected first. Each stripe in this method corresponds to a specific SIL and it is possible to perform a probabilistic seismic hazard analysis (PSHA) for each one separately. Consequently, N different ground motions may be selected for each of the m stripes (Cornell and Jalayer, 2002). The resulted $N \times m$ ground motions are then used for nonlinear transient analyses of the dam and the EDPs are computed. Shown in figure 12(c) is a sample plot of MSA with m up to 10. Discrete data points in each strip follow a log-normal distributional model.

Endurance Time Analysis (ETA) is a dynamic pushover procedure which estimates the seismic performance of the dam when subjected to limited number of pre-designed intensifying excitation, which are called endurance time acceleration functions (ETAF). The ETAFs are aimed to shake the dam from a low excitation level with a response in the elastic range to a medium excitation level where the dam experiences some nonlinearity and finally to a high excitation level, which causes the failure. All these responses ranges are experienced in a single time history analysis. Figure 12(d) shows the results of three ETA and also the mean curve. In this method, failure corresponds to a vertical line in ETA curve. The mean ETA curve is analogous to the one of the pushover analysis (POA) or median of IDA (Hariri-Ardebili, Saouma, and Porter, 2016).

Seismic Fragility Functions

A seismic fragility function expresses the probability that an undesirable event (violation of a limit state) will occur as a function of ground motion IM (potentially uncertain). It is usually expressed (and plotted) as 2D curve where the vertical axis bounded by 0 and 1 and the horizontal axis bounded below by 0 and above by infinity. Thus, the term "fragility curve" can be used instead of the fragility function. Note that the 3D plot of fragility functions is refereed to "Fragility surface". Usually, fragility curves are categorized into four main groups: a) Empirical: which is derived using the post-earthquake damage data, b) Analytical: which is derived based on transient structural analysis, c) Heuristic: which is derived based on expert opinion, and d) Hybrid: that combines aspects of two other methods.

The focus of this entry is on analytical fragility curves. The required data points for analytical fragility curves can be generated using the results of 1) CLA, 2) MSA, and/or 3) IDA. A lognormal cumulative distribution function (CDF) is usually used to quantify a fragility function (Porter, Kennedy, and Bachman, 2007). Based on another classification, the fragility curves can be derived either using either IM-based or EDP-based approaches: a) IM-based approach is suitable for the case where the LS threshold is defined based on IM capacity, and b) EDP-based approach is suitable when the LS threshold is defined based on EDP capacity.

Two types of LSs may be used in fragility function:

Global DI concept which varies from 0.0 to 1.0 and shows the overall damage state of the dam. A sample hybrid DI is proposed for gravity dams in terms of crack length, dissipated energy, and maximum drift (Hariri-Ardebili and Saouma, 2015).

Figure 13(a) shows a fragility surface where the two main axes are IM and $P\left[\text{DI} \geq \text{LS}|\text{IM}\right]$, and the third axis shows the variation of unknown LS (bounded to 0 and 1 in this example). As seen, increasing the LS increase the dispersion. Note that assuming a fixed value for LS, e.g. 0.75, changes the 3D fragility surface to a 2D fragility curve.

Local single-variable LS which are defined based on the dam type, modeling considerations, and engineering judgment. A list of these LSs is proposed by Tekie and Ellingwood (2003) for gravity dams, figure 13(b): a) LS1: Concrete material tensile failure at the neck, b) LS2: Foundation material compressive failure at the toe, c) LS3: Sliding at the dam-foundation interface, and d) LS4: Deflection at the top of the dam relative to the heel.

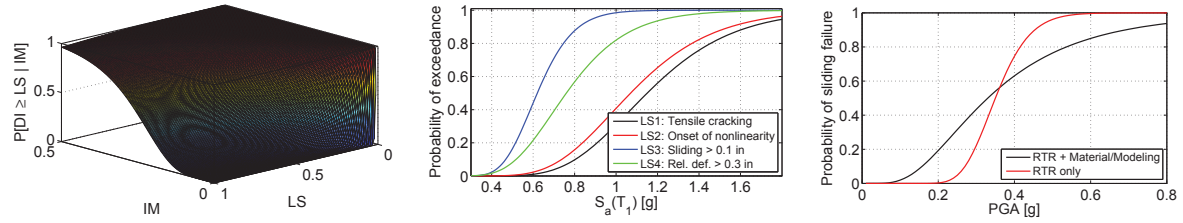

(a) Fragility surface based on DI (b) Fragility curves based on individual LS (c) Impact of β_{RTR} and β_{COM}

Figure 13: Seismic fragility curves for concrete dams

Software

Software used in all the reported analysis have been developed in house and specifically written for the applications intended. The deterministic analyses hinge on a specially designed pre-processor (that understand the language of dams such as crack, uplift, hydrostatic) (Haussman and Saouma, 2009), likewise for the finite element code merlin (Saouma, Červenka, and Reich, 2010) and the graphical post-processor (Haussman and Saouma, 2009). The probabilistic codes are all written in Matlab and are wrapped around Merlin for generating meshes and more importantly data-mining results to extract desired results.

Acknowledgments

The first author would like to acknowledge the support of the Electric Power Research Institute (EPRI) and the Tokyo Electric Power Company (TEPCO) for their financial support for the development of the static and dynamic versions of Merlin respectively. Matlab codes have been mostly developed through financial support of th Nuclear Regulatory Commission (NRC) within the context of a research project on the impact of AAR in nuclear reactors within a probabilistic framework.

References

Applied Technology Council (2012). *Seismic performance assessment of buildings, Volume 1: Methodology*. Tech. rep. ATC-58-1. Redwood City, CA: Federal Emergency Management Agency.

Army Corps of Engineers (1992). *Reliability Assessment of Navigation Structures*. ETL 1110-2-532. Washington, D.C.: Department of the Army, US Army Corps of Engineers.

Cornell, A. and F. Jalayer (2002). "Factored nonlinear displacement demand estimation methods for probability-based safety assessment". In: *Annual Meeting Research Digest No. 2002-7, A publication of the Pacific Earthquake Engineering Research Center*.

Dewey, R., R. Reich, and V. Saouma (1994). "Uplift Modelling for Fracture Mechanics Analysis of Concrete Dams". In: *ASCE J. of Structural Division* 120.10, pp. 3025–3044.

FEMA (2005). *Earthquake analyses and design of dams*. Tech. rep. Denver, Colorado: Federal Emergency Management Agency.

Hariri-Ardebili, M.A. and V. Saouma (2016). "Probabilistic seismic demand model and optimal intensity measure for concrete dams". In: *Structural Safety* 59, pp. 67–85.

Hariri-Ardebili, M.A. and V.E. Saouma (2015). "Quantitative failure metric for gravity dams". In: *Earthquake Engineering and Structural Dynamics* 44, pp. 461–480.

Hariri-Ardebili, M.A., V.E. Saouma, and K.A. Porter (2016). "Quantification of Seismic Potential Failure Modes in Concrete Dams". In: *Earthquake Engineering and Structural Dynamics*.

Haselton, C.B. et al. (2008). *An assessment to benchmark the seismic performance of a code-conforming reinforced concrete moment-frame building, PEER report 2007/12*. Tech. rep. Berkeley, Califprnia: Pacific Earthquake Engineering Research Center, University of California.

Haussman, G. and V. Saouma (2009). *Spider, a 3D Interactive Graphics Finite Element Post-Processor; User's Manual*. http://civil.colorado.edu/~saouma/pdf/spider.pdf.

Hillerborg, A., M. Modéer, and P.E. Petersson (1976). "Analysis of Crack Formation and Crack Growth in Concrete by Means of Fracture Mechanics and Finite Elements". In: *Cement and Concrete Research* 6.6, pp. 773–782.

Jalayer, F. (2003). "Direct probabilistic seismic analysis: implementing non-linear dynamic assessments". PhD thesis. Palo-Alto, CA: Stanford University.

Lee, J. and G. Fenves (1998). "Plastic-damage model for cyclic loading of concrete structures". In: *Journal of engineering mechanics* 124.8, pp. 892–900.

Lysmer, J. and R.L. Kuhlemeyer (1969). "Finite Element Model for Infinite Media". In: *ASCE Journal of Engineering Mechanics* 95.EM 4, pp. 859–877.

Porter, K. (2003). "An overview of PEER's performance-based earthquake engineering methodology". In: *Proceedings of the 9th International Conference on Applications of Statistics and Probability in Civil Engineering (ICASP9)*. San Francisco, CA.

Porter, K., R. Kennedy, and R. Bachman (2007). "Creating Fragility Functions for Performance-Based Earthquake Engineering". In: *Earthquake Spectra* 23, pp. 471–489.

Saouma, V. (2013). *Numerical Modeling of Alkali Aggregate Reaction*. 320 pages. CRC Press.

Saouma, V. and L. Perotti (2006). "Constitutive Model for Alkali Aggregate Reactions". In: *ACI Materials Journal* 103.3, pp. 194–202.

Saouma, V., L. Perotti, and T. Shimpo (2007). "Stress Analysis of Concrete Structures Subjected to Alkali-Aggregate Reactions". In: *ACI Materials Journal* 104.5, pp. 532–541.

Saouma, V., J. Červenka, and R. Reich (2010). *Merlin Finite Element User's Manual*. http://civil.colorado.edu/~saouma/pdf/users.pdf.

Saouma, V. et al. (2011). "A Simplified 3D Model for Rock-Structure Interaction with Radiation Damping and Free Field Input". In: *Bulletin of Earthquake Engineering* 9, pp. 1387–1402. DOI: s10518-011-9261-7.

Slowik, V. and V.E. Saouma (2000). "Water pressure in propagating concrete cracks". In: *ASCE Structural Engineering* 126, pp. 235–242.

Tekie, P.B. and B.R. Ellingwood (2003). “Seismic fragility assessment of concrete gravity dams”. In: *Earthquake Engineering and Structural Dynamics* 32, 2221–2240.

USGS 2003 (2003). *PSHA Interactive Deaggregation Tool, U.S. Geological Survey*. https://geohazards.usgs.gov/deaggint/2008/documentation.php.

Vamvatsikos, D. and C.A. Cornell (2002). “Incremental dynamic analysis”. In: *Earthquake Engineering and Structural Dynamics* 31, pp. 491–514.

5 DAM SAFETY
İstanbul Turkey 2018

International
5th National Symposium on
Dam Safety

October 27-31, 2018

NONLINEAR DYNAMIC BEHAVIOR OF HIGH ARCH DAMS

Jin-Ting WANG [1], Feng JIN[2], Chu-Han ZHANG[3]

ABSTRACT

The dynamic analysis of arch dams plays an important role in the earthquake design of new dams and the earthquake safety evaluation of existing dams. This paper focuses on the nonlinear dynamic behavior of high arch dams during strong earthquakes, which includes the opening and closing of contraction joints, cracking of dam concrete, and strengthening measures. The 210 m-high Dagangshan Dam in southwest China is analyzed as a case study using a comprehensive dam-water-foundation model. Firstly, the joint opening and the damage cracking of the dam are calculated, and the effect of cantilever reinforcement is investigated. Subsequently, seismic fragility are analyzed using the incremental dynamic analysis approach according to damage distribution and joint opening. Finally, some conclusions are presented.

Keywords: arch dam, contraction joints, cracking, seismic fragility.

INTRODUCTION

The seismic safety of arch dams is a widely discussed topic because the failure of an arch dam can result in unimaginable loss of human lives and substantial property damage. During a strong earthquake, the seismic response of arch dams may be nonlinear for two reasons. First, arch dams are built as an assemblage of monoliths by vertical contraction joints. The contraction joints may open and close cyclically and result in nonlinear response. The opening of the contraction joints of the Pacoima arch dam during the 1971 San Fernando and 1994 Northridge earthquakes (Swanson and Sharma, 1979; Hall, 1995) is an example. Second, the concrete may crack because of excessive stress in monoliths in the cantilever direction.

In last several decades, considerable research efforts have been devoted to nonlinear seismic response of arch dams. Some major influential factors, including contraction joint opening and closing (Zhang et al., 2000; Fenves et al., 1992; Lau et al, 1998; Du and Tu, 2007), damage evolution (Valliappan et al., 1999; Omid and Lotfi, 2017; Pan et al., 2009; Hariri-Ardebili, et al., 2016), strengthening measures (Zhang et al., 2000; Long et al., 2008), aging effect (Wang et al., 2011), dynamic dam-water-foundation interaction (Wang et al., 2012; Bayraktar et al., 2011), non-uniform seismic input (Wang et al., 2012), etc., have been considered in the safety assessment of arch dams against earthquakes. Wang et al. (2013) integrated a comprehensive model for analyzing the nonlinear earthquake response of arch dams, which takes into account the semi-unbounded size of foundation rock and compressible water, the opening of contraction joints, the cracking of the dam body, and the spatial variation of ground motions.

[1] Professor, Department of Hydraulic Engineering, Tsinghua University, Beijing, China, email: wangjt@tsinghua.edu.cn
[2] Professor, Department of Hydraulic Engineering, Tsinghua University, Beijing, China.
[3] Professor, Department of Hydraulic Engineering, Tsinghua University, Beijing, China.

In the seismic safety evaluation of dams, there exist epistemic (analysis modeling and material parameters) and aleatory (earthquake ground motion) uncertainties. Fragility analysis has become a useful tool for the seismic safety evaluation of dams to manage uncertainties, and meanwhile plays an important part in the framework of risk-based decision-making. Hariri-Ardebili and Saouma (2016) comprehensively reviewed the state-of-the-art of the seismic fragility analyses of concrete dams. Recently, Wang et al. (2018) analyzed the seismic fragility of arch dams according to damage distribution and contraction joint opening considering both epistemic and aleatory uncertainties.

Based on the analysis model (Pan et al., 2009; Wang et al., 2012; Wang et al., 2013), the nonlinear behavior of the Dagangshan dam in southwest China is analyzed as a case study. Firstly, the joint opening and the damage cracking of the dam are calculated and the effect of cantilever reinforcement is investigated. Subsequently, for three limit states, i.e., slight damage, moderate damage, and severe damage, seismic fragility curves are generated using the incremental dynamic analysis approach. Finally, some conclusions are presented.

NONLINEAR MODELLING OF DAM–RESERVOIR–FOUNDATION SYSTEM

Analysis procedure

The analyzed system is composed of concrete dam, flexible foundation rock, and reservoir. The nonlinear behavior, which resulted from contraction joint opening and concrete damage, is considered and identified as index for classifying limit states. The radiation damping of semi-unbounded foundation rock is also recognized in the investigation. Herein, the impounded water is assumed incompressible, and the dam–water interaction effects are represented using the generalized added mass technique (Kuo, 1982).

The nonlinear dynamic response of dam–reservoir–foundation system is analyzed using the analysis procedure developed in References (Pan et al., 2009; Wang et al., 2012; Wang et al., 2013) and performed using the commercial finite element software ABAQUS (2007). The radiation damping of infinite foundation is simulated by a 3D viscous-spring artificial boundary. The contraction joint is described using a contact boundary model. The plastic damage model is adopted to simulate the damage cracking of concrete materials during strong earthquakes. Figure 1 illustrates the nonlinear strain–softening constitutive relation, where σ and ε denote concrete stress and strain, respectively; E_0 is the initial (undamaged) elastic modulus; d_t is the tensile damage factor that varies from 0 (undamaged material with elastic behavior) to 1 (fully damaged material); G_f is the fracture energy; f_t is the tensile strength; ε_f is the maximum elastic and limiting tensile strains, respectively; and l_c is the characteristic length of concrete (commonly defined as thrice the maximum aggregate size).

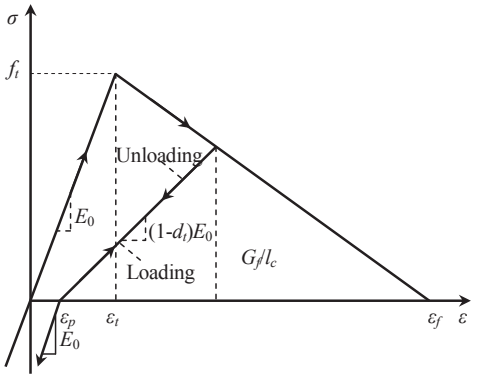

Figure 1. Softening curve of concrete under uniaxial cyclic loading

Finite element model

The Dagangshan dam was completed in 2015. The base and crest of the dam are at El. 925 m and El. 1135 m above sea level, respectively. The dam consists of 29 blocks, with a total crest length of 533 m. The thickness of the crown cantilever varies from 52 m at the base to 10 m at the crest.

Figure 2 shows the finite element model of the Dagangshan Dam foundation system and 28 contraction joints. The dam–foundation model is composed of 37,120 solid elements and 53,817 nodes. To simulate concrete damage, the dam is finely discretized into 26,235 elements and 41,862 nodes, and the mesh size is approximately 2 m in the vertical direction.

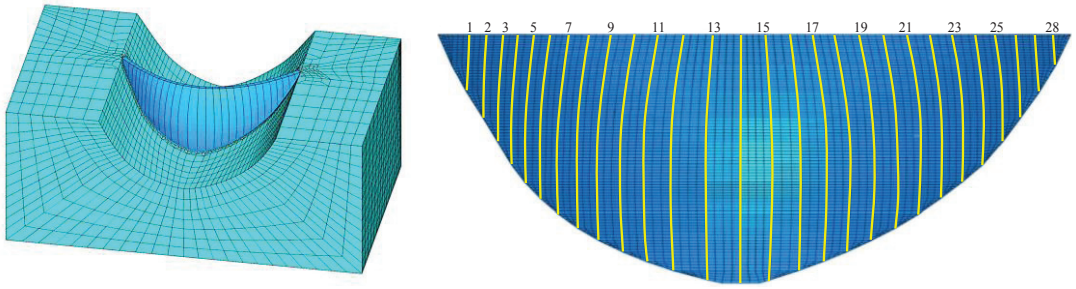

(a) dam–foundation system (b) dam and its contraction joints

Figure 2. Finite element discretization of the analyzed dam–reservoir–foundation system

Material parameters

The material properties of the concrete and foundation rock used in this study are selected mainly based on the design data. The material properties are defined as follows: (1) for the dam concrete, mass density = 2400 kg/m^3, initial dynamic elastic modulus = 31.2 GPa, and Poisson's ratio = 0.17; (2) for the foundation rock, density = 2650 kg/m^3, elastic modulus = 26 GPa, and Poisson's ratio = 0.25; and (3) for the reinforcing steel: density = 7850 kg/m^3, elastic modulus = 260 GPa, and Poisson's ratio = 0.3.

A nonlinear strain–softening constitutive relation shown in Figure 1 is adopted for the dam to describe the plastic–damage behavior of the concrete. The tensile strength f_t of the concrete is 3.12 MPa. The fracture energy G_f is assumed as 280 N/m based on experience. The limiting tensile strain ε_f is set to be 400 μm, and the characteristic length l_c is 0.45 m.

The material damping of the dam–foundation system is assumed to be of Rayleigh type. The damping ratio used in the first and fifth vibration modes of the dam–foundation system is 5%.

Applied loads and earthquake input

The applied static loads include the dam deadweight, hydrostatic and sediment pressures, and temperature loading. The normal water level is 5 m below the crest, and the sediment level is 125 m above the base.

The earthquake ground motion is assumed to be vertically and uniformly incident to the bottom artificial boundary and one-half of the specified amplitude value is used according to 1-D deconvolution. As proposed in Reference (Pan et al., 2009), the earthquake ground motion input is herein converted into the equivalent force applied on the artificial boundaries based on 1-D wave propagation theory. By this way, uniform ground motion is formed at the bottom artificial boundary and then transmitted to the dam-foundation interface.

NONLINEAR DYNAMIC RESPONSE UNDER DESIGN EARTHQUAKE

In this section, the nonlinear responses of the Dagangshan dam is analyzed when the design earthquake is considered. Figure 3 presents the three components of the design earthquake ground motion artificially generated based on the response spectrum specified in the China Specification of Seismic Design of Hydraulic Structures (State Economic and Trade Commission, 2000). The peak ground acceleration is 0.557 g in both stream and cross-stream directions with a 2% probability of exceedance in 100 years. The peak ground acceleration in the vertical direction is taken as 2/3 of that in horizontal directions, i.e., 0.371 g.

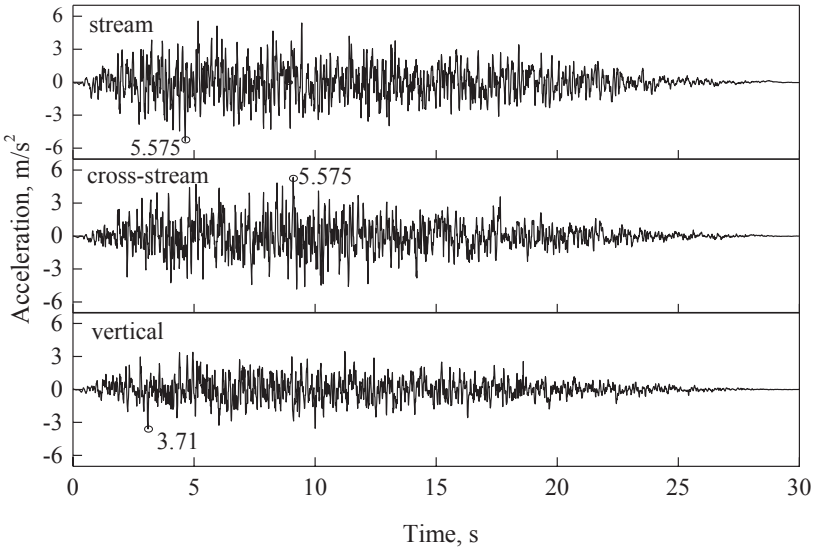

Figure 3. Three components of the design ground motion

Three analysis cases are considered. Case 1 assumes that the linear constitutive relationship is used for the dam concrete. Case 2 considers the damage cracking of the dam concrete. Case 3 further simulates the cantilever reinforcement for resisting the cantilever tensile stress.

Opening of Contraction joints

Figure 4 presents the envelopes of maximum joint opening in Case 1. It is apparent that the opening occurs at all the contraction joints during the specified earthquake excitation. The following conclusions are observed. (1) The peak values of joint opening occurs at the crest. They are 12.38 mm at the upstream face and 12.26 at the downstream face, respectively. (2) The joint opening continues downward to a certain depth. Some joints may fully open from the crest to the bottom. (3) The joint opening at the upstream face is roughly the same as that at the downstream face.

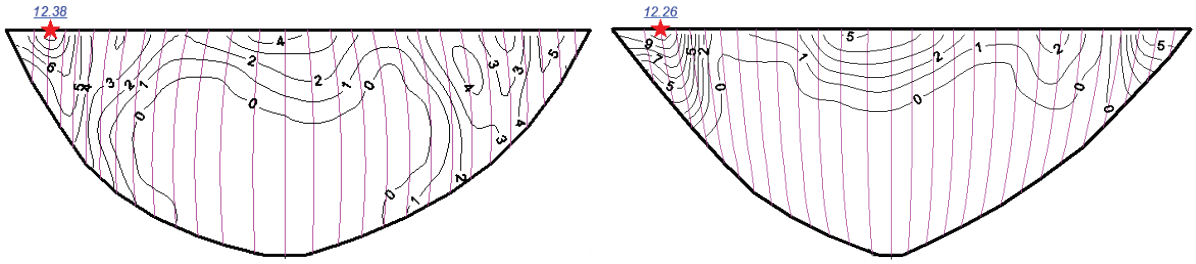

(a) upstream face (b) downstream face

Figure 4. Envelopes of maximum joint opening in Case 1

Tensile stresses

Considering that dam safety is usually controlled by tensile stresses during earthquakes, only the tensile stresses of concrete is discussed herein. The envelopes of tensile arch and cantilever stresses in Case 1 are shown in Figure 5. It is obvious that the tensile arch stress is released after joint opening, as shown in Figures 5 (a) and (c). The peak values of the tensile cantilever stress occur at the upper-middle portion of the dam. They are 3.51 MPa and 4.87 MPa on the upstream and downstream faces, respectively, which exceed the tensile strength of the dam concrete. This means that damage cracking will occur under the specified earthquake excitation.

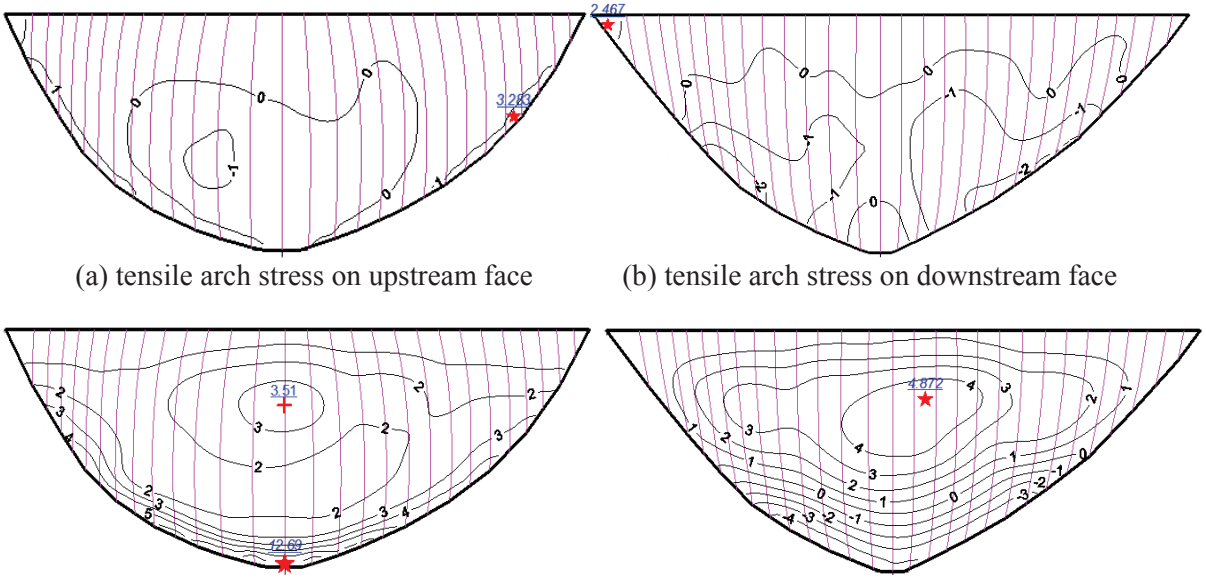

(a) tensile arch stress on upstream face (b) tensile arch stress on downstream face

(c) tensile cantilever stress on upstream face (d) tensile cantilever stress on downstream face

Figure 5. Envelopes of maximum tensile stresses in Case 1

Damage distribution

Figure 6 shows the calculated damage distribution on the upstream and downstream faces in case 2. It is observed that the damage on the upstream face appears in the dam body adjacent to the foundation rock. In contrast, the damage on the downstream face occurs on the upper-middle portion of the dam. The dam-foundation rock interface is a zone of stress concentration in the finite element analysis, and thus the calculated damage does not present the real state. Therefore, we focus on the damage the on the downstream face. Compared Figure 6 (b) with in Figure 5(d), it can be found that the damage distribution on the downstream face agrees with the tensile cantilever stress exceeding the tensile strength of dam concrete. In addition, it should be noted that the damage on the downstream face is distributed in the multiple stripes. This is attributed to the tensile stress release caused by cracking.

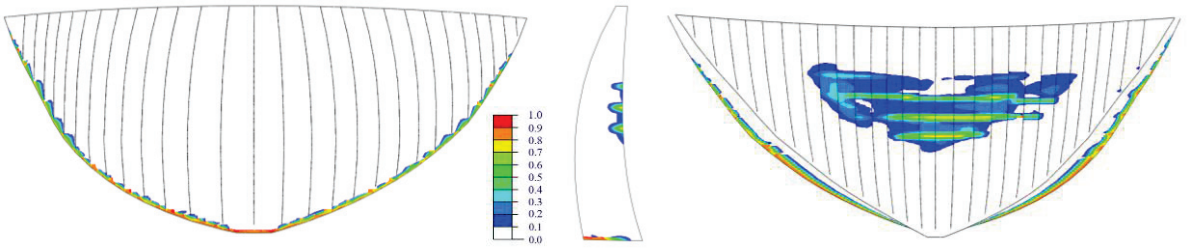

(a) upstream face (b) crown cantilever (c) downstream face

Figure 6. Concrete damage distributions of dam faces in Case 2

Effect of cantilever reinforcement

The closest active is only 4.5 km away from the Dagangshan dam site. Therefore, the design peak ground acceleration (0.5575 g) is not common in the practice of dam engineering. Considering the risk of earthquake damage, the cantilever reinforcement was placed in the potential cracking zone of

the Dagangshan dam for alleviating the extension and opening width of concrete cracks under strong earthquake. Figure 7 shows the calculated damage distribution on the upstream and downstream after placing the cantilever reinforcement (Case 3). It is observed that the damage zone after placing cantilever reinforcement is similar to that without reinforcement. However, the maximum damage factor is reduced. In addition, it can be observed from the damage distribution at the crown cantilever that the damage depth is also reduced. This is expected because that the reinforcing steel cannot prevent cracking, but can alleviate cracking. Therefore, the cantilever reinforcement is beneficial to the earthquake-resistant capacity of the Dagangshan dam.

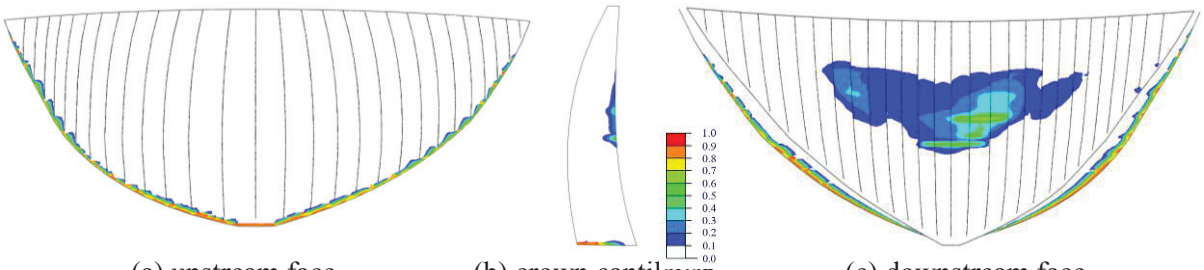

(a) upstream face (b) crown cantilever (c) downstream face

Figure 7. Concrete damage distributions of dam faces in Case 3

SEISMIC FRAGILITY ANALYSIS

Wang et al. (2018) investigated the seismic fragility analysis of the Dagangshan dam considering both epistemic and aleatory uncertainties. The nonlinear damage analyses were carried out at a set of ground motion levels, and the seismic fragility curves were subsequently generated using the incremental dynamic analysis approach. Herein, those analysis results are briefly reviewed. Interested readers may refer to the reference (Wang et al., 2018) for more details.

Limit states

The limit states are defined by damage distribution and joint opening. Three seismic damage levels, i.e., slight damage, moderate damage, and severe damage, are considered for generating fragility curves. The descriptions of the three limit states are listed in Table 1. It should be noted that abutment rock wedges may be capable of movements during strong earthquakes, and it is critical to the stability of arch dams. This will addressed in future investigations.

Table 1. Limit state criteria for classifying seismic damage and joint opening

Limit states	Descriptions
Slight damage (LS1)	Damage occurs on downstream surface, but no macro-cracking is observed. Dam is in linear elastic stage.
Moderate damage (LS2)	Macro-cracking occurs on the middle and upper of downstream face but not on the upstream face. Repair and reinforcement are needed to fully recover its performance.
Severe damage (LS3)	Macro-cracking appears from the downstream face to the upstream face, or joint opening is larger than 50 mm. The safety of people in the downstream is under threat.

Uncertain model parameters and ground motions

We selects tensile strength of concrete f_t, elastic modulus of concrete E_0, elastic modulus of foundation E_f, and damping ratio ζ of the system as uncertainty model parameters. The normal distribution is used for the concrete tensile strength, concrete modulus, and foundation modulus. Their mean, standard deviation, and variation coefficient are listed in Table 2. The damping ratio of the system is assumed uniform between 3% and 7%.

Table 2. Normally-distributed model parameters

Parameter	Mean (MPa)	Standard deviation	Coefficient of variation
f_t	2.5	0.5	0.2
E_0	2400	7.2	0.3
E_f	2000	6.0	0.3

Ten sets of three-component ground motions are considered. Each ground motion is scaled to 10 PGA levels with 0.1 g interval, i.e., 0.1, 0.2, 0.3, 0.4, 0.5, 0.6, 0.7, 0.8, 0.9, and 1.0 g. Every ground motion record is paired with the five model parameter samples. Therefore, 50 trials are performed at a given intensity level. Totally, five hundred nonlinear analyses are implemented to generate seismic fragility curves.

Seismic fragility curve

Seismic fragility curves of the Dagangshan Dam are obtained by the lognormal distribution fitting, as shown in Figure 8. The probability of occurrence of every limit state increases with the PGA level. When the PGA level is a constant value, the probability of slight damage is greater than moderate damage, and the probability of moderate damage is greater than that of severe damage. Based on Fig. 8, the occurrence probability of three limit states is 86 %, 51%, and 4%, respectively, for the design earthquake (0.5575 g).

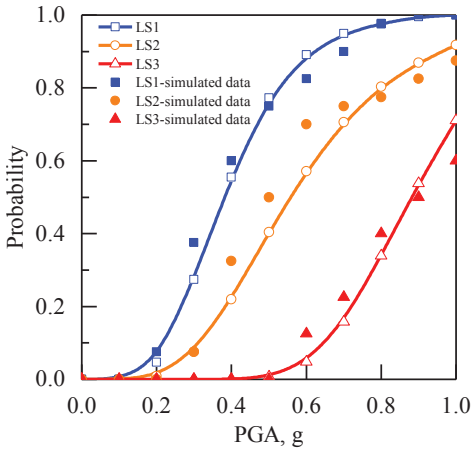

Figure 8. Seismic fragility for the defined three state limits

CONCLUSIONS

(1) Arch dams are usually built as independent monoliths separated by vertical contraction joints. During strong earthquakes, the contraction joints open and close cyclically, and the concrete cracks in the cantilever direction, which may cause the partially free block at the dam crest to uncontrollably release water. This is a potential failure mode of arch dams subjected to high intensity earthquakes.

(2) Considering the uncertainties in material parameters and ground motions, the Dagangshan dam may be damaged by near-filed strong earthquakes. Based on the seismic fragility analysis, the occurrence probability of severe damage is less than 5% under the design earthquake (0.5575g).

(3) The cantilever reinforcement cannot prevent cracking in the cantilever direction, but it can improve the integrity of dam concrete.

(4) The abutment stability is also critical to the seismic safety of arch dams. This paper does not address this issue.

ACKNOWLEDGEMENTS

This research is financially supported by the National Natural Science Foundation of China (Nos. 51639006 and 51725901). The authors express their sincerest gratitude for the support.

REFERENCES

ABAQUS Inc, 2007. "Abaqus Theory Manual". Version 6.7, ABAQUS, Inc., Providence, RI, USA.

Bayraktar, A., Sevim, B., Altunışık, A.C., 2011. "Finite element model updating effects on nonlinear seismic response of arch dam-reservoir-foundation systems". Finite Elements in Analysis and Design, 47(2), pp. 85-97.

Du, X., Tu, J., 2007. "Nonlinear seismic response analysis of arch dam-foundation systems-part II opening and closing contact joints". Bulletin of Earthquake Engineering, 5, pp. 121-133.

Fenves, G.L., Mojtahedi, S., Relmer, R.B., 1992. "Effect of contraction joints on earthquake response of an arch dam". Journal of Structural Engineering, ASCE, 118(4), pp. 1039-1055.

Hall, J.F., 1995. "Northridge earthquake of January 17, 1994 reconnaissance report, volume 1". Earthquake Spectra 11 (Supplement C), EERI 95-03.

Hall, J.F., 1998. "Efficient non-linear seismic analysis of arch dams". Earthquake Engineering and Structural Dynamics, 27(12), pp. 1425-1444.

Hariri-Ardebili, M.A., Furgani, L., Meghella, M., Saouma, V.E., 2016. "A new class of seismic damage and performance indices for arch dams via ETA method". Engineering Structures, 110, pp. 145-160.

Hariri-Ardebili, M.A., Saouma, V.E., 2016. "Seismic fragility analysis of concrete dams: A state-of-the-art review". Engineering Structures, 128, pp. 374-399.

Kuo, J., 1982. "Fluid-structure interactions: Added mass computations for incompressible fluid". Report No. UCB/EERC-82/09, University of California Earthquake Engineering Research Center, Berkeley.

Lau, D.T., Noruziaan, B., Razaqpur, A.G., 1998. "Modeling of contraction joint and shear sliding effects on earthquake response of arch dams". Earthquake Engineering and Structural Dynamics, 27(10), pp. 1013-1029.

Long, Y.C., Zhang, C.H., Jin, F., 2008. "Numerical simulation of reinforcement strengthening for high-arch dams to resist strong earthquakes". Earthquake engineering and structural dynamics, 37(15), pp. 1739-1761.

Omidi, O., Lotfi, V., 2017. "Seismic plastic–damage analysis of mass concrete blocks in arch dams including contraction and peripheral joints," Soil Dynamics and Earthquake Engineering, 95, pp. 118–137.

Pan, J.W., Zhang, C.H., Wang, J.T., Xu, Y.J., 2009. "Seismic damage-cracking analysis of arch dams using different earthquake input mechanisms". Science in China Series E: Technological Sciences, 52, pp. 518-529.

State Economic and Trade Commission, 2000. "Specification of seismic design of hydraulic structures, DL5073-2000". China Electric Power Press, Beijing, China (in Chinese).

Swanson, A.A., Sharma, R.P., 1979. "Effects of the 1971 San Fernando earthquake on Pacoima arch dam". Proc. 13th ICOLD, New Delhi, Q.51, R.3.

Wang, J.T., Jin, F., Zhang, C.H., 2011. "Seismic safety of arch dams with aging effects". Science China Technological Sciences, 54 (3), pp. 522-530.

Wang, J.T., Zhang, C.H., Jin F., 2012. "Nonlinear earthquake analysis of high arch dam–water–foundation rock systems". Earthquake Engineering and Structural Dynamics, 41(7), pp. 1157-1176.

Wang, J., Lv, D., Jin, F., Zhang C., 2013. Earthquake damage analysis of arch dams considering dam-water-foundation interaction". Soil Dynamics and Earthquake Engineering, 49, pp. 64-74.

Wang, J.T., Zhang, M.X., Jin, A.Y., Zhang, C.H., 2018. "Seismic fragility of arch dams based on damage analysis". Soil Dynamic and Earthquake Engineering, 2018, 109, pp.58-68.

Valliappan, S., Yazdchi, M., Khalili, N., 1999. “Seismic analysis of arch dams - a continuum damage mechanics approach”. International Journal of Numerical Methods in Engineering, 45(11), pp. 1695-1724.

Zhang, C.H., Xu, Y.J., Wang, G. L., Jin, F., 2000. “Non-linear seismic response of arch dams with contraction joint opening and joint reinforcements”. Earthquake Engineering and Structural Dynamics, 29(10), pp. 1547-1566.

TAILING DAMS – HOW DO WE MAKE THEM SAFER?

Dr Andy HUGHES [1]

ABSTRACT

Tailings dams continue to undergo failures at an unacceptable rate compared to water storage dams.

The consequence of failure can be widespread flows of tailings and impact over the landscape and water courses. This can be extreme in terms of life loss, environmental damage, social license to operate, company value, and mining industry sustainability. Any additional technology and information that enables an owner of a tailings dam to be more certain of its condition and thereby reduce the risk of failure is of tremendous value to reliable tailings and mine water management.

This approach has been successfully used to identify water flow paths through, under and around tailings dam in plan and elevation.

This paper, using tailings dam case studies, illustrates the procedure, findings, and the benefits of this methodology. The findings range from tailings dams where the methodology confirmed the design evaluations, to dams where new groundwater flow paths were identified. In the latter case, the dam designers were able to update the designs to mitigate for the new information and design a more safe and stable tailings dam with reduced risk of failure.

Keywords: tailings, dams, safety, investigation, leakage.

INTRODUCTION

Tailings dams and storage facilities are unique and different than water supply reservoir dams for many reasons: they store tailings (waste liability) versus water (resource asset); their construction and design evolve as the mine lives advance and tailings volumes increase while codes. In addition, regulations and technologies change; they embrace tailings properties, disposal methods and water management in dam design; and they store tailings in perpetuity.

Most of tailings dams are dynamic structures that grow in size and complexity over their operating life and must be maintained after closure. Their designs evolve with time and not always as originally envisaged because of many factors that range from global events, commodity prices and regulations that mine owners have no control over, to local operation, community, environmental, and other challenges.

Properly planned, designed, constructed, operated and maintained tailings dams provide safe and effective tailings storage facility (TSF) structures. Dams are raised by optimizing upstream, centreline and downstream methods to fit site conditions, land constraints and mine operations. TSFs use a host

[1] Director, Dams & Reservoirs Ltd, Newark, United Kingdom
e-posta: andy.hughes@damsandreservoirs.co.uk

of tailings and water management methods to optimize storage space, reduce operation costs, protect the environment, and maintain dam stability and safety.

Evolving designs continue to combine proven existing and new (disrupt mining) technologies to enhance the positive, progressive and collective ability to effectively manage tailings dams and TSFs. For example, several new non-intrusive technologies are now being used to help designers such as a method to identify seepage paths at depth through, under and around tailings dams that helps in the design of TSF and tailings dam stabilizations, expansions, and closures.

NON-INTRUSIVE INVESTIGATIVE TECHNOLOGY

Willowstick is a 'non-intrusive' technology which enables individual water paths to be identified and mapped both in plan and elevation. In so doing it identifies any leakages or seepages, any groundwater flows or confirms that there are no leakages.

The system is affected by metal features but even then the influence can be screened out in the modelling. Surveys are usually carried out within a week with results available on a daily basis.

This paper describes a geophysical technology that uses low volt, low amp, alternating electrical current to energize groundwater by electrodes placed in tailings water and seepage discharge to render two- and three-dimensional (2D and 3D) maps and Electric Current Distribution (ECD) models of seepage paths (Figure 1). The technology maps and models preferential groundwater flow paths like an angiogram that lets doctors to "see" blood vessels in a human body.

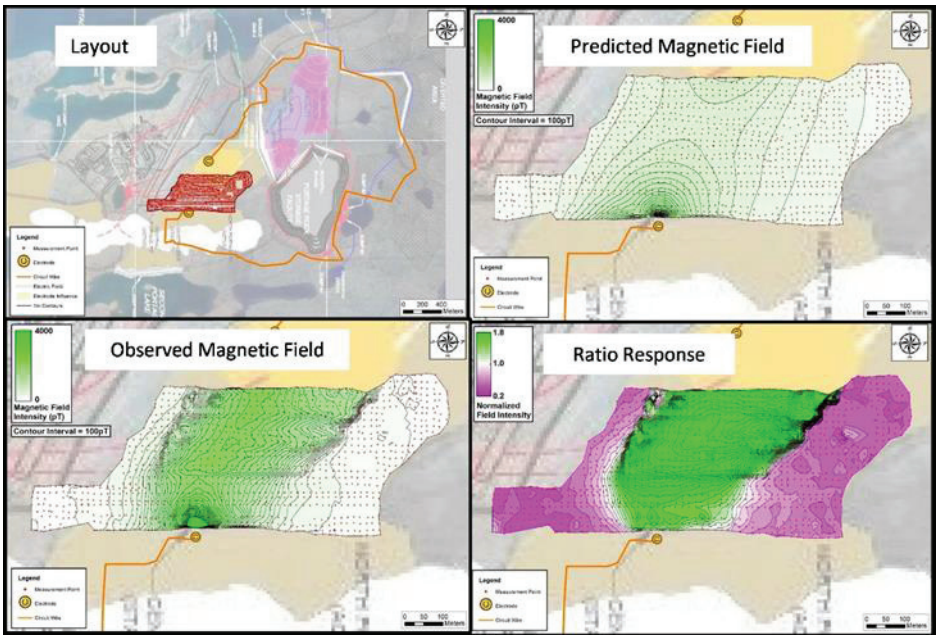

Figure 1. Steps to get data results and two-dimensional maps

The application of the technology to tailings dams is based on the principle that water increases the conductivity of earth materials through which it flows. As the signature, electric current travels between electrodes strategically placed upstream and downstream of the tailings dam, it concentrates in the more conductive zones, or highest transport porosity areas, where tailings water preferentially flows out of the TSF as seepage through, under, and around the dam.

An electric circuit is established in the water of interest. Measuring the resultant magnetic field at the surface reveals the electric current flow and distribution. Data is processed and compared to a

predicted magnetic field from a theoretical homogenous earth model to highlight deviations from the "uniform" model. 2D maps and 3D models are generated and interpreted in combination with known sub-surface data to enhance preferential seepage path definitions (Figures 2, 3 and 4).

The graphic shading shown in Figure 4 and in the subsequent tailings dam study figures in this paper span a shading spectrum from purple to green. Purple on the modelling represents actual water flow that is less than flow predicted by the "uniform" model. Green represents actual flow that is more than flow predicted by the "uniform" model. So, green most likely represents a seepage path.

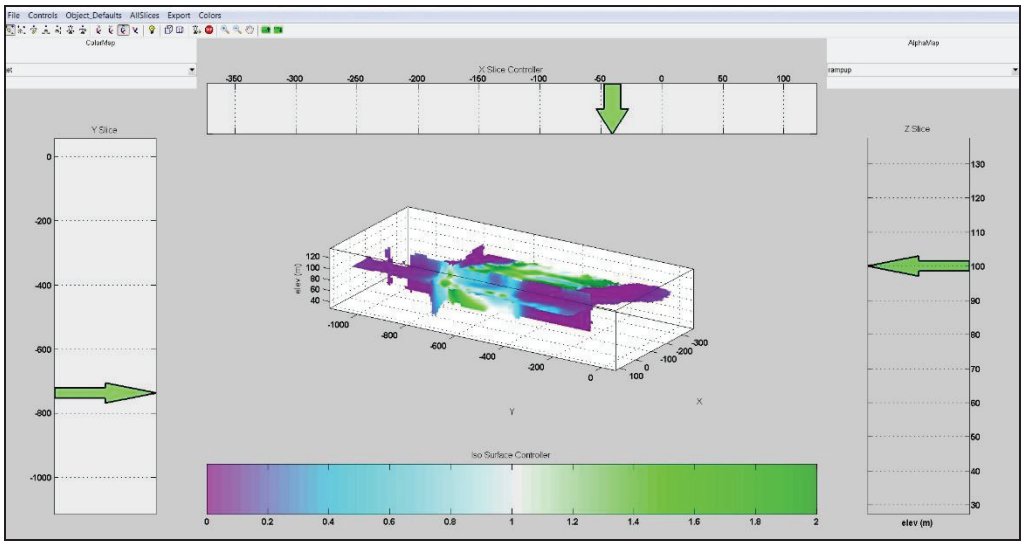

Figure 2. Three-dimensional inversion model

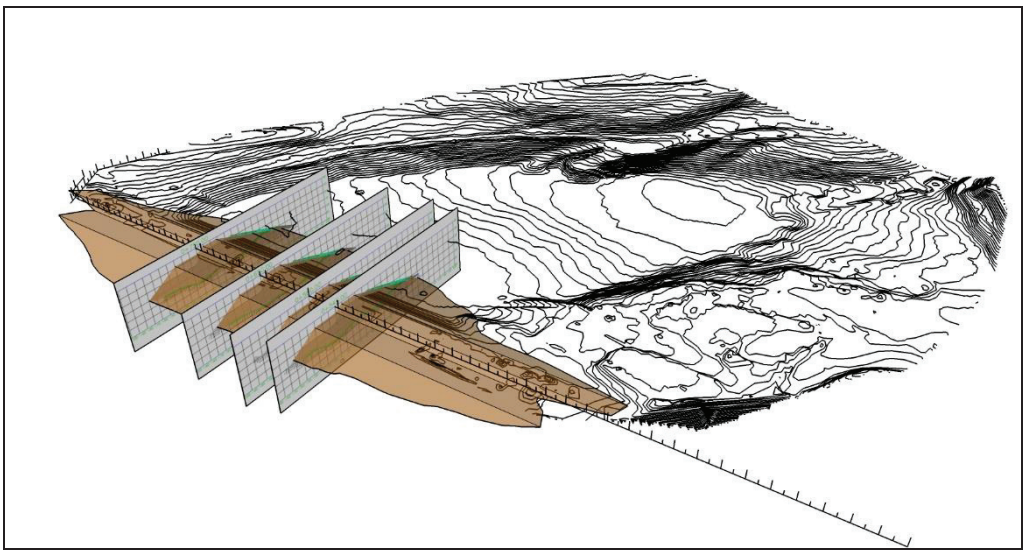

Figure 3. Three-dimensional site model

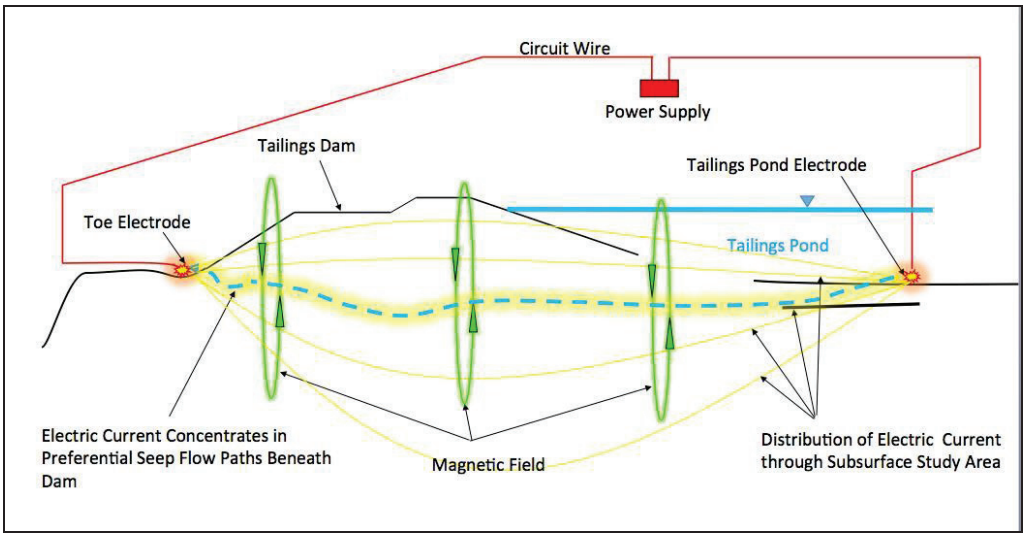

Figure 4. Survey setup

This paper, through three tailings dam studies, illustrates the procedures, findings and benefits of this technology. Results range from confirmation of design decisions to identifying new seepage paths. In the latter case, the designs are now being updated based on the new information to provide a more safe and stable tailings dam and reduce the risk of failure.

TAILINGS DAM STUDY 1

Tailings Dam Study 1 involves a TSF with two cells: original upper and smaller "old tailings" cell with tailings held by an old dam; and a lower "new tailings" cell with a new dam (Figure 5). A dike separates the cells. A settling pond and open pit are adjacent to the new dam.

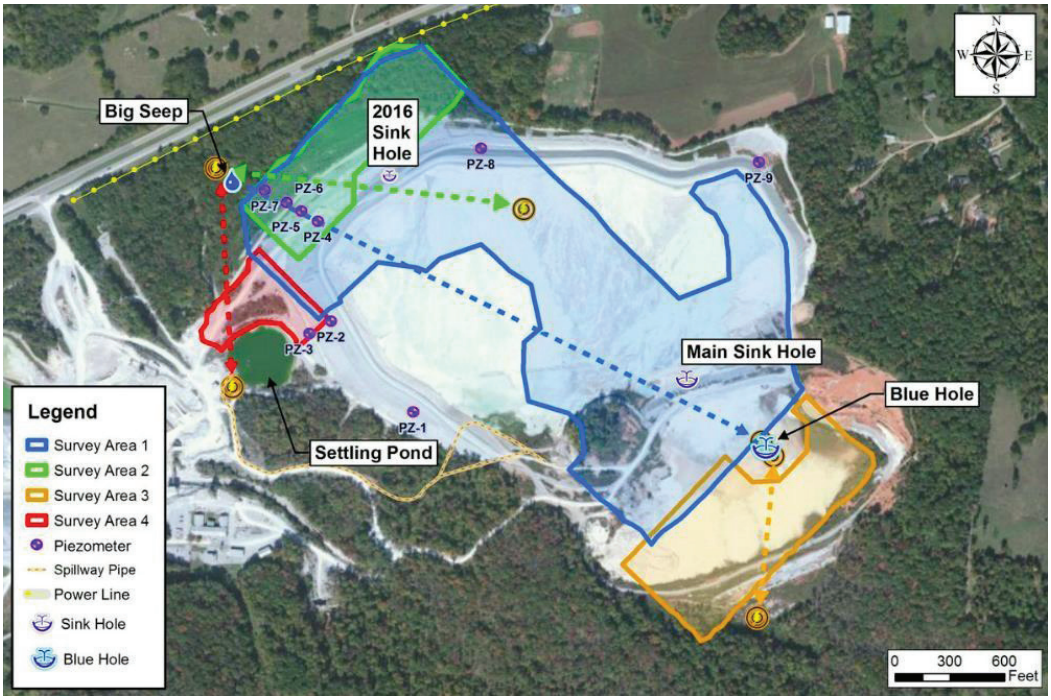

Figure 5. Four surveys planned to correlate sinkholes and seepages

Sinkholes were observed in tailings near both dams (Figures 6 and 7). Seepage was observed exiting from below both dams. The largest sinkhole is Blue Hole in the old tailings. The largest visible seepage is Big Seep at the toe of the new dam Figures 8 and 9). Blue Hole has existed for some time

and was not a concern. However, it was considered important to know how Blue Hole is connected to the new tailings and Big Seep. No turbidity was observed in the visible seepage.

Figure 6. Sinkhole in new tailings

Figure 1. Blue hole in old tailings

Figure 8. Blue hole

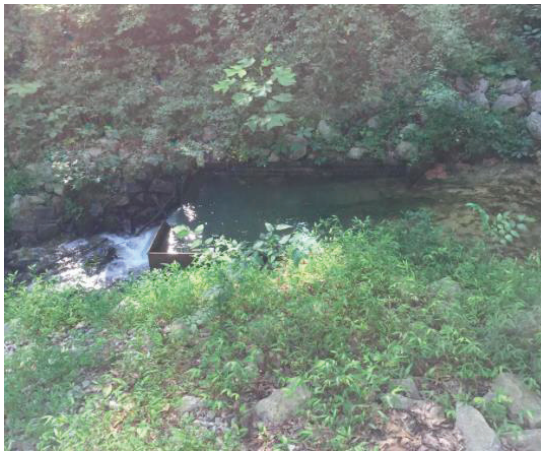

Figure 9. Outflow from Blue hole

There were concerns about potential internal erosion and piping in the old dam that could lead to failure and impact the new dam and pit. It was critical for workers safety and financial security that the pit is not at risk of receiving seepage and the old dam is safe. Four surveys were performed to identify seepage paths and facilitate the remedial works to protect the dams and pit if necessary.

Surveys 1 to 3 identified preferential flow paths that indicated seepage out of the TSF at its north-west, southeast and west locations as Seep Path A, B and C, respectively (Figure 10). Survey 4 was triggered by an earlier dye study where dye added to the tailings pond emerged in Big Seep. Electrodes were placed in the tailings pond and in Big Seep. Survey 4 identified a connection between tailings pond water and Big Seep by means of seepage from the TSF to Big Seep.

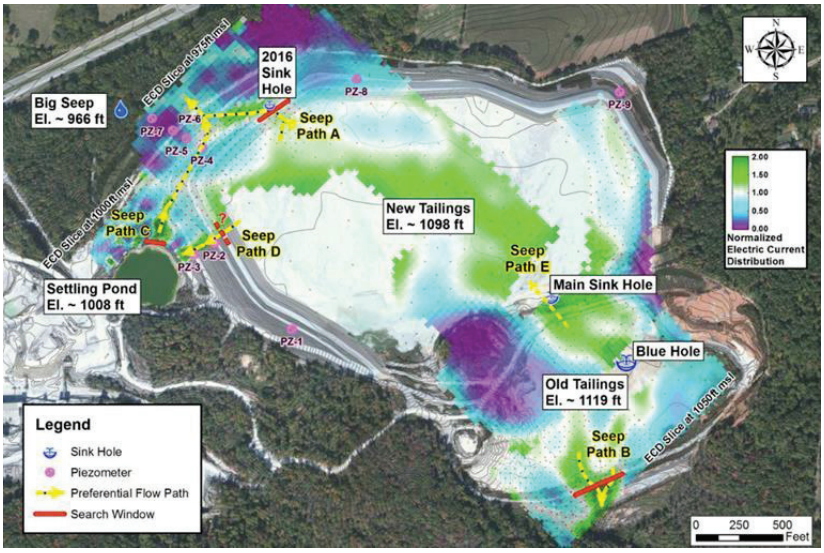

Figure 10. Investigation model showing seepage paths in yellow

Two paths were found where seepage preferentially flows out of the old cell: Seep Path B to the south; and Seep Path E under the divider dike. Seep Path B is of greater concern because it discharges out of the TSF. Seep Path E is of less concern because it discharges from the old cell to the new cell so is confined in the TSF.

Two paths were found where seepage preferentially flows out of the new cell. Seep Path A is the primary contributor to Big Seep. Seep Path D flows from the new cell to the settling pond. Seep Path D was not fully delineated because of limited access due to wet and soft tailings. Therefore, only the far edge (Survey 1) and downstream half (Survey 4) of the seepage path were identified.

Another seepage path was found contributing water to Big Seep. This is Seep Path C that originates out of the settling pond. With a strong, shallow anomaly, Survey 4 delineates where this seepage path leaves the settling pond and flows north-northeast. From there, Surveys 1 and 2 suggest that this seepage merges with Seep Path A before discharging at Big Seep.

Results are shown on Figure 11, which identifies the depth of the observed seepage path. The green shading indicates a greater concentration of the electric current than predicted as it focuses in the water bearing connection paths, or seepage paths. The blue and purple shading indicate a smaller amount of electric current, hence minimal, if any, seepage. The intensity of the magnetic field gives a direct correlation with water flow, the greater the intensity the greater the flow. The methodology only models flows and not stationary pore water within the fill.

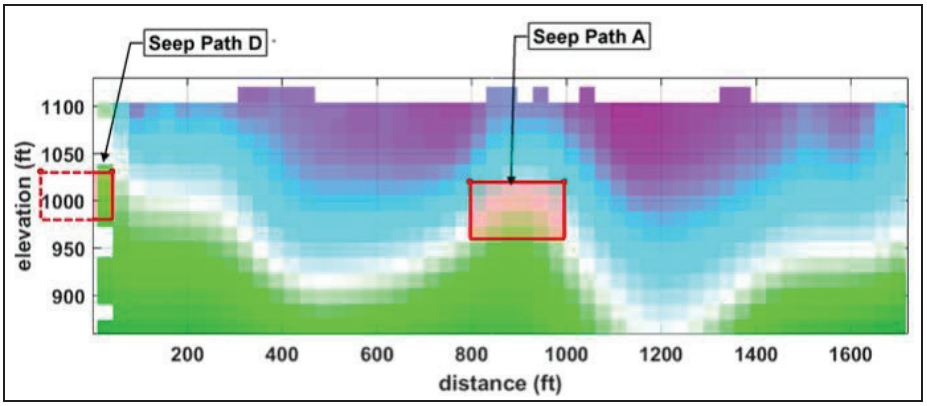

Figure 11. Vertical slice of survey model showing seepage path depth

TAILINGS DAM STUDY 2

Tailings Dam Study 2 involves a newly constructed tailings dam downstream of an original active TSF that was nearing capacity and upstream of the open pit (Figure 12). While the new dam was being built, seepage was observed at its downstream toe. A seepage survey was conducted to delineate the seepage paths and any risks that they might pose to the new dam and the open pit.

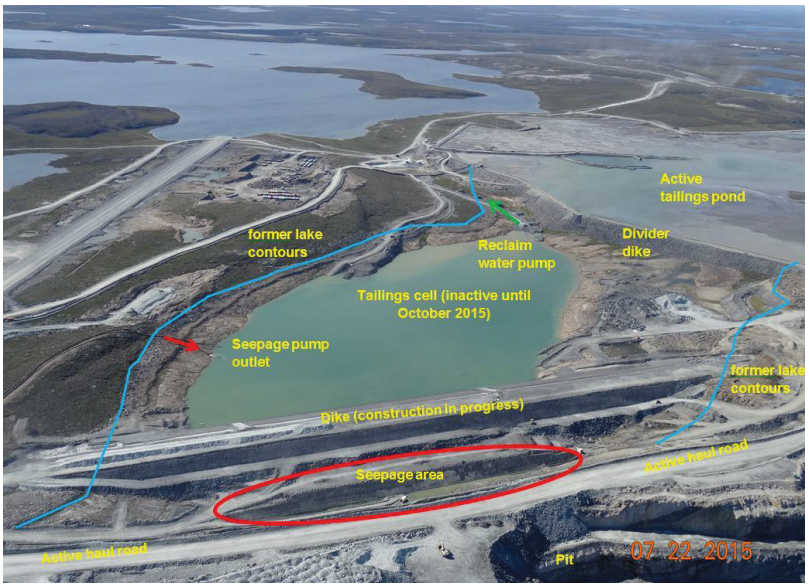

Figure 12. Tailings facility seepage area site plan

Two survey layouts were used with the same upstream electrode in the new tailings pond. For Survey 1, the downstream electrode was in the seepage discharge at the toe of the new dam. For Survey 2, it was in the seepage discharge in the open pit east of the dam (Figure 13).

Figure 13. Site dimensions for survey model

Survey 1 identified primary and secondary seepage paths under the dam (Figures 14 and 15). The plan and profile views show seepage path widths and depths. The green shading indicates seepage paths. The yellow lines are interpretations of connection paths between the two electrodes.

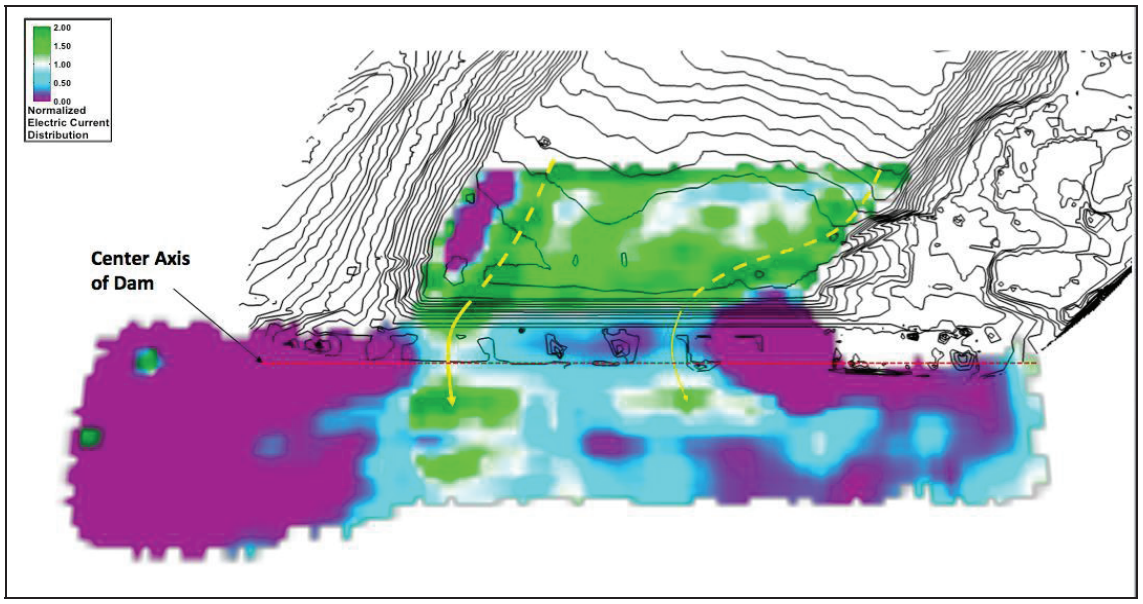

Figure 14. Model elevation slice showing two seepage paths under dam

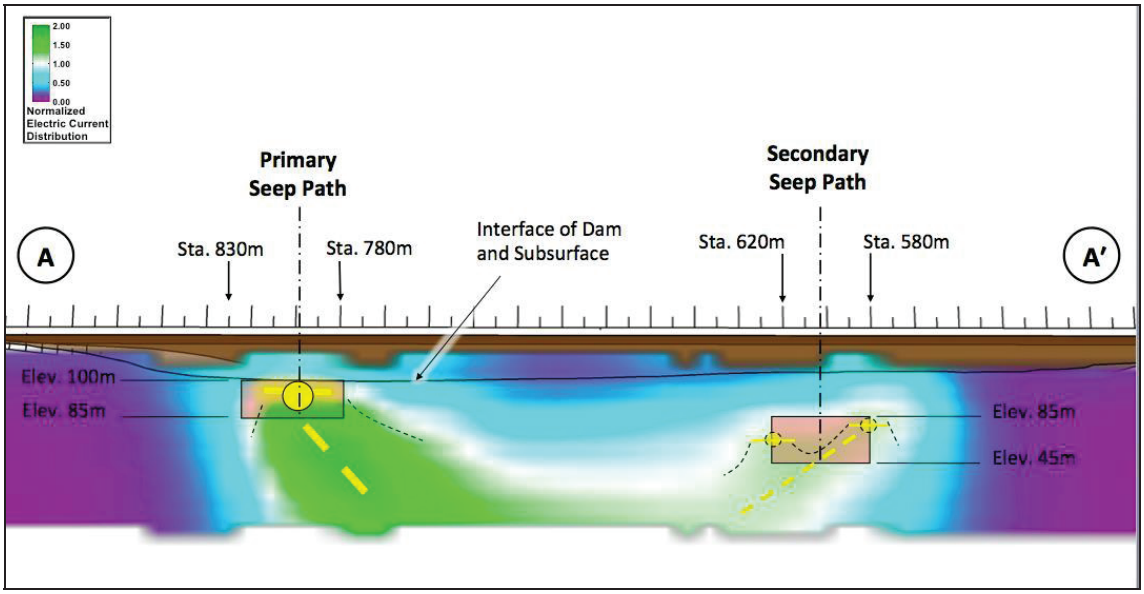

Figure 15. Model vertical slice along dam axis showing seepage path elevations

The results confirmed that there are no other seepage paths of any significance through or under the dam. This provided the confidence that piping and internal erosion were not concerns for the dam because the seepage paths that were identified are in the sub-surface foundation materials under the dam and not in the dam structure itself. Of course one has to consider whether foundation piping is an issue.

Geotechnical drilling was completed into the seepage path target areas identified by the survey. The drilling confirmed the survey findings, in as much as the drillings intercepted the flow paths. Remedial measures are now being planned that will be significantly less in cost than if the survey had not been completed and seepage paths not found – targeted remedial works.

TAILINGS DAM STUDY 3

Tailings Dam Study 3 involves a TSF with a tailings dam at the low end of a valley. A seepage collection pond is just downstream of the tailings dam. A waste rock dump occupies one of the valley

sides of the TSF. A 2-kilometre long drainage collection trench is aligned along the toe of the waste rock dump (Figures 16, 17 and 18).

Figure 16. Tailings aerial photo

Figure 17. Tailings facility site plan

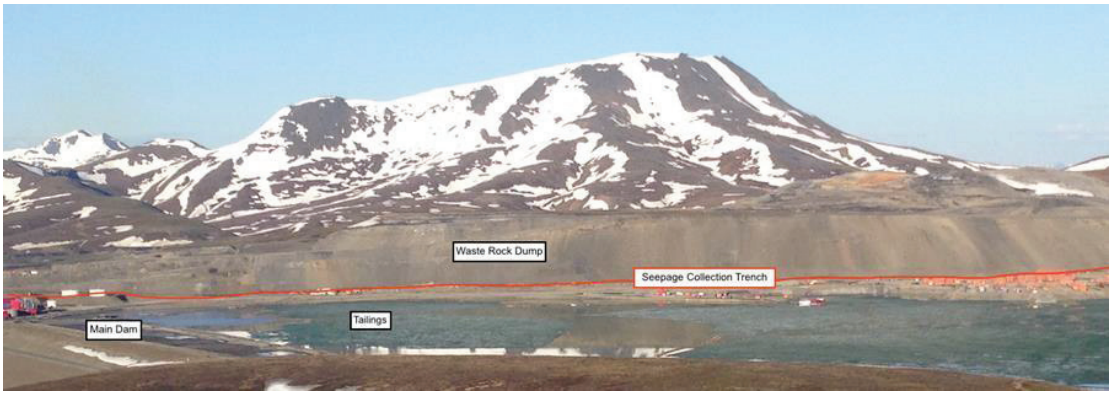

Figure 18. Tailings facility and waste rock dump

Seepage from the TSF is collected in the seepage collection system and is pumped back to the TSF (Figure 19). Additional contribution to the pumped back water is surface runoff from the seepage collection catchment area (Figure 20). There was concern that some "surface runoff" could also be seepage from the TSF through the left abutment of the tailings dam, and that there could be seepage from the TSF flowing under the seepage collection system and to the environment.

Water that escapes the waste rock dump drainage collection trench enters the TSF. However, over time as the TSF rises, the hydraulic gradient could switch from the TSF to the waste rock dump.

Figure 19. Tailings dam and seepage pond

Figure 20. Flow into seepage pond

The survey was conducted in two phases: Phase 1 to identify and delineate seepage patterns through, under, and around the tailings dam and seepage collection dam to stabilize them, if necessary, for raising the tailings dam; and Phase 2 to identify any deeper seepage paths that might pass under the waste rock dump drainage collection trench and flow to the TSF.

During Phase 1, a seepage path was unexpectedly found into the TSF under the wing wall part of the tailings dam (Figure 21, orange arrow). The seepage path is broad at first but narrows down. This seepage path conveys drainage into the TSF from the east hillside under the wing wall 5 to 6 metres below ground in what was confirmed to be a buried former drainage channel.

Figure 21. Surveys with flow paths

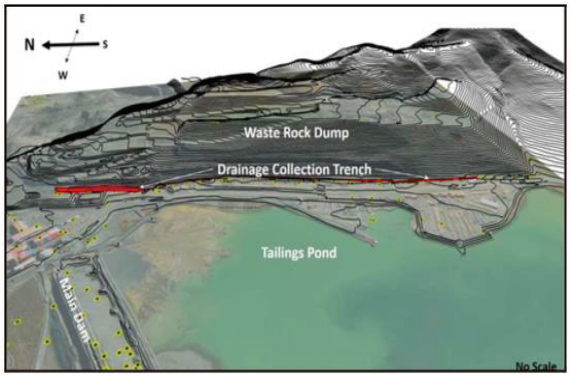

Figure 22. Site model

Seepage out of the TSF originates in the original stream channels under the TSF and converges to a single path in a rock underdrain that was built in the original creek channel under what is the highest part of the dam (Figure 21). The seepage flows through the rock underdrain to the seepage collection pond. There is no sign of seepage bypassing the seepage collection dam. The survey confirmed that the TSF and seepage collection system were performing as designed.

A third drainage path unrelated to TSF seepage was identified. Originating from the right hillside just downstream of the tailings dam, this drainage path conveys water to under the dam's right groin area (Figure 21, green arrows). Some of this water exits out from under the tailings dam near the bottom of the right groin. Some drainage, however, mixes with seepage from the TSF. All seepage and drainage were confirmed to be captured in the seepage collection pond.

No other seepage paths were identified through, under or around the tailings dam and seepage collection pond areas. The survey confirmed the design assumptions and performance expectations, and enabled planning to start for future tailings dam raises and seepage collection pond relocation to accommodate the increased footprint of an expanded tailings dam.

For the Phase 2 survey, solid yellow lines show primary seepage paths. Light yellow dash lines show secondary seepage paths. Black dashed circles show electric current preferentially flowing through and under the trench. Primary seepage paths were found to align with original drainages shown on pre-mining maps (Figure 23). Secondary seepage paths are under the trench but are shallower than primary seepage paths. The seepage path tops intercept the bottom of the trench.

The survey found that seepage from the waste rock dump was flowing under the dump along the top of the original ground surface. The model identified the depths of the primary seepage paths that were found to be just under the base of the drainage collection trench (Figures 23 and 24). The green in Figures 25 and 26 indicate seepage paths, while the purple indicates less water than predicted, hence minimal, if any, seepage.

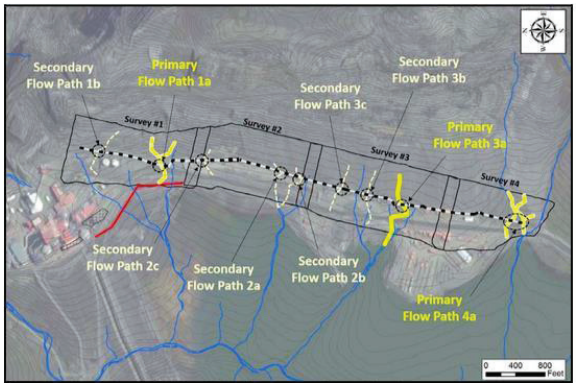

Figure 23. Plan view of seepage paths

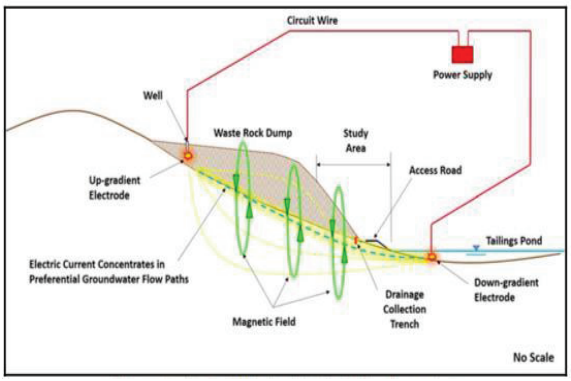

Figure 24. Cross section of survey layout

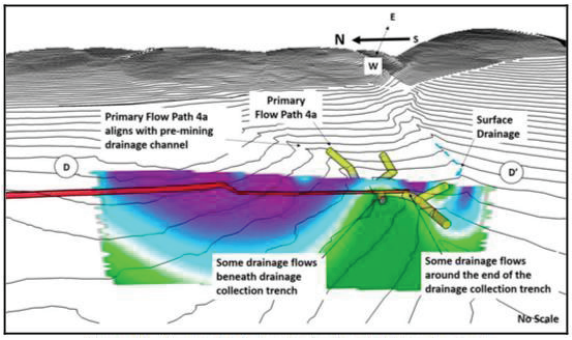

Figure 25. Slices of model

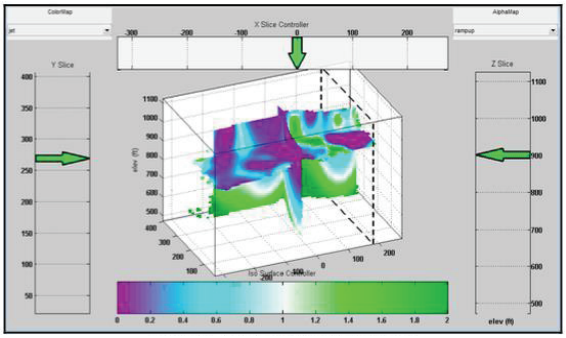

Figure 26. Model slice with seepage path

CONCLUSIONS

The three tailings dam studies show how Willowstick, a relatively inexpensive non-intrusive technology and an extremely quick survey method, can be used to supplement known geological, geotechnical, hydrological and groundwater information to enhance the knowledge of existing seepage conditions.

This knowledge can then be used to cost-effectively support and optimise the design of tailings dam stabilizations and future tailings dam raises including for ultimate closure and post-closure, and to provide long-term safety and stability for TSFs and tailings dams.

ACKNOWLEDGEMENTS

The authors gratefully acknowledge the support of AECOM and Willowstick Technologies in the preparation of this paper.

5th International Symposium on Dam Safety

October 27-31, 2018

RECENT ADVANCES IN ROCK-FILLED CONCRETE DAMS AND SELF-PROTECTED UNDERWATER CONCRETE

Feng JIN[1], Hu ZHOU[1] and Duruo HUANG[1]

1. Department of Hydraulic Engineering, Tsinghua University, Beijing, China

ABSTRACT

Rock-Filled Concrete (RFC) is an innovative sustainable mass concrete technology. It is formed by pouring self-compacting concrete onto the surface of an assembly of large rocks, and then filling the voids. The RFC technology combines advantages of both masonry and concrete in that it decreases cement consumption, lowers the temperature rise caused by hydration heat, and reduces shrinkage of concrete. The technology has been recently brought forward to an innovative environmentally-friendly self-protected underwater concrete (SPUC) for in-the-wet and underwater constructions with the aid of underwater protective agent. This paper aims at acquainting readers with a timely review of state-of-the-art rock-filled concrete dams and the self-protected underwater concrete technology, including (1) overview of RFC dams, (2) research on underwater protective agent and self-protected underwater concrete, and (3) engineering applications of SPUC.

1. Introduction

The Rock-Filled Concrete (RFC) is an innovative sustainable mass concrete technology invented by Prof. Feng Jin and Prof. Xuehui An in 2003. As shown in Figure 1, an assembly of large rocks is cemented with a high-performance self-compacting concrete (HSCC) to build gravity dams and arch dams. The technology combines advantages of both masonry and concrete while avoiding the limitations of each, in that it decreases cement consumption, lowers the temperature rise caused by hydration heat, and reduces shrinkage of the concrete (e.g. An *et al.* 2014; Jin *et al.* 2018a; Xie *et al.* 2015). The RFC technology is a subject of more than 20 national patents (e.g. Jin and An 2003; Jin *et al.* 2007, 2017) and has been recently recognized as a new dam construction technology by the International Commission on Large Dams. The RFC technology was awarded the 2017 National Invention Award (2nd class) by the State Council.

The RFC technology has been recently brought forward to a self-protected underwater concrete (SPUC) technology for underwater construction. The promise of SPUC is built on the successful development of the underwater protective agent (UPA), making SPUC being superior to traditional non-dispersible underwater concrete. In this paper, a timely review of state-of-the-art rock-filled concrete dams and the newly developed self-protected underwater concrete is provided, including (1) overview of RFC dams, (2) research on underwater protective agent and self-protected underwater concrete technology, and (3) engineering applications of SPUC.

2. Overview of Rock-filled Concrete Dams

The development of Self-Compacting Concrete (SCC) dates back to 1980s, when Prof. Okamura in the University of Tokyo invented a new type of concrete that is cohesive in preventing segregation, and could automatically fill the formwork with no need for vibration (Okamura and Ozawa 1995; Okamura 1997). This type of concrete coexisted in the United States was named as the Self-Consolidating Concrete. Immediately after its invention, the SCC technology was applied to a significant number of civil construction projects in Japan and regions beyond, such as anchorage construction of the Akashi-Kaikyo Suspension Bridge (Okamura and Ouchi 2003).

Yet, the SCC technology is not suitable for the construction of concrete dams, given high hydration temperature rise, large shrinkage and high material cost. At that time, there were calls for innovative and suitable dam construction materials to address the key challenges. In 2003, Professors Feng Jin and Xuehui An in Tsinghua University invented the Rock-Filled Concrete (RFC). It is a mass concrete technology, and can be formed by pouring high-performance self-compacting concrete onto the surface of an assembly of large rocks, and then filling the voids. By taking advantages from both masonry and concrete, the RFC technology frees vibration or roller compaction, decreases cement consumption, lowers temperature rise of hydration heat, reduces shrinkage of the concrete, making it a promising material for the construction of both gravity dams and arch dams. Since it was invented in 2003, more than 70 RFC gravity and arch dams have been completed or are under construction. Those dam heights range from 30 m to 90 m. The highest RFC dam under construction is 90 m high (the Songlin RFC gravity dam). To date, based on extensive practice in China, building an RFC dam can reduce the construction cost by 10% to 30% when compared with a conventional concrete dam or an RCC dam under the same condition.

(a) Formwork setting (b) rock leveling (c) HSCC pouring (d) sketch map

Figure 1. Construction process and sketch map of Rock-Filled Concrete

One notable example of the RFC dam is the Baijia double-curvature arch dam with a height of 69 m, which was completed and first impounded in 2015 (Figure 2). The Baijia hydropower station controls a drainage area of 962km², and is located in Shanxi Province, China. It is the highest RFC arch dam for the time being. The main part of the dam body is designed to C20 RFC and set with a 500mm thick HSCC impermeable layer, with an integrated pouring molding of the HSCC impermeable layer and dam body. It is also worth mentioning that a new type of impermeable layer structure is designed and placed on the upstream face of the RFC dam body to overcome potential weakness. The volume ratio of HSCC in RFC is lower than 45%, and the hydration temperature rise of the RFC is about 8-13^{o}C based on in-situ monitoring tests. No cooling pipes were used in the whole dam body.

Figure 2. (a) The Baijia RFC double-curvature arch dam (H = 69 m) under construction, (b) the impermeable layer before HSCC is poured, and (c) the photo taken after construction completed

3. Research and Applications of the Self-protected Underwater Concrete

An underwater protective agent (UPA) has been developed with the aim of producing an innovative self-protected underwater concrete (SPUC) for in-the-wet as well as underwater constructions without vibration, mixing or pressure control. The principle of self-protected underwater concrete is distinct from that of traditional non-dispersible underwater concrete (Yao *et al.* 1999), in that the UPA (a soluble polymer) is poured into water before pouring concrete. The water body is thereafter transformed into a UPA solution with a concentration of approximately 100 ppm. The structures of UPA molecules chains prevent cement particles from dispensation into water, so as to avoid segregation.

3.1 Laboratory tests of the underwater protective agent

The research of UPA focuses on its formulation and optimization specifically for the underwater environment (Jin *et al.* 2018b). To better understand the flow mechanism and underwater cementation process, a series of comparison experiments have been carried out, as demonstrated in Figure 3. To be more specific, three types of mortar have been poured into water, including the ordinary mortar (ref. Figure 3a), the traditional non-dispersible mortar (ref. Figure 3b) and the self-protected underwater mortar (ref. Figure 3c). Note that three types of mortar have the same mix and water-cement ratio, providing a reasonable basis for comparison among the three experimental cases. It is clearly observed in Figure 3(c) that the underwater protective agent could effectively prevent leakage of cement into water, making the water body being completely clear and no suspension. Obviously, the performance of self-protected underwater mortar is superior to those of the traditional non-dispersible mortar and ordinary mortar. It is also worth mentioning that the underwater protective agent (UPA) is designed harmless to marine biology

and environment, which has great promise as an edible material that could be used for green underwater construction.

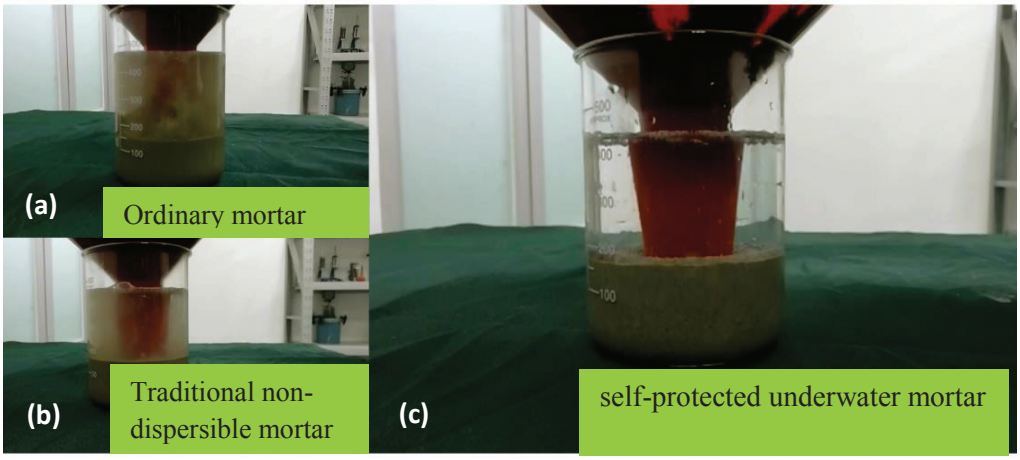

Figure 3. (a) Ordinary mortar, (b) traditional non-dispersible mortar, and (c) self-protected underwater mortar

3.2 Engineering Applications of the Self-protected Underwater Concrete

To date, the self-protected underwater concrete technology has been implemented into a number of engineering projects in China. In this section, several cases of repair and rehabilitation projects using SPUC are introduced.

3.2.1 Bottom Sealing of Piers in Tanjiang Bridge

The SPUC technology is implemented into a pier bottom sealing project in the Tanjiang Bridge located in Guangdong Province, China. Before pouring SPUC, a series of in-situ tests were conducted to validate its performance and optimize design. As shown in Figure 4, a pit was dig and paved with red, white and blue nylon sheets, followed by filling water and pouring UPA. The concrete was subsequently poured until the pit was filled with SPUC. After hardening, it was observed that the elevation difference between ground cast point and the location 5m away is merely 60 mm. The in-situ test results show that the average compressive strength of SPUC drill cores was 36.8 MPa, much higher than the design specification of 25 MPa.

In the following, the piers bottom sealing project in Tanjiang Bridge was carried out based on the success of in-situ test. The water depth is around 10-15 m. The thickness of bottom concrete is 3.5 m. Figure 5(a) shows area of concrete pouring, which is approximately 1000 m^2. The small circles denote 31 prescribed tremies with a diameter of 300 mm, through which the SPUC is poured into water. In actual construction process, only 24 tremies were virtually used given the excellent fluidity of SPUC. In total, 80% of consumed UPA was casted into the bottom water via tremies before pouring concrete. The remaining 20% UPA was thereafter casted into a tremie, followed by placing an insulate ball with a plug device. Concrete was poured into water via the tremie after the insulate ball plugged. We also guaranteed that the ends of tremies were

embedded into concrete with a depth of 500 mm. The separation distance between neighboring tremies is about 8 m. The slope of concrete surface is about 1:20 to 1:30.

Figure 4. In-situ tests of SPUC including (a) pouring concrete, (b) complete pouring and (c) drill cores after hardening in the Tanjiang bridge project

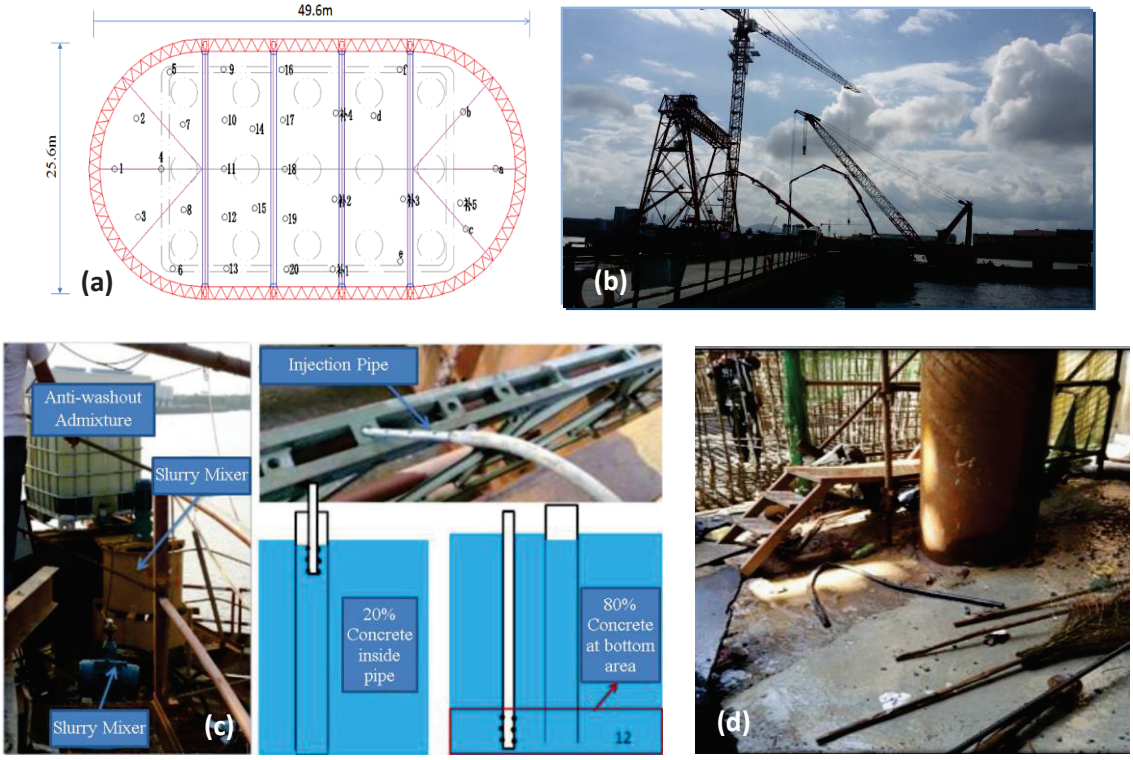

Figure 5. (a) Layout of SPUC construction, (b) construction of Tanjiang bridge, (c) dilution and casting of UPA, (d) piers bottom sealing after completed

The SPUC construction process was quite smooth, which lasts about 36 hours. A total amount of 2223 m^3 SPUC was poured. The average compression strength of drill cores is about 40 MPa, much higher than the design value of 25 MPa. It is also worth mentioning that flow rate in the surrounding water is around 1000 m^3 per hour, with a mud content of 0.95%. The SPUC technology guarantees sufficient compactness and pouring strength in such environment. The Tanjiang bridge project demonstrates the self-protected underwater concrete technology is suitable for underwater construction.

3.2.2 Rehabilitation project of Wanyao Dam

The SPUC was recently applied to the rehabilitation project of Wanyao dam located in Jiangshan, Zhejiang Province. The Wanyao reservoir is a large (Grade II) reservoir with irrigation, water supply, hydropower and flood control functions. The main dam of Wanyao reservoir is a roller-compacted concrete gravity dam with a height of 79 m. The length of dam crest is 390 m. It has been long subjected to severe seepage problem. Figure 6 shows the layout of rehabilitation project, where an impervious concrete face was installed at upstream face of the dam. The mix and quality measurement of SPUC in the project are shown in Tables 1 and 2, respectively. The SPUC was mixed at the mixer plant at the dam crest and casted via a funnel fixed at the crest and a tremie into the workspace underwater. The UPA was diluted and casted into water before pouring concrete. After completion, it is clearly seen in Figure 6(e) that the surface of SPUC is quite smooth without concrete pockmark after removing the side mold.

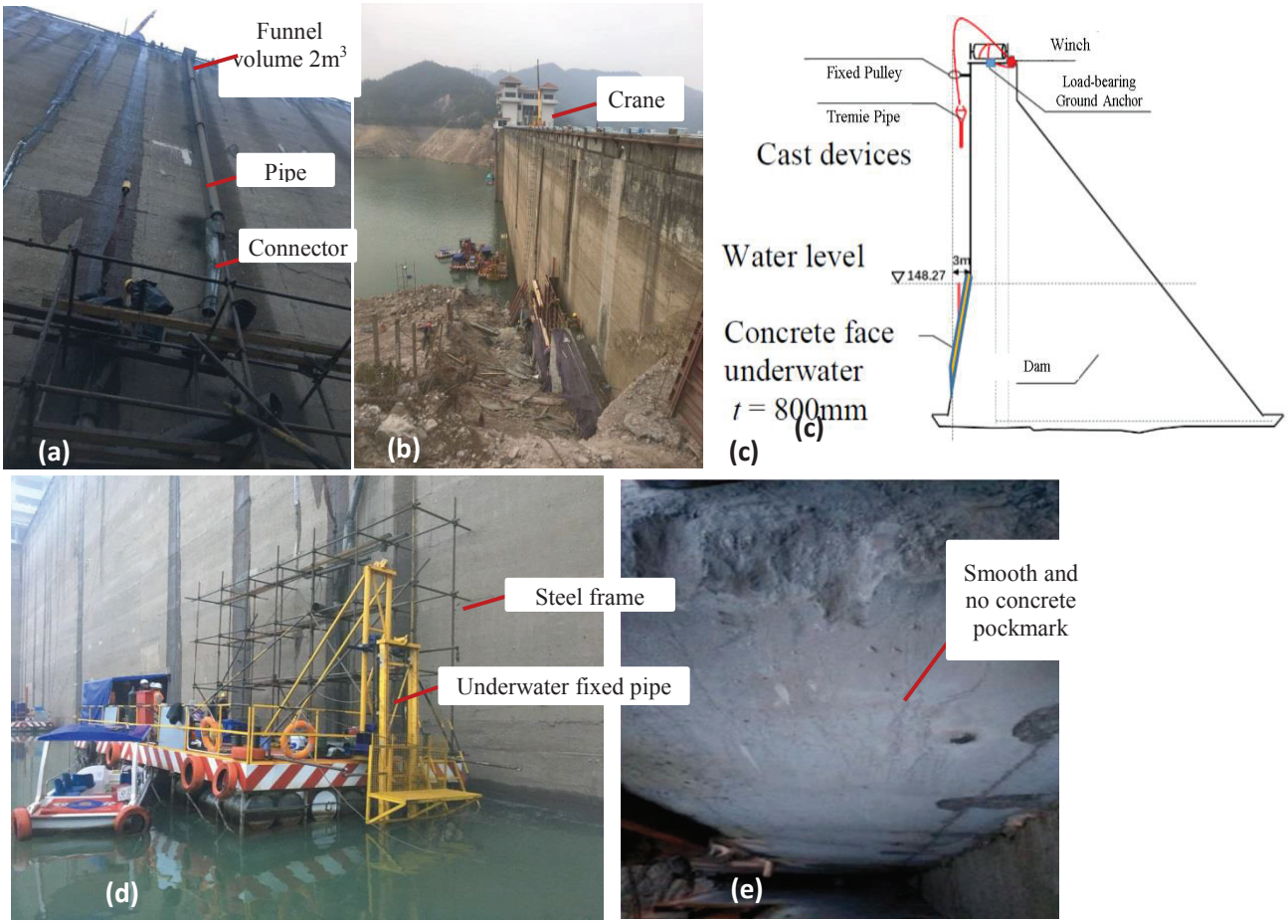

Figure 6. Layout of SPUC construction in Wanyao dam, casting plan during rehabilitation construction and after completion of the project

Table 1. Original mix for SPUC in the rehabilitation project of Wanyao Dam

Type of Material	Cement	Fly Ash	Natural Sand	Artificial Sand	Coarse Aggregate	Water	Superplasticizer
Amount per unit volume /(kg/m^3)	402	106	538	359	688	193	6.33

Table 2. Quality requirements of SPUC by standard mortar test

Test item	Initial value	After 30 min	After 60 min	After 90 min
Slump / mm	260	265	260	260
Slump flow / mm	660	670	660	650

4. Conclusions

This paper provides a timely review of state-of-the-art rock-filled concrete (RFC) dams and self-protected underwater concrete (SPUC) technology. The RFC technique is a subject of more than 20 Chinese patents. Since it was invented in 2003, more than 70 RFC gravity and arch dams have been completed or are under construction. It is also recognized as a new dam construction technology by the International Commission on Large Dams.

Recently, the RFC technology has been brought forward to an innovative self-protected underwater concrete technology for underwater and in-the-wet construction with no need for vibration and mixing. The SPUC technology leverages a newly invented underwater protective agent that could effectively prevent leakage of cement into water and was designed harmless to water environment. Laboratory tests, in-situ tests and engineering applications of the SPUC technology are introduced in this paper. The research and engineering applications on SPUC are still undergoing. It is believed that the innovative material and new construction technology will contribute to the long-term, sustainable, environment-friendly underwater and marine construction development in China and worldwide.

Acknowledgements

The authors thank the National Key R&D Program of China (Grant No. 2018YFC0406800), and National Natural Science Foundation of China (Grants No. 51239006, 51828902) for the financial supports. Researchers and engineers involved in the RFC and SPUC technologies are gratefully acknowledged for their contributions.

References

An X, Wu Q, Jin F, Huang M, Zhou H, Chen C and Liu C (2014). Rock-filled concrete, the new norm of SCC in hydraulic engineering in China. *Cement and Concrete Composites*, 54, pp. 89-99.

Jin F and An X (2003). Construction method for Rock-Filled Concrete dams, Chinese invention patent, patent number: ZL03102674.5

Jin F, An X and Zhou H (2007). Construction method for ordinary rock-filled concrete, Chinese invention patent, patent number: ZL200710100315.3

Jin F, Liu N, Zhou H, An X, Wang W and Li F (2017). Cementing rockfill dam, Chinese invention patent, patent number: 201710671580.0

Jin F, Zhou H and Huang D (2018a). Research on rock-filled concrete dams: a review. *Dam Engineering*, 29, pp. 101-112.

Jin F, Zhou H, Li F and Wan P (2018b). Self-protected underwater concrete in rehabilitation of hydraulic structures. *The 26th ICOLD World Congress*, July 1-7, Vienna.

Okamura H and Ozawa K (1995). Mix design for self-compacting concrete. *Concrete library of the JSCE,* 25, pp. 107-120 (Translation from Proc. ISCE, no 496/v-24, 1994.8)

Okamura H (1997). Self-compacting high performance concrete – Ferguson lecture for 1996. *Concrete International*, 19(7), pp. 50-54.

Okamura H and Ouchi M (2003). Applications of self-compacting concrete in Japan. *Proceedings of the 3rd International RILEM Symposium on Self-Compacting Concrete*, O. Wallevik and I. Nielsson, Ed., RILEM Publications,, pp. 3-5.

Xie Y, Corr DJ, Jin F, Zhou H and Shah SP (2015). Experimental study of the interfacial transition zone (ITZ) of model rock-filled concrete (RFC). *Cement and Concrete Composites*, 55, pp. 223-231.

Yao SX, Berner DE and Gerwick BC (1999). Assessment of underwater concrete technologies for in-the-wet construction of navigation structures. *Technical report INP-SL-1*, US Army Corps of Engineers.

International
5th National Symposium on
Dam Safety

October 27-31, 2018

THE DESIGN AND CONSTRUCTION OF GROUT CURTAINS AND CUTOFF WALLS FOR EXISTING DAMS

Donald BRUCE [1]

ABSTRACT

The use of grout curtains and concrete cutoff (diaphragm) walls has become common practice for the seepage remediation of existing dams in the U.S. in recent decades. Although the design, construction and performance of curtains and cutoffs for new dams is well known, there are very important nuances for remedial applications. This paper explores design concepts as related to system layout, construction issues, and instrumentation and monitoring details, based on experience from about 30 major rehabilitation projects. As further guidance, considerations are provided on the design of the Contract Documents (including Specifications), and Contractual Arrangements.

Keywords: Dam Remediation; Rock Grouting; Diaphragm Walls; Seepage Control; Instrumentation and Monitoring; Contract Documentation and Practices

INTRODUCTION

It is estimated that there are over 84,000 dams in the United States, totaling about 26,000 km (Bruce, 2018). About 14,000 of these structures meet a "High Hazard" classification in that if the dam were to fail, at least one human life would be lost. This does not even address the economic or environmental impacts of dam failure.

Only 4% (3,075) are Federally owned, and these mainly date from the earlier third of the Twentieth Century. Over 87% of the total are primarily classified as earth embankments, while no other category exceeds 3% of the total. The main primary purposes are recreation (35%), flood control (17%), fire protection in stock/small fish ponds (15%) and irrigation (10%), while less than 3% generate power. Many structures are multipurpose. Figure 1 summarizes their completion dates: about 50% were completed between 1950 and 1979, while the median age in the year 2018 is about 67 years.

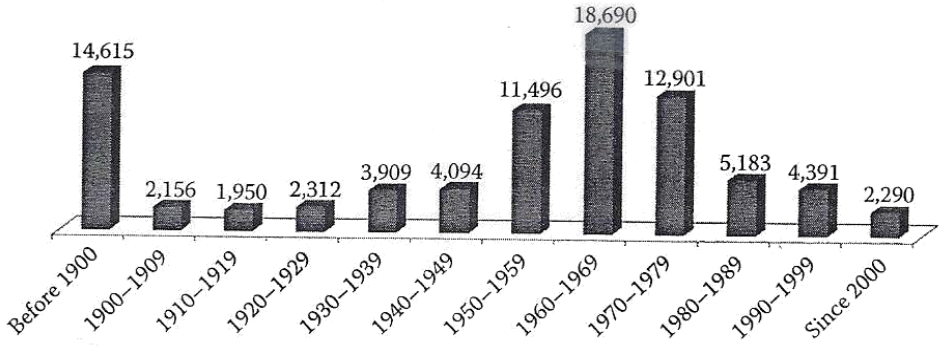

Figure 1. U.S. dams by completion date.
(From National Inventory of Dams, CorpsMAP, http://nid.usace.army.mil, 2010.)

[1] President, Geosystems, L.P., P.O. Box 237, Venetia, PA 15367, U.S.A., Phone: 724-942-0570, Fax: 724-942-1911, dabruce@geosystemsbruce.com.

Whereas it may be calculated from the National Inventory of Dams (2010) that the cumulative "end-to-end" length of all the U.S. dams is around 18,000 miles, preliminary estimates put the cumulative length of levees in the U.S. at over 120,000 miles. Only about 14% of this total may be regarded as federal, and referred to by Halpin (2010) as "robust." The balance includes municipal, local and agricultural structures often featuring little engineering design, patchwork construction and minimal periodic maintenance, since they were traditionally regarded as "simple" structures.

Certain design assumptions and construction techniques used in dams (let alone in the 180,000 km of levees) built prior to, say, 1970, would not be acceptable today, and have left behind fundamental flaws in some structures. Appropriate filter criteria for embankments and uplift/sliding issues in concrete dams are two obvious design related examples, while old approaches to rock surface preparation and foundation treatment would also fall into the unacceptable category. In addition, there are two overriding geological considerations which directly influence the serviceability, reliability, and performance of dams. These considerations are (i) the presence of solution susceptible carbonate and evaporite formations, and (ii) the potential for seismic activity.

Regarding point (i), there is a huge swath of karstic limestones and dolomites which outcrops from Pennsylvania to Alabama, while Martinez et al. (1998) have estimated that evaporites underlie about 40% of the contiguous 48 states. Regarding point (ii), there are highly seismic active zones centered on New Madrid, MO, and Charleston, SC, as well as the more famous seismic belts of the Western U.S. Very simplistically, therefore, lithology and seismicity — either alone or together — pose a clear and present threat to tens of thousands of water-retention structures nationwide, but especially to those in the basins of the central Mississippi-Missouri river system and its major tributaries such as the Tennessee and Ohio rivers, and to those in the Western states. To these concerns must be added the more transient, but equally destructive, threat posed by extreme weather events to embankments all across the country, but especially in the upper Midwest, the lower Mississippi, and central California.

Galvanized by the Gulf Coast tragedy of August, 2005, the Federal Government, in the form of the USACE (U.S. Army Corps of Engineers), developed and implemented a radically different approach to dam remediation prioritization, building on pioneering expertise and experience from the Bureau of Reclamation. This "risk-based" or "risk-informed" approach has since become a model for other bodies with large portfolios of dams, including the Tennessee Valley Authority and other major private utilities. This new approach has been the catalyst for the prioritized and expedited repair of many major structures in recent years.

Grout curtains and/or concrete cutoff (diaphragm) walls have long been used in dam construction, and many fine projects in Turkey have demonstrated the technology to great effect. However, the market in North America has largely focused on remedial solutions to existing embankments. Since 2005, there have been unparalleled levels of activity, as reflected in the case histories presented by Bruce (2012). The purpose of this paper is to highlight fundamental design issues – and solutions – which have developed in that time period spanning the implementation of about 30 major projects. To many readers, these may seem mundane or already too-well known, given the experiences and expertise of Turkish engineers. However, it is hoped that the paper will complement existing knowledge by highlighting design considerations specific to remedial applications.

CONSIDERATIONS FOR THE DESIGN OF REMEDIAL GROUT CURTAINS

The "design" of a curtain is not simply a drawing showing the location, depth and extent of a seepage reduction barrier. While always relying on – and reflecting – the input of specialty contractors, Designers must also specify certain construction practices to ensure the solution is implemented safely, efficiently and effectively. In addition, it is essential that the instrumentation and monitoring of the structure is designed properly to ensure safe dam safety during and after remediation is carried out. Therefore, design considerations are hereunder presented under three main headings: layout

concepts, construction requirements, and instrumentation and monitoring. The same groupings are used in the subsequent summary of considerations regarding diaphragm walls.

Design of Layout

- The length and depth of the curtain must be dictated by geological factors, and must therefore reflect the challenges of the hydrogeological model. In general, the curtain should terminate vertically and laterally into competent, low permeability rock. However, if the remediation is required to combat PFM's relating to subduction of embankment material into very permeable and/or erosion of fines within the upper parts of the rock formation (e.g., in epikarstic zones), then it may be acceptable to have a shallower, "floating" curtain provided a full seepage analysis confirms the safety and reliability of this design and additional supplementary interventions are constructed, e.g., a downstream toe filter berm.

- The location of the curtain is often dictated by preexisting access conditions, but is typically sited on the crest (good access road), a bench cut on the upstream face, or from within a grouting gallery. In any case, continuity must be assured between the curtain in rock and the core of the dam, in the case of a zoned embankment or the upstream part of the footprint of a concrete dam.

- The typical standard of care features a minimum of two rows of holes, inclined (within vertical planes) at about 10-15° off vertical, each row in opposite directions. This "criss-cross" pattern assures intersection and treatment of all joint sets, including those with vertical dip. Normally a third row of "tightening" and/or verification holes is installed between the two (already completed) outer rows. Where special "features" are found in the rock mass, one or more additional partial rows of holes can be installed as a "blister" on the upstream side of the curtain.

- A standard closure pattern is set, with Primaries at 10-12 m centers in each row. Full Secondaries can be anticipated, with variable intensities/frequencies of Tertiaries and even higher order holes, depending on the actual features discovered.

- The downstream row of holes should be completed before commencing on the upstream row and the Tightening/Verification row.

- The first stage (typically 2-5 m long) should be systematically downstaged in order to treat carefully the often critical upper rock horizons, and to provide, conceptually, a grouted "umbrella," hydraulically isolating the rock mass from the embankment itself. As noted below, special steps must be taken to assure that no fluids from the drilling, water testing, or grouting activities in the foundation can find their way into the embankment itself (except, of course, within and through the previously installed standpipes). Upstaging is preferred therebelow, provided the rock mass is mechanically stable, and no zones with major fluid losses or rod drops have been encountered during drilling.

- The "measures of success" must be explicitly described. These are typically one or more of the following:

  - a target residual permeability in the finished curtain (usually 5 Lugeons or less);
  - a reduction in seepage rates;
  - a major readjustment of piezometric surfaces within and below the dam;
  - elimination of "wet patches" on the downstream face of an embankment;
  - reduction of uplift pressures under a concrete dam.

Design of Construction

- First and foremost, the design must specify what is not acceptable in practice. For example, the use of air flush drilling in either embankment fills or foundation soils or rock is not permissible. Otherwise, the experience and expertise of the bidders should be exploited.

- Drilling through embankments is typically conducted with rotary sonic drilling, or dry double duplex. Such "no fluid" systems are specified by the USACE Engineering Manual 1807 (1997). Drilling in rock is most economically conducted with Water Powered, Down-the-Hole Hammers (Bruce and Lyon, 2017). Even with best and safest practice, piezometric "spikes" can be anticipated from nearby instruments, but these are normal, very transient, and will not constitute a construction PFM or a Dam Safety Issue.

- Deviation monitoring of boreholes is useful in deep curtains to ensure no untreated "windows" remain. However, only a limited number of holes to be monitored is typically warranted (say 10% of the total).

- Special care must be exercised in the placement and sealing of standpipes placed in an embankment. Details are provided in Bruce et al. (2018).

- In brief, the performance goals are (1) to ensure the annulus created around the standpipe when the drill casing is withdrawn is fully filled without damaging the dam, and (2) to hydraulically isolate the dam from the foundation by allowing a verifiable and effective treatment of the contact and the first, uppermost stage. Best practice is to use some form of Multiple Packer Sleeved Pipe (MPSP) system, such as originally developed at Oymapinar Dam, Turkey, by Rodio SpA in the late 1970's. Figure 2 provides a typical practical design detail.

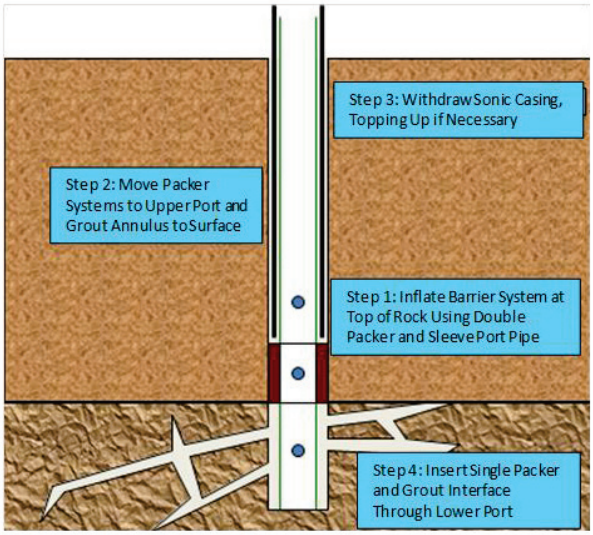

Figure 2. Separation of embankment and foundation.

- The design must address the maximum safe water testing and grouting pressures which can be used. Multistep water testing in the early Primary holes (or in preconstruction Investigation holes) will be of great value, coupled with the use of real-time injection parameter monitoring and analysis. Old-fashioned "rules of thumb" (e.g., 1 psi/ft) should not be relied upon exclusively (or at all!).

- The fluid and set grout properties must be clearly dictated in the design. The contractor will be responsible for achieving the properties and maintaining their consistency throughout the project. The key design requirements of contemporary, modified, balanced, stable grouts are as follows:

  - minimal bleed (≤ 1%);
  - pressure filtration coefficient of ≤ 0.08 $min^{-½}$;
  - initial set and hardening times;
  - Marsh Viscosities for a suite of High Mobility Grouts (HMG's) which will be used in sequence, viz 30-35 seconds; 40-45 seconds; 55-60 seconds; and > 90 seconds, as a minimum. How these are used (and changed) is described below.

- The grout take refusal criterion for each stage must be specified. Under normal conditions, it is reasonable to choose a value of about 2 liters/min over a 5-minute period at the target maximum pressure. Stages which encounter large voids/high flow volumes should be grouted with the highest viscosity mix feasible, and "rested" if the stage take exceeds a certain design volume, e.g., 5 m^3. Grouting is resumed after initial set of the grout has been achieved.

- Every stage should be water tested prior to grouting, with at least a single pressure test of minimum 5 minutes duration. Investigatory Verification hole stages should have more prolonged, multi-step tests, per Houlsby (1976).

Design of Instrumentation and Monitoring

- Each drilling, water testing and grouting operation must have specially-designed, real-time monitoring and recording instrumentation. Drilling parameters such as thrust, torque, penetration rate, etc., are integrated to provide a unit of "Specific Drilling Energy," i.e., a measure of the drillability of the ground. This is the "Measurement While Drilling" concept. Injection parameters are collected and integrated in real time to provide Lugeon values (for water) and Apparent Lugeon values (for grout, assuming the grout is, in fact, stable during injection). The development of the Apparent Lugeon value with time is the key to changing mix formulation in any given stage being grouted.

- It is now common practice for an Owner to specify that the contractor collects, presents and stores all his construction data in some form of an automated DMS (Data Management System). Contractors are often overwhelmed (initially at least) by the needs and scale of such a system. This must not be permitted by the Owner to occur: a fully compliant DMS must be up and running before production work commences. From the technical viewpoint alone, it is integral to informing all interested parties on the progress and effectiveness of the work (e.g., via Trend Analyses), and is therefore the only true basis for determining when the work is actually complete or if further work (e.g., higher order holes) is required, and where.

- The Contractor's DMS must be controlled by a suitably qualified grouting engineer (not just an IT specialist). There must be a similarly-equipped, dedicated and experienced engineer on the Owner's side. All parties must have access to all the information generated during the works.

- It is normally the case that the dam to be remediated will already have some intensity of instrumentation and, in fact, it is usually the case that the results of this instrumentation have highlighted the actual need for remediation, in concert with visual observations. Further instrumentation is invariably justified just before or during the grouting, to target specific "problem areas," or simply to ensure a broad coverage without data gaps. The result is a plethora of instruments, typically now configured to provide data in real time.

- It is essential for Dam Safety Assurance during construction that the Designer and the Contractor partner to collect, study and act upon these data in real time, regardless of whose contractual responsibility or liability it may be. The most efficient strategy is to create, prior to construction having commenced, a Joint Instrumentation Monitoring Plan (JIMP). This will identify which instruments are to be read, by whom, and at what frequency. The JIMP will also provide Threshold and Action Level guidance for each instrument, and identify courses of action when these levels are reached.

- A JIMP is implemented most effectively when the Designer and the Contractor can view the data while being physically in a joint "Mission Control" facility. In this way, the impact of the Contractor's work on the dam and its foundation can be judged in real time, and acted upon accordingly, as necessary.

- After the curtain or cutoff has been built, it is typical that little attention is paid to continuing to use the in-situ instrumentation to monitor the long-term efficiency of the cutoff. Even less attention is devoted to publishing such data so that the dam remediation community can have the benefit of a successful (or unsuccessful) case history. Such long-term monitoring is the responsibility of the Owner, and this should be regarded by them as an essential cost outlay – perhaps as part of the routine O&M budget.

- The typical dam and foundation instrument groups are well known, being piezometers, inclinometers, settlement monitoring, and seepage monitoring (e.g., via calibrated weirs). In addition, during drilling, grouting and cutoff wall construction, invaluable information on flow path geometry and dam response can be gained from electronic "trolls," installed in downstream holes to record pH and turbidity "hits." Construction activities can thus be a valuable tool in improving the hydrogeological model.

CONSIDERATIONS FOR THE DESIGN OF REMEDIAL CONCRETE CUTOFF WALLS

In many regards, the design requirements of concrete cutoff (diaphragm) walls are similar to those for grout curtains, and these similarities are outlined below. However, such cutoffs can be constructed by many different methods (Bruce 2012 and 2018). The basic classification considers :

- Category I Walls: The embankment and foundation materials are excavated under temporary supporting fluid (typically bentonite or polymer slurry) which is then displaced upwards and outwards by some type of final cementitious backfill material. There are many different types of wall excavation techniques, such as backhoe, clamshell (mechanical and hydraulic), hydromill cutter, or secant piling concepts.
- Category II Walls: For soil applications, the embankment and/or foundation materials are mixed in-situ by injecting cementitious binder delivered via large diameter augers (Deep Mixing Method), cutters (Cutter Soil Mix), or chain saws (TRD Method or "One Pass").

With this background – which requires a fundamental design decision to be made ab initio – the other key design considerations can be made in the same format as for grout curtains, above.

Design of Layout

- The length, depth and width of the wall must be primarily dictated by the driving PFM's and the geotechnical conditions. Careful considerations of the hydraulic gradients acting on the wall during service, and its fragility in a seismic event, must be considered in designing the hardened parameters of the wall, especially its strength and its stiffness. The permeability of such walls (usually specified as being $\leq 10^{-8}$ m/s) is typically easily achievable in the field using appropriate means, methods and materials (and testing methodologies!).

- The plan location of the wall must reflect the same issues as for grout curtain, but special attention must be paid to the location, width and stability of the working platform, since equipment of over an order heavier than grouting equipment is typically used.

- Careful attention must be paid to the design of the "connection" between the cutoff, and preexisting features such as hard, steep rock abutments, concrete structures such as powerhouses or spillways, and subsurface features such as bottom outlets or other through-going perforations.

- A common recent practice for remedial cutoffs in karstic conditions is the construction of a "composite wall" (Bruce et al. 2008). A two-row grout curtain is first installed, and then the cutoff wall is constructed between these two rows. The goals of the drilling and grouting program are to:

  - pretreat the foundation to prevent sudden and catastrophic loss of supporting fluid, and so loss of trench stability;
  - provide a site investigation of, relatively speaking, very high intensity, so that the dimensions of the wall (and especially its terminal depth) can be designed closely and economically;
  - allow the hydraulic cutoff effect of the wall to be extended into non-erodible rock, more economically by the grouting, as opposed to the diaphragm wall.

- Such pregrouting must be conducted to a high and consistent standard by a specialty contractor.

- As for any cutoff, specific performance goals must be set and verified, including:

  - reduction in seepage;
  - acceptable and logical piezometric performance;
  - elimination of other classic "signs of distress," e.g., settlements, sinkholes, muddy flows, damp patches, boils).

  In addition, the durability of the wall – typically a relatively thin membrane (0.8 – 1.5 m) subject to high differenial heads (100 m or more) – must be addressed.

Design of Construction

- Special and specific dam safety concerns likely to arise during construction must be clearly spelled out to prospective contractors so that they may address these in bids, and later in preconstruction submittals and construction work plans.

- As alluded to above, designs should address unacceptable construction methods, but encourage contractor originality and innovation, especially as contributing towards dam safety during construction.

- Each Contractor has its own particular mentality and preferences for means and methods, as well as for equipment. Each project's construction details must therefore be evaluated on this basis, with the prime concern being the safety of the dam during construction.

- A proper, stable, working platform (concreted if possible) is essential for a host of reasons, ranging from personnel safety to enhancing productivity.

- "Technique Demonstration Areas" – thoroughly analyzed and approved – are invariably of great value to all the project's stakeholders.

- Time is well spent up front in building high quality, weatherproofed bentonite and concrete materials storage and batching facilities, and maintenance shops.

- Development of mix designs and their approval by the Designer should not be allowed to negatively impact schedule and should be given high priority during the site mobilization phase.

- All preconstruction permits, etc., must be in place prior to site mobilization.

- The specification must confirm that all equipment is maintained regularly, and that all instrumentation is frequently recalibrated (if necessary).

- Individual cutoff wall elements, be they rectilinear wall panels, or secant piles, should be sized to minimize the number of inter-element joints, consistent, always, with dam safety concerns.

Design of Instrumentation and Monitoring

- The prime steps to be designed for a grout curtain – namely creation of the JIMP; automated real-time monitoring of construction parameters and dam response; and operation of a DMS – equally apply to cutoff wall operations.

- In addition, and in particular for cutoff wall projects which typically are of elevated scale, risk and scope, a comprehensive, formal Quality Control Implementation Plan is essential to design, and the effort needed for the drafting and implementation of this Plan should not be underestimated by the Contractor. This *project-specific* plan must address, as a minimum:

  – Site organization charts showing responsibilities, lines of communication and levels of authority of project personnel from all stakeholders;
  – Setting out methods and tolerances;
  – Bentonite or polymer slurry properties, production and testing;
  – Wall verticality and panel overlap (by at least 2 independent methods);
  – Wall tolerances;
  – Joint cleanliness criteria;
  – Concrete materials, batching, placement and testing;
  – Verification coring and in-situ permeability testing (and the use of an Optical Televiewer);
  – Management and communication of data and records (real time, and archived).

CONSIDERATIONS FOR THE DESIGN OF CONTRACT DOCUMENTS AND CONTRACTUAL ARRANGEMENTS

- Performance-based specifications are optimal, provided the fundamental performance goals are clearly and consistently stated.

- "Partnering" must be implemented rigorously, and with total commitment at all levels in each stakeholder.

- Contractual risks must be allocated fairly, with the Owner being responsible for the site conditions and for the potential impacts and benefits of any previous remediations (e.g., by pregrouting) on the project. Risks to the Owner can be managed in many ways in concert with his Designer:

  – Ensure <u>all</u> available site-specific data are made available at bid stage;

- Engage an appropriately qualified, experienced and resourced Design Engineer and Board of Consultants;
- Clearly define respective roles, responsibilities, and duties, especially for site inspection staff;
- Select a "Best Value" as opposed to "Low Bid" basis for Contractor selection;
- Insist on a "Partnering" environment as a means of resolving disputes;
- Select a qualified and experienced Specialty Contractor with appropriate human and mechanical resources;
- Encourage the bidders, via Performance Specifications, to bring their own ideas and expertise to the project;
- Ensure specification modifications are issued quickly by the Designer, and be sympathetic to requests for bid extensions;
- Allow budget for adequate short- and long-term instrumentation.

- There must be realistic project expectations, such as that:

  - The project will satisfy the design intent;
  - The project will be designed and built to the current state of practice and to appropriate referenceable standards of care;
  - Project schedule is actually attainable (especially in "tight" projects with multiple trades);
  - The work will not cause damage or detriment to adjacent preexisting structures;
  - Claims are inevitable, and must be evaluated strictly on merit (often not the case when Construction Managers operating on very small margins are involved).

- The principles of "Early Contractor Involvement" should be applied whenever feasible, and especially on particularly challenging projects, technically or schedule-wise.

- Particular details are provided in Bruce and Dreese (2010), which also provides guidance on the tasks and responsibilities which are to be allocated prior to drafting the project plans and specifications, and items to be addressed in these documents.

CLOSURE

The design of remedial curtains and cutoffs for existing dams involves a number of subtle, but critical, nuances in relation to the use of these same techniques in new dam construction. Careful attention must be paid to these issues during all phases of the delivery of a project. This paper presents a summary of observations and findings based on the particularly intense levels of seepage remediations on U.S. dams since 2005 in particular, in the hope that practitioners from other countries can benefit from these experiences. It is very easy in this day and age to become an "instant" internet expert, but it is also very easy to fail badly by ignoring practical experiences.

REFERENCES

Bruce, D.A., T.L. Dreese, and D.M. Heenan (2008). "Concrete Walls and Grout Curtains in the Twenty-First Century: The Concept of Composite Cut-Offs for Seepage Control," USSD Annual Conference, Portland, OR, April 28-May 2, 35 pp.

Bruce, D.A. and T.L. Dreese. (2010). "Specifications for Rock Mass Grouting," ASDSO Dam Safety Conference, September 19-23, Seattle, WA, 12 pp.

Bruce, D.A. (2012). "Specialty Construction Techniques for Dam and Levee Remediation," Spon Press, an imprint of Taylor and Francis, 304 pp.

Bruce, D.A. and R. Lyon (2017). "Recent Advances in Overburden and Down-the-Hole Drilling Techniques" 5th International Grouting, Deep Mixing, and Diaphragm Walls Conference,

International Conference Organization for Grouting (ICOG), Honolulu, Oahu, Hawaii, July 9-12, 10 pp.
Bruce, D.A. (2018). "Seepage Cutoffs for Dams and Levees: Lessons Learned from 40 Years of Remedial Construction in North America," International Commission on Large Dams (ICOLD) 26th Congress, 86th Annual Meeting, Vienna, Austria, July 1-7, 10 pp.
Bruce, D.A., T.L. Dreese, J. Cockburn (2018). "Remedial Grouting of Existing Embankment Dam Foundations: Lessons Learned (and Ignored)," International Commission on Large Dams (ICOLD) 26th Congress, 86th Annual Meeting, Vienna, Austria, July 1-7, 10 pp.
Halpin, E.C. (2010). "Creating a National Levee Safety Program, Recommendations from the National Committee on Levee Safety," ASDSO Dam Safety Conference, September 19-23, Seattle, WA, 22 p.
Houlsby, A.C. (1976) "Routine Interpretation of the Lugeon Water-Test." Quarterly Journal of Engineering Geology. 9, 303-313.
Martinez, J.D., K.S. Johnson and J.T. Neal. (1998). "Sinkholes in Evaporite Rocks." American Scientist, v. 86, no. 1, pp. 38-51.
National Inventory of Dams (NID). (2010). http://nid.usace.army.mil.
Weaver, K.D. and D.A. Bruce (2007). "Dam Foundation Grouting, Revised and Expanded Edition," American Society of Civil Engineers, ASCE Press, New York, 504 p.
U.S. Army Corps of Engineers (USACE) (1997). "Engineering and Design Procedures for Drilling in Earth Embankments," CECW-EG, Report No. 1110-1-1807, September 30.

5 DAM SAFETY
İstanbul Turkey 2018

5th International Symposium on Dam Safety

October 27-31, 2018

OVERVIEW OF DAMS IN THE MIDDLE EAST THROUGHOUT HISTORY AND DAM FAILURES IN THE LAST CENTURY IN THE WORLD

Gökmen TAYFUR

Dept. Civil Engineering
Izmir Institute of Technology Urla, Izmir, Turkey
Email: gokmentayfur@iyte.edu.tr

Abstract: The paper reviews the ancient dams built in the Middle East, especially in Turkey, Iran, and Egypt. The dams were used for irrigation and drinking water purposes. They were earthfill and/or rockfill embankment dams. Some date back to 3000 BC. Some were enormous like Marib Dam in Yemen with 720 m length, 60 m width and 15 height. Some are still in operation like Kesis Dam in Van. Most of them failed due to possible heavy flooding. In Medieval times; the construction of embankment dams had continued in the Middle East. Even, the first arch dam was built in Iran about 900 years ago. In 1350 AD, Iranians built 60 m high arch dam, which is still in use. In the dams built by Ottomans in the 19th century, also, pozzolanic cement was used to bind the stones and lead was used to assure the total impermeability. The dams were mostly masonary butress dams. The technology has been developed in this last century such that presently, there are multipurpose giagantic dams like Ataturk Dam in Turkey, and Aswan Dam in Egypt. Also, very high arch dams are being built with the state of the art technology such as Yusufeli Dam (270 m height) in Turkey and Kosar Dam (325 m height) in Iran. Dams has failed in the ancient times, medivel times and currently. The paper also highlights the dam failure types and continantel distributions and death tolls in this last century all over the world.

Keywords: Ancient dams, Medievel dams, Modern dams, Middle East, Dam Failures

INTRODUCTION

Dams have been built since 3000 BC. In fact, the first ancient dams were built in Anatolia, Mezopotamia, and Egypt (see Figure 1). The main purpose earlier was irrigation and drinking water supply. The dams were built as earthfill and/or rockfill dams due to the level of technology. Clay was used as plaster to bind the rocks and prevent the infiltration.

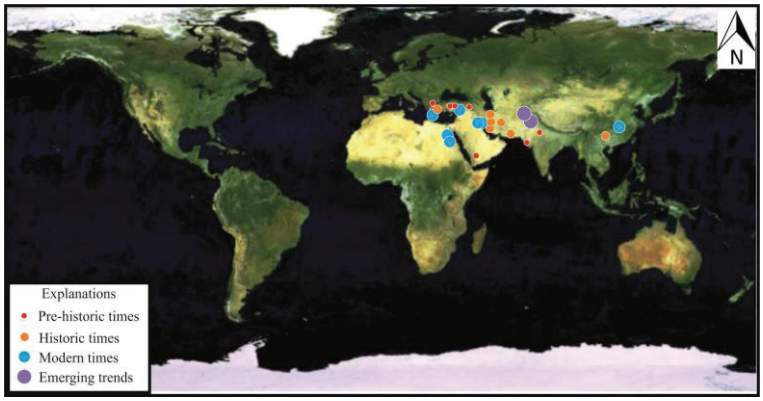

Figure 1. Dams in the Middle East

In medeivel times, we see the building of the first arch dam by Iranians. The one built in 1350 AD, 60 m high Kurit gravity arch dam, was the tallest arch dam until the beginning of the 20th century. In the 19th century, the dam's construction material also involved the cement and lead. Cement was used for binding, and lead was used for total impermeability. In the 20th century, large dams were built for the purpose of not only irrigation and drinking water supply but also for flood control, hydropower generation and even for recreation. There have been construction of many dams in recent years, especially in Turkey and Iran using the state of the art technology.

Dam failures have been inevitable throughout history. The common reasons used to be extreme flooding in ancient times. In this last century, ill-design, improper geological setting, ill-construction were the main reasons. The technological developments and experience has overcome these reasons but the extreme inflows and overtopping is still the main reason. The purpose of this study is to overview the ancient, medieval and modern dams in the Middle East and analyze the dam types, and failure types in the world in this last century.

ANCEINT DAMS IN THE MIDDLE EAST

Turkey

Various dams were dating back to the Hittite period (1600 BC) in Anatolia. Karakuyu Dam in Kayseri was constructed as the U-shaped crest with a total length of 400 m (Ozis et al. 2010). It was an earthfill dam and had 1.4 m wide and 8 m long sluice made of rectangular stones (see Fig. 2).

Figure 2 Karakuyu Dam

Golpınar Dam is one of the important dams from Hittite period in Anatolia (DSI 2008). The stones of the rockfill embankment have the size of a fist. The clay was used to strengthen the stones. Kesis Dam in Van is from the period of Urartian Kingdom (1000-500 BC). This dam along with the irrigation system still in use, storing about 20 million m^3 of water.

Iran

The history of the ancient dams in Iran dates back to 3000 years and shows that ancient Iranians were among the pioneers in dam construction in their efforts to develop water resources. The Darius Dam on Kor River dates back to 2500 years. Bahman Dam in Shiraz (Fig. 3) was built more than 2000 years ago. 1700 years old Mizan Dam in Shushtar is still in place. Amir Dam constructed by Buyids Dynasty, 35 km north of Shiraz, is 1000 years old.

Figure 3. Bahman Dam in Iran

Egypt

The embankment dams had been used very early in the ancient historical periods of Egypt. Loon (1992) reported that dam construction began about 6000 years BC in Egypt, which was used mainly for flood control and irrigation purposes. However, potable water supply and irrigation systems in Egypt have existed from the fourth millennium BC. Many small earthen dams and irrigations canals were built by ancient Egyptian to manage the Nile River water. The remains of one of the oldest and greatest known dams, Sadd-el-Kafara, built during the period of 2950 to 2750 BC, were found in Egypt in the Wadi el Garawi, 30 km south the capital city, Cairo (Saxena 2004). The dam site and a sketch for its dimension are shown in Figure 4. It was 107 to 113 m in crest length and 11 to 14 m in height. It was consisted from two masonry shoulders supporting a central core of sand and gravel. The core consisted of 60,000 ton of earth and rock-fill (Jansen 1980). The downstream wall was about 37 m wide, the upstream wall was about 29 m wide and they contained around 2,900 m^3 a mass of materials. These upstream and downstream walls were constructed from limestone ashlars. Each stone was roughly 30 cm high, 45 cm wide, 80 cm long and 23 kg (Fahlbusch 2017). Due to the erosion of the downstream face of the dam and lack of a spillway, it is believed that a flood destroyed it.

Figure 4. Sadd-Elkafara dam ruins and sketch for its cross-sectional dimensions (Schnitter 1994).

MEDIEVAL DAMS IN THE MIDDLE EAST

Turkey

In the Ottoman period of 1620 to 1839, two major water conveyance systems were built in Istanbul (Cecen 1987). The systems contained several dams. Four dams supported the Kirkcesme System and three dams supported the Taksim System (Fig.5). The dams have heights up to 17 m and crest lengths up to 104 m (Cecen 1987). These dams and systems are still in operation. Similarly, Elmalı Dam, constructed in 1893 on Asian side of Istanbul, is also still in operation.

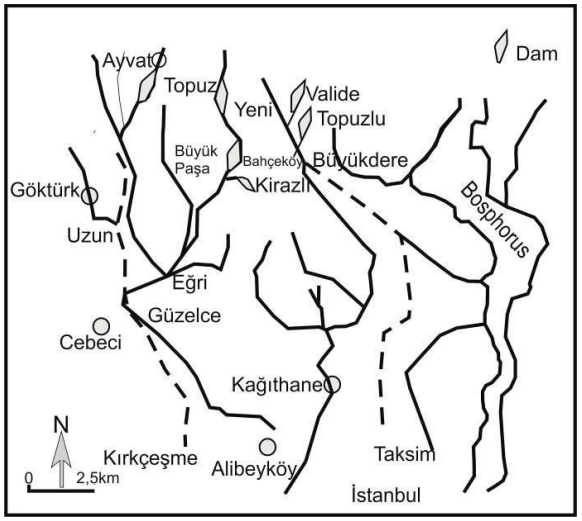

Figure 5 Kırkcesme and Taksim Systems

The Ottoman dams were constructed by two masonry walls with an impervious fill between them. The difference from the old techniques that pozzolanic cement was used to bind the stones and the lead was used to assure the total impermeability. The crest and the downstream of dams were lined with marble since there was no spillway.

Iran

Kebar Dam in the city of Ghom has a height of 25 m and it is believed to be the first arch dam built in the world about 700 to 900 years ago. Kurit gravity arch dam, located close to Tabas city was built in 1350 AD. Its height is 60 m and it was regarded as the highest dam in the world up to the beginning of the twentieth century (Fig. 6). During the Safavid Empire (1501-1736) water engineering progressed significantly and many storage and diversion dams and bridges were constructed in Esfahan and Mashhad, some of which still exist. Khaju Bridge and diversion dam and the Thirty – three Arch Bridge are two of the very famous and beautiful diversion dams and bridges in the city of Esfahan (Fig. 7) (Mahmoudian & Mahmoudian 2012).

Figure 6. Kurit Gravity Arch Dam in Tabas

Fig.7 Thirt-Three Arch Bridge in Isfahan

Egypt

The Aswan Low Dam built in 1902 is a gravity masonry buttress dam on the Nile River in Aswan, Egypt. The dam was built at the first waterfall of the Nile and it is located 690 km south-southeast of Cairo. It was the largest masonry dam in the world. The dam was designed to provide storage of annual flood water and supplement dry season flows to support greater irrigation development and population growth in the upper part of Egypt. The dam, originally limited in height by conservation concerns, worked as designed, but provided inadequate storage capacity for planned development. The dam was raised twice, in the periods of 1907–1912 and 1929–1933 for the height increase of 5 and 10 m, respectively (Novokshshenov 2011).

MODERN & PRESENT DAMS

Turkey

The construction of large dams started in late 1960s in Turkey. One of the largest one built in 1980s on Euphrates River is Ataturk Dam. It is the largest dam in Turkey and ranks sixth

amongst the largest earth-and-rock fill embankment dams in the world. The rockfill dam with the central core has a crest length of 1,820 m and height of 184 m. It is constructed to control flood water, irrigation and power generation. Most recently; Deriner Dam, which is a concrete double-curved arc dam on the Coruh River, 5 km east of Artvin in the northeast edge of Turkey was built in 2012 (Fig. 8). The main purpose of the dam is to produce hydroelectric power in addition to flood control.

Figure 8. Deriner Dam

Currently, Yusufeli Dam is being built, as a double-curvature arch dam with a height of 270 m in Artvin. It will have a crest length of 490 m and crest width of 15 m while being composed of about 3 million m^3 of concrete. The dam's spillway will be a service controlled chute type with a maximum discharge capacity of 8,000 m^3/s. The dam will have an underground power station (540 MW) that is 110 m long, 21.4 m wide and 45.2 m high.

Iran

Modern dam construction in Iran began in late 1950s. One of the most interesting dams from construction point of view is Kosar Dam which is located in a narrow gorge. The dam height is 144 m and the river width ranges from 6 to 8 meters. The dam abutments at both sides are sub-vertical from foundation up to the elevation 580 m at sea level (a.s.l). The riverbed is at elevation 500 m a.s.l. The gorge width at this elevation is about 40 to 50 m which makes the construction of the dam very difficult and costly within this height range. Hence, according to the natural shape of the site, an exclusive and quite different method of construction has been adopted. A 2 m thick metal platform was constructed at elevation 527 m a.s.l. (Fig.9). The gorge below this elevation has a discharge capacity of 2700 m^3/s. During wet season the flood currents flow along the river under the platform while the concreting of the dam is carried out above that. To carry out the construction work below this platform during dry season, a diversion system was constructed which consists of a 5 m diameter tunnel with a length of 500 and a 6 m high cofferdam (Farhangi 2003). Currently, Bakhtiari Dam, which is the highest double arch concrete dam in the world, is currently under construction on the Bakhtiari River within the Zagros Mountains on the border of Lorestan and Khuzestan Provinces. The height of the dam is 325 m. The Catchment area is 6,288 km^2 and the capacity of hydropower station is 1500 MW. Construction of the dam began on March 25, 2013.

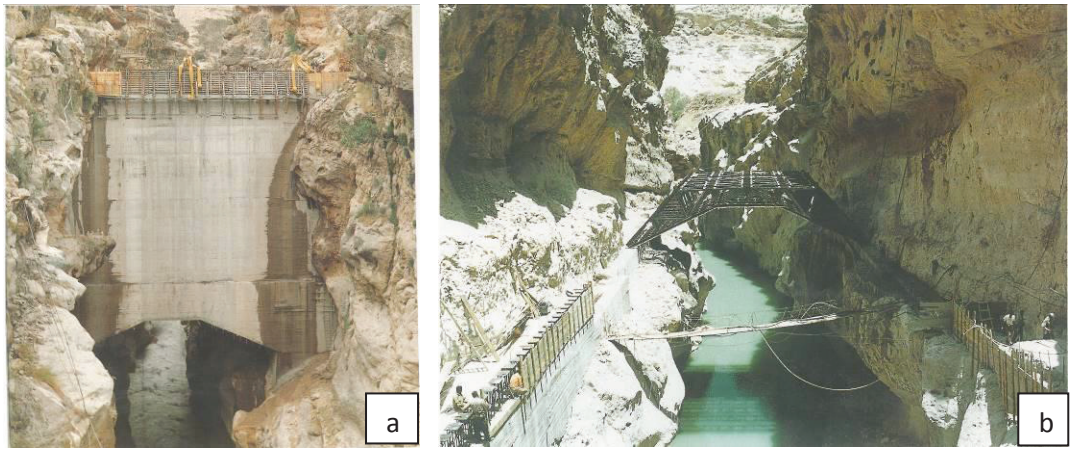

Figure 9. Kosar Dam; (a) dam on the platform, and, (b) Platform

Egypt

Aswan High Dam was constructed in 1970 in Aswan. It is a rockfill dam with grout curtain and clay core (Figure 10). Its total length is 3600 m and its height 111 m above the river bed. The storage capacity of its reservoir is 162 km^3. It has had significant impacts on the economy and culture in Egypt. The most important effect is that it converted a highly variable annual Nile flow into a predictable source of a constant supply. Water in the lake behind the Dam is available for release any time during the year, so seasonal variability can be manipulated to deliver supplies of water that match the optimal demand pattern (Schamp 1983).

Figure 10. Aswan Dam

DAM FAILURES IN THE LAST CENTURY

There are several types of dams such as embankment, gravity, butress, arch and RCC. Majority of the dams have been embankment dams and gravity dams. There are several causes of failures mainly; overtopping, piping and seepage, earthquake, extreme inflow, ill-desing, ill-foundation, ill-construction, poor meaintanance, and war. 78 major dam failures

occured all over the world from 1908 to 2018. The first dam failure was in 1908 in USA (**Hauser Dam in Montana).** It was a gravity dam and failed due to a foundation problem together with heavy flooding. The last one was in Kenya in 2018 (**Patel Milmet Dam in Solai**). It was an embankment dam and failed due to extreme inflows. Majority of dams failed were embankment (52%) and gravity (32%) ones and majority of the dam failure causes have been extreme inflows and overtopping (43%), ill-construction (16%), ill-design (13%) and ill-foundation (10%) (see Fig. 11).

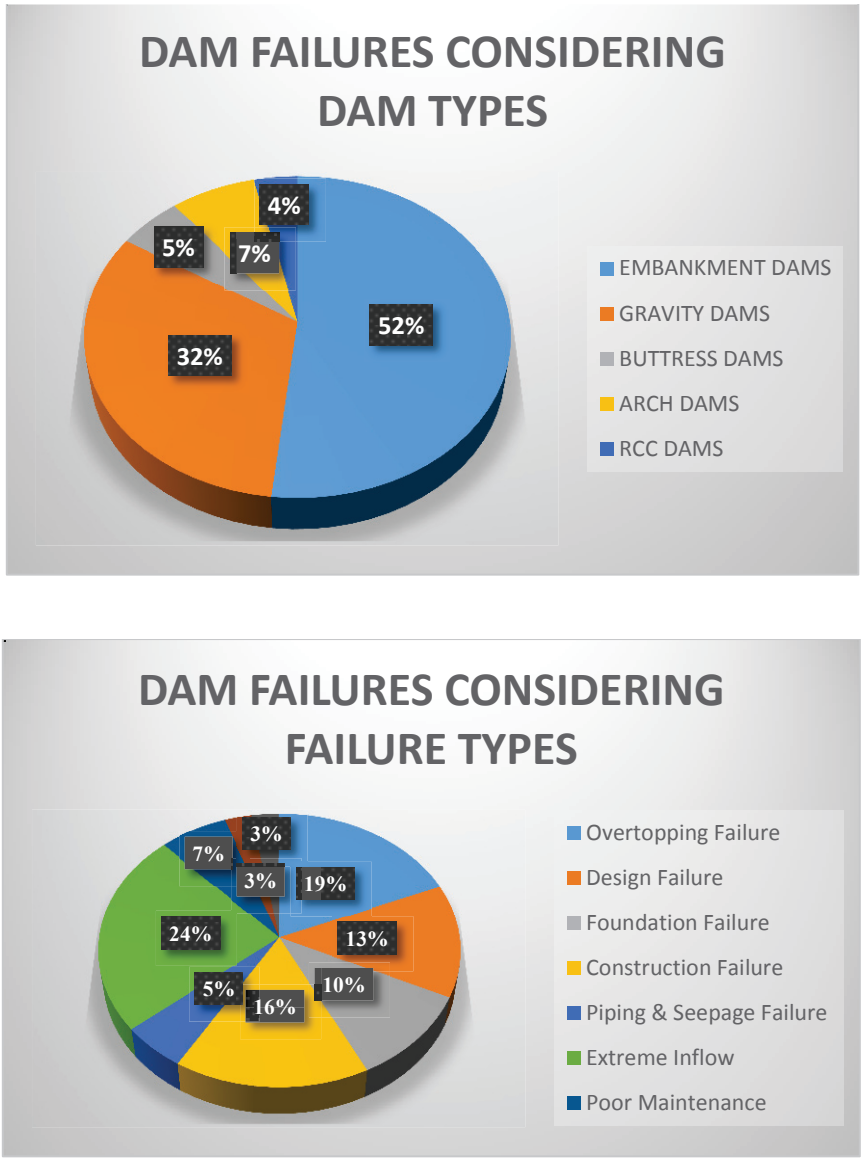

Figure 11. Dam failure percentages

Most dam failures have occured in North America (23%), Asia (27%) and Europe (31%). In America, 60% failures were embankment dams and 35% were gravity dams. In Europe, 46% were gravity ones and 23% were arch dams. In Asia and in Africa, most failed dams were embankment dams (in Asia 64% and in Africa 86%). In America and Europe, we see all kinds of dam failures. In Asia, extreme inflows and overtopping were the main culprits (totaling 64%). In Africa, the main reason was the ill-construction (50%), followed by overtopping (33%) and extreme inflows (17%).

1900-1925, mostly gravity dams failed (57%). The failure type was ill-design (45%). They were mainly in America (USA, Brasil) and in Europe. 1925-1950, mostly gravity dams failed

(100%). The failure reason was ill-foundation (38%) and the war (25%), happening mostly in Europe (83%) due to the II. World War. 1950-1975, dam failures happened mostly in Europe (44%), followed by Asia (31%), and America (19%). Dam types were embankment (43%), arch (29%) and butress (28%) dams. Failure types were ill-foundation (34%), extreme inflows (33%) and overtopping (20%).

1975-2000, we see dam failures in all continents, mostly in America (39%), followed by Asia (23%) and mostly the embankment dams failed (92%). The failure causes were widespread; extreme inflows, overtopping, piping & seepage, ill-construction, ill-design, and poor-maintenance.

2000-2018; dam failures occurred in America (44%), Asia (25), Europe (19%), and Africa (11%). Mostly embankment dams (64%) and gravity dams (27%) failed. Extreme inflows (35%), overtopping (24%) and ill-construction (21%) were the main failure causes.

Total death toll from dam failuers all over the world in this last century is **188,252**. The most single one is BANQIAO DAM in CHINA, an embankment dam, failed **in 1975** due to extreme inflows. **171,000 people died**. 17,252 deaths occurred from other ones in the last 100 years. Tigra Gravity Dam in India failed in 1917 due to piping and seepage under foundation resulting in 1000 death. Mohne Gravity Dam in Germany failed in 1943 due to bombing in the II. World War, resulting in death toll of 1580. Vajont Concrete Arch Dam in Iatly failed in 1963 due to a mass dam slide into the reservoir causing overtopping and detah of 2000 people. Sempor Embankment Dam in Indenosia failed in 1967 due to flash floods (2000 people died). Machchu- Embankment Dam in India failed in 1979 due to extreme inflows, causing 5000 deaths.

CONCLUDING REMARKS

Throughout history, societies of the world greatly benefited from building infrastructure for water resources systems management. By means of dam construction and operation, different civilizations managed to efficiently cover various water demands such as drinking water supply and irrigation. In ancient Egyptian civilization, people had constructed dams and canals to control Nile River flood and developed irrigation systems. The same tools still have been used in modern times. The Sabaens, ancient Yemen people, managed to keep their dam stood for over 1,000 years before the existence of concrete and the recent advanced construction technologies. Until the invention of cement, generally earthfill and/or rockfill embankment dams were built. Also, clay was used as a binding material.

Recent civilizations inherited the dam-technologies and developed them further. They substantially increased the application scale and implemented dam projects not only for water supply and irrigation but also for navigation, power generation, flood production, and recreational purposes. The differences between ancient and modern time dam-technologies are mostly found in the apparatus and the scale of applications with practically no differences in the fundamental principles used. For examples, Sadd el-Kafara in Egypt, the oldest known dam in the world, adopted the same building principle of modern embankment dams as it consisted from two masonry shoulders supporting a central core of sand and gravel. However, in this last century, especially in the last 50 years, huge dams were built and some are under construction around the world, including Turkey, Iran and Egypt with the state of the art knowledge, experience, and technology.

The number of dams have been increasing all over the world so is the number of disasters due to dam failures. Presently, as it has been the case, mostly embarkment dam and gravity dam

failures occur. Failures mostly happen in America (mainly USA and Brasil), Asia, Europe, and recently in Africa. Earlier casuses were mostly ill-design, improper geological setting and ill-construction. Recently, the major cause is being the sudden flashy extreme inflows as a result of climate change effects. This fact needs to be considered during the desining stage.

1. References

Cecen, K. (1987). Seldschukische und osmanische Talsperren. Historische Talsperren. Wittwer, Stuttgart, 275-295.

DSİ (2008). Hittite dam from 1250 B.C. towards today,. DSİ General Directorate, 5th Regional Directorate, report.

Fahlbusch, H. (2017). Early Dams. History Association. https://www.history.org.uk/.

Farhangi, B. (2003). Water melody in the passage of time. Tehran, Iran.

Jansen, R. B. (1980). Dams from the beginning. Dams and Public Safety (Part 1): 1-57.

Loon, M. (1992). The Beginning of the Middle Bronze Age in Syria. Ägypten und Levante/Egypt and the Levant, 3: 103-107.

Mahmoudian, S. and Mahmoudian, S. (2012) Water and water supply technologies in ancient Iran, chap 5. Evolution of water supply through the Millennia. IWA, London, 91-126.

Novokshshenov, V. (1993). Laboratory studies of the stone masonry in the Old Aswan DamArchived August 26, 2011, at the Wayback Machine., Materials and Structures 1993, Vol. 26, p. 103-110.

Öziş, Ü., Alkan, A. and Özdemir, Y. (2010). Ancient water works in Anatolia, Latest Trends on Cultural Heritage and Tourism, 3rd WSEAS International Conference on Cultural Heritage and Tourism (CUHT'10), 63-71.

Saxena, K. R. (2004). Sharma, V., Dams: Incidents and accidents. CRC Press.

Schamp, H. (1983). Sadd el-Ali, the High Dam of Aswan. Geowissenschaften in unserer Zeit (in German), **1** (2): 51–85.

PROCEEDINGS

5 DAM SAFETY
İstanbul Turkey 2018

5th International Symposium on Dam Safety

October 27-31, 2018

INSTRUMENT CHALLENGES AND MONITORING OF SHAHR-E-BIJAR DAM

A. Bagherzadeh KHALKHALI

ABSTRACT

The Shahr-e-Bijar dam is a 96.5 m high and 430 m long concrete faced rock-fill dam with reservoir volume of 105 million m^3. Construction of the dam was completed in April 2014. Monitoring of the dam behavior was based on the measurement data of instruments which installed in the dam body and the foundation as well as daily visual inspection. In this study, a two dimensional finite element analysis of SEB dam is carried out and the computed displacements and internal stresses compared with those measured in situ by the instrumentation. The rock-fill material is represented by the hardening soil model which is a modified version of Duncan and Chang's hyperbolic model.

The maximum recorded construction settlement is around 0.80 m at the maximum cross section and around 0.50 m at the sections on the abutments which correspond to 0.9% of the dam height. The deformations will further increase with first impounding and rising reservoir to full supply level and due to creeping of the rock-fill. The results of different instruments which are used for the settlement monitoring of the dam are shown that the accuracy of hydrostatic settlement cells is more than other instruments and the measured settlements by the magnetic plates around the inclinometer's tubes are usual below the actual settlement.

The stress arching within the dam body and abutments is recorded as 50 % in the middle of dam body and 60 % in the near of the banks. Also, during the construction, the shrinkage is mobilized within the dam body along the axis of dam at the first stage of construction and then by increasing the overburden's height, the expansion is recorded and increased up to the end of construction. The results are shown 65 mm as the maximum expansion which is mobilized at the middle part of the dam body.

Keywords: Monitoring, Concrete Faced Rock-fill Dam, FEM, Dam Behavior, Safety.

INTRODUCTION

Today, concrete faced rock-fill dams (CFRD) are very popular all over the world, especially in regions, which receive heavy rain and where impervious soil reserves are insufficient. In the current state of the art, the design of a CFRD is based on experience and engineering judgment [Cooke,1984]. CFRDs are gaining a worldwide recognition as the most economical type of dams to be constructed in extreme northern and sub-Antarctic regions. Use of the rock-fill material, which is not sensitive to the frost action and the construction technology allow lengthening the construction season. The total duration of the construction of CFRDs with regard to the total duration of construction of earth dams is on average reduced by one year. Since, these constructions are important structures; their behavior should be estimated realistically for both construction and reservoir filling stages. Finite element method is one of the available tools used in the prediction of structural behavior.

Deformations of CFRD dams start occurring during the construction. These deformations are caused by the increase of effective stresses during the construction by the consecutive layers of earth material and also by effects of creep of the material. Deformations may also be influenced by deformations of

the foundation, by transfer of stresses between the various zones of the dam and by other factors. After the construction is completed, the considerable movements of the crest and of the body of the dam can develop due to pressure of water during the first filling of the reservoir. The load of water and deformations of the rock-fill will be forced on concrete slab to deform. The concrete slab acts as an impervious membrane and any development of cracks in the slab would allow for water to penetrate the rock-fill of the dam and cause the structure to weaken or even loose stability. According to the working state, force distribution and hydraulic features of CFRD, proper zoning of dam filling material is carried out to take a full utilization of the material from structure excavation and to reduce the investment under the condition that the safety of operation is ensured. After filling of the reservoir, the rate of movement in the dam and in the concrete face generally diminishes with time, except for variations associated with periodic raising and lowering the level of the reservoir. In classic CFRDs where the concrete face is constructed after the end of construction of the rock-fill embankment, it is very important to estimate the displacements of the concrete face during the filling of the reservoir and to verify whether these displacements are lower than displacements compatible with the structural integrity of the concrete face. Most of the constructed CFRDs rest on the bedrock. However, there are some CFRDs constructed on soil foundations. Foundation conditions of the planned constructions call for studies to determine the range of possible movements of the concrete face slab during the construction of the dam and especially, during the filling of the reservoir.

Safety is the most important reason for observing the deformations of dams. Too large or unexpected deformations can be the only indication of potential problems of the dam or its foundation. Another reason for observing the deformations of dams, of less immediate concern but of potentially great long-range significance to engineering profession, is the need for better understanding of basic design concepts, stress-deformation characteristics, and geotechnical characteristics of soil and rock fill. The development of prediction methods, which allow a determination of deformations and stress distribution and comparison of predicted values with observed, constitutes very valid tools to control safety.

The key point in the analysis is down-to-earth modelling of the stress-strain relationships of rock-fill materials, preferably based on tri-axial test results. Considering the particle sizes of rock-fill material, up to 1.2 m diameter, the difficulty in obtaining experimental data, which in our case is lacking, becomes obvious. Although limited, the available tri-axial data in the literature indicate that rock-fill materials possess highly stress dependent, inelastic and non-linear stress-strain relationships [Marsal, 1967; Marachi et al., 1972; Duncan et al., 1980]. Among the material models used in the available studies carried out in recent years, Duncan and Chang's (1970) hyperbolic model is probably the most common. The hyperbolic model has been utilized in a number of similar research successfully [Khalid et al., 1990; Saboya and Byrne, 1993; Liu et al., 2002].

In the present study, the ''hardening soil model'', which is essentially a modified implementation of the hyperbolic model available in FLAC, is used to represent the rock-fill behavior [Schanz et al., 1999].

DAM CHARACTERISTICS

Shahr-e-Bijar (SEB) dam is a 96.5 m high and 430 m long concrete faced rock fill dam with reservoir volume of 105 million m^3. Construction of the dam was completed in April 2014 and impounding of the reservoir will be started during the next months. The dam is located in near of Rasht city, 40 Km, in the north of Iran. The main purpose of the dam is the water storage. Construction of the dam embankment was started in 2008 and finished in 2014. After the completion of rock-filling, the construction process had been given a halt for about 0.5 year until the major part of the settlement of rock-fill embankment was completed. The construction of concrete lining was continued after there.

SEB dam is 96.5 m high from the river bed and the side slopes are 2.0:1 and 1.6:1 (H:V) in the upstream and downstream embankment faces, respectively. The crest extends 437 m. The valley is 165 m wide and abutment slopes, on the average are 30 and 45 for the left and right abutments, respectively. Figure 1 shows the typical cross-section with different zones indicated.

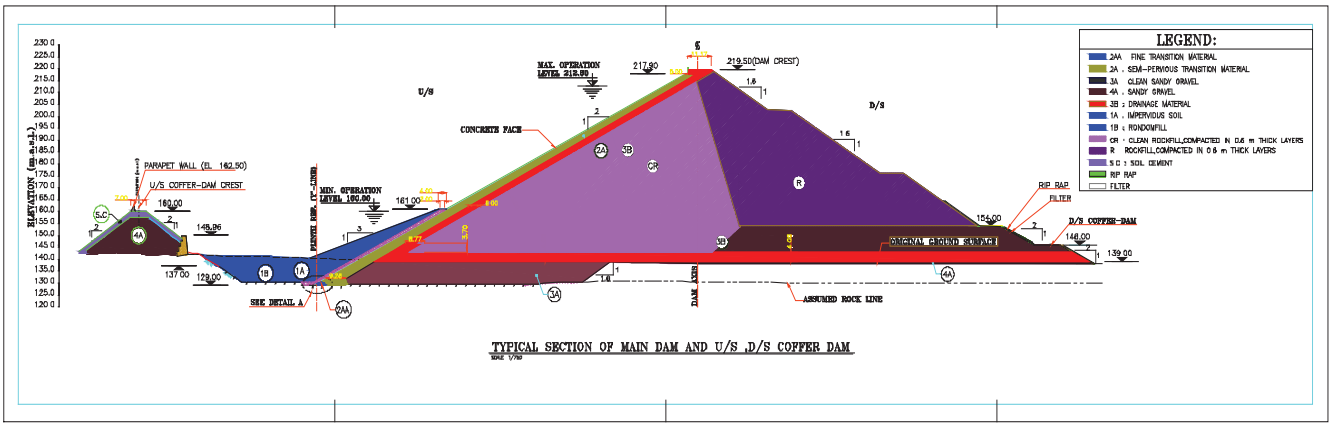

Figure 1. Typical cross section of SEB dam

Basic geological units in the dam site are sandstone, siltstone and limestone. Sandstone is the most common type of rock found in the region on which the dam rests. The details of zoning and construction are given in Table 1.

Table1. Materials and construction details of SEB dam

Zone	Material				Construction techniques	
	Type	Particle Sizes			Layers (m)	Compaction (12&15 t vibratory roller)
		D_{max} (mm)	Sand (%)	Fines (%)		
1A	Impervious fill	25	>50	>30	0.15	4 passes (static)
1B	alluvium	400		<20	0.30	4 passes
2A	Sieved rock (or alluvium)	75	35–55	3–10	0.15	6 passes (4 static + 6 dynamic)
2AA	Filter	40	38–60	5-12	0.15	6 passes
CR R	U/S & D/s Rock fill	300	16–35	<7	0.40	6 passes+150 lit/m^3 water
3B	Drainage	100	16-38	<3	0.25	6 passes

NUMERICAL SIMULATION

A modified version of Duncan–Chang model, has been utilized in the analyses. Since no large-scale tri-axial test results are available, pertinent works from the literature [Saboya and Byrne, 1993] with other experience in Iran are referred in selecting the hardening soil model parameters. Table 2 shows the selected parameters used in the numerical simulations. In hardening model, the secant modulus for primary loading corresponding to 50% of shear strength q_f is defined by Schanz et al. (1999) (Figure 2).

Table2. Range of hardening soil parameters used in the numerical simulation

Zone	γ [kN/m^3]	Φo	Δ Φ	K	n	R_f	K_{ur}	K_b	m
Transition	22	45	6.6	1000	0.40	0.85	2000	450	0.15
Main Rockfill	22	42	6.5	1100	0.35	0.82	2200	600	0.10
Secondary Rockfill	22	40	6.4	850	0.25	0.80	1700	400	0.05

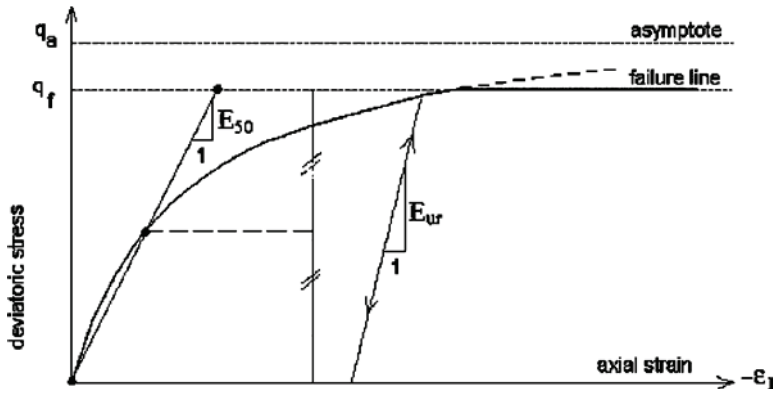

Figure 2. Hyperbolic stress-strain curve (Schanz et al., 1999)

Zones 2A and 2AA shown in Figure 1 are not expected to have a significant effect on the overall dam behavior and have not been included in the finite element analysis. The rock foundation of the dam is simulated base on the geotechnical laboratory tests. The analyses are carried out considering end of construction (EoC) conditions and are compared with the measured data by the installed instruments within the embankment.

The dam is simulated by assuming 2-D plane strain conditions. The finite element software, FLAC and GEOSLOPE-Sigma are employed. The rock fill embankment is modelled by 15- node triangular elements with the hardening soil as the material model. These elements have 12 interior stress points located at different coordinates from the element nodes where displacements are output. The concrete slab is model led by five nodded linear elastic beam elements. These elements have 50 cm thicknesses and 8 stress points. The material parameters of the concrete are shown in Table 3.

Table3. Linear elastic model parameters of the concrete slab

Material	E (MPa)	d (m)	c (kN/m^3)	m
Concrete	28,500	0.50	23.50	0.20

For a preliminary analysis, each construction stage was represented by a 5 m thick layer. It was observed that reducing the layer thickness renders the simulation better while extending the runtime. Finally, a layer thickness of 5 m was decided as agreeable. The last 6 m's of the dam from the top was not included in the mesh, since the parapet wall unnecessarily complicated the geometry, never the less the weight of the wall was taken into account in the model as a surcharge of 100 kPa.

INSTRUMENTATION OF THE DAM

Because it was the first example of its type in north of Iran, SEB dam was extensively instrumented in order to monitor the performance. Several types of instruments were used for monitoring the behavior. The instruments are listed below which are used for monitoring the dam at EoC.

- Hydraulic settlement cells located within the rock-fill (SC1-31)

– Total pressure cells, located within the rock-fill embankment (PC1-7)
– Vertical Inclinometers, located vertically in 3 main section of dam, (IS1-3)
– Magnetic settlement plates with 3 meters space around the vertical inclinometers,
– Electrical piezometers around the grout curtain and dam's foundation (EP 1-30)
– Cross arm extensometers within the embankments along longitudinal in three different level (150, 175 and 200 m.a.s.l.)

It is notable that one in-place inclinometer, 37 Electro-level cells and 12 three-dimensional joint-meters will be evaluated to monitor the rotation, displacement and movements of the concrete slab in the future.

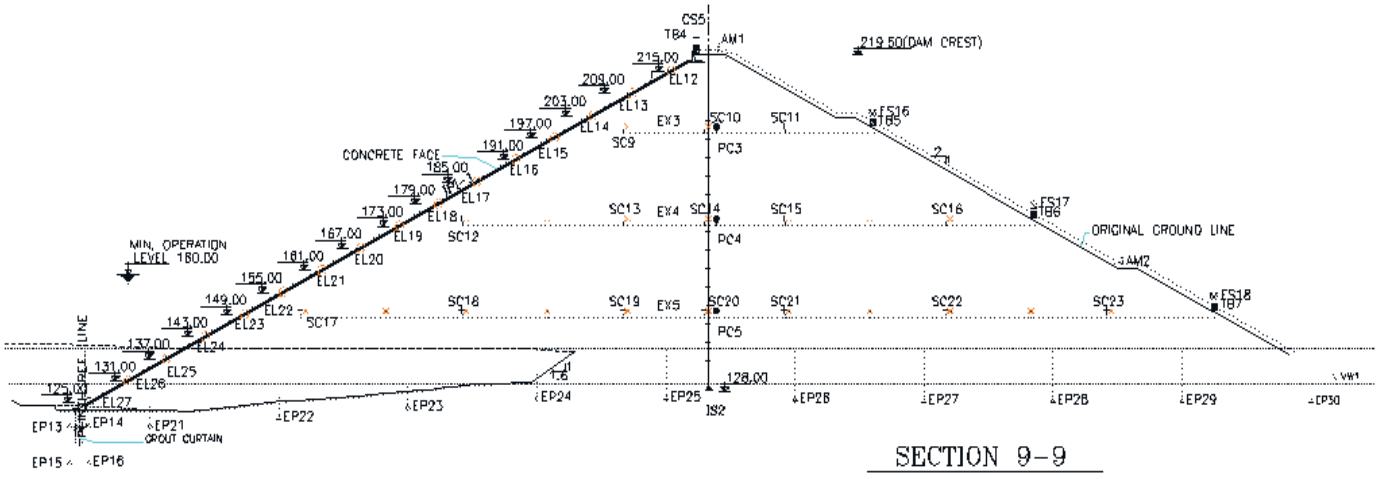

Figure 3. Instrumentation in the rock-fill embankment (Max. Cross Section)

As listed above, a total of 31 hydraulic settlement devices, 7 earth pressure cells and 3 inclinometers with magnetic settlement plates were installed at 3 cross-sections and three different elevations to control the behavior during the construction of dam. The locations of the devices at the maximum cross-section of the dam are shown in Figure 3. In the continue, the measured data of the instruments will be discussed and compared with the numerical simulation results at the end of construction for SEB dam. It is notable that this dam recently is going to first impounding.

SETTLEMENT

Dam deformations during construction were measured with hydrostatic settlement cells, fixed embankment extensometers and settlement gauges with combined inclinometer tubing. These instruments provided data of deformations along 3 sections within the dam body.

The maximum recorded construction settlement is around 0.80 m at the maximum cross section and around 0.50 m at the sections on the abutments. Measured settlement at the different depth of highest cross section is shown as Figure 4 during EoC. The construction settlements measured with the instruments were used for calculating the deformation moduli during construction E_{rc}:

$$E_{rc} = {}^{\gamma H d}/_{s} \qquad (1)$$

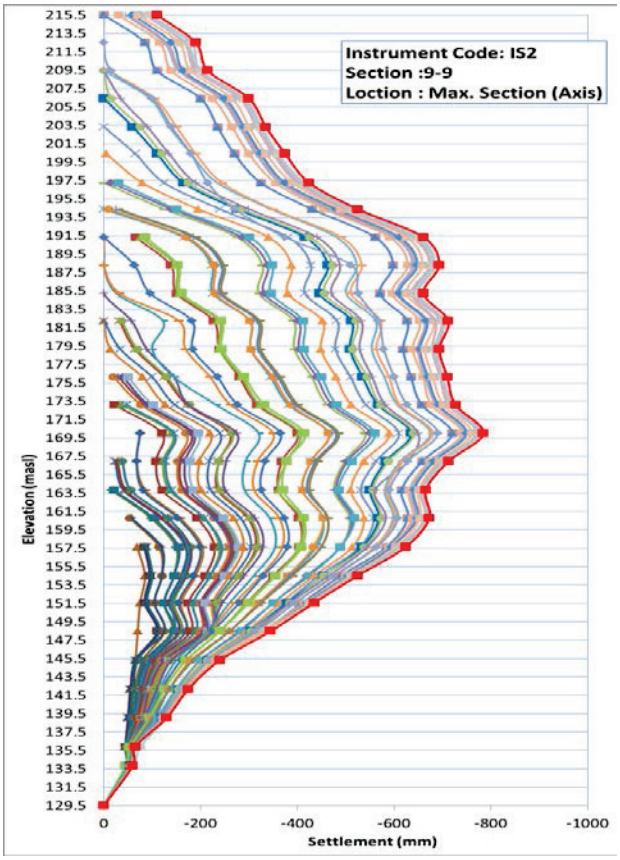

Figure 4. Measured settlement at the highest cross section during the construction.

γ = unit weight of fill above settlement plate,
H = height of fill above settlement plate,
d = thickness of fill below settlement plate,
s = recorded settlement of the settlement plate.

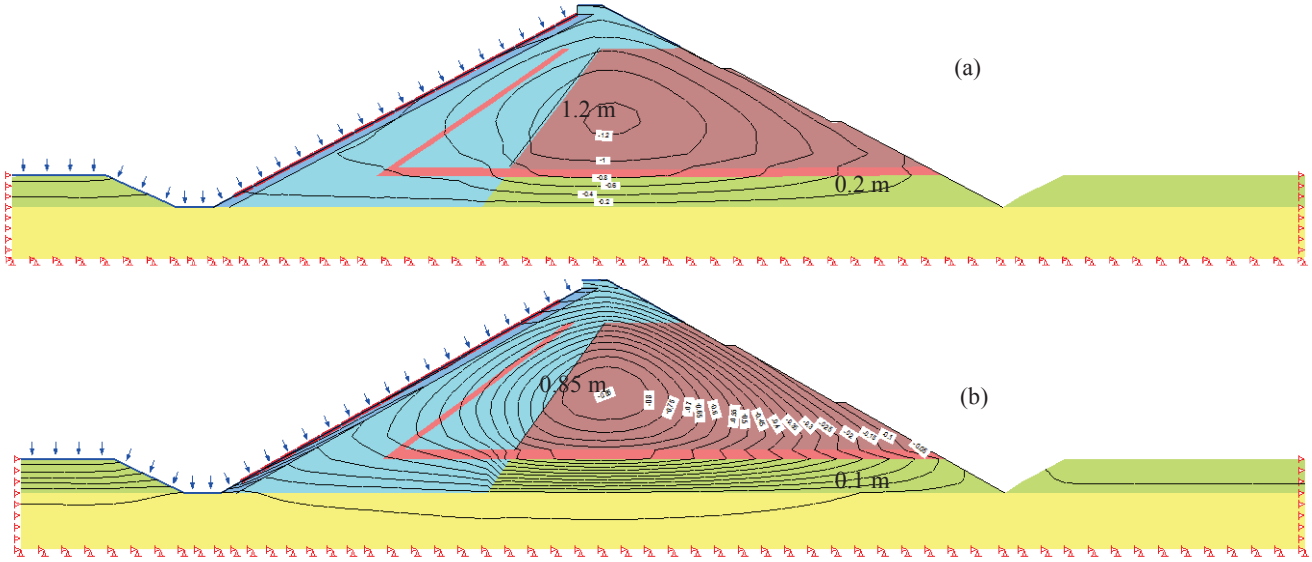

Figure 5. Calculated settlement at the highest cross section of SEB dam at EoC; (a)Linear elastic model (b)Hyperbolic Model

The back-calculated deformation moduli during construction are in the range of 60 MPa (upstream side) to 45 MPa (downstream side). Using these deformation moduli the dam settlements during construction were back-modelled using an elasto-plastic material model. The results are in good agreement with the monitored data. The calculated dam settlements comply well with the measured settlement as shown on Figure 4. According to numerical simulation, total settlement at the end of construction is defined by the linear elastic model equal to 0.85 m and 1.2 m by the Duncan-change hyperbolic model (Figure 5). In general view, the maximum dam settlement at the end of construction is about 0.8 m which corresponds to 0.9% of the dam height. Post-construction dam deformations

Figure 6. Vertical stress distribution in the highest cross section at EoC

generally occur due to the increased load from the reservoir, creep deformations, breakage of rock fill particles and softening of the rock fill due to wetting and saturation. The total maximum settlement at the dam crest was reported about 75 mm.

During the SEB construction, three main parameters were effective on the dam settlement. Void ratio of the compacted rock fill, Shape factor and breakable or creep capacity of the used materials to embank of dam were very effect on the mobilized deformations. According to the monitoring monthly and inspection daily, it is found that the void ratio is the main effective parameter on the total settlement of the dam.

The results of different instruments which are used for the settlement monitoring of the dam are shown that:

- Accuracy of hydrostatic settlement cells is more than other instruments.
- Measured settlements by the magnetic plates around the inclinometer's pipes are usual lower than the actual settlement.
- Reading errors of the hydrostatic cells are more than other cell.

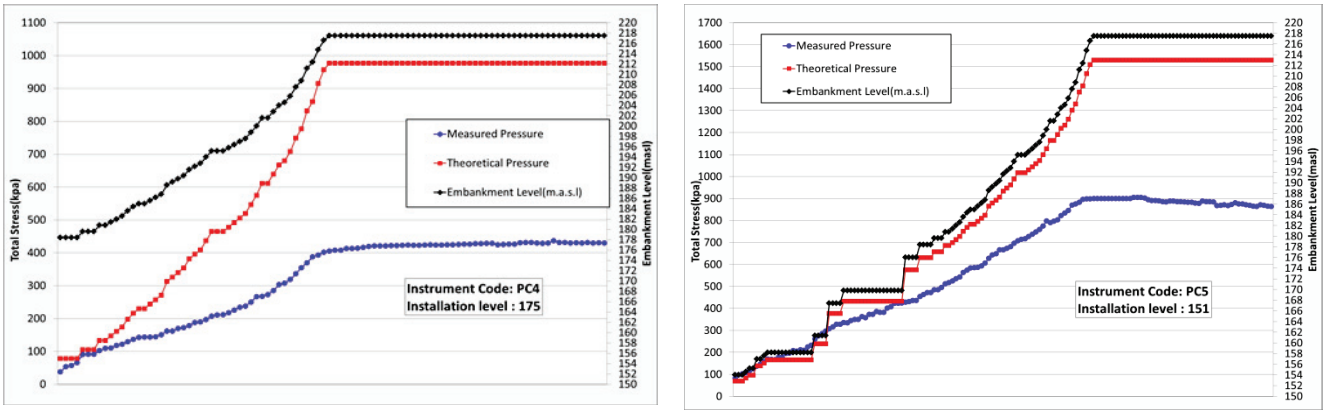

Figure 7. Measured total stresses at the highest cross section during the construction

TOTAL STRESSES

The comparison of predicted (Figure 6) and observed (Figure 7) total stresses for SEB dam at EOC is shown that the simulations and readings are similar from the trend view as well. But the theoretical value (overburden weight) and the measured data are not close together. As shown in Fig.7, the similar value is recorded for the measured vertical stress and the theoretical pressure at the first stage of EoC, but the difference of these pressures is increasing by the completion of dam body. The inclination of total pressure cells (from horizontal line) due to the construction displacement or rock fill creep movements is the main reason. To define the correction coefficient of stresses for SEB dam, the engineer is proposed the physical model of the dam to measure laboratory stresses path and then back-calculate the stresses in the filed condition. The stress arching, transfer the stresses from the dam body to the neighboring materials such as the abutment's rock, is recorded as 50 % in the middle of dam body and 60 % in the near of the banks.

EXTENSOMETERS

To measure the lateral movements within the dam body along the valley, 3 longitudinal extensometers are installed at three levels (151, 175 and 200). Figure 8 illustrate the photo of a fix installed point of this instrument as an example and its recorded data. As can be seen from the figure, during the construction, the shrinkage is mobilized at the first and by increasing the overburden's height, the expansion is recorded and increased up to the end of construction. The results are shown that lateral displacement equal to 65 mm as the maximum expansion which is mobilized at middle monitored elevation (175 m.a.s.l.). At the upper elevation, maximum expansion movements are limited to 34 mm. The upstream view of SEB dam at the end of construction with the above mentioned elevations is shown in Figure 9.

Generally, the lateral movements within the dam body are lower than the predicated values. Base on the simulations, lateral movement should be mobilized in the lower part (1/3 H) of the body more than other parts and the maximum movement is calculated about 100 mm. Comparison of the calculated and recorded data means that 65 percent of the predicted horizontal movement is actually mobilized.

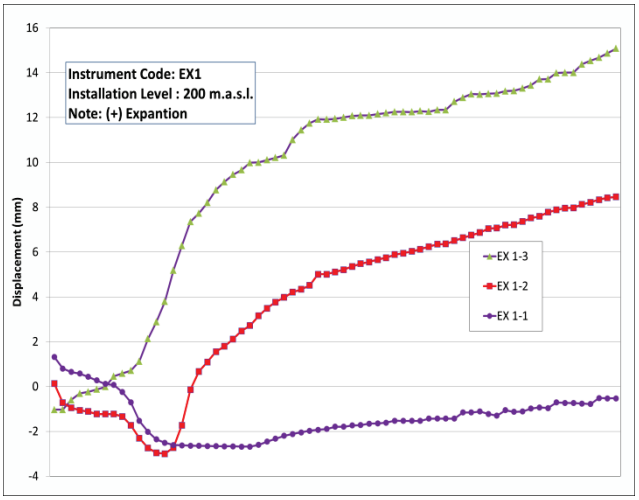

Figure 8. Measured lateral movement in the dam body at 200 m.a.s.l. by the extensometer.

Figure 9. Upstream view of SEB dam

CONCLUSIONS

In this study, a two dimensional finite element analysis of Shahr-e-Bijar (SEB) dam is carried out and the computed displacements and internal stresses compared with those measured in situ by the instrumentation. The rock-fill material is represented by the hardening soil model which is a modified version of Duncan and Chang's hyperbolic model.

The monitoring system of SEB dam has provided useful information on the deformation behavior of the dam during construction and the end of construction. The maximum recorded construction settlement is around 0.80 m at the maximum cross section and around 0.50 m at the sections on the abutments. According to numerical simulations, total settlement at the end of construction is defined by the linear elastic model equal to 0.85 m and 1.2 m by the Duncan-Change hyperbolic model. In general view, the maximum dam settlement at the end of construction is about 0.8 m which corresponds to 0.9% of the dam height. The deformations will further increase with first impounding

and rising reservoir to full supply level and due to creeping of the rock fill. Based on deformation monitoring at the downstream part of the dam, still a high rate of creeping is noticed. The results of different instruments which are used for the settlement monitoring of the dam are shown that the accuracy of hydrostatic settlement cells is more than other instruments and the measured settlements by the magnetic plates around the inclinometer's tubes are usual below the actual settlement.
The similar value is recorded for the measured vertical stress and the theoretical pressure at the first of end of construction, but the difference of these pressures is increasing by the completion of dam body. The inclination of total pressure cells (from horizontal line) due to the construction displacement or rock fill creep movements is the main reason. The stress arching within the dam body and abutments is recorded as 50 % in the middle of dam body and 60 % in the near of the banks.
During the construction, the shrinkage is mobilized within the dam body at the first along the axis of dam and then by increasing the overburden's height, the expansion is recorded and increased up to the end of construction. The results are shown that 65 mm as the maximum expansion which is mobilized at the middle elevation of the dam body. At the upper part of dam, maximum expansion movements are limited to 34 mm. Comparison of the calculated and recorded data means that 65 percent of the predicted horizontal movement is actually mobilized.

AKCNOWLEDGEMENT

Special thanks to Mr. Shantia from Yekom Consultants Engineers for their cooperation on this research.

REFERENCES

Cooke, J.B. (1984) Progress in rock-fill dams, (18th Terzaghi Lecture), Journal of Geotechnical Engineering, ASCE, 110(10), 1381–1414.

Duncan, J.M. and Chang, C.Y. (1970) Non-linear analysis of stress and strain in soil, Journal of Soil Mechanics and Foundations Division, ASCE, 96(SM5), 1629–1653.

Duncan, J.M., Byrne, P., Wong, K.S. and Babry, P. (1980) Strength, Stress-strain and Bulk Modulus Parameters for Finite Element Analyses of Stresses and Movements in Soil Masses, in Report No: UCB/GT/80–01, University of California at Berkeley.

Fitzpatrick, M.D., Cole, B.A., Kinstler, F.L. and Knoop, B.P. (1985) Design of concrete-faced rock-fill dams, Proc. of the Symp. ''Concrete Face Rock-fill Dams-Design, Construction, and Performance'', Journal of Geotechnical Engineering, ASCE, 111, 410–434.

Hunter, G. and Fell, R. (2003) Rock-fill modulus and settlement of concrete face rock-fill dams, Journal of Geotechnical and Geo-environmental Engineering, ASCE, 129(10), 909–917.

Khalid, S., Singh, B., Nayak, G.C. and Jain, O.P. (1990) Non-linear analysis of concrete face rock-fill dam, Journal of Geotechnical Engineering, ASCE, 116(5), 822–837.

Liu, X., Wu, X., Xin, J. and Tian, H. (2002) Three dimensional stress and displacement analysis of Yutiao concrete faced rock-fill dam, Proc. of 2nd Int. Symp. On Flood Defense, Science Press New York Ltd, Beijing, Vol. 1, pp. 1494–1500.

Marachi, N.D., Chan, C.K. and Seed, H.B. (1972) Evaluation of properties of rock-fill materials, Journal of Soil Mechanics and Foundations Division, ASCE, 98(SM1), 95–114.

Marsal, R.J. (1967) Large scale testing of rock-fill materials, Journal of Soil Mechanics and Foundations Division, ASCE, 93(SM2), 27–43.

Nobari, E.S. and Duncan, J.M. (1972) Movements in dams due to reservoir filling, Proc. ASCE, Specialty Conf. On Performance of Earth and Earth-Supported Structures, Purdue Univ., Lafayette, Indiana, pp. 797–815.

Saboya, F. Jr. and Byrne, P.M. (1993) Parameters for stress and deformation analysis of rock fill dams, Canadian Geotechnical Journal, 30, 690–701.

Schanz, T., Vermeer, P.A. and Bonnier, P.G. (1999) The Hardening Soil Model: Formulation and Verification, Beyond 2000 in Computational Geotechnics-10 years of Plaxis, Balkema, Rotterdam.

5th International Symposium on Dam Safety

October 27-31, 2018

EARTHQUAKE RESPONSE OF BHAKRA GRAVITY DAM

Barış SEVİM [1]

ABSTRACT

Dams are big structures which retain a huge water in their reservoir. So seismic response of these structures is important especially earthquake-prone areas. During an earthquake, reservoir affects the structural response of the dam. So reservoir must be considered to obtain more realistic behavior. Also, structure-fluid-soil interaction effects have considerably changed the response. Therefore earthquake response of such kind of structures must be determined. In this study, earthquake response of Bhakra Concrete Gravity Dam in India is examined. In the study, the dam is two-dimensionally modelled including dam-reservoir-foundation interaction. In finite element modelling, dam and foundation are represented by solid elements and the reservoir is represented by fluid elements. Linear time history analysis of the system is performed by conducting components of 1991 Uttarkashi Earthquake occurred in India. The earthquake record is applied to the system in upstream-downstream direction. According to analysis results, displacement and stresses changes in some nodes and sections are presented.

Keywords: Gravity dam, Earthquake response, Dam-reservoir-foundation interaction.

INTRODUCTION

Gravity dams are designed in such a way that its own weight resists the external forces. Also they can be easily constructed on site if the foundation is strong enough to bear dam's huge weight. So they are preferred to design and construct. Due to retaining a huge water in their reservoir, seismic response of these structures is important especially earthquake-prone areas. During an earthquake, reservoir affects the structural response of the dam. So reservoir must be considered to obtain more realistic behavior. Also, structure-fluid-soil interaction effects have considerably changed the response. Therefore earthquake response of such kind of structures must be determined. With the developing of computer systems, such kind of structures are modeled and analyzed using finite element method under huge earthquakes. In the literature, some recent studies consider linear and nonlinear dynamic response of gravity dams, damage mechanism, experimental and numerical investigation of reservoir-dam interaction systems etc. (Arabshahi and Lotfi, 2008, Phansri et al., 2010; Valamanesh et al, 2011, Ardebili et al., 2013; Wang et al., 2014; Altunışık and Sesli, 2015).

During in an earthquake, the reservoir are considerably affect the response of dam. So representation of reservoir is important to present realistic behavior of dam. Modeling and analysis of dynamic dam-reservoir-foundation interaction during earthquakes have gone through direct method. The discretized structural dynamic equation including dam-and foundation system subjected to ground motion can be formulated using finite element approach where the soil and structure are included within the same

Assoc. Prof. Department of Civil Engineering, Yildiz Technical University, Istanbul, Turkey,
e-posta: basevim@yildiz.edu.tr

model and analyzed in a single step in Eq. (1) (Khosravi et al., 2012;Mohsin et al., 2015; Varughese and Nikithan, 2016).

$$M_s\ddot{x}_e + C_s\dot{x}_e + k_s x_e = -M_s\ddot{x}_g \quad (1)$$

where, M_s, C_s, and k_s are the structural mass, damping and stiffness matrices, respectively. x_e, $\dot{x}_e$, $and\,\ddot{x}_e$ are is the nodal displacement, velocity and acceleration vectors, respectively. $\ddot{x}_g$ is ground acceleration. The reservoir produce a hydrodynamic effects during the earthquakes termed as Qp_e. So the discretized wave equation of reservoir is given as Eq. (2);

$$M_f\ddot{p}_e + C_f\dot{p}_e + k_f p_e + p_w Q^T(\ddot{x}_e + \dot{x}_e) = 0 \quad (2)$$

where, M_f, C_f, and k_f are the fluid (reservoir water) mass, damping and stiffness matrices, respectively. p_e is the nodal pressure and, $p_w Q^T$ is referred to as the coupling matrix. Dynamic equilibrium equation of the coupled system is obtained from Eq 1 and Eq 2 as given

$$M_c\ddot{x}_c + C_c\dot{x}_c + k_c x_c = F(t) \quad (3)$$

where M_c, C_c, and k_c are the coupled mass, damping and stiffness matrices respectively and F(t) is the dynamic load vector.

In the study, the dam is two-dimensionally modelled including dam-reservoir-foundation interaction. In finite element modelling, dam and foundation are represented by solid elements and the reservoir is represented by fluid elements. Linear time history analysis of the system is performed by conducting components of 1991 Uttarkashi Earthquake occurred in India. The earthquake record is applied to the system in upstream-downstream direction. According to analysis results, displacement and stresses changes in some nodes and sections are presented.

NUMERICAL EXAMPLE

In this study Bhakra Gravity dam is selected for the numerical example. The dam is situated in in the state of Himachal on the Satluj River in India. Satluj is a river coming from Himalayas. It is a perennial river but carries enormous water during floods and rains (Figure 1). The dam was the highest gravity dam when it was constructed with its 226 m height in 1963. The dam has 9.14 m and 190.5 m widths at crest and base, respectively. Some photos and 2 D geometry of the dam is given in Figure 2.

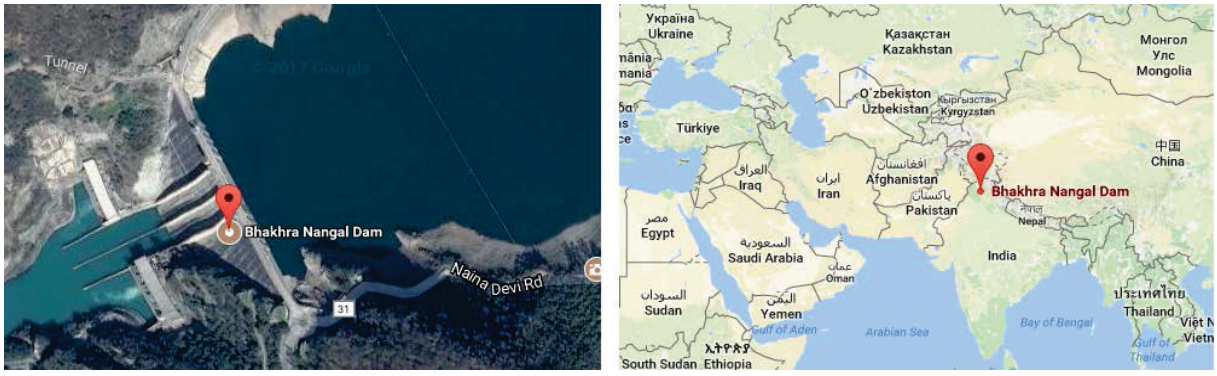

Figure 1. Location of Bhakra Gravity Dam

Figure 2. Some photos and 2 D geometry of Bhakra Gravity Dam

Finite element model of Bhakra dam is constituted two dimensionally by ANSYS (2017) software considering dam-reservoir-foundation (full reservoir) interaction effects (Fig. 4). The model includes geometrical dimensions given in Fig. 2. Dam body is represented using PLANE182 elements which are used for 2-D modeling of solid structures. The element has four nodes and has two degree of freedoms at each nodes such as X and Y translations. The element has the capabilities of plasticity, stress stiffening, large deflection, and large strain ANSYS (2017).

Finite Element Modelling of the Dam

In the modelling, reservoir is extended as 3 dam heights through upstream direction. Such a modeling neglects the effects on deflections, stresses, and natural frequencies of the dam (USACE, 2003; Sevim, 2011, Sevim vd., 2011a; Sevim vd., 2011b; Sevim vd., 2012). Reservoir is represented using FLUID29 elements which are used both modeling fluid domain and fluid-structure interaction. The element has four nodes with three degrees of freedom per node: translations in the nodal x and y directions and pressure. The translations, however, are applicable only at nodes that are on the interface.

Foundation is modelled using PLANE182 elements and extended as dam height through vertical and downstream directions. Also foundation is modeled on upstream direction under the reservoir. Boundary conditions for are fixed under and near side of the foundations. The foundation model should be preferred as massless in which only the effects of foundation flexibility are considered.

Material properties assumed in the modeling are given in Table 1. 4376 nodes and 418 PLANE182 elements for dam body, 2354 PLANE182 elements for dam foundation and 1452 FLUID29 elements for dam reservoir are used during the finite element modelling (Figure 3).

Table 1. Material properties of Bhakra dam-reservoir-foundation system

System	Element Type	Material Properties		
		Elasticity Modulus (MPa)	Poisson Ratio	Mass Density (kg/m^3)
Dam	PLANE182	25000	0.2	2500
Reservoir	FLUID29	2070	-	1000
Foundation	PLANE182	50000	0.3	-

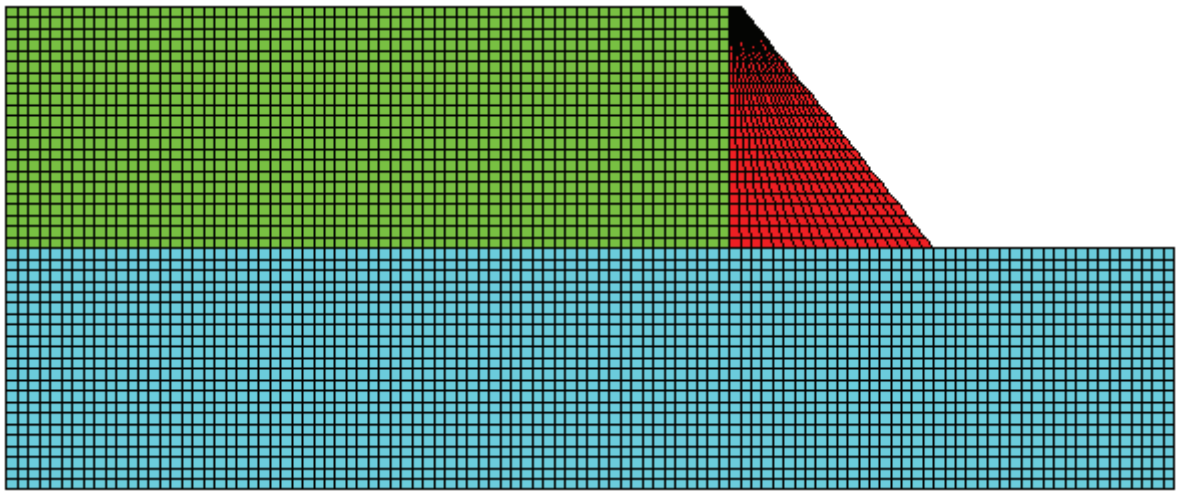

Figure 3. 2D finite element modeling of Bhakra Dam

Finite Element Analyses of the Dam

Before time history analyses of the dam, a modal analyses was performed to obtain mode shapes and natural frequencies which are used to calculate Rayleigh damping coefficients. In modal analysis, firs ten mode shapes are demonstrated as lateral and vertical bending modes. Also, the natural frequencies are changed between 0.97-4.33 Hz for first ten modes.

To investigate the seismic response of the dam, Uttarkashi Earthquake which was occurred in India was selected for seismic loads. Uttarkashi Earthquake occurred in 1991 under 10 km depth from the hypocenter with 7.0 magnitude (Url-1). As acceleration component, N85E (H) component obtained in Bhatwari station for Uttarkashi Earthquake was preferred. The acceleration time histories and spectral accelerations obtained for % 5 damping are plotted in Figs. 4-5, respectively for Uttarkashi Earthquake (Url-1).

In the study, N85E (H) component of the earthquake are applied to dam through upstream-downstream direction. Element matrices are computed using the Gauss numerical integration technique (Bathe, 1996). The Newmark method is used in the solution of the equation of motions. Damping matrices of the systems are considered by Rayleigh damping which is represented related to mass and stiffness matrices. Rayleigh damping constants are calculated within a frequency range 0.97-4.33 Hz assuming 5% damping ratios. Because of needed too much memory for the analyses, the first 18 seconds of the ground motion which are the most effective durations, are taken into account in calculations.

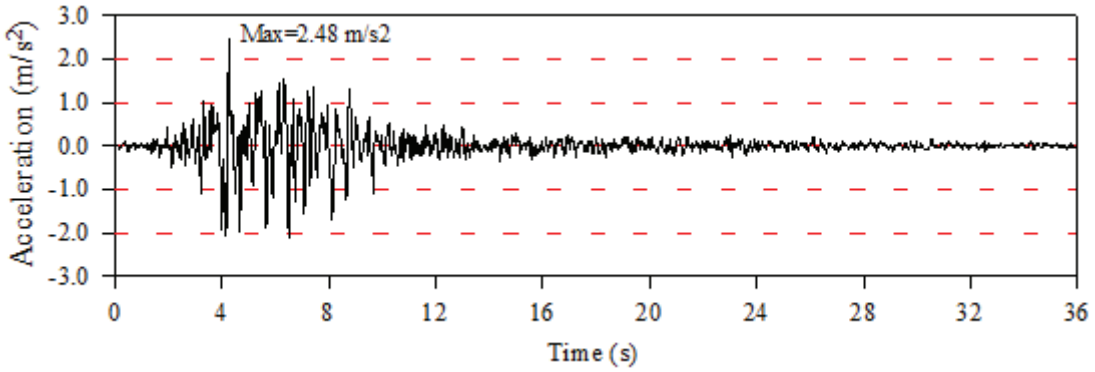

Figure 4. The time-histories of ground motion acceleration component of N85E (H)

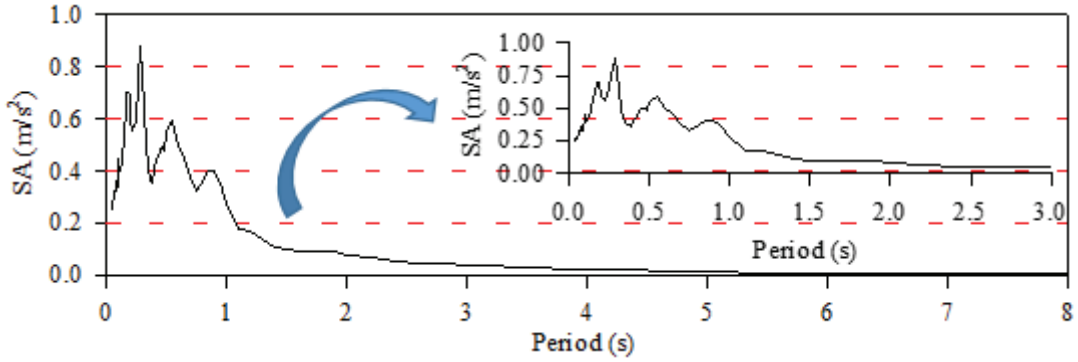

Figure 5. Spectral acceleration of ground motion component of N85E (H)

The time histories of lateral displacements at the crest point on downstream side of the dam are presented in Figure 6. According to Figure 6 the maximum displacement is obtained as 160 mm during 7-8 seconds.

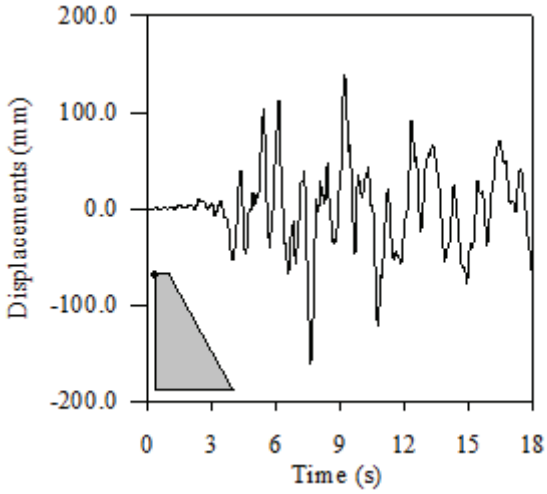

Figure 6. The time histories of lateral displacements at the crest point on the dam

The maximum lateral displacements of the dam through I-I section where the biggest values are occurred is given in Figure 7. As is seen in Figure 7 that the displacements are increased through the dam height, but the increasing ratio is decreased.

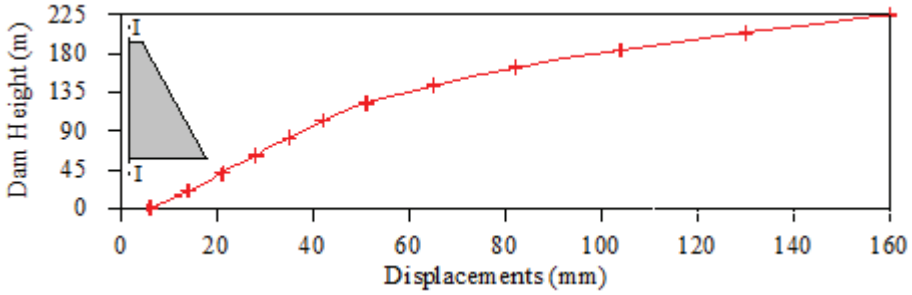

Figure 7. The maximum lateral displacements of the dam through I-I section

The time histories of maximum principal stresses at the base point on downstream side of the dam are presented in Figure 8. As is seen in Figure 8 that the maximum stress is obtained as 7 MPa during 9-10 seconds. The value of stress may be caused the damage on the dam when considered tensile stress of dam concrete.

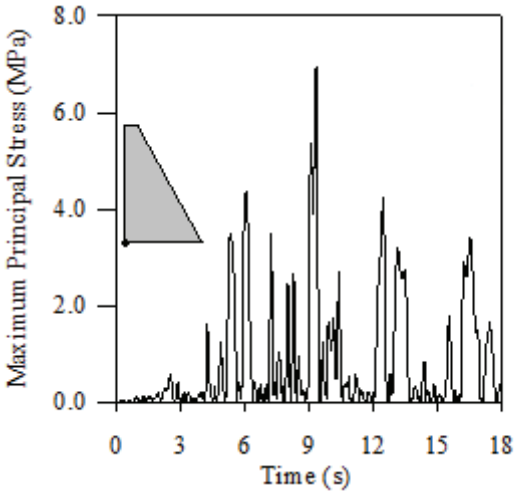

Figure 8. The time histories of maximum stresses at the base point of the dam

The maximum and minimum principal stresses of the dam through II-II section where the biggest values obtained are given in Figure 9 (a-b). As is seen in Figure 9 that the smallest stresses are occurred near 60-80 m from the upstream face of dam. But the biggest values for the stresses are obtained at upstream face of the dam.

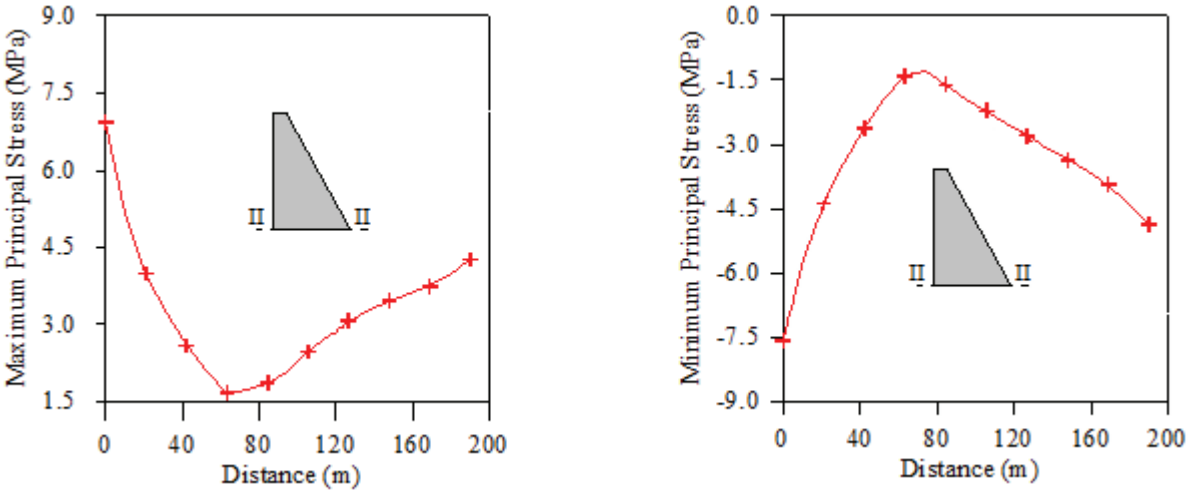

Figure 9. a) The maximum b) minimum principal stresses of the dam through II-II section

The maximum principal stresses that contour through the lateral direction is shown in Figure 10. It can be seen form Figure 10 that the maximum stresses occur at the base point on upstream face of the dam. Also it is possible that the limited tensile stress capacity of dam concrete may result in local damage to the base of the Bhakra Dam.

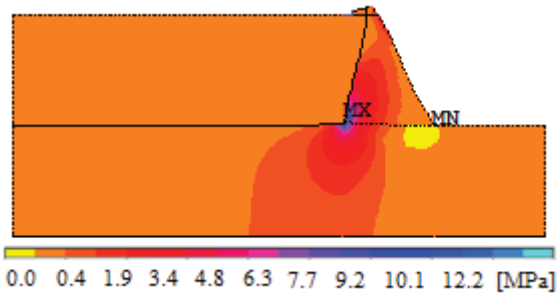

Figure 10. Maximum principal stress contour obtained from f 1991 Uttarkashi Earthquake

CONCLUSIONS

This study tells about the seismic response of Bhakra Gravity Dam in India. For the purpose, Bhakra Dam is modeled two dimensionally considering dam-reservoir-foundation interaction using ANSYS finite element software. Linear time history analyses of dam are performed by conducting 1991 Uttarkashi Earthquake in India. The following conclusions obtained from the study are specified.

- ✓ The first ten natural frequencies are estimated to range between 0.97-4.3 Hz from finite element analysis. Mode shapes are obtained as lateral and vertical bending modes.
- ✓ The displacements are increased through the dam height, but the increasing ratio is decreased. The maximum displacement is obtained as 160 mm during 7-8 seconds of the earthquake on the crest point of the dam.
- ✓ The maximum stress is obtained as 7 MPa during 9-10 seconds of the earthquake at the base point of the dam. The absolute value of smallest stresses are occurred near 60-80 m from the upstream face of dam. But the biggest values for the stresses are obtained at upstream face of the dam.
- ✓ According to 1991 Uttarkashi Earthquake results, It is possible to say that the limited tensile stress capacity of dam concrete may result in local damage to the base of Bhakra Dam.

REFERENCES

Altunisik, A.C and Sesli, H., 2015. "Dynamic response of concrete gravity dams using different water modelling approaches: Westergaard, Lagrange and Euler", Computers and Concrete, 16(3), 429-448.

ANSYS, Swanson Analysis System, USA, 2017.

Arabshahi, H and Lotfi, V., 2008. ''Earthquake response of concrete gravity dams including dam-foundation interface nonlinearities'', Engineering Structures, 30(11), 3065–3073.

Ardebili, M.A.H., Kolbadi, S.M.S., Mirzabozorg, A., 2013. "Smeared crack model for seismic failure analysis of concrete gravity dams considering fracture energy effects", Structural Engineering and Mechanics, 48(1), 17-39.

Khosravi, S., Salajegheh, J., Heydari, M.M., 2012. "Simulating of each concrete gravity dam with any geometric shape including dam-water foundation rock interaction using APDL", World Applied Sciences Journal, 17(3), 354-363.

Mohsin, A. Z., Omran, H. A., Al-Shukur, A.H.K., 2015. "Optimum design of low concrete gravity dam on random soil subjected to earthquake excitation, International Journal of Innovative Research in Science, Engineering and Technology, 4(9), 8961-8973.

Phansri, B., Charoenwongmit, S., Warnitchai, P., Shin, D.H., Park, K.H., 2010. "Numerical simulation of shaking table test on concrete gravity dam using plastic damage model", Structural Engineering and Mechanics, 36(4), 481-497

Sevim, B., 2011. "The effect of material properties on the seismic performance of arch dams", Natural Hazards and Earth Science, 11, 2253–2261.

Sevim, B., Altunışık, A.C., Bayraktar, A., Akköse, M., Calayır, Y., 2011a. "Water length and height effects on the earthquake behavior of arch dam-reservoir-foundation systems", KSCE Journal of Civil Engineering, 15(2), 295-303.

Sevim, B., Bayraktar, A., Altunışık, A.C., 2011b. "Investigation of water length effects on the modal behavior of a prototype arch dam using operational and analytical modal analyses", Structural Engineering and Mechanics, 37(6), 593-615.

Sevim, B., Altunışık, A.C., Bayraktar, A. 2012. "Earthquake behavior of Berke arch dam using ambient vibration test results", Journal of Performance of Constructed Facilities ASCE, 26, 780-792.

Url-1., 2017. http://www.strongmotioncenter.org, 08.03.2017.

USACE., 2003. "Time-history dynamic analysis of concrete hydraulic structures", Engineering Manual, EM 1110-2-6051, US Army Corps of Engineers, USA.

Valamanesh, V., Estekanchi, H.E., Vafai, A., Ghaemian, M., 2011. "Application of the endurance time method in seismic analysis of concrete gravity dams", Scientia Iranica, 18(3), 326–337.

Varughese, J. and Nikithan, S., 2016. "Seismic behavior of concrete gravity dams", Advances in Computational Design, 1(2), 195-206.

Wang, M., Chen, J., Fan, S., Lv, S., 2014. "Experimental study on high gravity dam strengthened with reinforcement for seismic resistance on shaking table", Structural Engineering and Mechanics, 51(4), 663-683.

5th International Symposium on Dam Safety

October 27-31, 2018

EFFECTS OF BASE WIDTH - DAM HEIGHT RATIO ON THE STRUCTURAL RESPONSE OF GRAVITY DAMS

Barış SEVİM [1]

ABSTRACT

Geometrical dimensions are the main parameters that affect the structural response of gravity dams. They are also important to determine the safest and most economical gravity dams. So this study is examined the geometrical dimensions effects on the structural response of gravity dams. For the purpose, three gravity dams are modeled in ANSYS finite element program to determine seismic response. In models, the dam height is selected with 200 m height, and the base lengths are selected as 100, 200, and 300 m. So three models are constituted considering base width (L) –dam height (H) ratio as 0.5, 1, and 1.5, respectively. The models also include dam-reservoir-foundation interaction. In finite element modeling, dam and foundation are represented by solid elements and the reservoir is represented by fluid elements. Linear time history analysis of the system is performed by conducting components of 1989 Loma Prieta Earthquake. The earthquake record is applied to the system in upstream-downstream direction. According to analysis results, natural frequencies, displacement and stresses changes in some nodes and sections are presented. The results show that the L/H ratios considerably affect the structural response of gravity dams.

Keywords: Base width-height ratio (L/H), Earthquake response, Gravity dam

INTRODUCTION

Due to retaining a huge water in their reservoir, seismic response of these structures is important especially earthquake-prone areas. One of the main effect on earthquake response of gravity dams are geometrical dimensions of dams. Because, dimensions of reservoir, foundation or geometry of dam body provide different response subjected to mode shapes, natural frequencies, displacement and stresses which are obtained from modal, static and dynamic analyses (USACE 2003). With the developing of computer systems, such kind of structures are modeled and analyzed using finite element method under huge earthquakes. In the literature, some recent studies consider modal, static and dynamic analyses of gravity dams (Millan et al., 2007, Phansri et al., 2010; Ardebili et al., 2013; Ziaolhagh et al., 2016).

In this study the geometrical dimensions effects on the structural response of gravity dams are investigated. For the aim, three gravity dams are modeled in ANSYS finite element program with 200 m height, and the base lengths are selected as 100, 200, and 300 m. So these three models are constituted considering base width (L) –dam height (H) ratio as 0.5, 1, and 1.5, respectively. In the study linear time history analysis of the system is performed by conducting components of 1989 Loma Prieta Earthquake. The earthquake record is applied to the system in upstream-downstream direction.

FORMULATION

During in an earthquake, the reservoir are considerably affect the response of dam. So representation of reservoir is important to present realistic behavior of dam. Modeling and analysis of dynamic dam-reservoir-foundation interaction during earthquakes have gone through direct method. The discretized

Assoc. Prof. Department of Civil Engineering, Yildiz Technical University, Istanbul, Turkey,
e-posta: basevim@yildiz.edu.tr

structural dynamic equation including dam-and foundation system subjected to ground motion can be formulated using finite element approach where the soil and structure are included within the same model and analyzed in a single step in Eq. (1) (Khosravi et al., 2012;Mohsin et al., 2015; Varughese and Nikithan, 2016).

$$M_s\ddot{x}_e + C_s\dot{x}_e + k_s x_e = -M_s\ddot{x}_g \quad (1)$$

where, M_s, C_s, and k_s are the structural mass, damping and stiffness matrices, respectively. x_e, $\dot{x}_e$, $and\, \ddot{x}_e$ are is the nodal displacement, velocity and acceleration vectors, respectively. $\ddot{x}_g$ is ground acceleration. The reservoir produce a hydrodynamic effects during the earthquakes termed as Qp_e. So the discretized wave equation of reservoir is given as Eq. (2);

$$M_f\ddot{p}_e + C_f\dot{p}_e + k_f p_e + p_w Q^T(\ddot{x}_e + \dot{x}_e) = 0 \quad (2)$$

where, M_f, C_f, and k_f are the fluid (reservoir water) mass, damping and stiffness matrices, respectively. p_e is the nodal pressure and, $p_w Q^T$ is referred to as the coupling matrix. Dynamic equilibrium equation of the coupled system is obtained from Eq 1 and Eq 2 as given

$$M_c\ddot{x}_c + C_c\dot{x}_c + k_c x_c = F(t) \quad (3)$$

where M_c, C_c, and k_c are the coupled mass, damping and stiffness matrices respectively and F(t) is the dynamic load vector.

NUMERICAL EXAMPLE

In this study, a concrete gravity dam with 10 m constant crest width and 200 m constant height (H) is selected as numerical example and base width (L) assumed as variably. Base width is calculated according to L/H ratio and the ratios are preferred as 0.5, 1.0, and 1.25, respectively. Therefore three different gravity dam models are decided for modeling. Finite element models of the dams are constituted two dimensionally by ANSYS (2017) software considering dam-reservoir-foundation (full reservoir) interaction effects (Fig. 1). Models are named as Model 1, Model 2, and Model 3, respectively for L/H ratios such as 0.5, 1.0, and 1.5 (See Figure 1).

In the finite element modeling, the dam body is represented using PLANE182 elements which are used for 2-D modeling of solid structures. The element has four nodes and has two degree of freedoms at each nodes such as X and Y translations. The element has the capabilities of plasticity, stress stiffening, large deflection, and large strain ANSYS (2017). In the modeling, reservoir is extended as 3 dam heights through upstream direction. Such a modeling neglects the effects on deflections, stresses, and natural frequencies of the dam (USACE 2003, Sevim 2011, Sevim *et al.* 2011, Sevim *et al.* 2012). Reservoir is represented using FLUID29 elements which are used both modeling fluid domain and fluid-structure interaction. The element has four nodes with three degrees of freedom per node: translations in the nodal x and y directions and pressure. The translations, however, are applicable only at nodes that are on the interface. Foundation is modeled using PLANE182 elements and extended as dam height through vertical and downstream directions. Also foundation is modeled on upstream direction under the reservoir. Boundary conditions for are fixed under and near side of the foundations. The foundation model should be preferred as massless in which only the effects of foundation flexibility are considered. The assumptions told above are generally use to model and evaluate the gravity dam. Material properties assumed in the modeling are given in Table 1. A mesh study is done to decide optimum mesh size. According to this investigations the numbers of nodes and elements used each model are listed in Table 2.

Table 1. Material properties assumed in finite element modeling of gravity dams

System	Element Type	Material Properties		
		Elasticity Modulus (MPa)	Poisson Ratio	Mass Density (kg/m^3)
Dam	PLANE182	35000	0.2	2500
Reservoir	FLUID29	2070	-	1000
Foundation	PLANE182	45000	0.3	-

Table 2. Numbers of Nodes and Elements used in finite element modeling of gravity dams

Models	Numbers of Nodes	Numbers of Elements		
		Dam PLANE182	Reservoir FLUID29	Foundation PLANE182
Model 1	3331	200	1200	1800
Model 2	3741	400	1200	2000
Model 3	6481	900	1800	3600

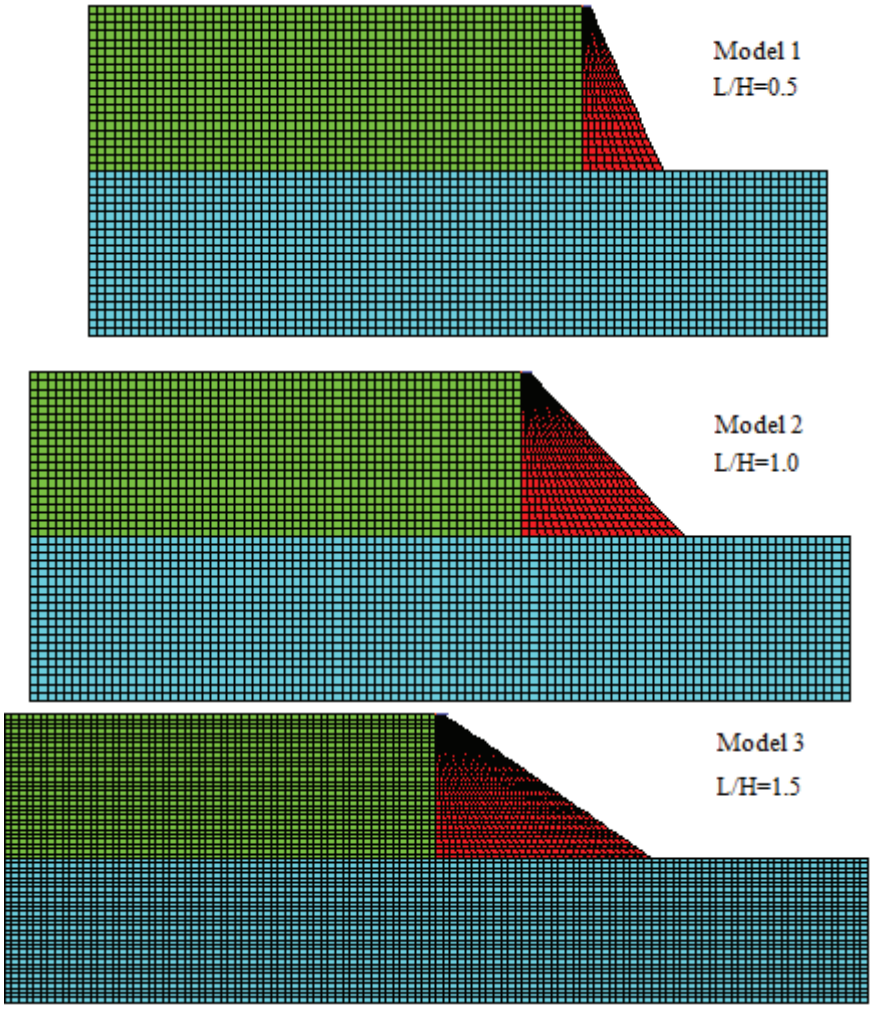

Figure 1. Finite element models of gravity dams

In this study, seismic response of gravity dams is investigated under 1989 Loma Prieta earthquake. East-west component (CLS090) of the earthquake is applied to models on upstream-downstream direction. The time histories of acceleration of CLS090 component are plotted in Figure 2 (Url-1

2017). In time history analyses, the element matrices are computed using the Gauss numerical integration technique (Bathe 1996). The Newmark method is used in the solution of the equation of motions. Damping matrices of the systems are considered by Rayleigh damping which is represented related to mass and stiffness matrices. Rayleigh damping constants are calculated considering first nine natural frequencies for each model assuming 5% damping ratios. Because of needed too much memory for the analyses, the first 15 seconds of the ground motion are taken into account in calculations for each model, which are the most effective durations.

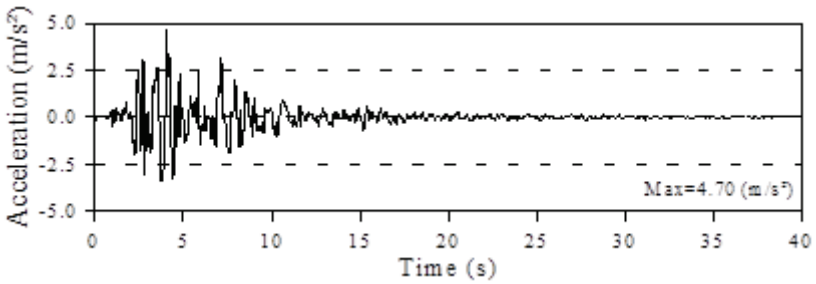

Figure 2. The time-histories of acceleration subjected to 1989 Loma Prieta earthquake

The time-history of the horizontal displacements at the crest point of gravity dam obtained from linear analysis are respectively presented in Figure 3 (a-c) from Model 1 to Model 3. As seen in Figure 3 that, when the maximum displacements are obtained for Model 1, the minimum displacements are occurred for Model 3. The maximum displacements at this point for each model are occurred as 41 cm, 21 and 18 cm, respectively. As is seen from Figure 3 that the frequency contents of the displacements of Model 2 and Model 3 are near to each other but different to those of Model 1. Also, the results show that the Model 3 provide minimum displacements. On the other hand the displacement at the crest point are nearly % 60 decreased from Model 1 to Model 2, and % 65 decreased from Model 1 to Model 3.

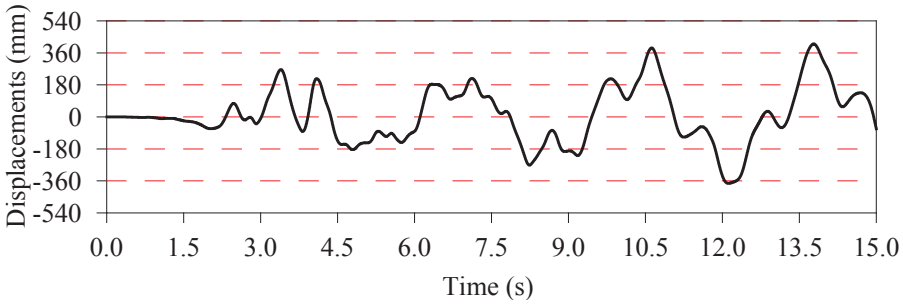

a) The time-histories of displacements occurred Model 1

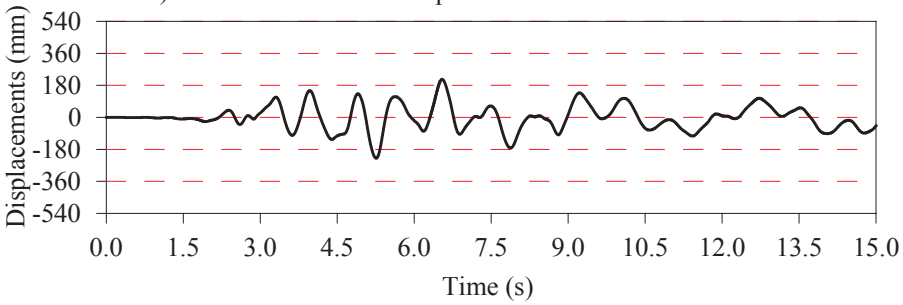

b) The time-histories of displacements occurred Model 2

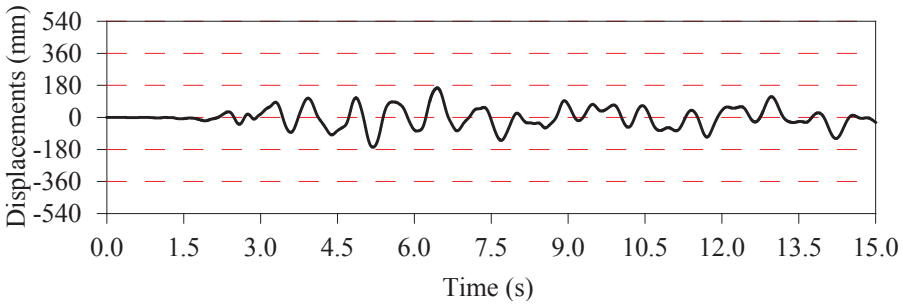

c) The time-histories of displacements occurred Model 3

Figure 3. The time-history of the horizontal displacements at the crest point of gravity dams

The time-histories of maximum principal stresses (tensile stress) for the most representative point of each dam model, which is base of downstream side of the dam for Model 1 and base of upstream side of the dam for Model 1, and Model 3 are plotted in Figure 4 (a-c), respectively. It is clearly seen from Figure 4 that the frequency contents of the stresses of Model 2 and Model 3 are near to each other but different to those of Model 1. The results show that the Model 3 has smaller stresses like the displacements results in Model 3. But Model 2 is more economic compare to Model 3 which has a little bigger stresses compared to Model 3.

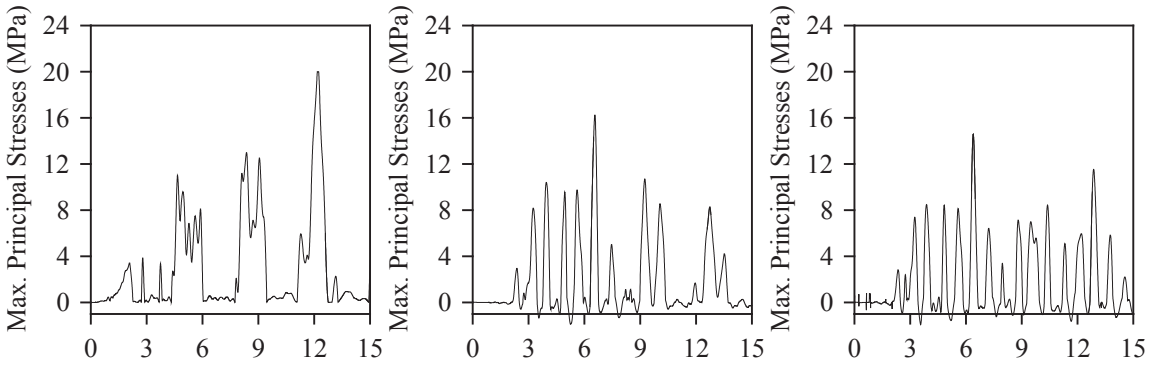

a) Model 1 b) Model 2 c) Model 3

Figure 4. The time-histories of maximum principal stresses

The maximum principal stresses that contour through the lateral direction at the instant at which the maximum stresses occur are shown in Figure 5 (a-c) for) for each model. It can be seen Figure 5 that the maximum stresses occur at the base point on downstream face of the dam except Model 1. The maximum principal (tensile) stresses obtained for each model are more than those of the limited tensile stress capacity of dam concrete. These may cause local damage on the dams. So more realistic representation, nonlinear time history analyses may be performed.

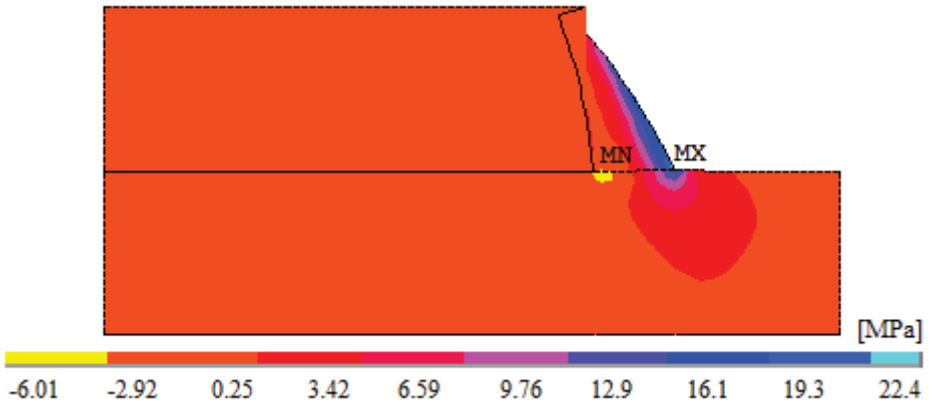

a) Model 1

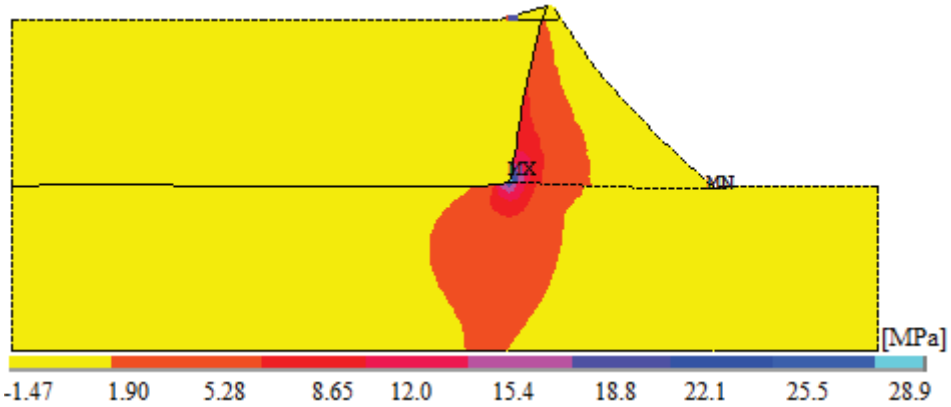

b) Model 2

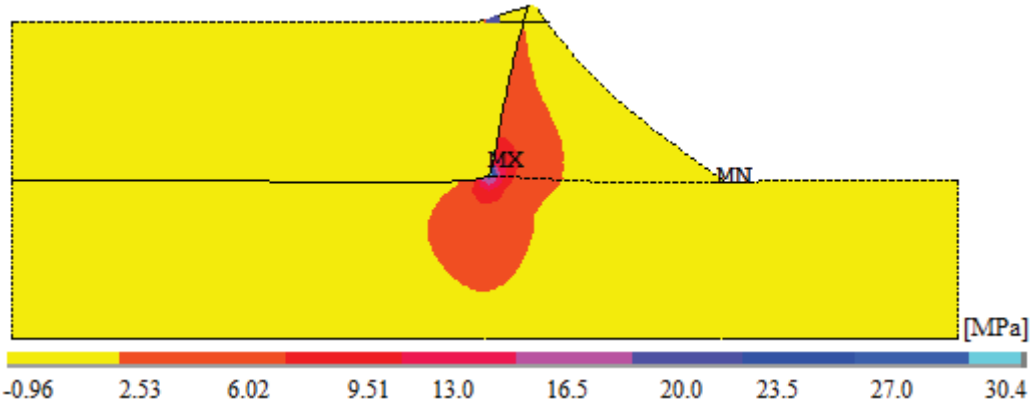

c) Model 3

Figure 5. Maximum principal stress contours obtained for each model

CONCLUSIONS

In this study, effects of geometrical dimensions of dam body on the seismic response of gravity dams are investigated. For the purpose, five gravity dam-reservoir-foundation systems are modelled considering different dam base width (L) - height (H) ratios considering 0.5, 1.0, and 1.5 ratios. In this study, the following observations and suggestion can be made:

- The frequency contents of the displacements of Model 2 and Model 3 are near to each other but different to those of Model 1. Also, the results show that the Model 3 provide minimum displacements. On the other hand the displacement at the crest point are nearly % 60 decreased from Model 1 to Model 2, and % 65 decreased from Model 1 to Model 3.
- The frequency contents of the stresses of Model 2 and Model 3 are near to each other but different to those of Model 1. The results show that the Model 3 has smaller stresses like the

displacements results in Model 3. But Model 2 is more economic compare to Model 3 which has a little bigger stresses compared to Model 3.

- The maximum principal (tensile) stresses obtained for each model are more than those of the limited tensile stress capacity of dam concrete. These may cause local damage on the dams. So more realistic representation, nonlinear time history analyses may be performed.
- According the result of the study, Model 2 and Model 2 have good seismic responses. But Model 2, where base width (L) - height (H) ratio is 1.0, has more suitable response. Because the displacement and stresses results are near to Model 2 results. Model 2 has nearly % 50 lower concrete volume. Such a difference provides more economy during construction.

REFERENCES

Ardebili, M.A.H., Kolbadi, S.M.S., Mirzabozorg, A., 2013. "Smeared crack model for seismic failure analysis of concrete gravity dams considering fracture energy effects", Structural Engineering and Mechanics, 48(1), 17-39.

Khosravi, S., Salajegheh, J., Heydari, M.M., 2012. "Simulating of each concrete gravity dam with any geometric shape including dam-water foundation rock interaction using APDL", World Applied Sciences Journal, 17(3), 354-363.

Millan, M.A., Young, Y. L. and Prevost, J.H. (2007), "The effect of reservoir geometry on the seismic response of gravity dams", Earthquake Eng. Struct. Dyn., 36, 1441-1459.

Mohsin, A. Z., Omran, H. A., Al-Shukur, A.H.K., 2015. "Optimum design of low concrete gravity dam on random soil subjected to earthquake excitation, International Journal of Innovative Research in Science, Engineering and Technology, 4(9), 8961-8973.

Phansri, B., Charoenwongmit, S., Warnitchai, P., Shin, D.H., Park, K.H., 2010. "Numerical simulation of shaking table test on concrete gravity dam using plastic damage model", Structural Engineering and Mechanics, 36(4), 481-497

Sevim, B., 2011. "The effect of material properties on the seismic performance of arch dams", Natural Hazards and Earth Science, 11, 2253–2261.

Sevim, B., Altunışık, A.C., Bayraktar, A., Akköse, M., Calayır, Y., 2011. "Water length and height effects on the earthquake behavior of arch dam-reservoir-foundation systems", KSCE Journal of Civil Engineering, 15(2), 295-303.

Sevim, B., Altunışık, A.C., Bayraktar, A. 2012. "Earthquake behavior of Berke arch dam using ambient vibration test results", Journal of Performance of Constructed Facilities ASCE, 26, 780-792.

Url-1., 2017. http://www.strongmotioncenter.org, 08.03.2017.

USACE., 2003. "Time-history dynamic analysis of concrete hydraulic structures", Engineering Manual, EM 1110-2-6051, US Army Corps of Engineers, USA.

Valamanesh, V., Estekanchi, H.E., Vafai, A., Ghaemian, M., 2011. "Application of the endurance time method in seismic analysis of concrete gravity dams", Scientia Iranica, 18(3), 326–337.

Varughese, J. and Nikithan, S., 2016. "Seismic behavior of concrete gravity dams", Advances in Computational Design, 1(2), 195-206.

Wang, M., Chen, J., Fan, S., Lv, S., 2014. "Experimental study on high gravity dam strengthened with reinforcement for seismic resistance on shaking table", Structural Engineering and Mechanics, 51(4), 663-683.

5th International Symposium on Dam Safety

October 27-31, 2018

STATIC ANALYSIS OF GRATCHE ARCH DAM – A CASE STUDY

Borjana BOGATINOSKA[1], Frosina PANOVSKA[1], Ana GRUPCHEVA[1], Stefanija IVANOVSKA[1], Dimitar KONDINSKI[1], Stevcho MITOVSKI[2], Ljupcho PETKOVSKI[3]

ABSTRACT

The advantages of building a curved (arch) dam were appreciated as early as Roman times (dam Kebar in Qom Providence, Iran, build in approx. 1300 AD). Arch dams act as an arch, accepting the loading from the upstream side and transferring it to the banks apropos the rock foundation. Dam sites, considered as favorable for arch dams, are to be composed of sound rock.

Several safety requirements are to be fulfilled in order to ensure the stability of all dam types, such as: functional (degree of satisfaction of the users' objectives), economic (ratio of cost/benefit), hydrological (acceptable risks for flood evacuation), hydraulic (conduits capacity), seepage (intensity of hydrodynamic process) and structural (dam's behavior at static and dynamic loads).

In the paper are given main findings regarding the stress-deformation state for static loads from the case study of Gratche arch dam, build on river Kochanska in 1959, in nearby of Kochani Municipality, Republic of Macedonia, with structural height of 43 m. The numerical analysis is conveyed with application of the code SOFiSTiK, based on the finite element method.

Keywords: Arch dam, static analysis, finite element method, SOFiSTiK.

INTRODUCTION

The dams, having in consideration their importance, dimensions, complexity of the problems that should be solved during the process of designing and construction along with the environmental impact are lined up in the most complex engineering structures [Novak et al., 2007; Tančev, 2013]. The number of constructed large dams in the world in specific periods is presented in Fig. 1. The ICOLD Register of dams lists around 45,000 dams higher than 15 m. According to the rapid population increase, foreseen to reach 10 billion inhabitants by the end of the century, more dams will have to be built in order various water demands to be satisfied.

Republic of Macedonia is located in the central part of the Balkan Peninsula, covering area of 25,713 km^2 with a population of about 2 million inhabitants. The rivers in Republic of Macedonia belong to three main river basins: (a) The Aegean basin, in which they flow out through the rivers Vardar and Strumica; (b) The Adriatic basin, to which they are taken away through the river Crn Drim (Black Drim); and, (c) The Black Sea basin, through the river Binachka Morava, which extends over a quite insignificant part. The biggest is the catchments basin of the River Vardar, which extends to some

[1] Student, Faculty of Civil Engineering, Ss Cyril and Methodius, Skopje, Republic of Macedonia, e-mail: borjana95@gmail.com
[2] Assistant Professor, Faculty of Civil Engineering, Ss Cyril and Methodius, Skopje, Republic of Macedonia, e-mail: smitovski@gf.ukim,edu,mk
[3] Full Professor, Faculty of Civil Engineering, Ss Cyril and Methodius, Skopje, Republic of Macedonia, e-mail: petkovski@gf.ukim.edu.mk

20,525 km^2 or 80% of the territory of the Republic of Macedonia. Total available surface water resources in the Republic of Macedonia are assessed as about 3,300 m^3 per capita annually.

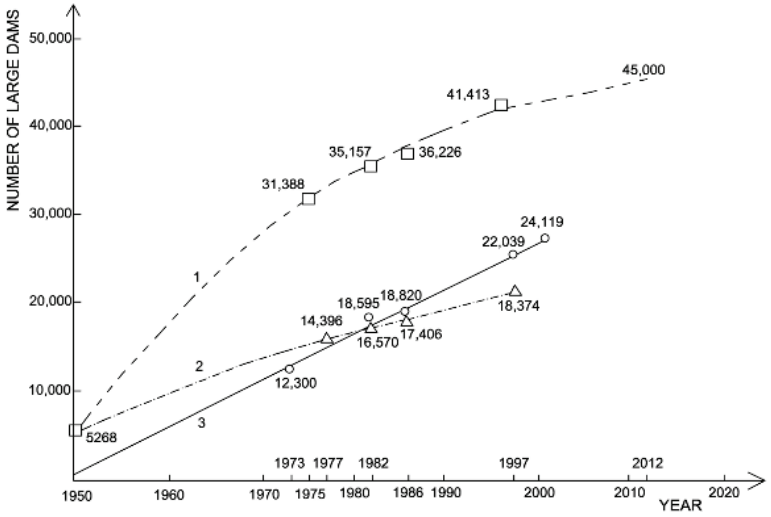

Fig. 1. Total number of constructed dam in the world [Jiazheng & Jing, 2000]. (1) Total number of dams in the world; (2) Number of large dams in the world except China; (3) Number of large dams in China.

The dam construction in Macedonia dates from 1938 when the Matka arch dam was constructed, located on the River Treska, in vicinity of Skopje, still in service. Up to now are constructed 27 large dams [Tančev et al., 2013]. Different types of dams are represented, having in consideration the various geological, topographical and hydrological conditions, among which 18 are embankment dams, 8 concrete arch dams and 1 concrete multiple arch dam. Latest constructed dam is St. Petka double curved arch dam, in nearby of Skopje, as final part of the cascade system on river Treska, along with dams St. Andrea and Kozyak, commissioned in August, 2012.

The assessment of the stability and the behaviour of dams during construction at full reservoir and during service period is of vital importance. The paper deals with numerical three-dimensional analysis of Gratche dam, performed with application of the program package SOFiSTiK.

GRATCHE DAM

During the period 1958/59 Gratche dam, was constructed in order to create reservoir purposed for irrigation of the rice fields in Kochansko Pole and for water supply of the industry in the city of Kochani. The dam has been constructed on Kochanska River, which flows through a canyon with very steep banks. The foundation is composed of crystal schists, decomposed at the surface in a zone of several meters. The height of the dam above the ground amounts to 29 m, while, above the highest point of the foundation is 43 m [Tanchev, 2014; YUCOLD, 1970]. On Fig. 1 is displayed the dam layout, where we can notice the steep banks and the relatively wide riverbed of the Kochanska River. The dam creates storage space of 2.4 million m^3. The first filling of the dam commenced in November, 1959, while the dam was commissioned in June, 1960. The dam is still in service, and without non-regular occurrences that can endanger its safety (cracks, increased leakage etc.).

In the horizontal sections of the dam the thickness is constant. The upstream face of the dam is vertical (Fig. 2). The radius of curvature of the horizontal arches varies very little – from 64.35 to 50.75 m, so that it can be considered constant. The central angle ranges within the limits from 136^o to 96^o. In the dam's body there have been incorporated 12,000 m^3 of concrete, with an average reinforcement of 40 kg reinforcing steel per 1 m^3 of concrete.

On Fig. 2, the part which is above the ground (1) is a thin reinforced concrete structure in the river bed, founded above a massive concrete block (2) connects the thick layer of river sediment (3). At the crest the dam is 150 m long and 1.0 m thick. Going downwards, the thickness increases and, near the concrete block amounts to 3.45 m. The massive concrete block in the foundation is 6.45 m wide and 14 m deep. It plays the role of a plug through the deposited sediment material, while at the same time serving also as a foundation of the dam. The spillway is completely separated from the dam's body and consists of four spillway spans, each 7 m wide. The overflow capacity is 120 m^3/s. The bottom outlet works accommodated in the central part of the dam has been provided with two gates, located in a small structure, immediately downstream of the dam. The pipe of the bottom outlet has a diameter of 1000 mm.

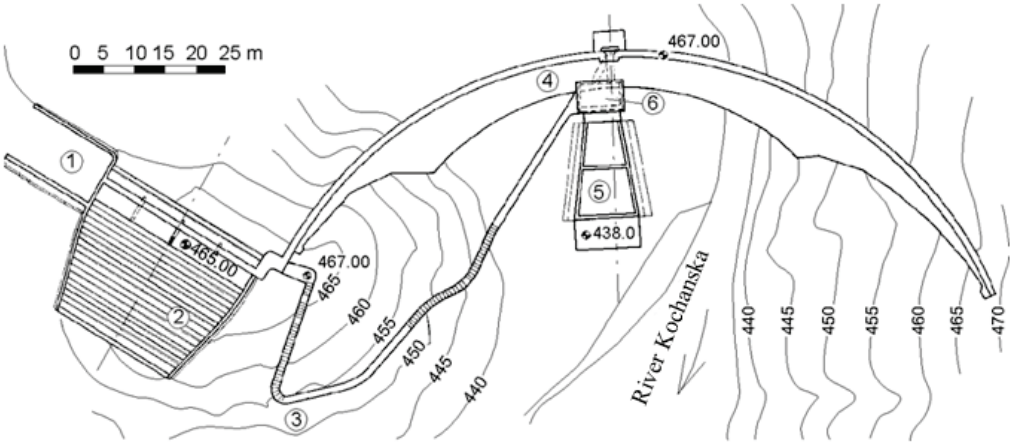

Fig. 2. Gratche dam, layout. (1) Plateau; (2) spillway; (3) roadway; (4) the dam's body; (5) stilling basin at the bottom outlet; (6) gate chamber at the bottom outlet.

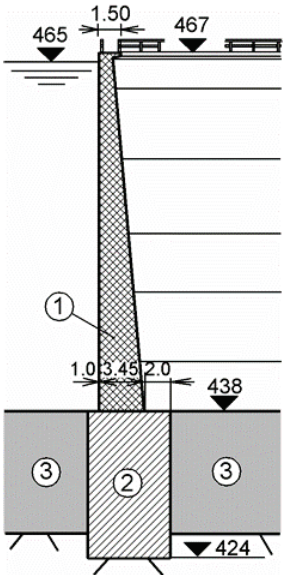

Fig. 2. Gratche dam, cross-section.

NUMERICAL MODEL

The static analysis of Gratche dam is conveyed with application of the program package SOFiSTiK, based on the finite element method. In order to perform the numerical analysis following steps are

undertaken: (1) choice of material parameters – constitutional laws (one of the most complex tasks during the analysis), (2) adoption of dam geometry and (3) simulation of the typical dam loading stages (empty and full reservoir).

The constitutional law for the concrete in the dam body and foundation is adopted according to EC 2, concrete grade CG 30 [Eurocode, 1992; ICOLD, 2009], directly applied form the material library of the code SOFiSTiK. On Fig. 2 are specified main input date for concrete.

Fig. 2. Input date for concrete, according to EC 2.

Parameter	Mark	Value	Unit
Density	γ	24.00	kg/m^3
Temperature coefficient	α	$1.00*10^{-5}$	
Elastic modulus	E	32837	MPa
Poisson ratio	ν	0.20	

The rock foundation is simulated as massless zone, by applying linear elastic constitutive law due to the fact that the rock foundation state is simulated only as initial stage in the model and the deformations in that zone are irrelevant for the dam behaviour. The input parameters for the rock foundation are modulus of elasticity E=10,000 MPa and Poissons's ratio ν=0.25, adopted according to reference [YUCOLD, 1970; Jovanovski et all, 2012].

The numerical model is composed of the dam body, concrete foundation and rock foundation. The dam body is limited by the dam site shape, and rock foundation, with length of 60.0 m upstream and 100.0 m downstream of the dam's central cantilever [ICOLD, 1987], while the rock foundation under the concrete foundation in the river bed is adopted at depth of 45.0 m (Fig .3). The rock foundation in the left and the right bank is adopted at length of 50.0 m on both sides of the dam crest. By such parameters is defined the non-deformable limit boundary condition. The discretization is conducted by capturing zones with different materials – concrete (dam body and foundation) and rock zone in groups. The dam's thickness is divided in 3 layers (groups).

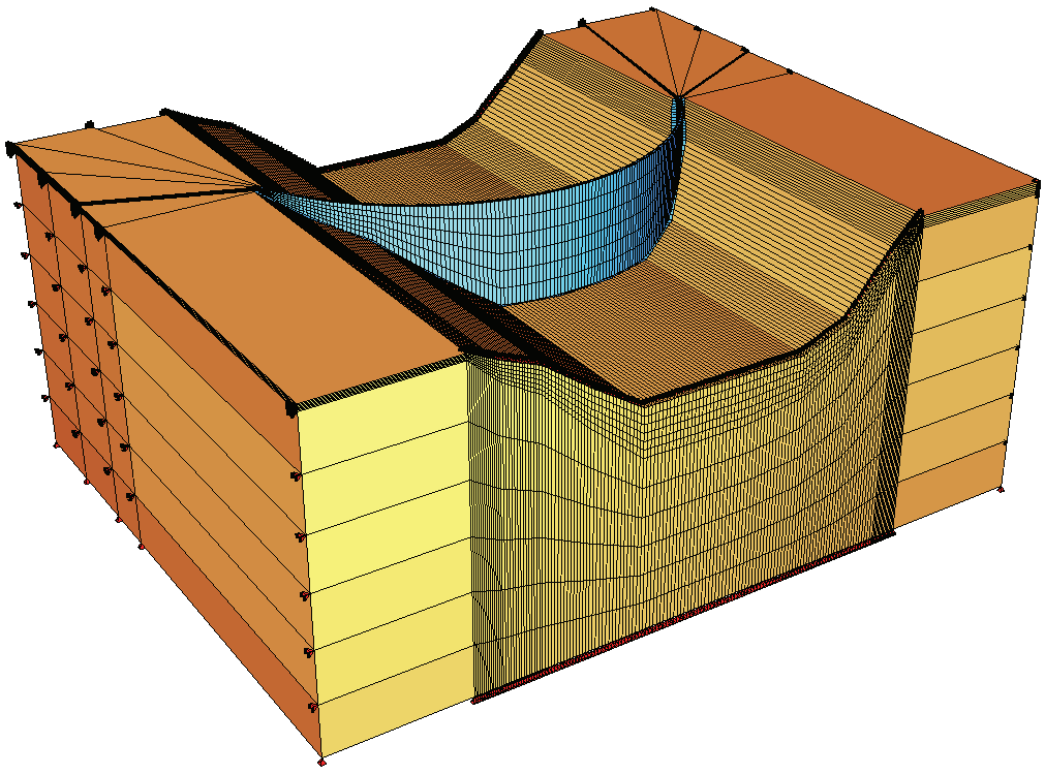

Fig. 3. Gratche dam model, spatial view from upstream side, number of elements E=6791.

The dam analysis includes simulation of state at full reservoir in case of low (winter period) and high temperatures (summer period). In case of Gratche dam there are no installed devices for temperature measurement within the dam body. Therefore, the temperature load (Fig. 4) is adopted in accordance with data from literature [ICOLD, 1987], as well and from previously performed analysis of such dams [Kokalanov et all, 2007; Mitovski, 2015]. Namely, the dam is divided in three groups along its thickness in order to apply various input values for the temperature, according to simulated loading stage (winter or summer period). The hydrostatic pressure on the dam is taken up to normal water elevation of 465.0 masl (Fig. 5).

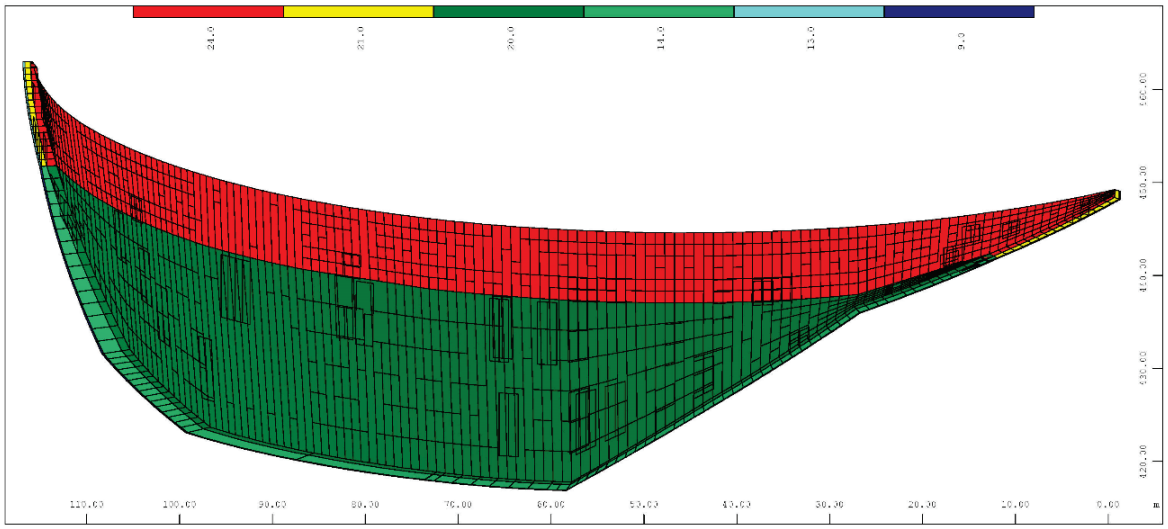

Fig. 4. Temperature load applied for summer period, T=9-24 ºC.

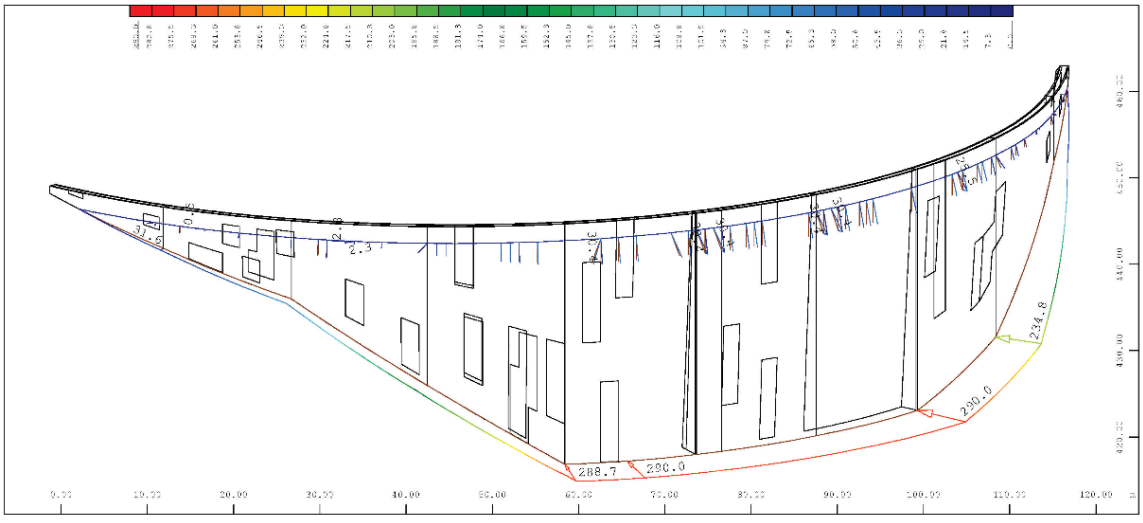

Fig. 5. Water load applied on dam body (full reservoir).

OUTPUT RESULTS

The dam state is assessed by analysis of the values and distribution of the displacements in the dam's body. The contour lines of the horizontal displacements (X-direction, „-"denotes displacement in downstream direction) for case at full reservoir and winter period are displayed in Fig. 6. The dam mainly deforms in downstream direction having in consideration that both temperature and hydrostatic load are acting in such direction. So, the maximal displacement occurs directly below the central at

zone of the dam crest, approximately at 70% of the dam height, value of 7.0 mm. The contour lines of the horizontal displacements for case at full reservoir and summer period are displayed in Fig. 7. In this case the dam mainly deforms in upstream direction having in consideration that temperature load is dominant in case of thin arch dam. In this case the maximal displacement occurs along great section of the dam crest, approximately on section of 1/3 of the crest length, value of 17.0 mm. In the central point of the dam crest the displacement is approximately 15 mm.

The isolines of the horizontal displacements (Y-direction, „-“denotes displacement towards the left bank) for winter period and full reservoir are displayed on Fig. 8. The maximal displacements occurs in the dam crest in vicinity of the right bank, with value of almost 3.0 mm. We can notice that there is analogue distribution in case of simulation of summer period (Fig. 9). Namely, the maximal displacements occurs on the same location, with somewhat increased value of 11.0 mm.

The distribution of the vertical displacements („-“denotes displacement in in gravity direction) for case at full reservoir and winter period are displayed in Fig. 10. The maximal displacement occurs at dam crest, approximately on ½ of dam's crest length, value of 1.0 mm. The distribution of the vertical displacements at full reservoir and summer period are displayed on Fig. 11. Also, similar as previous case, the temperature load causes displacements in opposite direction of the gravity apropos rising occurs. The maximal value of the displacements is 5.3 mm, located in the central part of the dam's crest.

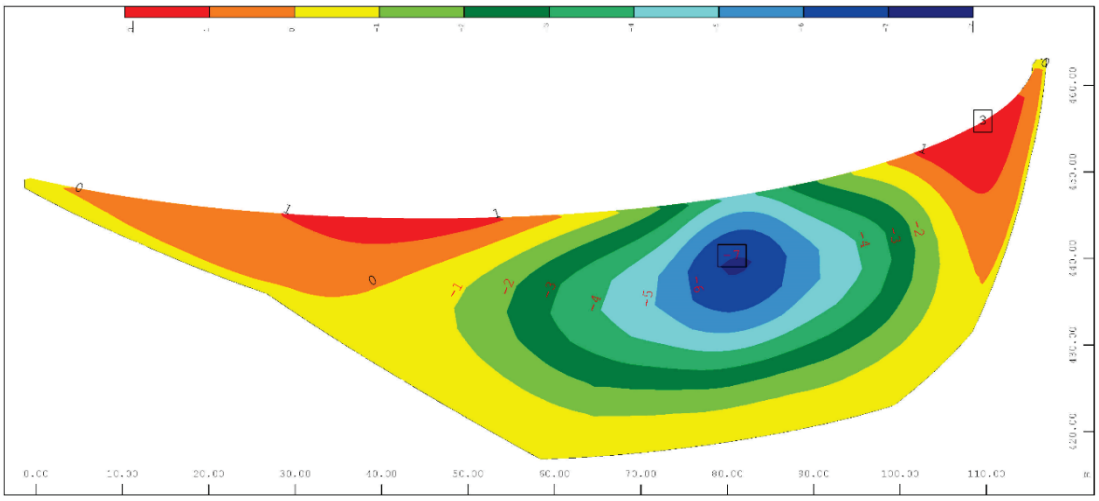

Fig. 6. Contour lines of summary horizontal displacements (X direction) at full reservoir and winter period.

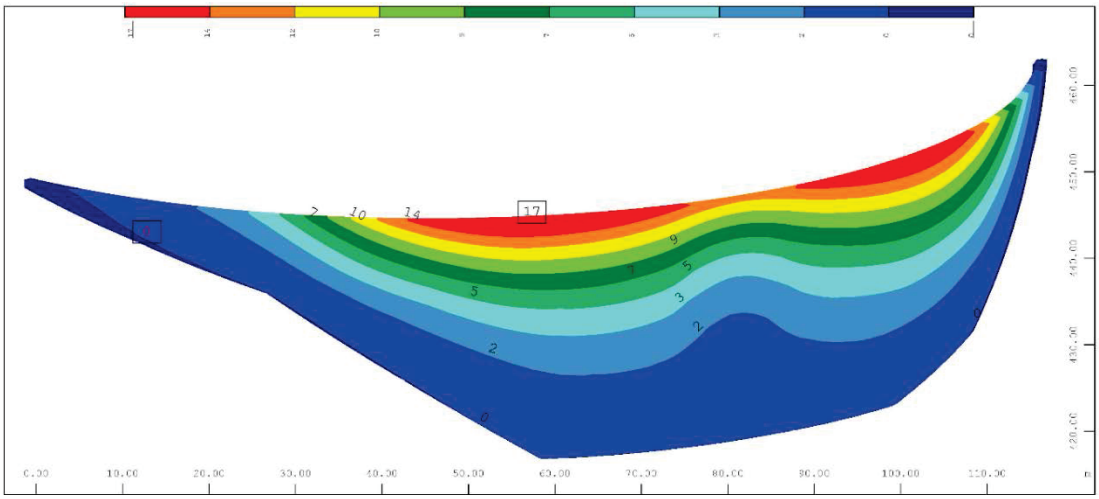

Fig. 7. Contour lines of summary horizontal displacements (X direction) at full reservoir and summer period.

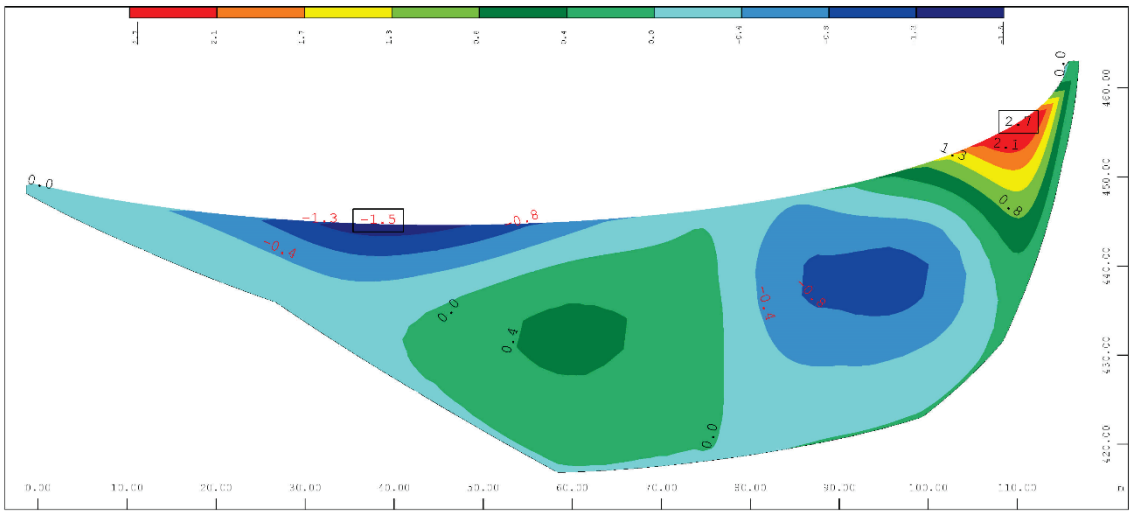

Fig. 8. Contour lines of summary horizontal displacements (X direction) at full reservoir and winter period.

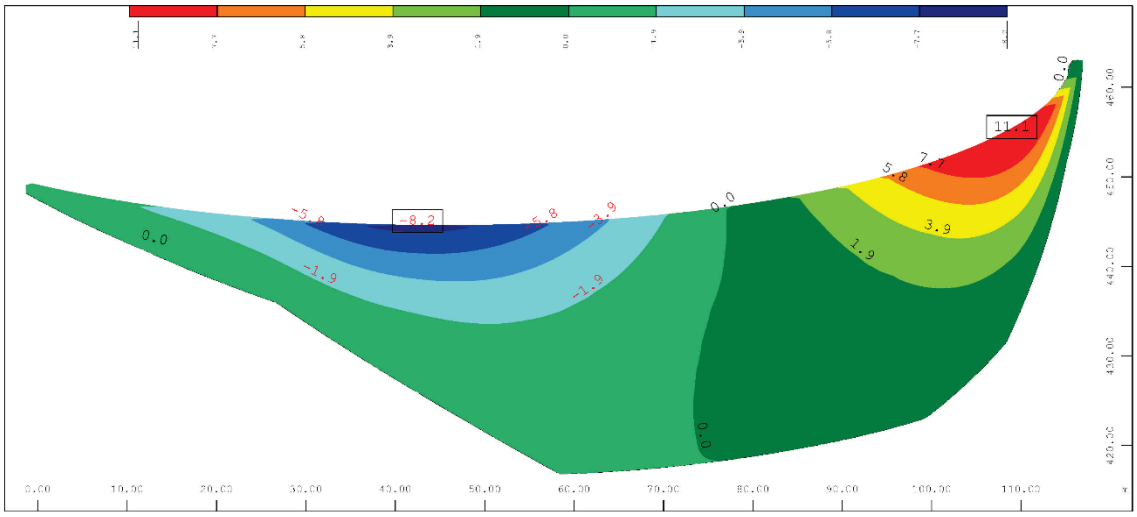

Fig. 9. Contour lines of summary horizontal displacements (X direction) at full reservoir and summer period.

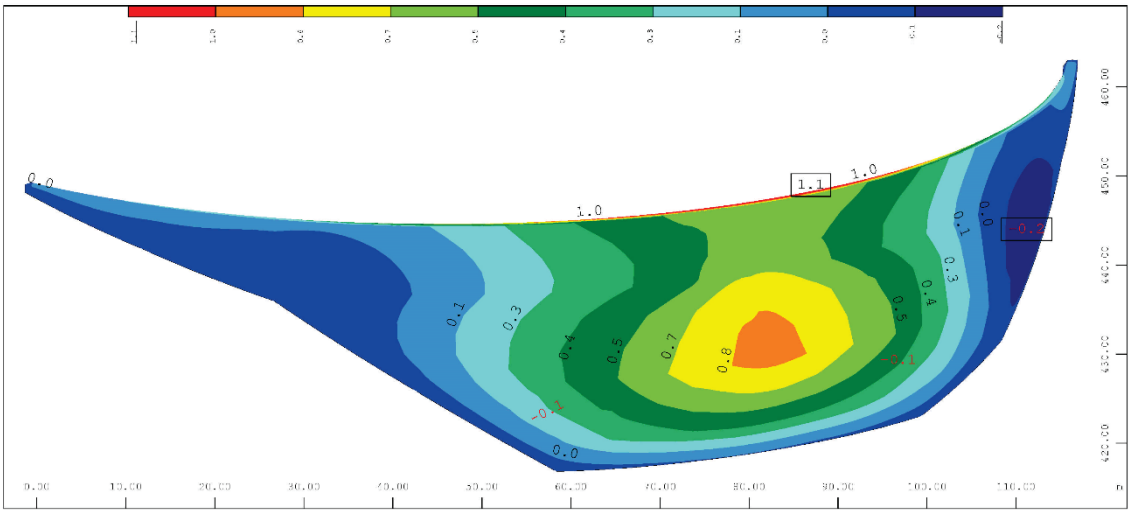

Fig. 10. Contour lines of summery vertical displacements at full reservoir and winter period.

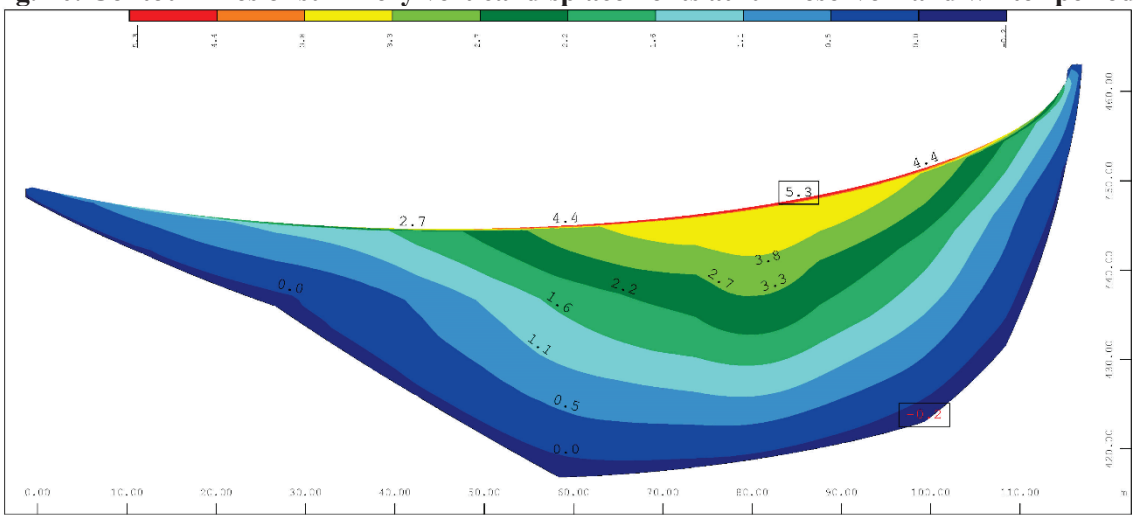

Fig. 11. Contour lines of summary vertical displacements at full reservoir and summer period.

On Fig. 12 are displayed main principal stresses for full reservoir state and temperatures for summer period. The stresses are in full compressive, reaching maximal value of 15.0 MPa at the right bank, at contact zone of the dam and the rock foundation.

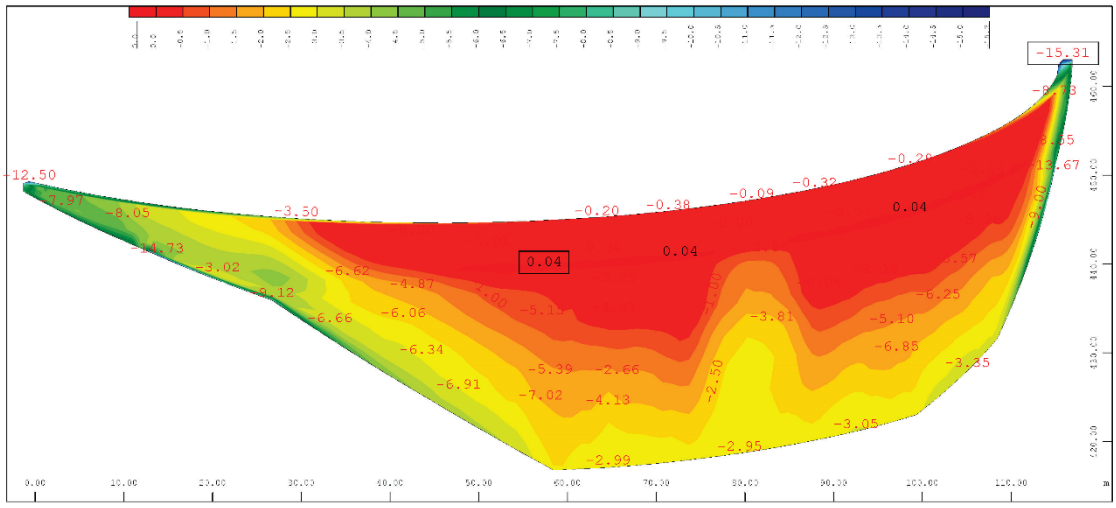

Fig. 12. Main principal stresses in the dam's body at full reservoir and summer period.

MONITORING DATA COMPARISON

The technical monitoring of the dams should fulfil two objectives: (1) to verify the conducted numerical analyses of the dam and to follow the dam behaviour in the service period, in order to detect eventual non-regular occurrences in the dam and the foundation, that could endanger the dam safety and (2) taking of timely and appropriate restoration measures. The concept of the technical monitoring system regarding the number of instruments, location, reading frequency etc. is primarily determined in dependence of the dam type and importance.

On Gratche dam is installed geodetic survey system for monitoring. Namely, by method of levelling is executed monitoring of the horizontal displacements of the central point (benchmark) of the dam crest during one year by total of 10 measurements. The partial measured displacements (compared to the "zero" measurement) of the specified benchmark point for 2017 are displayed on Fig. 13 [Elaborate, 2017] apropos the absolute displacement is approximately 25 mm. The water level in 2017 was varying between minimum elevation of 461.0 masl to maximum elevation of 465.0 masl, so we can take in to account that mainly the water level in the reservoir was at state of full reservoir. Also, on Fig. 13 are displayed the calculated horizontal displacements of the benchmark point, obtained with the numerical analysis, varying from winter period to summer period (the displacement curve is constructed by four points, simulating four periods within one year by additional simulation of two dam stages – for spring and autumn period, by varying input date for temperature). By comparation of the displacement curves we can conclude that there is good matching of the measured and calculated values for the displacements of benchmark point at dam crest for both – values and pattern.

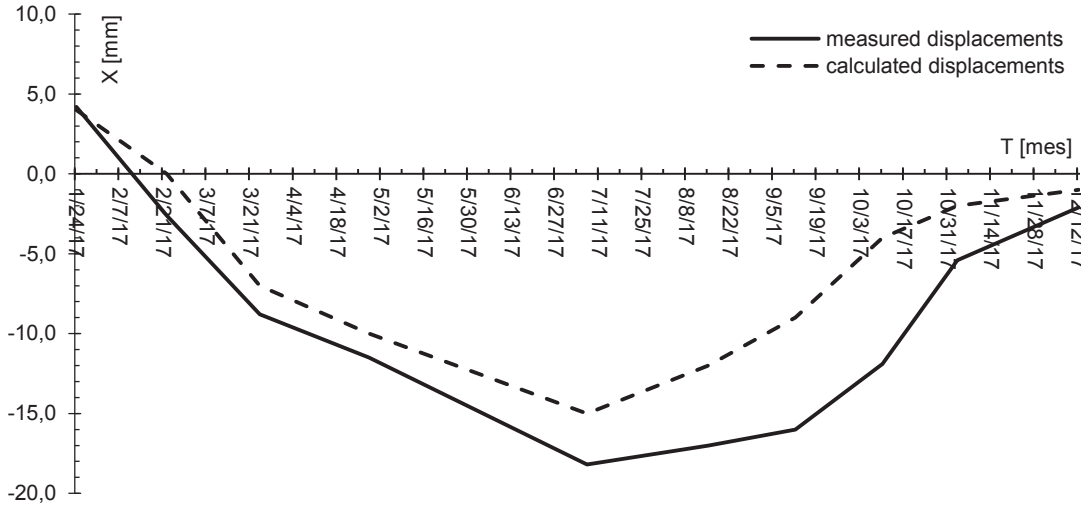

Fig. 13. Horizontal displacements of the benchmark point on dam crest for 2017 – measured and calculated values.

CONCLUSIONS

The prediction of the dam's behaviour during construction and service period is essential for ensuring and providing interval data for displacements and stresses, purposed for assessment of the dam stability within its life span. The dam behaviour is assessed by comparation of the measured and calculated date.

Maximum allowable stresses for usual loading state of the dam (self weight, temperature and hydrostatic pressure) should be less than 1/2 of specified compression strength and according to the

maximal calculated value of the principal stresses of around 15.0 MPa, such criteria is met. Namely, up to now there are no registered crack occurrences in the dam body.

The comparison of the calculated and measured horizontal displacements was undertaken. Namely, the deformation pattern and displacements values for both calculated and measured values shows good matching, analysed for period from winter to summer temperatures at full reservoir state. The comparison analysis gives valuable findings for the dam behaviour, and it serves as base for calibration process of the numerical model and installed monitoring instruments.

The obtained value for the displacements and stresses are in region of expected for arch dam with such dimensions, so we can conclude that the dam is stabile at action of static loads.

REFERENCES

Elaborate for analysis and assessment of the stability and functionality of dam Gratche with appurtenant structures and stability of the terrain around the dam and the reservoir for 2017, 2017. University Ss Cyril and Methodius, Civil Engineering Faculty – Skopje.

EUROCODE 2, 1992. "Design of concrete structures, European Committee for Standardization".

ICOLD Bulletin 145, 2009. "The physical properties of hardened conventional concrete in dams".

ICOLD Bulletin 30a, 1987. "Finite element methods in design and analysis of dams".

Jiazheng, P. & Jing, H. 2000. "Large Dams in China. A Fifty – Year Review". Beijing: China Water Power Press.

Jovanovski M., Gapkovski N., Pesevski I., Abolmasov B., 2012. "Engineering Geology", University Ss Cyril and Methodius, Civil Engineering Faculty – Skopje, Republic of Macedonia.

Kokalanov G., Tančev L., Mitovski S., 2007. "Analysis of the elastic behavior of La Acena arch – gravity dam" Ninth International Benchmark Workshop on Numerical Analysis of Dams, Proceedings, St. Petersburg, Rusia.

Mitovski S., 2015. „Static analysis of concrete dams by modeling of the structural joints", PhD thesis, Ss Cyril and Methodius University, Civil Engineering Faculty – Skopje.

Novak P. et all, 2007. "Hydraulic structures", Taylor & Francis Group, London.

Tanchev L., 2014. "Dams and appurtenant hydraulic structures", Second edition, A.A. Balkema Publ., CRC press, Taylor & Francis Group plc, London, UK

Tanchev, L., Petkovski L., Mitovski S., 2013. "Dam engineering in Republic of Macedonia: Recent practice and plans" International Symposium Dam engineering in Southeast and Middle Europe, Recent experience and future outlooks, Ljubljana, Slovenia

Yugoslav National Committee on Large Dams (YUCOLD), 1970. "Dams of Macedonia".

5th International Symposium on Dam Safety

October 27-31, 2018

EVALUATION OF 12 NOVEMBER 2017 Mw 7.3 – 30 KM SOUTH OF HALABJA IRAQ-IRAN BORDER EARTHQUAKE AND ITS EFFECTS ON DARBANDIKHAN DAM FROM A GEOLOGICAL PERSPECTIVE

M. Şefik İMAMOĞLU[1*], İdris BEDİRHANOĞLU[2], Çağrı MOLLAMAHMUTOĞLU[3]

ABSTRACT

In this study effects of the Mw 7.3 earthquake which occurred on 12 Nov 2017 around 30 Km south of Halabja near Iraq-Iran border were investigated from a geological perspective. The study is centered around the Darbandikhan region and specifically on the Darbandikhan Dam which was constructed on top of various geological formations each with different response characteristics with respect to strong ground motions. On-site investigations revealed substantial damage to the dam and immediate surroundings. The earthquake caused considerable depression zones in and around the dam body due to hydrodynamic effects and geological properties of the formations which carry dam foundation. Landslides and rockfalls were also observed on the slopes connecting to the dam structure. Some massive rocks on these slopes came loose and pose great danger due to their seemingly unstable states.

Key Words: Darbandikhan Dam, earthquake, landslide, damage.

INTRODUCTION

On 12.11.2017 at local time 21:18:17 (UTC 18:18:17) an earthquake with a magnitude of Mw 7.3 occurred at 30 Km south of Halabja near Iraq-Iran border on the Bitlis-Zagğros thrust belt. A scientific team was formed from the members of Dicle University College of Engineering in order to investigate the effects of the earthquake on-site. Assist. Prof. Dr. M. Şefik İmamoğlu from the Department of Geology of Mining Engineering, Assoc. Prof. Dr. İdris Bedirhanoğlu from the Department of Structures of Civil Engineering and CE Nihat Noyan from the Chamber of Civil Engineers/Diyarbakır branch arrived at the earthquake effected region on 14.11.2017 and started investigations just after three days passed the occurrence. Investigations were focused around the Darbandikhan region, especially on a nearby dam with the same name (Darbandikhan) and adjacent residential area since those locations were the most affected because of the earthquake. During the on-site tour the dam structure and its immediate surrounding and structures within the town with serious damages were investigated in detail.

THE Mw 7.3 EARTHQUAKE at 30 Km SOUTH of HALABJA - IRAQ-IRAN BORDER

On 12.11.2017 at 21:18:17 local time (UTC 18:18:17) an earthquake with magnitude of Mw 7.3 occured at 30 Km South of Halabja near Iraq-Iran border. The epicenter is located on the Bitlis-Zagğros suture belt and the earthquake was triggered due to the overthrust characteristics of the faults located within the so called belt.

USGS firstly announced the coordinates of the epicenter as **34.957°N** and **45.792°E** with a depth of 25 km but later revised the values and gave a new localiton which is shifted to the East with coordinates **34.905°N** and **45.956°E** with a depth of **19 km.** Due to this revision administrative location of epicenter was changed from Suleymaniyah-Iraq to Kermanshah-Iran as seen in Figure 1.

Figure 1. First and final epicenters announced and their distances with respect to Darbandikhan dam structure

The earthquake was felt in a vast region including Iraq's Baghdad, Basra, Mosul; Turkey's Diyarbakır, Van; Iran's Tabriz, Tehran and Ahvaz. Table 1 documents the major residential areas which are nearest to the epicenter and their populations.

Table 1. Nearest major residential areas to the epicenter of the earthquake and their populations (USGS)

ResidentialArea	Distance w/ respect to the firstly announced epicenter	Distance w/ respect to the revised epicenter	Population
Derbendikhan, Irak	19.7 km (12.3 mi)	31.8 km (19.8 mi)	>20,000
Halabja, Iraq	30.2 km (18.8 mi)	30.4 km (18.9 mi)	57,333
Pāveh Iran	52.4 km (32.6 mi)	39.6 km (24.6 mi)	17,779
Sarpol-e Ẕahāb, Iran	55.4 km (34.4 mi)	50.0 km (31.1 mi)	51,611
Suleymaniyah	75.0 km (46.6 mi)	87.3 km (54.3 mi)	723,170

Earthquake caused severe damage at the epicenter and immediate nearby with the classification of VIII level of Mercalli scale. As moving away from the epicenter the devastating effect of earthquake has diminished. For Batman which is 543 km far away level V, for Diyarbakir which is 612 km away approximately level IV is registered in terms of Mercalli scale. (Figure 2).

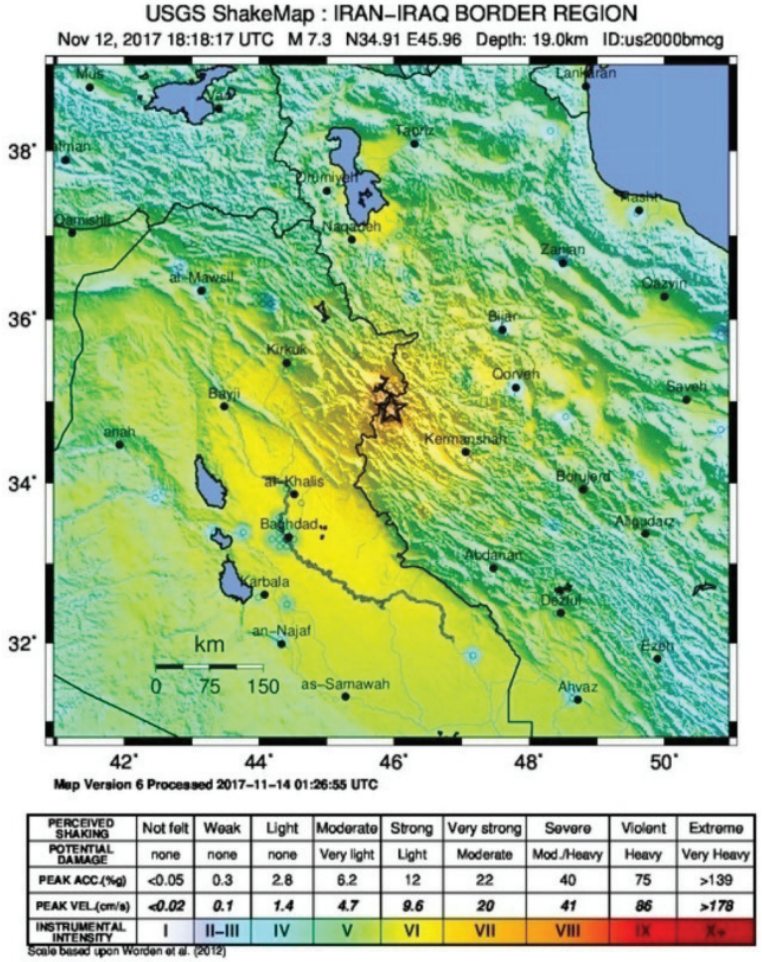

PERCEIVED SHAKING	Not felt	Weak	Light	Moderate	Strong	Very strong	Severe	Violent	Extreme
POTENTIAL DAMAGE	none	none	none	Very light	Light	Moderate	Mod./Heavy	Heavy	Very Heavy
PEAK ACC.(%g)	<0.05	0.3	2.8	6.2	12	22	40	75	>139
PEAK VEL.(cm/s)	*<0.02*	*0.1*	*1.4*	*4.7*	*9.6*	*20*	*41*	*86*	*>178*
INSTRUMENTAL INTENSITY	I	II–III	IV	V	VI	VII	VIII	IX	X+

Scale based upon Worden et al. (2012)

Figure 2. Earthquake Impact Map with Mercalli Scale (USGS)

The remarkable point here is that some regions which are closer to the epicenter but located on sturdy, solid ground were less effected than the regions which are farther but located on loose ground. Like the Kermanshah region Halabja and Darbandikhan regions were also affected up to VII level on the scale but they were not damaged to the level of Kermanshah due to the ground characteristics and structural quality. (Figure 3). Also since the Iraqi side is mountainous and residential areas scarce with lesser population figures, casualties and material loss were limited when compared to the Iranian side.

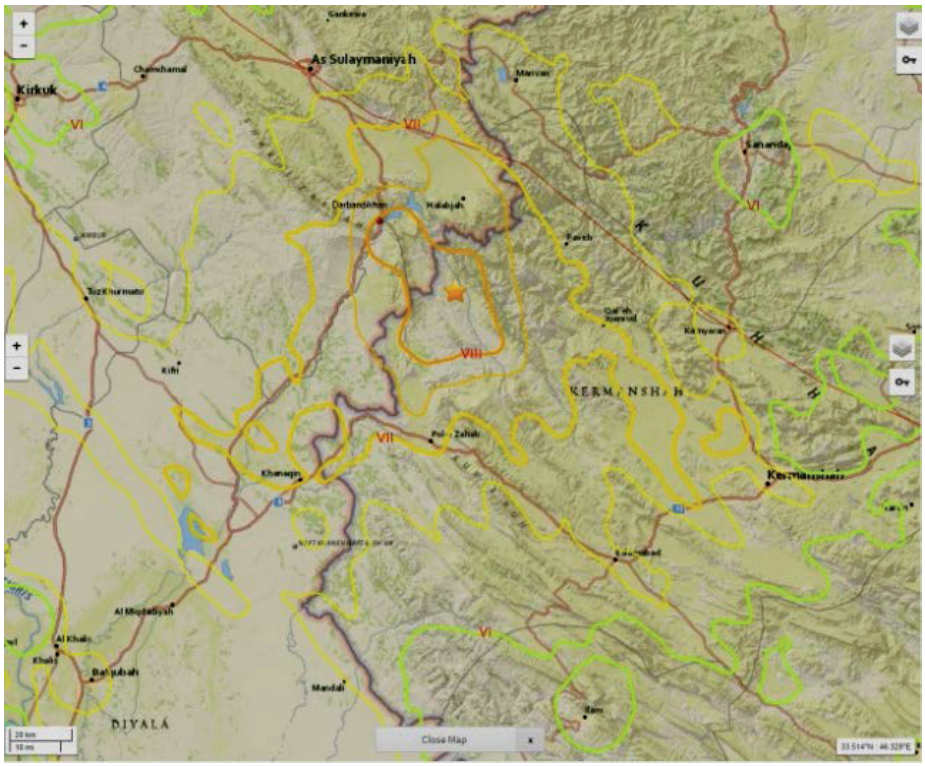

Figure 3. Earthquake Intensity Map (USGS)

SEISMIC ACTIVITY of MIDDLE EAST and SURROUNDING REGIONS

Middle East region is rich in terms of active fault zones which are capable to produce severely devastating earthquakes. African, Arabian and Indian plates are shifting to North-Northeast direction towards to the Eurasian plate. This movement causes to the squeezing of the Tetis oceanic plate and a compressional region with tectonically active properties is formed along the Bitlis-Zagğros suture belt. The resulting thrust effect when combined with the eastbound movement of the in-between Anatolian plate plays the main role in the regional seismic activity of the Middle East and surrounding regions. The northbound movement of the African plate and a rupture zone along Red Sea together cause a slip of Middle East region towards north, northwest direction with rates of 20-24 mm and 28 mm per year respectively (Figure 4). When this slip mechanism is arrested at some locations tremendous levels of stress develops and finally energy is discharged with ruptures and breaks which manifest themselves as earthquakes with a spectrum of magnitudes which depend on the size of the rupture occurring at these concentration points.

Bitlis-Zagğros suture belt is under the effect of a tectonically active compression zone with a length of over 300 Km. (Figure 5). The level of activity and rate of slip is lesser than the activity occurring in the Northern and Eastern Anatolian Fault zones which confine Anatolian plate. Thus occurrence of the earthquakes are rare on the suture belt when compared to the regions with active strike-slip faults. Nevertheless earthquakes with a magnitude over Mw 7 had happened on this suture belt when accumulated energy reached a threshold over time. (Figures 5-6).

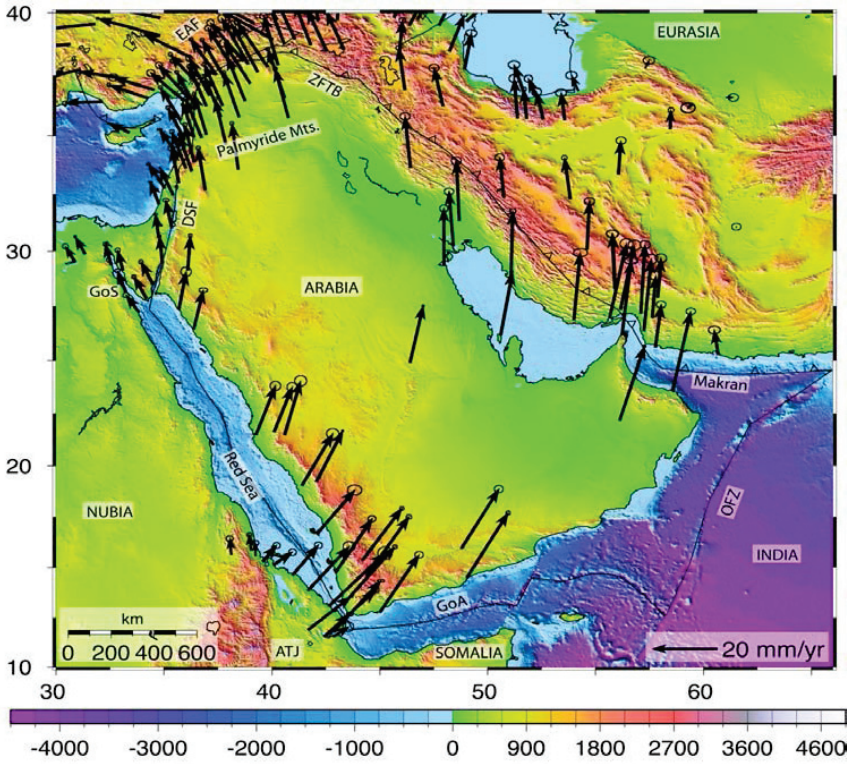

Figure 4. 1988-2005 Global Position System GPS results show slip rates and directions of the plates (it is estimated that the slip rate is 20-30mm/year) (Reilinger *et al.*, 2009, in Hafidh et al. 2012).

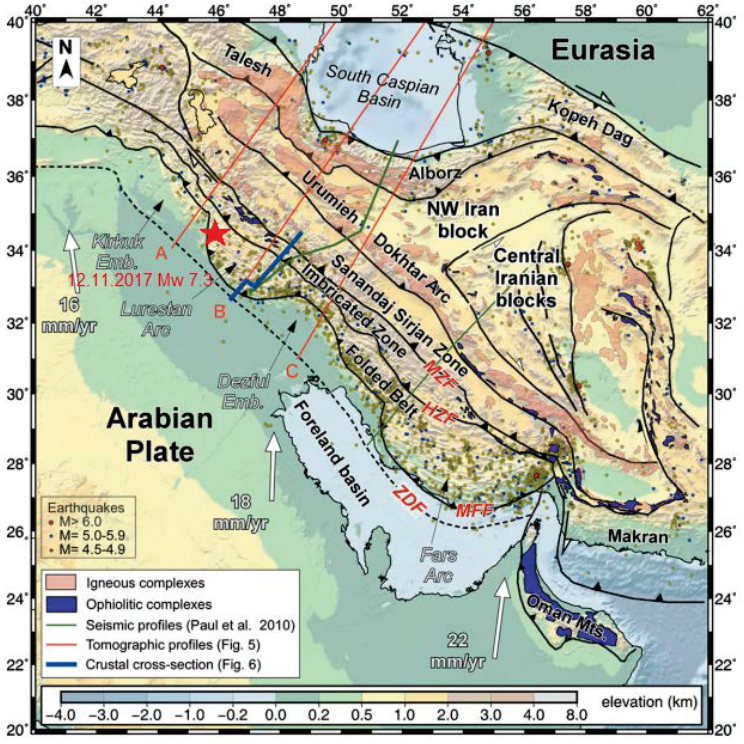

Figure 5. Major Tectonic Features along the Bitlis-Zagğros Suture Belt (Vergés J. Et all 2011)

The largest recorded earthquake which has occurred in the last 100 years is the earthquake which occurred in the Makran region, North of Gulf of Oman in 1945 with a moment magnitude of M8.1 (Figure 2). This severe earthquake caused a tsunami in the Gulf of Oman and Arabian Sea which resulted to the deaths of over 4000 people. In 1505 the Chaman Fault zone near Afghanistan Kabul fractured and devastated the nearby villages. In the same region on 30 May 1935 Suleymaniyah region, Quetta, Pakistan an earthquake (M7.6) caused deaths of 30000 to 60000 people (USGS).

The collision of the Arabian and Eurasian plates causes crust deformation along the Albroz and Kopet mountains in the Northern Iran. Thus Eastern Iran is susceptible to the strike-slip and reverse dip-slip faults which cause severe earthquakes. For example Dasth-e-Lut basin's southwest side was devastated by an earthquake with a magnitude of Mw 7.8 on 16 Sept 1978 which claimed lives of at least 15000 people.

1930 Hakkari Earthquake, 1975 Lice Earthquake and 2011 Van Earthquake are the major earthquakes of this seismic activeness which occurred as direct result of Bitlis-Zagğros suture belt in Turkey.

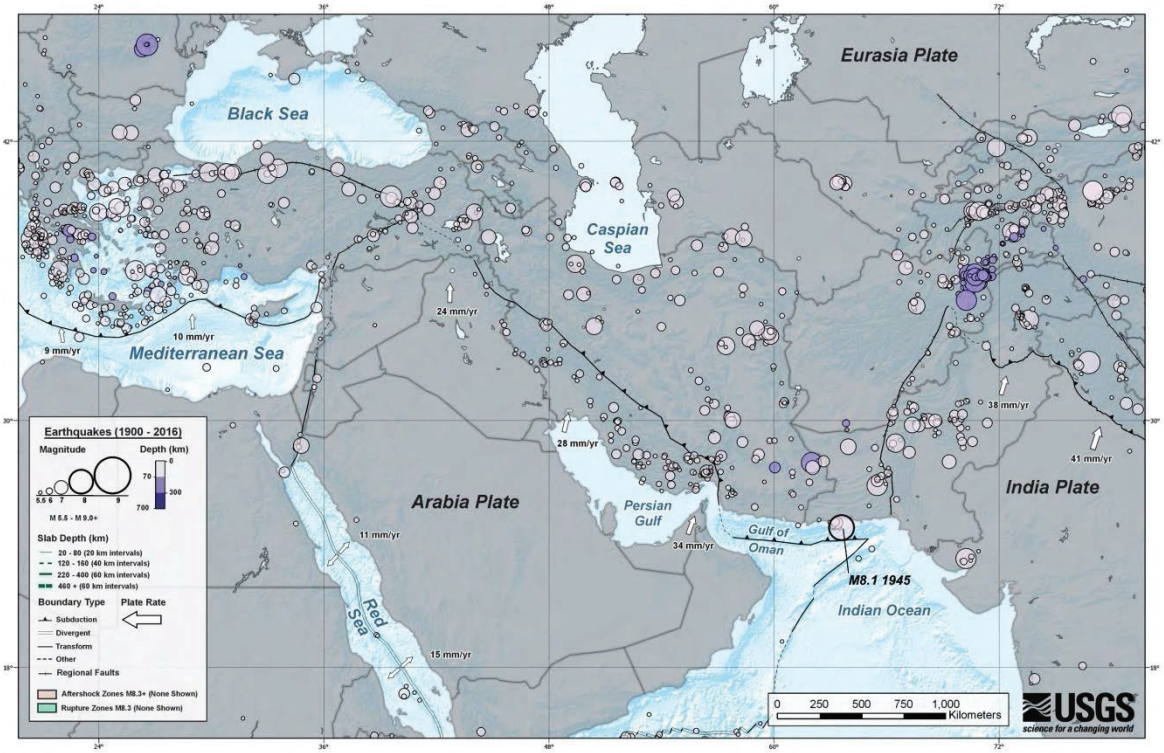

Figure 6. Earthquakes of Middle East between 1900-2016 with a magnitude over M 5.5 and slip of surrounding plates (USGS)

1930 Hakkari Earthquake occurred at Turkey-Iran border at 00:34 local time (UTC 21:34) on 7 May 1930 and devastated the city center of Hakkari. With a moment magnitude of 7.2M this earthquake resulted in the deaths of 2514 people and damaged around 3000 structures. 1975 Lice Earthquake occurred in the Lice district and surrounding villages of Diyarbakır province at 12.20 local time (UTC 09:20) with a magnitude of M 6.6. During the 23 seconds lasting severe earthquake 2385 people lost their lives and 8149 structures were damaged.

Last major earthquake of this mechanism in Turkey is the Van Earthquake in 2011 which has an epicenter located in the Tabanlı village of Van province. The severe (M 7.2) earthquake was felt in

almost the complete southeast region of Turkey including provinces Ağrı, Bitlis, Erzurum, Iğdır, Kars, Siirt, Bingöl, Muş, Diyarbakır, Tunceli, Batman, Erzincan which caused mass panic. In this earthquake thousands of structures were completely destroyed or heavily damaged beyond repair. Especially the RC structures in the downtown of Erciş district performed relatively poor and hundreds of them were annihilated. Due to the poor structural performance and severe damages earthquake took a heavy toll: 604 people mainly from Erçiş died and well over 2000 people injured.

EFFECTS of THE LAST EARTHQUAKE on THE DARBANDIKHAN DAM and SURROUNDING REGION

In order to assess the effect of the earthquake on the region we will briefly review the geology of the region.

Geology and the Ground Characteristics of the Darbandikhan Region

There are various kinds of lithological formations around the Darbandikhan district, Darbandikhan dam and surroundings. These formations consist of, from bottom to top, Tanjero, Sinjar, Kolosh, Khurmala, Fatha, Injana, Mukdadiye and Bai Hassan. (Sissakian V.K. 2000). The topmost layer is formed with recently formed alluvial deposits. (Figure 7-8).

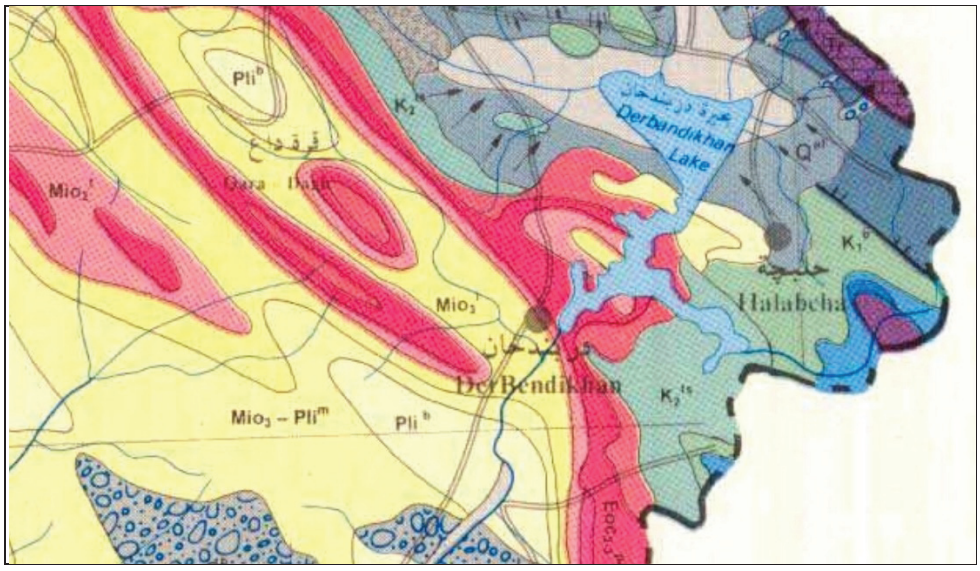

Figure 7. Darbandikhan Region's Geological Map (taken from 1/1000000 scale Geological Map of Iraq)

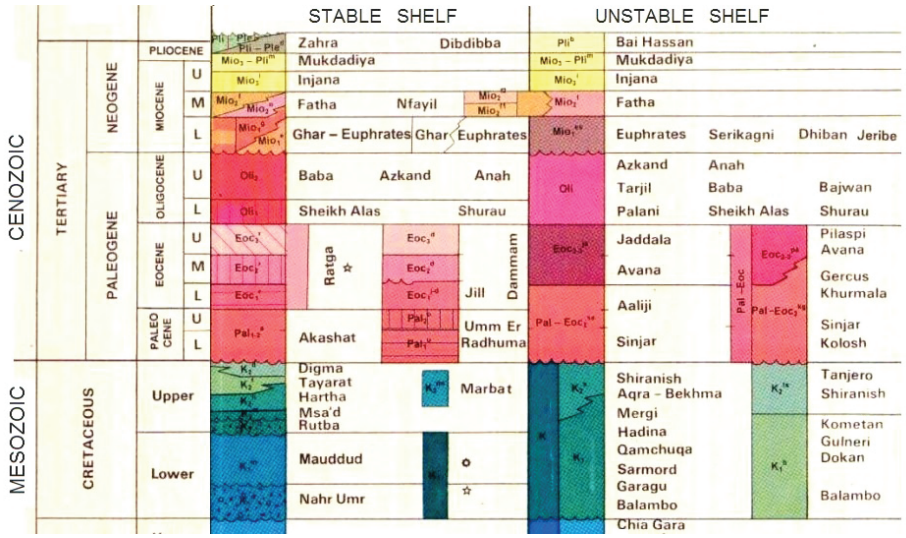

Figure 8. Stratigraphic vertical section of unstable settled layers around Darbandikhan region (taken from 1/1000000 scale Geological Map of Iraq)

Tanjero Clastik Formation (K_1^b -K_2^{ts})

This formation largely covers the Balombo-Tanjero region, south of Suleymaniyah. While bottom part of the formation is mainly consist of pelagic marls, upper part alternates between siltstone and argillaceous limestone. The greatest thickness of the formation is located between Rowarduz and Chuwarda where it reaches a thickness of 2000 m. The formation shifts to a flysch characteristics towards to southeast direction.

Sinjar Formation (Pal)

This formation is firstly defined in Sinjar region and manifested with algae reefs, lagoonal and nummulitic calcerous which settled on open shallows. Sinjar formation shows transitions with Kolosh formation and seems entwined together at many locations. While typical section thickness of the formation is around 176 m, the thickness around Darbandikhan region drops to 120 m. Due to its fossil content it is dated from early Eocene period and it is assumed to be lateral equivalent of the Becirman formation of Southeast Anatolian Region, Turkey.

Kolosh Formation (Eoc_3^{kg})

This formation is formed from, bottom to top, calcerous-marl, calcerous, shale, sandstone-shale, calcerous and 410 m thick blue shale – green sand layers. Formation largely manifests itself as a transition between the Kolosh formation itself and Sinjar formation around Darbandikhan region. While typical thickness of the formation is around 400 m it reaches above 1000 m around Darbandikhan region. Formation was settled on a narrow thalassic settlement and it is assumed to be lateral equivalent of the Germay formation of Southeast Anatolian Region, Turkey.

Khurmala Formation (Eoc_2^{kg})

As an inner carbonated shale product this formation is formed from dolomite, recrystallized limestone, partly sandy anhydride and gypsum. Calcerous layers of the formation intertwine with the fragments of the Kolosh formation. Formation is of local anhydride origin and formed as a narrow belt between Jabal and Maqlub. While average typical thickness of the formation is 185 m, bore holes at different locations give numbers from 115 m up to 606 m. The bottom contact region of the formation manifests

itself as intertwining with Kolosh formation and it is dated from Paleocene- Early Eocene periods. It forms a steep inclination with respect to south near the downstream side of the dam body. (Figure 9).

Fatha Formation (Mio_2^1)(Sub Fars Fm)

This formation is the largest and most economically important formation of Iraq. It mainly consists of anhydrite which is layered with alternating limestone and marl. It also includes gypsum and salt deposits. Formation, from bottom to top, starts with anhydride, mudstone and fine limestone sections and continues with conglomerates and carbonates. Salty parts are found in siltstone, mudstone and limestone sections and include anhydride and halite layers. Evaporites are generally found in marl sections. At these locations mudstone, siltstone and limestones are scarce. Near the basin boundaries marl and clastic sediments become dominant. Regional formation can be classified in two sub-parts: bottom sub and upper sub. They have respectively 220 meters and 400 meters of thickness. While bottom sub part is manifested with red mudstone, upper sub part is manifested with green-red mudstone, gypsum and recrystallized limestone. Total formation thickness is quite variable as it is changing from 600 m up to 900 m. Formation was settled down on an evaporite basin in a periodically small time duration. It is dated from middle Miocene period. As seen in Figure 9 district of Darbandikhan partly sits on this formation.

Figure 9. The Khurmala formation's limestones and Fatha fomration on top of it, northeast of Darbandikhan region

Injana Formation (Mio_3)

This formation consist of fine sediments of molasses which was deposited firstly onto shores and then later settled down on the river and lake beds. It has an average thickness of 620 m. The main body consists of a thin layer of calcerous sandstone which itself includes an even thinner layer of limestone and gravelly siltstone. Upper part continue with alternating sections of sandstone, siltstone, red mudstone. As we move from bottom to upper parts a transition from fine to coarser occurs in terms of grain size. The formation is assumed to be dated from later Miocene period. Some lower parts of the Darbandikhan district sit on this formation. (Figures 10, 11).

Mukdadiya Formation (Pli^{m})(Alt Bakhtiari Formation)
This formation consists of alternating sections of gravelly sandstone, sandstone and red mudstone. Sandstone part mostly includes river bed deposits and clay lumps in crosswise fashion. It is mainly formed with fine grain alternating sediments. Some sandstone layers show lateral expansions up to several kilometers. Around Darbandikhan region almost entirely it manifests itself as conglomerates. At some locations lateral expansions of the formation becomes so thin that lateral continuity almost cease to exist. This formation settled down rapidly on tributary environment. Gravels in the formation is mainly come from the highly folded Zagğros suture belt. Formation is dated from late Miocene period.

Figure 10. General view of formations which Darbandikhan district sits on (Qadr 2017 Google)

Figure 11. The Injana formation, one of many formations that make makes up Darbandikhan ground

Bai Hassan Formation (Plib)
Formation is entirely made up from clastic. This formation can be matched up with the Pliocene clastic formations of the Northern-Northeastern Syria and Southeast Turkey.

Effect of Earthquake on Darbandikhan Dam and Its Surroundings

Darbandikhan dam was built near north-northeast of Darbandikhan district on a narrow valley around 1956-1961 as a rockfill dam. The dam has an height of 128 m and a reservoir capacity of 3 billion m^3. The lateral dimension of the dam body is 535 meters and it is constructed on a narrow part of the thick limestone formation (Khurmala Fm.) which is eroded with the streams that are pouring in to Darbandikhan dam. The limestone formation itself sits on an alternating claystone-siltstone formation (Kolosh Fm.). (Figure 12). The dam structure is entirely sits on the alternating claystone-siltstone ground.

Figure 12. Darbandikhan (Derbendixan) Dam view of right bank

Both right and left banks of the dam lack proper levelling works and block stabilization. A closer investigation of the immediate surroundings of the dam revealed that the road on the right bank has cracks on it due to the failing of underlaying claystone-siltstone formation which has a steep slope. (Figure 13). Also it was observed that large limestone blocks were fallen and there are many unstable-loose blocks on the hillsides (Figure 16-17).

Figure 13. View of the cracks in the road owhich is on the right bank of Darbandikhan Dam

Figure 14. Unstable and loose rock blocks on the slopes of right bank of Darbandikhan dam

Another manifestation of the failing of the underlaying claystone-siltstone formation can be seen on the structures built on the hillside. One of these buildings were completely ruined and rest were severely damaged. (Figure 15).

Figure 15. A ruined structure on the right bank of Darbandikhan (Derbendixan) dam

Earthquake caused hydrodynamic effects in addition to the ground waves which resulted in deep lateral cracks around the clay core, especially on the downstream side of the dam structure. Cracks grow larger, up to 21 cm, as one moves towards the mid-section of the dam. (Figure 16). Due to erosion of the claystone and siltstone sections over time some very large limestone blocks resting on top became loose and lost their stability on the left hillside of the dam. During earthquake they became

fully unstable and fell downwards on to the dam body. (Figure 17). Also active landslides occurred at both hillsides during earthquake. (Figure 18).

Figure16. Major downstream crack occurred on the Darbandikhan (Derbendixan) Dam

Figure 17. Some very large limestone blocks on the left bank of the dam which became unstable and fallen

Figure 18. Active landslide occurred on the left bank of the dam and some fallen large blocks

Although many buildings were damaged only a few of them completely collapsed during the earthquake. This is partly because of the relative robustness of the Injana and Fatha formations beneath the town center of the Darbandikhan district and partly because of the underground water levels being very deep. The effects of earthquake on the structures in the city center will be discussed in detail in another study so we briefly mention this issue here.

CONCLUSIONS

The Bitlis-Zagğros thrust belt passes through the northern part of the Southeast Anatolian region, continues through the Iran-Iraq border region and reaches to the Himalayas.

Although it is relatively inactive with respect to the lateral strike slips in its neighborhood it is still quite capable of producing earthquakes up to a magnitude of 8.1. In fact some severe earthquakes occurred on the zone prove its importance from the perspective of strong ground motions.

The Iraqi side of the effected region experienced less devastation than the Iranian side. This because the populated areas are scarce, ground is more robust and the building equality is better in Iraqi side.

Close inspection of the buildings in Darbandikhan revealed that the locals have been unaware of the seismic activeness of the zone and disregarded the fact that it can produce severe earthquakes. This negligence also manifested itself in their way of life especially in the civil-structural constructions.

Thus new buildings should be constructed under strict codes which employs current modern engineering science, especially care should be given to earthquake based design. This latest earthquake should be an public awareness milestone just like the 1999 İzmit earthquake in Turkey.

The downstream part of the Darbandikhan dam structure was severely damaged with deep lateral cracks running through the entire body. Immediate measures should be taken for the dam safety and necessary repairment should be completed in a scientific manner.

Both hillsides of the dam possess great risk due to active landslides and rock falls. Detailed investigations should be carried for the landslide mechanisms and unstable blocks and necessary measures should be taken.

ACKNOWLEDGEMENTS

We deeply appreciate the supports of Diyarbakir Branch of Chamber of Civil Engineer and its member Civil Engineer Nihat Noyan who took a part in our investigation group. Dicle University Physics Department's graduate student Mr. Kadri Yusufwho accompanied us with his vehicle and also acted as our translator and guide. We also thank to the Dr. Ramazan Hamza Muhammed from Duhok University, Department of Geogly, and members of Duhok Seismology and Meteorology Institute; Head Dara Hasan Faraj, seismologs Bakir M Saeed Ali, Aras Muhammed Tofig, Omid Muhammed Mahsun, Borhan İbrahim Salih for their companionship during the on-site investigations. We need to also mention the helps of Union of Engineers Duhok Chamber members Abdul Emir and Diler Abo. We also wants to thanks Dicle University Engineering department and Dean of Engineering Faculty Prof. Dr. Abdullah Toprak, who made this site visit possible.

REFERENCES

Bedirhanoğlu, İ. ve İmamoğlu, M.Ş., 2017. "12 Kasım 2017 Halepçe Depremi Ön Değerlendirme Raporu". Dicle Üniversitesi Mühendislik Fakültesi Maden Mühendisliği Bölümü Genel Jeoloji Anabilim Dalı Başkanlığı, 29 Kasım 2017, DİYARBAKIR

Hafidh A. A. Ghalib, Ghassan I. Aleqabi, Eid Al-Tarazi, TawfiqGh. Al-Yazjeen,Omar Q. Ahmed, Bakir S. Ali, KhozgaQadr, Ali A. Ali, 2012. "A Proposal to Establish a Middle East Seismographic Network". Sulaimaniyah Kurdistan Directorate General of Meteorology and Seismology

İmamoğlu, M.Ş. ve Bedirhanoğlu, İ., 2017. "12 Kasım 2017 M 7.3 -Halepçe'nin 30 km Güneyi Irak-İran Sınır Bölgesi Depremi'nin Sismotektonik Ön Değerlendirme Raporu". Dicle Üniversitesi Mühendislik Fakültesi Maden Mühendisliği Bölümü Genel Jeoloji Anabilim Dalı Başkanlığı, 29 Kasım 2017, DİYARBAKIR

Jassim S. Z. and Goff J.C., 2006. "Geology of Iraq". Published by Dolin, Prague and Moravian Museum, Brno

Reilinger, R. F., 2009. "Seismotectonics of the Arabian Plate and its Boundaries". III, EOS Trans AGU,
90 (52), Fall Meeting Suppl. Abstract T54C-2011.

Sissakian V.K., 2000. "Geological Map of Iraq 1/1000000". State Republic of Iraq Ministry of Industry
and Minerals Company of Geological Survey and Mining, National Library Legal Deposit No: 141/2000 Baghdad Iraq

USGS, 2017. www.usgs.govs

Vergés J., Saura E., Cascıello E., Fernàndez M., Vıllaseñor A., Jıménez-Munt I. & García-Castellanos D., 2011. "Crustal-scale cross-sections across the NW Zagros belt: implications for the Arabian margin reconstruction". Geol. Mag. 148 (5–6), pp. 739–761. Cambridge University Press 2011 739 doi:10.1017/S0016756811000331

https://www.google.com.tr/maps/place/Derbendihan+Baraj%C4%B1,+Darbandikhan,+Irak (Rebin Qadr March 2017 Google)

5th International Symposium on Dam Safety

October 27-31, 2018

SEISMIC ANALYSIS OF CONCRETE-ROCKFILL COMBINATION DAM ON ELASTIC FOUNDATION

Ercan GEMİCİ [1], Fatih GÖKTEPE [2], Murat ŞAHİN [3]

ABSTRACT

Gravity dam is one of the most important structures of civil engineering designed to hold back large volumes of water. Concrete gravity dam and concrete-rockfill combined dam are two most commonly used dams, among others. The concrete-rockfill combined dam is fundamentally consist of an upstream concrete wall and a downstream sloping rockfill body to endure the water pressure together. The seismic stability of concrete gravity dams strengthened by rockfill buttressing has been noticed by many researchers and engineering science experts in recent years. The seismic response analysis of the concrete-rockfill combination dam can be carried out under both simplified methods and numerical analyses. The aim of this study is to investigate the seismic effects of backfill on dynamic response of composite dam on elastic foundation. For this purpose, the numerical model taking the effects of both empty and water-filled reservoir cases is developed by using finite element method. The concrete dam is considered as one of the complex structure because of geometrical dimensions with rock supports. Dynamic response analysis is performed for a series of concrete dams located in active seismic zones. According to dynamical analysis results, maximum displacement was 34.3 mm, maximum normal stress was 1288.7 kN/m^2 and maximum shear stress was defined 452.4 kN/m^2 in rockfill abutment.

Keywords: Concrete gravity dams, finite element method, dam safety, seismic stability

INTRODUCTION

Gravity dams are huge hydraulic structures which meet the requirements for electric power, irrigation, flood control, drinking and domestic water, etc. Dams are sometimes constructed from composite materials that are supported with rockfill, rather than only concrete. Rockfill placed as an abutment of concrete gravity dams has been strengthening method to upgrade the stability of existing dams for hydrostatic or seismic loads. The concrete gravity dams strengthened by rockfill buttressing has been attractive due to their advantages such as the low cost, the possibility of fast construction. Dams are designed by taking into consideration for instance; water, earthquake, wind, surcharge forces etc. The extreme loading situation of gravity dams includes earthquake loading. A great number of dams close at the fault line in the World. Therefore, the stability and safety of dams during strong earthquake have been a great deal of subject from researchers. Moreover, the stability of dam abutments is so important that is to be considered in particularly regions.

[1] Asst. Prof. Dr. Ercan GEMİCİ, Department of Civil Engineering, Bartın University, Bartın, Turkey, e-mail: egemici@bartin.edu.tr

[2] Asst. Prof. Dr. Fatih GÖKTEPE, Department of Civil Engineering, Bartın University, Bartın, Turkey, e-mail: fgoktepe@bartin.edu.tr

[3] Master Student Murat ŞAHİN, Department of Civil Engineering, Bartın University, Bartın, Turkey, e-mail: muratemirbeyoglu@gmail.com

The behavior of the rockfill-concrete gravity dams during the earthquake is considerable complex, such as the interaction between foundation–concrete body, water–dam body and dam body–rockfill abutment. The response to an earthquake is related to the seismic characteristics, the mechanical properties of rocks and sliding surfaces, and many other factors (Ghanaat 2002; Chopra and Zhang 1991), so dynamic analysis is far more complex than static analysis. There are different linear elastic boundary element methods (BEM) and finite element methods (FEM) which used to solve these complex problems. FEM lies in its flexibility in modeling complex section geometries and material conditions. The FEM reflects the mechanical properties of complex dam components (Zienkiewicz and Taylor 1989).

During the last three decades, measurement and interpretation of dam deformation is significant component of dam investigation and has been studied by several researchers on dam safety. (Jesung et al., 2009; Gu et al., 2011; Capra et al., 2015; Salazar et al., 2016; He et al., 2018) Researchers developed advanced analytical and numerical models to investigate for dam deformability in the seismic response of dams (Leger et al., 2007; De Sortis and Leclerc, 2011; Su et al., 2015).

Loh and Wu, 1996 have achieved the modal characteristics of the dam using ambient vibration and seismic response data considering the impact of the reservoir water level based on finite element analysis. Mouyeaux et al., 2018 has performed a probabilistic stability analysis for an existing earthfill dam using a Stochastic Finite Element Method (SFEM) and considering the spatial variability of soil properties based on field data. Hariri-Ardebili et al., 2016 have studied computer-aided parametric analysis on the finite element model of a typical concrete gravity dam. Yu et al., 2005 have investigated to stabilities of the abutments of gravity-arch dam using elasto-plastic finite element analyses. Oudni and Bouafia, 2015 have examined the earthquake damage response of concrete gravity dam using a finite element program. They specified that damage increases the intensity of displacement and the maximums of displacements values do not correspond to the maximums of amplitudes of the excitement.

The fundamental vibration period of composite dam systems is an important factor in the assessment of their dynamic or seismic behavior. Hatanaka, 1960 has worked to estimate the fundamental vibration period of dams with empty reservoirs. Okamoto, 1984 proposed simplified formulas to estimate the fundamental vibration periods of dams with empty and full reservoirs. Several researcher investigated to determine the fundamental vibration period of a dam for empty reservoir (Chopra, 1978; Fenves and Chopra, 1984; Rea et al., 1972).

The purpose of this work is to analyze the displacement and stress at the crust of rockfill the dam which were caused by the water load at different levels combined with the earthquake. It also summarizes the displacement and stress characteristics of the gravity dam rockfill abutment. The dam was modeled in three dimensions using the SAP2000 package program based on the finite element method.

SYSTEMS ANALYZED

In this study, seismic analysis of concrete-rockfill combination dam on elastic foundation is analyzed by using SAP2000. The mass concrete, the rockfill and the foundation is modeled based solid element. The representation of the concrete-rockfill combination dam on elastic foundation is schematically shown in Figure 1. The height of dam was selected as 35m, while the height of the rockfill was selected as 30m. Herein, the massless foundation assumption has been made to remove the effect of fundamental dynamic properties on the composite dam response. Moreover, the base excitation is applied to all foundation grid points simultaneously in the time domain. Actually, the foundation is acting as a large numerical shaking table without wave propagation in the foundation (Figure 1).

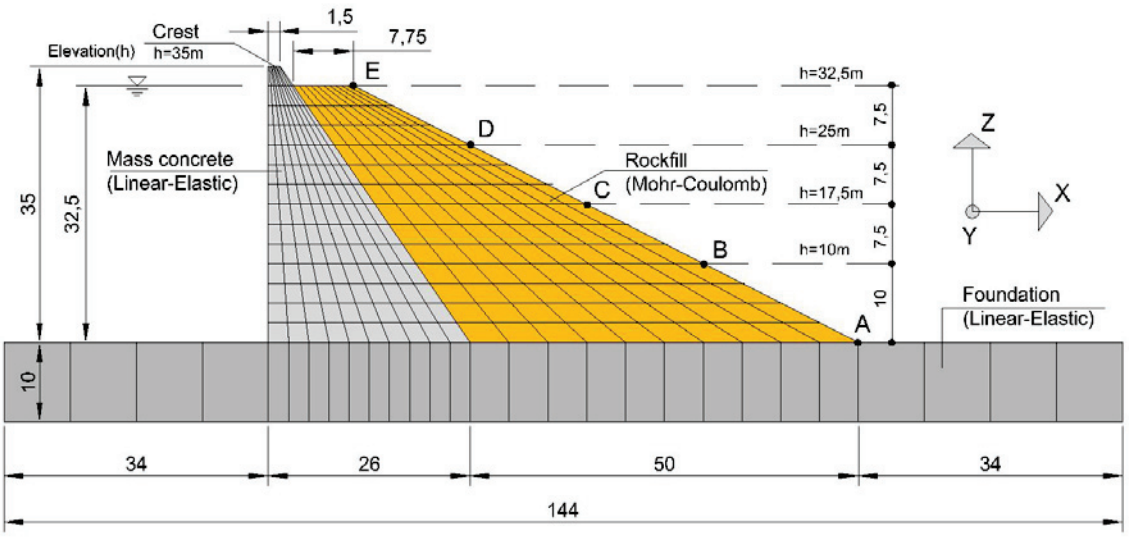

Figure 1. Idealization of the concrete-rockfill combination dam on elastic foundation

The plastic deformations of rockfill medium was directly achieved with Mohr–Coulomb failure criterion with a linear strength envelope defined using the internal rockfill friction angle. The essential parameters considered in FE model for the concrete and rock fill are summarized in Table 1.

Table 1. Material properties of the dam component

Material	Elastic Modulus E (MPa)	Poisson's ratio v (-)	Mass density ρ (kg/m^3)	Friction angle Ø (°)
Concrete	24000	0.2	2400	-
Rockfill	100	0.25	1950	37

The concrete-rockfill combination dam was investigated using 3D finite element model. These finite element model, which is considered with the base excitation, includes eight-noded finite elements. This type of element consist of three translational degrees of freedom at each node. Computational simulation of the concrete-rockfill combination dam has 7337 nodal points and 5790 solid elements. The dam and foundation materials are assumed to homogeneous and isotropic in linear modal time-history analyses under earthquake loading. The employed Finite Element mesh is shown in Figure 2.

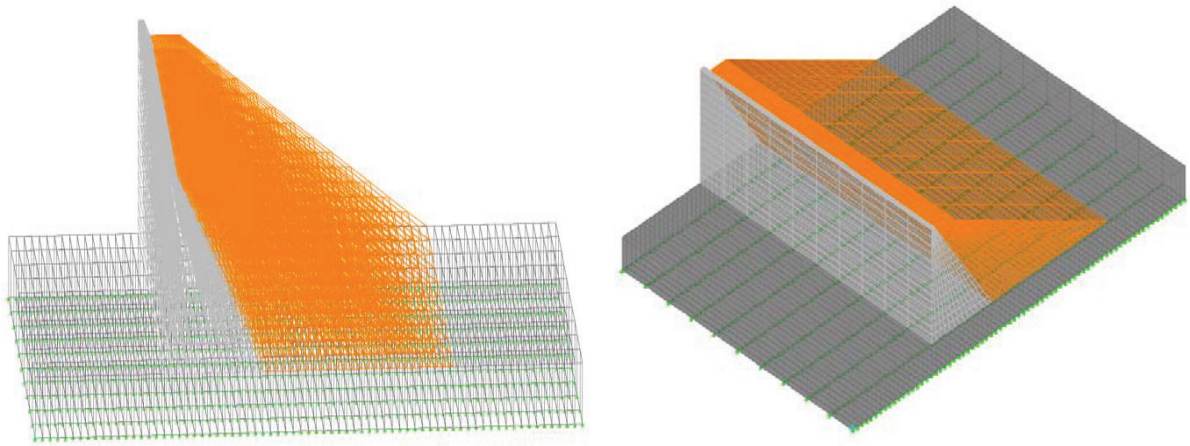

Figure 2. The employed Finite Element Model for the concrete-rockfill combination dam on elastic foundation

In order to investigate the seismic effects of backfill on dynamic response of composite dam on elastic foundation, the dam is subjected to the 1992 Erzincan earthquake acceleration record (M_s = 6.8) which can be seen acceleration (a), velocity (b) and displacement (c) of record showed in Figure 3. Note that, maximum acceleration of the east-west record is 0.5g. The acceleration was recorded in the which is about 0.75 km north-west of Erzincan city centre and an estimated 5 km from the epicenter. This is a near field strong ground motion record with high frequency content.

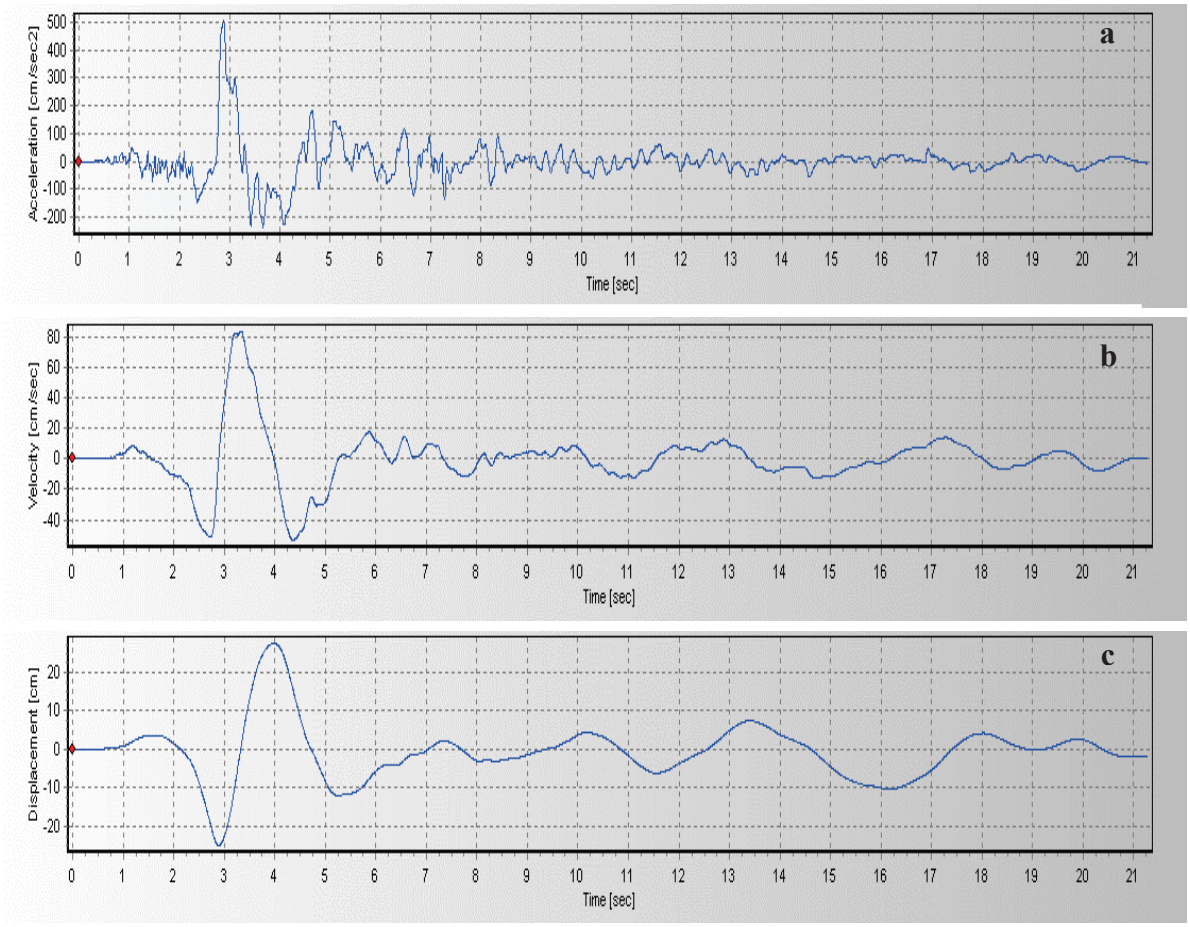

Figure 3. Base acceleration, velocity, and displacement for Erzincan earthquake.

NUMERICAL STUDIES AND RESULTS

The stress direction used in this study are given in Figure 4. Accordingly, S_{11} (in x direction), S_{22} (in y direction), S_{33} (in z direction) are normal stresses. S_{12} (in y direction on x surface), S_{13} (in z direction on x surface), S_{23} (in z direction on y surface) are shear stresses.

The displacement of rockfill abutment is shown in Figure 5. For the case of empty, half-empty and full reservoirs, the maximum displacement occurs in the middle of rockfill crust (C Point) for all situation according to x direction. The highest displacements have occurred when reservoir was empty When reservoir was fully, displacement value of rockfill crust top point 11.76% less than empty and 7.69% less than half-empty.

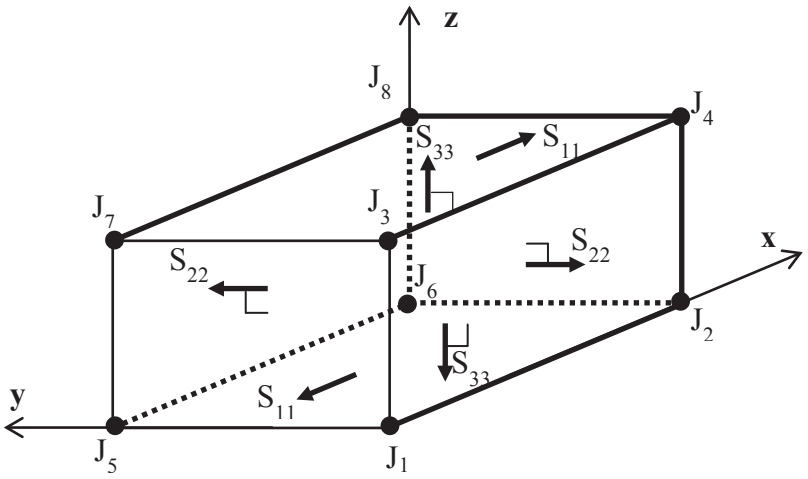

Figure 4. The stress direction used in this study

When comparing the maximum displacement according to water levels in the reservoir, the displacement of rockfill is reduced which full reservoir by 6.71% compared to empty reservoir and by 3.03 compared to half-empty reservoir (Table 2).

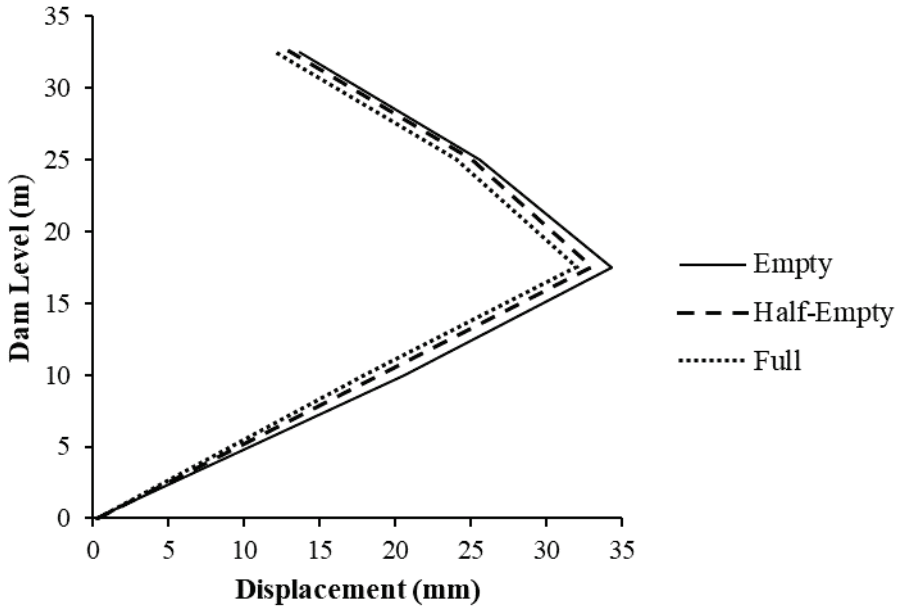

Figure 5. The displacement values that occur at different points of the dam

Table 2. The maximum displacement at the points for different reservoir conditions

Point	Dam Level (m)	Displacement (mm)		
		Empty	Half-Empty	Full
A	0	0.26	0.26	0.25
B	10	20.6	19	18
C	17.5	34.3	33	32
D	25	25.6	25	24
E	32.5	13.6	13	12

The values of maximum normal stress were observed for full reservoir condition as shown in Figure 6. As the water level in the reservoir decreases, both maximum normal stress and maximum shear stress are reduced.

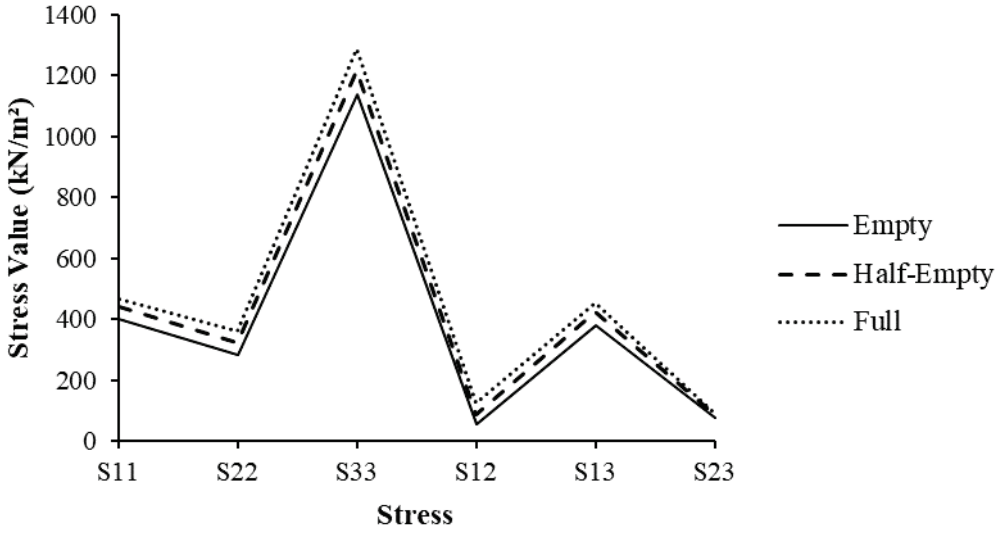

Figure 6. The normal and shear stress values for different reservoir conditions

According to the maximum normal stresses in x direction for water levels in the reservoir, the normal stresses of rockfill for full reservoir is increased by 16.38% and by 10.15% compared to the empty case and half-empty reservoir, respectively. Moreover, the maximum shear stresses reduced from the upstream to the crest (Table 3).

Table 3. The maximum normal and shear stress values for different reservoir conditions

Stresses	Stress (kN/m^2)		
	Empty	Half-Empty	Full
S_{11}	399.9	440.5	465.4
S_{22}	283.8	323.2	362.1
S_{33}	1138.8	1218.2	1288.7
S_{12}	56.4	87.5	125.7
S_{13}	380.5	425.6	452.4
S_{23}	76.0	85.1	92.7

CONCLUDING REMARKS

The purpose of this work is to analyze the displacement and stress at the crust of rockfill the dam which were caused by the water load at different levels combined with the earthquake. A simplified model is also proposed for dynamic analysis of concrete-rockfill combination dam on elastic foundation. Realistic analyzes of important structures such as dams, it is necessary to model them in three dimensions with the foundation soil of the structures. As earthquake effect will depend on the innage of the reservoir, analyzes for different water levels of reservoir should be made. The rockfill abutment can prevent or decrease concrete body downstream displacements of the dam during earthquakes. According to the results, the maximum displacement was found to be 34.3 mm and maximum normal stress was obtained 1288.7 kN/m^2 on the rockfill abutment. In addition to this, the maximum shear stress was 452.4 kN/m^2 for full reservoir. Note that, the places with maximum shear stresses demonstrate where the dam material can collapse. Also, the computed dynamic values are good enough for dam safety.

REFERENCES

Capra, A., Scaioni, M., Wieser, A., 2015. Editorial: Terrestrial Remote Sensing for Areal Deformation Monitoring. App. Geomatics, 7(2), pp. 61-63, DOI: 10.1007/s12518-015-0159-y.

Chopra, A. K., 1978. Earthquake resistant design of concrete gravity dams. J Struct Div (ASCE), 104: 953-971.

Chopra, A. K., Zhang, L., 1991. Earthquake-induced base sliding of concrete gravity dams, Journal of structural Engineering, Vol. 117, Issue 12 (December 1991) , https://doi.org/10.1061/(ASCE)0733-9445(1991)117:12(3698)

De Sortis, A., Paoliani, P., 2007. Statistical analysis and structural identification in concrete dam monitoring, Eng. Struct. 29 (1): 110–120.

Fenves, G., Chopra, A. K., 1984. Earthquake analysis and response of concrete gravity dams. Report No. UCB/EERC-84/10. Berkeley (California): University of California.

Ghanaat, Y., 2002. Seismic performance and damage criteria for concrete dams. In: Proceedings of the 3rd US-Japan workshop on advanced research on earthquake engineering for dams, San Diego, 22–23 June 2002.

Gu, C.S., Zhao, E.F., Jin, Y., Su, H.Z., 2011. Singular value diagnosis in dam safety monitoring effect values. Sci. China Technol. Sci. 54(5). http://dx.doi.org/10.1007/s11431-011-4339-7.

Hariri-Ardebili, M. A., Seyed-Kolbadi, S. M., Kianoush, M. R., 2016. FEM-based parametric analysis of a typical gravity dam considering input excitation mechanism, Soil Dynamics and Earthquake Engineering, Volume 84, May 2016, Pages 22-43.

Hatanaka, M., 1960. Study on the earthquake-resistant design of gravity type dams. In: Proceedings of the second world conference on earthquake engineering, vol. II. p. 82.1_82.16.

He, J. P., Jiang, Z. X., Zhao, C., Peng, Z. Q., Shi, Y. Q., 2018. Cloud-Verhulst hybrid prediction model for dam deformation under uncertain conditions. Water Science and Engineering, 11 (1): 61-67.

Jesung, J., Jongwook, L., Donghoon, S., Hangyu, P., 2009. Development of dam safety management system. Adv. Eng. Softw. 40 (8), http://dx.doi.org/10.1016/j.advengsoft.2008.10.009.

Leger, L., Leclerc, M., 2007. Hydrostatic, temperature, time-displacement model for concrete dams, J. Eng. Mech. 133 (3): 267–277.

Loh, C. H, Wu, T. S., 1996. Identification of Fei-Tsui arch dam from both ambient and seismic response data. Soil Dyn Earthq Eng. 15:465–83.

Mouyeaux, A., Carvajal, C., Bressolette, P., Peyras, L., Breul, P., Bacconnet, C., 2018. Probabilistic stability analysis of an earth dam by Stochastic Finite Element Method based on field data. Computers and Geotechnics, 101: 34-47.

Okamoto, S., 1984. Introduction to earthquake engineering. 2nd ed. Tokyo: University of Tokyo Press.

Oudni, N., Bouafia, Y., 2015. Response of concrete gravity dam by damage model under seismic excitation. Engineering Failure Analysis 58: 417-428.

Rea, D, Liaw, C. Y, Chopra, A. K., 1972. Dynamic properties of pine flat dam. Report UCB/EERC-72/07. Berkeley (California): University of California.

Salazar, F., Toledo, M. A., Onate, E., Suarez, B., 2016. Interpretation of dam deformation and leakage with boosted regression trees. Engineering Structures, 119 pp. 230-251, https://doi.org/10.1016/j.engstruct.2016.04.012.

SAP2000, 1997. "Integrated Finite Element Analysis and Design of Structures Graphic User Interface Manual", Computers and Structures, Inc., Berkley, California, USA.

Su, H. Z., Wen, Z. P., Chen, Z. X., Tian, S. G., 2016. Dam safety prediction model considering chaotic characteristics in prototype monitoring data series, Struct. Health Monit. 15 (6): 639–649.

Yu, X., Zhou, Y. F., Peng, S. Z., 2005. Stability analyses of dam abutments by3D elasto-plastic finite-element method: a case study of Houhe gravity-arch dam in China. International Journal of Rock Mechanics & Mining Sciences 42: 415–430.

Zienkiewicz, O. C., Taylor, R. L., 1989. The finite element method, v.2 Solid and fluid mechanics, dynamics and non-linearity. McGraw-Hill, London.

5 DAM SAFETY İstanbul Turkey 2018

5th International Symposium on Dam Safety

October 27-31, 2018

STRESS AND DEFORMATION SIMULATION OF A HIGH ASPHALT CORE ROCKFILL DAM ON THICK OVERBURDEN LAYERS

Enyue JI [1], Zhongzhi FU[2] , Shengshui CHEN[3], Qiming ZHONG[4]

ABSTRACT

In this paper, three dimensional finite element method(FEM) is used to analyze the stress and deformation of a high asphalt core rockfill dam on thick overburden layers. Firstly, the equivalent method is used to obtain the replacement rates and thus to deduce the simplified parameters of composite foundation. It is proved that the equivalent parameters can reflect reasonable stress and deformation of the dam. Then, 3-D FEM is used to simulate the stress and deformation of the dam by taking account the wetting deformation of the dam shell during the impoundment period. Based on the calculation results, the stress and deformation characteristics of dam body, overburden layers and the cut-off wall during post-construction, impoundment period are analyzed. In addition, the results indicate that the gravel pile treatment can reduce 13% settlement and 10% of the maximum horizontal displacement which is efficient for dam construction on thick overburden layers. The related research results can provide suggestions to the similar dam engineering.

Keywords: 3-D FEM, Asphalt core rockfill dam, Stress and deformation, equivalent method, Thick Overburden Layers.

INTRODUCTION

In recent years, hydropower development in China is more and more rapid. A large number of high earth rock dams have been designed or under construction, among which several earth rock dams can reach 300m height. However, many new dams have to be constructed on thick overburden layers as better sites are not available and removal of the existing overburden is technically or economically unfeasible. This adverse situation is often encountered along many hydropower-rich rivers in the southwest and northwest of China (Deng 2012, Xu et.al 2008), e.g. Yele asphalt core rockfill dam (Wang et.al 2010), Luding earth core rockfill dam and Changheba earth core rockfill dam. In view of the excellent ability to coordinate deformation of earth rock dams, earth rock dams are often the best or even the only choice in the construction of hydropower stations on thick overburden layers. Among them, earth core rockfill dams and asphalt core rockfill dam are often adopted as the first choice.
In order to forecast the actual stress and deformation of the dam, some numerical calculation methods are put forward in the past few decades. However, finite element method (FEM) (Akin 1982) is widely used and is proved to be the most effective method to predict stress and deformation behavior

[1] Post Ph. D, Department of Geotechnical engineering, Nanjing hydraulic insitude, Nanjing, China, e-posta: eyji@nhri.cn
[2] Senior Engineer, Department of Geotechnical engineering, Nanjing hydraulic insitude, Nanjing, China, e-posta: zzfu@nhri.cn
[3] Professor, Department of Geotechnical engineering, Nanjing hydraulic insitude, Nanjing, China, e-posta: sschen@nhri.cn
[4] Professor, Department of Geotechnical engineering, Nanjing hydraulic insitude, Nanjing, China, e-posta: qmzhong@nhri.cn

of dam engineering compared with the measured data. Zhang et.al (2016) studied the deformation characteristics of Shiziping earth core rockfill dam using field data and FEM and reasonable control measures for thick deposit dams are proposed. Zhou et.al (2016) studied the assessment of the crest cracks of the Pubugou rockfill dam by inserting inclination method into FEM. Stress and deformation analysis of the rock-fill dam with deep covering layer by static three dimensional finite element method is conducted by Sun et.al (2013). In general, dam engineering on thick burden layers is still a great challenge allover the word and needs to be further studied.

In this study, a case of a high asphalt core rockfill dam on thick overburden layers is further investigated using 3-D FEM. Firstly, the equivalent method is used to obtain the replacement rates and thus to deduce the simplified parameters of composite foundation. Then, stress and deformation behavior of the dam body and the cut-off wall is analyzed by the calculation results. Besides, the effect of gravel pile treatment is analyzed compared with the normal scheme without gravel pile treatment. The related research achievements can provide suggestions to similar dam engineering.

REPLACEMENT RATIO OF THE GRAVEL PILE COMPOSITE FOUNDATION

The maximum height of the dam in this project is 150m. The drilling tests reveal that the overburden layers is very deep, exceeding 400m, which is mainly composed of fine particle and have poor physical and mechanical indexes. Furthermore, the overburden layers contain a relatively weak silty clay layer with the possibility of liquefaction. Consequently, gravel piles are used to improve the modulus of the shallow overburden layers (Kang et.al 2016). The spacing of gravel piles under the dam body is 2.0*2.0m, and changes to 3.0*3.0m under the upstream and downstream ballast. The diameter of the gravel pile is 1.3m. The typical partition of the dam and geological section of overburden layers are shown in figure 1.

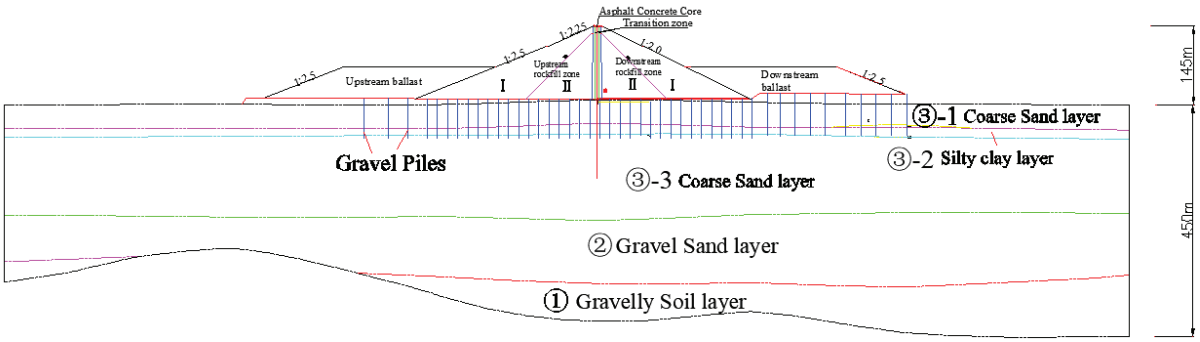

Figure 1 Typical partition of the dam and geological section of overburden layers

Replacement ratio of the composite foundation

Since the dam foundation is arranged with a huge number of gravel piles, if each gravel pile is taken into account, there will be too many elements, result in large amount of calculation. Therefore, it is necessary to study the equivalent method of simplifying the gravel pile into a composite foundation before performing the three-dimensional analysis of the whole dam. The equivalent method (Cui et.al 2014) is used to make the mechanical properties of the soil and the gravel pile in the composite foundation being equivalent to the mechanical properties of a homogeneous material. Thereby, the mechanical parameters of the equivalent homogeneous material can be obtained. Thus, the FEM mesh around the pile can be divided into a single material in the overall three-dimensional analysis.

The arrangement of the gravel piles in the dam foundation is plum-blossom shape, which is actually equivalent to a gravel pile wall after being simplified into a plane condition, as shown in figure 2. The equivalent simplification method is used according to the principle that the area of the gravel pile arranged in the plum-blossom shape is equal to the area of the gravel pile wall. Thus, the spacing and width of the equivalent gravel pile wall can be obtained.

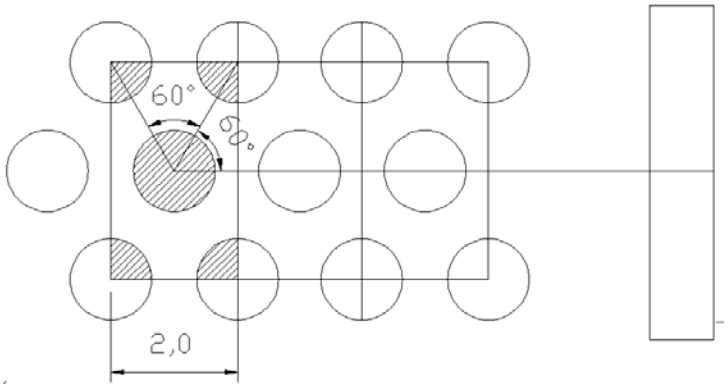

Figure 2 Equivalent schematic diagram of gravel pile composite foundation

According to the principle of area equivalent, the replacement rate of the plum-shaped gravel pile in the dam foundation can be calculated. The area of the shaded part in figure 2 is A_p, the total area is A, and the area of the gravel pile wall after equivalent replacement is the area of the rectangle in Figure 2. Consequently, the replacement ratio of the composite foundation when the spacing of gravel piles is 2.0*2.0m can be obtained as

$$m = \frac{A_P}{A} = \frac{\frac{1}{4}\cdot 4\cdot\frac{\pi d^4}{4}+\frac{\pi d^4}{4}}{2\times 2\sqrt{3}} = \frac{2\times\frac{\pi\times 1.3^4}{4}}{4\sqrt{3}} = 0.383 \tag{1}$$

Similarly, the replacement ratio of the composite foundation when the spacing of gravel piles is 2.0*2.0m can be obtained as

$$m = \frac{A_P}{A} = \frac{\frac{1}{4}\cdot 4\cdot\frac{\pi d^4}{4}+\frac{\pi d^4}{4}}{3\times 3\sqrt{3}} = \frac{2\times\frac{\pi\times 1.3^4}{4}}{9\sqrt{3}} = 0.17 \tag{2}$$

According to the literature (Gong 2002), the strength parameters of the composite foundation can be calculated by the equivalent method. For example, the cohesive force of composite soil can be expressed as

$$Cc = (1-m)Cs + mCp \tag{3}$$

Where Cs is the cohesive force of the soil, Cp is the cohesive force of the pile. Similarly, the friction angle of the composite soil can be expressed as

$$tg\varphi_c = (1-m)tg\varphi_s + mtg\varphi_p \tag{4}$$

Where φ_s is the friction angle of the soil, φ_p is the friction angle of the pile.

As a consequent, the parameters of E-V model (Duncan 1983) of the composite soil can be obtained by the method mentioned before which can be seen in table 3.

Table 1 FEM parameters of thick overburden layers

soil layer	buoyant density	Linear index		Nonlinear index		Parameters of Duncan *E-v* model						
		c	*φ*	φ_0	$\Delta\varphi$	*K*	*n*	R_f	*G*	*F*	*D*	K_{ur}
	g·cm^{-3}	kPa	°	°	°	-	-	-	-	-	-	-
4	1.37	-	-	47	5.6	836	0.35	0.79	0.32	0.1	4.8	1700
③-3	1.08	46	34	-	-	350	0.44	0.75	0.44	0.08	1.8	700
③-2	0.99	40	32	-	-	280	0.43	0.81	0.42	0.13	2	600
③-1	1.13	50	34	-	-	380	0.43	0.73	0.44	0.1	2	800
2	1.40	-	-	52	6	1300	0.48	0.70	0.40	0.01	3	2600
1	1.45	-	-	54	6	1500	0.45	0.68	0.42	0.01	3	3000
Gravel pile	1.45	-	-	48.3	5.6	1337	0.43	0.79	0.33	0.09	5.8	2674

Table 2 FEM parameters of dam materials

Dam materials	Construction density ($g \cdot cm^{-3}$)	Saturated density ($g \cdot cm^{-3}$)	c kPa	φ °	K	n	R_f	G	F	D	K_{ur}
Ballast	2.1	2.25	0	34	750	0.26	0.74	0.32	0.1	5.2	1500
Asphalt core	2.51	-	370	28	640	0.15	0.83	0.47	0	0	1200
Transition	2.09	2.3	0	50	950	0.25	0.89	0.39	0.12	6.5	1800
Upstream rockfill	2.18	2.3	0	48	1000	0.27	0.79	0.3	0.11	5.9	2100
Downstream rockfill	2.18	2.3	0	49	1288	0.24	0.84	0.3	0.11	5.3	2100
Residues	1.13	-	50	34	380	0.43	0.73	0.44	0.1	2	800

Table 3 Equivalent parameters of the overburden layers with gravel piles

overburden layers	ρ ($g \cdot cm^{-3}$)	c （kPa）	φ_o (°)	$\Delta\varphi$ (°)	K	n	R_f	K_{ur}	G	F	D
③-2(2m)	1.17	2.47	38.24	-	685	0.43	0.80	1394	0.39	0.11	3.46
③-3(2m)	1.22	2.84	39.48	-	728	0.44	0.77	1456	0.40	0.08	3.33
④(2m)	1.40	0	47.50	5.6	1028	0.38	0.79	2073	0.32	0.09	5.18
③-2(3m)	1.07	3.32	34.77	-	460	0.43	0.81	953	0.40	0.12	2.65
③-3(3m)	1.14	3.82	36.43	-	518	0.44	0.76	1036	0.42	0.09	2.48
④(3m)	1.38	0	47.22	5.6	921	0.36	0.79	1866	0.32	0.10	4.97

Verification of equivalent method

To verify the applicability of equivalent method mentioned previously, Z-1 and Z-2 schemes are conducted where Z-1 represents using the equivalent parameters in table 3 while Z-2 represents using the original parameters in table 1 and table 2.

According to the calculation results, the maximum values of the dam deformation of two schemes are listed in table 4. It can be seen that the maximum settlement of the Z-1 scheme model is 555.70 cm, and the maximum settlement of the Z-2 scheme is 567.50cm d in the post-construction. The difference of settlement between the two schemes is only 1.02%. In addition, the difference of settlement in is Impoundment period merely 0.9%. The FEM simulation results further indicate that the equivalent method is reasonable to deal with the composite foundation.

Table 4 Quasi-3D FEM results of the dam

Schemes	Conditions	Down maximum horizontal displacement /cm	Upstream maximum horizontal displacement /cm	Maximum settlement /cm
Z-1	Post-construction	107.62	-100.07	-555.70
	Impoundment period	137.29	-80.83	-560.80
Z-2	Post-construction	108.00	-100.13	-567.50
	Impoundment period	137.68	-80.76	-572.80

3-D FEM ANALYSIS FOR STRESS AND DEFORMATION

The wetting effect of upstream dam shell and floating force applied on the rockfill materials caused by water storage are all considered in the 3-D FEM calculation. The E-v model parameters are based on Table 1 and Table 2, and the equivalent parameters of composite foundation are from Table 3. 3-D finite element mesh of the dam is shown in figure 3.

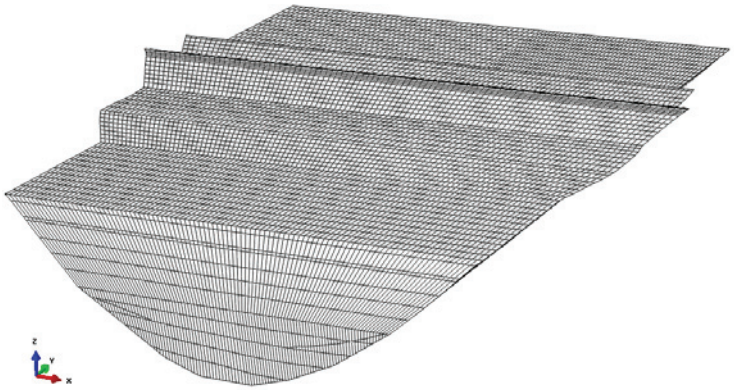

Figure 3 3-D finite element mesh of the dam

The main deformation of the dam

According to the parameters mentioned before, the main deformations of the dam including extreme horizontal displacement and settlement values are shown in table 5.

Table 5 The main deformation of the dam

Scheme	Conditions	Dam axis maximum horizontal displacement /(cm)	Dam axis maximum horizontal displacement /(cm)	Downstream maximum horizontal displacement /cm	Upstream maximum horizontal displacement /cm	Maximum settlement /cm
Z-3	Post-construction	113.70	-114.70	106.86	-89.56	-533.30
	Impoundment period	113.60	-115.40	128.56	-67.70	-523.50

Settlement of the dam

The settlement contours of the central section (X = 0) of the dam during post-construction and impoundment period are shown in figure 4. It can be seen that the maximum settlement of the dam is 533.30cm and 523.5cm, which is 0.83% and 0.81% of the maximum dam height respectively (644m including the depth of thick overburden layers). Besides, the maximum settlements are all located on the top surface of overburden layers due to the large settlement of the overburden layers, which is different from the conventional dams on the shallow overburden layers.

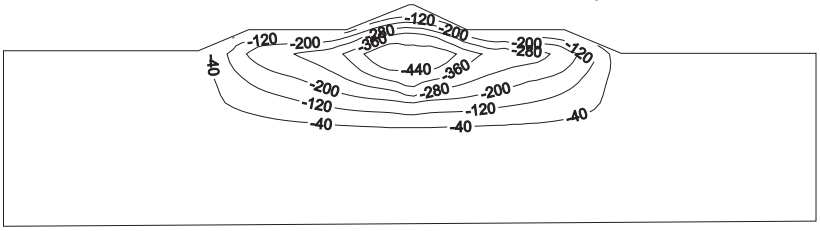

（a）Post-construction

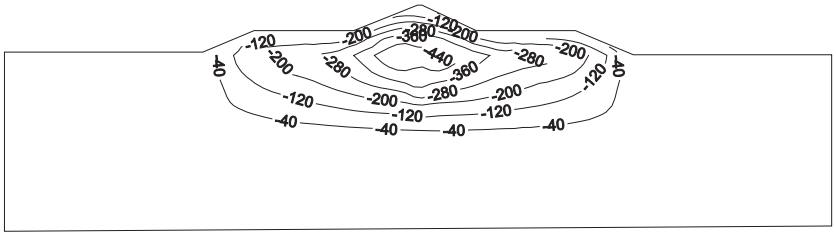

（b）Impoundment period

Figure 4 Settlement contours of the central section (X = 0) of the dam

Horizontal displacement of the dam

Figure 5 gives the horizontal displacement contour along the stream of the central section (X = 0). In figure 5, "+" means downstream displacement, "-" means upstream displacement. It is obvious that the horizontal displacement of the dam to the downstream is slightly larger than that to the upstream. The maximum horizontal displacement to the downstream is 106.86 cm and 128.56 cm, and the maximum horizontal displacement to the upstream is 89.56 cm and -67.70 cm, respectively. Both of the extreme horizontal displacements are located in the shallow overburden layers. Due to the water load on the asphalt concrete core and the anti-seepage wall, the maximum horizontal displacement to the downstream significantly increased by 20% from post-construction to impoundment period.

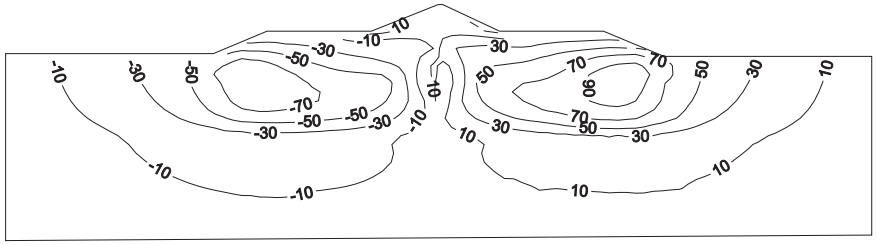

（a）Post-construction

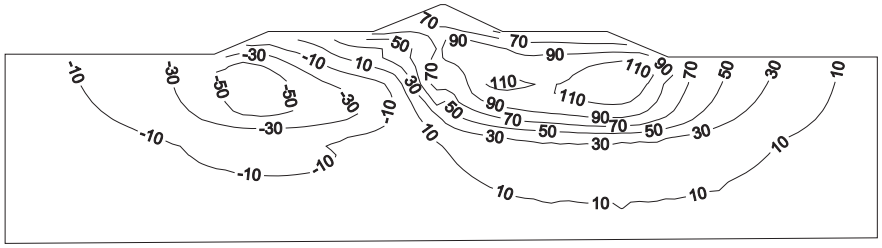

（b）Impoundment period

Figure 5 Horizontal displacement contours of the central section (X = 0) of the dam

The deformation properties of the asphalt concrete core wall is similar to the dam, and the difference is just reflected on the values.

Stress and deformation analysis of concrete cut-off wall

It is widely accepted that the stress and deformation of concrete cut-off wall are the major concern of the engineers during construction or impoundment period. To further study the stress and deformation properties of concrete cut-off wall, table 6 gives the main stress and deformation of the cut-off wall. The maximum settlement is 429.4cm and 423.8cm under post-construction and impoundment period condition, respectively.

Table 6 The main stress and deformation of the cut-off wall

Conditions	Maximum settlement /cm	maximum horizontal displacement along stream direction /cm	Maximum principal stress of upstream face/MPa	Minimum principal stress of upstream face/MPa	Maximum principal stress of downstream face/MPa	Minimum principal stress of downstream face/MPa
Post-construction	-429.40	19.95	168.71	-103.13	164.16	-103.33
Impoundment period	-423.80	114.59	168.18	-102.05	166.04	-103.91

Deformation analysis

The horizontal displacement contours of the cut-off wall along the stream direction of the dam are shown in figure 6. From construction to impoundment period, the maximum horizontal displacement along stream direction increases 95cm. The horizontal displacement of the upper part of the cut-off wall is larger than that of the lower part.

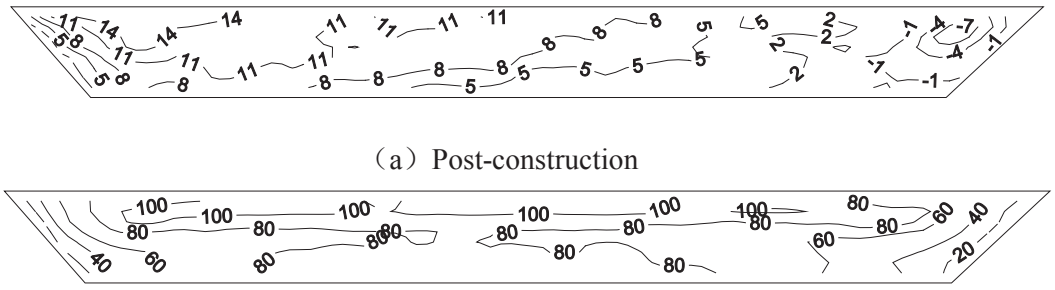

（a）Post-construction

（b）Impoundment period

Figure 6 Horizontal displacement contours of the cut-off wall

Figure 7 shows the settlement contours of the cut-off wall. The maximum settlement of the cut-off wall is 429.4cm and 423.8cm under post-construction and impoundment period condition, respectively. Due to the float pressure caused by impoundment of the reservoir, the maximum settlement slightly decreases by 5.6cm. Since the valley is the "V" shape, the settlement of the middle part of the cut-off wall is the largest compared with that of the valley parts.

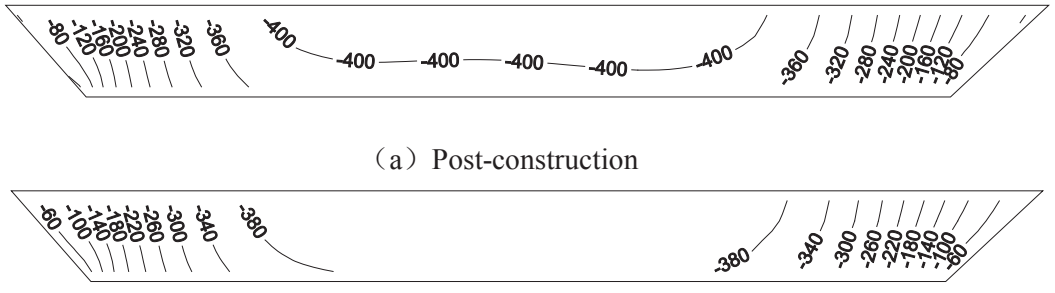

（a）Post-construction

（b）Impoundment period

Figure 7 Settlement contours of the cut-off wall

Stress analysis

The mesh of cut-off wall is divided into four layers along the direction of the river. Here, the outermost element on the left side of the dam axis is called the upstream face. Figure 7 gives the maximum principal stress contours on the upstream face of cut-off wall under post-construction period. It is obvious that the maximum principal stress locates near the bottom of the left and right sides of the cut-off wall, and the maximum value is 168.71MPa. Furthermore, the stress concentration

exists due to uneven settlement between the centre of the valley and the slope of cut-off wall. the major principal stress of the most areas on the upstream face of cut-off wall is less than 50MPa.

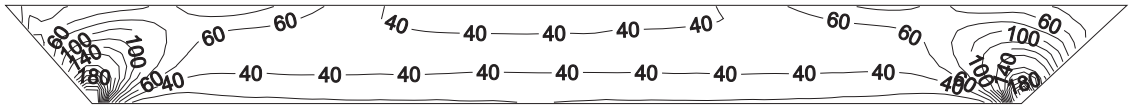

Figure 8 Maximum principal stress contours on the upstream face of cut-off wall

Figure 9 shows the minor principal stress contours on the upstream face of cut-off wall under impoundment period. In figure 9, tensile zones on the left and right sides of bank slopes exist. The maximum tensile stress is 103.13MPa (tension stress concentration). The concentration area is located at the top of the cut-off wall on the left and right banks.

Figure 9 Maximum principal stress contours on the upstream face of cut-off wall

The distribution of the principal stress on the downstream surface of the cut-off wall is similar to that on the upstream surface and is not listed here.

The effect of gravel pile treatment on the deformation of the dam

In order to analyse the treatment effect of the gravel piles, the scheme Z-4 which represents using original parameters of overburden layers is conducted to show the difference of deformation with Z-3. The parameters of Z-3 and Z-4 are exactly the same except the shallow foundation. According to the results of 3-D finite element calculation, the main deformations of the schemes Z-3 and Z-4 are given in table 7.

Table 7 The calculation results of schemes Z-3 and Z-4

Schemes	Conditions	Dam axis maximum horizontal displacement /(cm)	Dam axis maximum horizontal displacement /(cm)	Upstream maximum horizontal displacement /cm	Downstream maximum horizontal displacement /cm	Maximum settlement /cm
Z-3	Post-construction	113.70	-114.70	106.86	-89.56	-533.30
	Impoundment period	113.60	-115.40	128.56	-67.70	-523.50
Z-4	Post-construction	113.10	-115.40	121.61	-99.73	-609.70
	Impoundment period	113.50	-115.50	143.54	-78.19	-599.70

It can be seen from table 7 that the maximum settlement of scheme Z-4 without gravel pile treatment is 599.70cm during impoundment period. However, the maximum settlement of scheme Z-3 with gravel pile treatment is 523.50cm, which is 76.2cm smaller than scheme Z-4, reducing 13% settlement of the whole model. The results indicates that the gravel pile treatment is efficient for dam construction on thick overburden layers.

To further study the difference of schemes Z-3 and Z-4, figure 10 gives the differential settlement contour lines of two schemes. It can be seen that the maximum differential settlement locates in the shallow overburden layers and there is no big difference of the two schemes in deeper overburden layers. In addition, the gravel pile treatment can deduces 10% of the maximum horizontal

displacement of the dam. Considering the length of the paper, the horizontal displacement contour lines are not listed here.

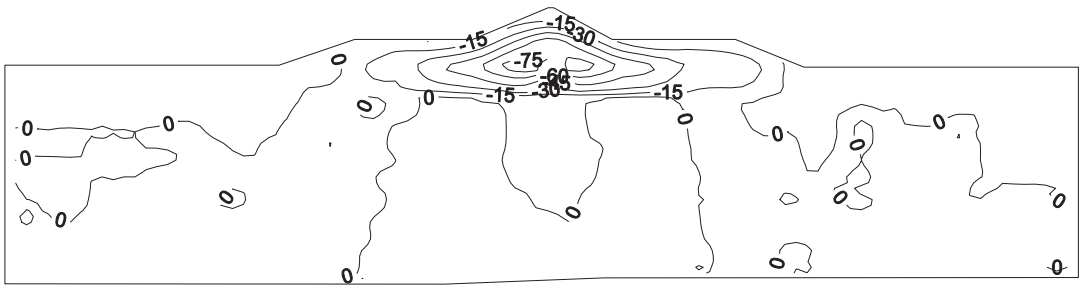

Figure 10 Differential settlement contour lines of schemes Z-3 and Z-4

CONCLUSIONS

1. To simplify the 3-D fem calculation, the equivalent method is used to obtain the replacement rates and thus to deduce the simplified parameters of composite foundation.
2. The results of main deformation of the dam reveals that the maximum settlement locates in the shallow overburden layers due to the deformation of the thick overburden layers.
3. Stress concentration and some tensile zones exist on the left and right sides of cut-off wall bank slopes due to the uneven deformation.
4. The results indicates that the gravel pile treatment can reduce 13% settlement and 10% of the maximum horizontal displacement which is efficient for dam construction on thick overburden layers.

AKNOWLEDGEMENTS

The authors gratefully acknowledge the financial support from the National Key Reasearch (2017YFC0404806), Development Program of China (51779152) and China Postdoctoral Science Foundation (2018M630578).

REFERENCES

Akin, J. E., 1982. Application and implementation of finite element methods . Academic press, New York.

Cui, X., et. al., 2014. “Deterioration of soil-cement piles in a saltwater region and its influence on the settlement of composite foundations”. Journal of Performance of Constructed Facilities, vol. 30, pp. 04014195.

Deng, M. J., 2012. “Advances in key technology for concrete face dams with deep overburden layers under cold and seismic conditions”. Chinese Journal of Geotechnical Engineering, vol. 34, pp. 985-996.

Duncan, J.M., Chang, C.Y., 1983. “Non-linear analysis of stress and strain in soils”. ASCE, Vo1.96.

Gong, X. N., 2002. Theory and engineering application of composite foundation. China Architecture & Building Press, Beijing, (in Chinese).

Kang, X., et. al., 2016. “Analysis of Pile-Soil Interaction of Gravel Pile Composite Foundation”. Electronic Journal of Geotechnical Engineering, vol. 21, pp. 29-87.

Sun, M., Chen, J., Chen, X., 2013. “Stress and deformation analysis of the rock-fill dam with deep covering layer by static three dimensional finite element method”. Yellow River, vol. 35, pp. 103-106.

Wang, W., Höeg, K., Zhang, Y., 2010. “Design and performance of the Yele asphalt-core rockfill dam”. Canadian Geotechnical Journal, vol. 47, pp. 1365-1381.

Xu, Q., Chen, W., Zhang, Z., 2008. “New views on forming mechanism of deep overburden on river bed in southwest of China”. Advances in Earth Science, vol. 23, pp. 448-456.

Zhang, H, et.al, 2016. “Deformation characteristics and control techniques at the Shiziping earth core rockfill dam”. Journal of Geotechnical and Geoenvironmental Engineering, vol.142, pp. 04015069 .

Zhou, W., Li, S. L., Ma, G., 2016. “Assessment of the crest cracks of the Pubugou rockfill dam based on parameters back analysis”. Geomechanics and Engineering, vol. 11, pp. 571-585.

5th International Symposium on Dam Safety

October 27-31, 2018

INFLUENCE OF DIFFERENT ORIENTATIONS AND REFERENCE AXES OF GROUND MOTIONS ON THE ENGINEERING DEMAND PARAMETERS OF AN EMBANKMENT DAM

Mohammad DAVOODI [1], Fariborz SANJARI [2]

ABSTRACT

In 2D time history analysis of embankment dams, as-recorded ground motion accelerations are generally used. Recorded accelerations depend on the orientation of the sensors as installed in the field, and by rotating the sensors, different accelerations are recorded for a specific ground motion. Considering that the orientation of sensors is random compared to the orientation of the structures and causative fault, it is necessary to consider the definite reference axes for earthquake records. The main objective of this paper is to compare all different orientation and reference axes of ground motion acceleration. To this aim, after selecting and scaling of earthquakes, the as-recorded horizontal components are rotated to: fault-normal/parallel direction, principal direction, direction related to GMrotIpp (NGA relationships) and maximum direction of response history analysis of 2DOF systems. In the next step, a numerical modeling of an embankment dam is developed using simplified approaches. Then as-recorded motions with various angles, as well as all four abovementioned reference axes, applied on the model to obtain the critical responses of the embankment dam. The results indicate that the orientation can significantly change the responses of the embankment dam. So it is necessary to perform parametric analysis to obtain critical responses.

Keywords: Reference axes, Embankment Dams, Critical orientation, Incidence angle

INTRODUCTION

Earthquake ground motions are generally recorded by digital accelerometers in three orthogonal components (two horizontal and one vertical). The vertical component is typically ignored and two horizontal shakings are used for the response history analysis of most structures. In two-dimensional time history analysis, a stronger horizontal component of the as-recorded ground motion is generally used to evaluate structural responses. However, the strength of horizontal earthquake ground motion depends on the orientation of the sensors as installed in the field. Simple trigonometric calculations demonstrate that by rotating the sensors, different waveforms are recorded for a specific ground motion. Considering that the orientation of the sensors is random compared to the orientation of the structures and causative fault, it is necessary to consider the definite reference axes for earthquake records. By reviewing literature, all reference axes of earthquake ground motions can be categorized as follows:

1) As-recorded ground motion records (Using recorded ground motion without rotating its axis)
2) Principal axes (PD)

[1] Associate Professor, Department of Geotechnical Engineering, International Institute of Earthquake Engineering and Seismology, Tehran, Iran, e-mail: m-davood@iiees.ac.ir
[2] Ph.D. Student, Department of Geotechnical Engineering, International Institute of Earthquake Engineering and Seismology, Tehran, Iran, e-mail: f.sanjari@iiees.ac.ir

3) Fault Normal and Fault Parallel direction (FN/FP)
4) Geometric Mean Independent of period and sensor orientations (GMRotIpp)
5) Maximum Spectral Demand (MSD)

Penzien and Watabe defined an orthogonal set of principal axes along which the variances of earthquake ground motion components have maximum, minimum and intermediate values, while the covariances are equal to zero. The involved procedure is similar to finding the principal directions of stresses in the classical strength of materials. The paper suggested moving window to calculate variances of components and showed that for the window of highest intensity the principal direction is toward earthquake epicenter (Penzien and Watabe 1974, Kubo and Penzien 1979, Kubo and Penzien 1979). Related researches investigated the response of structures subjected to principal component and various rotated ground motion records. Results of the analysis indicated that the responses due to principal components is higher than as-recorded accelerations, while the critical responses may occur in different directions (Reyes and Kalkan 2012).

Typically, ground motions that are recorded in stations less than 20 km away from the epicenter are known as the near-fault earthquake, however, the important characteristics and parameters of this type of earthquake should be taken into account (Stewart et al., 2001). Characteristics of near-fault earthquakes are directly related to the source mechanism, direction of fault rupture and location of the station with respect to the epicenter. The most important distinguishing features of near-fault earthquakes is the forward directivity. This phenomenon results in the accumulation of seismic energy in the fault normal direction and causes pulse-like motions (Somerville and Graves 1993; Somerville 2002; Mavroeidis and Papageorgiou 2003; Bray and Rodriguez-Marek 2004; Somerville 2005; Maniatakis et al., 2008; Lu and Panagiotou 2014) . Concerning this issue, it is assumed that the rotating of the ground motion components in the direction of FN / FP is a conservative method and suitable for the seismic evaluation of structures in the near-fault region. Therefore, the ASCE/SEI 7 Regulation states that in the near-fault region ground motion acceleration should be rotated in the FN/FP direction. While research shows that this direction does not always lead to a maximum response of structures (Kalkan and Kwong 2013; Davoodi et al., 2013; Hadiani et al. 2013).

The geometric mean of the response spectra of two horizontal ground motion components, which is commonly used as a response variable in predicting strong ground motion, depends on the orientation of the sensors. This results in different ground-motion intensity for the specific ground motion. This dependency is more pronounced in a strongly correlated motion such as that occurs in periods of 1 second or longer. Boore Introduced two orientation independent measurements as GMRotIpp and GMRotDpp. In these nomenclatures “GM” stands for geometric mean, “Rot” indicates rotations over all non-redundant angles, “D” and “I” shows period dependent and period independent respectively and “pp” stands for statistical percent percentile. Although the GMRotDpp measurement is independent of the orientation of the sensor, its important shortcoming is the dependence on the oscillator period. This means that GMRotIpp measurement leads to one definite angle for each ground motion acceleration. Therefore, the ground motion acceleration after rotating by this angle can be used in time history analysis (Boore et al., 2006).

The USGS seismic hazard maps and attenuation relationships used in regulations prior to NEHRP 2009 were based on probabilistic seismic hazard analysis and geometric mean (GM, GMRotI50). NEHRP 2009 provision utilizes maximum spectral demand (MSD) direction and deterministic seismic hazard analysis in the near-fault regions. Therefore, according to Baker and Cornell, when using the spectral acceleration, the value of the standard deviation must be taken into account. Because if the maximum value is defined by the mean value plus the standard deviation, if the GMRotI50 direction is used instead of as-recorded ground motion, due to the lower standard deviation of the GMRotI50, the probability of the earthquakes with a long return period is less predicted (Baker and Cornell 2006).

The ASCE / SEI-7-10 uses the Maximum spectral demand (MSD) to provide the site specific spectrum. The MSD direction is corresponding to the maximum spectral response of the single degree of freedom oscillator. The SDOF oscillator with 5% damping and period of T_i is subjected to each

horizontal component and responses is calculated as $A(t,T_i,x)$ and $A(t,T_i,y)$ By drawing the $A(t,T_i,x)-A(t,T_i,y)$ graph according to Figure 5 , the orientation corresponding to the point on the orbit farthest from the origin is identified as MSD. The mean value of the MSD is systematically greater than the GM and their ratio depends on oscillator period and is in the range of 1.1 to 1.5 (Huang et al., 2008; Huang et al., 2009).

The main objective of this paper is to investigate the Influence of different orientation and reference axes of ground motions on the dynamic response of an embankment dam. This investigation carried out with different incidence angle and regarding different reference axes. For this purpose, five well-known earthquake records have been selected from the PEER NGA database. then as-recorded motions have been transformed into four abovementioned directions. In the next step, as-recorded motions have been rotated to various angles from 0 to 360 degrees by 10-degree steps. Finally, the embankment dam responses subjected to rotated ground motion accelerations as well as all reference axes directions have been investigated. The results showed that, in general, reference axes directions did not always lead to the maximum responses, and it is necessary to perform parametric analysis with the different incidence angle of accelerations to obtain critical responses.

PROBLEM DESCRIPTION

Numerical Modeling of the Embankment Dams

Due to a large number of time history analyses and regarding that this type of analysis is time-consuming, homogeneous shear beam models were used for numerical modeling of dams. In accordance with the Figure 1, the governing differential equation of the dams excited by the ground motion can be extracted as follows (Das and Ramana 2010):

$$\frac{\partial^2 u}{\partial t^2}-\frac{G}{\rho}\left[\frac{\partial^2 u}{\partial z^2}+\frac{1}{z}\frac{\partial u}{\partial z}\right]=-\frac{\partial^2 u_g}{\partial t^2} \tag{1}$$

By solving this differential equation, the relative displacement at the height of the dam can be derived as follows.

$$u(z,t)=\sum_{n=1}^{n=\infty}\frac{2J_0\left[\beta_n(z/H)\right]}{\omega_n\beta_n J_1(\beta_n)}\int_0^t \ddot{u}_g \sin\left[\omega_n(t-t')\right]dt' \tag{2}$$

In this equation, J_0 and J_1 are Bessel functions, β_n is the zero value of the frequency function ($J_0\left(\omega_n H\times\sqrt{\frac{\rho}{G}}\right)=0$) and ω_n is the undamped natural frequency of the dam ($\frac{\beta_n}{H}\times\sqrt{\frac{G}{\rho}}$). By solving Equation 2, relative displacement at the height of the dam is obtained, then velocity and acceleration can be find by performing differentiation. In order to obtain absolute responses, the ground motion must be added up to the relative responses of the dam.

For considering nonlinear behavior of soils, an equivalent linear method (ELM) has been used. this method can approximately simulate the actual stress-strain path during cyclic loading by using modulus reduction and damping curves. The modules reduction and damping curves are derived from Darendeli general relationships (Darendeli 2001). Using a hyperbolic model and conducting multiple experiments on various soil types, Darendeli suggested the following relationships and coefficients.

$$\frac{G}{G_{\max}}=\frac{1}{1+\left(\frac{\gamma}{\gamma_r}\right)^a} \tag{3}$$

$$D_{Adjusted} = b \times \left(\frac{G}{G_{\max}} \right)^{0.1} \times D_{Masing} + D_{\min} \quad (4)$$

Where "γ_r" indicates reference strain (%),"a" is curvature coefficient, "Dmin" stands for small-strain material damping ratio (%), "b" is scaling coefficient, and "DAdjusted " is scaled and capped material damping (%). All unknown parameters of the model were computed using parametric analysis. Effective average shear strain and average confining stresses were utilized in the iterative process of equivalent linear approach.

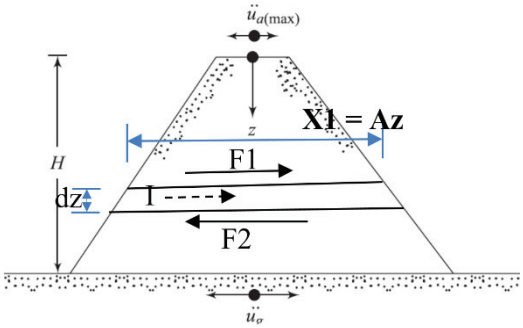

Figure 1. Shear beam method for evaluation of the embankment dams subjected to the ground motion acceleration (Das and Ramana 2010)

Ground Motion Input

To account for the random nature of earthquakes, five well-known ground motion records have been selected from PEER NGA database. these motions were recorded during the earthquake of Tabas 1978, Northridge 1994, Kobe 1995, Chi-Chi 1999 and Kocaeli 1999. Table 1 shows some important characteristics of these records. According to Iranian seismic code (Standard No. 2800 4th. Edition), all records have been scaled to 0.35g peak ground acceleration. Two horizontal component of scaled acceleration histories are depicted in Figure 2. Acceleration response spectra of two horizontal components and their ratio have been shown in Figure 3. The top and middle plots show the x and y component axis spectra, respectively, while the bottom shows the ratio of two horizontal components.

Tabel 1. Ground motions from PEER NGA database used as seeds for parametric analysis

Event name	Year	Station	Magnitude	Mechanism	Rrup (km)	Vs30 (m/sec)	Scale Factor	
							x_comp	y_comp
Tabas	1978	Tabas	7.35	Reverse	2.05	766.77	0.410	0.385
Northridge	1994	LA Dam	6.69	Reverse	5.92	628.99	0.823	1.086
Kobe	1995	KJMA	6.9	strike slip	0.96	312	0.416	0.555
Chi-chi	1999	TCU076	7.62	Reverse Oblique	2.74	614.98	1.016	0.817
Kocaeli	1999	Gebze	7.51	strike slip	10.92	792	1.342	2.435

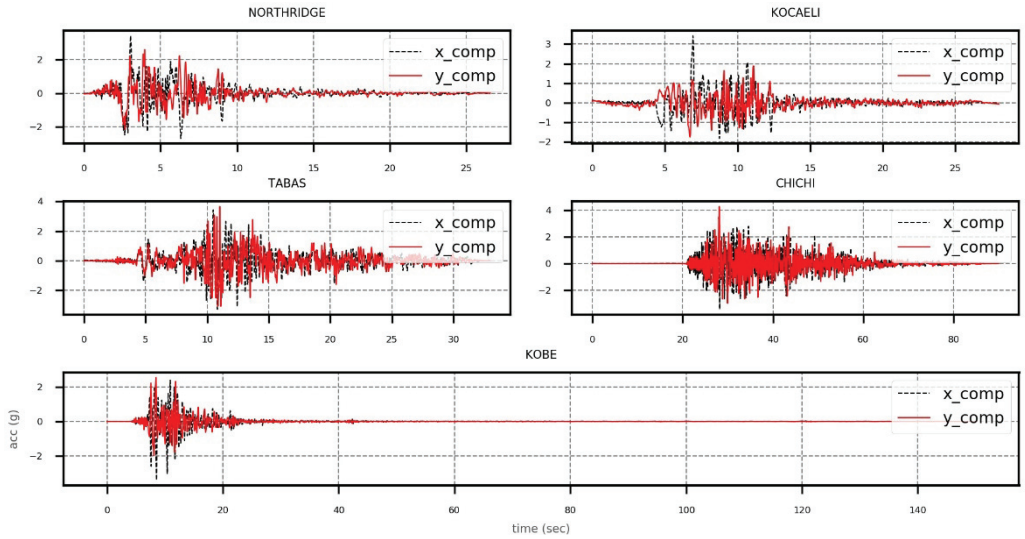

Figure 2. Acceleration time history of all selected ground motion records (two horizontal components)

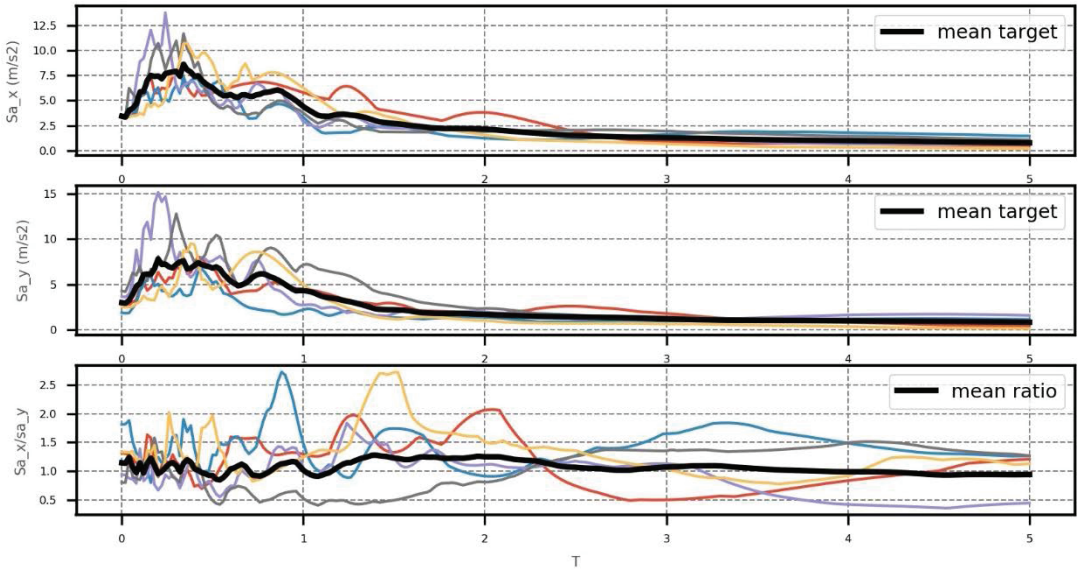

Figure 3. Response spectra for x axes (top), y axes (middle) and ratio of x to y (bottom)

THE ORIENTATION OF THE REFERENCE AXES

Principal Direction

according to the Penzien and Watabe principal directions of all selected ground motion records have been computed (Penzien and Watabe 1974). Moving window approach and optimization rule have been used to calculate these directions. regarding that calculated variance of each component depends on the length of the moving window, 3 different window length have been utilized. Results for a various window length of 3, 5, and 7 seconds have been reported in Tabel 2. For example, "PD_win7" stands for the principal direction of each ground motion record with moving window of 7-second length.

GMRotIpp

the direction independent of sensor orientation and oscillator period is defined as GMRotIpp (Boore et al., 2006). On the basis of research done by Boore et.al. this direction is sensitive to considered maximum oscillator period. So in present research not only this issue has been investigated, but also

the different types of responses (acceleration, velocity, displacement) and statistical percent percentile (pp) have been regarded. Figure 4 shows the median value (pp=50) and direction of GMRotI50 for maximum oscillator period of 5 second and acceleration response of Kocaeli ground motion. Tabel 2 shows GMRotIpp for percent percentile of 50 (pp=50) and for different response types.

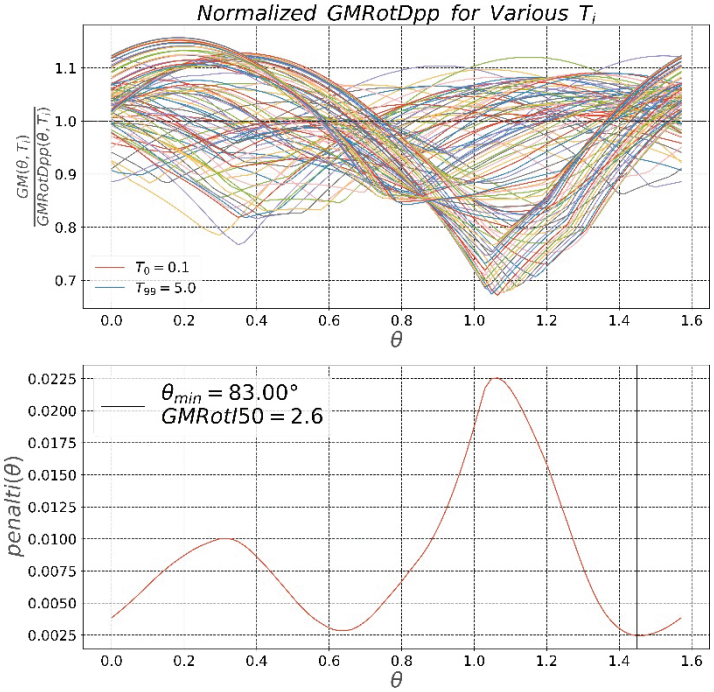

Figure 4. median value (pp=50) and direction of GMRotI50 for maximum oscillator period of 5 second and acceleration response of KOCAELI ground motion

MSD

According to Huang et.al. directions of maximum spectral demand have been computed for all selected ground motions (Huang et al., 2008; Huang et al., 2009). MSD direction and value depends not only on the period of SDOF system but also on the response type. Therefore, it is important to choose a proper response and period of structure for which the MSD direction is computed. In this paper, acceleration, velocity, and displacement response histories have been considered. Furthermore, the predominant period of both linear and equivalent linear system have been used. All computed MSD directions are reported in Tabel 2, for instance "MSD_acc_Teqlin" indicates MSD direction for acceleration response of SDOF system with characteristics (period, damping) of equivalent-linear model of an embankment dam. Figure 5 shows MSD values and directions for all selected ground motions at predominant period of 1 second. As can be seen from this figure, there is a distinct directionality in KOBE ground motion record at the period of 1 second. This issue can be inferred as near-fault earthquake characteristic.

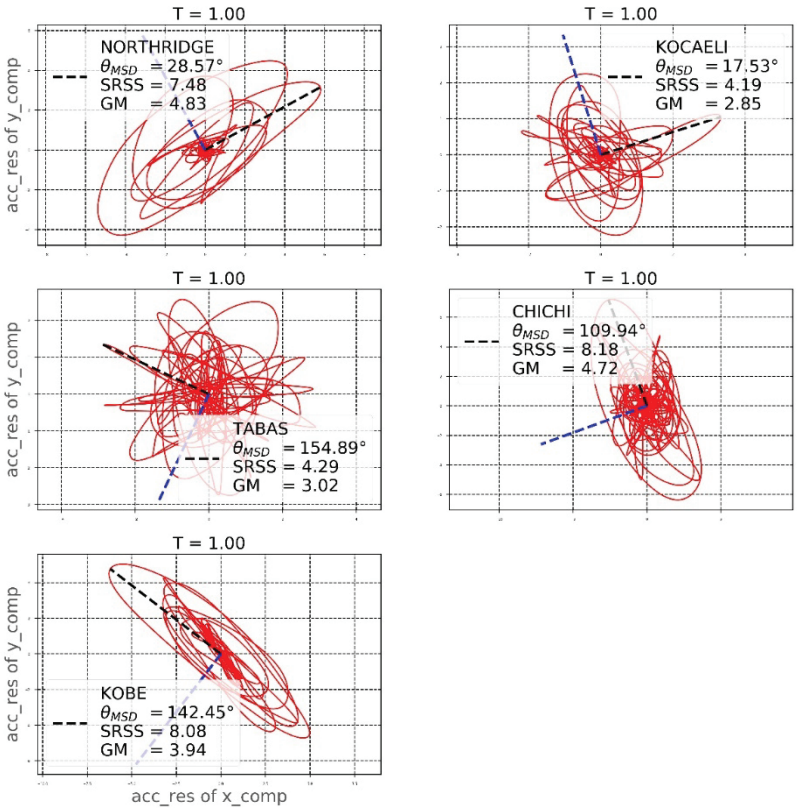

Figure 5. Directions and values of maximum spectral demand for all selected ground motions (Northridge, Kocaeli, Tabas, Chi-chi, Kobe)

according to the aforementioned definition, reference axes directions have been computed for all selected ground motion records and summarized in Tabel 2.

Tabel 2. All reference axis directions for 4 selected ground motions

Reference Axis	NORTHRIDGE	KOCAELI	TABAS	CHICHI	KOBE
GMRotI50_acc	67.00	83.00	7.00	50.00	79.00
GMRotI50_dis	22.00	22.00	22.00	22.00	22.00
GMRotI50_vel	59.00	86.00	4.00	26.00	26.00
MSD_acc_Teqlin	155.68	157.78	27.31	134.67	156.37
MSD_acc_Tlin	29.91	152.58	200.87	283.55	145.23
MSD_dis_Teqlin	335.14	337.28	207.26	314.76	336.45
MSD_dis_Tlin	210.26	332.56	21.81	102.97	324.66
MSD_vel_Teqlin	334.82	188.95	48.89	302.10	342.59
MSD_vel_Tlin	212.80	212.05	192.82	278.64	324.27
PD_win3	28.23	210.01	252.36	139.14	308.61
PD_win5	35.65	49.21	222.01	110.59	332.16
PD_win7	25.73	23.78	48.59	132.51	147.84

PARAMETRIC STUDY TO DETERMINE CRITICAL RESPONSES AND DIRECTIONS OF AN EMBANKMENT DAM

A typical embankment dam with height of 120 m was selected as a case study. Tabel 3 shows some important characteristics of the dam (Dakulas and Gazetas 1985).

Tabel 3. Characteristics of the dam used (Dakulas and Gazetas 1985)

Height	Average density (kg/m3)	Average Vs (m/s2)	Ccore/Cshell	h/H	Inhomogeneity	T1
120	2000	280	1	0	0	1.121

According to the aforementioned process (Numerical modeling of embankment dams), numerical modeling of the embankment dam was developed using the Python programming language. Figure 6 shows 4 mode shapes and periods of the selected dam.

To investigate the effects of ground motion directions on the response of the embankment dam, numerous parametric analyses were carried out. In order to perform these analyses, as-recorded ground motions were rotated to different angles in the range of 0-360 degrees in 10 degree steps. For each selected record, these 35 different directions as well as all 12 above-mentioned reference axes direction, added up to form an acceleration seed. Then linear and equivalent linear analyses of the dam were performed using each individual component of the acceleration seed. this process was repeated for all 5 selected records; and acceleration, velocity, and displacement responses of the dam crest were computed.

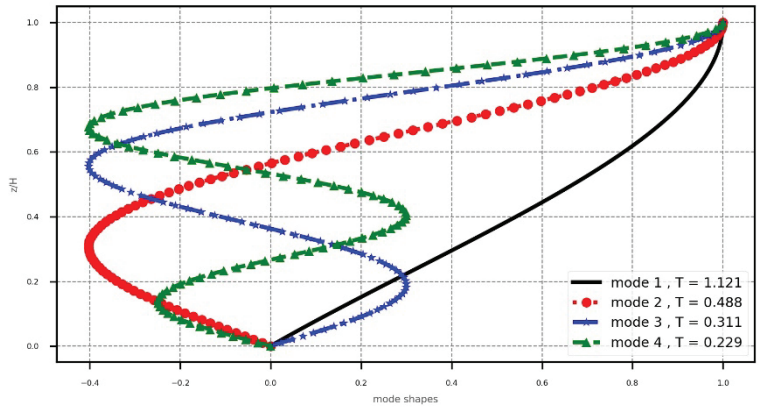

Figure 6. mode shapes and periods of the selected dam

0shows maximum crest velocities ad accelerations of the dam due to 4 ground motion records with different incidence angles in the equivalent linear model. In this figure solid lines show responses due to different orientation of records (0–360°, 10° steps) and asterisks indicate responses of reference axes directions. As can be seen from this figure, the orientation associated with the maximum responses do not coincide with reference axes directions. Also inferred from this figure are the critical orientation dependency on the ground motion records and considered responses. Figure 8 Compares the critical responses of all ground motion records, indicated by “max_res” with responses due to different reference axes directions in the equivalent linear analysis. It can be seen that the reference axes directions do not always lead to the maximum responses.

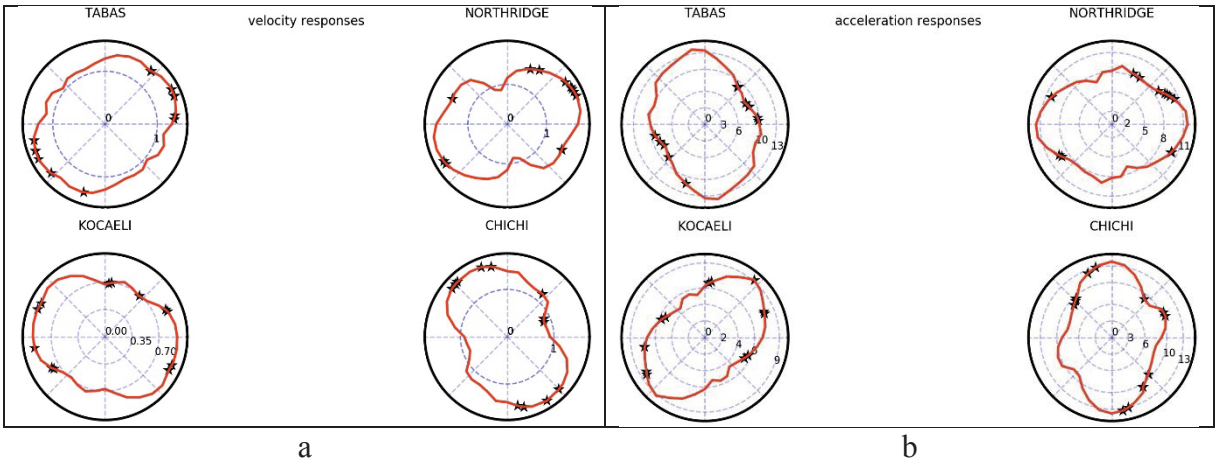

Figure 7. Maximum crest responses of the dam subjected to records with different incidence angles (solid lines show all orientations and asterisks show reference axes directions; a) velocity, b) acceleration

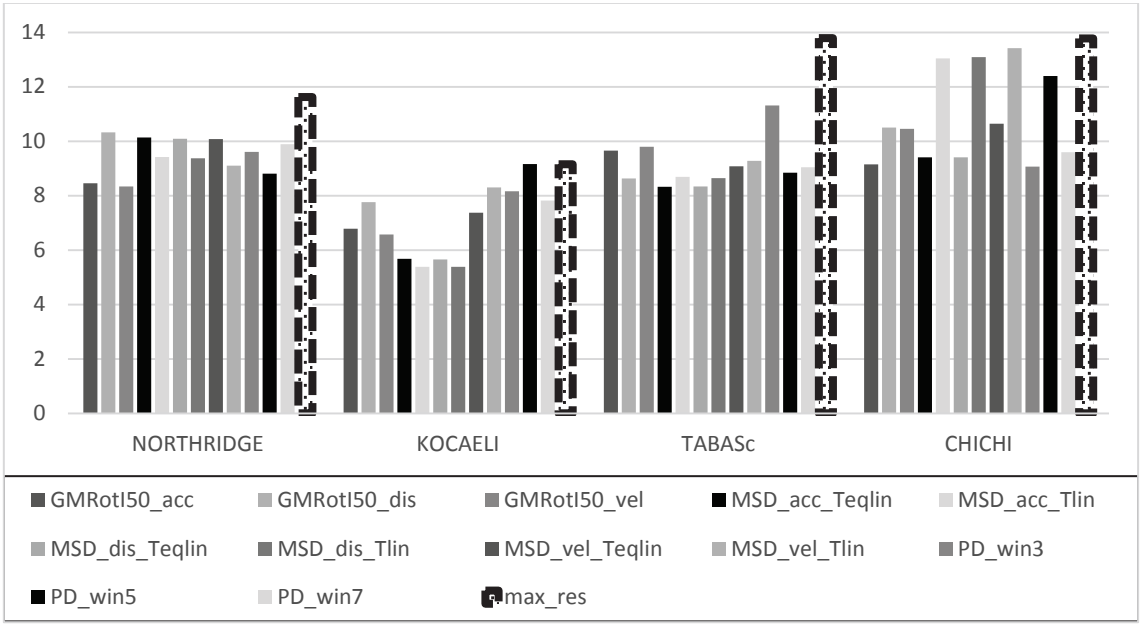

Figure 8. Maximum crest accelerations of the dam subjected to all selected ground motions with different incidence angles (equivalent linear analysis)

By investigating different responses, including displacement, velocity, and acceleration, due to linear and equivalent linear analyses, the important outcomes can be summarized as follows:

- Regarding only as-recorded motions almost always underestimate responses.
- generally, critical responses occur at directions other than reference axis directions.
- Critical directions obtained from linear models do not coincide with equivalent linear models.
- Critical directions are different for different response types.
- Although response spectrum of MSD direction is the envelope of all directions, time history analysis due to this direction does not lead to the critical response.

CONCLUSION

The main objective of this research is to investigate the influence of a different orientation of ground motions on some EDPs of the embankment dam. Furthermore, the comparison between all different reference axes was performed. To investigate this orientation dependence, each ground motion was rotated in 10˚ increments from 0˚to 360˚. These transformed motions as well as other reference axes directions were used as the input motions. A series of time history analysis of the embankment dam due to each record of input motions were carried out. The results showed that not only as-recorded motions but also the aforementioned reference axes directions do not always result in critical responses of the dam body. Therefore, a parametric study with regarding all non-redundant directions is needed to find the maximum desired EDPs.

REFERENCES

Baker, J. W. and C. A. Cornell (2006). "Which spectral acceleration are you using?" Earthquake Spectra 22(2): 293-312.

Boore, D. M., J. Watson-Lamprey and N. A. Abrahamson (2006). "Orientation-independent measures of ground motion." Bulletin of the seismological Society of America 96(4A): 1502-1511.

Bray, J. D. and A. Rodriguez-Marek (2004). "Characterization of forward-directivity ground motions in the near-fault region." Soil dynamics and earthquake engineering 24(11): 815-828.

Dakoulas, P. and Gazetas, G., 1985. A class of inhomogeneous shear models for seismic response of dams and embankments. *International Journal of Soil Dynamics and Earthquake Engineering*, *4*(4), pp.166-182.

Darendeli, M. B. (2001). "Development of a new family of normalized modulus reduction and material damping curves."

Davoodi, M., Jafari, M.K. and Hadiani, N., 2013. Seismic response of embankment dams under near-fault and far-field ground motion excitation. Engineering Geology, 158, pp.66-76

Das, B. and G. Ramana (2010). "Principles of soil dynamics, 2nd edn. Cengage Learning." Inc, Boston.

Hadiani, N., Davoodi, M. and Jafari, M.K., 2013. Correlation between settlement of embankment dams and ground motion intensity indices of pulse-like records. Iranian Journal of Science and Technology. Transactions of Civil Engineering, 37(C1), p.111.

Huang, Y.-N., A. S. Whittaker and N. Luco (2008). "Maximum spectral demands in the near-fault region." Earthquake Spectra 24(1): 319-341.

Huang, Y.-N., A. S. Whittaker and N. Luco (2009). "Orientation of maximum spectral demand in the near-fault region." Earthquake Spectra 25(3): 707-717.

Kalkan, E. and N. S. Kwong (2013). "Pros and cons of rotating ground motion records to fault-normal/parallel directions for response history analysis of buildings." Journal of Structural Engineering.

Kubo, T. and J. Penzien (1979). "Analysis of three dimensional strong ground motions along principal axes, San Fernando earthquake." Earthquake Engineering & Structural Dynamics 7(3): 265-278.

Kubo, T. and J. Penzien (1979). "Simulation of three
principal axes, San Fernando earthquake." Earthquake Engineering & Structural Dynamics 7(3): 279-294.

Lu, Y. and M. Panagiotou (2014). Characterization and Representation of Pulse-like Ground Motions Using Wavelet-based Cumulative Pulse Extraction.

Maniatakis, C. A., I. Taflampas and C. Spyrakos (2008). Identification of near-fault earthquake record characteristics. The 14th world conference on earthquake engineering Beijing, China, October.

Mavroeidis, G. P. and A. S. Papageorgiou (2003). "A mathematical representation of near-fault ground motions." Bulletin of the Seismological Society of America 93(3): 1099-1131.

Penzien, J. and M. Watabe (1974). "Characteristics of 3
Earthquake engineering & structural dynamics 3(4): 365-373.

Reyes, J. and E. Kalkan (2012). Relevance of Fault-Normal/Parallel and Maximum Direction Rotated Ground Motions on Nonlinear Behavior of Multi-Story Buildings. Proceedings of the 15th World Conference on Earthquake Engineering.

Somerville, P. and R. Graves (1993). "Conditions that give rise to unusually large long period ground motions." The structural design of tall buildings 2(3): 211-232.

Somerville, P. G. (2002). Characterizing near fault ground motion for the design and evaluation of bridges. Third National Conference and Workshop on Bridges and Highways. Portland, Oregon.

Somerville, P. G. (2005). Engineering characterization of near fault ground motions. Proc., NZSEE 2005 Conf.

Stewart, J. P., S.-J. Chiou, J. D. Bray, R. W. Graves, P. G. Somerville and N. A. Abrahamson (2001). Ground Motion Evaluation Procedures for Performance-Based Design. PEER Report 2001/09. Pacific Earthquake Engineering Research Center, University of California, Berkeley.

5 DAM SAFETY
İstanbul Turkey 2018

5th International Symposium on Dam Safety

October 27-31, 2018

SEISMIC RESPONSE OF MURUM CONCRETE GRAVITY DAM LOCATED IN SARAWAK, MALAYSIA

Kwan Ben SIM,[1] Raudhah AHMADI [2], Lidyana ROSLAN[3], Ahmed ABDULLAHI[4]

Meldi SUHATRIL[5]

ABSTRACT

In this paper, a three-dimensional dynamic finite element analyses of the Murum concrete gravity dam is presented. The dam is located in Sarawak, Malaysia, an area considered a low seismic zone. As a result, the Murum dam has never experienced any seismic damage in the past.. Nevertheless, this study aims to facilitate the research need to assess the response of the Murum hydroelectric power dam in under seismic loadings. Using ABAQUS software, a static linear analysis is employed to simulate the dam condition without seismic loading whereas a dynamic non-linear analysis evaluates the seismic response of the dam. The static response of the dam recorded stresses at the dam body which are within permissible limits. The dynamic response of the captured accelerations recorded at the crest of the dam as well as crack propagation in the dam body. The results show that under medium level shaking (0.1g<PGA<0.3g), a tensile zone is developed at the base of Murum Dam and critical cracking occurs. The dam is considered damaged and could cause flooding to happen at the downstream section. It is found that the maximum capacity of Murum Dam is up to 0.1g which is suitable for the low seismicity condition in Sarawak.

Keywords: Murum Dam, dynamic analysis, earthquake, three-dimensional finite element

INTRODUCTION

Hydropower dams built in areas of seismic activity can be vulnerable to earthquakes. This can be shown from previous incidents, e.g., Konya dam in India, Shih-Kang dam in Taiwan and the Zipingpu dam in China. The Konya dam suffered significant damage during the 1967 Konya earthquake (M 6.5). Cracks developed along the dam body, the reservoir leaked on the downstream section of the dam and concrete spalling occurred along the vertical joints between monoliths. According to Chopra and Chakrabarti (1973), the region in India where the 1967 Konya earthquake (M 6.5) occurred was considered a stable and almost non-seismic. In addition, Shih-Kang dam in Taiwan underwent

[1] Research student, Department of Civil Engineering, Universiti Malaysia Sarawak (UNIMAS), Kota Samarahan, 94300, Sarawak, Malaysia.
e-posta: 17030213@siswa.unimas.my
[2] Senior Lecturer, Department of Civil Engineering, Universiti Malaysia Sarawak (UNIMAS), Kota Samarahan, 94300, Sarawak, Malaysia.
e-posta: araudhah@unimas.my
[3] Lecturer, Department of Mechanical and Manufacturing Engineering, Universiti Malaysia Sarawak (UNIMAS), Kota Samarahan, 94300, Sarawak, Malaysia.
e-posta: rlidyana@unimas.my
[4] Assistant Professor, Department of Civil and Environmental Engineering, Dhofar University, Salalah, P.O. Box 2509, Salalah, Sultanate of Oman.
e-posta: aabdullahi@du.edu.om
[5] Senior Lecturer, Department of Civil Engineering, Universiti of Malaya (UM), 50603 Kuala Lumpur, Malaysia.
e-posta: meldi@um.edu.my

catastrophic failure due to the Chelungpu fault movement and ground shaking during the Chi-Chi earthquake (M 7.7) in 1999.

In the year 2008, 403 hydropower dams in China with a total capacity of 3.3 GW experienced some level damage during the Wenchuan earthquake (M 8.0). Although most of the dams are small earth dams, four of the damaged dams are of a considerable size with a height exceeding 100 meters. For example, the Zipingpu dam experienced cracking in its structure. Also the walls housing the power plant collapse resulting in a shut down and emptying of the reservoir(Jackson, 2012). In general, hydropower projects were disrupted as well as the flow of the river channels owing to the abundant rock falls and landslides (ICOLD, 2010). Although there were no failures among the dams, the Wenchuan earthquake clearly highlights the importance of seismic risk assessment and design for dams.

These case studies also demonstrate to the importance of conducting a seismic risk assessment for existing hydroelectric power (HEP) dams in seismic zones. Malaysia was considered a country with low seismic events until the recent years when the 2015 Ranau earthquake (M 6.0) struck Sabah, Malaysia. During this earthquake, minimum of 18 casualties with injuries were reported. Rock falls and damages to infrastructure were also experienced (USGS, 2015). Immediately following the earthquake, Malaysia started to be more aware of the seismic threats and the government has paid attention to the safety of critical infrastructure.

Sarawak, Malaysia is a low seismicity state which has similar conditions to Koyna, India. Sarawak has two active seismic faults which extend a 100km north to south trending Tubau fault which spans from Belaga in the south to Niah in the north, and the Kelawit Fault. Two earthquakes were caused by the Tubau Fault, one in May 2004 (M5.2) and another one in January 2010 (M3.5) (Yang et al., 2014).

In Sarawak, HEP dams are the main source of electric power. Murum dam is one of the many dams serving Sarawak, a concrete gravity arch type of dam which is located in Belaga. This dam has never experienced any earthquake events since its completion in 2014. As mentioned earlier, this is because Sarawak is a state with low seismicity condition. Furthermore, it is located 500 kilometers away from Ranau, Sabah, the centre of the recent earthquake. Since Murum dam is constructed in a region with low seismicity, researchers pay less attention to its seismic performance. Based on a study by Malla (2012), Murum dam is likely to experience large displacements when subjected to earthquake loadings due to the curved portion of the dam. The study showed that Ilsee dam in Switzerland, which is of similar design, could experience up to 2m displacement at the upper curved portion of the dam and up to 0.6m displacement at the upper straight portion.

In the present study, numerical finite element analyses are performed, first by considering the initial stress conditions of the dam body prior to seismic excitation. Static finite element analyses are conducted to simulate the dead load from the dam body as well as the hydrostatic load from the reservoir. Subsequently, nonlinear dynamic analyses are carried out to study the response of the dam during earthquake excitations.

MURUM DAM

Murum dam, shown in Figure 1, is a large 141m high concrete gravity dam possessing a slightly curved crest about 473 meters and supports a 944 MW power station. The reservoir has a capacity of $12x10^9$ m^3. The material properties are as tabulated in Table 1. The seismic design of the dam is based on ICOLD (2010) requirement, to withstand Operating Basis Earthquake (OBE) limit that is equivalent to 0.1g peak ground acceleration (PGA).

Figure 1 Murum concrete gravity dam in Sarawak

Table 1. Material properties for Murum Dam

Material	Value
Density	2643 kg/m3
Elastic Modulus (E)	31207 MPa
Poisson's ratio (v)	0.2
Dilation angle (ψ)	36.31˚
Compressive initial yield stress	13.0 MPa
Compressive ultimate stress	24.1 MPa
Tensile failure stress	2.9 MPa

NUMERICAL MODEL

Finite element analyses utilizing ABAQUS software are conducted to study the response of the Murum dam. To simulate the nonlinear constitutive behavior of concrete in the dam body, the concrete damage plasticity model (CDP) is employed in all the analyses (Azizan et al., 2017; Huang, 2015). CDP is a plastic-damage constitutive model for cyclic loading of concrete created by Lee and Fenves (1998) which models the scalar damage variable to signify the irreversible damage during the seismic excitation (Abaqus, 2014; Lee et al., 1998). The failure mechanisms of concrete in terms of tension cracks are employed in the study as seen in Figure 2. The finite element meshes from different angles are shown in Figures 3a-3d which consist of 7280 nodes and 5916 3D stress hexahedral elements (C3D8R), used for all the analyses.

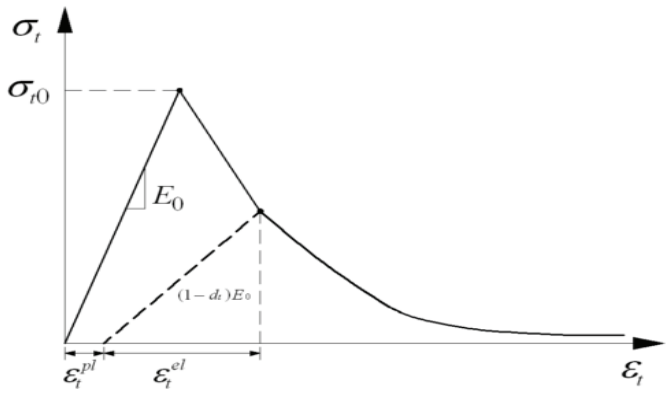

Figure 2. Concrete damaged plasticity (CDP) model in tension (ABAQUS 2014)

Figure 3a: Top view

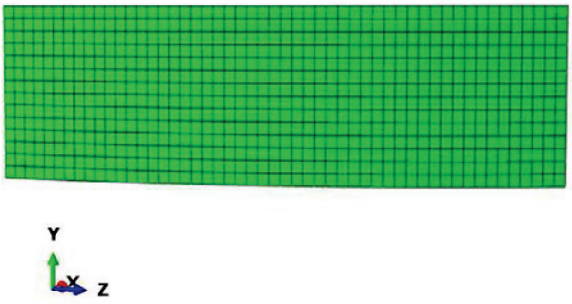

Figure 3b: Upstream face view

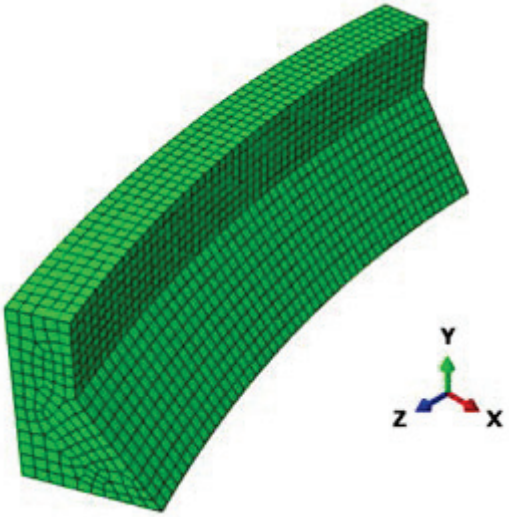

Figure 3c: Downstream 3-point view

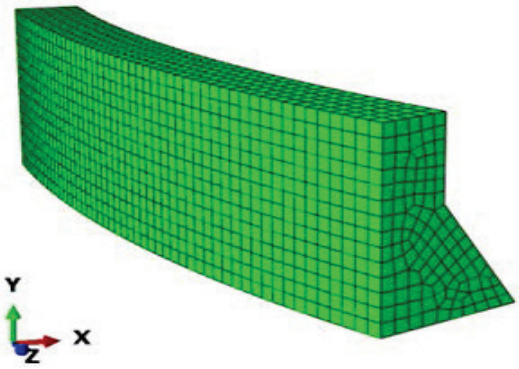

Figure 3d: Upstream 3-point view

STATIC ANALYSIS

Three Dimensional static analyses were performed in order to compute the initial conditions of the Murum dam before seismic events. Therefore, a static analysis was conducted before the dynamic analysis. The analysis takes into account the dead load from the dam itself as well as the hydrostatic pressure from the upstream face. The prescribed boundary condition for the static analysis are full fixity (displacements and rotation in all directions are zero) at the bottom boundary.

The results from static analysis of the dam as shown in Figure 4 shows that the stresses at the dam body are well within the permissible limits for normal static loads i.e. gravity load and hydrostatic pressure. Natural frequencies of the dam for mode 1, 2 and 3 are 2.16 Hz, 2.30Hz and 2.76Hz, respectively. In addition, the static mid crest displacement with a normal level reservoir is found to be 8.76mm which is within the permissible limit (Hariri-Ardebili et al., 2012). This confirms that the dam is well captured for the static analysis and more importantly, the following nonlinear seismic analysis.

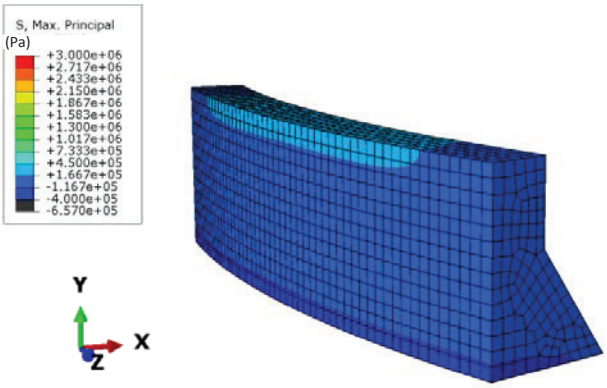

Figure 4 Major principal stress from ABAQUS software for Murum Dam before seismic events

NONLINEAR DYNAMIC ANALYSIS

Following the completion of static analyses and obtainment of the appropriate stress conditions, the nonlinear dynamic analyses were conducted to study the seismic response of the dam. Three sets of earthquake records originating from the 1999 Kocaeli earthquake (Mw 7.4) in Turkey have been chosen for the seismic excitation applied at the bottom boundary of the dam (Table 2). These ground motions are classified as long-distance earthquakes which are suitable for the seismicity conditions of Sarawak. These earthquake time histories are scaled to a PGA between 0.2g – 0.266g in order to assess any significant damage to the dam when the seismic excitation is double that of the initial designed earthquake value.

Table 2: Earthquake records used for the nonlinear dynamic analysis

Earthquake	Mw	Station	Record	Epicentral distance (km)	PGA (g)	PGV (cm/s)	PGD (cm)	Scaled PGAs (g)
Kocaeli, Turkey	7.4	Manisa	KOCAELI/MNS000	324.90	0.012	3.0	1.21	0.1
								0.2
Kocaeli, Turkey	7.4	Tosya	KOCAELI/TOS090	341.89	0.008	4.0	2.93	0.1
								0.266
Kocaeli , Turkey	7.4	Cekmece	KOCAELI/AFY000	223.07	0.015	2.64	1.66	0.1
								0.25

RESULTS OF NONLINEAR DYNAMIC ANALYSIS

Table 3 shows the nonlinear acceleration response at the mid crest of the dam for various scaled input motions. From the results, the mid crest acceleration values for all analyses fall within the expected range of values found in the literature (Dakoulas, 2013; Huang, 2015; Pelecanos et al. 2012).

Table 3: Nonlinear dynamic response of Murum Dam

Earthquake record	Original PGA (g)	Analysis	Results from nonlinear analysis	
		Scaled PGAs (g)	Mid crest PGA (g)	Amplification factor
Manisa	0.197	0.10	0.17	1.73
		0.20	**0.88**	**4.40**
Tosya	0.2	0.10	0.215	2.15
		0.266	0.45	1.70
Cekmece	0.1516	0.10	0.31	3.12
		0.25	0.81	3.22

Mid crest PGA response for Manisa seismic excitation scaled to PGA of 0.2g gives the highest seismic response of 0.88g PGA suggesting that an amplification factor of 4.4 occurs for that analysis. The amplification factors from all analyses fall within expected range values (Dakoulas, 2013; Huang, 2015). Although the amplification and magnitude of the mid crest accelerations varies to some degrees depending on the employed model and the seismic excitations input, it is envisaged that the high acceleration amplification response are caused by resonance. In the analyses, the external force which is the seismic loadings coincides with the natural frequency of the dam and causes the dam to accelerate at greater amplitudes.

Figure 5 shows the seismic response spectra of the mid crest from the nonlinear dynamic response. An average response spectrum is plotted and the maximum spectral acceleration is 1.22g at 0.08s. This period is vulnerable for any reservoir triggered earthquake (RTE) event which has a high chance to strike within years after the reservoir impoundment. Justification can be made from documented evidence from field observations of the Zipingpu dam in China, a large dam similar to the Murum dam, that has its crest accelerations logged by three strong motion instruments. The PGA at the crest of Zipingpu dam exceeds 2g PGA during the seismic event in May 2008 which caused a 0.74m displacement at the crest of the dam (Dakoulas, 2013).

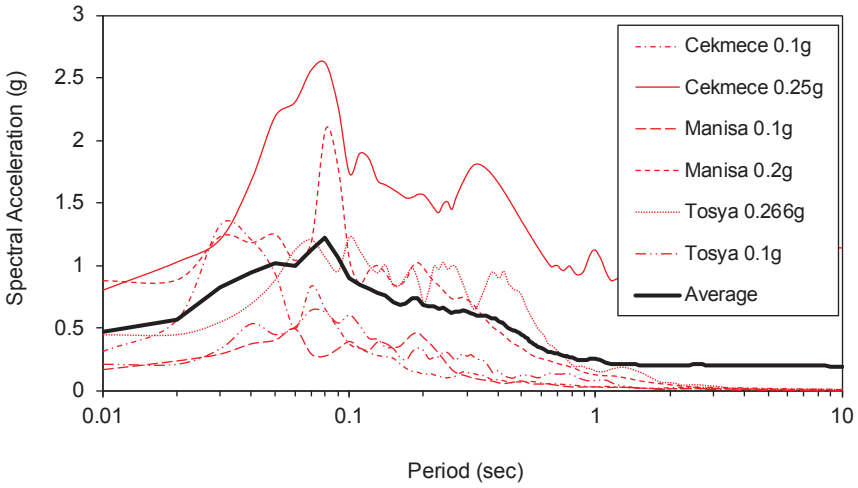

Figure 5: Seismic response spectra for (5% damping) for Murum Dam

From the nonlinear dynamic analyses, it can be seen that the Murum dam is safe from seismic excitations with a PGA of 0.1g. However, beyond that at 0.2g PGA, tensile zones develop and cracking starts to occur along the dam-foundation interface at the toe and heel of the dam. Figures 6 and 7 show the potential damage of the Murum dam subjected to Tosya 0.10g and 0.266g PGA.

Significant cracking occurs at the base of the dam which suggests that the dam has not failed but is considered severely damaged. Flooding will occur at the downstream section as the cracks will permit water from the reservoir to seep through. Severe cracks formation at the base of dam is less common but not surprising as similar crack profiles are reported by many researchers (Azizan, et al. 2017; Hariri-Ardebili et al., 2015).

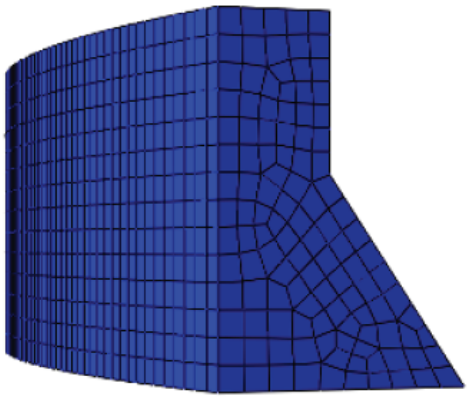

Max displacement: 0.512m

Figure 6: Insignificant seismic damage at the dam body caused by Tosya seismic excitation scaled at 0.1g

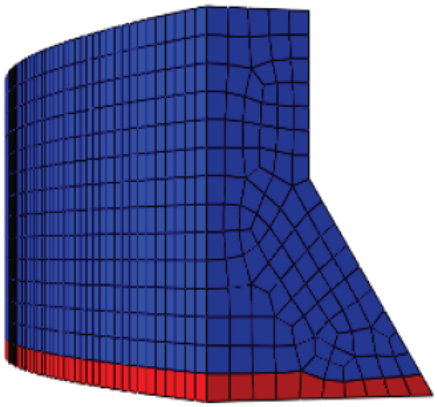

Max displacement: 1.298m

Figure 7: Seismic damage at bottom of the dam body caused by Tosya seismic excitation scaled at 0.266g

From the nonlinear dynamic analyses, it can be seen that all three earthquakes scaled beyond 0.2g PGA onwards caused tensile damage to the concrete material which is due to the changes in the major principal stress around the dam body. Major principal stress within the dam body during the Cekmece 0.25g earthquake is plotted in Figure 8. It can be seen that the maximum tension spreads at the uplift joint section. Here, the major principal stress is approaching the tensile strength of the concrete indicating the likelihood of tensile damage in the vicinity of the downstream face of the dam.

Referring to the major principal stress response history at the downstream section shown in Figure 9, largest values of the major principal stresses have exceeded the tensile strength of the concrete (>2.9 MPa), suggesting the high possibility of tensile damage in these areas. Figure 9 plots the major principal stress within the Murum dam body for Tosya 0.266g earthquake showing that the maximum tension is distributed at the base of the dam. A similar stress contour is also obtained for Manisa 0.2g earthquake. Although the major principal stress at the base for Tosya 0.266g earthquake (1.68 MPa) does not exceed the concrete tensile strength (2.9 MPa), tensile damage still occurs at the base, indicating that the dam material at the base has lost its tensile resistance.

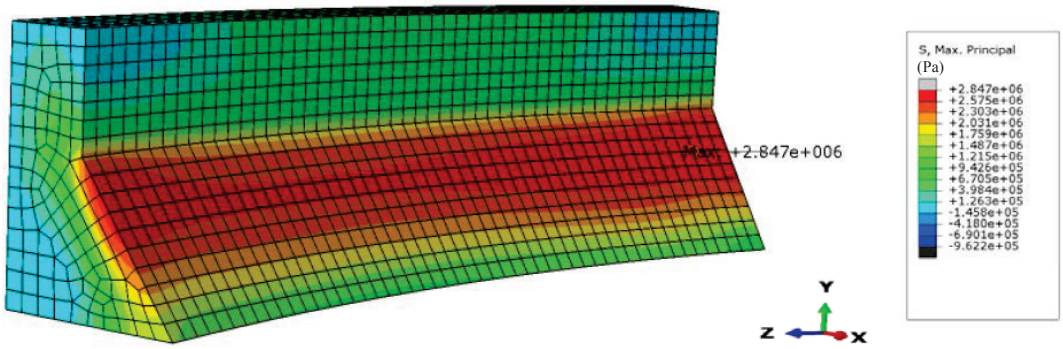

Figure 8: Response to Cekmece 0.25g seismic excitation: major principal stress at t=34.76s (downstream 3 point view)

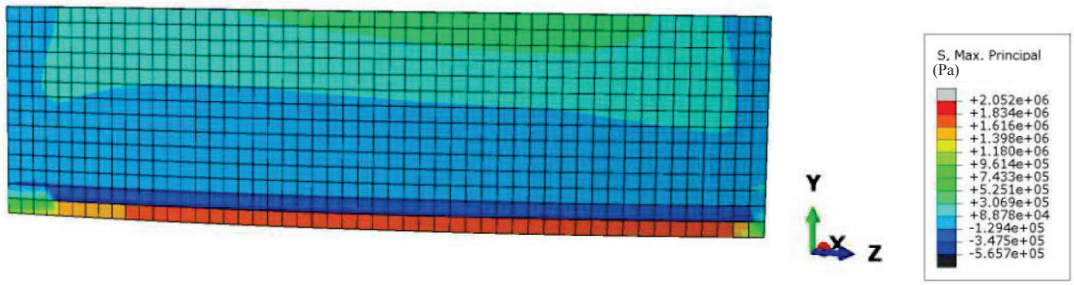

Figure 9: Response to Tosya 0.266g seismic excitation: major principal stress at t= 92.71s (upstream face)

CONCLUSION

The Murum dam is a newly constructed concrete gravity dam in Sarawak which has never experienced any earthquake damage. The present study employed a three dimensional static and nonlinear dynamic finite element analyses to study the dam response in the event of seismic excitations. The results show that the stresses and displacement were within good prediction of the static phase while for the dynamic phase, the crest accelerations obtained were also well predicted. The results show that under medium shaking (0.1g<PGA<0.3g), tensile zones develop at the base of the dam and critical cracking occurs. The dam is considered damaged and could cause flooding to happen at the downstream section. It is found that the maximum capacity of the Murum dam is up to 0.1g which is suitable for the low seismicity conditions in Sarawak.

ACKNOWLEDGEMENT

This authors wish to thank Universiti Malaysia Sarawak and Ministry of Higher Education, Malaysia for research funding through MyRA Special Short Grant 2015/2016, F02/SpSTG/1380/16/22.

REFERENCES

Abaqus. (2014). 6.14 Documentation. *Dassault Systemes Simulia Corporation*.

Azizan, N. Z. N., Majid, T. A., Nazri, F. M., & Maity, D. (2017). Incremental Dynamic Analysis of Koyna Dam under Repeated Ground Motions. *Malaysia Techinical Universities Conference on Engineering and Technology (MUCET 2017)*. https://doi.org/10.1088/1757-899X/318/1/012021

Dakoulas, P. (2013). Nonlinear seismic response of tall concrete-faced rockfill dams in narrow canyons. *Soil Dynamics and Earthquake Engineering*, *44*(1), 138. https://doi.org/10.1016/j.soildyn.2012.09.007

Hariri-Ardebili, M. a., & Mirzabozorg, H. (2012). Reservoir Fluctuation Effects on Seismic Response of High Concrete Arch Dams Considering Material Nonlinearity. *Journal of Civil Engineering Research*, *1*(1), 9–20. https://doi.org/10.5923/j.jce.20110101.02

Hariri-Ardebili, M. A., & Saouma, V. (2015). Quantitative failure metric for gravity dams. *Earthquake Engineering & Structural Dynamics*, *44*(3), 461–480.

Huang, J. (2015). Earthquake Damage Analysis of Concrete Gravity Dams: Modeling and Behavior under Near-Fault Seismic Excitations. *Journal of Earthquake Engineering*, *19*(7), 1037–1085. https://doi.org/10.1080/13632469.2015.1027019

ICOLD. (2010). *Selecting seismic parameters for large dams* (Vol. 72). https://doi.org/Bulletin 72

Jackson, J. (2012). 'Earthquake Hazards and Large Dams in Western China. *Probe International, April*.

K. Chopra, A., & Chakrabarti, P. (1973). The Koyna Earthquake and the Damage to Koyna Dam. *Bulletin of the Seismological Society of America*, *63*(2), 381–397.

Lee, J., & Fenves, G. L. (1998). A plastic-damage concrete model for earthquake analysis of dams. *Earthquake Engineering & Structural Dynamics*, *27*(9), 937–956.

Malla, S. (2012). Seismic Strengthening of an Arch-Gravity Dam. *15th World Conference on Earthquake Engineering (15WCEE)*.

Pelecanos, L., Kontoe, S., & Zdravkovic, L. (2012). Static and dynamic analysis of la villita dam in mexico, (9), 1045–1056.

USGS. (2015). M 6.0 - 14km WNW of Ranau, Malaysia. Retrieved October 24, 2017, from https://earthquake.usgs.gov/earthquakes/eventpage/us20002m5s

Yang, X. guang, & Chi, S. chun. (2014). Seismic stability of earth-rock dams using finite element limit analysis. *Soil Dynamics and Earthquake Engineering*, *64*, 1–10. https://doi.org/10.1016/j.soildyn.2014.04.007

5 DAM SAFETY
İstanbul Turkey 2018

5th International Symposium on Dam Safety

October 27-31, 2018

SEISMIC RESPONSE OF GRAVITY DAMS WITH RANDOM FINITE ELEMENT METHOD

M.A. Hariri-ARDEBİLİ[1], S.M. Seyed-KOLBADİ[1], V.E. SAOUMA[1], J. SALAMON[1]

ABSTRACT

The seismic response of gravity dams is typically derived under a deterministic finite element model for the dam-reservoir-foundation system. In the case where uncertainty in material properties should be incorporated into overall dam performance, the sensitive parameters can be treated as random variables. This paper presents the results of a study that considers the spatial distribution of random variables in the context of random field theory. Koyna Gravity Dam is used as a setting for numerical simulations. The concrete modulus of elasticity, mass density and tensile strength are all assumed to be random fields and generated based on the covariance matrix decomposition and midpoint discretization techniques. The anatomy of the random field seismic responses are presented first, followed by a set of parametric analyses. The impact of correlation length, a single- vs. double-random field, one- or two-dimensional material distributions, ground motion intensity and record-to-record variability and, lastly, dam class are all investigated herein. The uncertainty and dispersion of the seismic responses are quantified in each model; it is found that concrete heterogeneity affects the seismic performance evaluation and should be considered in a structural assessment and risk analysis.

Keywords: Uncertainty, Heterogeneous, Seismic, Probabilistic, Dam Class, Concrete.

INTRODUCTION

In general, the methods applied in structural analysis and design can be classified as either deterministic or probabilistic simulations. In the case where the finite element method (FEM), used to discretize the medium, is combined with statistics and reliability methods, the so-called probabilistic finite element method (PFEM) can be developed and applied to both linear and nonlinear systems. Based on the definition in [1], the term probabilistic or stochastic finite element method (SFEM) is employed in reference to a method that accounts for the geometric or material uncertainties in the structure, as well as the applied loads.

Random field theory and its applications are extensively used in the field of geotechnical engineering [3]. Emphasis is placed on the slope reliability analysis based on random FEM [2]. Studied the probabilistic seismic response of a heterogeneous soil profile with three parameters (i.e. shear modulus, damping, and Poisson's ratio) as the spatially random fields. These authors found that heterogeneity greatly affects the behavior of the soil profile, which induces differential movement at the ground surface.

In the case of concrete dam engineering, studies are very limited. The only research papers accessible are [9] and [5]. In all of these, concrete heterogeneity has been modeled based on the Weibull distribution law, while damage plasticity is used to simulate the failure process. These authors reported that when concrete heterogeneity is considered, the stress distribution is no longer smooth, which therefore better reflects the real-world situation.

The current conference paper is a shortened version of a journal paper published as [10].

[1] University of Colorado at Boulder

RANDOM FIELDS

In this section, an efficient random field generator is explained based on covariance matrix decomposition as well as a midpoint discretization method. The generator relies on a uniformly-distributed random field obtained by means of transformation from normally-distributed, homogeneous and isotropic random fields [3]; LHS is used to reduce the total number of simulations. The procedure, graphically illustrated in Figure 1, is described next:

Assuming that the random field, $H(x)$ is time-independent, one can decompose is as:

$$H(x) = \mu(x) + \alpha(x) \tag{1}$$

Where $\mu(x)$ is a mean value function, $\alpha(x)$ is a fluctuating component, and x presents the position vector.

$\mu(x)$ is a deterministic function, while $\alpha(x)$ is a random function with a zero mean and an auto-covariance function of:

$$C_{aa}(\xi, \sigma_0) = \sigma_0^2 \rho_{aa}(\xi) \tag{2}$$

Where $\xi = |x - x'|$ is the distance between any two arbitrary locations, δ_0 the (constant) standard deviation, and ρ_{aa} the auto-correlation function.

The midpoint method (MPM) is used to discretize the finite element domain [1]. The correlation matrix, C, is constructed from the discretized auto-correlation functions [4]. Matrix C is replaced by a set of k uncorrelated random variables ($r \langle\langle k$). This step is essential to reduce the required number of final realizations. The sum of the r largest eigenvalues is approximately equal to the trace of D (eigenvalue matrix of C):

$$D = Z^T C Z \tag{3}$$

Where Z is the eigenvector matrix of C.
If the r largest eigenvalues and eigenvectors are stored in an $r \times r$ matrix $\widetilde{D}$ and a $k \times r$ matrix $\widetilde{Z}$, then the target covariance matrix is approximately equal to:

$$\widetilde{C} = \widetilde{Z}\widetilde{D}\widetilde{Z}^T \tag{4}$$

This important feature allows applying Latin Hypercube sampling (LHS) in conjunction with random fields. Thus, the number of realizations should be $n \rangle r$ (and not $n \rangle k$), where $r \langle\langle k$. Then, generate a $n \times r$ matrix $\widetilde{P}$, in which each of the r columns is a random permutation of $1,...,n$. Next, generate matrix $\widetilde{Y}$ as a normalized version of $\widetilde{P}$, mapped on a normal distribution:

$$\widetilde{Y} = \Phi_{(0,1)}^{-1}\left(\frac{\widetilde{P}}{n+1}\right) \tag{5}$$

Estimate the covariance matrix of $\widetilde{Y}$ and factorize via the Cholesky decomposition

$$\widetilde{L}\widetilde{L}^{T} = \mathrm{cov}\left(\widetilde{Y}\right) \tag{6}$$

Where $\widetilde{L}$ is a lower triangular.
Compute a new matrix with a sample covariance equal to the identity

$$\widetilde{Y}^{*} = \widetilde{Y}\left(\widetilde{L}^{-1}\right)^{T} \tag{7}$$

Construct another new matrix $\widetilde{P}^{*}$ using the ranks of elements of the columns of $\widetilde{Y}^{*}$ (permutations of $1,...,n$). Also, construct matrix Q (or Q_{ij}) to specify the random component of variable $\widetilde{Y}$ in element i and realization j as:

$$Q = \overline{Q}\widetilde{D}^{1/2}\widetilde{Z}^{T} \tag{8}$$

In which:

$$\overline{Q} = \Phi_{(0,1)}^{-1}\left(\frac{\widetilde{P}^{*} - \widetilde{R}}{n}\right) \tag{9}$$

Where $\widetilde{R}$ is a random number uniformly distributed in (0, 1).
Lastly, compute the sampling matrix:

$$\widetilde{V} = F^{-1}\left[\Phi(Q)\right] \tag{10}$$

Where F^{-1} is a transformation with respect to a specified marginal statistic of the k variables. In the case of a uniform distribution, the sampling matrix can be rewritten as:

$$\widetilde{V} = L_B + (U_B - L_B)\left[\Phi(Q)\right] \tag{11}$$

Where L_B and U_B refer to the lower and upper bounds, respectively.

NUMERICAL EXAMPLE OF CASE STUDY DAM

Koyna Dam has been selected as a setting for running numerical simulations [8], [6]. This structure is 853 m long and 103 m high; the thickness at its base and crest are 70.2 m and 14.8 m, respectively, for the central non-overflow monoliths. Figure 1 shows the cross-section of the tallest non-overflow monolith, including the reservoir and the foundation. The finite element program was used to perform the transient analyses by implicit time integration. Two-dimensional plane strain quadratic elements are used for both the dam and foundation. 14 elements are present at the dam base and 24 along its height. 336 elements compose the dam body, which makes the medium-dense mesh acceptable for linear elastic analyses. Pressure-based fluid elements are placed in the reservoir domain. The fluid-structure interaction (FSI) is applied according to the method (Eulerian-Lagrangian approach) discussed in [7] where pressure in the fluid domain is coupled with solid domain's displacements. Both domains, the (massless) foundation and the reservoir extend three times the dam height {FERC-arch}. It is noteworthy that massless foundation might leads to slightly different response distribution in dam, particularly for relatively soft rocks (as radiation damping is ignored). However, since all simulations were with massless foundation, and since the primary interest is in the impact of concrete heterogeneity, results are not likely to be impacted by this limitation. Loads consist of: self-weight,

hydrostatic pressure (full reservoir), bottom sediment (wave reflection coefficient for the reservoir bottom materials assumed to equal 0.75), and seismic loads.

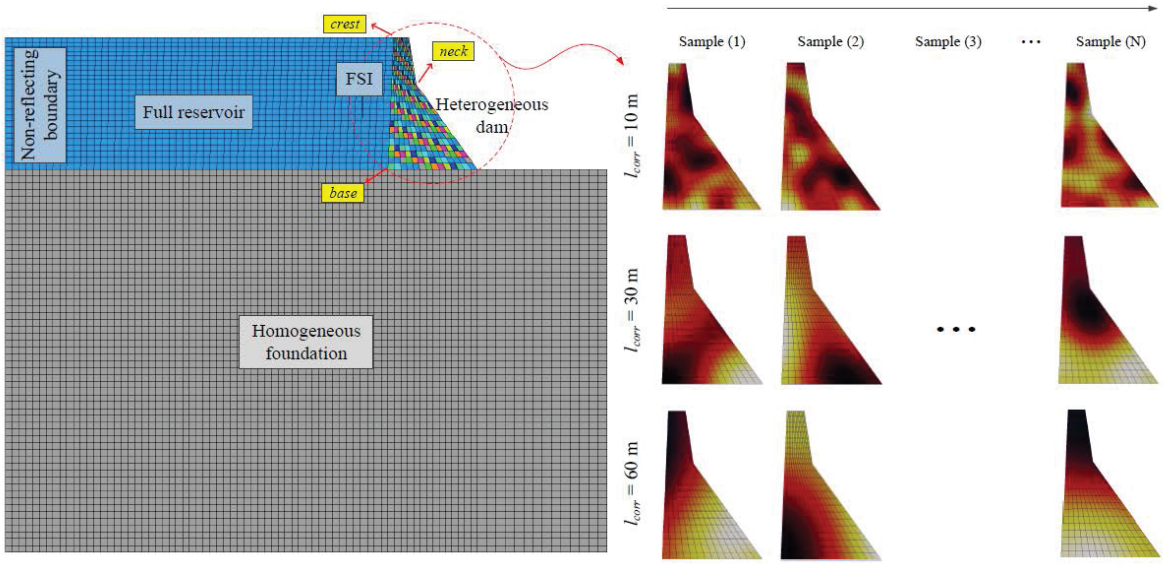

Figure 1. Finite element model of the coupled dam-reservoir-foundation system, including three realization of a heterogeneous dam with different correlation length

The foundation is assumed to be a homogeneous material with E_f=17 GPa, ν_f=0.18 and ρ_f=2700 kg/m^3. The mean concrete properties are: E_c=30 GPa, ν_c= 0.20, ρ_c=2643 kg/m^3 and f'_t= 2.2 MPa. In all heterogeneous models, the standard deviation, σ_0, is assumed to equal 0.5. For the modulus of elasticity, the bound is limited to (22, 38) GPa. Two models have been studied, namely:

Heterogeneous concrete: E_c is treated as a random field, with three different correlation lengths, i.e. l_{corr} = 10, 30 and 60 m. These lengths correspond to roughly 10%, 30% and 60% of the dam height. Figure 1 shows three samples for each correlation length. In some of the comparative models, ρ_c varies in addition to E_c. No correlation between ρ_c and E_c were accounted for. Since the linear elastic transient analyses are performed, thus, only these two parameters (i.e., E_c and ρ_c) might be random prior to perform the simulations. The randomness in f_t, if any, is included in post-processing the simulations. The maximum dam stresses are compared with f_t, (which is either constant, a random variable, or a random field).

Homogeneous concrete: E_c is treated as a random variable and sampled based on LHS. The maximum dam stresses are compared with f'_t, which is assumed to be either constant or a random variable.

RESULTS

Anatomy of Random Field Responses

In this section, various outputs from a group of random field models will be provided and the anatomy of the results discussed. This model can be considered as a pilot for all of the following sections. In this pilot model, l_{corr} equals 30 m. The concrete modulus of elasticity, E_c is assumed to be the only variable and is distributed randomly within the dam section (two-dimensional distribution). Other material properties are held constant. A total of 100 samples are drawn and, subsequently, 100 seismic analyses performed. The coupled system is excited with both horizontal and vertical components from

Koyna Dam recordings. Figure 2 shows the anatomy of these results. Each subplot can be explained as follows:

Figure 2(a) shows 100 individual horizontal displacement time histories (at the dam crest), along with their mean curve. The initial displacement is approx. 13 mm, with this value also being affected by the material heterogeneity. Dispersion of curves is dominant around the peak responses.
Figure 2(b) shows maximum horizontal displacements (three at the crest level, three at the neck discontinuity, and three at the base). At each location, the static, pure dynamic and total displacements are indicated separately. Results at the neck and base are shown as a function of crest displacement, which allows comparison of the degree of uniformity along the dam height. More uniform relative response corresponds to more homogeneous (less heterogeneous) model. For a homogeneous model (E_c treated as a random variable), these data should not reveal any dispersion.
Since dispersion is difficult to quantify based on the previous plot, Figure 2(c) shows the normal distribution fitted to the normalized displacements. Note that the displacement is normalized based on the mean value assuming that it follows the normal distribution. This plot thus reveals the dispersion of the 100 simulations generated based on the random field theory. For all the static, dynamic and total displacements, the response at the crest exhibits greater dispersion than that at the neck. Among the three displacement components, total response is the most highly dispersed. Although the static and dynamic responses are similar, still the dynamic response has a slightly higher dispersion.
Figure 2(d) shows the first (maximum) principal stress time history at the dam base (i.e. heel of the dam). The mean curve is included in this plot. Two sets of horizontal lines (corresponding to DCR) have also been drawn. One DCR^{mean} = 1.0 (using $f^{mean}{}_t$ = 2.2 MPa) is shown with a dashed line, while the 100 DCR^{rand} = 1.0 lines are obtained using random sampling from a truncated normal distribution (with COV of 0.1 and bounds set at 0.25 of the mean).
Figure 2(e) and 2(f) exhibit the CID-DCR curves for the dam base (thus far the most critical point of the dam). The former curve is based on a deterministic f_t while the latter has been computed based on random f_t. The green hatched area represents the region with $DCR\langle 1$ in which no damage is expected in the dam (stress is less than concrete strength). The major observations are:
The general trend of the mean curves are very similar; however, the random f_t model indicates a more uniform curve.
The dispersion of the random f_t model is much greater than deterministic f_t.
The mean curve just slightly exceeds the PTC, which is negligible.
In the random f_t model, the mean-plus-one STD case exceeds DCR for the range up to 1.2. In some of the individual random models, the curve exceeds PTC up to DCR = 1.5; under this condition, the dam should be analysed using nonlinear models.

Figures 2(g), 2(h) and 2(i) show the DSDR-DCR curves with deterministic, random, and random field assumptions, respectively. Two important points need to be highlighted: 1) the DSDR values are calculated based on element stresses and areas and thus some approximation is introduced into element stresses based on the contribution of each node; and 2) in practically no cases does DSDR exceed DCR = 1.0. This is because the nodal stresses are averaged in the elemental level. Hence, the results between DCR (0.2, 1.0) can be presented.
Random f_t results in a lower mean curve compared to the deterministic curve, while the dispersion basically remains unchanged. On the other hand, the random field f_t model does not affect the mean curve (with respect to the deterministic curve), yet it does increase the dispersion. There is no correlation between the E_c and f_t.

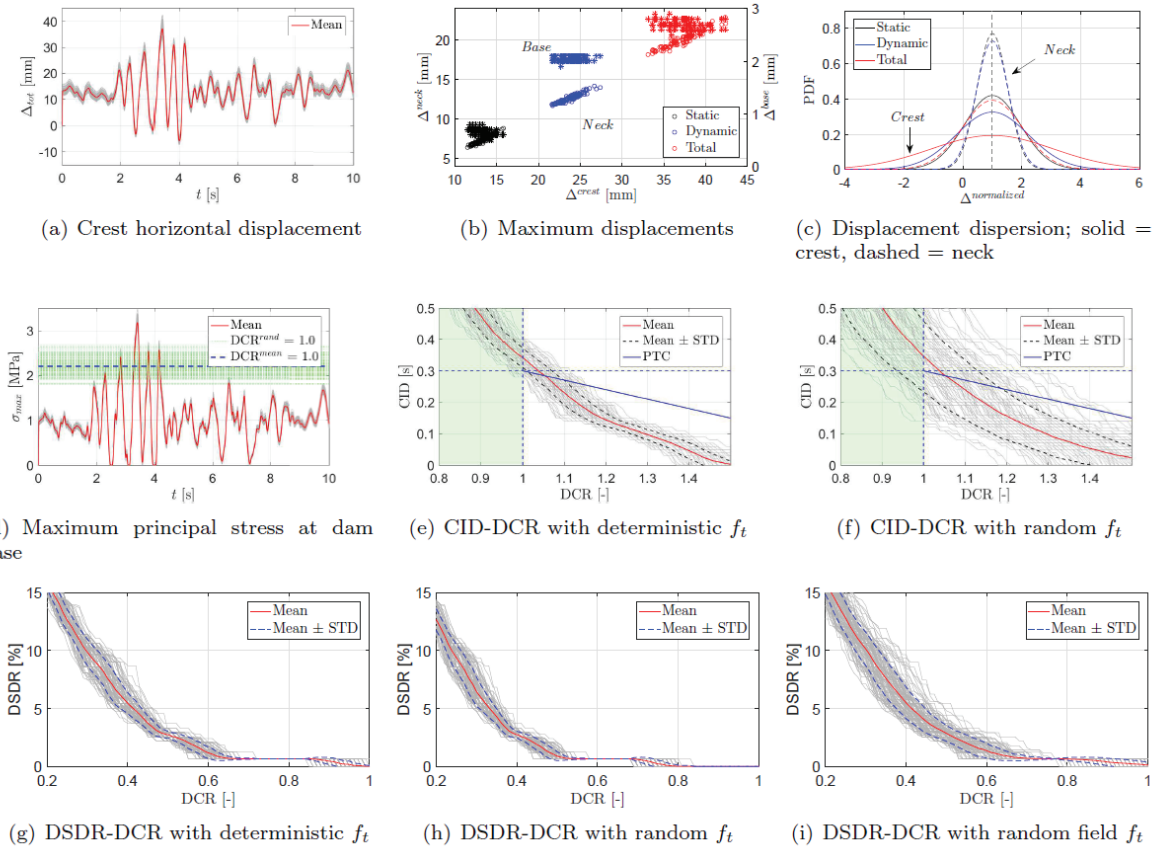

(a) Crest horizontal displacement (b) Maximum displacements (c) Displacement dispersion; solid = crest, dashed = neck

(d) Maximum principal stress at dam base (e) CID-DCR with deterministic f_t (f) CID-DCR with random f_t

(g) DSDR-DCR with deterministic f_t (h) DSDR-DCR with random f_t (i) DSDR-DCR with random field f_t

Figure 2. Anatomy of outputs from the random field simulation of a gravity dam

Impact of Spatial Correlation Length

In this section, the linear elastic analyses are performed with three heterogeneous models (l_{corr}=10, 30 and 60 m) and a homogeneous model. In all, four models are run and 100 samples drawn for each. For the heterogeneous models, the 2D distribution of E_c is shown in Figure 1. l_{corr} = 30 m indeed corresponds to the pilot model. Moreover, the comparative findings are summarized in Figure 3. Each subplot can be explained as follows:

Figure 3(a) shows the COV in displacement time history of the crest point. In general, the COV value varies between 0.05 and 0.2, yet some spikes appear at specific times. These spikes correspond to the peak displacement in the response history analyses. In the heterogeneous models, increasing the correlation length increases the COV. In the homogeneous model, the COV is nearly identical to the model with l_{corr} = 60 m.

Figures 3(b) and 3(c) display the mean and STD of the maximum displacement results at the crest and neck (the base has been neglected since its results are very small compared to the others).

Concrete heterogeneity has minimal effect on the mean displacement responses. Increasing the correlation length however increases the STD. The homogeneous model exhibits the highest STD (because it is assumed that its correlation length is infinity). A jump in STD occurs from l_{corr} 30 to 60 m.

Figure 3(d) shows the COV in the maximum (first) principal stress at the dam base with the displacement time history of the crest point. Once again, the higher correlation length increases the COV for the heterogeneous material. The homogeneous model reveals a higher dispersion and higher COV as well.

Figures 3(e) and 3(f) provide the variation in CID-DCR curves for the deterministic and random f_t models, respectively. For the deterministic f_t, the heterogeneous models have a higher COV

compared to the homogeneous model. Among each other, the model with the lower l_{corr} has a higher COV. For the random f_t model, the COV variation is more complex; it seems that for DCR< 1.15, a lower l_{corr} yields a lower COV and vice versa for DCR>1.15. For this model, no meaningful explanation can be forwarded for the homogeneous model variation (the curve associated with the homogeneous model fluctuates around the heterogeneous model outputs).

Figures 3(g), 3(h) and 3(i) show the variation in the DSDR-DCR curves for deterministic, random variable, and random field f_t models, respectively. No strict trends are evident in the deterministic and random models. In the random field model, a higher correlation length tends to increase the COV, and the homogeneous model returns the highest COV. In addition, the random field model increases the COV compared to both the deterministic and random models.

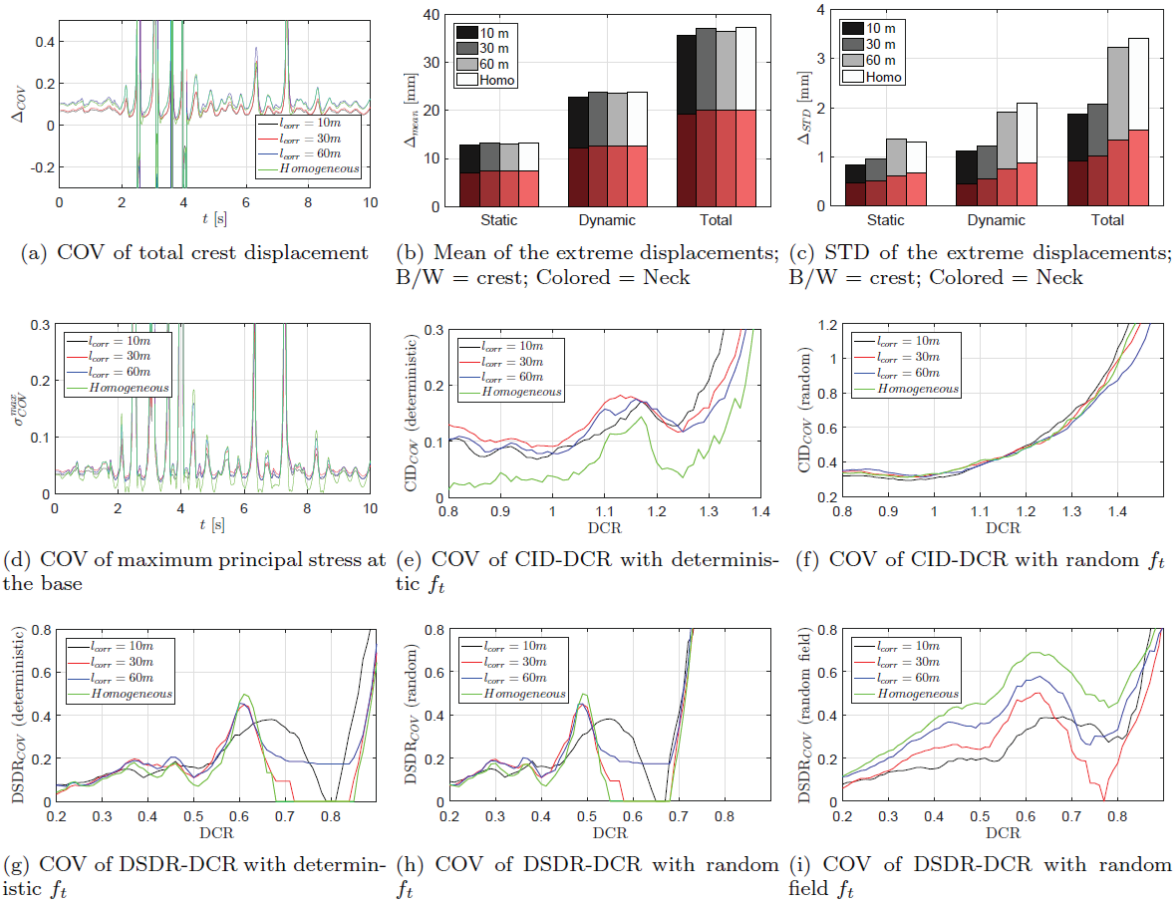

(a) COV of total crest displacement

(b) Mean of the extreme displacements; B/W = crest; Colored = Neck

(c) STD of the extreme displacements; B/W = crest; Colored = Neck

(d) COV of maximum principal stress at the base

(e) COV of CID-DCR with deterministic f_t

(f) COV of CID-DCR with random f_t

(g) COV of DSDR-DCR with deterministic f_t

(h) COV of DSDR-DCR with random f_t

(i) COV of DSDR-DCR with random field f_t

Figure 3. Impact of special correlation length on the variability of results

Impact of the Double Random Field Distribution

Thus far, all the models discussed have been based on just one random field model in the finite element simulation process (i.e. E_c). In this section, the impact of two simultaneous random fields will be investigated. The second random field is assumed to be the concrete mass density, ρ_c. An identical random field model is introduced for both parameters, in assuming a full correlation between them. The partial correlated or uncorrelated assumption may also be adopted, but such is not the subject of the present paper. Figure 4 compares the pilot model with the double random field model (both have a l_{corr} = 30 m). Each subplot can be explained as follows:

Figure 4(a) compares the displacement COV at the crest point. The double random field model exhibits a higher COV for nearly the entire time history. Under the spikes, the double random field model yields a much higher COV value.

Based on Figure 4(b), the double random field model has a higher COV. When averaged, the COV in the double random field model is twice that of the single random field model.
Figure 4(c) compares the COV resulting from the CID-DCR curves. In both the deterministic and random assumptions of f_t, the double random field distribution leads to a higher COV. Moreover, the random f_t model has a higher COV compared to the deterministic model.

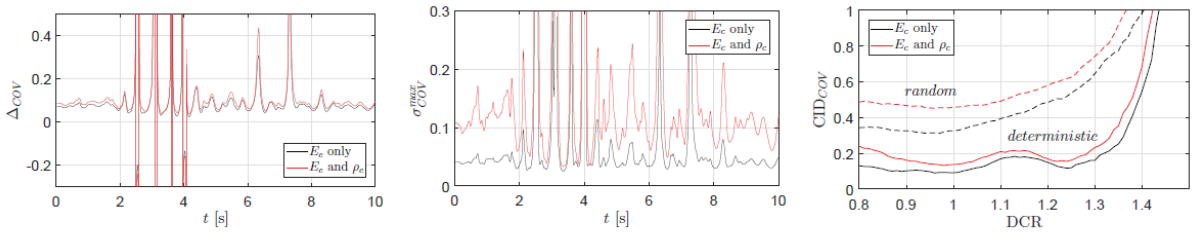

(a) COV of total crest displacement (b) COV of maximum principal stress at the base (c) COV of CID-DCR curves

Figure 4. Impact of a single- or double- random field assumption

CONCLUDING REMARKS

Overall conclusion is that the material heterogeneity is important in seismic response of the dams especially those deteriorated over the time. Detailed findings were presented in the various subsections and will not be repeated again in this section. The main findings can be summarized as follows:
Accounting for the randomness in f_t increases the dispersion of the cumulative inelastic duration curves at multiple DCR points. Subsequently, some of those curves exceed the performance threshold curve.
In the case of damage spatial distribution ratio curves, the random variable f_t model results in a lower mean compared to the deterministic model, while dispersion basically remains unchanged. On the other hand, the random field f_t model does not affect the mean (relative to the deterministic model), while it does increase dispersion.
Correlation length affects the variation in cumulative inelastic duration curves. For the deterministic f_t, heterogeneous models have a higher coefficient of variation compared to the homogeneous model. When compared among one another, the model with the lower l_{corr} has a higher coefficient of variation. As for the random variable f_t model, it appears that for demand capacity ratio less than 1.15, the lower l_{corr} has a lower coefficient of variation, and the converse is true for demand capacity ratio higher than 1.15. Moreover, for the damage spatial distribution ratio curves, the higher correlation length in the random field model increases the coefficient of variation.
It has been found that the response dispersion is also sensitive to the one- or two-dimensional spatial material distribution. In all displacement responses, stress responses, cumulative inelastic duration curves and damage spatial distribution ratio curves, the two-dimensional model leads to a higher coefficient of variation.
The dispersion in responses (either local, such as displacement and stress, or global like cumulative inelastic duration and damage spatial distribution ratio) depends on the contributing initial random fields. When assuming two random fields (even with full correlation), the coefficient of variation of the responses is considerably higher compared to the case with just one random field.
Local results (i.e. displacement and stress) are linearly proportional to the ground motion intensity measurement (both the mean and standard deviation). The global indices however are not linearly proportional to intensity measure. More specifically, the 3D surface of standard deviation - cumulative inelastic duration - intensity measure feature non-uniform patterns.

REFERENCES

[1] A. Der Kiureghian, J.-B. Ke, The stochastic Finite element method in structural reliability, Probabilistic Engineering Mechanics 3 (2) (1988) 83-91.

[2] D. Griffiths, J. Huang, G. A. Fenton, Influence of spatial variability on slope reliability using 2-D random fields, Journal of Geotechnical and Geoenvironmental Engineering 135 (10) (2009) 1367-1378.

[3] G. A. Fenton, D. V. Griffiths, Risk assessment in geotechnical engineering, Wiley, 2008.

[4] G. B. Baecher, J. T. Christian, Reliability and statistics in geotechnical engineering, John Wiley & Sons, 2005.

[5] H. Zhong, G. Lin, X. Li, J. Li, Seismic failure modeling of concrete dams considering heterogeneity of concrete, Soil Dynamics and Earthquake Engineering 31 (12) (2011) 1678{1689.

[6] M. A. Hariri-Ardebili, S. M. Seyed-Kolbadi, M. R. Kianoush, FEM-based parametric analysis of a typical gravity dam considering input excitation mechanism, Soil Dynamics and Earthquake Engineering 84 (2016) 22-43.

[7] M. A. Hariri-Ardebili, V. Saouma, K. A. Porter, Quantification of seismic potential failure modes in concrete dams, Earthquake Engineering and Structural Dynamics 45 (2016) 979-997.

[8] S. Bhattacharjee, P. Leger, Application of NLFM models to predict cracking in concrete gravity dams, ASCE Structural Engineering 120 (1994) 1255-1271.

[9] X. Tang, Y. Zhou, C. Zhang, J. Shi, Study on the heterogeneity of concrete and its failure behaviour using the equivalent probabilistic model, Journal of materials in civil engineering 23 (4) (2010) 402-413.

[10] Hariri-Ardebili, M. A., Seyed-Kolbadi, S. M., Saouma, V. E., Salamon, J., & Rajagopalan, B. (2018). Random finite element method for the seismic analysis of gravity dams. Engineering Structures, 171, 405-420.

5 DAM SAFETY
İstanbul Turkey 2018

5th International Symposium on Dam Safety

October 27-31, 2018

USING VECTOR-VALUED IMS IN PSDM OF CONCRETE DAMS

Mohammad ALEMBAGHERI [1]

ABSTRACT

In this paper, the efficiency of vector-valued intensity measures for predicting the seismic demand in gravity dams is investigated. The Folsom gravity dam-reservoir coupled system is selected and numerically analyzed under a set of two-hundred actual ground motions. First, the well-defined scalar IMs are separately investigated, then they are coupled to form two-parameter vector IMs. After that, IMs consisting of spectral acceleration at the first-mode natural period of the dam-reservoir system along with a measure of spectral shape (the ratio of spectral acceleration at a second period to the first-mode spectral acceleration value) are considered. It is attempted to determine the optimal second period by categorizing the spectral acceleration at the first-mode period of vibration. The efficiency of the proposed vector IMs are compared with scalar ones considering various structural responses as EDPs. Finally, the probabilistic seismic behavior of the dam is investigated by calculating its fragility curves employing scalar and vector IMs considering the effect of zero-response values.

Keywords: concrete dams; probabilistic seismic analysis; vector-valued; intensity measure; fragility

INTRODUCTION

In the approach of performance-based earthquake engineering (PBEE), the demand on a structure under a given earthquake should be properly estimated. To do this, the intensity of earthquake ground motion is measured by an intensity measure (IM), and the resulted structural response demanded under the earthquake is evaluated using engineering demand parameter (EDP). Then, the probability that earthquake will cause a prescribed level of demand in the structure is computed as a function of the defined IM. These probabilistic predictions of EDPs as a function of IMs can be obtained by statistical analysis of the results of nonlinear dynamic analyses under a set of earthquake ground motions (Baker, 2007). The robustness of the predictions is highly dependent on the selected IMs. Ground motion hazard models can be then combined with IM-EDP relations to compute the seismic reliability of structures.

Traditional IMs often include single-valued (scalar) parameters such as peak ground motion values or spectral responses, but it has been shown that vector-valued IMs consisting of multiple parameters of earthquake intensity may lead to better estimation (Baker and Cornell, 2004). A vector IM would contain more information about the ground motion than a scalar IM, and it has been shown that is more effective in predicting the response of building frames and bridges (Yakhchalian et al. 2015). Probabilistic seismic assessment of concrete dams using single-valued IMs has been well performed

[1] Assistant Professor, Department of Civil Engineering, Tarbiat Modares, Tehran, Iran
e-posta: alembagheri@modares.ac.ir

(Alembagheri and Ghaemian, 2013), but such study employing vector-valued IMs is very scarce. The formulation of probabilistic analysis of structures using single-valued IMs can be found elsewhere.

In this paper, application of vector-valued intensity measures for predicting the seismic demand in gravity dams is examined. For this purpose, Folsom gravity dam is selected as case-study and numerically modeled along with its full reservoir using the finite element method in an Eulerian-Lagrangian approach. A set of proper earthquake records including two-hundred actual ground motions are employed. The efficiency of the proposed vector IMs are compared with scalar ones considering various structural responses as EDPs.

VECTOR-VALUED INTENSITY MEASURES

The vector-valued IMs can increase estimation efficiency. Considering additional IM terms results in further explanation of a ground motion's effect on a structure so that the remaining unexplained statistical variability in EDP will be reduced. This means that fewer nonlinear dynamic analyses will be needed to characterize the relationship between the EDP and the IM. Multiple linear regression analysis can be performed on the cloud data with vector-valued IMs. Assuming a vector IM with two elements of IM_1 and IM_2, a linear functional form, after logarithmic transformation, can be again used to model the relationship between the mean value of EDP, $\lambda_{EDP|IM1,IM2}$, and IMs (Neter et al. 1996)

$$\ln(\lambda_{EDP|IM_1,IM_2}) = \ln\alpha_1 + \alpha_2 \ln(IM_1) + \alpha_3 \ln(IM_2) \tag{1}$$

where $\ln\alpha_1$, α_2 and α_3 are estimated coefficients obtained using multiple linear regression. The dispersion of EDP values given IM_1 and IM_2, $s_{EDP|IM1,IM2}$, can be then computed as

$$s_{EDP|IM_1,IM_2} = \sqrt{\frac{\sum_{i=1}^{N}[\ln(EDP_i \mid IM_1,IM_2) - \ln(\lambda_{EDP_i|IM_1,IM_2})]^2}{N-1}} \tag{2}$$

This method can be easily generalized to accommodate more IM parameters by simply adding additional terms to Eq. (1). Although there are some challenges with this method such as potential high correlation between adopted IMs, more extrapolations, and interaction between IM parameters, but the estimates of mean and standard deviation are obtained using low number of analyses as compared to other estimation methods.

In this study, the size of the vector IMs is limited to two parameters containing all possible dual combinations of the adopted scalar IMs. Also, a specific class of candidates is considered as potential vector IMs containing Sa(T1), which will be verified as an effective predictor of structural response for gravity dams, and a predictor $\Psi_{1,n}$= Sa(Tn)/Sa(T1) which is a measure of spectral shape. These parameters define two points on the acceleration spectrum of a ground motion. T_n is a second arbitrary period that can vary such that the value that optimally predicts the dam response is determined. The spectral shape predictor $\Psi_{1,n}$ has been shown to be a useful predictor of structural response (Cordova et al. 2000). It should be noted that the same procedure is easily applicable to vectors of a larger size.

Choosing an optimal IM is based on the criteria of efficiency (small variability of EDP for records with the same IM value), sufficiency, and ease of calculation. The adopted vector IMs are easy to calculate and familiar to many engineers. The efficiency is measured by dispersion coefficients computed from Eq. (2). The accuracy of the regression estimate using both scalar and vector IMs is increased by decreasing the standard deviation of the regression residuals or dispersion.

PROBABILISTIC SEISMIC ASSESSMENT

When a scalar IM is used, if ln(EDP|IM) is assumed to have a Gaussian distribution, then the estimated conditional probability of exceeding an EDP level edp given IM = im is computed as

$$P[EDP > edp \mid IM = im] = 1 - \Phi\left(\frac{\ln edp - \ln(\lambda_{EDP|IM})}{s_{EDP|IM}}\right) \tag{3}$$

where $\Phi(\cdot)$ is the cumulative distribution function of the standard Gaussian distribution. By plotting P[EDP>edp|IM=im] against various IM levels, the fragility curve is obtained. This prediction requires that the relationship between EDP and IM to be linear with constant variance after logarithmic transformation. This restriction may be appropriate only over a limited range of IM levels, but its advantage is reduced computational cost of the estimation.

Until now, it was assumed that EDP given IM has a lognormal distribution. However, it should be noted that the structural response of the dam may be zero under some earthquake ground motions. It is the case, for example, for the tensile damage imposed to the dam body. These zero quantities then have infinite logarithm, and they alter the estimation. So, to properly address this issue in computing the conditional probabilities, first it is required to account the probability of zero-response (ZR) parameters, through the following equation, in terms of the considered IM in the main prediction equation.

$$P[ZR \mid IM = im] = 1 - \Phi\left(im, \lambda_{ZR|IM}, s_{ZR|IM}\right) \tag{4}$$

where λZR|IM and sZR|IM are the mean and standard deviation of IM values corresponding to zero response parameters, respectively. Now the modified conditional probability is given by combining the two probabilities (Baker, 2007)

$$P[EDP > edp \mid IM = im] = (1 - P[ZR \mid IM = im]) \cdot \left(1 - \Phi\left(\frac{\ln edp - \ln(\hat{\lambda}_{EDP|IM})}{\hat{s}_{EDP|IM}}\right)\right) \tag{5}$$

where $\hat{\lambda}$ and $\hat{s}$ are sample mean and standard deviation, respectively, of the non-zero-response values. The same procedure can be employed for computing fragility curves when the vector IMs are used. Assuming that ln(EDP|IM1,IM2) is normally distributed with standard deviation of sEDP|IM1,IM2, the probability of exceeding an EDP level edp given IM = <IM_1, IM_2> and non-zero-response (NZR) values is

$$P[EDP > edp \mid IM_1 = im_1, IM_2 = im_2, NZR] = 1 - \Phi\left(\frac{\ln edp - \ln(\lambda_{EDP|IM_1,IM_2})}{s_{EDP|IM_1,IM_2}}\right) \tag{6}$$

This equation is similar to Eq. (3) used in the scalar case. The effect of zero-response values may be taken into account same as that described in Eqs. (4) and (5).

DAM MODEL AND GROUND MOTION SELECTION

The non-overflow monolith of Folsom gravity dam is chosen for the purpose of analysis. It is a well-shaped gravity dam that has been extensively studied in literature (Alembagheri, 2016). The dam is two-dimensionally modeled in plane-stress manner along with its full reservoir utilizing the finite element method, as shown in Fig. 1; the water-structure dynamic interaction is considered employing

Eulerian-Lagrangian formulation. The foundation is assumed rigid. The reservoir length is considered to be five times the dam height and non-reflecting boundary condition is assigned to its truncated far-end. The mesh has been sufficiently refined such that properly detects the nonlinear response of the dam body. The nonlinear behavior of mass concrete in tension is modeled using plastic-damage method. The stiffness degradation of mass concrete in tension, beyond its tensile strength (ft) is determined defining a tensile damage parameter (dt) which is assumed to be function of the plastic strains. This parameter can vary from zero, representing the undamaged material, to one, which represents total loss of strength. The considered constitutive behavior of mass concrete in this study is illustrated in Fig. 2. The behavior of mass concrete in compression is assumed linear. The material properties are tabulated in Table 1. They are assumed the same during static and dynamic analysis.

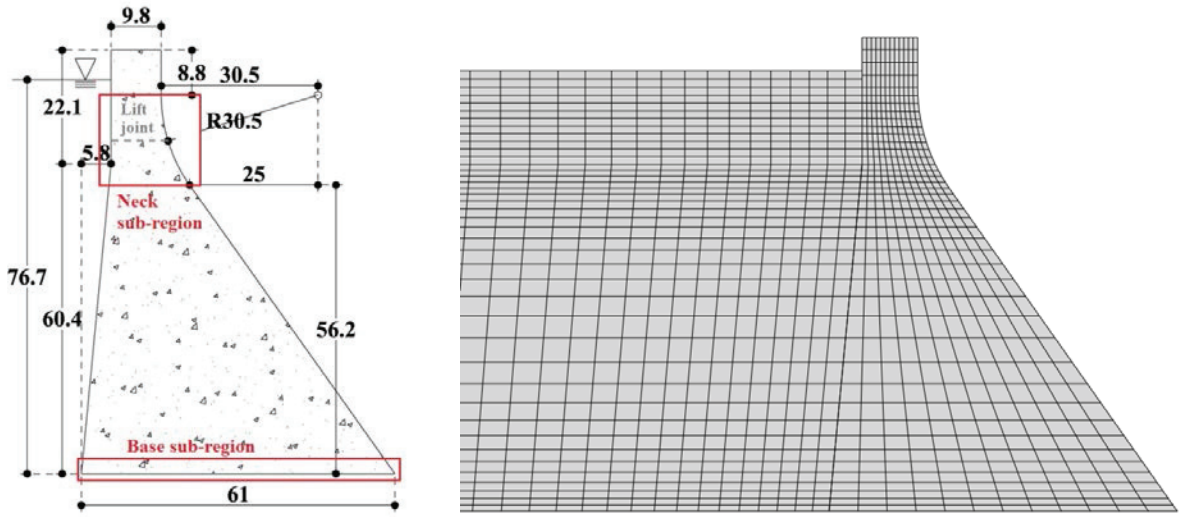

(a) **(b)**

Figure 1. (a) The tallest non-overflow monolith of Folsom gravity dam, the shown dimensions are in meters; (b) the finite element discretized mesh of the dam and part of the reservoir.

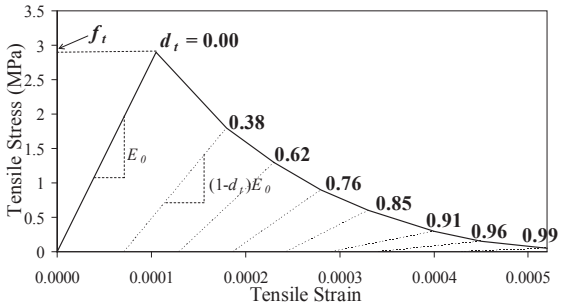

Figure 2. Stress-strain constitutive relation of dam concrete in uniaxial tension

Table 1. Material properties of dam concrete and reservoir water

Material	Property	Value
Concrete	Density (kg/m3)	2400
	Initial elastic modulus (GPa)	27.58
	Poisson's ratio	0.2
	Tensile strength (MPa)	2.9
Water	Density (kg/m3)	1000
	Bulk modulus (GPa)	2.07

The EDPs are the outcome of the nonlinear seismic finite element analysis of the dam-reservoir system. The adopted EDPs are crest maximum relative displacement (Δc), in cm, and two dimensionless local damage indices DI, from Eq. (7), which are separately calculated for the base and neck areas; they are the most susceptible areas to cracking. These areas are shown in Fig. 1(a).

$$DI_i = \frac{\int_i d_t \cdot dA_{e|i}}{\int_i dA_{e|i}} \qquad i = base\ or\ neck\ area \tag{7}$$

where $dA_{e|i}$ is the differential area of element e in area i. The summation is done on the entire area i, and shows the amount of damage that the dam may locally experience. DI_i varies between zero, showing no element cracks, to one indicating that all elements fully crack. Another EDP is defined as the energy dissipated through cracking damage process, ED, in MJ, which can be considered as a global measure of damage imposed to the dam body.

Two-hundred historical earthquake ground motions are used in the probabilistic analysis to investigate the effects of earthquake characteristics like intensity, frequency content and strong motion duration on the gravity dam's structural demands. This high number of records would lead to statistically meaningful response results. All of the records are extracted from PEER strong motion database, from the earthquake events with magnitude (M) range of 5 to 8. Their distances (R) vary between 30 to 60 km; they are recorded on ground with shear wave velocity more than 360 m/s which corresponds to rock or very dense soil class of the USGS soil classification. Gravity dams are normally constructed on such grounds. It has been attempted to avoid directivity effects by choosing records without near-fault and pulse-like characteristics. The distribution of the selected ground motions in M-R plane, shown in Fig. 3, indicates no statistical relationship between M and R. The acceleration response spectra of all 200 selected earthquake records are depicted in Fig. 4.

The dam is loaded statistically under the self-weight and the hydrostatic pressure of the full reservoir before dynamic analysis under the selected earthquake ground motions. The Rayleigh damping is employed that produce 5% critical damping in the first and third vibration modes of the coupled dam-reservoir system.

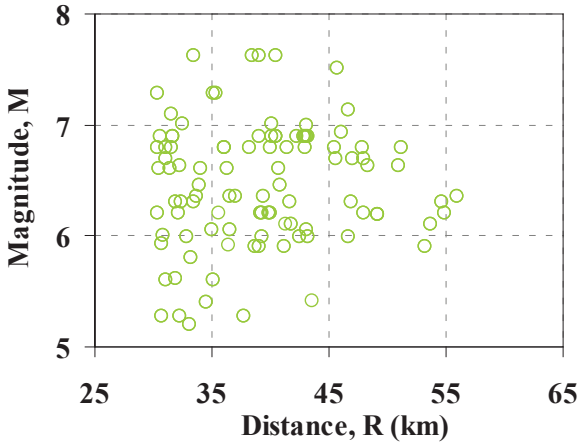

Figure 3. Distribution of the 200 earthquake ground motions in M-R plane.

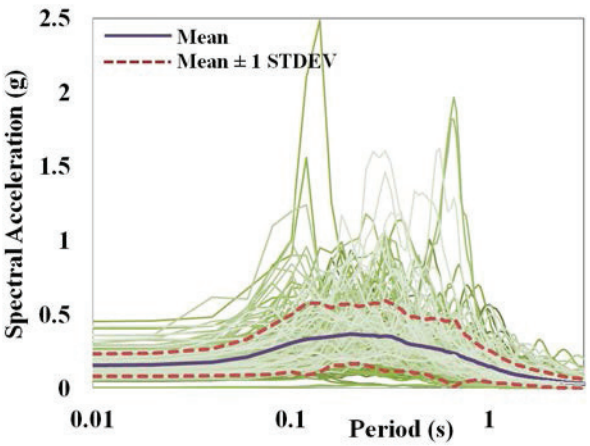

Figure 4. Acceleration response spectra of the selected earthquake records.

PREDICTION OF DAM RESPONSES

In this section, the prediction potential of the adopted IMs for various EDPs are investigated by assessing the dispersion of IM-EDP pairs considering both scalar and vector IMs; the optimal pair with the lowest dispersion is identified.

Single-valued IMs

Examples of regression of Δc as EDP are separately illustrated in Fig. 5 versus Sa(T1) and PGD as scalar IMs in logarithmic scale. Also shown are the normal distribution fits of the cloud data points in logarithmic scale. As it is observed, selecting scalar IM as Sa(T1) and PGD results in small and large residual standard deviation, respectively, which shows high and low efficiency. So, the trend in the cloud data can be clearly estimated more accurately using the Sa(T1) as single-valued IM. The calculated dispersion and goodness of fitting (R2) values for all possible IM-EDP pairs are tabulated in Table 2. From this table, the lowest variability belongs to Δc when it is coupled with various scalar IMs; DIneck shows almost the highest variability. The strong motion duration, TD, produces the largest dispersion values which shows its inefficiency in estimating the seismic demand of the dam structure, but Sa(T1) as IM has the lowest dispersion when it is considered with various EDPs. The highest R2 values also belong to the pairs with Sa(T1) as scalar IM.

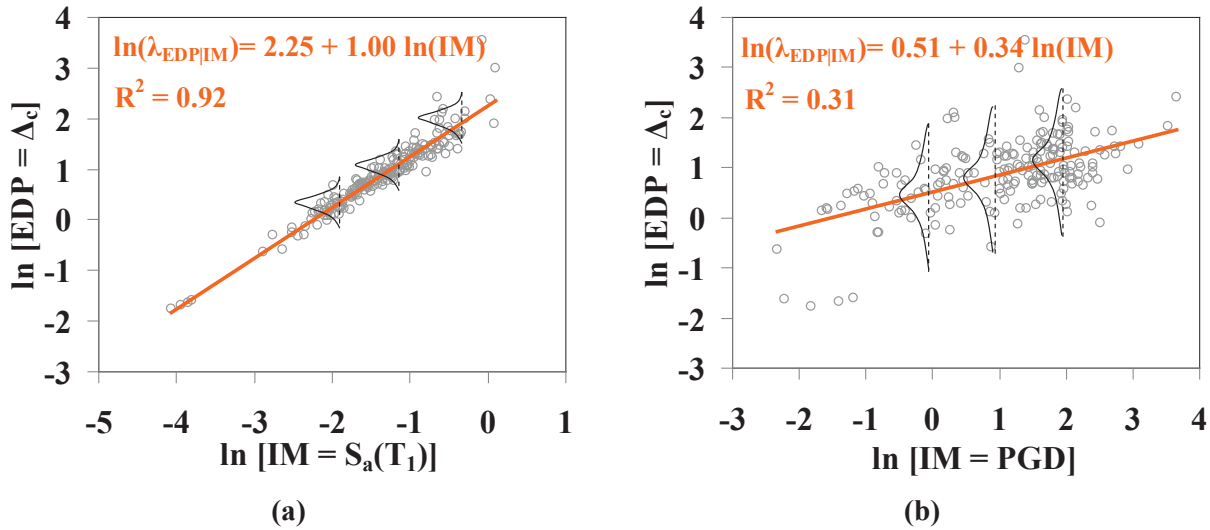

(a) (b)

Figure 5. Illustrations of estimating the conditional mean value from linear regression of ln(Δc) from cloud data: (a) IM = Sa(T1), (b) IM = PGD. The normal distribution of the data points obtained from the mean and standard deviation of the regression are also shown.

Table 2. Dispersion of EDP|IM considering single-valued IMs. The numbers in parentheses are the R2 values of the corresponding linear regressions.

Intensity Measure	Unit	Engineering Demand Parameter			
		Δc	DI_{base}	DI_{neck}	E_D
TD	sec	0.709 (0.02)	0.878 (0.01)	1.341 (0.00)	1.245 (0.01)
PGA	g	0.477 (0.55)	0.739 (0.30)	1.128 (0.29)	0.933 (0.37)
PGV	cm/s	0.467 (0.57)	0.685 (0.40)	1.214 (0.18)	0.948 (0.43)
PGD	cm	0.594 (0.31)	0.793 (0.19)	1.319 (0.03)	1.122 (0.19)
Sa(T1)	g	0.202 (0.92)	0.377 (0.82)	0.899 (0.55)	0.453 (0.87)
Sa(T2)	g	0.300 (0.82)	0.592 (0.55)	1.054 (0.38)	0.776 (0.61)
Sv(T1)	cm/s	0.595 (0.31)	0.817 (0.14)	0.797 (0.65)	1.141 (0.17)
Sd(T1)	cm	0.592 (0.31)	0.805 (0.17)	0.901 (0.55)	1.126 (0.19)

It was concluded that Sa(T1) is the best predictor between the other scalar IMs. For the 200 selected earthquake records, Sa(T1) varies between 0.017g to 1.110g. In this wide range, the dam may behave completely linear to highly nonlinear. To better assess its performance, the earthquake records are divided into four groups with the following Sa(T1) ranges: (1) 0.0-0.2g, (2) 0.2-0.4g, (3) 0.4-0.6g, and (4) more than 0.6g. It is noteworthy that in the first range, i.e. 0.0 < Sa(T1) < 0.2g, the dam responds completely linear or very slightly nonlinear without any cracking in the neck area. For Sa(T1) between 0.2-0.4g, the dam behaves moderately nonlinear, some records cause cracking in the neck area. In the third range, the nonlinear behavior extends, but when Sa(T1) is more than 0.6g, i.e. in the fourth range, the dam shows severe nonlinear response such that all records cause neck cracking. The dispersion values are re-computed considering these new ranges of Sa(T1), the results are shown in Table 3. The number of records that causes non-zero EDP values in each Sa(T1) group is also

reported in this table. The last column of the table shows the dispersion values considering all of the earthquake records. For Δc as EDP, this grouping reduces the dispersion to very small values when the dam behaves linearly to moderately nonlinear, i.e. in the first and second groups. But it increases the dispersion when the dam responds highly nonlinear in the third and fourth groups. However, the opposite trend is observed for the other EDPs that are directly related to the nonlinear response. In these cases, the dispersion decreases for higher Sa(T1) levels where the dam behaves completely nonlinear. For examples, the dispersion is decreased about 56%, 32% and 22% for DIbase, DIneck, and ED respectively, in the fourth range as compared with the entire range. So it is concluded that considering the earthquake records which are actually in (or are scaled to) the specific levels of Sa(T1), could result in lower dispersion and higher prediction potential for the gravity dam structural behavior.

Table 3. Dispersion of EDP|IM for IM as various ranges of Sa(T1). The numbers in parentheses show the number of earthquake records that cause non-zero response values in each group.

EDP	Variation range of Sa(T1)				
	0.0-0.2g	0.2-0.4g	0.4-0.6g	0.6-1.11g	0.0-1.11g
Δc	0.133 (68)	0.138 (84)	0.279 (31)	0.409 (17)	0.202 (200)
DIbase	0.376 (52)	0.271 (84)	0.201 (31)	0.165 (17)	0.377 (184)
DIneck	--- (0)	0.603 (10)	0.756 (21)	0.610 (17)	0.899 (48)
ED	0.488 (52)	0.346 (84)	0.363 (31)	0.353 (17)	0.453 (184)

Vector-valued IMs

To investigate the vector IMs, first suppose that EDP is Δc. The multiple linear regression of Δc in terms of vector IM = <Sa(T1),IM2>, in logarithmic scale, are illustratively shown in Fig. 6 separately for IM2 = PGA and PGD. The multiple linear regression for IM = <Sa(T1),PGA> would result in $\ln(\lambda_{\Delta c|Sa(T1),PGA}) = 2.38 + 0.939\ln(Sa(T1)) + 0.111\ln(PGA)$ with R2 = 0.92 and $s_{\Delta c|Sa(T1),PGA} = 0.198$. Comparing this result with the simple linear regression of $\ln(\lambda_{\Delta c|Sa(T1)})$ shown in Fig. 5(a), it is observed that both regression formula are approximately the same, with PGA contributes by low correlation coefficient of 0.111 which results in only 2% reduction in the dispersion. Choosing IM = <Sa(T1),PGD> leads to regression of $\ln(\lambda_{\Delta c|Sa(T1),PGD}) = 2.27 + 1.014\ln(Sa(T1)) - 0.009\ln(PGD)$ with R2 = 0.92 and $s_{\Delta c|Sa(T1),PGD} = 0.202$. From Table 2, PGD has low-efficient relation with Δc as EDP ($s_{\Delta c|PGD} = 0.594$), so it is observed that when one term of the vector IM has very lower correlation with EDP with respect to another term, it essentially contributes with very low coefficient in the multiple linear regression formula, and the resulted dispersion and R2 values will not be substantially affected. Considering IM = <PGA,PGD> would result in $\ln(\lambda_{\Delta c|PGA,PGD}) = 2.29 + 0.814\ln(PGA) + 0.173\ln(PGD)$ (R2 = 0.62, $s_{\Delta c|PGA,PGD} = 0.443$), so the weight of PGD is increased as the correlation of the first term, now PGA, with the selected EDP reduces.

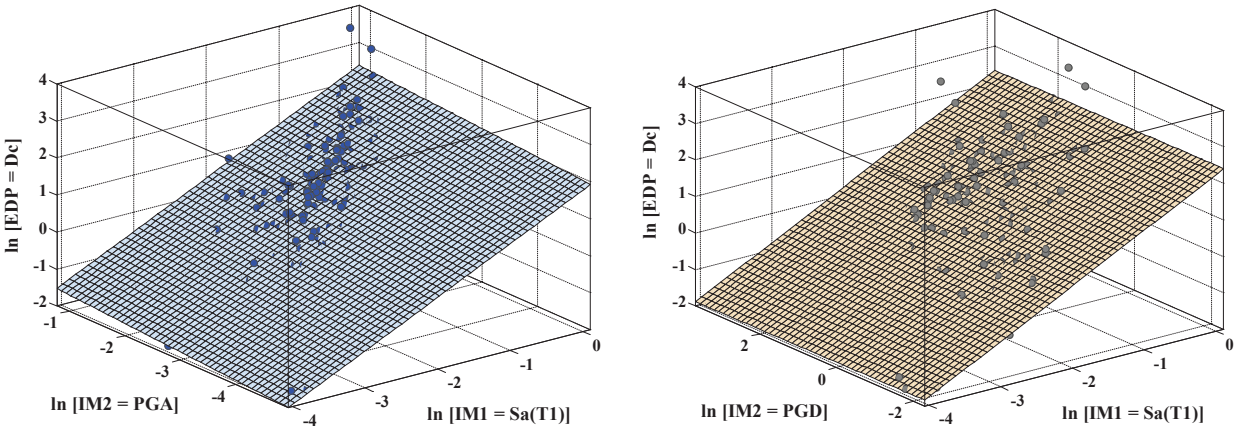

(a) **(b)**

Figure 6. Estimates of mean of ln(Δc) as a function of vector IM = < IM1 = Sa(T1) , IM2 > using multiple linear regression on the 3D cloud data: (a) IM2 = PGA, (b) IM2 = PGD.

The dispersion values for vector IMs consisting of all dual combinations of the scalar IMs are reported in Table 4 coupled with EDP = Δc and ED, and in Table 5 coupled with EDP = DIbase and DIneck. The above explanations can be again observed in these tables. Therefore, it is concluded that relative efficiency of the elements of a vector IM is a key point in their effects on the regression analysis. From Tables 4 and 5, it is observed that direct combination of scalar IMs to produce vector IMs can partly decrease the dispersion and increase the efficiency of the prediction model as compared to that obtained from more efficient component of the vector IM. The lowest dispersion belongs to vector IM = <Sa(T1),PGA>, coupled with Δc, with the value of 0.198 that shows about 2% reduction with respect to scalar IM = Sa(T1).

Table 4. Dispersion of EDP|IM1,IM2. The upper and lower triangles shows the dispersion values for the EDP as Δc and ED, respectively.

	IM2							
IM1	PGA	PGV	PGD	Sa(T1)	Sa(T2)	Sv(T1)	Sd(T1)	TD
PGA		0.414	0.443	0.198	0.297	0.451	0.445	0.463
PGV	0.881		0.457	0.202	0.295	0.434	0.437	0.463
PGD	0.936	0.939		0.202	0.300	0.520	0.522	0.573
Sa(T1)	0.455	0.452	0.452		0.201	0.202	0.202	0.203
Sa(T2)	0.773	0.738	0.766	0.441		0.297	0.296	0.301
Sv(T1)	0.969	0.912	1.044	0.454	0.776		0.594	0.592
Sd(T1)	0.955	0.909	1.036	0.454	0.771	1.099		0.590
TD	0.980	0.944	1.102	0.450	0.779	1.140	1.126	

Table 5. Dispersion of EDP|IM1,IM2. The upper and lower triangles shows the dispersion values for EDP as DIbase and DIneck, respectively.

	IM2							
IM1	PGA	PGV	PGD	Sa(T1)	Sa(T2)	Sv(T1)	Sd(T1)	TD
PGA		0.657	0.696	0.376	0.593	0.724	0.714	0.729
PGV	1.127		0.682	0.377	0.565	0.666	0.663	0.684
PGD	1.145	1.207		0.376	0.582	0.748	0.741	0.782
Sa(T1)	0.749	0.887	0.913		0.362	0.377	0.378	0.374
Sa(T2)	0.956	1.040	1.072	0.907		0.592	0.589	0.593
Sv(T1)	0.688	0.773	0.810	0.807	0.804		0.774	0.815
Sd(T1)	0.750	0.889	0.915	0.760	0.909	0.807		0.804
TD	1.146	1.211	1.330	0.912	1.054	0.805	0.914	

In the next step, the specific class of vector IMs composed of Sa(T1), which was verified as efficient predictor of dam responses, and Ψ1,n = Sa(Tn)/Sa(T1), where Tn is a second arbitrary period, is considered. The regression results are normalized to compute the fractional reduction in dispersion relative to that one obtained from the scalar IM = Sa(T1). If the fractional reduction is zero, then no efficiency is gained by including the given Ψ1,n. The optimal Tn that has the largest fractional reduction among all possible Tn values is the best choice that reduces the randomness. A plot of the fractional reduction in dispersion is shown in Fig. 7 for various EDPs. Also shown is the range of first (T1) to fifth (T5) natural periods of the dam-reservoir system. From this figure, the optimal Tn value is different for various EDPs, but it is located near or between T1-T5 range. The maximum fractional reduction in dispersion for Δc is as low as about 6%, while the reduction of 18% can be obtained for DIneck. Because the gravity dams are essentially first-mode dominated structures, the dispersion

reduction is low with respect to those obtained for building frames. The standard errors of estimation can be compared as (Baker and Cornell, 2004)

$$\frac{s_{scalar}}{\sqrt{N_{scalar}}} = \frac{s_{vector}}{\sqrt{N_{vector}}} \tag{8}$$

where Nscalar and Nvector are the number of records used in the analysis taking into account the scalar and vector IMs, respectively. So by 18% reduction in dispersion (svector = 0.82 sscalar), it is obtained that Nvector = 0.67 Nscalar. It means that by adopting more efficient vector-valued IM, the number of required records can be potentially reduced about 33%; however still maintain the same accuracy in the estimate of the mean response of the dam-reservoir system. This can lead to high reduction in computational cost.

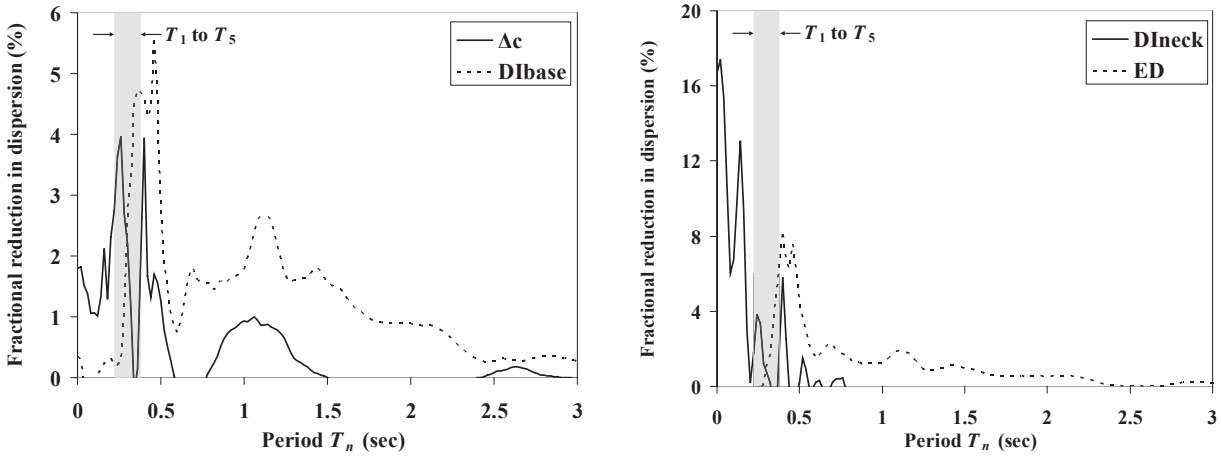

Figure 7. Fractional reduction in dispersion in terms of Tn for EDP as (a) Δc and DIbase, and (b) ED and DIneck. The first element of the vector IM is Sa(T1) and the second element is Ψ1,n = Sa(Tn)/Sa(T1).

To investigate the effects of Sa(T1) level on the obtained results, the same grouping of Sa(T1), as it was used for the scalar IM, is employed and the efficiency of including the Ψ1,n as second element of vector IM is separately assessed for each group. As a reminder, the groups of Sa(T1) levels are: (1) 0-0.2g, (2) 0.2-0.4g, (3) 0.4-0.6g, and (4) more than 0.6g. The dispersion values are computed considering the vector IM = <Sa(T1),Ψ1,n> for each group; the fractional reductions in dispersion are plotted for various EDPs in Fig. 8. Also shown is T1-T5 range of the dam-reservoir system. As it is observed, by limiting the computation in particular ranges of Sa(T1), much higher reduction in dispersion may be obtained. For 0.0 < Sa(T1) < 0.2g, since the dam stays linear or very slightly nonlinear, the reduction of dispersion is considerable just for EDP = Δc, where the optimal Tn is 0.22sec, which is the fifth-mode period of the dam-reservoir system, with approximately 15% reduction. This vector IM is comparable to the modal analysis method of estimating linear response which uses the spectral accelerations at the first and fifth modes of the system. If 0.2g < Sa(T1) < 0.4g, then the most reduction occurs for DIneck, with a significant value of 53% which corresponds to reduction of number of records by a scale of 4.5 (through Eq. 8), however, the number of records in this range of Sa(T1) which causes non-zero DIneck is just 10 records (Table 3). So the conclusion may not be very reliable. For the other EDPs the reduction is at-most below 7%.

Within the third range, i.e. 0.4g < Sa(T1) < 0.6g, the optimal Tn is located at 0.4 sec, a little more than T1, for all EDPs. In this range, most of the records cause some level of nonlinear behavior in the dam body. The highest reduction belongs to DIneck with the value of 39% which leads to 63% reduction in the number of records to obtain the same estimation accuracy when the vector-valued IM is used. For the other EDPs, if Tn varies between 0.4sec to 0.52sec, the reduction in dispersion is at least 40%

of the reduction seen at the optimal Tn. When 0.6 < Sa(T1), most of the records experience very large levels of nonlinearity, and the optimal Tn is located in a range higher than that was obtained for the third level. The maximum fractional reductions are 48%, 38%, 19% and 15% for ED, DIbase, Δc, and DIneck, respectively. Also the comparable reduction in dispersion can be obtained at a larger range of Tn as compared with other Sa(T1) groups. The dependence of Tn on the level of nonlinearity has been previously recognized for other structure types. The increase in Tn with increasing level of nonlinearity has been explained by the idea of an equivalent linear system in (Baker and Cornell, 2004).

From the above explanations, it is concluded that if Sa(T1) is low enough that few or no records cause nonlinearity, then the optimal second period Tn would be the fifth-mode period of the gravity dam-reservoir coupled system, and if Sa(T1) is large enough that most records cause nonlinear responses, then the optimal Tn would be larger than T1. Since the optimal second IM is dependent on the level of shaking or Sa(T1) value, using vector-valued IM in a fully probabilistic analysis would be more complicated, as it is required to switch IMs when integrating hazards from low to high levels.

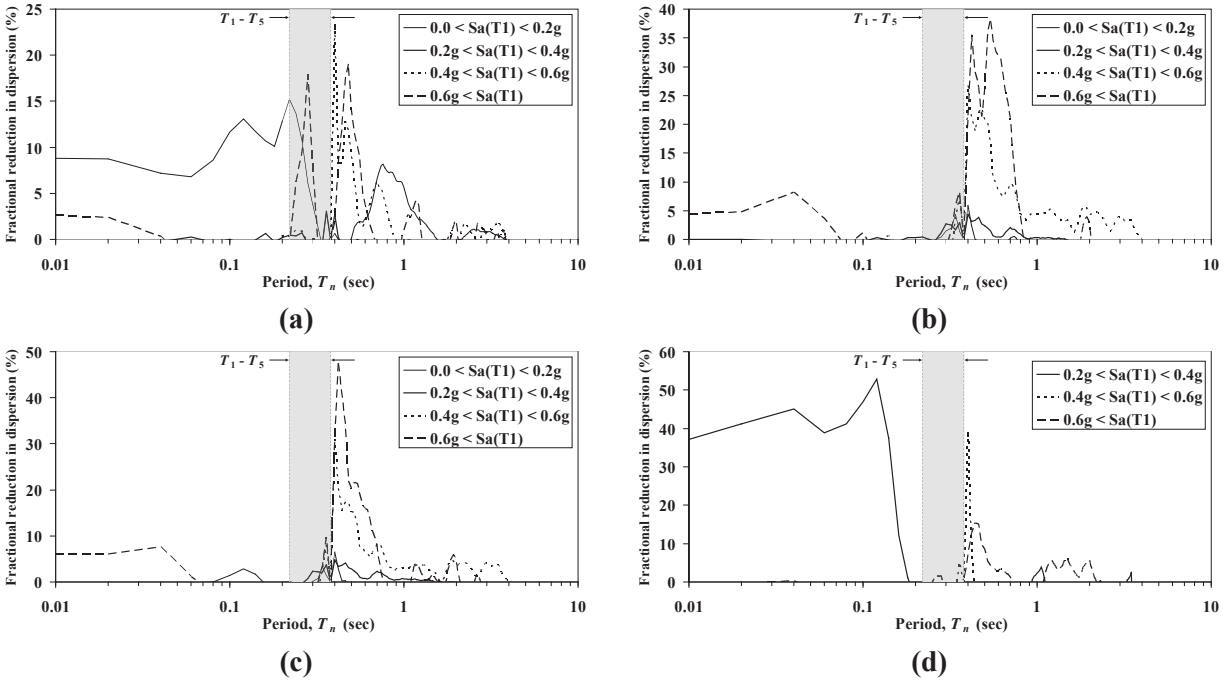

Figure 8. Fractional reduction in dispersion versus Tn for different Sa(T1) levels considering IM = <Sa(T1),Ψ1,n> : (a) EDP = Δc, (b) EDP = DIbase, (c) EDP = ED, (d) EDP = DIneck.

SEISMIC FRAGILITY CURVES

After investigating the efficiency of IM-EDP pairs considering both single- and vector-valued IMs, now the fragility functions can be computed from Eqs. (5) and (6) incorporating estimates of zero and non-zero response values at various IM levels. The actual distribution of zero response values for DIbase in terms of Sa(T1) along with the fitted cumulative standard normal distribution and the probability distribution of ZR response values obtained from Eq. (4) are shown in Fig. 9.

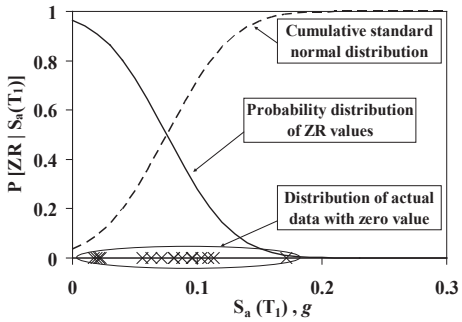

Figure 9. Actual distribution of zero response values for DIbase in terms of IM = Sa(T1) along with the fitted cumulative standard normal distribution and the probability distribution of ZR response values.

The fragility curves of DIbase ≥ 0.1, which corresponds to more than 10% base cracking, in terms of scalar IM = Sa(T1) are shown in Fig. 10 with and without considering zero-response (ZR) values. It should be noted that 16 records do not cause base cracking at all (Table 3). Because the probability of ZR values becomes actually zero for Sa(T1) > 0.2g as observed in Fig. 9, so the two curves in Fig. 10 are very close to each other.

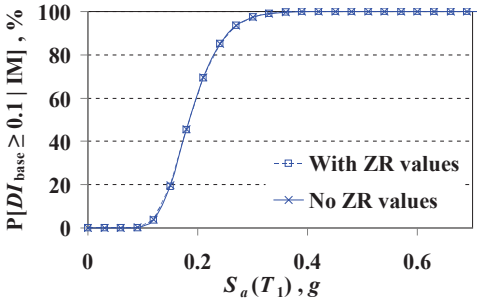

Figure 10. Fragility curve of DIbase ≥ 0.1 in terms of Sa(T1) with and without the effect of ZR values.

As another illustration, the seismic fragility curves are generated using scalar IMs = Sa(T1) and PGA, and vector IM = <Sa(T1),PGA>. They are depicted in Figs. 11(a), (b) and (c) to predict Δc ≥ 3cm, DIbase ≥ 0.1, and DIneck ≥ 0.01, respectively. The considered thresholds are subjective; their exact definition is beyond the scope of this study, however they are selected to illustratively compare the fragility curves. These fragility curves are with ZR values. There is not a large difference between the curves of the vector IM and one from scalar IM = Sa(T1), because as it was observed, considering PGA as an additional element does not essentially affect the IM-EDP relation. The ultimate goal is calculating the mean annual frequency of exceedence an EDP level from Eqs. (1) and (2). The reduction in variability is a good criterion to use vector IMs for accurate calculation. However, this calculation using vector IMs requires knowledge of vector ground motion hazard which is beyond the scope of this paper.

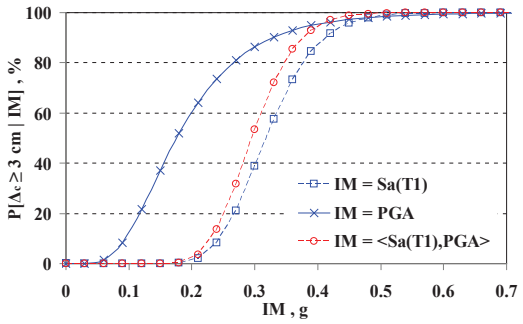

(a)

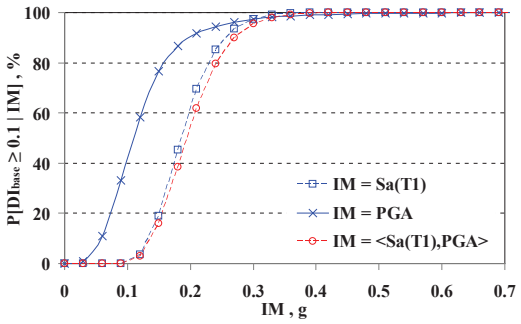

(b)

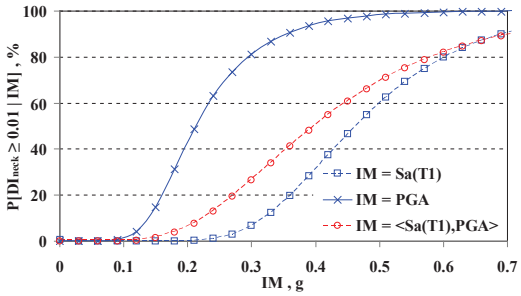

(c)

Fig. 11. Seismic fragility curves considering the scalar and vector IMs to predict: (a) Δc ≥ 3cm, (b) DIbase ≥ 0.1, and (c) DIneck ≥ 0.01

CONCLUSIONS

Application of vector-valued intensity measures for predicting the seismic demand in gravity dams was studied by numerical analysis of Folsom gravity dam-reservoir coupled system under a set of two-hundred actual ground motions. The efficiency of the defined IMs was examined through dispersion of IM-EDP pairs. Considering different well-established scalar IMs showed that the strong motion duration produces very high dispersion values, but Sa(T1) has the lowest dispersion when it is considered with various EDPs. It was found that categorizing Sa(T1) in specific levels could result in lower dispersion and higher accuracy of the prediction model.

Direct combination of the scalar IMs to produce two-parameter vector IMs showed that relative efficiency of the elements of the vector IM is a key point in their effects on the regression analysis. This type of vector IMs partly decrease the dispersion and increase the efficiency of the prediction model as compared to that obtained from more efficient component of the vector IM. Considering a specific class of vector IMs composed of spectral acceleration at the first-mode natural period of the dam-reservoir system along with a measure of spectral shape (the ratio of spectral acceleration at a second period to the first-mode spectral acceleration value), it was found that lower dispersion values with respect to the most-efficient scalar IM, i.e. Sa(T1), can be obtained. The optimal second period is different for various EDPs, but it is located near the range of the first to fifth natural period of the system. It was observed that by limiting the computation in particular ranges of Sa(T1), much higher reduction in dispersion may be obtained, however the optimal second period is dependent on the level of nonlinearity. If Sa(T1) is low enough that few or no records cause nonlinearity, then the optimal second period would be the fifth-mode period of the gravity dam-reservoir coupled system, and if Sa(T1) is large enough that most records cause nonlinear responses, then the optimal second period would be larger than T1. Finally, the probabilistic seismic performance of the dam was investigated by calculating its fragility curves employing scalar and vector IMs incorporating estimates of zero and non-zero response values.

REFERENCES

Baker, J.W., 2007. "Probabilistic structural response assessment using vector measures". Earthquake Engineering and Structural Dynamics, vol. 36, pp. 1861-1883.

Baker, J.W., Cornell, C.A., 2004. "Choice of a vector of ground motion intensity measures for seismic demand hazard analysis." 13th World Conference on Earthquake Engineering (No. 3384).

Yakhchalian, M., Nicknam, A., Amiri, G.G. 2015. "Optimal vector-valued intensity measure for seismic collapse assessment of structures". Earthquake Engineering and Engineering Vibration vol. 14, pp. 37-54.

Alembagheri, M., Ghaemian, M., 2013. “Incremental dynamic analysis of concrete gravity dams including base and lift joints”. Earthquake Engineering and Engineering Vibration vol. 12, pp. 119-134.

Neter, J., Kutner, M.H., Nachtsheim, C.J., Wasserman, W., 1996. “Applied Linear Statistical Models”. 4th ed. Boston: McGraw-Hill.

Cordova, P.P., Deierlein, G.G., Mehanny, S.S., Cornell, C.A., “Development of a two-parameter seismic intensity measure and probabilistic assessment procedure”. The Second US-Japan Workshop on Performance-Based Earthquake Engineering Methodology for Reinforced Concrete Building Structures, pp. 187-206.

Alembagheri, M., 2016. “Earthquake damage estimation of concrete gravity dams using linear analysis and empirical failure criteria.” Soil Dynamics and Structural Dynamics vol. 90, pp. 327-339.

COMPARISON OF PHYSICAL MODELING AND CFD SIMULATION OF FLOW OVER SPILLWAY IN THE ARKUN DAM

Muhammed UÇAR[1], Şerife YURDAGÜL KUMCU[2]

ABSTRACT

The Arkun Dam spillway and HEPP, located on the Çoruh River in north east of Turkey, was selected to conduct the comparison for hydraulic characteristics. This dam is planned and built to produce 780 GWh energy per year with 245 MW installed capacity. The experiments with 1/60-scaled physical model set up in Hydraulic Laboratory of State Hydraulic Works in Turkey. 130 m high dam body consists of earthfill structure and front side concrete cover. Gated ogee spillway chute is located on the dam body with 36 m width and 18.61 m design head for PMF discharge of 4570 m³/s. Flip bucket energy dissipater was selected at the end of the chute in order to control of water jet drop location and prevention of downstream erosion. Flow depth, discharge rate and pressure data were recorded for different flow conditions. The measuring devices utilized in the physical experiment were; ultrasonic flow meter for discharges, pressure measuring points for pressure, limnimeter for flow depth and Micro-Muline for velocity. Significant modifications were made on the original project with the experimental study. A comparative study was done in the study, so as to evaluate the compatibility of the computational fluid dynamics on modeling spillway flow. To compare the results of the physical model and the numerical model, discharge rating curves and pressures were compared. The reasonably good agreement of numerical models with the physical model in flow characteristics is shown.

Keywords: CFD, numerical modeling, spillway design, experimental hydraulics.

INTRODUCTION

Spillways design has always been one of the most leading parts of hydraulic engineering. To avoid overtopping and dam failure resulting casualties at the downstream, the spillway have to be designed for suitable discharges and according geometrical properties. Thus, the relationship between reservoir water level and the spillway discharge capacity named as discharge rating curve is utilized, basically. The curve also illustrates the gate opening ratios and discharge capabilities as a guide for power generation operation. The existing analytical formula with a fairly high degree of accuracy for simple geometries notwithstanding, complex geometries needs more accurate approaches. Physical model studies, provide almost excellent solutions within a range of scale limitations, are one of the widely

[1] Research Assistant, Department of Civil Engineering, Necmettin Erbakan University, Konya, Turkey, e-posta: muhammed.ucar.itulu@gmail.com

[2] Assoc. Professor, Department of Civil Engineering, Necmettin Erbakan University, Konya, Turkey, e-posta: yurdagulkumcu@gmail.com

used and safe way to obtain realistic results. However, the physical model has some disadvantages such as high costs and long construction durations. The alternative of the physical model is raised with developing technology in recent decades: computational fluid dynamics (CFD). The CFD codes are being developed to estimate complex fluid flow patterns accurately in the place of physical models. CFD technique has plausible results and relatively economical for most of the cases, nonetheless, reliability of the simulations for each type of cases needs evaluation before the employment in the construction. This is highly depending on both the competence and accurate utilization of the codes. It is necessary to obtain experimental data comparisons with analytical solutions and similar works to validate the numerical simulation results. Jacobsen and Olsen reported that the codes have been used for many fluid mechanics disciplines for more than 20 years as a standard tool such as for mechanical and aerospace engineering (2010). However, the method has not yet gained acceptance totally and being used for auxiliary tool to lessen the time and cost of the physical models. To lessen the need of physical modeling, the codes need to be improved and validated on a number of cases.

However lots of commercially available CFD packages defining the flow domain and boundary conditions with the same logic, the codes computing the mathematical expressions of the real sophisticated physical problems variously. Yet, most of the commercially available codes based on similar procedure: non-orthogonal unstructured grids with finite volume models, numbers of turbulence models and implicit multi grid solvers. Flow-3D has a distinction among the CFD codes, with having the orthogonal structured grid. Structured rectangular prism grid structure can be distributed relative to the need of the concentration, turns back to the user as more flexibility. Jacobsen and Olsen states that the volume-of-fluid method and fixed grid very well suits for the computation of geometrically complex free surface flows, even for hydraulic jumps. Hence, Flow-3D is one of the best spillway modeling code (2010). In order to compare the flow patterns over a standard ogee-crested spillway between physical model test results and CFD results, Savage and Johnson (2001) utilized Flow 3D. Kim and Park (2005) also investigated the flow structure over ogee spillway considering scale and roughness effects with the code. Usta (2014) utilized Flow-3D to check the reliability of the code with making comparison with Laleli dam spillway physical model.

This study is made on the comparison of the hydraulically methodologies, numerical and physical. Flow-3D is utilized for the numerical investigation, which solves the Reynolds-averaged Navier-Stokes (RANS) equations. Grid cells, which occupy computational space, are defined for just the surrounding area of the spillway and the approach channel. To make the comparison between the results of the physical model and the numerical model; discharge rating curves, velocity patterns and pressures were used. During the experimental study, many modifications have been made to facilitate smooth streamlines and to prevent destructive irregularities (Uyukluoglu, 2011). There is reasonably good agreement between the physical and numerical models in flow characteristics.

MATERIAL AND METHODS

Physical experiment

Arkun Dam spillway and flip bucket is physically tested at the Hydraulic Model Laboratory of State Hydraulic Works of Turkey (DSI) with a 1/60-scaled physical model. Construction materials of the model are selected as Plexiglas and conventional building materials as usual. The spillway has 36 m discharge channel in width with 3 gates at chute. Discharge channel has inclination of 14%. Ultrasonic flow meter is being used for measurements of discharge rates and Micro-Muline for flow velocities. Water surface profiles were measured by using a limnimeter with a scale to the nearest 0.1 mm. Pressures were measured using a piezometers board provided the average pressure reading at each pressure tap location. The piezometric heads were measured at the central axis of the spillway chute and flip bucket to check the cavitation risk (Uyukluoglu, 2011).

In order to investigate the flow characteristics and to evaluate the cavitation risk; flow depths, the pressures and flow rates were measured at various distances from the spillway crest (Km: 0+000.00). The model was operated for PMF=4570 m^3/s and belonging upstream reservoir elevation of 938.61 m. And also an alternative discharge is being used to observe the spillway characteristics under low discharge rates, that is 1523 m^3/s and having upstream reservoir elevation of 928.90 m.

Figure 1. General overview of the 1/60-scaled physical model (Uyukluoglu, 2011)

The cavitation is physically depended on the vapor pressure, the case occurs when the flow pressure is dropped under the vapor pressure anywhere of the spillway. The result is the vaporization of the water, seems like if it is boiling (Wagner, 1967). Due to the lack of bubbles escape probability under this type of physical condition, implosion occurs. The collapse of the bubbles provokes generation of the pressures fluctuations, high amount of vibrations and noise; the consequence is the structure failure (Vischer and Hager, 1997). The cavitation formation concurs flood time and the failure expands and hits to the downstream towns, meaning heavy loss. The risk of cavitation is checked by the amount of cavitation number formulated by the following equation.

$$\sigma = \frac{P - Pv}{\frac{1}{2}\rho U^2} \tag{1}$$

where; σ is the dimensionless cavitation number; P is the absolute pressure (N/m^2); P_v is the vapor pressure of the fluid (N/m^2); ρ is the fluid density (kg/m^3) and U is mean flow velocity (m/s). The critical cavitation number is the limit of the cavitation propagation (Kokpinar and Gogus, 2002). Falvey (1990) states that the critical cavitation number is σ =0.2, and cavitation will occur if σ<0.2.

To take precaution for the cases of cavitation risks, the structure of aeration devices is being utilized to channel air into flow naturally by the negative pressure. The devices, designed to deflect high velocity flow from the concrete surface and let to drop and dissipate energy, are located to the upstream of the first high risk location where the cavitation can be propagated. The devices positioned on the bottom of discharge channel with or without distribution duct and also positioned on the water contacting surfaces of the sidewalls of the structure (Chanson, 2002; Chanson, 2005).

The pressures on the spillway model measured and the calculations revealed that there is no risk of cavitation along the spillway. Some approach channel modifications were done to have uniform flow conditions among the structure (Uyukluoglu, 2011). Physical Model studies finalized after the observation of final design flow conditions on the spillway (Figure 2).

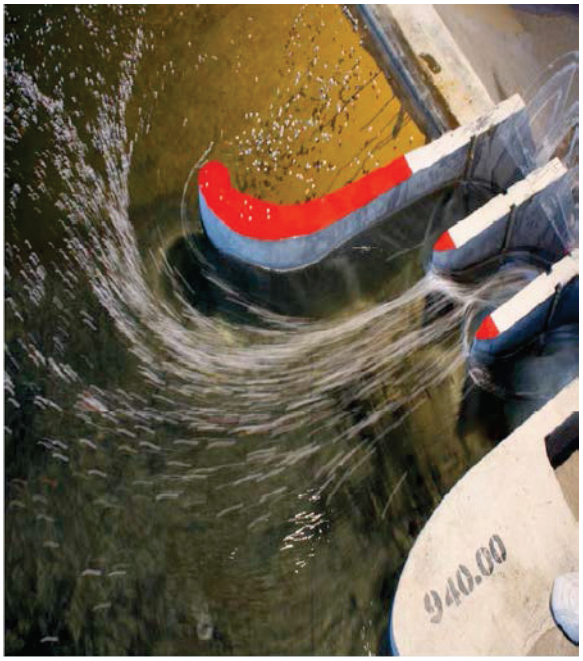

Figure 2. Streamlines and the Modifications (red) of the approach condition (Uyukluoglu, 2011)

Numerical Simulation

A special field of study of computer-based simulation techniques is named CFD serves for the researchers and practitioner of fluid mechanics. The method uses accepted flow equations such as the Navier- Stokes and continuity equations by discretization of the domain and solving the equations for each computational cell. Flow-3D uses the finite-volume method to solve the RANS equations. Computational domain is divided rectangular grid cells, called meshes, to facilitate the computation in every small part, named control volumes, to enhance the accuracy.

Volume of fluid method developed by Dr. Tony Hirt, has a systematic approach to advect fluid interfaces through a computational grid while keeping the interface sharp and well defined. Hirt and Sicilian (1985) improved the FAVOR method; Fractional Area/Volume Obstacle Representation, describing the obstructions while using the similar approach of VOF. The method is served for the definition of this study also. FAVOR method matches with the VOF method in the sense of description of cells that are empty, full, or partially filled with fluid.

To be able to define the computational environment, solid model of the dam is created by using AutoCAD-3D. After the 3D model is prepared, solid model of Arkun dam spillway are exported as the stereo lithographic (.stl) file format which is a common manner of users of Flow-3D. Arkun dam spillway solid model is presented in the Figure 3.

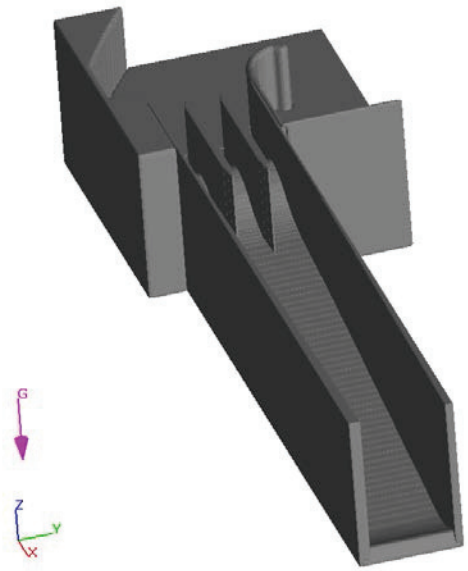

Figure 3: Arkun Dam Spillway solid model used in the CFD simulations

Flow-3D contains optional physical models describing the effects of turbulence, sediment scour, heat transfer, fluid solidification, surface tension, granular flows, moving solids, Lagrangian particles, solid deformation, cavitation, porous media and air entrainment. These additional items are derived as added to or modified the basic Navier-Stokes equations.

Flow-3D contains five turbulence models; the Prandtl mixing length model, the one-equation, the two equation k - ε and RNG models, and a large eddy simulation (LES) model. Renormalization group turbulence model is used in the study which solves the same equations with the k - ε model. Besides, constants of turbulence equations derived explicitly in the RNG model while standard k – ε model has empirical formation. Having said that, the RNG model is known to characterize the low intensity turbulence flows having strong shear regions, more accurately (Flow-3D User Manual). Physics tab is utilized to activate the turbulence model.

Main numerical parameters of the model setup are written in the Table 1.

Table 1. Main numerical parameters used in FLOW-3D

Option	Set up	Parameter
Fluid	Incompressible	ICMPRS=0
Viscosity	Newtonian fluid	IFVISC=1
Turbulence	Renormalized Group (RNG)	IFVIS=4
Pressure solver	General Minimal Residual (GMRES)	IGMRES=1
Momentum advection	First-order, upwind explicit scheme	IMPADV=0, IORDER=1
VOF advection method	Standard method (One Fluid Free Surface)	IFVOF=4
Time step control	Automatic	AUTOT=1

Two rectangular uniform grids with the mesh sizes as 0.5 meters (mesh block-1, MB1) and 1 meter (mesh block-2, MB2) are positioned concerning the relative significance. Total number of grid cells is approximately 5.127E+06.

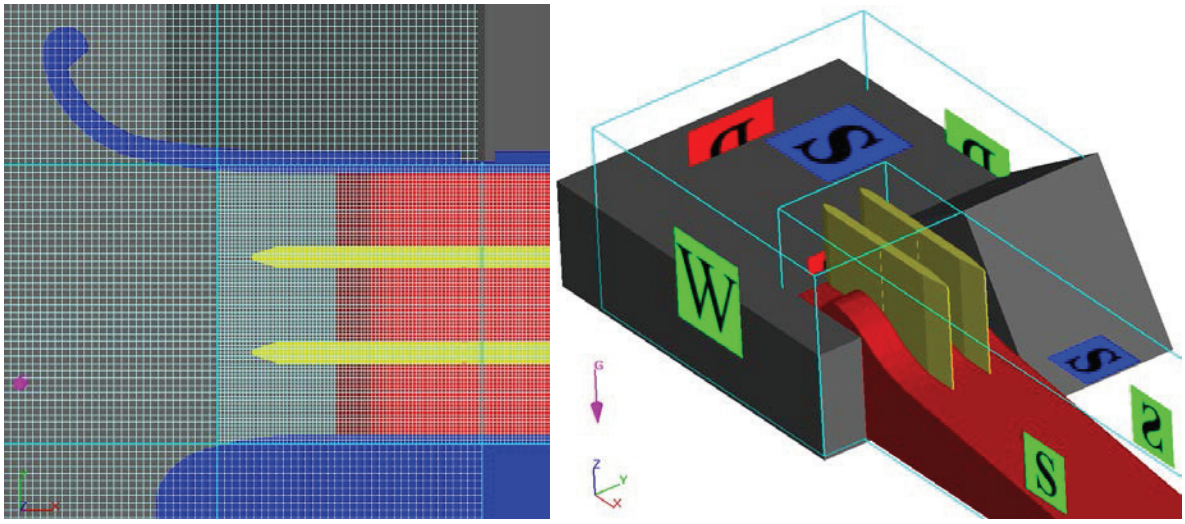

Figure 4: Mesh distribution of the Arkun Dam Spillway and boundary conditions.

Cartesian coordinate mesh has a natural characterization as having six different boundaries. As it is mentioned above and shown in the figure 4, overlapped two mesh blocks are used to model the spillway. While there are ten types of boundary conditions provided in the code, just the four types are implemented. Boundary conditions of the overlapping boundaries must be fixed as symmetry axis, thus MB1 x-min, y-min and y-max and MB2 x-max is arranged as symmetry axis. MB2 x-min & y-max are arranged as specified pressure, meaning the stagnation pressure attached to upstream reservoir level. The remaining boundaries can be read from table 2.

Table 2. Mesh block boundary conditions used in FLOW-3D

	Size	X-min	X-max	Y-min	Y-max	Z-min	Z-max
MB1	0,5 m	Symmetry	Outflow	Symmetry	Symmetry	Symmetry	Symmetry
MB2	1,0 m	Specified pressure	Symmetry	Wall	Specified pressure	Symmetry	Symmetry

DISCUSSION OF RESULTS

The flow rates over the spillway crest, free surface elevations, depth-averaged velocity distributions, and the pressures are the main comparison tool used between the physical model and the CFD model.

Flow rates of physical model (Q_{PM}) and the CFD model flow rates (Q_{CFD}) are stated in Table 3. Results are normalized to ease the evaluation. Probable Maximum Flood (PMF) parameters are noted as $(H_0)_{PMF}$=18.61 m and Q_{PMF}=4570 m^3/s. The discharge Q is normalized by Q_{PMF} and shown on the ordinate. Static head above crest, H_0, is normalized by the $(H_0)_{PMF}$ and shown in the abscissa in Figure 5. The relative percent difference in discharge for the relative percent difference $(H_0)/(H_0)_{PMF}$ is defined as $(Q_{CFD}- Q_{PM})/Q_{PM}$ $x100$. Table 3 shows the CFD model compatibility of discharge rate estimation.

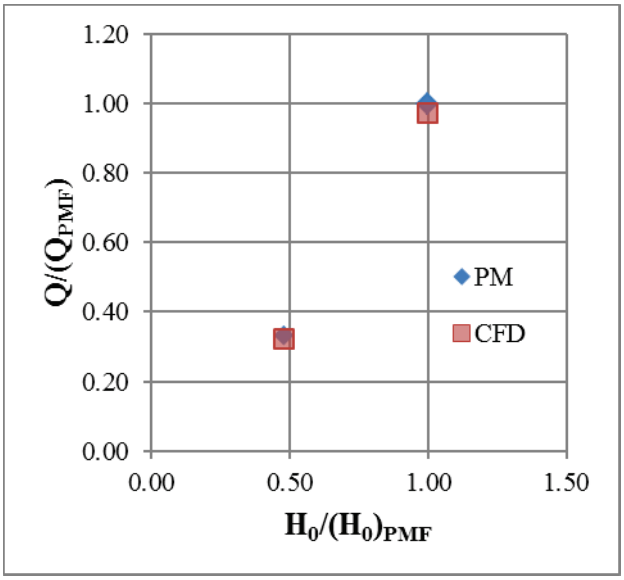

Figure 5: Normalized parameters of physical model (PM) and the numerical model (CFD) predictions

Table 3: Measured flow rate (scaled to prototype) versus computed flow rate

Q_{PM} (m^3/s)	Q_{CFD} (m^3/s)	Difference (m^3/s)	Percent Difference
1523	1477	46	3.02 %
4570	4440	130	2.85 %

Figure 6 shows the water surface profiles results of both the mathematical simulation and physical model observations for Q_{PMF}=4570 m^3/s. It is seen that, simulation gives reasonably good agreement for a given discharge and distance from the spillway crest. This means that, numerical solution can also be utilized as an alternative solution of water depth measurements.

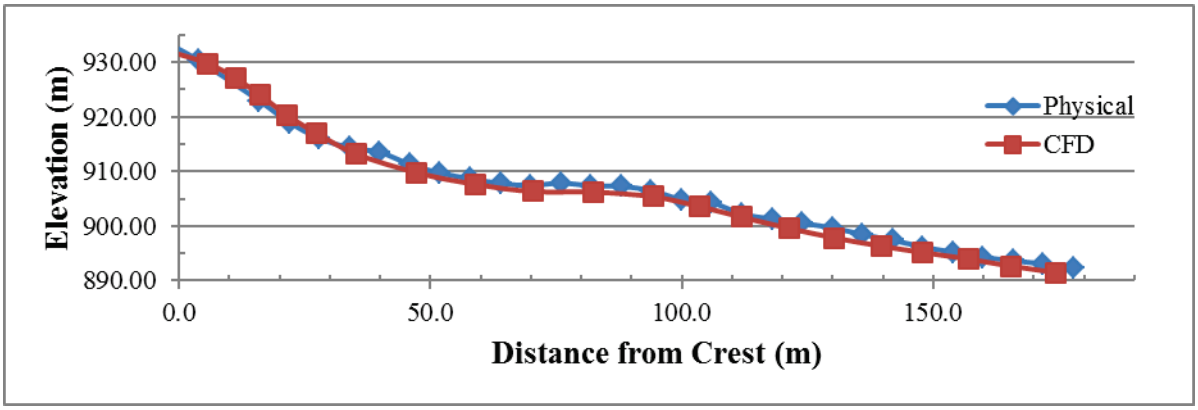

Figure 6: Water surface profiles of mathematical simulation and physical model observations for Q_{PMF}=4570 m^3/s.

Depth-averaged velocity for Q_{PMF} for CFD result and physical experiment comparison is illustrated in Figure 7, which is notably unacceptable. This can be explained by the insufficiency of mesh grid size, 0.5 meters mesh size is not proficient to estimate velocity. On the other hand, remaining results with the same size mesh were much more efficient than the velocity estimation.

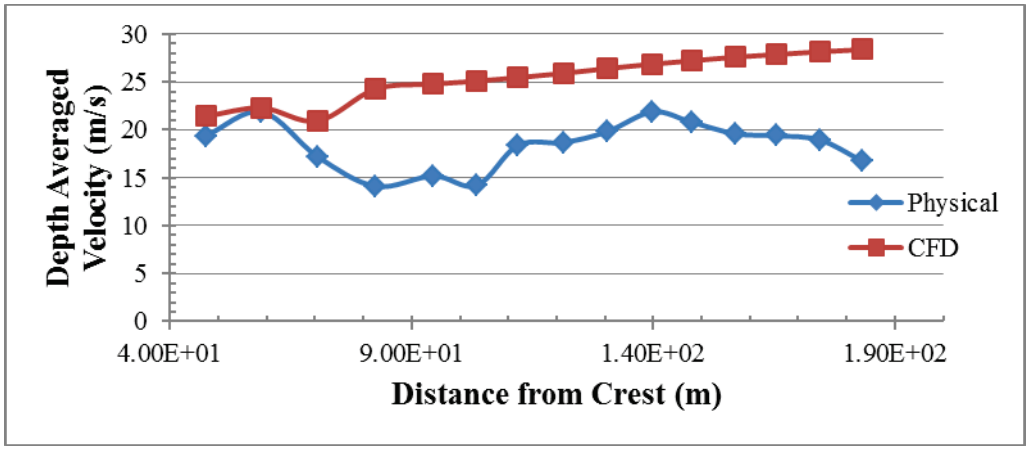

Figure 7: Depth-averaged velocity distribution for Q_{PMF}=4570 m^3/s

Table 4 shows the CFD model compatibility of pressure estimation. Averaged relative percent difference 7.6 %.

Table 4: Pressure comparison, physical (scaled to prototype) versus computed

Dist. From Crest (m)	P_{PM} (m)	P_{CFD} (m)	Difference (m)	Percent Difference
47.36	5.77	5.61	-0.16	2.9%
58.92	5.30	5.73	0.43	7.6%
70.48	5.51	6.45	0.94	14.5%
82.47	5.96	6.33	0.37	5.9%
94.46	5.86	6.45	0.59	9.2%
103.46	5.73	6.81	1.08	15.9%
112.01	5.85	5.43	-0.42	7.7%
121.43	5.41	6.39	0.98	15.3%
130.42	5.14	5.01	-0.13	2.6%
139.84	5.04	5.55	0.51	9.2%
147.97	4.68	4.35	-0.33	7.6%
156.96	4.77	4.77	0.00	0.0%
165.52	4.81	4.89	0.08	1.6%

Figure 8 demonstrates the pressure head distributions along the spillway surface, accepting the horizontal distance starting from the crest axis. Spillway average pressures for Q_{PMF}=4570 m^3/s presented to be compared.

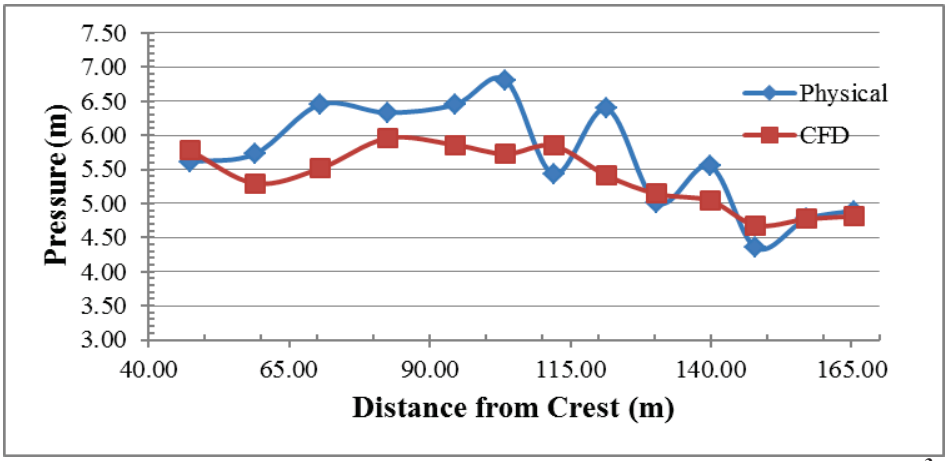

Figure 8: Comparison of CFD and physical model pressures for Q=4570 m^3/s.

CONCLUSIONS

As in hydraulic design, numerical modeling is raising in the field of engineering design disciplines. The numerical simulations providing a cost and time effective alternative to physical modeling with having the flexibility in studying in different conditions with more detailed hydraulic character information, nevertheless verification is needed. Having said that the CFD tools still have some limitations such as long run times, and numerical instabilities. Moreover the codes need proper usage, vital to select an appropriate mesh size and distribution, initial and boundary conditions for an accurate numerical solution.

The absolute percent differences between physical modeling and CFD simulation results in discharge estimation for Q_{PM} and Q_{CFD} are found very close to each other. Results showed that the CFD model gained a validation for this type of problems for discharge rate estimation within a range of 2.93 % for the average relative percent difference between the CFD model and the physical model.

Pressure comparison also showed that the code computes the pressure within averaged 7.6 % range, which is also acceptable. Velocity profile computation was insufficient. One can claim to clarify the key of the solution as the inadequateness of the mesh size, nevertheless, the code performed better estimations relative to the velocity results.

Even though numerical methods supplied continuously with increasing accuracy, it is needed to be emphasize that the physical model studies are still the benchmark of all alternative solution methods

REFERENCES

Chanson, H., Gonzalez, C.A., 2005. “Physical Modeling and Scale Effects of Air-Water Flows On Stepped Spillways”. J. Univ. SCI, 6A, 3,pp. 243–250.

Chanson, H., 2002. “The Hydraulics of Stepped Chutes and Spillways”. Balkema, Lisse, The Netherlands.

Falvey, H.T., 1990. “Cavitation in Chutes And Spillways”. Engineering Monograph 42, Water Resources Technical Publication, US Printing Office, Bureau of Reclamation, Denver.

Flow 3D, 2012. User Manual.

Hirt, C., Sicilian, J., 1985. "A Porosity Technique for the Definition of Obstacles in Rectangular Cell Meshes." Proc., Fourth Int. Conf. Ship Hydro., National Academy of Science, Washington, DC, USA.

Jacobsen, J, Msc., Olsen, N.R.B., Dr Ing., 2010. Proceedings of the Institution of Civil Engineers: Water Management; London Vol. 163, Iss. 6, pp. 283-288.

Kim, D.G., Park, J.H., 2005. “Analysis Of Flow Structure Over Ogee-Spillway In Consideration Of Scale And Roughness Effects By Using CFD Model”. Journal Of Civil Engineering, KSCE, Vol. 9, No. 2., pp. 161-169.

Kokpinar, M.A., Gogus, M., 2002. “High Speed Jet Flows Over Spillway Aerators”. Can. J. Civ. Eng. 29, pp. 885–898.

Savage, B.M., Johnson, M.C., 2001. “Flow Over Ogee Spillway: Physical and Numerical Model Case Study”. J. Hydraul. Eng. 127, (8), pp. 640–649.

Wagner, W.E., 1967. “Glen Canyon Diversion Tunnel Outlets”. J. Hydraul Div. ASCE, 93, (HY6), pp. 113–134.

Usta, E., 2014. “Numerical Investigation of Hydraulic Characteristics of Laleli Dam Spillway and Comparison with Physical Model Study”. Unpublished master’s thesis, METU, Ankara, TURKEY.

INVESTIGATING IMPACT OF DAMS ON ANNUAL MAXIMUM FLOWS OF RIVERS IN EUPHRATES BASIN, TURKEY

Muhammet YILMAZ[1], Fatih TOSUNOĞLU[1]

ABSTRACT

The Euphrates River basin is of critical importance for water, food and energy security and it is the largest of 26 river basins in Turkey. In order to effectively and efficiently use the water potential of the basin, many dams have been planned and constructed in the past 50 years. It is worth recalling that these dams may cause significant changes in the flow regimes of rivers. In the present study, we aimed to examine impact of dams on annual maximum flows of rivers in the Euphrates Basin. To achieve this purpose, pre and post-dam annual maximum flow records from several rivers, which are close to the considered dams, were collected. It is expected that the main statistical properties of these two periods should be different in the rivers affected by the dam. Significance of the difference is evaluated using parametric and non-parametric statistical tests, namely Student's t and Mann-Whitney U. According to test results, after Karakaya dam began operation, decreasing were observed at maximum flows of the stations 2124 and 2145 and the change was not observed in maximum flows of the station 2131. After Atatürk and Keban dams began operation, the change were not observed at maximum flows of the stations 2115 and 2149, respectively.

Keywords: Euphrates Basin, Annual maximum flows, Student's t test, Mann-Whitney U test.

1. INTRODUCTION

Dams, which are generally constructed across a river, ensure flood protection, hydropower generation, water for human consumption, irrigating for arid and semiarid lands, water supply for productive agriculture and also provides many economic and social benefits. It is a well known fact that hydrologic structures such as dam, hydroelectric power plant, flood protection structures and berms built on riverbeds can cause significant changes in the river hydrology streamflow regime characteristics, river morphology and river ecosystem (Simons and Senturk, 1977). Dams across the world has seriously shifted the global flow of water and sediment transport from continents to oceans via the world's river basins in recent years (Poff et al., 2007). The resultant hydrological alterations caused by dams can include changes in flood frequency and magnitude, reduction in overall flow, increased or decreased summer baseflows (Batalla et al., 2004). The effects of a dam on flow regime, will depend on its capacity in comparison with river runoff, its purpose (e.g. irrigation diversions, hydroelectric generation, flood control), and its operating rules.

A number of studies have been conducted to evaluate impacts of dams on the river flow worldwide. For example, Williams and Wolman (1984) indicate that dams shift the downstream flow regime of rivers. They investigated channel changes which have taken place downstream from 21 dams on rivers that were located mostly in western western United States and concluded that after dams were built, mean daily flows and average annual low flows were decreased. Batalla et al. (2004) analysed flow

[1] Research Assistant, Department of Civil Engineering, Erzurum Technical University, Erzurum, Turkey, e-posta: muhammet.yilmaz@erzurum.edu.tr
[1]Assistant Professor, Department of Civil Engineering, Erzurum Technical University, Erzurum, Turkey, e-posta: ftosunoglu@erzurum.edu.tr

records from 38 stations in the Ebro basin, searched hydrological effects of the dams. Their results indicated that dams have used significant changes to the flow regime especially on flood magnitude and monthly flow pattern. Assani et al. (2006) detected that due to the shifts induced by the dams were observed significant reduction in the frequencies of annual maximum flows of Canada's rivers. Zuo and Liang (2015) investigated the influence of dams on Shaying river flows, and used 55 years daily flow data belonging to 33 gauge stations. Two time series as before-impact and after-impact periods were considered They stated that the dams produced a decrease in maximum flows and minimum flows for 1-day, 3-day, 7-day, 30-day and 90-day of Shaying river. Mei et al. (2017) searched influence of dam on flood frequency and magnitude in United States, and indicated that there were observable reductions of the standard deviation for 32 out of the 38 river basins. Dogan et al. (2016) studied effect of Gokcekaya dam on Sakarya river flow pre and postdate in which dam began operation. They determined that while the dam decreased the maximum flows, it increased the minimum flows.

The main aim of this work is to evaluate effect of dams on annual instantaneous maximum flows (AIMF) ,which are usually used as basic parameter in the design of spillways (Yenigun and Ulgen, 2015). To achieve this purpose, significant changes for AIMF series span the period 1961-2015 belonging to 6 gauge stations in Euphrates basin were searched by comparing the pre and postdate in which dam began operation. For evaluate this statistical comparing, Student's t and Mann Whitney U tests are used. We believe that the findings of this study will supply a preliminary information for evaluate impact of dams which located in the Euphrates basin on AIMF series.

2. MATERIAL AND METHOD

2.1 Statistical tests

2.1.1 Anderson Darling test

The method proposed by Anderson and Darling (1952) tests the normality of the data. For calculate the test statistic (A^2), sample values are sorted from small to large and standardized. Cumulative Gaussian function value is expressed as k_i for i th variable (equation 1).

$$A^2 = -n - \frac{1}{n}\left\{\sum_{i=1}^{n}(2i-1)[lnk_i + ln(1-k_{n+1-i})]\right\} \quad (1)$$

(Stephens, 1974) modified Anderson-Darling test empirical distribution function. Modified test statistic, like this $T^* = (1 + 0.75/n + 2.25/n^2)A^2$. Upper tail probability is calculated as $\alpha = exp(1.2937 - 5.709T^{*2} + 0.0186T^{*2})$. α_0 is the significance level. If $\alpha < \alpha_0$, then the null hypothesis is rejected (Zhang, 1999).

2.1.2. Student's t test

Student's t test, parametric test, is often applied to assess for whether the two time series come from the same population. For instance, this test used to compare the means value of two groups. The t-test can be applied to two time series according to the standard deviation values equality or not. t test statistic is used as following formula at different standard deviations case.

$$t = \frac{\bar{x}_1 - \bar{x}_2}{\sqrt{\frac{{S_1}^2}{n_1} + \frac{{S_2}^2}{n_2}}} \quad (2)$$

where n_1 and n_2 are the sample lengths of the time series. Degree of freedom is given as,

$$d_f = \left(\frac{{S_1}^2}{n_1} + \frac{{S_2}^2}{n_2}\right) / \left[\frac{\left({S_1}^2/n_1\right)^2}{n_1 - 1} + \frac{\left({S_2}^2/n_2\right)^2}{n_2 - 1}\right] \quad (3)$$

t_o value d_f with degree of freedom is found from the t table. If t_o is less than t value which calculated by equation 2, then it can be said that these two groups came from two different populations (Sen, 2017).

2.1.3 Mann Whitney U test

The Mann Whitney U test is a nonparametric test that used to answer the question of whether there are differences between the two sample functions. The hypotheses tested in the Mann-Whitney U test are as follows.

H_o: Data sets n_1 and n_2 belong to the same populations.
H_1: Samples are examples of different populations.

To apply the Mann Whitney U test, two samples with sizes n_1 and n_2 are transformed into a single series and the sequence scores of the observations in the time series are found. Taking into account belongs to which series of the data, sort scores are collected according to series. The sum of the rank scores of the 1 st and 2.st observations is R_1, R_2 respectively. U_1 and U_2 test statistics are calculated using total ranking scores.

$$U_1 = n_1 * n_2 + \frac{n_1(n_1 + 1)}{2} - R_1 \quad (4)$$

$$U_2 = n_1 * n_2 + \frac{n_2(n_2 + 1)}{2} - R_2 \quad (5)$$

$$U = \min(U_1, U_2)$$

If n_1 and n_2 is greater than 10, the mean and standard deviation of U are found and the z test statistic is calculated as follows (Can et al., 2015).

$$\overline{U} = \frac{n_1 * n_2}{2} \quad (6)$$

$$S_u = \left[\frac{n_1 n_2 (n_1 + n_2 + 1)}{12}\right]^{1/2} \quad (7)$$

$$z = \frac{U - \overline{U}}{S_u} \quad (8)$$

If the absolute value of the calculated Z is greater than the $z_{1-\alpha/2}$ value of the normal distribution corresponding to α significance level, it is said that the samples belong to different populations.

3. STUDY AREA AND DATA

The Euphrates River basin, which is located at the southeastern Anatolia region of Turkey, has an area of 127,304 km2, average height of 1009,87, average precipitation of 540.1 mm/year, total streamflow of 31.61 km^3/yıl, and also the basin is the largest of 25 river basins in Turkey. There are 19 large dams in the basin. Atatürk Dam attracts attention due to the volume of water it collects in these dams while Keban and Karakaya dams are important in terms of height of the dam body. The Euphrates River

originates near the city of Erzurum, in the mountains of the eastern part of Turkey and it is the longest river in western Asia. As shown in Figure-1, the Euphrates basin is divided into three major sub-basins, as upper, middle and lower. In this study, annual instantaneous maximum flows records from six gauge stations are evaluated for effect of dams on river flows. The stations used in this study are given in figure 1. Streamflow records consist of periods in the range 42-55 years. As can be seen in Figure 1, all stations except one station (2149) are located in the lower basin. Table 1 gives the basic statistical characteristics of the AIMF series for each station and their observation period, median value, skewness coefficient, variation coefficients, location.

It is clearly seen from this table that skewness values are positive all stations and hence time series are right tailed distribution. Highest median value was observed at station 2115, which is located in the lower basin. The greatest coefficient of variations of the AIMF was detected at station 2131. Also the dams considered in this study are shown in Figure-1. The properties of the selected dams are given in table 2.

Table 1. Some statistical properties of the AIMF series at each gauge station

istasyon no	location	observation period	skewness	median(m^3/sn)	coefficient of variation
2115	lower	1968-2009	3.15	382.5	0.84
2124	lower	1963-2014	0.73	38.15	0.55
2131	lower	1961-2015	3.20	16.2	1.16
2135	lower	1967-2015	1.76	33	0.69
2145	lower	1963-2011	1.56	95.4	0.65
2149	upper	1964-2011	2.57	313.5	0.47

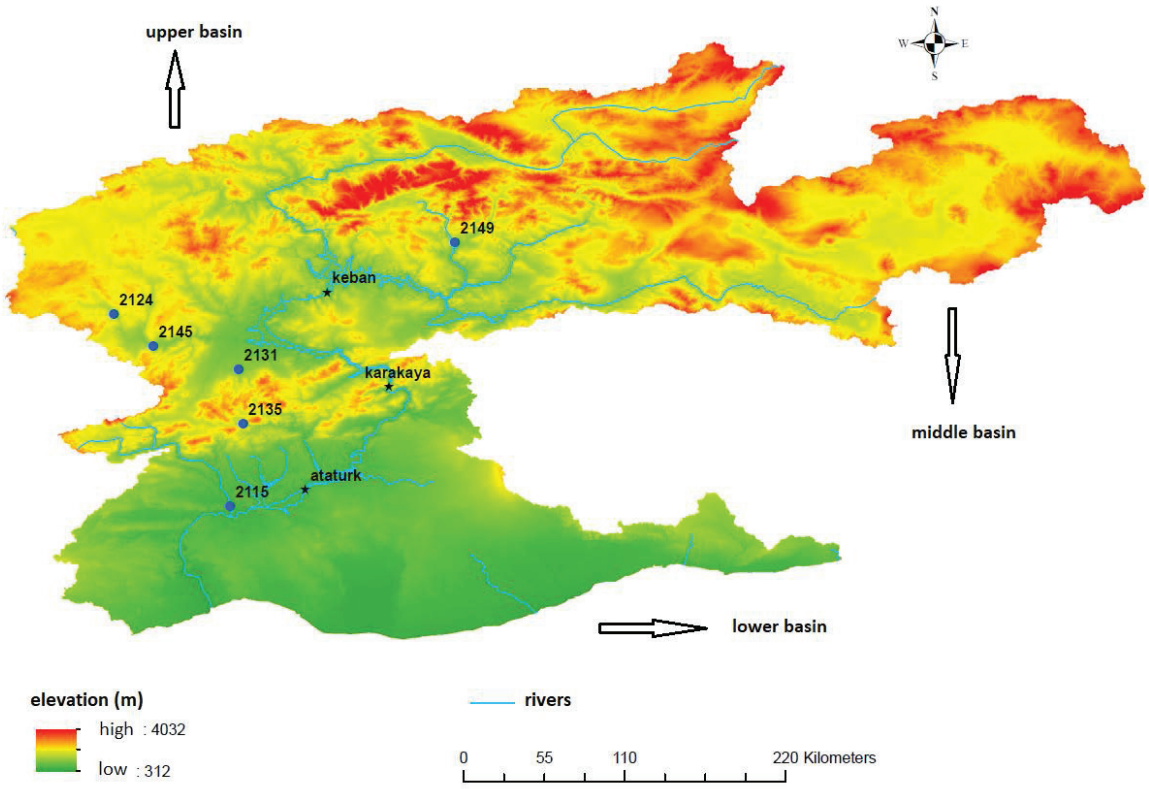

Figure 1. Stations and dams used in this study

Table2. Properties of selected dams

Dam	City	Type of dam	Beginning year of dam operation	elevation from base of dam (m)	Dam body volume (10^6 m^3)
Atatürk	Şanlıurfa	rockfill	1992	169	84.5
Keban	Elazığ	concrete weight + rockfill	1974	210	16.67
Karakaya	Diyarbakır	Concrete belt weight	1987	174	2

4. RESULTS

4.1 Anderson Darling test results

In this part of the study, Anderson Darling test was applied to test whether AIMF values of 6 gauge stations used in the study were normally distributed. The tests results (test statistic and p value for each AIMF series) are given in Table 3. As can be seen from the table that the considered AIMF series do not show a normal distribution as the computed p values are less than the 5% significance level. This findings imply that the Mann Whitney U must be applied to AIMF series to analyze the effect of the dams statistically.

Table 3. Anderson Darling test results applied to AIMF series

Station Number	AD test value	p value
2124	0.8921	0.0207
2145	2.0111	0.0005
2131	5.5009	0.0005
2135	1.44	0.00089
2115	3.9139	0.0005
2149	2.0271	0.0005

4.2 Mann Whitney U test results

The Mann Whitney U test used to evaluate statistical difference of the AIMF series before and after the year when the dam was began operation. Based on the locations of the stations and dams in the basin, we investigated impact of Karakaya dam on AIMF of station 2124, 2145, 2131, 2135; influence of Atatürk dam on AIMF of station 2115; effect of Keban dam on AIMF station 2149. The test statistics and p values that mentioned in the previous section have been computed and the results are presented in Table 4. It is clearly seen from the table that the z value of 2124 and 2145 stations is greater than 1.96 and implies a statistically significant decrease in AIMF values at significance level of 0.05. In other words, there is a statistical significant differences between the two AIMF series (before and after the year 1987) of the stations 2124 and 2145. No statistical significant decrease or increase was observed for the AIMF series of the other stations. However, the pre and post-dam AIMF series of the station 2131 can be considered as statistically significant at significance level of 0.10.

Table 4. Mann Whitney U test results

Station no	MN test statistic	p value	z
2124	173	0.003	-2.992
2145	170.5	0.01	-2.59
2131	271	0.075	-1.779
2135	280	0.522	-0.641
2115	163	0.178	-1.348
2149	142	0.508	-0.661

5. CONCLUSION

In this study, the effect of the dams located in the Euphrates basin on annual instantaneous maximum flows was investigated statistically. It is expected that there will be a change in flows after dams began operation. In this context, the statistical significance of this difference was analyzed by the nonparametric Mann Whitney U test and the following results were obtained.

According to the results of Mann Whitney U test, the maximum flow averages between 1963-1986 years belonging to 2124 station are statistically greater than the maximum flow averages between 1987-2014 years. The AIMF of this station have decreased after Karakaya dam began operation. This change in flows indicates that it may be the effect of the Karakaya dam. The maximum flow averages between 1963-1986 years belonging to 2145 station are statistically greater than the maximum flow averages between 1987-2011 years. Similarly, the same can be said for the 2145 station. But the changes in the AIMF of 2131 and 2135 stations have not been statistically determined. So it can be said that Karakaya dam was not affect the AIMF of these stations. The effects of Atatürk and Keban dams on the AIMF of 2115 and 2149 stations were investigated but not statistically significant.

As a result, the dams constructed on the rivers may bring significant changes over time in their characteristic features such as hydrological, morphological and sediment carrying capacity as well as flows. Especially the change in maximum flows is very important for the safety of the spillways of dams. There are very few studies investigating the effect of dams on maximum flows. This study only investigated the effect of dams in the on flows in the Euphrates basin. To fill this gap should be made to work like this throughout the Turkey. This study will be useful for researchers investigating the impact of dams on flows.

ACKNOWLEDGMENTS

This study was supported by Erzurum Technical University Scientific Research Coordination Unit (Project No. 2017/10). The authors also acknowledge the General Directorate of State Hydraulic Works, Turkey for providing the annual instantaneous maximum flow records used in this study.

REFERANCES

Anderson, T.W., Darling, D.A., 1952. Asymptotic Theory of Certain "Goodness of Fit" Criteria Based on Stochastic Processes The Annals of Mathematical Statistics, 23(2): 193-212.

Assani, A.A., Stichelbout, E., Roy, A.G., Petit, F., 2006. Comparison of impacts of dams on the annual maximum flow characteristics in three regulated hydrologic regimes in Quebec (Canada). Hydrol Process, 20(16): 3485-3501. DOI:10.1002/hyp.6150

Batalla, R.J., Gomez, C.M., Kondolf, G.M., 2004. Reservoir-induced hydrological changes in the Ebro River basin (NE Spain). J Hydrol, 290(1-2): 117-136. DOI:10.1016/j.jhydrol.2003.12.002

Can, I., Hizarcioglu, S., Tosunoglu, F., 2015. The impact of North Atlantic oscillation on the annual maximum flows in turkey, VIII. National Hydrology Congress, Sanlıurfa.

Dogan, E., Ceribasi, G., Akkaya, U., 2016. Investigation by Trend Analysis Method of Impacts of Dams on River Flow Regime: Sakarya River Example Karaelmas Science and Engineering 6(1): 50-55.

Mei, X.F., Van Gelder, P.H.A.J.M., Dai, Z.J., Tang, Z.H., 2017. Impact of dams on flood occurrence of selected rivers in the United States. Front Earth Sci-Prc, 11(2): 268-282. DOI:10.1007/s11707-016-0592-1

Poff, N.L., Olden, J.D., Merritt, D.M., Pepin, D.M., 2007. Homogenization of regional river dynamics by dams and global biodiversity implications. P Natl Acad Sci USA, 104(14): 5732-5737. DOI:10.1073/pnas.0609812104

Simons, D.B., Senturk, F., 1977. sediment transport techonology. water resources publications, USA.

Sen, Z., 2017. Innovative Trend Methodologies in Science and Engineering Turkish Water Foundation,Istanbul,Turkey

Stephens, M.A., 1974. EDF Statistics for Goodness of Fit and Some Comparisons. . Journal of the America Statistical Association, 347: 730-737.

Williams, G.P., Wolman, M.G., 1984. Downstream effects of dams in alluvial rivers. US Geological Survey, Professional Paper, 1286.

Yenigun, K., Ulgen, M.U., 2015. Trends in maximum flow on the axis of climate change and observation of its effect on dam safety, VIII. National Hydrology Congress, Sanlıurfa, pp. 343-354.

Zhang, P., 1999. Omnibus test of normality using the Q statistic. J Appl Stat, 26(4): 519-528. DOI:Doi 10.1080/02664769922395

Zuo, Q.T., Liang, S.K., 2015. Effects of dams on river flow regime based on IHA/RVA. Iahs-Aish P, 368: 275-280.

5 DAM SAFETY
İstanbul Turkey 2018

5th International Symposium on Dam Safety

October 27-31, 2018

EXAMINATION OF 3D NONLINEAR CREEP BEHAVIOUR OF A CONCRETE FACED ROCKFILL DAM CONSIDERING DAM BODY-FOUNDATION-CONCRETE SLAB INTERACTION

Memduh KARALAR[1], Murat ÇAVUŞLİ [2]

ABSTRACT

High concrete-faced rockfill (CFR) dams exhibit critical and variable deformations due to complicated geological condition, severe weather conditions, many material partitions and external loads. In this study, it is presented that how the creep behavior of dams changes under its own weight and reservoir water effect according to the numerical analyses. For this purpose, Ilısu dam, the concrete-faced rockfill dam built in Turkey, is selected to conduct by using FLAC3D software based on the finite difference method. In this model, Wipp-creep viscoplastic material model and burger-creep viscoplastic material model, which are special material models for time dependent analysis, are used for concrete slab and rockfill materials-foundation, respectively. Special interface elements are defined between the rockfill material-foundation and the concrete slab-rockfill material to provide interaction condition between the discrete surfaces. Numerical analyses are carried out for empty and full reservoir conditions of the CFR dam. According to the numerical analysis results, it is estimated that how much maximum horizontal displacements will be able in the Ilısu Dam in the future for both reservoir water level. Moreover, this study demonstrates that as the water level increases at the upstream side of the dam, the horizontal deformations occurring in the dam body obviously change and increase.

Keywords: Concrete-faced rockfill, Wipp-creep viscoplastic material model, Burger-creep viscoplastic material model, Creep analysis, Horizontal displacement behavior.

INTRODUCTION

Horizontal displacement is one of the most important deformation characteristic for high concrete faced rockfill dams and it is regarded as a key indicator for safety of these dams. Generally, there are two different types of deformations associated with these dams. First one is the horizontal displacement occurring from the dam's own weight and second one is the horizontal deformations which are perpendicular to the main axis of the dam. From past to present day, many researchers have investigated these dams. Soydemir and Kjaernsli proposed a technique for predicting the settlement of concrete faced rockfill dams for after 10 years of operation (Soydemir and Kjaernsli 1979). Then, this technique was edited this prediction technique (Clements R.P. 1984). Zhang et al. (2004) investigated a high concrete faced rockfill dam. A contact analysis method was performed. It was revealed in this study that whether the deformation of the CFR dam body is nonlinear or time dependent. Yu et al. examined the three dimensional (3D) effect of some major factors on the stability of an earth-rockfill

[1] Assistant Professor, Department of Civil Engineering, Bulent Ecevit University, Zonguldak, Turkey, e-posta: karalar@beun.edu.tr
[2] Research Assistant, Department of Civil Engineering, Bulent Ecevit University, Zonguldak, Turkey, e-posta: murat.cavusli@beun.edu.tr

dam, such as topography of the canyon and geometrical characteristics of the dam. It was suggested that it has to be careful to the canyon shape, gradient of the dam slope and height of the dam while performing 3D numerical analysis (Yu et al. 2005). Bayraktar et al. investigated the effect of the hydrostatic pressure on nonlinear behaviour of the concrete faced rockfill dam. It is revealed in this study that the hydrodynamic pressure of the reservoir water leads to increases in the maximum displacements and principal stresses of the dam (Bayraktar et al. 2009). Fang and Liu performed stress-strain analyses of a rockfill dam. It was indicated that especially after the foundation treatment, the displacement of the dam foundation clearly diminishes and it is well beneficial for the functioning of the core (Fang and Liu 2011). Zhou et al. examined the settlement analysis of the concrete faced rockfill dam. A creep model was used to model the rockfill during period of dam operation. Time dependent settlement behaviour of the CFR dam was studied with situ settlement-monitoring records and displacement back analysis (Zhou et al 2011). Xu et al. performed three dimensional simulation based on a modified generalized plasticity model and the concrete faced rockfill dam was monitored in detail. Numerical analyses and monitoring records were compared and numerical results agreed well with in situ monitoring records of the dam settlement. 70 cm maximum vertical displacement was observed in the dam body (Xu et al. 2012). Kim et al. was used a nonlinear and inelastic constitutive soil model to represent the behaviour of the concrete faced rockfill dam material. The finite elements analyses were performed to assess the displacements during both the construction and initial reservoir filling stages. The vertical and horizontal displacements increased along the height of the dam body for filling stages when compared with construction stage (Kim et al. 2014). Guo et al. proposed a method of deformation back analysis based on the response surface method and genetic optimization theory for the creep analysis of the high rockfill dams. The time dependent settlements in the dam body was obtained and estimated the performance of the rockfill dam (Guo et al. 2016). Rashidi and Haeri evaluated the behavior of the rockfill dams during construction and initial impounding using the numerical modeling and the instrumentation data. The finite difference model was created using FLAC software. Strain-hardening and strain-softening models were modified based on the data obtained from laboratory experiments and time dependent deformation-stress behaviour of the dam was acquired in detail in this study (Rashidi and Haeri 2017). Prampthawee et al. performed the time-dependent analyses of high rockfill dam. Three-dimensional finite element analyses without creep and with creep considerations of rockfill dam were performed and compared with the situ measurements (Prampthawee et al. 2017). Wen et al. performed the three dimensional numerical analyses and monitored the behaviour of the dam with a detailed deformation-monitoring system. Time dependent three dimensional settlements in the dam body were observed according to numerical analyses and obtained settlements- principal stresses of the dam were evaluated (Wen et al. 2017).
In this study, the viscoplastic behaviour of Ilısu Dam which is one of the largest concrete faced rockfill dam in the world is observed in detail and time dependent horizontal displacements are evaluated according to the numerical analyses.

ILISU CONCRETE FACED ROCKFILL DAM

The Ilısu Dam is part of the South-eastern Anatolian Project (GAP) and it is currently the largest hydropower project in Turkey. This construction was completed in 2017 year. The project area is 117 km away from the center of Mardin province and it was built in the boundaries of Ilısu village. General view of Ilısu dam is shown in the Fig. 1. This dam is the longest concrete faced rockfill dam in the world and it has 1775 m crest length. The project includes totally 44 million m^3 filling material, 3 diversion tunnels with a diameter of 12 m and length of 1 km, 3 power tunnels with a diameter of 11 m. Dam's precipitation area is 35509 km^2. The crest width is 8 m and dam body height is 130 m. The lake volume is 10.4 billion m^3. Maximum water elevation is 526.82 m and reservoir area is 318.5 km2. The project will generate 3.833 GWh power per year in average with an installed capacity of 1.200 MW. The slope of the upstream and downstream are 1:1.4 and slopes of the rockfill zones and transition zones are 2:1.5. The typical cross section of Ilısu dam and details are demonstrated in Fig. 2.

Figure 1. General view of Ilısu dam (DSI 2018).

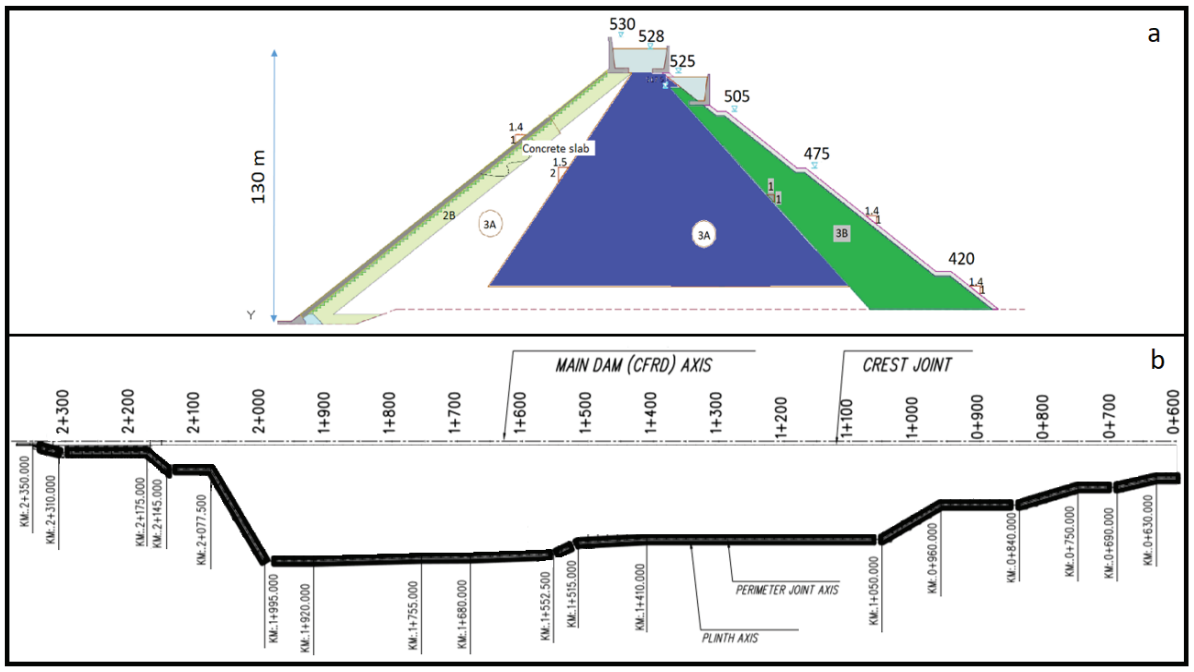

Figure 2. a) The typical cross section of Ilısu dam; b) change of dam body height along crest axis (DSI 2018).

The Ilısu dam was built as concrete faced rockfill dam and it was constructed using many different rockfill materials. While constructing Ilısu dam, rockfill materials were compacted by sheepsfoot rollers. This dam has 3 different filling materials such as basalt (3B), limestone (3A), bedding zone (2B) and a concrete slab was constructed on the surface of the dam. All filling materials have different mechanical properties and mechanical properties of the materials are selected from the laboratory experiments for numerical analyses as given in Table 1.

Table 1. Material properties of Ilısu Dam (DSI 2018).

Characteristics	*Specific Weight*	*Maximum Unit Weight*	*Porosity*	*Water Content*	*Air Content*	*Material Content*
Unit	g/cm^3	g/cm^3	%	%	%	%
2B	2.74	2.23	18.61	4.05	14.56	81.39
3A	2.68	1.99	25.75	7.78	17.97	74.25
3B	3.01	2.25	25.25	1.50	23.75	74.75

FINITE DIFFERENCE MODEL OF ILISU DAM

The three dimensional model of the concrete faced rockfill dam is created according to the original dam geometry. The finite difference model of dam has 5 different sections. Different sections that have various geometries, created 4 different blocks and these blocks are merged to constituted the 3D finite difference model of the dam body. Details of sections and blocks are shown in Fig. 3.

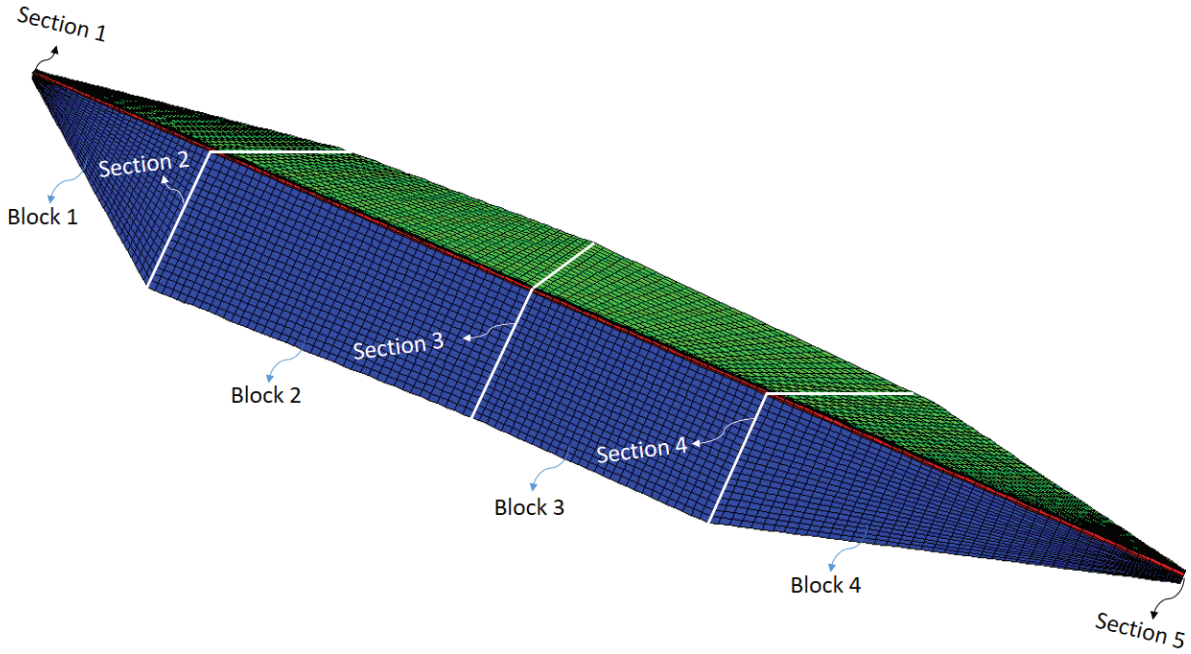

Figure 3. View of the blocks and sections of 3D finite difference model.

After the three dimensional model of dam body is created, the foundation is modelled and meshed in detail. The mesh detail of the dam and foundation is shown in the Fig. 4. Afterwards the foundation is extended toward downstream and the valley side as much as dam height. Also, it is extended three times of the dam height at upstream side of dam. Finally, height of the foundation is considered as much as the dam height. Total 1304547 finite difference elements are used in 3D finite difference model.

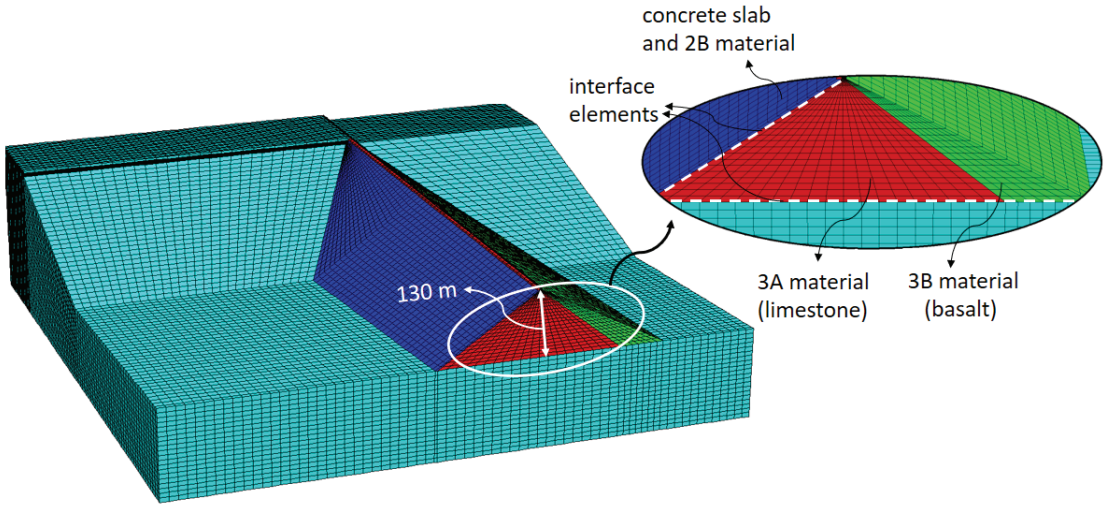

Figure 4. Detail of 3D Finite Difference Model.

Movement restricts of the 3D model must be performed before 3D model is analysed. So, the movement of the base of foundation is restricted in three directions (x, y, z). Moreover, the movement of the side surfaces of the model is allowed only in the vertical direction (z) and it is restricted in the horizontal directions (x, y). Material properties are defined for each volume as in the original dam project. Wipp-creep viscoplastic material model and burger-creep viscoplastic material model are defined for concrete slab and rockfill materials-foundation, respectively. The specific material parameters for these material models are considered in the numerical analyses. In addition, interface elements are defined between dam body-foundation and concrete slab-dam body to represent the interaction condition between discrete surfaces as shown in Fig. 5.

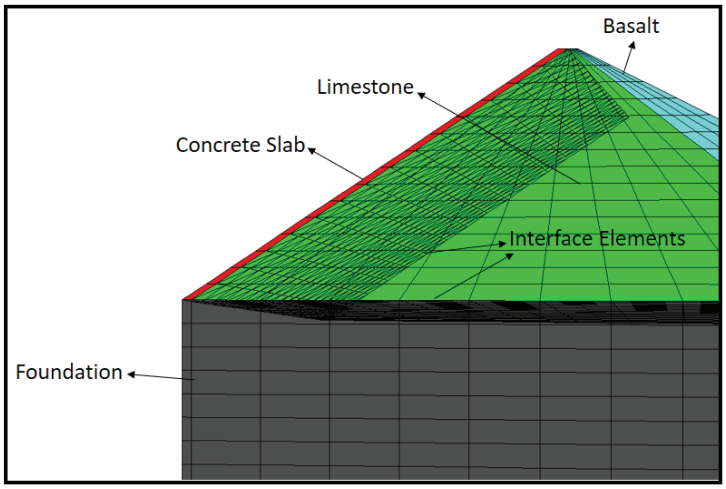

Figure 5. Interface conditions between dam body, foundation and concrete slab of the Ilısu dam.

Then, the reservoir water is modelled for 120 m (maximum water height) of reservoir water height and the reservoir-dam body-foundation system is created. Water loads are practiced to all nodal points at the upstream side of the dam considering hydrostatic pressure rules. Moreover, water table is created and modelled to represent water leakage into the dam body. Creating and meshing of the 3D model of Ilısu dam took a long time. Many problems are encountered during viscoplastic numerical analyses because three-dimensional finite difference model of the Ilısu dam has a great number of elements and nodes. For this reason, the finite difference mesh is changed several times and a new mesh is created so that the correct result can be achieved and the program will not fail. Mesh width is selected 10 m for numerical analyses.

NUMERICAL RESULTS

Three dimensional numerical results of the Ilısu CFR dam are presented in this section. As the first step of these analyses, only the foundation is collapsed under its self-weight for the empty reservoir condition of the dam. Then, all displacements which are obtained from the collapsed model are set to zero. This is implemented in order to exclude construction related all deformations. Afterwards, the dam body is placed on the settled foundation model and foundation-dam body system is collapsed under its self-weight. Behaviour of the dam is evaluated for empty reservoir condition of the dam for first step of the numerical analyses. According to second step of the numerical analyses, the reservoir water is modelled and foundation-dam body-reservoir interaction system of Ilısu dam is analysed for 120 m (maximum reservoir height) of the reservoir water height. According to numerical analyses, horizontal displacements which may take place in time, are evaluated for maximum reservoir condition in detail. Results are presented for empty and maximum reservoir condition of the dam as follows subsection and these results are compared with to each other.

EMPTY RESERVOIR CONDITION OF THE DAM

Deformation monitoring is one of the most important method for analysing the deformation characteristics of dams and provides a warning system for abnormal behaviour of the dam. So, observing the deformation behaviour of the dam body are vital for safety of these structures. Horizontal displacements are shown for initial condition (empty reservoir condition) of the dam in Fig. 6. When investigated the split half condition of the dam, in spite of horizontal displacements occurred in the negative direction at the upstream side of the dam, displacements took place in the opposite direction (positive) for the downstream side. Moreover, minimum horizontal displacement values are observed at the crest of the dam (Fig. 6). 3.43 cm horizontal displacement is obtained in the numerical analyses at the upstream side of the dam. 1.5 cm maximum horizontal displacement occurred at the downstream side of the dam and any displacement did not take place on the foundation. Moreover, any displacements did not occur on the surface of the dam body and the horizontal displacements increased from the crest to the foundation as seen from Fig. 6.

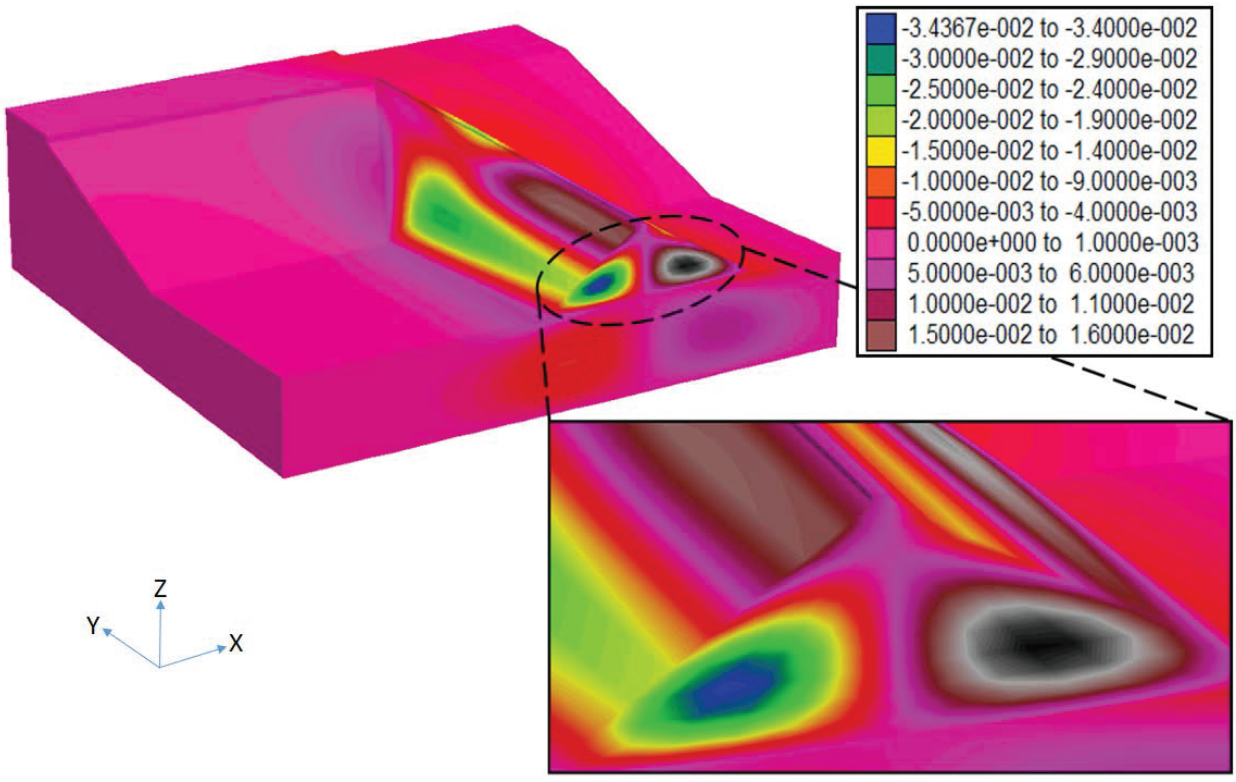

Figure 6. Horizontal displacements (m) for empty reservoir condition of the dam.

FULL RESERVOIR CONDITION OF THE DAM

Hydrostatic pressure is an important factor for the displacements of CFR dams. So, effect of the hydrostatic pressure on the dam behaviour are examined in detail in this section. Firstly, all displacements and principal stresses which are obtained from the empty reservoir condition of the dam are set to zero in order to exclude construction related the stresses and deformations. Then, reservoir water is modelled considering maximum reservoir level and effect of the hydrostatic pressure is taken into account in the all creep analyses. Horizontal displacement results are shown in Fig. 7-9. According to numerical results, reservoir water loads altered direction of the horizontal displacement vectors at the dam body and foundation for maximum reservoir condition when compared empty condition. In despite of the vertical settlement vectors are observed in the dam body for empty condition, traverse displacement vectors observed in the dam for maximum reservoir water condition due to the effect of the hydrostatic pressure, water flow and leakage as seen Fig. 7. Besides, deformed situation of the dam in time, is shown in Fig. 8. Bottom of the dam body is more deformed than the crest and deformation size is very critic at bottom of the dam. In addition, remarkable deformations are observed on the surface of the foundation as seen Fig. 8. Horizontal displacement results are presented in Fig. 9. When compared with empty condition of the dam, more horizontal displacements are observed in the dam body for maximum reservoir condition. 36.9 cm maximum displacement occurred on the dam body surface. In despite of any displacements did not take place on the surface of the foundation for empty reservoir condition, approximately 14 cm horizontal displacement is occurred for the maximum reservoir condition. Besides, 26 cm displacement is observed at middle of the dam body surface and all displacements took place in positive direction according to time depending creep analyses as seen Fig. 9. It is clearly seen from these numerical creep results the effect of the hydrostatic pressure on the horizontal displacement behaviour of Ilısu dam.

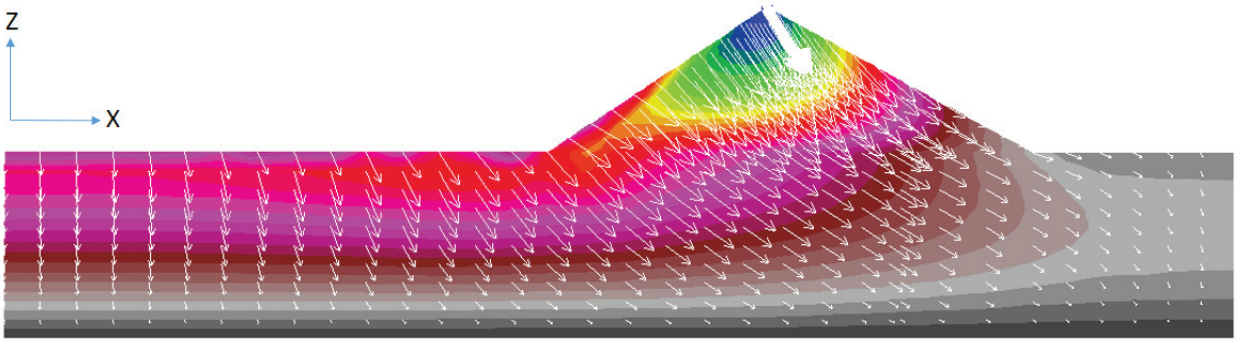

Figure 7. Displacements (m) for maximum reservoir condition of the dam.

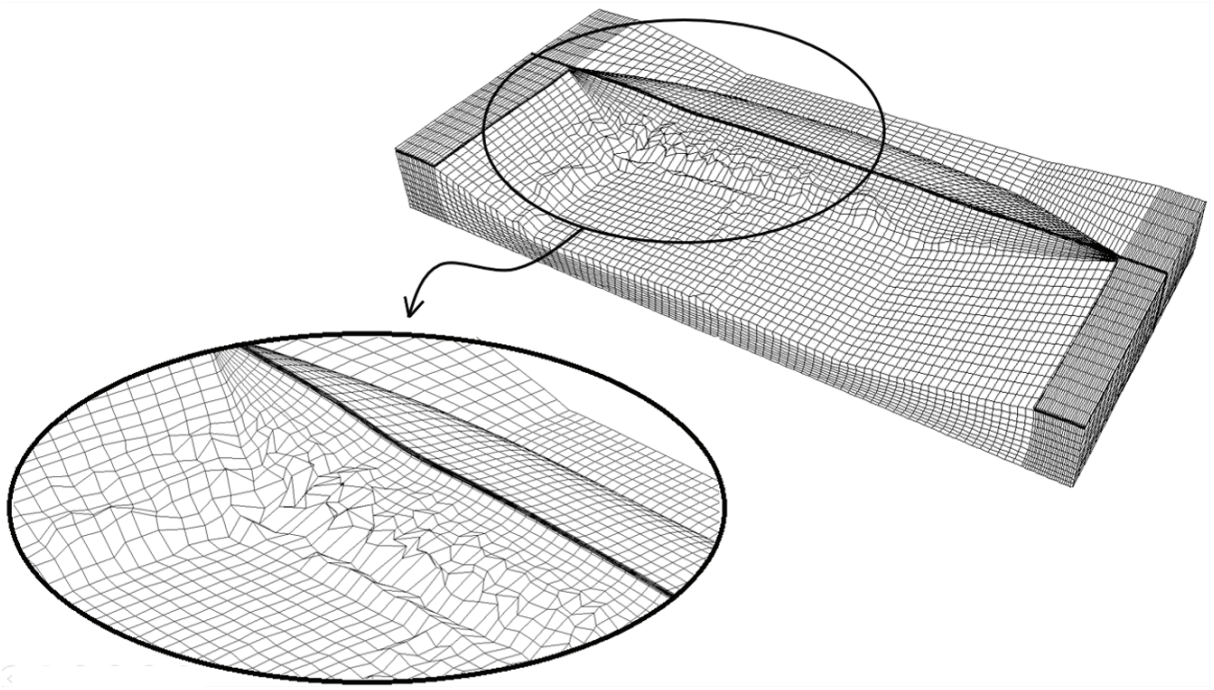

Figure 8. Deformed condition of the dam for maximum reservoir condition.

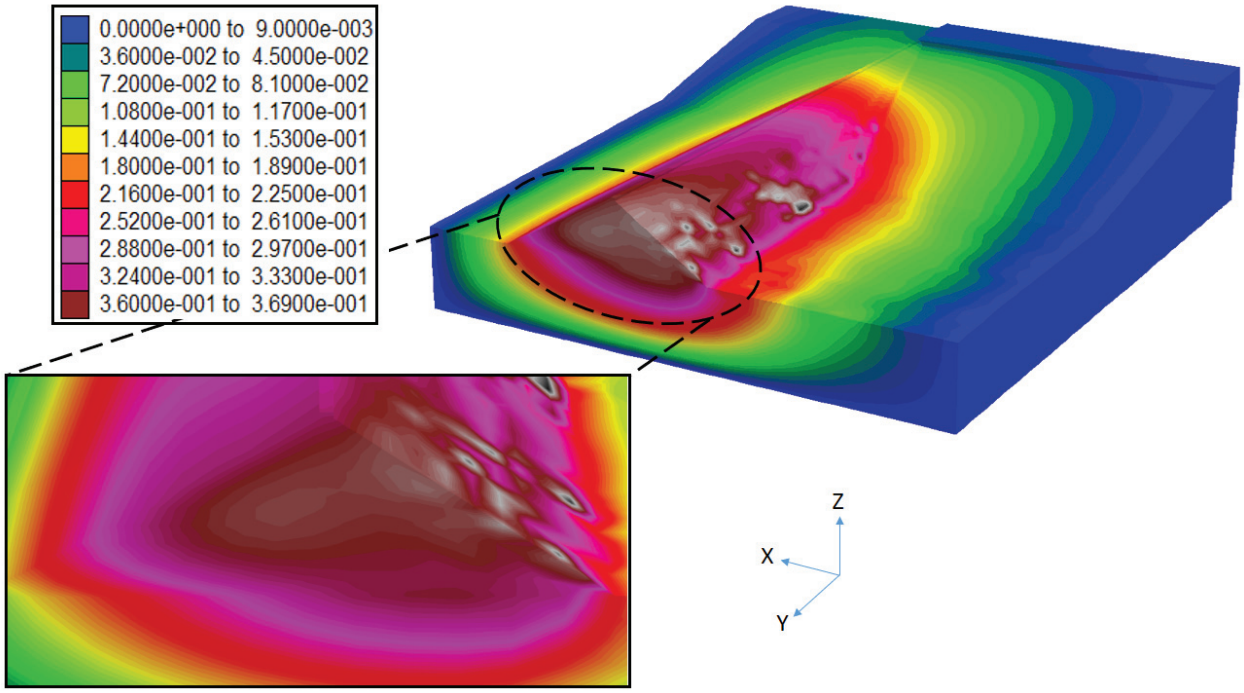

Figure 9. Horizontal displacements (m) for maximum reservoir condition of the dam.

CONCLUSIONS

Deformation control and monitoring is vital important for high concrete faced rockfill dams. For this reason, the horizontal displacements of the Ilısu dam is analyzed by 3D numerical modelling and nonlinear behaviour of the Ilısu dam is examined and evaluated in detail in this paper. Specific material models which use for numerical analyses are considered for the creep analyses and material properties are selected from experimental data. Firstly, numerical analyses are performed for empty reservoir condition of the dam. Then, reservoir water is modelled and viscoplastic creep analyses are

performed for maximum reservoir condition depending to the time in order to see deterioration of the rockfill materials in time. Numerical results are evaluated as below:

- According to the numerical analysis results, large horizontal displacement differences are observed between the empty and maximum reservoir condition of the dam. After the reservoir water contacted with the dam body, viscoplastic behaviour of the dam clearly changed and more displacements are observed in the dam body for maximum reservoir condition compared with empty reservoir condition.
- In spite of vertical displacement vectors occurred in the dam body for empty condition, traverse displacement vectors are observed in the dam body for maximum reservoir water condition due to effect of the hydrostatic pressure and water leakage.
- It is obviously seen from numerical analyses that bottom of the dam body is more deformed than the crest of the dam and deformation size is very critical at bottom of the dam. Moreover, remarkable deformations are observed on the surface of the foundation.

REFERENCES

Bayraktar A., Kartal M.E., Basaga H.B. (2009). ‘‘Reservoir water effects on earthquake performance evaluation of Torul Concrete-Faced Rockfill Dam’’ Water Science and Engineering, 2(1): 43-57.

Clements R.P. (1984) ‘‘Post-construction deformation of rockfill dams’’ J. Geotech. Eng. 110, 821-840.

DSI, General Directorate of State Hydraulic Works, Regional Directorate, Ankara, 2018.

Fang C., Liu Z. (2011). ‘‘Stress-strain analysis of Aikou rockfill dam with asphalt-concrete core’’ Journal of Rock Mechanics and Geotechnical Engineering. 3(2), 186–192.

Guo Q., Pei L., Zhou Z., Chen J., Yao F. (2016). ‘‘Response surface and genetic method of deformation back analysis for high core rockfill dams’’ Computer and Geotechnics, 74, 132-140.

Kim Y.S., Seo M.W., Lee C.W., Kang G.C. (2014). ‘‘Deformation characteristics during construction and after impoundment of the CFRD-type Daegok Dam, Korea’’ Engineering Geology, 178, 1–14.

Pramthawee P., Jongpradist P., Sukkarak R. (2017). ‘‘Integration of creep into a modified hardening soil model for time-dependent analysis of a high rockfill dam’’ Computers and Geotechnics, 91, 104–116.

Rashidi M., Haeri S.M. (2017). ‘‘Evaluation of behaviors of earth and rockfill dams during construction and initial impounding using instrumentation data and numerical modeling’’ Journal of Rock Mechanics and Geotechnical Engineering, 9(4), 709-725.

Soydemir C., Kjaernsli B. (1979) ‘‘Deformation of membrane-faced rockfill dams’’ 7th European Conf Soil Mech and Found Engrg. 3, pp. 120-126.

Yu Y., Xie L., Zhang B. (2005). ‘‘Stability of earth-rockfill dams: Influence of geometry on the three dimensional effect’’ Computers and Geotechnics, 32, 326–339.

Zhang B., Wang J.G., Shi R. (2004). ‘‘Time-dependent deformation in high concrete-faced rockfill dam and separation between concrete face slab and cushion layer’’ Computers and Geotechnics, 31, 559–573.

Zhou W., Hua J., Chang X., Zhou C. (2011). ‘‘Dam-reservoir-foundation interaction effects on the modal characteristic of concrete gravity dams’’ Structural Engineering and Mechanics, 38(1).

Wen L., Chai J., Xu Z., Qin Y., Li Y. (2017). ‘‘Monitoring and numerical analysis of behaviour of Miaojiaba concrete-face rockfill dam built on river gravel foundation in China’’ Computers and Geotechnics, 85, 230–248.

Xu B., Zou D., Liu H. (2012). ‘‘Three dimensional simulation of the construction process of the Zipingpu concrete face rockfill dam based on a generalized plasticity model’’ Computers and Geotechnics, 43, 143-154.

5 DAM SAFETY
İstanbul Turkey 2018

5th International Symposium on Dam Safety

October 27-31, 2018

THREE DIMENSIONAL NON-LINEAR SEISMIC BEHAVIOUR OF ILISU CONCRETE FACED ROCKFILL DAM

Memduh KARALAR[1], Murat ÇAVUŞLİ [2]

ABSTRACT

Concrete-faced rockfill (CFR) dams are commonly used due to their low cost and rapid construction advantages. Additionally, huge constructions of CFR dams play very important roles in national water and power management systems. In this study, Ilısu dam constructed in Turkey and completed in 2017, is selected for three dimensional (3D) non-linear seismic analyses to investigate the seismic response of a selected CFR dam under strong ground motion effect. 3D finite element model of Ilısu dam is modelled by using FLAC3D software based on the finite difference method. Mohr–Coulomb material model is considered for the mechanical behavior of the rockfill material and foundation in the 3D earthquake analyses. Moreover, Drucker-Prager nonlinear material model is used for concrete slab of the dam to represent nonlinearity of the concrete. Free field boundary condition that is special boundary condition for the nonlinear seismic analyses, is taken into account for the lateral boundaries of the 3D model. In addition, quiet artificial boundary condition is used for the bottom of the foundation in the 3D seismic analyses. The hysteric damping coefficients are separately calculated for all of the materials and these special damping values is defined to the FLAC3D software using special fish functions to capture the effects of variation of modulus and damping ratio with dynamic shear-strain magnitude. Nonlinear numerical analyses are performed for full reservoir conditions of Ilısu CFR dam. 1995 Kobe earthquake acceleration records are used in all time-history analyses and the non-linear earthquake behaviour of this dam presented. According to analysis results, horizontal deformations, vertical deformations and principal stresses on the dam body surface during earthquake are evaluated in detail. Consequently, it is clearly seen that the nonlinear seismic behavior of each nodal point on the dam body surface changes with the effect of the earthquake load.

Keywords: Concrete-faced rockfill dam, Kobe earthquake, Non-linear seismic analysis, Deformation behaviour, Principal stress behaviour.

INTRODUCTION

When two different tectonic plates come into contact with each other, earthquakes suddenly take place. Afterwards, the surface of the Earth immediately shakes by sudden release of energy in the elastic upper crust and the Earth randomly moves in all directions (x, y and z directions). So, all of the aspects of the strong ground motions has to take into account for monitoring of the CFR dam's safety (e.g. Yeow et al., 2016). Characteristic properties of seismic ground motions were initially observed by Hudson (1958) and Housner and Trifunac (1967). It was revealed that the ground motions which is about 20 km distance from the fault rupture are accepted as near fault seismic ground motions. These ground motions are so di

[1] Assistant Professor, Department of Civil Engineering, Bulent Ecevit University, Zonguldak, Turkey, e-posta: karalar@beun.edu.tr
[2] Research Assistant, Department of Civil Engineering, Bulent Ecevit University, Zonguldak, Turkey, e-posta: murat.cavusli@beun.edu.tr

long period pulses in their velocity time histories. The effect of the seismic loads on the earthquake behaviour of the CFR dams was examined by many investigators. Westergaard (1933) presented one of the most important results about the seismic effects on the dam-foundation-reservoir interaction behaviour. It was revealed the importance of the hydrodynamic pressure on the nonlinear behaviour of the dam body during near fault earthquakes. Afterwards, Chopra (1966) investigated the effect of water compressibility on the hydrodynamic pressure for the strong vertical-horizontal ground motions. Arici (2013) investigated the seismic performance of a CFR dam during near fault earthquake loads with focus on crack development. It was indicated that earthquake loads cause to the spreading of the cracks from the base of the plate to the middle height. Moreover, analyses of the factors affecting the face plate performance showed that increasing the reinforcement ratio is the most effective countermeasure to limit the damage expected during a strong earthquake. Yang and Chi (2014) developed a finite element limit analysis method to assess the seismic stability of the CFR dams. Andrianapoulos et al. (2014) revealed that predominant period of a dam's vibration is highly affected by the input motion characteristics and its height. It was presented that the peak acceleration of the dam's crest is governed by the stiffness of the foundation soil, the input motion characteristics and its height. Xu et al. (2015) developed an elastic-plastic dynamic analysis procedure for the CFR dams using the plastic-damage constitutive model and it was proposed that this procedure could be adopted in the analysis of interactions between soil and concrete structures. Cen et al. (2016) developed the concrete random mesoscopic damage model to assess the seismic damage behaviour of concrete slabs of the CFR dams. Han et al. (2016) investigated the seismic response of the CFR rockfill dam using finite element method. Parametric study showed that the vertical acceleration response of the rockfill dam is highly affected with the permeability of the rockfill materials comprising the dam body. In addition, study is indicated that the crest settlements can be significantly underestimated by ignoring the strong vertical ground motion. Zou et al. (2017) selected 16 different ground motions which include 8 pulse-like motions with rupture forward directivity e-ffepulctss ea mnd oti8 onsnon for numerical analyses. The seismic analyses indicated that the near fault pulse-like ground motion has a moderate impact on the dam acceleration and it has a remarkable impact on the residual deformation of dam and concrete slab damage, especially for the dam crest. Yazdani and Alembaghari (2017) assessed the seismic vulnerability of the rockfill dams located in near-fault areas. The dam-reservoir interaction system was examined under the selected pulse-like and non-pulse-like records and study was shown that earthquake characteristics other than pulse nature may govern the seismic responses. Moreover, it was indicated that the velocity and displacement response spectra at the fundamental period are the best options under the near fault earthquakes records with and without pulse nature for the seismic vulnerability of the coupled dam-reservoir system.
In this study, the nonlinear seismic behaviour of Ilısu Dam which was completed in 2017 is examined and evaluated in detail. 1995 Kobe earthquake is used in the seismic analyses and numerical analyses are performed for full reservoir condition of the dam. According to the 3D finite difference analyses, settlements, horizontal displacements and principal stresses are assessed for three various nodal points on the dam body surface. In addition, the deteriorations and fatigues in the rockfill materials are evaluated in detail.

ILISU DAM

The Ilısu Dam was completed in 2017 year and the project area is 117 km away from the center of Mardin province. Dam was built on the strong seismic zone in Turkey and it is part of the Southeastern Anatolian Project (GAP). This huge structure is currently the largest hydropower project in Turkey and it is the longest concrete faced rockfill dam (1775 m) in the world (Fig. 1).

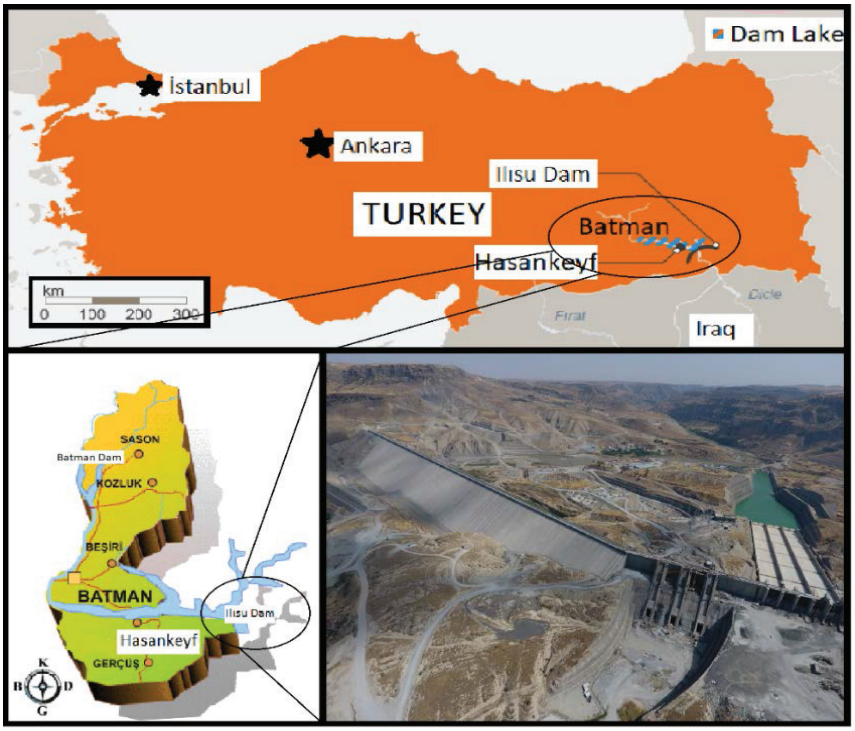

Figure 1. General view of Ilısu dam (DSI 2018).

The project includes totally 44 million m^3 filling material, 3 diversion tunnels with a diameter of 12 m and length of 1 km, 3 power tunnels with a diameter of 11 m. Dam's precipitation area is 35509 km^2. The crest width is 8 m and dam body height is 130 m. The lake volume is 10.4 billion m^3. Maximum water elevation is 526.82 m and reservoir area is 318.5 km^2. The project generates 3.833 GWh power per year in average with an installed capacity of 1.200 MW. Ilısu dam's location is showed in detail in Fig. 1. The slopes of the upstream side and downstream side of the Ilısu dam are 1:1.4 and slopes of the transition zones are 2:1.5. The typical cross section of Ilısu dam and details of the dam body height are demonstrated in Fig. 2.

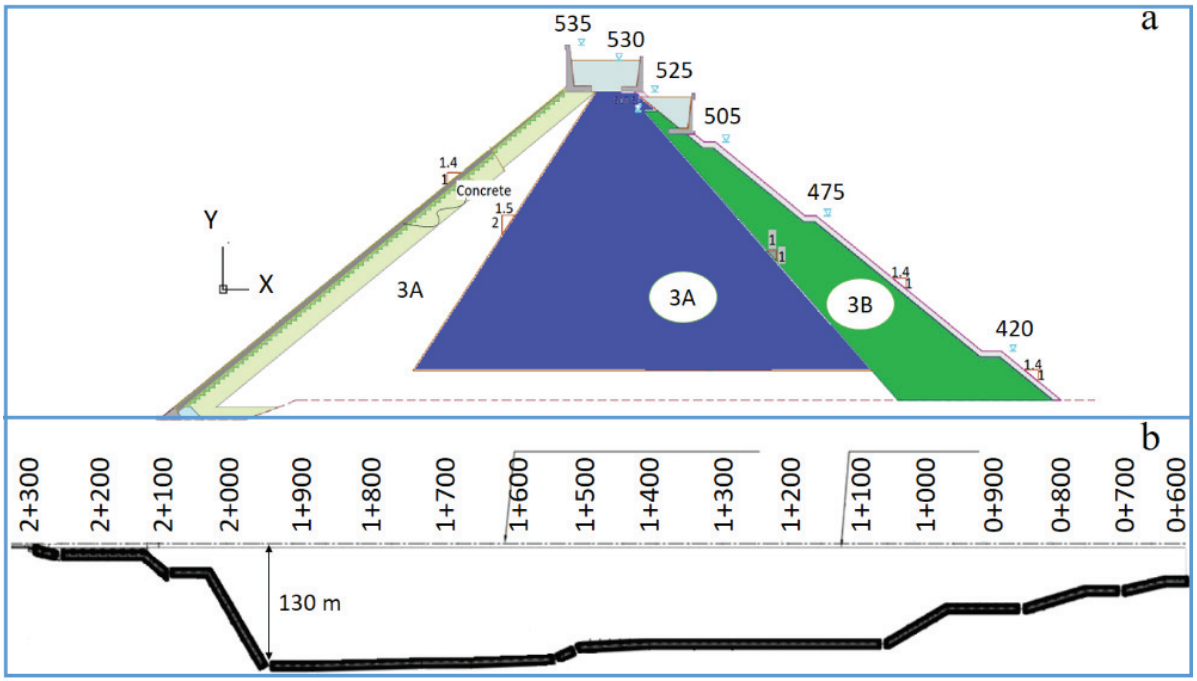

Figure 2. a) The typical cross section of Ilısu dam; b) Changing of the dam body depth along crest axis. (DSI 2018).

FINITE DIFFERENCE MODEL AND MATERIAL PROPERTIES OF ILISU DAM

While creating the 3D finite difference model of Ilısu dam, all rockfill materials and concrete slab that is built to hinder the leakage in the dam body are modelled as the original project of the dam. The 3D model of the dam body has 5 different sections and these section's geometrical properties are very different from each other. Each section has different heights along the dam body. While modelling Ilısu dam, these different sections are merged and finite difference model of the dam body is created. 3D finite difference model of the dam body has 4 various blocks. Details of the sections and blocks are presented in the Fig. 3.

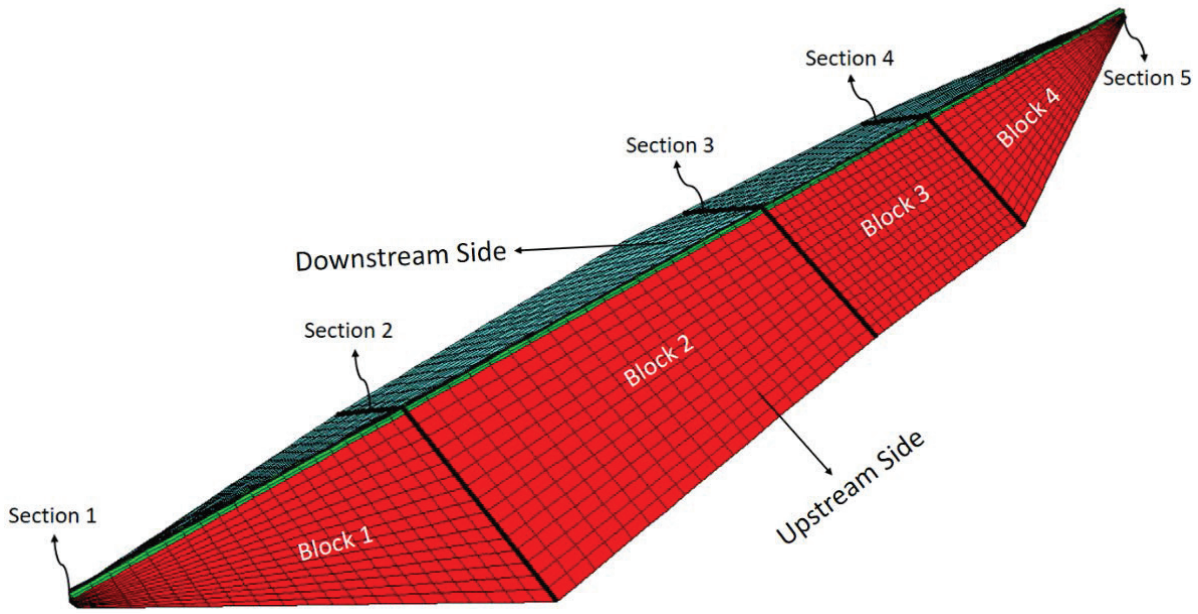

Figure 3. View of the section and blocks in the 3D finite difference model.

After the three dimensional model of dam body is modelled, the foundation and reservoir water are created in detail. While modelling the foundation, foundation is extended toward downstream and the valley side as much as dam height. Also, it is extended three times of the dam height at upstream side of dam. Finally, height of the foundation is considered as much as the dam height. These lengths and heights are the most critical conditions for the seismic analyses of the dams (Kartal et al. 2017). Total 1104547 finite difference elements are used in 3D finite difference model. Mohr Coulomb material model and Drucker Prager material model which are special nonlinear material models, are used for the rockfill material-foundation and concrete slab, respectively. Special fish functions are used while material model is defining to FLAC3D software. Moreover, special interface elements are defined between the rockfill material-foundation and the concrete slab-rockfill material to provide interaction condition between the discrete surfaces. Hysteretic damping models are usually employed to characterize damped dynamic properties of nonlinear mechanical systems. Various hysteretic damping models are calculated for all materials (rockfill materials, concrete slab and foundation) due to all materials have different characteristic properties. While defining these hysteric damping models to FLAC3D software, special fish functions are written and defined to the FLAC3D software. Free field boundary condition that is special boundary condition for seismic analyses, is defined to lateral boundaries of the 3D finite difference model for seismic analyses. This boundary condition is available for only lateral boundaries as seen Fig. 4 and it is made up of a combination of a load history and a viscous boundary. These viscous boundaries allow for an input of an earthquake motion while still absorbing incoming waves. In addition, quiet boundary (viscous boundary) condition is used for the bottom of the 3D model in the nonlinear earthquake analyses. Free field and quiet boundary conditions for the 3D finite difference model of Ilısu dam are shown in Fig. 4 and Fig. 5 in detail.

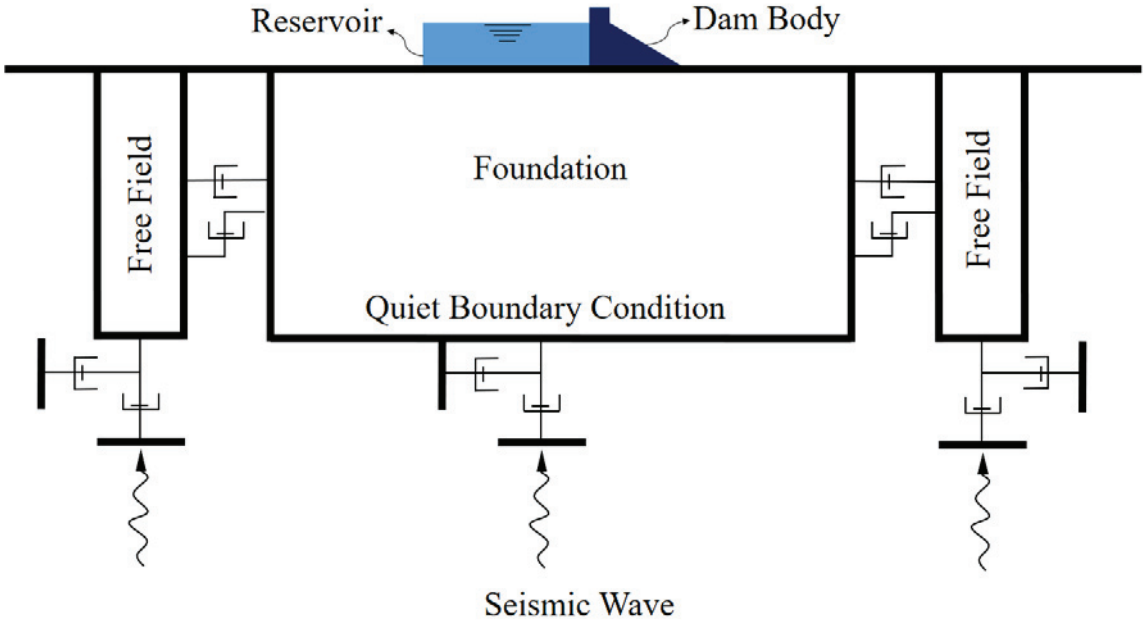

Figure 4. Boundary conditions for the 3d finite difference model.

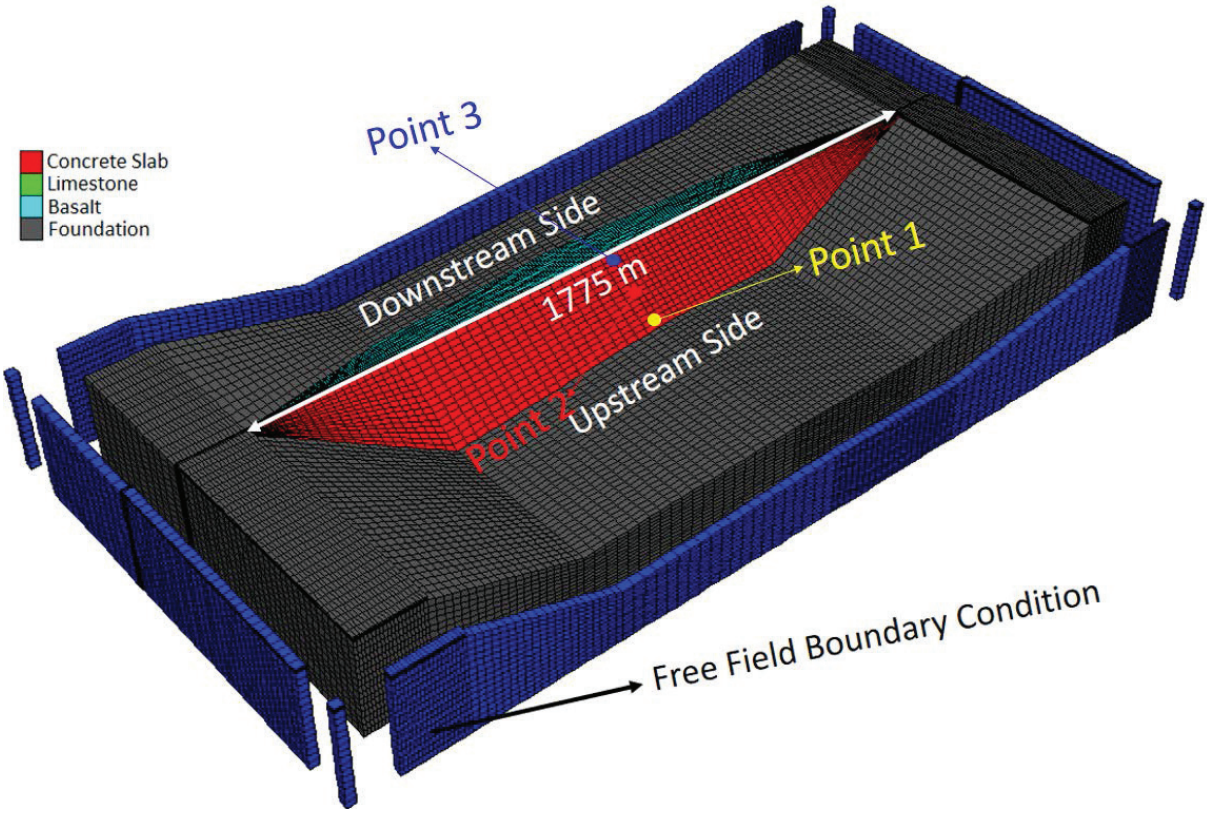

Figure 5. 3D finite difference model of Ilısu Dam.

Afterwards, the reservoir water is modelled considering the effect of the leakage in the dam body. Water height is taken into account as 130 m (full reservoir water level). While creating the reservoir water, water loads are calculated for each nodes of the dam's upstream side considering hydrostatic ware pressure. Then, water table is defined to the FLAC3D software using the special fish function to provide the leakage condition in the dam body. The creating and meshing of the three dimensional model of Ilısu dam took very long time. This process is not automated and so each process is

individually calculated. Many problems and errors are encountered during nonlinear seismic analyses due to three-dimensional finite difference model of the Ilısu dam has a great number of nodes and elements. So, the 3D mesh is changed many times and a new mesh is modelled so that the correct result can be achieved and the program will not fail. While analyzing the Ilısu dam, total 6 different mesh widths are created to find the correct mesh width. These widths are 10 m, 15 m, 20 m, 30 m, 40 m, 50 m, respectively. It is seen from numerical analyses that the maximum settlements on the crest of the dam do not change for less mesh width than 10 m (Fig. 6). So, mesh width is selected 10 m for seismic analyses.

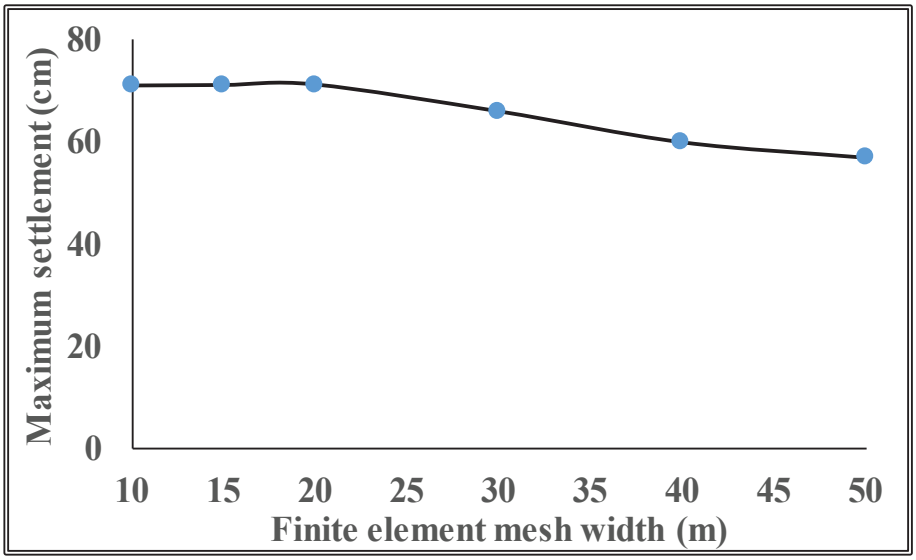

Figure 6. Settlement changes of the crest for different mesh widths.

The Ilısu dam was constructed as concrete faced rockfill dam and it was built using many various rockfill materials such as basalt (3B), limestone (3A) and bedding zone (2B). In addition, all rockfill materials have different mechanical properties. Mechanical properties of the rockfill materials are selected from the laboratory experiments for earthquake analyses as given in Table 1. Moreover, while constructing the Ilısu dam, these rockfill materials were compacted by sheepsfoot rollers.

Table 1. Material properties of Ilısu Dam (DSI 2018).

Characteristics	Specify weight	Unit Weight	Porosity	Water content	Air content	Material content
Unit	g/cm^3	g/cm^3	%	%	%	%
2B	2.74	2.23	18.61	4.05	14.56	81.39
3A	2.68	1.99	25.75	7.78	17.97	74.25
3B	3.01	2.25	25.25	1.50	23.75	74.75

GEOLOGIC BACKGROUND AND GROUND MOTION INPUTS

Turkey is located in one of the most actively deforming regions in the world. The tectonic faults in Turkey depends on relative motions among the African, the Aegean, the Arabian, the Anatolian, the Black Sea and the Eurasian plates. The neo-tectonics of Turkey is directed by three major elements: a) The Aegean–Cyprean Arc, a convergent plate boundary where the African Plate to the south is beneath the Anatolian Plate to the north; b) The North Anatolian Fault (NAF) Zone; c) The East Anatolian Fault (EAF) zone (Fig. 7). The East Anatolian Fault Zone (EAFZ) represents a plate boundary extending over 500 km between the Arabian and Anatolian plates. It is one of the largest currently active continental strike-slip faults in the world. Relative plate motion occurs with slip rates ranging from 6 to 10 mm/year and has resulted in destructive earthquakes in eastern Turkey as documented by historical records. It was showed in Figure 7 in detail. Moreover, the Ilısu dam was

built very close to the East Anatolian Fault (EAF). Due to its long and extensive historical record of the large earthquakes, the EAF zone provides an important natural laboratory to understand earthquake mechanics and fault behaviour over multiple earthquake cycles. Although the long historical record of the region, all historical earthquakes records for the East Anatolian Fault zone is not yet available. For many centuries, there have been large-magnitude (M>7) earthquakes in the EAF zone. In this study, 1995 Kobe earthquake is used for the nonlinear seismic analyses. This ground motion hit at 5:46 am on Tuesday, Jan. 17, 1995, in the southern part of Hyōgo prefecture, west-central Honshu and duration of it is 38 second. Accelerogram-time graphic of this earthquake is presented in the Fig. 8. Moreover, the time interval is selected as 0.005 sec in the nonlinear seismic analyses for the Kobe earthquake.

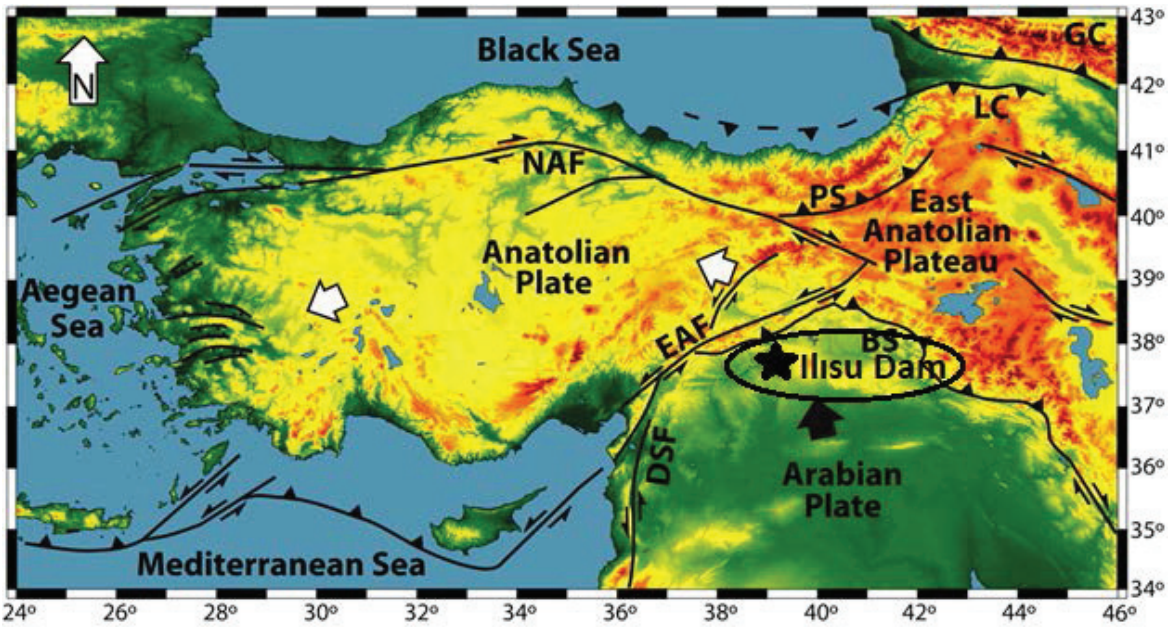

Figure 7. The fault map of Turkey and location of the Ilısu dam in seismic faults.

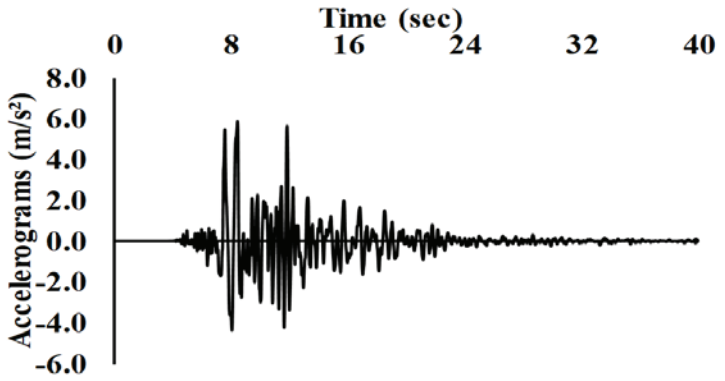

Figure 8. Accelerogram-time graphic of Kobe earthquake.

NUMERICAL RESULTS

In world countries where strong seismic ground motion occurs, such as Turkey, while constructing the huge water structure (e.g. CFR dams), we can never ignore the seismic characteristics of the zone. For this reason, the examination of the nonlinear seismic behaviour of such structures is vital importance in terms of the safety and future of these water constructions. In this study, the nonlinear seismic behavior of Ilısu dam that was constructed in a strong seismic region, is investigated graphically in detail. Firstly, the static analyses are performed for the empty condition of Ilısu dam and dam is collapsed under self-weight. Afterwards, nonlinear seismic analyses are performed only for the full

reservoir condition of the Ilısu dam considering various near fault ground motions. Kobe earthquake is used in the seismic analysis. While performing earthquake analysis for full reservoir condition of the dam, settlements, horizontal displacements, principal stresses that occurred from the construction phase of the dam, were not ignored. In the other word, before performed the seismic analyses, all displacements (vertical and horizontal) and principal stresses that are obtained from the collapsed 3D empty model, are set to zero in order to exclude the stresses and deformations. The numerical analysis algorithm for seismic analyses is shown in Fig. 9.

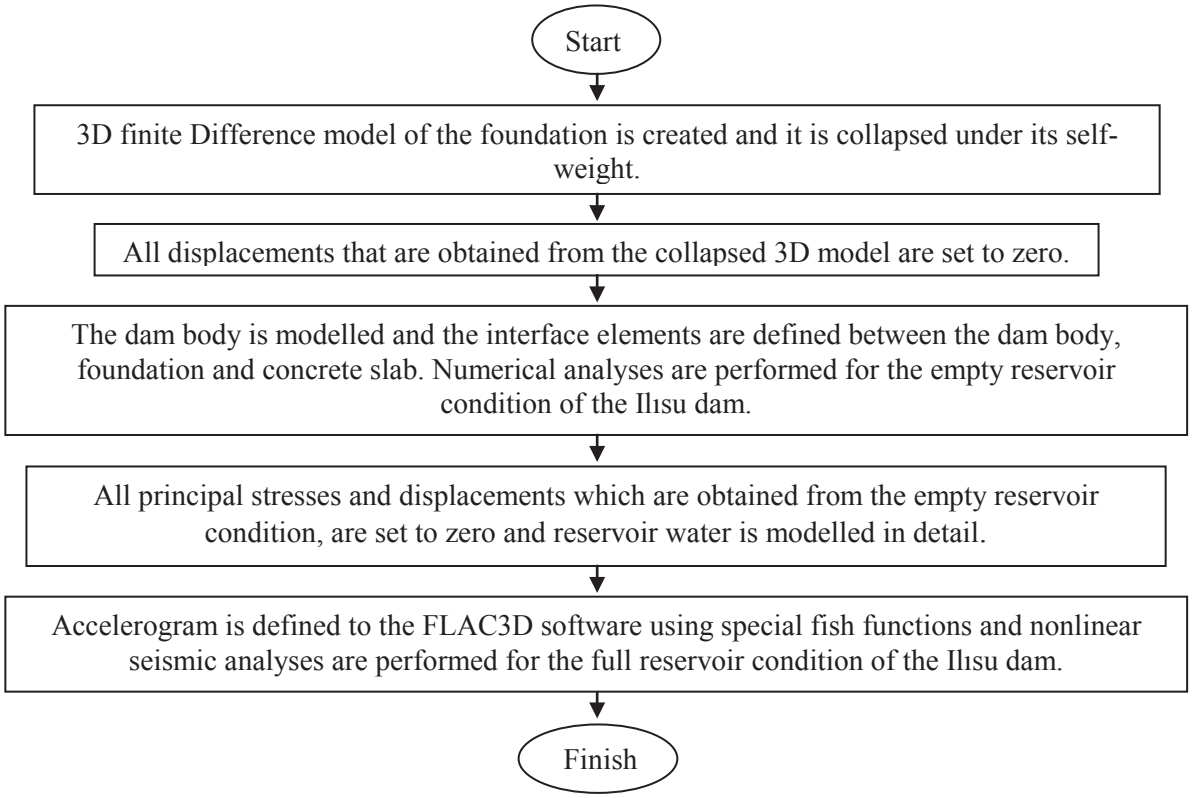

Figure 9. Numerical analysis algorithm for nonlinear seismic analyses.

Interaction elements should be defined between the dam bady-foundation-concrete slab to provide interaction between the discrete surfaces. Special shear (k_s) and normal (k_n) stiffness coefficients are calculated according to the mechanical properties of each rockfill material in this study. These coefficients and special friction values are defined between these surfaces to provide the interaction condition using the special fish functions. Normal- shear stiffness and friction values are considered as 10^8 Pa/m and 30^o between dam body and foundation. While detemining the boundary conditions of the 3D model, the special boundary conditions that are special for the nonlinear seismic analyses are used for the seismic analyses. Quiet boundary condition is defined for the bottom of the foundation to represented the viscous boundary condition. Moreover, the free field boundary condition is used for lateral surfaces of the 3D model. Accelerogram and period of the earthquake are defined to the FLAC3D software using special fish functions and these acceleration values are applied to the bottom of the 3D model considering x, y and z directions of the earthquake. As a result of the seismic analysis, the settlements, horizontal displacements and principal stresses are presented for three critical nodal points (Fig. 5) on the dam body surface and fatigue in the rockfill materials are evaluated in Fig. 10, 11, 12.

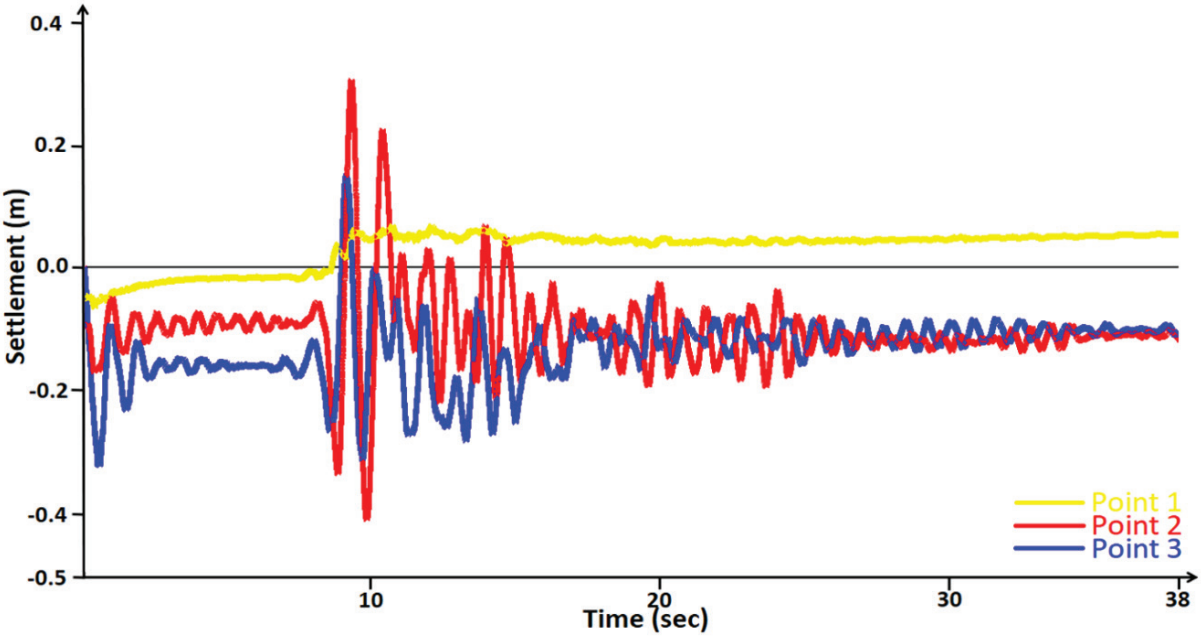

Figure 10. Settlement results for 3 various nodal points on the dam body surface.

Settlement results for these nodal points are shown graphically in Fig. 10. Maximum settlement is observed at Point 2 (middle nodal point). Moreover, minimum settlement occurred at Point 1. This important result is clearly shown that when compared to other points of the dam, more settlement occurs at the middle of the dam body surface during earthquake. 43 cm maximum settlement is observed on the Point 2 in the seismic analyses. In addition, 32 cm maximum settlement occurred on the Point 3 (top nodal point) at the 1.2th second of the earthquake. Finally, 7 cm maximum settlement is obtained on the Point 1 (lowest nodal point) as seen Fig. 10. In spite of no significant accelerations occurred between 24th and 38th second of the Kobe earthquake, significant settlements are observed for three nodal points between these seconds. This result is clearly shown the effect of the earthquake on the fatigue behaviour of the rockfill material.

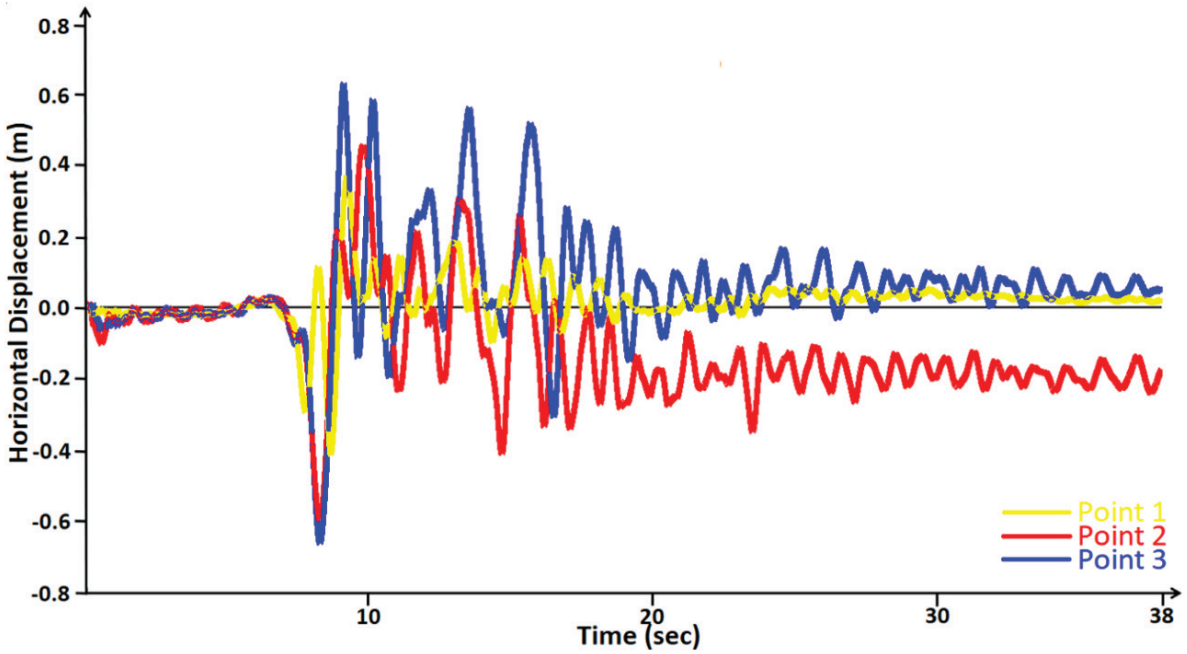

Figure 11. Horizontal displacement results for 3 various nodal points on the dam body surface.

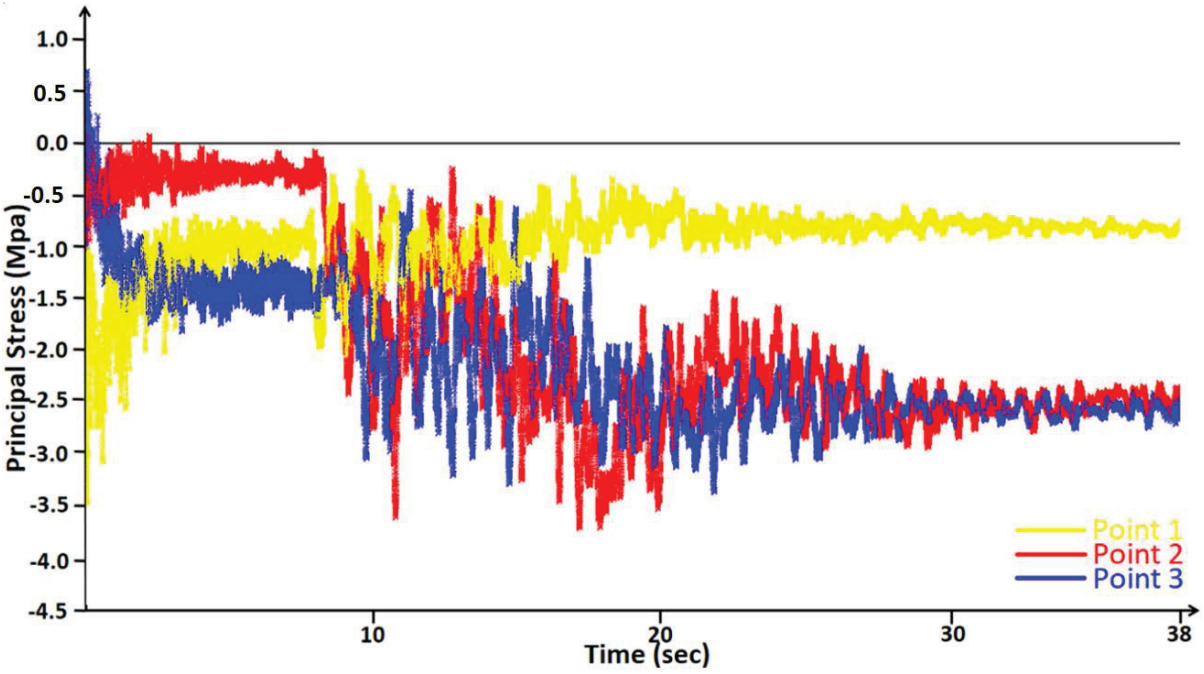

Figure 12. Principal stress results for 3 various nodal points on the dam body surface.

In Fig. 11, horizontal displacement results for three nodal points on the dam body surface are presented graphically. Maximum horizontal displacement is observed at Point 3 (top nodal point). Moreover, minimum displacement occurred at Point 1 (the lowest nodal point) as seen Fig. 11. 65 cm maximum horizontal displacement is observed for Point 3 and 45 cm maximum displacement is acquired for Point 1. No significant horizontal displacement is observed during first 7 second of the earthquake. But, in spite of no significant accelerations took place between 24th and 38th second of the Kobe earthquake, remarkable horizontal displacements are observed for three nodal points between these seconds. In Fig. 12, principal stress behaviour of the dam is shown graphically. Maximum principal stress is observed on the Point 2 at the 18th second of the earthquake. In addition, minimum stress occurred at Point 1 as seen Fig. 12. Approximately 3.7 Mpa maximum principal stress is obtained for Point 2 (middle nodal point) and 3.4 Mpa maximum stress is observed for Point 3. Moreover, significant principal stress values occurred for each nodal points at the last section of the earthquake (Fig. 12).

CONCLUSION

In this paper, the effect of Kobe earthquake on the nonlinear seismic behaviour of the Ilısu dam is examined in detail. The three dimensional finite difference model of the Ilısu dam is modelled using special fish functions and it is created according to the original dam project. The special material models are used for rockfill materials, foundation and concrete slab in the earthquake analyses. The earthquake accelerations are applied to the bottom of the 3D model. The effect of this important ground motion on the nonlinear earthquake behaviour of the Ilısu dam is evaluated as below:

- According to the numerical results, the settlement behaviour of Ilısu CFR dam clearly changes by the effect of ground motions of the Kobe earthquake. This result is obviously shown that while modelling and constructing a CFR dam, seismicity of the zone and the effect of these seismicity on the seismic behaviour of the dam are never ignored. During earthquake, maximum settlement occurs at middle sections of the dam body surface. Moreover, minimum settlement is observed at the lowest section of the dam body surface. This important result obviously shows the effect of the earthquake on the seismic behaviour of the dam.
- Significant horizontal displacements are observed on the dam body surface by the effect of the Kobe earthquake. During Kobe earthquake, maximum horizontal displacements are

observed at the middle sections of the dam body surface. In addition, minimum horizontal displacements occurred the lowest section of the dam body.

- During 38 seconds of the earthquake, remarkable principal stresses are observed on the dam body surface. The effect of the earthquake loads on the principal stress behaviour of the Ilısu dam is clearly seen from nonlinear seismic analyses.

REFERENCES

Andrianopoulos K.I., Papadimitriou A.G., Bouckovalas G.D., Karamitros D.K. (2014), Insight into the seismic response of earth dams with an emphasis on seismic coefficient estimation, Computers and Geotechnics, 55, 195-210.

Arici Y. (2013), Evaluation of the performance of the face slab of a CFRD during earthquake excitation, Soil Dynamics and Earthquake Engineering, 55, 71-85.

Cen W., Wen L., Zhang Z., Xiong K. (2016), Numerical simulation of seismic damage and cracking of concrete slabs of high concrete face rockfill dam, Water Science and Engineering, 9(3), 205-211.

Chopra A K. (1966) Hydrodynamic pressures on dams during earthquakes. Berkeley, Structures and Materials. Report no. 66-2A. University of California Berkeley, California, 45p.

DSI (2018), General Directorate of State Hydraulic Works, Regional Directorate, Ankara.

Han B., Zdravkovic L., Kontoe S., Taborda D. (2016), Numerical investigation of the response of the Yele rockfill dam during the 2008 Wenchuan earthquake, Soil Dynamics and Earthquake Engineering, 88, 124-142.

Housner, G. W. and M. D. Trifunac (1967). Analysis of accelerograms--Parkfield earthquake, Bull. Seism. Soc. Am. 57, 1193-1220.

Hudson, D. E. (1958). The Wilmont Survey Type Strong-Motion Earthquake Recorder, Earthquake Engineering Research Laboratory, California Institute of Technology.

Kartal, M.E., Cavusli, M., Sunbul, A.B. (2017), Assessing seismic response of a 2D roller-compacted concrete dam under variable reservoir lengths, Arabian Journal of Geoscience, 10: 488. https://doi.org/10.1007/s12517-017-3271-y, 2017.

Westergaard, H.M. (1933) Water pressures on dams during earthquakes. Am Soc Civ Eng Trans, 98(2); 418-433.

Xu B., Kong X., Hu Z., Zhou Y. (2015): Dynamic damage evaluation on the slabs of the concrete faced rockfill dam with the plastic-damage model, Computers and Geotechnics, 65, 258-265.

Yang X.g. and Chi S. c. (2014), Seismic stability of earth-rock dams using finite element limit analysis, Soil Dynamics and Earthquake Engineering, 64, 1-10.

Yazdani Y. and Alembagheri M. (2017), Seismic vulnerability of gravity dams in near-fault areas, Soil Dynamics and Earthquake Engineering, 102, 15-24.

Yeow et al., (2016) Wall building stiffness and strength effect on content sliding in Wellington seismic conditions, Earthquake Eng. & Structural dynamics, doi:10,1002/ege.2843.

Zou D., Han H., Liu J., Yang D., Kong X. (2017), Seismic failure analysis for a high concrete face rockfill dam subjected to near-fault pulse-like ground motions, Soil Dynamics and Earthquake Engineering, 98, 235-243.

5th International Symposium on Dam Safety

October 27-31, 2018

NUMERICAL ANALYSIS OF THE STRUCTURAL BEHAVIOUR OF ARCH DAMS USING SHELL FINITE ELEMENT FORMULATION

Sedat KÖMÜRCÜ [1], Murat YILMAZ[2]

ABSTRACT

Arch dams are widely preferred structures in terms of their strong structural behavior because of the arch geometry. Numerical analysis of the arch dams is a necessary not only to validate the structural performance of the existing arch dams but also to model and analyze modern dam constructions. Finite element models for the arch dams are generally very complicated in terms of having many unknown parameters. In this study, finite element analysis of an arch dam is performed with using a shell finite element formulation to investigate structural behavior of the arch dam. A four-node shell finite element is proposed and used for analyzing of an arch dam. The arch dam geometry is simplified with using a middle surface. The formulation is verified with arch dam example in the literature. Robustness of using a shell finite element formulation is indicated with the finite element analysis. Arch stresses at the upstream and downstream of the dam are presented as structural results. It is seen from the results, using a shell finite element is dramatically practical and effective for the structural analysis of the arch dams.

Keywords: Arch dams, Finite elements, Shell element, Structural behavior

INTRODUCTION

The development of new finite elements has been a significant subject in recent years. Shell finite elements have a wide using area for engineering applications. The main purpose of producing new element formulations is to increase the success of the finite element analysis using as sparse as possible finite element mesh. Different approaches can be tried to produce a simple and effective shell finite element. One of the methods is to formulate a shell element with combining membrane element and plate bending element. This method is very preferred way of producing shell element because of the simplicity of the formulation.

Various studies have been carried out for the formulation of finite elements. Groenwold and Stander studied on the combinations of membrane and plate elements (Groenwold and Stander, 1998). Bergan and Fellipa prepared a finite element formulation considering the out of plane displacement (Bergan and Felippa, 1985). Cook combined a hybrid method with out of plane rotation (Cook, 1986). Long and Xu studied to develop appropriate element models (Long and Xu, 1994). Pimpinelli worked on strain quadrilateral elements with drilling degree of freedom (Pimpinelli, 2004). Future work will be done to improve the results by making minor changes to existing element formulations.

[1] Research Assistant, Department of Civil Engineering, Istanbul Technical University, Istanbul, Turkey, e-posta: komurcus@itu.edu.tr

[2] Doctor, Department of Civil Engineering, Istanbul Technical University, Istanbul, Turkey, e-posta: yilmazmura@itu.edu.tr

Arch dams have a significant place among the all dam types. Remarkable studies have been done to analyze of arch dams. Rydzewski produced a significant study on the theory of arch dams (Rydzewski, 1965). Bernardou and Boisserie used the thin shell theory to analyze arch dam structures (Bernardou and Boisserie, 1982).

In this study, the plane stress element with drilling degree of freedom and the plate bending element are combined to obtain a shell end element with 6 degrees of freedom in each node and 24 degrees of freedom totally. The finite element is used to perform a numerical experiment for the analyzing of arch dams effectively.

FINITE ELEMENT FORMULATION OF SHELL ELEMENT

The shell finite element is obtained by combining the membrane element including the out of plane rotation and the plate bending element. Figure 1 shows the combination of membrane and plate element to obtain the shell element.

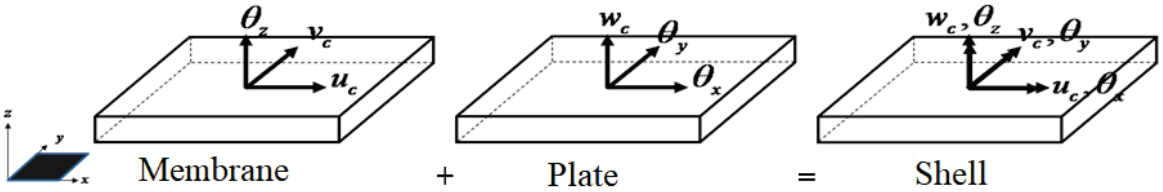

Figure 1. Shell element obtained by the combination of membrane and plate elements

u, v, and w be the displacements in the local x, y and z directions, respectively. θ_x, θ_y and θ_z are the rotations about the *x, y* and *z* directions, respectively. By writing the equilibrium equations in the x and y directions of the membrane element, the following equations are obtained by (Equation 1) and (Equation 2). Where *N* represents normal force and *q* is the load.

$$\frac{\partial N_x}{\partial x} + \frac{\partial N_{xy}}{\partial y} + q_x(x,y) = 0 \quad (\text{x } direction) \tag{1}$$

$$\frac{\partial N_y}{\partial y} + \frac{\partial N_{xy}}{\partial x} + q_y(x,y) = 0 \quad (y\ direction) \tag{2}$$

Normal force and strain relationships can also be expressed in matrix form as shown in (Equation 3). Where *E* and *v* are modulus of elasticity and Poisson ratio, respectively.

$$\begin{Bmatrix} N_x \\ N_y \\ N_{xy} \end{Bmatrix} = \frac{Eh}{(1-v^2)} \begin{bmatrix} 1 & v & 0 \\ v & 1 & 0 \\ 0 & 0 & \frac{1-v}{2} \end{bmatrix} \begin{Bmatrix} \frac{\partial u_c}{\partial x} \\ \frac{\partial v_c}{\partial y} \\ \frac{\partial u_c}{\partial y} + \frac{\partial v_c}{\partial x} \end{Bmatrix} \tag{3}$$

The following is the classical plate theory available in (Reddy, 2005). By writing the equilibrium equations in the x and y directions for the plate, the following equations are obtained as (Equation 4), (Equation 5) and (Equation 6). Where V and M are shear force and moment, respectively.

$$\frac{\partial V_x}{\partial x} + \frac{\partial V_y}{\partial y} + q(x,y) = 0 \qquad (vertical\ equilibrium) \tag{4}$$

$$V_y = \frac{\partial M_{xy}}{\partial x} + \frac{\partial M_y}{\partial y} \qquad (Moment\ about\ x\ axes) \tag{5}$$

$$V_x = \frac{\partial M_{xy}}{\partial y} + \frac{\partial M_x}{\partial x} \qquad (Moment\ about\ y\ axes) \tag{6}$$

If the V forces are placed in the vertical equilibrium equation, the governing differential equation is obtained as (Equation 7).

$$\frac{\partial^2 M_x}{\partial x^2} + 2\frac{\partial^2 M_{xy}}{\partial x \partial y} + \frac{\partial^2 M_y}{\partial y^2} + q(x,y) = 0 \tag{7}$$

Moment curvature relations can also be expressed in matrix form as (Equation 8). Where D is the flexural rigidity of plate.

$$\begin{Bmatrix} M_x \\ M_y \\ M_{xy} \end{Bmatrix} = -D \begin{bmatrix} 1 & \nu & 0 \\ \nu & 1 & 0 \\ 0 & 0 & \frac{1-\nu}{2} \end{bmatrix} \begin{Bmatrix} \frac{\partial^2 w}{\partial x^2} \\ \frac{\partial^2 w}{\partial y^2} \\ 2\frac{\partial^2 w}{\partial x \partial y} \end{Bmatrix} \tag{8}$$

The finite element equations can be obtained by using Virtual Work Theorem as (Equation 9).

$$\begin{aligned} &\int_A \left(N_x \frac{\partial \bar{u}}{\partial x} + N_{xy}\left(\frac{\partial \bar{u}}{\partial y} + \frac{\partial \bar{v}}{\partial x}\right) + N_y \frac{\partial \bar{v}}{\partial y} \right) dA + \\ &\int_A \left(\frac{\partial \bar{w}}{\partial x}\left(\frac{\partial w}{\partial x} N_x + \frac{\partial w}{\partial y} N_{xy}\right) + \frac{\partial \bar{w}}{\partial y}\left(\frac{\partial w}{\partial x} N_{xy} + \frac{\partial w}{\partial y} N_y\right) \right) dA + \\ &- \int_A \left(M_x \frac{\partial^2 \bar{w}}{\partial x^2} + 2M_{xy} \frac{\partial^2 \bar{w}}{\partial x \partial y} + M_y \frac{\partial^2 \bar{w}}{\partial y^2} \right) dA = \int_A \left(\bar{w} q(x,y) \right) dA \end{aligned} \tag{9}$$

The 12x12 membrane element system stiffness matrix K_M is obtained by combining the 8x8 membrane element stiffness matrix with adding the 4x4 out of plane rotation matrix (Equation 10).

$$\mathbf{K}_M = \begin{bmatrix} \mathbf{K}_8^{u_c, v_c} & \mathbf{K}_{8,4} \\ \mathbf{K}_{4,8} & \mathbf{K}_4^{\theta_z} \end{bmatrix} \tag{10}$$

The 12x12 stiffness matrix for the plate element K_P is obtained by neglecting the 4x4 mixed derivatives matrix as shown (Equation 11).

$$\mathbf{K}_P = \begin{bmatrix} \mathbf{K}_{12}^{w_c, \theta_x, \theta_y} & \mathbf{K}_{12,4} \\ \mathbf{K}_{4,12} & \mathbf{K}_4^{w_{cxy}} \end{bmatrix} \tag{11}$$

The 24x24 system stiffness matrix of the shell element is obtained by combining the stiffness matrices of the membrane element with the plate element as (Equation 12).

$$\mathbf{K}_M + \mathbf{K}_P = \begin{bmatrix} \mathbf{K}_{12}^{u_c, v_c, \theta_z} & \mathbf{0} & \mathbf{0} \\ \mathbf{0} & \mathbf{K}_{12}^{w_c, \theta_x, \theta_y} & \mathbf{K}_{12,4} \\ \mathbf{0} & \mathbf{K}_{4,12} & \mathbf{K}_4^{w_{cxy}} \end{bmatrix} \tag{12}$$

NUMERICAL ARCH DAM EXAMPLE

The finite element formulation is applied to the Grand Maison Arch Dam. The geometrical properties are used as expressed in the study of (Bernardou and Boisserie, 1982). They used the linear thin shell theory and conforming finite elements. The arch dam geometry is simplified with using a middle surface. Thus, the dam can be modelled using plane finite elements obtained in this study. Using plane elements instead of volume elements is a practical way of modelling huge structures such as dams. Analyze time considerably decrease using plane finite elements because of the degree of freedom of the system is decreased.

Model Properties

The material parameters used for the arch dam is shown in Table 1. These parameters are the elastic material parameters of the dam.

Table 1. Material parameters of the dam

Modulus of elasticity	$2x10^4$ MPa
Poisson ratio	0.2

The boundary conditions for the model is shown in Figure 2. Fixed ends represent the contact surfaces between the arch dam and soil surface. Free end represents top of the arch dam. Only ½ part of the dam is modelled in terms of symmetry using symmetrical boundary conditions. Using symmetrical boundary conditions is decrease the computational cost of the analyze effectively.

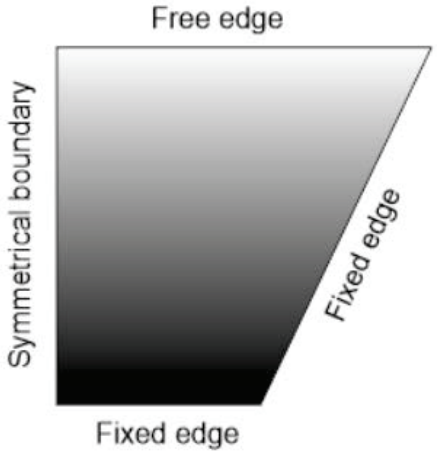

Figure 2. Boundary conditions of the dam

Results of the Finite Element Analysis

To test the performance of the element, Grand Maison Arch Dam is modelled, and stress values are analyzed. The stress values measured at the top of the crown cantilever and base of crown cantilever. Upstream and downstream stress values are calculated as shown in Table 2. Only hydrostatic loading is considered for the finite element analysis. The stress values are compared with the study of Bernardou and Boisserie in 1982. The results are compatible with their study in terms of the theory and finite element models.

Table 2. Stress values for the arch dam (MPa)

Study	Top of crown cantilever		Base of crown cantilever	
	Upstream	Downstream	Upstream	Downstream
Bernardou and Boisserie (1982)	-4.800	-2.883	2.753	-2.974
Present study	-4.955	-3.175	2.965	-3.156

CONCLUSION

In this study, a shell finite element having six degrees of freedom at each node and total of twenty-four degree of freedom is obtained. The membrane and plate element are combined to produce the shell element. Finite element analyzes are performed on the arch dam to investigate the performance of the shell element. As seen the compatible results with the Grand Maison arch dam example, the obtained shell element can be used for other similar arch dams making some simplifications such as using a middle surface. But these results are not the exact results for the arch dam structures and may be change with the effects of other types of loadings and conditions. Therefore, the designers and engineers should be cautious of the evaluation of the results of finite element analyzes.

REFERENCES

Bergan, P.G., Felippa, C.A., 1985. “A triangular membrane element with rotational degrees of freedom”. Comput. Meths. Appl. Eng, vol. 50, 25-69.

Bernardou, M., Boisserie, J.M., 1982. The Finite Element Method in Thin Shell Theory: Application to Arch Dam Simulation. Springer, New York.

Cook, R.D., 1986. “On the Allman triangle and a related quadrilateral element”. Comput. Struct., vol 22, 1065 1067.

Groenwold, A.A., Stander, N., 1998. “A 24 d.o.f. four-node flat shell finite element for general unsymmetric orthotropic layered composites”. Engineering Computations, vol. 15, N.4, 518-543.

Long, Y.Q., Xu, Y. 1994. “Generalized conforming quadrilateral membrane element with vertex rigid rotational freedom”. Comput Struct, vol 52, N.4, 749-755.
Pimpinelli, G., 2004. “An assumed strain quadrilateral element with drilling degrees of freedom”. Finite Elem Anal Des, vol. 41, 267-283.
Reddy, J.N., 2005. An Introduction to The Finite Element Method. McGraw-Hill, New York.
Rydzewski, J.R., 1965. Theory of Arch Dams. Pergamon Press, Oxford.

5th International Symposium on Dam Safety

October 27-31, 2018

EARTHQUAKE INDUCED PERMANENT DISPLACEMENT ASSESSMENT FOR ROCKFILL DAMS

Selda DURMAZ [1], Deniz ÜLGEN[2]

ABSTRACT

Rockfill is mostly preferred material for the dam construction at earthquake prone regions due to its high seismic energy absorption capacities. Increasing number of rockfill dams around the world provoke new studies on the dynamic behavior. This paper, intends to observe the dynamic response of concrete faced rockfill dams (CFRD). Therefore, a series of numerical analyses were conducted with a finite element method (FEM) based software. Since the rockfill material exhibits reduction in shear strength during the earthquake shakings, equivalent linear analysis procedure was followed. Thus, variation of shear modulus and damping properties were defined for the rockfill material. Effects of peak ground acceleration (PGA) of input motion, geometric properties as dam height, upstream and downstream slopes were scrutinized. Real earthquake records with different frequency contents were applied to the models. Newmark sliding block method is used to obtain the permanent displacement calculations. Evaluated results are represented in terms of permanent displacement (D), peak ground acceleration (PGA) and are compared with the case histories. Results of this study may be utilized for the preliminary design stage of concrete faced rockfill dams.

Keywords: Permanent displacement, Newmark sliding block analysis, Rockfill dams

INTRODUCTION

Concrete faced rockfill dams (CFRD) are both feasible way outs for difficult site conditions and applicable at seismically active regions for a good post-earthquake serviceability. While the Alto Anchicaya Dam was placed on a deep alluvium foundation, the Zipingpu Dam was built at a highly seismic area (Wen et al., 2017). Even the rockfill material provides seismic safety with high energy absorption capacity, some earthquake exposures yielded dam failures. Many failure examples indicate the inadequacy of the present information about the seismic design of CFRDs. Although the fundamental rules which dominate the behavior mostly revealed, the dynamic characteristic of CFRDs has not been understood completely yet. Basically earthquake induced permanent deformations are studied with the following approaches: 1) Numerical methods as finite element or finite difference methods; 2) Experimental methods as centrifuge test or shaking table tests have been carried out on dam models; 3) Deterministic methods as calculation of probability of likely deformations with correlations. Individual or combined applications of this methods were used to draw an overall frame for fill dams. Jibson (2007), Bray and Travasarou (2007), Rathje and Saygılı (2009) focused on the probabilistic studies to measure the contribution of uncertain parameters. Yield coefficient (k_y), initial fundamental period of dam (T_s), Arias intensity (I_a), peak ground acceleration (PGA), peak ground velocity (PGV) were utilized to establish probabilistic equations for the calculation of likely

[1] Research Assistant, Department of Civil Engineering, Mugla Sıtkı Kocman University, Mugla, Turkey, e-posta: seldadurmaz_22@hotmail.com

[2] Associated Professor, Department of Civil Engineering, Mugla Sıtkı Kocman University, Mugla,, Turkey, e-posta: denizulgen@gmail.com

permanent deformations of fill dams, embankments, natural slopes, compacted earth fills and municipal solid-waste landfills. Singh et al. (2007) studied on the results of 122 case histories of earth dams and embankments previously subjected to earthquakes. Newmark method based approaches were used to reevaluate the permanent deformations of these case histories. When the results are compared, in general, calculated ones are smaller than the site observations. Similarly, Meehan and Vahedifard (2013) reevaluated the results of 122 case studies of earth dams and embankments using 22 suggested numerical equations for the calculations of earthquake induced permanent displacements. Likewise, the results were coherent with the study of Singh et al. (2007), observed deformations in dam body were greater than calculated ones. Singh and Roy (2009) searched the earthquake induced crest settlement of 152 published case histories of embankment dams. Crest exhibits larger deformations when the fundamental period of embankment is close to the predominant period of earthquake. Furthermore, magnitude of earthquake and vertical component of seismic excitation cause same impact on the crest settlement. Wang et al. (2017) conducted a large scale shaking table test on a concrete-rockfill combination dam (CRCD). This dam type can be describe as a composition of concrete upstream wall and inclined rockfill downstream. According to the results of this study, despite the amplification increases with the height in the upper part of dam and the dam body is sensitive to low frequency components, general seismic performance of these dams are convincing. Zou et al. (2017) studied the influence of near-fault pulse-like ground motions on the seismic failure analysis of high CFRDs. This numerical study showed that dynamic response of the dam increases with the increasing ratio of peak ground velocity to peak ground acceleration (PGV/PGA). Additionally, even the acceleration records have the similar Arias intensities, pulse-like motion causes significant residual deformation increments. Furthermore, Pang et al. (2018) investigated seismic reliability of earth-rockfill dams utilizing generalized probability density evolution method considering the strain dependent material properties. His investigation yields a new parameter called “cumulative time of the factor of safety smaller than 1.0”. According to this study, reliability assessments can be done due to new index and the strain softening behavior should be taken into consideration.

Aforementioned studies generally capture all embankment types as earth dams, natural slopes, and earth and rockfill composition dams. CFRDs, on the other hand, are not studies specifically alone. In this paper, only results of the numerical study conducted for CFRDs were represented. Numerical dam models were subjected to seismic loadings and permanent displacements were calculated according to the Newmark sliding block method. Moreover, recorded case histories of compacted multi zone, multi zone rockfill, concrete faced rockfill, and concrete faced decomposed granite or gravel dams were utilized to crosscheck the numerically evaluated results.

MATERIALS AND METHODS

Numerical Dam Models

Intuitively, earthquake related parameters as PGA, relation between predominant period of excitation and fundamental period of dam, strain dependent parameters of fill and foundation material as damping and strength have much control over the earthquake induced deformations. Thus, influence of these parameters were scrutinized in this study numerically. Combination of different dam geometries, earthquake loadings, and material parameters were tested with a finite element based software. While creating the models, 50m and 200m dam heights; 1:1.2, 1:1.4, 1:1.6 and 1:1.8 slope inclinations were selected. In numerical models, dynamic loadings were provided from real earthquake records and paid attention them to have different frequency contents. Acceleration records of six real earthquakes having moment magnitude (M_w) from 6.5 to 7.5 were used (Table 1). Within the scope of this study, peak ground acceleration is utilized as an earthquake intensity measurement. In order to ascertain the existence of any impact of PGA, maximum values of acceleration records were scaled to 0.2g, 0.4g, and 0.6g levels. A summary of combined parameters are given in Table 2.

Since this is a parametric study, making no specification, fill material was assumed as any rock type appropriate for dam construction. Thus, constant values were used for the unit weight, Poisson's ratio and the cohesion and kept constant for all models. However, as given in Table 3, internal friction angle values of fill materials varied as 35, 40, 45, 50 degree, in order to investigate whether or not it has any effect on the dynamic response.

Table 1. Earthquakes used in analyses

Earthquakes	Date	Fault Mechanism	PGA	Predominant Period (s)	Moment Magnitude (M_w)
Cape Mendocino	1992	Thrust	0.39	0.24	7.2
Düzce	1999	Strike Slip	0.35	0.82	7.2
Kobe	1995	Strike Slip	0.50	0.44	6.9
Landers	1992	Strike Slip	0.65	0.08	7.3
Northridge	1994	Thrust	0.40	0.22	6.7
Tabas	1978	Thrust	0.11	0.54	7.4

Table 2. Used parameters in dam models

Dam height	50 m – 200 m
Crest width	5 m – 20 m
Slope inclination	1:1.2 - 1:1.4 - 1:1.6 - 1:1.8
Internal friction angle	35° - 40° - 45° - 50°
Earthquake	6 records
Peak ground acceleration	0.2g - 0.4g – 0.6g

Table 3. Material properties of rockfill

Unit weight (γ) (kN/m^3)	22
Poisson's ratio (υ)	0.2
Cohesion (C) (kN/m^2)	0
Internal friction angle (ϕ) (degree)	35° - 40° - 45° - 50°

Dynamic Analyses

Dynamic analyses of this study were conducted with a finite element based software, QUAKE/W. In this software, linear elastic model, equivalent linear model and non-linear model are available constitutive material models. Among these three options, equivalent linear model can be used for the cases in which earthquake like repeated loadings are present. Furthermore, equivalent linear analysis enables to consider the shear strength degradation throughout the cyclic loading. Repeated loads cause changes in dynamic material properties as decreasing in shear strength and increasing in damping. In QUAKE/W, the shear strength-strain and damping-strain variation curves can be defined by users to approximate the realistic response of structure. In the present study, damping and shear strength degradation curves were provided from the study of Jia and Chi (2012). Their study represent the strain dependency of 35 kinds of rockfill material and the results are summarized in terms of best fit, one standard division and two times standard division curves. In the present study, best fit curve was utilized. Used curves are given in Figure 1 and Figure 2. As stated above, equivalent linear analysis was used and this method follows an iteration procedure. Iteration procedure stars with the maximum values of parameters. Thus, maximum shear strength (G_{max}) must be defined at the beginning. While calculating G_{max}, dam models were divided into layers with ten meter thickness and the G_{max} values

were evaluated at the mid-point of each section. Besides, another important point is mesh generation for an accurate numerical simulation. According to Kuhlemeyer and Lysmer (1973), mesh size (ΔL) should be less than one-tenth to one-eighth of the wave length associated with the highest frequency component of the wave. This recommendation was considered during the mesh generation**.**

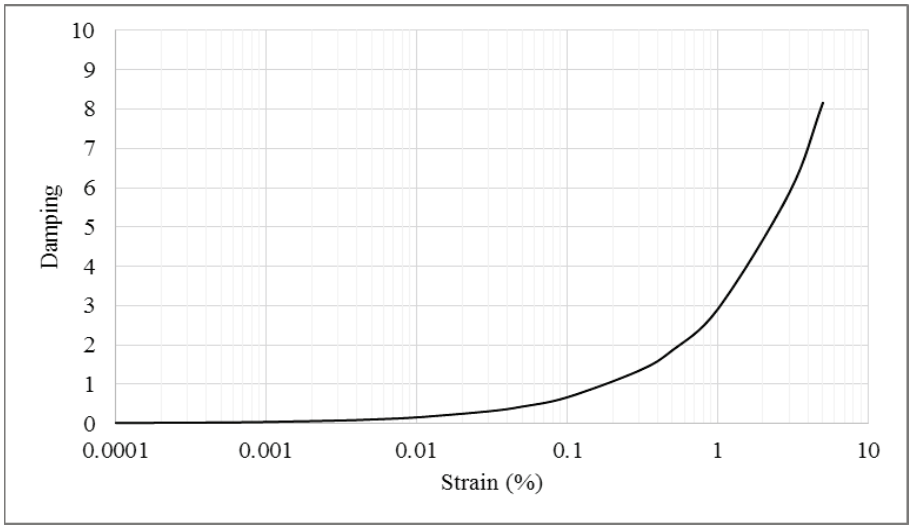

Figure 1. Damping versus strain values used in analyses Jia and Chi (2012)

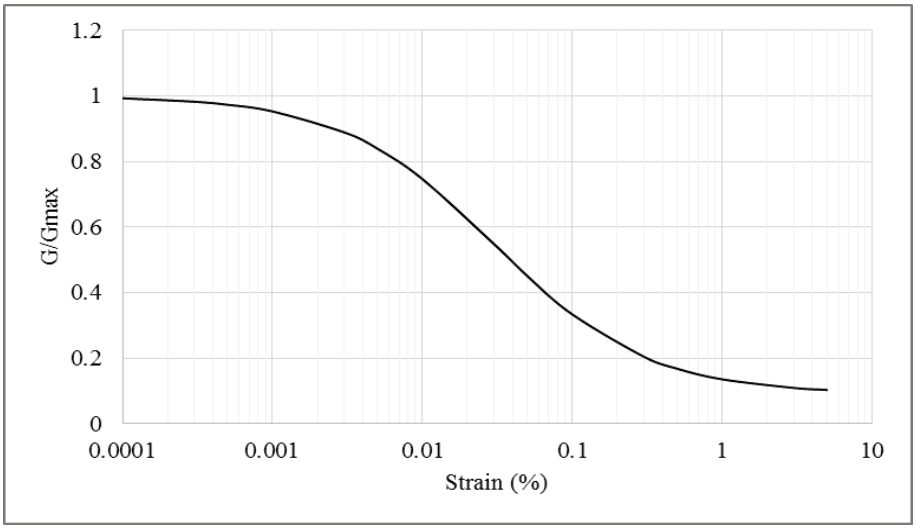

Figure 2. Shear modulus versus strain curve used in analyses Jia and Chi (2012)

Permanent Displacement

Earthquake induced permanent deformations are generally observed utilizing Newmark (1965) sliding block procedure. According to the method, every slip surface has a yield acceleration (a_y) and this acceleration can be defined as a threshold for the deformation initiation. Factor of safety of the related slip surface yields "1" for the yield acceleration. When the embankment is subjected to an acceleration greater than yield acceleration, deformations may be generated within the dam body. Double integration of exceeding accelerations yields permanent displacement. Herein, the main concern for the reliability of the results is the estimation of yield accelerations for the critical slip surfaces and pseudo-static analysis method can be used for the evaluation of yield acceleration. In this study, yield accelerations of predefined slip surfaces with three different sliding depths were obtained with a limit equilibrium based software, SLIDE. In order to apply pseudo-static analysis in SLIDE, required parameter is yield coefficient (k_y). According to the theory, effects of earthquake based forces can be simulate by multiplying the PGA with a yield coefficient. This multiplication represents

the horizontal force caused by dynamic loading. In the scope of this study, yield coefficients were applied as 1/2 and 1/3 of peak ground acceleration as summarized in the study of Kramer (1996).

By using earthquake induced acceleration from dynamic analyses and yield accelerations from pseudo-static analyses, permanent displacements were calculated. Maximum crest accelerations with different levels of PGA are represented in Figure 3 and 4 for 50m and 200m dams, respectively. A trend line is placed on the figures for the average values of the accelerations. Another finding is the variation of permanent displacement with the ratio of yield acceleration to PGA for 50m and 200m dam in Figure 5 and 6 respectively. Although, there is no upper limit for a critical deformation that can jeopardize the safety of structure, Hynes-Griffin and Franklin (1984) proposed the maximum allowable deformation as 100 cm. As seen in the Figure 5 and 6, this limit cannot be exceed if the ratio of yield acceleration to PGA is greater than 0.4.

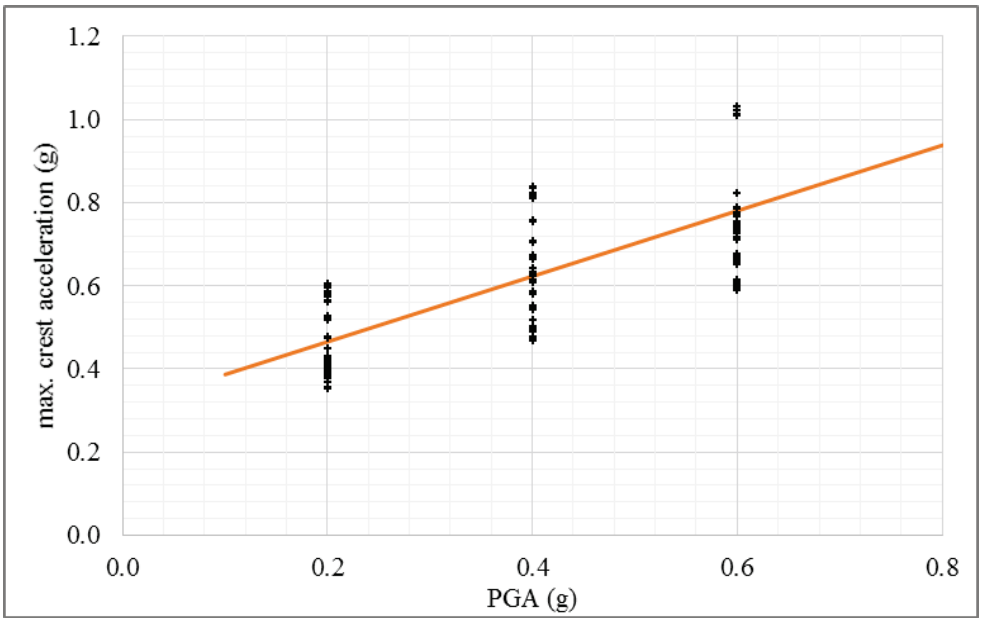

Figure 3. Relation between maximum crest acceleration and PGA for 50 m dam

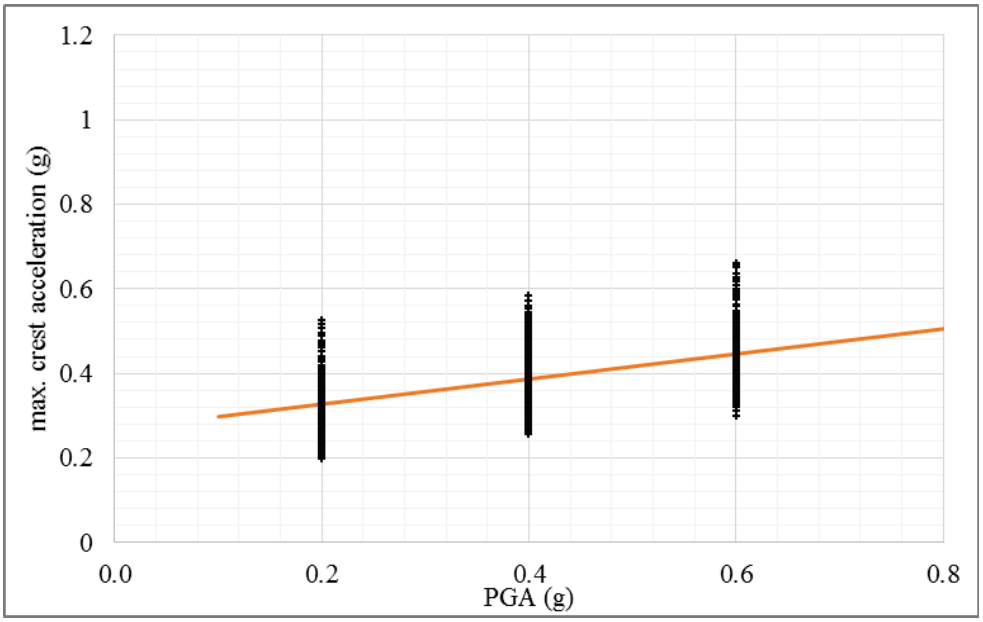

Figure 4. Relation between maximum crest acceleration and PGA for 200 m dam

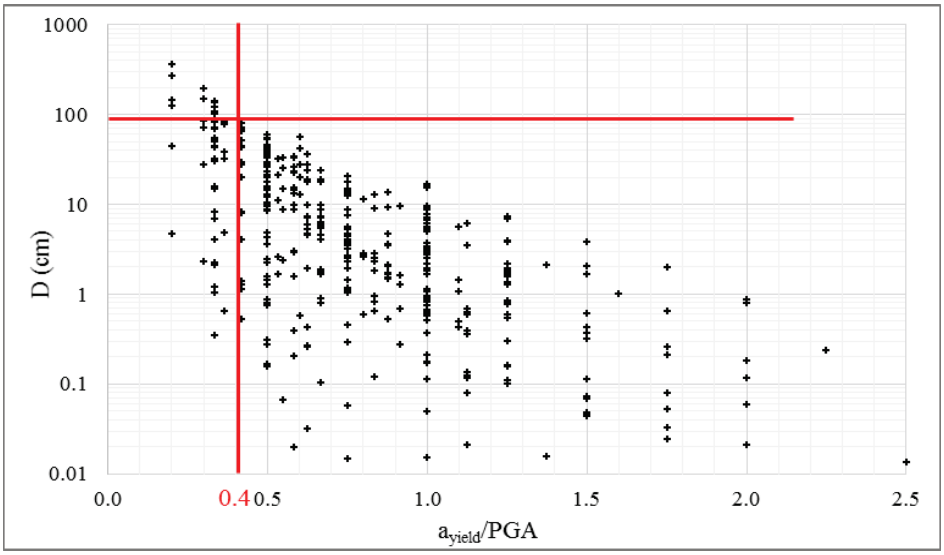

Figure 5. Variation of permanent displacement with the ratio of yield and maximum ground acceleration for 50 m dam

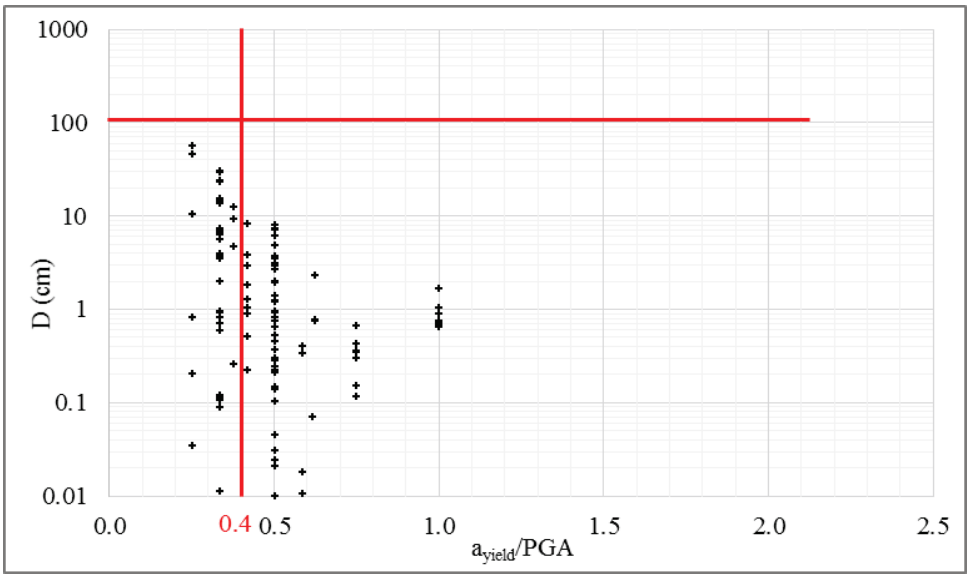

Figure 6. Variation of permanent displacement with the ratio of yield and maximum ground acceleration for 200 m dam

CASE STUDIES

In the present study, results of 54 case histories of embankments including compacted multi zone (type 1), multi zone rockfill (type 2), concrete faced rockfill (type 3), and concrete faced decomposed granite or gravel (type 4) dams were assessed. Table 4 shows the properties of dams and the causative earthquakes, and the exhibited horizontal deformations due to earthquake. Numerically evaluated horizontal displacements were represented as a range in terms of minimum and maximum values. Dam heights of the case studies varies in a wide range comparing with the numerical study, thus, assessments were made considering the a_{yield}/PGA ratios. Owing to the lack of instrumentation, researchers utilized attenuation relationships to obtain the maximum acceleration values of the earthquakes at dam site. Herein, used parameters are: Tp for predominant period of earthquake, T_D (s) for fundamental period of dam, a_{max}(g) for peak ground acceleration obtained with attenuation relations, M_w for moment magnitude of earthquake, a_y (g) for yield acceleration.

Table 4.Properties of case histories

Dam					Earthquake					a_y /PGA	Observed Displacement	Numerical Displacement	References
Name	Type	Height (m)	T_D (s)	a_y (g)	Date	M_w	a_{max} (g)	Distance (km)	T_p(s)		D(cm)	D(cm) D_{min}-D_{max}	
Anderson	2	73.2	1.08	0.34	10/17/89	7	0.26	16	0.32	1.31	2.1	0.02-4	Harder
Anderson	2	71.6	1.08	0.27	4/24/84	6.2	0.41	16	0.32	0.66	0.9	0.02-50	Bureau et al.
Austrian	1	21.5	0.79	0.21	10/17/89	7	0.58	11	0.32	0.36	30.5	0.05-90	Harder
Asagawara regulatory	1	56.4	0.53	0.08	10/23/04	6.8	0.12	24	0.32	0.67	40	0.02-50	Yasuda et al.
Baihe	1	66	0.89	0.06	7/28/76	7.8	0.2	150	0.52	0.30	700	0.9-110	Lingyao et al.
Brea	1	27.4	0.76	0.25	1/17/94	6.9	0.19	67	0.45	1.32	0.1	0.2-1	Abdel-Ghaffar and Scott
Chang	1	15.5	0.25	0.05	1/26/01	7.6	0.5	13	0.32	0.10	607	5-800	Singh et al.
Chofukuji	1	27.2	0.38	0.09	10/23/04	6.8	0.1	21	0.32	0.90	5	0.5-9	Yasuda et al.
Cogswell	3	8.5	0.69	0.15	6/28/91	5.6	0.26	4	0.25	0.58	4.1	0.01-30	Boulanger et al.
El Infiernillo U/S	2	148	1.58	0.13	9/21/89	7.2	0.12	116	0.56	1.08	3.3	0.01-10	Resendiz et al.
El Khattabi	4	27.5	0.37	0.18	2/24/04	6.4	0.25	21	0.25	0.72	1	0.05-15	EERI
EJ Chesbro	1	29	0.46	0.15	10/17/89	7	0.43	13	0.32	0.35	1.5	0.2-70	Harder
Fatehgadh	1	11.6	0.28	0.07	1/26/01	7.6	0.3	80	0.55	0.23	223	0.15-110	Singh et al.
Guadalupe	1	43.3	0.68	0.19	10/17/89	7	0.43	19	0.32	0.44	4.5	0.02-11	Harder
Guldurcek	1	68	0.91	0.27	6/6/00	5.9	0.13	19	0.27	2.08	1	0.02-1	Ozkan et al.
Hebgen	1	27.5	0.47	0.22	8/17/59	7.5	0.7	100	0.65	0.31	576	0.7-110	Seed et al.
Ishibuchi	3	53	0.63	0.28	5/26/03	7.1	0.27	85	0.42	1.04	0.1	0.01-10	Nagayama et al.
Kalaghoda	1	14.9	0.18	0.29	1/26/01	7.6	0.3	65	0.47	0.97	5	0.01-10	Krinitzsky and Hynes
Kalpong	3	27	0.35	0.1	9/14/02	6.5	0.1	21	0.27	1.00	0.1	0.01-10	Rai and Murty
Kanayatani	4	4	0.05	0.04	10/6/00	7.3	0.11	14	0.32	0.36	100	0.2-70	Matsuo
Kashi	1	16	0.25	0.14	8/23/85	7.4	0.25	21	0.32	0.56	30	0.01-60	Chonggang
Kashi	1	16	0.25	0.14	9/12/85	6.8	0.5	16	0.3	0.28	100	0.8-110	Chonggang
Kaswati	1	12	0.33	0.15	1/26/01	7.6	0.28	110	0.6	0.54	240	0.02-60	Singh et al.
Kawanishi	1	43	0.59	0.14	10/23/04	6.8	0.14	17	0.32	1.00	30	0.01-10	Yasuda et al.
Kitayama	1	25	0.34	0.15	1/17/95	7.1	0.3	31	0.32	0.50	75	0.01-80	Sakamoto et al.

Table 4.Continue

La Palma	1	10	0.12	0.05	3/3/85	7.8	0.46	80	0.38	0.11	183	2-700	De Alba et al.
La Villita	2	60	0.94	0.2	10/11/75	4.9	0.15	52	0.27	1.33	1.2	0.02-9	Elgamal et al.
La Villita	2	60	0.94	0.2	9/19/85	8.1	0.24	58	0.48	0.83	10.2	0.06-11	Elgamal et al.
Lexington	1	62.5	0.77	0.13	10/17/89	7	0.45	10	0.32	0.29	7.5	0.9-110	Harder
Long Valley	1	38.4	0.52	0.23	5/27/80	6.1	0.2	16	0.25	1.15	0.1	0.02-9	Lai and Seed
Lower Van Norman	1	24	0.38	0.19	2/9/71	6.6	0.6	13	0.27	0.32	0.1	0.1-70	Chaney
LA dam	1	47.3	0.6	0.15	1/17/94	6.9	0.43	7	0.32	0.35	2.4	0.2-70	Seed et al.
Makubetsu	1	26.9	0.42	0.18	9/26/03	8	0.25	141	0.5	0.72	70	0.01-12	Nagayama et al.
Matahina	2	86	1.08	0.17	3/2/87	6.5	0.24	11	0.28	0.71	25	0.01-11	Pender and Robertson
Miboro	2	131	1.43	0.23	8/19/61	7	0.15	16	0.32	1.53	5.2	0.09-7	Bureau et al.
Murayama	1	39	0.52	0.29	9/1/23	8.2	0.8	96	0.6	0.36	180	0.01-90	Seed et al.
Newell	2	55.5	0.75	0.25	10/17/89	7	0.43	10	0.32	0.58	23	0.8-40	Harder
Niwa Ikumine	1	15	0.23	0.07	07/12/93	7.8	0.28	71	0.36	0.25	0	0.02-130	Tani
Ono	1	36.6	0.52	0.27	9/1/23	8.2	0.8	96	0.6	0.34	24.4	0.2-70	Seed et al.
Oroville	1	235	2.74	0.21	8/1/75	6	0.11	7	0.25	1.91	0.1	0.02-2	Bureau et al.
Otani-Ike	1	27	0.65	0.15	12/21/46	8.3	0.8	45	0.32	0.19	0	2-700	Stroitel
Rudramata	1	27.6	0.28	0.07	1/26/01	7.6	0.3	80	0.55	0.23	433	2-600	Singh et al.
San Justo	2	41	0.51	0.27	10/17/89	7	0.26	27	0.32	1.04	0.1	0.01-10	Harder
Sasoi	1	20	0.27	0.3	1/26/01	7.6	0.2	120	0.32	1.50	9	0.6-6	Krinitzsky and Hynes
Shin-Yamam.	2	44.5	0.56	0.36	10/23/04	6.8	0.55	6	0.32	0.65	2	0.1-9	Yasuda et al.
Shivlakha	1	18	0.26	0.23	1/26/01	7.6	0.45	28	0.32	0.51	318	0.01-80	Singh et al.
Surgu	2	55	0.72	0.15	5/5/86	6.6	0.21	10	0.32	0.71	0.1	0.01-11	Ozkan et al.
Suvi	1	15	0.24	0.09	1/26/01	7.6	0.42	37	0.32	0.21	400	1.5-500	Singh et al.
Takami	2	120	1.31	0.37	9/26/03	8	0.33	140	0.5	1.12	0.1	0.01-10	Nagayama et al.
Tapar	1	15.5	0.21	0.12	1/26/01	7.6	0.15	43	0.32	0.80	50	0.9-10	Singh et al.
Tokiwa	1	33.5	0.49	0.2	1/17/95	7.1	0.2	10	0.32	1.00	0.1	0.01-10	Matsumoto et al.
Tsuboyama	1	20.5	0.29	0.13	10/23/04	6.8	0.13	19	0.32	1.00	7	0.01-10	Yasuda et al.
Vasona	1	10.4	0.19	0.46	10/17/89	7	0.4	9	0.32	1.15	2.7	0.01-10	Harder
Yamam regulatory	1	27.2	0.38	0.1	10/23/04	6.8	0.55	7	0.32	0.18	50	2-600	Yasuda et al.

CONCLUSION AND RESULTS

Seismic response of CFRDs has been searched with a series of dynamic analyses, and a wide range of variables have been examined. Among these parameters, earthquake induced permanent deformations, yield acceleration and peak ground acceleration of earthquake were dealt with in more detail. The study, also, includes the comparison of the results of the numerical analyses and observed dam deformation results.

As seen in Figure 3 and 4, the results are represented in terms of PGA and maximum crest acceleration. Since the upper part of the dams undergo more deformation variation of acceleration from bottom to top is important. Thus, this figures may serve for the estimation of crest acceleration. Despite the trend lines on the figures, an interval is seen for the amplifications. Moreover, acceleration amplification decreases with increasing dam height.

Change in permanent displacement with the ratio of yield to peak acceleration is summarized in Figure 5 and 6 for 50m and 200m dams, respectively. Since the source of permanent displacement is assumed as the difference between the yield acceleration and earthquake induced accelerations, this ratio is preferred. Similarly, Seed (1979) and Bray (2007) represented their studies in terms of same parameters. Variation of permanent displacement (U) with yield acceleration (k_y) and maximum ground acceleration (k_{max}) is given in Figure 7 and 8 respectively. As it is seen in the Figure 5 and 6, when the value of a_{yield}/PGA is greater than 0.4, observed deformations remain below the proposed 100cm limit. Furthermore, results of present study show similar tendency with the results of Seed (1979) and Bray (2007).

Results of 54 case studies were used for the validation of the present numerical study. However, available case studies include not only concrete faced rockfill dams but also other dam types similar to rockfill. Besides, dam heights of the case studies change in wide range, while numerical study deals with only two dam heights as 50m and 200m. Thus, a_{yiled}/PGA-D relations of the case studies are utilized for the assessments. Owing to this situation, some outliers exist in the results. However, numerically obtained results are in reasonable in agreement with the site measurements.

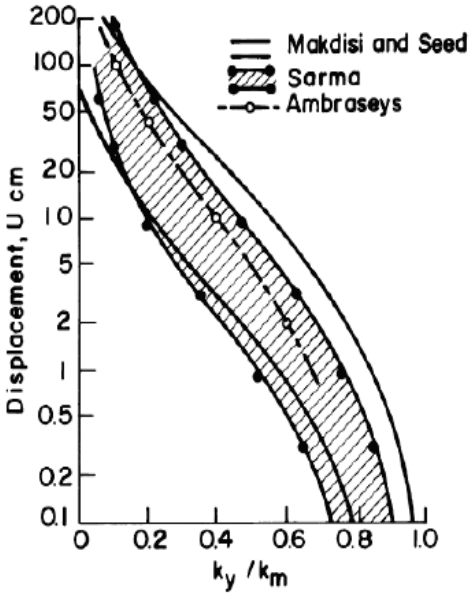

Figure 7. Computed displacement of embankment dams subjected to magnitude 6.5 earthquakes having little or no loss of strength due to earthquake induced deformations (Seed, 1979)

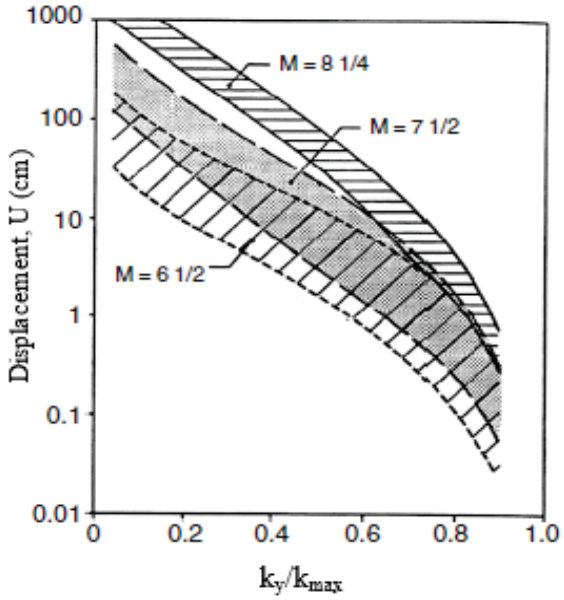

Figure 8. Variation of permanent displacement with yield acceleration (Bray, 2007)

REFERENCES

Abdel-Ghaffar, A.M. and R.F. Scott, 1979. "Analysis of earth dam response to earthquakes". J. Geotech. Eng., 105: 1379-1404.

Boulanger, R.W., J.D. Bray, S.M. Merry and L.H. Mejia, 1995. "Three-dimensional dynamic response analysis of Cogswell dam". Can. Geotech. J., 32: 452-464.

Bray, J. D., 2007. "Simplified seismic slope displacement procedures". 327-353, Earthquake Geotechnical Engineering, Pitilakis, K.D., Springer, Netherlands.

Bray, J.D., Travasarou, T., 2007. "Simplified procedure for estimating earthquake-induced deviatoric slope displacements". Journal of Geotechnical and Geoenviromental Engineering 133 (4): 381–392.

Bureau, G., R.L. Volpe, W.H. Roth and T. Udaka, 1985. "Seismic Analysis of Concrete face Rockfill Dams". In: Concrete Face Rockfill Dams-Design, Construction and Performance, Barry Cooke, J. and J.L. Sherard (Eds.). ASCE., ISBN: 0872625036,pp: 479-508.

Chaney, R.C., 1979. "Earthquake induced deformation in earth dams". Proceeding of the 2nd US National Conference on Earthquake Engineering, pp: 633-642.

Choggang, S., 1988. "Some experiences from damages of embankments during strong earthquakes in China". Proceeding of the 2nd International Conference on Case Histories in Geotech. Earthquake Engineering, pp: 729-735.

De Alba, P.A., H.B. Seed, E. Retamal and R.B. Seed, 1988. "Analyses of dam failures in 1985 Chilean earthquake". J. Geotech. Eng., 114: 1414-1434.

Earthquake Engineering Research Institute, 2004. "Preliminary observation on the Al Hoceima Morocco earthquake of 24 February, 2004". Special report. EERI, Oakland, CA, USA.

Elgamal, A.W., R.F. Scott and M.F. Succarieh, 1990. "La Villita dam response during five earthquakes including permanent deformation". J.Geotech. Eng., 114: 1443-1462.

Harder Jr., L.H., 1991. "Performance of earth dams during Loma Prieta earthquake". US Geological Survey Professional Paper, 1552: 3-26.

Hynes-Griffin M.E., Franklin A.G., 1984. "Rationalizing the seismic coefficient method". Misc. Paper No. GL-84-13, U.S. Army Engr. WES, Vicksburg, MS.

Jia, Y.F., Chi, S.C., 2012. "Application of rockfill dynamical characteristic statistic curve in mid-small scale concrete face dam dynamic analysis". 15th World Conference on Earthquake Engineering, 24-28 September, Lisbon.

Jibson, R. W., 2007 “Regression models for estimating coseismic landslide displacement”. Engineering Geology, 91(2): 209-218.
Kramer, S. L., 1996. “Geotechnical earthquake engineering”. Prentice-Hall Civil Engineering and Engineering Mechanics Series, Upper Saddle River, NJ: Prentice Hall, 673.
Krinitzsky, E.L. and M.E. Hynes, 2002. “The Bhuj, India, earthquake: Lessons learned for earthquake safety of dams on alluvium”. Eng. Geol., 66: 163-196.
Kuhlmeyer, R.L., Lysmer, J. 1973. “Finite element method accuracy for wave propagation problem”. Journal of the Soil mechanics and Foundation Division ASCE, 99(5): 421-427.
Lai, S.S. and H.B. Seed, 1980. “Dynamic response of long valley dam in the Mammoth lake earthquake series of May 25-27 1980”. Report 85/12, Univ. of Calif., Berkeley.
Lingyao, L., L. Kueifen and B. Dongping, 1980. “Earthquake damage of Baihe earth dam and liquefaction characteristics of sand and gravel materials”. Proceeding of the 7th World Conference on Earthquake Engineering, Istanbul, pp: 171-178.
Matsumoto, M., A. Nakamura, T. Sasaki and T. Iwashita, 1996. “Effects on Dams”. Soil Found., 36: 273-281.
Matsuo, O., 2000. “Report on the Western Tottori Prefecture earthquake of October 6, 2000”. In: Report of 33rd Tech. of US-Japan Natural Resources Development Program, Japan.
Meehan, C. L., Vahedifard, F. 2013. “Evaluation of simplified methods for predicting earthquake-induced slope displacements in earth dams and embankments”. Engineering Geology, 152(1): 180-193.
Nagayama, I., Y. Yamaguchi, T. Sasaki, A. Nakamura, H. Kawasaki and D. Hirayama, 2004. “Damage to dams due to three large earthquake occurred in 2003, in Japan”. US-Japan Natural Resources Development Program, Japan.
Newmark, N.M., 1965. “Effects of earthquakes on dams and embankments”. Géotechnique, 15: 139–160.
Ozkan, M.Y., M. Erdik, M.A. Tuncer and C. Yilmaz, 1996. “An evaluation of Surgu dam response during 5 May 1986 earthquake”. Soil Dyn. Earthquake Eng., 15: 1-10.
Pang, R., Xu, B., Kong, X., Zou, D., Zhou, Y. 2018. “Seismic reliability assessment of earth-rockfill dam slopes considering strain-softening of rockfill based on generalized probability density evolution method”. Soil Dynamics and Earthquake Engineering, 107, 96-107.
Pender, M.J. and T.W. Robertson, 1987. “Edgecumbe earthquake: Reconnaissance report”. Bull. N. Z. Natl. Soc. Earthquake Eng., 20: 201-249.
Rai, D.C. and C.V.R. Murty, 2003. “North Andaman (Diglipur) earthquake of 14 September 2002”. India.
Resendiz, D., Romo, M.P. and E. Moreno, 1982. “El infiernillo and la villita dams: Seismic behavior”. J.Geotech. Eng., 108: 109-131.
Rathje, E. M., & Saygili, G. 2009. “Probabilistic assessment of earthquake-induced sliding displacements of natural slopes”. Bulletin of the New Zealand Society for Earthquake Engineering, 42(1): 18.
Sakamoto, S., H. Yoshida, Y. Yamaguchi, H. Satoh, T. Iwashita and N. Matsumoto, 2002. “Numerical simulation of sliding of an earth dam during the 1985 Kobe earthquake”. Proceeding of the 3rd US-Japan Workshop on Advanced Research on Earthquake Engineering for Dams, June 22-23, San Diego, California, pp: 416.
Seed, H.B., I.F. Makdisi and P. De Alba, 1978. “Performance of earthen dams during earthquakes”. J. Geotech. Eng., 104: 967-994.
Seed, H. B. 1979. “Considerations in the earthquake-resistant design of earth and rockfill dams”. Geotechnique, 29(3): 215-263.
Singh, R., D. Roy and S.K. Jain, 2005. “Analysis of earth dams affected by the 2001 Bhuj earthquake”. Eng. Geol., 80: 282-291.
Singh, R., Roy, D., Das, D. 2007. “A correlation for permanent earthquake-induced deformation of earth embankments”. Engineering Geology, 90(3-4), 174-185.
Singh, R., Debasis, R. 2009. “Estimation of earthquake-induced crest settlements of embankments”. American Journal of Engineering and Applied Sciences, 2(3), 515-525.

Stroitel, G., 1969. “Design and investigation of seismically stable dams in Japan”. Power Technol. Eng. (Formerly Hydrotech. Construct.), 3: 946-955.
Tani, S., 2000. “Behavior of large fill dams during earthquake and earthquake damage”. Soil Dyn. Earthquake Eng., 20: 223-229.
Wang, J., Yang, G., Liu, H., Nimbalkar, S. S., Tang, X., Xiao, Y. 2017. “Seismic response of concrete-rockfill combination dam using large-scale shaking table tests”. Soil Dynamics and Earthquake Engineering, 99, 9-19.
Wen, L., Chai, J., Xu, Z., Qin, Y., Li, Y., 2018. “A statistical review of the behaviour of concrete-face rockfill dams based on case histories”. Géotechnique, 68(9), 749-771.
Yasuda, N., M. Kondo, T. Sano, H. Yoshioka, Y. Yamaguchi, T. Sasaki and M. Tomita, 2005. “Effect of the mid Niigata prefecture earthquake in 2004 on dams”. US Japan Natural Resources Development Program, Technical Report.
Zou, D., Han, H., Liu, J., Yang, D., Kong, X. 2017. “Seismic failure analysis for a high concrete face rockfill dam subjected to near-fault pulse-like ground motions”. Soil Dynamics and Earthquake Engineering, 98, 235-243.

5 DAM SAFETY
İstanbul Turkey 2018

5th International Symposium on Dam Safety

October 27-31, 2018

AN INVESTIGATION OF ENERGY DISSIPATION IN CONVERGENT STEPPED SPILLWAYS USING FLOW 3D MODEL

Seyed Sajad AALİ[1], Abbas Ali GHEZELSOFLOO [2]

ABSTRACT

Extra kinetic energy dissipation of flow at downstream of large dams is one of the most significant concerns. The stepped spillway is one of the most effective hydraulic structures to dissipate the extra kinetic energy of flow. Because of its specific features and advantages, stepped spillways have gained popularity among hydraulic engineers over the last two decades. In many cases, spillways require convergence to meet the economic demands and topographic and geological conditions of the specific site. This study aims to investigate the rate of energy dissipation on convergent stepped spillway using Flow 3D numerical model. Physical experimental data conducted were used to verify the numerical modeling results. The results showed that there is a good agreement between Flow 3D results and experimental data. In order to investigate the effects of different conditions on energy dissipation using convergent stepped spillway, the spillway of Chandir Dam was modeled. The rate of energy dissipation was compared among different types of spillway geometry including smooth spillway, convergent spillway, stepped spillway and convergent stepped spillways with four different training wall convergence angles including 5º, 10º, 15º and 20º. The most energy dissipation rate has averagely been observed at 10º convergence angle. Mentioned convergence angle was considered as the optimum angle. Using 10º convergent stepped spillway not only reduces 16 percent of operating costs but also increases the rate of energy dissipation comparing with the common stepped spillway.
Keywords: Energy dissipation, Stepped spillway, Flow 3D numerical model, Convergence

INTRODUCTION

Stepped spillway consists of steps, which start from near crest and continue to the spillway downstream. Due to the significant impact of stairs on the amount of energy dissipation, mentioned spillway has attracted a great deal of attention among dam engineers. In this case, extra energy is dissipated along the conveyance part of spillway including steps (large roughness). Therefore, less amount of energy should be dissipated at the spillway downstream and smaller stilling basin will be required as well. Not only physical models cannot present perfect results because of complex flow patterns and scale effects but also they cannot provide a clear understanding of governing physics of these kinds of cases alone. In order to understand the governing physics of problems properly, it is necessary to analyze both experimental and numerical studies for each case. The stepped spillway has recently gained popularity among engineers due to compatible construction method with new construction materials such as RCC (roller compacted concrete). The ideal behavior of this type of

[1] Postgraduate of Civil Engineering, Department of Civil Engineering, Khavaran Institute of higher Education, Mashhad, Iran,
e-posta: sajad.aali@yahoo.com

[2] Assistant Professor, Department of Civil Engineering, Islamic Azad University, Mashhad, Iran,
e-posta: ghezelsofloo@gmail.com

spillway depends on correct design, optimum build quality, suitable flow conditions and regular maintenance. A large amount of energy dissipated along the conveyance structure (stepped chute) results in size and cost reduction of downstream energy dissipaters or stilling basin. A stepped spillway reduces the flow velocity and increases the rate of aeration that is why the cavitation risks of stepped spillways are less important than other cases. However, due to the economic considerations and some limitations including topographic conditions and geologic features of the site, spillway training walls should be converged. For smooth transitions the maximum convergence angle should not exceed $\alpha = \tan^{-1}(1/3Fr)$ to provide an acceptable transition and avoid cross-waves, wave run-up and uneven distribution of flow across the channel (USBR, 1987). Overall, there is a fundamental question to be answered. How will different factors affect flow characteristics in case of stepped spillways? There are a number of studies about different kinds of flow characteristics over stepped spillways. To simulate main characteristics of air-water two-phase flow over a stepped spillway taken as a popular measurement for the energy dissipation, one of the Computational fluid dynamics (CFD) methods and turbulence models called the finite volume and the RNG K-Ɛ, respectively were used. The obtained results of the study showed a close agreement with the experimental case (Cheng et al., 2006). In order to simulate flow over stepped spillways with four different configurations of steps Fluent software was used and three turbulence models such as standard K-Ɛ, RNG K-Ɛ, and K-ω models were applied to conduct the numerical analysis. The findings of the study showed that RNG K-Ɛ model had the nearest results to the experimental one. In addition, based on the results, energy dissipation was increased by larger steps spillways thanks to the creating larger vortexes (Danesh Faraz et al., 2014). Two-dimensional unsteady flow using V-flow code obtained by CFD were carried out by Vosoughifar et al (2013) for laminar flow without any turbulence models over a stepped spillway. Their result made a comparison of the obtained results of different applications of models based on the mass imbalance to show a useful index of the fluid flow solution and an accuracy criterion. A specific, two-dimensional, physical model was built to determine some hydraulic parameters such as the inception point location, velocities, air concentrations and the energy dissipation by Hunt et al (2010). A remarkable study to investigate the main characteristic of the flow over a stepped spillway with different configurations of steps by numerical simulation was carried out by Tabbara et al (2005). The finite element method of CFD methods was used by ADINA software and K-Ɛ model was used thanks to the turbulent flow. The findings of their study indicated a close agreement between the computed water surface profile and the measured one, as well as the energy dissipation. Eghbalzadeh and Javan (2012) made a noticeable attempt to investigate the volume of fluid (VOF) and the Mixture methods for numerical simulation of air-entrainment in skimming flow over stepped spillways by fluent software. Simulated results were compared with the experimental ones so that the obtained findings highlighted that free surface is simulated better by the Mixture method than the VOF method. Because of the paucity of studies about convergent stepped spillway, this research aims to examine flow characteristics including flow depth, velocity, and energy dissipation over stepped spillways with different angles using Flow 3D. CFD is a particular kind of numerical analysis done to solve different patterns of fluid flow in various situations. Using CFD techniques to simulate flow patterns not only save more time and money but also provide more detailed results comparing with experimental studies. Next section deals with the method of the study. First, the numerical model is introduced. Second, the modeling method is presented. Third, for the validation of numerical results, experimental data of the study performed by Hunt et al (2008) were used. Numerical results obtained by Flow 3D software is compared with Hunt experimental results. Finally, spillway of Chandir dam was modeled with varying training wall convergence angles to examine flow characteristics and the rate of energy dissipation. The result section investigates flow characteristics including velocity and flow depth with different spillway geometries. Averaged energy dissipation is evaluated at different converging angles and finally, the suitable convergence angle is introduced.

Numerical methods

CFD a branch of fluid mechanics is a way to simulate flow patterns in which standard flow equations such as Navier-Stokes and continuity equations are discretized and solved for each computational cell.

Flow 3D is a powerful, accurate and comprehensive CFD software that analyzes various physical flow processes and concentrates on the free surface and multi-phase applications. This software divides the domain of flow into the rectangular grid cells and solves the equations governing the fluid flow with finite-difference or finite-volume approximations. Flow 3D is a highly practical method to model three-dimensional phenomena, complex situations, and both steady and unsteady flows. In this paper, we face a three-dimensional phenomenon. Because variables should be solved not only in X and Z directions but in Y direction due to the convergence angle. The most important equations used by Flow 3d to simulate flow characteristics for incompressible flow are RANS and continuity equations:

$$\frac{\partial}{\partial_{x_i}}(u_i A_i) = 0 \tag{1}$$

$$\frac{\partial_{u_i}}{\partial_t} + \frac{1}{V_F}(u_i A_i \frac{\partial_{u_i}}{\partial_{x_j}}) = \frac{1}{\rho}\frac{\partial_P}{\partial_{x_i}} + g_i + f_i \tag{2}$$

Numerical model validation

In order to validate the numerical results of Flow 3D software, Experimental setup of a physical model, which performed to evaluate water surface along the wall with varying convergence angles, was simulated. Prototype design parameters for convergent stepped spillway presented by Hunt et al., (2008) are shown in Table 1.

Table 1. Prototype Design Elements and Dimensions

Design elements	Spillway slope (H:V)	Spillway width	Step height (m)	Convergence angle	Training wall height	Stilling basin length	Stilling basin wall height	End sill height	Maximum discharge	Maximum head
Prototype dimensions	3:1	100 m	0.3	0,15,30, 52°	4.3 m	18.2m	6.7 m	0.6 m	763 CMS	2.4 m

Figure 1 shows a comparison of numerical and experimental results for free surface elevation along the wall with varying convergence angles. As shown below, there is a good agreement between numerical and experimental results. Results of Flow 3D software is compatible findings of the experimental study. Increasing the convergence angle of the training wall causes higher elevation of the free surface along the wall.

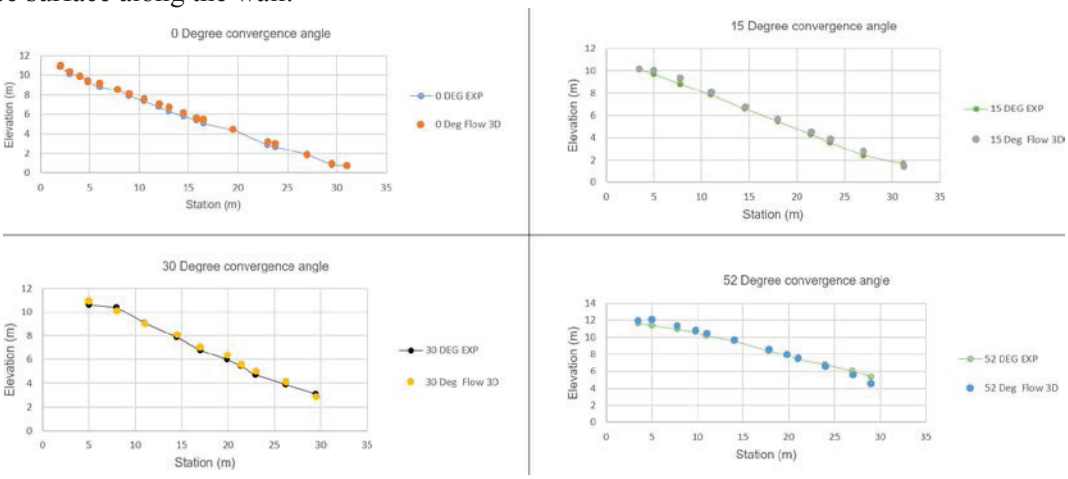

Figure 1. Comparison of numerical and experimental results for free surface elevation along wall with varying convergence angles

Case study and numerical modeling

Chandir dam is a reservoir dam constructed across the Chandir River in North Khorasan province, Iran. The main purpose of this dam is four-fold. First, optimum use of total basin runoff. Second, satisfying the need of agriculture sector. Third, supplying drinking water and developing welfare facilities and amenities. Fourth, preventing downstream flood damage. In this study, the authors used Chandir dam dataset to investigate the effect of converging stepped spillway on flow characteristics and examine the rate of energy dissipation in different geometries. Table 2 presents the raw data for numerical modeling.

Table 2. Spillway Design Elements and considered parameters

Design elements	Spillway slope (H:V)	Spillway width	Step height	Convergence angle	Training wall height	Stilling basin wall height	Maximum discharge	Crest elevation	Bed elevation
dimensions	5:3	61.2 m	0.5 m	0,5,10, 15 and 20^{o}	5 m	7 m	1400 CMS	836 m	803.5 m

At the first step, different geometries of convergent stepped spillway were modeled by AutoCAD software. Geometries were exported as Stereo lithography (STL) files in order to import them as solids in Flow 3D. A sample of modeled stepped spillway is shown in figure 2.

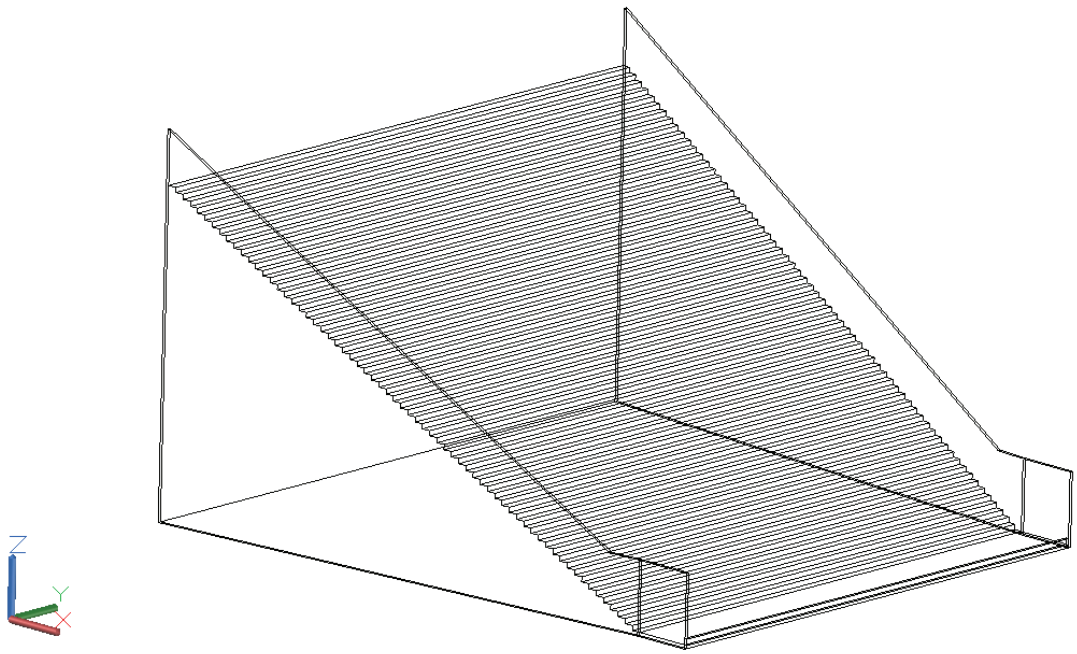

Figure 2. A sample of modeled Stepped spillway with 5^{o} converging training wall

At the second step of the numerical modeling procedure, general specifications were defined to Flow 3D according to table 3.

Table 3. General specifications

Units	Fluid	Flow mode	Step height	Finish time
SI	Water at 20oC	Incompressible	0.5 m	7

For simulating accurately, physical models were selected according to the nature of the phenomenon. Due to the turbulent flow, a turbulent model should be chosen. As it mentioned before, Danesh Faraz et al (2014) compared three turbulence models including RNG, K-ω, and K-Ɛ. They found that the RNG model had relative superiority among the rest. On the other hand, it was recommended to use RNG or K-Ɛ turbulence model if the air entrainment model is desired (Flow Science, Inc., 2008). RNG model was considered as the turbulence model. Table 4 shows selected physical models.

Table 4. Physical models

Air entrainment	
Gravity	Z component = -9.81
Viscosity and Turbulence	Viscous flow & RNG model

Boundary conditions were defined according to table 5.

Table 5. Boundary conditions

Xmin	Xmax	Ymin	Ymax	Zmin	Zmax
VFR	Outflow	Symmetry	Symmetry	Wall	Symmetry

It is worth noting that the Xmin boundary includes 1400 CMS maximum water discharge and 36.5m water elevation.
At the last stage, the hydrostatic pressure was defined as an initial condition.

Results and discussion

Convergence angles including 0, 5, 10, 15 and 20^o under the maximum discharge were modeled and flow characteristics such as flow depth and velocity were analyzed for each spillway configuration. Due to the nature of the phenomenon, variation of flow characteristics occurs in all three directions. The most important factors composing total hydraulic head are flow depth and flow velocity. Figure 3 and figure 4 show velocity magnitude and flow depth, respectively. Flow velocity distribution across channel width is relatively uniform at 0, 5 and 10^o convergence angles. However, at 15 and 20^o convergence angles cross-waves, wave run up and uneven distribution of flow occur more which cause unwilling state at the downstream terminal structure. Figure 4 demonstrates that the maximum flow depth is right after the spillway crest. The more side walls converge, the higher flow depth occurs along training walls. The maximum rate of flow depth (6.41m) occurs in 20^o convergence angle. It con result that converging training walls lead to increasing flow depth and decreasing velocity magnitude along training walls. However, exactly opposite situation occurs along the centerline of the channel. It is worth mentioning that the Froude number is maximum along the training walls and minimum along the centerline.

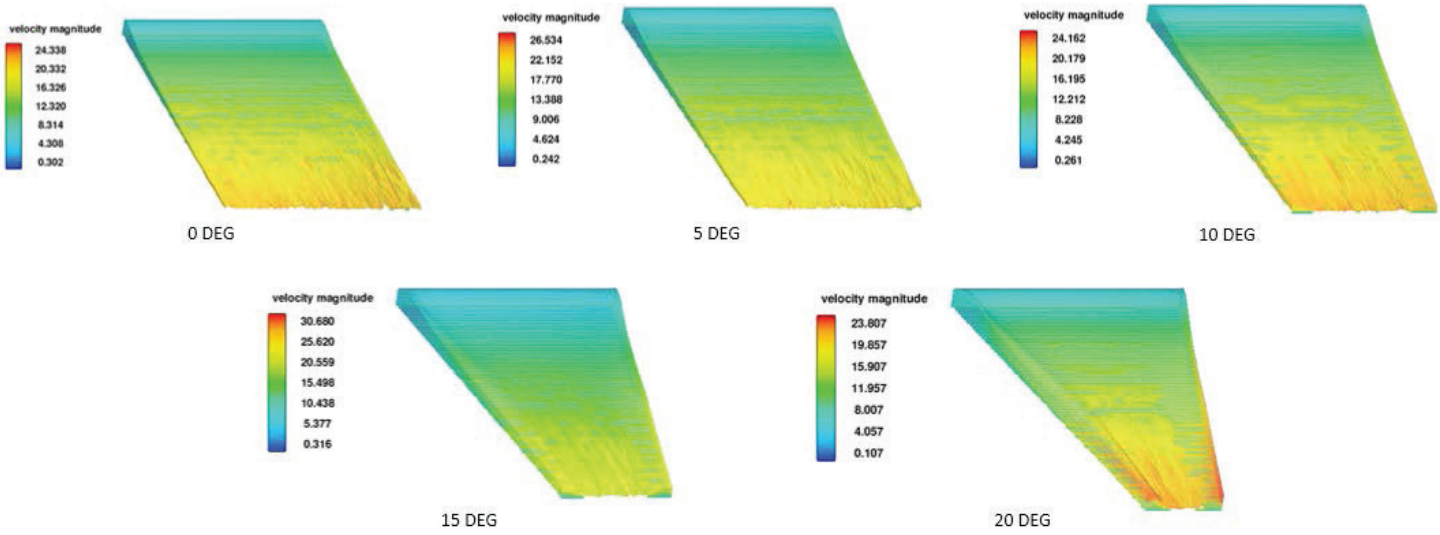

Figure 3. Velocity magnitude for each convergence angle

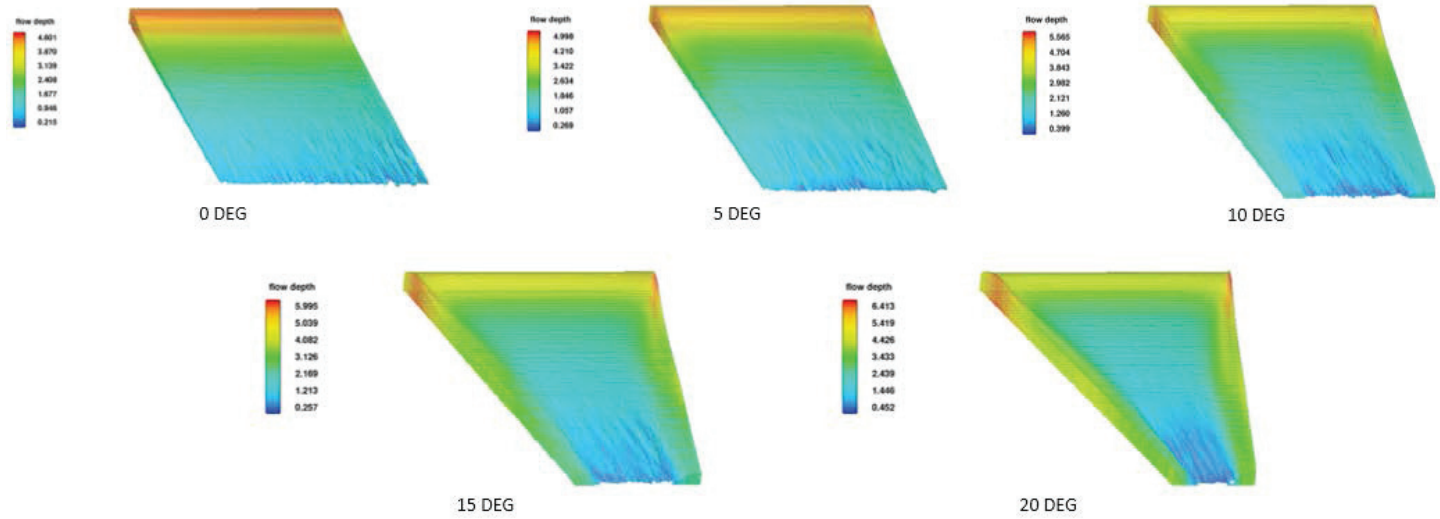

Figure 4. Flow depth for each convergence angle

To examine the rate of energy dissipation, the total hydraulic head was measured in 5 points at both crest level cross-section and tail water cross-section (right after the final step) for each spillway. Total hydraulic head at the crest level cross section was equal to 38m for each geometry because, at the crest level cross-section, flow depth and spillway crest widths were equal. After that, total hydraulic heads of tail water cross-section (right after the final step) were measured at 5 points located in the centerline, near the left and right training walls and ¼ of width and ¾ of width for each geometry. As an example, Figure 5 shows general plan of stepped spillway with 20^{o} converging training walls and figure 6 demonstrates the locations of points at the cross section a-a.

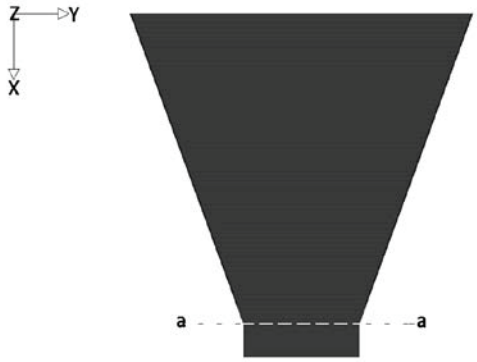

Figure 5. General plan of stepped spillway with 20^{o} converging training walls

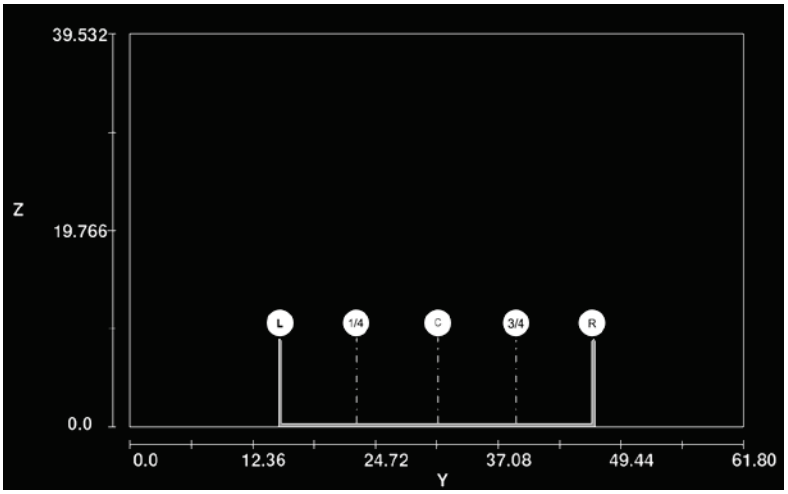

Figure 6. Locations of points for measuring total hydraulic head at the cross section a-a.

Total hydraulic heads of mentioned points presented in table 6 for each spillway.

Table 6. Total hydraulic head in different points of each spillway

Convergence angle	Lef wall	1/4	Center line	3/4	Right wall
0	20	22	27	22	20
5	17	24	24	24	17
10	16	24	22	24	16
15	20	22	24	22	20
20	24	17	24	17	24

In order to calculate the rate of energy dissipation in each point, below equation, was used.

$$\frac{H_{up} - H_{down}}{H_{up}} = \Delta E \qquad (3)$$

Where H_{up} and H_{down} are total hydraulic heads of upstream and downstream respectively. ΔE is the rate of energy dissipation in each point at the tail water cross-section. Figure 7 demonstrates the average rate of energy dissipation for each convergent stepped spillway.

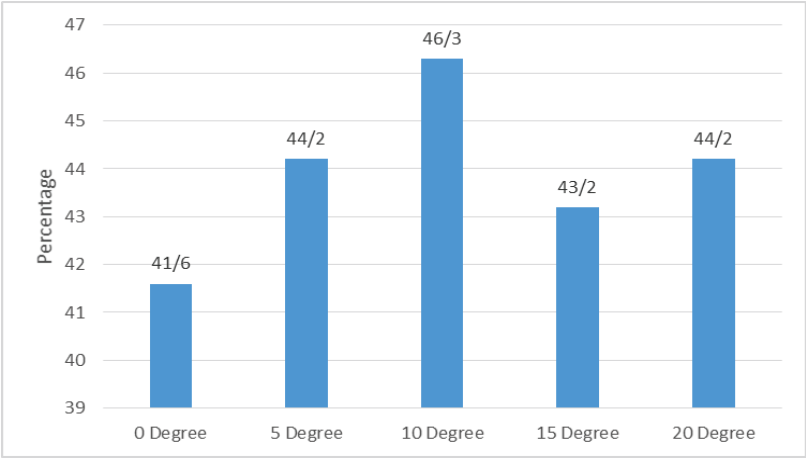

Figure 7. The rate of average energy dissipation in each convergent stepped spillway

As shown above, the stepped spillway with 10° convergence, training wall angle yields the most energy dissipation rate. This convergence angle contains the more gradual transition compared with 15 or 20° convergence angles so that undesirable cross waves, wave run up and uneven flow distribution across the channel would be reduced. Stepped spillways with an optimum convergent

angle not only increase the rate of energy dissipation but also cut project costs by reducing dimensions of conveyance structure and downstream stilling basin. In this case study, 10^o convergent stepped spillway reduces 16 percent of operating costs compared to the simple stepped spillway.

Conclusion

In order to design or rehabilitate spillways with the best performance, dam engineers have recently encountered many challenges and limitations including inadequate spillway capacity of aging watershed dams, economic demands, topographic and geological conditions. The stepped spillway is one of the most effective spillways. Because of the mentioned limitations and considerations, converging training walls of the conveyance structure is obligatory. Due to the lack of information about convergent stepped spillways, in this study, flow over the stepped spillway with different training wall convergence angles including 5º,10 º,15 º and 20 º was simulated using Flow 3D software. First, numerical results compared with experimental data and showed a good agreement. Next, data of the Chandir dam presented. Then, numerical modeling method was discussed. Before the last stage, the main flow characteristics such as velocity and flow depth were illustrated. Finally, total hydraulic heads and average energy dissipation of each spillway were calculated. Findings of the present study are outlined below.

- Flow velocity distribution across channel width is relatively uniform at zero, five and ten degrees convergence angles.
- The maximum flow depth occurs right after the spillway crest.
- The more side walls converge, the higher flow depth occurs along training walls.
- Converging training walls leads to increasing flow depth and decreasing velocity magnitude along training walls.
- Froude number is maximum along the training walls and minimum along the centerline.
- 10^o convergence training wall angle yields not only the most energy dissipation rate but also relatively uniform flow distribution across the channel compared to higher convergence angles.
- 10^o convergent stepped spillway reduces 16 percent of operating costs compared to simple (parallel training walls) stepped spillway.

REFERENCES

Cheng, X., Chen, Y., & Luo, L. (2006). Numerical simulation of air-water two-phase flow over stepped spillways. Science in China Series E: Technological Sciences, 49(6), 674-684.

Daneshfaraz, R., Sadeghfam, S., & Kashani, M. 2014. Numerical simulation of flow over stepped spillways. Research in Civil and Environmental Engineering, 2, (04), 190-198.

Eghbalzadeh, A., & Javan, M. (2012). Comparison of Mixture and VOF Models for Numerical Simulation of Air–entrainment in Skimming Flow over Stepped Spillways. Procedia Engineering, 28, 657-660.

Hunt, S. L., & Kadavy, K. C. (2010). Energy dissipation on flat-sloped stepped spillways: Part 2. Downstream of the inception point. Transactions of the ASABE, 53(1), 111-118.

Hunt, S. L., Kadavy, K. C., Abt, S. R., & Temple, D. M. (2008). Impact of converging chute walls for roller compacted concrete stepped spillways. Journal of hydraulic engineering, 134(7), 1000-1003.

Reclamation, U. B. O. (1987). Design of small dams. Water Resources Technical Publication, 860p.

Tabbara, M., Chatila, J., & Awwad, R. (2005). Computational simulation of flow over stepped spillways. Computers & structures, 83(27), 2215-2224.

Vosoughifar, H. R., Dolatshah, A., Shokouhi, S. K. S., & Nezhad, S. R. H. (2013). Evaluation of fluid flow over stepped spillways using the finite volume method as a novel approach. Strojniški vestnik-Journal of Mechanical Engineering, 59(5), 301-310.

5th International Symposium on Dam Safety

October 27-31, 2018

PREDICTION OF EMBANKMENT DAM BREACH WIDTH

Alper AYDEMİR [1], Aytaç GÜVEN [2]

ABSTRACT

Dam failures are disasters that have many irreversible outcomes such as life loss, economical loss and negative environmental impacts. Dam accidents could be prevented by predicting possible consequences of different failure modes.

Dams are economically high investment cost projects and any dam breach experiments are limited with small scaled dam body models because of economic reasons. Breach width is a key parameter which directly influences physical quantities as the amount of water or dam body material that is suddenly scattered to downstream since the amount of eroded material or peak discharge occurred by breach is directly proportional with the width of gap formed in dam body.

In this study gene expression programming (GEP) technique was used to develop a mathematical expression for predicting breach width of earth fill dams. Historical dam failure data obtained from the literature were used for training and validating processes of modeling. Results of this study shows that GEP technique could be well used to predict the breach width occurred by piping failures which is the most common cause of dam failures.

Keywords: Dam Breach, Piping, Dam Safety, Gene Expression Programming

INTRODUCTION

Dams are barriers constructed on waterways to store water for different purposes. Critical role of dams on regional economy makes them attractive for decision makers and engineering firms including design and construction. Electricity generation, irrigation, recreation, flood control etc. are some benefits of the dams. Construction of dams needs high investments during project period. But nowadays most of the dams are constructed for multiple purposes, so economic return of initial costs take less time.

Main idea behind the dam projects is building a barrier across water way and to store water. Multipurpose dams mean water should be stored safely and could be distributed in different ways. But problems that could occur during project or operation stages make dams vulnerable for many hazards. Dam failures are disasters that have many irreversible outcomes such as life loss, economical loss and negative environmental impacts. Dam accidents could be prevented by predicting possible consequences of different failure modes.

[1] Asst. Prof. Dr., Civil Engineering Department, Nuh Naci Yazgan University, Kayseri, Turkey, e-posta: aydemir@nny.edu.tr

[2] Professor, Department of Civil Engineering, Gaziantep University, Gaziantep, Turkey, e-posta: aguven@gantep.edu.tr

Dams can be categorized according to height, volume, purpose, body type and materials used in body of dam. All these categories include primitive elements to identify dam properties which have significant role on dam failure. For instance, piping could be the most significant mode for an earth dam but it could not be main parameter in another dam project such as concrete dam. Federal Emergency Management Agency (FEMA) define these failure induced parameters as failure modes (FEMA, 2008). Failure modes are used to identify failure mechanism of dams during breach.

Dams are economically high investment cost projects and any dam breach experiments are limited with small scaled dam body models because of economic reasons. Many different experimental dam breach studies could be found in the literature but most of dam are based on simulation run on reduced model of investigated dams. Importance of dam breach parameters and difficulties occurred during experimental studies force dam safety engineers to use various predictive methods for breach parameters.

Breach width is a key parameter which directly influences physical quantities as the amount of water or dam body material that are suddenly scattered to downstream since the amount of eroded material or peak discharge occurred by breach is directly proportional with width of gap formed in the dam body. Breach formation depends on different factors such as embankment geometry, material composition, construction methods, type and degree of embankment crest and slope protective cover, reservoir dimensions, inflow to the reservoir during failure, and the mode of failure (D.C. Froehlich, 2008). Occurrence of dam breach includes many different parameters which also contain unpredictable uncertainties so accuracy in estimation techniques plays a crucial role in dam risk studies directly.

DAM BREACH PARAMETERS

Dam breach is a sudden accident which makes these disasters unpredictable and uncontrolled. Measurement of changes or recording any other actions during a dam failure could be impossible. But defining these accidents could lead to identify causes of dam failures. Dam breach could be investigated with various parameters. Most widely used ones that are found in literature are:

- Breach Width
- Breach Side Slope
- Failure Time
- Peak Breach Discharge

Dam breach parameters give practical information about dam breach process. Inundation zone of a dam failure is the area that could be affected by dam failure. In other words, land which would be partially or totally damaged by water released from dam reservoir after dam breach. Each of dam breach parameter directly influences size of hazard. For example, if breach width increases than peak breach discharge increases also. Because eroded material and amount of released water is generally related with the size of gap occurred on dam body face. On the other side, the amount of released material could force the sides to have different shapes and this creates breach side slope. Any of these parameters should be carefully investigated. If possible during or after dam failure all of evidences such as side slopes, breach top or bottom size, time difference between start and end of the failure should be measured. Measured dam failure data is essential for dam safety examinations. Each dam is unique for construction or design stages but in general any historical dam failure data could give an idea about fail mechanism to dam safety engineers.

Mathematical expression for the expected values of the final width and side slope of a trapezoidal breach along with its formation time was developed by using 74 embankment dam failure data and results indicated that variances of the predicted quantities to be calculated as well (D.C. Froehlich, 2008).

In another study, fuzzy algorithm was used for estimating average breach widths of embankment dams. 69 embankment dam failure data were used to develop and test the fuzzy logic model. Application of this model also presented for estimating average breach widths of two case studies. Fuzzy logic model results uncertainty band is found to be approximately ±0.51 order of magnitude smaller than the ±0.56 order of magnitude achieved with the best available regression equations models. Results show that fuzzy logic model is capable of estimating average breach width better than regression equation models (Elmazoghi, 2013).

Dam breach parameters were also modeled by using gene expression models by Sattar (2014), and a new empirical formula of physical meaning for prediction of non-dimensional key dam breach parameters was presented. Gene expression model was obtained with 140 dam failure cases data from a database and %75 of data was separated and used for training as well as %25 of data used to validate the model. The results of the gene expression based study indicated that uncertainties of 20 to 40% are calculated for the developed GEP models with reservoir shape factor and dam erodibility being main influential predictors.

United States Bureau of Reclamation (USBR) reviewed the current methods for predicting embankment dam breach parameters and numerically modeling dam breach events (Wahl, 1998). Key findings of the USBR study include:

- There is presently both a need and opportunity to achieve significant improvements in technology used to analyze embankment dam breach processes. The potential benefits to be achieved from this effort may significantly aid risk assessment studies, in which thresholds of dam failure, probabilities of failure, and consequences of failure are all of prime importance.
- When population centers are located close to dams, accurate prediction of breach parameters is crucial to development of effective emergency action plans, design of early warning systems, and characterization of threats to lives and property.
- Warning time is the most important parameter affecting potential loss of life due to dam failure.
- The primary benefits of improved prediction of breach initiation and formation times will accrue to the population within a few kilometers of the structure, but this is also the region which historically has the greatest risk for loss of life.
- The distinction between breach initiation time and breach formation time has not been clearly made in the literature or the available case study data; this impacts the ability to accurately predict warning time.
- Although breach initiation time is critical to the determination of loss of life, there is little guidance in the literature for its prediction. Numerical dam breach models have the potential to predict breach initiation times, but are not widely used and are not based on observed breach erosion mechanisms.
- Breach parameter prediction equations based on analyses of dam failure case studies have significant uncertainty, breach formation time is especially difficult to predict.
- Much valuable information is available from embankment failures that continue to occur each year, but it is often lost because local authorities have other pressing needs during a crisis and are not aware of the type of data that would be of most use to dam breach researchers. The formation of a standing forensic team that could promptly investigate incidents of dam failure and dam survival of extreme events (e.g., overtopped but not failed) would be extremely valuable.

Breach Shape

Breach formation could be usually defined as a growing simple trapezoid shape that includes an empirical model. Shape of an breach used in practice given in Figure 1 (Altinakar et al., 2011).

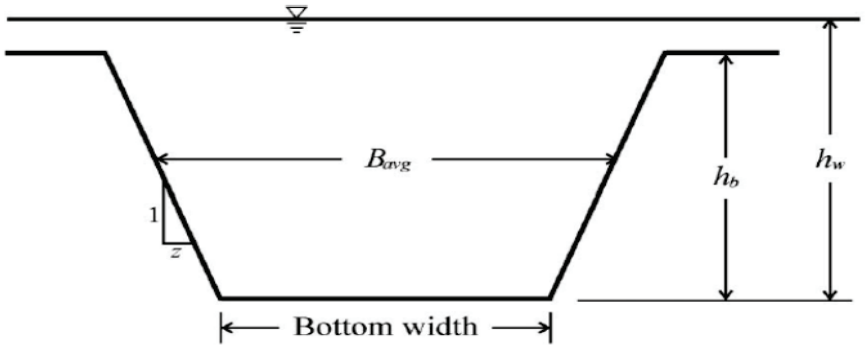

Figure 1. Breach Shape

Most of studies found in the literature uses breach formation type as trapezoidal. This process could be explained in three variations of the empirical model of breach formation commonly used to evaluate the dam failures which are shown in Figure 2 as Models A, B, and C. Each of the three models assumes that a breach begins to form at the top of a dam and grows with time into the shape of a triangle or a trapezoid. Terms such as the height, average width, and side slope of the final trapezoidal opening in the dam was used to describe the geometry of breach. Model A is the first phase of process. In Model A breaches develop initially in the shape of triangles until the bottom of the breach reaches its lowest elevation. Than expansion begins as the breach start to take its well-known trapezoidal shape. In Model B, during base width of trapezoidal shape increases linearly also maximum height and width of the breach are increases. Model C considers the bottom width of the trapezoidal breach as constant. When all of the three models are compared with observations obtained from the past embankment dam failures and the experimental studies, then it could be concluded that Model A represents the breach development better than Model B and Model C (D.C. Froehlich, 2008).

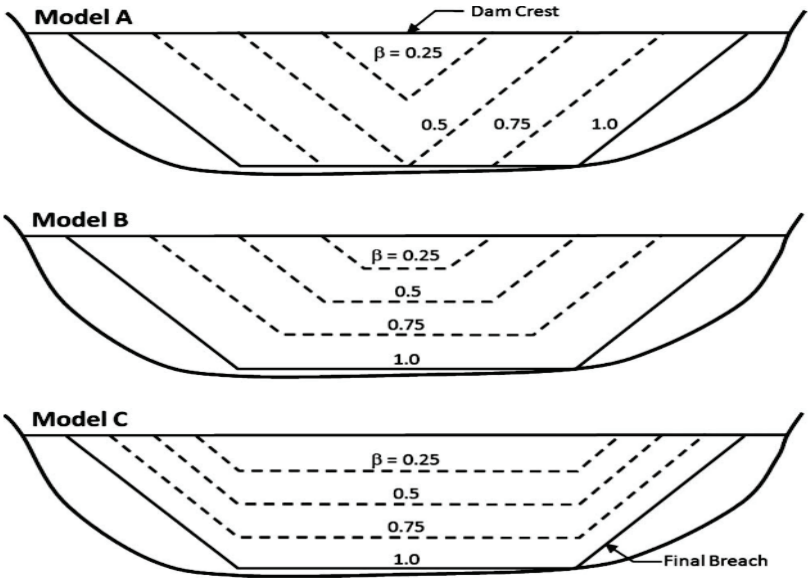

Figure 2 Breach Formation Types

Breach Width

Breach width is distance between sides of breach. Any trapezoidal shape have many different width that could change according to place that is measured. Average breach width is generally used for preventing possible confusions.

Existing Methods for Predicting Breach Parameters

Dam failure mechanism is one of major topics for water resources engineering research. High cost and many other deficiencies faced in experimental studies forced scientists to find new solutions to predicting possible consequences of dam failures. Empirical models obtained from the historical dam failure data are one of widely used solutions for breach parameter estimation. Stages of finding a suitable model starts with obtaining breach parameters of previously failed dams. Collected data combined with other measured ones from different size, shape, material or type dam fail data which is the main complexity lies on the basis of these models. As every dam project is unique for construction method, dam body type, dam body material, foundation type and properties then these projects must be investigated with its own properties. Most of models found in the literature are based on empirical models generated from the historical dam failures. If detailed examination needed to observe fail mechanism of a dam, than it is obvious to use all related data. But when researchers use historical dam failure data these unique could not be defined as its natural form. Accuracy of empirical dam breach parameter estimation models depends on the correlation between the measured historical dam failure data and the investigated dam data. This means if the observed dam properties such as dam type, dam height, reservoir volume, dam body type, earthquake data, foundation conditions, maximum probable flood are suitable with each other than empirical models could give better results. Many unique differences in dam projects make this correlation impossible for most of real life problems. Empirical methods found in the literature and practically used for estimating the breach width researches are using historical dam failure case studies. The most widely used models will be given in this section.

Johnson and Illes Method (1976)

This study was first research in the literature which investigated breach width problems. They used case studies of earth, gravity and arch dams. Breach was described as triangular to trapezoidal shape as the breach develops (Johnson & Illes, 1976). Formulation of Johnson and Illes method for earth fill dams is given in Equation 1:

$$0{,}5h_d \leq B \leq 3h_d \tag{1}$$

Federal Energy Regulatory Commission Method (FERC) (1987)

FERC is an independent agency that regulates and licenses electricity, oil, natural gas, and hydropower projects. Results of FERC study shows that breach width 2-4 times of h_d (FERC, 1999). Formulation of FERC study could be given as;

$$2h_d \leq B \leq 4h_d \tag{2}$$

Singh and Snorrason Method (1982):

This method was developed by using 20 case study data of historical failures. They investigated relationship between breach width and dam height. For this purpose breach width versus dam height measured values were plotted and results of this research shows that breach width changes between 2 and 5 times of dam height (Singh & Snorrason, 1984). Formulation can be given as:

$$2h_d \leq B \leq 5h_d \tag{3}$$

Froehlich Method (1995):

Froehlich revised his previous studies and used 63 dam failure data for investigating dam breach parameters. Prediction equations of each parameter were obtained from multiple regression analysis and suggested k_0 constant for formulation. The factor k_0 indirectly account for the effect of large inflows to a reservoir during an overtopping failure, which are not included in the estimate of V_w and which would increase the ultimate breach width (David C. Froehlich, 1995). Froehlich suggested following equation for average breach width:

$$\underline{B} = 15\, k_0\, V_w^{0,32}\, {H_b}^{0,19} \tag{4}$$

where;

k_0 = If the failure mode was overtopping 1,4 otherwise 1,0
V_w = volume of reservoir at the time of failure (million m^3)
H = Final breach height (meters)

PREDICTION OF DAM BREACH WIDTH USING GENE EXPRESSION PROGRAMMING

Engineers are solving problems to cope with nature and human needs. During this process it's important to clearly understand natural events such as earthquakes, flood, hurricane etc. But these events sometimes could be unpredictable or maybe detailed examination process needed to understand what will happen in future. Therefore, engineers must understand past events and collect enough data to make assumptions about next generations. But time could be a challenging barrier for problem solving. Solving complex problems which include millions of data and time consuming analysis forced engineers to use advantage of computers. Artificial intelligence techniques have evolutionary abilities based on psychology and biology to learn new properties for adapting changing environmental conditions. These techniques mimic living organisms to solve scientific problems (Koza, 2003).

GEP, a genotype/phenotype genetic algorithm (linear and ramified) which uses character linear chromosomes composed of genes structurally organized in a head and a tail. The chromosomes function as a genome and are subjected to modification by means of mutation, transposition, root transposition, gene transposition, gene recombination, and one- and two-point recombination. The chromosomes encode expression trees which are the object of selection. The creation of these separate entities (genome and expression tree) with distinct functions allows the algorithm to perform with high efficiency that greatly surpasses existing adaptive techniques (Ferreira, 2001).

Accurately prediction of unknown parameters in water resources or any other civil engineering problems are crucial. Especially safety of construction mainly depends on possible future consequences of any defects that could be faced during design or operation period. Many studies could be found on literature which used artificial intelligence techniques to predict solutions of natural problems.

GEP based empirical models were used for daily reference evapotranspiration estimation by Guven et al. (2008). Statistical measures such as average, standard deviation, minimum and maximum values, as well as criteria such as mean square error and determination coefficient were used to measure the performance of the model developed by employing GEP. Results of the study indicated that the new equation produces quite satisfactorily results and can be used as an alternative to the conventional models (Guven et al., 2008). Hydraulics and hydrologic problems include many uncertainties and unpredictable parameters. Taking only a few parameters into the modeling process is still a challenging operation. Reference evapotranspiration using routing weather data from the tropical seasonally dry regions used with Gene Expression Programming to estimate evapotranspiration. Results revealed that GEP model is fairly a promising approach with the advantage to provide successfully simple algebraic formulas ease to use without recourse to the full set of meteorological

data requirement for accurately estimate evapotranspiration (Traore & Guven, 2013). In another study 140 historical dam failure cases were used to develop new empirical formula for prediction of non-dimensional key dam breach parameters with gene expression programming. Dam type, failure mode and dam erodibility were picked as additional predictors to mostly used dam breach estimation parameters. Using parametric and uncertainty analysis results, the reservoir shape factor, the dam erodibility, and the dam failure mode are found to have large weights and influence on output predictions in suggested models (Sattar, 2014).

RESULTS AND DISCUSSION

Historical dam failure data obtained from Sattar (2014) was used to provide input data to GEP model. 140 embankment dam failure data from different countries and different dam types was used to identify accuracy of the prediction process. Selected failures were from various countries and various dam types. This makes the proposed model applicable to different types of embankment dams. GEP was used in this study to predict the dam breach width which is one of most important dam breach parameter for embankment dams. 75% of all data was used for training and the remaining 25% was used for the testing period. Predicted values of average breach width are plotted against measured values as seen in Figure 3 where Figure 3.a. shows training and Figure 3.b. shows testing results obtained by using all dam failure database.

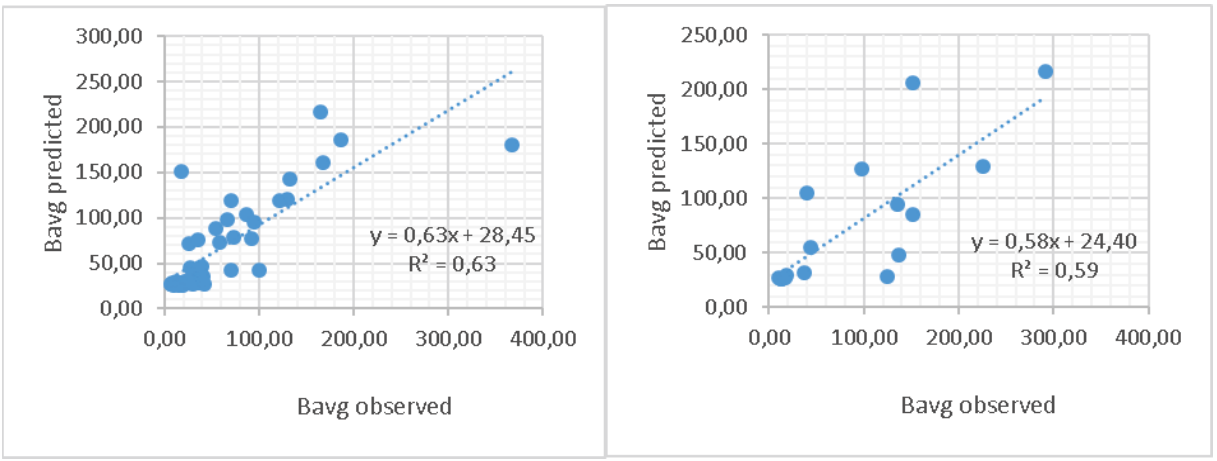

Taking the results of all database used model into account, it could be said that the GEP model developed for the prediction of breach width has good correlation with the measured data. International Commission on Large Dams (ICOLD) mostly use dam height (and also other parameters such as volume of water stored in reservoir) for classifying dams. Dams which have dam height less than 15 meter are called small dams and larger than 15 meters are called large dams. So dams are classified according to size for comparing the effect of dam height on prediction methods. Figure 4.a and 4.b show training and testing data sets results, respectively. The coefficient of determination (R^2) for testing data sets of large dams is 0,52 which is less than the correlation obtained for all dam database values (R^2= 0,59).

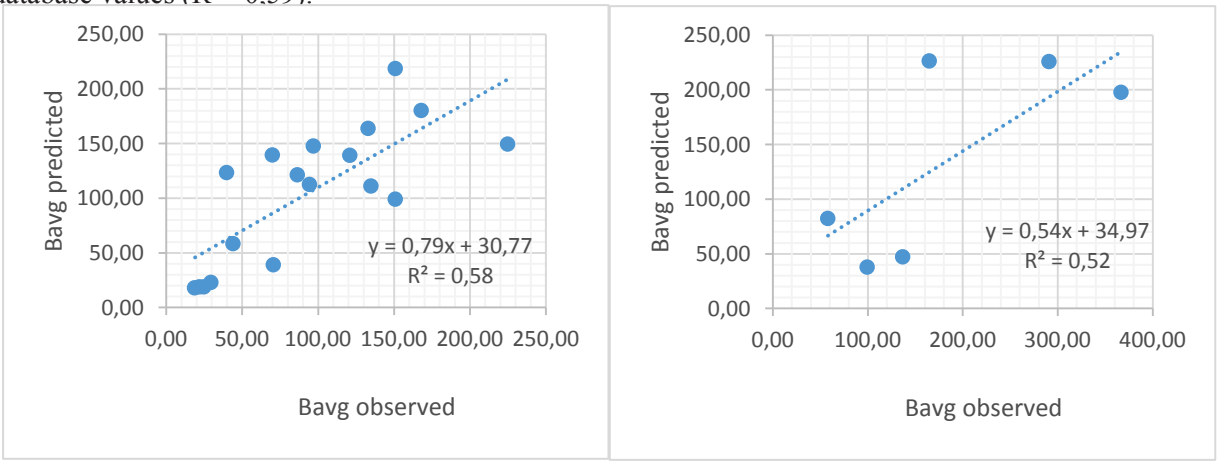

Figure 2 Predicted (GEP) and observed (measured) values of H>15m dams
(a) training, and (b) testing sets.

Small dam values were also used as input data to predict the dam breach width. Figure 5.a. shows training and Figure 5.b. shows testing results of GEP model based on small dam database values.

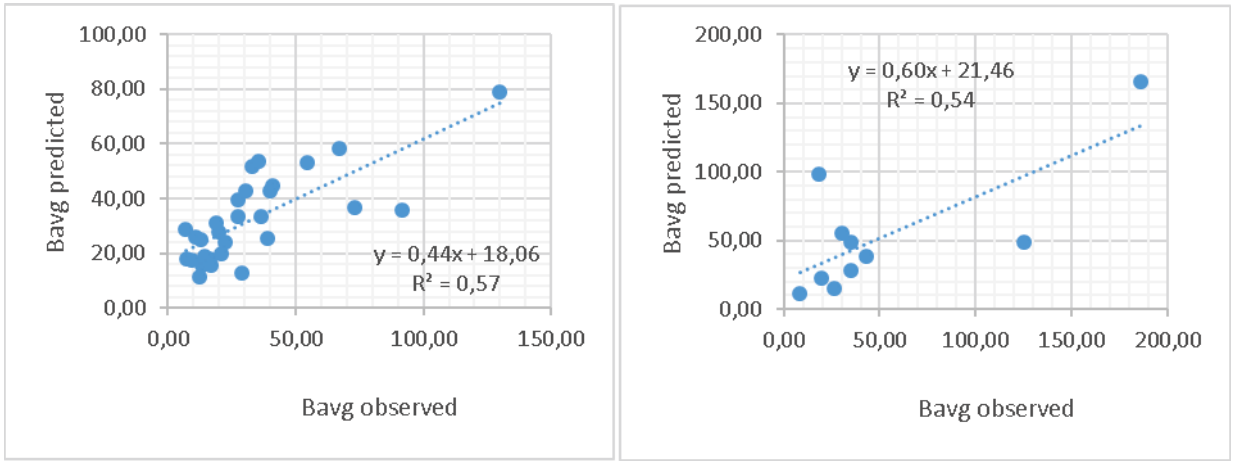

Figure 3 Predicted (GEP) and observed (measured) values of H<15m dams (a) training, and (b) testing sets.

Database was also separated according to dam failure mode to determine the effect of dam failure type on dam breach parameter prediction. Figure 6.a. shows training and Figure 6.b. shows testing results of GEP based on the piping failure mode.

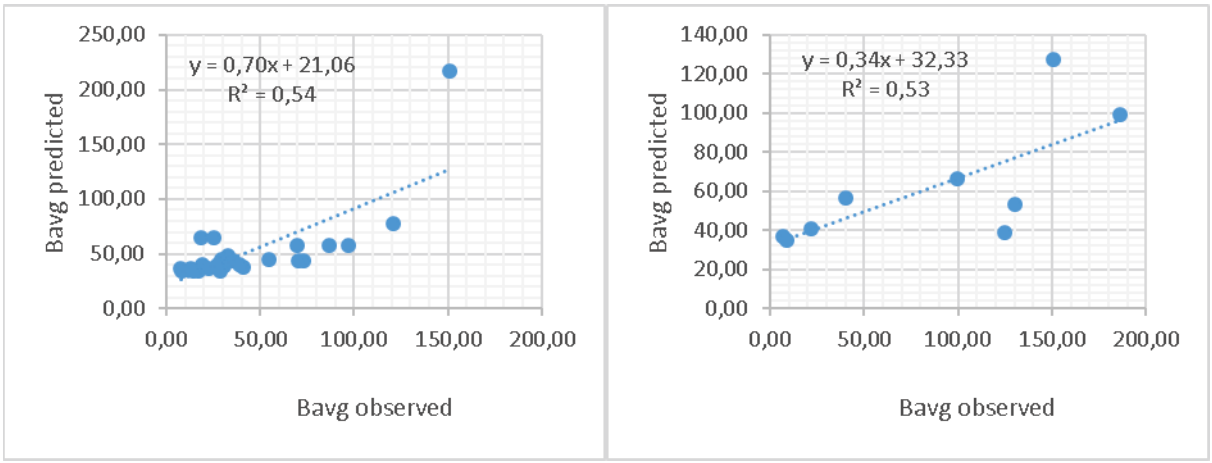

Figure 4 Predicted (GEP) vs measured values of piping failure mode dams (a) training, and (b) testing sets.

Database also includes the data of overtopping failure mode. Dams failed by overtopping failure were used to predict the breach width. From Figure 7 it can be seen that GEP model which uses overtopping failure mode dam values as input data have best accuracy in results for training (Figure 7.a.) and testing (Figure 7.b.) data sets when compared with the previously obtained correlations for other variations (training data set R^2= 0,86 test data set R^2= 0,69).

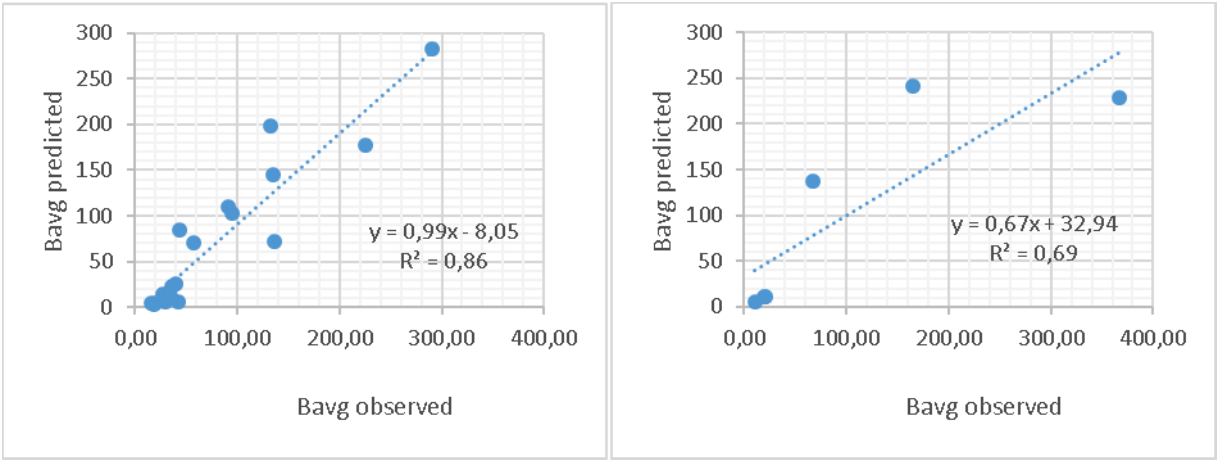

Figure 5 Predicted (GEP) and measured overtopping failure mode dams (a) training, and (b) testing sets.

Results of failure mode separated data for both piping and overtopping failures have less correlation when compared with the model proposed for small dams. But failure mode data based models allow users to investigate the effect of failure mode on breach width for any kind of embankment dams.

All suggested models using GEP for dam breach width prediction include and equation that could be used for practically estimating possible breach width. Equations obtained from the GEP models developed for breach width prediction process are given in Table 1.

Table 1 Average Breach Width Estimation Equation

Input Data	$\overline{B}$ (B_{avg}) Equation	Equation Number
All Database	B_{avg}= (226.94435/(Vw+34.923675))*(Vw+3.8877408)	(4)
h_d >15 meter	B_{avg} = (-233.85582)*(((-Vw)-1)/(Vw+22.437815))	(5)
h_d < 15 meter	B_{avg}= (3.4451127*Hw)+Vw	(6)
Piping Failure Mode	B_{avg}= 0.4579953*(Vw+Hd+70.62219)	(7)
Overtopping Failure Mode	B_{avg} = (-11.541182)*(((Hw/Hd)*Vw)/(Vw+10.212183))* ((-0.1196869)*Hd)-16.71026	(8)

CONCLUSIONS

Prediction of important dam breach parameters which could give clue for future researches was investigated in this study. Results showed that gene expression programming technique could give successful results when used within dam breach parameter prediction studies. If the amount of data used during the training and testing process could be increased then these artificial intelligence techniques could give better results. This study also noted that if the database is separated according to dam size or dam failure type, it will also effect prediction results. Equations allow users to find observed situations' possible results in less time. The proposed models could be well used in all dam breach width prediction studies for all types of embankment dams.

REFERENCES

Altinakar, M. S., Al-riffai, M., Bergman, N., Bradford, S. F., & States, U. (2011). Earthen Embankment Breaching. *Journal of Hydraulic Engineering*, *137*(12), 1549–1564. https://doi.org/10.1061/(ASCE)HY.1943-7900.0000498

Elmazoghi, H. G. H. G. (2013). Fuzzy algorithm for estimating average breach widths of embankment dams. *Natural Hazards*, *68*(2), 229–248. https://doi.org/10.1007/s11069-012-0350-y

Federal Emergency Management Agency (FEMA). (2008). *Risk Prioritization Tool for Dam*. Washington D.C.

FERC, F. E. R. C. (1999). Engineering guidelines for the evaluation of hydropower projects. *Washington DC*, *20426*(July).

Ferreira, C. (2001). Gene Expression Programming: a New Adaptive Algorithm for Solving Problems, 1–22. Retrieved from http://arxiv.org/abs/cs/0102027

Froehlich, D. C. (1995). Embankment dam breach parameters revisited. In *International Water Resources Engineering Conference - Proceedings* (Vol. 1, pp. 887–891).

Froehlich, D. C. (2008). Embankment dam breach parameters and their uncertainties. *Journal of Hydraulic Engineering*, *134*(12), 1708–1721. https://doi.org/10.1061/(ASCE)0733-9429(2008)134:12(1708)

Guven, A., Aytek, A., Yuce, M. I., & Aksoy, H. (2008). Genetic programming-based empirical model for daily reference evapotranspiration estimation. *Clean - Soil, Air, Water*, *36*(10–11), 905–912. https://doi.org/10.1002/clen.200800009

Johnson, A., & Illes, P. (1976). A classification of dams failures. *Int. Water Power Dam Constr.*, *28*(12), 43.

Koza, J. R. (2003). *Genetic Programming : On the Programming of Computers By Means of Natural Selection Complex Adaptive Systems*. Retrieved from papers2://publication/uuid/5DADD85F-EE2F-42E1-8BF8-2CC6959C4FA0

Sattar, A. M. A. (2014). Gene expression models for prediction of dam breach parameters. *Journal of Hydroinformatics*, *16*(3), 550. https://doi.org/10.2166/hydro.2013.084

Singh, K. P., & Snorrason, A. (1984). Sensitivity of outflow peaks and flood stages to the selection of dam breach parameters and simulation models. *Journal of Hydrology*, *68*(1–4), 295–310. https://doi.org/10.1016/0022-1694(84)90217-8

Traore, S., & Guven, A. (2013). New algebraic formulations of evapotranspiration extracted from gene-expression programming in the tropical seasonally dry regions of West Africa. *Irrigation Science*, *31*(1), 1–10. https://doi.org/10.1007/s00271-011-0288-y

Wahl, T. (1998). Prediction of Embankment Dam Breach Parameters—A literature review and needs assessment. *U.S. Bureau of Reclamation Dam Safety*, (July).

NOTATIONS

$\bar{B}$ (B_{avg}) : Average breach width
H : Final breach height (meters)
h_b (H_b) : Final breach height (meters)
h_d (H_d) : Height of dam (meters)
h_w (H_w) : Hydraulic depth of water at dam at failure, above breach bottom
k_0 : If the failure mode was overtopping 1,4 otherwise 1,0)
V_w : volume of reservoir at the time of failure (million m^3)
z : Side slope ratio
β : Breach progression parameter

5th International Symposium on Dam Safety

October 27-31, 2018

REMEDIES FOR THERMAL STRAIN RELATED PROBLEMS

Alper ALDEMİR [1]

ABSTRACT

Dams are one of the most valuable structural types as far as their multi-functional nature is considered. They are very important for societies as mankind requires artificially created water supplies to withstand the fluctuations in the available water. In addition, these structures generate electricity in order to balance the energy demands of settlements. Therefore, the design and assessment of these structures is still prominent concerns of researchers. Due to the immense size of dam structures, the construction stage is also a problem to be solved. Especially, the concrete gravity dams require another investigation to unveil whether the structure is in trouble due to excessive thermal strains demanded by hydration process and/or unequal cooling of the concrete layers. Unfortunately, these thermal analysis often govern the mixture design or the construction plan, resulting in the modification of the final design. The solutions to the excessive thermal strain demands are i. the increase in the pozzolan ratio in the cementitious material, ii. The decrease in the construction speed (i.e. reduction in the sizes of concrete blocks) and iii. the reduction in the compressive strength. In the scope of this study, the possible solutions to excessive thermal demands will be investigated. To this end, the deepest section of Gunduzler Dam, which is a roller compacted concrete gravity dam still being constructed in Eskisehir province, is utilized. The efficiency of the mitigation techniques will also be examined in this study. The optimum pozzolan ratio in cementitious material along with the optimum placement duration between successive horizontal layers will be analyzed.

Keywords: Thermal analysis, efficiency, optimum pozzolan ratio, optimum construction speed

INTRODUCTION

Dams are one of the most important structural types as far as their multi-functional nature is considered. They are very important for societies as mankind requires artificially created water supplies to withstand the fluctuations in the available water. In addition, these structures could supply necessary water to generate electricity in order to balance the energy demands of settlements. Therefore, the design and assessment of these structures is still prominent concerns of researchers. These structure unfortunately generally lie in seismic prone regions and they are in direct contact with its surrounding media (i.e. foundation rock and impounded water). In addition, these structures are immense in size, making their numerical models more complex. Consequently, researcher have been trying to identify the behavior of dam structures under extreme demands (i.e. earthquake excitations, or huge landfalls causing large waves, etc.).

[1] Assistant Professor, Department of Civil Engineering, Hacettepe University, Ankara, Turkey, e.mail: alperaldemir@hacettepe.edu.tr

The research on dam structures has started in the beginning of 20TH century. The studies concentrated on the understanding of the interaction between the reservoir and the dam body and resulted in many methods to simulate the real behavior (Westergaard 1933, Kuo 1982, Medina and Dominguez 1989, Wang and Chopra 2008). Then, the researchers tried to perform some experiments to test the mathematical findings (Hatanaka 1955, Niwa and Clough 1980, Bertero et al. 1984, Uchita et al. 2005 and Phansri et al. 2015). Afterwards, these experimental and numerical developments resulted in more advanced methods that consider interaction with the utilization of boundary elements and/or interface elements (Dasgupta and Chopra 1979, Medina et al. 1990 and Bhattacharjee and Leger 1994). There were also some efforts to simplify these advanced modelling techniques to propose more user-friendly and design oriented procedures (Fenves and Chopra 1985.a and b).

The other research topic for dam structures is definitely the thermal related problems. Due to the immense size of dam structures, the construction stage is also a problem to be solved. Especially, the concrete gravity dams require another investigation to unveil whether the structure is in trouble due to excessive thermal strains demanded by hydration process and/or unequal cooling of the concrete layers. Unfortunately, these thermal analysis often govern the mixture design or the construction plan, resulting in the modification of the final design. The solutions to the excessive thermal strain demands are i. the increase in the pozzolan ratio in the cementitious material, ii. The decrease in the construction speed (i.e. reduction in the sizes of concrete blocks) and iii. the reduction in the compressive strength. To this end, researchers propose some hydration energy curves to estimate the temperature change (or related strain and stress values) due to the placement of mass concrete (Malkawi et al. 2003). Generally, the thermal analyses governs the size of the monoliths during the construction. If the monolith dimensions come out to be less than expected, the commonly utilized solution was to change the mixture design. In the scope of this study, the possible solutions to excessive thermal demands will be investigated. To this end, the deepest section of Gunduzler Dam, which is a roller compacted concrete gravity dam still being constructed in Eskisehir province, is utilized. The efficiency of the mitigation techniques will also be examined in this study. The optimum pozzolan ratio in cementitious material along with the optimum placement duration between successive horizontal layers will be analyzed.

DESCRIPTION OF GUNDUZLER DAM

Gunduzler is located at the province of the city of Eskisehir (i.e. nearly 28km to the city center of Eskisehir). It is planned to serve for irrigation purpose. It is design as Roller Compacted Concrete (RCC) dam. It has a maximum height of 61m and a crest length of 419m (Figure 1). It lies on the second seismic zone in Turkey (i.e. PGA values reaching up to 0.2g). The seismic design of Gunduzler dam resulted in a vertical upstream slope and a slope of 1:0.7 at the downstream face (Figure 1). The mixture design of Gunduzler dam was composed of 80kg/m^3 of cement and 40kg/m^3 of fly ash.

DESCRIPTION OF NUMERICAL MODEL FOR THERMAL ANALYSES

The thermal analyses of Gunduzler dam was performed in ANSYS v13.0 multi-physics program. The numerical model is shown in Figure 2. The numerical model was composed of 8-node shell elements (i.e. for both thermal and structural analyses). Approximately 2800 elements were utilized during the analyses. The thermal analyses also considered the staged construction used during the construction stage of Gunduzler Dam by activating the birth-and-death property. The heat of hydration – time curve given in Figure 3 was used during the thermal analysis as suggested by Malkawi et al. (2003). For the sake of simplicity, the given heat of hydration curve was idealized by using two lines.

(a) Location of Gunduzler Dam

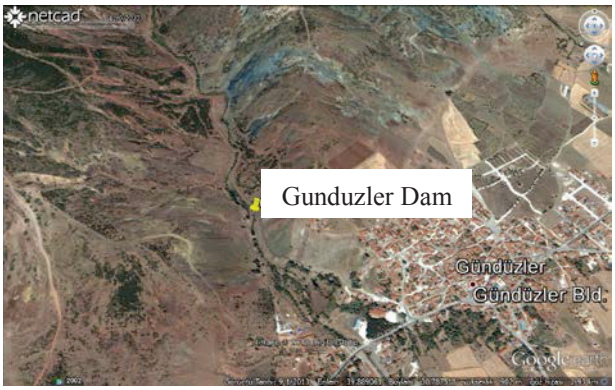

(b) Satellite View of the Location of Gunduzler Dam

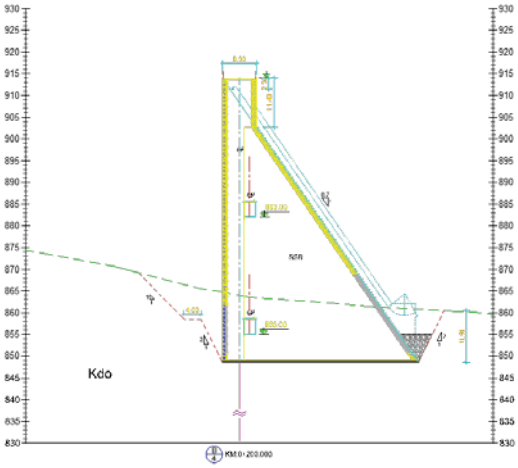

(c) Deepest Section of Gunduzler Dam

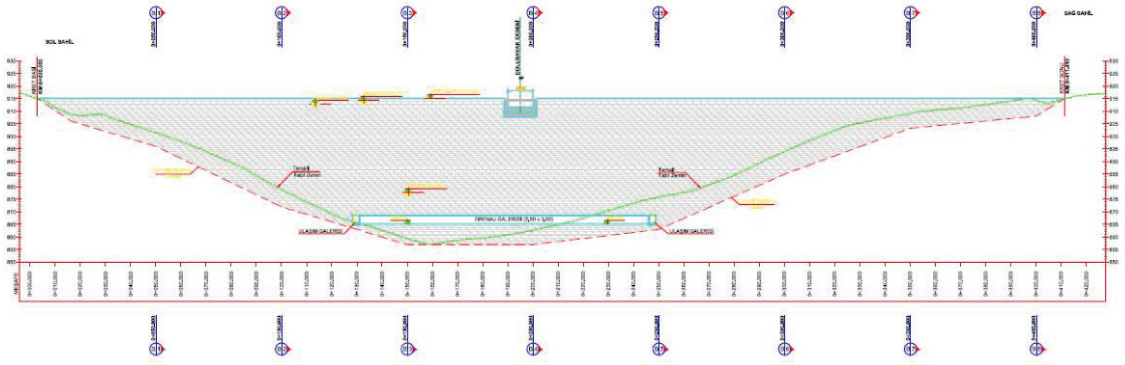

(d) Profile View of Gunduzler Dam

Figure 1. Gunduzler Dam

The necessary parameters for modelling concrete and foundation rock are presented in Table 1. These parameters are assumed to be consistent with the literature available data (Lee et al. 2008, Malkawi et al. 2003, Noorzaei et al. 2006 ve Kim 2010). In numerical models, the convection coefficient was taken as constant by neglecting the effect of formwork.

Table 1. Material Properties used in the Numerical Models

	RCC
Density (kg/m^3)	2.400
Specific Heat (J/kg/ C^o)	963
Modulus of Elasticity (MPa)	19.000
Coefficient of Expansion (1/ C^o)	6,5x10^{-6}

Conduction Coefficient (J C°/s/m)	2,1
Convection Coefficient (J/s/m²)	10.3
Poission Ratio	0.2

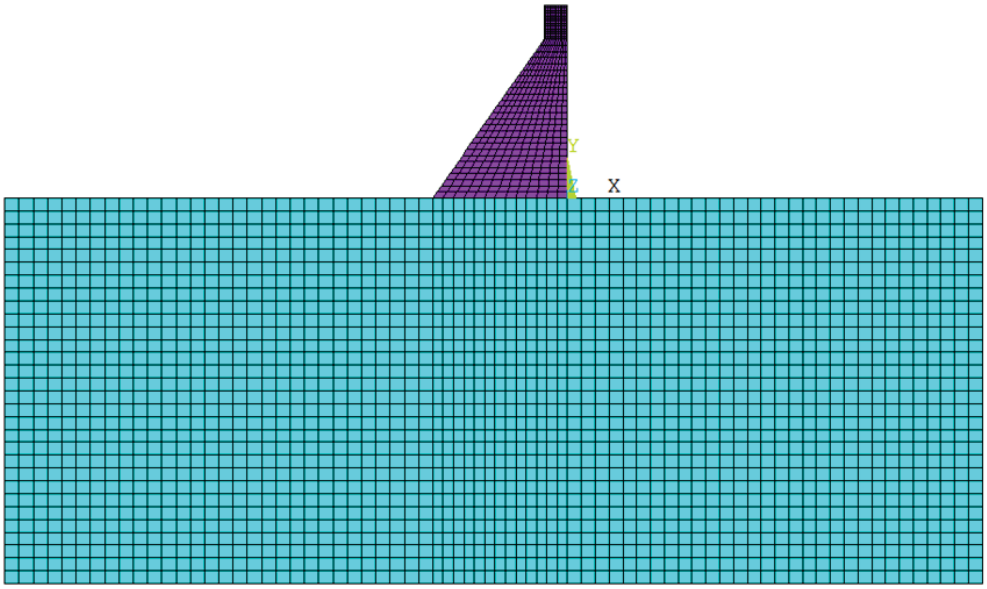

Figure 2. Details of Numerical Model

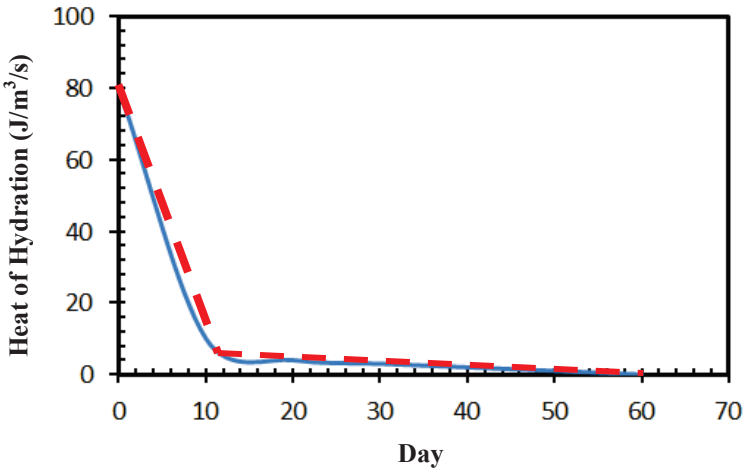

Figure 3. Used Heat of Hydration Curve during Thermal Analysis

THERMAL ANALYSES

In this part, a different perspective other than changing the thickness of the monolith was tried to be presented for possible remedy to reduce the temperature changes inside the dam body. This reduction apparently lead decreased strain and stress levels in the dam body. Therefore, the thickness of the monoliths could indirectly be increased. The first parameter was selected as the start of the project. The average temperatures between 1990 and 2010 recorded in Eskisehir are given in Table 2. These values are used to determine the necessary convection value on the dam body. In addition, the thickness of monolith in numerical models was assumed to be 13m.

Table 2. Average Temperatures recorded in Eskisehir

Year	Jan	Feb	Mar	Apr	May	Jun	Jul	Aug	Sep	Oct	Nov	Dec	Ave.
1990									15.80	11.70	7.70	2.90	9.53
1991	-1.40	-1.10	6.20	9.60	12.70	18.40	21.40	20.80	15.90	11.70	5.60	-1.50	9.86
1992	-4.10	-4.10	2.60	9.90	13.70	18.40	19.20	22.40	15.40	13.60	4.10	-1.40	9.14
1993	-4.50	-1.00	4.10	9.00	13.70	17.90	20.50	20.90	16.90	12.50	3.60	3.10	9.73
1994	2.70	1.30	5.10	12.10	15.50	18.80	22.30	22.00	20.50	14.30	4.80	0.20	11.63
1995	2.50	3.30	4.90	8.50	15.50	20.30	20.10	20.70	17.30	9.30	2.20	2.30	10.58
1996	-0.30	2.70	2.20	7.10	16.10	18.10	22.30	21.20	15.40	9.90	6.00	5.00	10.48
1997	1.00	-0.70	2.00	5.70	15.50	18.80	20.80	18.60	13.70	10.80	5.80	2.50	9.54
1998	0.40	1.90	2.10	12.00	13.90	18.20	22.10	22.70	16.80	12.00	7.30	3.30	11.06
1999	2.50	2.30	5.10	10.50	15.50	18.90	22.70	22.10	17.30	12.50	5.40	4.00	11.57
2000	-4.40	-0.90	3.30	12.30	14.20	18.40	23.30	21.00	17.10	10.60	6.30	0.60	10.15
2001	2.40	2.70	10.30	10.30	14.10	20.20	23.80	22.20	18.30	11.30	5.60	1.50	11.89
2002	-5.30	2.60	7.00	9.30	14.70	19.30	23.40	21.00	16.60	11.60	6.10	-2.40	10.33
2003	4.80	-1.40	1.00	7.60	16.40	20.40	21.70	22.40	15.80	12.90	5.70	0.50	10.65
2004	-0.30	1.10	5.40	9.60	14.00	18.80	21.70	20.60	17.50	12.80	5.70	1.40	10.69
2005	2.10	1.50	4.90	10.00	14.70	18.20	22.40	22.80	16.80	9.50	5.20	2.50	10.88
2006	-2.80	-1.80	5.80	11.30	14.80	19.40	21.10	24.60	16.60	12.60	3.90	-0.70	10.40
2007	0.00	1.50	5.40	7.50	17.80	20.80	23.80	23.90	17.70	12.60	4.90	0.60	11.38
2008	-3.50	0.00	8.40	11.50	14.30	20.20	21.90	23.40	17.00	11.70	6.80	1.50	11.10
2009	0.90	3.10	4.60	10.00	14.80	20.40	22.20	21.00	16.50	14.50	6.00	4.60	11.55
2010	2.40	5.70	6.70	10.20	16.40	19.40	23.30	25.30	19.00	10.80	10.00	4.90	12.84
Ave.	-0.25	0.94	4.86	9.70	14.92	19.17	22.00	21.98	16.85	11.87	5.65	1.69	10.71

Effect of Start Date of the Construction

The start of the construction could have an effect on the temperature distribution of the dam body as the convection between the dam body and the atmosphere sometimes could lead to extreme changes in temperature. To this end, the start of the construction was taken as a parameter in this study. There were four different start dates, i.e. January (coldest month), April (mild temperature after coldest month), August (warmest month) and October (mild temperature after warmest month).

Start Date as January

The thermal analysis was conducted by taking the start date of the construction as January. The results are given at the end of the construction in Figure 4.

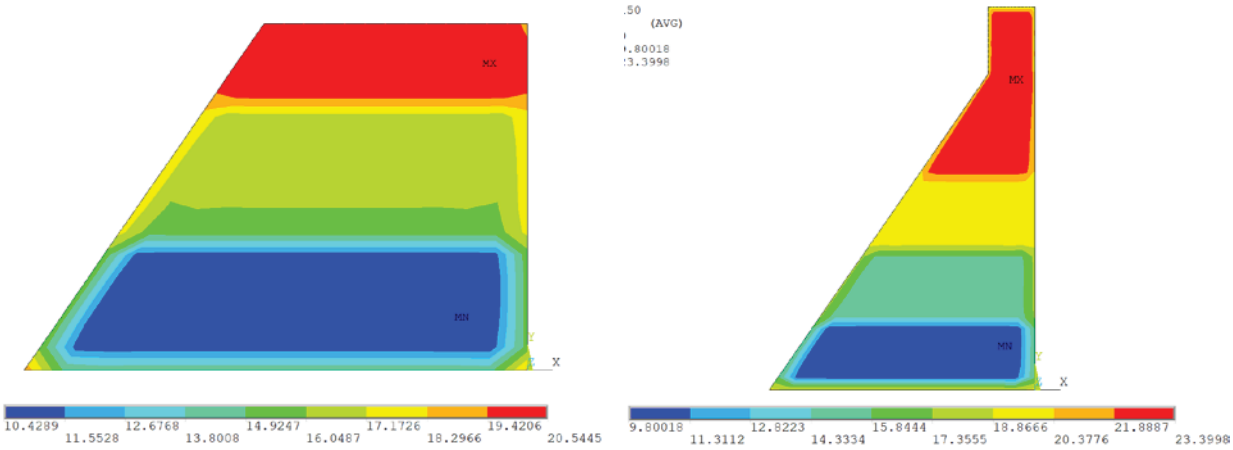

Figure 4. Temperature Distribution of the Dam Body for January as the Start Date of Construction

Start Date as April

The thermal analysis was conducted by taking the start date of the construction as January. The results are given at the end of the construction in Figure 5.

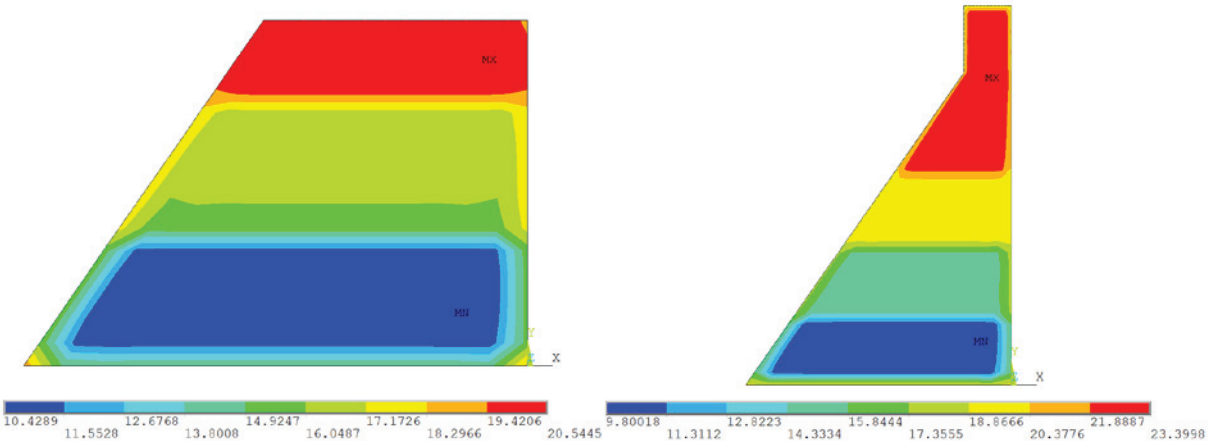

Figure 5. Temperature Distribution of the Dam Body for April as the Start Date of Construction

Start Date as August

The thermal analysis was conducted by taking the start date of the construction as January. The results are given at the end of the construction in Figure 6.

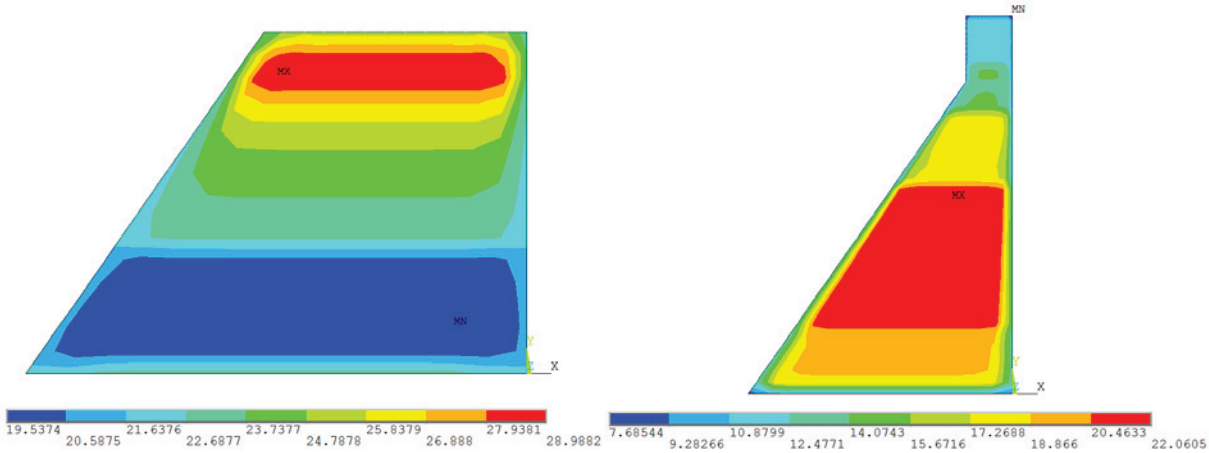

Figure 6. Temperature Distribution of the Dam Body for August as the Start Date of

Start Date as October

The thermal analysis was conducted by taking the start date of the construction as January. The results are given at the end of the construction in Figure 7.

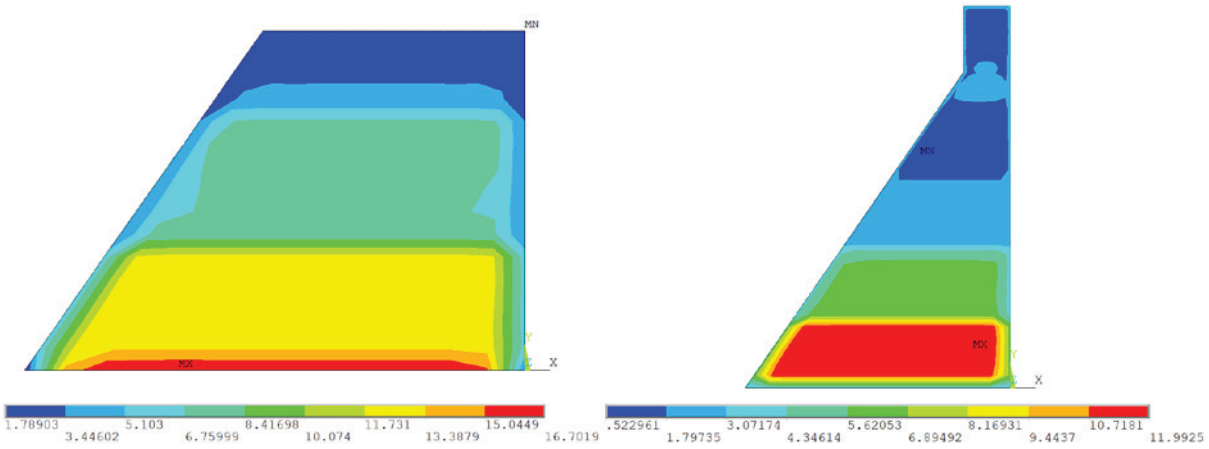

Figure 7. Temperature Distribution of the Dam Body for October as the Start Date of Construction

From Figures 4-7, it is clear that the start date of the construction affects the temperature distribution due to the heat of hydration. It is also apparent that the best choice for the start date of the construction of the Gunduzler Dam is the month October. Therefore, it could be stated that the start date of the construction could positively affect the temperature changes inside the dam body. And, the start date of the construction should be taken into account in order to limit the temperature rise in the dam body due to the heat of hydration.

Effect of the Delay Time between Successive Horizontal Lift Joints

The lift joints could be placed after some delay time in order to reduce the temperature values in the dam body. The effect of this delay time was also investigated in this study. To this end, four different values for the delay time, i.e. 1, 3, 7 and 10 days, are considered. The analysis results are given for a dam built starting in January.

One-day Delay Time

The thermal analysis was conducted by taking the delay time between successive horizontal lift joints as 1 day. The results are given at the end of the construction in Figure 8.

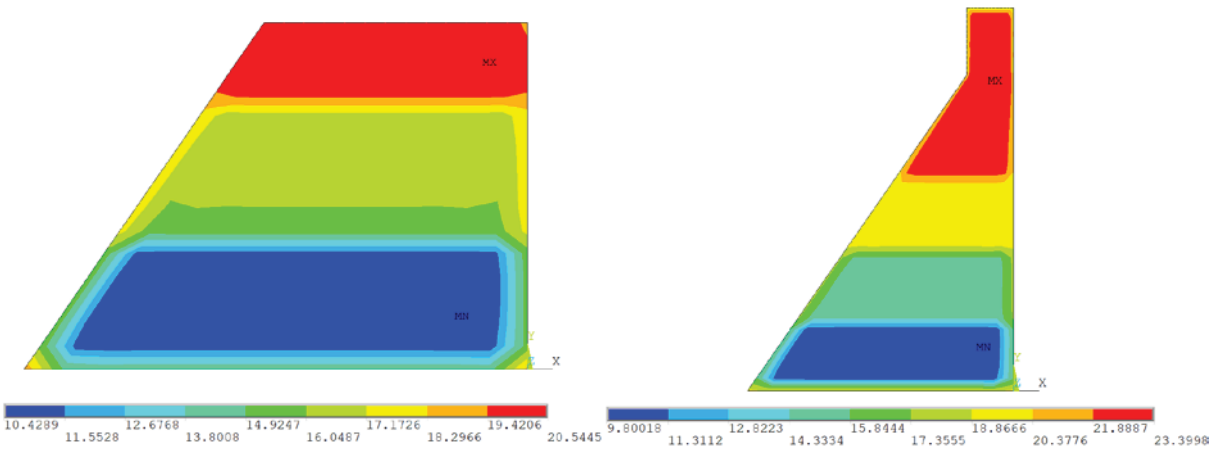

Figure 8. Temperature Distribution of the Dam Body for 1-day Delay Time

Three-day Delay Time

The thermal analysis was conducted by taking the delay time between successive horizontal lift joints as 3 days. The results are given at the end of the construction in Figure 9.

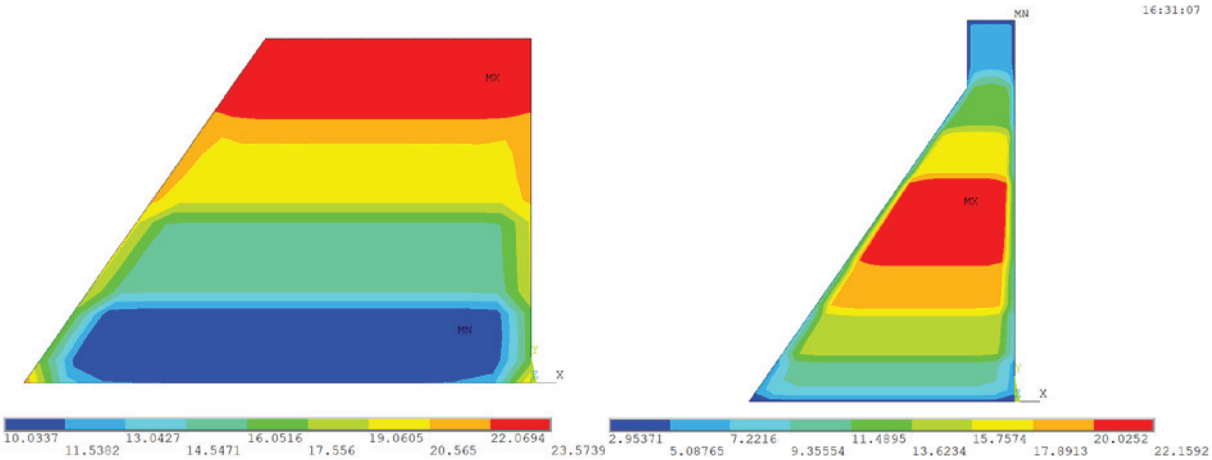

Figure 9. Temperature Distribution of the Dam Body for 3-day Delay Time

Seven-day Delay Time

The thermal analysis was conducted by taking the delay time between successive horizontal lift joints as 7 days. The results are given at the end of the construction in Figure 10.

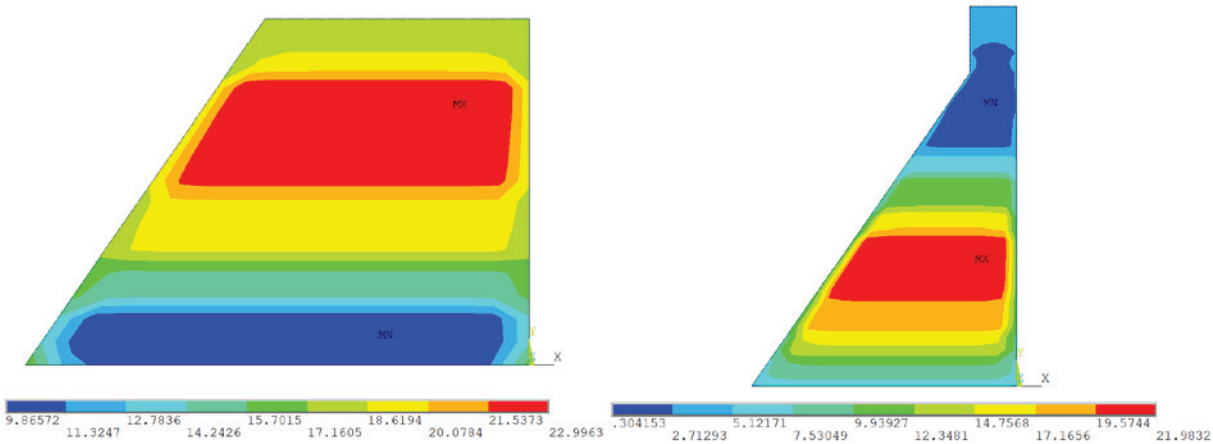

Figure 10. Temperature Distribution of the Dam Body for 7-day Delay Time

Ten-day Delay Time

The thermal analysis was conducted by taking the delay time between successive horizontal lift joints as 10 days. The results are given at the end of the construction in Figure 11.

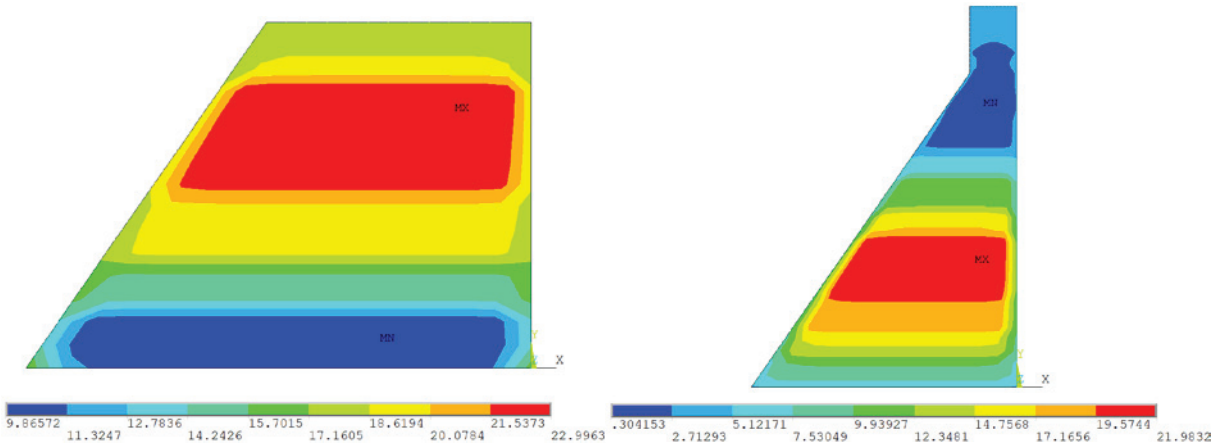

Figure 11. Temperature Distribution of the Dam Body for 10-day Delay Time

From Figures 8-11, it is clear that the delay time between successive horizontal lift joints could have some limited effect on the temperature increase in the dam body. 7-day delay time between successive horizontal lift joints was detected to have the maximum influence on the temperature distribution. The percentage decrease was determined as approximately 6%. And, after 7-day delay time between successive horizontal lift joints, there was no change in temperature distribution (i.e. the effect of delay time seemed to reach a convergence). Therefore, the temperature distribution throughout the dam body could be improved by adjusting the construction time between the successive lift joints.

CONCLUSION

The thickness of monoliths of concrete dams are generally determined by conducting thermal analysis. The excessive theremal strains could be caused by large changes in temperatures inside the dam body due to the heat of hydration. The general trend among design engineers to solve this issue is to the increase in the pozzolan ratio in the cementitious material, to decrease the construction speed (i.e. reduction in the sizes of concrete blocks) or to reduce the compressive strength of the used concrete mixture. In the scope of this study, the possible different solutions to the excessive thermal demands was investigated. To this end, the deepest section of Gunduzler Dam, which is a roller compacted concrete gravity dam still being constructed in Eskisehir province, was utilized.

The conducted numerical analysis revealed that the start date of the construction affects the temperature distribution due to the heat of hydration (Figures 4-7). It is also apparent that the best choice for the start date of the construction of the Gunduzler Dam is the month October. Therefore, it could be stated that the start date of the construction could positively affect the temperature changes inside the dam body. And, the start date of the construction should be taken into account in order to limit the temperature rise in the dam body due to the heat of hydration.

It was also shown that the delay time between successive horizontal lift joints could have some limited effect on the temperature increase in the dam body (Figures 8-11). 7-day delay time between successive horizontal lift joints was detected to have the maximum influence on the temperature distribution. The percentage decrease was determined as approximately 6%. And, after 7-day delay time between successive horizontal lift joints, there was no change in temperature distribution (i.e. the effect of delay time seemed to reach a convergence). Therefore, the temperature distribution throughout the dam body could be improved by adjusting the construction time between the successive lift joints.

REFERENCES

Bernal, D. and Youssef, A., 1998. "A Hybrid Time Frequency Domain Formulation for Non-Linear Soil-structure Interaction", Earthquake Engineering and Structural Dynamics, vol. 27, pp. 673-685.

Bertero V.V., Aktan A.E., Charney F.A. and Sause R., 1984. "Earthquake Simulation Tests and Associated Studies of a 1/5th-scale Model of a 7-story R/C Frame–wall Test Structure", Report No: UCB/EERC-84/05, University of California, Berkeley, California.

Bhattacharjee, S.S. and Leger, P., 1994. "Application of NFLM Models to Predict Cracking in Concrete Gravity Dams", Journal of Structural Engineering ASCE, vol. 120, N. 4, pp. 1255-1271.

Dasgupta,G. and Chopra, A.K., 1979. "Dynamic Stiffness Matrices for Viscoelastic Half Planes", Journal of Engineering Mechanics Division, ASCE, vol. 105, N. 5, pp. 729-745.

Fenves, G. and Chopra, A.K., 1985.a. "Simplified Earthquake Analysis of Concrete Gravity Dams: Separate Hydrodynamic and Foundation Interaction Effects", Journal of Engineering Mechanics, vol. 111, N. 6, pp. 715-735.

Fenves, G. and Chopra, A.K., 1985.b. "Simplified Earthquake Analysis of Concrete Gravity Dams: Combined Hydrodynamic and Foundation Interaction Effects", Journal of Engineering Mechanics, vol. 111, N. 6, pp. 736-756.

Hatanaka, M., 1955. "Fundamental Considerations on the Earthquake Resistant Properties of Earth Dam", Disaster Prevention Research Institute, Bulletin No:11, Kyoto, Japan.

Kim, S.G., 2010. "Effect of Heat Generation from Cement Hydration on Mass Concrete Placement", Graduate Theses and Dissertations.

Kuo, J.S.H., 1982. "Fluid – structure Interactions: Added Mass Computations for Incompressible Fluid", Report No: UCB/EERC-82/09, University of California, Berkeley, California.

Lee, Y., Choi, M.S., Yi, S.T. and Kim, J.K., 2009. "Experimental Study on the Convective Heat Transfer Coefficient of Early-age Concrete", Cement and Concrete Composites, vol. 31, pp. 60 – 71.

Malkawi, A.I.H., Mutasher, S.A. and Qui, T.J., 2003. "Thermal-structural Modeling and Temperature Control of Roller Compacted Concrete Gravity Dam", Journal of Performance of Constructed Facilities ASCE, vol. 17, N. 4, pp. 177 - 187.

Medina F. and Dominguez, J., 1989. "Boundary Elements for the Analysis of the Seismic Response of Dams including Dam-water-foundation Interaction Effects", Engineering Analysis with Boundary Elements, vol. 6, N. 3, pp. 152:157.

Medina, F., Dominguez, J., and Tassoulas, J., 1990. "Response of Dams to Earthquakes including Effects of Sediments", Journal of Structural Engineering ASCE, vol. 116, N. 11, pp. 3108–3121.

Niwa, A. and Clough, R.W., 1980. "Shaking Table Research on Concrete Dam Models", Report No: UCB/EERC-80/06, Earthquake Engineering Research Center, University of California, Berkeley, California.

Noorzaei, J., Bayagoob, K.H., Thanoon, W.A. and Jaafar, M.S., 2006. "Thermal and Stress Analysis of Kinta Dam, Engineering Structures", vol. 28, pp. 1795 - 1802.

Phansri, B., Charoenwongmit, S., Yooprasertchai, E., Park, K., Warnitchai, P. and Shin, D., 2015. "An Experimental Study on Shaking Table Tests on Models of a Concrete Gravity Dam", KSCE Journal of Civil Engineering, vol. 19, N. 1, pp. 142-150.

Uchita, Y., Shimpo, T. and Saouma, V., 2005. "Dynamic Centrifuge Tests of Concrete Dam", Earthquake Engineering and Structural Dynamics, vol. 34, N. 12, pp. 1467–1487.

Wang, J. and Chopra, A.K., 2008. "EACD-3D: A Computer Program for Three Dimensional Earthquake Analysis of Concrete Dams Considering Spatially - Varying Ground Motion", Report No: UCB/EERC-2008/04, Earthquake Engineering Research Center, University of California, Berkeley, California.

Westergaard, H.M., 1933. "Water pressures on dams during earthquakes". Transactions of the American Society of Civil Engineers, vol. 98, pp. 418–433.

5th International Symposium on Dam Safety

October 27-31, 2018

ENVIRONMENTAL IMPACTS OF LARGE DAMS : YUSUFELI DAM EXAMPLE (ARTVIN/ TURKEY)

Ayla BİLGİN [1]

ABSTRACT

Dams are considered as a clean energy source. However, major ecological losses occur during the construction of the dam, the precious agricultural areas are destroyed and the living spaces of the creatures are destroyed. Among social and environmental issues discussed in recent years, dams and HEPPs have an important place. Although collecting large dams offers many benefits, there are many irreversible negative environmental effects for the environment. The environmental risks of dams, physicochemical risks, biological risks, economic, social and cultural risks, health and safety risks are evaluated in 4 main categories. Identification of the hazards that may arise in the construction and operation of a dam will provide a planned approach to sustainable resource management by preventing ecological degradation. Yusufeli Dam and Hydroelectric Power Plant are built on the Coruh River which is one of the most important rivers of the Black Sea Basin. Çoruh River has a length of 376 km and 354 km is within the boundaries of our home. There are 3 dams built on the river. These are Muratli, Borçka and Deriner dams. In this study, Yusufeli Dam was evaluated within the scope of environmental effects of large dams.

Keywords: Environmental Impacts, Environmental Risk, Yusufeli Dam,

INTRODUCTION

Dams have been promoted as an important tool for meeting water and energy needs, and some as a long-term, strategic investment capable of providing a large number of benefits typical of all major infrastructure projects. Large dams are constructed with the aim of establishing an industrial base with regional development, employment creation and export capacity (WCR, 2001).

Until 1970s, large dams were introduced as an important means of meeting human needs for water and energy. The World Commission report on Dams 2000, an independent assessment based on case studies from all over the world, has shown that many dams perform poorly in terms of the intended benefits and delivery of services. In addition, the negative environmental and social impacts of large dams were largely unexpected or low. The construction of dams results in physical, chemical and biological changes to natural ecosystems. Most dams have been created by focusing on maximizing the short-term economic use of water, resulting in little or no long-term consequences of changes in flow volumes, flow patterns and water quality (McCartney et al. 2001). Today, environmental problems such as economic and technical problems are taken into consideration in the design of dams (Ishida et all. 2003)

[1] Dr.Lecturer, Department of Environmental Engineering, Artvin Coruh University, Artvin, Turkey, e-posta: ayla.bilgin@gmail.com

The environmental, social and health-related consequences of large dam projects are internationally remarkable (Baviskar and Singh 1994). Although dams are important for water and energy supply, flood management and irrigation, millions of people are often exposed to negative health and social impacts in less developed countries (Goldsmith and Hildyard 1984).

ENVIRONMENTAL IMPACTS OF BIG DAMS

The establishment of a large dam with high savings capacity may have multilateral and significant impacts. These effects can be classified as physical, biological, social, economic, political and ecological effects. In general, the environmental impact of the dam lake can be examined as "negative and destructive environmental effects of dams" (Jashni, and Chamanchi, 2007) .

In order to investigate the effects of dams on ecosystems, a wide range of data is required for both abiotic and biotic components of ecosystems. To fully assess the impact of a dam on the ecosystem; hydrology of the river (both at the dam and downstream site); hydraulic characteristics of the river; water quality; geomorphological features (ie sediment transport); aquatic biota and habitat requirements; coastal vegetation and its associated fauna; information on direct use of the river and its associated resources by the local population is required (Nilsson and Dynesius, 1994).

Rivers are natural corridors important for the flow of energy, substances and species, and are often key elements in the regulation and maintenance of landscape biodiversity (Nilsson and Jansson, 1995). The changes caused by the dams directly and indirectly affect the heterogeneity of habitats and ultimately the ecological integrity of river ecosystems. Dams cause changes throughout the river systems. The most obvious effect of storage reservoirs is the permanent destruction of ecosystems by land. The most common downstream effect of large dams is the decrease in the variation of water discharge throughout the year. Total discharge can be reduced if the evaporation rates are high and / or the water is removed directly from the reservoir (Ward and Stanford, 1995). In many countries resettlement is being carried out due to the large dam construction (Table 1).

While evaluating the environmental risks of dams, they are evaluated under four main headings (Muhlbauer, 2004).;
- Physicochemical risks
- Biological Risks
- Economic, social and cultural risks
- Health and safety risks

These risks are also considered as sub-headings and are given in Figure 1.

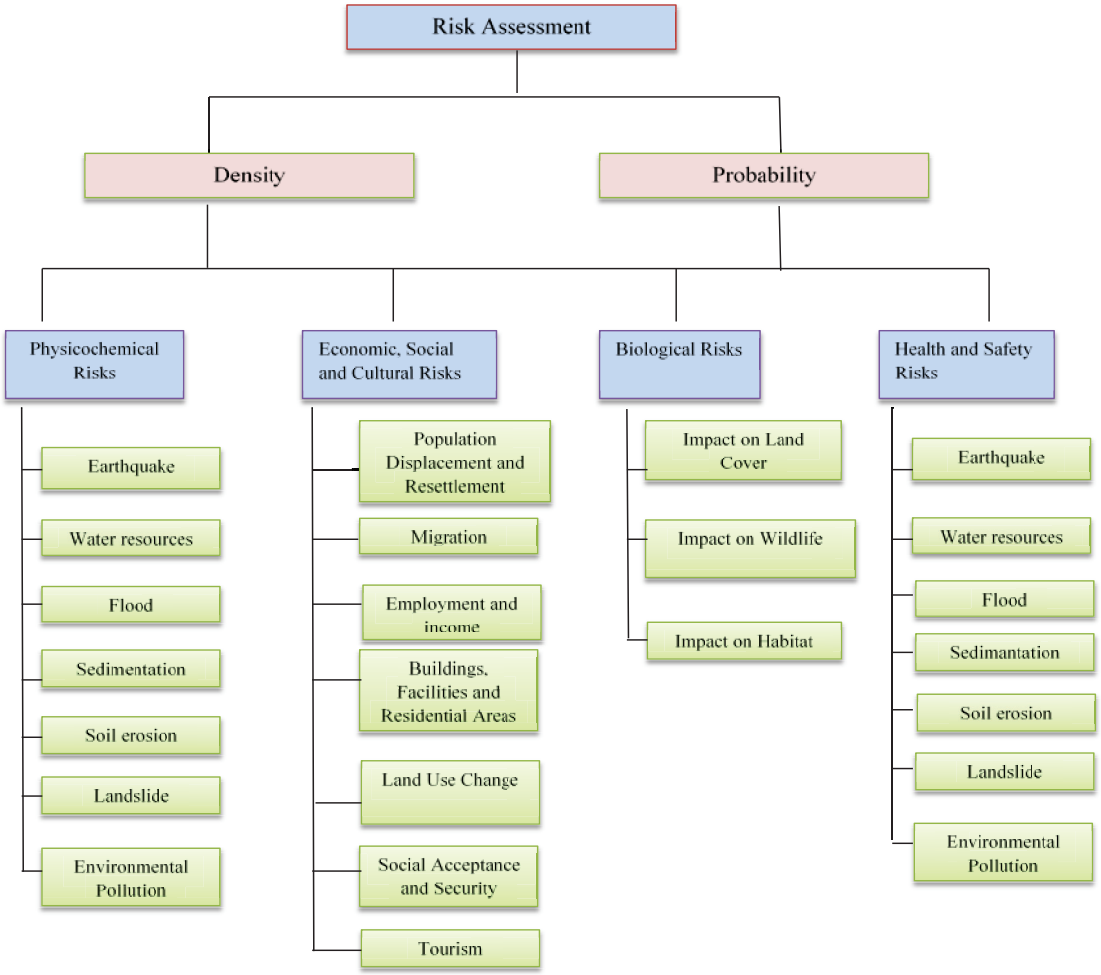

Figure 1. Environmental Risk Assessment of Dams (Muhlbauer, 2004).

Table 1. Countries and number of people who are resettled due to large dams in the world (Bilgin 2015)

Dams	**Country**	**Resettlement**
Three Gorges China	China	1,250,000
Upper Krishna II	India	220,000
Sardar Sarovar	India	127,000
Aswan High Dam	Egypt	100,000
Kossou Ivory	Coast	85,000
Akosombo	Ghana	84,000
Longtan	China	73,000
Mahaweli I–IV	China	60,000
Kariba	Zambia and Zimbabwe	57,000
Sobradhino	Brazil	55,000

EVALUATION OF YUSUFELI DAM

The Yusufeli Dam is built on the Coruh River. The height of the dam body is 270 meters and it will be the 7th in the world's highest dams list. The Yusufeli Dam will have 540 MWe installed power and is planned to produce 1 billion 888 million kilowatt hours of electricity annually. This amount corresponds to the production of 7 thousand in Turkey's electricity consumption. The Yusufeli Dam, which has a storage capacity of 2 billion 130 million m3, has the highest storage capacity among the HEPPs to be established and operated on the Coruh River. The storage capacity of the dam corresponds to approximately 30% of the annual flow of the Coruh River (http://www.enerjiatlasi.com/hidroelektrik/yusufeli-baraji.html).

Initial work for the Yusufeli Project, a part of the Coruh River Hydroelectric Development Master Plan, was launched in 1970, but the tender for the dam project was made in 2010. State Water Works data gore; the project will cover 0.6% of Turkey's annual energy needs. When the Yusufeli Dam, which is a large-scaled dam, is completed, an area of 3,241 hectares will be under the water. The project will cause Yusufeli district center and 3 villages to be completely , and 16 villages and land to be partially under the water (KD, 2011).

Dam and HEPP projects are evaluated within the scope of EIA Regulation according to their capacities. However, since the Yusufeli Dam Project was included in the investment program prior to 1997, it was exempted from the EIA within the scope of the EIA Regulation under the title of ’Legal Excluded Projects Ancak. Therefore, an ”Environmental Impact Assessment“ report has not been prepared. In 2006, Encon Environmental Consultancy Ltd. was established to meet the requirements of international credit institutions involved in project finance. Sti. has prepared a report under the name of rapor Yusufeli Dam and HEPP Environmental Impact Assessment tarafından. The report is not a report that has to be applied to the EIA Regulation and is only for the purpose of receiving international credit support.

CONCLUSION

Along with the developing technology, the damage in the environment is increasing. However, it has harmful effects on environment and human life during dam construction phase. Environmental impact assessment studies are required before starting dam construction and other investment studies. Preparing environmental legislation of dams construction is provides both legal responsibilities and a planned approach. Taking the results of environmental assessment seriously and using them in practice can reduce some of destructive effects.

REFERENCES

Bilgin, A., 2015. "Yusufeli Barajı Çevresel Risk Değerlendirmesi", Yusufeli Barajının İlçeye Etkileri, Türker Matbaacılık.

Baviskar, A., Singh, A.K. 1994. "Malignant growth: The Sadar Sarovar dam and its impact on public health". *Environmental Impact Assessment Review* 14:349–358.

Goldsmith, E., Hildyard, N. 1984. The Social and Environmental Impact of Large Dams. Wadebridge: Wadebridge Ecological Centre.

Muhlbauer, W.K., 2004. "Pipeline Risk Management Manual: Ideas, Techniques and Resources". 3rd edit. Gulf Professional Publishing, Elsevier, Oxford, UK

Ishida, S., Kotoku, M., Abe, E., Fazal, M.A., Tesuchihara, T., Imaizumi, M., "Construction of Subsurface Dams and Their Impact on the Environment," Material and Geo Environment, Vol. 50, No. 1, 2003, pp.149-152.

KD, 2011. Kaçkar Dağları ve Yusufeli Bölgesi Yönetim Planı, 121syf.

McCartney, M.P., Sullivan, C. and Acreman, M.C., 2000. "Ecosystem Impacts of Large Dams", UNEP,2001.

Nilsson, C. and Dynesius, M. 1994." Ecological effects of river regulation on mammals and birds: a review". *Regul. Rivers: Res. Manage*. 9, 45-53.

Nilsson, C., Jansson, R. 1995. "Floristic differences between riparian corridors regulated and free-flowing boreal rivers". Regul. Rivers: Res. Manage., 11, 55-66

Ward, J.V., Stanford, J.A. 1995. " Ecological connectivity in alluvial river ecosystems and its disruption by flow regulation". *Regulated Rivers: Research and Management*, 11, 105-119.

WCR, "World Commission Report, Dams and development: A new framework for decision-making", December, 2001.

5 DAM SAFETY
İstanbul Turkey 2018

5th International Symposium on Dam Safety

October 27-31, 2018

PHYSICAL MODELING OF SUBMERGED FLOW UNDER SLUICE GATE: INVESTIGATION OF SCALE EFFECTS AND DYNAMIC SIMILARITY

Ali YILDIZ [1], Ali İhsan MARTI[2]

ABSTRACT

Sluice gates are used as the energy dissipation structures besides controlling water level in the reservoirs. In some cases, steps and baffle blocks are placed at the stilling basin after the sluice gate to produce a submerged hydraulic jump and improve energy dissipation. Submerged hydraulic jump is formed as a result of strong turbulence forces, so that the hydraulic design of these structures should be made carefully. Physical models are built in the laboratories to represent its real-world prototype; however some scale effects may arise between models. Two open channel setups, called as model and prototype, are used in this study. The experiments of the study are performed on these channels using identical Froude Numbers and geometric scaling ratio of 4:1. The flow depths at four different points are measured from model and prototype for 2 different gate openings and 30 discharge values. The results showed that there is %93 consistency between model and prototype, whereas this consistency was not observed at turbulence existing regions due to scale effects.

Keywords: Dimensional Analysis, Physical Modeling, Hydraulic Similitude, Froude Similarity, Scale Effect.

INTRODUCTION

Dams and water structures are used for water supply which have very significant role in human being. When designing a dam, safety should be considered besides to economical benefits. While designing and making hydraulic calculation of a dam, any mistake should be avoided because dams store large amount of water in their reservoir. In the case of a dam body damaged, this amount of water can cause major destruction and loss of human life. Excessive water in the dam reservoir is transferred by spillways to downstream side in a safe and controlled manner. Therefore spillway has an important role in terms of operation and stabilization of the dam. After specifying type of spillway, the position of spillway on dam is determined and hydraulic calculations are made. For the dam to be safe, spillway must be able to evacuate floods before the dam is damaged. %22 of the dam's failures are caused by inadequate spillway capacity and their wrong operation (ICOLD, 1995).

In some cases, spillways are equipped with sluice gates and these gates have lifting devices to control flow rates by changing opening under the gate. Sluice gates provide controlled release of the water and prevent the instant floods pass to downstream side after heavy rainfall. In addition, sluice gates provide more water storage in the reservoir by keeping water level in the maximum level. Flat and radial gates are usually used in spillways. In energy generating dams, the water level in the reservoir

[1] Res. Asist., Department of Civil Engineering, Konya Teknik University, Konya, Turkey, e-posta: aliyildiz@selcuk.edu.tr
[2] Dr., Department of Civil Engineering, Konya Teknik University, Konya, Turkey, e-posta: alihsan@selcuk.edu.tr

should be kept at maximum level for efficient energy production; therefore, these types of dams may be equipped with sluice gates. In spite of these benefits of the sluice gates, If the sluice gates are damaged, suddenly opened gates can cause a 1000-years of overflow. This means that the covers must be designed correctly and securely.

In the design stage of dams, physical modeling techniques are mainly used. Scaled models are constructed in the laboratory and hydraulic similarity rules are used on this model to design actual construction to be built. A physical model represents the prototype (actual structure) and is used as a tool to find most technical and economical solution (Novak, 1984). The reliability of a physical model depends on the correct construction. If the model is built incorrectly, the data obtained from model will increase the error rate in the calculations. There are some numerical ratios and scales that must be taken into account when constructing the physical model. The scale ratio be used in the model is important, because the greater scale ratio increases cost of building the model. The size of laboratory environment in which the model is to be built affects the model size; small-scaled models take small space than large-scaled models. However, as the scale of the model is reduced, scale effects are more observed in the results. Therefore, scale ratio should be determined carefully to minimize scale effects besides construction time and costs. Scale effect arises from coefficient of force ratios between model and prototype is not kept constant (Hughes, 1993). Incorrect modeling of flow conditions, turbulence intensity and fluid properties also cause scale effects (Yalin, 1971).

In this study, physical modeling of hydraulic structures has been studied. Two experimental setup called model and prototype were used. The prototype experimental setup was built 4 times larger than model also a sluice gate and a step are placed to both models. Froude similitude was applied to the results obtained from model and prototype, and results are evaluated in terms of hydraulic similarity rules.

MATERIAL AND METHOD

Dimensional Analysis and Hydraulic Similarity

For the practical solution of many hydraulic problems, mathematical and experimental methods have been developed to solve them. Today, important hydraulic structures are designed and built after model studies have been done. Dimensional analysis and hydraulic simulation applications allow engineers to simplify and organize experiments and analyze their results. The principle of dimensional homogeneity is the basis of dimensional analysis. Dimensional homogeneity is a condition that must be satisfied by all mathematical equations expressing a physical phenomena and it is defined as the necessity of all dimensions of equations being the same. It is called “dimensional homogeneity”. In general, all physical relationships can be expressed with basic dimensions such as force (F), length (L), and time (T) or mass (M), length (L) and time (T). Expressions of some basic quantities in hydraulic engineering are given in Table 1.

Table 1. Expression of some basic quantities

Quantity	Sembol	Dimension
Velocity	V	LT^{-1}
Discharge	Q	L^3T^{-1}
Pressure	P	ML^{-2}
Shear Stress	τ	ML^{-2}
Specific Density	ρ	$ML^{-4}T^2$
Total Head	H	L
Head Lost	h_k	L

Hydraulic Models

Hydraulic models are manufactured in a certain scale ratio to provide all the important characteristic of the prototype (Geometric similarity) and design conditions (Kinematic similarity and Dynamic similarity). A physical model is completely similar to its-real world prototype if it satisfies these three criteria (Geometric, Kinematic and Dynamic Similarity)

Geometric Similarity: There is a constant ratio between the corresponding lengths in the model and the prototype (Equation 1).

$$\frac{L_{model}}{L_{prototype}} = L_{ratio} \text{ or } \frac{L_m}{L_p} = L_r \text{ and } \frac{A_{model}}{A_{prototype}} = \frac{L^2_{model}}{L^2_{prototype}} = L^2_{ratio} = L^2_r \quad (1)$$

Kinematic Similarity: Kinematic ratio exists between model and prototype if path of the water particles are similar and velocities of these particles have same ratio (Equation 2-5).

$$\text{Velocity Ratio} \quad ; V_{Ratio} = \frac{V_m}{V_p} \quad (2)$$

$$\text{Time Ratio} \quad ; T_{Ratio} = \frac{T_m}{T_p} \quad (3)$$

$$\text{Discharge Ratio} \quad ; Q_{Ratio} = \frac{a_m}{a_p} \quad (4)$$

$$\text{Acceleration Ratio} \quad ; a_{Ratio} = \frac{a_m}{a_p} \quad (5)$$

Dynamic Similarity: If the ratio of the forces in model and prototype are equal, there is dynamic similarity in geometrically and kinematically similar systems. While dynamic similarity is applied, some common "Dimensionless Numbers" are used such as Froude Number and Reynolds Number. Which number will be used changed depending on the type of flow condition. For example Froude Number is suitable for open channel flow and Reynolds number is suitable for pipe flow.

First of all a dimensionless number should be determined between model and prototype. In dynamic similarity, Buchingham Pi Theorem is used to determine which dimensionless number will be used.

Buchingham Pi Theorem

When the number of physical magnitudes or variables is four or more, Buchingham Pi Theorem is a very important tool used to organize these quantities into a minimum number of significant dimensionless groups that will form an equation (Buckingham, 1914). Dimensionless groups are called as "π terms". Numbers of the physical quantities (velocity, density, pressure ex.) are determined and called "n". "r" is the number of basic dimensions (mass-L, length-L, time-T ex.) which problem includes.

Dimensionless analysis of experimental setup is made to determine dimensionless parameters.

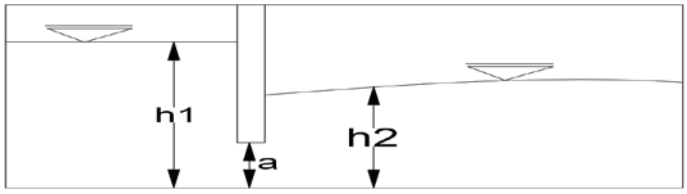

Figure 1. General scheme of sluice gate

Parameters affecting velocity of flow (V) under a sluice gate can be grouped as;

$$V=(h_1, h_2, a, b, \rho, g) \quad (6)$$

where h_1 is upstream flow depth, h_2 is downstream flow depth, a is gate opening, b is width, ρ is density and g is gravity.

According to equation 6, there are 7 physical parameters n=7 and there are 3 basic dimension (F, L, T) r=3. Number of the π terms is 7-3=4.

Π_1 expressed as;

$$\pi_1 = V * (h_1)^a * (\rho)^b * (g)^c = F^0 * L^0 * T^0 \quad (7)$$

$$\pi_1 = \frac{L}{T} * (L)^a * (\frac{F}{L^3})^b * (\frac{L}{T^2})^c = F^0 * L^0 * T^0 \quad (8)$$

$$\pi_1 = \frac{V}{\sqrt{h_1 * g}} \quad \text{(Froude Number)} \quad (9)$$

Π_2 expressed as;

$$\pi_2 = h_2 * (h_1)^a * (\rho)^b * (g)^c = F^0 * L^0 * T^0 \quad (10)$$

$$\pi_2 = L * (L)^a * (\frac{F}{L^3})^b * (\frac{L}{T^2})^c = F^0 * L^0 * T^0 \quad (11)$$

$$\pi_2 = \frac{h_2}{h_1} \quad (12)$$

Π_3 expressed as;

$$\pi_3 = a * (h_1)^a * (\rho)^b * (g)^c = F^0 * L^0 * T^0 \quad (13)$$

$$\pi_3 = L * (L)^a * (\frac{F}{L^3})^b * (\frac{L}{T^2})^c = F^0 * L^0 * T^0 \quad (14)$$

$$\pi_3 = \frac{a}{h_1} \quad (15)$$

Π_4 expressed as;

$$\pi_4 = b * (h_1)^a * (\rho)^b * (g)^c = F^0 * L^0 * T^0 \quad (16)$$

$$\pi_4 = L * (L)^a * (\frac{F}{L^3})^b * (\frac{L}{T^2})^c = F^0 * L^0 * T^0 \quad (17)$$

$$\pi_4 = \frac{b}{h_1} \quad (18)$$

Froude Similarity

Froude number is defines as ratio of the gravity forces to the inertia forces. Therefore the similarity between model and prototype is called "Froude Similarity" when this ratio is used. Discharge ratio, velocity ratio and length ratio are got from Froude Similarity expressed below.

$$Fr_r = \frac{Fr_p}{Fr_m} = 1 \quad (19)$$

Ratio of the Froude Numbers of model and prototype accepted as Fr_r=1;

$$Fr_r = \frac{V_r^2}{g_r L_r} = 1 \quad (20)$$

and

$$g_r = 1 \text{ so } V_r^2 = L_r, \ V_r = \sqrt{L_r} \quad (21)$$

By using of Equation 21,

$$\text{Velocity Ratio} \quad ; V_r = \sqrt{L_r} \quad (22)$$

$$\text{Time Ratio} \quad ; T_r = \sqrt{L_r} \quad (23)$$

$$\text{Acceleration Ratio} \quad ; a_r = 1 \quad (24)$$

$$\text{Discharge Ratio} \quad ; Q_r = L_r^{5/2} \tag{25}$$

$$\text{Force Ratio} \quad ; F_r = L_r^3 \tag{26}$$

Experimental Setups: Model and Prototype

Experimental studies have been carried out in Hydraulic Laboratories of Civil Engineering Department of Konya Teknik University in order to investigate scale effects on solution and modeling of hydraulic problems. In these studies, two open channel systems which have different dimensions were used. While working principles of two systems are same, only difference between them is their size.

In experiments, the small open channel system was considered as a "Model" and the large open channel system was considered as a "Prototype". It is assumed that the prototype has never been built and the experimental data obtained from model have been used to predict the outcome of the prototype according to Hydraulic Similarity rules. Then, the actual data obtained from the prototype was compared with the data get by model and scale effects were investigated.

Model setup has 4 m long, 0,075 m wide, 0,25 m depth and zero slope. The model setup is a simple flume which is made of plexiglas (Figure 2). Water flow in the model is provided by a pump. The pump send water from reservoir to the beginning of the channel via pipes then water passing through the channel fall into reservoir again end of the channel. Discharge is regulated by a valve that controls pump.

Figure 2. General view of Model

Flow rate through the channel is determined by reservoir at the end of channel. The valve under the reservoir is closed and water accumulation is provided in the reservoir then the volume change is calculated by measuring the rise of water with time. Model system and measurement reservoir can be seen in Figure 3.

Figure 3. Reservoir for measuring discharge in Model

Prototype setup has 6.5 m long, 0.6 m wide and 0.5 m depth and zero slope (Fig. 4.). Side walls and bottom of the prototype is made of 1.2 cm thick laminated glass. The purpose of using thick glass is to prevent breakage of glass under small force and allow to channel carry excess loads. Water flow in

prototype is provided by two pumps which are connected in parallel to system. Discharge value through the pumps is controlled by frequency changer in the panel which pumps are connected.

Figure 4. General view of Prototype

Discharge values are read by ultrasonic flowmeter placed on pipe (Figure 5.). Prototype system works same principle with model system.

Figure 5. Ultrasonic flowmeter

There is a geometric ratio L_r=4 between model and prototype. In other words, everything that was done in the model was also made in the prototype 4 times bigger. First, geometric ratio is provided between channel widths; If the width of channel is 0,075 m, width of the prototype should be 0,30 m. Flow condition is submerged flow in both model and prototype in experiments. 2 different gate openings are used for both systems. Gate opening used in the prototype is 4 times larger than the model because of the geometric ratio L_r=4. In the model gate openings are $(a_1)_m$=0,0145 m, $(a_2)_m$=0,02 m and in prototype gate openings are $(a_1)_p$=0,0145*4=0,058 m, $(a_2)_p$=0,02*4=0,08 m .

(a) **(b)**

Figure 6. Gate openings (a) for model $(a_2)_m$=0,02m and (b) for prototype $(a_2)_p$=0,08m

In experiments a step is placed to model and prototype. This step turns flow regime from subcritical to supercritical and causes submerged hydraulic jump near the gate. The dimensions of step is

0,025x0,075x0,15 in model and 0,1x0,3x0,6 in prototype Figure 7. Geometric ratio is taken into account when determining the distance of step from gate. While the distance between gate and step is 0,3 m in model, this distance is 1,2 m in prototype.

(a) **(b)**

Figure 7. Steps used in (a) model and (b) prototype

RESULTS

First of all water surface profiles are compared to determine how the flow profiles of the model and prototype are consistent with each other and whether they are consistent with the "Froude Similarity". When comparing the free surface profiles, it was also investigated that is there a difference between profiles due to scale effect. When looked to Figure 8, there is high consistency between model and prototype in terms of water surface profiles. Steps change flow regime supercritical to subcritical and cause a submerged hydraulic jump near the gates.

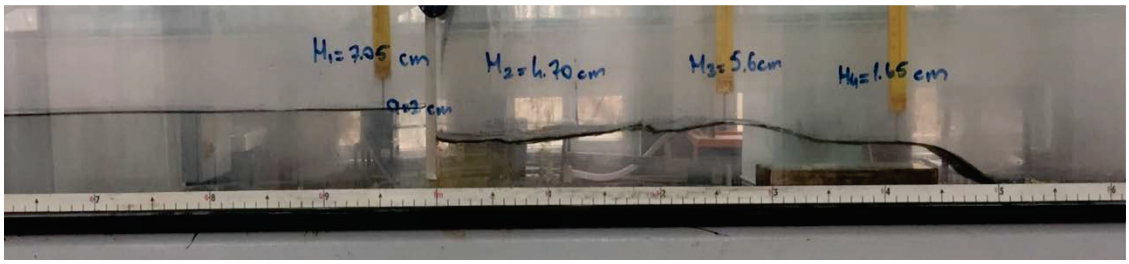

(a)

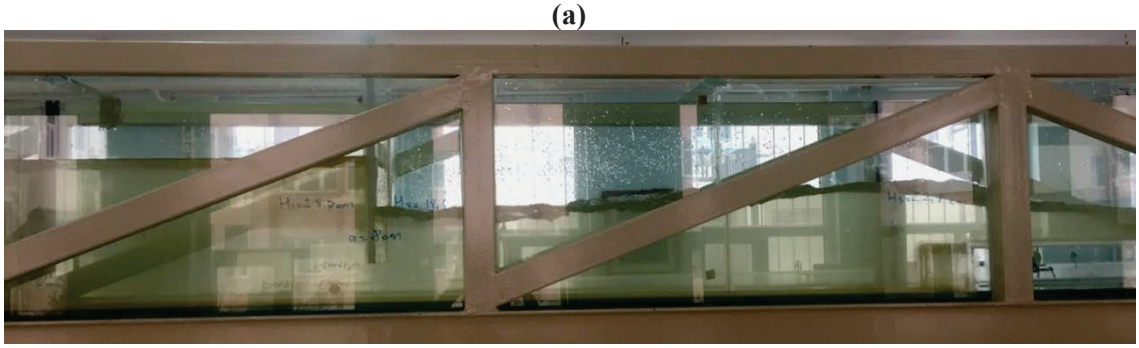

(b)

Figure 9. Water surface profile in (a) model and (b) prototype

Experiments are carried out on two different gate openings with geometric ratio L_r=4. To compare models, there must be a ratio of discharges between model and prototype. This ratio is called discharge ratio and calculated as $Q_r=L_r^{2,5}=4^{2,5}=32$. In other words, 32 times of the discharge values of model should be got in prototype. Same procedure is also valid for flow depths, however flow depths ratio is calculated as $H_r= L_r=4$ and 4 times of flow depths of model should be got in prototype. For this purpose, flow depths in model and prototype are measured at 4 different points (Figure 9).

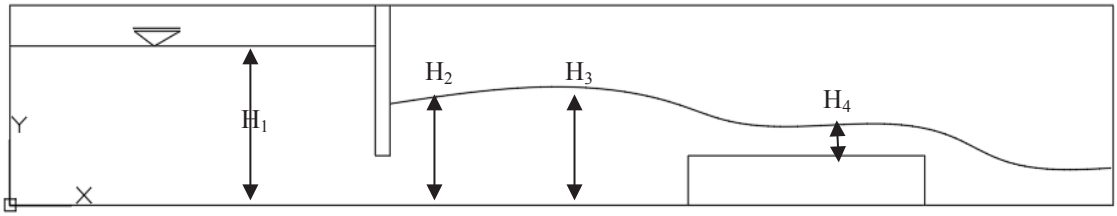

Figure 9. Measurements point in model and prototype

Results, get from model and prototype, are given in Table 2 and Table 3.

Table 2. Flow depths get from 4 different measurements point for gate openings; $(a_1)_m$=0,0145 m and $(a_1)_p$=0,058 m

Model Setup (a_{model}=0.0145m, b_{model}=0.075 m)							
H_1	H_2	H_3	H_4	Q(lt/sn)	Fr_2	Fr_3	Fr_4
4.65	4.00	4.25	1.10	0.267	0.14	0.13	0.98
5.35	4.15	4.60	1.30	0.357	0.18	0.15	1.03
6.90	4.30	5.05	1.55	0.498	0.24	0.19	1.10
8.60	4.20	5.50	1.70	0.640	0.32	0.21	1.23
Prototype Setup ($a_{prototype}$=0,058 m, $b_{prototype}$=0,03 m)							
H_1	H_2	H_3	H_4	Q(lt/sn)	Fr_2	Fr_3	Fr_4
18.30	15.70	17.00	4.40	8.580	0.15	0.13	0.99
21.00	16.30	18.30	5.10	11.090	0.18	0.15	1.02
27.20	16.80	20.50	6.20	15.960	0.25	0.18	1.10
34.00	16.50	22.50	6.90	20.470	0.33	0.20	1.20

Table 3. Flow depths get from 4 different measurements point for gate openings $(a_2)_m$=0,02 m and $(a_1)_p$=0,08 m

Model Setup (a_{model}=0.02m, b_{model}=0.075 m)							
H_1	H_2	H_3	H_4	Q(lt/sn)	Fr_2	Fr_3	Fr_4
4.15	4.03	4.15	1.00	0.272	0.14	0.14	1.16
5.00	4.33	4.75	1.24	0.393	0.19	0.16	1.21
5.95	4.60	5.17	1.48	0.539	0.23	0.20	1.27
6.03	4.60	5.24	1.50	0.553	0.24	0.20	1.28
6.95	4.70	5.53	1.65	0.649	0.27	0.21	1.30
7.05	4.70	5.60	1.70	0.685	0.29	0.22	1.32
Prototype Setup ($a_{prototype}$=0,08 m, $b_{prototype}$=0,03 m)							
H_1	H_2	H_3	H_4	Q(lt/sn)	Fr_2	Fr_3	Fr_4
16.80	16.30	16.80	4.10	8.850	0.14	0.14	1.13
20.00	17.50	18.90	5.00	12.550	0.18	0.16	1.19
24.00	18.50	21.00	6.00	17.280	0.23	0.19	1.25
24.50	18.55	21.20	6.10	17.950	0.24	0.20	1.27
28.10	18.60	22.50	6.75	21.580	0.29	0.22	1.31
28.70	18.60	22.80	6.80	21.900	0.29	0.21	1.31

When flow depths and discharge values get from model and prototype are compared, there is high consistency with the values of L_r=4 and Q_r=32 used in Froude similarity.

Table 4. Ratio of the flow depths when flow rate ratio Q_r=32 is provided for gate openings; $(a_1)_m$=0,0145 m and $(a_1)_p$=0,058 m

$(H_1)_p/(H_1)_m$	$(H_2)_p/(H_2)_m$	$(H_3)_p/(H_3)_m$	$(H_4)_p/(H_4)_m$	$(Q)_p/(Q)_m$
3.94	3.93	4.00	4.00	32.14
3.93	3.93	3.98	3.92	31.06
3.94	3.91	4.06	4.00	32.04
3.95	3.93	4.09	4.06	31.99

Table 5. Ratio of the flow depths when flow rate ratio Q_r=32 is provided for gate openings; **$(a_1)_m$=0,02** m and $(a_1)_p$=0,08 m

$(H_1)_p/(H_1)$m	$(H_2)_p/(H_2)_m$	$(H_3)_p/(H_3)_m$	$(H_4)_p/(H_4)_m$	$(Q)_p/(Q)_m$
4.05	4.04	4.05	4.10	32.54
4.00	4.04	3.98	4.03	31.93
4.03	4.02	4.06	4.05	32.07
4.06	4.03	4.05	4.07	32.47
4.04	3.96	4.07	4.09	33.25
4.07	3.96	4.07	4.00	31.95

The flow depths obtained from the both model were divided by the gate opening to obtain dimensionless relative depths. The relative depths and Froude Numbers are shown on the graphs for different gate openings and measurement points.

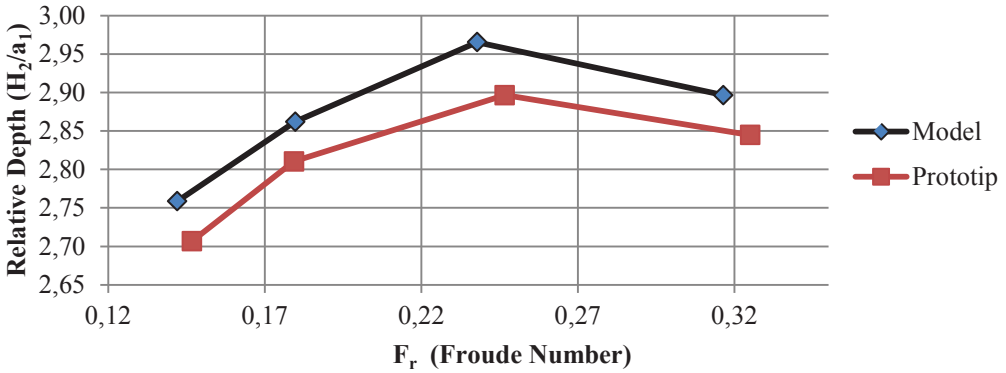

Figure 10. Comparison of relative flow depths for $(a_1)_m$=1,45 cm , $(a_1)_p$=5,8 cm , measurement point-2;H_2

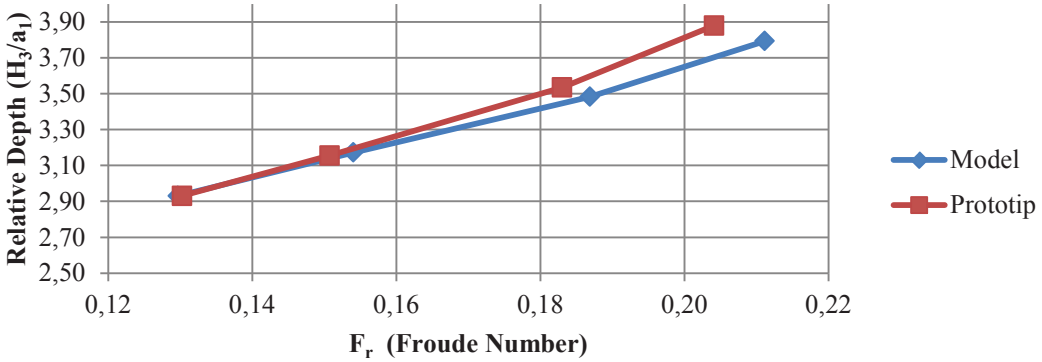

Figure 11. Comparison of relative flow depths for $(a_1)_m$=1,45 cm , $(a_1)_p$=5,8 cm , measurement point-3;H_3

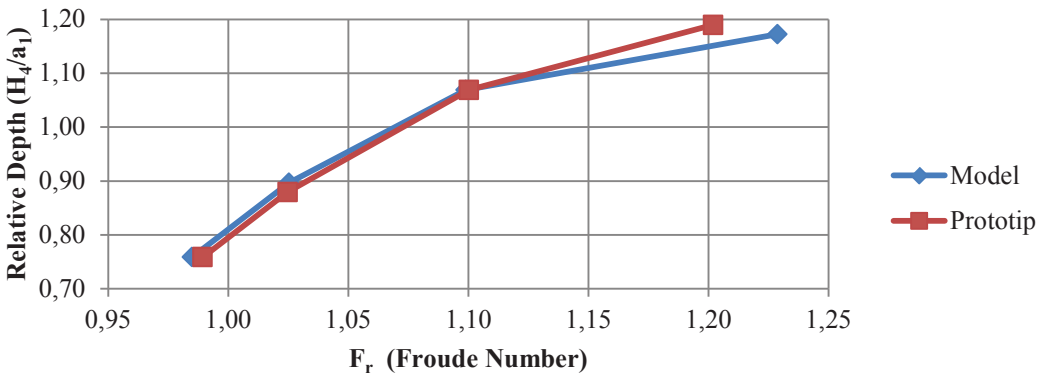

Figure 12. Comparison of relative flow depths for $(a_1)_m$=1,45 cm, $(a_1)_p$=5,8 cm, measurement point-4;H_4

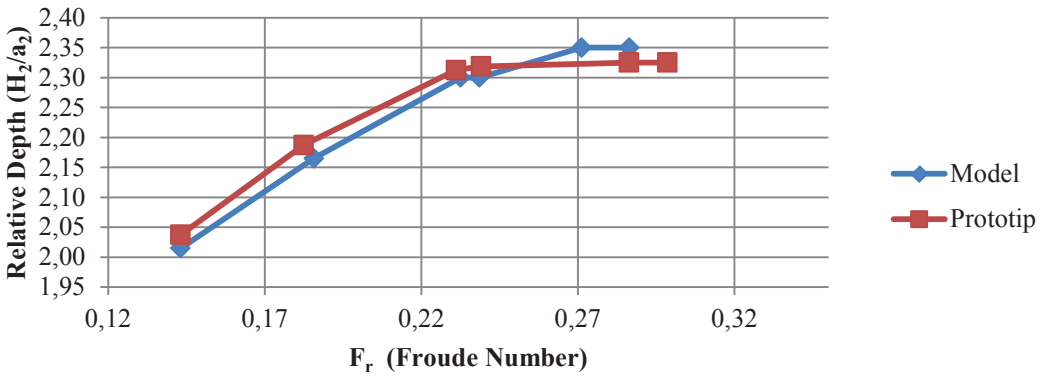

Figure 13. Comparison of relative flow depths for $(a_2)_m$=2,00 cm , $(a_2)_p$=8,00 cm , measurement point-2;H_2

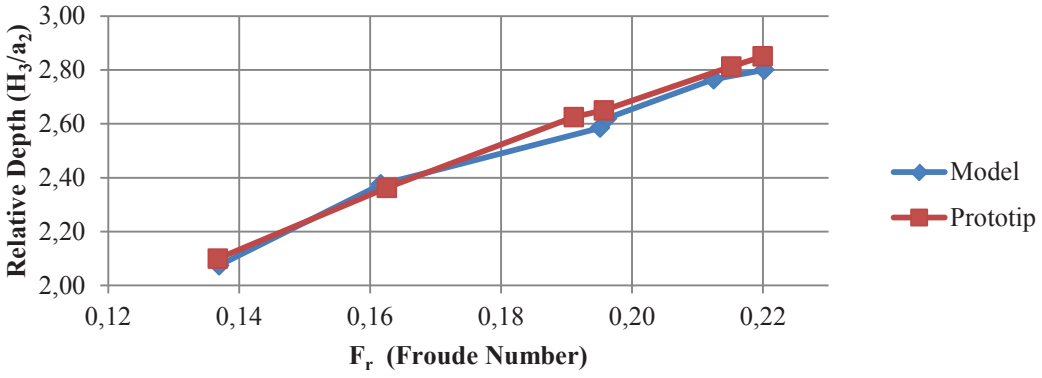

Figure 14. Comparison of relative flow depths for $(a_2)_m$=2,00 cm , $(a_2)_p$=8,00 cm , measurement point-3;H_3

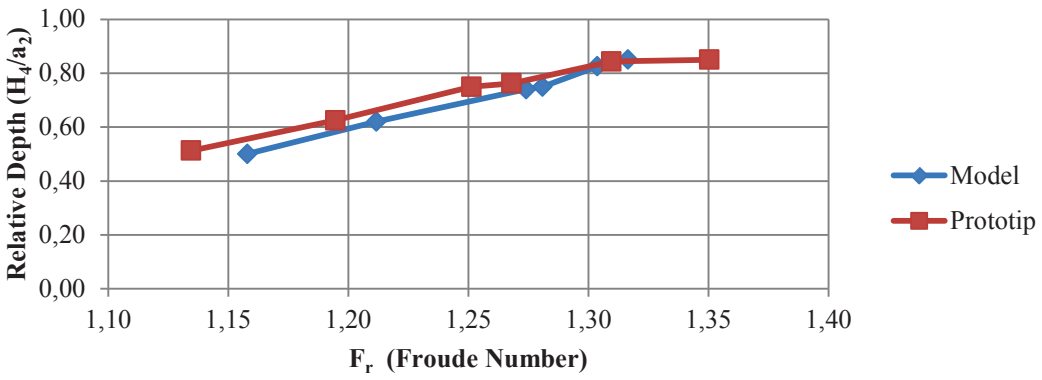

Figure 15. Comparison of relative flow depths for $(a_2)_m$=2,00 cm , $(a_2)_p$=8,00 cm , measurement point-4;H_4

It can be seen from graphs Froude Numbers and relative flow depths of model and prototype very close to each other. However results of measurements from the H2 point with gate opening (a1)m=0,0145m and (a2)=0,058m, did not agree with each other. The main reason for his high amount of turbulences due to low gate opening.

Although flow profiles are observed with high consistency in both model, there may be some differences in water movement and behavior due to scale effects. In cases where turbulence is large, results are not consistent with each other. This difference can be seen clearly in the submerged hydraulic jump. There was more waving in the prototype compared with the model where submerged hydraulic jump occurs. As a result of scale effects, some hydraulic events, which cannot be observed in the model, can be observed in the prototype. Whereas there is no vortex in the model, a serious vortex is observed in the prototype before the sluice gate (Figure 15.). As a result of vortex, air drawn into water can damage construction; also objects floating on the water can be attracted. The prototype used in experiments was constructed in the lab, but when this prototype is built in large scale in real life, these hydraulic events can have serious consequences and can lead to damage.

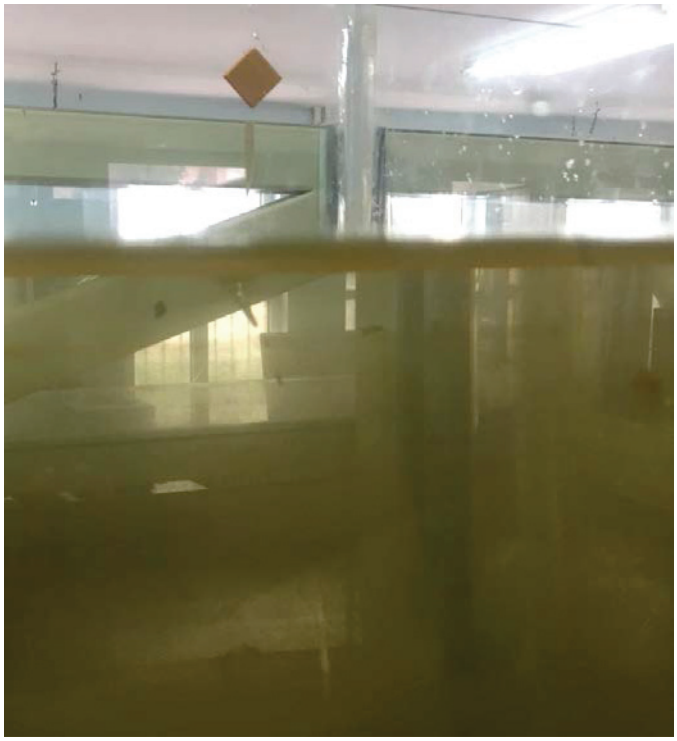

Figure 16. Vortex occurred in upstream side of sluice gate

CONCLUSIONS

In this study, the behavior of flow under sluice gate is modeled by a physical model and Froude Similarity. Froude model gave satisfactory results in cases where the flow continues in one direction and turbulence is low. There are differences between model and prototype in terms of flow depths where turbulence is high.

REFERENCES

Buckingham, E. 1914. On physically similar systems- Illustrations of the use of dimensional equations. Physical Review 4, 345-376

Hughes, S.A., 1993, Advanced series on ocean engineering, 7. Physical Models And Laboratory Techniques in Coastal Engineering, Londra, 27-33.

International Commission of Large Dams, 1995, Dam Failures and Statistical Analysis, ICOLD bulletin 99, Paris, 75-80.

Novak, P., 1984, "Scaling factor and scale effects in modeling hydraulic structures", Scale Effects In Modelling Hydraulic Structures, Esslingen, 1-5.

Yalın, M.S., 1971, Theory of hydraulic models, E. M. Wilson, Macmillan, Londra, 35-36.

5th International Symposium on Dam Safety

October 27-31, 2018

THE IMPORTANCE OF SURFACE WATER AND GROUNDWATER RESOURCES FOR THE SUSTAINABILITY OF THE KARABURUN PENINSULA, İZMİR, TURKEY

Bahadır ÖZTÜRK [1], Alper BABA [2]

ABSTRACT

Karaburun Peninsula is located in the western part of Turkey. The Peninsula has large agricultural land and farming pattern specific to the region. The region is also of great importance for tourism. Especially in summer, the population increases by several times. About 90 percent demand for drinking and irrigation water in the Peninsula is supplied from groundwater sources. There are many uncertificated wells have been drilled in the region. However, seawater intrusion was observed due to excessive water extraction from the drilling in the coastal areas of the Peninsula. Seawater intrusion has been being monitored since 2013 in some parts of the Peninsula. Water demands increase last decades. Therefore, the General Directorate of State Hydraulic Works (DSİ) has constructed a pond (Mordoğan) and four dams (Karareis, Alaçatı, Bozköy, and Salman) for the drinking and irrigation purposes. Mordoğan Pond and Salman Dam meet the irrigation water demand of the Peninsula by irrigating 130 ha and 170 ha agriculture land as well, respectively. Excessive water extraction affects the salinization of the groundwater resources and climate change seriously affects the occupancy rate of dams. Both surface water and groundwater resources must be monitored for the sustainability of the water resources in this region.

Keywords: Water resources, seawater intrusion, sustainability, Karaburun Peninsula

INTRODUCTION

Water is an essential resource for numerous nations and its scarcity is a major concern in peninsula and islands. Increasing population, climate change and their potential hydrologic effects put uncertainties to water resources management of these regions (Middelkoop, et al., 2001). Loucks, et al. (2000) explains sustainable water resources management as an idea that accentuates the need to consider the future as well as the present. Water resources that are figured out how to fulfill the changing demands set on them, now and on into the future, without degradation, can be called sustainable. As the water demand increases, the importance of determining the quality and quantity of the water resources increases. Quality and quantity are of major factors that shape the sustainability of water resources. Management and sustainability of water resources of the coastal aquifer of peninsula and islands are very important. These regions are affected by many negative factors such as seawater intrusion. Over-pumping of groundwater in these regions results in seawater intrusion problems (Ben-Asher, 2000; Elhatib v Günay, 1993; Gordu et al., 2001; Yazıcıgil and Ekmekci, 2003; Karahanoglu et al., 2003; Demirel, 2004; Çamur and Yazıcıgil, 2005; Louvat et al., 1999; Edmunds and Milne, 2001; Mansour et al., 2017). This phenomenon is especially common in Mediterranean regions because of the semi-arid conditions. Seawater intrusion-mixing or

[1] Ms. Student, Department of Civil Engineering, İzmir Institute of Technology, İzmir, Turkey, e-posta: bahadirozturk@iyte.edu.tr

[2] Professor, Department of Civil Engineering, İzmir Institute of Technology, İzmir, Turkey, e-posta: alperbaba@iyte.edu.tr

replacing saltwater with freshwater in an aquifer is one of the main contaminating factors in most of the coastal aquifers (Bear et al., 1999). Seawater intrusion is also a threat to the sustainability of the water supply for the people living in the coastal areas and for their economy (Cassardo and Jones, 2011; Gain et al., 2012). Seawater intrusion reduces freshwater storage in coastal aquifers and can result in the abandonment of freshwater supply wells when concentrations of dissolved ions exceed drinking-water standards (Barlow, 2003). Seawater intrusion is a widespread problem that is affecting water quality, vegetation and soil in coastal aquifers.

Karaburun Peninsula is one of the biggest peninsulas in Turkey. The Peninsula consists of Urla, Çeşme, and Karaburun districts where is a touristic center. The population of the peninsula shows great difference due to the season, in summer the population can increase dozens of times by winter. Most of the water resources, which is used in the Peninsula, are belongs to groundwater resources (Baba, et al., 2015). Extraction too much groundwater from the coastal aquifers of the Peninsula resulted in seawater intrusion (Baba, et al., 2015). The aim of this study to evaluate the Karaburun Peninsula water resource and its importance for sustainability of the region.

STUDY AREA

Karaburun Peninsula is located in the city İzmir in the western part of Turkey by covering an area of 171.000 ha (Figure 1). The Peninsula generally has a rather rugged earth structure. The Bozdağ mass extending in the north-south direction forms the highest section of the peninsula with a height of 1212 meters (Akdağ Hill) (Figure 2). The mountains descend steeply to the sea, and this has affected the settlement of the Karaburun Peninsula. Some parts of Mordoğan, Yeni Liman, Badembükü and Denizgiren areas are plains. Along the İzmir Gulf, the North and West coasts lie in a very scenic lane and are very frequent (İZKA, 2014).

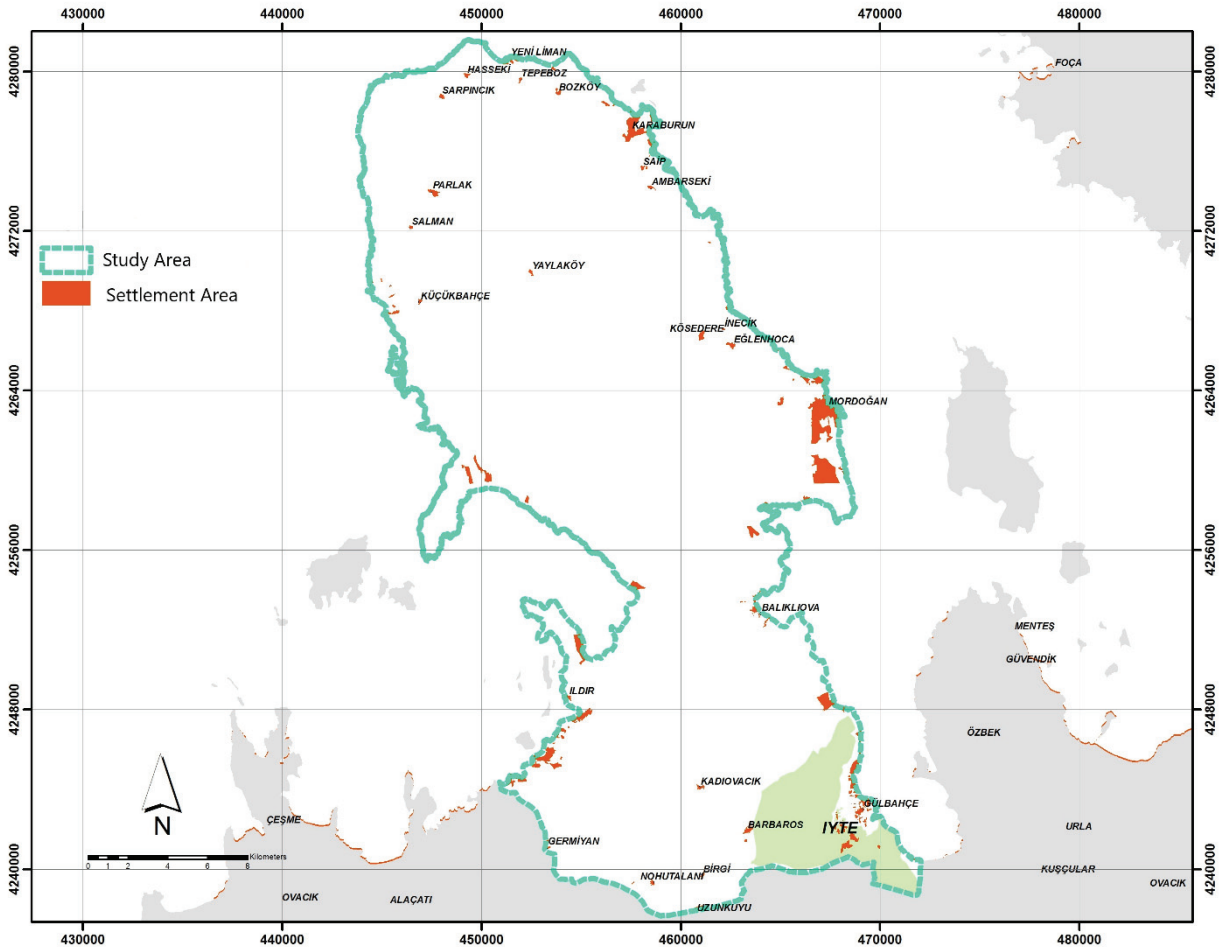

Figure 1. Location map of Karaburun Peninsula

The peninsula almost completely reflects the Mediterranean climate in terms of macroclimate (Mater, 1982). According to the indices of precipitation activity and continentality, the region is located in the "semi-moist marine climate" class on an annual average basis (Mater, 1982; Sezer, 1988).

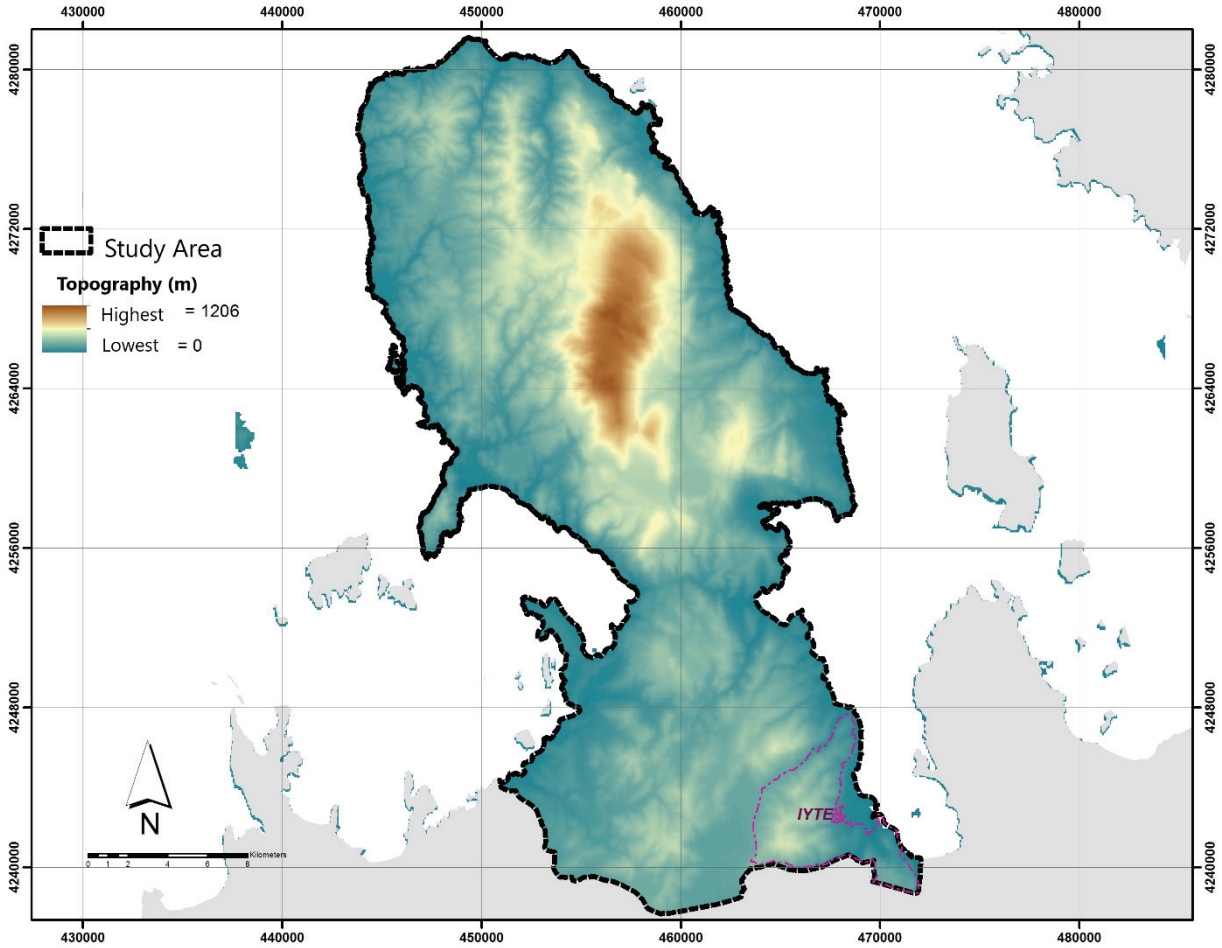

Figure 2. Morphological map of study area

POPULATION AND WATER DEMAND OF PENINSULA

Population growth and tourism put a pressure on water resources in the Peninsula, especially in summer times. Loucks, et al., (2000) explained the difficulty of water resources management because of the future uncertainties for individuals, animals, agriculture and industrial needs of water. However, there are some techniques that are used for population projection to predict the future water demand approximately. In this study, Turkish Banks of Provinces regulation is used to determine the possible future population and water demand of Çeşme and Karaburun Districts in the Peninsula by using past recorded populations, up to the year 2050. Except for Alaçatı and Çeşme regions, summer house population is not included in the calculation of population projection. For other regions only settled population is used. While calculating the water demand, tourist populations of Alaçatı and Çeşme City Center are accepted as 10.000 and 22.500, respectively. About 5% of trade and 10% of seepage loss is included in water demand calculations for each region. Also, animal, agricultural, industrial and special needs of water are neglected since the lack of information, but human consumption only is investigated. Figure 3 and Figure 4 shows projected population and water demand (l/s) of Çeşme and Karaburun Districts.

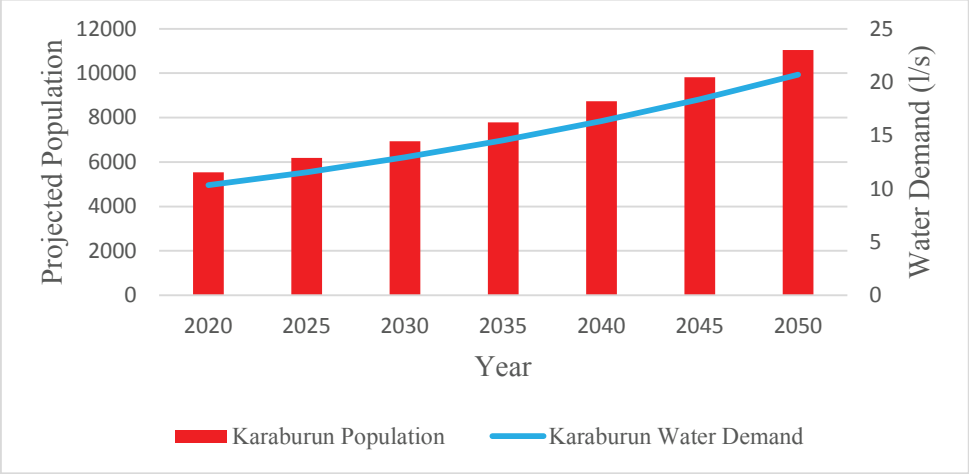

Figure 3. Projected population and water demand chart of Karaburun District

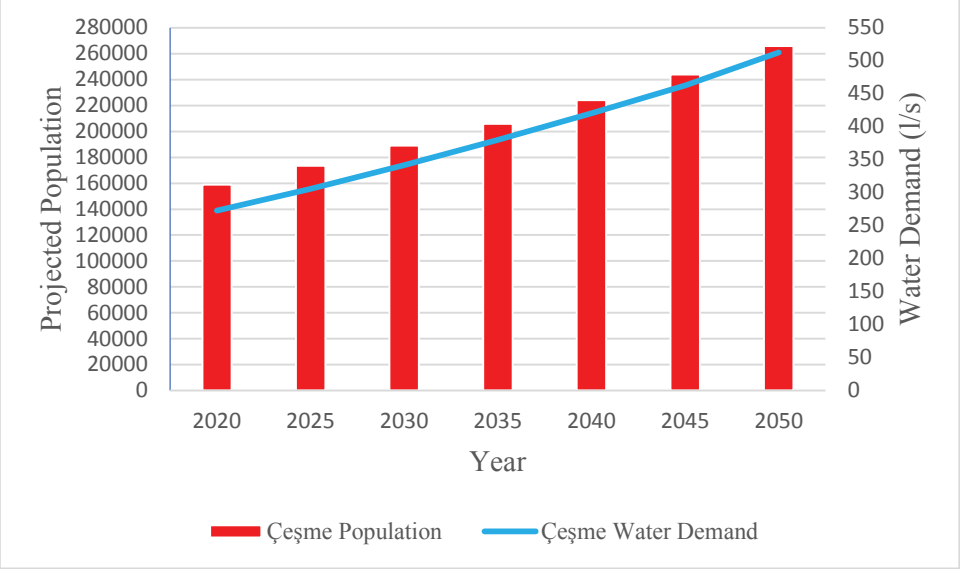

Figure 4. Projected population and water demand chart of Çeşme District

Populations and water demand of Çeşme and Karaburun districts are predicted to be 265.821 and 11.044 people, 512.3 l/s and 20.7 l/s, respectively by the calculations done according to Turkish Banks of Provinces regulations.

SURFACE WATER OF PENINSULA

In order to supply the water demand of the Peninsula in terms of human consumptions and agricultural needs, the General Directorate of State Hydraulic Works (DSİ) has constructed Mordoğan Eğlenhoca Pond, Karareis Dam, Alaçatı Kutlu Aktaş Dam, Bozköy Dam and Salman Dam in the districts (Figure 5). Salman, Karareis, and Bozköy Dams are not being used for water supply for the moment but according to DSİ, they will be being used at the end of 2018. Table 1 gives information about the surface water of the peninsula (Table 1). Mordoğan Eğlenhoca Pond, Karareis Dam and Salman Dam are planned to supply irrigation water to agriculture lands in the Peninsula as well as human consumptions. Alaçatı Kutlu Aktaş Dam and Bozköy Dam are planned to supply water for human consumption only. Some portion of the drinking water of the Çeşme District is supplied from the Alaçatı Kutlu Aktaş Dam which has high storage

capacity (Figure 6). However, water levels are on the decline in the dam in recent years as a result of climate change. The occupancy rate of the dam is 20% in August 2018. Therefore, the Karareis dam is planned for the water needs of the Çeşme by DSİ. Karareis dam is not active yet (Figure 7). Mordoğan Pond and Salman Dam meet the irrigation water demand of the Peninsula by irrigating 130 ha and 170 ha agriculture land as well, respectively.

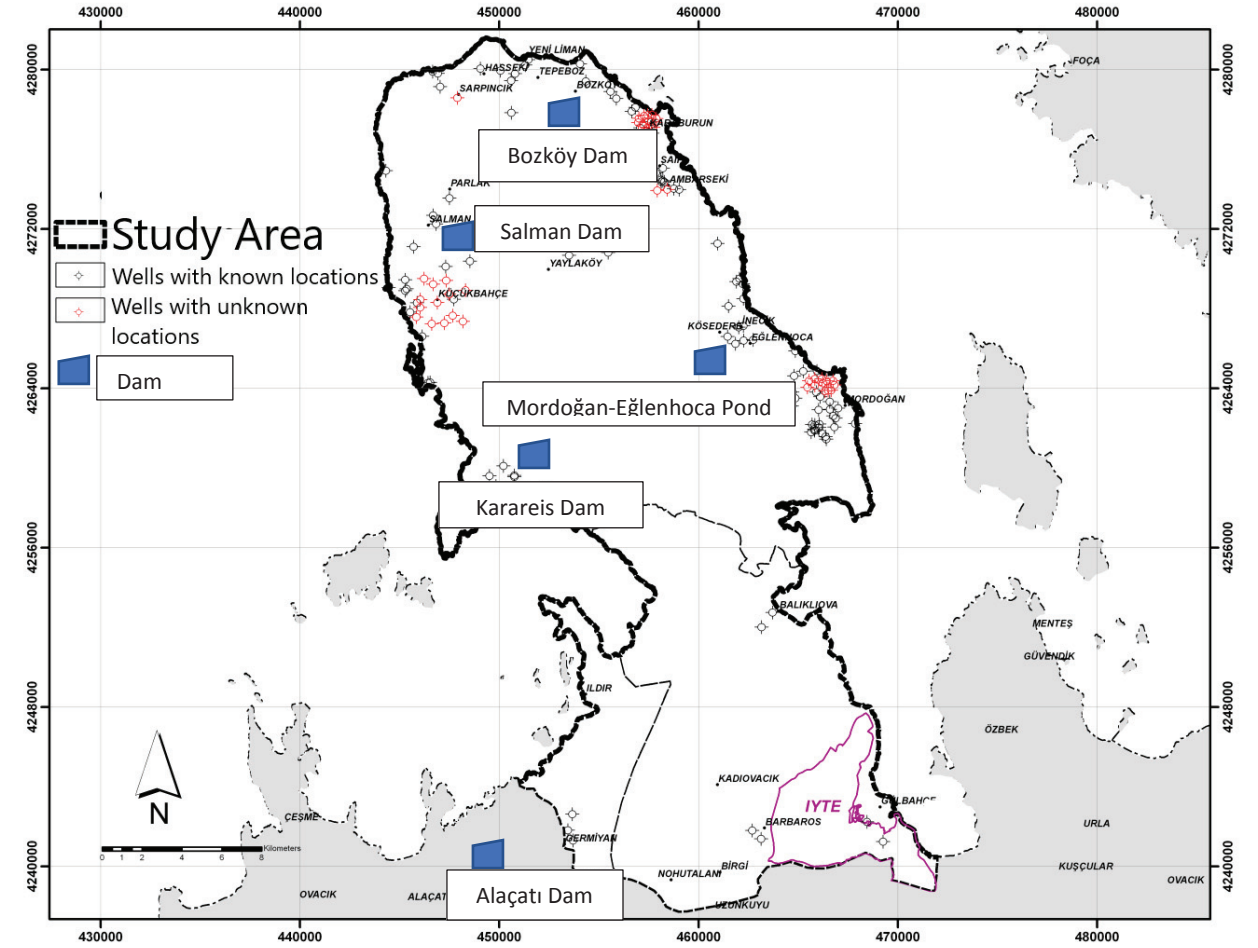

Figure 5. Surface and groundwater resources in study area

Figure 6. Picture from Alaçatı Kutlu Aktaş Dam

Figure 7. Picture from Karareis Dam

Table 1. Information about surface structures of the Peninsula

Structure Name		**Mordoğan Eğlenhoca Pond**	**Karareis Dam**	**Alaçatı Kutlu Aktaş Dam**	**Bozköy Dam**	**Salman Dam**
Stream		Kuşkudan	Camiboğazı	İmamlı	Uzundere	Sudeğirmeni
District		Karaburun	Karaburun	Çeşme	Karaburun	Karaburun
Basin		Küçük Menderes	Küçük Menderes	Küçük Menderes	Küçük Menderes	Küçük Menderes
Purpose		Human Consumption & Irrigation	Human Consumption & Irrigation	Human Consumption	Human Consumption	Human Consumption & Irrigation
Storage Capacity (hm^3)		1.57	2.84	16.61	3.653	4.13
Planned Water Supply (l/s)	Human Consumption	22.51	90.06	92.59	62.79	28.54
	Irrigation	13.95	35.83	-	-	24.73

GROUNDWATER RESOURCES OF PENINSULA

Groundwater plays an important role in the sustainability of the Karaburun and Çeşme Districts by meeting an important amount of the water need (Baba, 2013). A significant proportion of Çesme District's water is supplied from the wells located in the southwestern parts of the Karaburun Peninsula. The major percentage of water is pumped to Çeşme from Ildır region, but this excessive abstraction of groundwater resulted in seawater intrusion in the region (Figure 8). The average flow rate of water obtained from these wells is 200 l/s in the summer. The total number and discharge capacities of the state-owned deep wells in the Peninsula is given in Table 2. These wells have been used for drinking water. Out of these wells, there are more than a thousand uncertificated wells especially in the rural areas of the Peninsula (see Figure 5). Most of these wells have been used for domestic and agricultural use. In addition, karst structures are tectonically controlled in the region. Tectonic zones are EW and NNE trending. Along the tectonic zones, karstic springs have been seen in different part of Peninsula (Figure 9). The average flow of karst springs reaches up to 420 l/s in Ildırı region.

Figure 8. Picture from wells in Ildır Region

Figure 9. Picture from springs in Ildır Region

Table 2. Total number of deep wells which is supply drinking water in Peninsula

	Karaburun District	Çeşme District
Number of wells	14	15
Flowrate (l/s)	261	121

SEAWATER INTRUSION IN THE PENINSULA

Seawater intrusion has been seen in different parts of coastal aquifers of Peninsula. Geometrical characteristics of the aquifers and their state of interaction with the sea were studied by Baba et al (2015). In addition, Mansour et.al (2017) monitored Karareis region where is located in the extreme western end of Karaburun Peninsula (Figure 10). The results of this study showed that the aquifer of Karareis region is very sensitive to increased pumping rates; therefore, authors mentioned that appropriate management techniques should incorporate time-dependent maximum total pumping values that should not be exceeded in the Karareis region. In this study groundwater monitoring was done from 2016 to 2017 in the same region. The results show that seawater intrusion increases each year in this region.

Figure 10. Location map of Karareis Region and wells

Determination of seawater intrusion in Karareis Region is very important since there are approximately 750 summer houses and about 60 ha of agricultural land presents in the region. In order to determine the seawater intrusion, two monitoring wells (SK-2, SK-7) were monitored. In both wells, automatic groundwater data loggers (Schlumberger Mini Diver) were installed. The automatic data loggers recorded electrical conductivity, water level and temperature values every hour. The data loggers recorded temperature and electrical conductivity (EC) values from October 2016 to November 2017. The collected data from the data loggers were grouped as seasons as can be seen from the Figure 11- Figure 14. SK-7 is about 300 m and SK-2 is about 1200 m far from the sea. The electrical conductivity reached highest levels in the irrigation period. Based on the observations between October 2016 and January 2017, the electrical conductivity varied from 1900 to 37000 µs/cm in the borehole SK-7. The electrical conductivity reached its highest level in January 2017. Extreme groundwater was used for agricultural activity in this period. SK-2 has not under the risk at that moment. But results show that agricultural well has been affected SK-2. Distribution of groundwater level change is directly related with pumps works for agricultural activity in this region.

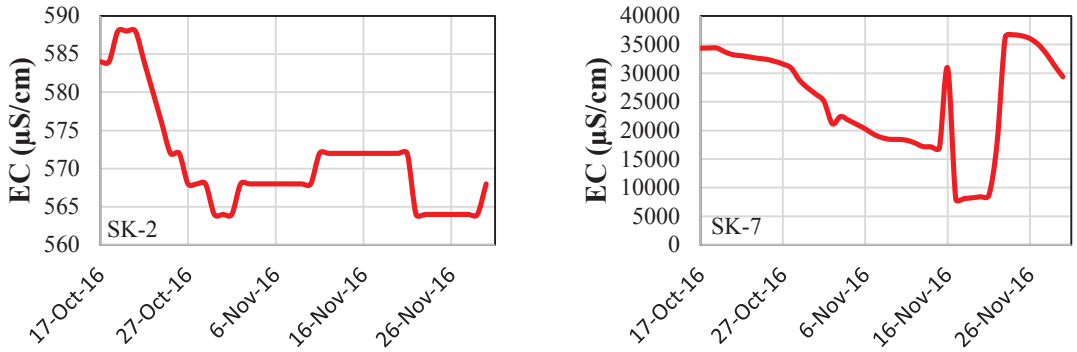

Figure 11. Electrical conductivity values for SK-2 and SK-7 for the period of 2016-Fall

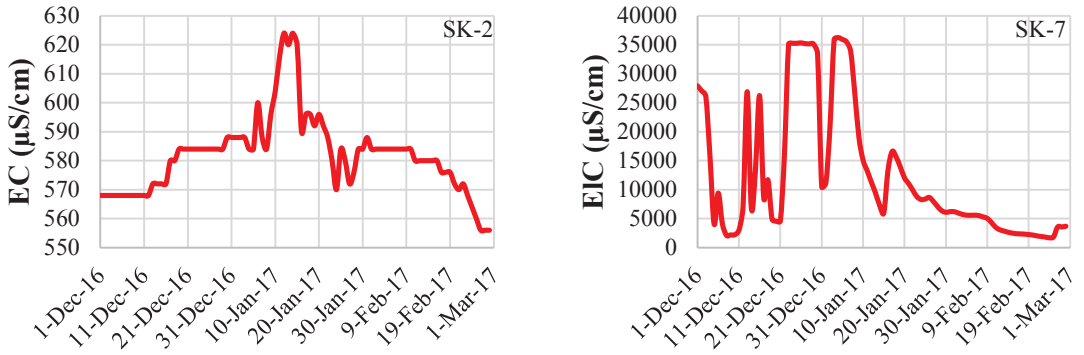

Figure 12. Electrical conductivity values for SK-2 and SK-7 for the period of 2017-Winter

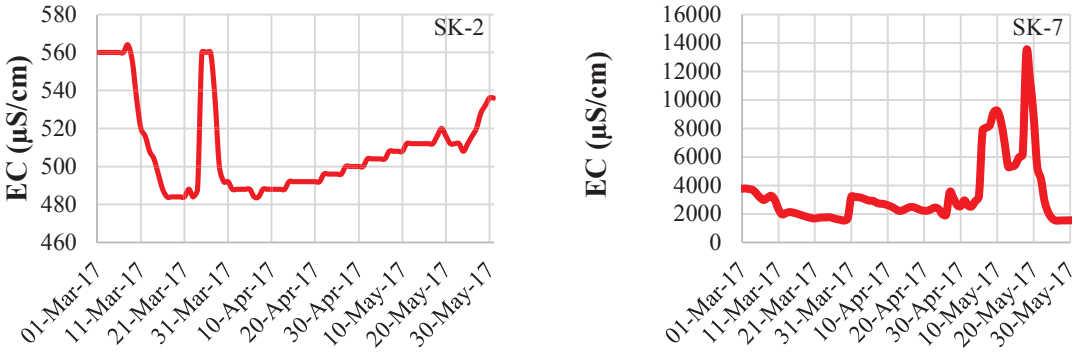

Figure 13. Electrical conductivity values for SK-2 and SK-7 for the period of 2017-Spring

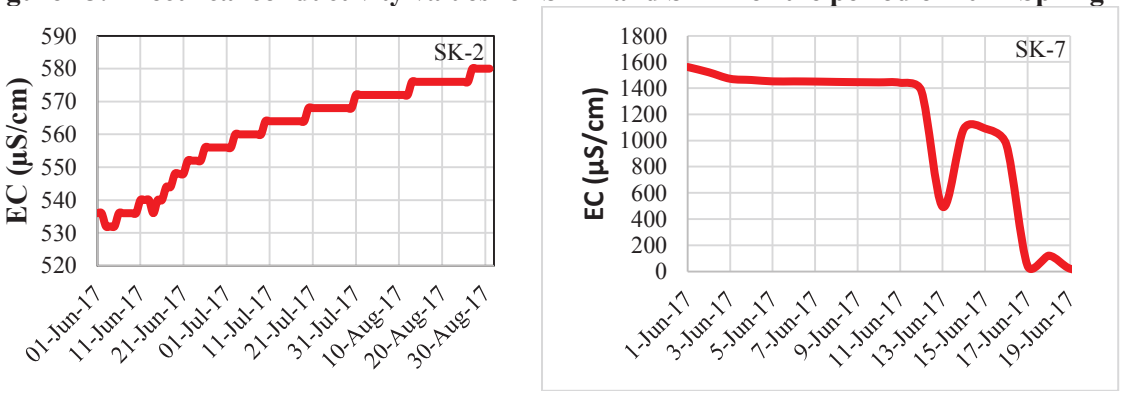

Figure 14. Electrical conductivity values for SK-2 and SK-7 for the period of 2017-Summer

RESULTS AND CONCLUSION

Sustainability and management of water resources in islands and peninsula are very important. Quality and quantity of the water resources (both surface and subsurface) must be studied for the sustainability and management of water resources. The coastal aquifers of this region are under stress with demand exceeding the supply of groundwater resources. Over pumping from coastal aquifers is responsible for the elevated rate of seawater intrusion in these regions such as Karareis. Seawater intrusion is directly influencing the quality of water resources in the coastal region. In addition, water levels are on the decline in the dam in recent years as a result of climate change in the Mediterranean region. Therefore; it's

important to increase groundwater recharge and built underground dams to prevent more evaporation. In addition, agricultural activity should be controlled in the coastal region. Monitoring of groundwater resources is very essential for this kind of sensible region.

Acknowledgements: This study was funded by the Scientific and Technological Research Council of Turkey (TUBİTAK) through project number 113Y042.

REFERENCES

Baba, A. (2013). *Gülbahçe Geothermal Resource Development Project.* İzmir: İZKA DFD Project.

Baba, A., Gündüz, O., Şimşek, C., & Elçi, A. (2015). Investigation of seawater intrusion in coastal aquifers: a case study from Karaburun Peninsula, Turkey. *36th IAHR World Congress.*

Barlow, P. (2003). *Ground Water in Freshwater-Saltwater.* Virginia: U.S. Geological Survey.

Bear, J., Cheng, A., S. Sorek, D. O., & Herrera, I. (1999). *Seawater intrusion in coastal aquifers: concepts, methods and practices.* Springer.

Ben-Asher, J., Beltrao, J., & Costa, M. (2000). Modelling the effect of sea water intrusion on groundwater salinity in agricultural areas in Israel, Portugal, Spain and Turkey. *International Symposium on Techniques to Control Salination for Horticultural Productivity.* Antalya, Turkey.

Camur, M. Y. (2005). Effects of the planned Ephesus recreational canal on freshwater-seawater interface in the Selcuk sub-basin, Izmir. *Envıronmental Geology, 48*, 229-237.

Cassardo, C., & Jones, J. (2011). Managing water in a changing world. *Water*, 618–628.

Demirel, Z. (2004). The history and evaluation of saltwater intrusion into a coastal aquifer in Mersin, Turkey. *Journal of Environmental Management, 70*, 275-282.

Edmunds, W. M. (2001). Palaeowaters in Coastal Europe: Evolution of Groundwater since the Late Pleistocene. *Geological Society of London*.

Elhatip H., G. (1993). Analysis of sea water intrusion associated with karstic, channels beneath Ovacık plain, Southern Turkey. *Hydrogeological Processes in Karst Terranes (Proceedings of the Antalya Symposium and Field Seminar).* Antalya.

Gain, A., Giupponi, C., & Renaud, F. (2012). Climate change adaptation and vulnerability assessment of water resources systems in developing countries: A generalized framework and a feasibility study in Bangladesh. *Water*, 345–366.

Gordu F., M. L. (2001). Simulation of Seawater Intrusion in the Goksu Delta at Silifke, Turkey. *First International Conference on Saltwater Intrusion and Coastal Aquifers—Monitoring, Modeling, and Management.* Essaouira, Morocco.

İZKA. (2014). *Peninsula Sustainable Development Strategy.* İzmir Development Agency.

Karahanoglu, N., & Doyuran, V. (2003). Finite element simulation of seawater intrusion into a quarry-site coastal aquifer. *Environ Geol*, 456-466.

Loucks, D. P., Stakhiv, E. Z., & Martin, L. R. (2000). Sustainable Water Resources Management. *Journal of Water Resources Planning and Management*, 43-47.

Louvat, D. M. (1999). Origin and residence time of salinity in the Aspo groundwater system. *Applied Geochemistry 14 (7)*, 917–925.

Mansour, A. Y., Baba, A., Gündüz, O., Şimşek, C., Elçi, A., & Murathan, A. (2017). Modeling of seawater intrusion in a coastal aquifer of Karaburun Peninsula, western Turkey. *Environmental Earth Sciences*.

Mater, B. (1982). *Relations between Classification and Use of Land in Urla Peninsula.* İstanbul Üniversitesi.

Middelkoop, H., Daamen, K., Gellens, D., Grabs, W., Kwadijk, J. C., Lang, H., Wilke, K. (2001). Impact Of Climate Change On Hydrological Regimes And Water Resources Management In The Rhine Basin. *Climatic Change*, 105-128.

Sezer, İ. (1988). A new index experiment on climate and vegetation classification. *Aegean Geography Journal*, 161-202.

Yazicigil H., Ekmekci M. (2003). Perspectives on Turkish ground water resources. *Ground Water, 41, 3*, 290-291.

5 DAM SAFETY
İstanbul Turkey 2018

5th International Symposium on Dam Safety

October 27-31, 2018

EFFECT OF RESERVOIR BOTTOM ABSORPTION ON THE HYDRODYNAMIC RESPONSE OF DAM-RESERVOIRS DURING EARTHQUAKE

Ender DEMİREL[1]

ABSTRACT

While it's well known that the reservoir absorption effects can result in significant change in the hydrodynamic response of dam-reservoirs during earthquake, effects of absorption of the reservoir banks are less understood and more complex to simulate due to three-dimensionality of the reservoir geometry. In this study, a three-dimensional numerical solver is developed for the investigation of reservoir bank absorption effects on the hydrodynamic response of large dam-reservoirs during earthquake. Absorption effects are considered employing an absorbing boundary condition based on the damping coefficient of the reservoir material. In order to reduce the computational domain, an effective non-reflecting boundary condition is implemented for the transmission of the pressure waves at the far-end of the computational domain. Numerical tests on two-dimensional cases have demonstrated that the proposed computational model can accurately simulate hydrodynamic response of dam-reservoirs considering absorption effects.

Keywords: Earthquake, dam-reservoir, reservoir bottom absorption, OpenFOAM, simulation.

INTRODUCTION

Accurate prediction of earthquake induced hydrodynamic pressures in dam-reservoirs is required to provide design guidelines for large dams. Compressibility effects in water owing to the shocks during earthquake significantly affect hydrodynamic response of high-head dams. Previous studies in the literature revealed that the hydrodynamic forces acting on arch dams were underestimated when the compressibility effects are neglected (Chopra, 1967). Analytical and numerical solutions of the acoustic pressure equation provide satisfactory results for the estimation of hydrodynamic forces acting on dam body (Aydin and Demirel, 2012). Breakthrough developments in computer technology in recent years made it possible to simulate earthquake induced surface waves, which may be critical in design of embankment and arch dams for energy considerations (Demirel and Aydin, 2016).

[1] Associate Professor, Department of Civil Engineering, Eskisehir Osmangazi University, Eskisehir, Turkey, e-posta: edemirel@ogu.edu.tr

In order to perform realistic simulation of hydrodynamic response of earthquake excited dam-reservoirs, reservoir bottom absorption effects should be consider since compressible pressure waves are partly absorbed by the reservoir material during earthquake. Absorption effects can be incorporated into the mathematical model implementing appropriate boundary conditions on the reservoir boundaries. In this study, a parallel computational model is developed based on an open source CFD (Computational Fluid Dynamics) code for the realistic simulation of large dam-reservoirs during earthquake considering both compressibility and absorption effects. An effective non-reflecting boundary condition is applied at the far-end of the computational domain in order to reduce computational time and to prevent the reflection of pressure waves. Numerical simulations are performed on two-dimensional reservoir geometries with inclined dam-faces using different damping parameters. Results are compared with the numerical results in the literature to see accuracy and reliability of the numerical model.

NUMERICAL MODEL

Earthquake induced hydrodynamic pressures in the reservoir are governed by the following pressure equation including compressibility effects:

$$-\frac{1}{c^2}\frac{\partial^2 p}{\partial t^2}+\nabla^2 p=0 \tag{1}$$

Where c (=1438 m/s) is the sound speed in water to represent compressibility effects due to immediate consequence of an earthquake. Equation (1) is valid for the incompressible fluid when the sound speed is set to a large value, which means that any disturbance in the pressure field is perceived in the computational domain at an infinitely small time.

Figure 1. Three-dimensional view of dam-reservoir geometry subjected to earthquake

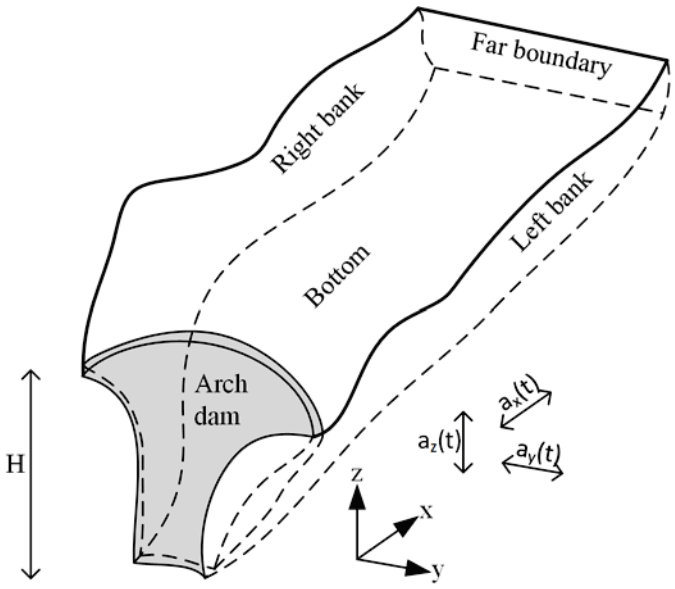

For the realistic simulation of earthquake excited dam-reservoirs, appropriate boundary conditions are defined on dam body, reservoir bottom, reservoir banks and far-end of the computational domain (Fig. 1). The following boundary condition is used on the dam face to apply the earthquake disturbance:

$$\left.\frac{\partial p}{\partial n}\right|_{dam}=-\rho a_n \tag{2}$$

Where n is the unit normal vector on the dam face, ρ is the fluid density and a_n is the acceleration component normal to the dam body. Absorbing boundary condition is used at the reservoir boundaries to include absorption effects by the reservoir material as follows:

$$\left.\frac{\partial p}{\partial n}\right|_{reservoir} = -\rho a_n - q\frac{\partial p}{\partial t} \tag{3}$$

Where q is the absorption coefficient of the reservoir material and given by Fenves and Chopra (1984) as

$$q = \frac{1-\alpha_r}{c\left(1+\alpha_r\right)} \tag{4}$$

in which α_r is reflection coefficient of the reservoir boundary and defined as the ratio of the reflected waves to the normally incident compressibility waves. It should be noted that the reflection coefficient can be considered as variable in the present model depending on the spatial variation of the reservoir material over the field.

Sharan's boundary condition (Sharan 1987) is used at the far-end of the computational domain for the transmission of compressibility waves at the boundary without reflection of pressure waves back into the reservoir domain:

$$\left.\frac{\partial p}{\partial n}\right|_{far} = -\frac{\pi}{2H} - \frac{1}{c}\frac{\partial p}{\partial t} \tag{5}$$

Where H is the water depth in the reservoir. Free-surface effects are neglected in this study since the contributions from the free-surface waves can be neglected for the hydrodynamic response of large dam-reservoirs.

RESULTS AND DISCUSSION

Present computational model is first validated for a two-dimensional reservoir geometry in this conference paper even if the model is three-dimensional since two-dimensional analytical solutions are available in the literature. Two-dimensional dam-reservoir geometry is schematically shown in Fig. 2 along with the boundary conditions. Dam-face is fully inclined with 60° inclination angle.

Figure 2. Schematic view of two-dimensional dam-reservoir geometry

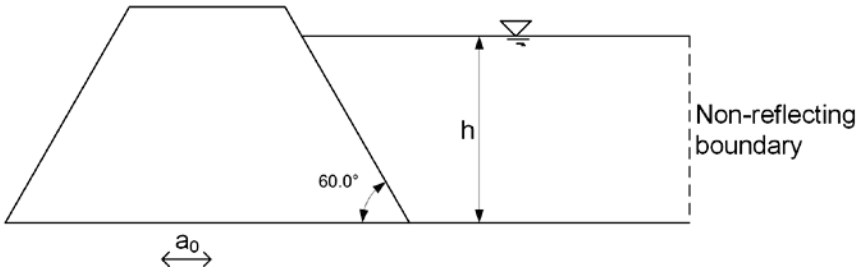

Dam-reservoir geometry is subjected to a constant a_0 acceleration in horizontal direction and the dimensionless pressure coefficient along the dam-face is defined as:

$$C_p = p/\left(\rho a_0 h\right) \tag{6}$$

Numerical simulations are performed for the dam-reservoir geometry given in Fig. 2 for different reflection coefficients of reservoir materials and distributions of pressure coefficients are compared with the finite element results of Sharan (1991) in Fig. 3. The good agreement between the present and the finite element results for different damping coefficients clearly shows that the present computational model can accurately predict hydrodynamic pressures on inclined dam-faces.

Figure 3. Comparison of the present results with the literature for different reflection coefficients

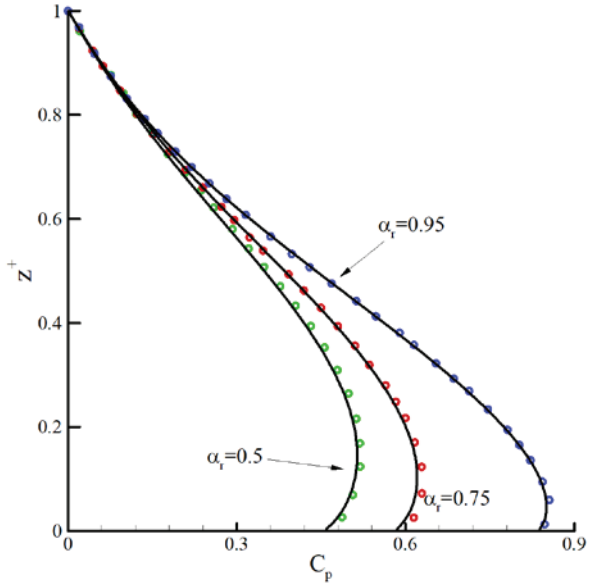

In order to see the time variation of hydrodynamic forces on the dam-face, dam-reservoir geometry is subjected to the harmonic excitation $a_x(t) = \alpha g \cos(\omega t)$, where ω is the angular frequency of the excitation. Drag force on the dam-face is obtained integrating hydrodynamic pressures over the dam face and non-dimensionalized as:

$$C_D = F_D / \left(\rho \alpha g h^2 \right) \tag{7}$$

Time variation of hydrodynamic forces on the dam-face is depicted in Fig. 4 for different reservoir bottom reflection coefficients. Time scale is non-dimensionalized with respect to the period of the excitation in the plot. It is seen in the figure that the reflection coefficient is not much effective on the time variation of the hydrodynamic forces. However, high reflection coefficient results in greater hydrodynamic forces than that in low reflection coefficient since the energy of the pressure waves are partly absorbed by the reservoir material. Thus, large dams are overdesigned when the reservoir bottom absorption effects are not considered in the numerical model.

Figure4. Time variation of drag coefficient for different reservoir bottom reflection coefficients.

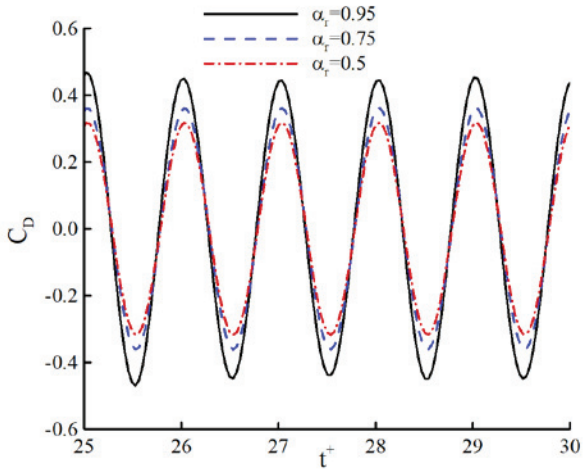

CONCLUSIONS

A three-dimensional computational model has been developed for the prediction of hydrodynamic forces on dam faces during earthquake. Compressibility and reservoir bottom absorption effects are considered in the model. The length of the reservoir is reduced with the application of an effective non-reflecting boundary condition at the far-end of the computational domain. The numerical model is validated with the numerical results reported in the literature for two-dimensional geometries. Comparisons of the hydrodynamic pressures over the dam-face with the finite element results show that the present model can accurately simulate hydrodynamic response of dam-reservoirs with fully inclined dam-faces.

REFERENCES

Chopra, A.K. 1967. "Hydrodynamic pressures on dams during earthquakes." J. Eng. Mech., Div., vol. 93, pp. 205-223.

Aydin, I., Demirel, E. 2012. "Hydrodynamic modeling of dam-reservoir response during earthquakes." *J. Eng. Mech.*, vol. 138, pp. 164-174.

Demirel, E., Aydin, I. 2016. "Numerical simulation and formulation of Wave run-up on dam-face due to ground oscillations using major earthquake acceleration records." J. Eng. Mech., vol. 142,pp. 1-8.

Fenves, G., Chopra, A.K. 1984. "Earthquake analysis of concrete gravity dams including reservoir bottom absorption and dam-water-foundation reservoir interaction." Earthq. Eng. Struct. Dyn., vol. 12, pp. 663-680.

Sharan, S. K. 1987. "Time-domain analysis of infinite fluid vibration." Int. J. Numer. Methods Eng., vol. 24, pp. 945-958.

Sharan, S. K. 1991. "Efficient finite element analysis of hydrodynamic pressure on dams." Computers and Structures, vol. 42, pp. 713-723.

SEDIMENTATION PROBLEM IN DAM RESERVOIRS; HASANLAR DAM RESERVOIR AS AN EXAMPLE

Erhan DEMİR [1], İbrahim BİROĞLU [2]

ABSTRACT

The first connotation that comes to mind as regards dam safety is usually the safety or durability of the dam body and related hydraulic structures. The safety of the dam and related hydraulic structures will not be so important singly if the storage facility of the dam can not serve due to various reasons. Therefore, as regards dam safety, the safety of quality and quantity of water, reliability of reservoir, upstream and downstream facilities as well as the dam body and related structures should be understood as a whole. From this point of view, taking the necessary precautions to prevent the filling of the effective storage capacity of the dam with sediment, at least for the economic life of the dam is essential for providing safety and reliability of the facility. In this paper, the Hasanlar Dam has been outlined as an example for the problem of sedimentation in dam reservoirs.

Keywords: Active volume, sedimentation, dam reservoir.

ÖZET

Baraj güvenliği denilince akıllarda oluşan ilk çağrışım genellikle, baraj gövdesi ve ilgili sanat yapılarının güvenliği ya da sağlamlığı olmaktadır. Çeşitli nedenlerle hizmet gayesini ifa edemeyen depolama tesisinin, baraj gövdesi ile birlikte ilgili sanat yapılarının sağlamlığı ya da güvenliği tek başına bir önem arz etmeyecektir. Dolayısıyla baraj güvenliği denilince, baraj gövdesi ve ilgili sanat yapıları ile birlikte depolanan suyun miktarının ve kalitesinin, rezervuarının, memba ve mansap tesislerinin güvenliği de bir bütün olarak anlaşılmalıdır. Bu açıdan bakıldığında Baraj rezervuarlarında bırakılan aktif hacmin, söz konusu barajın en azından ekonomik ömrü boyunca sediment ile dolmasını önlemeye yönelik gerekli tedbirleri almak, tesisin güvenliğinin ve güvenilirliğinin temini için elzemdir. Bu bildiride Hasanlar Barajı, barajlarda yaşanan rüsubat problemi için bir örnek olarak ana hatlarıyla ele alınmıştır.

Anahtar Kelimeler: Aktif hacim, sediment birikimi, baraj rezervuarı.

[1] State Hydraulic Works (DSİ), Department of Surveying, Planning and Allocation, Deputy Head, Civil Engineer (M.Sc.), Ankara, Turkey
e-mail: erhandemir@dsi.gov.tr

[2] State Hydraulic Works (DSİ), Department of Surveying, Planning and Allocation, Manager of Erosion and Siltation Control Branch, Forest Engineer (M.Sc.), Ankara, Turkey
e-mail: ibiroglu@dsi.gov.tr

INTRODUCTION

The dam safety issue, together with the environment affected by the dam, is a very important (vital) element for a dam, but it is not sufficient by itself. A storage facility should be reliable as well as safe to provide service as envisaged throughout its planned economic operating life.

Considering that the main source of the services provided by a storage facility is water, ensuring the reliability of both the quantity and the quality of the water provided by the storage facility is at least as important as the structural security of the dam.

In the dams, the deposition of silts above the projected level in the planning phase causes the dead volume to be filled in a short time and cause a decrease in the volume of active storage. This situation may decrease the planned regulation rate of dam and cause disruption of it's water supplying services for drinking, industrial usage and agricultural irrigation. If the dam has power generation purpose than ıt is also cause damages to hydroelectric power plant turbines and may negative effect of energy production. Again, this situation may cause negative environmental effects especially in the downstream of the dams.

The siltation is a rather minor problem for many dams but may reduce by decades the possible long life of 50 % of them and may be a key problem within few years or few decades for over 10% of large or small dams.[1]

There are two main measures that are usually applied to reduce the amount of sediment which comes with water in to a dam reservoir. The first one is to prevent erosion, which is the source of the sediment, with appropriate measures in the places where erosion occur and the other is to trap the sediment which is activated before reaching the reservoir with suitable places and appropriate measures.

In spite of all sediment control measures taken in the upstream of the dam, if there is still sedimentation problem in a dam reservoir and if this situation is considering as a big risk for the operation of the dam facilities than there are different solutions can be applied such as cleaning of the reservoir or transfering the sediments from the reservoir to the downstream.

Although there are many solutions to sedimentation problem for dam reservoirs, it is necessary to determine which of these solutions is the most appropriate and economical solution because the local datas for each dam are different. One of the important local datas is sediment yields of the basin for determining the right sedimentation solution. But it is not very easy to know sediment yields of basins precisely before operation period of dams since the sediment yields of basins are not the same and differ from one basin to another.

HASANLAR DAM'S RESERVOIR

There are various empirical formulas and modeling tools for the determination of the yield of sedimentation for a selected point in the basin. One of them is RUSLE (Revised Universal Soil Loss Equation), which is widely used to produce specific models depending on the region.

Models such as WaTEM/SEDEM (The Water and Tillage Erosion Model and Sediment Delivery Model) erosion model, the EPM (Erosion Potential Model) model, the SATEEC (The Sediment Assessment Tool for Effective Erosion Control) model or the PISA (Previsione Interrimento Serbatoi Artificiali) model requires important datas that are difficult to obtain or collect.

It is also known that air stereography is another method based on the superimposition of aerial photographs of the reservoir which is taken at appropriate time intervals.

In the determination of the sediment yield of the basin, direct measurement methods such as bathymetric measurements are more reliable than models or empirical formulas. But like many other direct measurement methods, it is costly, time-consuming and laborious.

In this paper, the Hasanlar Dam has been outlined as an example for the problem of sedimentation in dam reservoirs. At the planning stage how much the sediment yield olf the basin was predicted, now how much calculated by the DEMIS and what does the bathymetric measurements show. All these will be tried to summarize in this paper.

Hasanlar Dam and it's basin

Hasanlar Dam is a storage facility proposed by DSİ (State Hydraulic Works) within the boundaries of Düzce Province under the planning report of 'Düzce - Efteni Project' on Küçük Melen River. At the planning stage the dam had three main purposes which are water supply for drinking, water supply for agricultural irrigation and flood control. During operation period of the dam, in 1991, a hydroelectric power plant was built and thus generating energy is added to the purposes of the dam. The location of the dam in Turkey is shown in Figure 1.

Figure 1: The location of the Hasanlar Dam in Turkey (Base map is taken from Google Earth)

The construction of the dam started in 1965 and was completed in 1972 and was subsequently flooded with water. The main characteristics of the dam are given in Table 1 and the current photographs are given in Figure 2 and Figure 3.

Table 1: Characteristic Informations of Hasanlar Dam [2]

Type of dam	Rock fill with clay core
Height from the River Bed	70,80 m
Height from the Dam Foundation	72,80 m
Body fill volume	1.651.000 m^3
Minimum water intake level (MWL)	227,50 m
Operating water level (OWL)	255,50 m
Spillway crest elevation (small spillway)	255,50 m
Spillway crest elevation (big spillway)	267,36 m

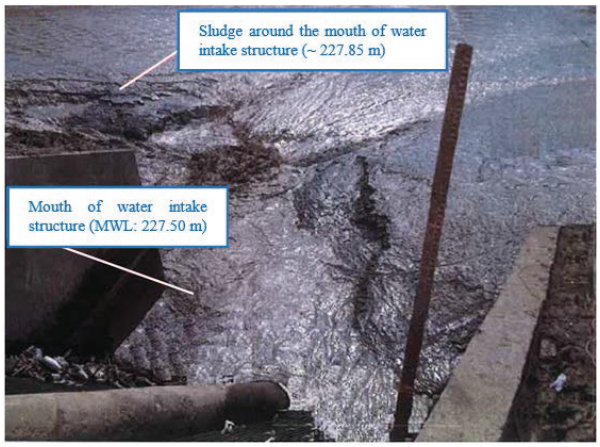

Figure 2: A view from the mouth of water intake (2018, [3])

Figure 3: view of the reservoir (2018, [3])

Hasanlar Dam is located in the Küçük Melen River basin, which is a sub-basin of the Western Black Sea Basin. The drainage area of the Hasanlar Dam is about 695 square kilometers and it is shown in Figure 4.

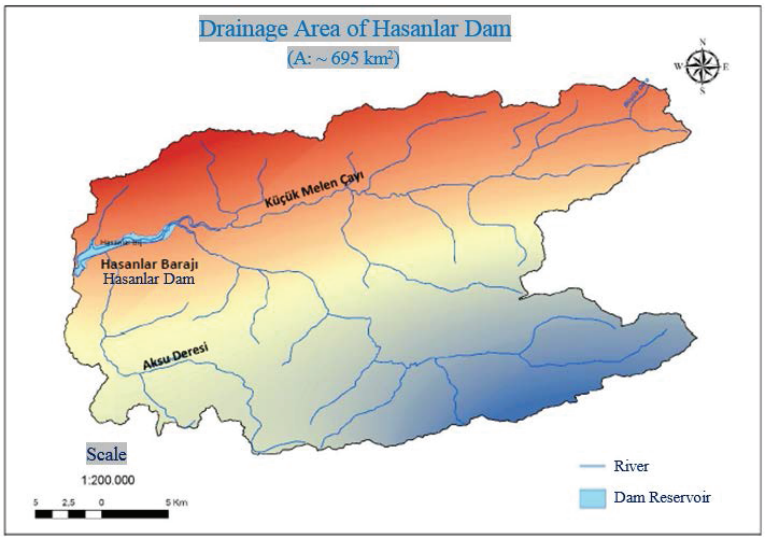

Figure 4: The drainage area of Hasanlar Dam (DEMİS)

Sediment Situation of Hasanlar Dam's Reservoir

For sediment situation of the basin, '*There is no information about the amount of sediment which is carried by the rivers in the project area since there are no studies on the rivers in the Küçük Melen Basin. However, it is estimated that the sediment yield is higher in Aksu, Asar and Uğur Suyu rivers located in the Küçük Melen basin and therefore it is proposed that the weirs which are proposed to be built on these rivers should be gated. For Hasanlar Dam reservoir, 160 m^3/km^2/year sediment yield is estimated and the dead volume in the reservoir is calculated according to this estimation.*' is written in the planning report of Düzce - Efteni Project (Chapter III, page 19).

In the planning report, the sediment yield of the basin for the reservoir is estimated as 160 m^3/km^2/year and corresponding 5.000.000 m^3 dead volume in the dam reservoir reserved to store the sediment for 50 years.

A model, called as DEMİS (Dynamic Erosion Model and Monitoring System), has been developed by the General Directorate for Combating Desertification and Erosion (General Directorate of ÇEM) together with the Ankara University Faculty of Agriculture to predict the water erosion of Turkey. DEMİS is a GIS (Geographical Information Systems) based dynamic model using the Russle (Revised Universal Soil Loss Equation) method.

The drainage area of Hasanlar Dam was studied by using the DEMİS model and the situation of erosion obtained. Five different categories from very light to very severe situations in the basin are given in Table 2.

Table 2: Situation of erosion for Hasanlar Dam's drainage area (DEMİS)

Hasanlar Dam	Categories					Total
	Very Light	Light	Moderate	Severe	Very Severe	
Area (ha)	56.513	2.003	1.960	3.863	5.099	69.438
Percentage (%)	81,39	2,88	2,82	5,56	7,34	100,00

According to the results produced by DEMİS, 81,39 % of the basin is very light, 2,88 % is light, 2,82 % is moderate, 5,56% is severe and 7,34 % is very severe erosive.

Also produced by DEMİS for the basin of Hasanlar dam; Vegetation and land use factor map (shown in Figure 5), the soil erosion susceptibility factor map (shown in Figure 6), the sediment transmission rate map (shown in Figure 7) and the map of soil losses carried by rivers (shown in Figure 7).

The sediment yield of the basin for the reservoir is calculated as 205 m^3/km^2/year by DEMİS.

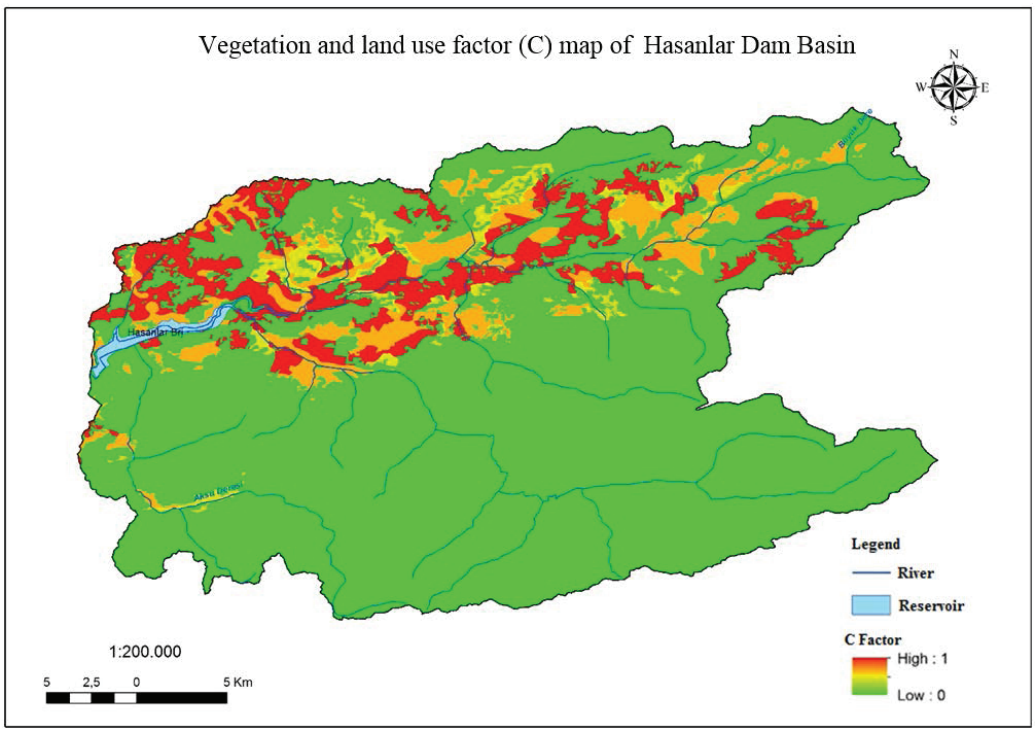

Figure 5: Vegetation and land use factor map of Hasanlar Dam basin (DEMİS)

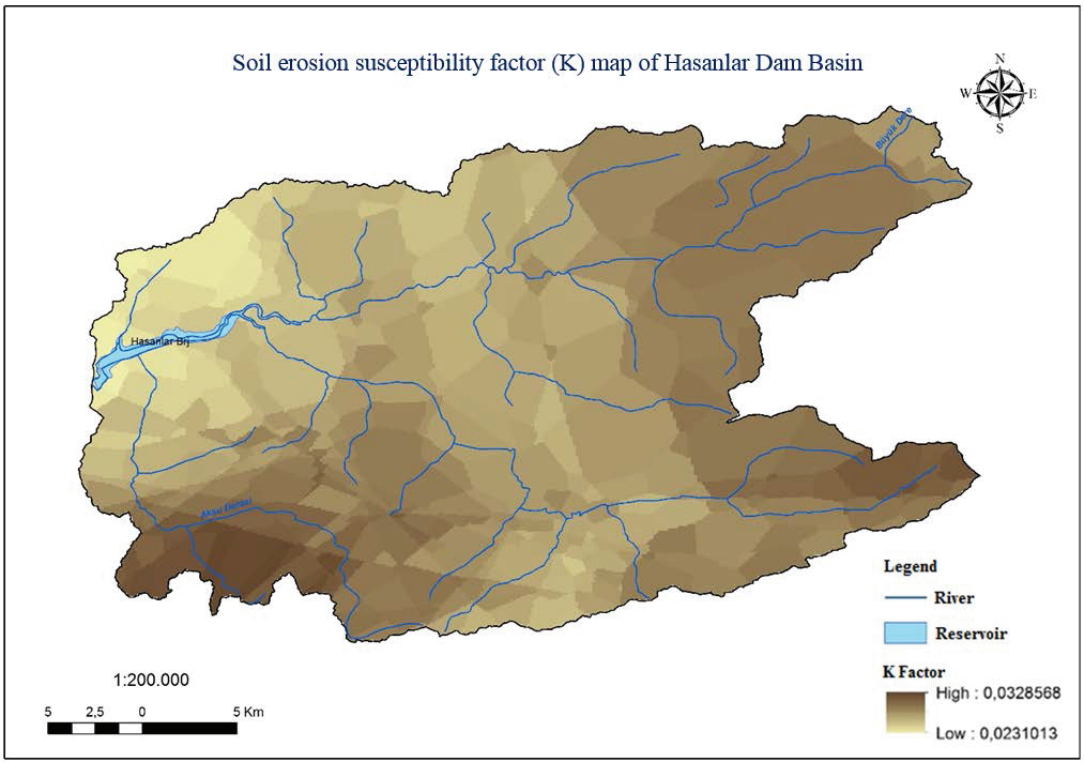

Figure 6: Soil erosion susceptibility factor map of Hasanlar Dam basin (DEMİS)

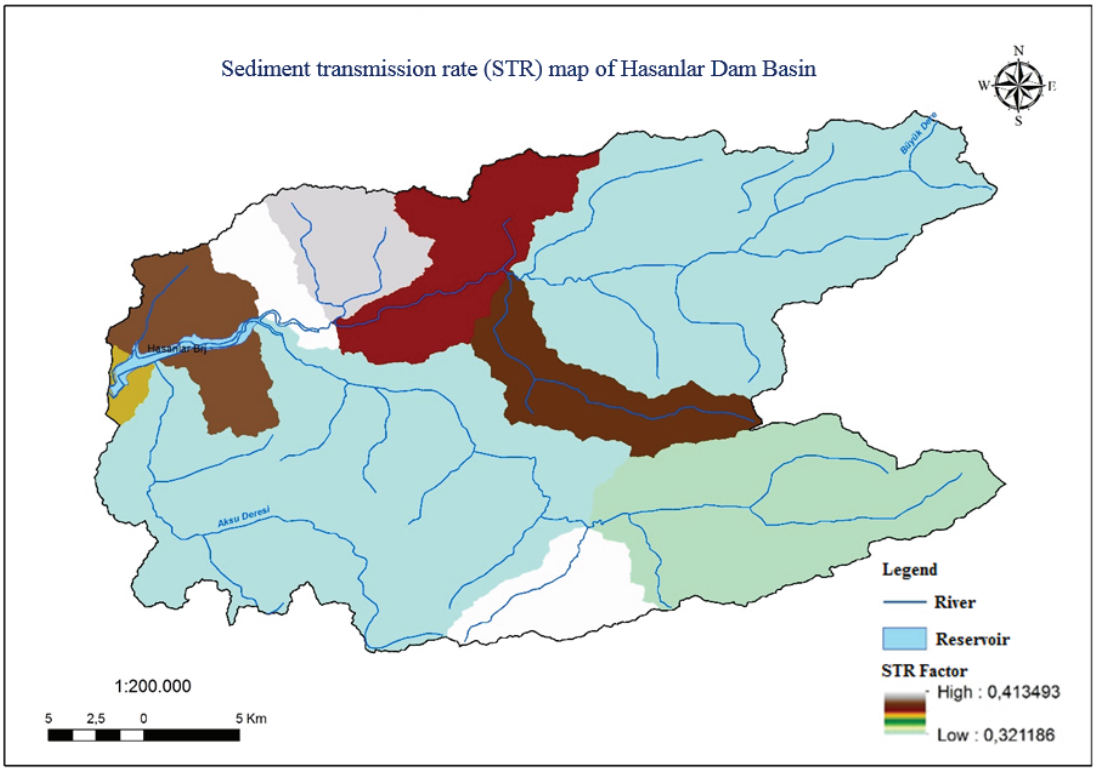

Figure 7: Sediment transmission rate map of Hasanlar Dam basin (DEMİS)

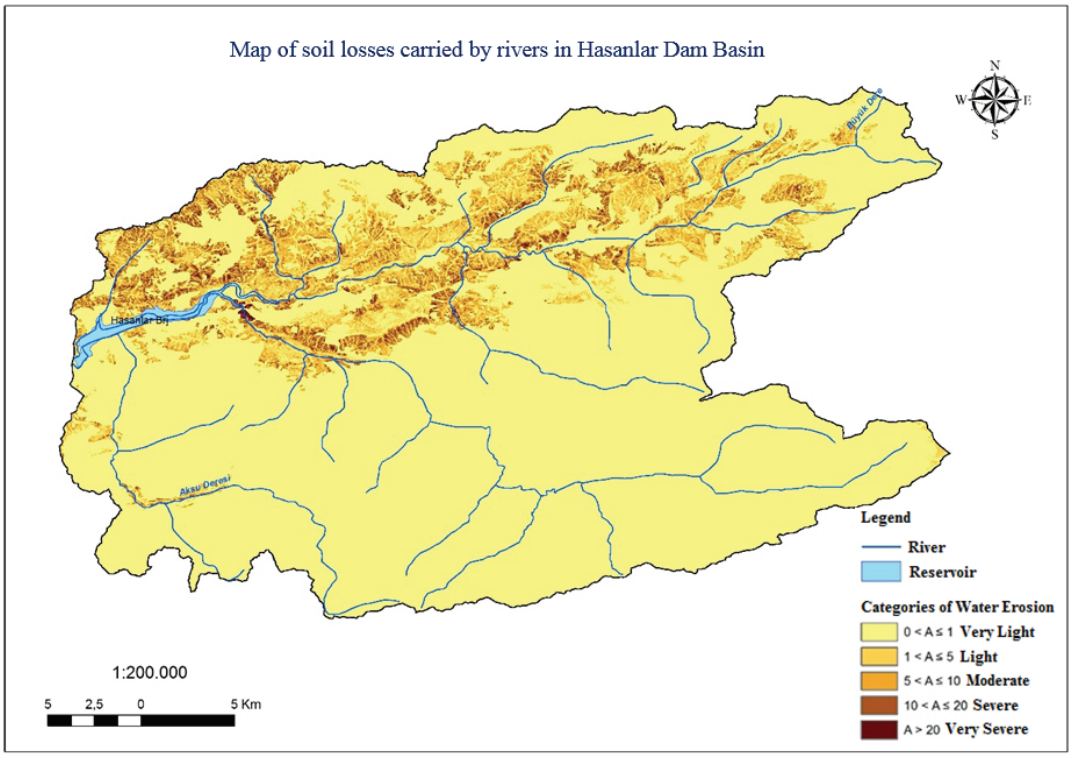

Figure 8: Map of soil losses carried by rivers in Hasanlar Dam basin (DEMİS)

In years 1974, 1979, 1999 and 2014, bathymetric measurements were made in order to observe the amount of sediment deposited in the reservoir. Table 3 shows the elevation and the corresponding volume values of the reservoir obtained from the bathymetric measurements taken in 1974, 1999 and 2014.

Table 3: The elevation and the corresponding volume values of the Hasanlar Dam reservoir according to the years of measurements [4]

Elevation (m)	Measurement in 1974 (m^3)	Measurement in 1999 (m^3)	Measurement in 2014 (m^3)
227,50 (MWL)	3.200.000	45.000	18.000
230	4.850.000	425.000	308.000
235	10.300.000	3.485.000	2.910.000
240	17.448.000	8.850.000	7.740.000
245	26.150.000	16.025.000	14.942.000
250	36.620.000	25.488.000	37.410.000
255,50 (OWL)	50.630.000	38.490.000	37.415.000
260	64.048.000	51.520.000	50.295.000
265	81.152.000	67.935.000	66.880.000

When the measurement values in Table 3 are taken into consideration, it is seen that almost all of the dead volume of Hasanlar Dam, which has been flooded in 1972, has been almost completed in about 30 years, and that the sediment storage rate of the dam decreases gradually compared to the first years.

RESULTS AND RECOMMENDATIONS

Taking the necessary measures to prevent the active volume left in the dam reservoirs from filling with sediment at least during the economic life of the dam is very important to ensure the safety and reliability of the storage facilities. Therefore, especially in the active basins in terms of sedimentation, the measures to be taken against sedimentation and erosion should be taken into account in the selection of the dam site location at the planning stage together with the other important criteria like the geological formations, reservoir operation levels, water quality and quantity, land acquisition and/or resettlement status, the existing public works structures etc.

There are various modeling tools and empirical formulas for the determination of the sediment yield of basins. The calculated or predicted sediment yields for the same basin may vary according to the chosen method and the differences between results (outputs) may be significant. While a selected calculation method can give values very close to the truth for a particular basin, it can not produce accurate results for another basin which is thought to have similar characteristics. Therefore, determination of the sediment yield of a basin should be done by using with a number of methods which are considered to be suitable for the basin and the results (outputs) of methods should be supported and questioned by site surveys.

In addition, sediment observations should be continued in appropriate periods for the dams which are critical especially in the active basins in terms of sedimentation. According to the results of the observations if the dead volume of reservoir will expire before scheduled date and if this situation presents a risk for the safety / reliability of the dam, the measures for the solution of the sediment problem should be developed.

THANKS

We would like to thank Mr. Suat ŞAHİN for his contribution to the data produced with the DEMİS model.

REFERENCES

[1] URL**:** http://www.hydrocoop.org/dams-with-significant-siltation-problems/

[2] "Düzce - Efteni Project Planning Report", DSİ Archives, Ankara 1971

[3] DSİ, Surveying, Planning and Allocation Department, Erosion and Sediment Control Section Archives

[4] DSİ, Surveying, Planning and Allocation Department, Map Section Archives

5 DAM SAFETY
İstanbul Turkey 2018

5th International Symposium on Dam Safety

October 27-31, 2018

EVALUATING THE EFFECTS OF NON-SEQUENTIAL CONSTRUCTION OF CASCADE RESERVOIRS ON POTENTIAL ACTIVE WATER STORAGE CAPACITY

Şahnaz TİĞREK[1], Emrah YALÇIN[2]

ABSTRACT

Reservoir sedimentation is a very serious problem in Turkey, as it is in many countries. Deposited sediment in reservoirs causes water storage capacity losses, thus reducing potential benefits that could be gained from hydropower generation, irrigation, water supply and flood control. Although the useful life of a reservoir is generally determined from the rate of dead storage capacity loss, the basin applications more than often have appeared to commission the farthest downstream ones of cascade planned projects first due to their higher internal rates of return. Hence, at design stage of such reservoirs, sediment yield estimations are based on the existing upstream conditions at that time as it is not known when the upstream dams will be constructed. This uncertainty can lead to enormous dead volume allocations to remain on the safe side in determining minimum operation levels and, hence, positioning intake structures. In this study, the inability to be used entire potential water storage capacity resulting from inappropriate basin management practices is presented with the example of Botan Creek. The results show that the total active storage of the farthest downstream three dams could be increased about up to 38.47% (337.85 hm^3) according to optimization studies to be conducted.

Keywords: Reservoir sedimentation, cascade reservoirs, Botan Basin, Alkumru Dam, Turkey

INTRODUCTION

Reservoir sedimentation is a fact especially in semi-arid regions where the stream-flow shows a considerable variation from season to season or over a period of years that leads to high-rate erosion and sediment transport processes (Altun et al., 2004). Deposited sediment in reservoirs causes water storage capacity losses, thus reducing potential benefits that could be gained from hydropower generation, irrigation, water supply and flood control. In addition to storage loss, the combination of sediment trapping and flow regulation can cause dramatic impacts on streambed degradation, acceleration rates of bank failure, and increase scour at downstream structures such as bridges (Sumi and Hirose, 2009).

Nowadays, as the number of dams and their ages increase, the importance of managing the disturbed sediment balance of rivers has more clearly emerged in achieving sustainable development of basin storage capacities (Tigrek and Aras, 2012; Tigrek et al., 2009). Reservoir sedimentation is a complex phenomenon that is influenced by many factors such as watershed sediment production, rate of transportation and mode of deposition, and thus should be assessed specifically for the predicted

[1] Associate Professor, Department of Civil Engineering, Batman University, Batman, Turkey, e-mail: sahnaz.tigrek@batman.edu.tr
[2] Assistant Professor, Department of Civil Engineering, Kirsehir Ahi Evran University, Kirsehir, Turkey, e-mail: emrah.yalcin@ahievran.edu.tr

service life of each project in the planning stage or for extending the predicted service life of existing dams (Sumi and Hirose, 2009). Although there are some studies to foresee sediment distribution within reservoirs (Chaudhuri, 2017) and capacity loss over the years (Altun et al., 2004; Khaba and Griffiths, 2017), there is a gap in the literature concerning the dead storage capacity allocations of cascade reservoir schemes within the scope of integrated river basin development planning and management.

In the planning of a cascade reservoir system in a watershed, an integrated approach focusing on the optimization of whole system energy production and water needs is a must to obtain maximum potential benefits from that watershed (Yalcin and Tigrek, 2017a; Yalcin and Tigrek, 2017b). Since sedimentation is a fact and will continue throughout the lifetime of cascade reservoir projects, it should be estimated for the whole basin in this planning stage. By doing this, it is possible to account trapped sediment amount at the upstream of each reservoir in a cascade manner by considering only the intermediate catchments that contribute sediment transport between dam projects. Hence, minimum dead storage capacities to be allocated for each project are determined according to these accounted sediment amounts regarding the assumed useful life of these structures.

Although the useful life of a reservoir is generally determined from the rate of dead storage capacity loss as a common practice, the basin applications more than often have appeared to commission the farthest downstream ones of cascade planned projects first due to their higher internal rates of return. In addition, the duration of realization of an upstream project can be longer than expected due to financial, environmental and social considerations. Hence, at the design stage of such reservoirs, sediment yield estimations are based on the existing upstream conditions at that time as it is not known when the upstream dams will be constructed. This uncertainty can lead to enormous dead volume allocations to remain on the safe side in determining minimum operation levels and, hence, positioning intake structures. More dead storage capacity means a larger lake volume, a bigger dam body, and a wider inundation area or a lower energy production.

In the present study, the inability to be used entire potential water storage capacity resulting from inappropriate basin management practices is presented with the example of Botan Creek. The allocated dead storage capacities of the three most downstream cascade hydropower projects, one of which has been in operation while the other two are under construction, on the mainstream of Botan Creek are re-evaluated under the developed upstream conditions as if that the projects were constructed and taken in operation in order from upstream to downstream. Accordingly, the effects of non-sequential construction of these dam projects on the potential active water storage capacity of Botan Creek are assessed by comparing the allocated and re-evaluated dead reservoir volumes.

STUDY AREA

In Turkey, there are 26 basins in terms of hydrology. Of these hydrologic basins, 22 are river basins and the others are enclosed basins having no flow to the sea. The basin of the Tigris River contains the second largest flow volume (after the Euphrates River Basin) of all the rivers in the country. The Tigris River flows through the south-eastern Anatolia Region of Turkey, and there are four main tributaries, namely Garzan, Bitlis, Botan and Batman Creeks, running into the main channel of the river. The Botan Basin is a recent developing sub-basin of the Tigris River, and it is selected as the case of this study to pose a possibility of reconsideration in the planning stage.

The Botan hydropower system consists of the Narli Dam and HEPP Project, the Oran Dam and HEPP Project, the Keskin Dam and HEPP Project, the Pervari Dam and HEPP Project, the Cetin Dam and HEPP Project, and the Alkumru Dam and HEPP Project, as depicted in Figure 1 (EIE, 1986; Hidrokon, 2009; Limak, 2006; Su Yapi, 2007). Moreover, there is an in-basin diversion from Mukus Creek to Pervari Dam with a transmission canal with a capacity of 30 m^3/s (Su Yapi, 2007).

After the compilation of the reconnaissance studies for the Botan Basin in 1986, the basin

development process was initiated with the start of the construction of the most downstream project, Alkumru Dam, in 2008. To date, only the Alkumru Project was taken into operation in 2011, and the Cetin and Pervari projects have still been under construction since 2011 and 2014, respectively. The completionratiosof.

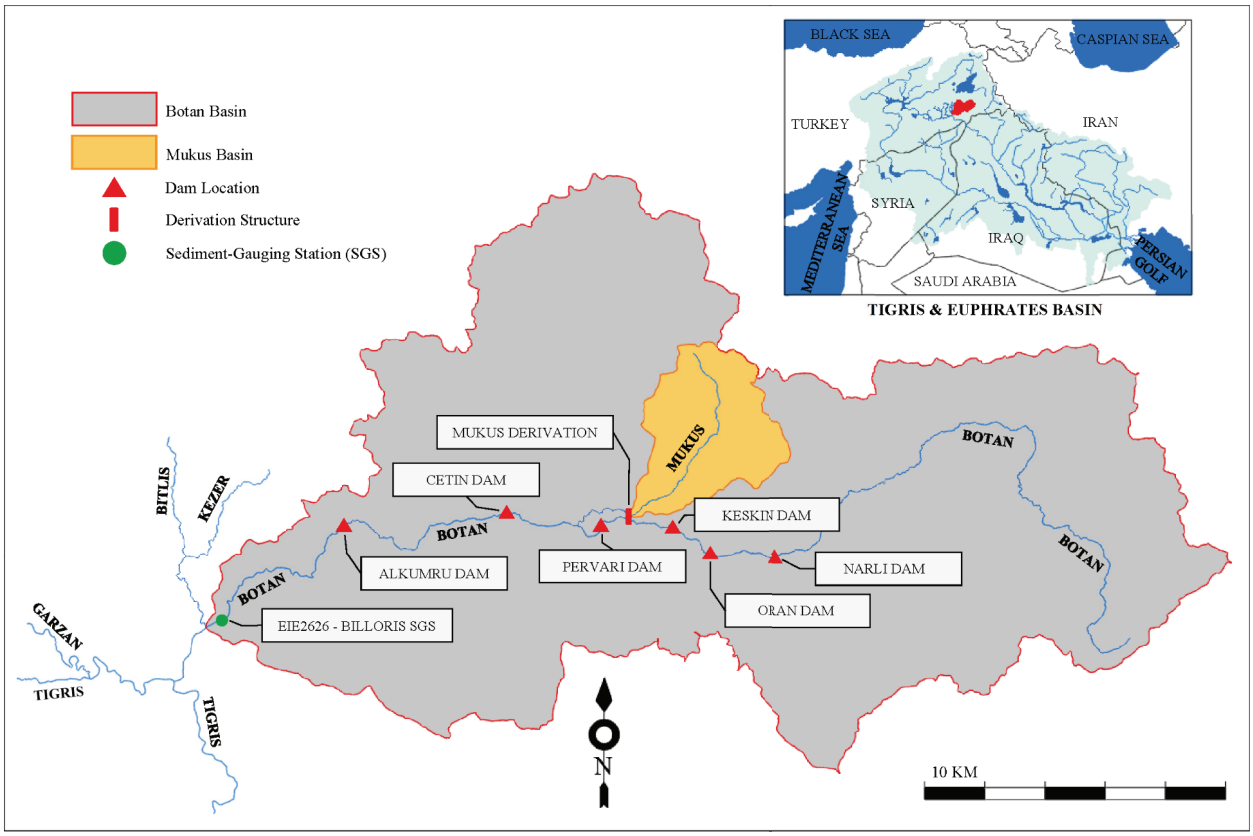

Figure 1. Location map of the study area

these projects have just reached, in turn, 12 percent in mid-2016 and 30 percent in mid-2017, and still, no dates have been set for their commissioning. The topographical and technical properties of these single-purpose projects are detailed in Table 1. Besides, while a three-year pre-license has been granted for the Keskin Project in 2017, there is no activity related to the realization of the other two most upstream dam projects (Enerji Atlasi, 2018).

Table 1. Characteristics of the Pervari, Cetin and Alkumru projects

Characteristics	Unit	Pervari	Cetin	Alkumru
Purpose	-	Energy	Energy	Energy
Drainage Area	km^2	4288.1	7066.2	7562.5
Thalwag Elevation	m	820.0	678.0	542.0
Maximum Water Level	m	980.0	822.0	647.0
Minimum Water Level	m	930.0	760.0	611.8
Total Volume at Maximum Water Level	hm^3	237.41	613.95	417.20
Active Storage	hm^3	144.41	458.71	275.02
Dead Storage	hm^3	93.00	155.24	142.18
Tailwater Level	m	820.0	647.0	541.8
Design Discharge	m^3/s	160.00	315.49	277.00
Penstock: Number/Diameter/Length	-/m/m	1/6.4/125	1/9.4~4.0/313[a]	3/4.7/124
Energy Tunnel: Number/Diameter/Length	-/m/m	1/7.15/600	1/9.4/5302	1/8.4/443
Number of Units	-	4	5	3
Gross Head/Net Head	m/m	160.0/158.8	175.0/162.6	105.2/103.9
Turbine Type	-	Francis	Francis	Francis

Notes: [a] The inner diameter of the penstock gradually decreases from 9.4 m to 4.0 m between the shaft and the power plant.
Sources: Hidrokon (2009); Limak (2006); Su Yapi (2007).

When the available pre-feasibility and feasibility reports of the Alkumru, Cetin and Pervari projects are examined, it is observed that the sediment yield estimates related to the determination of dead volume allocations were conducted by assuming that the existing upstream conditions at those times would not change throughout the intended lifetime of these structures (Hidrokon, 2009; Limak, 2006; Su Yapi, 2007). It is clear that the reason for such an assumption is the uncertainty of the commissioning date of the upstream reservoirs. As a result, initiation of the basin development process from the most downstream reservoir project caused dead volume allocations in excess of what is necessary for the reservoirs to remain on the safe side in determining minimum operation levels and, hence, positioning intake structures.

SEDIMENT ANALYSIS FOR DEAD VOLUME ALLOCATIONS

To reanalyze the allocated dead reservoir storages in the Alkumru, Cetin and Pervari projects and to find an answer to the question of what would be the increase in the maximum possible active storage capacities of these reservoirs when these projects were constructed in sequence from upstream to downstream, the sediment transport analysis conducted by EIE (General Directorate of Electrical Power Resources Survey and Development Administration) (2000) using the data collected at the Billoris sediment-gauging station (Station Id: EIE 2626) is utilized. Billoris station located downstream of these projects is the only station on Botan Creek which has daily sediment records (Figure 1). The results of this analysis, based on 314 sediment samples obtained in the period of 1971-1999, indicate that the suspended sediment yield in the basin is 489 t/year/km², and the submerged specific weight is 1.33 t/m^3, as detailed in Table 2.

Instead of using directly the suspended sediment yield determined for the drainage area of the station in calculating the sediment amount to be deposited in the reservoirs, this yield is projected to the net drainage areas of the reservoirs by using the ratio of the sediment amounts derived from the regional suspended sediment rating curve developed for the streams of Turkey. Accordingly, for each of the dam projects, the net drainage area that contributes to sediment transport is calculated by subtracting the drainage area controlled by the upstream projects from the total drainage area of the reservoir. The long-year mean annual suspended sediment amounts corresponding to the calculated net drainage areas of Billoris station and the three reservoirs are computed directly from this regional rating curve equation, given in Table 2. By multiplying the suspended sediment yield of Billoris station with the computed long-year mean annual suspended amount ratio among the reservoir and the observation station, the suspended sediment yield corresponding the net drainage area of the reservoir is calculated for each of the projects.

Table 2. Characteristics and statistics of the Botan Creek - Billoris SGS

Station No	EIE 2626
Net drainage area	8761.2 km^2
Elevation	457 m
Observation period	1971-1996 (Discharge) 1971-1999 (Suspended sediment)
Number of sediment samples	314
Suspended sediment rating curve of the station	$Q_{S\text{-}SGS} = 0{,}0391Q^{2{,}2818}$ (Coefficient of determination, $R^2 = 0.769$) $Q_{S\text{-}SGS}$: *Daily mean suspended sediment amount (t/day)* Q: *Daily mean discharge (m^3/s)*
Degree of dispersion	56.2% sand 43.8% clay+ silt
Submerged specific weight	1.33 t/m^3
Suspended sediment amount	4282671 t/year 3220053 m^3/year
Suspended sediment yield	489 t/year/km² 368 m^3/year/km²
Regional suspended sediment rating curve developed for the streams of Turkey	$Q_{S\text{-}REG} = 6{,}2106A^{1{,}3605}$ (Coefficient of determination, $R^2 = 0.787$) $Q_{S\text{-}REG}$: *Long-year mean annual suspended sediment amount (t/year)* Q: *Net drainage area (km^2)*
Long-year mean annual suspended sediment amount for the net drainage area of the station	1435461 t/year

Sources: EIE (2000).

To account for bed load accumulations in the reservoirs, the calculated suspended sediment yields should be increased with a ratio between 15% to 400% depending on the vegetation cover, topographic situation, forest areas, land use, river bed slope and hydrological properties of the catchments. Although this ratio is taken as 25% in the engineering hydrology report of Botan Creek (EIE, 1991), in this study, the annual total sediment amounts are determined under the assumption that the bed load is 30% of the suspended sediments. Thus, the annual sediment amounts are calculated by multiplying the increased suspended sediment yields with the net drainage areas, and the reservoir volumes equivalent to the amounts of sediment that will be deposited during the 50-year economic lifetime of the projects are designated as dead storages. Accordingly, assuming the horizontal deposition of sediments across the reservoirs, corresponding water levels to the total sediment amounts, or dead storages, are read from the volume-area curves of the reservoirs, shown in Figure 2.

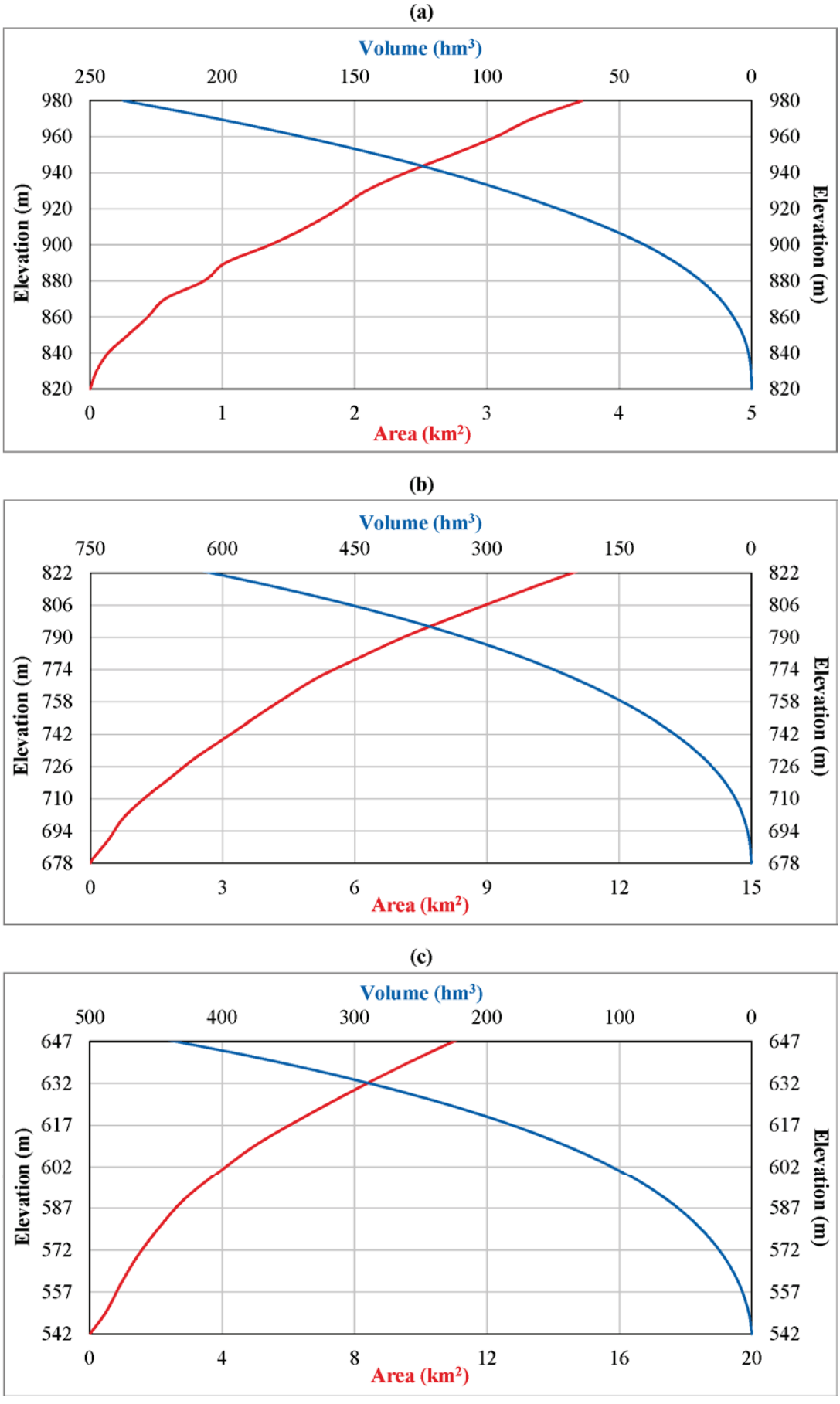

Figure 2. Volume-area curves of the (a) Pervari, (b) Cetin and (c) Alkumru reservoirs

The above calculations are conducted for both of the sequential and current non-sequential development states of the Botan Basin. When examining the current development case, the drainage areas are considered as the net drainage areas without taking into account the catchments controlled by the upstream projects such as were done in the design stage of these projects. For the full upstream development case, the intermediate basin areas between two cascade projects are considered as the net drainage areas assuming that all the projects of the Botan hydropower system were constructed in order from upstream to downstream. In both cases to be assessed, the Pervari Project is evaluated separately, with and without taking into account the Mukus Derivation.

RESULTS AND DISCUSSION

According to the pre-feasibility and feasibility reports of the Alkumru, Cetin and Pervari projects, the allocated dead volumes in the reservoirs are 142.18, 155.24 and 93.00 hm^3 respectively (Hidrokon, 2009; Limak, 2006; Su Yapi, 2007). While conducting the design process of these projects, these volumes were determined by taking into consideration the existing upstream conditions at those times. However, for the Alkumru Project, although the total sediment amount was found to be 175 hm^3, the reservoir dead storage volume was decreased to 142.18 hm^3 considering that the upstream plants could be commissioned in the 50-year economic lifetime period of the project. In addition, the dead storage volume of Pervari Reservoir was determined by considering that the flows of Mukus Creek would be diverted to the reservoir by a transmission canal.

When these volumes are re-analyzed with the same point of view as in these reports, the amounts of sediment that will be deposited during the economic lifetime of the projects are found to be 171.33, 156.22 and 83.50 hm^3 for the Alkumru, Cetin and Pervari reservoirs respectively, as detailed in Table 3. These amounts are close to the ones given in the pre-feasibility and feasibility reports of the projects. In addition, it is observed that the effect of the Mukus Derivation on the dead storage volume of Pervari Reservoir is an increase of 4.32 hm^3 (approximately %5) in the total sediment amount to be accumulated (Table 3). The profit of this water transfer can be optimized as a function of derivation cost and energy production considering the decrease in the active storage volume of the reservoir.

Table 3. Reanalysis of the allocated dead volumes in the Pervari, Cetin and Alkumru reservoirs considering the current non-sequential development state of the Botan Basin

	Unit	Pervari (without Mukus Derivation)	Pervari (with Mukus Derivation)	Cetin	Alkumru
Drainage area	km^2	4288.1	4288.1	7066.2	7562.5
Net drainage area	km^2	4288.1	4288.1 + 505.6	7066.2	7562.5
Long-year mean annual suspended sediment amount for the net drainage area of the reservoir	t/year	543038	572663	1071398	1175054
Suspended sediment load	t/year	1620143	1708530	3196498	3505752
Bed load	t/year	486043	512559	958949	1051726
Total sediment load	t/year	2106186	2221088	4155447	4557478
	m^3/year	1583598	1669991	3124396	3426675
Economic lifetime period	year	50	50	50	50
Total sediment amount	hm^3	79.18	83.50	156.22	171.33
Corresponding water level to the total sediment amount in the reservoir	m	923.04	925.21	760.20	615.06
Allocated dead storage in the reservoir	hm^3	93.00	93.00	155.24	142.18

As a result of repeating the same calculations to investigate dead storages required for the scenario corresponding to the sequential development of the Botan Basin, the total sediment amounts are found to be 4.21, 43.87 and 4.49 hm^3 for the Alkumru, Cetin and Pervari reservoirs respectively, as detailed in Table 4. These results indicate that the computed sediment amounts are significantly lower than the allocated dead volumes in the reservoirs. Considerable decreases are also found in the water levels corresponding to the computed sediment amounts in the reservoirs. An increase of only 4.32 hm^3 in the accumulated sediment amount of Pervari Reservoir resulting from the Mukus Derivation leads to a 26.45 m rise in the water level corresponding to the lifetime sediment accumulation (Table 4).

Table 4. Determination of dead volumes for the Pervari, Cetin and Alkumru reservoirs considering the sequential development of the Botan Basin

	Unit	Pervari (without Mukus Derivation)	Pervari (with Mukus Derivation)	Cetin	Alkumru
Drainage area	km^2	4288.1	4288.1	7066.2	7562.5
Net drainage area	km^2	46.3	46.3 + 505.6	2778.1	496.3
Long-year mean annual suspended sediment amount for the net drainage area of the reservoir	t/year	1146	30771	300852	28886
Suspended sediment load	t/year	3419	91805	897586	86182
Bed load	t/year	1026	27542	269276	25855
Total sediment load	t/year	4445	119347	1166861	112037
	m^3/year	3342	89735	877339	84238
Economic lifetime period	year	50	50	50	50
Total sediment amount	hm^3	0.17	4.49	43.87	4.21
Corresponding water level to the total sediment amount in the reservoir	m	826.80	853.25	725.24	552.41

The results from these computations demonstrate that the total dead storage of the farthest downstream three dam projects of the Botan hydropower system could be decreased up to 86.54%, corresponding to an increase of 38.47% (337.85 hm^3) in the total active storage for the analyzed system projects, as detailed in Table 5 and Table 6. This possible increase, which is even higher than the active storage of Alkumru Reservoir, in the total active reservoir volume of the three cascade projects can only be obtained by lowering the minimum operation levels and, hence, the positions of the power intakes to those corresponding the computed sediment amounts in the reservoirs.

Table 5. Comparison of the determined total sediment amounts against the allocated dead volumes in the Pervari, Cetin and Alkumru reservoirs

Project	Allocated dead storage in the reservoir (hm^3)	Reanalysis for the current development state		Analysis for the sequential basin development	
		Total sediment amount (hm^3)	Difference (%)	Total sediment amount (hm^3)	Difference (%)
Pervari (with Mukus Derivation)	93.00	83.50	-10.22	4.49	-95.17
Cetin	155.24	156.22	0.63	43.87	-71.74
Alkumru	142.18	171.33	20.50	4.21	-97.04
Total	390.42	411.05	5.28	52.57	-86.54

Table 6. Comparison of the maximum possible active storage capacities against the allocated active volumes in the Pervari, Cetin and Alkumru reservoirs

Project	Allocated active storage in the reservoir (hm^3)	Reanalysis for the current development state		Analysis for the sequential basin development	
		Active storage (hm^3)	Difference (%)	Active storage (hm^3)	Difference (%)
Pervari (with Mukus Derivation)	144.41	153.91	6.58	232.92	61.30
Cetin	458.71	457.73	-0.21	570.08	24.28
Alkumru	275.02	245.87	-10.60	412.99	50.17
Total	878.14	857.51	-2.35	1215.99	38.47

The life storages of the reservoirs will only be marginally reduced by an uneven distribution of the sediments within the reservoirs. However, it shall be mentioned that under the made assumption that the sediments would be deposited horizontally across the reservoirs starting from the lowest sections first, the sediment levels would rise almost to the levels of the power intakes. It may, therefore, become necessary that local protection measures be implemented at a later stage of the economic lifetime of the hydropower schemes in order to ensure satisfactory operation of the intake structures (Ilisu Dam and HEPP Engineering and Consultancy Services Consortium, 2008).

Although, in this assessment, the minimum operation levels of the reservoirs are considered to be equal to the corresponding water levels to the total sediment amounts, this consideration is only a prerequisite to further investigations for optimizing minimum operation levels and, hence, active storages of the reservoirs, in terms of maximum energy production. In such an optimization study, the net head can be at the forefront for a hydropower plant, while for another plant, the active storage can come to the forefront in maximizing energy to be produced. The sequential construction case of cascade reservoirs mentioned in this study provides wider ranges of head and active storage than the ones in the non-sequential basin development case in maximizing the energy productions of the system projects. Thus, more energy can be produced as a result of the optimization studies to be conducted under these wide-range constraints.

CONCLUSIONS

In this study, the effects of non-sequential construction of cascade reservoirs on potential active water storage capacity are assessed with the example of Botan Creek. The three most downstream cascade projects of the Botan hydropower system started to be constructed and taken in operation in order from downstream to upstream are analyzed in terms of their dead storage capacities allocated without taking into account the catchments controlled by the upstream projects. The results show that if the system projects were constructed and taken in operation in order from upstream to downstream, the total active storage of these three reservoirs could be increased about up to 38.47% (337.85 hm^3) according to optimization studies to be conducted.

This assessment can be improved in terms of energy production by optimizing the minimum operation levels of the system reservoirs under the minimum water level constraints ranged from the water levels corresponding to the computed sediment amounts to the maximum water levels of the reservoirs. Accordingly, the amount of loss in the energy production due to the inability to use all the potential water storage capacity of the system reservoirs resulting from such an improper watershed management practice can be demonstrated clearly.

REFERENCES

Altun, S., Sarvary, I., Tigrek, S., 2004. "Prediction of reservoir siltation case studies for Turkey". HYDRO 2004, Porto (in CD).

Chaudhuri, D., 2017. "Empirical approaches in prediction of reservoir sediment distribution - An experience of 57 reservoirs in the USA and India". International Journal of Sediment Research, vol. 32(2), pp. 260-276.

EIE (General Directorate of Electrical Power Resources Survey and Development Administration), 1986. The Tigris River, Botan Creek Reconnaissance Report, Publication No: 86–53. General Directorate of Electrical Power Resources Survey and Development Administration, Ankara (in Turkish).

EIE (General Directorate of Electrical Power Resources Survey and Development Administration), 2000. Suspended Sediment Data and Sediment Transport Amounts for Surface Waters in Turkey, Publication No: 20–17. General Directorate of Electrical Power Resources Survey and Development Administration, Ankara (in Turkish).

EIE (General Directorate of Electrical Power Resources Survey and Development Administration), 1991. Botan Creek Engineering Hydrology Report. General Directorate of Electrical Power Resources Survey and Development Administration, Ankara (in Turkish).

Enerji Atlasi, 2018. Botan Creek. Retrieved from http://www.enerjiatlasi.com/akarsular/botan-cayi.html (11 June 2018).

Hidrokon (Hidrokon Engineering Consultancy Incorporated Company), 2009. Cetin Dam and HEPP Feasibility Report. Hidrokon Engineering Consultancy Incorporated Company, Ankara (in Turkish).

Ilisu Dam and HEPP Engineering and Consultancy Services Consortium, 2008. Ilisu Dam and HEPP, Flood Hydrology and Sediment Transport. Ilisu Dam and HEPP Engineering and Consultancy Services Consortium: Colenko Power Engineering Limited, IM Maggia Engineering, Dolsar Engineering and Rast Engineering Services Limited, Ankara.

Khaba, L., Griffiths, J.A., 2017. "Calculation of reservoir capacity loss due to sediment deposition in the Muela reservoir, Northern Lesotho". International Soil and Water Conservation Research, vol. 5(2), pp. 130-140.

Limak (Limak Hydropower Plant Investments Incorporated Company), 2006. The Alkumru Dam and HEPP Project Feasibility Report. Limak Hydropower Plant Investments Incorporated Company, Ankara (in Turkish).

Su Yapi (Su Yapi Engineering and Consultancy Incorporated Company), 2007. The Tigris River, Botan Creek, Pervari Dam and HEPP Establishments Pre-Feasibility Report (Appendix 3A). Su Yapi Engineering and Consultancy Incorporated Company, Ankara (in Turkish).

Sumi, T., Hirose, T., 2009. "Accumulation of sediment in reservoirs". Water Storage, Transport, and Distribution - Encyclopedia of Life Support Systems (edited by Takahasi, Y.). UNESCO and EOLSS Publishers/UNESCO, Singapore, pp. 224-252.

Tigrek, S., Aras, T., 2012. Reservoir Sediment Management. CRC Press, London.

Tigrek, S., Gobelez, O., Aras, T., 2009. "Sustainable management of reservoirs and preservation of water quality". Technological Perspectives for Rational Use of Water Resources in the Mediterranean Region (edited by El Moujabber, M., Mandi, L., Trisorio-Liuzzi, G., Martín, I., Rabi, A., Rodríguez, R.). Centre International de Hautes Etudes Agronomiques (CIHEAM), Bari, pp. 41-53.

Yalcin, E., Tigrek, S., 2017a. "The Tigris hydropower system operations: the need for an integrated approach". International Journal of Water Resources Development, pp. 1-16.

Yalcin, E., Tigrek, S., 2017b. "Optimization of the Garzan hydropower system operations". Arabian Journal of Geosciences, vol. 10:374.

5th International Symposium on Dam Safety

October 27-31, 2018

PRECISE ESTIMATION OF PEAK FLOWS FOR DIFFERENT RETURN PERIODS: THE CASE OF CORUH BASIN, TURKEY

Fatih TOSUNOĞLU[1], Muhammet YILMAZ[1] , Sezai YILDIZ[2]

ABSTRACT

The magnitude of peak flows for various return periods play important role in design, planning and management of the water structures. In order to avoid high cost and large damage, the precise prediction of the peak flows is needed. In the present study, we aim to produce an accurate peak flow quantile estimates for various return periods. For this purpose, ten widely used probability distribution functions are considered to model annual instantaneous peak flows of a gauge station in the Çoruh basin, where various hydroelectric power plants and dams have been planned and designed in recent years. To define the best fitted distribution function among candidates, five powerful and commonly used model selection techniques, namely Akaike Information Criterion, Bayesian Information Criterion, Kolmogorov-Smirnov test, Anderson Darling test, Cramér-von-Mises test, have been applied. According the results of these techniques, the Gamma and Weibull distributions have been identified as the best fitted models. Finally, the peak flow quantiles in various return periods (10, 20, 50, 100 and 200, 500, 1000 and 10000 years) have been computed using the best fitted distributions. The findings from this study would be useful in proving information for determining the design flow values of hydraulic structures in the basin.

Keywords: Coruh basin, Peak flow, Model selection techniques, Probability distribution function.

1. INTRODUCTION

Flood frequency analysis is the one of widely used methods for planning, design and management of the hydraulic structures in any area of the world. Flood frequency analysis studies typically involve determining the best-fit univariate probability distribution function of annual peak flows observed at gauge stations and flood peak values, which are used in design of hydraulic structures, are then estimated for various return periods. In order to avoid extensive costs or large damages, precise definition of probability distributions is needed. A large number of studies have been published in scientific literature related to flood frequency analysis that propose the use of a variety of probability distribution functions to describe annual peak flow frequency distributions. For instance, Haktanir (1991) applied seven commonly used probability distributions (lognormal, Gumbel, smemax, log-Boughton, loglogistic, Pearson-3 and log-Pearson-3) to model annual flood peaks series longer than 21 observations of 112 unregulated natural streams in 23 major basins in Turkey. According to the evaluations of several goodness of fit tests, a single definite distribution did not appear to be the most suitable consistently for all the sample series taken, but the log-logistic and log-Pearson-3 models scored a larger number of better fits. Buyukkaracığan and Kahya (2009) used two and three parameter

[1]Civil Engineering Department, Engineering and Architecture Faculty, Erzurum Technical University Erzurum, Turkey
[2]State Hydraulic Works (DSI), Artvin, Turkey

log-normal, Gumbel, Pearson-3, logPearson-3, Log-Boughton, log-logistic and general extreme value distributions to characterize annual peak series of 12 gauge stations located in Konya Basin, Turkey. Based on chi squared and Kolmogorov-Smirnov goodness-of-fit tests, Log-Pearson 3 was found to be more suitable distribution type than the others. Opere et al. (2006) evaluated various probability distributions to describe annual maximum flow series from 28 river gauging stations located in the Nile Equatorial basin, Kenyan/Tanzanian. The Chi-Square and Kolmogorov–Smirnov statistics showed that the Generalized extreme value (GEV) and Extreme value type 1 (EV1) are the best candidates. Afreen and Muhammed (2012) considered gamma (G2) and generalized logistic (GLO) distributions for modelling annual maximum flows observed in six catchments in Pakistan. The exceedance quantiles for each catchment with return periods of 2, 5, 10, 25, 50 and 100 years were estimated using the inverse functions of the fitted distributions, which were defined by various model selection criterions. Li et al. (2016) fitted the Generalized Extreme Value (GEV) and Generalized Pareto distribution (GPD) models to the annual maximum (AM) series and the peaks over a threshold (POT) series in the Heihe River basin, China. The statistical Kolmogorov- Smirnov and Anderson Darling tests employed for defining the most suitable distribution type, which is then used to estimate extreme flood events for different return periods. Many other studies, not presented, can be found in Haddad and Rahman (2010), Seckin et. al. (2010), Can and Tosunoglu (2013).

In the present study, we aim to provide an accurate estimation of annual peak flows under different return periods. To achieve this aim, various probability distributions are fitted to annual peak flows observed in the rivers of Çoruh basin, Turkey. Five commonly used model selection techniques including Akaike Information Criterion, Bayesian Information Criterion, Anderson Darling, Cramér–von Mises and Kolmogorov-Smirnov tests are used to determine the most appropriate model among candidates. Then, the best fitted distribution is applied to compute extreme flood quantiles under different return periods, which can be helpful for the decision makers in the planning, design and management of hydraulic structures in the basin.

2. MATERIAL and METHODS

2.1 Probability distributions

The following distributions are considered for the current study; Weibull (WBL), two parameter and three parameter Lognormal (LN2 and LN3), Gamma (GAM), Pearson type-III (P3), Normal (NORM), Extreme Value type-1 (EV1), Generalized Extreme Value (GEV), Logistic (LOGIS) and log-Logistic (LLOGIS). Description of the considered probability distribution function are presented in table 1. Parameters of the distributions are estimated using the maximum likelihood method.

Table 1. General description of Probability Distribution Functions used in this study

Distribution	Probability Distribution Function (PDF)	Parameters
WBL	$f(x) = \frac{\beta}{\alpha}\left(\frac{x}{\alpha}\right)^{\beta-1} exp\left[-\left(\frac{x}{\alpha}\right)^{\beta}\right]$	β = shape parameter (β>0) α = scale parameter (α>0)
LN2	$f(x) = \frac{1}{x\sigma_y\sqrt{2\pi}} exp\left[-\frac{1}{2{\sigma_y}^2}\left(logx - \mu_y\right)^2\right]$	μ_y = shape parameter (μ_y>0) σ_y = scale parameter (σ_y>0) k = threshold parameter
LN3	$f(x) = \frac{1}{(x-k)\sigma_y\sqrt{2\pi}} exp\left[-\frac{1}{2{\sigma_y}^2}\left(\log(x-k) - \mu_y\right)^2\right]$	
GAM	$f(x) = \frac{x^{\beta-1}}{\alpha^{\beta}\Gamma(\beta)} exp\left[\frac{-(x)}{\alpha}\right]$	β= shape parameter (k>0) α = scale parameter (α>0) k= threshold parameter Γ = gamma function
P3	$f(x) = \frac{(x-k)^{\beta-1}}{\alpha^{\beta}\Gamma(\beta)} exp\left[\frac{-(x-k)}{\alpha}\right]$	
NORM	$f(x) = \frac{1}{\sigma\sqrt{2\pi}} exp\left[\frac{-1}{2}\left(\frac{x-\mu}{\sigma}\right)^2\right]$	μ = location parameter σ = scale parameter (σ>0)
EV1	$f(x) = \frac{1}{\sigma} exp\left[-\frac{(x-\mu)}{\sigma} - exp\left(-\frac{(x-\mu)}{\sigma}\right)\right]$	μ = location parameter σ = scale parameter (σ>0)
LOGIS	$f(x) = \frac{1}{\sigma}\exp\left(\frac{x-\mu}{\sigma}\right)\left[1+\exp\left(\frac{x-\mu}{\sigma}\right)\right]^{-2}$	μ = location parameter σ = scale parameter (α>0) β = shape parameter
LLOGIS	$f(x) = \frac{\beta}{x}\left(\frac{x}{\sigma}\right)^{\beta}\left[1+\left(\frac{x}{\sigma}\right)^{\beta}\right]^{-2}$	
GEV	$f(x) = \frac{1}{\sigma}\exp\left[-(1+\beta z)^{-1/\beta}\right](1+\beta z)^{-1-1/\beta}$	μ = location parameter σ = scale parameter (α>0) β = shape parameter $\left(z = \frac{x-\mu}{\sigma}\right)$

2.2. Model selection techniques

There are several ways of defining the 'most suitable fit' or 'optimum' distribution for flood frequency analysis. Haddad and Rahman (2010) mentioned that multiple criteria, which take into account which of the selected distributions provides the best estimation accuracy with reduced uncertain. Each of the criteria has own pros and cons, which are related to the true distribution, the size of the available sample, probability model type, parameter estimation method. Among various techniques, Anderson Darling test (AD), Akaike Information Criterion (AIC), Bayesian Information Criterion (BIC), Chi-squared (χ^2), Cramér–von Mises (CvM) test, Kolmogorov-Smirnov (KS) test are the most widely used methods in hydrology field. Laio et. al. (2009) suggested that at least two model selection techniques (e.g. AIC or BIC with AD) should be used for a more reliable selection of the best fitted distribution. In this study, five model selection techniques, namely AD, AIC, BIC, CvM and KS, are considered. The general formulas of the considered techniques are given by;

$$AD = -n - \frac{1}{n}\sum_{i=1}^{n}[(2i-1)\ln(F(x_i)) + (2n+1-2i)\ln(1-F(x_i))] \quad (1)$$

$$AIC = -2\mathrm{L} + 2k \quad (2)$$

$$BIC = -2\,log\,L + klog(n) \tag{3}$$

$$CvM = \frac{1}{12n} + \sum_{i=1}^{n}\left[F(x_i) - \frac{2i-1}{2n}\right]^2 \tag{4}$$

$$KS = max|F(x_i) - \bar{F}(x_i)| \tag{5}$$

In these formulas, n is the number of observations, $F(x_i)$ denoted cumulative distribution function of the distribution, L is the log-likelihood maximized function, k is the number of the distribution parameters and

3. STUDY AREA and DATA USED

The Coruh basin, which is located in northeastern Turkey, was selected as the study area. The basin comprises 19,748 km^2 of drainage area, which is approximately 2.53% of Turkey and it can be defined as three main sub-basins, namely lower, middle and upper. The total length of Çoruh River is 431 km and it is the fastest flowing river in Turkey (Buyukyildiz, 2014). The Çoruh basin and its rivers have a high economic importance to Turkey because it is largely undeveloped but has economically exploitable hydropower potential (Berkun, 2010). During last decade, a number of dams and hydroelectric power plants (HEPP) have been planned and some are under construction while some are already in operation. In the present study, annual peak flow records of gauge station 2135 are used for flood modelling. The main reason for using peak flow data of this station is that the gauge station is located in at the entrance of Yusufeli dam and hydro-electric project which is located in the middle part of the basin. With a storage capacity of 2.13x10^9 m^3 and a double-curvature arch dam with a height of 270 m, it is one of the largest dam of a multidam project in North East Turkey. Location map of the Coruh basin, the gauge station and Yusufeli dam is given in Figure 1.

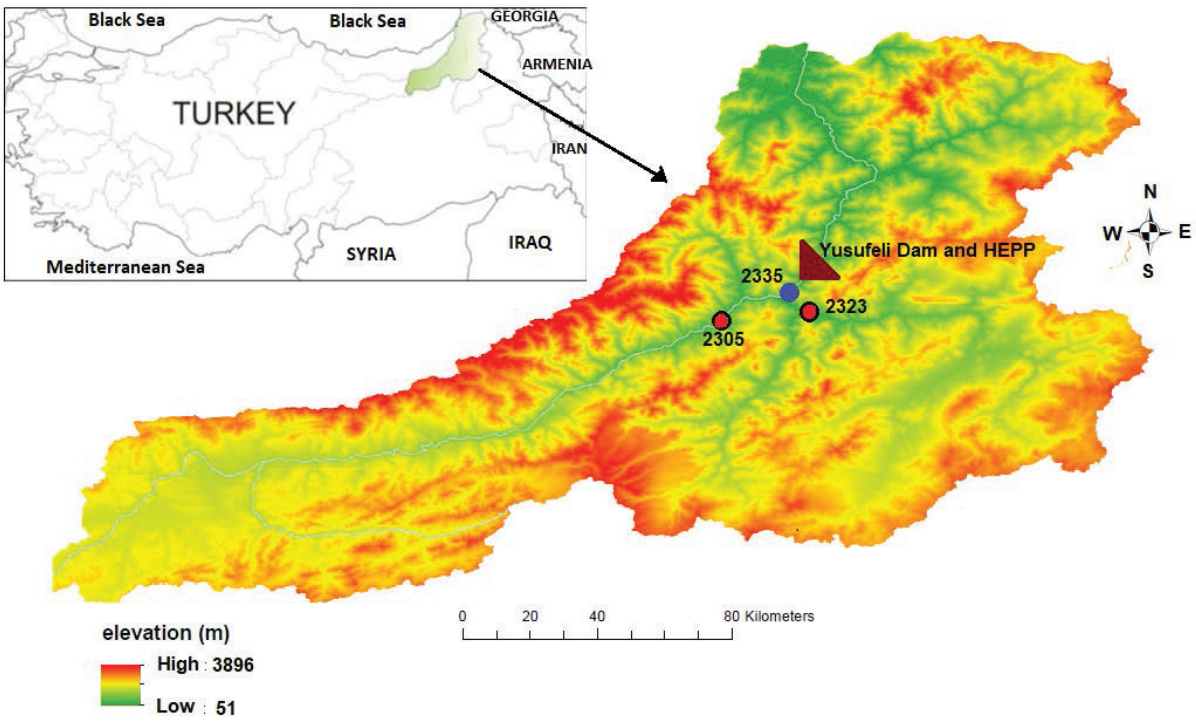

Figure 1. Location map of the study area (Çoruh basin) and gauge stations used in this study

3.1. Preliminary Data Analysis

In this study, annual instantaneous peak flows covering of period 1993–2011 from are considered flood modelling. It is worth to remember that record length must be 25 years at least in order to ensure validity of the modelling results statistically. To have statistically valid observation length (for period of 1987-2011), we used univariate and multivariate regression models. Annual peak flow records of the stations 2305 and 2323, which have a very strong positive correlation with the record of the station 2335, were used as inputs of the regression models. To define the best regression model, determination coefficient (R^2) and Root Mean Square Error (RMSE), which can be computed as follows, were used.

$$R^2=1-\frac{SSE}{SS_Y} \qquad SSE=\sum_{i=1}^{n} e_i^2 \qquad \text{and} \qquad SS_Y=\sum_{i=1}^{n}(y_i-\bar{y})^2 \tag{6}$$

$$RMSE=\sqrt{\frac{1}{n}\sum_{i=1}^{n}(y_i-\hat{y}_i)} \tag{7}$$

Where, y_i denotes observations and $\hat{y}_i$ are estimated values using the regression model. Minimum value of RMSE and highest R^2 indicate the best model. Summary of the developed regression models is given in Table 1.

Table 2. RMSE and R^2 values of the developed regression models

Output station	Input station	RMSE	R^2
2335	2305	124.591	0.811
2335	2323	127.482	0.802
2335	2305 and 2323	98.749	0.881

Based on the results that provided the Table 1, the best regression model can be written as;

$$Q_{2335} = 0.1481 + 0.6836 \times Q_{2305} + 0.4342 \times Q_{2325} + e \tag{8}$$

It is worth noting that the linear regression analysis requires all variables to be multivariate normal. Hence, prior to fit regression models to the data sets, we used logarithmic transformation fulfill the normality requirement. After computing Q values in Eq.(8), an inverse logarithmic transformation was used to obtain real annual peak flows (Figure 2).

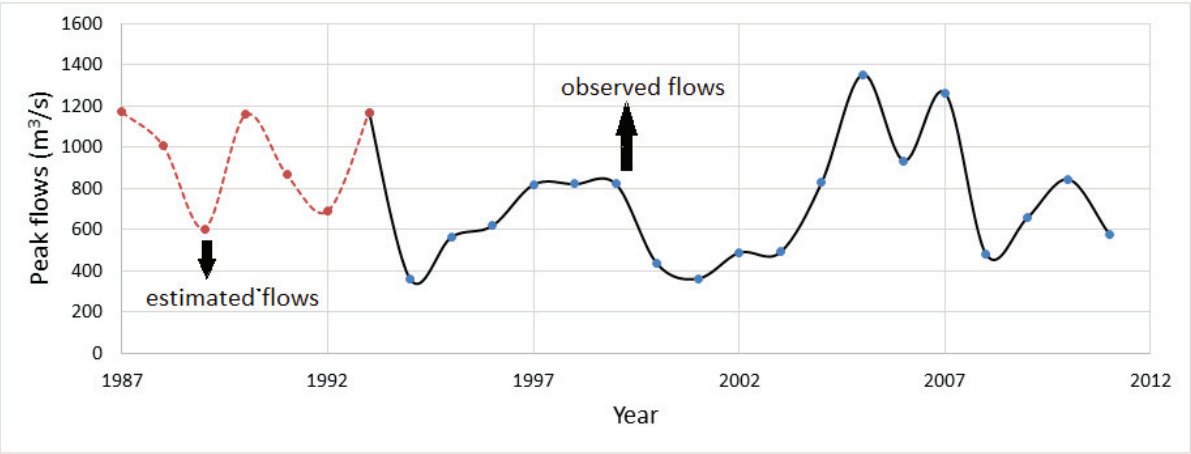

Figure 2. Time series of the annual instantaneous peak flows of the station 2335

4. RESULTS

4.1. Stationarity and Independence Tests

In this part of the study, stationarity and independence, which are essential assumptions in conventional flood frequency analysis, was checked. The Mann-Kendall trend test was used to evaluate stationarity while simple autocorrelation function was employed for independence analysis. Trend test results and autocorrelation plot are presented in Table 3 and Figure 3, respectively. From the table 3, it can be seen that the considered data series do not show significant decreasing or increasing trend, which implies that the data is stationary. Also, it is obvious from the Figure 3 that the computed autocorrelation coefficients (from 0 to 20 lags) are within the 95 % confidence limit and it implies independence of the data series.

Table 3. Mann-Kendall test results (stationarity analysis)

Station Number	MK test statistic (S)	Computed Z value	Critical value of Z (α=0.05)	Trend
2335	-27	-0.607	±1.96	No

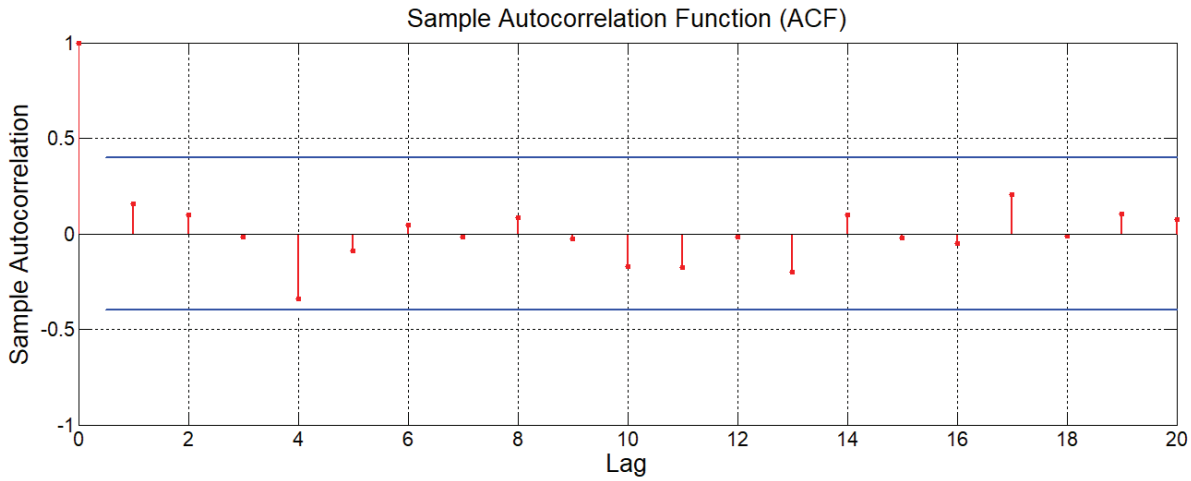

Figure 3. Autocorrelation plots of the annual peak flow series (independence analysis)

4.2. Performance evaluation of Probability distributions

After proving existence of the stationarity and independence in the data series, Weibull (WBL), two parameter (LN2) and three parameter Lognormal (LN3), Gamma (GAM), Pearson type-III (P3), Normal (NORM), Extreme Value type-1 (EV1), Generalized Extreme Value (GEV), Logistic (LOGIS) and log-Logistic (LLOGIS) were fitted. Their parameters were estimated using the maximum likelihood method. Performances of the candidate distributions were compared by means of the AD, AIC, BIC, CvM and KS criterions and their test statistics for each distribution were computed. The results are given in Table 3.

Table 3. Results of the model selection methods for the candidate probability distributions

	WBL	LN2	GAM	LOGIS	NORM	EV1	GEV	LLOGIS	P3	LN3
AD	0.3858	0.3258	**0.3189**	0.4531	0.4709	0.3294	0.3469	0.3474	0.3307	0.3268
CvM	0.0581	0.0501	**0.0484**	0.0612	0.0705	0.0510	0.0525	0.0531	0.0493	0.0503
KS	**0.1047**	0.1483	0.1271	0.1154	0.1123	0.1467	0.1307	0.1453	0.1571	0.1484
AIC	356.13	355.45	**355.25**	358.81	357.20	355.73	357.57	357.25	356.59	357.45
BIC	358.57	357.89	**357.69**	361.24	359.63	358.17	361.22	359.68	360.24	361.10

The best fitted distributions are shown in bold.

Based on the model selection results, the Gamma and Weibull distributions were found to be the most suitable models for describing annual peak flow records. The four criterions (AD, CvM, AIC and BIC) produced the minimum value for Gamma while only KS test provided the lowest statistic value for Weibull distribution. Hence, the Gamma and Weibull distributions were selected as the best fitted and second fitted models, respectively. For visual evaluation, probability density function (PDF) and cumulative distribution function (CDF) of the Gamma and Weibull distributions against the empirical PDF and CDFs were plotted in Figure 4.

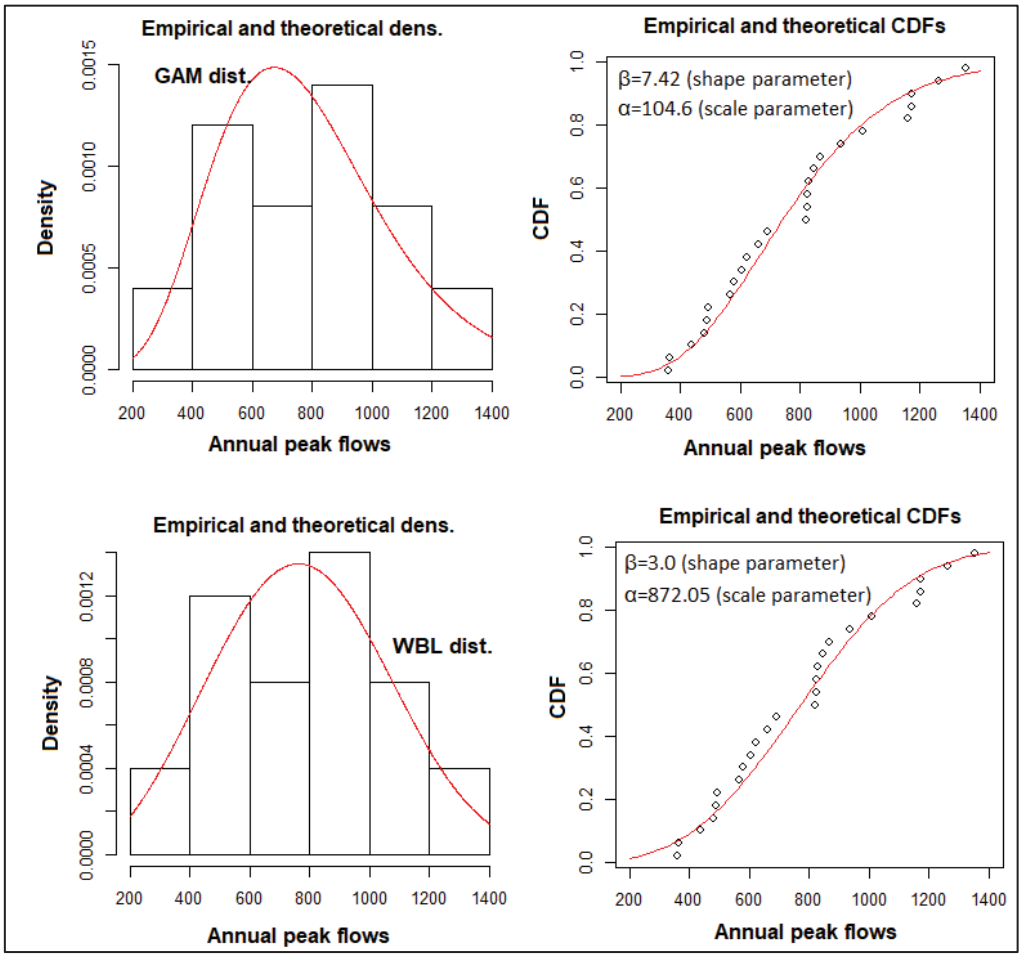

Figure 4. Empirical and theoretical PDF and CDF plots of the best fitted distributions

4.3. Quantile estimation

After acquiring the best-fitted probability distribution for annual peak flows of the station 2335, it can be easily used to calculate quantile estimates for different return periods or conversely, to estimate the return period for a certain peak flow magnitude. The return period exceeding a given flood magnitude can be computed as;

$$T(q) = \frac{1}{P(Q > q)} = \frac{1}{1 - P(Q \leq q)} = \frac{1}{1 - F(q)} \quad (9)$$

Where $\boldsymbol{F(q)}$ denotes the cumulative distribution function. The rarer the event is, the lower its probability of exceedance and therefore the greater its return period. Then, magnitude q for any return period is evaluated in a straight forward manner by replacing F by its value from Eq. (9). In this study, annual peak flow quantiles were computed for 10, 20, 50, 100 and 200, 500, 1000 and 10000 years. 95% confidence bands of the computed quantiles were also calculated and the results are given in Table 4.

Table 4. The estimated peak flow quantiles (with 95% confidence bands) for different return periods

		Gamma distribution			Weibull distribution		
T	**P**	**LB (m^3/s)**	**Point (m^3/s)**	**UB (m^3/s)**	**LB (m^3/s)**	**Point (m^3/s)**	**UB (m^3/s)**
10	0.9	976	1157	1371	1005	1152	1321
20	0.95	1077	1297	1562	1086	1258	1456
50	0.98	1195	1467	1800	1171	1375	1614
100	0.99	1278	1588	1973	1224	1452	1722
200	0.995	1356	1704	2141	1271	1521	1822
500	0.998	1454	1851	2357	1325	1605	1944
1000	0.999	1524	1959	2518	1361	1662	2030
10000	0.9999	1746	2302	3034	1465	1830	2286

LB: Lower bound at 5% level of significance.
UB: Upper bound at 5% level of significance.

5. CONCLUSIONS

In order to obtain safe and economical dam design, precise estimation of project flow values for various return periods is needed. For instance, maximum peak flows corresponding to 10-25-50-100 years are used to design diversion structures while the design of spillways needs flow values of 1000-10 000 years. In the present study, we aim to compute flood values that can be useful for designing hydraulic structures in Çoruh basin. For this purpose, ten commonly used probability distribution functions are employed for modelling annual peak flow time series from one station, which is located in the entrance of Yusufeli dam. Based on the five model selection methods, it was found that the annual peak flow data were best fit with the Gamma and Weibull distributions. Finally, the best fitted distributions were used to calculate peak flow quantiles that have recurrence intervals of 10, 20, 50, 100 and 200, 500, 1000 and 10000 years. The authors believe that the calculated peak flow values can be used by decision makers in planning and design of hydraulic structures (e.g. spillway) in the Yusufeli dam.

ACKNOWLEDGMENTS

The authors sincerely thank the General Directorate of State Hydraulic Works, Turkey for providing the annual instantaneous peak flow records used in this study.

REFERENCES

Afreen, S., Muhammad, F. 2012. “Flood frequency analysis of various dams and barrages in Pakistan”. Irrigation and Drainage, vol. 61, pp.116–128.

Berkun, M. 2010 “Hydroelectric potential and environmental effects of multidam hydropower projects in Turkey”. Energy for Sustainable Development, vol.14, pp. 320–329.

Buyukyidiz, M. 2014. “Monthly streamflow time series modelling of Coruh River”. International Scientific Conference People, Buildings and Environment, Kroměříž, Czech Republic.

Buyukkaracigan, N., Kahya, E. 2009. “Flood frequency analysıs of annual peak flows in Konya basin streams”. Technical Sciences Journal of Technical-Online, vol. 8(3), pp. 246-261.

Can, I., Tosunoglu, F. 2013. “Estimating T-year flood confidence intervals of rivers in Coruh Basin, Turkey.” Journal of Flood Risk Management, vol. 6(3), pp.186–196.

Haddad, K., Rahman, A. 2010. “Selection of the best fit flood frequency distribution and parameter estimation procedure: a case study for Tasmania in Australia”. Stochastic Environmental Research Risk Assessment, vol. 25(3), pp.415–428.

Haktanir, T., 1991. “Statistical modelling of annual maximum flows in Turkish rivers”. Hydrological Sciences Journal, vol.36(4), pp. 367-389.

Laio, F., Di Baldassarre, G., Montanari, A. 2009. “Model selection techniques for the frequency analysis of hydrological extremes.” Water Resources Research, vol. 45(7), W07416.

Li, Z., Wang, Y., Zhao, W., Xu, Z., Li, Z. 2016. **“**Frequency analysis of high flow extremes in the Yingluoxia watershed in Northwest China”. Water, vol.(8), pp.1-15.

Opere, A.O., Mkhandi, S., Willems, P. 2006. “At site flood frequency analysis for the Nile equatorial basins”. Physics and Chemistry of the Earth, vol. 31, pp.919-927.

Seçkin, N., Yurtal, R., Haktanir, T., Dogan, A. 2010. “Comparison of probability weighted moments and maximum likelihood methods used in flood frequency analysis for Ceyhan river basin”. Arabian Journal for Science and Engineering. vol. 35(1), pp.49–69.

5th International Symposium on Dam Safety

October 27-31, 2018

INVESTIGATING THE LONG-TERM PROSPECTS OF PRECIPITATION AND COMPARISON BETWEEN GFDL-ESM2G AND MIROC-ESM MODELS IN KASHAFROOD RIVER BASIN

Armin AHMADİ [1], Abbas Ali GHEZELSOFLOO[2] Amirhossein Aghakhani AFSHAR[3]

ABSTRACT

The rivers condition in arid and semi-arid area extremely effected by climate change and rainfall patterns. The purpose of this study is to investigate the impacts of climate change on precipitation in Kashafrood river Basin (KB) in northeast of Iran by using Soil and Water Assessment Tool (SWAT) in historical period (1995-2011) and future periods: near future (2014-2042), intermediate future (2043-2071) and far future (2072-2100). The precipitation was analyzed and compared by MIROC-ESM and GFDL-ESM2G models in the Coupled Model Intercomparison Project Phase 5 (CMIP5) under two Representative Concentration Pathways (RCP) scenarios (RCP2.6 and RCP8.5). In order to calibrate and validate the hydrologic models in 5 runoff stations, Sequential Uncertainty Fitting Program (SUFI-2) was used. The results indicate that SWAT models is suitable for assessing water resources components in this basin. Also, climate change impacts on this area shows that precipitation in GFDL-ESM2G model under RCP2.6 and RCP8.5 comparing between future periods and the historical period increasing about 29.2-60.6% and mentioned component in MIROC-ESM model tends to increase around 4.9-48.6% in the future periods. Furthermore, GFD-ESM2G model comparing to MIROC-ESM model in RCP2.6 (RCP8.5) in near, intermediate and far future periods increases 23.15% (8.08%), 27.84% (12.13%) and 18.69% (23.13%), respectively.

Keywords: Climate change, CMIP5, RCPs, Precipitation, SWAT.

INTRODUCTION

The influence of climate change on water resource availability for human consumption has drawn the attention of scientists all over the world (Zuo et al. 2015; Rodrigues et al. 2014; Faramarzi et al. 2009). In the context of climate change and changes in precipitation frequency (Zuo et al., 2015), studies have shown global warming has led to ecosystem degradation and water crisis (Falkenmark and Rockström 2006) and exacerbated water scarcity in the arid and semi-arid regions. More than 600 million people are currently living in the areas with less than 500 m^3 per capita, thus enduring severe shortage of water (Pereira et al. 2009). Therefore, there are a great deal of researches concerning the

[1] Student, Department of Civil Engineering, Mashhad Branch, Islamic Azad University, Mashhad, Iran,
e-posta: armin.mailbox@gmail.com
[2] Assistant Professor, Department of Civil Engineering, Mashhad Branch, Islamic Azad University, Mashhad, Iran,
e-posta: ghezelsofloo@gmail.com
[3] Postgraduate, Department of Water Engineering, Faculty of Civil Engineering, University of Tabriz, Tabriz, Iran,
e-posta: a.s.a.a.6269@gmail.com

increasing threat of water scarcity at regional and global scales (Vörösmarty et al. 2010). As a result, in the context of global warming, a comprehensive assessment of water resources is a vital part of understanding the availability of water and improving water management towards sustainable, efficient, and equitable use of scarce freshwater resources. Furthermore, climate change has been a main influencing factor on water resources in river basin and there has been an interaction between climate change and water resources (Faramarzi et al. 2009). Climate change also influences the spatial and temporal variability of water resources in a basin (Vörösmarty et al. 2010). Due to the high variation and low rate of precipitation in arid and semi-arid area such as KR, it can directly or indirectly impacts many sectors of the economy and can lead to severe human losses (Anyamba et al. 2014). Many studies are available for precipitation assessment on global and regional scale (Pal et al. 2004; Shongwe et al. 2009; Sillmann et al. 2013; Sylla et al. 2010; Chen 2013; Singh et al. 2014; Giorgi et al. 2014). but a new focus is needed on the catchment scale (Rockström et al. 2010). Iran is a country located in arid and semi-arid climates of the Middle East region mostly characterized by low rainfall and high temperature as a result of higher evapotranspiration demand. Its water balance is relatively delicate threatened by water scarcity that can significantly aggravate due to climate change (IPCC 2007). Arguably, climate change is one of the major challenges confronting Iran; its adverse effects on water resources can impact the environment and the economy, particularly the agricultural sector. There is a strong demand from decision makers for predictions about the potential impacts of climate change on the interval and amount of precipitation, which have consequences on sustaining and managing water resources appropriately and diminishing water scarcity problem that has become noticeable (Ternik et al. 2013). In Northeast of Iran, Kashafrood River is the longest river in this region and providing surface water for Mashhad city. Due to its extreme dry weather this basin has been suffering from water scarcity and pollution (Aghakhani Afshar et al. 2016). Up to now, water scarcity related to climate change in the Kashafrood catchment have not been well considered in analysis of climate change and climate policy construction. Therefore, the main objective of this study has been to assess the potential future climatic changes on the precipitation in KB and based on phase 5 of the Coupled Model Intercomparison Project (CMIP5; Taylor et al. 2012). The Soil and Water Assessment Tool (SWAT) as a semi-distributed hydrological model has been used to provide more insights into the mechanisms of land surface and hydrological processes and are regarded as a powerful tool for simulating hydrological processes and assessing the effects of climate change on water resources spatiotemporally (developed by United States Department of Agriculture (USDA); Arnold et al. 1998). For sensitivity analysis we applied SUFI-2. SUFI-2 is a tool, multi-site calibration, and uncertainty analysis and it is capable of analyzing a huge number of parameters and measured data from many gauging stations simultaneously. SUFI-2 algorithm is efficient when we are dealing with computationally intensive, complex large-scale models and it is easily linked to SWAT (In the SWAT-CUP software). For impact assessment studies and reliable future simulations, scientists have to rely on models. For example, the General Circulation Models (GCMs) provide numerical simulations of the global climate system, while hydrological models are physically-based numerical models for simulating regional hydrological processes. The main objective of this study is first to calibrate and validate a hydrologic model in a large-scale basin in Iran with uncertainty analysis. The second objective is to estimate the amount of precipitation at the sub-basin level on a monthly time-step considering the impact of water resources management practices in Kashafrood river basin.

MATERIAL AND METHODS

The study area is situated in the northeastern part of Iran in Razavi Khorasan Province (RKP), namely the Kashafrood Basin (KB). KB is the biggest watershed in RKP with area of 16870 km^2 and known as a large-scale watershed. Kashafrood River is the longest river in this area and its total length is about 285 km. Geographically, KB is located approximately between latitudes 35° 35′ N and 37° 07′ N and longitudes 58° 15′ E and 61° 13′ E (Figure. 1). The catchment topographical elevation varies from 390 m above sea level in the southeast part to 3302 m above sea level in the northwest part, with a mean elevation of 1846 m above sea level and a mean slope is 4.7%. Due to mountainous

topographical conditions, Climate of KB is cold, semi-arid with low annual rainfalls as well high evapotranspiration in summer. The mean annual precipitation of the area is measured about 340 mm with high spatial variation. Also, the mean annual maximum and minimum temperatures are 20.6 and 7.1 °C, respectively (Afshar et al. 2017). Therefore, focusing on the climate change is important in this area for the present and also future time periods. In this study, input data consist of Digital Elevation Model (DEM), land-use map from IRS satellite imagery (Based on field investigation), soil map, climatologic data (containing 34 rainfall stations, 12 temperature stations located inside the basin for 1992 to 2011) and Monthly runoff data (Sar Asiab Shandiz (SARASSHA), Zire Band Golestan (ZIRBAGOL), Golestan Jaghargh (GOLHAGHR), Hesar Dehbar (HESDEHB) and Kartian (KARTIAN)) are required. Torogh and Kardeh dams are respectively lies in south and north of Mashhad as a most populated city in this area providing water for agricultural and drinking sectors (Fig. 1). Fig. 1 shows the topography KB, and the location of gauging and meteorological stations. Also, land-use map in the KB (presented in Fig. 2) is distributed as follows: pasture (50.9%), agricultural land-generic (28.6%), winter wheat (15.6%) and others such as forest, urban, range and water (4.9%) Heterogeneous mix of silt, sand and clay is predominant soil type at the northern and center part of watershed, whereas, dominant soil type of the eastern and southern of basin are silt and clay (Afshar et al. 2017).

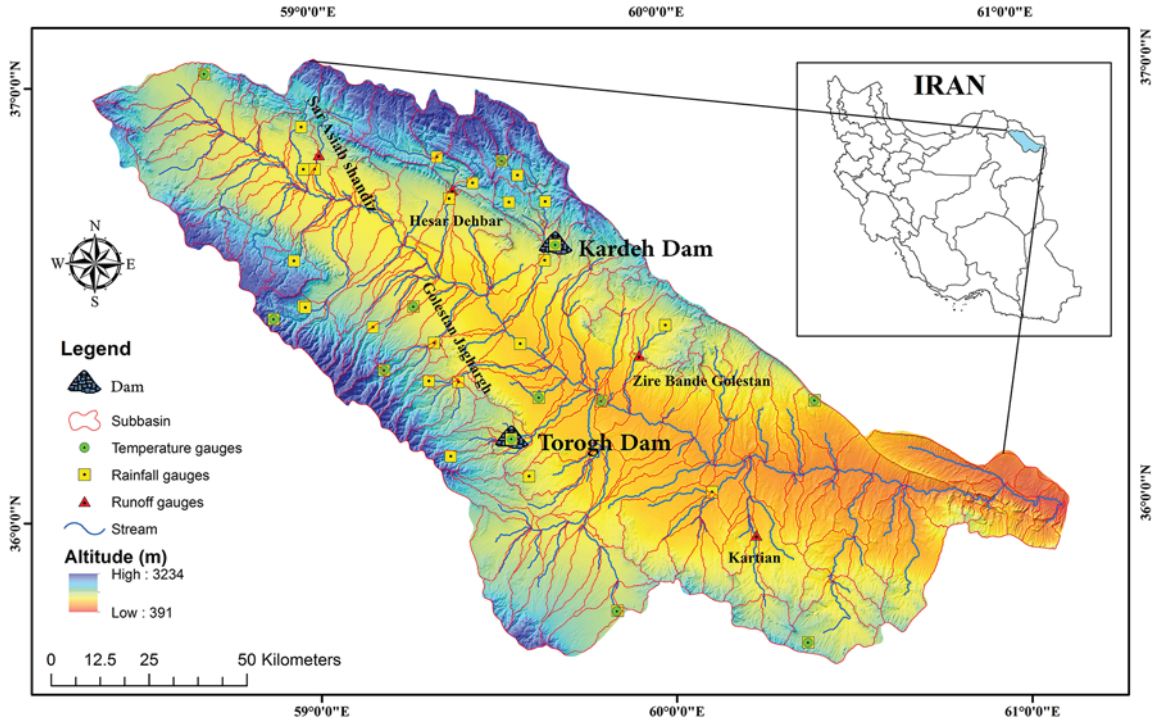

Figure 1. DEM (digital elevation model) map and the location of gauging and meteorological stations in KRB.

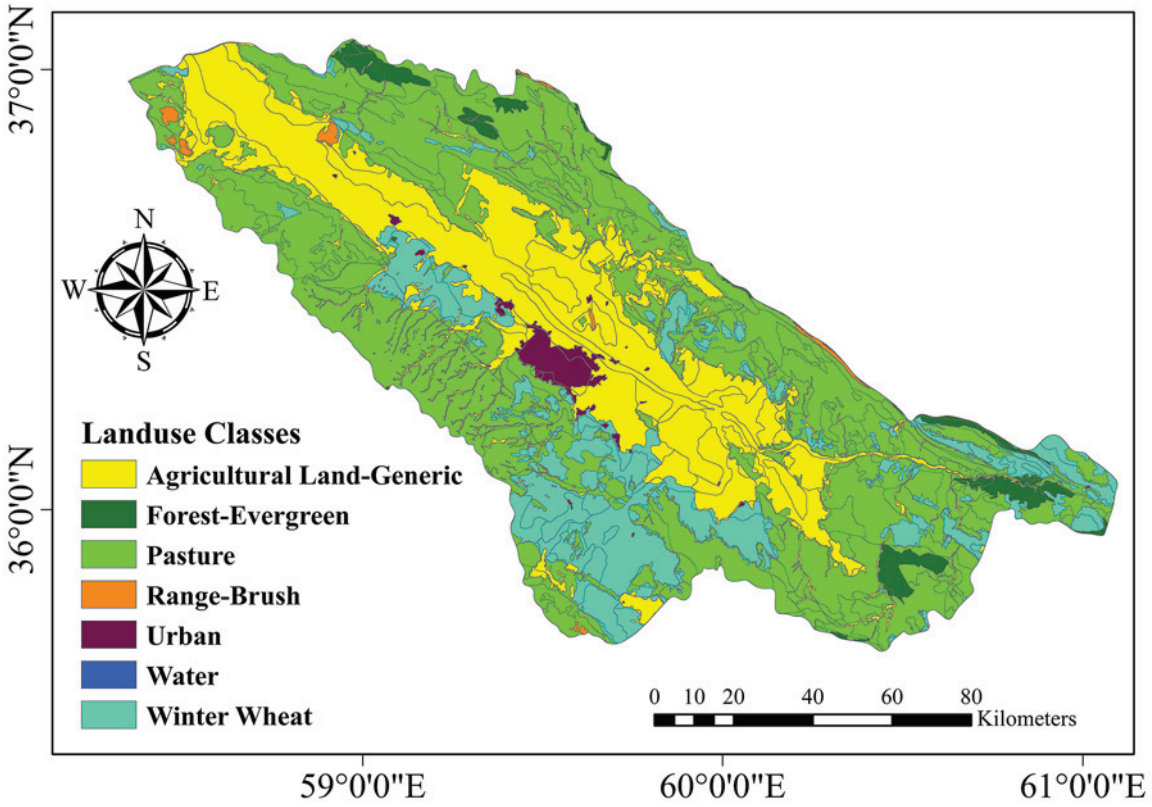

Figure 2. Land use map of Kashhafrood river basin

The SWAT model which operates at a daily time step for simulating the precipitation was used in this study. Digital Elevation Model (DEM) is used in SWAT model to delineate a river basin. The delineated river basin is divided into sub-basins, which are further divided into unique land-use/soil/slope units called Hydrologic Response Units (HRUs). The delineation of HRUs are performed by superimposing the soil, land use and slope map. In this study, the watershed is divided into 217 sub-basins and with a threshold area of 4852 hectares and the total of 635 HRUs was defined in the model with threshold values of 20, 20 and 10% for land-use, soil and slope class, respectively. Then, for slope discretization, the multiple slope option with two classes of 0-21 and >21% was selected. (Afshar et al. 2017)

SUFI-2 optimization algorithm was applied for parameter estimation and sensitivity analysis. Identifying the sensitive parameters in the watershed was the primary objective of calibration to controls the runoff. According to all parameters constant and then varying each parameter within the prior range (One-at-a-time method) the sensitivity analysis was carried out. Each model consists of uncertainty in predictions due to the uncertainty associated with input data and model parameters. SUFI-2 algorithm can narrow down the range of uncertainty by identifying a range of parameters that reduce overall uncertainty in the output. The model output is quantified by 95% prediction uncertainty (95PPU) calculated at 2.5% and 97.5%. The performance of SWAT model was evaluated by using the goodness-of-fit criteria, such as coefficient of determination (R^2), Nash-Sutcliffe Efficiency (NS), R and P-factor. R-factor is the ratio of average thickness of 95PPU band to standard deviation of observed data, whereas P-factor is the percentage of observed data enclosed in 95PPU (Abbaspour et al. 2007). The maximum value of P-factor is 1, which means 100% of the observed data is bracketed by the 95PPU. The lower value of the R-factor indicates better model performance. The overall time period used in our analysis is 1992–2011. The first three years (1992–1995) were used as warm-up period to alleviate the effects of unknown initial conditions and subsequently this time period is excluded from the analysis. We divided the discharge data set into two periods 1995–2000 (Validation period) and 2001–2011 (Calibration period).

In CMIP5 outputs, Sixty-one climate change models were used to simulate the present and future climates all over the world. Then, 14 models were selected to be used in this study. Table 1

summarized the general information and name of associated institutions on each of the 14 models. CMIP5 unlike the CMIP3, uses the new Representative Concentration Pathways (RCPs) which is provided in Table 2. The RCPs according to their radiative forcing level by 2100 are named. These scenarios include four RCP scenarios named RCP2.6, RCP4.5, RCP6.0, and RCP8.5 (Van Vuuren et al. 2011). Also, the RCP2.6 and RCP8.5 were used in this study to investigate the future climate impacts in precipitation. In the present study, in order to downscale the precipitation data BCSD method was chosen (Aghakhani Afshar et al. 2016), therefore, all outputs of the 14 Models of the fifth report were downscaled into grids of 0.5 degrees resolution to have a better comparison between simulated and observed data.

Table 1. GCMs (Global Climate Models) used in this study.

Model name	Organization
HadGEM2-ES	MOHC, Met Office Hadley Centre, UK
GFDL-CM3	NOAA, Geophysical Fluid Dynamics Laboratory, USA
GFDL-ESM2M	
GFDL-ESM2G	
MIROC5	MIROC, Centre for Climate System Research, Japan
MIROC-ESM	
MIROC-ESM-CHEM	
IPSL-CM5A-LR	IPSL, Institute Pierre Simon Laplace, France
IPSL-CM5A-MR	
NorESM1-M	NCC, Norwegian Climate Centre, Norway
BCC-CSM1.1	BCC, Beijing Climate Centre, China
CSIRO-Mk3.6.0	CSIRO-QCCCE, Commonwealth Scientific and Industrial Research
CCSM4	NCAR, National Center for Atmospheric Research, USA
CESM1(CAM5)	NSF-DOE-NCAR, Community Earth System Model Contributors

Table 2. Overview of representative concentration pathways (RCPs).

RCPs	Scenario
2.6	Peak in radiative forcing at ~3:1 Wm2 (~490 ppm CO2 equivalent) before 2100 and then decline (the selected pathway declines to 2.6Wm2 by 2100)
4.5	Stabilization without overshoot pathway to 4.5 Wm2 (~650 ppm CO2 equivalent) at stabilization after 2100
6.0	Stabilization without overshoot pathway to 6 Wm2 at (~850 ppm CO2 equivalent) stabilization after 2100
8.5	Rising radiative forcing pathway leading to 8.5 Wm2 (~1370 ppm CO2 equivalent) by 2100

After downscaling the climatic data of 34 rainfall and 12 temperature stations for the mentioned CMIP5 models, the following steps were taken to select the best CMIP5 models which are the most adapted ones to the observed data (Aghakhani Afshar et al. 2016):

First, the historical data of 4 stations in the vicinity of each of the reference stations (Observational stations) with intervals of 0.5 degrees were extracted by using ArcGIS. Then by using Inverse Distance Weight (IDW) as an interpolation method, the historical data of reference stations were obtained having the information of 4 stations in the vicinity. After that, according to the precipitation data as an important component in the climate subject and using the Thiessen's polygon averaging method, the fifth Assessment Report (AR5) models were evaluated with Nash-Sutcliffe Efficiency (NS), Percent of Bias (PBIAS), Coefficient of determination (R^2) and Ratio of the root mean square error to the standard deviation of measured (RSR) criteria. Regarding the values of the

performance parameters in table 3, it was set up for a performance rating of the simulation models (Moriasi et al. 2007).

$$NS = 1 - \frac{\sum_{t=1}^{T}(x_{obs,t} - y_{model,t})^2}{\sum_{t=1}^{T}(x_{obs,t} - \bar{x}_{obs})^2} \quad (1)$$

$$PBIAS = \frac{\sum_{t=1}^{T}(x_{obs,t} - y_{model,t})}{\sum_{t=1}^{T} x_{obs,t}} \times 100 \quad (2)$$

$$R^2 = \left\{ \frac{\sum_{t=1}^{T}(x_{obs,t} - \bar{x}_{obs}) \times (y_{model,t} - \bar{y}_{model})}{\left[\sum_{t=1}^{T}(x_{obs,t} - \bar{x}_{obs})^2\right]^{0.5} \times \left[\sum_{t=1}^{T}(y_{model,t} - \bar{y}_{model})^2\right]^{0.5}} \right\}^2 \quad (3)$$

$$RSR = \frac{\sqrt{\sum_{t=1}^{T}(x_{obs,t} - y_{model,t})^2}}{\sqrt{\sum_{t=1}^{T}(x_{obs,t} - \bar{x}_{obs})^2}} \quad (4)$$

Where in these equations, $x_{obs,t}$ and y_{model} are the observed and CMIP5 model simulation values at time unit of t, $\bar{x}_{obs}$ and $\bar{y}_{model}$ are the mean of observed and simulated data values at the entire time period of the evaluation.

Finally, MIROC-ESM and GFDL-ESM2G were selected as the best climate models (Table 4) based on the values introduced in Table 3.

Table 3. Model performance ratings based on the range of NS, PBIAS, R2 and RSR values.

Rating	NS	PBIAS	R2	RSR
Very Good (VG)	0.75 < NS ≤ 1.00	PBIAS ≤ ±10.00	0.866 ≤ R2 < 1.00	0 ≤ RSR ≤ 0.5
Good (G)	0.65 < NS ≤ 0.75	±10 ≤ PBIAS < ±15	0.733 ≤ R2 < 0.866	0.5 < RSR ≤ 0.6
Satisfactory (S)	0.50 < NS ≤ 0.65	±15 ≤ PBIAS < ±25	0.60 ≤ R2 < 0.733	0.6 < RSR ≤ 0.7
Unsatisfactory	NS < 0.50	PBIAS ≥ ±25	R2 < 0.6	RSR > 0.7

Table 4. Performance of evaluation criteria for CMIP5 models.

Models	Criteria Evaluation			
	NS	PBIAS	R^2	RSR
HadGEM2-ES	0.57 (S)	-17.15 (S)	0.69 (S)	0.73 (US)
IPSL-CM5A-LR	0.71 (G)	-15.65 (S)	0.81 (G)	0.61 (S)
NorESM1-M	0.88 (VG)	-4.74	0.92	0.51 (G)
BCC-CSM1.1	0.62 (S)	-11.01 (G)	0.74 (G)	0.67 (S)
CCSM4	0.43 (US)	-28.15	0.52	0.79 (US)
MIROC-ESM	***0.95 (VG)***	***-2.88***	***0.97***	***0.33 (VG)***
CSIRO-MK3.6.0	0.51 (S)	-27.44	0.60 (S)	0.71 (US)
GFDL-ESM2M	0.66 (G)	-10.4 (G)	0.79 (G)	0.64 (S)
GFDL-ESM2G	***0.92 (VG)***	***-2.93***	***0.94***	***0.37 (VG)***
CESM1(CAM5)	0.55 (S)	-26.36	0.63 (S)	0.68 (S)
GFDL-CM3	0.48 (US)	-26.03	0.54	0.74 (US)
MIROC-ESM-	0.78 (VG)	-5.25	0.71 (S)	0.66 (S)
IPSL-CM5A-MR	0.85 (VG)	-4.96	0.85 (G)	0.46 (VG)
MIROC5	0.60 (S)	-25.75	0.71 (S)	0.68 (S)

- VG: Very Good, G: Good, S: Satisfactory and US: Unsatisfactory

RESULTS AND DISCUSSIONS

Calibration, sensitivity analysis was performed on 29 parameters. The sensitivity analysis shows that most of the 20 parameters of hydrology are sensitive to river discharge. These parameters are presented in Table 5. These sensitive parameters have a vital role for the model calibration and parameter changes during iteration processes. In SUFI-2, after each iteration the goodness-of-fit between the observed and simulation runoff discharge is calculated. Then new parameter ranges are suggested for next iterations. All processes of calibration and validation have been done with twenty parameters with NS as an objective function for each of the 5 runoff stations separately. Also, the minimum value of objective function threshold for the behavioral samples is chosen to be 0.5. Simulation number of 500 is set for each iteration was chosen for uncertainty analysis until the performance criteria were satisfied (Abbaspour et al. 2007). The final range of the posterior parameters after 6 successive iterations (Totally 3000 runs) as well the fitted values of parameter are listed in Table 5.

Table 5. Most sensitive parameters used for the SWAT model development.

Parameters	range	Parameters	range	Parameters	range
SFTMP	-1.81 to -1	PCPMM	-0.325 to -0.177	ESCO	0.41 to 0.501
SMTMP	-1.92 to -0.95	CN2	0.197 to 0.281	SLSUBBSN	96.5 to 109.5
SMFMN	7.5 to 8.95	SHALLST	460.8 to 510.5	SURLAG	9.6 to 12.2
SOL_K	-0.32 to -0.15	SOL_AWC	0.21 to 0.28	ALPHA_BF	0 to 0.08
SOL_BD	-0.167 to -0.095	GW_DELA	132.7 to 159	TIMP	0.5 to 0.7
CH_K2	101.5 to 114	GW_REVA	0.085 to 0.115	RCHRG_D	0.229 to 0.32
CH_N2	0.102 to 0.13	EPCO	0.29 to 0.41		

Figure 3 presented the uncertainty analysis results of SUFI-2 for the calibration and validation periods at the 5 main hydrological stations in the KB and also, the shaded band (95PPU) contains all uncertainties from the different sources. The simulated result and measured monthly discharges shows that the SWAT model overestimated low flow and underestimated peak flow for some years especially in the recession part during the simulation period (Figure 3). The reason of that might be caused by measuring the input data and associating with the model. By considering the residuals and the statistical results, the model is ready for validation analysis. According to the Table 6, the model performance criteria were quite satisfactory for such a large-scale basin and SWAT model set-up is suitable to evaluate the precipitation in the KB.

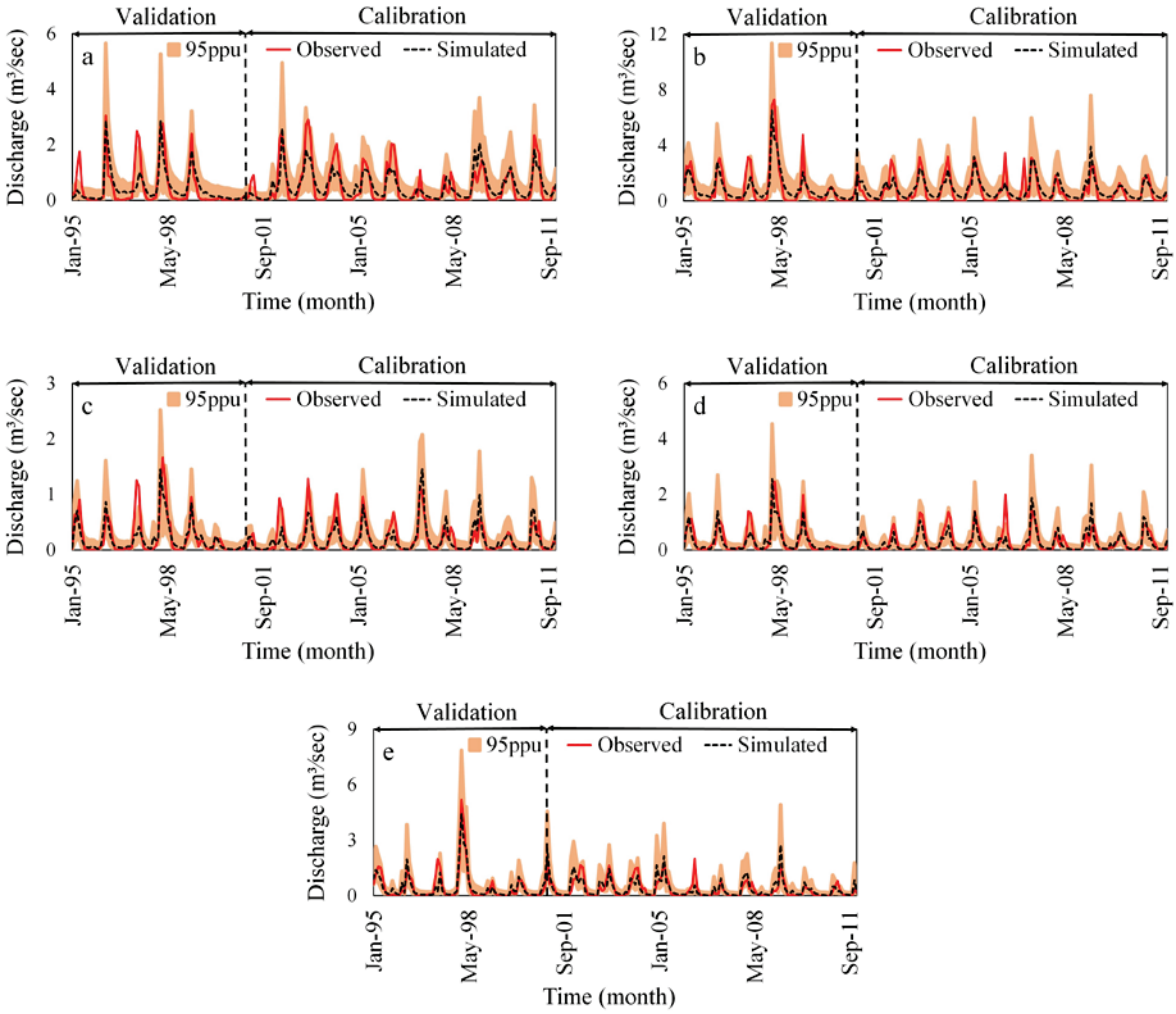

Figure 3. Calibration and validation of SWAT model at: a) SARASSHA, b) ZIRBAGOL, c) GOLJAGHR, d) HESDEHB and e) KARTIAN.

Table 6. Goodness-of-fit statistics between modeled and observed runoff for stations.

Stations	Calibration Period				Validation period			
	R^2	NS	R-	P-	R^2	NS	R-	P-
SARASSH	0.7	0.7	1.10	0.57	0.6	0.6	0.96	0.56
ZIRBAGOL	0.6	0.6	1.29	0.58	0.8	0.8	0.92	0.65
GOLJAGH	0.6	0.6	0.95	0.63	0.7	0.7	0.81	0.64
HESDEHB	0.6	0.6	0.92	0.74	0.8	0.8	0.75	0.78
KARTIAN	0.6	0.6	0.90	0.66	0.8	0.8	0.58	0.67

The spatial variations of precipitation in KB during the historical future time periods (2014-2042, 2043-2071, and 2072-2100) in MIROC-ESM and GFDL-ESM2G models under both scenarios (RCP 2.6 and RCP 8.5) are presented in Fig. 4, 5, and 6.

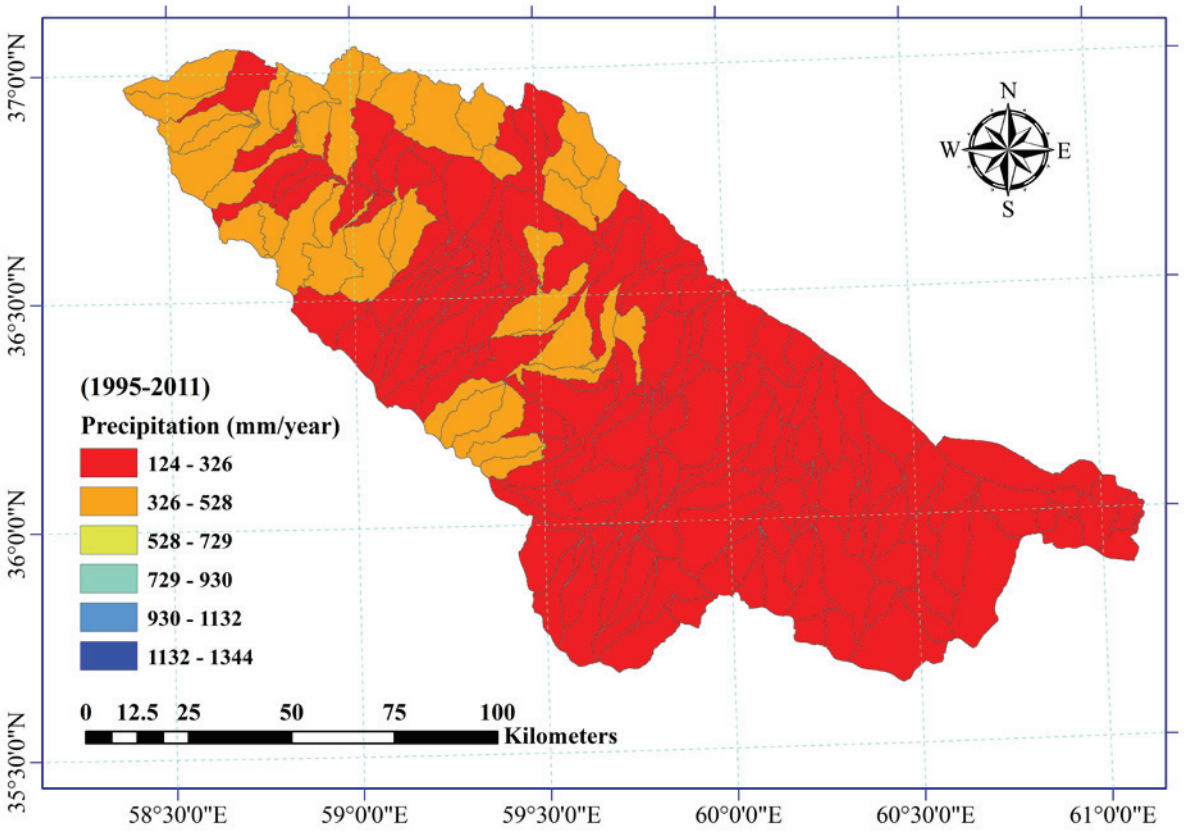

Figure 4. Spatial distribution of precipitation over the KB in historical period.

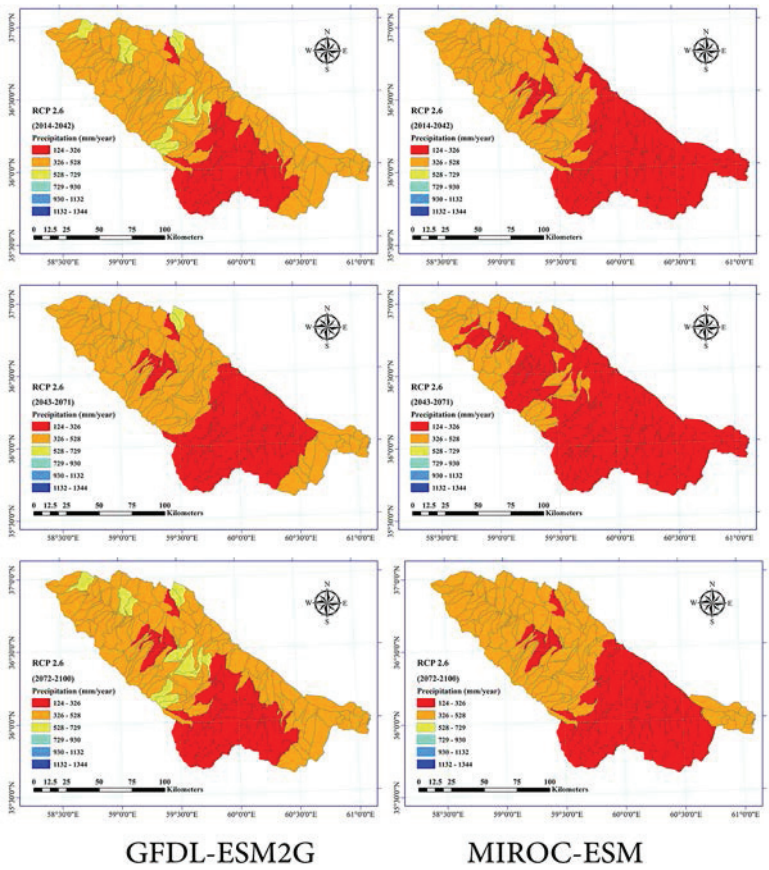

Figure 5. Spatial distribution of precipitation over the KB for both models and under RCP 2.6 in future periods.

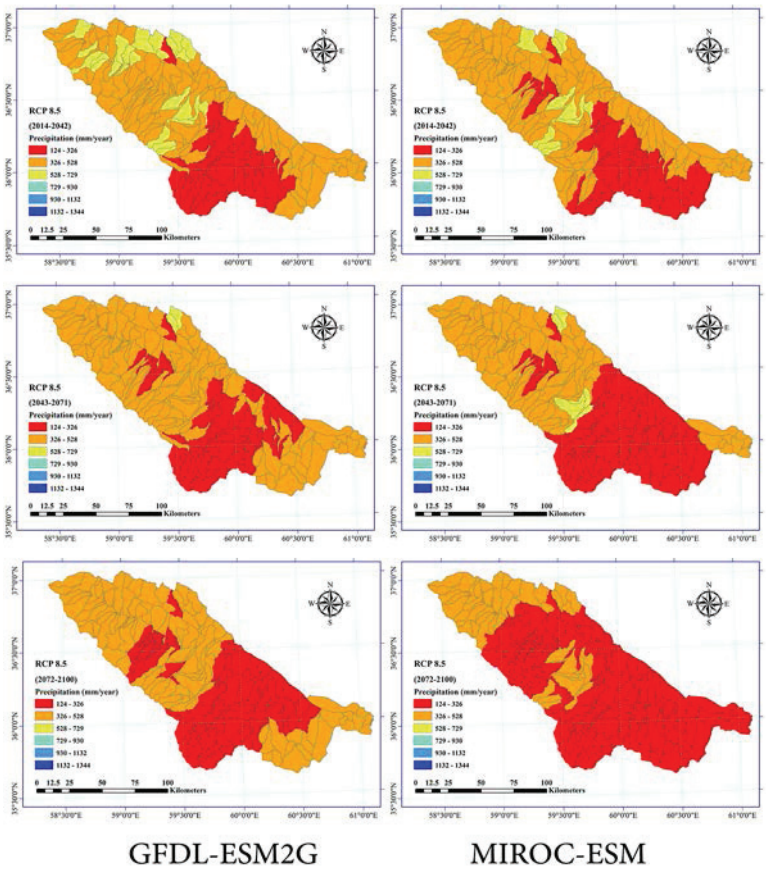

Figure 6. **Spatial distribution of precipitation over the KB for both models and under RCP 8.5 in future periods.**

The simulation results shows that in the northern part of the values of precipitation would be higher than the southern part. The results shows almost the same pattern for different time periods. However, there are some differences in sub-basin scale and amount of precipitation. The mean annual precipitation in near future under RCP 2.6 (RCP 8.5) in GFDL-ESM2G and MIROC-ESM models respectively is about 393 (402) and 319 (372) mm/year. Beside, in intermediate future period the mean value of this component under RCP 2.6 and RCP 8.5 in GFDL-ESM2G (MIROC-ESM) simulated about 348 (272) and 373 (332) mm/year, respectively. Mean annual precipitation in far future period simulated by GFDL-ESM2G (MIROC-ESM) model under RCP 2.6 and RCP 8.5 is about 394 (332) and 323 (263) mm/year. The results shows that in near and intermediate periods in both models under RCP 8.5 amount of precipitation simulated higher than RCP 2.6, while in far future under RCP 2.6 the mean annual of the mentioned component simulated higher than the other scenario. Furthermore, the average annual precipitation is calculated by GFDL-ESM2G model in KB in all future periods and under both scenarios is higher than the other selected model. By comparing the amount of precipitation in historical and future periods the condition of the study area will be improved and in all future periods precipitation will increase.

CONCLUSION

The SWAT model and SUFI-2 Algorithm in this study was successfully applied to quantify the precipitation in KB at different spatial and monthly time step. Calibration and validation of the model in five hydrometric stations represented a good performance of the model in simulation of hydrological processes. In comparison between GFDL-ESM2G with MIROC-ESM In near, intermediate, and far future periods under RCP 2.6 (RCP 8.5) GFDL-ESM2G estimated the mean annual precipitation about 23.1% (8%), 27.8% (12.1%), and 18.6% (23.1%) more than the other

model. the results of this study may provide reliable information about precipitation on sub-basin scale for policymakers.

REFERENCE

Abbaspour, K.C., Yang, J., Maximov, I., Siber, R., Bogner, K., Mieleitner, J., Zobrist, J. and Srinivasan, R. (2007). Modelling Hydrology and Water Quality in the Pre-Alpine/Alpine Thur Watershed Using SWAT, Journal of Hydrology, 333(413-430), doi:10.1016/j.jhydrol.2006.09.014.

Afshar, A. A., Hassanzadeh, Y., Pourreza-Bilondi, M., & Ahmadi, A. (2017). Analyzing long-term spatial variability of blue and green water footprints in a semi-arid mountainous basin with MIROC-ESM model (case study: Kashafrood River Basin, Iran). Theoretical and Applied Climatology, 1-15.

Aghakhani Afshar, A., Hassanzadeh, Y., Besalatpour, A.A. and Pourreza-Bilondi, M. (2016). Climate change forecasting in a mountainous data scarce watershed using CMIP5 models under representative concentration pathways, Journal of Theoretical and Applied Climatology, 125(3-4), 1-17, doi: 10.1007/s00704-016-1908-5.

Anyamba, A., Small, J. L., Britch, S. C., Tucker, C. J., Pak, E. W., Reynolds, C. A., ... & Linthicum, K. J. (2014). Recent weather extremes and impacts on agricultural production and vector-borne disease outbreak patterns. PloS one, 9(3), e92538.

Chen, H. (2013). Projected change in extreme rainfall events in China by the end of the 21st century using CMIP5 models. Chinese Science Bulletin, 58(12), 1462-1472.

Falkenmark M, Rockström J (2006). The new blue and green water paradigm: breaking new ground for water resources planning and management. J Water Resources Planning and Management. 132:129–132.

Faramarzi M, Abbaspour KC, Schulin R, Yang H (2009). Modeling blue and green water resources availability in Iran. J Hydrological Processes. 23:486–501.

Giorgi, F., Coppola, E., Raffaele, F., Diro, G. T., Fuentes-Franco, R., Giuliani, G., ... & Torma, C. (2014). Changes in extremes and hydroclimatic regimes in the CREMA ensemble projections. Climatic change, 125(1), 39-51.

IPCC (2007). Climate Change 2007: Impacts, Adaptation, and Vulnerability. Exit EPA Disclaimer Contribution of Working Group II to the Third Assessment Report of the Intergovernmental Panel on Climate Change, edited by ML. Parry et al. Cambridge University Press. Cambridge. UK.

Moriasi D, Arnold JG, Van Liew M, Bingner R, Harmel R, Veith T (2007). Model Evaluation Guidelines for Systematic Quantification of Accuracy in Watershed Simulations. J Soil and Water Division of American Society of Agricultural and Biological Engineers, 50:885-900.

Pal, J. S., Giorgi, F., & Bi, X. (2004). Consistency of recent European summer precipitation trends and extremes with future regional climate projections. Geophysical Research Letters, 31(13).

Pereira LS, Cordery I, Iacovides I (2009). Coping with Water Scarcity: addressing the challenges. Springer Verlag: Dordrecht. doi: 10.1007/978-1-4020-9579-5.

Rockström J, Karlberg L, Wani SP (2010). Managing water in rainfed agriculture—the need for a paradigm shift. J Agricultural Water Management. 97:543–550.

Rodrigues DB, Gupta HV, Mendiondo EM (2014). A blue/green water based accounting framework for assessment of water security. J Water Resources Research. 50:7187–7205.

Shongwe, M. E., Van Oldenborgh, G. J., Van Den Hurk, B. J. J. M., De Boer, B., Coelho, C. A. S., & Van Aalst, M. K. (2009). Projected changes in mean and extreme precipitation in Africa under global warming. Part I: Southern Africa. Journal of climate, 22(13), 3819-3837.

Sillmann, J., Kharin, V. V., Zwiers, F. W., Zhang, X., & Bronaugh, D. (2013). Climate extremes indices in the CMIP5 multimodel ensemble: Part 2. Future climate projections. Journal of Geophysical Research: Atmospheres, 118(6), 2473-2493.

Singh, D., Tsiang, M., Rajaratnam, B., & Diffenbaugh, N. S. (2014). Observed changes in extreme wet and dry spells during the South Asian summer monsoon season. Nature Climate Change, 4(6), 456.

Sylla, M. B., Gaye, A. T., Jenkins, G. S., Pal, J. S., & Giorgi, F. (2010). Consistency of projected drought over the Sahel with changes in the monsoon circulation and extremes in a regional climate model projections. Journal of Geophysical Research: Atmospheres, 115(D16)

Taylor, K. E., Stouffer, R. J., & Meehl, G. A. (2012). An overview of CMIP5 and the experiment design. Bulletin of the American Meteorological Society, 93(4), 485-498.

Terink W, Immerzeel WW, Droogers P (2013). Climate change projections of precipitation and reference evapotranspiration for the Middle East and Northern Africa until 2050. International Journal of Climatology 33(14):3055-3072.

Van Vuuren DP, Edmonds J, Kainuma M, Riahi K, Thomson A, Hibbard K, Hurtt GC, Kram T, Krey V, Lamarque JF, Masui T, Meinshausen M, Nakicenovic N, Smith SJ, Rose SK (2011). The representative concentration pathways: an overview. J Climatic Change. 109:5–31.

Vörösmarty CJ, Mclntyre PB, Gessner MO, Duegeon D (2010). Global threats to human water security and river biodiversity. J Nature. 467:555–561.

Zuo D, Xu Z, Peng D, Song J, Cheng L, Wei S, Abbaspour KC, Yang H (2015). Simulating spatiotemporal variability of blue and green water resources availability with uncertainty analysis. J Hydrological Processes. 29:1942–1955.

5th International Symposium on Dam Safety

October 27-31, 2018

HOW TO CONSTRUCT A LARGE-SCALE DISTORTED PHYSICAL MODEL TO REALISTICALLY STUDY DAM BREAK FLOWS

Gökmen TAYFUR[1], M. Şükrü GÜNEY , Gökçen BOMBAR , Tanıl ARKIS

ABSTRACT

This paper, step by step, describes how to build a realistic distorted physical model of a real dam to study dam break flows. The construction involves several stages; (1) designing, and construction of (2) infrastructure, (3) dam reservoir, (4) dam body, (5) downstream area, (6) Creek and highway, and (7) town buildings. Designing stage involves the selection of actual dam whose model needs to fit to the available space at chosen horizontal and vertical scales and it has a settlement at the downstream section. To construct infrastructure, dam reservoir, dam body and downstream sections; topographic maps, bathymetry, land use maps, settlement maps, and hydrological reports are required. Also, required are the construction machines and material (iron bars, metal poles, cement, bricks, roof cover panels, etc.), granular filling material (sand, gravel, soil, etc), metal sheets and welding machine to build cross-sections and thus reflect the actual topography, pipes, canal and drainage hole to collect surface flows, wooden material for reflecting buildings, motor and lifting mechanism to lift dam body. Building the cross-sections (transects) and placing them at the right place at the right elevation in the physical model was a tedious and delicate work. So was the concreting and smoothing the surface such that it reflects the actual topography of prototype and the roof to protect the model from climatic conditions. All these require willingness of government agencies to provide data, hydrological maps, hydrological reports, and residential and topographical maps, field trips, skilled technicians, patience, talent and man and machine power. Drainage of experimental flows and surface flows due to rainfall were achieved with the constructed drainage system. The surface topography of upstream reservoir and downstream section were replicated as close as possible and infiltration was prevented by the right surface treatment of the experimental area.

Keywords: Distorted model, Physical model, Design, Upstream reservoir, Dam body, Downstream area, Urkmez Town, Urkmez Dam

INTRODUCTION

Dam break flow simulations, in the literature, has been commonly performed in a laboratory flume. For sudden break simulations, a moveable metal gate is used (Fig.1). When the gate in a flume is in place water backs up the gate, then the gate is suddenly lifted resulting in sudden dam break flows.

[1] Dept. Civil Engineering , Izmir Institute of Technology Urla, Izmir, Turkey
Email: gokmentayfur@iyte.edu.tr

Figure 1. Dam break experiment using movable metal gate in a laboratory flume
(https://www.google.com.tr/search?q=laboratory+dam+break+flow+experiment+photo)

Using the similar setup in Figure 1, Palumbo et al (2008) made dam break flow experiments on moveable bed using 6 m long flume. Greco et al (2008) studied gradual dam break flows using a flume. Instead of a gate, they build a dam body constructed from a compacted sand (Fig.2).

Figure 2. Gradual dam break experiment using compacted sand dam body in a laboratory flume
(https://www.google.com.tr/search?q=laboratory+dam+break+flow+experiment+photo)

Morris et al (2008) took further step by building a dam body in a field right at downstream section of an actual dam (Fig.3a). It was an earth filled dam having 6 m height (see Fig. 3b). They also constructed the scaled model of the physical dam model in the laboratory for more controlled and detailed investigation (Fig.3c).

(a)

(b)

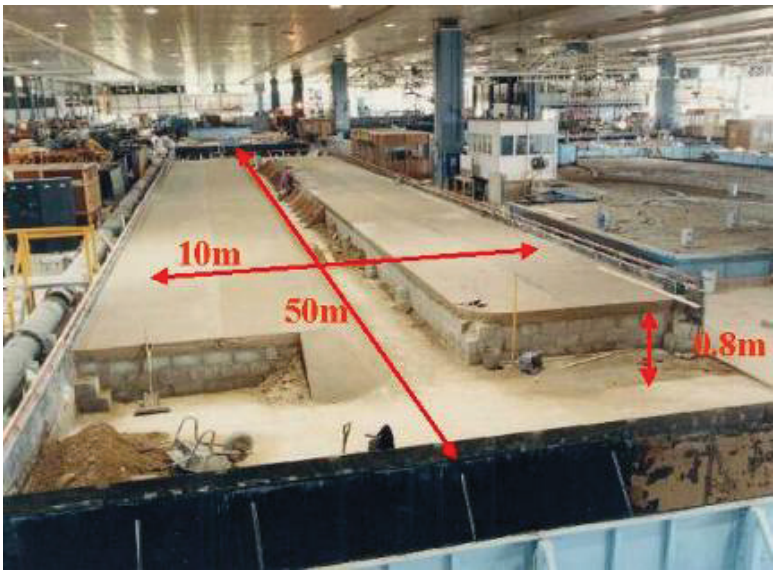

(c)

Figure 3. (a) The place of experimental dam in the field, (b) Dam break experiment in the field, and (c) Dam break experiment in the laboratory (Morris et al. 2008)

Laboratory dam break flow experiments having a settlement at downstream section has also been attempted with simple experiments. For example; Frazao and Zech (2007) used a system as depicted in Fig.4 where there is a single object right at the downstream section. Their system is simple set up in a laboratory flume having moveable gate, as described in Fig.1

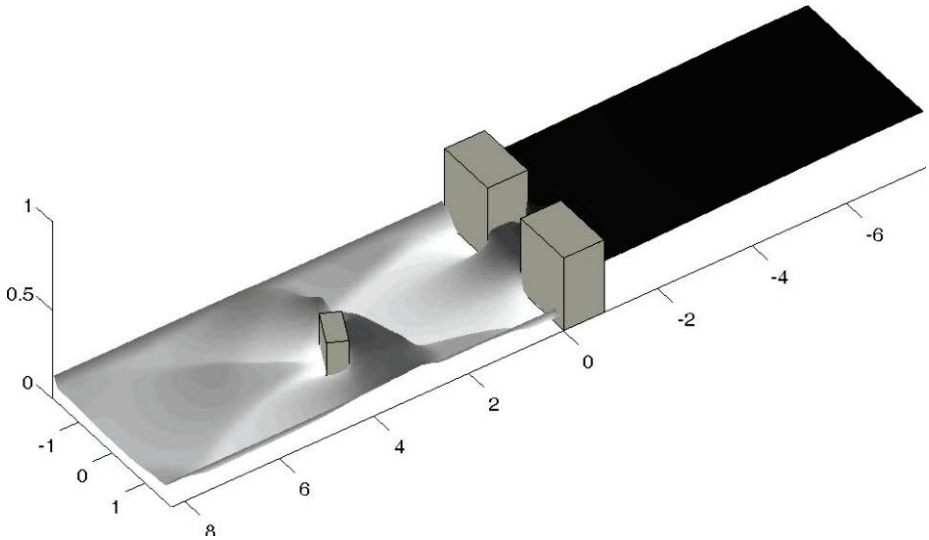

Figure 4. Schematic representation of an experimental set up (Frazao and Zech 2007)

Testa et al (2007) built a better representation of a dam break flow experiments having a settlement at downstream section (Fig.5). Their physical model tried to reflect the creek and the flooding area with topographical detail, to a certain extend. The creek was built 50 m long as having a concrete surface. The settlement area was reflected in a simple fashion with 14 cubic concrete objects having 15 cm side length. They were placed in an ordered fashion as shown in Fig.5. The tank was used for dam reservoir. Although, it is a more realistic representation as compared to the other experiments, it is still a simple design since the dam reservoir and the buildings were not represented in a realistic manner. Furthermore, the topography of the downstream area is not detailed.

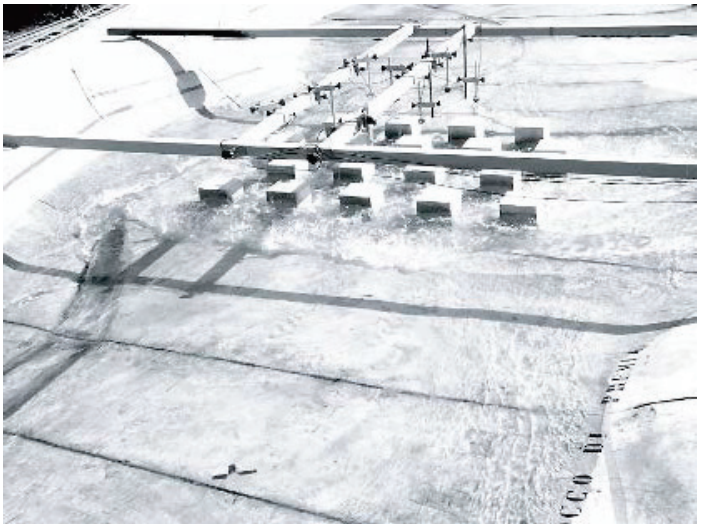

Figure 5. Experimental set up (Testa et al 2007)

As summarized above, dam break flow experiments had been generally carried out in a laboratory flume using a moveable gate or a simple sand compacted dam body. Few studies had attempted to reflect the reality to a certain extend. To the knowledge of the authors, there is no dam flow experiments; reflecting actual dam reservoir, dam body and downstream area with actual topography and settlements. Such a work requires a distorted physical model design. This study is presenting such a work which may be the first very comprehensive physical dam break flow model in the world. It could be beneficial for those who may be planning to construct such physical model in the sense that it would save time and guide them with respect to designing, required material and apparatus, construction details and procedures, etc.

DISTORTED PHYSICAL MODEL CONSTRUCTION

A distorted physical model comprising dam reservoir, dam body and the village at its downstream was designed and constructed in the scope of TUBİTAK 110M240 project to investigate the flood wave propagation due to dam break (Guney et al 2013, 2014, 2015). Construction of this distorted physical model involves several steps, such as (1) designing, and construction of (2) infrastructure, (3) dam reservoir, (4) dam body, (5) downstream section (creek, road), (6) buildings.

Designing Stage

At this stage, one needs to first consider the available space for the model to be constructed and accordingly the actual dam to be chosen. The dam, including its upstream and downstream sections, needs to be at a right size such that its physical model can fit to the available space. For this purpose, one needs to pay attention to the horizontal and vertical scales. If one were to use the same scale for both horizontal and vertical directions, in contrast to the upstream and downstream sections, dam body height would be too short and accordingly water level behind the dam body would be too shallow such that the dam break flood wave cannot even be generated to measure flow depths and velocities. Therefore, the model needs to be constructed as distorted. Second, if the objective is to study the dam break flow effects on urban areas, then there should be settlement at its downstream section. Urkmez Dam satisfied this criteria due to two reasons: (1) it fits to 300 m^2 available space at Dokuz Eylul University (DEU), Hydraulic Laboratory open area, with 1/150 horizontal and 1/30 vertical scales, (2) there is Urkmez Town, with its 10000 population (becomes 20000 in summer time) at its downstream area. Figure 6 shows the dam reservoir, dam body, and Urkmez town. Figure 7 shows the available open space at Hydraulics Laboratory of DEU. Table 1 summarizes the geometric characteristics of Urkmez Dam (prototype) (dam reservoir and dam body) and its distorted physical model, with the applied vertical and horizontal scales. For example; an object with a size of 6 m height and 75 m length in prototype would be reflected in the distorted physical model with dimensions of 20 cm height and 50 cm length. A flow depth measured 10 cm in the physical model experiment corresponds to 3 m height flooding depth in the field.

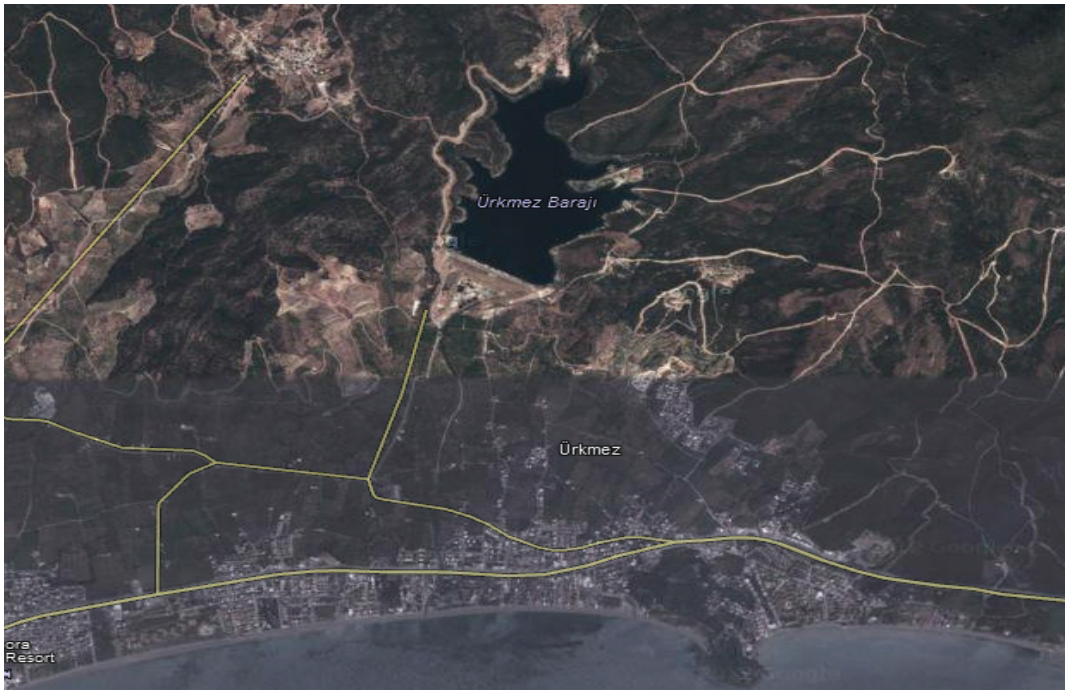

Figure 6. The general view of the studied area (maps.google.com)

Figure 7. Available space for the physical model construction

Table 1. The geometric characteristics of the prototype and physical model

Characteristics	Prototype	Physical model
Crest length (m)	426	2.84
Crest width (m)	12	0.08
Dam height from base(m)	32	1.07
Lake volume at minimum level (m^3)	375 000	0.556
Lake volume at maximum level (m^3)	8 625 000	12.778
Lake volume at normal level (m^3)	7 950 000	11.778
Lake active volume (m^3)	7 575 000	11.222

Infrastructure

Infrastructure is an important part of the model. It should be constructed carefully such that it should carry the heavy weight of the physical model and drain the experimental flows. First, drainage pipes are placed. One needs to make simple computation so that the chosen size of pipes can drain the area. For the drainage purpose, 300 mm diameter 2 pipes were first placed in the experimental area (Fig.8). The bottom floor on which the physical model is constructed was first leveled, filled with fine gravel and then compacted (Fig.9). Before pouring the concrete, canal for collecting the surface waters and drainage hole for entrance of drainage pipes are to be constructed (Fig.10). The compacted surface was placed with iron bars of 8 mm diameter and a concrete was poured over and leveled (Fig.11). The constructed of drainage system successfully drained the experimental flows and surface flows due to rainfall. The compacted surface supported by the iron bars and concrete was strong enough to carry the whole load on it.

Figure 8. Placement of drainage pipes

Figure 9. Leveling ground

Figure 10. Canal and drainage hole for draining surface water

Figure 11. Pouring concrete

Dam Reservoir

To construct the dam reservoir, the cross sections at every 50 m are first determined by using the related maps obtained from DSI (State Hydraulics Works). Then, they are drawn for the distorted model considering the scales (Fig.12).

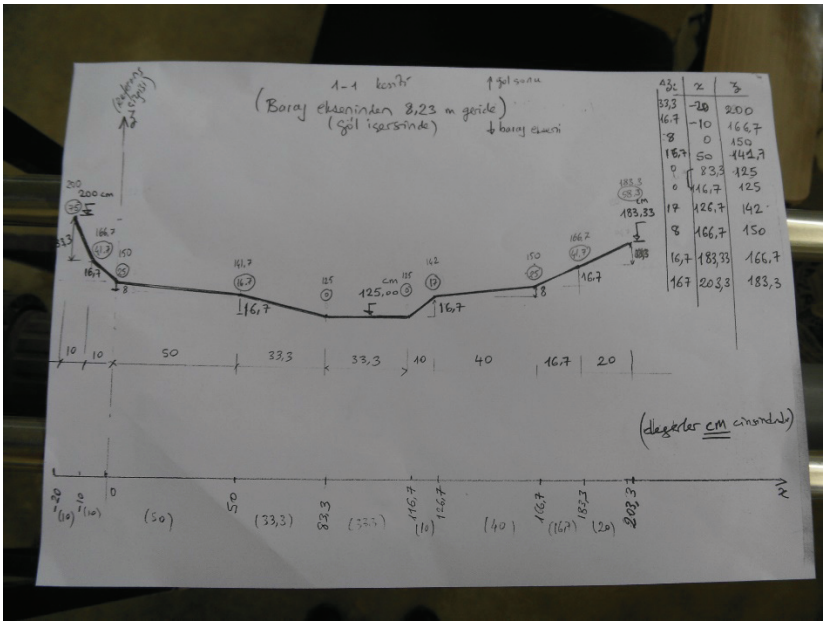

Figure 12 Drawing of an intersect (cross-section)

Once the cross-sections were drawn, they were then manufactured in the laboratory using metal sheets and welding (Fig.13).

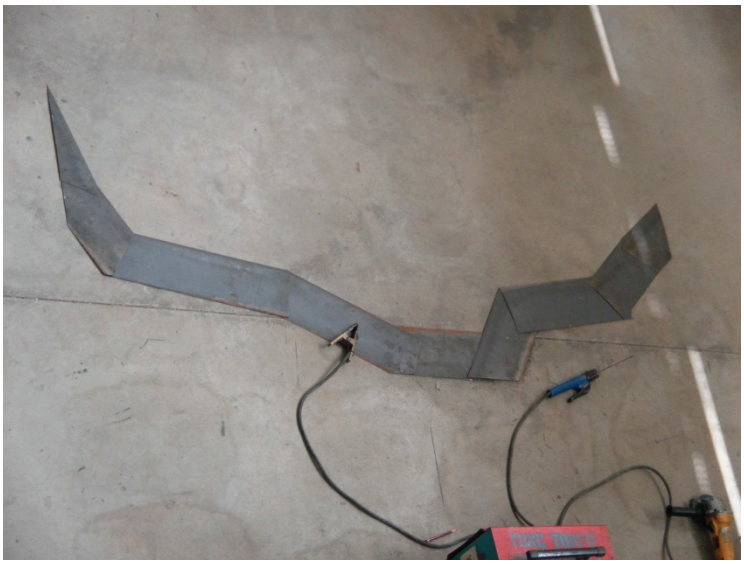

Figure 13. Construction a cross-section using metal sheet

The manufactured cross sections were then placed in the experimental area at the pre-specified related locations (Fig.14).

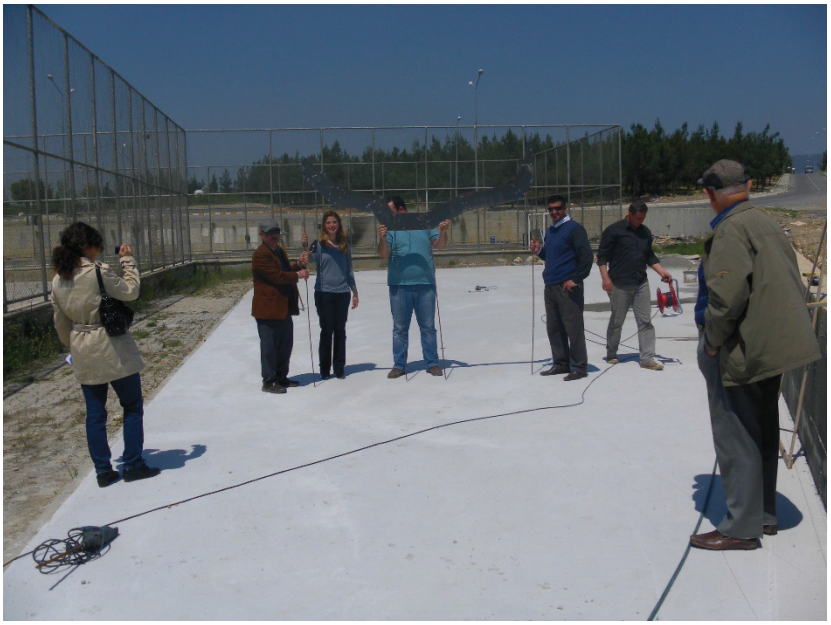

Figure 14. Placement of a metal sheet cross-section

Thus, dam reservoir was first built by placing all the metal cross sections, connecting them together (Fig.15). Construction of metal cross-sections and placement in the filed require masonry skills. The one in Figures 15 and 16 is a very skilled technician at the Hydraulics lab of DEU.

Figure 15. Placement of metal sheets for dam reservoir

Then, brick walls around the reservoir were built (Fig.16). Then the reservoir is filled with granular material (Fig.17).

Figure 16. Construction of brick wall around the dam reservoir

Figure 17. Filling granular material at dam reservoir

A concrete was then poured over the surface and smoothed to exactly replicate the topography of the reservoir (Fig. 18). The surface was treated in order to prevent any infiltration. The final view of the dam reservoir is presented in Figure 19.

Figure 18. Pouring concrete at dam reservoir

Figure 19. Final view of dam reservoir

The major concern at this stage was to replicate the topographic surface as close as possible and not to allow any infiltration of water from the reservoir. These were carefully achieved.

Downstream Section

The same procedure used in the construction of a dam reservoir is applied to construct the topography of the downstream area, including Urkmez Creek and the Highway (see Figures 20-25). For the Creek and Highway construction, field trips were carried out several times to see them in place. Impermeable surface was also achieved in the downstream section.

Figure 20. Placement of metal bars cross sections

Figure 21. Filling granular material before concrete pouring

Figure 22. Concrete pouring

Figure 23. Leveling surface

Figure 24. Downstream topography and the Creek view

Figure 25 View of highway

Urkmez Town

By the help of the maps obtained from Izmir Water and Sewage Department (IZSU), the residential area of Urkmez town was created together with the road and bridge, following the distorted scales, in the downstream area, using wooden material (Fig.26). The wooden blocks were cut into rectangular prismatic pieces at dimensions of residential buildings and houses, following the vertical and horizontal scales. Then, each piece is glued and screwed into its respective spot on the concrete floor. 10 cm height corresponds to one-floor building while 40 cm height corresponds to 4 flor building. Some buildings were adjacent, and those were all reflected as one wooden block. The location of each building, its height, its placement and direction were all carefully paid attention. The wooden blocks were screwed into the floor. First screw was screwed into the floor, its top was cutoff (Fig.26), and then the wooden block was mounted onto the screw by screwing. While doing so, the blocks were arranged according to its real position in the field. As seen in Fig.27, hundreds of wooden blocks were used to reflect the whole buildings in the residential area.

Figure 26. Screws prepared for mounting buildings

Figure 27. Residential area

Seferihisar-Kusadası highway passing through the town was also built (Fig.28). In addition, to protect the instruments from outside (meteorological) conditions and to be able to work at any day of any season, the roof was constructed at the top of the experimental area. Figure 29 shows the final version of the downstream area.

Figure 28 Highway

Figure 29. Final version of the downstream area

Dam Body

Figure 30 shows the placement of the dam body, which is constructed by screwing the metal sheets and the pump (motor) which is used to lift the body in order to create dam break. Figure 30 shows the gate for trapezoidal breach. Also, there was a gate for triangular breach and a gate for sudden break.

Figure 30. Trapezoidal dam body

Figure 31 presents the final version of the constructed distorted physical model for Urkmez Dam, including reservoir, dam body and downstream area together with Urkmez Creek, the Highway, and the residential area.

Figure 31. Final version of the physical model

The experiments were successfully carried out and flow depths and velocities were measured at different locations in the downstream section. Flood wave movements were recorded. Figures 32 and 33 show two shots from an experiment. The instrumentation and experimental results are published in conference (Guney et al 2013) and journal (Guney et al 2014, 2015) papers and reported in the final project report (Tayfur et al 2014).

Figure 32. Dam break

Figure 33. Dam break flood wave movement

CONCLUDING REMARKS

The construction of a distorted physical model of an actual dam, together with its reservoir, dam body, downstream area, the creek, the highway and the buildings in residential area, requires a very careful thinking, design, creativity, machine and man labor, machine and construction materials, and very skilled personnel. It requires courage, patience and well organized team work. The work presented herein is an exceptional and may be the first in its kind in the world. The experimental physical model has a potential to be used for further experimental scientific studies such as the investigation of plants (trees) on the flood wave. The dam body can be constructed as an earthfill, as it is the actual case in prototype and gradual breaks can be studied, which is the objective of the authors for the future.

AKNOWLEDGEMENTS

The authors thank TUBITAK for the financial support through 110M240 project. The authors would like to thank Prof. Dr. Turhan Acatay for his valuable suggestions and Technician İsa Ustundag for his talented patience. Also, the authors thank to the graduate students Sumeyra G. Sahin, Esra Berberoglu, Dogus Bayram, and Prof. Sebnem Elci for their contribution during the construction of the physical model.

REFERENCES

Frazao, S.S. and Zech, Y. 2017. 'Experimental study of dam break flow against an isolated obstacle', *Journal of Hydraulic Research*, 45, Extra Issue, 27-36.

Greco, M., Pontillo, M., Iervolino, M. and Leopardi, A. 2008. '2DH numerical simulation of breach evolution in an earth dam.' In Altinakar, Kökpınar, Aydın, Çokgör ve Kırkgöz (Eds) Riverflow2008, Volume 1, 661-667, Kubaba, ISBN 978-605-60136-1-4.

Guney MS, Tayfur G, Bombar G, Bayram D (2013) Experimental investigation of flood propagation due to trapezoidal breach in the distorted physical model of Urkmez Dam. International Perspectives on Water and Environment, IPWE2013, Izmir

Guney MS, Tayfur G, Bombar G, Elci S (2014). 'Distorted physical model to study sudden partial dam break flows in an urban area.' Journal of Hydraul Engineering, 140(11).

Guney, M.Ş., **Tayfur**, G., Arkış, T. ve Bombar, G. 2015. 'Experimental and numerical investigation of flood propagation due to trapezoidal breach in the distorted physical model of Ürkmez Dam.' *Dam Engineering*, 25(4), 171-187.

Morris, M.W., Hassan, M.A.A.M. ve Samuels, P.G. 2008. 'Development of the HR BREACH model for predicting breach growth through flood embarkments and embarkment dams.' In Altinakar, Kökpınar, Aydın, Çokgör ve Kırkgöz (Eds) Riverflow2008, Volume 1, 679-687, ISBN 978-605-60136-1-4.

Palumbo, A., Soares-Frazao, S., Goutiere, L. Pianese, D. and Zech, Y. 2008. 'Dam-break flow on mobile bed in a channel with a sudden enlargement.' In Altinakar, Kökpınar, Aydın, Çokgör ve Kırkgöz (Eds) Riverflow2008, Volume 1, 645-654., Kubaba, ISBN 978-605-60136-1-4.

Tayfur, G. Guney, M.S., Elci, S., Haltas, I ve Bombar, G. 2014. Investigation of dam break flows experimentally and numerically—Application to real dams at GIS environment. TUBITAK Project Report, Ankara, 2014 Project number: 110M240. (in Turkish).

Testa, G., Zuccala, D., Alcrudo, F., Mulet, UJ., Frazao, S.S. (2007). 'Flash flow experiment in a simplified urban district.' *Hydraulic Research*, 45, Extra Issue, 37-44.

International
5th National Symposium on
Dam Safety

October 27-31, 2018

COMPARISON OF HECRAS 1D AND 2D DAM BREAK FLOW SIMULATIONS: CASE STUDIES OF URKMEZ DAM

Gül S. ŞAHİN[1], C. Melisa KAYA[2], GÖkmen TAYFUR[3]

ABSTRACT

Dams are constructed to provide benefits to society, hydropower generation, including water supply management and flood control. However, floods caused by failure of a dam is quite catastrophic for lives, properties and environment**.** Flow models for dam break scenarios ensures crucial information about land use planning and risk managment to minimize flood losses. In this study, estimation of flood innundated areas caused by flood triggered by failure of Urkmez Dam in Izmir is carried out by using HEC-RAS one-dimensional (1D) unsteady flow routing model (full Saint Venant equations) and two dimensional model (2D) (full Saint Venant equations or Diffusion wave equations). The aim of the paper is to assess the risk of a dam failure potential by comparing performances of 1D and 2D simulations. Two models were compared considering the required data, cpu (numerical simulation) time, data preparation, inundated area, flood velocity, flood depth, and travel time of flood waves.

Keywords Dam Break, Flood routing, Flood mapping, HEC-RAS 1D model, HEC-RAS 2D model

1. INTRODUCTION

A dam is a structure to store water for providing drinking water, energy generation and flood control. However, dam breaks are important events that require special attention. They can have hazardous results. Dam breaks can be partial or complete, resulting in large quantities water flow at downstream area. They can cause environmental disaster, resulting in loss of life and property. As a result; dam break analysis is a significant interest for civil engineers.

Zeyzoun Dam failed in 2002 in Syria (Fig.2). Flood affected 80 km2 and destroyed 4 villages with 251 homes (Chanson 2009). Also, some important farm land at Hatay was submerged during the failure (Kocaman 2007). In Fig.2, a top view one of the submerged village and the remaining part of dam body can be seen.

[1] Graduate Student, Department of Civil Engineering, Izmir Institute of Technology , Izmir, Turkey, e-mail: gulsahin@iyte.edu.tr
[2] Asistant Professor, Department of Geomatic, Izmir Katip Celebi University, Izmir, Turkey, e-mail: caglamelisa@gmail.com
[3] Professor, Department of Civil Engineering, Izmir Institute of Technology, Izmir, Turkey, e-mail: gokmentayfur@iyte.edu.tr

Figure 1: Teton Dam Failure

(a) Submerged Village, (b) Remaning Part of Dam Body

Figure 2: Zeyzoun Dam Failure

Dam break flow analysis become important to investigate the consequences. Many computational researches take part in literature about floods. Some flood analyses were performed for Wac Bennett Dam at British Columbia using three different hydraulic models (Hicks and Peacock 2005). Hec-Ras, River 1-D and SSARR were used for the comparison and they observed that flood routing and flood level forecasting can easily be performed by Hec-Ras model by using the required input data: channel geometry, boundary conditions, tributary inflows and channel resistance.

The objective of the paper is to assess the risk of Urkmez Dam failure by comparing performances of 1D and 2D simulations. Two models were compared considering the required data, cpu (numerical simulation) time, data preparation, inundated area, flood velocity, flood depth, and travel time of flood waves.

1.1 Study Area

The studied dam is located in Urkmez, which is located 90 km south of Izmir, Turkey (Fig.3). The region is subjected to the Mediterranean Climate, receiving annually 600-800 mm precipitation.

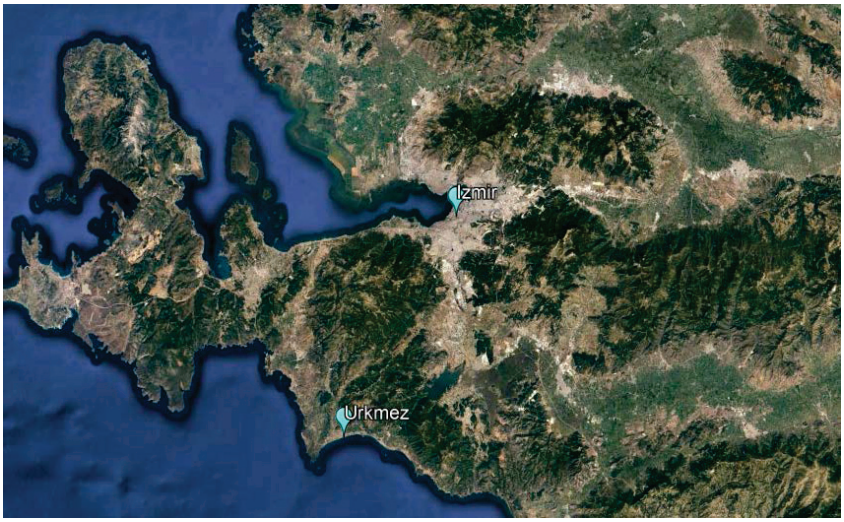

Figure 3: Location of Urkmez

Urkmez Dam was constructed for irrigation and potable water in 1990. The characteristics of the dam is given at Table 1.

Table 1: Urkmez Dam Characteristics

Characteristics	Value
Crest length (m)	426
Crest width (m)	12
Height from base (m)	32
Reservoir volume at minimum level (m^3)	375,000
Reservoir volume at maximum level (m^3)	8,625,000
Reservoir volume at normal level (m^3)	7,950,000
Lake active volume (m^3)	7,575,000

Study area of Urkmez Dam reservoir, dam body and the residential area can be seen in Figure 4.

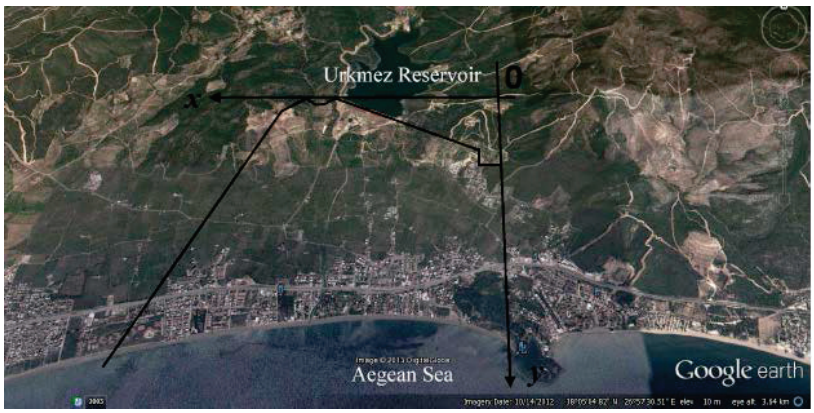

Figure 4: Urkmez Dam Reservoir

2. PRESENTATION OF MODELS

In many river modelling applications, it is assumed that the flow is one-dimensional (1D) St Venants equations. When studying flow over complex floodplains, the assumption that flow is 1D may no longer be valid. 2D unsteady flow varies in time and along two spatial dimensions. The governing principles of 2D unsteady flow are the same as for 1D flow; the conservation of mass and momentum.

2.1 1D Continuity and Momentum Equation

The continuity equation describes the preservation of mass in a given control volume. It states that the net mass flux equals the change in storage. The 1D form of the St. Venant continuity equation can be written in the following form:

$$\frac{\partial(Q)}{\partial x} + \frac{\partial A}{\partial t} = q \quad (1)$$

Where Q is the flow rate, A is the cross sectional area and q is the lateral inflow. The momentum equation is based on Newtons second law of motion, stating that the sum of the forces acting on an element equals the rate of change of momentum. The formulation of the momentum equation will be different depending on what forces that are being considered. Taking pressure, gravity and frictional resistance into account, the 1D momentum equation can be written as:

$$\frac{\partial V}{\partial t} + g\frac{\partial}{\partial x}\left(\frac{V^2}{2g} + h\right) = g(S_0 - S_f) \quad (2)$$

Where V is the flow velocity, g is the gravitational acceleration, h is the water depth, S_o is the bed slope and S_f is the friction slope.

The 2D form of the continuity equation states, just as the 1D form, that the net mass flux into the control volume equals the change in storage in the control volume. The difference is that the mass fluxes are now calculated in 2 dimensions. The 2-dimensional continuity equation can be written as:

$$\frac{\partial H}{\partial t} + \frac{\partial(hu)}{\partial x} + \frac{\partial(hv)}{\partial y} = q \quad (3)$$

Where H is the water surface elevation, h is the water depth, u and v are the depth averaged velocities in the x- and y-direction, and q is the source term, representing inflow from external sources such as precipitation (Chaudhry, 2008).

As in the 1D case, the momentum balance is based on the principle that the sum of forces acting on an element equals the rate of change of momentum. Considering forcing from gravity, eddy viscosity (momentum exchange), friction and the Coriolis effect, the 2D momentum balance equations can be written as follows. Momentum balance in the x-direction:

$$\frac{\partial u}{\partial t} + u\frac{\partial u}{\partial x} + v\frac{\partial u}{\partial y} = -g\frac{\partial H}{\partial x} + v_t\left(\frac{\partial^2 u}{\partial x^2} + \frac{\partial^2 u}{\partial x^2}\right) - c_f u + fv \quad (4)$$

The momentum balance in the y-direction:

$$\frac{\partial v}{\partial t} + u\frac{\partial v}{\partial x} + v\frac{\partial v}{\partial y} = -g\frac{\partial H}{\partial y} + v_t\left(\frac{\partial^2 v}{\partial x^2} + \frac{\partial^2 v}{\partial x^2}\right) - c_f v + fu \quad (5)$$

where H is the water surface elevation, ν_t is the eddy viscosity coefficient, c_f is the friction coefficient , f is the Coriolis parameter and v and u are depth averaged velocities in the x and y directions, respectively (Brunner, 2016a). The first term in the momentum equations represents the local acceleration ($\partial u/\partial t$ in equation 4, corresponding term in 5), the second term ($u\partial u/\partial x + v\partial u/\partial y$ in 4, corresponding term in 5) is the convective acceleration, other terms stand for the forcing from gravity, eddy viscosity, bed friction, and Coriolis force. Using the Manning's formula, the friction coefficient c_f can be expressed as following (in the x-direction):

$$c_f = \frac{n^2 g|u|}{R^{4/3}} \quad (6)$$

where n is Manning's roughness, g the gravitational accelaration, u the velocity in the x-direction and R the hydraulic Radius.

3. DATA

Topographic map scale 1:1,000 (UTM Zone 27/WGS84 3°) were used for the creation of digital elevation model (DEM) of about 10 cm spatial resolution for Urkmez Basin. All the cross-sections used in HEC-GEO RAS and z values were extracted from Triangulated Irregular Network (TIN) surface. Geometric data like the stream centreline, banks, flow direction, land use, bridges/culverts, ineffective flow areas were created by using HEC-GEO RAS in GIS (Geographical Information Systems) environment. Also, flow area (2D mesh), weir parameters - inlet, dam bridge data were created in HEC-RAS for 2D Modeling. Data pertaining to the dam and the reservoir were provided from the State Hydraulic Works (DSI). Reservoir volume-elevation curve was provided from DSI.

4. METHODOLOGY

The modelling procedure involves three steps: (1) Geometric configuration is based on the cross-sections in the 1-D model was produced and 1D Dynamic Routing was simulated in HEC -RAS determine the resulting flood at downstream side of Urkmez Dam, (2) Floodplain discretized into grid cells and two-dimensional unsteady flow analysis is performed for Dam break analysis across and along the flow path at downstream side of Urkmez Dam, (3) The GIS based flood maps produced by HEC-RAS is overlapped to DEM to delineate the flood inundated areas. So-obtained results for dam breach analysis compared performance of 1D and 2D simulations. Two models have been compared with required data for simulation, data preparation time, inundated area, flood velocity, flood depth and travel time of flood waves. The flow chart of the methodology is illustrated in Figure 5.

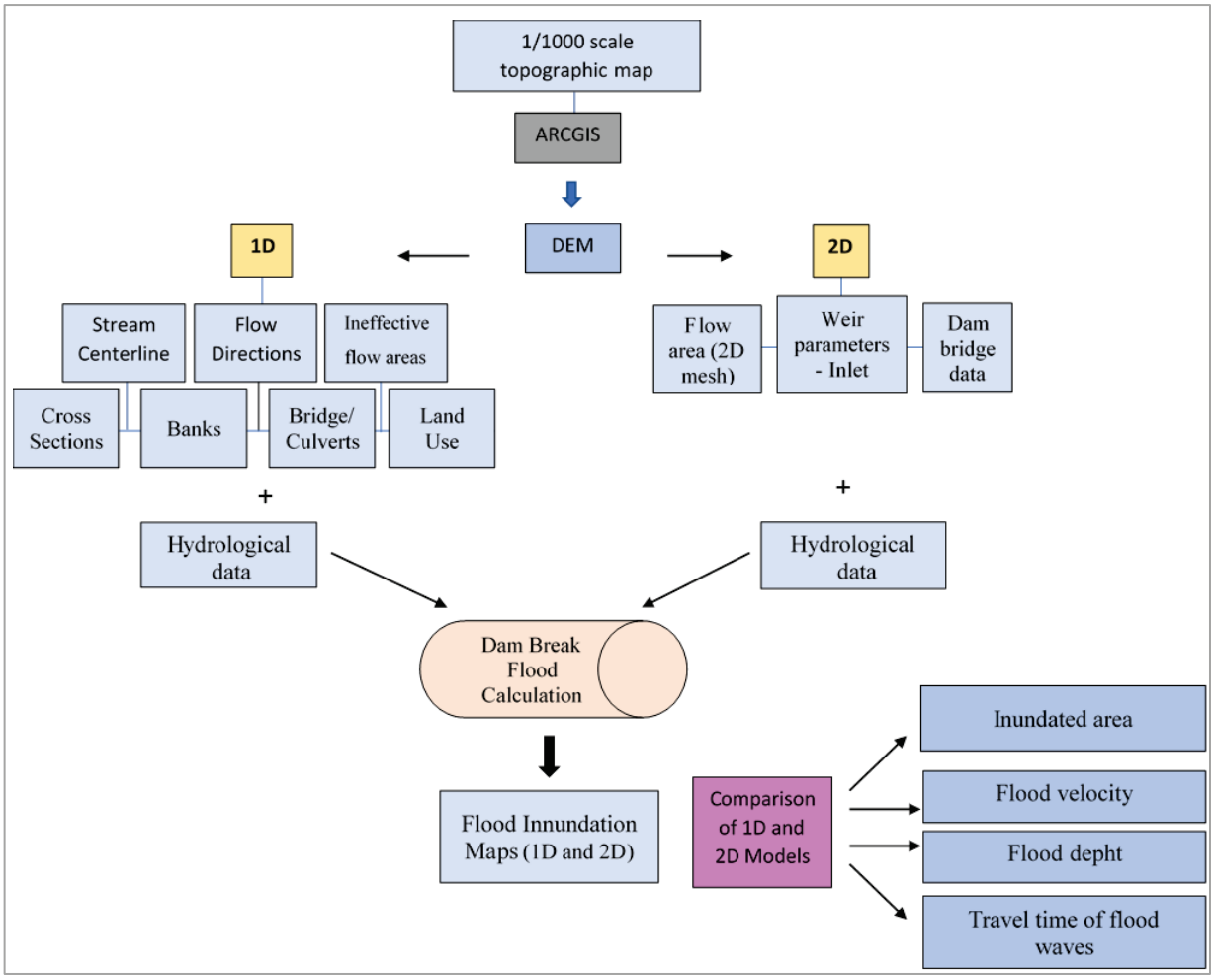

Figure 5: Flow Chart of Methodology

5. RESULT AND DISCUSSION

The simulations were carried out using HEC-RAS one-dimensional (1D) unsteady flow routing model and two-dimensional model (2D) for a sunny day failure at Urkmez Dam. The results have been compared with required data for simulation, data preparing process, inundated area, flood depth and flood velocity of flood waves. While the geometric configuration is based on the cross-sections in the 1-D model (Figure 6), 2-D model relies on finite element mesh resolution (Figure 7). For the one-dimensional model used for simulation; stream centerline, flow paths, banks, cross sections, and land use type were created in Hec-GeoRAS. On the other hand 2D mesh, weir parameters, inlet, dam bridge data were created in HEC-RAS for 2D modeling. All geometric data created based on the same Digital Elevated Model which was produced using the topographic mapping scale 1:1,000 (UTM Zone 27/WGS84).

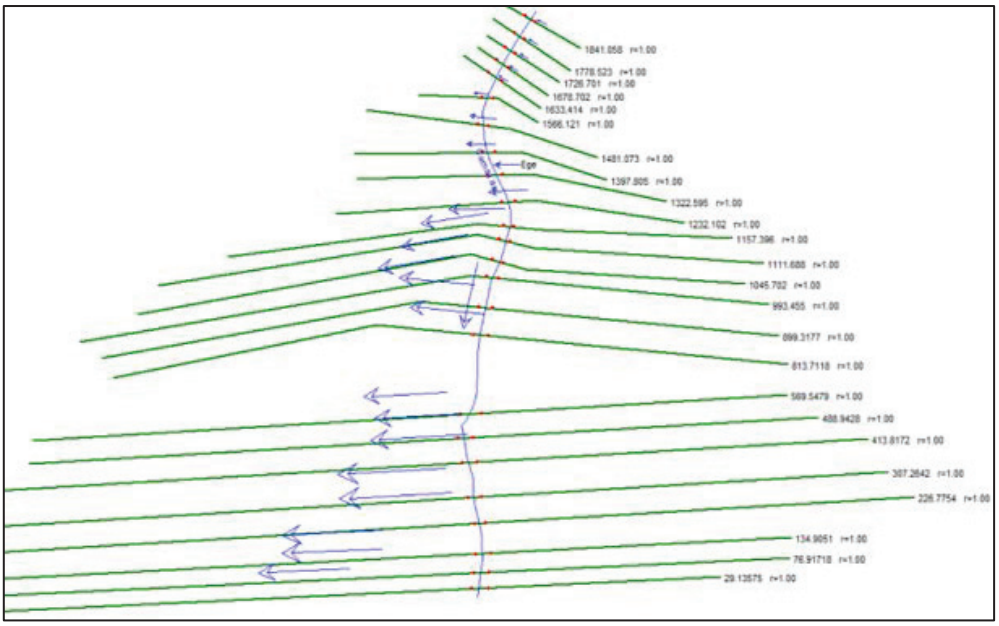

Figure 6: Urkmez Creek Cross Sections

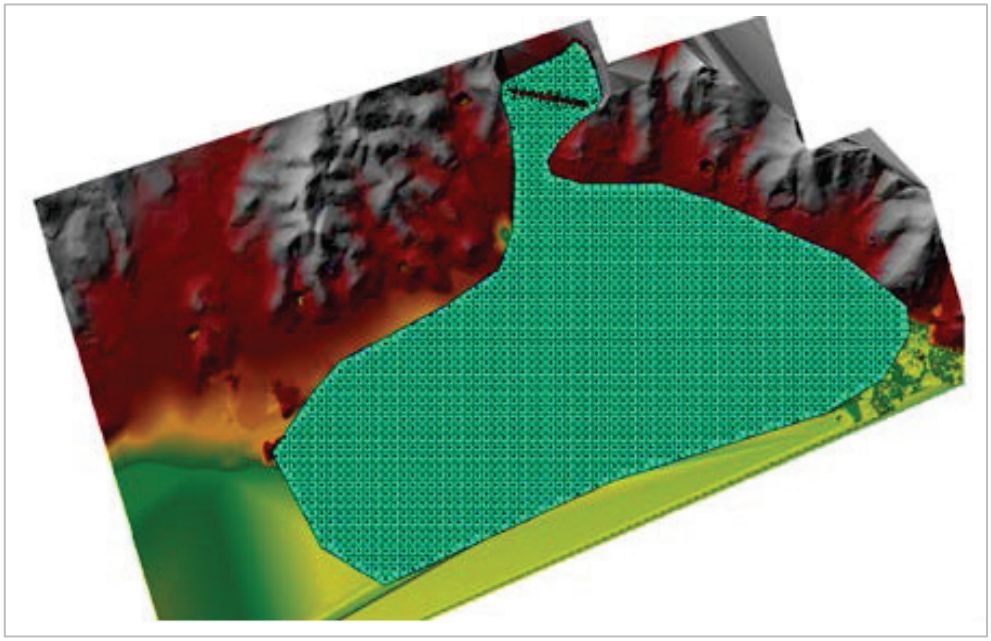

Figure 7: 2D Flow Area

According to simulation results of 1D hydraulic model;

- About 280 ha area will be inundated
- Maximum flood depth in upstream side reached to 7.53 m and 1.94 m in the downstream side.
- Flood velocity varied from 16.01 m/s to 0.018 m/s.
- The highest velocity was observed on the right side (in the flow direction) at a distance of about 280-300 meters from the reservoir.
- The maximum velocity was reached in about 1.5 minutes.

The inundated area predicated for the whole site by the 1D unsteady hydraulic model is shown in Figure 8.

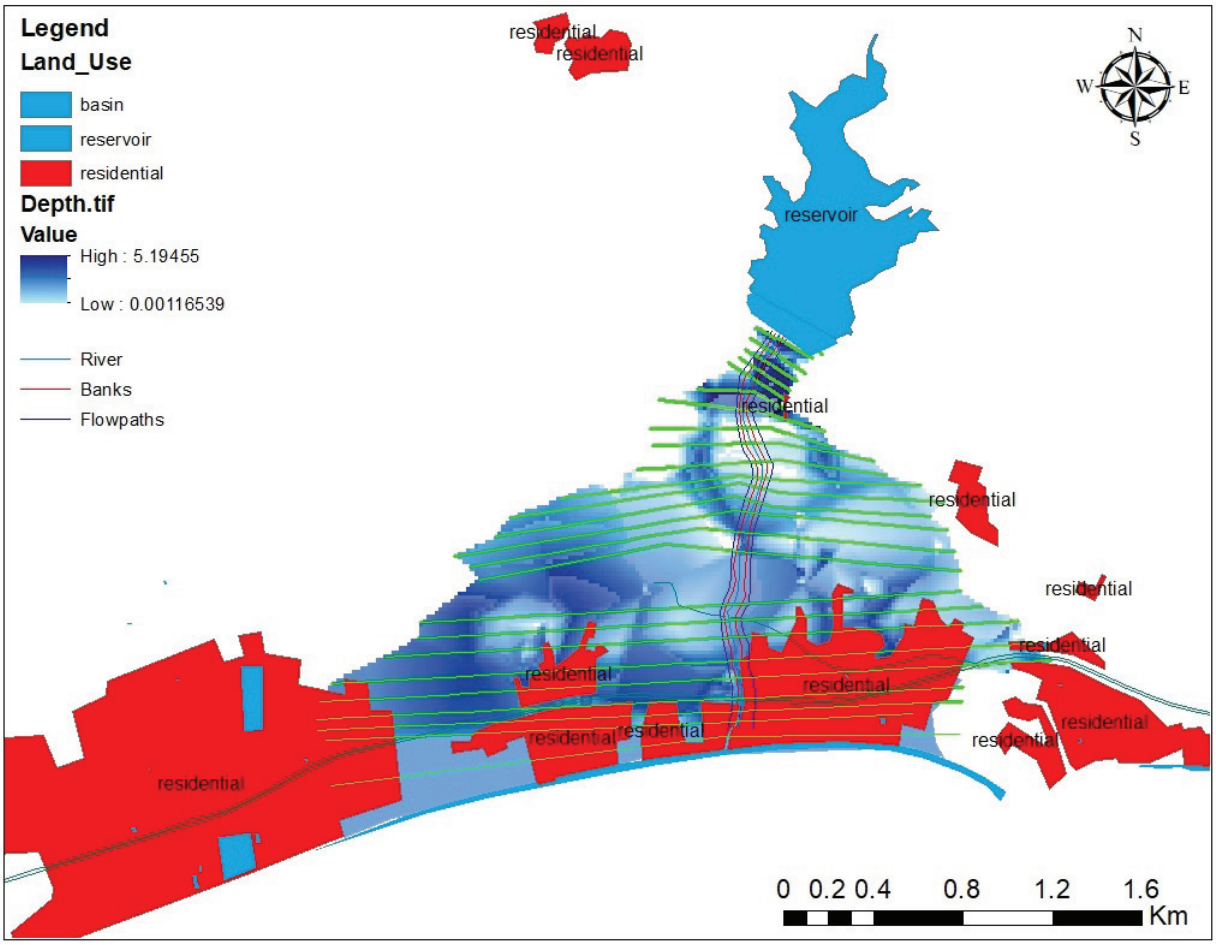

Figure 8: Inundation areas were predicted by the 1D modeling

2D hydraulic model simulations revealed that;

- About 300 ha area will be inundated,
- Maximum flood depth in upstream side reached to 6.25 m and 0.24 m in the downstream side.
- Flood velocity varied from 28.1 m/s to 0.24 m/s.
- The highest velocity was observed on the right side (in the flow direction) at a distance of about 300 meters from the storage area.

- The maximum velocity was reached in about 1 minute.

Figure 9 shows the time series of inundation predicted by the 2D model.

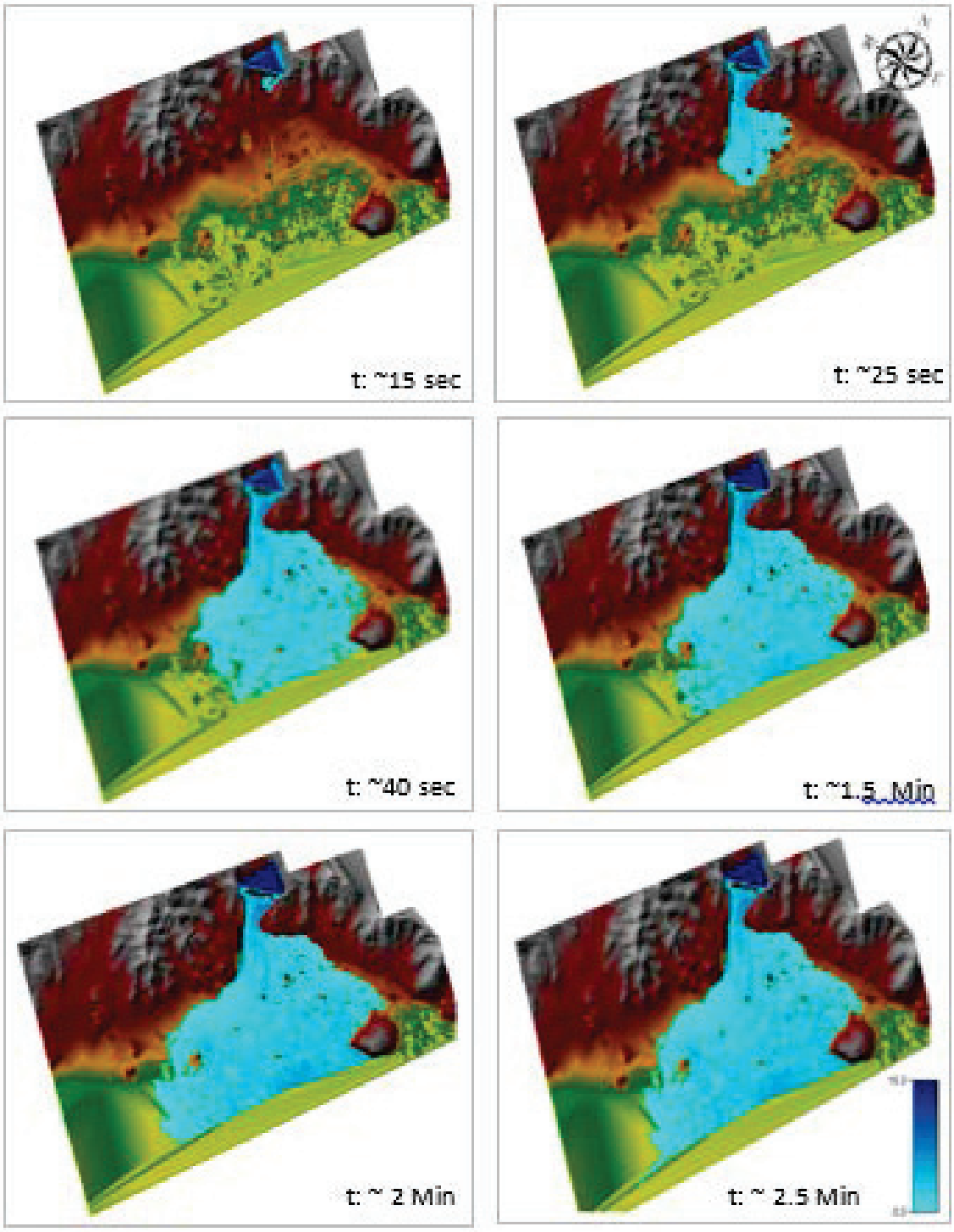

Figure 9: The process of inundation predicted by the 2D modeling

Although 1D results reached to higher water depth, it had a slower travel time. 2D results demonstrated lower water depth but showed a faster travel time, as shown in Figures 10 and 11. While

the maximum velocity was reached in about 2 minutes in 2D modelling, it was reached in about 1.5 minutes in 1D modelling (see Figures 12 and 13).

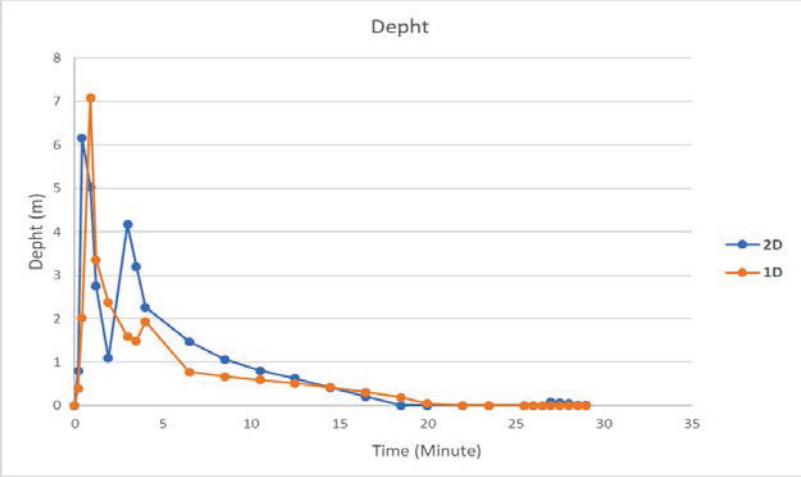

Figure 10: Flow depth in upstream site

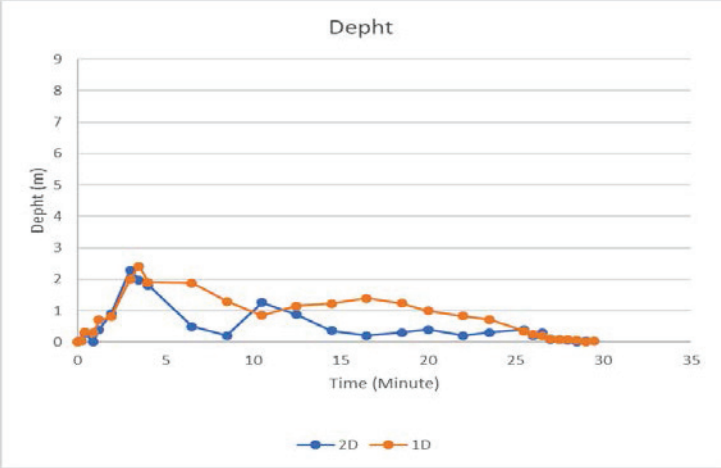

Figure 11: Flow depth in downstream

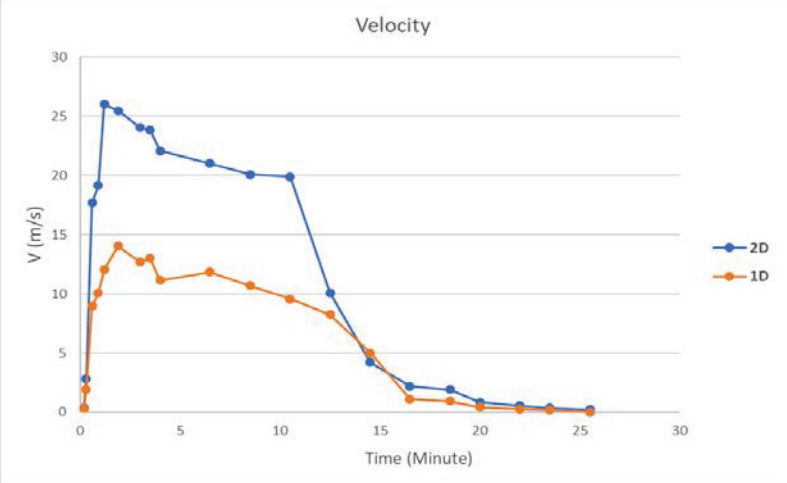

Figure 12: Flow velocities in upstream

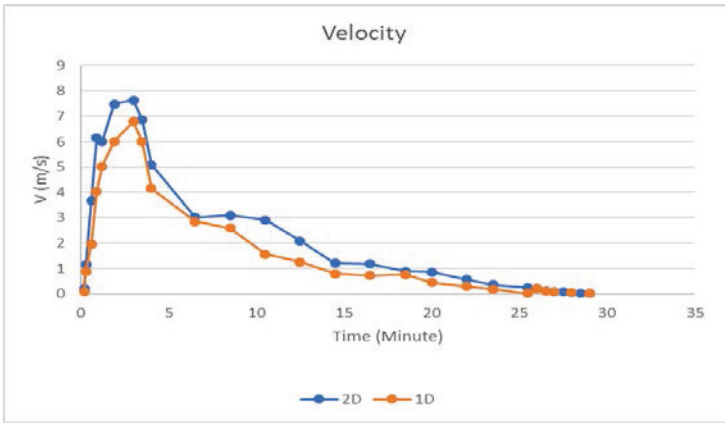

Figure 13: Flow velocities in downstream

6. CONCLUSIONS

The aim of this paper is to assess Urkmez Dam failure potential risk with dam breach analysis by comparing performance of 1D and 2D simulations. The one-dimensional model needs more detailed input data, so the data preparation period takes a longer time. Simulation results show that the areas to be submerged are approximately the same. However, the estimated size of the inundated area in the 2D model is about 5 percent larger. At the same time, the depth observed in 1-dimensional model is higher than the 2-dimensional simulation results, but the time to reach the maximum speed is slower than the 2-D model.

REFERENCES

Chanson H, 2009. "Application of the method of characteristics to the dam break wave problem" Journal of Hydraulic Research Vol. 47, No:1, pp. 41-49.

Kocaman S, 2007. "Experimental and Theoretical Investigation of Dam Break Analysis" PhD Thesis. University.

Hicks F, Peacock T, 2005. "Suitability of Hec-Ras for Flood Forecasting" Canadian Water Resources Journal 30(2), pp. 159-174.

Chaudhry M.H, 2008. "Open Channel Flow" 2nd Edition, Berlin, Springer.

Brunner, G.W, 2016 Hec-Ras River Analysis System: Hydraulic Reference Manual, Version 5.0, US Army Corps of Engineers, Hydraulic Engineering Center.

5th International Symposium on Dam Safety

October 27-31, 2018

SHORT TERM OPERATION OF RESERVOIR SYSTEM WITH NEURAL NETWORK MODEL BASED ENSEMBLE STREAMFLOWS AND STOCHASTIC OPTIMIZATION

Gökçen UYSAL [1], Aynur ŞENSOY[2]

ABSTRACT

Short term operation of small reservoirs are challenging due to limited storage and multiple usage such as water supply, energy or flood control. Operators need a reliable forecasting system and robust operational tools in order to operate systems in an efficient manner. The aim of the research is to develop hourly real-time control system of a multi-purpose reservoir using neural network model based streamflow forecasts and stochastic optimization techniques. There are different approaches to develop forecasting systems based on hydrological models such as physical, conceptual, stochastic models and soft computing technique etc. Most of these models require proper meteorological forecast data as direct input. On the other hand, instead of a deterministic forecast data set, ensemble meteorological data provide multiple spread members which can incorporate uncertainty with non-parametric way. In this study, single system ensembles are produced by perturbation of model inputs such as precipitation, temperature and snow depth data. Hourly ensemble streamflow forecasts are produced by neural network model and perturbed forcing input data. Multi-Layer Perceptron model with fast Levenberg-Marquardt algorithm is employed to optimize the weights of network. While 60 % of the data set is used in training and cross-validation processes, remaining (40 %) data is used as testing of the model. Later, a selected event is tested in multi-stage stochastic open-loop optimization to estimate short term control decision trajectories. Neural network model based ensemble forecasts provide probabilistic reservoir inflow forecasts which can be used in short term operation. Initial results are promising to be used in real-time operation of downstream control and water supply. The methodology is valuable especially for relatively small catchments to account for uncertainty in decision mechanism.

Keywords: Artificial neural network, multi-stage stochastic optimization, reservoir, dam operation

INTRODUCTION

Optimal operation of reservoirs are a common problem for many decades (Wurbs, 1993; Chang and Chang, 2001; Labadie 2004; Rani and Moreira, 2010). The challenges arise due to many factors such as storage capacity, water and energy needs, risk and consequences of operating strategy etc. Strategies or policies are composed of a series of decisions for the storage or release of water for multiple purposes such as release from turbines and spillways, withdrawals for irrigation, water supply etc. In order to satisfy a robust real-time operation policy, extensive investigation has been done on the optimization models for reservoir systems (Mays, 1989; Faber and Stendinger, 2001; Che

[1] PhD., Department of Civil Engineering, Eskisehir Technical University, Turkey,
e-posta: gokcenuysal@anadolu.edu.tr
[2] Associate Professor, Department of Civil Engineering, Eskisehir Technical University, Turkey,
e-posta: asensoy@anadolu.edu.tr

and Mays, 2015). Generally, the optimization problem of the system is challenging due its nonlinear, non-convex and its dynamic structure. Besides, stochasticity is inherent in reservoir system operation. According to Labadie (2004), "Unregulated inflows, net evaporation rates, hydrologic parameters, system demands, and economic parameters should often be treated as random variables, giving rise to a complex large-scale, nonlinear, stochastic optimization problem." Many optimization models are not suitable for integrating risk and uncertainty in the system. One solution is to set a stochastic optimization which can incorporate uncertainties. At this point, the main problem might be having more complex system than deterministic equivalents because of increasing disturbance vectors, states etc. Tree-Based Model Predictive Control (TB-MPC) is an innovative method to consider ensemble forecasts with an adaptive control (Raso et al., 2014).

Small capacity reservoirs hold considerable challenge due to their restricted capacity and correspondingly shorter response time in real-time operation (Uysal et al, 2018). In this study, hourly short-term operation of a relatively small water supply reservoir suffering from flood control restriction is tackled under a stochastic optimization control problem. To that end, multiple inflow trajectories (so-called ensembles) are generated from a hydrological forecasting model, in which case the primary source of uncertainty is assumed to be the forecast error. Artificial Neural Network (ANN) employing several formats and learning algorithms is preferred as a forecasting tool according to its ability to identify highly nonlinear processes. Firstly, ANN model is trained and tested with hourly observed data (inflow, prec, temp but also snow data). Later, forecasted ensembles are used in an open-loop multi-stage stochastic optimization.

METHODOLOGY

The details of the methodology is described under two main subtitles:

i. The first task is to set and implement a hydrological model. At this point, a neural network model is used to mimic hourly inflows into the dam reservoir lake. Forcing variables of precipitation, temperature and snow measurement data are explicitly perturbed and provided to the calibrated and validated model.
ii. Subsequently, outputs of the hydrological model become the backbone of the stochastic set-up of the optimization model. A stochastic version of the reservoir system optimization model is developed and implemented under RTC-Tools model (Schwanenberg et al., 2015). Produced inflow data are used in open-loop multi-stage stochastic model.

Neural Network based Ensemble Streamflows

An Artificial Neural Network (ANN) is characterized by its architecture that represent the pattern of connection between nodes, its method of determining the connection weights, and the activation function (Fausett, 1994). Multi-Layer Perceptron (MLP) is a method of feedforward network that has interconnected neurons arranged into three layers: input layer, a hidden layer and an output layer. The information can only pass through input vector to forward layers and the network uses backpropagation algorithm in the training stage. The output of node j, y_j is obtained by the following equation:

$$y_j = f\left(XW_j - b_j\right) \tag{1}$$

where, $X = (x_1, \ldots, x_i, \ldots, x_n)$, $W_j = (w_{1j}, \ldots, w_{ij}, \ldots, w_{nj})$ and X is information from previous nodes, w_{ij} represents the connection weight from the i^{th} node in the preceding layer to this node, where b_j is bias, f is the activation function.

The sigmoid function is used in the hidden layer since it is a bounded, monotonic, nondecreasing function that provides a graded, nonlinear response (ASCE, 2000). This function is preferred since it enables a network to map any nonlinear process. The network is trained using a Levenberg-Marquart

(LM) technique, since it is more powerful than the conventional gradient techniques (Hagan and Menhaj, 1994). The typical performance function is used for training feedforward neural networks is the mean sum of squares of the network errors. The network weights and biases are initialized by the MATLAB software internally. The data is pre-processed and standardized within [0.1-0.9] in order to trim outliers and provide all variables into same scale.

Multi-Stage Stochastic Tree-based Model Predictive Control

Deterministic Model Predictive Control (MPC) considers a discrete time-dynamic system according to

$$x^k = f\left(x^{k-1}, x^k, u^k, d^k\right) \tag{2}$$

$$y^k = g\left(x^k, u^k, d^k\right) \tag{3}$$

where x, y, u, d are the state, dependent variable, control and disturbance vectors, respectively. Also, $f()$ and $g()$ are functions representing an arbitrary linear or nonlinear water resources model. Under the assumption of knowing the realization of the disturbance d over the time horizon, the simultaneous (aka collocated) MPC has below objective function and constraints:

$$\underset{u, x \in \{0,\ldots,T\}}{min} \sum_{k=1}^{N-1} J\left(x^k, u^k, d^k\right) + E\left(x^N, u^N, d^k\right) \tag{4}$$

$$\text{s.t.:} \quad h\left(x^k, y^k, u^k, d^k\right) \le 0, \quad k = 1,\ldots,N \tag{5}$$

$$x^k - f\left(x^{k-1}, x^k, u^k, d^k\right) = 0 \tag{6}$$

where $J()$ is a cost function associated with each state transition, $E()$ is an additional cost function related to the final state condition, and $h()$ represents hard constraints on control variables and states, respectively. In this case, the related model (reservoir simulation equations) becomes an equality constraint of the optimization problem in Equation 6.

The problem is extended through multi-stage stochastic set-up by changing d^k with d_j^k where j denotes the ensemble index $(j = 1,...,M)$ and k denotes the time instant $(k = 1,...,N)$.

$$\underset{u, x \in \{0,\ldots,T\}}{\min} \sum_{j=1}^{M} p_j \sum_{k=1}^{N-1} J(x_j^k, u_j^k, d_j^k) + E(x_j^N, u_j^N, d_j^N) \tag{7}$$

where p_j stands for the probability of the ensemble member, M stands for the number of the ensembles.

Definition of control variable u_j^k identifies the approach for stochastic MPC set-up. Multi-stage stochastic optimization (so called Tree-based MPC, TB-MPC) is improved version which uses scenario trees for disturbance, states and control trajectories (Raso et al., 2014).

Application

The developed methodology is applied to a water supply reservoir of Yuvacık dam located in the southern part of Kocaeli city, Turkey. It has approximately 51.2 hm^3 storage volume at maximum operating level. The dam operation requires two main tasks are as water supply and flood protection as the downstream region is an industrial area. The total catchment area is about 258 km^2. Moreover, the basin has a wide elevation range between 80 – 1550 m, thus resulting in snowmelt runoff during

spring seasons. The excessive water is mainly released from a gated spillway that is located on the dam body.

There are several objectives which should be considered for a proper hourly operational decision support system. These are;

i. The reservoir should be operated within lower and upper elevation limits.
ii. The excess water is released from a controlled spillway with a discharge curve above a certain level.
iii. A time-dependent variable guide curve should be taken into account.
iv. Spillway operation (due to wear and tear of the gates) should be as much as minimum.
v. The maximum spillway release should be restricted because of the downstream condition.
vi. The restriction between consecutive spillway discharges should be considered.
vii. Continuity in water supply (withdrawn from the reservoir) should be maintained according to city needs.

Neural network architectures (models) are derived by trial and error approach. Hydro-meteorological data records are provided from automated weather and flow measurement stations. In this study 10 hidden neurons are used in one single hidden layer. The network formulation is defined below:

$$Q_{in} = f(Q_{in(n-48)}, \mathrm{P}_{(n)}, T_{(n)}, SD_{m(n)}, SD_{h(n)}) \tag{8}$$

where, Q_{in}, f, P, T, SD_m, SD_h and n stands for inflow into reservoir, neural network model, total precipitation, air temperature, snow depth at mean elevation, snow depth on higher elevation and time index, respectively.

Finally, ANN based hydrological model results (training and testing) are evaluated with four performance criteria for the assessment. These are, the coefficient of determination (R^2), Nash-Sutcliffe Efficiency (NSE), Root Mean Square Error (RMSE) and Mean Absolute Error (MAE) denoted as:

$$R^2 = \left[\frac{\sum_{t=1}^{n} \left(Q_m^t - \bar{Q}_m\right)\left(Q_o^t - \bar{Q}_o\right)}{\sqrt{\sum_{t=1}^{n} \left(Q_m^t - \bar{Q}_m\right)^2} \sqrt{\sum_{t=1}^{n} \left(Q_o^t - \bar{Q}_o\right)^2}} \right]^2 \tag{9}$$

$$NSE = 1 - \frac{\sum_{t=1}^{n} \left(Q_o^t - Q_m^t\right)^2}{\sum_{t=1}^{n} \left(Q_o^t - \bar{Q}_o\right)^2} \tag{10}$$

$$RMSE = \sqrt{\frac{\sum_{t=1}^{n} \left(Q_m^t - Q_o^t\right)^2}{n}} \tag{11}$$

$$MAE = \frac{\sum_{t=1}^{n} \left|Q_o^t - Q_m^t\right|}{n} \tag{12}$$

RESULTS

Preliminary results are presented as (i) hydrological modelling (training and testing of the neural network based hydrological model, forecasting of an ensemble set of inflows for a selected event) and (ii) testing of produced ensemble forecast data in multi-stage stochastic optimization model. The results are evaluated under these two main subtitles.

Neural Network based Ensemble Streamflows Results

The data is divided into two main parts (time periods) in the application. Hourly data (from 01 January 2010 to 31 October 2012) are provided from automated stations and different input combinations are tested. Subsequently, only input combination described in Equation 8 (referred to methodology) is used in the model and its results (due to its higher performance) are presented in the study. It should be noted that the training part (including 9528 time steps, 01 January 2010 – 01 January 2011) is randomly divided into 85 % and 15 % for training and cross-validation (stopping criterion), respectively. The model is tested through an excluded period (including 6525 time steps, 01 February 2011 – 31 October 2012).

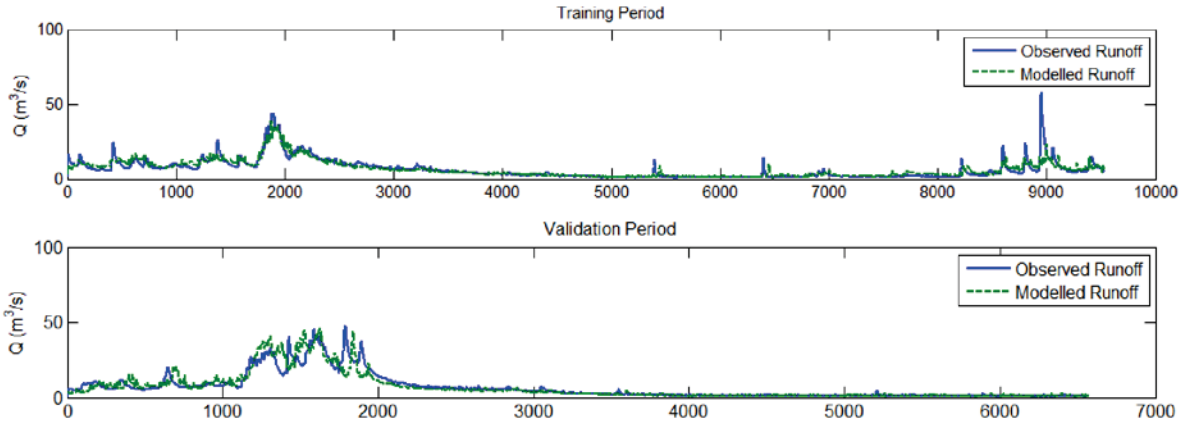

Figure 1. Training and testing model results against observed inflows [x-axis in hours]

The performances of the hydrological modeling results are tested with four performance metrics. The results are presented in Table 1. According to that, hourly hydrological model can provide reasonable performance to be used in a forecasting study.

Table 1. Performances of the hydrological modelling

Period	R^2	NSE	RMSE [m^3/s]	MAE [m^3/s]
Training	0.79	0.78	3.0	1.5
Testing	0.81	0.78	3.9	1.8

An event (13 days) is selected to be forecasted in April when both rainfall and snowmelt are effective on the reservoir inflow. Model inputs are perturbed independently with normal distribution using 51 members for precipitation N(0, 30 %), temperature N(0, 10%) and snow depth N(0, 5%) data. Figure 2 represents the produced inflow forecasts against observed discharge (red line indicates ensemble forecast while blue is observed one and green lines are optimal control trees produced by tree reduction technique integrated into TB-MPC).

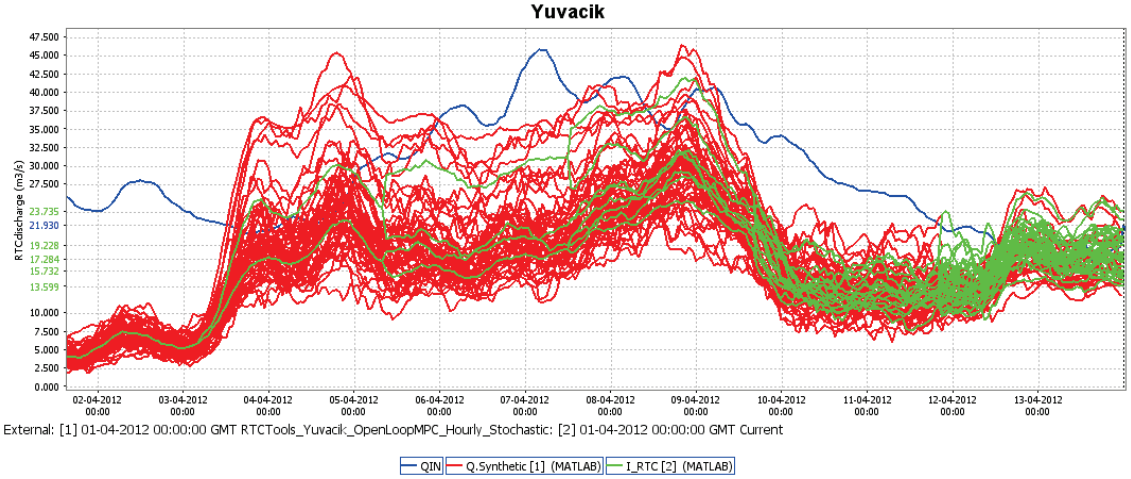

Figure 2. Deterministic and ensemble forecasts generated

Multi-stage stochastic TB-MPC is employed in open-loop mode using reduced ensemble forecasts The model also produces states and optimized variables in rooted tree form. It should be also noted that a high level initial forebay elevation is selected in order to consider full-reservoir case. The results are evaluated in forebay elevation and spillway discharges as shown in Figure 3.

According to preliminary findings, ANN integrated TB-MPC open-loop model offers pre-releases in order to empty the reservoir pool for an expected event. Different than conventional deterministic counterparts, the model results (optimization variable and state) are in tree form that can include resolution of the uncertainty along with time horizon. This means that ensemble spread can provide knowledge of the uncertainty and the model can capture this information in stochastic optimization.

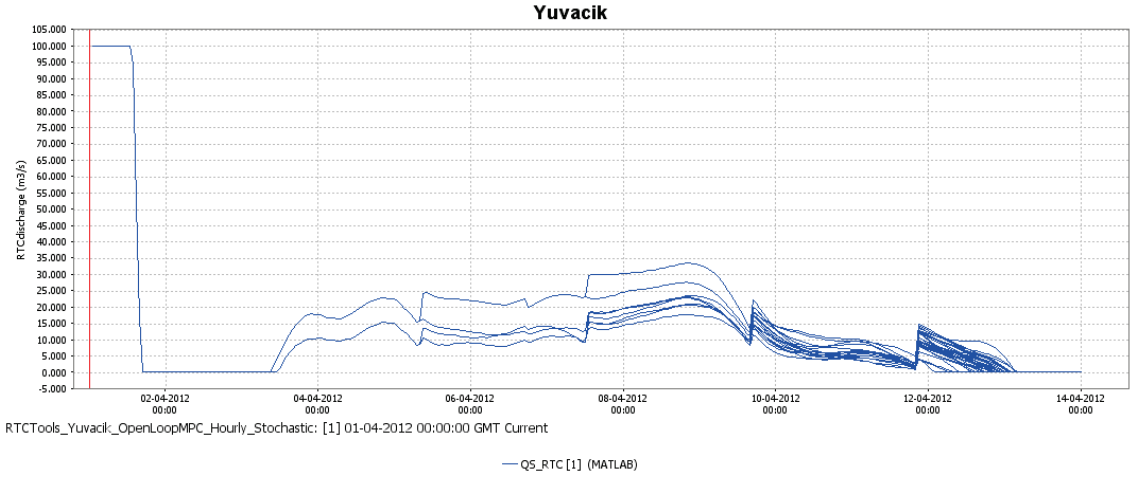

(a)

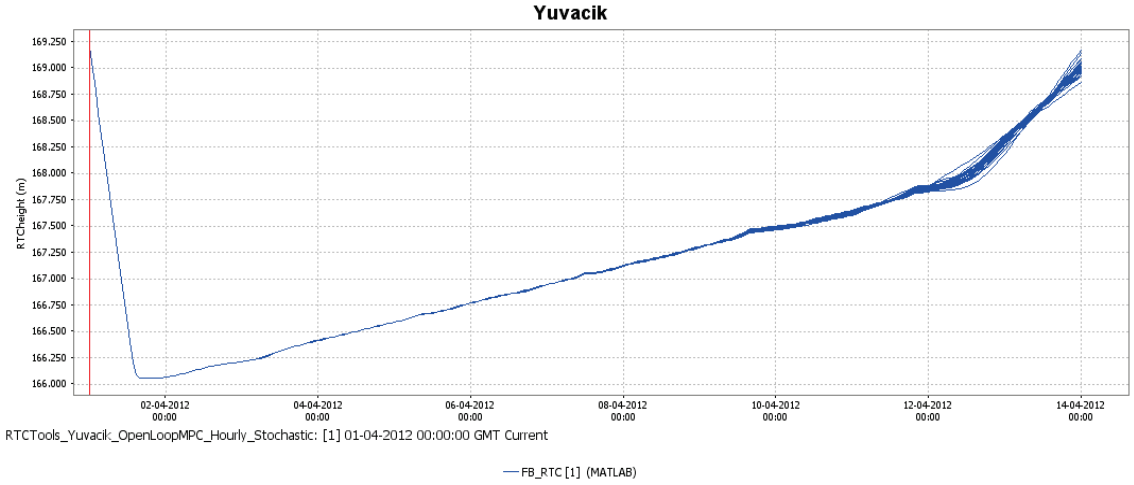

(b)

Figure 3. Open-loop TB-MPC results (a) Spillway discharge [m^3/s] (b) Forebay elevation [m]

CONCLUSIONS

Hourly model set up in real-time management and consideration of uncertainty in decision support mechanism are still lack in operational systems. This study contributes this gap and offers integrated management tools with innovative technologies such as neural network and real time control (with multi-stage stochastic optimization). According to preliminary findings, one can note bellows:

- Hourly neural network forecasting model is promising to be used in operational studies; however the model still necessitates assessment of different input combinations and advanced improvement techniques.
- Production of ensemble spread can provide spread in the inflows thus resulting uncertainty assessment for operators rather than deterministic single trajectories.
- Multi-stage stochastic method such as TB-MPC provides the resolution of the uncertainty contrary to its conventional equivalents.

AKNOWLEDGEMENTS

This study is supported by Anadolu University Scientific Research Projects Commission under the grant No: 1705F189.

REFERENCES

ASCE Task Committee on Application of Artificial Neural Networks in Hydrology, 2000. "Artificial neural networks in hydrology. I: Preliminary concepts". Journal of Hydrologic Engineering, 5(2), 115-123.

Chang, L.C., Chang, F.J., 2001. "Intelligent control for modelling of real Hydrological Processes, 15(9), 1621-1634.

Che, D., Mays, L.W., 2015. "Development of an optimization/simulation model for real-time flood-control operation of river-reservoirs systems". Water Resources Management, 29(11), 3987-4005.

Faber, B.A., Stedinger, J.R., 2001. "Reservoir optimization using sampling SDP with ensemble streamflow prediction (ESP) forecasts". Journal of Hydrology, 249(1-4), 113-133.

Fausett, L., 1994. "Fundamentals of neural networks: architectures, algorithms, and applications" Prentice-Hall, Inc. Upper Saddle River, NJ, USA ©1994 ISBN:0-13-334186-0

Hagan, M.T., Menhaj, M. B., 1994. "Training feedforward networks with the Marquardt algorithm". IEEE transactions on Neural Networks, 5(6), 989-993.

Labadie, J.W., 2004. "Optimal operation of multireservoir systems: state-of-the-art review. Journal of Water Resources Planning and Management, 130(2), 93-111.

Mays, L.W., 1989. "Hydrosystems engineering simulation vs. optimization: why not both?". IAHS Publ:225–231

Rani, D., Moreira, M.M., 2010. "Simulation–optimization modeling: a survey and potential application in reservoir systems operation". Water Resources Management, 24(6), 1107-1138.

Raso, L., Schwanenberg, D., van de Giesen, N.C., van Overloop, P.J., 2014. "Short-term optimal operation of water systems using ensemble forecasts". Advanced in Water Resources, 71, 200–208.

Schwanenberg, D., Becker, B.P.J., Xu, M., 2015. "The open real-time control (RTC)-Tools software framework for modeling RTC in water resources sytems". Journal of Hydroinformatics, 2015, 17, 130–148.

Uysal, G., Alvarado-Montero, R., Schwanenberg, D., Şensoy, A., 2018. "Real-time flood control by tree-based model predictive control including forecast uncertainty: A case study reservoir in Turkey". Water, 10(3), 340.

Wurbs, R.A., 1993. "Reservoir-system simulation and optimization models. Journal of Water Resources Planning and Management". 119(4), 455-472.

5th International Symposium on Dam Safety

October 27-31, 2018

ASSESSMENT OF LANDSLIDE GENERATED IMPULSE WAVES IN DAM RESERVOIRS

Hakan ERSOY[1], Murat KARAHAN[2], M. Oğuz SÜNNETCİ[3], Aykut AKGÜN[4], Tuğçe ANILAN[5], Arzu FIRAT ERSOY[6], Kübra TEZEL[7], Bilgehan KUL YAHŞİ[8], Hasan H. ÖZTÜRK[9]

ABSTRACT

In this study, effects of the impulse waves caused by the reviving of the Havuzlu paleo-landslide, which is located 8 km to the upstream of Artvin Dam, were investigated using 3D simulation-based numerical analyses. 3D solid model of the corresponding area was created using raster data. The topography was modelled in 1/10000 scale and the landslide was introduced as a 300*200*40 m (width*length*depth) mass with 2.1 million cubic meters volume. Following the creation of 3D solid model of both the study area and landslide, the solid models were imported to the FLOW-3D software. The material properties of the landslide, whose boundaries were determined via field studies, were introduced to the software, and boundaries of the area to be analyzed and the number of meshes were determined. Maximum water level in the dam reservoir was accepted to be 504 meters, and renormalization group (RNG) was used as turbulence model. The results indicate that the landslide material would reach 35.2 m/s velocity and the resulting wave would move towards the dam body at 34.3 m/s speed with a height of 2 meters at the dam body, which will not cause any problems for the dam body.

Keywords: Landslide, dam, reservoir, impulse wave

[1]Assoc.Prof., Department of Geological Engineering, Karadeniz Technical University, Trabzon, Turkey, e-mail: blavetirraa@hotmail.com
[2] Res. Assist. Department of Geological Engineering, Karadeniz Technical University, Trabzon, Turkey, e-mail: muratkarahan21@gmail.com
[3] Res. Assist. Department of Geological Engineering, Karadeniz Technical University, Trabzon, Turkey, e-mail: moguzsunnetci@ktu.edu.tr
[4] Prof., Department of Geological Engineering, Karadeniz Technical University, Trabzon, Turkey, e-mail: aykut.akgun@ktu.edu.tr
[5] Asst. Prof., Department of Civil Engineering, Karadeniz Technical University, Trabzon, Turkey, e-mail: tugcekoc@ktu.edu.tr
[6] Assoc.Prof., Department of Geological Engineering, Karadeniz Technical University, Trabzon, Turkey, e-mail: firat@ktu.edu.tr
[7] Geological Eng., Department of Geological Engineering, Karadeniz Technical University, Trabzon, Turkey, e-mail: tezelkubra@gmail.com
[8] Dr. Geological Eng., Dept. of Geological Engineering, Karadeniz Technical University, Trabzon, Turkey, e-mail: bilgehankul@ktu.edu.tr
[9] DSİ 26. Regional Directorate, Artvin, Turkey e-mail: dsi26@dsi.gov.tr

INTRODUCTION

About 10% of more than 300 large dam collapses reported worldwide are caused by the landslide formed on the valley slopes at dam reservoir sites (Tezel 2015) and 85% of these landslides occurred within the next two years after the filling of the dam reservoir (Riemer 1995). The research indicated that forming of new landslides and/or reviving of paleo-landslides in dam reservoir areas are induced by the elevation of pore water pressure in the valley slopes following water impoundment in the reservoir (Wang et al. 2004; Fawu et al. 2006; Kaczmarek 2015). Much research described in the literature has demonstrated that heavy rainfall impact and changes of reservoir water level in the dam sites are the most effective parameters on the stability of the valley slopes (Corominas & Moya 1999; Iverson 2001; Vichas et al. 2001; Liu et al. 2004; Wang et al. 2007; Tsai 2008; Matsuura et al. 2008; Deying et al. 2010; Pinyol et al. 2012). In the literature, the 1963 Vajont landslide disaster occurred in Italy is a most well-known example caused by the water impoundment and related sudden changes of hydrostatic groundwater pressure (Kilburn & Petley 2003). Artvin Dam is the one of the most important projects in the master plan of the Çoruh River Basin (Figure 1a). This dam is a 180 m high and 278 m long arch-gravity dam. Construction of the dam began in 2010 with the supervision of Turkey General Directorate of State Hydraulic Works and the dam started to produce hydropower energy in 2015 with the installed capacity of 340 MW. The reservoir behind the dam has a catchment capacity of 167 million cubic meters. With this capacity, the water level of the dam reservoir increased 500 m and reached the toe of a huge paleo-landslide located 8 km southwest of the dam axis in an upstream direction (Figure 1b).

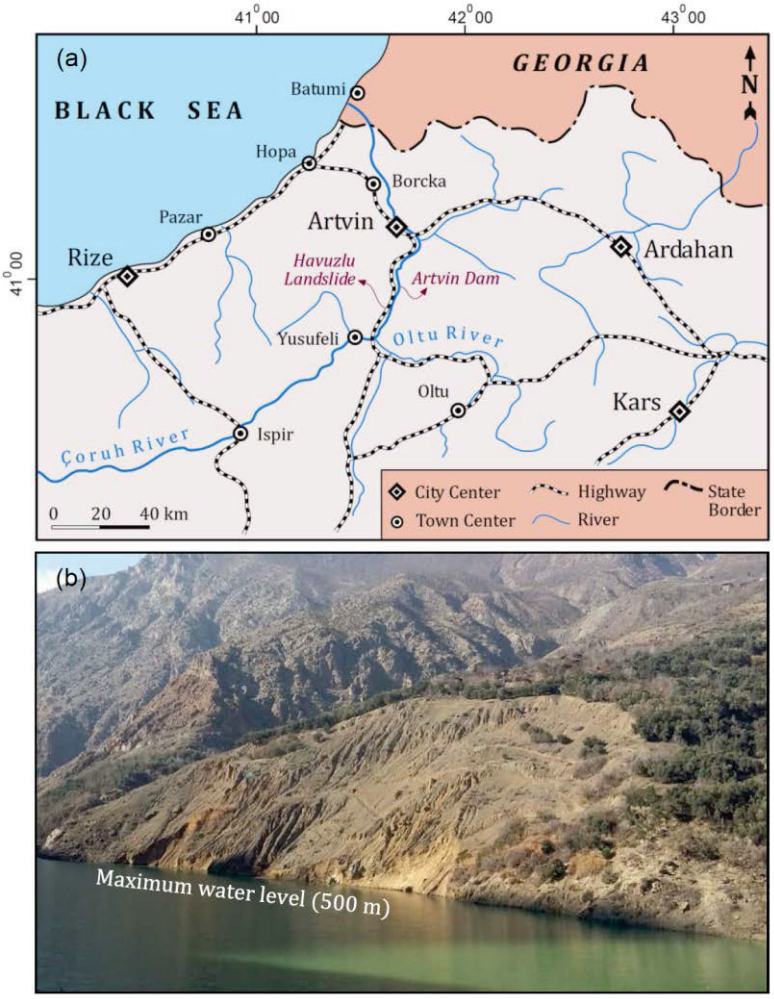

Figure 1. Location map of the study area (a) and Havuzlu paleo-landslide area (b)

Within the scope of this study; (1) vertical and horizontal homogeneity of paleo-landslide materials were investigated using borehole applications, resistivity and seismic surveys, (2) index and strength properties of the materials were determined with the laboratory and field in-situ tests, (3) stability analyses were evaluated using LE and FEM for different conditions, (4) the periodic surface monitoring systems were integrated at the site such as laser distance meter to predict the behavior of landslides during the active duration of the dam and finally (5) the effect the landslide generated impulse waves on the dam body was evaluated.

GEOLOGICAL SETTING

The eastern Pontides, which is one of the tectonic and geological provinces of Turkey, are subdivided into two different zones based on structural differences and lithological properties (Özsayar et al. 1981). While the Upper Cretaceous and Miocene volcano-clastic rocks are dominant lithology in the Northern Zone, the Southern Zone is represented by mainly pre-Upper Cretaceous aged sedimentary rocks (Arslan & Aslan 2006; Eyüboğlu et al. 2007). The study area with complex geological and tectonic features is located in the Northern Zone.

Paleozoic basement metamorphic containing mainly gneiss, micaschist and Paleozoic-Triassic aged magmatic complex consisting of gabbro, microgabbro, phyllite, tonalite were controlled and directed by the thrust faults in the north-south direction in the region. These basement rocks cut by Jurassic aged granites. Liassic-Dogger aged units overlying the basement rocks contains mainly metasandstone, metasiltstone, phyllite, dolerite, basalt, andesite and dacite. These all lithologic units cut by Upper Cretaceous-Paleocene aged granitic rocks. Havuzlu paleo-landslide materials located on the Jurassic aged units (Figure 2).

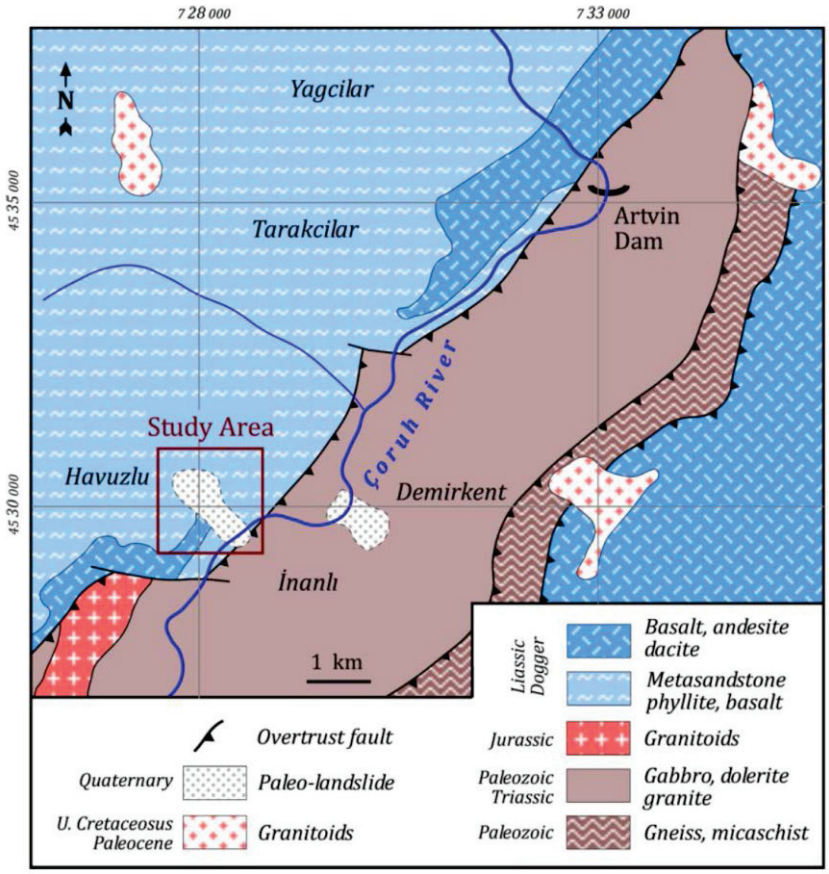

Figure 2. Geological map of the study area

According to probability of exceedance distribution corresponding to return period, an iso-acceleration map was prepared by Erdik et al. (2006) taking into account active faults and using appropriate attenuation relations for Turkey. Although there are no active faults in the study area and around vicinity, the earthquake with magnitude above 6.0 were recorded for the instrumental period (Şaroğlu et al. 1992). For that reason, the peak horizontal ground acceleration (PHA) value was taken as 0.20 g for the study area according to this map.

FIELD INVESTIGATIONS AND SITE CHARACTERIZATION

In the first stage of the study, after the boundaries of paleo-landslide (surface contact between main rock and landslide material) were determined with field observations, 21 boreholes were drilled and electric resistivity surveys in 20 different profiles were carried out to characterize 3D model of the paleo-landslide materials. Based on the drilling logs, the geophysical surveys were planned as the line lengths between 300 and 600 meters. As a result of evaluation of the data obtained from 1602-meter boreholes and the resistivity surveys in different profiles, 3D physical model and 1/2500 scaled engineering geological map of the paleo-landslide materials was prepared (Figure 3) according to IAEG (1976).

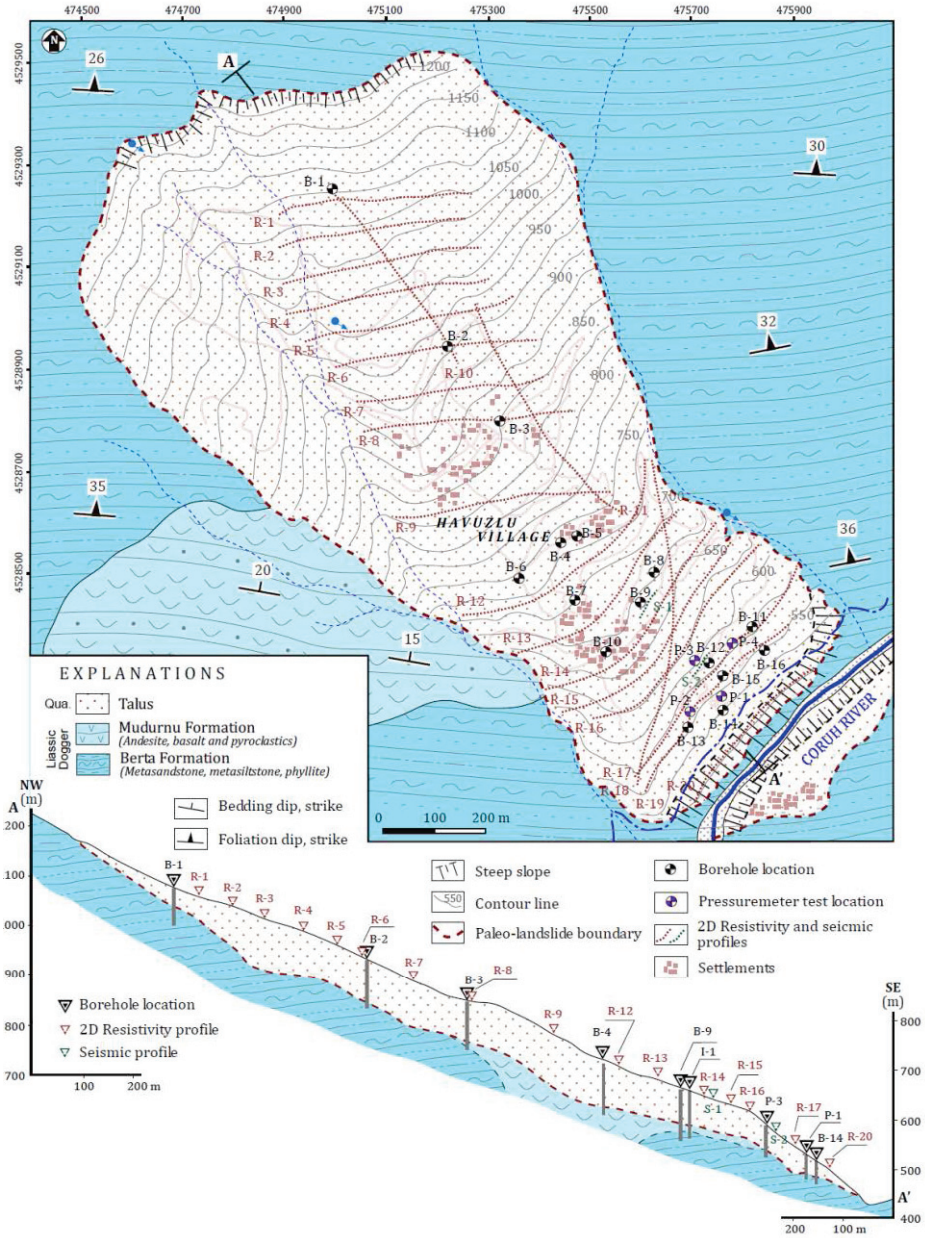

Figure 3. Engineering geological map of the study area

The length of the landslide material is about 1650 m, while the width varies between 450 and 950 meters. The altitudes of the paleo-landslide toe and the main scarp are about 450 and 1230 m respectively. The maximum thickness of the landslide material with an average thickness of 65 meters is over 100 meters. This maximum thickness was reported in borehole logs prepared in the area where the landslide width is least. The field observations, borehole logs and resistivity applications showed that the volume of the paleo-landslide material was about 85 million cubic meters.

Ten boreholes were chosen as piezometer wells to measure groundwater levels for all seasons, but groundwater movement was not recorded in these wells. Surface water originated from precipitation percolated through landslide material to fractured basement rock and this water resurfaced as seasonal contact springs. In addition, pressuremeter tests were conducted at 2 m intervals in four different boreholes (P1, P2, P3 and P4) to determine vertical homogeneity of the landslide materials. All data obtained from borehole applications, geophysical surveys and in-situ tests were evaluated as a whole and the landslide materials were divided into two different zones (Table 1).

Table 1. Classification of the landslide materials as a function of depth and pressuremeter modulus, limit and net limit pressure values for the different zones

Depth (m)	Pressuremeter Modulus (E_M) (kPa)	Limit Pressure (P_L) (kPa)	Net Limit Pressure (P_{LN}) (kPa)	E_m / P_L	Classification	
					Menard (1975)	Briaud (1992)
0-15	1200-7000	300-800	150-550	4.0-8.8	Loose sand	Loose sand
15-	2500-18000	800-1350	400-1200	4.1-13.3	Dense sand	Compact sand

The thickness of the upper zone varies between 15 and 20 meters and the thickness of the lower zone varies depending on the bedrock depth. The bedrock was characterized with two different lithologies. While the volcanic rocks in the Mudurnu Formation were only observed in the boreholes carried out in the landslide material between 600 and 900 m altitude, whereas the metamorphic rocks in the Berta Formation were also cut with the boreholes carried out on other altitudes. The results of the pressuremeter tests showed that while the upper zone of the landslide materials was described as "loose sand", the other zone was classified as "dense or compact sand" according to Menard (1975) and Briaud (1992).

The laboratory tests were performed on the undisturbed samples obtained from five different boreholes and two test pits for determination of index and strength properties of the paleo-landslide materials. Although taking samples from boreholes is difficult issue for cohesionless soils, the undisturbed samples were obtained from the zones containing clay more than 10%. All samples were classified considering the index properties according to the USCS (ASTM 2006) and the landslide materials were generally described as SC (clayey sand) class. In the study, UU direct shear tests were preferred to determine strength parameters and residual strength values were used because the paleo-landslide materials (previously failed) for two different zones. The results of the tests are given in Table 2 and Table 3.

Table 2. Some geotechnical properties of the studied paleo-landslide materials

Borehole Number	Depth (m)	Grain size distribution (%)				Atterberg limits (%)			USCS
		Gravel	Sand	Silt	Clay	LL	PL	PI	
B13	20-21	16	41	30	13	-	-	-	SM
B12	50-52	22	29	35	14	41	25	16	SC
B7	58-60	20	55	17	8	37	23	14	SC
B6	30-31	29	40	20	11	41	25	16	SC
TP 1	2.5-3.0	30	49	16	5	30	17	13	SC
TP 2	2.5-3.0	29	53	13	5	27	15	12	SC

Table 3. Shear strength parameters of the paleo-landslide materials

Sample No	Depth (m)	Cohesion (kPa)	Friction angle (ϕ) (degree)
B6	30.5	28	21
B6	40.1	30	20
B12	10.0	14	28
B12	20.6	18	24
B13	40.0	34	25
TP1	2.5	26	30

STABILITY ANALYSIS OF THE PALEO-LANDSLIDE

There are many large and small paleo-landslides in the Coruh River Basin where many large-scale dams under construction. The effect of the rising pore water pressure in the materials depending on the dam reservoir could make the paleo-landslide materials active. With the sliding of the paleo-landslide material into the reservoir, huge water waves create significant damage at the dam, power plant and settlements in the basin. Considering this situation, the stability of the Havuzlu paleo-landslide material was evaluated using different analysis techniques for different cases. At first stage, limit equilibrium (LE) analysis was performed using Slide v5.0 (Rocscience 2003) software to determine the factor of safety (FOS) of the paleo-landslide material for operating water level (500 m) of the dam lake. The Mohr-Coulomb criterion was used, and the Morgensten-Price method was chosen for combined slide type analyses.

In addition to LE methods, numerical analysis-based methodology such as the finite element (FE) method was used for slope stability analysis in the study. To determine Poisson ratio values of paleo-landslide material, seismic refraction methods using the Geometrics ES3000 12-channel exploration seismograph in two different profiles were performed. Using the obtained data, Poisson ratio values were calculated according to the equation suggested by Tezcan *et al.* (2006) and Lanston (1990) using P and S-wave velocity values.

$$\upsilon = \left[(V_P/V_S)^2 - 2\right] / 2\left[(V_P/V_S)^2 - 1\right] \quad (1)$$

where; ν: Poisson ratio, V_P and V_S: P and S wave velocity (m/s)

The input parameters obtained from the boreholes, in-situ and laboratory studies for the limit equilibrium and numerical analysis are summarized in the Table 4.

Table 4. The values used in LE and numerical analysis for slope stability

Depth (m)	Pressuremeter Modulus (E_M) (kPa)	P-Wave Velocity (P_v, m/s)	S-Wave Velocity (S_v, m/s)	Poisson ratio (ν)	c (kPa)	ϕ (degree)	Unit weight (kN/m^2)	Saturated unit weight (kN/m^2)
0-15	5000	800	420	0.31	21	31	18.6	19.9
15-	10000	1050	550	0.32	28	23	19.1	20.1

Generally, a fraction of peak acceleration (about 1/2 to 2/3 of PGA) is used for pseudo static slope stability analyses because maximum acceleration is not constant during an earthquake. For the studied area, the PHA value was taken as 0.2 g for 475-year return period and this maximum value was preferred for the stability analysis considering to the importance of the landslide generated impulse waves for dam body. According to the analyses results, the FOS values were determined as 1.21 and 0.87 respectively for without and with horizontal ground acceleration (Figure 4).

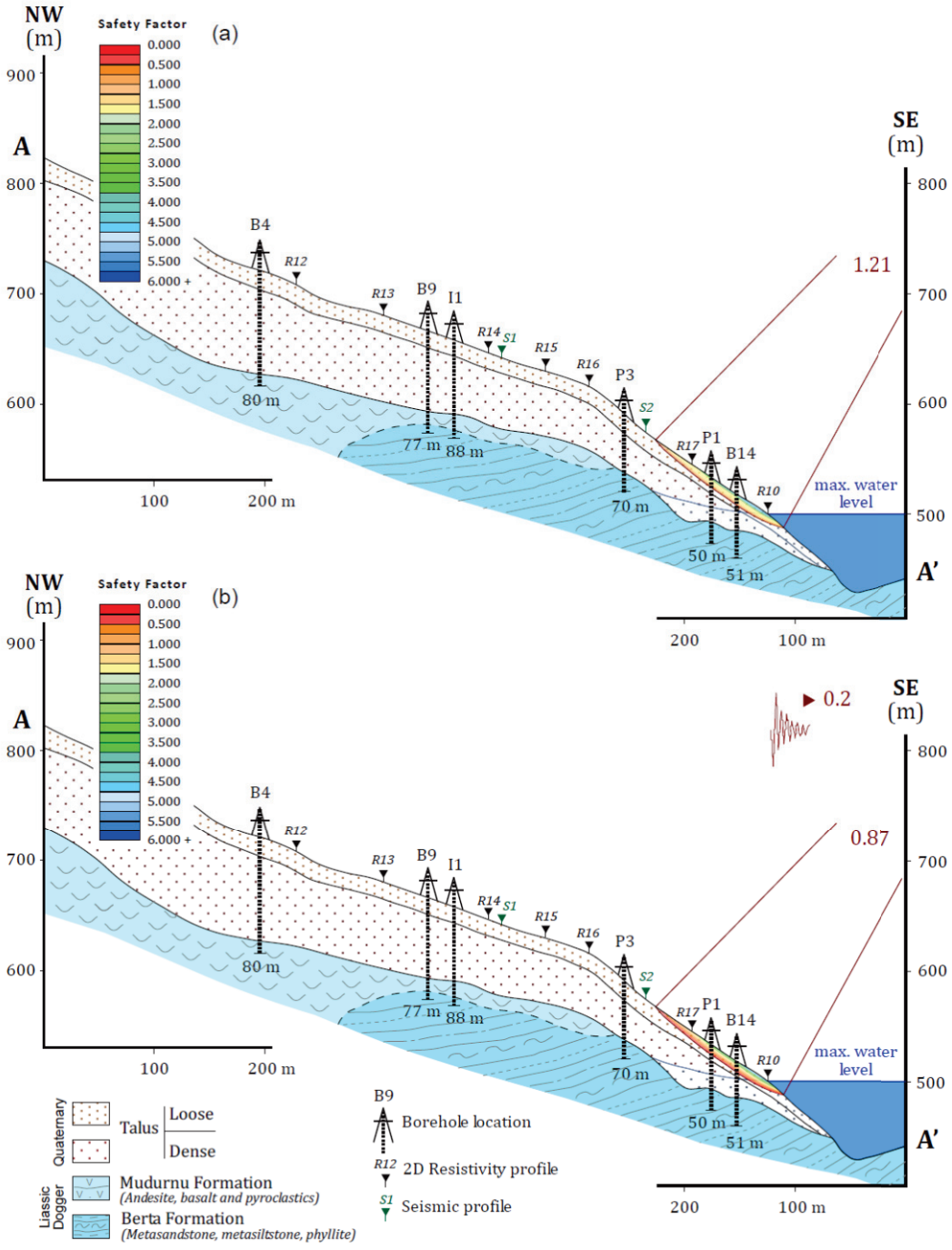

Figure 4. Limit equilibrium (LE) analyses for the A-B cross section (without and with horizontal ground acceleration)

Using the two-dimensional hybrid element model including the Shear Strength Reduction (SSR) analysis was used to evaluate the slope stability. Together with the SSR analyses using Phase^2 software (Rocscience 2006), Stress Reduction Factor (SRF) values for the paleo-landslide materials were determined as 0.81 for seismic load (Figure 5).

FOS and SRF values obtained from both methods are very close to each other and these values are less than 1, which means the results are consistent and the studied paleo-landslide material will unstable for pseudo static case.

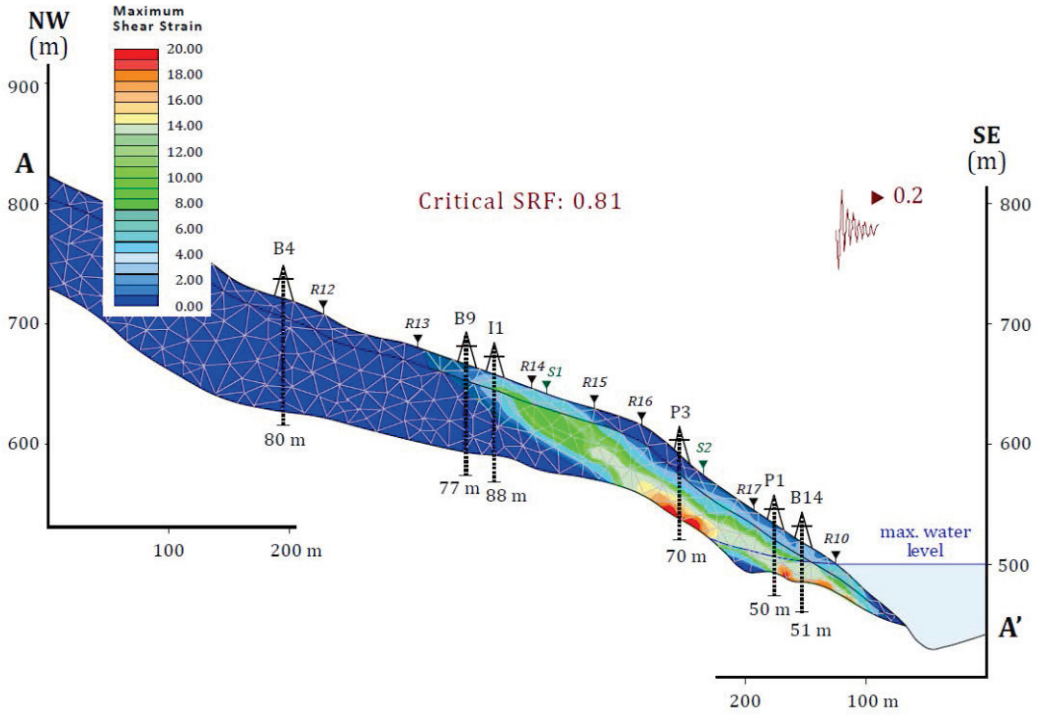

Figure 5. Finite element (FE) based SSR analysis for the A-B cross section

EFFECTS OF THE LANDSLIDE GENERATED IMPULSE WAVES

Impulse waves formed by impact of landslides in dam reservoirs represent a significant hazard for coastal areas and dam body in Çoruh River Basin. Thus, determining the height of the landslide induced wave is the most essential issue due to designation of the minimum freeboard to prevent dam overtopping. In the study, to estimate the height of the impulse waves by the impact of the possible landslide into the water body, the following equation (Equation 2) suggested by Heller (2007) was used and wave height value was calculated 2.6 m on Artvin Dam body.

$$H_{(r,\gamma)} = (3/2)\, P^{4/5}\, cos^2\,(2\gamma/3)\,(r/h)^{-2/3}\, h \qquad (2)$$

where;

$H_{(r,\gamma)}$ (m) : wave height at a given position (for dam body)
P : impulse product number (0.44 from Equation 3)
h (m) : still water depth at a given position (120 m for dam body)
γ (^{o}) : wave propagation angle (70^0)
r (m) : radial distance from the dam body in the wave basin (8000 m)

Impulse product parameters (P) was calculated following equations proposed by Heller et al. (2009) and found as 0.44 for Artvin Dam.

$$P = FS^{1/2} M^{1/4} \{cos[(6\alpha/7)]\}^{1/2} \qquad (3)$$

where;

P : impulse product parameter
F : slide Froud number, $F = v_s / (g\, h)^{1/2}$
v_s (m/s) : slide impact velocity (24 m/s)
g (m/s^2) : gravitational acceleration (9.81 m/s^2)
h (m) : still water depth at a given position (120 m for dam body)

S : relative slide thickness (S = s / h = 0.5)
s (m) : average slide thickness (60 m)
M : relative slide mass [$M = \rho_s \forbidden_s / (\rho_w\ b\ h^2) = 0.57$]
ρs (kg/m^3) : bulk slide density (1950 kg/m^3)
ρw (kg/m^3) : water density (1000 kg/m^3)
$\forbidden_s$ (m^3) : bulk slide volume (2.1 million m^3)
b (m) : slide width on the reservoir (500 m)
α (°) : slide impact angle (degree) (33°)

Slide impact velocity (or landslide velocity) is the one of the fundamental parameters for modeling waves caused by reservoir landslide and it highly depends slide impact angle which is equal to the average angle of shear plane. In the study slide impact velocity was calculated using the Equation 4 proposed by Körner (1976) and found at 24 m/s for a 33-degree slide impact angle (α) value obtained from the surface of rupture in Figure 5 and 6.

$$v_s = \sqrt{2g\ \Delta Z_{sc}(sin\alpha - tan\delta\ cos\alpha)} \tag{4}$$

where;
v_s (m/s) : slide impact velocity
g (m/s^2) : gravitational acceleration (9.81 ms^{-2})
ΔZ_{sc} (m) : drop height of the center of gravity of the slide (150 m)
α (°) : slide impact angle (33°)
δ (°) : dynamic bad friction angle (frictional angle of the landslide material, 23°)

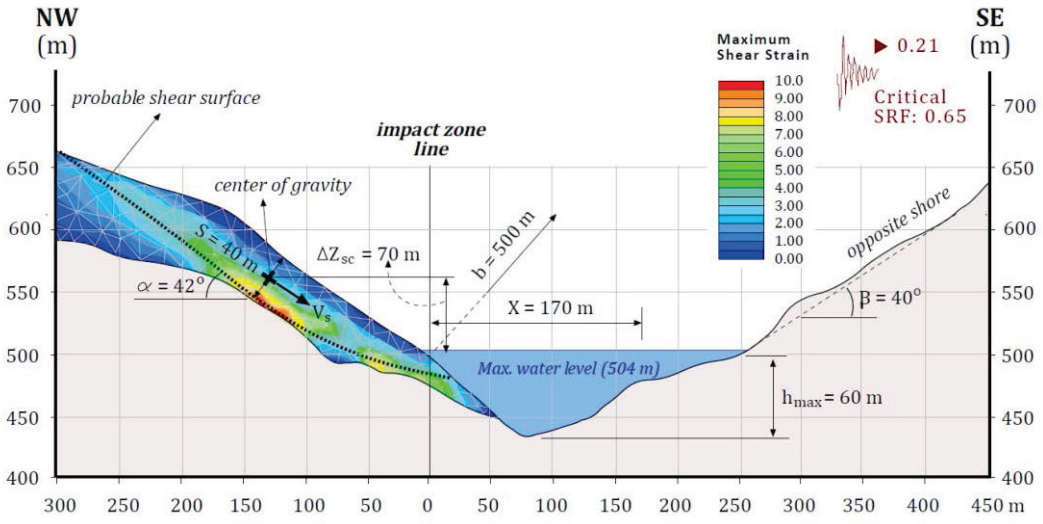

Figure 6. The view of the governing parameters, reservoir and opposite shore geometry in the finite element model

CONCLUSIONS

Although there have been no incidents of dam collapse caused either by mishandling of engineering procedures or the lack of adequate geological characterization, many landslides have occurred around lake areas, derivation tunnels, filled spillway beds and power plants in Turkey. Mass movement problems on a small scale have been seen in the reservoir area and its surroundings in almost every dam project. In recent years, numerous plans for dams have been projected in the Eastern Black Sea

Region, especially in the Çoruh Basin. The building of most of them has begun and this situation brought the mass movement issue in this topographically rough basin along with it.

The Artvin Dam project, the subject of this study, is a striking example of the negative effects of not determining the geological characteristics of the reservoir area in detail when choosing the location of the dam. 8 km southwest of the planned dam there is a 1650 meter-long, 450-900 meter-wide, up to 100-meter-thick and 80 million m^3 paleo-landslide. The dam started to hold water in the September of 2015 and the toe section of the paleo-landslide was left in the dam reservoir. Although the studies into paleo-landslides started 30 years ago, the stability analysis with effects of the dam lake was only started in 2015.

In this study, after 21 borehole applications of a total of 1602 meters, 20 different electric resistivity surveys and two seismic reflections with different profile applications, the horizontal and vertical homogeneity of the landslide material was determined, and the physical and mechanical characteristics of these materials were determined with field and laboratory tests. In the light of this data, the stability of the landslide material was evaluated with limit equilibrium and numerical analyses. In addition, laser distance measurement techniques were used to periodically trace the landslide material. The obtained results and the recommendations are listed below:

1. LE and FEM-SSR methods were used in the stability analyses. While FOS was obtained as 1.21 and 0.87, respectively for without and with horizontal ground acceleration, SRF value was found as 0.81 with PGA. These values show that there is a mass movement risk for only pseudo static situation.

2. In the study the new surface after a possible landslide was modeled and the safety factor was determined to be 4.65 using a limit equilibrium method for the new surface. This value of safety factor shows that the landslide is not regressive.

3. Especially in the models that were obtained by numerical analyses, it is seen that the top elevation of the failure surface is approximately 650 meters. The highest point of the landslide is at the 1170-meter elevation. This situation shows that it is not possible for the 80 million m^3 paleo-landslide mass to slide and it is more likely for local failures to happen.

4. In the analysis that considers that the dam lake is at maximum operation status and considering the ground acceleration, it was determined that 3.5 million m^3 of material will be unstable and when the topographical situation is considered, it was calculated that 2.1 million m^3 of this material might slide into the dam lake. Because the reservoir area is narrow in the area where the landslide could occur, it is thought that the reservoir area could be filled with the materials. For this reason, a 2500-meter-long bypass tunnel was proposed for the dam to continue its function. After the proposal, the construction of the tunnel was finished in May 2015.

5. It is essential to determine the heights of the possible waves that might happen upstream of the Artvin Dam due to sudden mass movement into the reservoir during a possible landslide. To determine height of the landslide generated impulse wave for the dam body, empirical equations based “impulse product parameter” and “slide Froud number” were used for the dam body. Because the height of the wave to strike the dam was calculated as 2.61 meters and the freeboard of the arch-gravity dam was designed as 12 m, overtopping for the dam body are not expected. But, it is recommended to take the necessary precautions and prepare an immediate action plan for risky areas along the valley slopes of the Artvin Dam.

6. Due to the characteristics of the landslide material it is essential, during the dam operations, to utilize change controls of the water levels and to prevent sudden level changes. Also, it is recommended that settlements in the paleo-landslide area be moved.

ACKNOWLEDGMENTS

Karadeniz Technical University (Turkey) Scientific Research Fund. (Project No: FSI-2017-6871) partly supported this study.

REFERENCES

Arslan, M. and Aslan, Z., 2006. "Mineralogy, petrography and whole-rock geochemistry of the Tertiary Granitic Intrusions in the Eastern Pontides, Turkey" Journal of Asian Earth Sciences, 27, 177-193

ASTM 2001. "Standard Practice for Correction of Unit Weight and Water Content for Soils Containing Oversize Particles" In: Annual Book of ASTM Standards. ASTM D4718, Philadelphia, PA.

ASTM 2005. "Standard Test Method for Monitoring Ground Movement Using Probe-Type Inclinometers" In: Annual Book of ASTM Standards. ASTM D6230, Philadelphia, PA.

ASTM 2005. "Standard test methods for liquid limit, plastic limit and plasticity index of soils. In: Annual Book of ASTM Standards" ASTM D4318, Philadelphia, PA.

ASTM 2006. "Standard practice for classification of soils for engineering purposes (Unified Soil Classification System)" In: Annual Book of ASTM Standards. ASTM D2487, Philadelphia, PA.

ASTM 2007. "Standard test method for particle-size analysis of soils. In: Annual Book of ASTM Standards" ASTM D422, Philadelphia, PA.

ASTM 2011. "Standard test method for direct shear test of soils under consolidated drained conditions. In: Annual Book of ASTM Standards" ASTM D3080, Philadelphia, PA.

ASTM 2016. "Standard test method for prebored pressuremeter testing in soils" In: Annual Book of ASTM Standards. ASTM D4719, Philadelphia, PA.

Briaud, J.L., 1992. The Pressuremeter, Taylor and Francis, London.

Corominas, J., Moya, J.. 1999. "Reconstructing recent landslide activity in relation to rainfall in the Llobregat River basin, Eastern Pyrenees Spain" Geomorphology, 30, 79–93,

Deying, L., Kunlong, Y., Chin, L., 2010. "Analysis of Baishuihe landslide influenced by the effects of reservoir water and rainfall" Environmental Earth Sciences, 60, 677–687,

Erdik, M., Şeşetyan, K., Demircioğlu, M.B., Durukal, E. 2006. "Ulaştırma Bakanlığı Demiryolları Limanlar ve Havameydanları İnşaatları Deprem Teknik Yönetmeliği için Deprem Tehlikesi Belirlenmesi" BÜ Kandilli Rasathanesi ve Deprem Araştırma Enstitüsü, Istanbul, Turkey (in Turkish).

Eyuboglu, Y., Bektaş, O., Pul, D. 2007. "Mid-Cretaceous olistostromal ophiolitic mélange developped in the back-arc basin of the Eastern Pontide magmatic arc (NE Turkey)" International Geology Review, 49, 1103–1126,

Fawu, W.F., Peng, X., Zhang, Y., Huo, Z., Takeuchi, A., Araiba, K. & Wang, G. 2006. Landslides and slope deformation caused by water impoundment in the Three Gorges Reservoir, China. The 10th IAEG International Congress, 137, 1–13, Nottingham, United Kingdom.

Heller, V. 2007. Landslide generated impulse waves - Prediction of near field characteristics. PhD thesis, ETH Zurich.

Heller, V., Hager, W.H., Minor, H.E. 2009. Landslide generated impulse waves in reservoirs - Basics and computation. In: Boes, R. (ed) VAW Mitteilung, 211, ETH Zurich.

IAEG (International Association of Engineering Geology) 1976. Engineering geological maps: a guide to their preparation. Unesco Press, Paris, France.

Iverson, R.M. 2001. "Landslide triggering by rainfall infiltration" Water Resources Research, 36,1897-1910,

Kaczmarek, H., Tyszkowski, S., Banach, M. 2015. "Landslide development at the shores of a dam reservoir (Włocławek, Poland), based on 40 years of research". Environmental Earth Sciences, 74, 4247–4259,

Kilburn, C.R.J., Petley, D.N. 2003. "Forecasting giant, catastrophic slope collapse: lessons from Vajont, Northern Italy" Geomorphology, 54, 21–32,

Langston, C.A., Furlong, K.P., Vogfjord, K.S., Clouser, R.H., Ammon, C.J. 1990. “Analysis of teleseismic body waves radiated from the Loma Prieta earthquake”. Geophysical Research Letters, 17, 1405-1408

Liu, J.G., Mason, P.J. 2004. “Landslide hazard assessment in the Three Gorges area of the Yangtze River using ASTER imagery: Zigui–Badong” Geomorphology, 61, 171–187

Matsuura, S., Asano, S., Okamoto, T. 2008. “Relationship between rain and/or meltwater, pore-water pressure and displacement of a reactivated landslide” Engineering Geology, 101, 49–59

Özsayar, T., Pelin, S., Gedikoğlu, A. 1981. “Cretaceous in the eastern Pontides” Black Sea Technical University Earth Science Bulletin, 1, 65–114 (in Turkish with English abstract).

Pinyol, N., Alonso, E., Corominas, J., Moya, J. 2012. “Canelles landslide: modelling rapid drawdown and fast potential sliding” Landslides, 9, 33–51,

Riemer, W. 1995. “Landslides and reservoirs” In: Bell, D.H. (ed) Proc 6th Int Symp on Landslides, Christchurch, Additional papers, reports, discussion. International Association of Engineering Geology, 3, 213–224, Balkema Publishers, Rotterdam.

Rocscience 2003. Slide v5.0, 2D limit equilibrium slope stability analysis software. Rocscience, Toronto.

Rocscience 2006. Phase2-A 2D Finite Element Program. Rocscience Inc., Toronto.

Şaroğlu, F., Emre, O., Kuşçu, I. 1992. “Active Fault Map of Turkey”. General Directorate of Mineral Research and Exploration of Turkey (in Turkish).

Tezcan, S.S., Özdemir, Z., Keçeli, A. 2006. “Seismic Technique to Determine the Allowable Bearing Pressure for Shallow Foundations in Soils and Rocks” Acta Geophysica, 57, 400-412,

Tezel, K. 2015. Engineering Geological Assessment of Havuzlu (Yusufeli, Artvin) Landslide. MSc thesis, Karadeniz Technical University.

Tsai, T.L. 2008. “The influence of rainstorm pattern on shallow landslide” Environmental Geology, 53, 1563-1569,

Vichas, C., Skourtis, C., Stiros, S. 2001 Kinematics of a landslide over The Polyphyton Reservoir (Greece). In: Proceedings of 10th Int Symp of Deformation Measurements. Int Federation of Surveyors, Orange, California, 71–77.

Wang, F.W., Zhang, Y.M., Huo, Z.T., Matsumoto, T., Huang, B.L. 2004. “2003 Qianjiangping landslide, Three Gorges Reservoir” China. Landslide, 1, 157-162,

Wang, H.B., Xu, W.Y., Xu, R.C., Jiang, Q.H., Liu, J.H. 2007. “Hazard assessment by 3D stability analysis of landslides due to reservoir impounding” Landslides, 4, 381-388

5th International Symposium on Dam Safety

October 27-31, 2018

FLOOD SIMULATION OF THE OBRUK DAM

Şerife YURDAGÜL KUMCU [1], Mustafa ALTINAKAR[2]

ABSTRACT

The Obruk Dam is located on the Kızlırmak River which is the longest river having the origin and the end both in Turkey. The aim of the Obruk Dam is supplying energy and water for irrigation. Obruk Dam and HEPP have 4 turbines and each has 93.75 m^3 / s discharge capacity and 52.70 MW installed capacity.

When the turbines of Obruk Dam work full capacity, they supply the discharge of 375 m^3 / s at the downstream of the river bed. Moreover, if the river branches joining to main stream are added to river discharge, there is flood risk in Osmancık district center and Kumbaba village and also in agricultural land through the river. In March 2012, 4 turbines were actively operated because of the high water level of the dam and flood occurred at the downstream.

In this study, in order to show flood scenerios of the Obruk Dam during the 4 turbines under operational caonditions; DSS-WISE and HEC-RAS 1-D mathematical models are used. The flood scenerios and water depths are compared with each other and also with the 10-m DEM satellite image having obtained during flooding under the same operating conditions.

.

Keywords: Obruk Dam, Flood, DSS-WISE, HEC-RAS.

INTRODUCTION

Flood is unexpected overflow that of a large amount of water beyond its normal limits submerges land that is usually dry and it happens in unexpected place and in unexpected time. Overflowing the river from its bed damages the lands surrounding it, the infra structures of the settlements and the living things. As a result, the socio-economic life has trouble. (Uşkay ve Aksu, 2002; Kılıçer and Özgüler, 2002).

Flood is the most common natural disaster seen in the world. Floods usually occur after prolonged rainfall or heavy and sudden rainfall, especially on highly inclined and impervious land areas. 40% of the economic losses resulted by natural disasters due to flooding in the world. Moreover, more than half of all catastrophic deaths are also caused by floods (Ministry of Forestry and Water Affairs, Upstream Basin Flood Control Action Plan 2013-2017). During the previous 2006-2015 decade, floods were the first cause of disaster deaths in all African UN regions, in Central and South America, as well as in Central, South and West Asia. The estimated economic losses from natural disasters in 2016 (US$ 153.9 billion) was the fourth highest since 2006, almost 12% above the annual 2006-2015 damages average (US$ 137.6 billion). This increase in total costs is related, in part, to the US$ 59

[1] Assoc. Professor, Department of Civil Engineering, Necmettin Erbakan UniversityKonya, Turkey, e-posta: yurdagulkumcu@gmail.com

[2] Professor, National Center for Computational Hydroscience and Engineering, Mississippi, US, e-posta: altinakar@ncche.olemiss.edu

billion damages reported for hydrological disasters, an amount representing 1.74 times the annual average. Of this amount, US$ 22 billion are attributable to a flood in China, while US$ 10 billion to another flood in the USA.

Although the number of the earthquake took the largest share in natural disaster occurrences (78% for the period 1900-2013) in Turkey, it followed by floods (22 % for the period 1900-2013) at top ten natural disasers up to international disasters database, EM-DAT records as seen in Figure 1.

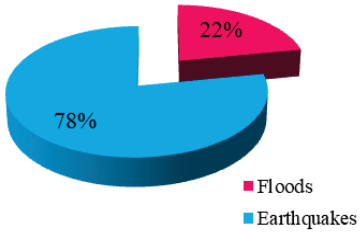

Figure 1. The most effective disasters to Turkey between 1900-2013 (Source: "EM-DAT: The OFDA/CRED International Disaster Database)

The annual average economic loss due to flooding in our country is $ 100,000,000 and the annual investment in projects to reduce the control and losses of the workers is $ 30,000,000. Some floods experienced in Turkey and their results are tabulated in Table 1.

Table 2. Floods in Turkey

Year	Number of floods	Loss of life	Inundated area (ha)	Loss of cost (US$)
1989	10	1	9500	1900000
1990	26	57	7450	206000000
1991	23	23	15770	14000000
1992	14	1	690	11000000
1993	2	-	60	43000
1994	9	4	1680	1200000
1995	20	164	201100	1100000000
1996	4	1	11000	1200000
1997	1	-	1390	60000
1998	2	57	7000	600000000
1999	1	3		
2000	4	-	8.066	
2001	42	8	43.297	
2002	27	27	510	
2003	21	7	64.200	
2004	23	3	25.750	
2005	25	14	13.855	
2006	24	45	85.810	
2007	22	11	1.050	
2008	10	2	10	
2009	84	59	3.250	
2010	110	25	44.279	
2011	56	13	202	
2012	36	15	18.615	
Toplam	484	229	308.894	
Source :DSI				

FLOOD SIMULATIONS of OBRUK DAM

The Kızılırmak is Turkey's longest river that originates and also flows into its territories. It has the second largest drainage basin in Turkey. Its length is 1355 km and the basin area is 8 211 385 ha. The General Directorate of State Hydraulic Works (DSİ) is carring out bedding, flooding and similar flood preventing works in various sections of Kızılırmak River, especially Osmancık center in order to reduce flooding and to reduce its effects.

The Obruk Dam and HEPP located in the Çorum province of Turkey on the Kılırmak River. It's purpose is producing energy and irrigation. Obruk Dam and HEPP have 4 turbine units each have the discharge capacity of 93.75 m^3/s with 52.70 MW installed capacity. When all turbines are under operation, its capacity i s rising to 93.75*4=375 m^3/s. Osmancık district center and Kumbaba village are inundated with the combination of the water flow discharging from all turbines and kızıırmak tributaries. In March 2012, because of the 4 turbines were actively operated because of the high water level of the dam reservoir, and additionally tributaries of Kızılırmak River, flood events occurred at the downstream of the dam and Osmancık. Operation conditions of Obruk Dam and some views belong to inundated areas are seen Table 2 and in Figure 2, respectively.

Table 2. Operation conditions of Obruk Dam

Water Resource	Maximum Discharge (m^3/s)						
	Frequencies (Year)						
	2	5	10	25	50	100	500
Spillway	744	965	1156	1398	1589	1751	5000
Bottom outlet	169	169	169	169	169	169	169
Turbine 1	93.75	93.75	93.75	93.75	93.75	93.75	93.75
Turbine 1+2	187.5	187.5	187.5	187.5	187.5	187.5	187.5
Turbine 1+2+3	281.25	281.25	281.25	281.25	281.25	281.25	281.25
Turbine 1+2+3+4	375	375	375	375	375	375	375
Havva creek	15.1	24.9	30.9	38	42.9	47.5	59
Arkıl Creek	58.3	92.8	113.9	138.5	155.3	170.8	210.2
Dodurga Creek	16	28.3	36.7	47.3	55.3	63.1	81.4
Eminoğlu Creek	18	29.7	36.8	45.1	50.7	55.9	69.1
Balıklı Creek	50.7	92	124.7	170.8	207.6	246.3	330.4
Çomu Creek	73.7	125.8	165.1	217.8	258.4	300	393.4

Figure 2. Views from flooding of Obruk Dam and Inundated areas of Osmancık District

MATERIALS and METHODOLOGY

Two of the 4 turbines of Obruk Dam are under operation in normal operational conditions but third and the last turbines, respectively had to be taken into operation because of the increasing precipitation, in March, 2012. Discharges coming from the tributaries were also joined to main channel and Kızılırmak River overflowed from the river main bed. During the flood, operation conditions of turbines, spillway and the discharges coming from the tributaries are tabulated in Table 3, 4 and Table 4, respectively.

Table 3. Operation conditions of turbines of Obruk Dam

Operation duration, T (h)	Number of turbines under operation	Discharge Q (m^3/s)
0	2	187.50
50	3	281.25
54	4	375.00

Table 4. Operation conditions of the spillway of Obruk Dam

Time		Frequancy time (year)
h	**s**	**2**
0	0	80
40	144000	350
60	216000	650
80	288000	744
100	360000	650
120	432000	350
160	576000	100
180	648000	80

Table 5. Discharges joining from tribitories to main channel

Constant 2 year-frequency flood discharges of creeks	
Creek	Discharge, Q (m^3/s)
Havva	24.9
Arkıl	92.8
Dodurga	28.3
Eminoğlu	29.7
Balıklı	92.0

In the last decades, numerical modeling studies have rapidly increased by development of computer technologies. Numerical models are generally modeled in 1D (Whyte and Barich, 2013). At the time and the use of current 1D models is not sufficient as the flow conditions are can not be fully described with 1D models as flood is a very complex phenomena. Bacuse of that, some concerns about reliability of the results arised (Cox, J.N., 2010). 2D solutions enable flow continuity with horizontal and vertical components of the flow (Cook, A. C. 2008). Furthermore, the use of high resolution geographical information and remote sensing system has made it very easy to access the project data to be used. It is necessary to use all the advantages offered by new technologies in order to make the

most effective use of time and risk assessment by minimizing the loss of life and property at the time of any flood.

In this study, DSS-WISE and CCHE-MESH models and HEC-RAS models, which are one-dimensional models, are used. The results obtained are compared with each other and with the satellite image obtained during flooding under the same operating conditions.

DSS-WISE is Secure, web-based graphical user interface and map server providing analytical capabilities and a decision support system for dam/levee security. It has simplified data entry in 12 easy steps with real-time validation of user input. User input is kept to a strict minimum. It prepares input data automatically using national databases (USGS, NED DEM, levees, bridges, classified land-use/cover) and provides automated, two-dimensional flood modeling/mapping capabilities with cell sizes from 20 ft. to 200 ft. It also displays inundation extent periodically during the simulation. In 80% of the cases, it prepares the results available in less than one hour.

CCHE-MESH is an efficient 2D mesh generator for both structured and unstructured meshes. It supports mesh generations. It is capable of digitization of block boundary, 2D mesh generation of quality structured, 2D rectangle mesh generation, 2D quality of algebraic mesh generation, 2D hybrid mesh generation and 2D quality triangle mesh generation and fast bed interpolation.

HEC-RAS is a software allows the user to perform one-dimensional steady flow, one and two-dimensional unsteady flow calculations, sediment transport/mobile bed computations, and water temperature/water quality modeling.

During the study 10 m sensitive DEM belonging to area were used. 8 flood measurement lines and 29 flow measurement points were added along to Kızılırmak River to measure water depths and profiles as much possible as sensitive. Along the river 334 cross-section were used to define the river bed.

DISCUSSION and RESULTS

After defining the operational conditions of the turbines and spillway of the Obruk Dam, the program run for various scenarios. Figure 3 shows the measurement points, lines and the region indicated on the google map.

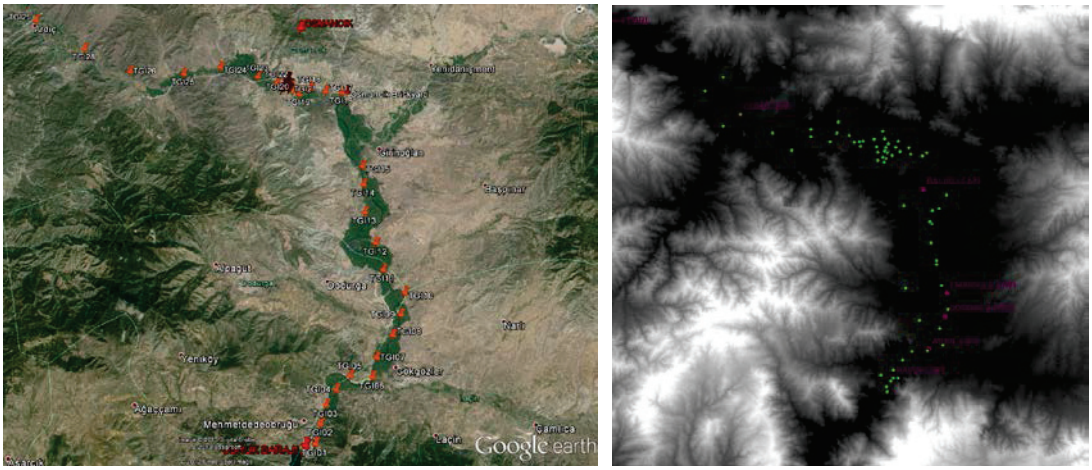

a) b)

Figure 3. Study area and measurement lines and points on a) Google Map b)10 m DEM

DSS-WISE allows describing measurement sections, measurement points and describing creeks. Moreover, water measurements can be observed during the program running time, whenever and whereever needed. In this part of the study, in order to see the water spreading area and water depth variation with time, flood maps belonging to 6h, 18h and 72h are given at the same map on the Figure 4.

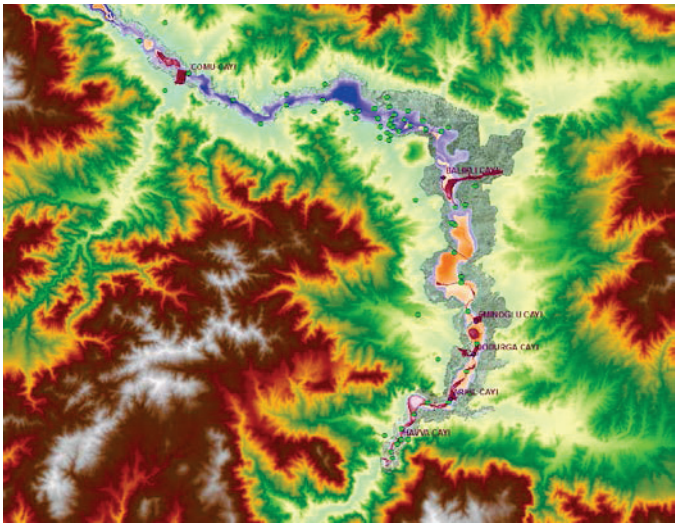

Figure 4. Comparisons of the flood maps belonging to runs of T=6h, 18h ve72h

Water depth variations with time in some stations are given Figure 5. The water depths observed at the station are tabulated in Table 6.

Table 6. Water measurement stations

Station	Region
TGI31	Just downstream of the Obruk Dam
TGI34	Girinoğlan
TGI36	Osmancık-right bank
TGI37	Osmancık-left bank

It is clearly seen Figure 5 that, at station TGI31, water depth is increasing 0.80 m while it also reaches 0.80 m around left bank of the Osmancık district at TGI 37 with time. It is obvious from this figure that, some settlements are inundated with increasing water levels.

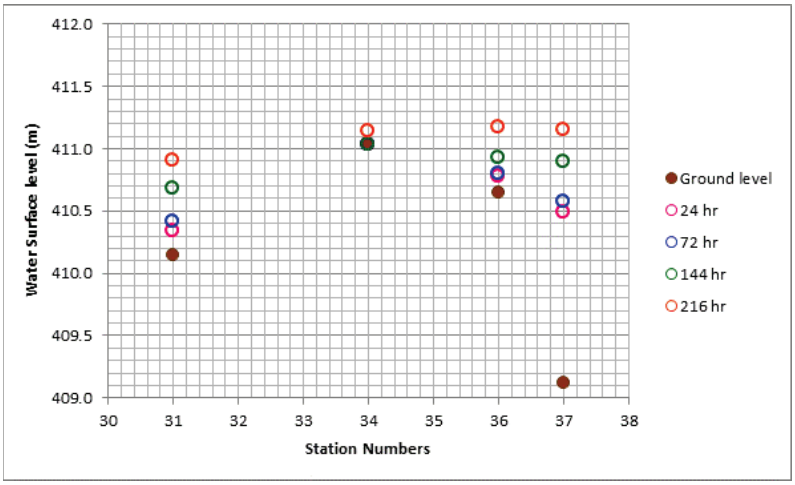

Figure 5 Increasing of Water level at the station of TGI31, TGI34, TGI36 and TGI37

CONCLUSIONS

Flood Simulation of Obruk Dam on the Kızılırmak Basin has been studied with DSS-WISE and HEC-RAS. Inundation areas of Kızılırmak basin has been figured out. It is clear that, if all turbines of Obruk Dam are under operation, some residential districts and their centers are inundated. Water depth of Kızılırmak River overflows and it reches about 0.80 cm around the Osmancık and Kumbaba center.

AKNOWLEDGEMENTS

I would like to express my sincere thanks to my supervisor Prof. Dr. Mustafa ALTINAKAR and NCCHE team for their invaluable guidance, continued interest, patient and encouragement throughout this enjoyable study.

This work was supported by the Scientific and Technological Research Council of Turkey (TÜBİTAK). Grant No: 1059B191200317.

REFERENCES

Cook, A. C., 2008. "Comparison of one-dimensional HEC-RAS with two-dimensional FESWMS model in flood inundation mapping". MS dissertation, May 2008, Purdue University,West Lafayette, Indiana, US.

Cox, J. N., 2010. "Advantages and practicality of using a 2D hydrodynamic model in comparison to a 1D hydrodynamic model in a flood prone area" Bachelor of Engineering (Civil), University of Southern Queensland,Faculty of Engineering and Surveying.

EM-DAT, 2018. "The OFDA/CRED International Disaster Database"

Onuşluel G. ve Harmancıoğlu N. B., 2002. Su kaynaklı doğal afet: Taşkın. TMH-Türkiye Mühendislik Haberleri, sayı:420-421-422, sayfa: 131-132.

"Upstream Basin Flood Control Plan". 2013-2017. The Ministry of Forestry and Water Affairs

Uşkay, S. and Aksu, S., 2002. "Ülkemizde Taşkınlar, nedenleri, zararları ve gereken önlemler". TMH-TMH, No.420-421-422, pp. 133-136.

Kılıçer, Ü. and Özgüler, H., 2002. "Türkiye'de Taşkın Durumu". TMH, No. 420-421-422, pp.142-144.

Whyte, D. and Barich, N., 2013. "Comparing 1D and 2D modelling and implications of outcomes for development planning and approvals" 8th Victorian Flood Conference, 13-15 February 2013, Melbourne, Australia.

5 DAM SAFETY İstanbul Turkey 2018

5th International Symposium on Dam Safety

October 27-31, 2018

EXPERIMENTAL AND NUMERICAL MODELLING OF DAM SPILLWAYS

Şerife YURDAGÜL KUMCU [1]

ABSTRACT

Each dam structure stands specific design according to the topography and climatic conditions of the intended purpose and the region to be constructed. Because of these specifications, each water structure is unique and needs to be projected differently.

In the process of designing of hydraulic structures, in order to describe the phenomena many parameters should be included, so it is not possible to define it exactly mathematically. In this point engineers try to avoid to do mistakes and to find the most appropriate solutions in these structures, which are very expensive to construct. The problems that can be seen after the dam structure is constructed and moreover opened to operation can cause the loss of life and property which cannot be compensated. It is not economical either. Physical and numerical model studies prevent the dam structure from these losses.

The experimental tests and mathematical model studies in hydraulic studies are the measures of the accuracy of the study. If there is no time, area and labor limitations experimental studies may be preferable. Otherwise, mathematical model studies, which use high performance computers, may be another choice to test the structure before constructing it.

As a result, any modeling within the possibilities before the construction of the hydraulic structures is important in terms of preventing serious damages of life and property losses. In this study, experimental and numerical study of a dam spillway will be presented. Differences and similarities will be shown in hydraulic view.

Keywords: Dam spillway design, Experimental study, Numerical study, Spillway structure.

INTRODUCTION

One of the most focused subjects in hydraulic engineering has been the hydraulic design of spillways. It is vital to pass flood flows efficiently and safely to downstream of dams, appropriately planned spillways are required. A hydraulic model is still a precision device for the experimental investigation of flow over a spillway structure, which can give reliable information only if it is designed correctly. Physical models are capable of being most realistic. While the hydraulic modeling is still the widely accepted and utilized mechanism for the experimental investigation of flow over a spillway structure, as it requires experiments, has scaling problems, has measurement difficulties and needs operating

[1] Associate Professor, Department of Civil Engineering, Necmettin Erbakan University, Konya, Turkey, e-posta: syurdagulkumcu@konya.edu.tr

costs, numerical simulations for hydrodynamic processes has become alluring with increasing computer processing capacity and without the necessity of time & budget consuming physical build-up progress (Johnson and Savage, 2006). Having said that, these numerical results still needs calibration and validation with hydraulic model results. The problems involving fluid flow are being solved by a branch of numerical modeling named as Computational Fluid Dynamics (CFD). In this study, in order to evaluate the capability of the computational fluid dynamics on modeling spillway flow a comparative study was also made by using results obtained from physical modeling and computational fluid dynamics (CFD) simulation. A commercially available CFD program, which solves the Reynolds-averaged Navier-Stokes (RANS) equations, was used to model the numerical model setup by defining cells where the flow is partially or completely restricted in the computational space. It was shown that there were many modification needed after project design with experimental and numerical study and there is reasonably good agreement between the physical and numerical models in flow characteristics.

PHSICAL MODELLING

Flow pattern is very difficult to solve as its structure is very complex. Dynamic effects are generally not to be taken into consideration or some equations and definitions are getting simplified doing by assumptions because of the complexity of the flow phenomena.

It is the fact that ignoring the dynamic influences in the design process causes very important problems during the construction and operating stages of the hydraulic structure. Hydraulic modeling is needed to prevent these problems because it has a great deal of precaution for predicting any fault that may occur during construction. As a result, it enables advantages in saving time and cost. For this reason, in case of building huge or extraordinary structures, in order to predict the deficiencies, modeling of the structure in a reduced scale may provide loss of life and property.

Material and Methods

The 1/60-scaled physical model of the Kopru Dam spillway, composed of plexiglas and conventional building materials, was built and tested at the Hydraulic Model Laboratory of State Hydraulic Works of Turkey (DSI) as shown in Figures 1 and 2 (Özcan, 2011). The spillway has a contraction symmetrically; 125 m in width at crest and 100 m in width at flip bucket. Discharge channel has a 0.8/1 ratio slope and 72 m in length and the submerged flip bucket has 15 m radius.

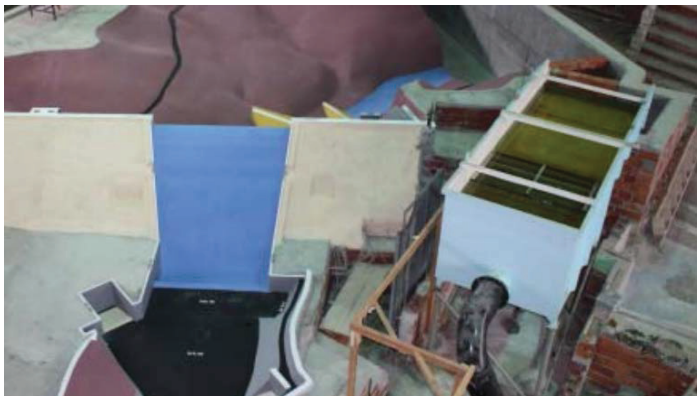

Figure 1. Sharp crested rectangular weir for flow rate measuring and silencer system (Özcan, 2011)

Figure 2. 1/60-scaled physical model with PMF discharge (Özcan, 2011)

Three different upstream reservoir elevations are set as given in Table 1 to run the model. By a control gate positioned far downstream of the model and the downstream tailwater elevations was regulated.

Table 1. Prototype scale operating conditions for upstream and downstream of Köprü Dam

Chosen for	Discharge (m^3/s)	Upstream reservoir elevation (m)	Downstream tailwater elevation (m)
Q_{100} (equals 1/3 Q_{PMF})	1754	413.73	324.20
2/3 Q_{PMF}	3500	415.72	328.30
Q_{PMF}	5223	417.31	331.00

Some modifications were done to obtain uniform flow conditions before and among the chute. Cavitation risks were tested along the spillway. It is figured out that the available aeration device was not sufficient, and there was cavitation risk. To satisfy the need, distribution duct and damps are added to the aeration system (Bureau of Reclamation, 1990). After observing final design for the approach flow conditions and spillway, physical model studies finalized (Figure 2).

Similarly to Kopru Dam, a 1/50-scaled physical model of the Kavsak Dam spillway and stilling basin was built and tested at the Hydraulic Model Laboratory of State Hydraulic Works of Turkey (DSI). The model was constructed of plexiglas and was fabricated to conform to the distinctive shape of an ogee crest. The spillway has 45.8 m in width and 57 m long with a bottom slope of 125%. The length of the stilling basin is about 90 m. A control valve was used to set the flow in the physical model. The model was operated at four different upstream reservoir elevations as given in Table 2. The 3rd and 4th runs in Table 2 belong to corresponding Q_{1000} and Q_{10000} discharge values of the project. The downstream tailwater elevations was adjusted by another control gate located far downstream of the model. Figure 3 and 4 show the general view of the physical model and the some modifications done along the discharge channel, respectively.

Figure 3. Original project given by the project designer (Kumcu, 2010)

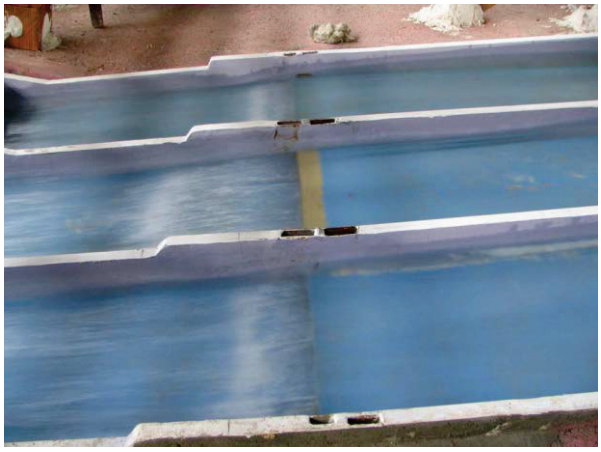

Figure 4. Modification made on the discharge channel (Kumcu, 2010)

Table 2. Upstream and downstream operating conditions of the Kavsak Dam

Run	Upstream reservoir elevation (m)	Downstream tailwater elevation (m)
1	306.55	168.00
2	311.35	174.50
3	314.00	178.90
4	316.50	182.55

NUMERICAL SIMULATION

The purpose of commonly used mathematical models is to calculate the changes in all equations which express the mixture, transport and reactions in a simplified form. Analytical solutions of the equations for every situation may or may not be practical. For this reason, it may be necessary to implement the solutions in a computer using mathematical solution methods such as finite difference or finite element. Depending on the characteristics of the problem, it may be necessary to set up and use much simpler or more complicated models with this basic relation. The mathematical formulation of the problem is the reduction of the physical problem to a set of either algebraic or differential equations subject to certain assumptions.

Material and Methods

The simulations of the flow over the both spillway were modeled in a commercially-available CFD package FLOW-3D Version 11.2. To solve the RANS equations, the program implements finite-volume method. B.D.Nichols and C.W.Hirt (1975), and more completely in C.W.Hirt and B.D.Nichols (1981) expressed that free surfaces are modeled with the Volume of Fluid (VOF) technique, trademarked as TruVOF. This technique facilitates three important functions for free surface flow; location and orientation of free surfaces within computational cells, tracking of free surface motion through cells, and a boundary condition applied at the free surface interface. A cell porosity technique termed the fractional area/volume obstacle representation of FAVOR method (C.W.Hirt 1992) is used by the program to identify the location of the flow obstacles. Staggered grid technique is being used at discrete times to compute the average values for the flow parameters (pressures and velocities) for each cell (Vesteeg and Malalasekera 1996, Kumcu et al., 2017)

FLOW-3D version V11.2 was used to simulate flow over the Kopru Dam along with the renormalized group turbulence model. A rectangular non-uniform grid was defined using by mesh planes in the computational domain shown in Figure 5. Mesh planes provides mesh size distribution relative to the need; neighboring cell sizes has some ratio in between two mesh plane and this mesh intensification facilitates focusing on the most effective parts. Total number of grid cells was approximately 6.82E+06.

FLOW-3D version V10.0 was used to simulate flow over the Kavsak Dam along with the renormalized group turbulence model. A rectangular grid was defined in the computation domain shown in Figure 6. Total number of grid cells was approximately 6.24E+06 in which only 4.36E+06 of them were active.

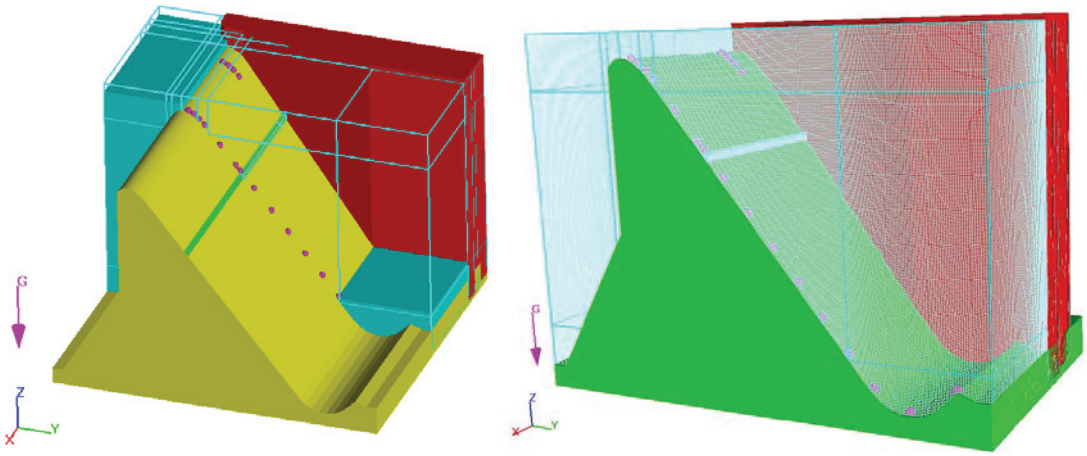

Figure 5: Kopru Dam Spillway solid model used in the CFD simulations, mesh planes & grids

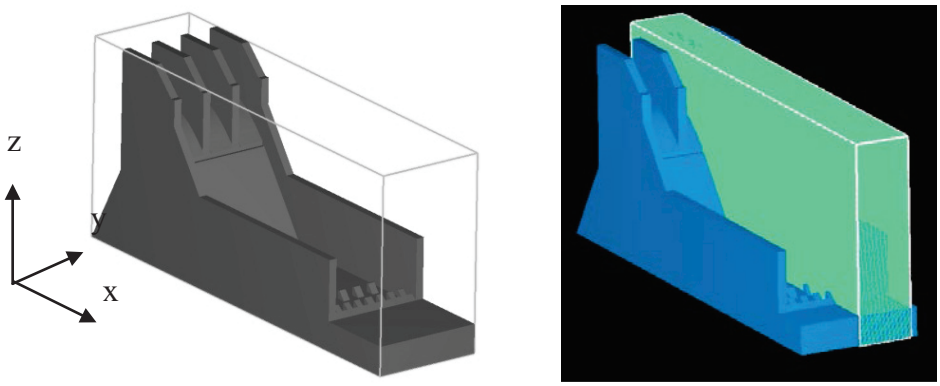

a) b)

Figure 6: Solid model and solid model with mesh of the Kavsak Dam Spillway used in the CFD simulations (final design)

DISCUSSION of RESULTS

The flow rates over the spillway crest are used to compare the differences between the physical model and the CFD model for both Kopru Dam and Kavsak Dam.

Physical model measured flow rates (Q_{PM}) and the numerically calculated flow rates from the CFD model (Q_{CFD}) belonging to Kopru Dam are shown in Table 3. To simplify the assessment of the results, those have been normalized in Figure 4. The Probable Maximum Flood (PMF) parameters are noted as $(H_0)_{PMF}$=7.31 m and Q_{PMF}=5223 m^3/s. The discharge Q is normalized by Q_{PMF} and shown on the ordinate and the static head above crest, H_0, is normalized by the $(H_0)_{PMF}$ and shown in the abscissa in Figure 4. The relative percent difference in discharge and the relative percent difference at a given $(H_0)/(H_0)_{PMF}$ is defined as $(Q_{CFD}- Q_{PM})/Q_{PM}\,x100$. Table 3 shows that the CFD model agrees within 2.0 % in average with the physical model.

Table 3: Measured flow rate (scaled to prototype) versus computed flow rate

Q_{PM} (m^3/s)	Q_{CFD} (m^3/s)	Difference (m^3/s)	Percent Difference
1754	1799	45	2.57 %
3500	3579	79	2.26 %
5223	5284	61	1.17 %

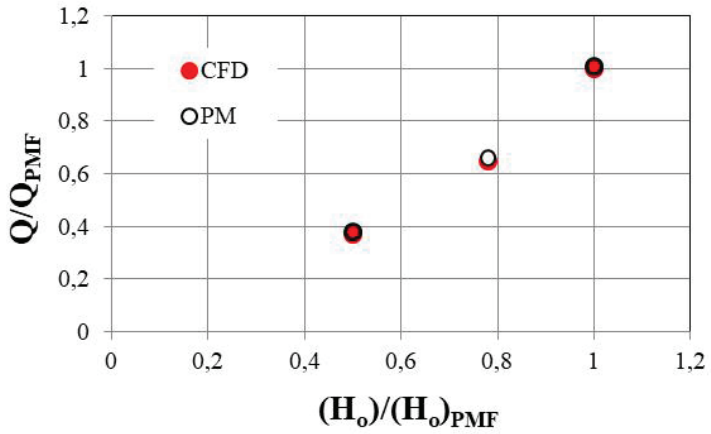

Figure 4: Normalized parameters of physical model (PM) and the numerical model (CFD) predictions for Kopru Dam

Table 4 shows the physical model measured flow rates (Q_{PM}) and the numerically calculated flow rates from the CFD model (Q_{CFD}) for Kavsak Dam. The results have been normalized to allow a comparison in their simplest form in Figure 5. The 10000 years return period parameters, $(H_0)_{10000}$=16.46 m and Q_{10000}=5053 m^3/s, from physical model are used as the basis. In Figure 7 the static head above crest, H_0, is normalized by the $(H_0)_{10000}$ and shown in the abscissa. The discharge Q is normalized by Q_{10000} and shown on the ordinate. Using the physical model and its discharge as observed standard, the relative percent difference in discharge is calculated in Table 4. The relative percent difference at a given $(H_0)/(H_0)_{10000}$ is defined as $(Q_{CFD}- Q_{PM})/Q_{PM}\, x100$ and shows that the CFD model agrees within 3.2% in average with the physical model.

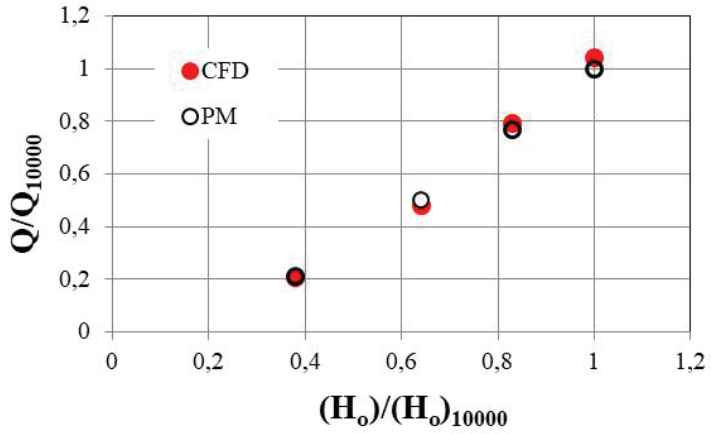

Figure 5: Comparison between the physical model (PM) and the numerical model (CFD) predictions for flow rates over spillway

Table 4: Comparison of observed flow rate versus computed flow rate (prototype scale)

Run	Q_{PM} (m^3/s)	Q_{CFD} (m^3/s)	Per cent difference
1	1000	1034	3.4
2	2500	2415	3.4
3	3856	4001	3.7
4	5053	5170	2.3

CONCLUSIONS

The absolute percent differences between physical modeling and CFD simulation results in discharge estimation for Q_{PM} and Q_{CFD} are found very close to each other. The flow rate results show that the CFD model provided a reasonable solution. The average relative percent difference between the CFD model and the physical model was obtained as 2.0 % and 3.2 % for the Kopru Dam and Kavsak Dam, respectively..

Through the hydraulic jump region, various difficulties experienced mainly due to effects of high turbulence and flow bulking, the CFD measured results for depth-averaged velocities fit generally the physical model data. The ability of numerical methods in the design and analysis of spillway flows are observed.

Even though numerical methods supplied continuously with increasing accuracy, it is needed to be emphasize that the physical model studies are still the benchmark of all alternative solution methods.

REFERENCES

Bureau of Reclamation, 1990. Cavitation in Chute and Spillways. Engineering Monograph No.42. U.S.

Hirt, C.W., Nichols, B.D.,1981. Volume of Fluid (VOF) Method for the Dynamics of Free Boundaries, Journal of Computational Physics, vol. 39, No:201.

Hirt, C.W., 1992. Volume-fraction techniques: Powerfull tools for flow modeling, Flow Science Rep. No. FSI-92-00-02, Flow Science Inc., Santa Fe, N.M.

Johnson, M.C., Savage, B.M., 2006. Physical and Numerical Comparison of Flow Over Ogee Spillway in the Presence of Tailwater, ASCE-Journal of Hydraulic Engineering, vol. 12, No:132, 1353-1357.

Kumcu, Ş. Y., 2010. Model Report of Spillway Structure of Kavsak Dam and HEPP. Report No: 1005. General Directorate of State Hydraulic Works-Hydraulic Model Laboratory, Ankara (in Turkish).

Kumcu, S.Y., Kokpinar, M.A., Guler, I.O.,2017, KSCE Journal of Civil Eng., vol. 21, No:994.

Nichols, B.D., Hirt, C.W., 1975. Methods for Calculating Multi-Dimensional, Transient Free Surface Flows Past Bodies. Proc. First Intern. Conf. Num. Ship Hydrodynamics, Gaithersburg, ML, Oct. 20-23. Özcan, Ç., 2011. Hydraulic Model Studies of Kopru Dam and HEPP. Report No: Hi-1011. General Directorate of State Hydraulic Works-Hydraulic Model Laboratory, Ankara (in Turkish).

Vesteeg, H.K., Malalasekera, W., 1996. An Introduction to Computational Fluid Dynamics, Longman Scientific and Technical, New York.

5th International Symposium on Dam Safety

October 27-31, 2018

FLOOD WAVE PROPAGATION SOLUTION COMPARISON AFTER DAM-BREAK EVENT BY USING DIFFERENTIAL WAVE AND DYNAMIC MOMENTUM METHODS

Hasan Oğulcan MARANGOZ[1], Tuğçe ANILAN[2], Emre AKÇALI[3], Arzu FIRAT ERSOY[4], Hakan ERSOY[4], Murat KARAHAN[5]

ABSTRACT

The impact of destruction wave, occurring after dam-break events, to settlement areas may be much more efficient than flood waves occurring due to rainfall. Therefore, structural and non-structural precautions to be taken in advance have vital importance. These precautions to be taken can be considered according to where border of flood waves can reach and what the hydraulic parameters are. For this reason, it is necessary to obtain available data (topography, geotechnical, hydraulic etc.) and using modelling software with high accuracy. Nowadays, numerical modelling and simulation of flood waves due to the event of a dam failure can be provided by different computational fluids dynamics (CFD) software. However, the contents of these methods and equations used in this software may significantly affect the results.

In this paper, flood propagation analysis of Atasu Dam, located 17 km South from Trabzon province center, is performed with using 2 different type of CFD software. One of the HAD software used in the numerical model of the flood propagation analysis belonging to the same study area is **Saint Venant dynamic wave** and the other is **diffusive wave** equations. Thereafter, the floodplain areas were obtained by 1D and 2D analyzes and the results were compared. Finally, according to the results obtained with both software; the flood wave heights at the city center vary by a maximum of about 0.5 meter and their arrival time is about 5 minutes. Therefore, while borders of flood wave propagations are generally compatible with each CFD software, it varies considerable at some places where the numbers of houses are raised, and slopes are decreased.

Keywords: 2D analysis, dam-break, flood propagation, St. Venant equations. diffusive wave equation

[1] Civil Eng., Department of Civil Engineering, Karadeniz Technical University, Trabzon, Turkey, E-mail: hasanogulcan@gmail.com
[2] Asst. Prof., Department of Civil Engineering, Karadeniz Technical University, Trabzon, Turkey, E-mail: tugcekoc@ktu.edu.tr
[3] Dr. Civil Eng., DSİ 22. Regional Directorate, Trabzon, Turkey, E-mail: emreakcali@dsi.gov.tr
[4] Assoc.Prof., Department of Geology Engineering, Karadeniz Technical University, Trabzon, Turkey, E-mail: firat@ktu.edu.tr
[5] Assoc.Prof., Department of Geology Engineering, Karadeniz Technical University, Trabzon, Turkey, E-mail: blavetirraa@hotmail.com
[6] Res. Assist. Department of Geology Engineering, Karadeniz Technical University, Trabzon, Turkey, E-mail: muratkarahan21@gmail.com

1.INTRODUCTION

Dams can be classified as a safe engineering structure, yet they are also one of the most dangerous engineering structures in the event of damage or failure. Natural disasters such as earthquakes, floods, and landslides, which are frequently observed in our country, cause loss of life and property in the regions where they occur. It can be stated through historical evidence that earthquakes are not necessarily impactful on dam failures [Table 1]. Floods, on the other hand, are considered as the main natural disaster causing the highest damage along with other harms to dam bodies [Table 2]. The failure of the 267-meters-high Vajont Arch Dam in Venice, Italy in 1923 is accepted as one of the most catastrophic disasters in the history, caused by a ceaseless precipitation in the area and resulted the death of more than 2000 people as the reservoir water overtopped the dam body. Likewise, 48 people died in Kenya in 2018 May when 70 million m^3 reservoir water broke free after the failure of Patel Dam as a result of ceaseless heavy rain. This disaster showed that the dams can fail in modern day and the importance of precipitation effect on dam safety. Generally speaking, technical and methodological deficiencies were the main cause of the failure of dams which were built before 1930s. Considering the period from then until now, it can be stated that current dam failures are generally caused by floods [Table 2]. Gleno Dam, which was built in 1923 in Middle Italian Alps, failed during the filling process of the reservoir because of structural faults and deficiencies, resulting the death of 356 people. Built in 1924 in USA, the failure of St. Francis Dam is another dam failure disaster where the dam failed after 2 years because of structural causes and 600 people died (Rogers, 2013).

Different studies in the literature that are conducted on dam failure and wave propagation through numerical simulation software were investigated. Wurbs (1987) compared 6 of the 1-dimensional models that are used to investigate dam failure-induced flood waves, using finite difference method. The simplified dam-break prediction model (SMPDBK) of Natural Weather Service (NWS) yielded the best result in the comparison. Singh (1988) conducted a study on the geometry of breaches during the failure of gradual earth-dams. In the study, triangular, rectangular and trapezoidal-shaped breaches were taken into account to compare water discharge rate from the reservoir. Broad-crested weir hydraulics model was used for the solution of the problem. In another study, 2-dimensional flood simulations were carried out to investigate the effects of the failure of St. Francis Dam in 1928. Also, the analyses were repeated with different Manning's Roughness Coefficients (Begnudelli and Sanders, 2007). Elçi et al. (2017) created 1-dimensional in-stream model using HEC-RAS software and 2-dimensional flood propagation model using FLO-2D software for the scenario of instant failure of Porsuk and Alibey dams. Parameters such as water height, propagation area, flood propagation velocity and arrival time were compared in the analyses.

Today, a dam failure incident can be numerically simulated and the areas under the risk of flood can be realistically determined using computational fluid dynamics (CFD) software. The type and application of the precautions against the hazard becomes easier as flow-rate, velocity, and water surface parameters in the determined area are known. When the applications that are conducted using CFD software are evaluated, it is seen that shallow water equations known as the Saint Venant Equations are often used in the 1- and 2-dimensional analyses for flood calculations. Saint Venant equations can be used both as is and by neglecting some of the terms in the equations (Demirpençe, 2001). In this study, solutions of dynamic momentum equations, which includes all terms in the equation to the iterations, and diffusive wave equations, which excludes convective accelerations, are compared for the same calculation area, thus, details on sensitivity of the solutions and usability of the equations with respect to terrain structure are explained. In the study area, numerical flood analysis calculations were carried out by 2-dimensional modelling and diffusive wave equations using HEC-RAS CFD software. The compared software, SOBEK CFD, was adopted from the results of another study (NFB, 2014) and 1-dimensional in-stream models and 2-dimensional wave propagation models in urban areas were compared. Therefore, differences in the output parameters between 1- and 2-dimensional analyses are presented in the Results section of this study.

Table 1. Dam Failure Types and Their Percentages (Abay et al., 2015)

Failure Type	%	Cause of Failure
Overtopping	34	Improper spillway design; bed load accumulation in spillway; scouring of dam crest
Foundation Problems	30	Differential settlements; slide and slope instability; high toe-water pressure, uncontrolled seepage
Piping and seepage	20	Internal collapse due to piping; seepage and collapse along hydraulic structures such as sluice way; cracks in dam body
Pipes and valves	10	Infiltration of backfill material through junctions or cracks
Other	6	Earthquake, vegetation, animal influence, etc.

Table 2. Major Dam Failure Incidents with Death Counts Above 50 (Abay vd., 2015)

Row	Dam	Year	Country	Death Count	Cause of Failure
1	Banqiao/Shimantan	1975	PRC	171.000	Catastrophic rain
2	Machchu 2	1979	India	5.000	Overtopping
3	Sempor	1967	Indonesia	>2.000	Overtopping
4	South Fork	1889	USA	2.209	Excessive rain
5	Vaiont	1963	Italy	2.000	Overtopping
6	Tigra	1917	India	1.000	Seepage to foundation
7	Panshet	1961	India	1.000	Body collapse
8	Puentes	1802	Spain	608	Soft soil
9	St. Francis	1928	USA	600	Geological instability
10	Malpesset	1959	France	423	During construction
11	Gleno	1923	Italy	356	Design error
12	Val di Stava	1985	Italy	268	Design error
13	Koshi	2008	Nepal	250	Excessive rain
14	Dale Dike	1864	England	244	Improper construction
15	Canyon Lake	1972	USA	238	Flood
16	Kantale	1986	Sri Lanka	180	Improper management
17	Tangiwai	1953	N. Zealand	151	Crater lake flood
18	Bouzey	1884	Algeria	150	Slide
19	Vega de Tera	1959	Spain	144	Body collapse
20	Mill Nehri	1874	USA	139	Design error
21	Buffalo Creek	1972	USA	125	Excessive rain
22	Sella Zerbino	1935	Italy	111	Geo. Instability/Flood
23	Vratsa	1966	Bulgaria	107	Mud and water flood
24	Situ Gintung	2009	Indonesia	98	Exc. Rain/ Imp. Mang.
25	Certej	1971	Romany	89	Body collapse
26	Bilberry	1852	England	81	Excessive rain
27	Austin	1911	USA	78	Design error
28	Sayano/Shushenskaya	2009	Russia	75	Turbine break-off
29	Eder ve Möhne	1943	Germany	70	Intentional collapse
30	Shakidor	2005	Pakistan	70	Excessive rain

2. STUDY AREA

Atasu Dam is a 118-meter-high rockfill dam with concrete coating on upstream face, located in Maçka district of Trabzon city, towards the upstream of Değirmendere Stream. It has 35 million m^3 of reservoir storage volume, 745.50 m^3/s spillway and 141 m^3/s sluice way discharge rate capacity. It was constructed for the purposes of flood control, drinking-running water supply and energy production, and began operation in 2010. Atasu Dam is classified as a large dam in every category of the World Commission on Dams' classification.

Figure 1. View of the Study Area

Although Atasu Dam is at a distance of 17 km from the urban areas of Trabzon city center, it is only 2 km away from settlements like Temelli, Barışlı, Hızarlı, Gayretli, Alaçam, Armağan and Akoluk. Thereby, this gives an idea about the potential hazard on the settlements near the dam body in case of a dam failure.

3. METHODOLOGY

3.1. Preparing Geometric Data

Digital Elevation Model (DEM), which is the base of the model geometry, was created by processing the 1/5000 scaled photogrammetric maps of the study area in WGS 1984 datum system using ArcGIS. Approximately 170000 4 to 8 edged, 100*100 cm grids were used in the HEC-RAS software for 2-dimensional flood analysis. Flood control walls, bridges, culverts and embankments were not defined in the analysis software as they were already included in the processing stage of the DEM, while buildings in the flood area are added to the DEM at a later stage via 3-dimensional spatial analysis using ArcGIS software [Figure 2].

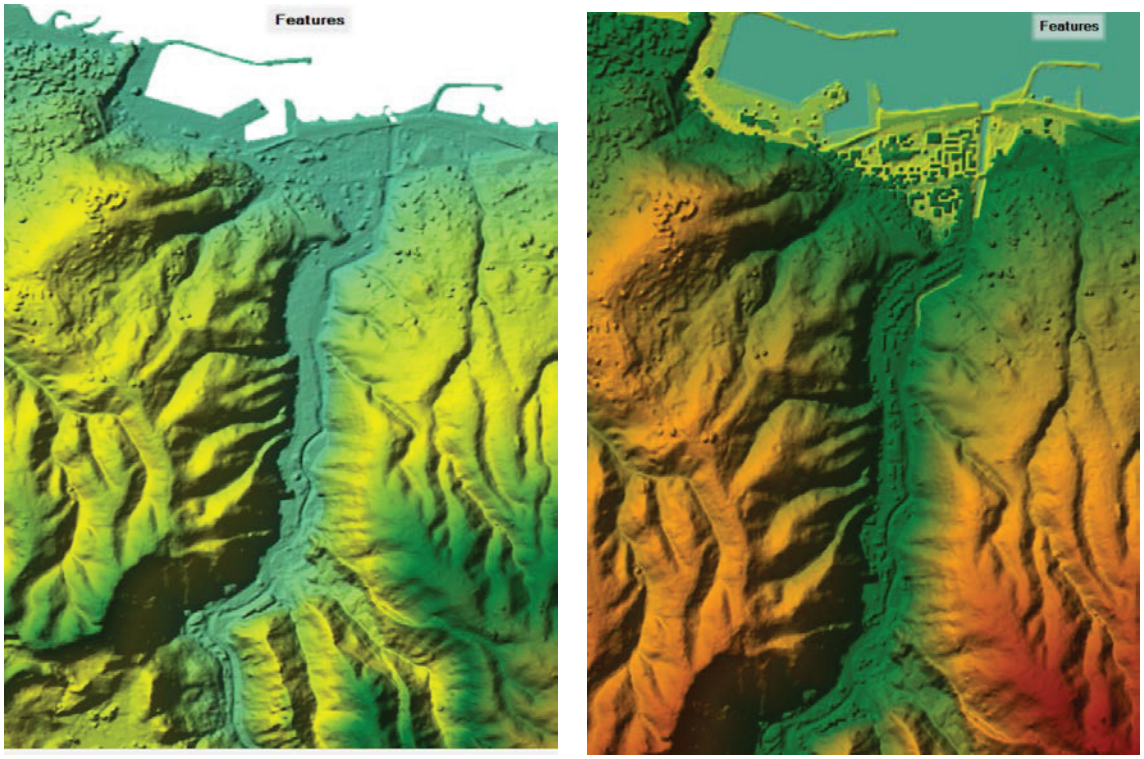

Figure 2. Adding Buildings in the Study Area into the Digital Elevation Model

3.2. Calculation of Design Flood Flow Rates

Two different flow rates were used in the failure analyses of the Atasu Dam. One of them is the rainfall-induced peak flow rate of the stream which would be responsible for the failure of the dam. The other one is the flood flow rate which will arise after the peak flow rate causes the dam failure by damaging the body. In the analyses, one of the hydraulic unknowns was the entrance coordinates of the flood flows caused by the dam failure. Then, flow rate values in the city center or other settlements were determined by repulsing the obtained hydrograph through the downstream.

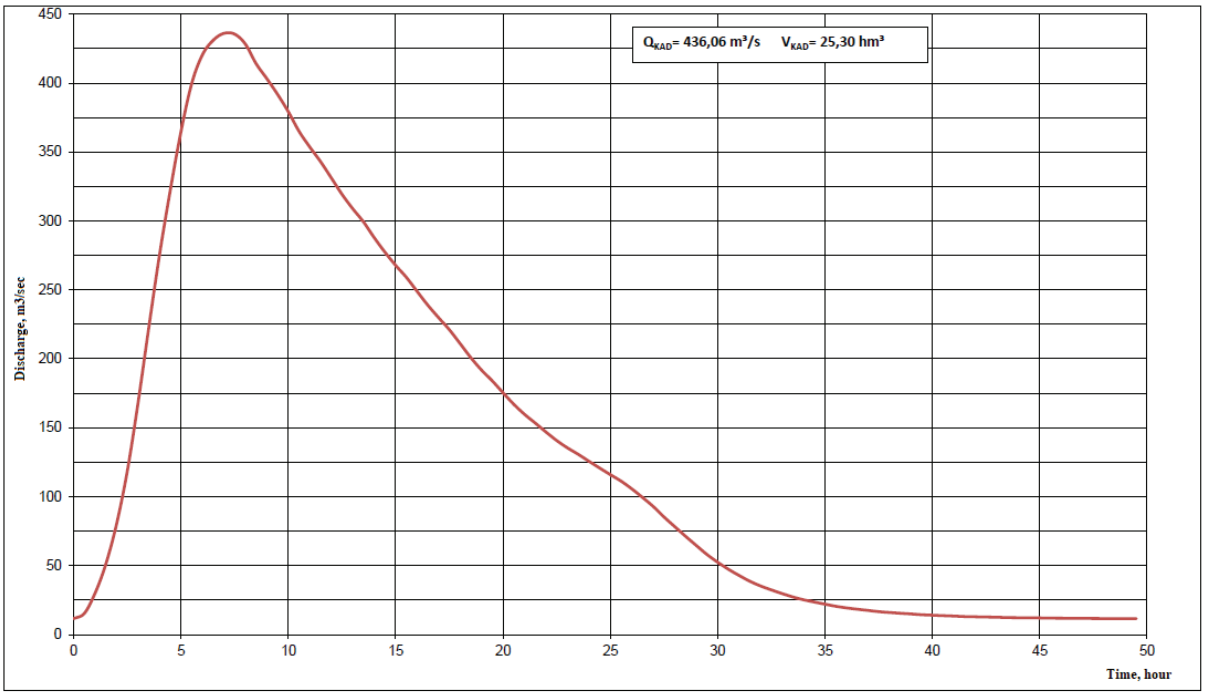

Figure 3 – Catastrophic Hydrograph Repulsed to the Dam Axis (NFB, 2014)

The catastrophic flood flow rate responsible for the failure of the dam was calculated in accordance with synthetic method of General Directorate for State Hydraulic Works (DSİ) as 436.06 m^3/sec and the flood outputs were compared based on this value. The flood hydrograph coordinates after the dam failure have been determined using HEC-HMS (USACE) software in a previous study (NFB, 2014). The input parameters for the hydrologic model are catastrophic flow rate, dam parameters, time of failure, elevation-volume curve [Table 3] and the dam failure-induced hydrograph coordinates of the first cross-section towards downstream [Table 4]. The hydrograph coordinates of the last cross-section, on the other hand, are one of the output parameters.

Table 3. Elevation-Volume Curve of Atasu Dam Used in the Hydrologic Model (NFB, 2014)

Elevation (m)	Volume (hm^3)
202	0
210	0.02
220	0.25
230	0.85
240	1.93
250	3.65
260	6.05
270	9.17
280	13.13
290	17.99
300	23.79
310	30.63
320	38.71
330	48.15
340	58.99
350	71.34

Table 4. Flow rates in the event of failure of Atasu Dam through catastrophic flood (m^3/sec) and some of the hydrograph coordinates (NFB,2014)

Time (sec/min/h)	Flow rate (m^3/sec)	Time (sec/min/h)	Flow rate (m^3/sec)	Time (sec/min/h)	Flow rate (m^3/sec)	Time (sec/min/h)	Flow rate (m^3/sec)
0:00	0.0	15:00	267.5	6:00	52.1	21:00	12.0
0:15	0.3	15:15	262.6	6:15	49.5	21:15	11.5
0:30	42919.6	15:30	259.5	6:30	47.1	21:30	11.0
0:45	18.9	15:45	253.2	6:45	44.6	21:45	11.0
1:00	26.3	16:00	248.4	7:00	42.1	22:00	11.0
1:15	35.3	16:15	242.7	7:15	40.0	22:15	11.0
1:30	45.7	16:30	238.4	7:30	38.1	22:30	11.0
1:45	58.2	16:45	233.3	7:45	36.5	22:45	11.0
2:00	72.7	17:00	229.4	8:00	35.1	23:00	11.0
2:15	89.5	17:15	224.8	8:15	33.5	23:15	11.0
2:30	108.5	17:30	221.3	8:30	32.1	23:30	11.0
2:45	130.5	17:45	215.9	8:45	30.5	23:45	27.4
3:00	155.5	18:00	211.3	9:00	29.1	0:00	60.3
3:15	181.5	18:15	205.4	9:15	28.0	0:15	75.6
3:30	208.5	18:30	200.3	9:30	27.1	0:30	71.9
3:45	235.3	18:45	195.4	9:45	26.0	0:45	72.1
4:00	261.8	19:00	191.2	10:00	25.1	1:00	69.4
4:15	286.8	19:15	187.4	10:15	24.0	1:15	69.4
4:30	310.6	19:30	184.2	10:30	23.1	1:30	67.1
4:45	331.3	19:45	179.4	10:45	22.5	1:45	67.0
5:00	352.2	20:00	175.2	11:00	22.0	2:00	64.9
5:15	374.3	20:15	170.9	11:15	21.0	2:15	64.1
5:30	385.7	20:30	167.2	11:30	20.0	2:30	61.7
5:45	405.8	20:45	163.0	11:45	19.5	2:45	61.4
6:00	423.3	21:00	159.2	12:00	19.0	3:00	59.8
6:15	422.3	21:15	155.9	12:15	18.5	3:15	59.5
6:30	433.9	21:30	153.2	12:30	18.0	3:30	58.1
6:45	430.6	21:45	149.5	12:45	17.5	3:45	57.7
7:00	438.7	22:00	146.1	13:00	17.0	4:00	56.4
7:15	433.0	22:15	143.0	13:15	16.5	4:15	55.7
7:30	437.4	22:30	140.1	13:30	16.0	4:30	54.2
7:45	429.3	22:45	137.5	13:45	16.0	4:45	53.8
8:00	430.2	23:00	135.1	14:00	16.0	5:00	52.8
8:15	419.1	23:15	132.5	14:15	15.5	5:15	52.3
8:30	416.0	23:30	130.1	14:30	15.0	5:30	51.4
8:45	406.8	23:45	127.5	14:45	14.5	5:45	51.0
9:00	404.8	0:00	125.1	15:00	14.0	6:00	50.2
9:15	395.5	0:15	122.5	15:15	14.0	6:15	49.5
9:30	392.6	0:30	120.1	15:30	14.0	6:30	48.5
9:45	383.6	0:45	117.5	15:45	14.0	6:45	48.1
10:00	380.5	1:00	115.1	16:00	14.0	7:00	47.5
10:15	370.8	1:15	113.0	16:15	13.5	7:15	47.1
10:30	366.3	1:30	111.1	16:30	13.0	7:30	46.5

The time to failure of dam body and other breach parameters were calculated through the equations of Froehlich (1995) with the assumption that the kadastrfal flow will overtop the dam body and propagate through a trapezoidal breach. The K_0 value in Equations 1 and 2 is a constant coefficient which is adopted as 1.4 in the events of overtopping. V_w is the storage volume at normal water level. h_b is the height of the breach.

$$B_{mean}(m)=0.1803 \times K_o \times V_w^{0.32} \times h_b^{0.19} \quad (1)$$

$$T_f(hour)= 0.00254 \times V_w^{0.53} \times h_b^{(-0.90)} \quad (2)$$

Mean breach width and time to failure were determined as 163.91 meters and 0.35 hours respectively via *Equation 1* and *2* [Figure 4]. Z_b coefficient is expressed as 1/inclination and it is important for determining the edge inclinations of breaches. The inclination is adopted as 1 for the event of overtopping (NFB, 2014) [Figure 4].

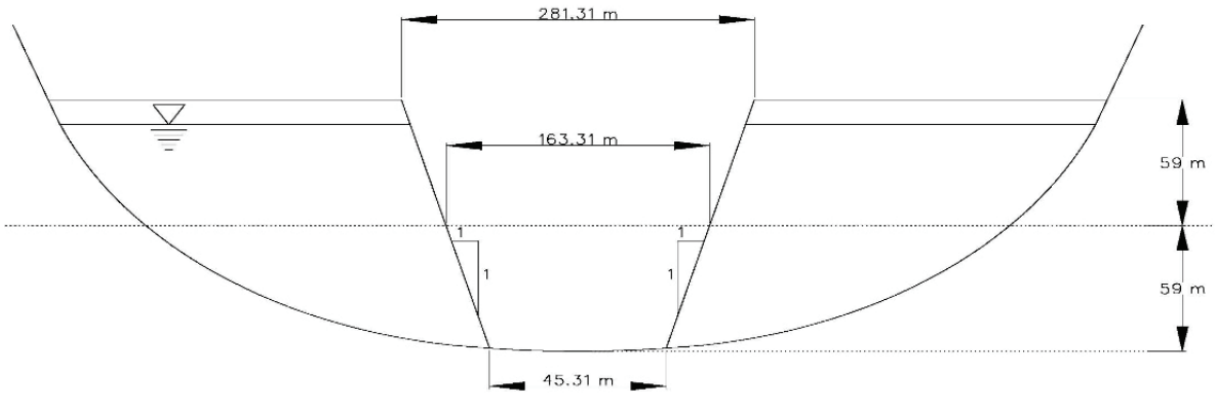

Figure 4. The final condition of the breach after the overtopping of the dam (NFB, 2014)

3.3. Motion Equations

Dam failure problems can be simulated by shallow water equations. In open channel hydraulics, shallow water equations predicate that the stream's length is much higher than its depth. Therefore, the movements that are taken into account in flood calculations solved with these equations do not take place in the depth aspect. The inclination of the stream which the equations will be used for must be partly over 0.001. The equation consists of 2 sub-equations as conservation of mass and momentum. The problems can be solved along a line (1-dimensional) or area of each grid (2-dimensional) by using convenient boundary conditions and iterations. The momentum equation in Saint Venant equations is composed of local acceleration term, conserved acceleration term, pressure force term, gravity force term and friction force term. These terms are also known as the dynamic momentum equations. When dynamic momentum equation is used for a flood analyses, all the terms in the equation are included in the calculation and iteration. As for the diffusive equation the local acceleration and conserved acceleration terms are neglected, then it is solved by combining with conservation of mass. In 1-dimensional flood calculations, the calculation is conducted along the possible propagation direction of water, and only one dimension is present in the equations spatially. The Saint Venant equations become usable for grid solutions when their integral is taken spatially as in Equation *3* and *4* (Thi, 2011).

$$\frac{dQ}{dt}+\frac{1}{A}\frac{d}{dx}\left(\frac{Q^2}{A}\right)+g\frac{dy}{dx}-g\left(S_0-S_f\right)=0 \quad (3)$$

$$\frac{dQ}{dx}+\frac{dA}{dt}=0 \quad (4)$$

The 1- and 2-dimensional numerical failure simulations of Atasu Dam for the same study area were conducted by Saint Venant equations using HEC-RAS in this study and SOBEK in the previous study (NFB, 2014). The studies that conducted using whole Saint Venant equations via SOBEK software (NFB, 2014) and using diffusive wave equations via HEC-RAS software were compared in this study. The diffusive equations are obtained as shown below by neglecting local and conserved inertia terms in St. Venant equations and combining it with continuity equations:

$$\frac{dQ}{dt} + C\frac{dQ}{dx} = D_h\left(\frac{d^2Q}{dx^2}\right) \tag{5}$$

Although this approach was used as diffusive wave approach in many previous studies, it was stated by some researchers (Kaya and Ülke, 2013) that diffusive waves can also have inertia effects. The impact of molecular diffusion can be neglected in practical applications. Additionally, if mean values of Q and C are used along the cross-section, the value of D_h becomes higher than sheer turbulence diffusion. This is why the change in velocity in the cross-section is the biggest effect that causes diffusion (Yüksel, 2013). Therefore, for the solution with diffusive wave equations, the propagation of water in 1 or 2 directions is largely due to the acceleration caused by floor inclination.

3.4 Results of Flood Analyses

The results of solutions by HEC-RAS and SOBEK software are presented in this section. Below is the comparison of outer limits of flood waves that are calculated by diffusive and dynamic momentum equations after a catastrophic flood-induced dam failure [Figure 5].

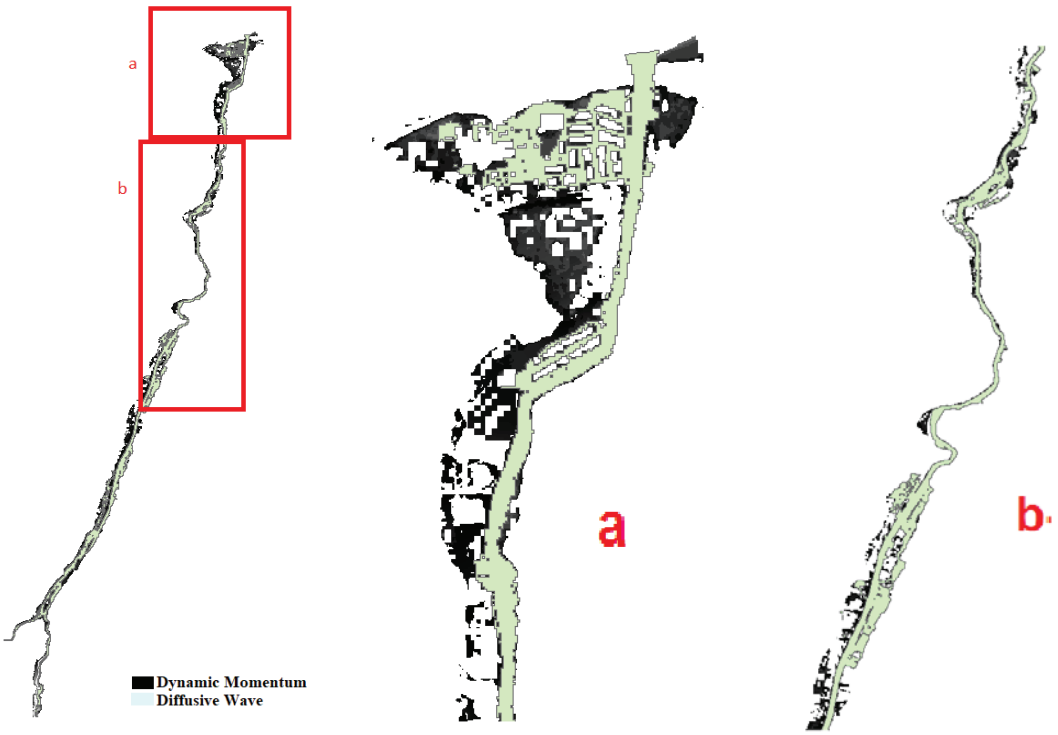

Figure 5. Overlapping flood boundaries of Diffusive and Dynamic Momentum Equations (a-Close view from city center) (b-Close view from Değirmendere)

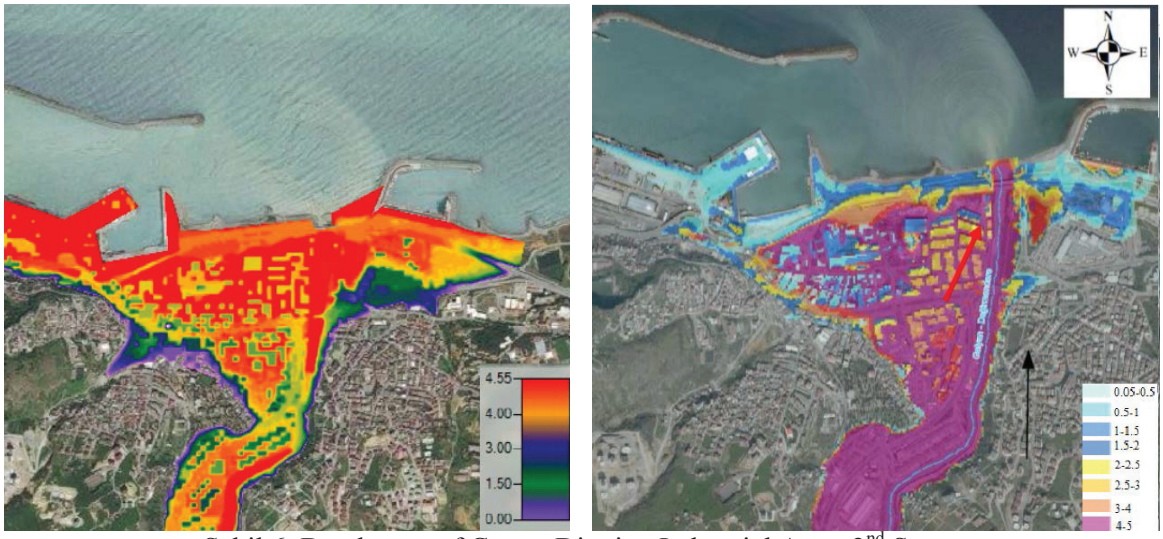

Şekil 6. Depth map of Center District, Industrial Area, 2nd Street
a-Diffusive Wave b-Dynamic Wave

The water velocity values in the main stream are between 3 and 16 m/sec for both models after the failure of the dam because of a catastrophic flood. The flood propagation areas differ in city center and where main stream deviates [Figure 5]. The maximum flood depth reaches 5 meters in some locations of city center for dynamic wave solution, while it's nearly 5.5 meters for diffusive wave solution. The minimum flood depth is between 3 and 5 centimeters for both solutions. The flood wave reaches Esiroğlu settlement after approximately 20 minutes in both solutions. The wave reaches the sea through the industrial area of city center after 50 minutes in dynamic wave solution and 55 minutes in diffusive wave solution. The insufficient bridges along the flood area are similar in both models. Also, the Trabzon Airport is out of the risky area in solutions with both equations.

4. RESULTS

In this study, the dam failure-induced flood wave analysis was conducted with diffusive wave method and it was compared with dynamic wave equations for study area. It is seen that the compared parameters such as flood boundaries and flood depths differ between both models. Additionally, the time for the flood wave to reach city center differ for about 5 minutes between the models. It can be seen that the results of diffusive and dynamic momentum equations significantly differ in 2-dimensional grid solutions because of the presence of buildings and bridges. This situation can also be observed in the areas where elevation increases or decreases instantly. The neglection of local and conserved acceleration properties in diffusive wave equations is the main reason of this. It is seen that the results of diffusive and dynamic wave equations differ especially in areas like external building walls and bridge abutments, where significant changes in acceleration and velocity values are expected.

Another difference in the results of the analyses is the properties of flood propagation in some areas of the main stream. The 1-dimensional modelling of the main stream in SOBEK software means that the dynamic wave equations are solved along the flow direction and thus only accelerations in this direction are considered. Therefore, solutions partly differ for the areas where the inclination gets lower and lateral accelerations become more important. Nonetheless, it is observed that flood propagation and other properties are in accord for the areas that are 2-dimensionally modelled. In HEC-RAS software, all propagation was conducted in 2 dimensions and thus 2-dimensional movements in both stream bed and urban areas are taken into account.

It is of vital importance that the results of both equations have significant differences especially for the areas with dense urbanization. The dynamic wave equations will yield more accurate results for

urbanized flood propagation analyses in this regard. Besides, it is considered that diffusive wave equations will yield more accurate and exact results for the areas where terrain inclinations don't get lower and areas that are distant from urbanization (e.g. flood analysis in a rural area), because of the convenience of solution with computer software. Likely, an increase in downstream length and the condition where the area has a constant inclination also improves the correctness of the 1- and 2-dimensional diffusive wave equations.

REFERENCES

Abay, O., Baykan, N., 2015. "Tarih boyunca barajların elden çıkma nedenleri'', Su Yapıları Sempozyumu, Ankara, s. 157-166.

Begnudelli, L., Sanders, B.F., 2007. ''Simulation of the St. Francis Dam-break flood'', ASCE Journal of Engineering Mechanics, 133(11), pp. 1200-1212.

Demirpençe, H., 2001. "Akarsularda taşkın öteleme metotlarının karşılaştırılması", Türkiye İnşaat Mühendisliği XVI Teknik Kongre ve Sergisi, ODTÜ, Ankara.

Elçi, Ş., Tayfur, G., Haltaş, İ., Kocaman, B., 2017. ''Baraj yıkılması sonrası iki boyutlu taşkın yayılımının yerleşim bölgeleri için modellenmesi'', İMO Teknik Dergi, 482, s. 7955-7975.

Froehlich, D.C., 1995. ''Peak outflow from breached embankment dam'', Journal of Water Resources Plannig and Management, 121(1), pp. 90–97.

Kaya B., Ülke A. 2013. ''Taşkınların ötelenmesinde diferansiyel kuadratur yöntemi'', Taşkın ve Heyelan Sempozyumu, Trabzon, s. 59-68.

NFB Mühendislik, 2014. "Atasu Barajı taşkın analizi", Technical Report, Ankara.

Singh, V.P., 1988. ''Analysis of gradual earth-dam failure''. Journal of Hydraulic Engineering. 114(1). pp.21-42.

Rogers D., 2013. ''The St. Francis dam failure'', Shlemon Specialty Conference Dam Foundations Failures and Incidents, May 16-17, Colorado.

Thi N.T.V., 2011. ''One dimensional Saint-Venant system'', University of Orleans Master 2 Puf Hcmc Mathematics, France, p 45.

Yüksel, Y., 2013. "Advanced Fluid Mechanics", Beta Basım Yayım, Ankara, pp. 413.

Wurbs, R.A., 1987. ''Dam-breach flood wave models'', Journal of Hydraulic Engineering, 113(29), pp. 29-46.

5th International Symposium on Dam Safety

October 27-31, 2018

AUTOMATIC EARTHQUAKE DETECTION & SAFETY MEASUREMENTS FOR MONITORING THE DAMS USING GPS ZIGBEE AND GSM TECHNOLOGIES

Mohammed Shoaib SYED [1], Shaik Abdul Khader JILANI [2]

ABSTRACT

An electronic based real time monitoring system is proposed in the vicinity of large dam regions. The proposed system focuses on providing instantaneous seismic status along with geographic location near the vicinity of dam due to Earthquake and disasters. Real time monitoring systems could be used to monitor the locations of seismic/disaster dam regions to safeguard the downstream population. In this study the possibility of detecting the earthquake and disasters by using Seismic Sensors, ZigBee and GPS is stated. The Aim of this investigation is to tracking Earthquake/Disasters which is in the specified range. By combining ZigBee wireless network and GPS module we can make powerful and reliable monitoring system near the vicinity of the dam region which can track both indoor and outdoor dam safety applications. GPS gives latitude and longitude values of the geographical location of the seismic activity and ZigBee wireless network connects the nodes in the network. The affected location can be visualized in Google Earth in real time using the interface developed in this investigation. ZigBee pro series 2 modules are configured in API mode to construct better wireless network and MATLAB code is developed to interface Google Earth for real time visualization.

Keywords: Seismic Sensors, ZigBee, GPS, GSM, and Dam safety

INTRODUCTION

Storage of fresh water has become one of the primary tasks for modern day human sustenance. Large dams and reservoirs play key role in sustenance and development of any country. They serve variety of purposes like providing drinking water, Water for Agriculture, electricity generation, flood control etc. However, construction of large Dams is not free from demerits. Due to geographical constraints majority of large dams are constructed in highly seismic areas, this situation can be noticed in countries like NEW ZEALAND, IRAN, TURKEY, LATIN AMERICA, USSR etc., etc. However well planned and constructed dams built on competent foundations, embankment materials, generally perform well. Still Marcuson and Silver (1987) advise that in Situ improvements made to large dam foundations and embankments are most challenging aspect of seismic improvement. Aerobiology, Biophysical Studies through integration of ZigBee communication protocols in fixed wing air vehicle for dam regions was done by Prof. Shaik Abdul Khader Jilani et al. (4th International LTBD Conference held on 17-19th October 2017 at Tehran Iran).

[1]Assistant Professor, Department of Physics, School of Sciences, MANUU Poly DBG Satellite Campus, Maulana Azad National Urdu University, Gachibowli, Hyderabad-500 032, Telangana State, India.
e-posta: dr.smdshoaib@manuu.ac.in Phone: +91-04023006612-15, Web: www.manuu.ac.in

[2] Professor, Department of Electronics & Communication Engineering, MITS, Madanapalli-517325, Chittoor District, Andhra Pradesh, India.
e-posta: jilani_s_a_k@yahoo.com

Before construction of reservoir infrastructures, large dam projects are generally evaluated according to the latest developments in engineering standards with respect to floods, seismic hazards and other causes of failure, such as over tapping of the dam, foundation defects, and karts or slope instability (Mouvet et al 2001, BWG 2002 ASDSO 2010). Also events such as the Sichuan earthquake in May 2008, and the fact that no single dam collapsed during this quake (Although many of them have suffered damage) plainly support this practice (Wieland 2008).

In the present investigation an electronic based smart network is proposed in the vicinity of dam region. The system focuses on providing instantaneous information of affected location because of operation of dam and natural calamities like earthquake. It is expected that by providing status information to the dam security or dam safety emergency team about the disasters/earthquake it will be possible to pin point and identify the level of damage experienced by the dam so that necessary action can be initiated. However, Dr. Shaik Abdul Khader Jilani et.,al designed two major modules for automatic tracking of victims at sacred congregation for earthquake seismic regions using GPS, ZigBee and GSM Technologies. (SEE7th International Conference on Seismology and Earthquake Engineering held on 18-21 May 2015 at Tehran Iran). The present investigation is focused on Earthquake detection by using these following GPS, ZigBee and GSM Technologies for dam safety measurements. **S**torage dams are subjected to various treats, Martin Wieland (Front. Archit. Civ. Eng. China 2010, 4(1): 56–64 DOI 10.1007/s11709-010-0005-6) listed out seismic hazards. Fault movement causing structural distortion. Mass movement like rock falls, power houses, Electro mechanical devises causing damage to gates and cracking and Puncturing. Ground movement due to liquefaction and densification of soil, causing distortions in dams are some of the major treats. These are additional treats noticed with in the vicinity of the dam in addition to natural treats like earthquake and floods. Therefore, our proposed model emphasizes on monitoring damages caused by both types of hazards. Some problems such as usability and safety illustrated by Peyret F et al. (2000) and Goodrum, P.M. et al. (2006). A critical review was done and experienced on landslide monitoring by using the embedded system, M.G Angeli et.al.,(2000).For personal wireless networks, one area of commercial interest has been short-distance; low-power, and low-cost, wireless communication was used, A. Rozyyev and H. Hsbullah (2010). Now there is high demand for Engineers who have knowledge or interested in wireless communication and embedded system. Remote monitoring system with wireless network was used to support rescue operations, ICCAS (2013). The communication mediums were optical fiber, infrared, generally wireless radio and twisted pair Cheok, G. S et al. (2000) and Mc Cullouch, B et al. (1997).

SOFTWARE and HARDWARE IMPLEMENTATION

The firmware is software written for embedded systems. Rather than a disk drive it is stored in flash convertor chips or read-only memory. It often runs with limited computer hardware resources: little memory, screen no keyboard or small, Nam Kim et al. The GeoZigBee wrist watch device also includes a low power TIDGET sensor, flash memory and a ZigBee wireless data link, A Brown (1992). İn the present investigation is real time subject location detection and tracking system using Global Positioning System (GPS) module, and ZigBee modules, GPS tracking system, United States Patent.

In order to implement the proposed model, the following Hardware and Software modules are required. They are:

1. Seismic Sensor Node
2. Data Transmission/Reception System
3. Data Analysis and Alerting Software
4. Power source for Seismic Sensor Nodes.

Seismic Sensor Node:

Each Seismic Sensor Node consists of high-sensitivity acceleration sensor, Microcontroller, GPS module and ZigBee module. Acceleration sensor converts the vibrations in to analog electrical signal

and this analog signal is fed to A/D converter of microcontroller which in turns digitizes the data. GPS receiver module connected to microcontroller estimates the geographical location of Sensor Node with the help of GPS satellite constellation. Microcontroller compiles the message with the data collected from accelerometer Sensor and GPS receiver along with node information and send it to master node. Each Seismic node powered with portable solar panel and battery bank, which allows us to place the module in any location on the dam. Figure 2(a) depicts the Seismic Sensor Node module

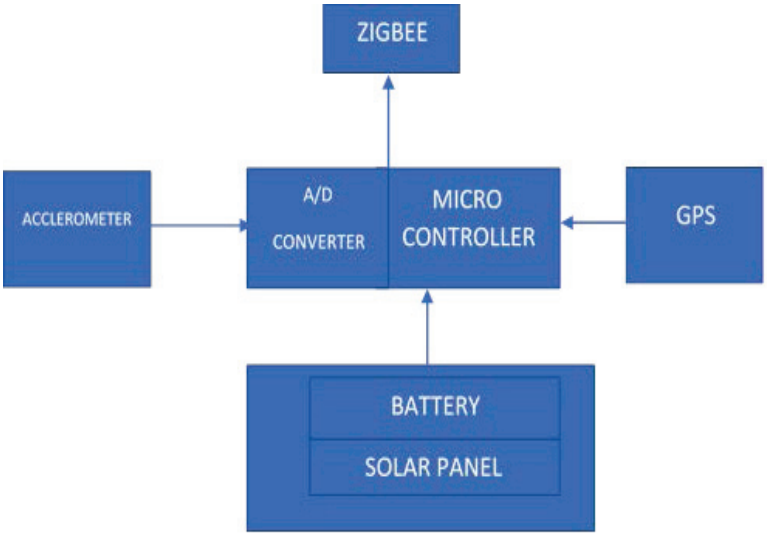

Figure 2(a) Seismic Sensor Node Module

Data Transmission/Reception System:

In the present work two communication schemes are used. One for communication between Sensor Nodes and Master Node and another between Master Node and Monitoring System. Between Sensor Node and Master Node ZigBee protocol is used which can cover few square kilometres. This protocol helps to gather seismic information from various Nodes to Master Node. Between Master Node and Monitoring System additional GSM/GPRS communication link is used which allows to transmit data via internet.

Data Analysis and Alerting Software:

In present work MATLAB is used for Data Analysis and Alerting. MATLAB is scientific language which consists of many tool boxes that allows the user to develop code for any Engineering application. Many Artificial intelligence and machine learning tools of MATLAB allows us to predict and estimate damage status. MATLAB is interfaced with Google Earth Software to pin point location and level of damage in real time.

Power Source for Seismic Sensor Nodes:

Since the number of Seismic Sensor Nodes need to be placed at different locations on and near the dam vicinity and wired power may not possible in all places, a standalone individual power source is designed for all Seismic Sensor Nodes. It consists of solar panel and rechargeable battery.

GLOBAL POSITIONING SYSTEM (GPS)

GPS was created and realized by the U.S Department of Defence (USDOD) and was originally run with 24 satellites. İt was established in 1973 to overcome the limitations of previous navigation systems. Lu, M., Chen; W. and Chan, W.H. (2004) Dileepa Jayakody et.al., and Srilanka Railway Department (2007) N.D future plans. GPS is maintained by anyone with a GPS receiver, J.M. Falco et.al. (2006) Chung-ChengChiu, et.al.,(2007) Torjusen, H. Et.al., (2001) and K. Michael, A et.al., (2006). The Russian Global Navigation satellite (GLONASS) was for use by the Russian military

only until 2007. Global Positioning System techniques is also used in landslide monitoring, J.A Gili et.al., (2000). There are also planned Chinese Compass navigation system and Galileo positioning system of the European Union (EU) Jaselskis, E. J. and El-Mislami, T (2003) Peyret, F et.al., (2000). The receiver uses the messages it receives to determine the transmit time of each message and computes the distance to each satellite, Dileepa Jayakody et., al. Many GPS units shows derived information such as direction and speed, calculate from position changes Alison Brown, et., al. Therefore receivers use four or more satellites to solve for the receivers location time and date Peter Williams et.al., (2004). The United States Department of Defence runs a freely available and highly accurate positioning system called GPS, A. Arciniegas, (2005). İn the present investigation Sıte Seismimicity Reports, Historic Seismicity Plots, Safety of Dam Data Base and Seismicity can be studied through this GPS, ZigBee and GSM Technologies.

The GPS receiver used in the proposed work is shown in fig 2(b) which can be capable of receiving signals from up to 65 GPS satellites and transfers them into the precise position and timing information. It supports UART and protocols. Operates with supply voltage of 3.6V~6.0V.

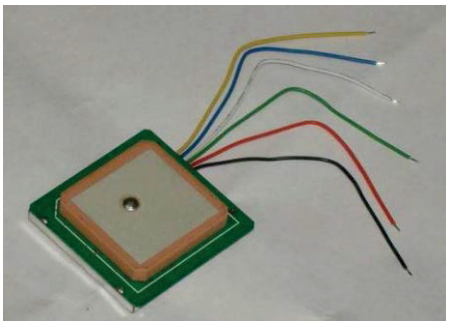

Fig. 2 (b) GPS 634R

ZIGBEE MODILE

XBee-PRO 802.15.4 ZigBee models used for data transmission between Seismic Nodes and Master Node is shown in Fig 2(c). It supports Point-to-Multipoint network topology and operates at 2.4 GHz licence free wireless communication channel and consumes less than 1 in sleep mode. ZigBee goal is the applications that require reliable communications, due to mesh topology, with low data transmission rate and long live batteries, Won-Suk Jang and Miroslaw J. Skibniewski. ZigBee sensor network was also used for patient localization and air temperature monitoring during emergency response to crisis, SENSORCOMM (2008). In the present investigation we are trying to use this application in disaster management Mc Cullouch et al. (1997). It provides the ability to run for years on inexpensive batteries for a host of monitoring applications: Lighting controls, AMR (Automatic Meter Reading), wireless telemetry, shade controls, detectors, environment controls, HVAC control, home security, and heating control etc, Song. J et.al., (2006). In the present investigation this ZigBee is utilized for dam safety application.

Fig. 2(c) ZigBee series2

Google Earth Software:

Google Earth is a software program that renders 3D representation of Earth based on images sent by satellites. It maps the Earth by superimposing aerial photography, satellite images, and GIS data onto a 3D globe. Google Earth Software can be interfaced with GPS for real-time location determination and it also provides latitude, longitude and altitude and terrain information with different view angles. We developed MATLAB interface for Google Earth for analysis. Fig 2(d) depicts the aerial view of Srisialam dam of South India.

Fig. 2(d) Google Earth view of Srisailam Dam

DISCUSSION AND CONCLUSIONS

The Paper Summarizes the Key areas of progress with reference to case histories involving various applications for natural calamities/disasters and seismic mitigation. Experiences around the world show that the large improvements in a dam project are achieved when the environmental effects of a dam are considered. The Real time earthquake detection and tracking using ZigBee and GPS has been developed for dam safety measurements based on GPS-634R ZigBee Series-2 modules. The system is tested for the distance up to 120 meters. Since the system is compact, low cost and consumes less power it is attractive for developing into various applications of Dam Safety measurements. The present system uses ZigBee and GPS receiver because of their high power. With the help of ZigBee, GPS and Google Earth Software we track the object even if the object is inside the large dams. By using the Mesh topology we have to extend the range also. Once a patent is secured the technology could be used to detect and estimate the earthquake over the Dam regions. The present system uses ZigBee and GPS receiver in the movable/ stationary base mobile or stations module which has the following advantages and most suitable for dam safety measurements they are,

1. No subscription fee or licence fee of any type is required. It is lifelong 100% free because GPS and ZigBee work independent of any service provider.
2. ZigBee module consumes vey less power (nearly 100 times compared to GSM module) therefore Solar Cell based module can be designed and utilized.
3. If the earthquake is happen with in the vicinity of dam safety base station there is no need of GSM module. Therefore the present system can be operated in areas where GSM coverage is not available.
4. The coverage area of ZigBee can be extended to 40 miles in open areas like large dams and reservoirs for dam safety applications.
5. More number of ZigBee modules can be used for the dam safety measurements as the radiation

levels are very low compared to GSM.

AKNOWLEDGEMENTS

The Author is thankful to **Dr. Mohammad Aslam Parvaiz** Sir Honorable Vice Chancellor MANUU and **Dr. Shakeel Ahmad** Sir Former Joint Secretary UGC, New Delhi and Pro Vice Chancellor MANUU Central University, Hyderabad for their encouragement to do Current Challenging Research Activities in our Central University for the overall development of Students, Faculties and Institution.

REFERENCES

[1] Marcuson W.F. and Silver M.L (1987) "Shake –Proof Dams" Civil Engineering 57, (12), pp 44-47.
[2] Mohammed Shoaib Syed, Abdul Khader Jilani Shaik, 17-19th October 2017, "Aerobiology, Biophysical Studies through integration of ZigBee communication protocols in fixed wing air vehicle for dam regions" ISBN No.978-3-85125-564-5.
[3] Mouvet L., Mueller R.W. and Pougatsch, H. 2001 Structural safety of dams according to the new Swiss legislation. *Proc. ICOLD European Symposium*, Geiranger, Norway
[4] BWG, 2002 Sicherheit der Stauanlagen. Richtlinie. Bundesamt für Wasser und Geologie, Biel, 119 pp.
[5] ASDSO (2010) Association of State Dam Officials, Lexington, KY, USA. http://www.damsafety.org
[6] Wieland, M. 2008 Effects of the 12 May 2008 Sichuan earthquake on dams – preliminary assessment. www.waterpowermagazine.com
[7] Mohammed Shoaib Syed, Abdul Khader Jilani Shaik, 18-21st May 2015, Automatic tracking of Victims at Sacred Congregation for Earthquake Seismic Regions using GPS, ZigBee and GSM Technologies, ISBN No. 978-964-6490-53-6.
[8] Martin Wieland, Features of seismic hazard in large dam projects and strong motion monitoring of large dams Front. Archit. Civ. Eng. China 2010, 4(1): 56–64 DOI 10.1007/s11709-010-0005-6.
[9] Peyret, F.; Betaille, D. and Hintzy. G. (2000) High-precision application of GPS in the field of real-time equipment positioning. Automation in Construction, Elsevier, 9(3) p. 299-314.
[10] Goodrum, P.M.; McLaren, M.A. and Durfee, A. (2006) The application of active radio frequency identification technology for tool tracking on construction job sites Automation in Construction, Elsevier, 15(3), p. 292-302.
[11] Angeli M.G., Pasto A., and Silvano S., "A Critical Review of Landslide Monitoring Experiences" Eng. Geol., Vol.55, pp 133-147, Feb 2000.
[12] A. Rozyyev and H. Hsbullah, (2010). "Comparisons of routing protocols for child tracking in wireless sensor network," IEE, pp. 1238-1243.
[13] Remote motoring system with wireless network to support rescue operations, 13th International Conference on Control, Automation and Systems ICCAS 2013, PP.251-254, Oct 2013.
[14] Cheok, G. S.; Lipman, R. R.; Witzgall, C.; Bernal, J. And Stone, W.C., NIST construction automation program No. 4: non-intrusive scanning technology for construction status determination. NISTIR 6457, BFRL, NIST, Gaithersburg, MD, USA, January, 2000.
[15] Mc Cullouch, B. Automating field data collection on construction organizations. Proceedings of Construction Congress V, ASCE, Minneapolis, Minnesota, USA, October 5-7, 1997, p. 957-963.
[16] Won-Suk Jang and Miroslaw J. Skibniewski, Wireless network-Based Tracking and Monitoring on Project Sites of Construction materials.
[17] ZigBee Sensor Network for Patient Localization and Air Temperature Monitoring During Emergency Response to Crisis, Second International Conference on Sensor Technologies and Applications, SENSORCOMM 08, pp 233-238, Aug 2008.
[18] N.Watthanawisuth, N. Tongrod, T.kerdcharoen, and A. Tuantranont Real-time monitoring of GPS-tracking tractor based on ZigBee multi-hop mesh network.
[19] Song, J.; Ergen, E.; Haas, C.T.; Akinci, B. And Caldas, C. Automating the task of tracking the delivery and receipt of fabricated pipe spools in industrial projects. Automation Construction, Elsevier, 15(2), 2006, p. 166-177.

[20] J.M. Falco, R. Casas, A. Macro, J.L. Falco., (2006) Guiding support for 'Way-finding' in unknown buildings: design and evaluation. Proceeding of ICCHP, Lecture Notes in Computer Science, and Computers Helping People with Special needs, Linz, Vol.4061, pp. 724-731.
[21] Chung-ChengChiu, Min-Yuku, Hung- Tsung, Chen Nat, June (2007). "Motorcycle Detection and Tracking System with Occlusion Segmentation," Image Analysis for Multimedia Interactive Services. Santorini, Vol.2, pp. 32-32.
[22]Torjusen, H., Lieblein, G., Wandel, M., Francis, C.A., (2001). Food system orientation and quality perception among consumers and producers of organic food in hedmark Country, Norway. J. Food Quality preference 12 (3), 207-216.
[23] K. Michael, A. Mcnamee, M.G. Michael, (2006). The emerging ethics of human centric GPS tracking and monitoring, International Conference on Mobile Business, Copenhagen, Denmark, IEEE computer society, Washington, 25-27th July, pp. 34-44.
[24] GPS tracking system, United States Patent 5, 379, 224.
[25] Lu, M., Chen; W. And Chan, W.H. (2004). Discussion of "building project model support for automated labor monitoring", Journal of Computing in Civil Engineering. ASCE, 18(4), p. 381-383.
[26] Dileepa Jayakody, Mananu Gunawardana, Nipuna wicrama Surendra, Dayan Gayasri Jayasekara, Chanaka Upendra, supervisor, Rangana De Silva. GPS/GSM based train tracking system-utilizing mobile networks to support public transportation was proposed.
[27] Srilanka Railway Department (2007), n.d., future plans. www.railway.gov/lk/future_plan.html.
[28] http://www. Wikipedia.org
[29] http://ftp1.digi.com/support/documentation/90000866_A.pdf
[30] http://sites.google.com/site/xbeetutorial/xct
[31] http://en.wikipedia.org/wiki/Global_Positioning_System
[32] Gili J.A., Corominas J. and Rius J using Global Positioning System Techniques in Landslide Monitoring Eng. Geol. Vol.55., pp.162-192, Feb 2000.
[33] Jaselskis, E. J. and El-Mislami, T. (2003), Implementing radio frequency identification in the construction process, Journal of Construction Engineering and Management. ASCE, 129(6), p. 680-688.
[34] A. Brown, M. May, B. Tanju, (2000). "Benefits of Software GPS Receiver for Enhanced Signal Processing,"GPS Solutions 4(1), summer, pp 56-66.
[35] Peter Williams, Deere & Company 1996. "Satellite Precise Positioning for Agriculture and Farming" FCC Rural Satellite Forum, January 27, 2004.
[36] A. Arciniegas, S. Takahashi, and A. Torres, "Soft computing techniques for analysis of kidnapping crimes in Colombia," CHISPS, pp. 30-35, April 2005.
[37] Nam Kim, Young-Jun Song, Dong-Woo Kim, and Jae-Hoeing Ahn. Children location Detection in School Zone.
[38] A. Brown, "The TIDGET – A Low Cost GPS Sensor for Tracking Applications," ION 5th International Technical Meeting, Albuquerque, September 1992.
[39] M. Young, (1989).The Technical Writer's Handbook. Mill Valley, CA: University Science.
[40] ABI Research, The market for RFID readers. Technical Report from ABI Research 2005, Document code RRRFR available online at: http://www.abiresearch.com/ Products/market research/RFID_Readers, accessed on September 5, 2006.
[41] Alison brown, Jacob Griesbach, and Bruce Bockius, GPS tracking Location-Based service using Wristwatch GeoZigBee Sensors.

5 DAM SAFETY
İstanbul Turkey 2018

5th International Symposium on Dam Safety

October 27-31, 2018

OPTIMIZATION OF THE LABYRINTH WEIR PERFORMANCE

Mosbah BEN SAID [1], Ahmed OUAMANE[2]

ABSTRACT

Current climate conditions, extension of hydrological data records and the development of new methods for extreme flood estimation have shown the inadequacy of a significant number of spillways to evacuate increased extreme floods, which create a new challenge for safety of dams. Consequently, dam designers and operators are seeking solutions to adapt the capacity of the evacuation of both the existing and new spillways dams. The non-rectilinear spillway form offers an effective solution to increase discharges capacity for both existing and new dam projects. The objective of this work is to optimize the labyrinth spillway, in particular the rectangular plan form. In this framework, standard labyrinth weir shape modifications are aimed to improve the hydraulic performance and to reduce the construction cost. These modifications concern the entrance shape, the basis length and the height of the side walls. The experimental results show that these enhancements have a positive impact on economic and hydraulic performance compared to standard labyrinth.

Keywords: Spillway, Labyrinth, Physical Models, discharge capacity..

INTRODUCTION

The loss of the water storage capacity due to the silting of the reservoir and insufficient spillway capacity as a result of extreme floods pose real problems for dam reservoirs in the recent years.
Free flow spillways weir such as labyrinth weir provides an efficient and safer flood control structure compared to gated weirs. It could be an adequate solution not only to increase the storage capacity and to improve the safety of existing dams, but also to reduce considerably the cost of new dam projects.

Despite their structural complexity and less hydraulic efficiency compared to the rectangular labyrinth especially for heads H*/P of less than 0.5 (Ouamane & Lemperiere 2013 and Ben said & Ouamane 2018), the triangular and trapezoidal plan shape are still widely studied and used to increase the crest length and thus the specific flow rates of spillway.

[1] Researcher, Scientific and Technical Research Center on Arid Regions, Biskra University, Biskra, Algeria,
e-posta: bensaid.mosbah@fgmail.com
[2] Professor, Department of Civil Engineering and hydraulic, Biskra University, Biskra, Algeria,
e-posta: aouamane@yahoo.fr

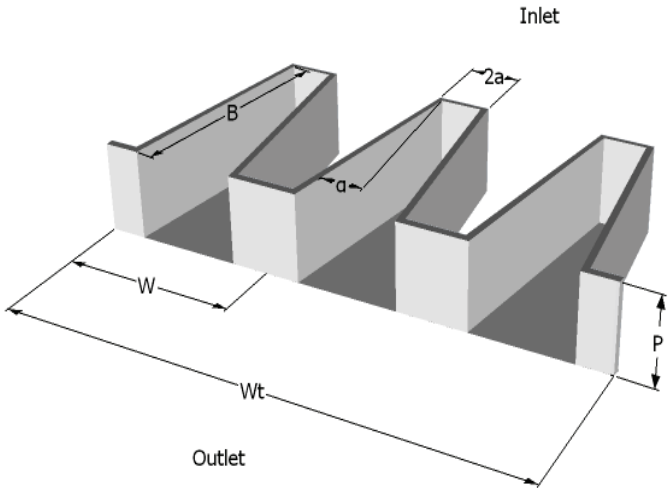

Figure 1. Labyrinth weir with the main geometric parameters

In an effort to show the efficiency to use the rectangular labyrinth weir to increase the discharge capacity, a comparison study between rectangular and trapezoidal labyrinth weir has been conducted in reservoir and channel applications. To adapt the labyrinth weir to the reduced crest dam, a physical mode was fabricated with up and downstream overhangs thus leads to reduce the footprint without affecting the developed crest length of the labyrinth. On the same model, two modifications of the downstream alveoli were conducted to reduce the volume of steel-reinforced concrete and thus make its use more economic. The first one took an inclined bottom shape and the second was formed as a stepped downstream section.

Experimental setup

The experimental tests were conducted at the Laboratory of Hydraulic developments and Environment, University of Biskra, Algeria. Two facilities were used for physical modeling: a rectangular flume (Fig. 3-2) for channelized applications and a reservoir test facility to simulate dam (Fig. 3-3). The rectangular flume having a section of 1 ×1 m wide and deep, and 12 m long and the simulation basin is characterized by square shape with 3x3 m and height 1.1 m.

The experimental system is equipped with two pumps, which deliver up to 180 l/s. The discharges are measured using two flowmeters, one ultrasonic and the other electromagnetic. The water depths are measured by a series of ultrasonic level sensors. The assembly operates within a closed circuit. The tested models were constructed from sheet metal 2 mm thick. A schematic of the channel and reservoir test facility are shown in figures 2 and 3.

Figure 2. Reservoir test facility

Figure 3. Rectangular flume test facility

Table 1. Characteristic of models

Model	n°	n	L	Wt	P	B	W_u	a	b	r	L/Wt	W/P	a/b	B/P
	-	-	cm	cm	cm	cm	cm	cm	cm	cm	-	-	-	-
Rectangular Labyrinth	01	6	355	90.8	15	25	15	9	6	3	3.91	1	1.5	1.66
Trapezoidal Labyrinth	02	6	358	90	15	27	15	-	-	-	3.96	1	-	1.8
Labyrinth with up-and downstream overhang	03	4	494	99.2	20	50	25	13.5	11.3	-	4.98	1.25	1.2	2.5

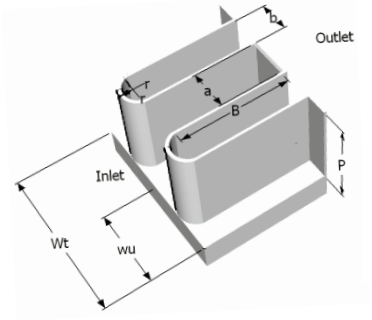

Figure 3. Rectangular labyrinth

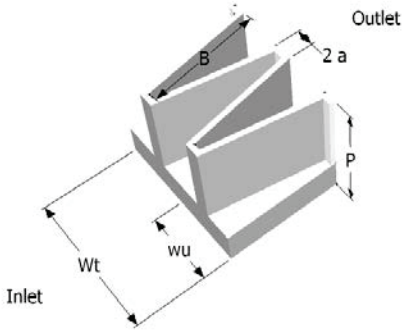

Figure.4 Trapezoidal labyrinth

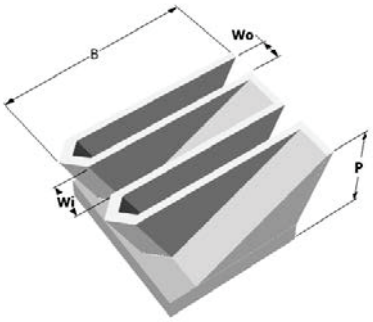

Figure 5. Labyrinth with up-and Downstream overhangs

RESULTS AND DISCUSSION

The obtained experimental results for the tested configuration are presented as a function between the relative upstream head and the discharge coefficient derived from the linear weir discharge equation (Poleni equation).

$$C_w = f(H^*/P) \tag{1}$$

where;

$$C_W = \frac{Q}{W\sqrt{2g}H^{*3/2}} \tag{2}$$

In equation (2):
C_w: Discharge coefficient of the tested model
Q: Discharge (m^3/s)
H^*: Total upstream head (m).
W: total width of weir (m)

Comparison between rectangular and trapezoidal labyrinth weir
In reservoir application :

In this case, the labyrinth weir models were tested in the reservoir test facility to simulate the weir position in reservoir dam (the inlet channel width equal 4 times the labyrinth total width). Using the equation (2), the discharge coefficient for two configurations, rectangular and trapezoidal labyrinth weir shape in plan view was calculated and compared for the same developed crest length ratio L/W equal 4. The experimental results have shown clearly that the rectangular labyrinth weir was the most efficient than the trapezoidal shape, especially for low and moderate relative heads (H^*/P <0.6).

For the relative head H^*/P equal 0.3, the discharge coefficient with rectangular labyrinth shape is around 13 per cent more efficient than the model with trapezoidal shape. However, this advantage decreases progressively to reach 5 per cent for a relative head H^*/P equal to 0.5. This decreasing efficiency with H^*/P increasing is mainly caused, by the nappe interference and the progressive development of submergence of the downstream alveoli. For highest heads $H/^*P$>0.6, the two configuration show similar performance.

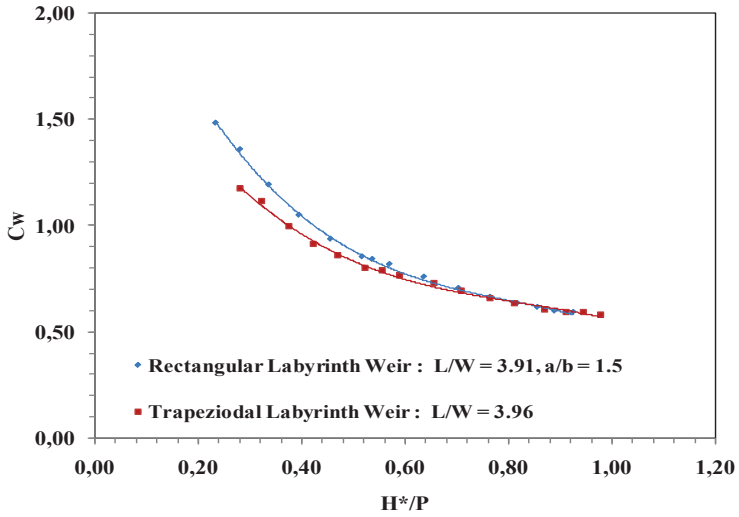

Fig. 6. Discharge capacity comparison between Rectangular and Trapezoidal labyrinth in-reservoir application

In-channel application

Many exciting labyrinth weirs are used as control structures in streams, canals and rivers. In this context, an experimental study has been conducted in-channel application on two models, rectangular and trapezoidal labyrinth shape, to determine the most relevant shape. For this case, the inlet channel width equal to the total labyrinth width.

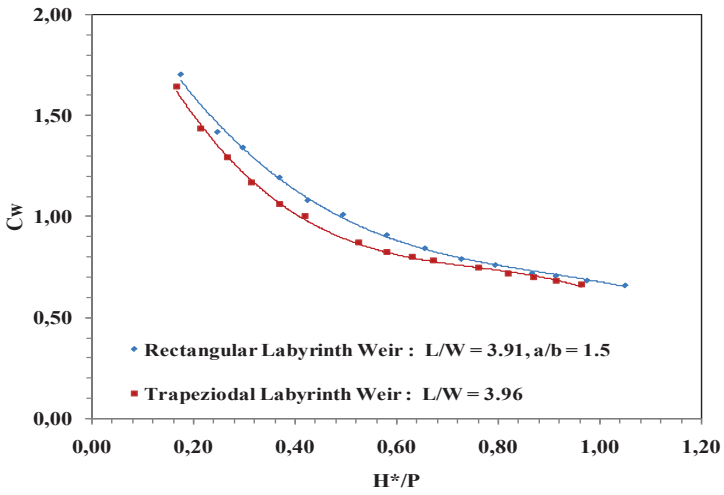

Fig. 7. Discharge capacity comparison between Rectangular and Trapezoidal labyrinth in-channel application

As shown in the graphic (2), the rectangular labyrinth weir is more efficient than the trapezoidal configuration for most of the tested range (H^*/P). Tests on these two configurations have shown that the rectangular form performance is around 10 per cent greater than the trapezoidal shape for values of $H^*/P < 0.8$. However, the efficiency is about 3 % beyond this value. In addition to the hydraulic efficiency, a labyrinth with rectangular shape in plan of view has a reduced dimensions compared to trapezoidal shape, which reduce its construction cost and makes its use more convenient for restricted place.

Labyrinth with overhangs

The use of the overhangs permits to design a labyrinth weir with a limited basis length and, therefore, to be placed on a reduced crest length of dams. For that, a labyrinth model with upstream and downstream overhangs has been fabricated and tested to verify the overhangs influence on the labyrinth performance. According to the experimental results represented in term of discharge as a function to the relative upstream head (figure 4), the labyrinth weir with up-and downstream overhangs provides discharges until 4.5 higher than the linear weir for low relative heads ($H^*/P < 3$) and it is around 3 times for moderate relative heads ($H^*/P \approx 5$).

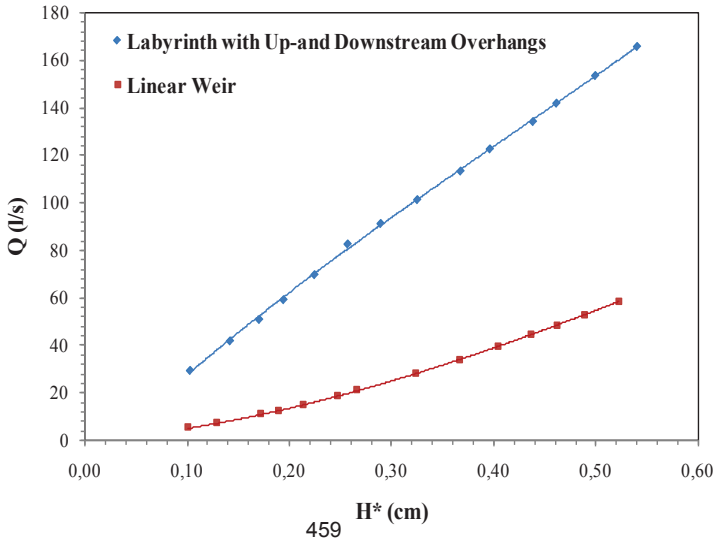

Fig.8. Comparison between discharge capacities of labyrinth and linear weir

Labyrinth with filling downstream alveoli

The economical weir is mainly defined by the volume of reinforced concrete consumed by the structure. Consequently, to reduce the construction cost of the labyrinth weir which could be significantly affected by the increase of the free wall, the partially filling of the downstream alveoli with ordinary concrete could thus to be the best solution. Thus, an experimental study of the effect of the downstream alveoli filling has been carried out on two shapes of filling, the first one with inclined downstream shape and the second is with stepped downstream shape, and the two cases are compared to reference mode (without filling).

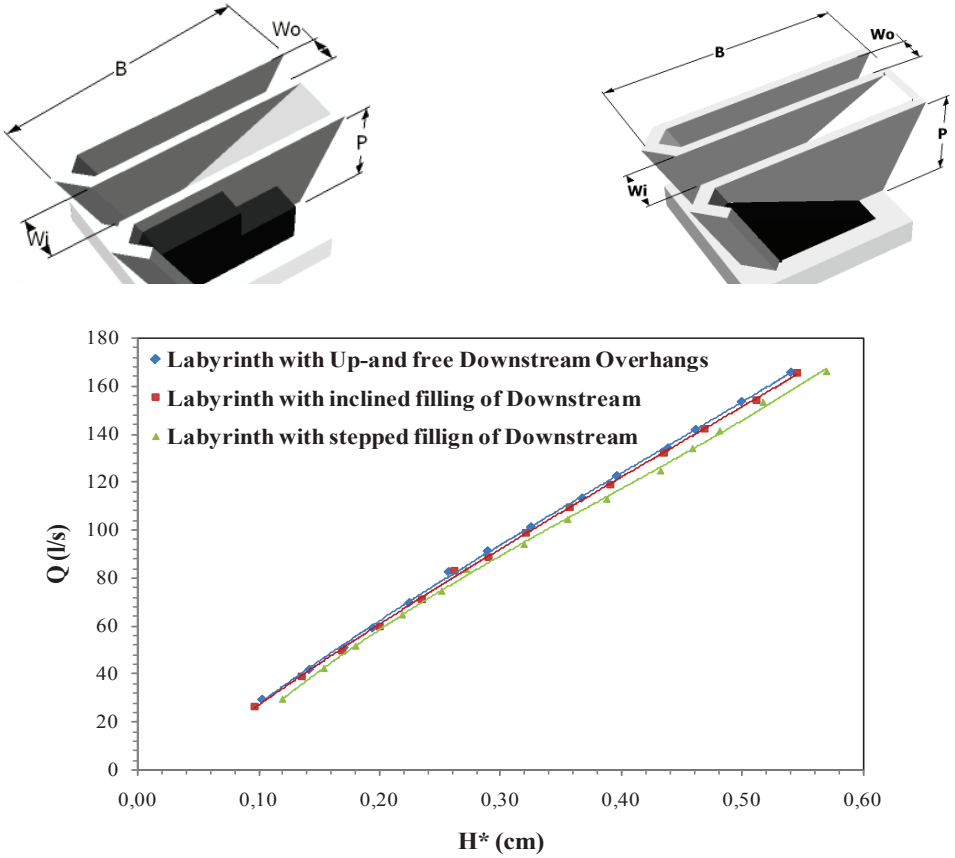

Fig.11. Discharge capacity of labyrinth weir with varied downstream shape

Practically no significant change in the weir efficiency is observed when the downstream is designed with inclined shape. For the downstream designed with two steps 8.5 cm high for each one, the obtained results have shown that the adoption of stepped downstream does not reduce the discharge capacity of more than 6%. Regarding the energy dissipation and construction cost, this option seems to be the best design even if the labyrinth designed with stepped downstream was more hydraulically efficient.

CONCLUSION

An experimental study was conducted to study the performance of the rectangular labyrinth shape designed with some improvements. an experimental study was conducted to study the performance of the rectangular labyrinth shape designed with some improvements. The adoption of a rounded entry

shape instead of a flat shape allowing an increase of the rectangular labyrinth weir efficiency compared to trapezoidal labyrinth weir. In addition to the hydraulic efficiency for both application in-reservoir and channel application, a rectangular labyrinth weir could more convenient for restricted space of emplacement and more economical thanks to reduced dimensions.

The labyrinth weir designed with overhangs could be useful tool to increase the safety and storage capacity of many existing dams. However, for large discharges, increase of free wall high would be necessary to evacuate important volume of water which eventually requiring an additional costs.
In order to construct a labyrinth weir with lower cost possible, two filling types of the downstream alveoli have been tested. The first one with inclined downstream shape and the second is with stepped downstream shape. The experimental results have shown that the head/discharge curves of the two weirs, with inclined downstream and without filling downstream, are similar. It seems thus that the choice of the rectangular labyrinth weir could be an economical alternative.

REFERENCES

Ben Saïd, M., Ouamane A., 2011. "Study of optimization of labyrinth weir". Labyrinth and Piano Key Weirs, pp 67-74. ©2011 Taylor & Francis.

Ben said, M., and Ouamane, A., 2018. "Remodelling labyrinth weir geometryto increase performance" Hydropower. & Dams Issue one. pp. 74-79

Ouamane A., and Ben Said M., 2010 "Economic conceptions of the labyrinth weir allowing the improvement of the management of floods and the increase of the useful capacity of the reservoir" Rheinisch-Westfälische Technische Hochschule Aachen, Germany, Publication No. 158, Published by Shaker Verlag, Germany.

Ouamane, A. and Lempérière, F., 2013 "Improvement of the form of labyrinth weirs", Proceedings, International Conference on Labyrinth and Piano Key Weirs - PKW 2013, Paris, France

5th International Symposium on Dam Safety

October 27-31, 2018

RELATIONSHIP BETWEEN SEDIMENT TRANSPORT AND SCOUR GEOMETRY FOR HIGH FLOW VELOCITIES AT THE LABYRINTH SIDE WEIRS

Mustafa TUNÇ [1], Muhammet Emin EMİROĞLU[2]

ABSTRACT

The weirs are a hydraulic structure that are often used in engineering applications. Scour occurs at the side weir region due to high flow velocity in the main channel. In the meantime, the sediment transports to the evacuation channel over the side weir. The purpose of the current study is to investigate the variation of the maximum scour depth and scour geometry around the labyrinth side weir for high flow velocities. In this study, triangular labyrinth side weirs with different crest heights and different weir opening lengths were tested in the hydraulic laboratory in a large experimental flume. Quartz sand with median grain diameter of 1.16 mm is used as bed material. A series of experiments are carried out for flow velocities between 0.5 and 1.2 m/s. It has been observed that the scour depth around the weir and the amount of sediment spilled over the side weir increases, with increasing the flow velocity. For the values of flow velocities 1 to 1.2 m/s, dunes with high dimensions and more sediment transport in the alluvial bed are observed in experiments tested. Precautions for safety of hydraulic structure should be taken at the scouring regions.

Keywords: Labyrinth side weir; Scour; Safety; Alluvial stream; Flow velocity.

INTRODUCTION

It is possible to damage or even demolish the structure by increasing the scour problem which is common in stream structures. For this reason, especially scours seen in the mouths of water intake, scour at the downstream of the spillways, scour around the piers of the bridge and scour of the energy breaker structures constitute a big risk for hydraulic structures. In our country, which is rich in rivers, efforts should be made to solve these problems.

It is desirable that the water supplied to the sedimentation pool and the transmission channel by embossing in streams contain as few as possible fewer sediment. Otherwise, problems such as sediment accumulation in sedimentation channels and transmission channels, erosion of the turbines in hydroelectric power plants at the short period in which water power plant is discharged occur. In addition, continuous water intake due to sediment accumulation in the water intake structures may not be possible. In our country, most of the water intake structures constitute lateral water intake structures (Tunc, 2014).

[1] Research Assistant, Department of Civil Engineering, Firat University, Elazig, Turkey,
e-posta: mtunc@firat.edu.tr
[2] Professor, Department of Civil Engineering, Firat University, Elazig, Turkey,,
e-posta: memin.emiroglu@gmail.com

Onen (2005) conducted a series of experiments by examining the maximum scour depth at rectangular cross-section channel under free over flow conditions and under subcritical flow conditions. In the case of clear water scour and live bed scour, the maximum scour depth change around the side weir was investigated experimentally. Emiroglu et al. (2007) 104M394 TUBITAK project at the labyrinth side weir flow characteristics of the side weir and the change of the bed topography of the ground for the clear water scour have been experimentally examined. Dilek (2011), clear water scour at the subcritical flow regime conditions along a straight cohesive material bed (clay+sand mixture), in the case of free over flow, at the L=25 and 50 cm weir openings and at the classical side weirs with a crest height of p=7 and 12 cm at the main canal. Rosier et al. (2011) studied the geometry of the bed shapes at the classical rectangular side weir area placed at a rectangular channel. Paris et al. (2012), an experimental study was carried out to determine the relationship between the bed morphology and the flow. Emiroglu et al. (2017) carried out a series of experiments in order to reduce the scour by using anti-vortex plates at the labyrinth side weirs. In Tunc and Emiroglu (2018), bed topographies were determined for live bed scour at labyrinth side weirs.

When the studies in the literature are examined, there are a few studies on the scour depth of lateral flow in alluvial-bed channel. It is seen that most of them are carried out for low discharges and for classical side weirs. Due to the limited number of studies in the literature about scour geometry around the labyrinth side weirs placed on streams, a complete theoretical basis has not been established on this subject.

In the present study, it is aimed to investigate the maximum scour depth, bed topography and sediment transport for high discharges at an alluvial bed. Thus, the usability of labyrinth side weirs at open channels for security will be determined.

FORMATION OF BED SHAPES

With the movement of the solid grains, some properties such as flow velocity, turbulence effect, shear stress near the alluvial bed will change with the movement of the grains because the flow will spend a certain amount of energy. This change will be more effective with the amount of moving grain. When the flow velocity is increased, the flatness of the bed is replaced by the slightly wavy ripples. These ripple forms are similar to the shape created by the wind on the sand or on the shore by ripples (Figure 1). If the flow depth is high, the ripples start to appear with the increase of the critical flow velocity (V_c) which activates the grains. The ripples begin to form in some parts of the alluvial bed by a continuous accumulation of sediments, while a small number of sediments are removed. In the direction perpendicular to the flow axis, small sediment accumulations are formed close to each other. The transitions at the downstream of these sediment accumulations hold the grains in motion. Thus, the height of the sediment accumulation increases with time, the upstream faces are flat, the downstream faces are upright. The slope of this formed ripple is close to the slope of the solid material under water. When the sediment grains come up to the upstream of the ripples, they continue to act as if they were on the base of the ripples, but when they reach the top of the ripple, its movement is prevented due to the loop formed behind the ripple and the ripple moves towards the downstream at a rate lower than the average velocity (Bayazıt, 1971; Tunc, 2014).

Figure 1. Sand ripples formed in a movable bed (Tunc, 2014)

As the velocity increases, the sediment grains are dragged without the opportunity to move from one ripple to another. Therefore, the increase in ripple height slows down and is fixed completely after a while. In this region, while the height of the ripples remains constant, the ripple length increases continuously. Therefore, the ratio of the ripple height to the ripple length is reduced by increasing the flow velocity. However, the flow movement increases and the amount of sediment transported increases. If the flow velocity reaches larger values, the ripples disappear completely and take the form of an almost plane. With the velocity reaching to a certain size, the transition from ripples to the flatfoot is not a moment, first a transition zone where the ripples are in some regions and in some regions is seen. V_c, V_0, V_1, V_2 values; fluid, flow and sediment grain properties. There, V_c=Critical flow velocity, V_0=The velocity at which the ripples begin to appear, V_1=The velocity at which the rise in the ripple height begins to stabilize, V_2=The velocity of the ripples decreases and the velocity of the ripples is very large. Goncharov (1964) has obtained some approximate formulas.

$$\frac{V_0}{V_{kr}} = \left(\frac{d}{y}\right)^{1/12} \quad , \quad \frac{V_2}{V_{kr}} = 2{,}5\left(\frac{y}{d}\right)^{1/12} \quad , \quad V_1 = 0{,}25\,V_0 + 0{,}75\,V_2 \tag{1}$$

$$H_{max} = \frac{y}{2\,log\left(1{,}6\,\frac{y}{d}\right)} \quad L = 11\,H_{max} \tag{2}$$

where y=flow depth, L=weir opening length, H_{max}=the maximum value of the weir height.

Yalin (1964) proposed Equation (3):

$$\frac{H}{y} = \frac{1}{6}\,\frac{\tau_0 - \tau_{kr}}{\tau_0} \tag{3}$$

As the velocity increases, the shapes at the alluvial bed change. Firstly, consists of short and three-dimensional ripples. Then there are dunes whose dimensions are larger (lateral length than ripple) (Figure 2). The length of the ripples is 30 cm and their height is less than 3 cm. When the base is covered with ripples, there is no change in the surface of the water. Yalin (1964); In the ripple type, while giving the L~1000d approach, the ripple length is related to the grain diameter and the L~5y approach in the dunes emphasized that the ripple length depends on the depth of the flow. Ripples do not occur on sand floors (i.e. coats of coarse material) covered with grains greater than 0.6 mm. Chabert and Chauvin (1963) developed the, d diameter (4) for other materials:

$$d = 0{,}6\sqrt{\frac{1{,}6\,\gamma}{\gamma_s - \gamma}} \qquad (4)$$

Figure 2. Dunes occurring on movable bed (Tunc, 2014)

EXPERIMENTAL STUDY

In this study, the scour depths around the triangular labyrinth side weir in a rectangular cross-section straight channel with movable bed were investigated experimentally for steady-flow conditions and free over flow cases. Labyrinth weir crest is not straight in the plane as the weir crest. The equilibrium scour depth (d_{se}); It is determined that it is dependent on the flow velocity (V_1), the critical flow velocity (V_c), the weir crest height (p), and the side weir opening length (L). The apex angle of the labyrinth weir was taken as 90 [illegible] to determine the scour geometry and the amount of sediment carried around triangular labyrinth weir by changing the flow velocity between 0.5 and 1.2 m/s. For this purpose, a series of experiments were carried out for the crest heights of p=7 and 16 cm and for the side weir opening length L=25 and 40 cm.

The present experimental study was carried out at the experiment setup presented in Figure 3, the plan and the sections. Thresholds are placed on the upstream and downstream ends of the main canal. A quartz sand with d_{50}=1.16 mm was placed between the two thresholds. With the experiments conducted in the laboratory, the wet specific gravity of quartz sand was 26.49 kN/m^3 and the dry specific gravity was 26 kN/m^3. To ensure steady-flow conditions, perforated bricks are installed at appropriate sections of the channel. The bed material was placed in the center of the side weir.

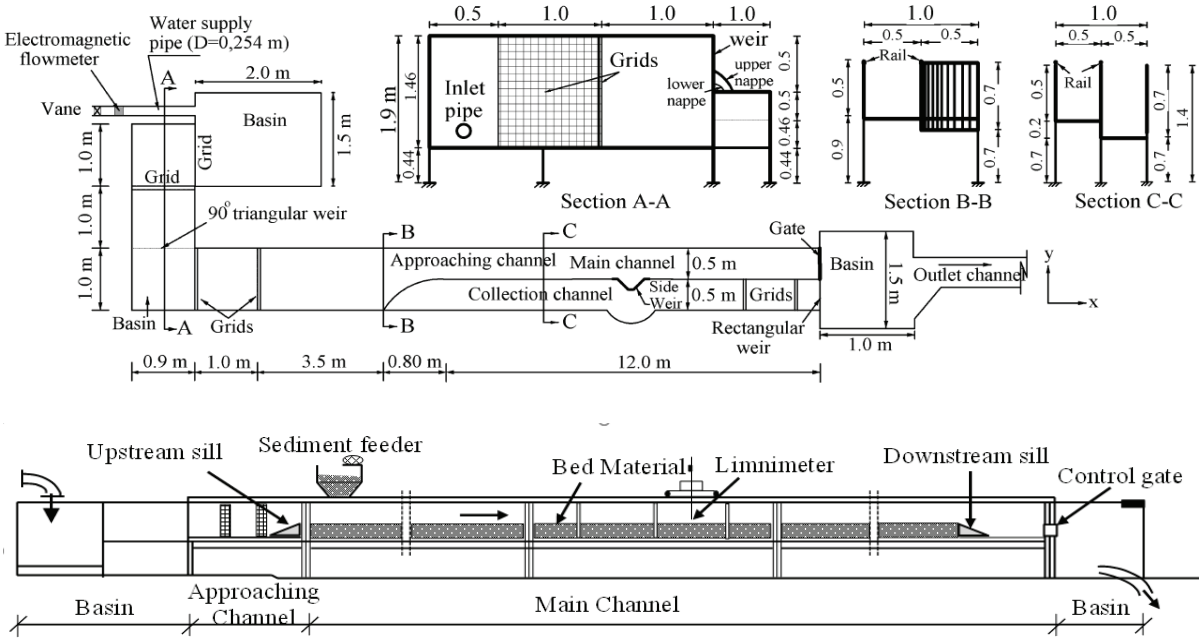

Figure 3. Plan and cross-sections of the experimental setup

The experiments were carried out at a discharge of 35-110 L/s. The flow depth (y_1) was measured at the upstream end of the side weir in the channel axis. The discharge at the main channel is calculated from the equation V_1=Q (B.y_1). Novak and Cabelka (1981) proposed to take a minimum nap thickness (y_1-p) of 0.03 m to minimize the surface tension. Therefore, in this study, minimum nap height was taken as 0.03 m. The experiments were carried out under steady-flow conditions, in the case of free over flow conditions and in the case of live bed scour conditions.

Before each experiment, the sand was mixed, compacted and the floor was smoothed, and water was slowly introduced into the channel. The water was slowly rising from the ramp in front of the threshold at the upstream end of the channel, while a second 0.20 m high threshold was placed above the threshold on the downstream side. In addition, the flow from the side weir was prevented. In this way, the flat shape of the sediment in the bed is prevented. After the water level was equal across the entire channel, the required flow was reached and the second threshold above the threshold at the downstream side was slowly removed. However, the shape of the sand in the alluvial bed was prevented from deterioration, so that the flow through the side weir was ensured and the experiment was started. By keeping the flow constant, the flow depth (y_1) at the channel is adjusted to the desired extent by radial gates at the end of the channel. Experiments continued for up to 900 minutes.

After the test was completed, an additional threshold of 0.20 m was placed on the threshold downstream of the straight channel so that the valve was closed slowly to prevent the topography occurring at the bed so that the water was slowly evacuated from the channel. After all these operations, the bed topography was determined with the help of digital limnimeter.

RESULTS AND DISCUSSION OF THE EXPERIMENTAL TESTS

In this experimental study, for different flow velocities, p=7 and 16 cm crest height from the bottom of the sand, L=25 and 40 cm opening length for the side weirs, in the case of live bed scour channel topography changes and spilled sediment discharges were examined. Figure 4 shows that the sediment transport is maximum, while in Figure 4, sediment transport is minimum. When Figure 4 is examined, it is seen that maximum sediment transport occurs at the lowest crest height (p=7 cm) and lowest weir opening (L=40 cm). It is observed that the minimum sediment transport is carried out at the labyrinth

side weir with the highest crest height (p=16 cm) and the highest weir opening length (L=25 cm). The formation of dunes in different sizes was observed at the alluvial bed channel.

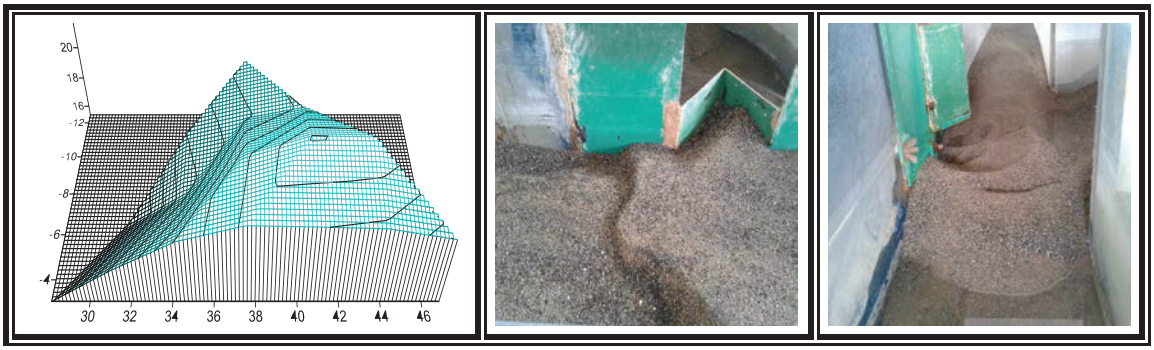

(a)

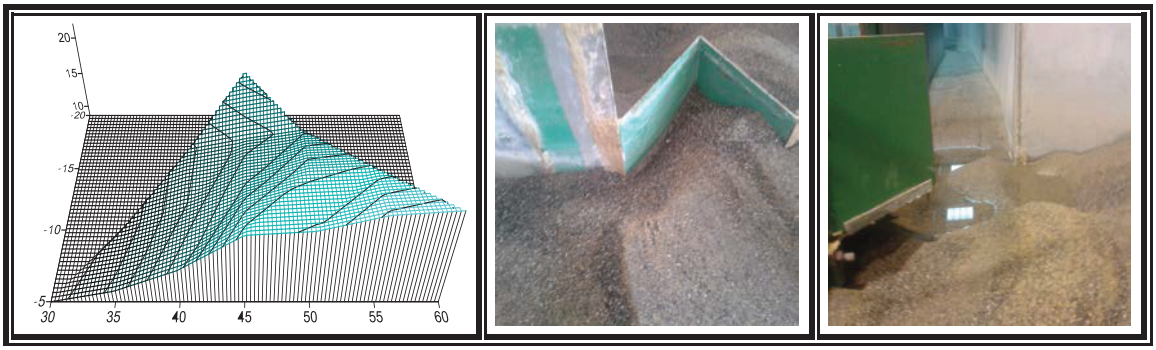

(b)

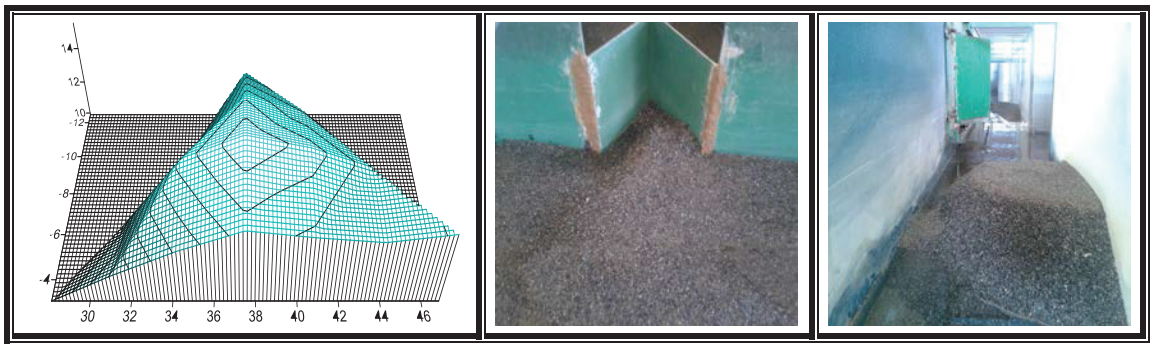

(c)

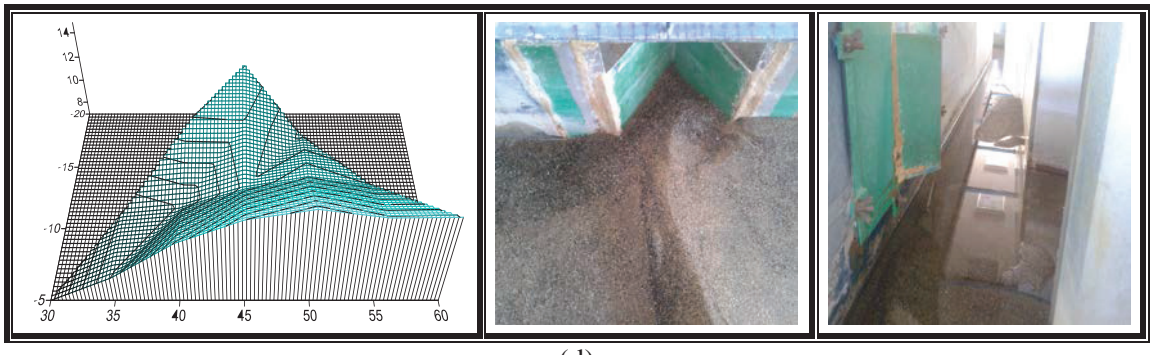

(d)

Figure 4. Pictures and bed topography obtained from the experiments: (a) p=7 cm, L=25 cm, V_1=0.833 m/s (b) p=7 cm, L=40 cm, V_1=1.0 m/s, (c) p=16 cm, L=25 cm, V_1=0.947 m/s, (d) p=16 cm, L=40 cm, V_1=0.565 m/s

When Figure 5 and 6 is examined, it is observed that the sediment discharge (Q_s) which is evacuated by the increase of the flow velocity (V_1) increases. The maximum Q_s is the experiment; p=7 cm, L=40 cm and V_1~1 m/s. Q_s; in is the minimum experiment; p=16 cm, L=25 cm, and V_1~0.6 m/s. It is concluded that; as the weir crest height increase, the spilled sediment discharge decreases and as the weir opening length increase, the spilled sediment discharge increases.

As soon as the dunes were formed and the bed was continuously in motion, the sediment transport occurred at a high level and the amount of spilled bed material was continuously increased with the increase of flow velocity (Figure 6).

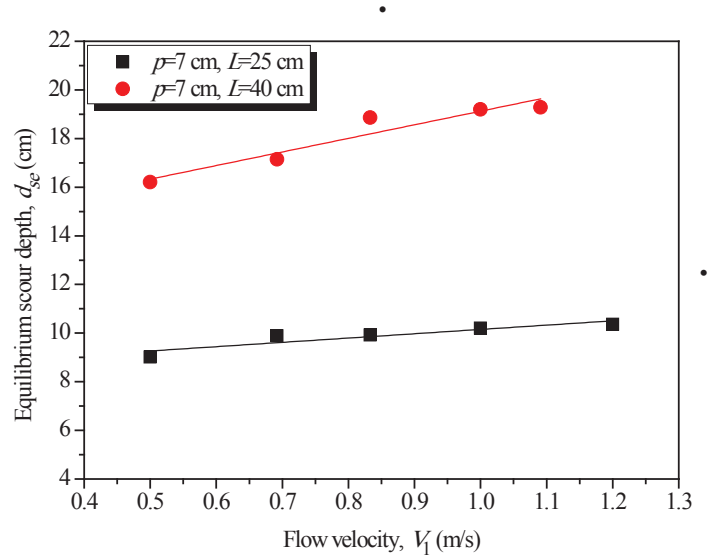

(a)

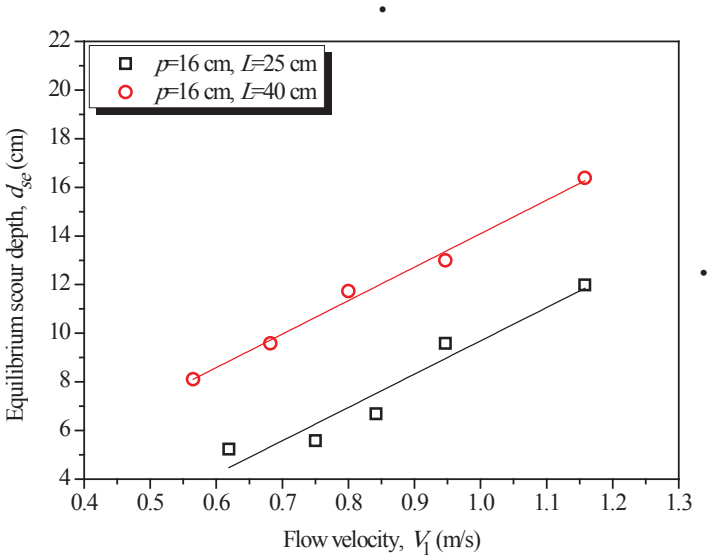

(b)

Figure 5. Equilibrium scour depth change over flow velocity: (a) for p=7 cm, (b) for p=16 cm

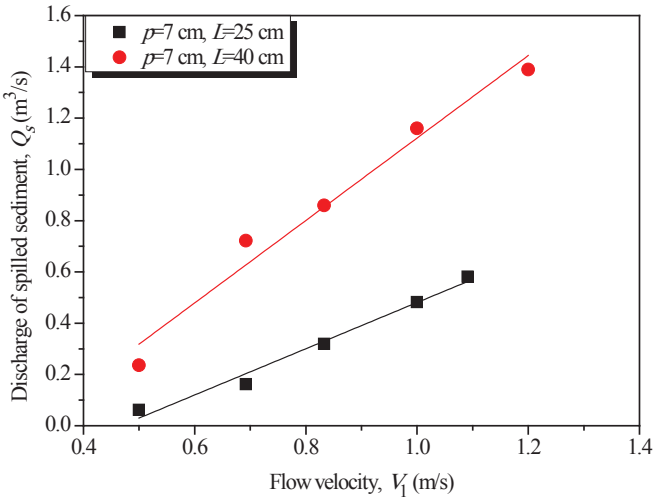

(a)

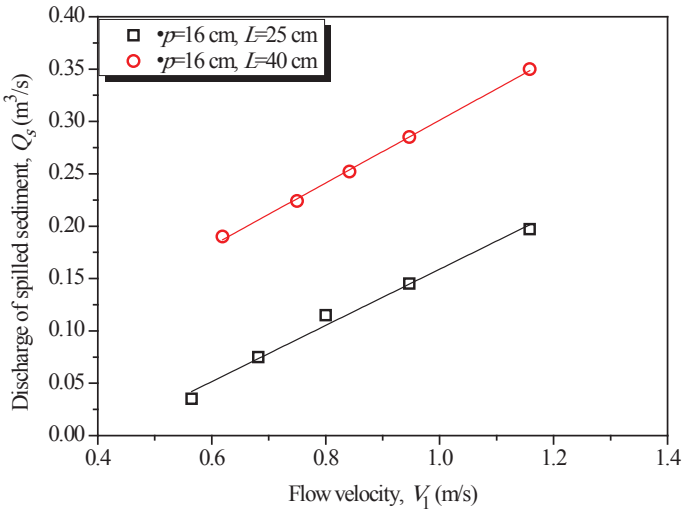

(b)

Figure 6. Discharge of spilled sediment over flow velocity: (a) for *p*=7 cm, (b) for *p*=16 cm

CONCLUSIONS

- Increased flow velocity (V_1) increased the spilled sediment discharge (Q_s).
- It was observed that the spilled sediment discharge (Q_s) decreased with the increase of the weir crest height (p).
- It was observed that the spilled sediment discharge (Q_s) decreased with the decrease of the weir opening length (L).
- For the values low flow velocity, it is generally observed that the formation of dunes at the alluvial bed is observed.
- For the values high flow velocity, it is generally observed that the formation of dunes at the bed is observed.
- In the transition from the ripple form to the dune form, higher scour depths were observed with the change of the bed roughness.
- Increased lateral flow caused a change in the bed topography. Therefore, the maximum change in bed topography was observed under these conditions, since the maximum sediment transport was carried out in the minimum span and minimum crest heights.

REFERENCES

Bayazit, M., 1971. Hareketli Tabanlı Akımların Hidroliği, İTÜ İnşaat Fakültesi Matbaası, İstanbul (in Turkish).

Chabert, J. and Chauvin, J.L., 1963. Formation des dunes et des rides dans les modeles fluviaux, *Bull. du Centre de Recherché et d'Essais de Chatou*, No.4.

Emiroglu, M. E., Gogus, M., Tunc, M., and Islamoglu, K. (2017). Effects of Antivortex Structures Installed on Trapezoidal Labyrinth Side Weirs on Discharge Capacity and Scouring. Journal of Irrigation and Drainage (ASCE), 143(4).

Emiroglu, M. E., Kaya, N. ve Ozturk, M., 2007. Labirent yan savaklardaki akımın ve su alma bölgesindeki oyulmanın kıvrımlı bir kanal boyunca incelenmesi, TÜBİTAK Proje No: 104M394 (in Turkish).

Goncharov, N. V., 1964. Dynamics of Channel Flow, Israel Program for Scientific Translation, Jerusalem.

Melvılle, B. W. and Chiew, Y. M., 1999. Time scale for local scour at bridge piers, *Journal of Hydraulic Engineering, ASCE*, 125(1), 59-65.

Novak P. and Cabelka J., 1981. Models in Hydraulic Engineering, Pitman Publishing Limited, London.

Onen, F., 2005. Hareketli tabanlı akarsularda yanal akımın hidrodinamiğinin incelenmesi, Doktora tezi, Yıldız Teknik Üniversitesi, Fen Bilimleri Enstitüsü, İstanbul, 174s (in Turkish).

Paris, E., Solari, L., and Bechi, G. (2012). "Applicability of the De Marchi hypothesis for side weir flow in the case of movable beds." Journal of Hydraulic Engineering, 10.1061/(ASCE)HY.1943-7900.0000566, 653-656.

Rosier, B., Boillat, J. L., and Schleiss, A. J. (2011). "Influence of lateral water withdrawal on bed form geometry in a channel." Journal of Hydraulic Engineering, 10.1061/(ASCE)HY.1943-7900.0000472, 1668-1675.

Tunc, M., Emiroglu, M. E. (2018). Investigation of Live-Bed Scour at Labyrinth Side Weirs. Fırat University Turkish Journal of Science & Technology, 13(1), 129-136.

Tunc, M. (2014). *An investigation of the hydrodynamics of flow at the labyrinth side weirs in the movable bed rivers*, Firat University, Graduate School of Science (in Turkish).

Yalin, M.S., 1964. Geometrical properties of sand waves, *Jour. Hyd. Div., ASCE*.

5th International Symposium on Dam Safety

October 27-31, 2018

A COMPARISON OF RADIAL-GATED AND FREE-FLOW OGEE FLOOD SPILLWAYS IN CASE OF YEDIGÖZE DAM

Neşe AÇANAL[1], Tefaruk HAKTANIR[2]

ABSTRACT

A free-flow ogee flood spillway is designed for Yedigöze Dam as an alternative to the present radial-gated one, so that both yield the same maximum water surface elevation during routing of the Probable Maximum Flood. The length of the free-flow spillway turns out to be about 10 times that of the radial-gated one for the same routing performance. This huge difference is due to very small volume of the available surcharge storage of Yedigöze Dam, which is about4 % of the total volume of its Probable Maximum Flood. Although the costs of the reinforced-concrete columns carrying the trunnion supports and of six steel radial gates and of the lifting mechanisms along with the hoisting motors of the radial-gated spillway may require considerably high monetary values, the costs of large volume of excavation and of large volume of concrete needed for the free-flow spillway may amount to considerably high magnitudes as well.

Keywords: flood routing over ogee spillways

INTRODUCTION

For the operation of the gates of the existing radial-gated ogee spillway of Yedigöze Dam, in its 'Final Feasibility Report' it is stated that: "The gates will be opened partially after the lake water surface elevation reaches 235.0 m (top of active pool) during an incoming flood hydrograph. The managers will not allow the lake water surface elevation to overpass 236.5 m by adjusting the partial gate openings. If the lake water surface elevation cannot be dropped below 236.5 m by partial gate openings and it has a tendency to rise, then the managers will open the gates fully at 236.5 m." (SANKO 2007). This is a reasonable multi-stage operation policy, and it suggests somewhat like a trial-and error partial gate openings rule starting out at 235.0 m up to a final critical water surface elevation of 236.5 m. However, this policy does not suggest any quantitative gate opening values against some critical lake water surface elevations; rather, it leaves the gate operation in a vague manner to the discretion of the managers.In the pertinent table of routing computations in this report, the maximum water surface elevation reached during routing of the Probable Maximum Flood (PMF) is 238.4 m, which leaves a freeboard of 1.6 m below the dam crest elevation of 240.0 m (SANKO 2007).

The 15-stage operation model is the final phase of various studies of stepwise partial gate openings strategy since 1990s (e.g., Açanal and Haktanır 1999a, 1999b, Açanal et al. 2000, Haktanır and Kişi 2001, Haktanır et al. 2013), and it is cited by a few international publications. So far, this model is applied to a few dams in Turkey during a couple of M.Sc. and Graduation Project studies at Erciyes

[1] Dr., Department of Civil Engineering, Erciyes University, Kayseri, Turkey
eposta: neseacanal@gmail.com
[2] Prof., Department of Civil Engineering, Nuh Naci Yazgan University, Kayseri, Turkey
eposta: thaktan@gmail.com

University. Actually, the operation of spillway gates by partial gate openings in a stepwise manner is a classically known approach. For example, a five-stage gate operation rule is given in its final project for Catalan Dam on Seyhan River in Turkey, and it specifies five constant-magnitude release discharges for five regions each between the two ofsix critical lake water surface elevations,the first one being the top of active pool and the sixth onethe dam crest elevation minus the freeboard(DSİ, 1987). For example, it is stated in this project that: "In the first region which is the region between the water surface elevations of 118.6 m and 125.15 m, a constant spillway discharge of 1200 m^3/s will be released from the lake." (DSİ, 1987).In order to keep the spillway discharge at a constant magnitude of 1200 m^3/s while the lake water surface elevation is rising from 118.6 m up to 125.15 m, which is a head increase of more than six meters, it would be difficult to adjust the partial gate openings. With increasing upstream head, the spillway gates will have to be gradually encroached in order to keep the released discharge constant, which will necessitate a difficult-to-manage spillway gate adjustment operation. As another example, in the final project of the Ilısu Dam, whose active pool capacity is one of the largest in Turkey, it is stated that: "The spillway gates will be adjusted to makethe outflow discharge equal the inflow discharge in order to keep the lake water surface elevation at the maximum operation level; and the spillway gates will be fully opened if the lake level cannot be kept at top of active pool elevation and starts to increase." (DSİ, 2010). Again, this is a rather indefinite and intangible rule of gate operation which requires personal judgment and trial-and-error by the managers. A similar approach is presented in the HEC-5 model of the Hydrologic Engineering Center of US Army Corps of Engineers (HEC 1998), also. Hence, the strategy of the 15-stage operation model of keeping the partial openings of the spillway gates at a constant value between any two adjacent critical lake water surface elevations for a couple of hours during either the rising or the falling limb of any flood is easier to implement than the policy of trying to keep a constant spillway discharge while the lake water surface elevation is steadily increasing or decreasing during routing of a flood hydrograph from the dam.

The objective of this study is twofold. First, it is aimed to apply the 15-stage operation model for the routing of the Probable Maximum Flood over the radial-gated flood spillway of Yedigöze Dam. Second, an alternative free-flow spillway is to be designed to yield the same maximum lake water surface elevation when the Probable Maximum Flood (PMF) is routed as that by the existing radial-gated one.

MATERIALS AND METHOD

Materials

The (lake storage, hm^3)↔(lake water surface elevation, m) relationship as a numerical table, the flow rates of the PMFall over its time base,and the relevant dimensions of the ogee spillway and of the gates like gate width, gate height, trunnion elevation, gate seat elevation, etcetera are taken directly from the final feasibility report of Yedigöze Dam (SANKO 2007). The ordinates of the PMF are computed with the help of a third-degree polynomial interpolation at time increments of 12 minutes ($\Delta t = 0.2$ h).

15-stage Operation Model for Gated Flood Spillways

The 15-stage operation model is explained in concise but sufficient detail in a relevant publication (Haktanir et al 2013). Therefore, the analytical and numerical methods of this model will not be repeated here. Yet, a brief summary may be worth making. The lake water surface elevation upon the entrance of the incoming flood is assumed to be the top of the active pool. Initially, the surcharge storage is divided into 15 equal volumes, and the upper elevations of these sub-surcharge storages (H-sub-storage-i's) are initial candidates of the critical lake levels (Hcr_i's) which form the ceiling elevations of the stages. In each stagea different gate opening is set. Ten decision flood hydrographs are formed bydividing half of the PMF into ten segments by multiplying the PMF by the ratios of 0.05, 0.10, …, 0.45, 0.50. Beyond those, five more decision hydrographs are computed by multiplying

the PMF by the ratios of 0.5, 0.6, 0.7, 0.8, 0.9, 1.0, the PMF being the highest probable flood hydrograph. Initially, a set of possible gate openings (d's) consisting of between 40 and 100 values is assigned. The first gate opening is 'fully closed' (d = 0 m). The set of possible gate openings for any dam is formed at 10 cm increments from fully closed to 2 m, then at 20 cm increments from 2 to 4 m, at 50 cm increments from 4 to 10 m, and at 1 m increments beyond 10 m up to the fully opened (free flow) case.In numerical values this set is: 0.0, 0.1, 0.2, …, 1.9, 2.0, 2.2, 2.4, …, 3.8, 4.0, 4.5, 5.0, …, 9.5, 10., 11., 12, …, fully open. The design head for large dams can be as high as 20 ~ 30 meters while for small dams it can be as small as 10 m or even a smaller value.To begin with, the first decision hydrograph (5 % of PMF) is routed with the gates in closed position and with the full discharge of the shaft spillway like the energy penstock, and the maximum lake water surface elevation (Hmax) formed is taken as Hcr_1. If this Hmax happens to be greater than the top elevation of the first sub-surcharge storage, then the gates are opened 10 cm instead of being closed and the routing of 0.05×PMF is repeated. Hmax which is close to but a little smaller than H-sub-storage-1 is taken as the first critical lake level (Hcr_1). Next, the second decision hydrograph (0.10×PMF) is routed with the gate opening of the first decision hydrograph. Because 0.10×PMF is twice as much as 0.05×PMF, the lake water surface elevation passes above the first critical lake level (Hcr_1) before reaching the peak of the outflow hydrograph. At that instant, the gate opening is increased to the next higher value in the initial set of possible gate openings and Hmax in this case is computed. If this Hmax turns out to be greater than the top elevation of the second sub-surcharge storage, then the gates are opened to the next higher value in the possible set of gate openings and the routing of 0.10×PMF is repeated. The gate openings are increased stepwise until Hmax becomes close to but a little smaller than H-sub-storage-2, and Hmax is taken as the second critical lake level (Hcr_2). This procedure is repeated for each one of the 15 stages rising upwards one by one, the final stage being in the 15^{th} sub-surcharge storage and the final flood hydrograph being the PMF. When the PMF is routed, the managers of the dam will not realize its true magnitude and they will open the gates as much as the value determined for the first stage. Because of its huge magnitude, the PMF will cause the lake level to rise above the first critical level with the gate opening of the first stage in a very short time. Immediately when the lake water surface level passes Hcr_1, the gates will be opened as much as the value determined for the 2^{nd} stage. In this manner, during routing of the PMF, the top elevations of all the stages from the first to the 14^{th} stage will be passed, the lake level will rise to be in the 15^{th} surcharge sub-storage and the gates will be opened as required for the 15^{th} stage.The gate opening of the 15^{th} stage will be such a value that the final maximum lake water surface elevation reached will be below the dam crest elevation by a freeboard specified initially. The details of the numerical algorithms, especially for determining those times for passage from one stage to the next stage are given in relevant publications (Açanal et al 2000, Haktanır et al 2013).In order to simplify the rules of the 15-satge operation model in a practical way, the same critical lake levels are accepted during the falling limb of any flood hydrograph also. With the purpose of draining the surcharge storage a little faster back to the maximum operation elevation (top of active pool), the gate opening of the N'th stage is kept the same down to the (N–2)'nd stage. Hence, the same critical lake levels and the gate openings determined during the rising limbs of the 15 decision hydrographs is used as they are during the falling limb also with the exception of shifting the gate openings two stages below.Computation of the spillway discharge within any stage is done by the method for partially-opened radial-gated ogee spillways given in the 'Spillways' Chapter of the classical book: *Design of Small Dams* (USBR 1973).

The 15-stage operation model determines a few more sets of 15 critical lake levels (Hcr_i's) and 15 gate openings (d_i's) after having computed the first solution which allocates the 15 sub-surcharge storages to 15 decision flood hydrographs at proportionate magnitudes. The PMF has an extremely small probability of occurrence. Therefore, small-magnitude floods like 0.3×PMF, 0.4×PMF, 0.5×PMF have actually higher probabilities of occurrence than those of high-magnitude floods like PMF, 0.9×PMF, 0.8×PMF, and it may be more realistic to attempt to attenuate the small-magnitude floods and let huge outflow peaks be released during routing of high-magnitude floods. Therefore, the 15-stage operation model deliberately constricts the gate openings at the initial stages in a stepwise manner, which yields smaller peaks of the outflow hydrographs when small-magnitude decision floods are routed. But, the constriction of the gate openings at small floods causes their critical lake

levels to be pushed further upwards leaving smaller sub-surcharge storages for higher floods. And, this reduction in peaks of small floods comes at the expense of larger peaks of the outflow hydrographs of high-magnitude floods like PMF, 0.9×PMF, 0.8×PMF, , 0.7×PMF. The 15-stage operation model determines as many more sets of 15 Hcr_i'sand 15 d_i's as allowed by the available surcharge storage. Finally, the computations are stalled by numerical instability due to shrinking of higher sub-surcharge storages.For those dams having fairly large surcharge storages, the 15-stage operation model finds quite a few more sets of operation rules (e.g. Haktanır et al 2013). For those dams having too small a surcharge storage, like the Yedigöze Dam of this study,the model can find only a few different sets of operations, or even cannot come up with any solution at all.

After having applied it to a few dams having radial-gated ogee flood spillways, it is noticed that the 15-stage operation model gives better results for dams having surcharge storages greater than 15 % of the total volume of the Probable Maximum Flood (PMF). In this study, the 15-stage operation model isapplied to the existing radial-gated spillway of Yedigöze Dam,although it has too small a surcharge storage, which is only about 4 % of the total volume of the PMF.Therefore, the 15 gate openingsalong withthe 15 critical lake water surface elevations for Yedigöze Dam aredetermined by a trial-and-error approach. The maximum turbine discharge of 380 m^3/s given in the mentioned report (SANKO 2007) is released during the entire time base of the incoming flood.The 15 critical lake levels and the 15 gate openings obtained as such still yield a plausible routing of the Probable Maximum Flood, with an advantage of not having to make instant crucial decisions during routing of an immense flood.Table 1 gives the 15 critical lake levels and the 15 gate openings obtained for Yedigöze Dam.

Table 1. A reasonable set of 15 critical lake levels and 15 gate openings determined by trial-and-error for routing of the Probable Maximum Flood of Yedigöze Dam over its radial-gated spillway.

Lake water surface elevation at the beginning = 235.0 m									
Critical lake surface elevations and gate openings during the rising limb of the outflow hydrograph:									
Lake surface elvn (m)	235.0	235.2	235.4	235.6	235.8	236.0	236.3	236.7	237.0
Gate opening (m)	0.0	0.0	0.5	1.0	1.5	2.0	2.5	3.0	3.5	4.0
Critical lake surface elevations and gate openings during the rising limb of the outflow hydrograph (continued):									
Lake water elvtn (m)	237.0	237.2	237.4	237.6	237.8	238.0	238.3	238.4	
Gate opening (m)	3.5	4.0	5.0	6.0	8.0	10.0	12.0	fully opened	
Operation during the falling limb of the outflow hydrograph:									
Lake surface elvn (m)	238.4	238.3	238.0	237.8	237.6	237.4	237.2	237.0	236.7
Gate opening (m)	fully opened			12.0	10.0	8.0	6.0	5.0	
Operation during the falling limb of the outflow hydrograph (continued):									
Lake surface elvn (m)	236.7	236.3	236.0	235.8	235.6	235.4	235.2	234.9	
Gate opening (m)	5.0	4.0	3.5	3.0	2.5	2.0	1.5	1.0	

Length of Free-Flow Ogee Spillway and Routing of the PMF

The length of the free-flow ogee spillway considered as an alternative to the existing radial-gated one is computed by the method in the book: *Design of Small Dams* (USBR 1973). Initially, the elevation of top of active pool, the maximum allowed water surface elevation during routing of the Probable Maximum Flood, the length of the spillway approach channelare given; and, after a few trial routings, the spillway length satisfying the maximum allowed water surface elevation constraint is computed along with the outflow hydrograph. To begin with, the peak of the outflow hydrograph is assumed to equal 70 % of the peak of the PMF. After having determined the discharge coefficient which equals the multiplication of four coefficients given in the relevant charts of the 'Spillways' Chapter of

Design of Small Dams (USBR 1973), the spillway length is computed by the free-flow spillway discharge equation.Iterations for the spillway design discharge and hence the spillway lengthare repeated until (1) the spillway design discharge becomes equal to the peak of the outflow hydrograph when the PMF is routed and also (2) the maximum water surface elevation reached during routing of the PMF is equal to the initially specified value.Computing the length of the flood spillway according to the peak of the outflow hydrograph is more realistic and more economical than taking the peak of the inflow hydrograph as the spillway design discharge, because a shorter spillway length is computed. The routing effect of a free-flow spillway will be more efficient if there is a fairly large volume of surcharge storage above the maximum operation elevation (top of active pool), and the difference between the peaks of the PMF and the outflow hydrograph will be great.The details of this iterative algorithm are presented at the 8th National Hydrology Congress (Haktanır et al 2015).

RESULTS, DISCUSSIONS, AND CONCLUSION

The routing computations for both the alternative free-flow and the existing radial-gated spillways are done with a time step of Δt = 0.2 hours (12 minutes).The net length of the existing radial-gated spillway is 66 meters (SANKO 2007) while that of the free-flow spillway whose crest elevation is necessarily equal to top of the active pool turns out to be 698 meters. This huge difference in lengths of the free-flow and radial-gated spillways is due to two constraints. The first one is the requirement that the crest elevation of the free-flow spillway be equal to the top of active pool. And, the second constraint is the very small total surcharge storage of this dam between the elevations of 235.0 and 238.4 m. As mentioned before, the surcharge storage within the 3.4 meter band between these elevations is just about 4 % of the total volume of the PMF of the Yedigöze Dam (SANKO 2007). The crest elevation of the existing radial-gated spillway is 221.5 m and its design head is 16.9 m, whereas the same values for the alternative free-flow spillway are 235.0 m and a mere 3.4 m. Therefore, the gated spillway is far more advantageous in releasing discharges over it due to much higher heads. Figure 1 shows the outflow hydrographfrom the existing radial-gated spillway routed by the 15-stage operation model together with the Probable Maximum Flood given in the Final Feasibility Report (SANKO 2007) as the inflow hydrograph. Figure 2 shows the outflow hydrograph of the Probable Maximum Flood routed from the alternative free-flow spillway.Hence, this dam has almost no routing capacity, which is obvious from Figures 1 and 2.

Although the costs of the reinforced-concrete columns carrying the trunnion supports and of six steel radial gates and of the lifting mechanisms along with the hoisting motors of the existing radial-gated spillway may require considerably high monetary values, the costs of large volume of excavation and of large volume of concrete needed for the alternative free-flow spillway may amount to pretty high magnitudes as well.

Presently, the authors are working on other research studies. The objective of bringing forth the 15-stage operation model once again by implementing it to Yedigöze Dam is to try to attract the attention of the technical and administrative personnel in charge with the hope that this model be applied to an actual dam in Turkey as a pilot study. The second objective is to present the computer programs for (1) the design of the free-flow ogee spillway and (2) the 15-stage operation model to anybody interested.

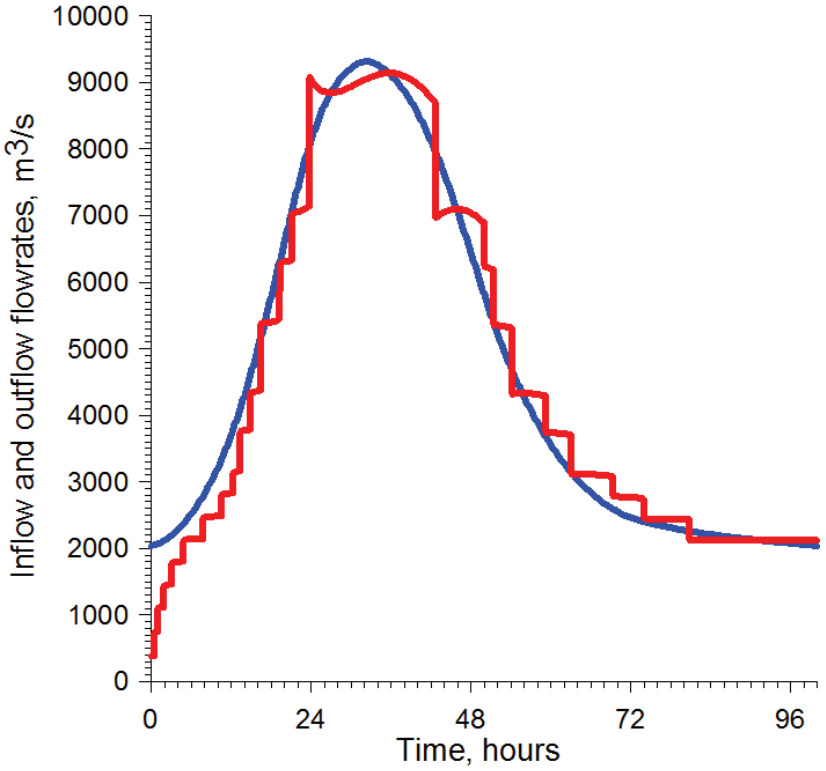

Figure 1. Routing of the Probable Maximum Flood given in the 'Final Feasibility Report of Yedigöze Dam' from the existing radial-gated spillway by the 15-stage operation model.

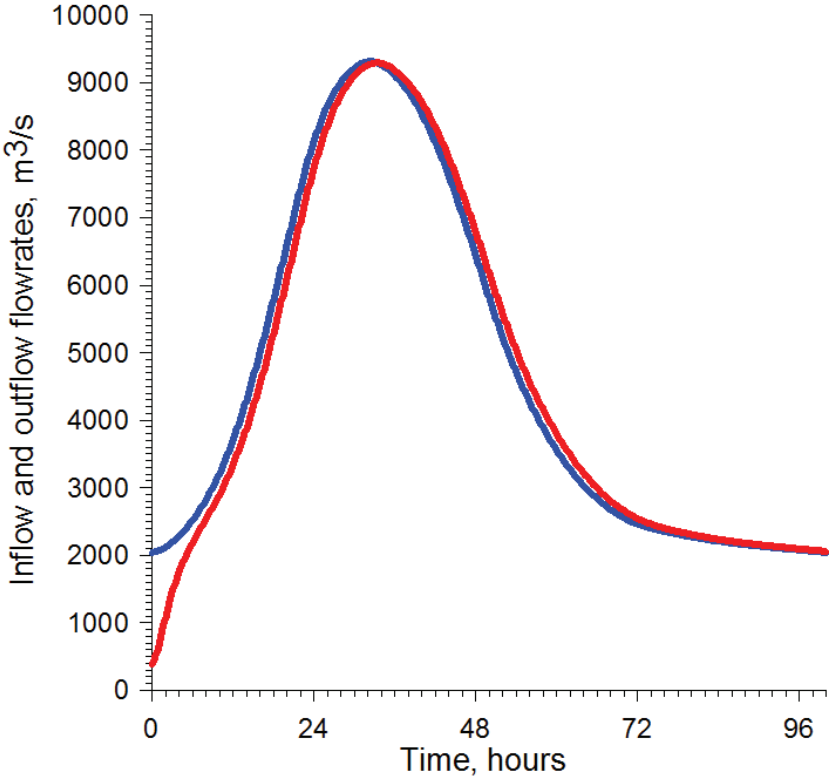

Figure 2. Routing of the Probable Maximum Flood from the alternative free-flow spillway.

REFERENCES

Açanal, N. and Haktanır, T., 1999a."Five stage flood routing for gated reservoirs by grouping floods into five different categories according to their return periods". Hydrological Sciences Journal, vol. 44(2), pp. 163–172.

Açanal, N. and Haktanır, T., 1999b."Six-stage flood routing for dams having gated spillways". Turkish Journal of Engineering and Environmental Sciences, Tübitak, vol. 23(6), pp. 411–422.

Açanal, N., Yurtal, R., Haktanır, T., 2000."Multi-stage flood routing for gated reservoirs and conjunctive optimization of hydroelectricity income with flood losses". Hydrological Sciences Journal, Vol. 45(5), pp. 675–688.

DSİ, 1987. Final Project of Çatalan Dam and HPP, Sheet No. 43: Routing of the Probable Maximum Flood (In Turkish). General Directorate of State Water Works, Investigation, Planning and Allocations Division, Yücetepe, Ankara.

DSİ, 2010. Final Project of Ilısu Dam and HPP, Report No: 14.160/0030-Rev.1 Hydraulic Report of the Flood Spillway and Routing of the Probable Maximum Flood (In Turkish). General Directorate of State Water Works, Investigation, Planning and Allocations Division, Yücetepe, Ankara.

Haktanır, T. and Kisi, Ö., 2001."Ten-stage discrete flood routing for dams having gated spillways". Journal of Hydrologic Engineering, ASCE, vol. 6(1), pp. 86–90.

Haktanır, T., Çıtakoğlu, H., Açanal, N., 2013."Fifteen-stage operation of gated spillways for flood routing management through artificial reservoirs". Hydrological Sciences Journal, vol. 58(5), pp. 1013–1031.

Haktanır, T., Çıtakoğlu, H., Çobaner, M., 2015."Computation of ogee profile free flow spillway and routing of design flood (In Turkish)". VIII. National Hydrology Congress, 8–10 October 2015, Harran University, Şanlıurfa, Proceedings, pp. 242–253.

HEC, 1987. Engineering and Design Management of Water Control Systems, Engineer Manual EM-1110-2-3600. US Army Corps of Engineers, Hydrologic Engineering Center, Davis, CA, USA.

HEC, 1998. HEC-5 Simulation of Flood Control and Conservation Systems, Users' Manual Version 8.0. US Army Corps of Engineers, Hydrologic Engineering Center, Davis, CA, USA.

SANKO, 2007. Final Feasibility Report of Yedigöze Dam and Its HPP (In Turkish). SANKO Engineering and Consulting Inc., Çetin Emeç Bulvarı, 6.ncı Cadde, No: 61/7, 06520, Balgat/Ankara.

USBR, 1973. Design of Small Dams, Second edition,US Department of The Interior, Bureau of Reclamation, US Government Printing Office, Washington DC.

5th International Symposium on Dam Safety

October 27-31, 2018

FREQUENCY ANALYSES OF ANNUAL FLOOD PEAKS OF STREAMS IN FIVE BASINS OF THE BLACK SEA

Neşe AÇANAL[1], Hatice ÇITAKOĞLU[2], Tefaruk HAKTANIR[3], Gülsüm YAZICI[4]

ABSTRACT

Based on (1) Chi-square and (2) probability-plot correlation coefficient goodness-of-fit tests, (3) visual inspections of histograms of the observed series together with the probability density functions, and (4) visual inspections of elements of the observed series marked by the Cunnane plotting position formula together with the cumulative distribution functions, the probability distribution models of the Generalized Maximum Values and of the 3-Parameter Log-Normal whose parameters are computed by the method of probability-weighted moments are deemed most suitable for the observed series of annual flood peaks with record lengths in the range of 31 to 74 years with an average length of 49 years on 43 natural streams having no dams on upstream parts in five major basins discharging to the Black Sea. Either one of these two models can be chosen as the best because mostly they yield close values for the flood peaks over the range of average return periods from 1.11 to 10,000 years.

Keywords: flood frequency analysis, flood peaks in Black SeaRegion

INTRODUCTION

Flood frequency analysis is a classical approach to estimate the average return periods of peaks of measured real-life floods and those of probable future floods of higher magnitudes. Flood peaks discharging into the inlets of drainage systems in urban areas are commonly calculated on the basis of their average return periods. In the final project of any dam, the flood hydrographs of various average return periods are given along with the probable maximum flood. Endless cases of flood frequency applications can be mentioned. For example, in a study, the operation of gates of radial-gated spillways of a couple of dams in Turkey is done considering the magnitudes of floods categorized according to their return periods (Açanal and Haktanır 1999). Because of the significance of this topic in design of water structures in general, the World Meteorological Organization also has published reports regarding this subject, the last one as Chapter 5 in *Guide to Hydrologic Practices Volume II* (WMO 2009). And, maybe thousands of papers and a few books related to flood frequency analysis are published (e.g. Ghorbani et al 2010, Haktanır 1992, Rao and Hamed 2000).

Frequent flooding causes considerable damages in the Black Sea Region of Turkey. Therefore, the objective of this study has been to apply frequency analyses on the annual flood peaks series with

[1] Dr., Department of Civil Engineering, Erciyes University, Kayseri, Turkey
eposta: neseacanal@gmail.com
[2] Dr., Department of Civil Engineering, Erciyes University, Kayseri, Turkey
eposta: hcitakoglu@erciyes.edu.tr
[3] Prof., Department of Civil Engineering, Nuh Naci Yazgan University, Kayseri, Turkey
eposta: thaktan@gmail.com
[4] M.Sc. student, Department of Civil Engineering, Erciyes University, Kayseri, Turkey
eposta: gyazici@erciyes.edu.tr

record lengths greater than or equal to 30 years observed at as many natural streams as available in five major basins in Turkey discharging to the Black Sea. Among these, the West Black Sea and the East Black Sea Basins are classified as congregated basins comprising many small to medium sized creeks discharging directly to the sea, and their down-most sections contacting the sea extend over a large part of the Black Sea shoreline. All of the streams in these two basins should be considered to convey unregulated flows because there are no dams on them.

MATERIALS AND METHOD

Materials

As shown in Figure 1, Basin #13, the West Black Sea Basin, begins at the far western border of Turkey in the Thrace region and extends towards east all the way past the city of Sinop covering almost half of the Black Sea shore. Basin #22, the East Black Sea Basin, beginning close to the eastern boundary of Basin #13, extends all the way to the eastern border of Turkey flanking Georgia (Figure 1). Basin #12, the Sakarya Basin, is drained by the Sakarya River as the main channel, and most of it lies within the northern parts of the Inland Anatolia Region and its western boundary is adjacent to the eastern parts of the Marmara and Aegean Regions of Turkey (Figure 1). Basin #15, the Kızılırmak (Red River) Basin, is drained by the Kızılırmak River as the primary channel, and most of it is positioned in the northeastern parts of the Inland Anatolia Region while its northern tributaries are located in the Black Sea Region between Basins #13 and#22 (Figure 1). Most of Basin #14, the Yeşilırmak (Green River) Basin, is positioned south of the leeward sides of the Black Sea Mountains. As Basins #13 and #22 extend within fairly narrow bands all along the coast of the Black Sea and are positioned in the windward areas between the shoreline and the summits of the Black Sea Mountains, some of the other three basins, #12, #15, and #14, have parts extending southwards into the Aegean and Inland Anatolia Regions (Figure 1).

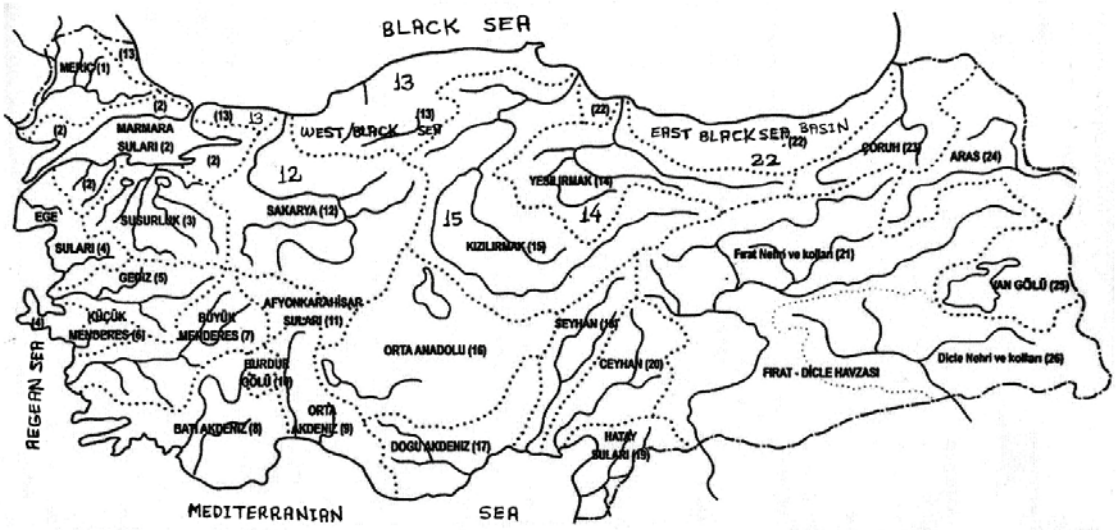

Figure 1. Map showing the five basins discharging to the Black Sea together with all 26 basins of Turkey.

All the data of the annual flood peaks having a record length of at least 30 years measured at those stream-gauging stations which are not located downstream from any dams are taken from the gauged stream flows year books published by the General Directorate of State Water Works (DSİ 1935–

2014). Altogether 43 such recorded series of annual flood peaks with an average length of 49 elements are obtained and used in the analyses.

Method

Taking into consideration the information in a relevant and fairly recent report by the World Meteorological Organization (WMO 2009) and previous studies performed in Turkey (e.g. Haktanır 1992, Seçkin et al 2010), the 3-parameter log-normal (LN3), generalized extreme values (GEV), generalized logistic (GLO), Pearson-3 (P3), and log-Pearson-3 (LP3) are deemed as potential probability distributions to represent the distributions of the annual flood peaks series of natural streams in the study basins. The 2-parameter distributions of Gumbel and 2-parameter log-normal (LN2) are left out. The log-Pearson-3 distribution is more comprehensive than LN2 because LN2 is a special version of LP3 having zero skewness for the log-transformed series. Similarly, the Gumbel distribution is a special form of GEV having a skewness coefficient of +1.14, and GEV is more comprehensive than Gumbel incorporating a flexible skewness coefficient (SC) which can vary over the widest possible range of $-\infty < SC < +\infty$. The parameters of the potential probability distributions are computed by three methods, which are conventional moments (-MOM), maximum-likelihood (-ML), and probability-weighted moments (-PWM). Hence, five probability distributions and three parameter estimation methods result in 15 (=5×3) distribution models.

In this study, the choice of the best-fit probability distribution model is based on an overall evaluation of a few different criteria. The first one is the classical Chi-square goodness-of-fit test. Because the number of parameters of all 15 distribution models is the same (three), the choice of the better-fit model can be made simply by the smallest magnitude Chi-square statistic. The number of sub-divisions for the histograms of the elements in the observed series and of the elements expected by a theoretical distribution (K) is computed by the empirical Sturges formula ($K = 1 + 3.3 \times \log_{10}(N)$, N being the sample length) like many other studies. Briefly, the Chi-square goodness-of-fit test produces a single number which reflects the conformity of the histogram of the observed elements to the histogram of the expected elements by a potential probability distribution. Here, a straightforward ranking of distributions according to Chi-square statistic magnitudes is not followed. Rather, those first few models having Chi-square statistics close in magnitude are all considered as potentially good enough, and the other evaluation criteria are taken into account to further refine the choice for the better distributions or the best one.

The second evaluation criterion is the visual inspection of the histogram of the relative frequencies of the observed elements of the sample series drawn together with the scale-adjusted probability density functions of the potential distributions all placed in the same graph. The ordinates of the probability density function of any candidate distribution are multiplied by the sub-division length (Δx) when drawn together with the relative frequencies histogram because the area under the histogram equals Δx, not 1.

The third evaluation criterion is the probability plot correlation coefficient (PPCC) goodness-of-fit test which was originally proposed by Filliben (1975) and later has become a popular goodness-of-fit test. In this test, the expected magnitudes of the elements of the observed sample series as computed by a potential probability distribution are compared with the observed magnitudes. The non-exceedence probabilities of the elements of the observed series are estimated by a suitable plotting position formula depending on their rank numbers in the ordered series, and the expected magnitudes of the elements assumed to have those non-exceedence probabilities are computed by the quantile function of the potential distribution. If that distribution is a perfect fit to the observed series, then the expected magnitudes should be equal to the observed magnitudes, and the correlation coefficient of N observed magnitudes against N expected magnitudes should be equal to 1. Closer the correlation coefficient to 1, better the fit of that distribution to the observed series. In this study, the Cunnane plotting position formula is used in estimation of the non-exceedence probabilities of the elements of the observed sample series as done by Adeloye and Montaseri (2002).

The fourth evaluation criterion is drawing the frequency curves (cumulative distribution functions) of a few distribution models, which exhibit better performances both in the Chi-square and PPCC goodness-of-fit tests, on a Gumbel graph paper together with the elements of the observed sample series marked in the graph by the Cunnane plotting position formula, and visually observing the agreement and disagreement of these curves firstly with the tendency of the plotted sample points and with each other in the interval of exceedence probabilities (Pex) of: $0.0001 \leq Pex \leq 0.9$, or equally in the interval of average return periods (T) of: 1.11 years $\leq T \leq$ 10,000 years. Personal judgment also is taken into account. For example, a distribution whose quantile function (inverse of cumulative distribution function) seems to follow the plotted points over their entire range up to the highest-magnitude one (the greatest-value element of the observed series) but then increases sharply at a fast rate beyond that is discarded. As an example, mostly, the quantile function of the Generalized Logistic distribution whose parameters are computed by the method of maximum-likelihood (GLO-ML) shows such unreasonably higher rates of increase with increasing return periods.

RESULTS AND DISCUSSIONS

Careful assessment of all those four criteria along with the personal judgment acquired by similar previous studies have led to choosing the probability distributions of GEV-PWM and LN3-PWM for most of the annual flood peaks series recorded at the gauging stations in these five basins. For a majority of these observed series, the LN3 distribution whose parameters are computed by the method of maximum likelihood, LN3-ML, also turns out to be almost as good as LN3-PWM; but, for the sake of generality LN3-PWM is chosen. The GEV distribution whose parameters are computed by the method of probability-weighted moments, GEV-PWM, is superior to the other GEV models, which are GEV-MOM and GEV-ML. For some series, Pearson-3 and log-Pearson-3, whose parameters are computed by the methods of moments and probability-weighted moments are also close to the chosen distributions, but again, for the sake of generality, either GEV-PWM or LN3-PWM has turned to be the most reasonable choice. GEV-PWM and LN3-PWM usually yield quantiles (flood peaks) close to each other in these five basins.

Tables 1, 2, 3, 4, 5 present the summary results of the best-fit distributions chosen for the annual flood peaks series of the natural streams in those five basins in Turkey discharging to the Black Sea. As seen in these tables, the flood producing mechanisms of the natural streams in these five Black Sea basins show drastic differences. For example, for a few cases a smaller size drainage area generates much higher annual flood peaks than a larger size watershed. There should be topographic, morphologic, land use, and precipitation causes for those differences. Investigation in that direction is out of the scope of this study, and straightforward frequency analyses on the series of annual flood peaks measured at some stream-gaging stations are applied in the manner summarized above. Nonetheless, the ratios of (Mean annual flood peak, liters/s) ÷ (Drainage area, km^2) of the streams in Basins #13 and #22, which are covering most of the shore line of the Black Sea, are fairly consistent.

Table 1. Summary information of frequency analyses on annual flood peaks (AFP) series observed in Basin #12 (Sakarya Basin)

Station ID	Drainage area (km^2)	Record period and length of series(*)	Mean-AFP / Drainage area (l/s /km^2)	Variation and Skewness coefficients	Best distribution model	AFPs having return periods 50, 100, 500, 1000,
1203 Beşdeğirmen	3938.4	1936 – 2011 74	9	0.841−2.93	GEV-PWM	130, 164, 276, 343, 684
1219 Yağbasan	410.8	1953 – 2011 55	270	0.483−0.54	GEV-PWM	245, 268, 317, 336, 392
1222 Rüstümköy	2021.6	1953 – 2014 61	79	0.505−0.70	LN3-PWM	363, 403, 495, 534, 667
1224 Aktaş	4342.2	1963 – 2014 50	5	0.667−2.24	GEV-PWM	63, 78, 123, 149, 272
1226 Meşecik	7140.0	1963 – 2011 48	10	0.716−1.20	LN3-PWM	237, 284, 410, 472, 716
1233 Karaköy	2003.2	1959 – 2013 54	116	0.600−1.33	LN3-PWM	652, 764, 1053, 1191, 1717
1237 Dokurcun	1073.4	1956 – 2014 57	63	0.763−1.90	LN3-PWM	246, 310, 499, 600, 1040
1250 Kınık	232.8	1981 – 2014 33	208	0.732−1.50	GEV-PWM	166, 214, 375, 475, 1022

Table 2. Summary information of frequency analyses on annual flood peaks (AFP) series observed in Basin #13 (West Black Sea Basin)

Station ID	Drainage area (km^2)	Record period and length of series(*)	Mean-AFP / Drainage area (l/s /km^2)	Variation and Skewness coefficients	Best distribution model	AFPs having return periods 50, 100, 500, 1000,
1302 Yakabaşı	1988.0	1953–2013 60	116	0.410 +1.24	GEV-PWM	494, 558, 720, 796, 1075
1307 Azdavay	1097.6	1963–2011 49	102	0.453 +0.40	GEV-PWM	238, 260, 304, 321, 370
1314 Karabük	5086.8	1963–2011 49	59	0.534 +0.84	LN3-PWM	734, 831, 1062, 1166, 1533
1319 Gökçesu	786.3	1965–2013 45	96	0.831 +2.77	LN3-PWM	276, 346, 549, 656, 1119
1327 Afatlar	953.6	1968–2013 45	121	0.438 +0.35	GEV-PWM	244, 266, 312, 330, 382
1330 M.Şevketpaşa	23.1	1966– 012 44	742	1.28 +5.27	LN3-PWM	69, 93, 168, 211, 418
1331 Bartın	1342.0	1970–2013 36	330	0.657 +1.35	GEV-PWM	1422, 1720, 2578, 3035, 5058
1334 Beşdeğirmenler	1342.0	1965–2011 47	60	0.550 +3.72	GEV-PWM	160, 192, 286, 337, 577
1335 Derecik	13300.4	1964–2010 47	73	0.603 +1.60	GEV-PWM	2706, 3231, 4710, 5483, 8810
1338 Ortaköy	104.8	1981–2011 31	979	0.691 +1.12	LN3-PWM	318, 379, 542, 622, 933
1339 Çiftekese	105.2	1981–2011 31	446	0.666 +2.17	GEV-PWM	1422, 1720,2578, 3035, 5058

Table 3. Summary information of frequency analyses on annual flood peaks (AFP) series observed in Basin #15 (Kızılırmak Basin)

Station ID	Drainage area (km^2)	Record period and length of series(*)	Mean-AFP / Drainage area (l/s /km^2)	Variation and Skewness coefficients	Best distribution model	AFPs having return periods 50, 100, 500, 1000,
1501 Yamula	15581.6	1938–2003 66	29	0.406 +0.92	LN3-PWM	910, 1002, 1214, 1306, 1617
1517 Şefaatli	8592.4	1953–2003 50	7	0.557 +0.76	GEV-PWM	144, 159, 190, 203, 240
1535 Söğütlühan	6606.5	1963–2013 50	47	0.356 +0.36	LN3-PWM	568, 611, 703, 740, 859
1538 Çeltikçibaşı	1962.0	1971–2013 42	69	0.744 +2.15	GEV-PWM	408, 484, 685, 786, 1188
1539 Bulakbaşı	1642.0	1972–2013 42	105	0.469 +0.79	GEV-PWM	396, 446, 567, 621, 808
1541 Çadırhöyük	16762.8	1981–2013 31	7	0.527 +0.21	GEV-PWM	248, 269, 309, 323, 361

Table 4. Summary information of frequency analyses on annual flood peaks (AFP) series observed in Basin #14 (Yeşilırmak Basin)

Station ID	Drainage area (km^2)	Record period and length of series(*)	Mean-AFP / Drainage area (l/s /km^2)	Variation and Skewness coefficients	Best distribution model	AFPs having return periods 50, 100, 500, 1000,
1402 Kale	33904.0	1939–2013 70	20	0.393 +1.18	LN3-PWM	1383, 1520,1836, 1974, 2439
1412 Şeyhoğlu	3668.8	1954–2013 58	15	0.707 +0.94	LN3-PWM	168, 195, 260, 291, 400
1413 Durucasu	21667.2	1955–2012 58	14	0.486 +0.70	LN3-PWM	672, 739, 890, 954, 1164
1414 Sütlüce	5409.2	1956–2012 57	22	0.435 +0.41	LN3-PWM	240, 260, 302, 319, 373
1418 Gömeleönü	1608.0	1964–2013 50	108	0.373 +1.94	LN3-PWM	325, 355, 425, 455, 557
1422 Çiçekbükü	1714.0	1969–2013 45	47	0.532 +1.62	LN3-PWM	206, 240, 328, 370, 533
1424 Çırdak	1032.8	1969–2012 44	32	0.457 +0.73	LN3-PWM	69, 75, 90, 96, 114
14A014 Kurtun	1342.0	1964 – 2013 48	244	0.960 +2.08	LN3-PWM	239, 292, 438, 510, 802

Table 5. Summary information of frequency analyses on annual flood peaks (AFP) series observed in Basin #22 (East Black Sea Basin)

Station ID	Drainage area (km^2)	Record period and length of series**(*)**	Mean-AFP / Drainage area (l/s /km^2)	Variation and Skewness coefficients	Best distribution model	AFPs having return periods 50, 100, 500, 1000,
2202 Değirmencik	635.7	1967–2013 47	152	0.432 +1.79	GEV-PWM	221, 259, 369, 427, 680
2213 Dereli	713.0	1962–2004 43	183	0.598 +2.00	LN3-PWM	391, 474, 706, 824, 1312
2215 Çamlıkdere	445.2	1965–2013 48	185	0.311 +1.45	GEV-ML	153, 170, 213, 233, 307
2218 Şimşirli	834.9	1963–2009 47	199	0.510 +2.14	LN3-PWM	437, 531, 804, 947, 1563
2228 Bahadırlı	191.4	1962–2013 47	349	0.577 +1.24	LN3-PWM	218, 252, 336, 375, 519
2232 Topluca	763.2	1964–2013 50	234	0.437 +3.12	LN3-PWM	423, 507, 753, 883, 1441
2233 Tozköy	223.1	1964–2013 50	195	0.248 +1.07	GEV-PWM	74, 82, 101, 109, 142
2238 Arıcılar	1024.4	1965–2013 49	155	0.440 +0.51	LN3-ML	341, 377, 462, 498, 622
2245 Gökçeli	232.8	1969–2013 45	1177	0.649 +1.79	LN3-PWM	786, 925, 1290, 1465, 2139
2247 Gocallı	1859.2	1968–2013 45	213	0.556 +1.28	GEV-PWM	1052, 1240, 1752, 2010, 3077

(*): There are some missing data in some years for some of the stations.

The figure showing the histogram of the observed elements in the series together with the scale-adjusted probability density functions of the LN3-PWM and GEV-PWM distributions, followed by the figure showing the points plotted by the Cunnane plotting position formula and the quantile functions of the LN3-PWM and GEV-PWM distributions in a Gumbel graph paper for one station in each basin are given in Figures 2, 3, 4, 5, 6, 7, 8, 9, 10, 11, respectively.

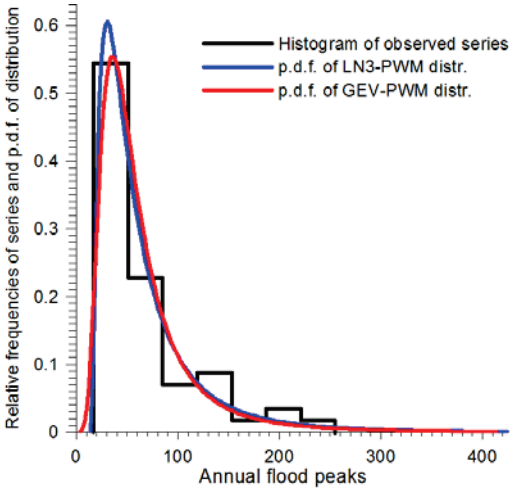

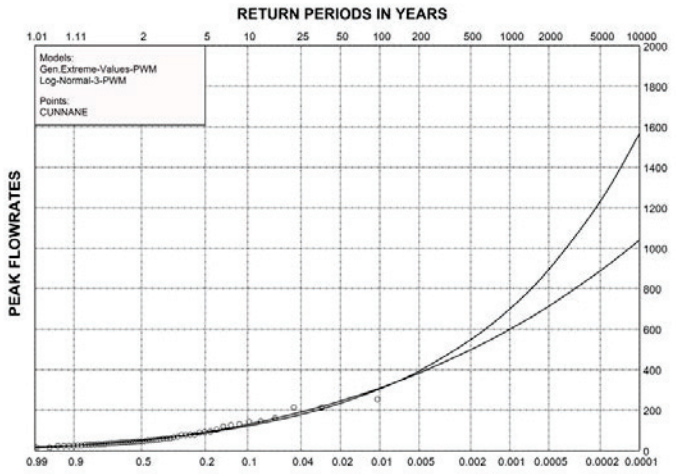

Figure 2 **Figure 3**

Figure 2. Histogram of the observed series of AFPs measured at stream-gauging station 1237–Dokurcun in Basin #12 (Sakarya Basin) along with the probability density functions of LN3-PWM (chosen) and GEV-PWM distributions.

Figure 3. Elements of the observed series of AFPs measured at stream-gauging station 1237–Dokurcun in Basin #12 (Sakarya Basin) marked by the Cunnane plotting position formula along with the curves of the quantile functions of the LN3-PWM (chosen) and GEV-PWM distributions.

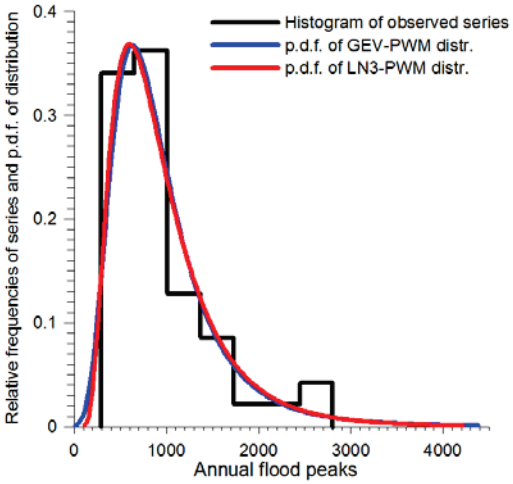

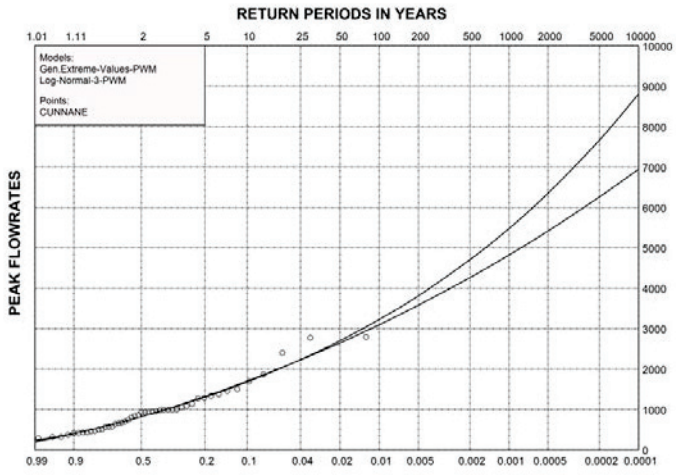

Figure 4 **Figure 5**

Figure 4. Histogram of the observed series of annual flood peaks measured at stream-gauging station 1335–Derecik in Basin #13 (West Black Sea Basin) along with the probability density functions of LN3-PWM and GEV-PWM (chosen) distributions

Figure 5. Elements of the observed series of AFPs measured at stream-gauging station 1335–Derecik in Basin #13 (West Black Sea Basin) marked by the Cunnane plotting position formula along with the curves of the quantile functions of the LN3-PWM (chosen) and GEV-PWM distributions.

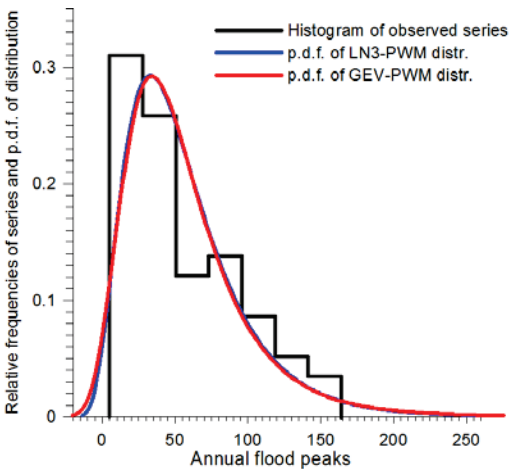

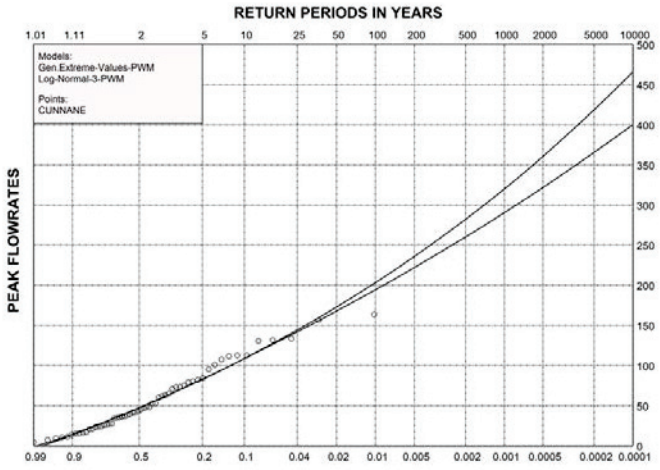

Figure 6 **Figure 7**

Figure 6. Histogram of the observed series of annual flood peaks measured at stream-gauging station 1412–Şeyhoğlu in Basin #14 (Yeşilırmak Basin) along with the probability density functions of LN3-PWM (chosen) and GEV-PWM distributions

Figure 7. Elements of the observed series of AFPs measured at stream-gauging station 1412–Şeyhoğlu in Basin #14 (Yeşilırmak Basin) marked by the Cunnane plotting position formula along with the curves of the quantile functions of the LN3-PWM (chosen) and GEV-PWM distributions.

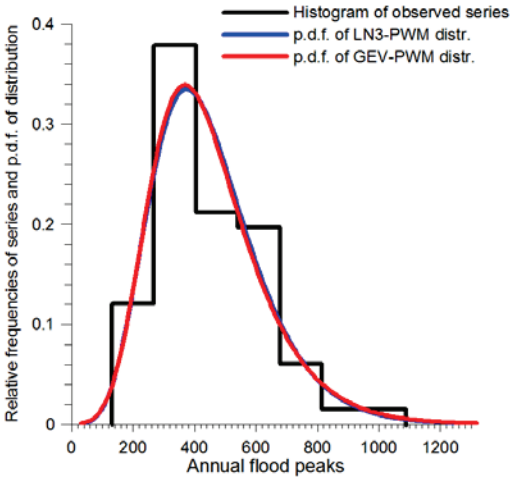

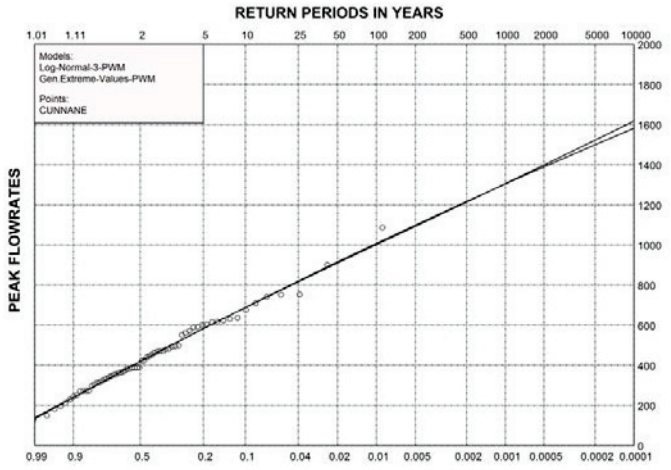

Figure 8 **Figure 9**

Figure 8. Histogram of the observed series of annual flood peaks measured at stream-gauging station 1501–Yamula in Basin #15 (Kızılırmak Basin) along with the probability density functions of LN3-PWM (chosen) and GEV-PWM distributions

Figure 9. Elements of the observed series of AFPs measured at stream-gauging station 1501–Yamula in Basin #15 (Kızılırmak Basin) marked by the Cunnane plotting position formula along with the curves of the quantile functions of the LN3-PWM (chosen) and GEV-PWM distributions.

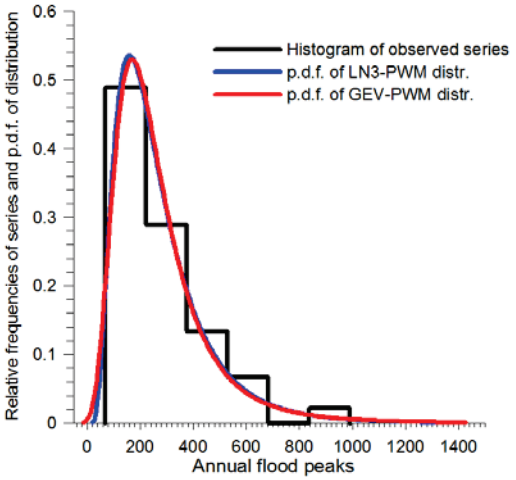

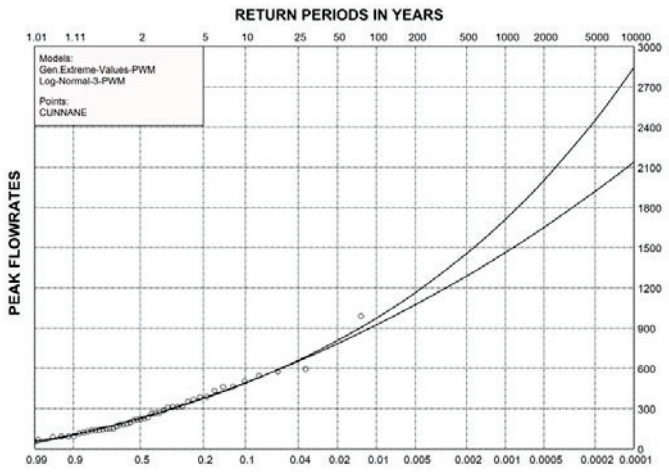

Figure 10 **Figure 11**

Figure 10. Histogram of the observed series of annual flood peaks measured at stream-gauging station 2245–Gökçeli in Basin #22 (East Black Sea Basin) along with the probability density function s of LN3-PWM (chosen) and GEV-PWM distributions

Figure 11. Elements of the observed series of AFPs measured at stream-gauging station 2245–Gökçeli in Basin #22 (East Black Sea Basin) marked by the Cunnane plotting position formula along with the curves of the quantile functions of the LN3-PWM (chosen) and GEV-PWM distributions.

CONCLUSIONS

Based on (1) Chi-square and (2) probability-plot correlation coefficient goodness-of-fit tests, (3) visual inspections of the histograms together with the probability density functions, and (4) visual inspections of the frequency curves together with elements of the observed series marked by the Cunnane plotting position formula, the probability distribution models of the Generalized Maximum Values and the 3-Parameter Log-Normal whose parameters are computed by the method of probability-weighted moments (GEV-PWM and LN3-PWM) are deemed most suitable for the observed series of annual flood peaks with record lengths in the range of 31 to 74 years with an average length of 49 years on 43 natural streams having no dams at upstream parts in five major basins discharging to the Black Sea. Either one of these two models can be chosen as the best because mostly they yield close values for the flood peaks over the range of average return periods from 1.11 to 10,000 years.

REFERENCES

Açanal, N. and Haktanır, T., 1999."Five stage flood routing for gated reservoirs by grouping floods into five different categories according to their return periods". Hydrological Sciences Journal, vol. 44(2), pp. 163–172.

Adeloye, A.J. and Montaseri, M., 2002."Preliminary streamflow data analyses prior to water resources planning study". Hydrological Sciences Journal, vol. 47(5), pp. 679-692.

DSİ, 1935 – 2014..... Year Book of Gauged Stream Flows (In Turkish). General Directorate of State Water Works (DSI), Department of Investigation, Planning, and Allocations, Yucetepe, Ankara, Turkey.

Filliben, J.J., 1975."The probability plot correlation test for normality". Technometrics, vol. 17(1), pp. 111-117.

Ghorbani, M. A., Ruskeepaa, H., Singh, V. P., Sivakumar, B., 2010."Flood frequency analysis using Mathematica". Turkish Journal of Engineering and Environmental Sciences, vol. 34, pp. 171–188.

Haktanır, T., 1992."Comparison of various flood frequency distributions using annual flood peaks data of rivers in Anatolia". Journal of Hydrology, vol. 136(1-4), pp. 1-31.

Haktanır, T., Çıtakoğlu, H., Çobaner, M., 2013."Estimation of return periods of peak flowrates of the probable maximum floods of three dams by frequency analysis" (in Turkish)National Symposium on Floods and Land Slides, 24–26 October 2013, Trabzon, Turkish Chamber of Civil Engineers, Karadeniz Technical University, Proceedings, pp. 521–532.

Rao, A.R. and Hamed, H.H., 2000.Flood Frequency Analysis. CRC Pres, LLC, 2000 N.W., Corporate Blvd., Boca Raton, FA 33431, USA.

Seçkin, N., Yurtal, R., Haktanır, T., Doğan, A., 2010."Comparison of probability weighted moments and maximum likelihood methods used in flood frequency analysis for Ceyhan River Basin". The Arabian Journal for Science and Engineering, vol. 35(1B), pp. 49–69.

5th International Symposium on Dam Safety

October 27-31, 2018

COMPARISON OF 2D HYDRAULIC MODELS FOR FLOOD SIMULATION ON THE MERT RIVER TURKEY

Neslihan BEDEN [1], Vahdettin DEMİR[2], Hesham ALRAYESS [3], Aslı ÜLKE KESKİN[4]

ABSTRACT

As well as all over the world, Turkey exposures to floods more frequently as a result of climate change. The study area, Mert River is located in Samsun city north of Turkey and also frequently exposed to floods and flood management studies in the region are carried out in progress by local administrations. The aim of this study is to compare different hydraulic modeling methods on Mert River, mainly related to floodplain modeling. Therefore, different hydraulic models have been applied to the Mert River. Two types of 2D models are examined in this paper, these are respectively MIKE 21 and FLO-2D. In this study a comparison of the simulation results of models are performed. By these comparisons, the benefits and limitations of the models in flood forecasting are trying to show. The analysis of the results shows that there is a consistency between different 2D models and that the reliability of the results strongly depends on the sufficiency of the available data.

Keywords: Flood modeling, MIKE 21, FLO-2D.

INTRODUCTION

Flood disasters are the most important natural disaster succeeding the earthquakes. extreme precipitation, heavy populated areas, industrialization, unplanned urbanization along the river banks, debris fan, intense deposits on the river bed, rapid urbanization are the main causes of the floods. Also, it is expected that climate change will exasperate and accelerate the hydrological cycle. Thus, magnitude and frequency of future floods can increase (Kvocka et al., 2015). However, unplanned urbanization and failures in disaster management are main factors that turn floods into disasters. In order to minimize flood damage, analysis of the floods with various frequencies and determination of the inundated areas be carried out. Floods are not completely preventable, but if the flood-prone areas are known in advance, most of the damage can be reduced. Therefore, in order to reduce the loss of life and property in floods, it is necessary to estimate the water levels of river cross-sections for expected floods in urbanized areas (Sahoo and Sreeja, 2015). Also, the estimation of the flood inundation locations is very essential for development of insurance maps of risk assessments and effective management plans for reducing future flood risk.

[1] Lecturer, Department of Construction, Kavak Vocational School, Samsun University, Samsun, Turkey, e-posta: neslihan.beden@omu.edu.tr
[2] Research assıstant, Department of Civil Engineering, KTO Karatay University, Konya, Turkey, e-posta: vahdettin.demir@karatay.edu.tr
[3] PhD researcher, Department of Civil Engineering, Ondokuz Mayis University, Samsun, Turkey, e-posta: hesham.majed@hotmail.com
[4] Assistant Professor, Department of Civil Engineering, Ondokuz Mayis University, Samsun, Turkey, e-posta: asli.ulke@omu.edu.tr

Flood inundation mapping and identifying the flood risk zones are primary steps for formulating any flood management strategy (Patel et al., 2017). Understanding the effects of flood inundation in terms of area, depth and time is mandatory for efficient flood risk management. 1D modeling approaches could be useful mainly for artificial channels however it has limitations for overflow analysis (Srinivas et al., 2009). In situations such as overflowing of water from the channels, 1D models become meaningless. Then it becomes a 2D phenomenon and the use of a 2D model is more suitable. Also, model type selection in flood modeling depends on many aspects. These aspects are mainly the catchment area and both spatial and temporal data availability.

In this study, Mert river floods are modeled by using 2D numerical models. There are many studies in the literature comparing various flood models. Hunter et al. (2008) described benchmark testing of six two dimensional (2D) hydraulic models (DIVAST, DIVASTTVD, TUFLOW, JFLOW, TRENT and LISFLOOD-FP) in terms of their ability to simulate surface flows in a densely urbanized area in their study. Banks et al. (2014) presented a review of currently available flood damage assessment tools and their abilities. Crispino et al. (2015) discussed a comprehensive comparison between 1D and 2D modelling of floods in meandering channels, to guide practitioners in the confident choice of a tradeoff between complexity and accuracy.

Tools that model flood inundation and perform damage assessment have historically been directed at planning for disaster response or developing flood insurance rate maps (Flo-2D Software, 2012; FEMA, 2008, Banks et al., 2014).

The comparison of 2D hydraulic models for simulating flash floods over the Mert River is the aim of this study. For this purpose, the dynamic behavior of Mert River in Turkey was modelled by using numerical analysis of advanced modelling tools; MIKE 21 FM and FLO-2D. Hydraulic modelling consists in simulating the river flows. The two-dimensional modelling includes a significant improvement in calculating hydraulic variables and also the delineation of flood zones.

CASE STUDY AREA AND DATA USED

Mert River (41.279 latitude and longitude: 36.352 coordinates) located in the district of Samsun Canik and Ilkadim and to the Middle Black Sea was selected. Figure 1 shows the study area. The Mert River has an important place in terms of drinking and irrigation water provided to Samsun through its history. This river has a total of six bridges, including a 5-divided road bridge and a pedestrian bridge. The first, second and third bridges of the Mert River are located on the coast of the Black Sea and are used for intercity road transportation. The fourth and fifth bridges are built on the Mert River and are used for road transport between Canik and Ilkadım districts (Demir, 2015). Mert river has a 740 km^2 precipitation area. The selected watershed maximum precipitation is 70.8 mm in November, the minimum precipitation is 29.4 mm in August, and the annual average precipitation is 674.8 mm. Flow discharges for different return period floods are obtained from State Hydraulic Works Samsun Office and given in Table 1. Manning roughness coefficients are obtained with field surveys. Values of 0.022, 0.026, 0.045, 0.030 were used for concrete, bush-wooded and woodland for river banks respectively and 0.03 for the river bed (Chow, 1959). 1/1000 scale topographic map which improved with field surveys has digitized and used in this study as a base map.

Mert river flooding occurred on 3 July 2012. This is preferred because it is a high level of loss of life and property. Mert river was chosen as the study area because of the flood disasters that happened in the past. In 4.7.2012, an extreme flood disaster occurred in Mert river (Figure 2). With this event, especially the industrial zone took a severe economic damage and 10 people lost their lives as a result of the inundated basements. Discharge of flood was measured 570 m^3/s by State Hydraulic Works in 04.07.2012. Flood models are calibrated with 2012 flood event discharge value and watermarks at the study area.

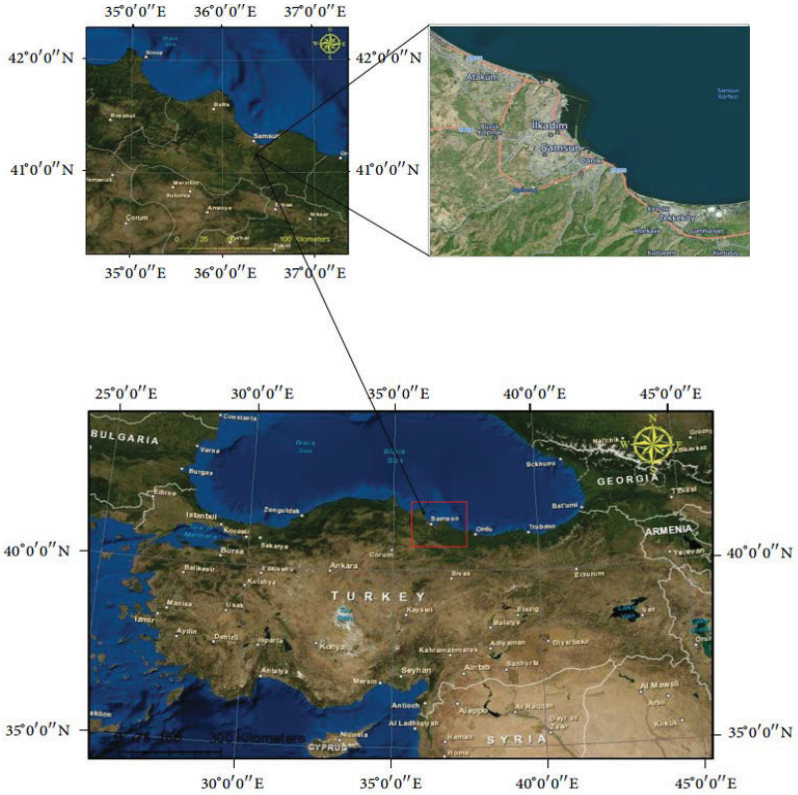

Figure 1. Study area, Google-Earth Images

Table 1. Flood values of different return periods of Mert River.

Return Periods	5	10	25	50	100	500	1000	10000
Discharge (m^3/s)	440.2	522.3	719.4	863.9	1029.1	1453.3	1722.4	2660.0

Figure 2. 2012 Mert river flood

FLOOD MODELING

Two-dimensional flood inundation models have become an integral part of flood risk assessment in both urban and rural areas, providing a means of converting catchment discharge into inundation extent, depth and in some cases flow velocity. These models vary in complexity from solutions of the two-dimensional shallow water equations to storage cell models based on Manning's equation (Neal et al., 2010).

MIKE 21 FM

MIKE 21 Flow Model FM is a two-dimensional modeling system which based on a flexible mesh approach. Model is suitable for free surface flows. MIKE 21 has a basic computational component Hydrodynamic Module. The Hydrodynamic Module is based on the numerical solution of the two-dimensional shallow water equations -the depth- integrated incompressible Reynolds-averaged Navier-Stokes equations. Thus, the model consists of continuity, momentum, temperature, salinity and density equations. In the horizontal domain, both Cartesian and spherical coordinates can be used. However, being a general modeling system for 2D and 3D free surface flows it may also be applied for studies of inland surface waters, e.g. overland flooding and lakes or reservoirs (DHI, 2016; Ulke et al., 2017). In base of MIKE 21 HD, continuity equation write as follows;

$$\frac{\partial s}{\partial t} + \frac{\partial}{\partial x}Uh + \frac{\partial}{\partial x}Vh = F_s \tag{1}$$

$$\frac{\partial s}{\partial t} + U\frac{\partial U}{\partial x} + V\frac{\partial U}{\partial y} + g\partial_x s + \frac{g}{C^2 d}U\sqrt{U^2+V^2} + \frac{\partial}{\partial x}\left(K_{xx}\frac{\partial U}{\partial x}\right) + \frac{\partial}{\partial y}\left(K_{yy}\frac{\partial U}{\partial y}\right) = F_s \tag{2}$$

$$\frac{\partial s}{\partial t} + U\frac{\partial V}{\partial x} + V\frac{\partial V}{\partial y} + \frac{\partial s}{\partial x} + \frac{g}{C^2 d}V\sqrt{U^2+V^2} + \frac{\partial}{\partial x}\left(K_{xx}\frac{\partial V}{\partial x}\right) + \frac{\partial}{\partial y}\left(K_{yy}\frac{\partial V}{\partial y}\right) = F_s V_s \tag{3}$$

In Equations 1-2 and 3 definitions are; s: height, h: water level, U and V are the notations of the depth averaged velocity components of Cartesian, C: the Chezy component, Kxx and Kyy: the eddy viscosity, F: source term, and Vs and Us: the velocity components at the source. The program has a toolbox for flood damage assessment that integrates with ArcGIS, which can calculate damage per unit area in any specified currency. However, the user must supply specific depth–damage estimates for various land uses (Banks et al., 2014). Training is available for both urban and river applications of MIKE powered by DHI softwares. Each course costing €1,050 (DHI, 2018). MIKE Flood license fees begin at $18,500 (Banks et al., 2014).

FLO-2D

FLO-2D is one of the package programs produced and developed by O'Brien for 2D hydraulic models. FLO-2D is widely used in flood models made in recent years. The program models the flow of water depending on time (O'Brien, 2006). FLO-2D, a commercial software, is a program that simulates the flow of sludge and rubble with finite difference methods based on second-order rheological conditions. FLO-2D is a finite volume model, including Herschel-Bulkley (HB) rheology, which represents a viscous fluid. This rheological model can model the rubble flow of muddy type with sufficient clay content (Hsu et al., 2010). FLO-2D is a dynamic flood-displacing model that can simulate river and surface flows. The model solves the full dynamic wave momentum and continuity equations (Equation 4-8) for square grid elements using the finite difference method. Thus, the two-dimensional propagation of the flood wave in the grid elements system is calculated (Elci et al., 2017).

$$\frac{\partial U}{\partial t} + \frac{\partial F}{\partial x} + \frac{\partial G}{\partial y} = S \tag{4}$$

$$U = \begin{bmatrix} h \\ h_u \\ h_y \end{bmatrix} \tag{5}$$

$$F = \begin{bmatrix} h \\ h_{uu} \\ h_{uv} \end{bmatrix} \tag{6}$$

$$G = \begin{bmatrix} h \\ h_{uv} \\ h_{vv} \end{bmatrix} \tag{7}$$

$$S = \begin{bmatrix} 0 \\ -gh\frac{\partial Z}{\partial x} - g\frac{n^2 u\sqrt{u^2+v^2}}{\frac{1}{h^3}} \\ -gh\frac{\partial Z}{\partial y} - g\frac{n^2 v\sqrt{u^2+v^2}}{\frac{1}{h^3}} \end{bmatrix} \tag{8}$$

In Equations 4-8 definitions are; h: flow depth; u: velocity x direction; v: velocity y direction; g: acceleration; Z: water surface elevation, n: Manning roughness coefficient. (Tayfur, 2017; Ying et al., 2009). The single-user license price of the program is at $3495. Also, RiverFlo-2D is capable for hydrodynamic modeling of river and can be purchased for $3950. FLO-2D has online courses which has a cost that ranging from $50 to $200. Course prices depends on to the course duration, location, and course type. (Banks et al., 2014).

RESULTS

The results of both MIKE 21 and FLO-2D models are given side by side in Figure 3-5 for Q100, Q500 and Q1000 respectively.

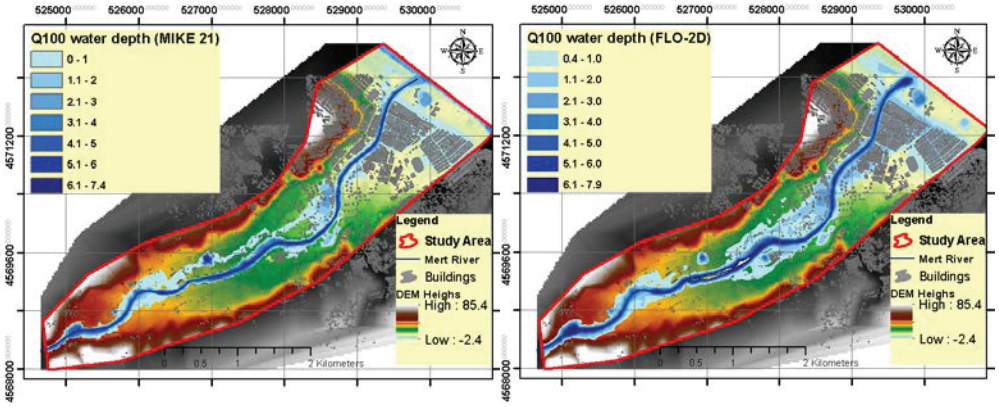

Figure 3. Water depth results for Q100 for MIKE 21 and FLO-2D

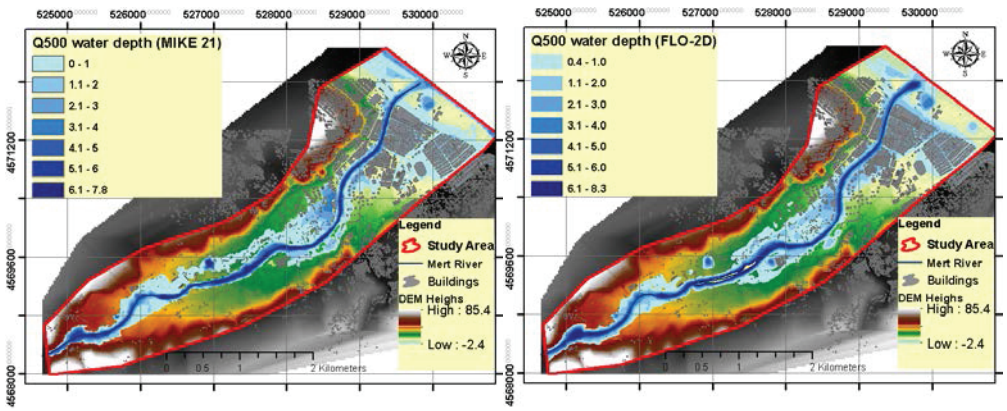

Figure 4. Water depth results for Q500 for MIKE 21 and FLO-2D

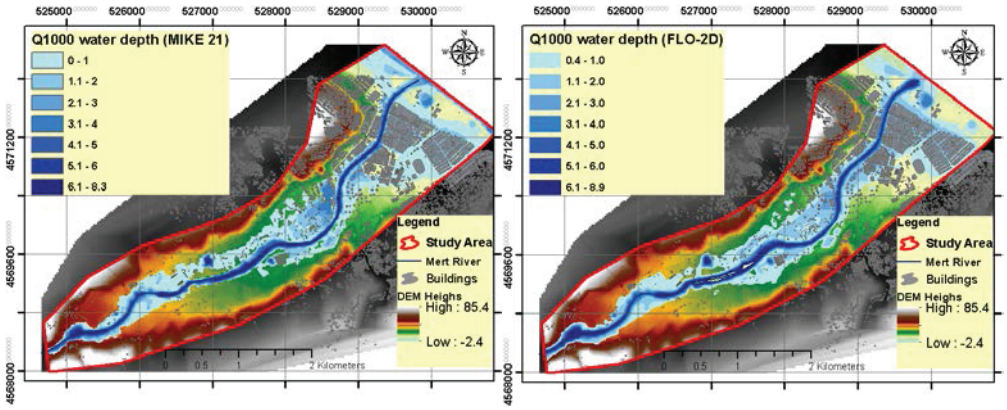

Figure 5. Water depth results for Q1000 for MIKE 21 and FLO-2D

The water depths and DEM (digital elevation model) are in meters. According to the results, the propagation areas are similar. There is a small difference between MIKE 21 and FLO-2D water depth results. Authors have used same boundary conditions in modeling phase which were flood hydrographs, base map, bed resistance, study area boundaries and initial conditions. In Figure 6 flood propagation areas of MIKE 21 and FLO-2D results are shown with superpositioning respectively. Information on flood exposed areas is given on the Table 2.

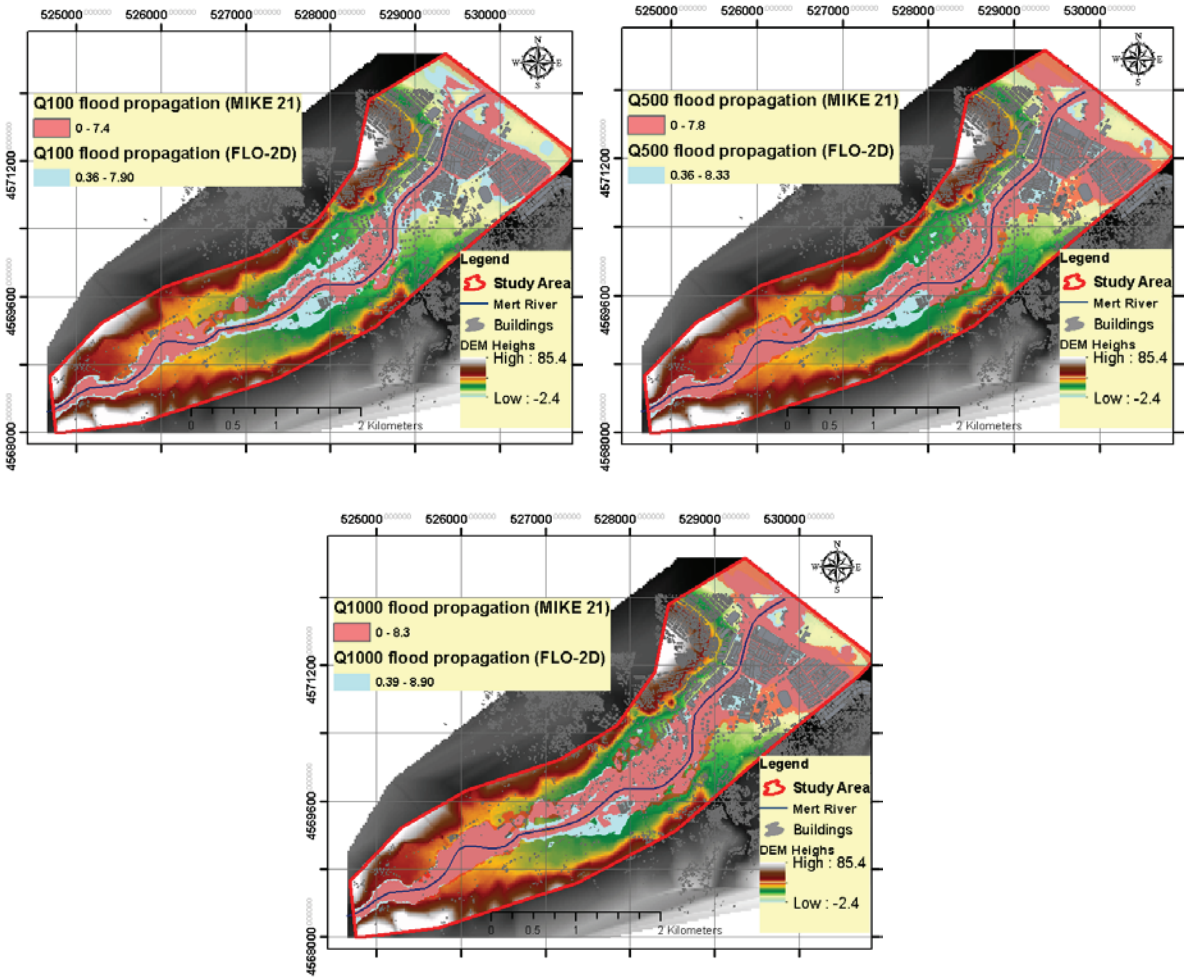

Figure 6. Flood propagation comparisons of MIKE 21 and FLO-2D results

Table 2. Flood propagation areas (km^2)

	Q100	Q500	Q1000
MIKE 21	2.75	3.10	3.50
FLO-2D	2.81	3.26	3.67

The FLO-2D propagation areas of Q100, Q500 and Q1000 discharges are 2.1%, 5.2%, and 4.8% higher than that of MIKE 21, respectively. At water depths, there is about a 0.5 m difference between the two model results.

CONCLUSION

Numerous models have been developed for numerical analysis of floods. A major part of them is the computer software which is widely used in literature. In this study Mert river which were exposed to floods frequently was selected as study area. Q100, Q500 and Q1000 discharges are modeled by two different flood model; MIKE 21 and FLO-2D. According to the results it is expected that future floods will suffer great damage to the study area. The obtained results are sufficient for this study however results have some differences. According to the authors, these differences may originate from the different mesh approaches of the selected models. Studies on this subject are underway. This paper is a part of a study which is developing by authors with more specific manner.

ACKNOWLEDGMENT

The authors would like to thank the State Hydraulic Works Samsun Office for obtaining data and also DHI Turkey Office for the provision of the MIKE powered by DHI software.

REFERENCES

Banks, J.C., Camp, J.V. & Abkowitz, M.D., 2014. Adaptation planning for floods: a review of available tools. Natural Hazards, Vol. 70, Issue 2, 1327–1337.

Chow, V.T., 1959, Open-channel hydraulics: New York, McGraw-Hill, 680 p.

Crispino, G., Gisonni, C., Michele Iervolino, M., 2015. Flood hazard assessment: comparison of 1D and 2D hydraulic models. International Journal of River Basin Management, Vol.13, Issue 2, 153-166.

Demir, V., 2015. Mert Irmagi (Samsun) Taskin Haritalarinin Cografi Bilgi Sistemleri Yardimiyla Belirlenmesi. Ondokuz Mayis University, Master Thesis (In Turkish) Graduate School of Sciences, 110 pages.

DHI (Danish Hydraulic Institute), 2016. MIKE 21 Flow model FM, hydrodynamic module Reference Manual.

DHI (Danish Hydraulic Institute), 2018. Course schedule 2018; https://www.dhigroup.com/upload/publications/course-calendar/DK_2018_CourseDescription_MIKE21FlowModelFM_HydrodynamicModellingUsingFlexibleMesh_UK.pdf?_ga=2.60871020.1755804274.1534840640-2040704720.1522075546 Accessed 21.08.2018.

Elçi, Ş., Tayfur, G., Haltas, I., ve Kocaman, B., 2017. Baraj Yıkılması Sonrası İki Boyutlu Taşkın Yayılımının Yerleşim Bölgeleri İçin Modellenmesi. Teknik Dergi, 7955–7976.

FEMA (2008) HAZUS user group success story: using HAZUS for flood loss estimates and CRS flood mitigation planning.

Flo-2D Software I, 2012. Flo-2D: technical papers. https://www.flo-2d.com/flo-2d-pro/. Accessed 21.08.2018

Hsu, S.M., Chiou, L.B., Lin, G.F., Chao, C.H., Wen, H.Y., and Ku, C.Y., 2010. Applications of simulation technique on debris-flow hazard zone delineation: A case study in Hualien County, Taiwan. Natural Hazards and Earth System Science, Vol. 10, Issue 3, 535–545.

Hunter, N.M., Bates, P.D., Neelz, S., Pender, G., Villanueva, F.I., Wright, N.G., Liang, D., Falconer, R.A., Lin, F.B., Waller, S., Crossley, A.J., Mason, D.C., 2008. Benchmarking 2D hydraulic models for urban flood simulations. Proceedings of the Institution of Civil Engineers: Water Management, vol. 161, N.1, 13-30, ISSN 1741-7589.

Kvocka, D., Falconer, R.A., Bray, M., 2015. Appropriate model use for predicting elevations and inundation extent for extreme flood events. Nat Hazards Vol. 79, 1791–1808.

Neal, J.C., Fevtrell, T.J., Bates, P.D. and Wright, N.G., 2010. A comparison of three parallelisation methods for 2D flood inundation models. Environmental Modeling & Software, Vol. 25, Issue 4, 398-411.

O'Brien., 2006. FLO-2D user's manual, Version 2006.01. FLO Engineering, Nutrioso.

Patel, D.P., Ramirez, J.A., Srivastava, P.K., Bray, M., Han. D., 2017. Assessment of flood inundation mapping of Surat city by coupled 1D/2D hydrodynamic modeling: a case application of the new HEC-RAS 5. Nat Hazards, Vol. 89, 93-130.

Sahoo. S.N., Sreeja. P., 2015. Development of Flood Inundation Maps and quantification of flood risk in an Urban catchment of Brahmaputra River. ASCE-ASME J Risk Uncertain Eng Syst Part A Civil Eng, Vol. 3, A4015001.

Srinivas. K., Werner. M., Wright. N., 2009. Comparing forecast skill of inundation models of differing complexity: the case of Upton upon Severn. Taylor & Francis Group, London

Tayfur, Gökmen. 2017. "Baraj Yıkılma Sonucu Meydana Gelen Taşkın Dalgası Simülasyonu Gerçekleştirme Aşamaları." Su vakfı, Su külliyesi 5:1–15 (In Turkish).

Ulke A., Beden, N., Demir, V., and Menek, N., 2017. Numerical modeling of Samsun Mert River floods, European Water 57: 27-34

Ying, Xinya, Jeff Jorgeson, and Sam S. Y. Wang. 2009. "Modeling Dam-Break Flows Using Finite Volume Method on Unstructured Grid." Engineering Applications of Computational Fluid Mechanics 3(2):184–94.

5th International Symposium on Dam Safety

October 27-31, 2018

SEDIMENT YIELD OF ANKARA-NALLIHAN- BOZYAKA RESERVOIR BASIN

Oğuz DEMİRKIRAN[1] Suat AKGÜL[1] Yakup KÖŞKER[1] Oğuz BAŞKAN[1]

ABSTACT

Assessment of basin sediment yield has great importance for the studies on planning and managing soil and water resources. This study was carried out between 2006 and 2011 in Ankara - Haymana - Nallıhan - Bozyaka Reservoir Basin, which has 22.51 km^2 basin area, in order to determine the sediment yield in the basins. As a result of bathymetric studies carried out in two different years in the reservoir at the basin exit, the amount of sediment accumulated in the reservoir was calculated and the sediment yield of the basin was determined as 7.41 tons ha $year^{-1}$.

From the empirical methods, using USLE, the maximum amount of soil loss of the basin was calculated to 108,308 tons $year^{-1}$. Some of the sediment delivery ratio equations in the literature have been applied and the best result in the basin has been Boyce method with 7.76 tons ha $year^{-1}$.

Key Words: Bathymetry, Sediment yield, USLE, Sediment delivery ratio, Bozyaka, Reservoir

INTRODUCTION

The leading factor causing decrease in the storing volume of water storage structures is the amount of sediment from the basin transported by water. It is important to continue to carry out research studies aiming at the determination of sediment yield from basins especially during those periods when extrem rainfall events are frequent due to climate change.

During the projecting stage of water structures, dead volume calculation are being made to determine their economical lives. In the determination of the dead volumes, it is necessary to make a realistic estimation for the sediment amount that will reach to reservoir from the basin. In the determination of the sediment amount, empirical methods were widely used up to nowadays (Çelik, 1994). Among these methods, Gross Erosion Ratio Method is the most widely used method in Turkey. On the other hand, there are other methods that are used worldwide. Universal Soil Loss Equation is one of these methods and it determines the soil loss as a function of soil type, plant cover, topography and precipitation in the basin (USDA, 1978).

Despite these methods, measurement is the most accurate method for the determination of the sediment yield from a basin. The measurements are made via sampling from the rivers and the amount of sediment transported is determined by using the sediment rating curves. On the other hand, for the catchments where reservoir constructions were completed, sediment yield calculations are made through bathymetric measurements. Through bathymetric measurements, it is possible to determine the sediment fill ratio of the reservoir, the sediment amount accumulated in the reservoir as of years, the capacity loss of the reservoir and the remaining economical life of the reservoir. The direct measurement of the sediment yield gives us opportunity to make comparisons with empirical methods and thus will facilitate to determine the most suitable empirical method and the correction coefficients to be used in basins where direct measurements are not made.

In this study, it was aimed to determine the amount of sediment accumulated in Bozyaka dam located within the boundary of Nallıhan county of Ankara province as of m3 year-1, ton year-1 and ton ha-1year-1.It was also aimed to find out the relationship between the sediment accumulated in the dam and the sediment amount determined through empirical methods and thus investigate the possibility of using these empirical methods in similar basins.

[1] Toprak Gübre ve Su Kaynakları Merkez Araştırma Enstitüsü Müdürlüğü – Ankara - TÜRKİYE
oguz.demirkiran@tarim.gov.tr, yakup.kosker@tarim.gov.tr, suat.akgul@tarim.gov.tr, oguz.baskan@tarim.gov.tr

MATERIAL and METHOD

Material

Location of the Basin

The dam, where small portion of its basin is in the boundary of Bolu province, is located in Nallıhan county and 5 km at the northeast of Bozyaka village. The distance between the dam and the Soil Fertilizer and Water Resources Central Research Institute is about 180 km.

The basin area of the dam is 22.510 km^2 and crest coordinate values as of is 3 64 206 East, 44 61 512 North.

Topographic and Drainage Characteristics of the Basin

The elevation distribution map of Bozyaka basin was prepared using Digital Elevation Model (Figure 2.1). As can be seen from the figure, the direction of the basin is towards West. The basin relief was found as 510 m which is calculated from the minimum and maximum elevations of the basin. The slope of the basin, where terrestrial elevation differences are frequent, was calculated as 19.9%.

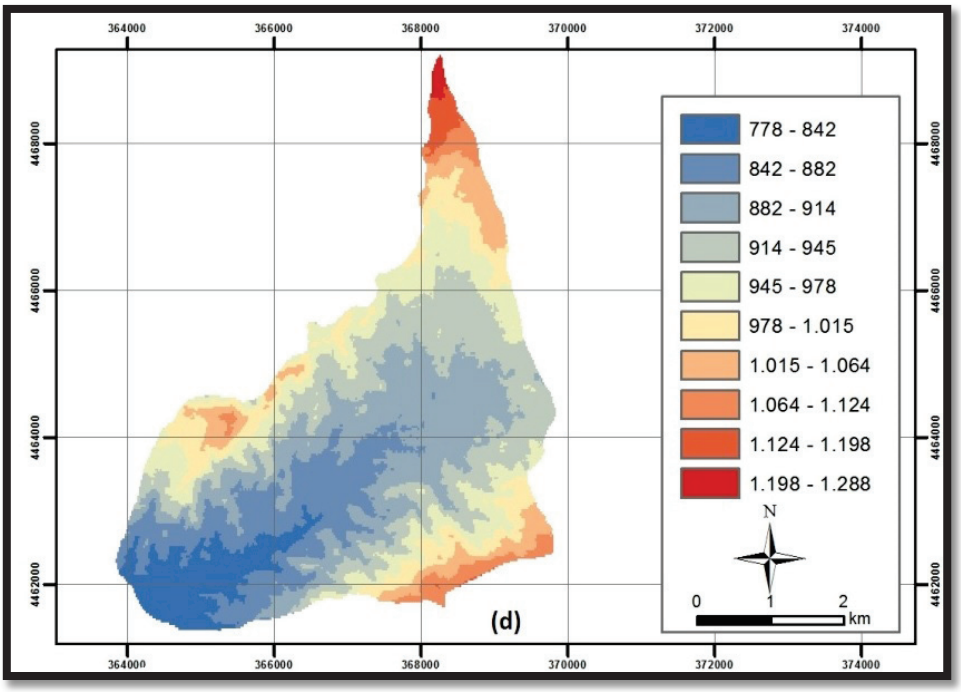

Figure 2.1. Elevation Map of Bozyaka Basin

The Area-Elevation values calculated from the topographic map of Bozyaka Dam Basin was given in Figure 2.2. About 88% of basin area is located between 778-1000 m elevations, and the remaining 12% of the basin area is located between 1000-1288 m elevations.

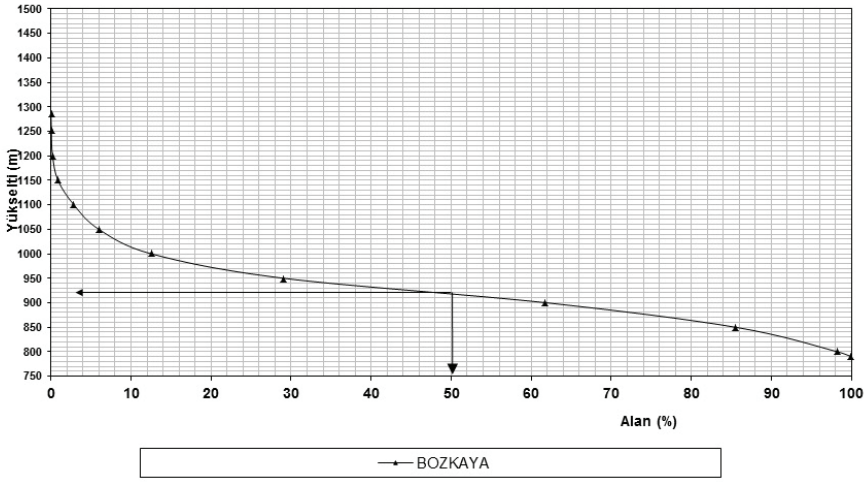

Figure 2.2 Area-Elevation Curve of Bozyaka Basin

Some of the other topographic and drainage parameters of the study basin were calculated and given in Table 2.1.

Table 2.1. Some characteristics of the basin

		Bozyaka Basin
Basin Topographic Characteristics		
1.	Havza Area (km^2)	22.51
2.	Perimeter (km)	23.44
3.	Minimum Elevation (m)	778
4.	Maximum Elevation (m)	1288
5.	Basin Relief (m)	510
6.	Basin Direction	East
7.	Average Elevation of the Basin (m)	1038
8.	Average Slope of the Basin (%)	19.9
Drainage Characteristics		
1.	The Length of Main Waterways (km)	9.7
2.	Total Length of Waterways (km)	37.7
3.	Main Waterway Profile Slope (%)	2.61
4.	Drainage Density (m/km^2)	1674.81
5.	Water Ways Frequency	1.199

Soil Characteristics and Plant Cover of the Basin

Almost the whole basin (96.45%) is covered by Brown Forest Soils formed on parent material which is rich of lime. Profiles are in the form of A(B)C and the horizons interpenetrate to each other gradually. Horizon A is well apparent due to being well developed. It is dark brown and crumbly. It has a porous or granular structure. Below the horizon CaCO3 is found. Brown Forest Soils are generally formed under wide leaved forest cover. The effective soil formation processes in these soils are calsification and podzolization. These soils have a good drainage capacity. About 3.55% of the basin area is covered by Alluvial Soils.

The biggest land use class in Bozyaka dam basin is rainfed agricultural lands with 31,20%. This followed by vegetation transition areas (25,25%), sparsely vegetated areas (25,02%), coniferous forest lands (9,00%) and natural grasslands (6,98%).

Method

The calculation of sediment accumulation from volume difference

The main objective in this method is to determine the amount of sediment accumulated in the dam within two time intervals following each other. For that reason, the active volume for a certain water level of the dam is determined within 5-year interval, and the sediment accumulation is calculated through the reduction in the active volume. In the bathymetric measurements echo-sounder (z value), laser positioning system (depiction of x,y value during the 1. measurement), GPS (depiction of x,y value during the 2. measurement) and a labtop computer were used. During the bathymetric measurements, elevation (z) and coordinate values (x, y) were gathered in the computer simultaneously. The coordinate and depth values gathered (x,y,z) were evaluated in Surfer^{tm} Software and a value for each point of the dam base was produced. Linear Triangulation Method was used in producing these values.

The same methods were employed during the second measurements, and active water volumes were calculated. The decrease in the active water volumes between the two time intervals gave us the amount of sediment in m3 accumulated in the dam. In order to define this amount in tons, the average bulk density of the sediment was taken as 1.50 gr cm-3 (Özbek vd., 1995).

The Calculation of Sediment Amount with Universal Soil Loss Equation (USLE)

The annual potential soil loss in the study basin was calculated using Universal Soil Loss Equation developed by Wischmeier et al. (1971) to be used in agricultural lands.

Sediment delivery ratio

The equations given in Table 3 were used to determine the sediment yield taking into account the maximum soil loss. (Karaş et al., 2012).

The Calculation of sediment amount of the basin using EIEI Equation

A logarithmic correlation was found between the basin area and annual sediment yield as a result of the evaluations of the long years data (1966-1975) of the 56 stations countrywide belonging to the Former General Directorate of Electrical Power Resources Survey and Development (Sevinç, 1993). The Correlation coefficient is 0.87 and the relation is given in Equation 1.

$$Log\ Q_s = 0.97688 + 1.10309 \log A \qquad (1)$$

Qs: Annual Average Sediment Amount x 103, ton year-1
A: Drainage Area (km2)

RESULTS

The calculation of sediment accumulation from volume difference

The first measurements in Bozyaka Dam were made in 2006. At the date of measurement, the water level was determined as 60 cm below crest of spillway. During the bathymetric measuremets, coordinate and depth values at 50 666 points were gathered. The coordinates were depicted using laser positioning system. The measurements were made at random routes parallel to each other on the dam surface. According to the data, the deepest point at the date of measurement was at 789,9 m level. This shows us that the maximum depth of the dam as of 2006 was 10,7 m. The bathymetric map of the basin prepared as a result of evaluating the gathered data in Surfer Software was given in Figure 3.1.

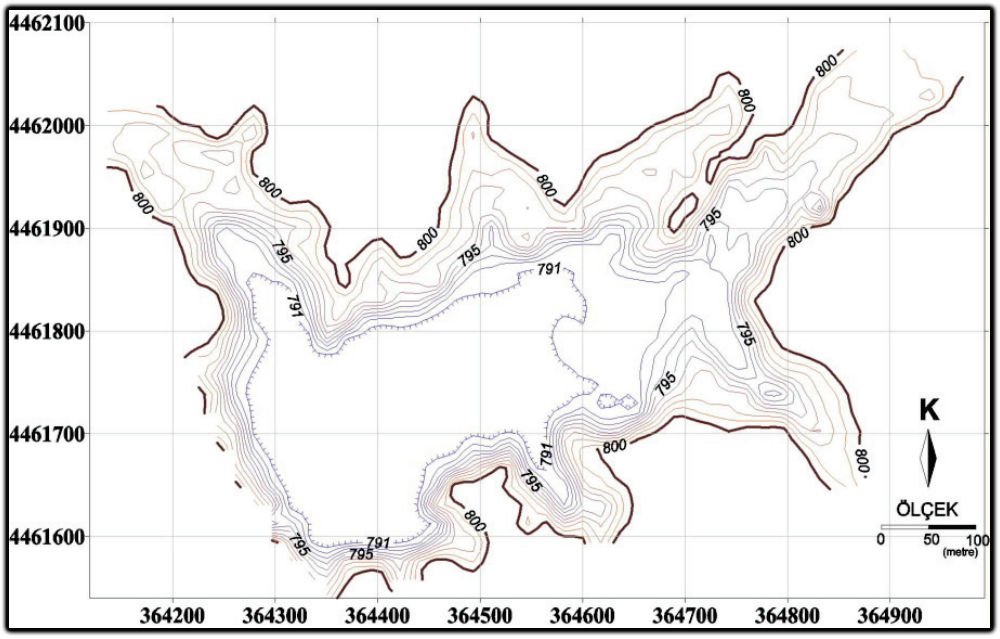

Figure 3.1 Bathymetric Map of Bozyaka Dam (2006)

The second measurements were made in 2011. The coordinates of the points which depth measurements were made were gathered using GPS. During the second measurements, the water level of the dam was determined as 797 m. In the bathymetric measurements, depth and coordinate values belonging to 8 850 points were gathered. As a result of evaluations, the depth recorded at deepest point was determined as 791,1 m. This showed us that the dam became 1,2 m shallow according to the first measurement. The base map of the dam and the cross-sections, which were prepared using depth and coordinate values at the dam base through Surfer Software, were given in Figure 3.2.

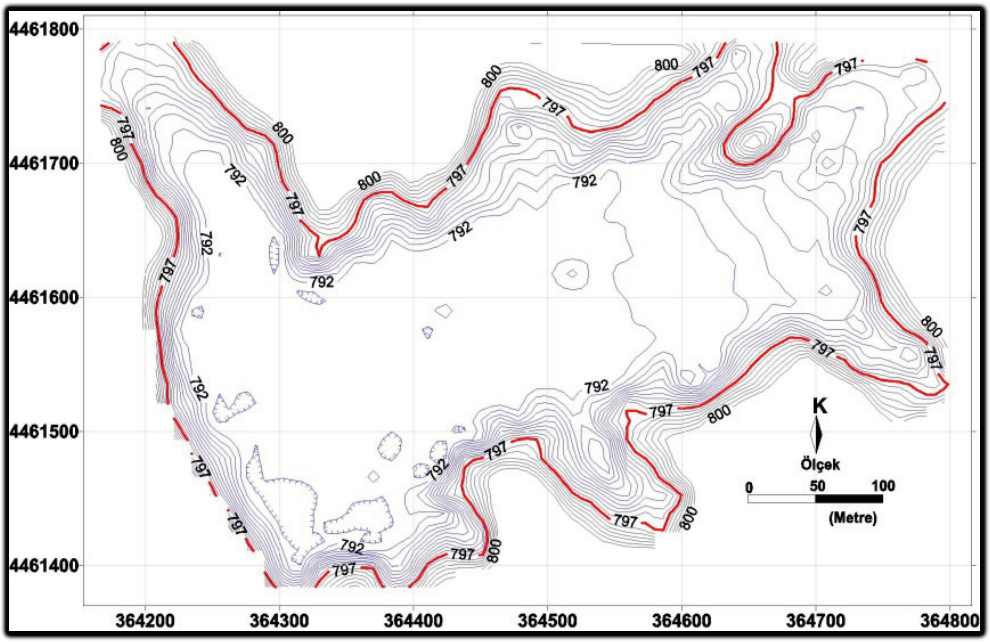

Figure 3.2 Bathymetric Map of Bozyaka Dam (2011)

As a result of using the bathymetric maps belonging to each period, fractional volumetric calculations were made. The calculations showed that 55 566 m3 sediment was accumulated on the dam base

during 5 years period. According to the bulk density of the sediment, this amount was determined as 83 349 tons. The annual amount was found as 16 670 tons.

The Calculation of Sediment Amount with Universal Soil Loss Equation (USLE)
The R (rainfall erosivity) value of Bozyaka Basin was taken from Erpul et al., 2009. The R value in megajoule/ha/year x mm/hour is 1534, and this is equal to 37,7 ton/ha/year x mm/hour. Only one R value was taken for the whole basin.

For the K (soil erodibility) value of Bozyaka basin, 50 soil samples from different points were taken and soil samples were analysed to determine their texture, organic matter content and hydraulic conductivity in the laboratory. These values have been put into the Wischmayer equation and the respective K values for each location were determined. Because the coordinates of these locations were known, the values were evaluated in Arc Map and K data layer for the catchment was prepared. The K values in the catchment have varied between 0,082 and 0,54. The LS 8topographic index) distribution map of Bozyaka basin was determined by using digital soil model (DEM). As a result of the evaluations, LS value for the basin has been found to vary between 0,00 and 10,26.

The C (cropping factor) layer of the basin has been determined using the land use classes in CORINE model. According to CORINE, 7 land use classes were determined for the basin. As a result of the evaluations, C valuse were found to vary between 0.001 and 0.4 in Bozyaka basin. The P (conservation practice factor) has been taken as 1 as there was no conservation practice taken in the basin.

As a result of evaluations using USLE map prepared for Bozyaka basin, the soil loss in the basin has been evaluated in 8 classes. As can be seen from the Figure 3.3, the potential erosion areas of the basin have soil loss values varying between 0,0 and 133,84 ton/ha/year. As a result of the evaluations of these areas, the maximum sediment amount that could come from the basin has been calculated as 108 380 ton/basin/year.

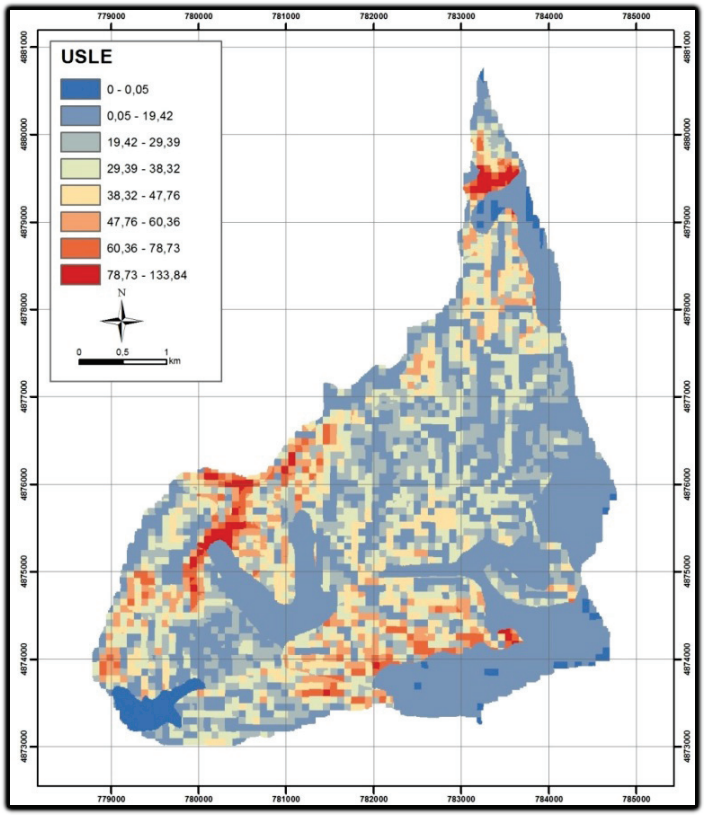

Figure 3.3 USLE Map of Bozyaka Basin

Sediment Delivery Ratios
Depending on the sediment yield determined through bathymetric measurements, the sediment delivery ratio for the catchment was calculated as 0.15. When compared with empirical methods, the closest result to the real measurements was produced by Boyce equation with 0.16. When Vanoni equation was used, the sediment delivery ratio was calculated as 0.28.

The Calculation of sediment amount of the basin using EIEI Equation
Basin sediment yield defined as a funcion of basin area was determined by using Equation 1. As the result of calculations, sediment yield of the basin was found as 3.272 ton year^{-1}.

CONCLUSIONS and DISCUSSION

As a result of bathymetric measurements, annual sediment yield of Bozyaka basin was calculated as 16.670 tons, and the sediment amount from a unit land was found as 7.41 tonha-1year-1. This amount has been evaluated as very high when compared with studies at similar catchments. As a result of evaluating USLE data, the maximum soil loss that could come from Bozyaka basin was calculated as 48,12 tonha-1year-1. From these results, it can be said that the real sediment delivery ratio of the basin is 0.15. The sediment yield from unit area was calculated using EIEI Equation and the amount of sediment from the unit area was calculated as 1,45 tonha-1year-1.

The basin is covered by two great soil groups and 96,45% of the basin is covered by Brown Forest Soils and the remaining 3,55% is covered by Alluvial Soils. About 26,66% of the basin has flat, close to flat and gentle slopes and consequently is not affected from erosion. The area affected from medium level erosion cover only 0,51% of the basin and these areas have generally medium slope and medium to shallow soil depth. The remaining 72,83% of the basin has very severe and severe erosion and the soils are very shallow and the lands are formed of steep lands.

The biggest land use class in Bozyaka dam basin is rainfed agricultural lands with 31,20%. This followed by vegetation transition areas (25,25%), sparsely vegetated areas (25,02%), coniferous forest lands (9,00%) and natural grasslands (6,98%). Rainfed agricultural lands, sparsely vegetated areas and natural grasslands are the main causative factor for erosion. In addition, very high erosion from the basin can be attributed to the fact that 3/4th of the basin is subject to severe to very severe erosion with shallow soils and steep lands.

On geological perspective, marn units that are under physical and chemical degradation were also subject to very severe erosion.

Demirkıran and Köşker (2007), have calculated the sediment yield of Ankara-Yenimahalle-Güvenç Dam, that has an area of 17.655 km2, as 1.76 tonha-1year-1. The plant cover of the basin is mainly formed of rangelands and arid agricultural lands with 21% average slope. They carried out a similar study in Samsun-Havza-Kuşkonağı Dam Basin. They calculated the sediment yield of the basin, having an area of 11.563 km2, and average slope of 7,1%, as 1.67 tonha-1year-1. (Demirkıran et al. 2013). Another study they carried out was in Ankara-Haymana-İkizce Dam Basin and calculated the sediment yield as 1.50 tonha-1year-1. (Demirkıran et al. 2017). The basin area of İkizce Dam is 51.425 km2, the average slope is 6,5%. Demirkıran vd. (2018), The sediment yield of Kızılkoyun Dam Basin was calculated as 2.14 ton ha-1year-1. The researchers have indicated that the size and the geological characteristics of the basin have close relation with the sediment yield that could come from the basin.

REFERENCES

Çelik E.H (1994). Uluborlu (Isparta) Barajının Yapım Maaliyetiyle Havza Islah Maaliyetinin Karşılaştırılması. İstanbul Üniversitesi Orman Fakültesi Dergisi. Seri:A, Cilt: 44, Sayı:2 Sayfa No:69-77, Istanbul

Demirkıran O, Köşker Y (2007). Ankara-Yenimahalle-Güvenç Gölet Havzası Sediment Verimi. III. Ulusal Su Mühendisliği, Sayfa:357-368, Gümüldür-İzmir

Demirkıran O, Erel A, Dengiz O (2013). Samsun Havza Kuşkonağı Gölet Havzası Sediment Verimi. 3. Ulusal Toprak ve Su Kaynakları Kongresi, Bildiriler Kitabı SayfaNo: 290-298, Tokat

Demirkıran O, Köşker Y, Akgül S, Başkan O (2017). Ankara Haymana İkizce Gölet Havzası Sediment Verimi. 5. Uluslararası katılımlı Toprak ve Su Kaynakları Kongresi. Bildiriler Kitabı Cilt 1 s. 591-605, Kırklareli

Demirkıran O, Köşker Y, Akgül S, Başkan O (2018). Ankara Haymana Kızılkoyun Gölet Havzası Sediment Verimi.Toprak Su Dergisi. Cilt:7, Sayı:1, Sayfa No: 49-56, 2018, Ankara

EEA. 2000. CORINE land cover 2000. European Environment Agency http://image2000.jrc.it.

Karaş E, Demirkıran O, Oğuz İ, Cebel H (2012). Comparison of Sediment Delivery Rations in Güvenç Basin. International Soil Science Congress on "Land Degradation and Challenges in Sustainable Soil Mnagement", 15-17 Mayıs 1912, Çeşme-İzmir-Türkiye

Özbek H, Kaya Z, Gök M, Kaptan H (1995). Toprak Bilimi (Çeviri). Ç, Ü, Ziraat Fakültesi Genel Yayın No, 73, Ders Kitapları Yayın No: 16, Adana

Sevinç A N (1993). Havza Sediment Verimi (Basılmamış), Ankara.

Soil Survey Staff, 1999. Soil Taxonomy (Second Edition), United States Department of Agriculture Natural Resources Conservation Service, Agriculture Handbook, Number 436, USA, https://www.nrcs.usda.gov/Internet/FSE_DOCUMENTS/nrcs142p2_051232.pdf

USDA (1978). Predicting Rainfail Erosion Losses-A Guide To Conservation Planning.USDA Handbook 573. GPO, Washington, DC, USA

Wischmeier W H, Johnson C B, Cross B V (1971). A soil erodibility nomograph for farmland and construction sites. J. Soil and Water Conserv. 26:189 -193. USA

5th International Symposium on Dam Safety

October 27-31, 2018

ASSESSMENT OF SEDIMENT CAPTURE PERFORMANCES OF COANDA AND TYROLEAN INTAKES BY EXPERIMENTS

Şebnem ELÇİ [1], Oğuz HAZAR[2]

ABSTRACT

Intake structures on channels or in reservoirs are frequently used to divert/withdraw a certain amount of water discharge for various purposes of use i.e. irrigation, potable water supply and generation of hydroelectric power. Hydrologic, geotechnical, topographic and climatic factors directly affect the type of the intake structures which will be constructed. Factors such as excessive rain or snow melt and greater river bed slopes can result in high turbidity flows and in that case bottom intake structures such as Coanda and Tyrolean type intakes might be preferred for their better screening of sediments as compared to frontal and lateral intake structures. To perform this task, diverted water is captured by a transversal rack and a gallery located in the control crest is utilized. With a proper design of the intake, the quality of the diverted water can be increased by screening out most of the sediments in the flow.

Previous studies on the bottom intake structures, presented empirical equations relating the diverted water amount per unit width to hydraulic head, discharge coefficient and void ratio of the bar clearance to the total length; based on experiments. Most studies focused on the discharge coefficient and the parameters affecting this coefficient such as hydraulic and rack characteristics. Presented study focused on the sediment capture performances of these two specific type intake structures though experimental work. A novel sediment feeding system designed specifically for this study is utilized in the experiments. Sediment feeding system allowed the user to control the frequency and amount of the feeding of sediments to the channel. The rack slopes varied from 10 to 30 degrees for both intake structures. Study results pointed out a new parameter including sediment characteristics should be considered for a proper design of Tyrolean and Coanda type intakes, as well as rack and hydraulic characteristics.

Keywords: Tyrolean intakes, Coanda intakes, high turbidity flows

INTRODUCTION

Bottom intake stuructures, if designed properly, can filter the entrance of the sediments to the intake structure. In the design of the structure, it is necessary to consider different aspects. The efficiency of the intake structure depends on various factors such as the shape of the bars, clear spacing between the bars (void ratio), flow approximation conditions and quantity, the angle of the rack, length, sediment rate, etc. It is assumed that flux over the rack is one-dimensional, flow decreases progressively, hydrostatic pressure distribution acts over the rack in the flow direction and energy level or energy head can be considered constant along the rack. Several researchers have studied this problem using analytical models. Noseda (1955) studied the clear water flow through different racks.

[1] Professor, Department of Civil Engineering, Izmir Institute of Technology, Izmir, Turkey, e-posta: sebnemelci@iyte.edu.tr

[2] Graduate Student, Department of Civil Engineering, Izmir Institute of Technology, Izmir, Turkey, e-posta: hazaroguz@gmail.com

Differences between measured and calculated depth profiles are generally found at the beginning of the rack due to the consideration of hydrostatic pressure distribution, and at the edge of the rack when friction effects are neglected (Brunella et al., 2003). Noseda (1955) defined a variable discharge coefficient for horizontal rack case and subcritical approximation flow:

$$C_q = 0{,}66m^{-0{,}16}\left(\frac{h}{l}\right)^{-0{,}13} \quad (1)$$

where l is referred to distance between the centerline of two consecutive bars, m is the void ratio and h is the height of water measured in the vertical direction. Once all the parameters are defined, several researchers (Frank, 1956; Kuntzmann and Bouvard, 1954; Noseda, 1955) have proposed the wetted rack length necessary to derive a defined flow rate. The value of the wetted rack length proposed by Noseda (1955) is obtained with the following equation:

$$L = 1{,}1848\frac{h}{C_q m} \quad (2)$$

where L is the wetted rack length.

In the studies conducted by Yılmaz (2010) and Şahiner (2012); comprehensive sets of experiments at METU, related to Tyrolean intakes were done. As results of these studies it was stated that; the water capture efficiency first decreases with increasing θ up to value of about 15° and then increases with increasing value of θ up to the value of about 27° and finally decreases again with increasing θ. For a constant discharge, the WCE attains almost the same maximum values at two different screen slopes of about θ = 5° and θ = 27° in the figures of small L/e. They stated that, θ = 27° should be selected to reduce the risk of clogging of the bar openings due to the presence of sediment in the flow in practical applications.

In different studies, researchers investigated the behaviour of clear water over the rack with different slopes, bar spacing and shapes, but not many studies could be found where sediment was fed into the sytem and the sediment characteristics were provided as parameter. So this study aims to fulfill this gap in the literature via series of experiments.

Experimental Setup:
Experiments were conducted in the hydraulics laboratory of Izmir Institute of Technology, utilizing a setup specifically designed for this study. Two types of intakes structures – Tyrolean and Coanda types were built so that screen slopes could be modified as desired during the experiments. Figure 1 shows the Coanda type intake used during the experiments. A fine net attached frame that has the ability to trap the sediments was placed under the rack and this setup was placed on top of a a 200 l capacity empty tank which enabled the measurement of water capture efficiency of the system. Figure 2 shows the frame used in the experiments. 300 g of sediments having d=0,8 mm was fed into the system by a novel sediment feeder system designed specifically for this study. Sediment feeding system was designed using Arduino which is an open-source electronics platform used for building interactive prototypes. The sediment feeding system allowed the user to control the frequency and amount of the feeding of sediments to the channel which is 20 cm wide and 2 m long and the intake structure consequently. Figure 3 shows the sediment feeding system used in the experiments.

The water capture efficiency and the sediment capture efficiency of the two types of intakes were evaluated through experiments. The angle of rack inclination, θ was selected as 10°, 20° and 30° in the experiments. Each experiment was repeated 3 times and the average values of these experiments are presented in the study. The spacing between the bars of the rack were 1 mm, which resulted in a void ratio of 0,09 (m=0,09) for the Coanda type and 0,07 (m=0,07) for the Tyrolean type intakes. The experiments continued for three minutes after the feeding of the experiments started and a constant discharge (Qt=2,4 l/s) was maintained. Water height above the weir (h) was measured as 1,4 cm via a

point gauge for the given discharge. Considering that 300 g of sediment was fed into the system for three minutes, concentration of the sediments was calculated as 0,7 g/l during the experiments. This value is comparable to a turbid river in nature. The wetted rack length varied for each experiment and presented in Table 1.

Figure 1. Coanda type intake used in the experiments.

Figure 2. Frame used to capture the sediments.

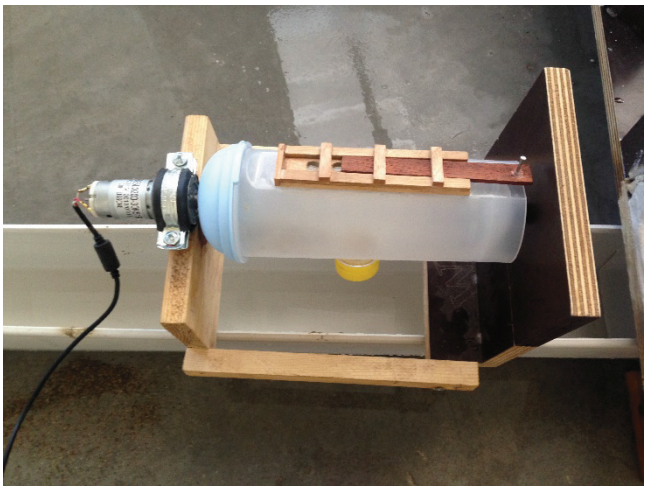

Figure 3. Sediment feeding system used in the experiments.

Table 1. Parameters utilized in the experiments. Here Θ is the angle of rack inclination, m is the void ratio defined by the ratio of the spacing between the bars to the total distance, L is the wetted rack length, h is the water height above the weir, Qi is the water entering into the intake, Qt is the total discharge diverted to the intakes via a channel, WCE is the water capture efficiency of the intake, St is the total amount of sediments fed into the system, Si is the amount of sediments captured by the intakes and Cin/Ct is the ratio of concentration of the sediments captured by the intake to the total sediment concentration fed into the system.

Intake type	Θ (°)	m	L (cm)	h (cm)	Qi (l/s)	Qt (l/s)	WCE (%)	St (g)	Si(g)	Cin/Ct
Coanda	10	0,09	10,7	1,4	1,14	2,4	48	300	62,4	43,8
Coanda	20	0,09	21,5	1,4	1,45	2,4	60	300	158,2	87,3
Coanda	30	0,09	29,3	1,4	1,53	2,4	64	300	210,4	110,0
Tyrolean	10	0,07	14,7	1,4	0,72	2,4	30	300	48,5	53,9
Tyrolean	20	0,07	28,8	1,4	1,02	2,4	43	300	65,7	51,5
Tyrolean	30	0,07	36	1,4	1,12	2,4	47	300	117	83,6

Results and Conclusions:

In order to evaluate the water capture efficiency and the sediment capture efficiency of the two types, contant discharge of Qt=2,4 l/s was passed through a channel flowing into the intake structures. Water velocity was measured by an Accoustic Doppler Velocimeter (ADV) and discharge was calculated accordingly. Water height above the weir was measured as 1.4 cm by a point gauge. According to the results, Coanda type intake had shorter wetted rack length due to the difference in its design and the wetted rack length increased as the rack slope angle increased.

Calculated discharge coefficients and wetted rack lengths using the equations proposed by the researchers (Equations 1 and 2) were compared to the observed wetted rack lengths. Only one value for each intake type could be calculated since the proposed equations are for horizontal intakes and do not consider the angle of rack inclination. Wetted rack lengths were calculated as 30,3 cm and 36 cm for Coanda and Tyrolean types respectively. These values were very close to 30° of rack inclination values of the wetted rack lengths: 29,3 cm and 36 cm observed in the experiments. This can be explained by the positioning of the racks, which approaches to horizontal as the angle of rack inclination increases.
Both water capture efficiency (WCE) and sediment release efficiency (SRE) were calculated for each case and presented in the Table 1. Coanda type intakes have significantly higher water capture efficiency as compared to Tyrolean type intakes. As the rack angle increases water capture efficiency also increased, although this increase was not linear. As for the sediment release efficiency both intakes performed well at low rack angles. Coanda intake performed slightly better at 10 degrees, but it was observed that at the other angles (20 and 30 degrees) Tyrolean intake performed better. In order to investigate the optimum angle for both intake types experiments in small increments of angles is found necessary. Ratio of concentration of the sediments captured by the intake to the total sediment concentration fed into the system was also found an efficient parameter to test the efficiency of the intakes. At higher angles, it was observed that Coanda type intake can both capture water and sediments at a higher rate as compared to Tyrolean type. Thus, the sediment size and void ratio of the intakes should be investigated for a proper evaulation of the performances of the two types of the intakes.

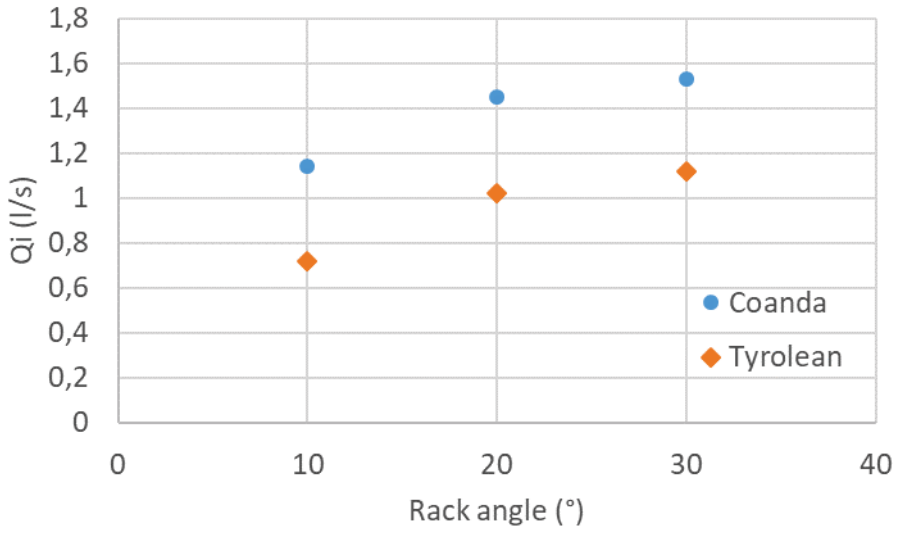

Figure 4. Comparison of discharges captured by the two types of intakes at different rack angles.

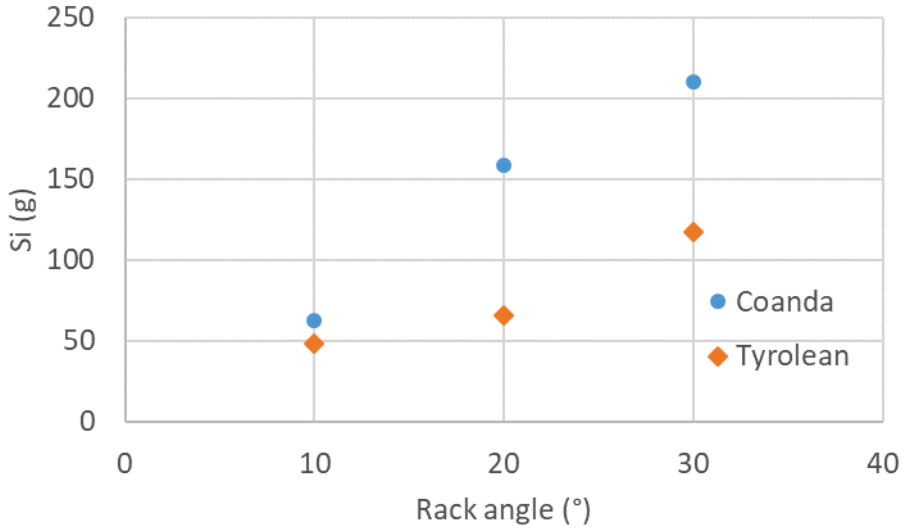

Figure 5. Comparison of sediments captured by the two types of intakes at different rack angles.

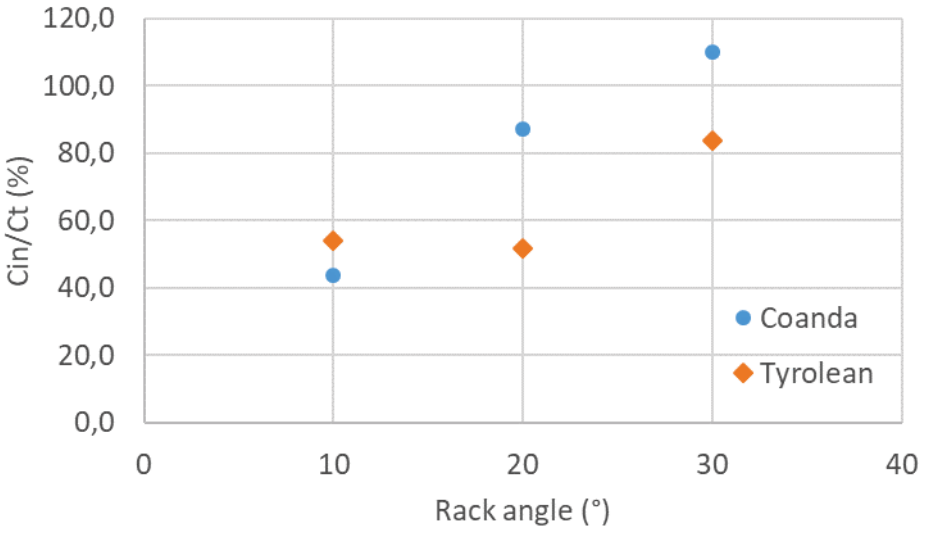

Figure 6. Comparison of conentration ratios captured by the two types of intakes at different rack angles.

ACKNOWLEDGEMENTS

We would like to thank to Ozan Sertkaya for his valuable help during the experiments.

REFERENCES

Brunella, S., Hager, W. H. and Hans-Erwin Minor, H.E., 2003. “Hydraulics of bottom rack Intake”. J. of Hyd. Eng. ASCE, 129 (1), 1-10.

Frank, J., 1956. “Hydraulische Untersuchungen für das Tiroler Wehr”. Der Bauingenieur, 31 (3), 96-101 (in German).

Kuntzmann, J. and Bouvard, M., 1954. “Etude the´orique des grilles de prises d’eau du type ‘en-dessous”. La Houille Blanche, 9 (9/10), 569–574 (in French).

Noseda, G., 1955. “Operation and Design of Bottom Intake Racks”. 6th International Association of Hydraulic Research Congress, La Haye, (17), 1–11.

Şahiner, H., 2012. “Hydraulic Characteristics of Tyrolean Weirs Having Steel Racks and Circular-Perforated Entry”. Thesis Submitted in Partial Fulfillment of The Requirements for the Degree of Master of Science in the Department of Civil Engineering The Middle East Technical University, Ankara,Turkey.

Yılmaz, N.A., 2010. “Hydraulic Characteristics of Tyrolean Weirs”. Thesis Submitted in Partial Fulfillment of the Requirements for the Degree of Master of Science in the Department of Civil Engineering The Middle East Technical University, Ankara, Turkey.

5th International Symposium on Dam Safety

October 27-31, 2018

DEVELOPMENT OF SOFTWARE TO PREDICT THE MODAL PARAMETERS AND STRUCTURAL BEHAVIOR OF SINGLE CURVED ARCH DAMS

Ebru KALKAN [1], Ahmet Can ALTUNIŞIK [2], Hasan Basri BAŞAĞA [3], Barış SEVİM [4]

ABSTRACT

The dams are among the most important building elements and fields of study of Civil Engineering when considering the reasons such as the duties they undertake, the difficulties in construction stages and high cost. Analyzes carried out by expert engineers are also taking considerable time due to the difficult and challenging of parts of modeling, analysis and interpretation. In the scope of this paper, general engineering software has been developed in order to facilitate the analysis of the dam which takes considerable time due to the reasons explained above and to have a quick knowledge about the structural behavior. Modal analysis, static analysis and dynamic analysis results can be obtained by considering the soil-structure interaction for single curved arch dams within the scope of the developed software. As the initial model, a single curved Type-1 arch dam selected that is one of five types of arch dam, presented in the "Arch Dams Symposium" in 1968. Detailed studies have been carried out on the reference type 1-arch dam, built on a certain scale in the laboratory environment and verified by environmental vibration tests, taking into account the different scales (1, 10, 20, 30, ..., 500) through the finite element model created by the ANSYS program. In the analyses, dam height, material property, mass, soil class, seismic load reduction factor, effective ground acceleration coefficient, soil-structure interaction etc. are used as variable parameters. In the end of analyses, static and modal analysis results (frequency, period, displacement, strain and deformation) with the most appropriate equations obtained by the regression analysis, dynamic analysis results (displacement, stress and deformation) are expressed by the equations of field. Software interface has been developed using the EXCEL program in order to combine the large number of formulas, equations and results obtained.

Keywords: Arch dam, modal parameters, software, structural behavior, Type-1 arch dam.

INTRODUCTION

With the development of the technology age and the concept of time being so important, there is an increasing trend towards software operations to ensure ease of process. Peng and Law (2002) introduced a software framework, which will serve as the core for collaborative structural analysis

[1] Dr., Department of Civil Engineering, Karadeniz Technical University, Trabzon, Turkey, e-posta: ebrukalkan@ktu.edu.tr
[2] Professor, Department of Civil Engineering, Karadeniz Technical University, Trabzon, Turkey, e-posta: ahmetcan8284@hotmail.com
[3] Asst. Prof. Dr., Department of Civil Engineering, Karadeniz Technical University, Trabzon, Turkey, e-posta: hasanbb69@hotmail.com
[4] Assoc. Prof. Dr, Department of Civil Engineering, Yildiz Technical University, Istanbul, Turkey, e-posta: basevim@yildiz.edu.tr

program development. Özdemir (2004) analyzed the effects of main and interdependence of data on linear regression and knowledge transfer by aiming to mathematically and structurally define reciprocal dependency structure between two periodic-stochastic hydrological processes. Mittrup and Hartmann (2005) studied on software development for structural control of dams. For this purpose, it is selected Ennepe Dam that gravity dam. The correctness of the software is proved by the tests conducted at the Ennepe Dam and the usage of the application has been recommended. Beşiktaş (2010) used the data of some flow observation stations in the Eastern Black Sea Region to estimate flow rates of previously unmeasured points by using the regression analysis method the flow continuity curves. Şahin (2009) presented a new algorithm developed to minimize the torsional effects in asymmetric tall buildings. Qiujing et al. (2012) aimed to estimated horizontal displacements, stress and safety of high arch dams during construct and first water storage. Parameters are selected as water level, change of temperature, time, elasticity modulus of rock and concrete. It is aimed to develop formula for obtained dynamic characteristic of historical arch bridges by Bayraktar et al. (2014). Within the scope of the Sümerkan (2014) thesis, he developed a formula based on environmental vibration data and finite element analysis to predict the natural frequencies of post-tensioned balanced console bridges. Serhatoğlu (2015) examined the dynamic characteristics and performances of historical minarets. For this purpose, in the scope of the thesis, experimental works and finite element analyses are carried out on 15 historical minarets in Bursa. Within the thesis of Atmaca (2016), software named structGIS is developed in order to complete the earthquake inventory of the existing building stock, which is one of the important stages of earthquake damage estimation and loss reduction studies. Many studies conducted on the subject show that the software and scaling studies are getting more and more important (Chan et al. 2010, Gu and Özçelik 2011, Xiang et al. 2011, Cheng 2012, Yılmaz and Şahin 2013, Altunışık et al. 2018a, 2018b, 2018c, 2018d).

Software is being developed and continuously updated to facilitate the works done in many areas of engineering and to provide save time. It is seen that the need for software is increasing day by day when the researches done are examined. Within the scope of study, it is aimed to obtain the results of the structural behavior of arch dams under dynamic analysis depending on the desired parameters

SCOPE AND USAGE AREA OF SCALING

Scaling is a work that can be done in every area, by shrinking large elements or systems and by enlarge small elements or systems in a certain way to make it easier to work on. The main purpose of the scaling concept used in many areas is basically the same, and the main purpose is to simplify the work by making the hard and time-consuming systems smaller and simpler to test. The study areas of Civil Engineering are multi-story buildings, dams, airports etc. examining and testing such prototypes is a very expensive, time-consuming and difficult-to-control process. For this reason, it is very easy and convenient to do the desired work on the small models created by scaling the prototype. Due to the similarity between the prototype and the model, the results obtained in the small model will be interpreted so that the behavior of the prototype can be predicted.

In its broadest terms, there are two main ways to relate the model to the prototype. Similarity conditions are derived from the relevant field equations if the system has a mathematical model or by dimensional analysis if the mathematical model of the system is not valid. In dimensional analysis, all parameters and variables that affect the behavior of the system have to be known. The obtained equation is the dimensionless product of system parameters and variables. Thus, similarity conditions can be created on the basis of the generated equation.

Since there is a corresponding mathematical model for the frequency value, similarity relations are obtained with depending on the geometric, mass and material scales and the results are compared with each other. Mathematical formulas of different systems are changing. For example, the frequency formula of the simple column element whose results are known is chosen. The obtained similarity formula can be generalized and used in different systems.

By establishing a relationship between the prototype and the scaled model of the column;

$$\frac{f_{n(\text{Model})}}{f_{n(\text{prototype})}} = \frac{\sqrt{E_m}\,S}{\sqrt{E_p}} \quad \Rightarrow \quad f_{n(m)} = S\sqrt{\frac{E_m}{E_p}}\,f_{n(p)} \tag{1}$$

Eq. 1 is a similarity formula obtained for the frequency value. The general formulas expressing the scale model and prototype between the similarity relation established by using mathematical models of displacement, principal stress and principal strain, are presented in Table 1.

Table 1. Similarity formulas for displacement, principal stress and principal strain

Structural Behavior	Formül
Frequency	$f_m = S\frac{\sqrt{E_m}}{\sqrt{E_p}} f_p$
Displacement	$\delta_m = \frac{E_p}{E_m}\frac{1}{S^2}\delta_p$
Principal Stress	$\sigma_m = \frac{1}{S}\frac{\gamma_m}{\gamma_p}\sigma_p$
Principal Strain	$\varepsilon_m = \frac{1}{S}\frac{\gamma_p}{\gamma_m}\frac{E_p}{E_m}\varepsilon_p$

These formulas are formed by using a column sample. In the example, the prototype is used for the real column size and the model is called for the scaled columns. For the application of the formulas to the dam, a small scaled dam with a laboratory model are named as a prototype and the enlarged scale dams are named as model and the similarity formulas are rearranged (Table 2).

Table 2. Rearranged similarity formulas for displacement, principal stress and principal strain

Structural Behavior	Formül
Frequency	$f_m = \frac{1}{S}\frac{\sqrt{E_m}}{\sqrt{E_p}} f_p$
Displacement	$\delta_m = \frac{E_p}{E_m}\frac{\gamma_m}{\gamma_p} S^2\,\delta_p$
Principal Stress	$\sigma_m = S\frac{\gamma_m}{\gamma_p}\sigma_p$
Principal Strain	$\varepsilon_m = S\frac{\gamma_p}{\gamma_m}\frac{E_p}{E_m}\varepsilon_p$

TYPE-1 ARCH DAM

There are five types of arch dams with different geometries proposed in the symposium "Arch Dams (1968)" held in England in 1968. From this dam types, in order to study in the laboratory were selected model small-scaled Type-1 arch dam. The Type-1 arch dam has geometry that a constant radius, angle and a single curvature. The geometrical characteristics of the Type-1 arch dam are shown in Figures 1 and 2.

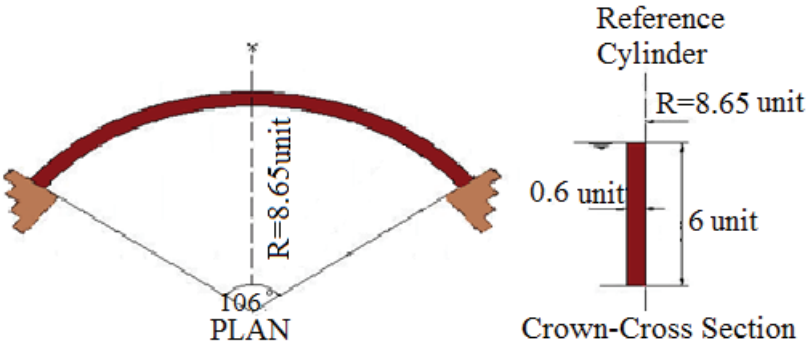

Figure 1. Geometry properties of Type-1 Arch Dam (Arch Dams, 1968)

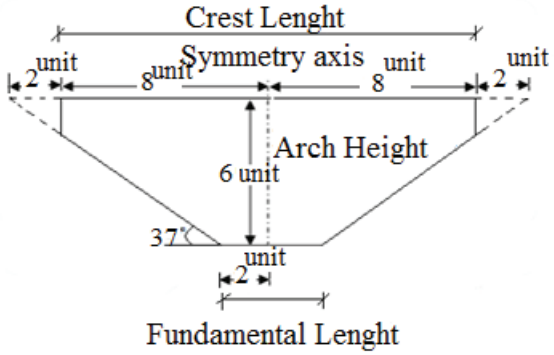

Figure 2. The cross-section of the valley where the Type-1 arch dam is located

Constitution of Laboratory Model

In the Type-1 arch dam whose dimensions are given in units, 1 unit=10cm is selected and the laboratory model is created. According to the obtained data, the dam height (H) is 60cm, the crest and the base width are 6cm and the crest length of the dam is calculated as 171.13cm in the upstream face and 160.03cm in the downstream face. In the studies conducted within the scope of the thesis, the dam model has been developed to include base and reservoir in order to realistically determine the dynamic behavior of the Type-1 arch dam (Sevim 2010). The three-dimensional soil-structure interaction model and laboratory model of the Type-1 arch dam prepared according to these properties and the dimensions of this model are given in Figure 3.

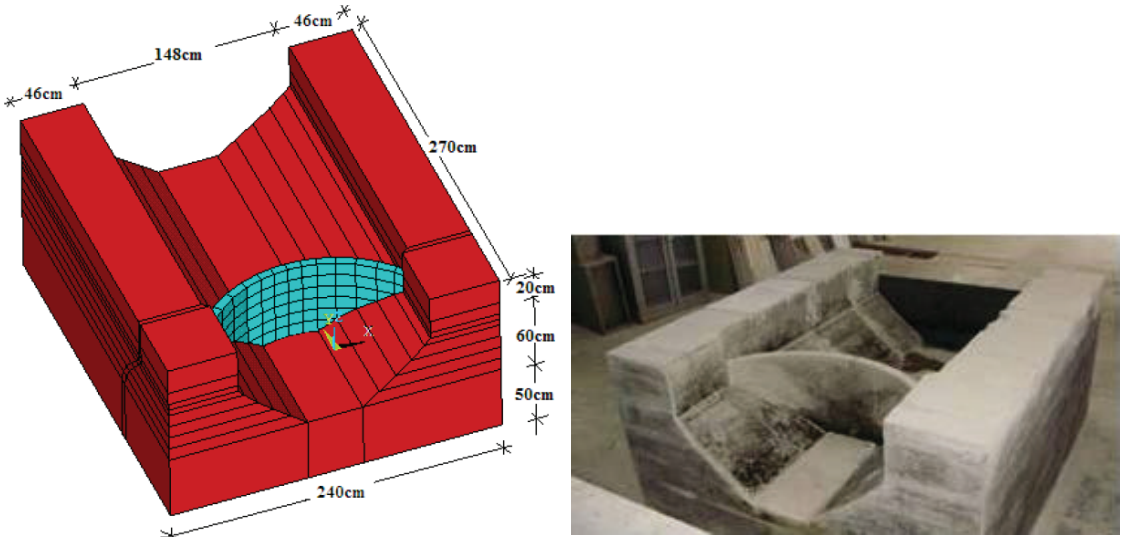

Figure 3. 3D and laboratory model of Type-1 arch dam

Modal Parameters of Laboratory Model of Type-1 Arch Dam

By using the finite element model of the Type-1 arch dam formed in the thesis study done by Sevim (2010), is purposed developing the software to predict the static, dynamic characteristics and structural characteristics of the dams. Non-destructive experimental measurements such as ambient vibration and forced vibration tests are conducted on the dam body to extract the natural frequencies. Table 3 summarizes the first nine numerically and experimentally identified natural frequencies.

Table 3. Numerical and experimental first nine natural frequencies

Mod Number	Frequency Values (Hz)		
	Finite Element Analysis	Ambient Vibration Test	Forced Vibration test
1	348.87	339.2	340
2	364.81	372.6	372
3	510.22	552.3	552
4	658.45	619.8	616
5	680.42	----	----
6	701.66	----	----
7	740.70	741.1	740
8	793.32	----	----
9	836.73	839.0	828

Results of Finite Element Model of Type-1 Arch Dam

In order to verify the results given in Table 3 and obtain the displacements with principal stresses and strain, finite element model of the Type-1 arch dam is constituted in ANSYS software (2016). It is aimed to use these results as initial and references parameters for scaling.

The analyses are carried out Soil-structure interaction conditions. Empty reservoir condition is taken into consideration. For the next studies, it is aim to investigate the reservoir and dynamic load effects on structural response. Modal analyses are done and first ten natural frequencies, period values and mode shapes are obtained. Table 4 presents the related results. In the finite element analysis, the material properties are selected as E=150000MPa for dam body and foundation according to the updated finite element results by experimental measurement.

Table 4. Dynamic characteristics of Type-1 arch dam for soil-structure interaction

Mod Number	Finite Element Analysis Results		
	Frequency (Hz)	Period (s)	Mod Shape
1	344.58706	0.002020	Anti-Symmetrical Mode
2	361.20676	0.002768	Symmetrical Mode
3	505.56430	0.001978	Symmetrical Mode
4	652.08387	0.001534	Anti-Symmetrical Mode
5	674.36188	0.001483	Vertical Mode
6	860.11709	0.001163	Vertical Mode
7	890.79624	0.001125	Symmetrical Mode
8	917.23440	0.001090	Vertical Mode
9	954.16860	0.001048	Symmetrical mode
10	958.79734	0.001043	Symmetrical mode

Static analyses of the Type-1 arch dam are carried out under its own weight considering empty reservoir water and soil-structure interaction. Displacements, principal stresses and principal strains are calculated at the all nodal points of upstream and downstream faces (Figure 4) of dam body. A

total of 346 nodal points are located on the upstream and downstream faces of dam body. 10 critical nodal points are selected to display the changes of displacements and internal forces.

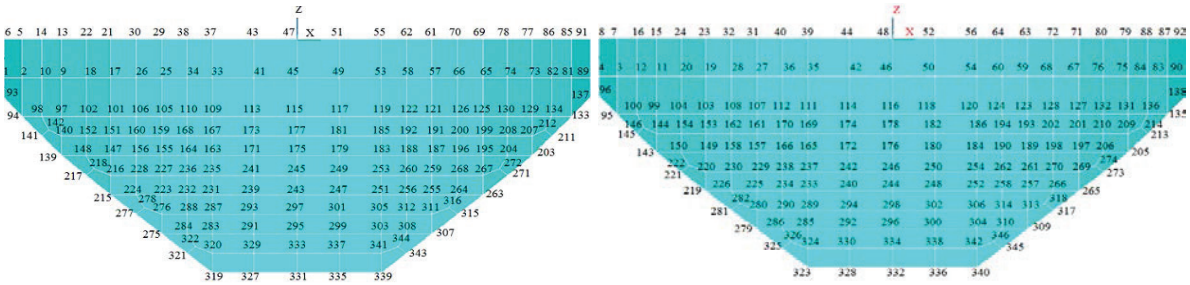

a) Upstream Surface b) Downstream Surface

Figure 4. Nodal points numbers of upstream and downstream surface of Type-1 arch dam

Determination of Real Arch Dam Model Results

To investigate the real arch dam response using scaling laws and similarity requirements with related formulas, four different arch dams (Model-1, Model-2, Model-3 and Model-4) are selected as an example. Table 5 present the detail information such as scaling factors, arch heights, arch interior radius and thickness with modulus of elasticity considered in the analyses to reflect the real arch dam models (Model-1, Model-2, Model-3 and Model-4).

Table 5. Dynamic characteristics of Type-1 arch dam for soil-structure interaction

Type-1 Arch Dam	Scale	Arch Height (m)	Arch Interior Radius (m)	Crest and Fundamental Thickness (m)	Modulus of Elasticity (MPa)
Prototype	1	0.60	0.8650	0.06	15000
Model-1	335	201	289.78	20.1	34000
Model-2	400	240	346.00	24.0	34000
Model-3	416.67	250	360.42	25.0	34000
Model-4	450	270	389.25	27.0	34000

Considering frequency formula in Table 2 and the frequency values of prototype Type-1 arch dam given in Table 4 including soil-structure interaction, the first natural frequencies of Model-1 and Model-2 are calculated;

$$f_{m_1} = \frac{1}{S}\frac{\sqrt{E_{m_1}}}{\sqrt{E_p}} f_p$$

$$f_{m_1} = \frac{1}{335}\frac{\sqrt{34000}}{\sqrt{15000}} 344.58706 = 1.548611\,\text{Hz} \quad (2)$$

$$f_{m_2} = \frac{1}{S}\frac{\sqrt{E_{m_2}}}{\sqrt{E_p}} f_p$$

$$f_{m_2} = \frac{1}{400}\frac{\sqrt{34000}}{\sqrt{15000}} 344.58706 = 1.2969786\,\text{Hz} \quad (3)$$

Table 6 presents the first ten natural frequencies of scaled arch dam models (Model-1, Model-2, Model-3 and Model-4) using finite element analysis and related formula soil-structure interaction. It can be seen from these table that there is a good agreement between finite element results and related formula (for frequencies, displacements, principal stresses and principal strains) of all models.

Table 6. The first ten natural frequencies of scaled arch dam models using FE analyses and formula for soil-structure interaction

Mod Numbers	Frequency (Hz)							
	Model-1		Model-2		Model-3		Model-4	
	ANSYS	Formula	ANSYS	Formula	ANSYS	Formula	ANSYS	Formula
1	1.5486	1.5486311	1.297	1.2969786	1.2451	1.2450895	1.1529	1.1528698
2	1.6233	1.6233228	1.3595	1.3595329	1.3051	1.3051411	1.2085	1.2084736
3	2.2721	2.2720894	1.9029	1.9028749	1.8267	1.8267453	1.6914	1.6914444
4	2.9306	2.9305726	2.4544	2.4543545	2.3562	2.3561615	2.1816	2.1816485
5	3.0307	3.0306936	2.5382	2.5382059	2.4367	2.4366582	2.2562	2.256183
6	3.8655	3.8655082	3.2374	3.2373631	3.1078	3.1078437	2.8777	2.8776561
7	4.0034	4.0033854	3.3528	3.3528352	3.2187	3.2186961	2.9803	2.980298
8	4.1222	4.1222028	3.4523	3.4523449	3.3142	3.3142246	3.0688	3.068751
9	4.2882	4.2881912	3.5914	3.5913601	3.4477	3.4476782	3.1923	3.1923201
10	4.309	4.3089935	3.6088	3.6087821	3.4644	3.4644031	3.2078	3.2078063

Dynamic Analysis Results of Laboratory Model of Type-1 Arch Dam

Under the time-dependent changing loads, it seems that there are disproportional between displacements, principal stresses and principal strains values obtained from the prototype and different scale of dam. In other words, the ratio of values obtained at any nodal points on between the dams that enlarged at a certain scale and prototype are not the same as the ratios of values at the between different nodal points on dams. This shows that the values obtained at result of dynamic analysis (displacement, principal stress and strain) can not be generalized with a single formula. For this reason, a regression analysis is used, which is a statistical method for obtaining of the results of large scale real systems according to the prototype results, achieving the desired data by fitting a curve between the results. In regression analysis, which is a parametric study, a curve is obtained by performing a regression analysis with the results of analyzes obtained with different combinations of the desired data in Type-1 arch dam, it is reached the result together with the formula of curve. It has been seen that the expression of the desired values using a single curve at all the nodal points on the dam is not a correct approach. Thus, developed different formulas are reflected the results of each nodal point in the dam.

Selection of Analysis Parameters

Taking into consideration soil-structure interaction of the Type-1 arch dam, it is obtained a total of 102 unit finite element models as 1, 10, 20, ..., 500 times scale. When the scales are expressed as arch height, they take values ranging between 0.60-300m and these values are also the first parameter for regression analysis. In the Modulus of Elasticity selected as the second parameter, for each model is taken into consideration nine different concrete strength class as C14/16, C16/20, C18/22.5, C20/25, C25/30, C30/37, C35/45, C40/50 and C45/55. Based on these two parameters, 918 different models are created and 3672 response spectrum analysis is applied by considering four different soil classes that is Z1, Z2, Z3 and Z4. All analyses are performed with ANSYS (2010) finite element program.

The results obtained in each of the nodal points for 102 different models with respect to nine different concrete strength classes are arranged, making them suitable for regression analysis. The data for each nodal point is obtained for all ground classes, fixed conditions and soil-structure interaction model, and a total of 2768 txt files have been created.

The first step is to evaluate whether there is any relationship between the obtained data or a linear or non-linear relationship if there is a relationship. Within the scope of this study, the desired graphics are created with EXCEL software and the relationship between the data is examined in detail. As a result of the review, a linear relationship is generally determined in the scatterplot of the data

pertaining to displacement. Nonetheless, nonlinear relationships exist at some nodal points. For this reason, it is evaluated which kind of range is suitable in each nodal points for the displacement results. Scatterplots of some nodal points related to displacement are given in Figure 5. Once the trendline of the obtained scatterplot is constructed, the R^2 value indicating how the gradient represents the data is readable. It is seen that these values are about 97-98% for some nodal points shown in Figure 5.

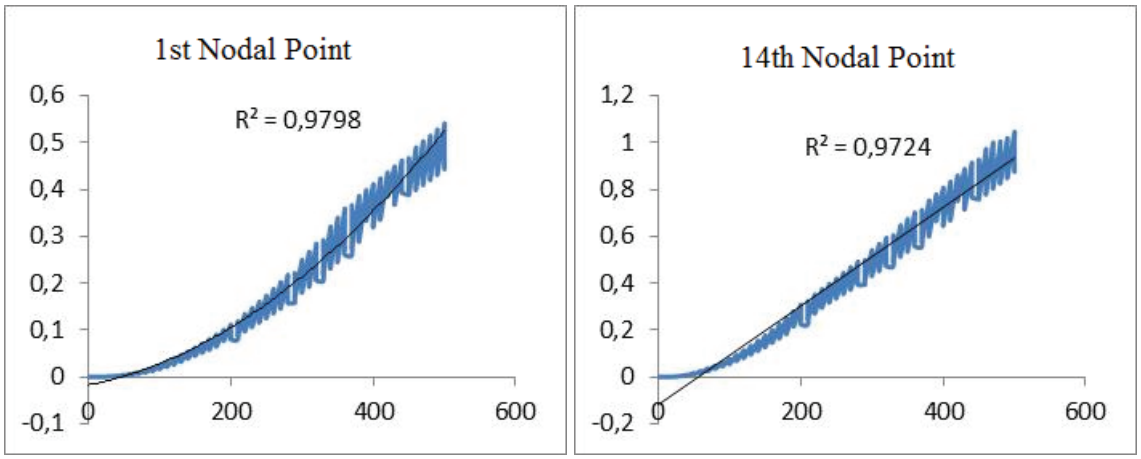

Figure 5. Scatterplots of the displacement results for some nodal points

Application of Appropriate Regression Analyzes for Results

Two-parameter regression analyses are performed by considering the scale and the modulus of elasticity as parameters. Linear regression analysis is performed at nodal points where the linear relationship is valid for the displacement results. However, for the non-linear relationship, the program code of the 2nd degree regression analysis based on the Least Squares Method given in the thesis study by Başağa (2009) is rearranged according to the two-parameter method.

Comparison of ANSYS and Regression Analysis Results

The results of the regression analysis are compared with the results obtained from the ANSYS program and the error rates are examined. When the results are analyzed, it is seen that 10% of the error rates are not exceeded. When comparing for the 50-times scaled of Type-1 arch dam, error rates reach 20-40%. This height is considered as the lower limit because the error rate at the scale value corresponding to a dam height of 30m is high. The upper limit used in the regression analysis is 300 meters arch height which corresponds to 500-times scale. It is decided that the formulas obtained for this reason are suitable for dam heights between 30m and 300m. It appears that errors of the predicted results of the formulas of any arch height value in outside these limits will more than 10%. Figure 6 shows the comparison the error rates of the results obtained according to different selected parameter values in some nodal points.

Development of Software

In the scope of the work done in Type-1 dam, it is not easy to present the desired results due to the reasons such as the excess of the variable parameters and the combination of these parameters, long and specific of the formulas obtained for each nodal point. It is a very difficult process to find and store a desired data from within the plenty data. For this reason, it is aimed to develop a software that will only allow the results of the desired data to be obtained at a selected nodal point and display various graphs and contour diagrams of these results. With the help of the software designed in the EXCEL program, the parameters are asserted the user selection and the static and dynamic analytical results are displayed with the formulas obtained from the regression analysis of the desired nodal

point at the arch dam. At the same time, depending on the selected parameters, the change on sectional and the contour diagrams of the results of the arch can be obtained at any nodal point.

Displacement			
500 Scale, Ao=4, R=1, C30/37, Z1			
Nodal Points	ANSYS	Formula	%Error
1.	1,912806	1,872897	2,086368
10.	3,043458	3,221922	-5,86386
19.	7,591565	7,561946	0,390151
31.	12,77068	12,48698	2,22151
37.	16,31958	16,74372	-2,59896
47.	28,29404	27,3858	3,21
48.	28,33737	27,3858	3,358014
50.	14,99984	14,2395	5,068934
72.	12,42	12,21506	1,65014
81.	2,167173	2,332794	-7,64224
90.	1,977952	1,872897	5,311278
105.	6,075831	6,33973	-4,34342

Maximum Principal Strain			
350 Scale, Ao=4, R=1, C20/25, Z1			
Nodal Points	ANSYS	Formula	%Error
1.	0,000115	0,000116	-0,91788
10.	0,000179	0,000183	-2,2075
19.	0,000349	0,000356	-2,0922
31.	0,000561	0,000552	1,591474
37.	0,000556	0,000551	0,91254
47.	0,000682	0,000676	0,910996
48.	0,000489	0,000491	-0,37904
50.	0,000453	0,000444	1,864185
72.	0,000494	0,000496	-0,23052
81.	0,000197	0,000203	-3,1155
93.	0,000106	0,000103	2,319356
105.	0,000328	0,000327	0,396926

Figure 6. Comparison of the results obtained for some nodal points

The Figurations for the appearance and use of the developed software are shown in detail in Figures 7-10.

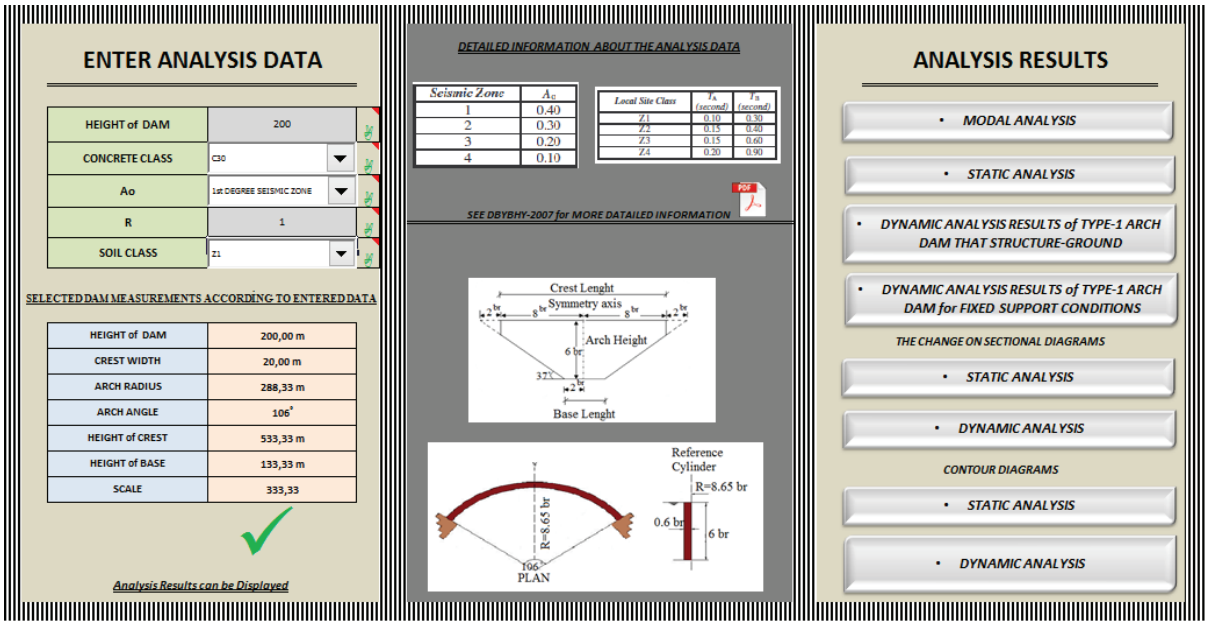

Figure 7. Input of data into home page of the software

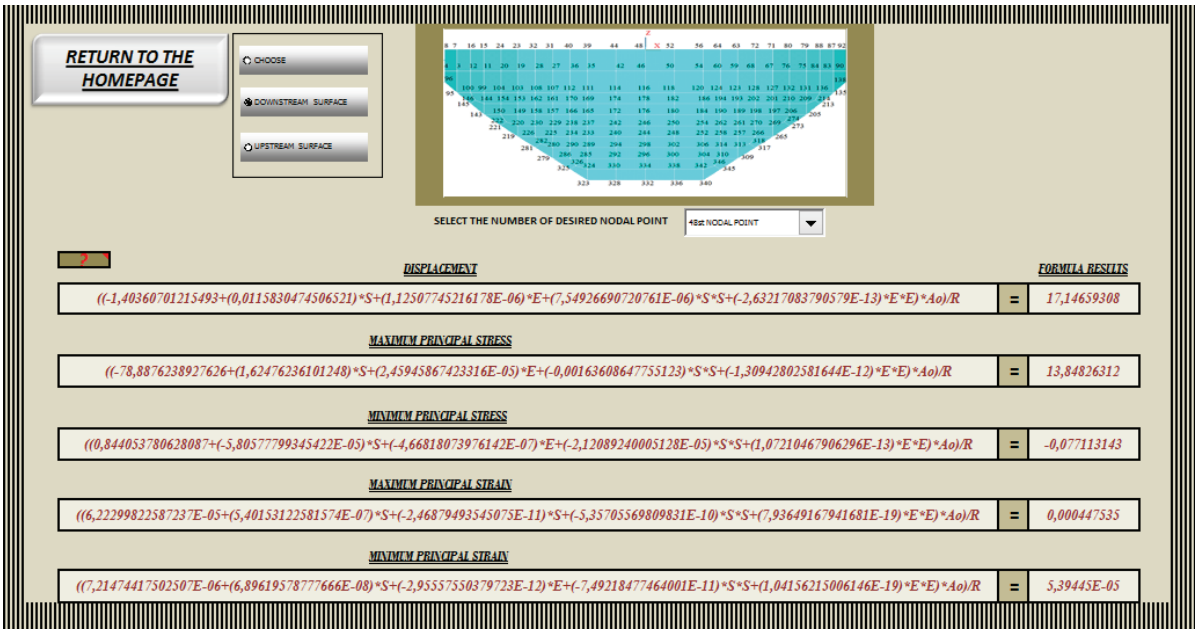

Figure 8. Displaying the related formulas and results of 48 nodal point at dynamic analysis results page of Type-1 arch dam that building ground interaction

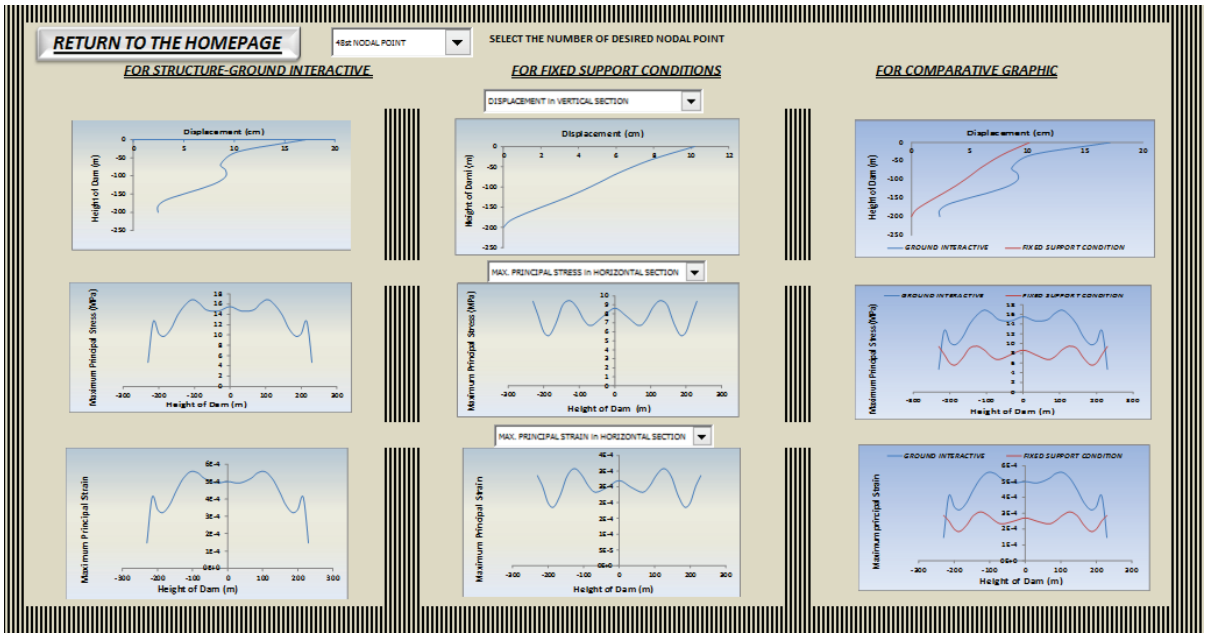

Figure 9. Displaying the change on sectional diagrams of 48th nodal point at section diagrams page obtained with dynamic analysis

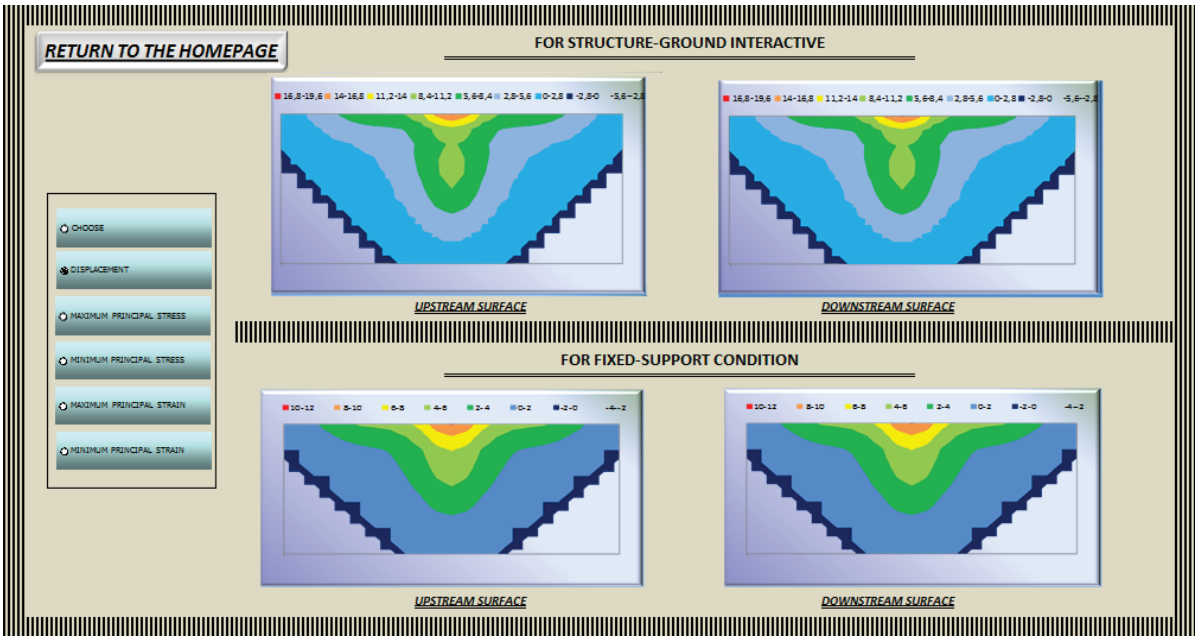

Figure 10. Displaying the change on sectional diagrams of 48th nodal point at section diagrams page obtained with dynamic analysis

CONCLUSION

In this study, engineering software is developed to predict the structural behavior of arch dams. By using the finite element model of the Type-1 arch dam modeled in the laboratory, dams are scaled to different heights and dynamic analyses are made. Taking into consideration the fixed support conditions and structure-foundation interaction of the Type-1 arch dam, it is obtained a total of 102 unit finite element models as 1, 10, 20, ..., 500 times scale. When the scales are expressed as arch height, they take values ranging between 0.60-300m and these values are also the first parameter for regression analysis. Modulus of elasticity are selected as second parameter and nine different concrete strength class (C14/16, C16/20, C18/22.5, C20/25, C25/30, C30/37, C35/45, C40/50 and C45/55) are considered for each structural model. Based on these two parameters, 918 different models are created and 3672 response spectrum analyses are applied by considering four different soil classes that is Z1, Z2, Z3 and Z4. All analyses are performed with ANSYS (2010) finite element program. The data for each nodal point on Type-1 arch dam is obtained for all ground classes, fixed support conditions and soil-structure interaction model, and a total of 2768 txt files are created. For regression analysis, the first step is to evaluate whether there is any relationship between the obtained data or a linear or non-linear relationship if there is a relationship. As a result of the review, a linear relationship was generally determined in the scatterplot of the data pertaining to displacement. Nonetheless, nonlinear relationships exist at some nodal points. However, it is seen nonlinear relationship in the scatterplot of data of the principal stress and principal strain. In each of the 346 nodal points on the arch body, a total of 13840 formulas are created represented of five different structural behavior, including displacement, maximum and minimum principal stresses, and maximum and minimum principal strains. The results of the regression analysis are compared with the results obtained from the ANSYS program and the error rates are examined. When the results are analyzed, it is seen that 10% of the error rates are not exceeded. In the scope of the work done in Type-1 dam, it is not easy to present the desired results due to the reasons such as the excess of the variable parameters and the combination of these parameters, long and specific of the formulas obtained for each nodal point. For this reason, it is aimed to develop a software that will only allow the results of the desired data to be obtained at a selected nodal point and display various graphs and contour diagrams of these results.

REFERENCES

Altunışık A.C., Kalkan E., Başağa, H.B., 2018a. "Development of Engineering Software to Predict the Structural Behavior of Arch Dams". Advances in Computational Design, vol. 3, N.1, pp. 87-112.

Altunışık A.C., Kalkan E., Başağa, H.B., 2018b. "Creation of Similarity Requirement with Field Equations in Steel Bearing Systems". The Open Civil Engineering Journal, vol. 12, N.1, pp. 134-149.

Altunışık A.C., Kalkan E., Başağa, H.B., 2018c. "Structural behavior of arch dams considering experimentally validated prototype model using similitude and scaling laws". Computers and Concrete, vol. 22, N.1, pp. 101-116.

Altunışık A.C., Kalkan E., Başağa, H.B., 2018d. "Structural Response Relationship Between Scaled and Prototype Concrete Load Bearing Systems Using Similarity Requirements". Computers and Concrete, vol. 21, N.4, pp. 385-397.

Arch Dams., 1968. "A review of British research and development". Proceedings of the Symposium held at the Institution of Civil Engineers, March, London, England.

Atmaca, H., 2016. "System Development for Full Scale Modeling and Analysis of Building Inventory". Master Thesis, Yıldız Technical University, İstanbul, Turkey.

Başağa, H.B., 2009. "An Approach for Reliability Analysis of Structures: Improved Response Surface Method". PhD Thesis, Karadeniz Technical University, Trabzon, Turkey.

Bayraktar, A., Türker, T., Altunışık, A.C., 2014. "Experimental frequencies and damping ratios for historical masonry arch bridges". Construction and Building Materials, vol. 75, pp. 234-241.

Beşiktaş, M., 2010. "Determination of Flow Duration Curves by Regression Analysis in the Eastern Black Sea and Current Estimation". Master Thesis, İstanbul Technical University, İstanbul, Turkey.

Chan, Y.K., Lu, Y.K., Albermani, F.G., 2010. "Performance-based structural fire design of steel frames using conventional computer software", Steel and Composite Structures, vol. 10, N.3, pp. 207-222.

Cheng, J., 2012. "Development of computational software for flutter reliability analysis of long span bridges", Wind and Structures, vol. 15, N. 3, pp. 209-221.

Gu, Q., Özçelik, Ö., 2011. "Integrating OpenSees with other software-with application to coupling problems in civil engineering". Structural Engineering and Mechanics, vol. 40, pp. 85-103.

Mittrup, I., Hartmann, D., 2005. "Structural monitoring of dams using software agents". Computing in Civil Engineering, ASCE, pp. 1-7.

Özdemir, Y., 2004. "Information Transfer via Regression among Periodic-Stochastic Hydrologic Processes". PhD Thesis, Dokuz Eylül University, İzmir, Turkey

Peng, J., Law, K.H., 2002. "A prototype software framework for internet-enabled collaborative development of a structural analysis program". Engineering with Computers, vol. 18, pp. 38-49.

Qiujing, Z., Guoxin, Z., Haifeng, L., Yi, L., Bo, Y., 2012. "Study on regression analysis and simulation feedback-prediction methods of super high arch dam during construction and first impounding process", Earth and Space, ASCE, pp. 1024-1033.

Serhatoğlu, C., 2015. "Numerical and Empirical Investigation of Dynamic Performance of Historical Masonry Minarets in Bursa". Master Thesis, Uludağ University, Bursa, Turkey.

Sevim, B., 2010. "Determination of Dynamic Behavior of Arch Dams using Finite Element and Experimental Modal Analysis Methods", PhD Thesis, Karadeniz Technical University, Trabzon, Turkey.

Sümerkan, S. 2014. "Natural frequency formula for post tensioned balanced cantilever bridges", Master Thesis, Karadeniz Technical University, Trabzon, Turkey.

Şahin, A., 2009. "Digital Signal Processing, Dynamic Characteristic Identification and Finite Element Model Updating Software for Experimental and Operational Modal Testing of Structures: SignalCAD-ModalCAD-FemUP", PhD Thesis, Karadeniz Technical University, Trabzon, Turkey.

Xiang, J., Jiang, Z., Wang, Y., Chen, X., 2011. "Study on Damage Detection Software of Beam-like Structures". Structural Engineering and Mechanics, vol. 39, N. 1, pp. 77-91.

Yılmaz, O., Şahin, A., 2013. "Educational Software Development for Design of Steel Structures Lesson". Sigma Journal of Engineering and Natural Sciences, vol. 31, N. 4, pp. 571-581.

5th International Symposium on Dam Safety

October 27-31, 2018

THE DIFFERENT METHODS FOR THE DESIGN OF RESERVOIR CAPACITY AT GAZİPAŞA GÖKÇELER DAM

Tuğba ÖZKOCA[1], Cenk SEZEN[2], Aslı ÜLKE KESKİN[3]

ABSTRACT

The reservoirs are designed to provide a balance between the flows of the river. Critical period methods are those in which the required reservoir capacity is equated to the difference between the water released from an initially full reservoir and the inflows, for periods of low flow. In this study, the capacity-yield-reliability relationship for single reservoir named Gökçeler Dam was investigated. Mass Curve, Residual Mass Curve, Moran Probability Matrix Method, Hardison's method and Minimum Flow approach was used in this study for determining reservoir capacity. The observed monthly and annual mean flow data observed for a period 1991-2015 of DSI-17039 Gökçeler River Gazipaşa Flow Gauging Station in East Mediterranean Basin in Turkey were used. For 0% probability of failure, the highest reservoir capacity resulted for methods Mass Curve, Residual Mass Curve and Minimum flow approach at the range between 52,48 to 52,94x10^6 m^3 for draft equal 63%. Conversely, for Hardison's methods when the high value of probability of failure (5% and 10%) were used for estimation, reservoir capacity values resulted at the range between 25,52 to 19,56 x10^6 m^3 for draft equal 60%. In Moran Probability Matrix method, the reservoir capacity was determined as 200 x10^6 m^3.

Keywords: Capacity-Yield-Reliability Relationship, Reservoir Capacity, Gökçeler River, Antalya

INTRODUCTION

Storage reservoirs are important components of water resource systems. Reservoirs are constructed on rivers in order to respond to the water demand during periods where inflow is less than the demand. Determination of the required capacity, i.e. the operation study, for a river reservoir is done using a data set corresponding to a period of time (Aksoy, 2001).

The adequacy and reliability of the water supplies from surface water resources are largely dependent upon the ability of these reservoirs to provide sufficient water storage during the critical dry periods. Therefore, in the design of reservoirs, the risk of failure should be taken into account as a reservoir of a given size can provide a certain yield only with a certain probability because of the random nature of inflows (Bayazit and Onoz, 2000).

The critical period in water resources systems, as well as the accumulation wells in planning, designing and operating the reservoirs is also very important in determining the reservoir volume (Rao, at al., 2001). If the reservoir capacity is deemed to be full at the beginning of the critical period, the reservoir will be completely empty at the end of the critical period.

[1] MSc., State Hydraulic Works, 13th Regional Directorate, Antalya, Turkey
e-mail: tugbasafak@dsi.gov.tr

[2] MSc., Department of Civil Engineering, Faculty of Engineering, Ondokuz Mayıs University, 55139, Atakum, Samsun, Turkey
e-mail: cenk.sezen@omu.edu.tr

[3] Dr. Lecturer, Department of Civil Engineering, Faculty of Engineering, Ondokuz Mayıs University, 55139, Atakum, Samsun, Turkey
e-mail:asli.ulke@omu.edu.tr

The accumulation volume capacity corresponds to the need at the accepted risk level. If a risk-free operation is designed for the reservoir then the concept of the ideal accumulation reservoir is involved. The ideal accumulation reservoir is neither full of water nor empty (Bayazıt, 1982).

In this study, Monthly and annual mean flow data observed for a period 1991-2015 of DSI-17039 Gökçeler River Gazipaşa Flow Gauging Station in East Mediterranean Basin in Turkey are used. Three probabilities of failure (0%, 5% and 10%) are considered for reservoir capacity estimation. The percentage of the draft is taken 63% for the the Mass Curve, Minimum Flow and Residual Mass Curve methods and 60% and 80% for the Hardison's Generalized method so as to estimate reservoir capacity.

METHODS

The methods used to determine the volume of the reservoir are theoretically divided into three parts but the distinction between these groups is not very clear. First group is termed "critical period techniques" which depend on analyzing those events when the yield exceeds demand. In the second group, an important part of which is subsection of probability matrix methods. The third group consist of those procedures, which are based on generated data (McMahon and Mein, 1986).

Critical Period Techniques

The critical period is defined as a period during which reservoir goes from a full condition to an empty condition without spilling in the intervening period. Therefore, for a given inflow and demand record critical period is the period in which the largest storage capacity is required. If a reservoir is designed with that capacity, it will completely empty at the end of the critical period, if it is assumed full at the beginning of that period. It should be pointed out that such a capacity supplies the demand at an accepted level of risk (Aksoy, 2001).

Mass Curve Method

This method is also known as the Ripple mass curve method after the developer of this method. This is a simple method, which is commonly used to estimate the required storage capacity of a reservoir in project planning stage. The method uses the most critical period of recorded flow to compute storage (Ripple, 1883). The steps in the mass curve methods procedure are as follows: Firstly, mass curves are created for the proposed dam site using monthly and annual flow data. Secondly, the inclination of the cumulative draft line are decide for the graphical scales. After that, show the cumulative draft line on the same graph with the mass curve for the reservoir. Then, the largest intercept between the mass inflow curve and the cumulative draft line is determined and measured. (McMahon and Mein, 1986).

Residual Mass Curve Methods

Residual Mass Curve Method is a slightly more complicate version of the mass curve. However, it is more suitable to decide the storage volume (McMahon and Mein, 1986). This method is graphical saves the additional space needed for plotting curve and to accentuate more clearly the crests and troughs of the cumulative flow records. Additionally, measure the largest intercept between the mass inflow curve and draft lines.

Minimum Flow Approach

In determining the reservoir volume by the minimum flow method, first 5, 10, 20 ... monthly total flows are found from the flow observations. The values found are pointed at the time axis corresponding to 5, 10, 20 … months respectively to obtain a curve of minimum flows. Then, as shown in Figure 1, when critical storage (C_{crit}) is determined, the maximum intercept between the draft line and the drought curve is utilized (McMahon and Mein, 1986).

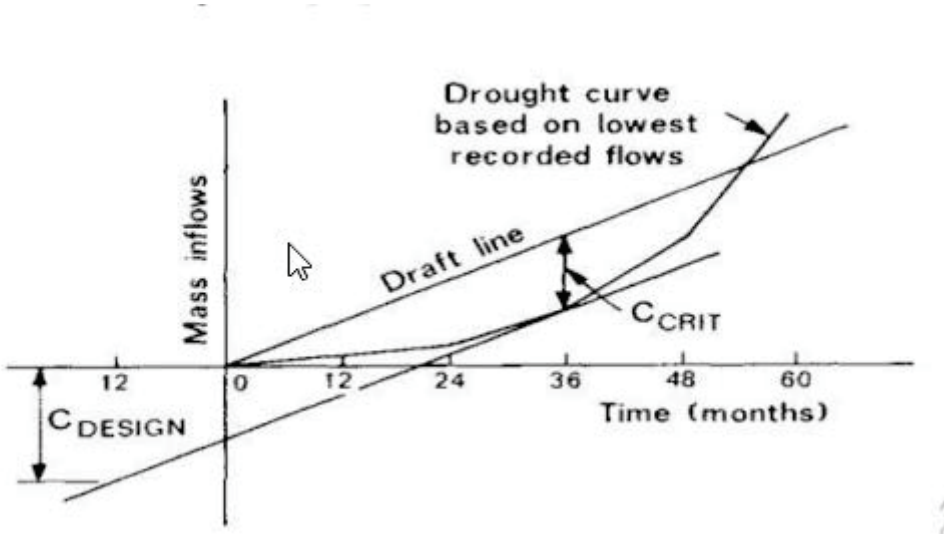

Figure 1. Reservoir capacity-yield analysis by minimum flow approach(McMahon and Mein, 1986)

Hardison's Generalised Methods

Hardison (1965) generalized Langbein's probability directing method utilizing theoretical dispersions of yearly flows and accepting serial correlation to be zero.This equivalent to Moran's (1954) except that Hardison used a simultaneous model rather than mutually exclusive type adopted by Moran (McMahon and Mein, 1978). The annual storage estimates were shown graphically for Lognormal, Normal and Weibull distributions of annual flows.

Using by Hardison's methods for reservoir capacity firstly the appropriate distribution type depends on parameters (mean, standard deviation, coefficient of variation and coefficient of skewness) compute. At that time if the coefficient of skewness of the logarithms of flow is greater than -0.2, accept a log- normal distribution. If the coefficient of skewness of the absolute flows is less than 0.2 or if the coefficient of variation of the flows is less than 0.25 accept a normal distribution. Additionally accept a Weibull distribution if neither a log- normal nor a normal distribution is selected except when the logarithms of the flows have a negative skew coefficient greater than 1.5 (McMahon and Mein, 1986). The reservoir capacity can then be determined by multiplying the reservoir capacity obtained from the graphs by the average.

Moran Probability Matrix Method

The Moran probability matrix method in which annual flows are used is expressed in terms of a basic unit of current, draft and volume. This method does not directly provide the necessary reservoir capacity. However, the required capacity for a selected capacity value can be found by means of trial capacity based on the probability of vacancy of the reservoir found from the probability distribution (Bacanlı and Koç, 2006).

Probability theory of storage systems, which has now developed into an active branch of applied probability is formulated by Moran (Moran,1954). Calculated reservoir volume estimates are independent of initial states. This is in contrast to the critical period techniques and is one of the advantages of the matrix method. Non-permanent data can be used. When annual flows are taken as independent, the sequence of flows is insignificant.

CASE STUDY

The East Mediterranean basin, which is shown in Figure 2, is one of the twenty- five basin in Turkey. The precipitation area of the basin is 21682,8 km^2 and average annual flow is 7835.6 hm^3. There are Bıçkıcı, Delice, Gökçeler and Musa streams in the basin. There are three flow gauging stations around the basin where the project is located (Table 1).

Table 1. Number, names and area of station in the Eastern Mediterranean basin

Number	Stream	Name	Area(km^2)
D17A039	Gökçeler	Gazipaşa	139.4
D17A027	Bıçkıcı	İnceğiz	134.0
D17A038	Sedre	Kocaoğlanlı	158.0

The Gökçeler stream falls into the Mediterranean Sea within the boundaries of Antalya province. The location of the Gökçeler dam is given in Figure 2.

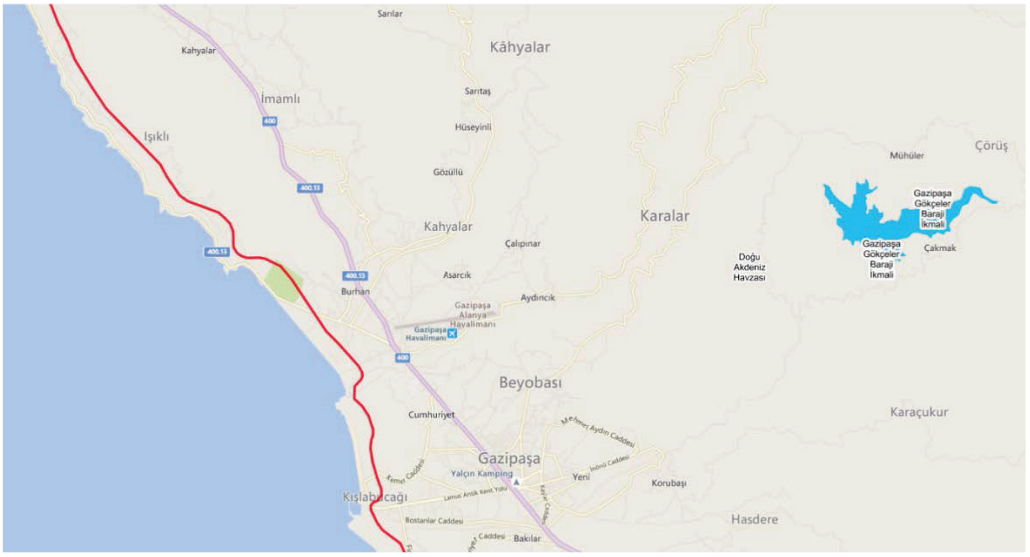

Figure 2. Gökçeler dam

Monthly flow of Gökçeler Dam are monthly current values of flow gauging stations D17A039. The flow values of the station 1991-2015 are available. In the study, it is aimed to determine the necessary storage volume with different methods in the literature. Evaporation losses are not taken into consideration since the reservoir capacities to be obtained by different methods are intended to be compared. Table 2 shows the statistical data for D17A039 Gazipaşa Flow Gauging Station.

Table 2. The statistical data for D17A039 Gazipaşa Flow Gauging Station.

Statistics	Monthly	Annually
Data Length	300	25
Mean	7.27	87.25
Standard Deviation	3.55	42.64
Coefficient of Variation	1.110	0.489
Coefficient of Skewness	1.955	0.509

RESULT

In this study, the capacity-yield-reliability relation for single reservoir named Gökçeler Dam was researched as a case study. In this regard, reservoir capacity of Gökçeler Dam was calculated by using Mass Curve, Residual Mass Curve, Moran Probability Matrix Method, Hardison's Method and Minimum Flow approach.

Mass Curve Approach

The Mass Curve approach was utilized for the period 1991-2015 (300 months). The monthly data was used so as determine the reservoir capacity by this method. As a draft ratio 63%, which was planned for this dam, is selected. Accordingly, the draft corresponds to 4.58×10^6 m^3 (63% of monthly mean flow) was taken into consideration. Consequently, for the 63% draft ratio probability of failure 0%, the storage capacity was determined as 52.48×10^6 m^3. The calculation reservoir capacity by Mass Curve approach was indicated in Fig. 3.

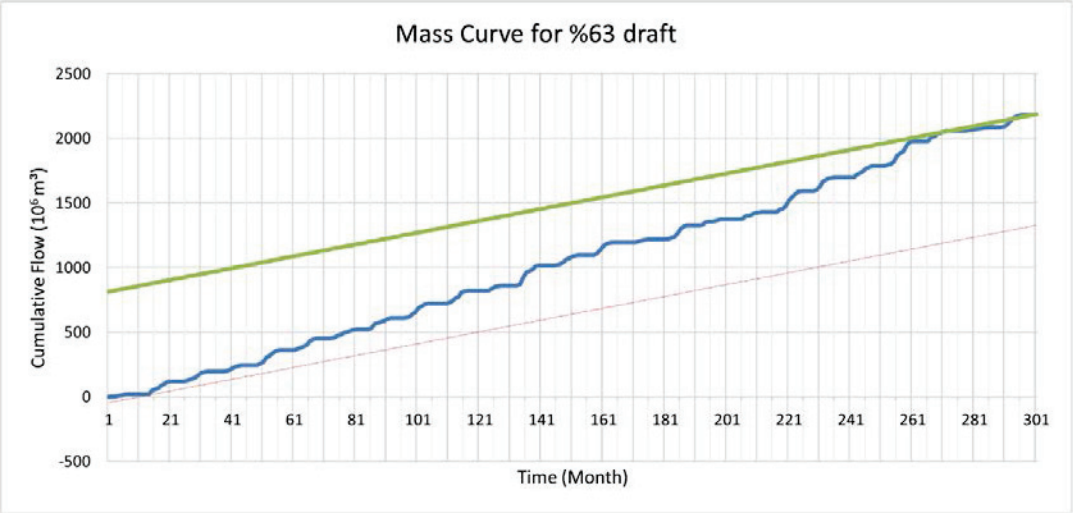

Figure 3. Determination of Reservoir Capacity by Mass Curve Approach

Minimum Flow Approach

The reservoir storage capacity was also calculated by Minimum Flow approach for draft ratio 63% probability of failure 0%. In this regard, as the mean draft volume 1374.23x106 m3 was taken into account. Accordingly, reservoir storage capacity was calculated as 52.74x106 m3 by Minimum Flow approach. The analysis as regards Minimum Flow approach can be seen in Table 3 and Fig. 4, respectively.

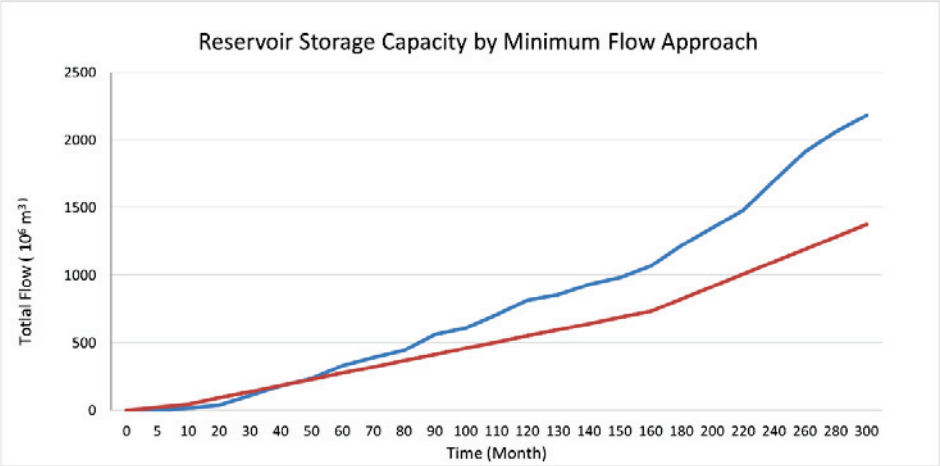

Figure 4. Determination of Reservoir Capacity by Minimum Flow Approach

Table 3. Minimum Flow Approach for the Reservoir Storage Capacity for Draft 63%

Time Period (Month)	Lowest Total Flow for that time period (10^6 m3)	Draft (%63) (10^6 m³)	Reservoir Capacity
5	0.136	22.90	22.77
10	14.571	45.81	31.24
20	38.873	91.62	**52.74**
30	107.988	137.42	29.44
40	180.069	183.23	3.16
50	233.17	229.04	-4.13
60	330.831	274.85	-55.98
70	390.337	320.65	-69.68
80	444.884	366.46	-78.42
90	559.335	412.27	-147.07
100	608.616	458.08	-150.54
110	704.994	503.88	-201.11
120	814.394	549.69	-264.70
130	855.97	595.50	-260.47
140	931.952	641.31	-290.64
150	982.036	687.12	-294.92
160	1067.025	732.92	-334.10
180	1218.318	824.54	-393.78
200	1350.244	916.15	-434.09
220	1479.424	1007.77	-471.65
240	1698.253	1099.38	-598.87
260	1913.248	1191.00	-722.25
280	2062.897	1282.62	-780.28
300	2181.319	1374.23	-807.09

Residual Mass Curve Approach

The reservoir storage capacity was calculated thanks to this approach by using monthly data for the draft 63% and probability of failure 0%. Accordingly, reservoir capacity was determined as 52.945×10^6 m^3 by Residual Mass Curve approach. The analysis of Residual Mass Curve method can be seen in Fig. 5.

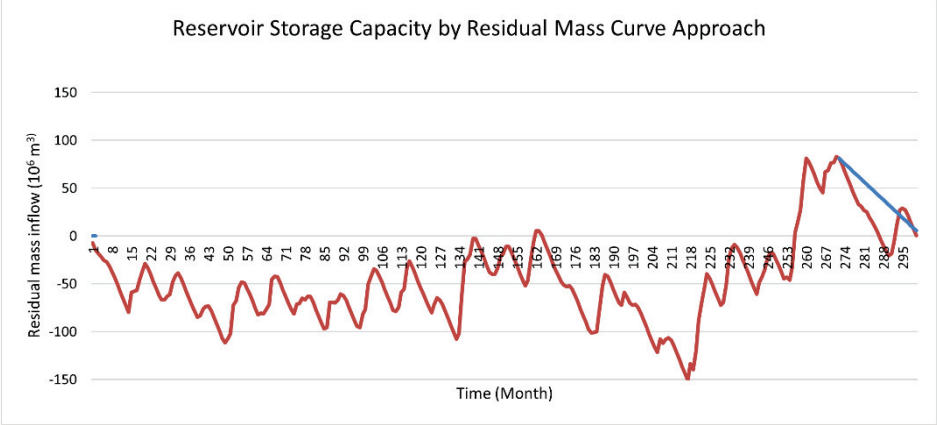

Figure 5. Determination of Reservoir Capacity by Residual Mass Curve Approach

Hardison's Generalized Method

In order to calculate the reservoir storage capacity by Hardison's Generalized method, different draft ratios and probability of failures were utilized as indicated in Table 4. In this context, for the draft 60% and probability of failure 10%, 5%, the reservoir storage capacity was calculated as 19.56×10^6 m^3 and 25.52×10^6 m^3. On the other hand, for the draft 80% and probability of failure 10%, 5%, the reservoir capacity was determined as 55.34×10^6 m^3 and 83.21×10^6 m^3.

Draft	Probability of Failure (10^6 m^3) (%)	Weibull Reservoir Capacity	C (10^6 m^3)	$C_{adjusted}$ (10^6 m^3)
60	10	0.25	22.23	19.56
	5	0.33	29.34	25.52
80	10	0.75	66.68	55.34
	5	1.2	106.68	83.21

Table 4. Hardison's Generalized Method for the Reservoir Storage Capacity

Reservoir capacity was adjusted because of the annual autocorrelation effect. The adjustment process was carried out by means of the study of McMahon and Mein (1986) (Appendix A, Fig. A-3) and $C_{adjusted}$ values were presented in last column of Table 4.

Moran Probability Matrix Method

To determine the reservoir capacity by Moran Probability Matrix method, it was assumed that initial reservoir capacity is 200×10^6 m^3 and the intervals were selected as 20×10^6 m^3 so as to constitute the matrix. The matrix was shown in Table 5. Final result for the matrix after the iterations was given in Table 6.

Table 5. Moran Probabilty Matrix for the Reservoir Storage Capacity

Units	0	1	2	3	4	5	6	7	8
0	0.40	0.28	0.16	0	0	0	0	0	0
1	0.28	0.12	0.12	0.16	0	0	0	0	0
2	0.16	0.28	0.12	0.12	0.16	0	0	0	0
3	0.00	0.16	0.28	0.12	0.12	0.16	0	0	0
4	0.08	0.00	0.16	0.28	0.12	0.12	0.16	0	0
5	0.04	0.08	0.00	0.16	0.28	0.12	0.12	0.16	0
6	0.04	0.04	0.08	0.00	0.16	0.28	0.12	0.12	0.16
7	0	0.04	0.04	0.08	0.00	0.16	0.28	0.12	0.12
8	0	0	0.04	0.08	0.16	0.16	0.32	0.60	0.72

Table 6. Final Result for the Matrix after the Iterations

Result
0.011
0.011
0.018
0.027
0.049
0.067
0.148
0.136
0.533

CONCLUSION

In this study, the reservoir storage capacity of single reservoir named Gökçeler Dam, which is situated in East Mediterranean Basin in Turkey, was determined by using Mass Curve, Minimum Flow, Residual Mass Curve, Hardison's Generalized and Moran Probability Matrix methods. In this respect, monthly and annual mean data for the period of 1991-2015 which belong to DSI-17039 Gökçeler River Gazipaşa Flow Gauging Station were utilized. According to the official documents, draft ratio and total volume of the reservoir were stated as 63% and 56.8 $x10^6$ m^3, respectively. In this regard, as the draft ratio and probability of failure were selected as 63% and 0% respectively so as to determine the reservoir capacity by Mass Curve, Minimum Flow, Residual Mass Curve approaches. On the other hand, for the probability of failure 10% and 5% and draft ratio 60% and 80%, reservoir capacity was calculated by using Hardison's Generalized method.

Finally, the failure ratio was specified for an assumed reservoir capacity according to Moran Probability Matrix method. As a result, the reservoir storage capacity was calculated between $52.48x10^6$ m^3 and $52.945x10^6$ m^3 by Mass Curve, Minimum Flow, Residual Mass Curve methods. While the reservoir capacity ranged between $19.56x10^6$ m^3 and $83.21x10^6$ m^3 according to Hardison's Generalized Method. Finally, the probability of failure was specified as %1.1 for the assumed reservoir storage capacity $200x10^6$ m^3 by Moran Probability Matrix method.

REFERENCES

Aksoy, H., 2001. "Storage capacity for river reservoir by wavelet-based generation of sequent peak algorithm". Water Resource Management, 15,423-437.

Bacanlı, Ü.G., Koç, A.C., 2006. "Moran Olasılık Matris Yöntemiyle Hazne Tasarımı: Yenidere Barajı Örneği". Süleyman Demirel Üniversitesi, Fen Bilimleri Enstitüsü Dergisi, 10-2,255-261

Bayazit, M., Önöz, B., 2000. "Conditional distributions of ideal reservoir storage variables". Journal of Hydrologic Engineering, 5(1), 52-58.

Bayazit, M.,1982. "Ideal reservoir capacity as afunction of yield and risk" .Journal of Hydrology, 58,1- 9.

Hardison, C.H. 1965. "Storage to augment low flows" Reservoir Yield Symposium.

McMahon, T. A, Mein, R. G. 1978." Reservoir capacity and yield", Amsterdam: Elsevier Scientific Publishing Company .

McMahon, T.A., Mein, R.G. 1986. "River and reservoir yield", Littleton Colorado: Water Resources Publications.

Moran, P, A. 1954. "Probability theory of dams and storage system". Australian Journal of Applied Science, 5, 116-126.

Rao,Z., Moore, I.N.,O'Connell, P.E. Jamieeson, D.G., 2001. "An interactive management system for operational control of Kirazdere Reservoir(Turkey)". Water Resource Management, 15, 223-234

Ripple, W., 1883. "Capacity of storage reservoirs for water supply". Institution of Civil Engineers. 71,270-278.

So many large dams were constructed
for irrigation of lands
and also production of electricity.
DSA desires to be a non-profit organization
for providing
"dam safety concept" in Turkey.

ATA

We are thankful to executive committee
of ATA Companies Group
for their contribution